AD-A070 386 AIR FORCE MATERIALS LAB WRIGHT-PATTERSON AFB OH F/G 22/2
PROCEEDINGS OF THE USAF/NASA INTERNATIONAL SPACECRAFT CONTAMINA--ETC(U)
1978 J M JEMIOLA
UNCLASSIFIED AFML-TR-78-190 NL

1 OF 13
AD
A070386

(14) AFML-TR-78-190,
NASA-CP-2039

LEVEL II

2

AD A070386

(6)

PROCEEDINGS OF THE USAF / NASA INTERNATIONAL SPACECRAFT CONTAMINATION CONFERENCE

CAPTAIN J. M. JEMIOLA
EDITOR

(10) James M./Jemiola

(11) 1978

(12) 1220p.

SCIENTIFIC INTERIM REPORT, FOR PERIOD 7 to 9 MARCH 1978

(9)

(16) 7340

(17) 07

D D C
JUN 26 1979
C

Approved for public release; distribution unlimited.

This report is the result of a joint U.S. Air Force and NASA sponsored conference held 7-9 March 1978 at the United States Air Force Academy, Colorado.

DDC FILE COPY

AIR FORCE MATERIALS LABORATORY
AIR FORCE WRIGHT AERONAUTICAL LABORATORIES
AIR FORCE SYSTEMS COMMAND
WRIGHT-PATTERSON AIR FORCE BASE, OHIO

NATIONAL AERONAUTICS AND SPACE ADMINISTRATION
MARSHALL SPACE FLIGHT CENTER
HUNTSVILLE, ALABAMA

NASA
National Aeronautics and
Space Administration

012 320

79 06 25 069 LB

NOTICE

This report has been reviewed by the Information Office (IO) and is releasable to the National Technical Information Service (NTIS). At NTIS, it will be available to the general public, including foreign nations.

This technical report has been reviewed and is approved for publication.

James M Jemiola
JAMES M. JEMIOLA
Project Engineer

FOR THE COMMANDER

J. M. KELBLE, Chief
Nonmetallic Materials Division

If your address has changed, if you wish to be removed from our mailing list, or if the addressee is no longer employed by your organization please notify AFML/MBE, W-PAFB, OH 45433 to help us maintain a current mailing list.

Copies of this report should not be returned unless return is required by security considerations, contractual obligations, or notice on a specific document.

AIR FORCE/56780/29 May 1979 — 300

REPORT DOCUMENTATION PAGE	**READ INSTRUCTIONS BEFORE COMPLETING FORM**
1. REPORT NUMBER AFML-TR-78-190 — 2. GOVT ACCESSION NO.	3. RECIPIENT'S CATALOG NUMBER
4. TITLE (*and Subtitle*) PROCEEDINGS OF THE USAF/NASA INTERNATIONAL SPACECRAFT CONTAMINATION CONFERENCE	5. TYPE OF REPORT & PERIOD COVERED Scientific Interim 7-9 March 1978 6. PERFORMING ORG. REPORT NUMBER
7. Editor Capt J. M. Jemiola	8. CONTRACT OR GRANT NUMBER(s)
9. PERFORMING ORGANIZATION NAME AND ADDRESS Air Force Materials Laboratory Wright-Patterson AFB, Ohio 45433	10. PROGRAM ELEMENT, PROJECT, TASK AREA & WORK UNIT NUMBERS 62102F, Project 7340 Work Unit 73400774
11. CONTROLLING OFFICE NAME AND ADDRESS NASA Marshal Space Flight Center Huntsville, Alabama 35812	12. REPORT DATE 13. NUMBER OF PAGES
14. MONITORING AGENCY NAME & ADDRESS(*if different from Controlling Office*) Air Force Materials Laboratory Wright-Patterson AFB, Ohio 45433	15. SECURITY CLASS. (*of this report*) Unclassified 15a. DECLASSIFICATION/DOWNGRADING SCHEDULE

16. DISTRIBUTION STATEMENT (*of this Report*)

Approved for public release; distribution unlimited.

17. DISTRIBUTION STATEMENT (*of the abstract entered in Block 20, if different from Report*)

18. SUPPLEMENTARY NOTES

This report is the result of a joint USAF and NASA sponsored conference held 7-9 March 1978 at the United States Air Force Academy, Colorado.

19. KEY WORDS (*Continue on reverse side if necessary and identify by block number*)

spacecraft contamination
satellite contamination
contamination modeling

20. ABSTRACT (*Continue on reverse side if necessary and identify by block number*)

An International Spacecraft Contamination Conference, sponsored by the USAF and NASA, was held from 7-9 March 1978. The proceedings contain over fifty papers dealing with subjects including: 1) spacecraft modeling, 2) determination of basic material properties, 3) thruster plume characteristics and modeling, 4) contamination prevention and control, and 5) contamination kinetics and effects. An executive summary and the transcripts of both a panel discussion and a question and answer session are also included.

DD FORM 1 JAN 73 1473 EDITION OF 1 NOV 65 IS OBSOLETE

79 06 25 069

PREFACE

The USAF/NASA International Spacecraft Contamination Conference was held at the USAF Academy from 7-9 March 1978. The conference provided USAF, NASA, industry, and university groups working in the spacecraft contamination technology area the opportunity to present their results and to formulate new development plans. Spacecraft contamination technology encompasses a broad based technology effort composed of expertise running from basic materials characterization to spacecraft design engineering. The conference provided a medium for a comprehensive presentation of results from programs in these diverse disciplines. The technology base formed at the conference and contained in this document has immediate and direct application to design and test requirements for on-going and planned USAF, NASA, and industry space systems.

We would like to thank Brig. Gen. Forrest S. McCartney, Deputy for Space Systems Communications, Space and Missile Systems Organization, for presenting a keynote address which provided thorough and positive guidance as to the contamination concerns of the satellite user community. We would like to thank Col. John E. Brooke, Assistant Director of Science and Technology, USAF Systems Command, and Dr. Robert E. Smylie, Acting Associate Administrator for Aeronautics and Space Technology, National Aeronautics and Space Administration, for their approval and endorsement of the conference. We would also like to thank Lt. Gen. James R. Allen, Superintendent, USAF Academy, for supporting the conference, including arrangements for accommodations, transportation, meals, and facilities, and Brig. Gen. William T. Woodyard, Dean of Faculty, USAF Academy, for his welcoming address. In particular, thanks are extended to Captains Mark Torreano and William Denton, Directorate of Conferences, USAF Academy, for their outstanding support at the conference. Members of the Conference Program Committee are K. Baerwald, E. N. Borson, L. Leger, C. R. Maag, J. A. Muscari, S. Price, H. E. Scott, D. Stewart, F. C. Witteborn, and J. W. Youngblood.

J. M. Jemiola
E. R. Miller
Co-Chairmen, USAF/NASA International
Spacecraft Contamination Conference

TABLE OF CONTENTS

TABLE OF CONTENTS (Continued)

TABLE OF CONTENTS

TABLE OF CONTENTS (Continued)

PAGE

SESSION VI (Continued)

PROCEEDINGS OF THE USAF/NASA
INTERNATIONAL SPACECRAFT CONTAMINATION CONFERENCE

Executive Summary

SESSION I	Ray O. Rantanen Martin Marietta Aerospace Denver, CO 80201 Eugene A. Zeiner Aerojet ElectroSystems Azusa, CA 91702
SESSION II	Carl Maag Aerojet ElectroSystems Azusa, CA 91702 Ernest B. Ress Martin Marietta Aerospace Denver, CO 80201
SESSION III	Ken Baerwald and Donald L. Young NASA Jet Propulsion Laboratory Pasadena, CA 91103
SESSION IV	Lubert J. Leger NASA Johnson Space Center Houston, TX 77058 Don Wallace IBC Berkeley Irvine, CA 92715
SESSION V	Robert G. Moss Ford Aerospace Palo Alto, CA 94303 Thomas A. Hughes McDonnell Douglas Astronautics St. Louis, MO 63166
SESSION VI	Jack Gilligan IITRI Chicago, IL 60616 Jack Triolo NASA Goddard Space Flight Center Greenbelt, MD 20771

SESSION VII Eugene N. Borson
Aerospace Corporation
Los Angeles, CA 90009

Edgar R. Miller
NASA Marshall Space Flight Center
Huntsville, AL 35812

SESSION I - CONTAMINATION MODELING/MATERIALS AND COMPONENTS

T. A. Hughes, McDonnell Douglas Astronautics, St. Louis, Missouri, discussed the behavior of mass loss of materials in vacuum by chemical reaction kinetics equations. The application of these equations to various systems and the effects of temperature and time were discussed in detail. It was noted the required parameters for the mass loss equations can be obtained through thermogravimetric analysis techniques.

E. A. Zeiner, Aerojet ElectroSystems, Azusa, California, presented the basic structure of a model to predict contaminant deposition on spacecraft surfaces. A brief summary of the source, transport and effects equations were presented in complex form. The model was stated as being able to address diffusion limited and surface desorption limited mass loss processes. Since a copy of this paper was not available, a thorough review was not possible.

A. P. M. Glassford, Lockheed Research Laboratory, presented outgassing rates of multilayer insulation components (MLI). The components tested were aluminized mylar, goldized mylar, dacron net, silk net, nylon net, and Tissuglas. Data were presented for mass loss rates at various temperatures for each component with water as the identified predominant outgassing species. Questioning after the presentation revealed that associated testing at Lockheed indicates that successive layers are purely an additive effect in determining outgassing rates.

N. J. Pugel, Denver University, Colorado, reported on thermogravimetric analysis work she performed at Martin Marietta Corporation, Denver Division. The problems and techniques of dynamic and isothermal thermogravimetric analysis were presented. Data for DC 92-007 white thermal control paint, silver-teflon, RTV 566, and astroquartz fabric were presented. A comparison between mass loss rates for predictions from dynamic TGA parameters and isothermal tests was made for RTV 566 and DC 92-007. It was pointed out that an in-depth test program is currently underway at Martin Marietta to totally understand the ramifications of dynamic TGA testing since it can be used in a timely fashion for materials evaluation at laser induced temperatures, as well as ambient spacecraft temperatures. The effect of sample size, configuration, and temperature sweep rate on the low temperature, low available mass components will be studied in detail during this effort.

A. Zwaal, European Space and Technology Center, presented the application of two vacuum systems at ESTEC in determining outgassing rates of materials in vacuum. Outgassing data for eight nonmetallic coatings and multilayer insulation blankets used on Spacelab were presented. Water regain measurements were discussed for the materials, as well as condensation coefficients for the MLI blankets at several collector and source temperature combinations. Quartz crystal microbalances were used as the primary sensor in the tests.

SESSION II - CONTAMINATION MODELING/SPACECRAFT

This session presented a series of papers which dealt with the definition of the induced environment and the effects from the induced environment upon a spacecraft. Inherent in defining the induced spacecraft contaminant environment is the development of the methodology and physics of the processes taking place. Over the past eight to ten years, a number of approaches have been developed to analytically model a spacecraft environment. These analytical models have evolved and are continuing to evolve into sophisticated computer programs which can predict the induced environment of a spacecraft from launch through the free flight phase. These programs take into account the geometry of the spacecraft, as well as the contaminant source, transport, and effects characteristics as a function of time and temperature. The papers in this session could be broken up into two basic categories. The first series of papers dealt with the modeling of the induced environment and its effect relationship on specific spacecraft and instruments. The remaining papers dealt with the modeling of key contaminant transport mechanisms and the flight verification of one of the transport mechanisms.

The initial two papers presented in this session evaluated the induced environment of the Spacelab payloads and a cryogenically cooled infrared telescope facility. This work had been sponsored by NASA over the past four years and led to the development of a generalized systems level contamination computer model called the Shuttle/Payload Contamination Evaluation (SPACE) program. The primary conclusions developed indicated that a totally contaminant free environment acceptable to all payloads could not be provided uniquely through design. However, through optimizing the design of instruments and identifying appropriate constraints and operational planning, based upon individual payload mixes and mission objectives, the Shuttle Orbiter environment would be suitable for sensitive instruments. The next two papers dealt with the development of computer modeling programs which could treat the flight phase and the launch-to-flight phase. These programs were developed under Air Force sponsorship and represented analytical modeling approaches to solving current military contamination problems.

The next two papers dealt with key elements of the transport mechanisms of the contaminant. A direct simulation Monte Carlo program was presented which was capable of analyzing the non-equilibrium, three-dimensional external environment in the vicinity of the Shuttle Orbiter. The flowfield variables computed in the Monte Carlo analysis included the density, velocity, and temperature distribution throughout the flowfield; the back scattered flux density; the flux density incident on each element of the Shuttle Orbiter surface; and the molecular column density as viewed from the payload bay in a specific direction. Two important considerations were noted concerning the mechanism of back scattered flux density. First, in many instances it was the only mechanism for contaminating critical surfaces of a spacecraft and second, for most modeling approaches, such as the SPACE program, the back scatter flux densities were calculated from a single collision model as opposed to the more expensive Monte Carlo approach presented in this paper. Another key aspect of the transport of contaminants presented in this session was the relationship of charged particles and their attraction to surfaces of a spacecraft by the electrostatic forces between the particle and the charged spacecraft surfaces. The source of particles could be the natural environment; charged particles emitted from the spacecraft or outgassing particles ionized by electric fields around the satellite. This phenomena plays an important role in the transport of spacecraft contaminants of satellites at very high earth orbits where the return flux or back scattered flux is not the predominant phenomena. The final paper presented the results of an experiment performed on the Atmospheric Explorer-D satellite to measure the back scattered flux from venting neon gas into the velocity vector of the satellite at low earth orbit and measuring the returned neon by a mass spectrometer. The measured back scattered flux compared favorably to calculations based upon single collision theory.

Considerable growth has been seen in the recent years in the development of analytical tools and spacecraft modeling of the induced environment. Although there are still areas associated with specific contaminant source and transport characteristics that need to be resolved, the key areas where additional work is required are in the modeling of surface deposition and effects upon critical surfaces and the acquiring of laboratory and flight data to validate and substantiate the models. This includes the model input data used and the methodology and physics represented by the models.

SESSION III - ROCKET EXHAUST PLUMES

Unlike sources of spacecraft contamination which outgas passively, a rocket engine can only perform its function by expelling relatively large quantities of gases at extremely high velocities. These gases are often accompanied by unburned liquid droplets or solid particles which may still be burning after exiting the nozzle. The impaction of these condensible gases, liquid droplets, or solid particles on scientific instruments or thermal control surfaces is of serious concern to the spacecraft designer.

Locating instruments and sensitive surfaces away from the direction in which small attitude control or large orbit-insertion engines point is not the simple solution it may at first appear. Viscous effects within the rocket nozzle result in a large radial Mach number variation at the nozzle exit. The result of this variation is that the boundary layer flow near the nozzle wall expands to large angles with respect to the nozzle centerline. While the percent mass contained in the boundary layer may be small, the absolute quantity may be significant and the expansion of these gases around the nozzle lip and over the spacecraft may be a source of contamination which greatly exceeds all others on the spacecraft.

Unfortunately, the physics of the boundary layer expansion are not well understood; prediction of the backflow mass and momentum flux distribution is thus a region of great uncertainty.

Coupled with the problem of describing the complete exhaust plume flowfield are concerns related to the identification of potential contaminants. Rocket engines for spacecraft application may include solid propellants, liquid bipropellants, liquid monopropellants, ion drive, pulsed plasma, or other mass expulsion devices. Not only do each of these engines utilize entirely different propellants and chemistries, but the constituents produced by any given engine type may differ greatly with design and operation.

The rocket exhaust plume session of this conference included papers which addressed a wide range of contamination concerns, including analytical predictions, spacecraft flight data, ground testing, and space experiments. Large solid rocket motors, liquid bipropellant engines, and monopropellant thrusters were discussed.

The first three papers pertained to the contamination environment produced by large solid rocket motors. Maag opened the session with a survey of available test data and flight experience. Barsh et al concerned themselves with payload contamination from the plume of the Interim Upper Stage (IUS) motor. Their postulated mechanisms for backflow from the engine over the payload included charging effects, collisional scattering effects, and boundary layer turbulence. A contaminant deposition on the order of 10^{-6} gm/cm^2 was predicted for the IUS payload. The method of approach outlined by Leising and Greenfield in the third paper was entirely different from that of Barsh et al. The validity of the Leising and Greenfield methodology for calculating high angle boundary layer expansion effects was checked against an experiment flown aboard an Air Force Block 5D spacecraft. The same procedure was then used to predict, with good results, the contamination and heat flux originating from the orbit-insertion solid rocket motor and impacting the science platform of the Voyager spacecraft.

The contaminants produced by the Space Shuttle liquid bipropellant attitude control and vernier thrusters was discussed by Stechman. The thruster design characteristics and operation were related to the quantity of unreacted propellants expelled. Weaknesses in the presently available tools for predicting contaminant generation were said to be in the areas of combustion modeling and accountability for film cooling and mixture ratio stratification.

The next two papers were extremely interesting to anyone actively involved in the calculation of liquid bipropellant or monopropellant exhaust plume effects. Scott and Frazine characterized the backflow plume contamination potential of a 22N thrust bipropellant engine over a range of operating conditions and configurations. Mass flux measurements were reported over angles of up to 150° from the nozzle centerline. An exponential decay of mass flux with increasing angle was revealed. Infrared transmission and laser interference measurements yielded additional information on contaminant deposits. McCay et al reported plume contamination measurements from an aged monopropellant thruster over a wide range of operating conditions. As with the work by Scott and Frazine, a variety of diagnostic tools were brought to bear during the examination, including quartz crystal microbalance, a mass spectrometer, a laser Raman and Raleigh scattering system, and an electron beam. Data were taken not only for individual pulses in a train but also during pulse transients, revealing quantities of undecomposed hydrazine in the plume. A radical change in the quantity of raw hydrazine occurred during the testing, even though engine performance was apparently not seriously degraded.

In the final paper of the session, Molinari presented a concept for a test facility which would allow testing of propulsion systems in the space environment and a characterization of the resultant exhaust plumes. To be designed primarily for large thrust engines, the Plume Contamination Effects Module is to be flown into earth orbit aboard the Space Shuttle, the test firing conducted in the Shuttle bay, and the entire facility then returned to earth with its data package.

In general, the ideas and information presented during the session were outstanding for a first conference of this nature. It is hoped that future conferences will be equally valuable and that increased participation by other nations will render them international in more than name.

SESSION IV - CONTAMINATION MONITORING

Session IV, Contamination Monitoring, can be divided into two parts, one part covering details of the Shuttle Induced Environmental Contamination Monitor (IECM) and the second part covering methods and techniques for general ground contamination monitoring.

In the first paper Ed Miller presented a general overview of the IECM, including some details of each of the individual instruments in the IECM. Rudy Ruff's presentation on the IECM mass spectrometer gave a detailed description of the hardware plus an analysis of and the rationale for use of this instrument to determine on-orbit mass column densities. The IECM series concluded with a paper presented by Dan McKeown covering the quartz crystal microbalance systems to be used on the IECM. Details of both the Temperature-Controlled Quartz Crystal Microbalance (TQCM) and the Cryogenic Quartz Crystal Microbalance (CQCM) were presented.

Don Wallace (this session's co-chairman) presented a paper in which he addressed some considerations necessary to use quartz crystal microbalances for quantitative measurements. Ray Kruger then described an approach to evaluating the cleanliness of a thermal vacuum chamber using a cold finger to collect any contaminant followed by analysis with a residual gas analyzer.

Herbert Nuss described using a molecular beam scattering technique to determine the amount of surface contamination present on an optical surface. Herman Scott described the infrared transmittance spectra and index of refraction of cryodeposits which formed during the firing of a monomethyl hydrazine, nitrogen tetraoxide engine. This paper was originally planned to be presented in Session VI but was exchanged with another paper. Paper number eight, in which two methods of measuring surface contamination, one using internal reflection spectroscopy and the other using front surface quarter wave coated dielectric mirrors, was presented by Carl Maag. In the final paper of the session, Ernest Crutcher presented a method for identifying the contamination source or the history of contamination exposure by detailed examination of contaminants using light microscopy and related techniques.

SESSION V - CONTAMINATION PREVENTION AND CONTROL

A. Hiltz, G. E., described a method for vacuum stripping RTV silicones which are used as space shuttle tiles and high outgassers to obtain low outgassing materials and low overall cost. RTV is mixed, cured, and post-cured as usual, then vacuum stripped at 350°F and 10^{-6} torr for 48 hours. This reduced TML and VCM to well within acceptable levels. Thermal conductivity was reduced about 25 percent, specific heat was unchanged, tensile strength and modulus were slightly higher, failure strain was slightly lower, thermal expansion coefficient was unchanged, bond strength was essentially unchanged, and flatwise tensile was slightly lower. Vacuum stripping effectively reduced outgassing of RTV foams and did not degrade physical or mechanical properties.

R. Dawbarn, ARO, presented data showing that up to 50 percent of the particulate from rocket motors are submicron size Al_2O_3. Particle size is bimodal, with a peak at 0.1μ. Particle size does not increase with motor size; it may actually decrease. Particle size distribution may be very different for firings in space compared to tests on earth. The fine oxide particles are major potential spacecraft contaminants.

R. Richmond, NASA/JSFC, discussed the effectiveness of teflon-coated beta cloth in preventing contamination of payloads in the Shuttle Orbiter payload bay. A test setup using Bray oil to represent hydraulic fluid and a thermoelectrically-cooled QCM was described, as was the testing procedure. Absorption and desorption rates as a function of temperature were plotted. Desorption is nonlinear with temperature, increasing exponentially with temperature. The condensation coefficient of the Bray oil was 1 at -25°C or lower. The teflon-coated beta cloth reduced molecular flux of the oil by almost an order of magnitude.

W. Loeb, Gnostic Concepts, described the properties and applications of Parylene C for protective coating of surfaces and tie-down of particulate contaminants. A coating thickness of .15 mils was enough to tie down light particles inside hybrid circuits. A coating .4 mils thick was partially successful in tying down lead shot. Complete coverage .1 mil thick could be achieved with a 31 mil diameter hole in the hybrid package lid. Electrical and physical properties of Parylene C and compatibility with various circuit elements were discussed. Slight increases in conductor capacitance, wire bond strength, emissivity, and microwave line loss could occur. Low resistivity unglazed resistors had unacceptably high resistance increases. No other adverse effects were reported.

C. Cunniff, AF Geophysics Lab, discussed the cleaning and handling procedures used to assure cleanliness of a cryogenically cooled IR telescope which was launched on a Hi-Star rocket and recovered after the flight. Surface cleaning and cleanliness control were described in detail. Visually clean was accepted as an adequate standard for surface contamination control. Ten successful launches resulted in a map of 90 percent of the sky at 11 and 22 micron wavelengths which identified some 3200 celestial objects.

A. Hoffman, JPL, described methods for controlling particulate contamination on the Viking and Voyager spacecraft. Very clean facilities and restraints on personnel, such as special clothing and limited access, were required. Monitoring was done by light scattering monitors, visual, wipe samples, and air monitors such as isokinetic probes and disc samples. Particle counters and disc samples provided reasonable indications of contamination problems. Air conditioning and HEPA filters were used at the launch facility to protect the spacecraft from particulate contamination. A HEPA filter failed on Viking causing contamination. The number and likely source of Voyager disc sample particles were given. A Voyager shroud tore, possibly from high speed N_2 purge gas impinging on the shroud. A number of particle occurrences over the first 120 days were plotted. Particle appearance usually followed an event such as pyrotechnic device firing and decreased in frequency with time.

M. Barsh, Aerojet, described the procedure for cleaning more than 10,000 second surface fused silica mirrors. Visually clean was not accepted as an adequate criterion. Scrubbing with milk of magnesia and detergent scrubbing, plasma discharge cleaning, applying and peeling collodion, and repeated solvent wiping were evaluated. Auger analysis was used to determine surface cleanliness. A mixture of trichloroethane and ethanol proved most effective in removing surface deposits. Two cleanings after the surfaces were "visually clean" reduced deposit thickness from several hundred angstroms to less than 10 angstroms. Additional cleanings were ineffective. Cleanliness was verified by limiting the net extract from cloths used to wipe 200 mirrors to a weight of .0002 grams or less.

E. Yadlovsky, Colorado State University, reported the results of a study of puncture discharge from surface dielectrics on geosynchronous satellites. Surface potentials as high as 20 KV were measured on ATS-5 and ATS-6. The experimental setup and test results for silverized teflon samples were described. Puncture craters and breakdown occur at 10 KV for 1 mil teflon and 24 KV for 3 mil teflon. Teflon and silver from the backing are ejected and transported to nearby surfaces, as are particles and electrons. Approximately 10^{13} fast electrons are emitted during discharge, flowing primarily at 90° to the surface. Positive particles with a minimum energy of 30 Kev are emitted primarily at 90° to the surface at a rate of about 7×10^{12} particles/event. The particles probably are ionized carbon. Both molten teflon and charged particles probably redeposit on spacecraft surfaces causing contamination.

SESSION VI - SPECIAL TOPICS AND EFFECTS

J. P. Pipes described the array of sensitive contamination measuring instruments used in the AEDC Mark I space chamber for assessment of the contamination level and types present. Measurements associated with testing of the Global Positioning System Satellite in the Mark I facility indicated that the results from multiple internal reflectance spectroscopy and quartz crystal microbalances could be combined to provide quantitative data on contaminant (DC 704) as thin as two molecular layers thick.

E. A. Zeiner presented results of source kinetics outgassing tests performed at AESC on RTV 566 adhesive and DC 92-007 white paint. These test data were the foundation for the mass transport model presented by the author in a previous session. The basic results indicated that the mass release of most polymeric source materials could be considered as consisting of three distinct components which were being diffusely emitted simultaneously at any given temperature. Two of the components could be associated with bulk diffusion processes while the third component appeared to be associated with activated thermal decomposition. The net mass deposition rate on a typical target surface at anytime was generally the difference between the incident mass flux and re-emission mass rate. The rate was only remotely related to the total amount of volatile material in the source itself.

C. K. Liu discussed the practical test of the effects of a contaminant on the optical and thermal properties of specific thermal control coatings and transparent solar cell cover glass. The source of contamination is material outgas products from several commonly used materials and rocket plume products. He stressed that this was a low cost test for screening purposes and only the first stage of a more detailed study using more comprehensive insitu environmental exposure and contamination effect measurement facilities.

J. A. Muscari presented the results of an ongoing program to evaluate the effects of RTV 560 silicone outgassing products on the solar absorptance of silver-teflon thermal control materials. The equipment in which the experiments were carried out also was described. Changes in solar absorptance of the silver-teflon surfaces before and after exposure to two different UV sources were shown as a function of exposure time. The results, although preliminary, seemed to indicate that contaminants from RTV 560 do not significantly affect the solar absorptance of the silver-teflon surface or undergo UV-induced changes.

Otto K. Hussman provided a background for his results by describing the M.B.B. combined environmental test facility in which the materials were tested. In order to protect the transparent layer of second surface mirrors from UV damage he proposed a surface interference film which would either absorb the UV or reflect the UV before entering the suprasil layer. He showed results that indicated that ZnS and Al_2O_3 do improve the stability of the second surface mirrors. In addition, he proposed to use a transparent electrically conductive film as a top layer to reduce the damage to the dielectric layer from charge buildup discharge.

SESSION VII - PANEL DISCUSSION

This session was not summarized.

SESSION I

CONTAMINATION MODELING/MATERIALS AND COMPONENTS

OUTGASSING OF MATERIALS IN THE SPACE ENVIRONMENT

A THERMOKINETIC APPROACH

T. A. Hughes

McDonnell Douglas Astronautics Company - St. Louis

St. Louis, Missouri 63166

ABSTRACT

Previous efforts to model the outgassing of polymers on spacecraft have been partly empirical and partly educated guesses. None of these approaches have been successful in effectively describing the process in terms of time and temperature in such a manner that outgassing could be predicted in advance so that valid assessments could be made of its effects on various optical systems.

This report provides a fresh approach to this problem by relating the outgassing to basic chemical reaction kinetics, which provides a powerful tool for such estimations and also provides an insight to the basic mechanisms involved. The general equations of the total outgassing quantity are derived, as well as the outgassing rates, as functions of time and temperature. The results are shown to be consistent with experimental data obtained in earlier programs. While there is much evidence that suggests outgassing is primarily a first-order reaction, the equations are presented here for both first-order and other-than-first-order reactions.

The power to the reaction-kinetics approach lies in its applicability whether the outgassing mechanism is due to desorption, diffusion, thermal decomposition or evaporation. It also illuminates those situations where only minor constituents of the parent material outgas, or where the entire substance may outgas.

To implement the use of this approach certain thermokinetic parameters must be measured for each material of interest. It is suggested that the necessary data can be obtained through sensitive thermogravimetric analysis (TGA) techniques.

This work was performed under a Continuing Independent Research and Development Program on Spacecraft Contamination, funded by the McDonnell-Douglas Astronautics Company - St. Louis.

1.0 INTRODUCTION

The outgassing of polymers in space can occur due to several mechanisms:

- Chain scission
- Desorption
- Improper catalyst/resin ratio or inadequate mixing or curing
- Evaporation

Chain scission occurs when a fragment of a molecular chain breaks off due to heat or radiation. While this process is normally associated with elevated temperatures, it will also occur at lower temperatures though at greatly reduced rates. Desorption occurs when absorbed gases or solvents become volatile in the vacuum of space. Frequently these may be noncondensable gases which are more correctly termed offgassing species. The occurrence of improper catalyst/resin ratio, which may be also due to nonuniform distribution of these components, leaves a residue of low molecular weight monomer or prepolymer and/or catalyst which because of its low molecular weight, is much more easily volatilized in the vacuum of space than the parent polymer. Also such materials can be expected to diffuse through the bulk material to the surface.

The processes of chain scission and of evaporation imply that the entire mass of the substance is ultimately available for outgassing. Where desorption or diffusion and vaporization of catalyst or monomer occurs, these processes involve only a small fraction of the parent material. These latter processes also have lower activation energies and therefore outgas much more readily than a decomposition process. The active mass of material available for outgassing (as contrasted with the total mass) will be seen to be a very important quantity as it enters into many of the equations and can influence the validity of the currently accepted NASA/ASTM Micro-VCM outgassing test. Also from a very practical standpoint it is probable that thermal-vacuum degassing of a material prior to service will provide a significant benefit only in the case where the outgassing is primarily desorption or diffusion.

It must also be recognized that multiple outgassing mechanisms may occur simultaneously. In certain cases multiple fractions may diffuse to the surface, each having its own kinetics, or a high rate diffusion process plus a slow rate decomposition process may occur concurrently. This may have obscured the interpretation of experimental data in earlier work and the use of the kinetics approach can resolve many of those problems once the constants are known.

The Micro-VCM test (ASTM E595-77)[1] is currently employed for evaluating materials as possible sources of contamination on a spacecraft. This test is essentially a go/no-go test which measures the mass loss of a specimen in 24 hours under vacuum at a fixed temperature of 125°C, and the amount of the outgassed material which will condense on a surface at 25°C. However, this test will not provide any clues as to the amount of contamination that might occur with more typical spacecraft temperatures and for the extended durations spacecraft are required to be in service.

This technical note describes a method for providing such information by a thermokinetics approach. It will be shown that this approach is a very powerful tool for such estimations and, in addition, sheds light on the specific mechanisms involved.

2.0 OUTGASSING PARAMETRICS

2.1 Basic Reaction Kinetics

The outgassing of polymeric materials is accompanied by a weight loss of the source which can be described by reaction rate kinetics. The rate of weight loss, whether due to decomposition, desorption, diffusion or evaporation, is a function of the instantaneous reacting weight (w) and is:[1,2,3,4]

---

1. Superscripts in text designate references at end of paper

$$\frac{dw}{dt} = -k\,w^n \qquad (1)$$

The exponent n is the order of the reaction and k is a proportionality constant which is temperature dependent. This temperature dependence is assumed to follow the Arrhenious principle:

$$k = A\,e^{-E/RT} \qquad (2)$$

where E is the activation energy, R is the gas constant and A is a proportionality constant which is independent of temperature.

Substituting Eq (2) in Eq (1) and integrating from initial conditions (w_0, t_0) to any subsequent time (w, t) the residual weight remaining may be expressed as:

for n = 1

$$w = w_o\,e^{-kt} \qquad (3a)$$

$$w = w_o\,e^{-tA\,e^{-E/RT}} \qquad (3b)$$

for n ≠ 1

$$w = \left[w_o^{1-n} - kt(1-n)\right]^{\frac{1}{1-n}} \qquad (4a)$$

$$w = \left[w_o^{1-n} - (tA\,e^{-E/RT})(1-n)\right]^{\frac{1}{1-n}} \qquad (4b)$$

However, for outgassing purposes, it is the weight loss that we are primarily interested in, or the fraction of the original weight that is lost. The latter is obviously ($1-w/w_0$), and we can rewrite Eqs (3) and (4) to give weight loss directly as a function of time, temperature and the thermokinetic constants as:

for n = 1

$$1 - \frac{w}{w_o} = 1 - e^{-kt} \qquad (5a)$$

$$1 - \frac{w}{w_o} = 1 - e^{-tA\,e^{-E/RT}} \qquad (5b)$$

for n ≠ 1

$$1 - \frac{w}{w_o} = 1 - \left[1 - \frac{(1-n)kt}{w_o^{1-n}}\right]^{\frac{1}{1-n}} \qquad (6a)$$

$$1 - \frac{w}{w_o} = 1 - \left[1 - \frac{(1-n)tAe^{-E/RT}}{w_o^{1-n}}\right]^{\frac{1}{1-n}} \qquad (6b)$$

It is apparent from Eq (5) that the total quantity of outgassing products (as a fraction of the total material initially present) in a first-order reaction is a relatively simple exponential, and can be simply plotted or otherwise described. However, for reaction orders other than unity (Eq (6)), the fraction lost is a function of the finite amount present initially, as well as a function of time and thermochemical constants. In the case of zero-order reactions (n = 0) the rate of weight loss is invariant, and may be controlled by some other factor such as available surface area or rate of heat input. The evaporation of liquids are frequently zero-order as in the case of glycerine[5] or DC-704 silicone oil[6]. There is strong evidence that most outgassing is primarily first-order, but the possibility of nonunity orders cannot be ruled out pending more exact testing and analysis.

The value of the reaction constant A usually has a basis in the underlying reaction. In bimolecular reactions (second-order), the value of A may be interpreted as the number of molecules colliding.[7] However, in unimolecular reactions (first-order), the value of A is believed to be related to the frequency of oscillation of the atoms within the molecule, which is usually of the order of 10^{13} per sec. Deviations from this value however are not unusual. Data on the decomposition of TFE Teflon[8] for instance shows it to be a first order reaction with $A = 4.73 \times 10^{18}$ sec^{-1} and E = 80,500 cal/mole.

One of the assets of the thermokinetic approach is that the numerical value of the activation energy provides a clue to the specific mechanism involved in outgassing. The orders of magnitude of activation energies for polymers are:[9] 1-10 kcal/mole for desorption; 5-15 kcal/mole for diffusion and evaporation; and 20-80 kcal/mole for thermal decomposition. As discussed briefly in a later section, the values of the activation energy and specific reaction constant can be determined from TGA experiments.

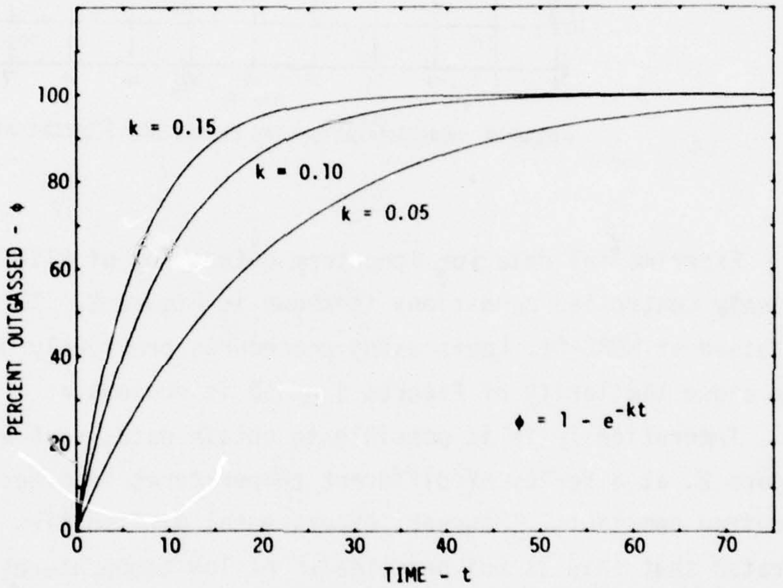

FIGURE 1 PREDICTED OUTGASSING ASSUMING A FIRST-ORDER REACTION

2.2 <u>Comparison of Theory with Experimental Results</u>

A plot of the total accretion of outgassed product with time is shown in Figure 1 for several reaction rate coefficients, assuming a first-order reaction (Eq 3a). This figure shows a high initial rate, and the rate decaying with time, with the total quantity outgassed becoming asymptotic to the total available amount of reactant.

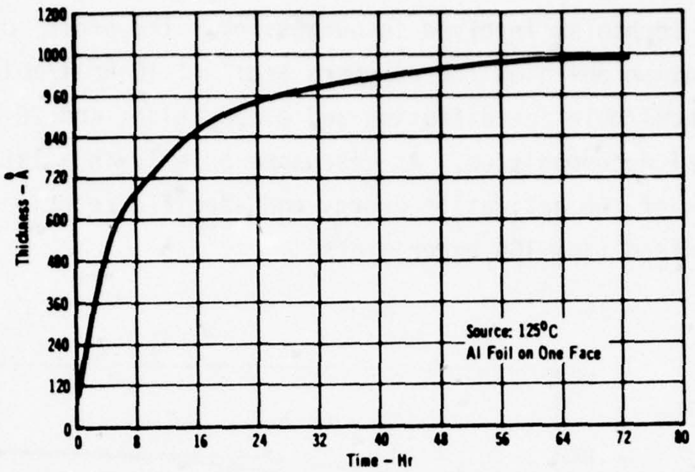

FIGURE 2 MEASURED OUTGASSING OF RTV-602 SILICONE AT 125°C

Experimental data for long term outgassing of RTV-602 under closely controlled conditions is shown in Figure 2. This data was obtained at MDAC-St. Louis using procedures previously described.[6,10] The close similarity of Figures 1 and 2 is obvious.

Theoretically it is possible to obtain data, such as shown in Figure 2, at a series of different temperatures in order to obtain the required constants. However, experimental difficulties have demonstrated that this is not practical. At low temperatures contamination rates are so low that the test becomes prohibitively long, and difficult to distinguish between chamber background and true contamination. At high temperatures, the heat-up time of the Knudsen cell allows the more volatile fractions to evaporate before the temperature stabilizes at the test temperature.

A considerable body of outgassing data exists, run under varying conditions and temperatures. Invariably the data have all the hallmarks dictated by Equation 3: rapid outgassing initially, an exponentially decaying rate, and the total quantity assuming a nearly asymptotic value. As an example, the data of[11] covered a number of different materials, measured at different temperatures by different techniques. Those data should conform (if first-order reactions) to a simplified version of Equation 3a where the fraction outgassed (ϕ) is:

$$\phi = 1 - e^{-kt} \tag{7}$$

The empirical equations contained in[11] have been rearranged to this form and are shown in Table I. The values of k are expected to vary due to the differing materials and temperatures. The essential point here is whether the data conforms to the general $1 - e^{-kt}$. This correlation appears quite good.

Table I Outgassing of Silicones

Material	Source Temperature °C	Measurement Technique	Fraction Outgassed (t = Hours)
RTV-602	140	Knudsen Cell QCM	$1.002 - e^{-0.579t}$
Modified RTV-602	180	Knudsen Cell IR Ellipsometry	$1.02 - e^{-0.917t}$
RTV-560	140	Knudsen Cell Vis. Ellipsometry	$0.99 - e^{-0.383t}$
RTV-566	50	2.5"x2.5" Flat Plate QCM	$1.01 - e^{-0.539t}$

Curran and Millard in a recent paper[16] have presented data on the contamination of a satellite in a geosynchronous orbit. Their data is shown in Figure 3, and which, except for a translated zero-point, shows the characteristics expressed by Eq 3a.

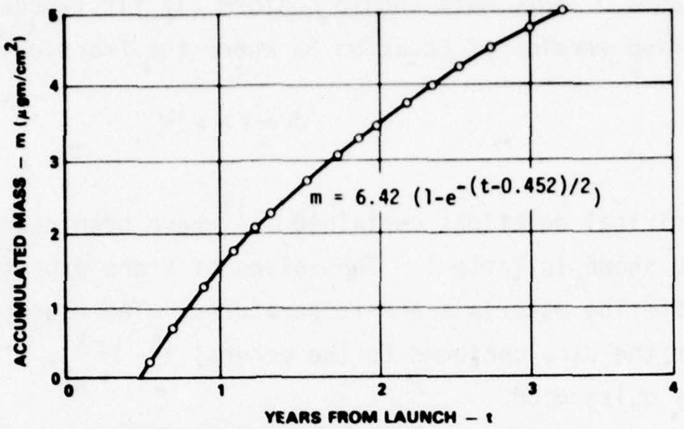

FIGURE 3 CONTAMINATION MEASURED ON A GEOSYNCHRONOUS SATELLITE AFTER CURRAN AND MILLARD (REF 16)

2.3 Estimated Outgassing as a Function of Activation Energy

The first-order reaction equation (Eq 3b) can be manipulated to:

$$\ln(\ln w_0/w) = \ln t + \ln A - E/RT \qquad (8)$$

which provides a convenient form for estimating the amount of outgassing that will occur. Figures 4 and 5 show this data for 25°C and 125°C respectively. In both cases, the specific reaction constant, A, was assumed* to be 1×10^{13} $\sec^{-1}$. The maximum total weight loss (TWL) permitted under NASA requirements (1% in 24 hrs at 398K) is also shown for reference. While the scale of the ordinate on Figures 4 and 5 is ln (ln w_0/w), the scale is marked in units of the equivalent fraction (ϕ) of outgassed material with $w_0/w = 1/(1 - \phi)$. The separate

---

*the correct unit for A is W^{1-n}/t; however for first-order reactions assumed here, this becomes reciprocal time. It might be noted also that the units of k, A and t can present a trap for the unwary. They must be consistent.

scale to the right on these two figures shown the effect of higher (10A) and lower (0.1A) multiples of the assumed A.

For comparison with the NASA limits of outgassing based on the Micro-VCM test, a linear plot of Equation 3b is shown in Figure 6.

It is apparent from these figures that if the activation energy is higher than about 36,300 cal/mole ($A = 10^{13} sec^{-1}$), that the material will pass the test even though ultimately all of the material will outgas. Also when the activation energy is substantially less than 36,000 cal/mole, in the diffusion range for instance (5-15 kcal/mole), that the outgassing will be very rapid and such a material will satisfy NASA requirements only if the total reactant is less than 1% of the

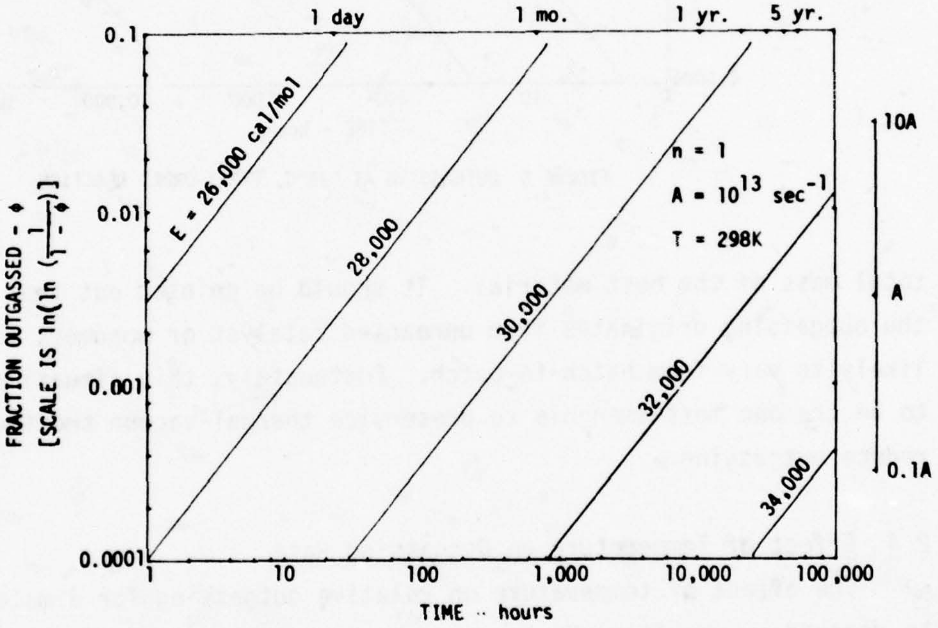

FIGURE 4 OUTGASSING AT 25°C, FIRST-ORDER REACTION

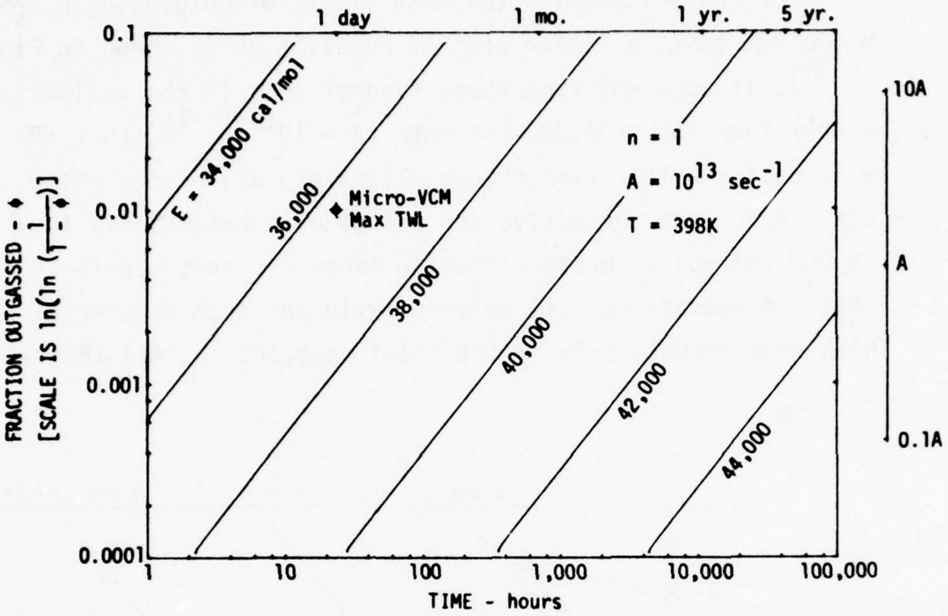

FIGURE 5 OUTGASSING AT 125°C, FIRST-ORDER REACTION

total mass of the host material. It should be pointed out that where the outgassing originates from unreacted catalyst or monomer, this is likely to vary from batch-to-batch. Fortunately, this situation appears to be the one most amenable to preservice thermal-vacuum treatment to reduce outgassing.

2.4 Effect of Temperature on Outgassing Rate

The effect of temperature on relative outgassing for a material may be derived by rewriting Eq 1:

$$\frac{dw}{dt} = -A e^{-E/RT} w^n$$

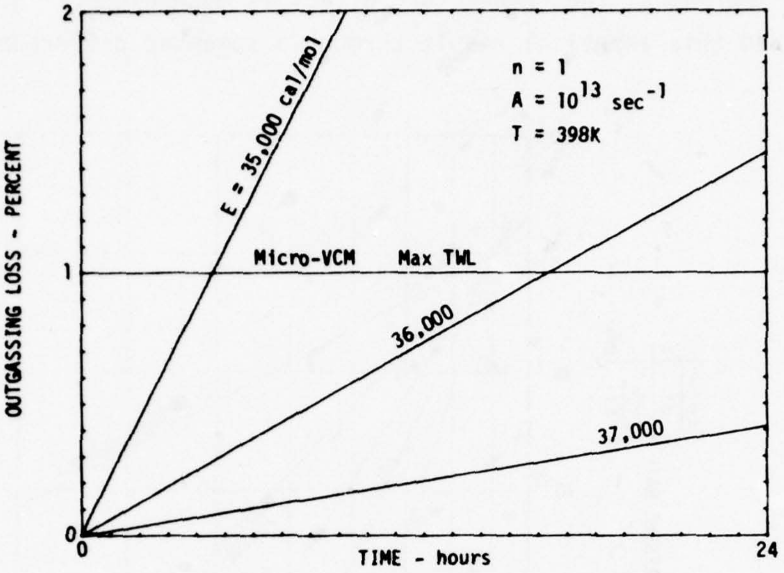

FIGURE 6 OUTGASSING AT 125°C, FIRST-ORDER REACTION

and

$$\frac{dw/w^n}{dt} = -Ae^{-E/RT}$$

were dw/w^n is the fractional weight loss. By writing this equation for two temperatures and dividing, we have

$$\frac{\left[\frac{dw/w^n}{dt}\right]_{T_2}}{\left[\frac{dw/w^n}{dt}\right]_{T_1}} = e^{\frac{E}{R}\left\{\frac{1}{T_1}-\frac{1}{T_2}\right\}} \tag{9}$$

Thus we see that the relative rate of fractional weight change with temperature will vary for different activation energies. The effect of temperature on the outgassing rates relative to 125°C for various energies of activation is shown in Figure 7. It is seen that as the energy level increases, the temperature effect is much higher. Scialdone[9] obtained this identical result through a somewhat different approach.

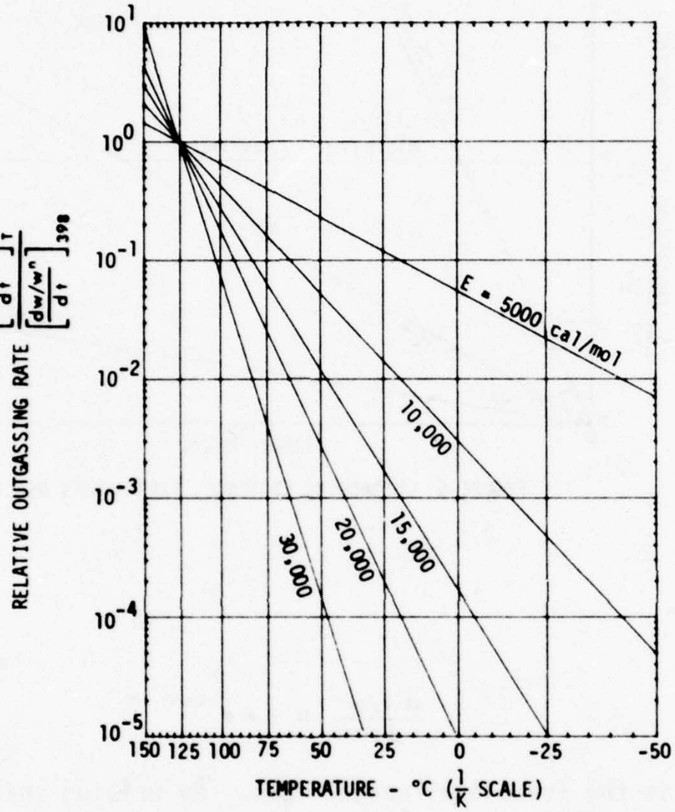

FIGURE 7 EFFECT OF TEMPERATURE ON OUTGASSING RATES REFERENCED TO 125°C

2.4 Effect of Time on Outgassing Rate

Equation (1) described the outgassing rate as a function of active mass available for outgassing. The integrated form of that equation (Eq 3 and 4) described how the active mass changed with time. By substituting Eq (3) and (4) into Eq (1) we find that the rate of change of available mass (which is the outgassing rate) is:

for n = 1

$$\frac{dw}{dt} = -kw_o e^{-kt} \tag{10a}$$

for n ≠ 1

$$\frac{dw}{dt} = -k\left[w_o^{1-n} - kt(1-n)\right]^{\frac{n}{1-n}} \tag{10b}$$

Equation (10a) shows that the outgassing rate for a first-order reaction would decay exponentially with time, the same result which has been determined empirically[6,10,11,12].

For a zero-order reaction, Eq (10b) shows that the outgassing rate is constant at all times, and which has been previously noted as occurring with simple liquids and monomers. For other than zero-order or first-order reactions, the rate will vary in a complex manner, which has been observed by several investigators[13,14,15]. It can be seen from Equation (10b) that the reaction rate for $0 \leq n < 1.0$ will decrease to zero in a finite time:

$$t = \frac{w_o^{1-n}}{(1-n)k} \tag{11}$$

However, for reaction orders of 1.0 or larger the rate can never reach zero, though for practical purposes it may become insignificant after long time periods.

Figure 8 illustrates the typical shapes of outgassing rate curves for various reaction orders, with the assumption of equal rate constants. Figure 9 makes the same rate constant assumptions and shows how the total outgassed quantity varies with time for different reaction orders. The equal rate assumption is made for purposes of illustration only. With real materials they can be expected to vary widely.

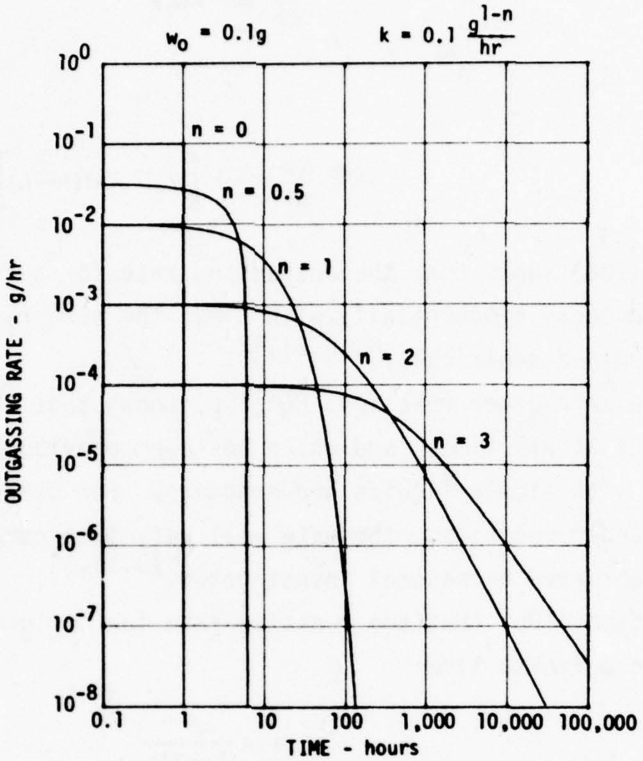

FIGURE 8 EFFECT OF REACTION ORDER ON OUTGASSING RATES

3.0 DETERMINATION OF CONSTANTS

The determination of the constants for use in the kinetics approach to outgassing is a complex subject and will be only briefly reviewed here.

The constants can be determined by outgassing measurements made at a series of constant temperatures. However, there are a number of flaws in this approach:

- Long test durations are needed to fully characterize the data (70-100 hours), even at high temperatures (125-200°C).
- Loss of material (low energy of activation material) during heat-up to test temperature.
- At low temperatures, measurement of the minute quantities are extremely difficult and subject to gross errors.

Because any test will likely be used not only for initial evaluation of material, but also for evaluating individual mixes of material used in production, it is desirable that a shorter test be available. In this respect even the Micro-VCM test requires a minimum of 3 days to run, when the pre- and post-test conditioning is included.

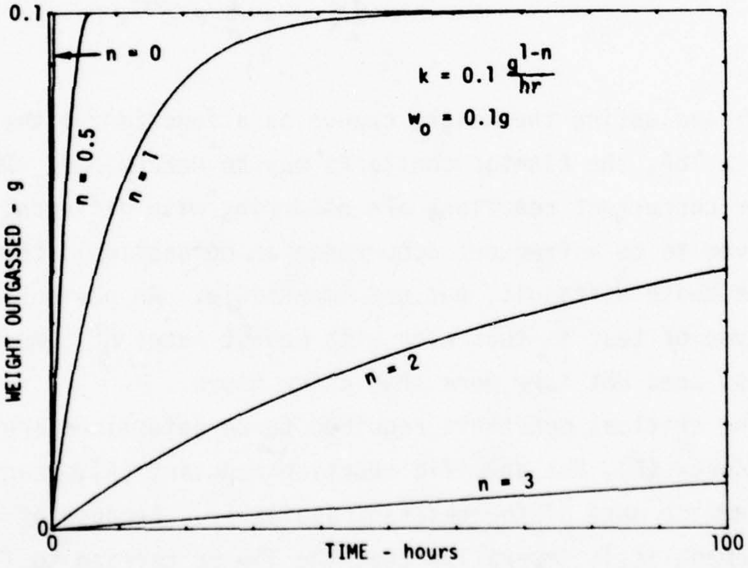

FIGURE 9 EFFECT OF REACTION ORDER ON TOTAL QUANTITY OUTGASSED WITH TIME

The approach that is likely to be most applicable is dynamic thermal gravimetric analysis. In this test, the specimen is exposed to a constant rate of temperature rise, usually beginning at room temperature. With a constant rate of temperature change:

$$\frac{dT}{dt} = \beta$$

$$dt = \frac{dT}{\beta}$$

so the basic equation:

$$dw = -Ae^{-E/RT}w^{n}dt$$

can be expressed in terms of temperature:

$$\frac{dw}{w^{n}} = -\frac{A}{\beta}e^{-E/RT}dT \qquad (12)$$

By evaluating the weight change as a function of the temperature during a TGA, the kinetic constants may be determined. When consecutive or concurrent reactions are occurring with different constants (believed to be a frequent occurrence in outgassing), the data analysis becomes quite difficult, but not impossible. An obvious advantage of this type of test is that even with modest rates of temperature rise, the test need not take more than a few hours.

The critical constants required to be determined are the activation energy (E), the specific reaction constant (A), reaction order (n), and the mass of the reactant available. Because of the last requirement it is imperative that the TGA be carried to final constant weight, and that it be conducted in the atmosphere of operational service (vacuum).

4.0 CONCLUSIONS

Previous attempts to model the outgassing of materials have not been completely successful, due to a lack of understanding of the mechanisms and materials participating. However, the application of chemical reaction rate kinetics appears to offer a valid approach to resolving this problem. To implement this approach it will be necessary to have knowledge of various constants, which presumably can be obtained through thermalgravimetric analysis. With the constants available, this method will provide the systems engineer with a comprehensive model to predict outgassing as a function of both time and temperature. If the TGA data indicates an outgassing species is a minor constituent of the bulk material, the kinetics technique is capable of identifying a preservice vacuum outgassing procedure that should effectively eliminate that source. Under circumstances in which normally inert material is illuminated by intense electromagnetic energy, this technique should be capable of a reasonable estimate of outgassing that would occur under the temporary highly elevated temperatures.

REFERENCES

1. C. David, Thermal Degradation of Polymers in Comprehensive Chemical Kinetics, Vol. 14: Degradation of Polymers, C. H. Bamford and C. F. H. Tipper (ed); pps 28-32; Elsevier Publishing Co., N.Y., 1975.

2. E. S. Freeman and B. Carrol, The Application of Thermoanalytical Technique to Reaction Kinetics. The Thermogravimetric Evaluation of the Decomposition of Calcium Oxalate Monohydrate, J. Phys. Chem., 662, 394-397, 1958.

3. J. J. Lohr, D. E. Wilson, F. M. Hamaker, and W. J. Stewart, Accelerated Testing of the Mechanical and Thermal Integrity of Polymeric Materials, AIAA/ASME 8th Structures, Structural Dynamics and Materials Conference, Palm Springs, CA, 1967.

4. H. H. Horowitz and G. Metzger, A New Analysis of Thermogravimetric Traces, Analytical Chemistry, 35, 10, 1464-1468, Sep 1963.

5. W. A. Riehl, Considerations on the Evaporation of Materials in Vacuum, 46th National Meeting, AIChE, Los Angeles, CA, Feb 1962.

6. T. A. Hughes, T. E. Bonham, T. H. Allen, Investigation of Contamination Effects on Thermal Control Materials, AFML TR 76-5, Contract F33615-73-C-5091, Mar 1976.

7. F. H. Getman, F. Daniels, Outlines of Theoretical Chemistry, 6th Ed., p. 341 (1937), John Wiley and Sons, Inc., N.Y., N.Y.

8. S. L. Madorsky and S. Straus, Note on the Thermal Decomposition of Polytetrafluorethylene as a First Order Reaction, J. Res NBS, Physics and Chemistry, 64A, 6, 513-4, Dec 1960.

9. J. J. Scialdone, Environment of a Spacecraft Produced by its Own Outgassing, International Conference on Evaluation of Space Environment on Materials, Toulouse, France, Centre National D'Etudes Spatiales, June 1974.

10. T. H. Allen, T. A. Hughes, B. C. Price, A Study of Molecular Contamination, Proceedings IES/AIAA/ASTM/NASA Eighth Space Simulation Conference, Nov 1975 (NASA SP-379).

11. T. A. Hughes and T. E. Bonham, Spacecraft Contamination: Outgassing of Silicone Polymers, Proceedings of 22nd Annual Technical Meeting, IES, Apr 1976.

12. T. A. Hughes, T. H. Allen, R. M. F. Linford, T. E. Bonham, Investigation of Contamination Effects on Thermal Control Materials, Report AFML TR 74-218, Contract F33615-73-C-5091, Jan 1975.

13. F. J. Shittko, Measurement of Gas Emission from Solid Surfaces, Vacuum 13, 525-537, Dec 63.

14. H. von Munchausen and F. J. Shittko, Investigation of the Outgassing Process of Silicone Rubber, Vacuum 13, 549-553, Dec 1963.

15. D. A. Wallace, Use of the Quartz Crystal Microbalance for Outgassing and Optical Contamination Measurements, J. Vac Sci and Tech, 9, 1, 462-6 (1972).

16. D. G. T. Curran and J. M. Millard, Results of Contamination/Degradation Measurements on Thermal Control Surfaces of a Operational Satellite, AIAA 12th Thermophysics Conf. Albuquerque, N. Mex., June 1977, AIAA Paper 77-740.

A Multinodal Model for Surface Contamination Based upon the Boltzmann Equation of Transport

by

E. A. Zeiner
Aerojet ElectroSystems Company

Abstract

A composite analytical model to compute the deposition rates of volatile condensible materials (VCM) on the surfaces of a multinodal enclosure is derived using a Fick diffusion model for the VCM mass loss rates from the source material, an exponential-Langmuir model to account for the reemission rates of deposited VCM, and a Krook relaxation model of the Boltzmann equation to characterize the scattering and transport properties of the VCM between the enclosure nodes.

1. Introduction

The first step in accounting for the influence of filmwise contamination on the sensitive surfaces of a satellite is to determine the amount of contamination deposition on each such receptor surface as time of flight progresses. The second step is to evaluate the thermo-optical effects of these surface deposits. This report describes the properties of an analytical model which has been recently developed to compute the deposition of the volatile condensible materials (VCM) which diffuse out of a nonmetallic source and are eventually deposited on a remote receptor surface.

The overall model (or algorithm) is a composite of these "sub"-models which characterize the basic processes involved in the transfer of the VCM from its host source to the receptor. The first such process is that of source kinetics. This involves the mechanisms by which the VCM moves through the bulk of the host source when the ambient pressure is sufficiently reduced and is eventually released at the source surface. Fick's First and Second Laws for unsteady-state diffusion are employed to model this process. The second process is that of the reemission of the VCM from the receptors on which the adsorbed molecules reside for a short period of time. Based upon experimental evidence[1,2] this process exhibits an exponential reemission rate for very small deposits which becomes a constant rate independent of the deposit thickness[3] where relatively large deposits exist. This latter constant large-mass reemission rate can be identified with the classical Langmuir evaporation mass rate for pure substances, which is a function of the saturation vapor pressure.

The third process is the mass transfer of the VCM molecular streams between the receptor surfaces nodes. This transport model couples the source and reemission kinetics with the relative geometry of the surface nodes which make up the bounding enclosure. The basis for such a statistical model is the Boltzmann equation for the velocity destribution function (VDF) of the VCM streams. The general intractability of this equation usually requires a simplification of the collision integrals of the Boltzmann equation, which will still permit utilization of the resulting macroscopic flux vectors (velocity moments) for VCM vapor densities varying from continuum viscous flow (Navier-Stokes equations) to collisionless free molecule flow. For this algorithm, the Krook[4] single-relaxation approximation is applied using the "two-stream Maxwellian" distribution of Lees[5]. The initial Maxwellian originates at the enclosure surfaces following source emission, receptor scatter, and receptor reemission as a boundary condition, and then "relaxes" to the uniform Maxwellian of the VCM vapor, which can be approximated as an ideal random gas in local equilibrium with the enclosure surfaces.

The final result is a set of ordinary second-order nonlinear nonhomogeneous differential equations which are coupled together by experimentally determined capture coefficients and the view factors of the nodal surfaces. The collisional properties using the Krook approximation of a symmetric collision frequency parameter restrict this model to gas interactions between similar molecules.

2. Source Kinetics

The release of the VCM from the source material is modeled as a surface-mediated diffusion process. By this is meant that the classical diffusion of VCM molecules through the bulk of the source matrix is influenced by the kinetics of these molecules when they reach the surface of the source and are released. The bulk diffusion process is characterized by a mass diffusion coefficient, while the surface process is characterized by a surface residence time or, its inverse, a rate constant. Both of these parameters are temperature-dependent and must be experimentally determined. A third parameter which must also be empirically determined is initial quantity of "active" (capable of release from the source) VCM within the source. This obviously specifies the initial uniform concentration.

The governing equation is the one-dimensional form of Fick's Second Law for unsteady state as follows:

$$\frac{\partial C_i}{\partial t} = D_i\left(\frac{\partial^2 C_i}{\partial x^2}\right) \tag{1}$$

where

$C_i(x,t)$ = mass concentration of the i^{th} active component in the source, $g\text{-}cm^{-3}$

D_i = i^{th} component mass diffusion coefficient, $cm^2 - s^{-1}$

x = transverse position in the source coating measured from the free surface, cm

The one-dimensional model is sketched at the left of Figure 1.

The initial concentration of VCM in the source is considered to be uniform so that

$$C_i(o,x) = C_{oi} = \left(\frac{\mu_i \; W_s}{A_s \; h}\right) \; g\text{-}cm^{-3} \tag{2}$$

where

C_{oi} = initial mass concentration (density) of the i^{th} active component in the source, $g\text{-}cm^{-3}$

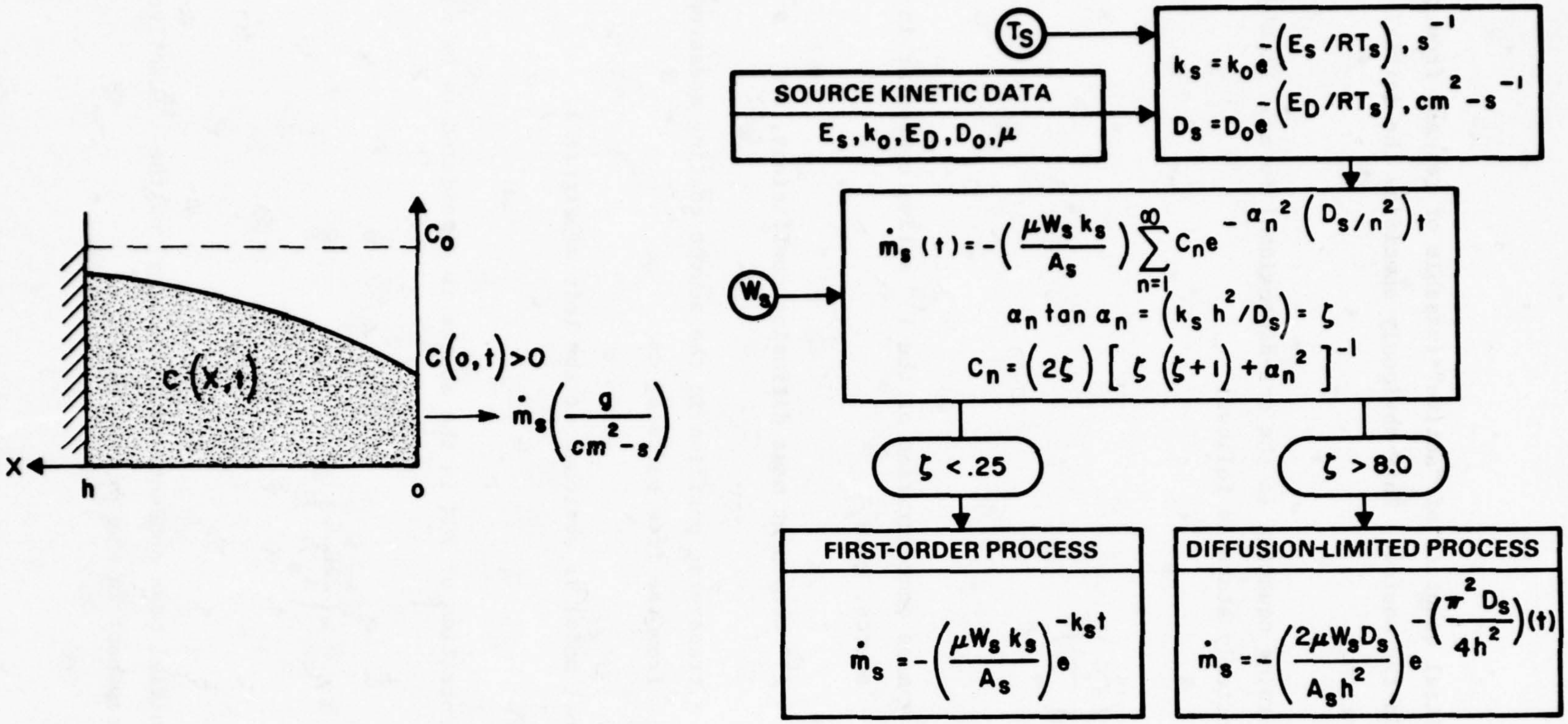

SOURCE VCM EMISSION KINETICS MODEL

FIGURE 1

μ_i = weight fraction of the i^{th} component in the source coating

W_s = total weight of the source coating prior to outgassing, g

A_s = free emission surface of source, cm^2

h = thickness of the source coating, cm.

The source mass loss rate is computed from Fick's First Law[6]

$$\dot{M}_s(t) = A_s \sum_{i=1}^{N} D_i \left[\frac{\partial}{\partial x} C_i(x,t)\right]_{x=0}, \ g\text{-}s^{-1} \tag{3}$$

where

N = number of active components in the source.

It is convenient to define two kinetic parameters for a typical source component.

$$k_{si} = \tau_{si}^{-1} \tag{4a}$$

$$\zeta_i = \left(\frac{h^2 k_{si}}{D_i}\right) \tag{4b}$$

where

τ_{si} = surface residence time for the i^{th} component on the source surface, s

k_{si} = i^{th} component surface rate constant, s^{-1} (also "jump frequency")

h = source coating thickness, cm.

ζ_i is a dimensionless kinetic parameter which specifies the relative importance of surface kinetics to diffusion kinetics for the ith component. A small value of ζ_i indicates that the component has high internal mobility;hence the outgassing is determined primarily by a first-order surface process while a large value of ζ_i indicates a component which is internally diffusion limited.

The complete solution of equation (1) for the total source mass loss rate is given by

$$\dot{M}_s(t) = -W_s \sum_{i=1}^{N} \sum_{n=1}^{\infty} \mu_i\, k_{si}\, C_{ni}\, e^{-\alpha_{ni}^2 D_i t/h^2} \quad \text{g/s} \tag{6a}$$

$$\alpha_{ni} \tan(\alpha_{ni}) - \zeta_i = 0 \tag{6b}$$

where

$$C_{ni} = \frac{2\zeta_i}{\zeta_i(\zeta_i+1) + \alpha_{ni}^2}$$

α_{ni} = real and positive rates of the transcendental equation (6b).

When $\zeta_i \leq .1$, all the terms of the infinite series in equation (6a) for $n \geq 2$ are negligible and $\alpha_{1i}^2 \cong \zeta_i$. Equation (6a) then simplifies to a first-order source process.

$$\dot{M}_s(t) = -W_s \sum_{i=1}^{N} \mu_i\, k_{si}\, e^{-k_{si} t}, \text{ g/s.} \tag{7}$$

Exponential kinetics also exists for the general model of equation (6) after sufficient time has elapsed for the exponential terms for $n \geq 2$ in the infinite series to vanish. This "relaxation" time, t^*, is physically the time required for the mass concentration to establish a cosine-like distribution in the source.

The source mass loss rate after the relaxation period is simply the asymptotic solution of equation (6a) when only the fundamental term of the series prevails. The resulting equation is

$$\dot{M}_s(t \geq t^*) = -W_s \sum_{i=1}^{N} \mu_i \, k_{si} \, C_{1i} \, e^{-\alpha_{1i}^2 D_i t/h^2}, \text{ g/s.} \qquad (8)$$

For values of $\zeta_i \geq 10$, the fundamental root, α_{1i}, assumes a constant value of $(\pi^2/4)$. This indicates a strongly diffusion-limited process, which can also be simply modeled using exponential kinetics

$$\dot{M}_s(t \geq t^*) \quad -W_s \left(\frac{8}{\pi^2}\right) \sum_{i=1}^{N} \mu_i \, k_{Di} \, e^{-k_{Di} t}, \text{ g/s.} \qquad (9)$$

where

$$k_{Di} = \left(\frac{\pi^2 D_i}{4h^2}\right), \text{ a diffusion rate constant for the } i^{th} \text{ component, } s^{-1}.$$

The characteristics of outgassing during the transition, or relaxation period, when about 40% of the VCM released must be analyzed by equations somewhat different from (6), since during the initial diffusion process many terms of this series are required. This addition to the source kinetics is currently being prepared. A summary of the surface-mediated diffuse-source kinetics model is shown in Figure 1.

3. VCM Reemission Kinetics

VCM reemission kinetics covers the processes by which condensed VCM desorbs, evaporates, or sublimates from the receptor surface. When sufficient VCM has been deposited on a receptor, the mass reemission rate is constant. If the condensed VCM is a pure substance, this constant reemission rate is dependent upon the saturation vapor pressure through Langmuir equation

$$\dot{M}_L = \frac{A_Q}{\sqrt{2\pi R}} \sqrt{\frac{M}{T_Q}}\, P_\ell \qquad (10)$$

where

$\dot{M}_L$ = Langmuir bulk reemission rate, g/s

M = VCM atomic weight, AMV

T_Q = receptor temperature, °K

P_ℓ = VCM saturation vapor pressure, torr

R = universal gas constant, cal/g-mole-°K.

When the receptor surface is only partially covered, the reemission rate can be related to a temperature-dependent residence time. The rate at which mass leaves a receptor is then the VCM mass deposited on the receptor divided by this residence time. Experiments[7] have shown that a small mass is adsorbed more or less permanently (in vacuum at 10^{-7} torr) on the receptor surface. An equation expressing the VCM reemission rate can then be written

$$M_e(t) = \frac{1}{\tau_e}\left[M_Q(t) - M_a\right] \qquad (11)$$

where

$\dot{M}_e(t)$ = reemission rate, g/s

τ_e = temperature dependent residence time, s^{-1}

$M_Q(t)$ = VCM mass on receptor, g

M_a = VCM permanently adsorbed on receptor, g

The residence time can be shown thermodynamically[8] to have temperature dependence as

$$\tau_e = \tau_o e^{\Delta E_e/RT} \quad (12)$$

where

τ_o = approximately the lattice normal vibrational period, s

ΔE_e = heart of deposition for the process, cal/g-mole

It is easy to see that a first-order reemission rate constant, K_e, similar to that in the source kinetics model, equation (7), can be expressed as the reciprocal of this residence time.

The reemission rate is then essentially a first order process when surface coverage is less than complete.

To account for a continuous process varying from a first-order reemission with small deposits to the constant (zero^th order) mass loss rate limit, when bulk VCM exists, an exponential function is suggested as an initial approximation. The resulting equation bridging equations (1) and (11) becomes

$$\dot{M}_e = -\dot{M}_L \left[i - e^{\frac{k_e}{\dot{M}_L}(M_a - M_Q)} \right] \quad (13)$$

where

$\dot{M}_L$ = Langmuir constant mass loss rate at surface saturation, g/s

$k_e = 1/\tau_e$, reemission rate constant, s^{-1}

The reemission kinetic model is summarized in Figure 2, which illustrates the typical relationships of the parameters at specific receptor temperature. Experimental work has shown that the constant-bulk Langmuir reemission process does not occur until a receptor mass deposit far in excess (>1500 Å thick) of an idealized monolayer coverage exists. The possible explanation for this is that as the VCM leaves the receptor surface, a critical coverage exists where the remaining material tends to draw together and form clusters or islands on the surface. Electron photomicrographs have shown this behavior when the average surface coverage is as much as 500 Å. This is the point where the cohesive surface forces in the VCM exceed the adsorption forces of the VCM to the receptor surface.

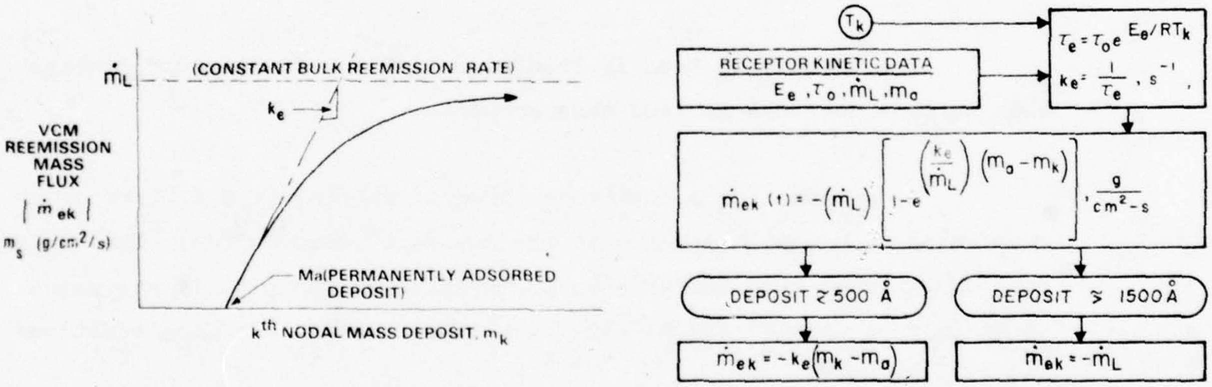

Figure 2. Receptor VCM Reemission Kinetics Model

4. Multinode Transport Model

The transport model mathematically describes the properties of the flow field as the VCM streams between the enclosure nodes. In so doing, it accounts for the intermolecular scattering in the flow field with the boundary conditions ascribed by the source and receptor kinetic models described previously. It is derived in a sequence of three steps. The first is an approximation for the collision integrals in the Boltzmann transport equation which results in a solution of the velocity distribution function (VDF) throughout the flow field. This flow field is statistically modeled by a VDF which relaxes exponentially by repeated binary collisions from its prescribed initial free-molecule value at the nodal surfaces to that of an equilibrium continuum field VDF which is an isotropic background throughout the enclosure. Secondly, the mass flux vector which impinges on each enclosure nodal receptor surface is obtained by integrating VDF over all velocity space (momentum space). The result is the Maxwell integral equation for the first velocity moment. For an N-order multinodal enclosure, this results in a consistent set of N ordinary second-order nonlinear nonhomogeneous differential equations which compute the net mass deposition rate on each node as a function of the source mass loss rate, the nodal reemission rates, and the incident flux of the uniform continuum background. Finally, the mass flux of the continuum field is itself formulated in terms of the source mass loss and nodal reemission rates.

A. The Krook-Boltzmann Relaxation Equation

The starting point for the developing of a statistical analysis for the behavior of gas dynamics is the well known Boltzmann equation. In the absence of external forces on a monatomic homogeneous gas, this can be written[9]

$$\left(\frac{\partial}{\partial t} + \underline{v}\cdot\nabla\right.\ f\ (\underline{r},\underline{v},t) = B(ff') \qquad (14)$$

where

$f(\underline{r},\underline{v},t)$ = single-particle velocity distribution function (VDF), molecules/cm^3, at position $\underline{r}$ in space, with thermal velocity $\underline{v}$ at time t.

$B(f,f')$ = bilinear Boltzmann collision integral in functional form.

When the collision probability between two classes (speeds) of molecules is finite, the collision integral can be separated in two parts.[10] One part defines an integral operator for the VDF before scattering, which accounts for the decrease in the VDF due to local removal of molecules, while the second part is a creation collision integral which accounts for molecules added locally to the VDF. The so-called Krook equation[4] expresses this separation by a linearized collision parameter between two VDFs which represent the dynamic state of the gas. This suggests a "relaxation" type process by which each of the VDFs approach each other symmetrically by repeated binary collisions. The Boltzmann collision integral of equation (14) is then approximated by

$$B(ff') \approx -K(f - f_o) \qquad (15)$$

where

K = symmetric collision - frequency parameter, s^{-1}

f_o = local Maxwellian VDF

The left side of equation (14) can be interpreted as representing the change in the number of molecules having a VDF of (f) as one follows along a path in phase space through the gas. The Krook simplification proposes that the loss and gain are both proportional to K(i.e., the symmetry of collision), and that the after-collision molecules (f') obey the local continuum Maxwellian VDF. This "two-stream Maxwellian" distribution can be shown[11] to agree with the free-molecule solution at the surface boundaries as well as that of continuum flow regardless of the system geometry. A further simplification assumed for this application is that the continuum field VDF is an absolute Maxwellian, being uniform throughout the enclosure volume but varying in time. This implies the absence of a mass average velocity for this background gas.

Equation (14) combined with (15) can be integrated along a generic direction in physical space which coincides with the velocity vector. The result is a integrable form of the Krook equation

$$\left(\frac{\partial}{\partial t} + v\frac{\partial}{\partial r} + K\right) f\,(r,v,t) = K\,f_o(v,t) \tag{16}$$

This can be readily integrated using the Laplace transform to give the value of the VDF at a remote field point (r_k) from a boundary source point (r_j) in the direction ($\hat{\Omega}$) of the speed (v) as follows.

$$f_k(r,v) = f_j(v,t-r/v)e^{\frac{-K}{v}(r_k-r_j)} + f_o(v,t-r/v)\left[1-e^{\frac{-K}{v}(r_k-r_j)}\right] \tag{17}$$

This is Krook's equation for an enclosure with a spatially isotropic continuum VDF in a direction parallel to the velocity vector. The situation is illustrated in Figure 3.

The translation argument of the time dependent source and field functions indicates that the mass is moving at a finite velocity, hence a time lag of $(r_k - r_j)/v$ is indicated for the field point r_k to be influenced by a flux propagating from source r_j at speed v. If this time lag interval is small compared to the time interval over which the source is changing, then it becomes negligible. This is obviously the case when photons are propagating.

It also applies in the case of satellite structures where the distances between nodes is on the order of tens of meters while molecular velocities are on the order of hundreds of meters per second, since a significant change in the source mass loss rates requires at least several minutes. Thus the final expression for Krook's equation applied to the present systems becomes

$$f_k(r,v,t) = f_j(v,t)e^{\frac{-K}{v}(r_k - r_j)} + f_o(v,t)\left[1 - e^{\frac{-K}{v}(r_k - r_j)}\right]. \qquad (17a)$$

B. Enclosure Boundary Conditions

The boundary conditions that need to be specified are the VDF functions at the boundary, f_j, and for the continuum field, f_o. In this simplified model, it is assumed that no average mass velocity develops for continuum flow; hence both VDFs are absolute Maxwellians. The source Maxwellian is assumed to result from a hypothetical equilibrium VCM gas behind the j^{th} source node which results in a cosine distribution of direction relative to the surface normal $(\hat{j})$ with a Maxwellian speed

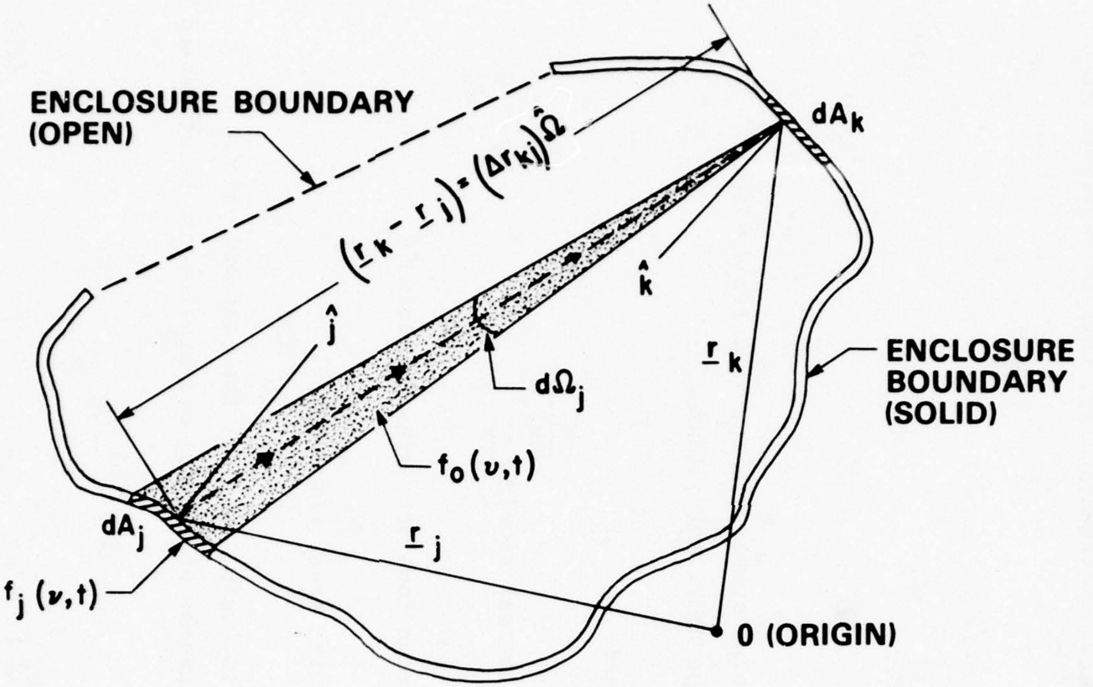

$\underline{r}_j, \underline{r}_k$ = DISPLACEMENT VECTOR TO j^{th} AND k^{th} NODES, cm

$\hat{j}, \hat{k}$ = INWARD SURFACE NORMALS TO j^{th} AND k^{th} NODES

$\hat{\Omega}$ = DIRECTION OF VELOCITY VECTOR, $\underline{V} = |\underline{V}|\,\hat{\Omega}$

f_j, f_o = MAXWELLIAN VELOCITY DISTRIBUTION FUNCTIONS FOR FREE-MOLECULE FLOW AT j^{th} SURFACE AND IN CONTINUUM FLOW FIELD (0), RESPECTIVELY, MOLECULES/cm^3

Figure 3. Enclosure Geometry for Krook Relaxation Model and Mass Intensity

distribution along each radial direction[13]. This further specifies free molecule flow at the surface. Mathematically, this is expressed as

$$f(v,t) = n_j(t)\left(\frac{\beta_j}{\pi}\right)^{3/2} v^2 e^{-\beta_j v^2} \tag{18}$$

where

$n_j(t)$ = molecular number density associated with j^{th} surface node, molecules/cm^3

β_j = $\frac{4}{\pi \bar{v}_j^2}$ and

$\bar{v}_j$ = mean thermal speed $= \sqrt{\frac{8kT_j}{\pi m}}$

k = Boltzmann constant, ergs/molecule-°K

m = molecular mass, g/molecule.

In a completely analogous fashion, the continuum field Maxwellian which is independent of spatial orientation can be expressed

$$f_o(v,t) = n_o(t)\left(\frac{\beta_o}{\pi}\right)^{3/2} v^2 e^{-\beta_o v^2} \tag{19}$$

where

$n_o(t)$ = molecule number density for uniform field, molecules/cm^3

β_o = $\left(4/\pi\bar{v}_o{}^2\right)$.

Since the field Maxwellian is isotropic, it could be integrated along the complete path length to the source node; hence it can be considered directly correlated as if it originated within the surface.

C. Mass Intensity and the Incident Nodal Mass Flux

In fluid mechanics, the principle objective is to determine the macroscopic properties of the flow field such as the average mass velocity, the pressure, shear stresses, and the average energy flow. These average properties, which are functions of the molecular velocity, are calculated at a field point by simply integrating the VDF weighted by the property function over all velocity space. This is formally expressed by

$$\overline{Q}(\underline{r},t) = \int_{\text{All } \underline{v}} Q(\underline{v})\ f(\underline{r},\underline{v},t)\ d\underline{v} \tag{20}$$

where

$Q(\underline{v})$ = molecular property (mass, momentum, energy)

$d\underline{v}$ = element volume of velocity space.

Another macroscopic average can be obtained for the transport of the property (Q) in a given direction ($\hat{\Omega}$) across an elemental area normal to that direction. This is obtained by integrating the VDF, now weighted by the property times the projected velocity component, over the hemisphere above the area. The result is called the "property flux vector" and is expressed by

$$\overline{Qv}(r,t) = \int_{\text{half } \underline{v} \text{ space}} Q(\underline{v})\ (\underline{v}\,\hat{\Omega})\ f(\underline{r},\underline{v},t)\ d\underline{v} \tag{21}$$

Thus, the mass flux (vector) is obtained from equation (21) when $Q(\underline{v})$ is designated the molecular mass, and the mass flux is then identified with the first moment of the VDF.

This can be evaluated at the j^{th} source node which will define a "molecular mass intensity," which is analogus to the intensity in radiation heat transfer, for Maxwellian emission from the j^{th} node. The total hemispherical mass loss rate into the enclosure is obtained from the first moment of equation (18).

$$\dot{m}_j(t) = m \int_{(2\pi)} \int_0^{\infty} v \cos \theta_j\ f_j(v,t)\ dv\ d\Omega \tag{22}$$

where

$\dot{m}_j(t)$ = mass flux leaving j^{th} node, g/cm^2-s

$d\Omega$ = $\sin \theta_j d\theta_j\ d\phi$.

Since the integrals can be separated, the integration over the speeds yields

$$\dot{m}_j(t) = -\int_{(2\pi)} \frac{m}{\pi}\left(\frac{n_j(t)}{2\sqrt{\pi\beta j}}\right)\cos\theta_j d\Omega,\ \mathrm{g/cm^2\text{-}s}. \tag{23}$$

The second integration assumes azimuthal symmetry and ranges θ_j from (0) to ($\pi/2$) thus covering the hemispherical half-space over the j^{th} node. The result is

$$\dot{m}_j(t) = \frac{mn_j(t)}{2\sqrt{\pi\beta_s}}\ ,\ \mathrm{g/cm^2\text{-}s}. \tag{23a}$$

Recalling the definition of β_j in equation (18),

$$\dot{m}_j(t) = \frac{m\bar{v}_j}{4} n_j(t). \tag{23b}$$

From equation (23) and the definition of uniform intensity, the mass intensity is then defined as

$$I_j(t) = \frac{1}{\pi}\left[\frac{mn_j(t)}{2\sqrt{\pi\beta_j}}\right] = \frac{\dot{m}_j(t)}{\pi}\quad \mathrm{g/cm^2\text{-}s\text{-}sr}. \tag{24}$$

where

$I_j(t)$ = constant molecular emission intensity from the j^{th} node, g/cm^2-s-sr

An analogous result can be obtained for the intensity of the field mass flux vector since it can be mathematically considered as a source at j^{th} node. The expression becomes

$$I_o(t) = \frac{1}{\pi}\left[\frac{m\, n_o(t)}{2\sqrt{\pi\beta_o}}\right] = \frac{\dot{m}_o(t)}{\pi} \tag{25}$$

where

$I_o(t)$ = constant molecular emission from the field, g/cm^2-s-sr.

$n_o(t)$ = uniform molecular density in the enclosure, g/cm^3.

The differential mass flux on the k^{th} receptor node due to a differential source element dA_j node can be obtained by applying equation (22) with the VDF derived in equation (17). Symbolically, the desired equation becomes

$$d\phi_{j,k}(t) = \int_o^\infty m\, v\, f_k(v,t)\, dv \cos\theta_k\, d\Omega_j \tag{26}$$

where

$\phi_{j,k}(t)$ = mass flux incident on a unit area of the k^{th} node from the j^{th} differential source node, g/cm^2-s.

$d\Omega_j$ = the solid angle subtended at a point in k by the j^{th} node.

If source and field Maxwellians defined by equations (18) and (19) are put into equation (17a) and then the integration indicated in equation (26) is applied, the following expression for the differential mass flux is obtained.

$$d\phi_{j,k} = mn_j {\frac{\beta j}{\pi}}^{3/2} \int_o^\infty v^3 e^{-\beta_j v^2 - \frac{k}{v}(r_k - r_j)} dv \cos\theta_k \, d\Omega_j + ---$$

$$--- + mn_o \left(\frac{\beta_o}{\pi}\right)^{3/2} \int_o^\infty v^3 \left[1-e^{-\frac{k}{v}(r_k-r_j)}\right] e^{-\beta_o v^2} dv \cos\theta_k \, d\Omega_j . \qquad (27)$$

It is convenient to define the following function[11]

$$G_n(\alpha_n) = \frac{1}{2} \int x^3 e^{-x^2 - \gamma_n/x} dx = <e^{-\gamma_n/x}> \qquad (28)$$

where

$\gamma_n = K\sqrt{\beta_n}(v_j - r_k)$, (n= j,o).

The two integrals of equation (27) can be expressed in terms of function (28),

$$\int_o^\infty v^3 e^{-\beta_j v^2 - \frac{k}{v}(r_k - r_j)} \, dv = \frac{1}{2\beta_j} G_j(r) \tag{29a}$$

$$\int_o^\infty v^3 \; 1-e^{\frac{-k}{v}(r_k - r_s)} \; e^{-\beta_o v^2} \, dv = \frac{1}{2\beta_o} \left[1-G_o(r) \right] . \tag{29b}$$

The solid angle that the jth differential area subtends relative to the kth node is

$$d\Omega_j = \frac{\cos\theta_j \, dA_j}{(r_k - r_j)^2} \tag{30}$$

Now, combining equations (29) and (30) into equation (27) and integrating over a finite source node (A_j) and finite receptor node (A_k), the incident mass flux becomes

$$\phi_{j,k} = \dot{m}_j \frac{1}{A_k} \int_{A_k}\int_{A_j} \frac{G_j(r) \cos\theta_j \cos\theta_k}{\pi(r_k - r_j)^2} \, dA_j \, dA_k + \text{---} \tag{31}$$

$$\text{---} + \dot{m}_o \frac{1}{A_k} \iint \frac{1-G_o(r) \quad \cos\theta_j \quad \cos\theta_k}{\pi(r_k - r_j)^2} \, dA_j \, dA_k .$$

A mean geometrical molecular transmittance and absorptance can be defined analogous with the characteristics of radiation heat transfer[14] in a scattering and emitting gas as follows

$$(T_{jk}\ F_{jk}) \equiv \frac{1}{A_k} \int_{A_k}\int_{A_j} \frac{G_j(r)\ \cos\theta_j\ \cos\theta_k}{\pi(r_k - r_j)^2}\ dA_j\ dA_k \qquad (32a)$$

$$(\alpha_{jk}\ F_{jk}) = \int_{A_k}\int_{A_j} \frac{1 - G_o(r)\ \ \cos\theta_j\ \cos\theta_k}{\pi(r_k - r_j)^2}\ dA_j\ dA_k \qquad (32b)$$

where

T_{jk} = mean geometrical molecular transmittance from the jth to the kth node

α_{jk} = mean geometrical molecular absorptance from the jth to the kth node

F_{jk} = diffuse angle factor from the jth to the kth node

The final form for the mass flux from the jth node incident on the kth node is then finally

$$\phi_{j,k} = (T_{jk}\ F_{jk})\dot{m}_j + (\alpha_{jk}F_{jk})\dot{m}_o . \qquad (33)$$

D. Multinode Mass Flux Coupling and Deposition Equations

Equation (33) accounts for the transport of molecular Maxwellian streams between two nodes as indicated. The molecules accounted for by this equation are a composite of two Maxwellian classes, those identified with the source j^{th} node hence at a temperature of T_j and those of the continuum field Maxwellian at temperature T_o. The flux is entirely contained within a volume bounded by the surfaces of the nodes and all straight lines which pass through both nodes. Clearly, this relationship must be extended to include molecules streaming from a node with class temperatures differing from the nodal temperature and should encompass enough nodal surfaces to geometrically describe the system being modeled.

With reference to Figure 4, an "enclosure" is composed of two types of nodes. There are N nodes which form the boundary of the enclosure. These N nodes include open areas, or holes, which are single nodal surfaces which neither scatter (anechoic) or reemit flux. The remainder of the nodes both scatter incident flux and reemit from masses deposited on their surfaces. Each of these "active" nodes is characterized by its area (A_k), its temperature (T_k), by an reemission mass rate ($\dot{m}_{ek}$) at the nodal temperature, and by a group of N capture coefficients (σ_{ik}) which represent the probability that molecules of a Maxwellian class at T_i will reside on the node surface long enough to become accommodated to the nodal temperature, T_r. The fraction of the incident stream that is not accommodated is assumed to be "elastically" scattered; hence it retains its class identification. Both of the emerging streams, the scattered stream at say T_i and the reemitted one at T_k, are assumed to be Maxwellian streams with a cosine

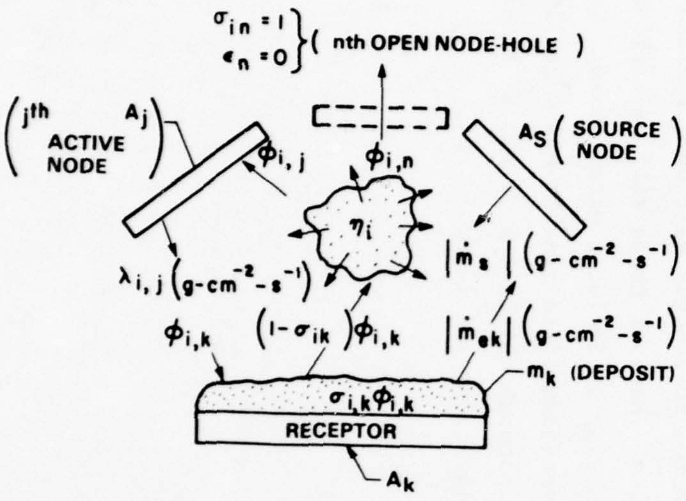

1. INCIDENT MOLECULAR FLUX OF i^{th} CLASS MAXWELLIAN FLUX AT T_i FROM j^{th} NODE TO k^{th} NODE

$$\phi_{i,k} = \sum_{j=1}^{N} \left[\left(\tau_{ikj} F_{kj} \right) \lambda_{ij} + \left(\alpha_{ikj} F_{kj} \right) \eta_i \right]$$

2. EMERGENT FLUX DUE TO ELASTIC SURFACE SCATTERING AND VCM REEMISSIONS

$$\lambda_{i,k} = \left(1 - \sigma_{ik}\right) \phi_{i,k} + \delta_{ik} \dot{m}_{ek}$$

3. DEPOSITION RATE ON k^{th} RECEPTOR NODE

$$\dot{m}_{dk} = \sum_{i=1}^{N} \left(\sigma_{ik} \phi_{i,k} + \delta_{ik} \dot{m}_{ek} \right) - \sum_{S} \sigma_{sk} F_{ks} \dot{m}_s$$

Figure 4. Enclosure Geometry and Mass Balance Equations

distribution relative to the surface normal.[15] Free-molecule flow is assumed to exist in the immediate vicinity of a nodal surface which becomes "relaxed" within a mean free path of the surface; the so-called Knudsen layer.

The other class of nodes is the source nodes. These are characterized again by their area (A_s), by their temperature (T_s), and by their mass loss rates ($\dot{m}_s$). These nodes may be actually superimposed over one or more of the other nodes or they may be a single-point jet into the enclosure. They do not participate in the scattering and reemission processes. All of the VCM components which are released by the same source are considered as separate VCM sources. In the development of the flux coupling equations which follow, a single VCM component is assumed, to simplify the notation.

With the assumption of each node either totally accommodating and reemitting at its temperature or elastically scattering, it is clear the enclosure VCM gas will be comprised of N Maxwellian classes of molecules. Each of these will be incident and reemitted on each node, resulting in N^2 local mass fluxes. Concomitantly, there will be N continuum field classes which are isotropic throughout the enclosure through which each of the N^2 local surface Maxwellians is relaxing by collision.

The mass flux coupling and mass deposition equations for the enclosure can be derived by considering a VCM mass rate balance on a typical nodal surface, say the k^{th} node, as indicated in Figure 4. The equation for the incident flux of i^{th} class molecules on the k^{th} receptor is obtained by summing over all the enclosure nodes, including the k^{th} node, and over the continuum field fluxes:

$$\phi_{i,k} = \sum_{j=1,N} \left[(T_{ikj}\ F_{ks})\ \lambda_{i,j} + (\alpha_i k_j F_{kj})\ \eta_i \right] \tag{34}$$

$$i,k,j = 1, ---, N$$

where

$\phi_{i,k}$ = total incident mass flux at class temperature T_i on the k^{th} node, g/cm^2-s

$\lambda_{i,j}$ = total mass released from the j^{th} node at temperature T_i, g/cm^2-s (this flux is identical with $\dot{m}_j(t)$ as expressed in previous equations)

η_i = equilibrium field mass flux at T_i (this flux is identical with $\dot{m}_o(t)$ as expressed in previous equations), g/cm^2-s

T_{ikj} = mean transmittance of i^{th} class molecules from the k^{th} node to the j^{th} node

α_{ikj} = mean absorptance of i^{th} class molecules from the k^{th} node to the j_{th} node

F_{kj} = diffuse angle factor from the k^{th} node to the j^{th} node.

In equation (34), use has been made of the reciprocity which is applicable to the scattering process.[14] This is

$$\left.\begin{aligned} A_j\,T_{ijk}\,F_{jk} &= A_k\,T_{ikj}\,F_{kj} \\ \alpha_{ijk} &= (1 - T_{ijk}) \end{aligned}\right\} \qquad (35)$$

The equations for the VCM reemission mass flux can again be identified from Figure 4 and can be expressed as

$$\lambda_{i,k} = (1 - \sigma_{ik})\phi_{i,k} - \delta_{ik}\dot{m}_{ek} \qquad (36)$$

$$i,k = 1,---,N$$

where

σ_{ik} = mean capture coefficient for i^{th} class molecules on the k^{th} node

$\dot{M}_{ek}$ = VCM remission mass flux from the k^{th} node at T_k, (this is intrinsically a negative value, hence the minus sign in equation (36)), g/cm^2-s

$$\delta_{ik} = \begin{cases} 1, & i=k \\ 0, & i\neq k \end{cases} \quad \text{Kronecker delta function}$$

Finally, the nodal mass deposition rates are obtained by summing the accommodated fractions of the incident fluxes with that from the source and subtracting the reemission rate.

$$\dot{m}_{dk} = \sum_{j=1,N} \sigma_{ik} \, \phi_{i,k} + \dot{m}_{ek} - \sigma_{sk} \, T_{sks} \, F_{ks} \, \dot{m}_{s} \qquad (37)$$

where

$\dot{m}_{dk}$ = mass deposition rate for all class molecules on the k^{th} node, g/cm^2-s

$\dot{m}_{s}$ = mass loss rate from the source node at T_s (this is intrinsically a g/cm^2-s negative value, hence the minus sign).

σ_{sk} = mean capture coefficient for s^{th} class source molecules at T_s on the k^{th} node

T_{sks} = mean transmittance for source molecules at T_s from the k^{th} node to the source node

F_{ks} = diffuse view factor from the k^{th} node to the source node.

Now, equations (34) and (36) can be combined to give N^2 linear equations which couple the incident nodal fluxes with the nodal reemission rates and the incident flux from the equilibrium field molecules. This is expressed in matrix format as

$$\left[Y(T_{ikj}\ F_{ks},\ \sigma_{ik}) \right] \left\{ \phi \right\} = \left[G(T_{ikj}\ F_{kj}) \right] \left\{ \dot{m}_e \right\} + \left[H(\alpha_{ikj}\ F_{kj}) \right] \left\{ \eta \right\} \quad (38)$$

where

$\left[Y \right]$ = $(N^2 \times N^2)$ - matrix whose elements are functions of the transmittances, the view factors, and the capture coefficients

$\left\{ \phi \right\}$ = (N^2) - vector whose elements are the incident mass fluxes, g/cm^2-s

$\left[G \right]$ = $(N^2 \times N)$ - matrix whose elements are functions of the transmittances and the view factors

$\left\{ \dot{m}_e \right\}$ = (N) - vector whose elements are the mass reemission fluxes, g/cm^{2-s}

$\left[H \right]$ = $(N^2 \times N)$ - matrix whose elements are functions of the absorptances and the view factors

$\left\{ \eta \right\}$ = (N) - vector whose elements are the incident mass fluxes from the field distribution, g/cm^2-s

Equation (38) can be combined with equation (37), thereby expressing the fundamental mass deposition equations in a concise matrix format:

$$\left\{ \dot{m}_d \right\} = \left[I - S(\sigma_{ik})\ Y^{-1} G \right] \left\{ \dot{m}_e \right\} + \left[S(\sigma_{ik})\ Y^{-1} H \right] \left\{ \eta \right\} - \dot{m}_s \left\{ B(\sigma_{sk} T_{sks} F_{as}) \right\} \quad (39)$$

where

$\left\{ \dot{m}_d \right\}$ = (N) - vector whose elements are the nodal mass deposition rates, g/cm^2-s

$\left[S \right]$ = ($N \times N^2$) - matrix whose elements are the N^2 capture coefficients

$\left\{ B \right\}$ = (N) - vector whose elements are the capture coefficients, the transmittance and the view factors between the receptor nodes and the source

$\left[I \right]$ = ($N \times N$) - identity matrix

When free molecule flow conditions exist through the enclosure, the (α) all vanish and the (T) become unity, and the (H) matrix vanishes. Equation (39) reduces to

$$\left\{ \dot{m}_d \right\} = \left[I - SY^{-1}G \left\{ \dot{m}_e \right\} - \dot{m}_s \quad \left\{ B(\sigma_{sk} \; F_{ks}) \right\} \right. . \tag{40}$$

At the other end of the collision spectrum the (α) become unity, and the (T) vanish. Further $\left[Y \right] \rightarrow \left[I \right]$, $\left[G \right] \rightarrow 0$, and $\left[H(\alpha F) \right] \rightarrow \left[H(F) \right]$. Then, the general deposition equation (39) becomes

$$\left\{ \dot{m}_d \right\} = \left[S \; H(F_{kj}) \right] \left\{ \eta \right\} - \left\{ \dot{m}_e \right\} . \tag{41}$$

This shows how the mixing by a very large collision rate (or vanishingly small collision mean free path) substantially homogenizes all of the nodal emission to make up the uniform equilibrium field VCM.

E. Continuum Mass Flux

As shown in equation (39), the nodal deposition rate is linearly dependent on the isotropic continuum flux (η) from the continuum molecules. This continuum, by assumption, is considered to consist of a homogeneous mixture of N vapors with uniform density and N classes of temperatures identified with the nodal temperatures. When continuum conditions exist within the enclosure, all the mass fluxes released from the source and reemitted from the nodes becomes homogenized into the continuum. Since the continuum implies a very large number of intermolecular and surface collisions, it is assumed that the fraction of the total continuum vapor at a particular class temperature will be in the same ratio as the surface area at that temperature to the total bounding area of the enclosure. Thus, each emission and reemission flux regardless of its temperature at release is separated into the N continuum vapors according to this area ratio mixing rule. The incident continuum mass flux is the same on all nodes by virtue of its isotropy.

With these basic properties of the continuum flow field, it is possible to independently derive the continuum nodal mass fluxes in terms of the geometry of the enclosure, the source emission rate, the nodal reemission rate, and the capture coefficients. This is done by performing an instantaneous mass balance within the system enclosure. This simply states the conservation of mass (the continuity equation) of classical continuum fluid mechanics. It is also analogous to the "pumping speed" expression used to evaluate vacuum pumping systems in vacuum chamber technology.[16]

Assuming that continuum flow exists in the enclosure, the rate of change in the total i^{th} continuum class mass in the enclosure is equal to the rate of generation from the source and the nodal reemissions less that adsorbed by capture at the nodal surfaces. Mathematically this is expressed as:

$$\frac{d}{dt}(mN_i) = \left(\frac{A_i}{A_T}\right)\left[A_s\dot{m}_s + \sum_{j=1,N} A_j\dot{m}_{ej}\right] - \frac{1}{4v_o}(mN_i)\,v_i \sum_{j=1,N} A_j\sigma_{ij} \qquad (42)$$

where

N_i = total number if i^{th} class continuum molecules in the enclousre, molecules

A_i = area of the i^{th} node and T_i, cm^2

$A_T = \sum_{j=1,N} A_j$, the total enclosure boundary area, cm^2

v_o = total enclosure volume defined by the envelope of all straight lines passing through two or more nodes, cm^3

$\bar{v}_i = \sqrt{\frac{8kt}{\pi m}}$, the average thermal speed of the i^{th} class of Maxwellian molecules, cm/s

m = molecular mass, g.

The continuum mass flux for the i^{th} class can be expressed as

$$\eta_i = \left(\frac{\bar{v}_i}{4V_o}\right) . \ mN_i \tag{43}$$

where

η_i = incident mass flux of continuum i^{th} class molecules on all nodes, g/cm^2-s

An ordinary linear nonhomogeneous differential equation for the i^{th} continuum mass flux is then obtained by introducting equation (43) into equation (42) which results in the following expression:

$$\dot{\eta}_i + P_i\eta_i = Q_i \left[A_s\dot{m}_s + \sum A_i\dot{me}_s\right] \tag{44}$$

where

$$P_i = \left(\frac{\bar{v}_i}{4V_o}\right)\sum A_i\sigma_{ij}, \ s^{-1}$$

$$Q_i = \left(\frac{A_i\bar{v}_i}{4V_oA_t}\right), \ cm^{-2}\text{-}s^{-1}$$

For the entire system, the N coupled continuum mass fluxes can be conveniently expressed in matrix format by generalizing equation (44). This set of N equations becomes:

$$\left\{\dot{\eta}\right\} + [P]\left\{\eta\right\} = (A_s\dot{m}_s)[Q] + [Q]\left\{\dot{me}\right\} \tag{45}$$

where

$[\eta]$ = (N) - vector whose elements are the nodal continuum mass fluxes, g/cm^2-s

[P] = (N x N) - diagonal matrix whose elements are the P_i values of equation (44), s^{-1}

[Q] = (N x N) - diagonal matrix whose elements are the q_i values of equation (44), cm^{-2}-s^{-1}

[A] = (N x N) - matrix whose elements are the nodal surface areas, cm^2.

If equation (39) is differentiated with respect to time and equation (45) is substituted in, an ordinary second order differential equation is derived which is linearly dependent upon the continuum flux vector, (η_i). There are then two independent matrix equations which are linearly dependent upon η, equation (30) and its time derivative. If they are combined to eliminate η, a set of N ordinary nonlinear second-order nonhomogeneous differential equations results as follows:

$$[A']\left[\dot{m}_d^{\cdot}\right] + \left\{\dot{m}_d\right\} - [B']\left\{\dot{m}_e^{\cdot}\right\} - [C']\left\{\dot{m}_e\right\} = -\left[\ddot{m}_s\left\{D'\right\} + \dot{m}_s\left\{E'\right\}\right] \qquad (46)$$

where

$$[A'] = \left[SY^{-1}\ HP^{-1}\right]\left[SY^{-1}\ H\right]^{-1}$$

$$[B'] = \left[SY^{-1}\ HP^{-1}\right]\left[SY^{-1}\ H\right]^{-1}\left[I\text{-}SY^{-1}\right]G$$

$$[C'] = \left[SY^{-1}\ H\right]\left[P^{-1}AQ\right] + \left[I - SY^{-1}\ G\right]$$

$$\{D'\} = \left(\frac{As}{AT}\right)\left[SY^{-1}\ H\right]\left\{Ai/\sum_j A_i\sigma_{ij}\right\}$$

$$\{E'\} + \{B\} - \left[SY^{-1}\ HP^{-1}\right]\left[SY^{-1}\ H\right]^{-1}\{B\}.$$

Equation (46) is the desired final result of the deposition model. Its format is clarified if first-order reemission kinetics is assured as in equation (11). Assuming that the permanently adsorbed VCM is negligible, the mass rate elements of the deposition equation become:

$$\begin{aligned} \left\{ m_d \right\} &= \left\{ m \right\} \\ \left\{ \dot{m}_e \right\} &= -[K_e]\ m \end{aligned} \qquad (47)$$

where

$\left\{ m \right\}$ = (N) - vector whose elements are the specific nodal mass deposit, g/cm^2

When the results of equation (47) are introduced into equation (46), a set of N ordinary second-order nonhomogeneous differential equations for the nodal mass deposition results:

$$[A']\left\{\ddot{m}\right\} + [I + B'K_e]\left\{\dot{m}\right\} + [C'K_e]\left\{m\right\} = -\left[\ddot{m}_s\left\{D'\right\} + \dot{m}_s\left\{E'\right\}\right. \qquad (48)$$

which is the deposition equation for very thin deposits.

Equation (48) can be readily solved for the nodal deposition $\left\{m\right\}$ using numerical computation procedures. Since the condition of free molecule flow causes the [H] operator to vanish, the thin-deposit equation (48) simplifies to become:

$$\left\{\dot{m}\right\} + [I - S\ G]\left\{m\right\} = -\dot{m}_s\left\{B\right\} \qquad (49)$$

which is equivalent to equation (40). Equation (48) indicates the basic "damping" influence of the continuum flow field. In order to provide the smooth transition from continuum flow to free molecule flow and vice versa, it is necessary to continually evaluate the changes in the mean geometric transmittances of each node, since these change with the local densities due to the subsequent changes in the collision frequency and the mean free path. Thus, the elements of the matrix operators [Y], [G], [H] and the vector operator $\{B\}$ are functionally dependent on the variable flux vectors $\{\dot{m}_e\}$, $\{\eta\}$, and $\{\phi\}$. This nonlinearity is introduced by the time variations in the magnitude of the fluxes as the source is depleted of VCM. Under free-molecule conditions, when the field is collisionless, the equations becom linear.

Thus, the reduced equation (49) is a significant simplification with constant linear operators and can be solved formally using matrizant methods of matrix calculus together with Sylvestor's theorem for functions of matrices.

A summary of the equations for the multinodal surface contamination model is presented in Figure 5.

- **NODAL SURFACE MASS FLUX EQUATIONS**

$$\left[\mathcal{Y}(T,F,\sigma)\right]\{\phi\} = \left[\mathcal{G}(T,F)\right]\{\dot{m}_e\} + \left[\mathcal{H}(1-T,F)\right]\{\eta\}$$

- **CONTINUUM FIELD MASS FLUX EQUATIONS**

$$\{\dot{\eta}\} + \left[P(A,\bar{\upsilon},V_O,\sigma)\right]\{\eta\} = \left[AQ(A,q,\bar{\upsilon},V_O)\right]\{\dot{m}_e\} + A_S\,\dot{m}_S\,[Q]$$

- **NODAL MASS DEPOSITION RATE EQUATIONS**

$$\{\dot{m}_d\} = \left[\mathcal{S}(\sigma)\right]\{\phi\} + \{\dot{m}_e\} - \dot{m}_S\,\{B(T,F,\sigma)\}$$

- **COMBINED MULTINODE DEPOSITION EQUATION**

$$[A']\{\ddot{m}_d\} + \{\dot{m}_d\} - [B']\{\ddot{m}_e\} - [C']\{\dot{m}_e\} = -\left[\ddot{m}_S\{D'\} + \dot{m}_S\{E'\}\right]$$

- **DEPOSITION EQUATION FOR FREE-MOLECULE FLOW**

$$\{\dot{m}\} + \left[I - \mathcal{S}\,\mathcal{Y}^{-1}\,\mathcal{G}\right]\{m\} = -\,\dot{m}_S\,\{B\}$$

AEROJET ELECTROSYSTEMS COMPANY

Figure 5. Summary of the Basic Equations of the Multinodal Surface Contamination Model

5. Computational Procedures

To compute the mass deposition on any node with the general conditions of the transitional Knudsen flow, equation (46) must be solved using a digital computer program. The interrelationship of the various equations developed in the previous sections are indicated in the information flow diagram of Figure 6.

Figure 6 depicts three analytical procedures which must be followed prior to exercising the deposition algorithm. These are identified by the double-border rectangles in the upper section of Figure 6. First, the system configuration must be divided into the nodal surfaces which will define the system enclosure. A node is defined as a segment of the enclosure boundary which has a uniform temperature and a uniform mass deposit. The size of a node is dependent only on these two criteria. A system from a small sensor to a large orbiting satellite can be modeled. Once the geometrical characteristics of the enclosure system have been determined, this data is introduced into a geometrical view factor program which is used to compute the diffuse view factors which interconnect the nodes. Many such programs using contour integration and/or finite element integration are available as they are most frequently employed in problems of radiation heat transfer. The third analytical procedure required to support the contamination algorithm is a transient thermal analyzer which can continually compute the nodal and source temperatures over the time period desired. If the system is in a space orbit, the environmental ultraviolet and charged particle fluxes, Φ, should also be computed concurrently with the orbital temperature profiles.

Another very important segment of the overall algorithm is the experimental data base in the four areas indicated on Figure 6 by the circles near the four corners. These test efforts provide the basic

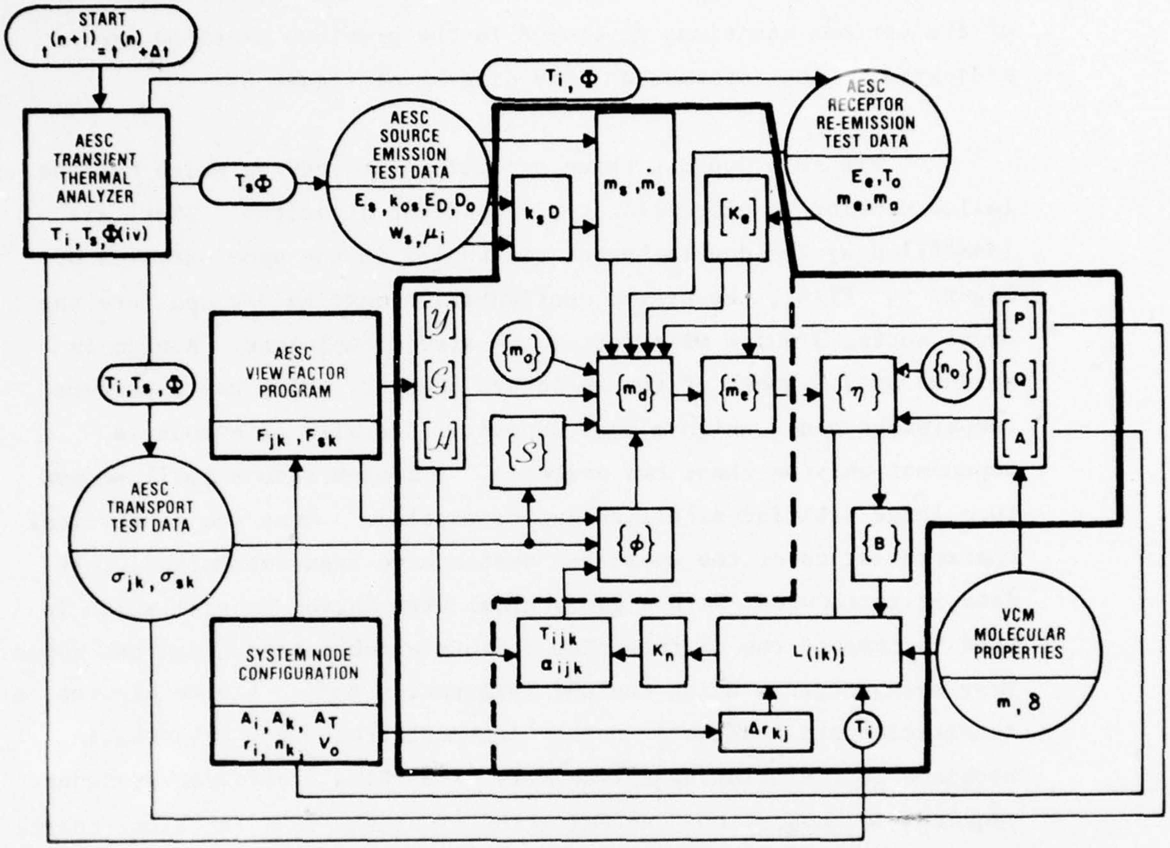

AEROJET AESC
ELECTROSYSTEMS COMPANY

Figure 6. Contamination Model Information Flow Diagram

kinetic and transport properties of the sources and their VCM as a function of the temperature of the nodes and of the environmental ultraviolet and particle fluences. Significant progress has been made on obtaining such data for the source emission kinetics, the VCM reemission kinetics, and the capture coefficients which are the transport descriptors for surface collisions.

This data is sufficient if the analysis is to cover only the free-molecule regime. If the scattering influence for transition and continuum flow is necessary, then two VCM molecular properties, the molecular mass (m) and its collision diameter (δ), are needed. For simple monatomic inert gases, fairly good information already exists. However, for the complex polymeric VCM molecules that are released by the source materials used in space, there is virtually no data, and extrapolation from the inert gases is poor at best. Much work is needed in this area.

Another complication enters the computational aspects when transition flow must be considered. This is the problem that the differential equations become nonlinear in that the elements of the operators $|Y|$, $|G|$, $|H|$, and $\{B\}$ become functions of the dependent variables. This requires continual reiteration and computation of the mean free paths and the mean geometric absorptance and transmittance. To use the procedures as indicated on Figure 6, it is implicit that T_{ijk} can be calculated independently of F_{jk}. Generally, as was shown previously, this is not true. However, with relatively simple nonreentrant surfaces, approximate formulas can be used based upon the techniques of radiation heat transfer.[14]

The solution technique is to select an initial orbital time $t^{(o)}$ at which the initial nodal deposit vector is $\{m_o\}$ and the initial continuum flux vector is $\{\eta_o\}$. At the injection of orbit these are both near zero. The temperatures are then computed. Then, for the time interval, Δt, the temperatures are assumed constant so that the values of the source and receptor kinetic parameters are constant. For this brief period of isothermal conditions, a mass deposition vector is calculated which is then used to determine the scattering mean transmittance for the next Δt interval. Prior to each new Δt, the coefficients of the dependent operators must be recomputed based upon the conditions during the last interval. The informational flow for this loop calculation is outlined in Figure 5 by the dotted boundary. If scattering collisions are negligible, then this block of subprograms is bypassed and the problem solution continues with constant matrix coefficients.

6. Applications

To date, only the free-molecule section of the model has been applied to practical problems. Since only a limited data base presently exists, the results must be considered preliminary, but many of the phenomena attributed to contamination have been at least qualitatively verified on several complex Air Force satellites. Classification of these programs prohibits presentation of the results.

Another relevant application was to use the model to design the apparatus and procedures to measure the kinetic and transport properties of the source materials. It is clear that the nodal coupling is significant and that the configuration of the testing apparatus must be simple enough to permit a closed-form solution of the basic equation (49) in a vacuum chamber. The configuration, sketched in Figure 7, consists of a cylindrical vacuum chamber evacuated to less than 10^{-7} torr with its top, bottom, and sides completely shrouded by LN_2 jacketing. Four quartz crystal microbalances (QCMs)

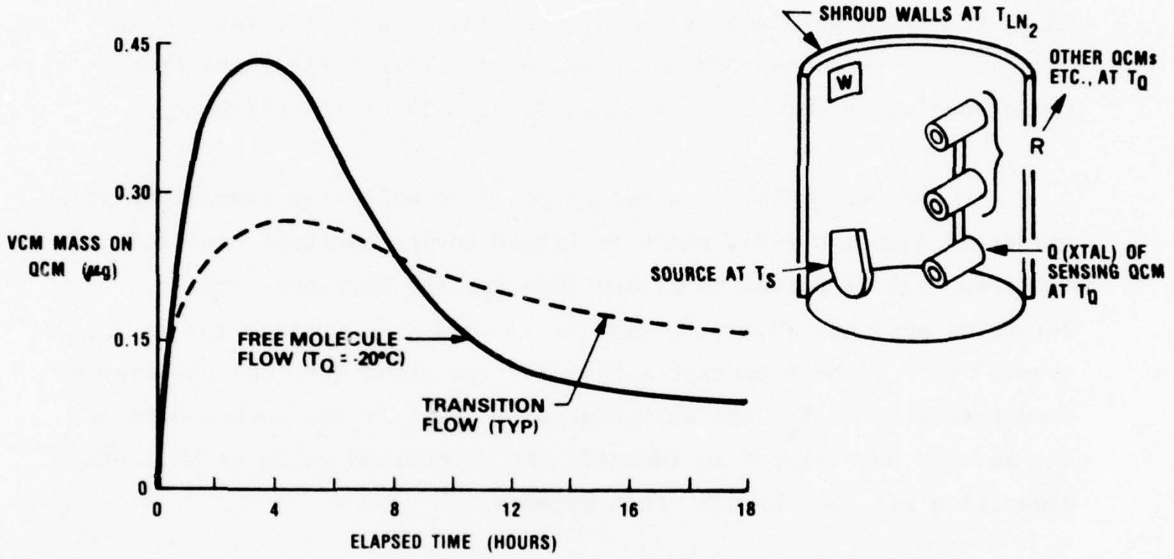

- **DEPOSITION RATE EQUATION**

$$\dot{m}_Q + k_Q m_Q = -F_{QS}\,\sigma_{SQ}\,\dot{m}_S,\ g/cm^2/s$$

- **MASS DEPOSITION ON INITIALLY CLEAN QCM WITH 1st ORDER SOURCE KINETICS**

$$m_Q(t) = \frac{F_{QS}\,\sigma_{SQ}\,\mu W_S\,k_S}{A_S\,(k_Q - k_S)}\left(e^{-k_S t} - e^{-k_Q t}\right),\ g/cm^2$$

Figure 7. VCM Mass (μg) Deposited on a QCM Area 0.316 cm^2 Located 5.0 cm from a 2.54-cm-diameter Source of RTV-566 (0.2% Catalyst) Coated with 70 mg and Maintained at 125°C for 24 Hours.

were positioned at distances varying from 2 inches to 6 inches in front of a 1-inch-diameter disk specimen coated with the source material. The source was maintained at the desired emission temperature between 40°C and 150°C while the QCMs were all collectively held from near LN_2 temperatures (-170°C) to about 25°C. With this configuration the apparatus, labeled the Molekit (Molecular Kinetics Test Facility), can be modeled as a four-node system: the source as a 1-inch-diameter disk, the 1/4-inch-diameter sensing crystal of a particular QCM as another, the remaining QCM cases which can reflect flux, and finally the shroud walls which were assumed to be molecularly anechoic.

When the Molekit is evacuated, free molecular conditions will exist and equation (49), which is linear having constant coefficient matrices, can be solved in closed form for the four-node system. Referring again to Figure 7, let the subscript Q identify the sensing crystal at T_Q, the subscript R identify the other QCMs and the support structure also at T_Q, the subscript S to identify the source held at T_s, and the subscript W to identify the cryoshroud walls at LN_2. The deposition rate on the QCM then becomes:

$$\dot{m}_Q + \sum_j Z_{Qj} m_j = -F_{QS}\sigma_{SQ}\dot{m}_S, \quad (j=Q,R,S,W) \tag{50}$$

where

$$Z_{QQ} = k_Q \frac{\begin{bmatrix} 1-(F_{SW}F_{US} + F_{SQ}F_{QW}F_{US} + --- \\ --- + F_{UQ}F_{QS}F_{SW})(1-\sigma_{SQ})(1-\sigma_{QW}) - \ldots \\ \ldots - F_{SQ}(1-\sigma_{QS}) - F_{WQ}F_{QW}(1-\sigma_{QW}) \end{bmatrix}}{\left[1 - F_{SW}F_{WS}(1-\sigma_{QW})(1-\sigma_{SQ})\right]}$$

$$Z_{QR} = \frac{(A_R k_R) \left[(F_{RS}F_{SW}F_{UQ} + F_{RW}F_{WS}F_{SQ})\ (1 - \sigma_{QS})(1 - \sigma_{QW}) + \text{---} \right. \\ \left. \text{---} + F_{RS}F_{SQ}(1 - \sigma_{QS}) + F_{RW}F_{WQ}(1 - \sigma_{QW}) \right]}{A_Q \left[1 - F_{SW}F_{WS}(1 - \sigma_{SQ})(1 - \sigma_{QW}) \right]}$$

$$Z_{QS} = \frac{-(A_S k_S) \left[F_{SQ} + (F_{SR}F_{RW}F_{WQ} - F_{RW}F_{WR}F_{SR})(1 - \sigma_{SQ})(1 - \sigma_{SW}) - F_{SW}F_{WQ}(1 - \sigma_{SW}) \right]}{A_Q \left[1 - (F_{RW}F_{WR} + F_{QW}F_{WQ})\ (1 - \sigma_{SQ})\ (1 - \sigma_{SW}) \right]}$$

$$Z_{QW} = 0$$

Equation (50) has assumed that all the active nodes are reemitting with first-order processes associated with depositions of less than about 500 Å. The rate constants are k_Q, k_R, and k_S for reemission from the QCM, the support structure, and the source, respectively. k_W, the LN_2 shroud reemission rate constant, is considered to be negligible; hence there is no loss of deposition. However, it is still probable that scattering does occur from the cryogenic shroud walls, hence the presence of the wall capture coefficient, σ_{SW}, in equation (50).

Equation (50) computes the QCM deposition considering all the nodes in a fully coupled system. This is the required model when the spacing between the source disk and the QCM is less than about 1 inch. As this spacing is increased, the view factors diminish rapidly until, at distances greater than 2 inches, the QCM is coupled only to the source node. With this configuration, equation (50) is dramatically simplified to the intuitively obvious equation

$$\dot{m}_Q + k_Q m_Q = -F_{QS}\sigma_{SQ}\dot{m}_s. \qquad (51)$$

If the source mass loss rate, $\dot{m}_s$, can be expressed in an integrable form, equation (51) can be readily integrated. Assuming first-order source kinetics of equation (7) for a source with only one component, the integration of equation (51) using equation (7) for the source, rate assuming an initially clean QCM, gives

$$m_Q(t) = \frac{F_{QS}\sigma_{SQ}W_S k_S}{A_s(k_Q-k_e)}\left(e^{-k_s t} - e^{-k_Q t}\right), \text{ g/cm}^2. \qquad (52)$$

Equation (52) shows that the deposition rises to a peak value and then reemits off to zero. The permanently adsorbed layer has been assumed negligible. Figure 7b shows the results of vacuum test data on RTV-566 adhesive compound which represents free molecular conditions. The source was at 125°C while the QCMs and internal support structure were at -20°C. With assumed molecular properties, the "damping" influence of the continuum field can be estimated. A simplified transition model with constant attenuation was used to estimate these effects and compare with free-molecule flow.

The transition flow deposition curve is also shown, with the dotted line, in Figure 7b. The "damping" effect is clear. This is a very real condition when a small cavity surrounds the source as it gasses. For instance, it is highly probable that the total mass loss (% TML) obtained in SRI-JPL tests will be somewhat less than that exhibited in a large vacuum chamber.

References

1. Glassford, A.P.M., "An Analysis of the Accuracy of a Commercial Quartz Crystal Microbalance," paper No. 76-438 presented at the AIAA 11th Thermophysics Conference, San Diego, Cal., 1976

2. "Investigation of Contamination Effects on Thermal Control Materials," AFML-TR-74-218 Final Technical Report, Jan. 1975 (McDonnell Douglas Aerospace Corporation)

3. Buckley, D.H. and Johnson, R.L., "Evaporation Rates for Various Organic Liquid and Solid Lubricants in Vacuum to 10^{-8} Millimeters of Mercury at 55°F to 1100°F," NASA TN D-2081, National Aeronautics and Space Administration, Washington, DC, 1963

4. Bhatnager, Gross, and Krook, in Physical Review (94) pp. 511-525, 1954

5. Lees, L. and Liu, C., "Kinetic Theory Description of Plane Compressible Covette Flow," in Rarefied Gas Dynamics, Supp. 1, 1961

6. Jost, W., Diffusion in Solids, Liquids and Gases, Academic Press, N.Y., 1952

7. Adamson, A.W., Physical Chemistry of Surfaces, John Wiley and Sons, 3rd Ed., 1976

8. Lyubitov, Y., "Molecular Flow in Vessels" in Journal of the Institute of Crystallography, Academy of Sciences of the USSR, Moscow, 1967 (Translation by W. Furrey and J. Wood for the Consultant Bureau, N.Y.)

9. McCune, J.E., Morse, T.F., and Sandri, G., "On the Relaxation of Gases Toward Continuum Flow" in Rarefied Gas Dynamics, p. 115, Supp. 2, Vol. 1, Academic Press, 1963

10. Willis, D.R., "Linearized Covette Flow with Large Knudsen Numbers," in Rarefied Gas Dynamics, p. 429, Supp. 1, Academic Press, 1961

11. Shen, S.F., "A General Transfer Equation Approach for the Transition Regime of Rarefied Gas Flows and Some of its Applications," in Rarefied Gas Dynamics, p. 112, Supp. 2, Vol. II, Academic Press, 1963

12. Patterson, G.N., Molecular Flow of Gases, John Wiley and Sons, N.Y., 1956

13. Nocilla, S., "The Surface Reemission Law in Free-Molecule Flow," in Rarefied Gas Dynamics, p. 327, Supp. 2, Vol. I, 1963

14. Siegel, R. and Howell, J., Thermal Radiation Heat Transfer, McGraw-Hill, 1972

15. Nocilla, S., "On the Interaction Between Stream and Bodies in Free-Molecule Flow," in Rarefied Gas Dynamics, p. 169, Supp. 1, 1961

16. Dushman, S. and Lafferty, J., Scientific Foundations of Vacuum Technique, John Wiley and Sons, Inc., 1962

OUTGASSING RATE OF MULTILAYER INSULATION

A. P. M. Glassford and C. K. Liu
Lockheed Palo Alto Research Laboratory

1.0 INTRODUCTION

Multilayer insulation (MLI) is used extensively in space systems in applications where high thermal resistance plus very light weight are required, such as the insulation of cryogenic systems, and a variety of critical external surfaces such as the back side of radiators. MLI consists of many thermal radiation shields arranged in series, usually interleaved with a low conductance spacer material to reduce thermal conduction between shields. To achieve maximum thermal resistance a great many shields in series are required, and consequently the shields and spacers are made of very lightweight materials so as to avoid excessive weight. Shields are customarily made by vacuum depositing a 500-1000 Å layer of gold or aluminum on one or both sides of Mylar or Kapton substrates with nominal thickness in the range 0.25 - 2.0 mils. The actual thickness of the metal film is adjusted to obtain the desired low emittance value for low radiation heat transfer. Commonly used spacing materials include netting made from silk, nylon or Dacron, or very thin glass fibers, such as 'Tissuglas' and 'Dexiglas' cloths.

Since MLI materials are very light weight, the total mass of MLI is relatively small in most applications. On the other hand, because of the many layers required the total surface area can be extremely high, making MLI a significant outgas source, and, because the surface to volume ratio is high, the major outgas product is water vapor. MLI outgassing can affect overall system performance in two principal ways. Firstly, outgassing products can degrade the performance of the MLI system itself by raising the gas pressure between the shields sufficiently for gaseous conduction to become significant. Insulation degradation can also occur if sections of the MLI are cold enough to cause condensation of outgas products, which will raise the emissivity of the shields and increase the radiation heat transfer. Secondly, as an outgassing source MLI can degrade the performance of associated systems. MLI outgassing can delay the attainment of low pressures in test chambers and vacuum enclosures, while on the ground and in orbit outgas products can condense on optical and thermal control surfaces. This latter situation is probably the most critical current MLI-caused problem area, because of the increasing use of cryogenic sensor systems. Outgassed water vapor can also contribute to the contaminant cloud surrounding an orbiting spacecraft.

In order to minimize or eliminate problems introduced by MLI outgassing, careful design studies must be made for which an outgassing data base is required. The type of data needed for such analyses are outgassing rates per unit area as a function of time for the various temperature histories of specific interest for all materials of interest. However, temperature history can take an infinite variety of forms, so it is impossible in practice to obtain sufficient data to represent all situations. A more practical approach is to obtain isothermal outgassing rate data at various specific temperatures, and then to estimate the rates for other constant or varying temperature situations by use of analytical models. The work reported in this paper is directed towards this end. Isothermal outgassing rate data have been obtained for a range of temperatures for a selection of commonly-used MLI shields and spacers. An attempt has been made to incorporate the data into various previously-proposed analytical models. The reported work is part of an Independent Research program in progress at Lockheed and further data and analyses of the type described will become available from this program in the near future.

MLI outgassing rates have been measured as a function of time in previous programs.(1), (2), (3) These previous measurements were all based upon pressure measurements. This limited the available sensitivity of the measurement, and depended, in principle, on the assumption that the outgas products would not be adsorbed on the apparatus walls. These limitations were aggravated when measurements at temperatures other than ambient were made. In the present tests a technique based on collection of the outgas species on a cooled quartz crystal microbalance (QCM) was used. The technique permits between one and three orders of magnitude better sensitivity and accuracy to be achieved, while variable sample temperature operation presents no additional problem.

2.0 EXPERIMENTAL PROGRAM

2.1 Sample Material

The types and specifications of the materials tested to date are listed in Table 1. Additional shield materials will be tested, including Mylar with a single coat of both aluminum and gold, Kapton with various types of coating and 'Dexiglas' glass fiber cloth.

2.2 Test Schedule

The test schedule to date is shown in Table 2. The range of test temperatures selected for each material includes the ambient temperature of 25°C; a maximum temperature of about 125°C; the lowest temperature for which the outgassing rate is measurable; and as many isotherms

---

1. Keller, C. W., High Performance Thermal Protection Systems," Rept. LMSC A-964947, Dec. 1969, Lockheed Missiles & Space Company, Sunnyvale, California, pp 4.1-4.26.
2. Glassford, A. P. M., Outgassing Behavior of Multilayer Insulation Materials, J. Spacecraft and Rockets, Vol. 7, No. 12, Dec. 1970, pp. 1464-1468
3. Parmley, R. T., Smith, F. J., Glassford A. P. M., Coleman, J., and Stevenson, D. R., Effect of Environment on Insulation Materials - Vols. 1 and 2. NASA-CR 120978 and 120979 (1973), Final Report, Contract NAS 3-14342, Lockheed Missiles & Space Company, Inc.

between these limits are deemed necessary to establish the temperature variation of outgassing rate over this range. A complete set of isotherms has been obtained for double-aluminized Mylar and Dacron net. The remaining materials have been tested only at 25°C so far in order to complete a representative comparison of materials before this conference.

TABLE 1. MULTILAYER INSULATION MATERIAL SPECIFICATIONS

MATERIAL	NOMINAL DIMENSIONS	MANUFACTURER'S NAME/STYLE
Double-aluminized Mylar	-0.25 mils thick	National Metallizing Div.,
Double-goldized Mylar	-500 to 1000Å metal film -8.7x10^{-4} gm/cm^2 (Al) -1.1x10^{-3} gm/cm^2 (Au)	Standard Pack. Corp., Cranbury, N. J. 08512
Dacron Net	-8.7 hex. meshes/cm^2 -6.7 mils thick -6 x 10^{-4} gm/cm^2	Apex Mills 49 W. 37th Street New York, N. Y. 10018 - Style B-4A
Nylon net	-$13\frac{1}{4}$ hex. meshes/cm^2 -9 mils thick -1.4x10^{-3} gm/cm^2	Sears Roebuck (any store)
Silk Net	-32.5 hex. meshes/cm^2 -5 mils thick -6x10^{-4} gm/cm^2	John Heathcoat Company 108 W. 39th Street New York, N. Y. 10018 Silk Illusion Net
Tissuglas (Glass Fiber Paper)	-0.6 mils thick -4.2x10^{-4} gm/cm^2	Pallflex Prod. Corp. Kennedy Drive Putnam, Conn. 06260 - Style 60G

TABLE 2 - TEST SCHEDULE

Material	Nominal Samples Area - In^2	Test Temperatures - $^\circ C$
Double-Aluminized Mylar	~1600	-54; -34; -8; 25; 50; 81; 121
Double-Goldized Mylar	1728	25
Dacron Net	~3000	2.5; 12/5; 25; 57.2; 126
Silk Net	1536	25
Nylon Net	1903	25
Tissuglas	3056	25

The duration of each isothermal test was one week. This period represented a balance between obtaining adequate long term data, and completing the test program in a reasonable time. One week permits a convenient practical turn-around schedule, while the data for this period can be reliably extrapolated to several weeks duration.

2.3 Apparatus Description

The experimental outgassing rate measurements were made by using the Thermal Analysis Apparatus (TAA), shown in Figure 1. The principal components of the TAA are a sample pot, a collector QCM, and a system of shrouds which are thermally grounded to a liquid nitrogen reservoir. The sample pot is a cylindrical container with a small orifice in one end. Its base contains an electrical resistance heater and a platinum resistance thermometer. It is supported by a strut attached to the cooled shrouding, which serves as a thermal link. The sample pot temperature can be controlled to any value above 120°K by balancing the electrical heat input to the pot against the heat leak along the strut to the shrouds.

AD-A070 386 AIR FORCE MATERIALS LAB WRIGHT-PATTERSON AFB OH F/G 22/2

PROCEEDINGS OF THE USAF/NASA INTERNATIONAL SPACECRAFT CONTAMINA--ETC(U)

1978 J M JEMIOLA

UNCLASSIFIED AFML-TR-78-190 NL

2 OF 13
AD
A070386

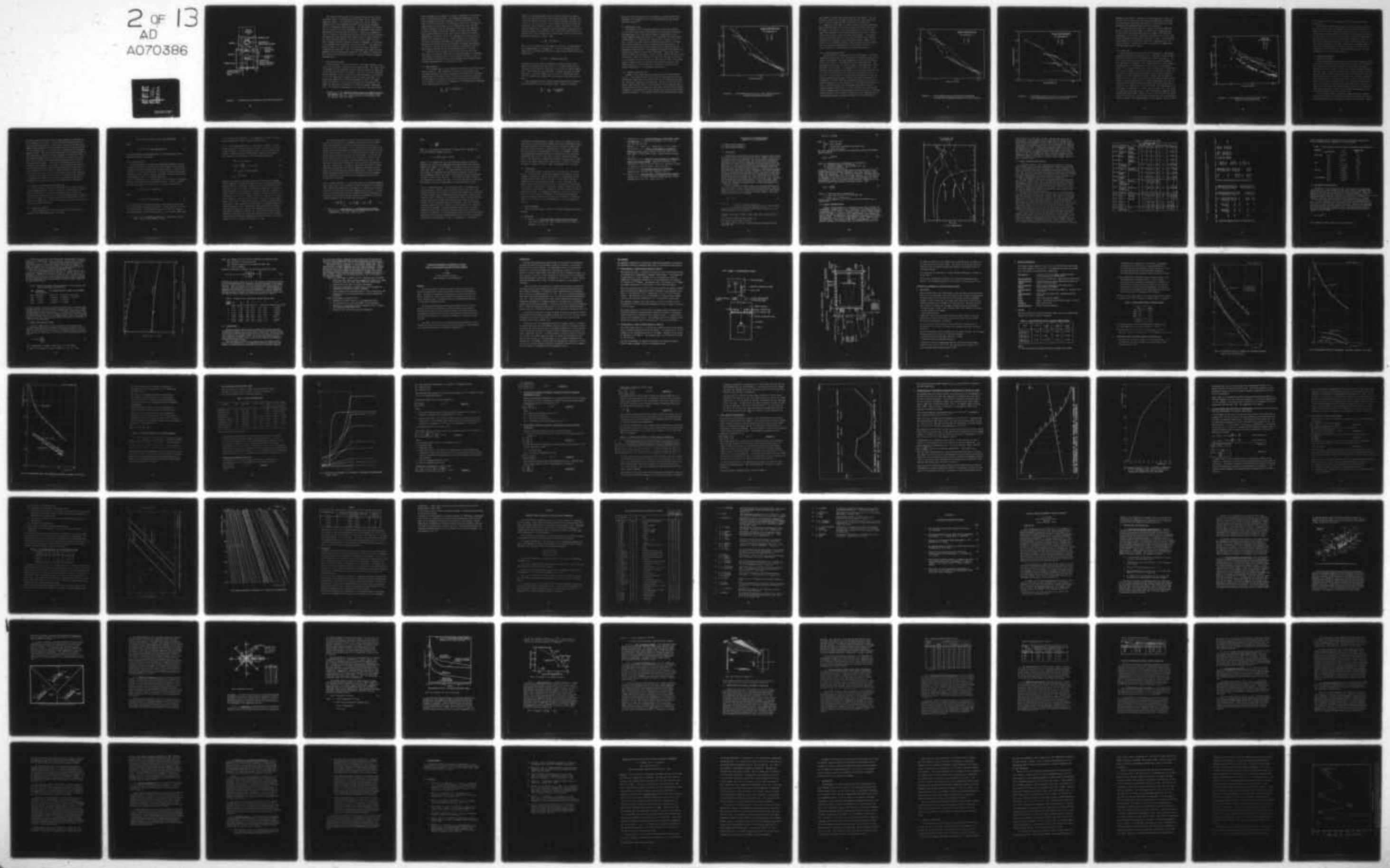

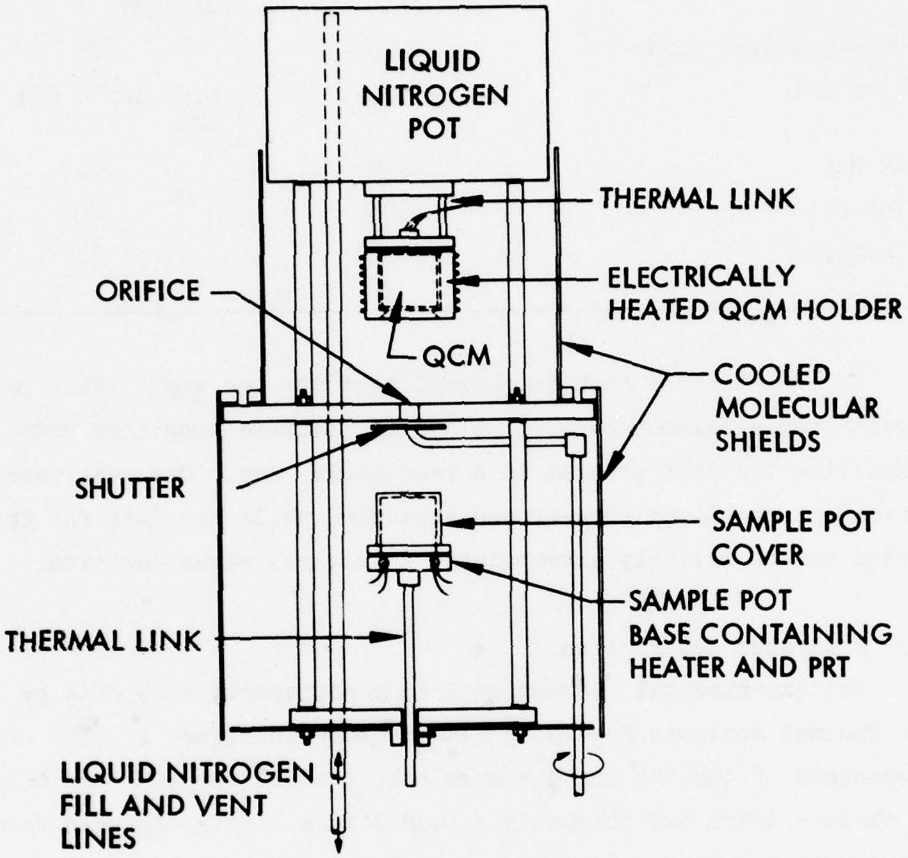

FIGURE 1 - SCHEMATIC OF THERMAL ANALYSIS APPARATUS

The collector QCM, mounted in an aluminum holder with an electric resistance heater, is positioned along the normal line of sight of the sample pot orifice. The QCM views the sample pot orifice through a shuttered hole in the shielding structure, permitting the impinging flux to be interrupted when appropriate. The QCM normally cools naturally to about 84°K, at which temperature all significant outgas species impinging on its surface will be condensed. However, its temperature can be controlled to any temperature between 84°K and 420°K by balancing electrical heat input against heat leakage along its support struts to the liquid nitrogen reservoir. The QCM is a Celesco Model 700 unit, which contains a built-in platinum resistance thermometer. The accuracy of this QCM has been established in a previous work.(4) The apparatus shown in Figure 1 is enclosed in a bell jar which can be evacuated to a pressure less than $2x10^{-7}$ torr. The fundamental data output from the apparatus are QCM frequency and temperature, and sample pot temperature. These data are recorded continuously as a function of time by automatic instrumentation.

2.4 Experimental Procedure

At the beginning of the test the area of the sample material is measured, and the sample is inserted in the sample holder. The sample holder is assembled with the apparatus, and the distance between the sample pot orifice and the QCM surface is measured. The bell jar is then evacuated and the apparatus cooled by filling the liquid nitrogen pot. Evacuation to 10^{-5} torr takes about 3 minutes, while cooldown of the QCM to its equilibrium temperature of 84°K and attainment of $2x10^{-7}$ torr takes about 40-60 minutes. As soon as the apparatus has been evacuated the sample pot temperature is adjusted to a selected constant temperature value. Above-ambient temperatures can be reached in less than one-half

---

4. Glassford, A. P. M., Analysis of the Accuracy of a Commercial Quartz Microbalance, Progress in Astronautics and Aeronautics, Volume 56, Allie M. Smith, Ed., American Institute of Aeronautics and Astronautics, New York, (1977).

hour by heating the pot rapidly, followed by adjustment of the electric power to the equilibrium value. For subambient temperatures the pot cools naturally with the main apparatus, reaching temperatures of the order of -50°C in two hours. The experiment consists of collecting the outgas product from the sample pot by condensation on the cold QCM. Collection begins as soon as the QCM has cooled below the temperature at which the outgas products can condense. The main outgas product from most MLI materials is water vapor, which condenses in vacuum at temperatures below about 155°K. This temperature is reached about 25 minutes after beginning the test. Outgas products are collected for one week, during which time sample pot temperature control, liquid nitrogen pot refilling and data recording are performed automatically. At the end of the test period data recording is terminated, electric power inputs switched off, and the apparatus allowed to warm up.

From time to time during a test, as well as at the end of the test period, the QCM was warmed up in a controlled manner, to determine the evaporation characteristics of the accumulated deposit. This involves heating the QCM at about 1-2°K per minute and recording the QCM frequency and temperatures as a function of time.

2.5 Data Reduction

It is assumed that all the molecular flux striking the 84°K collector QCM is condensed. This assumption is correct for H_2O, which is the principal component, and almost certainly possesses the lowest molecular weight among the outgassed species. The error introduced by equating the molecular flux collected by the QCM to the absolute flux striking it is therefore considered to be negligible. The molecular flux impinging on the QCM is therefore given by

$$\frac{\dot{m}}{A}_Q = \frac{df}{dt} \times S \text{ gms/cm}^2\text{/sec}$$

where f is the QCM frequency, and S is the QCM sensitivity constant (4.43×10^{-9} gm/cm^2/Hz for the Celesco Model 700A QCM). The mass flux at the QCM surface is related to the total mass leaving the sample pot orifice, $\dot{m}_o$, by a view factor. For an infinitely thin orifice the distribution of flux leaving it should be cosine. The effect of finite orifice thickness is to reduce the flux at large angles and increase it along the normal. The magnitude of this effect has been measured in a previous test, and is allowed for by introducing a factor of 0.98 in the equation relating $\dot{m}_o$ to $(\dot{m}/A)_Q$. Thus

$$\dot{m}_o = \frac{\dot{m}}{A}_Q \times (0.98 \pi r^2)$$

where r is the distance from the sample pot orifice to the QCM surface. The outgassing rate of the sample, $\dot{Q}$, is found by dividing $\dot{m}_o$ by the sample area. The area used is the total exposed area, which is twice the nominal area.

$$\dot{Q} = \dot{m}_o/(2 \times \text{nominal sample area})$$

All data are recorded from the beginning of evacuation and plotted against time elapsed since this event. The evacuation times given in this paper thus include the time required to adjust the sample temperature to the selected equilibrium value. Although this time can range from zero, for the 25°C sample, up to 2 hours for temperatures below -50°C the average time required for equilibrium was less than one-half hour.

The frequency/time data obtained during QCM warm-up are related to the evaporation rate of the collected deposit, $(\dot{m}_e/A)$, as follows

$$\frac{\dot{m}_e}{A} = -\frac{df}{dt} \times \frac{(4.43 \times 10^{-9})}{0.81}$$

The factor 0.81 is introduced in this equation to allow for the flow resistance of the aperture in its case through which the QCM crystal views the exterior.(4)

2.6 Experimental Data

The results of the experiments conducted to date are discussed below in three main groups - measurements at 25°C on several materials, and measurements for a comprehensive range of temperatures on both double-aluminized Mylar and Dacron net. In all cases, the data consist of measurements of outgassing rate versus time for a period of 6 to 7 days. At the end of this period the QCM was slowly heated to identify the collected components by their reevaporation characteristics. In all cases, the principal outgas component was H_2O, identified by its evaporation characteristics. The evaporation of water from a QCM of this type has been studied in some detail previously(4) and so H_2O can be identified with some certainty. In most tests no species but water could be detected. Since the sensitivity of this test is about 0.5 per cent it is concluded that in most cases at least 99.5 per cent of the outgas species collected under the specified test conditions was H_2O. The single exception to this conclusions -- Dacron net tested at above ambient temperatures -- is discussed in Section 2.6.3.

2.6.1 Ambient Temperature Data

Figure 2 shows outgassing rate versus time for several materials at 25°C. It is apparent that Dacron net has a significantly lower outgassing rate than either silk or Nylon net, and is clearly the preferred net, based upon outgassing considerations. The data for the three nets suggest that detailed studies of the variation of the outgassing rate of silk and Nylon net with temperature would serve little practical purpose. Tissuglas is a commonly used spacer, and has been used in several flight systems by Lockheed. It is generally used in MLI systems having a higher

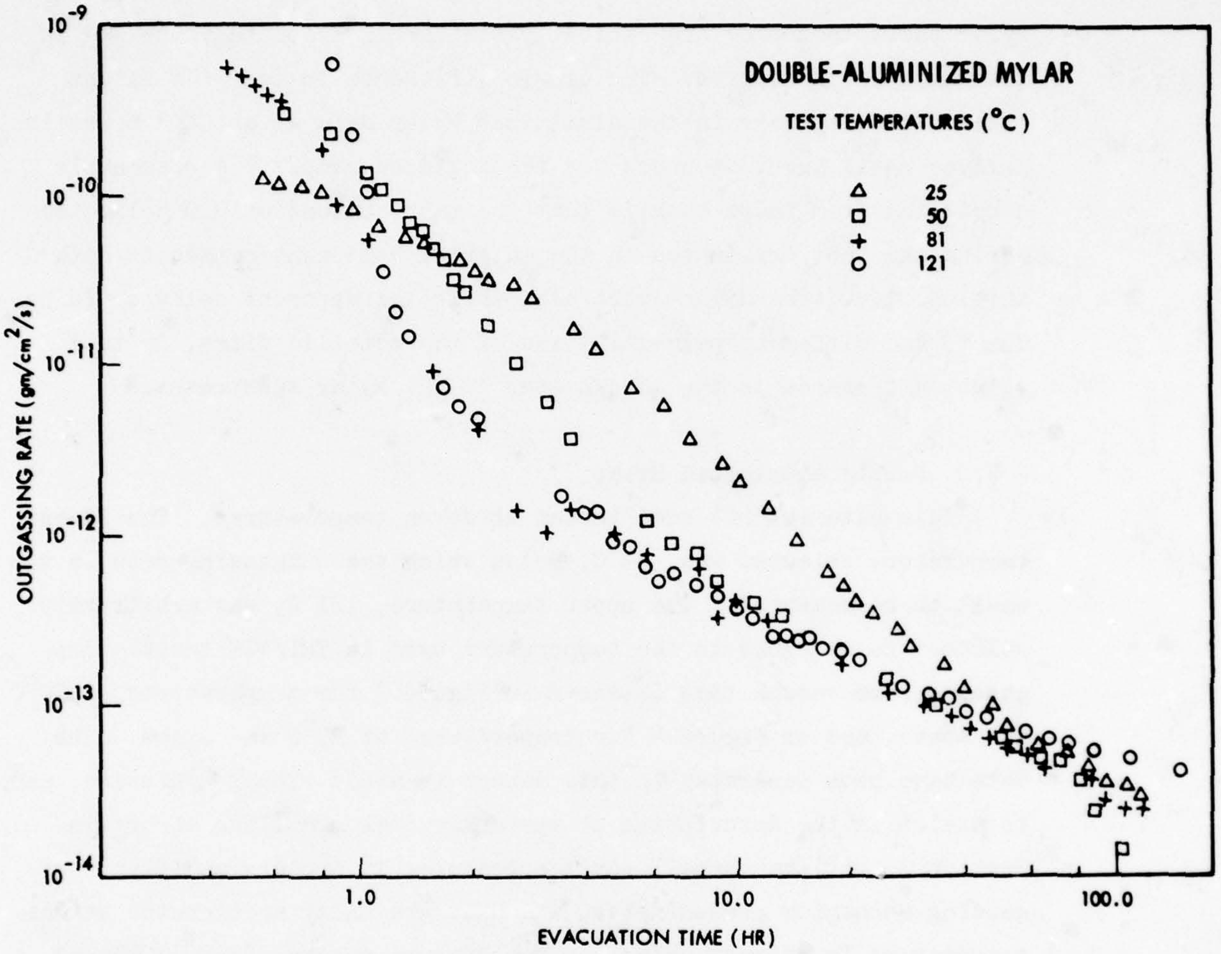

FIGURE 2 - OUTGASSING RATE AT 25°C FOR VARIOUS MULTI-LAYER INSULATION MATERIALS

total number of layers than systems which use net spacers. The data therefore indicate that Tissuglas-spaced MLI will outgas between one and two orders of magnitude more than Dacron net-spaced MLI.

Comparison of the data for double-goldized and double-aluminized Mylar shows that they are basically similar in absolute value and in the shape of the curves. The single difference is that the slight 'knee' which appears in the aluminized Mylar data at about 3 hours is delayed until about 4½ hours for the golidzed sample. A reasonable conclusion from these data is that the major amount of H_2O collected during the test originates in the material component common to both shields, i.e., the Mylar substrate, while the apparent delay could be due to the different permeabilities of the metallic films, or to a slight difference in the thicknesses of the Mylar substrates.

2.6.2 Double Aluminized Mylar

This material has been tested at seven temperatures. The lowest temperature selected was -54°C, below which the outgassing rate is too small to be measured. The upper temperature, 121°C, was arbitrarily selected to be close to the temperature used in TML/VCM tests. Outgassing rate versus time is shown in Figure 3 for temperatures of 25°C and above, and on Figure 4 for temperatures of 25°C and below. The data have been separated in this manner to avoid visual confusion, and to assist in the description of the analytical modelling effort in Section 3. At the three lower temperatures it appears as if one outgassing mechanism predominates, which is gradually accelerated as the temperature is raised. When the temperature reaches 25°C, a second mechanism appears to become significant at times greater than about 14 hours. Further raising of the temperature accelerates the first mechanism still further until it is over within an hour, and several slower mechanisms now become predominant in the time period of interest. Further heating does not produce a reduction in the outgassing rate at long evacuation times, as would be expected if a limited number of

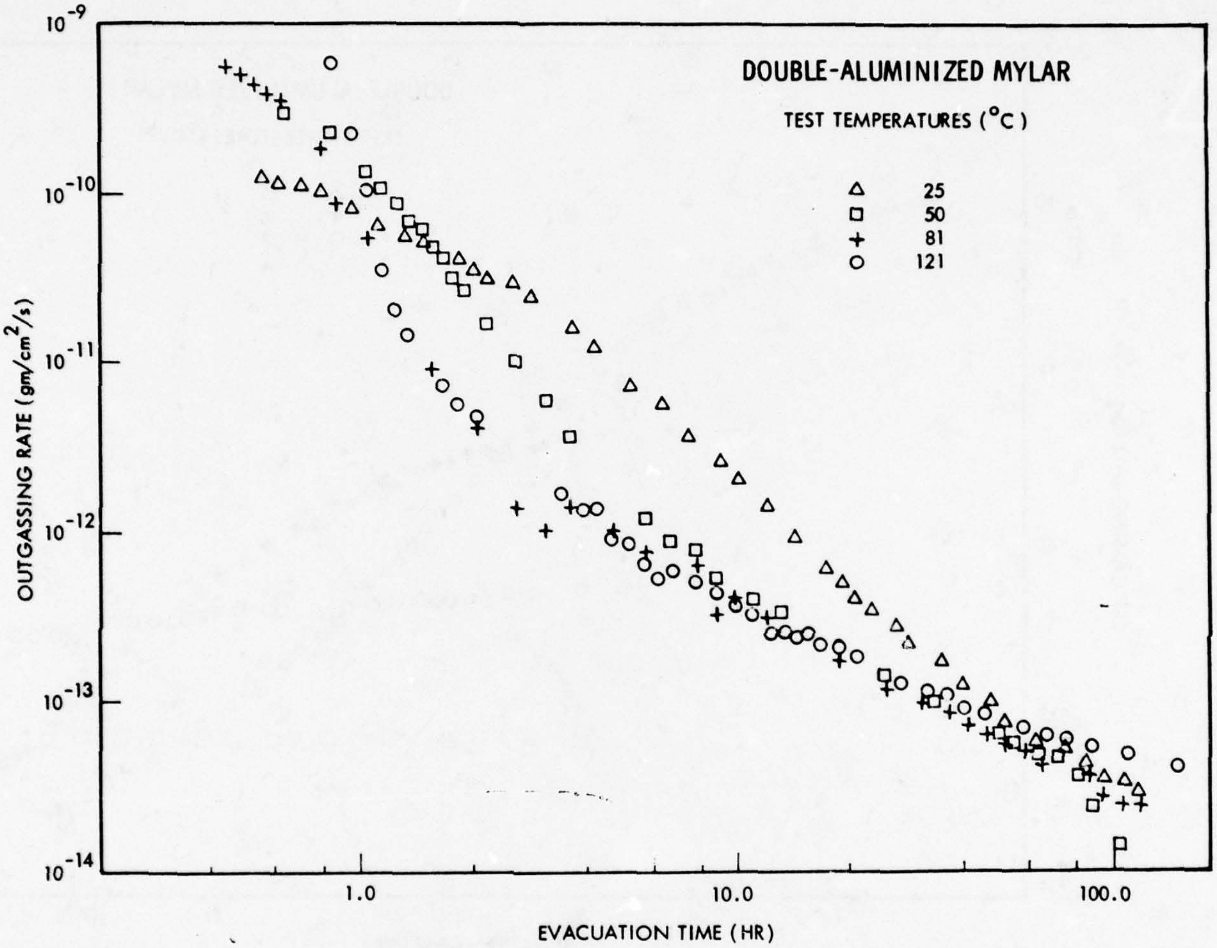

FIGURE 3 - OUTGASSING RATE OF DOUBLE-ALUMINIZED MYLAR FOR TEMPERATURES OF 25°C AND ABOVE

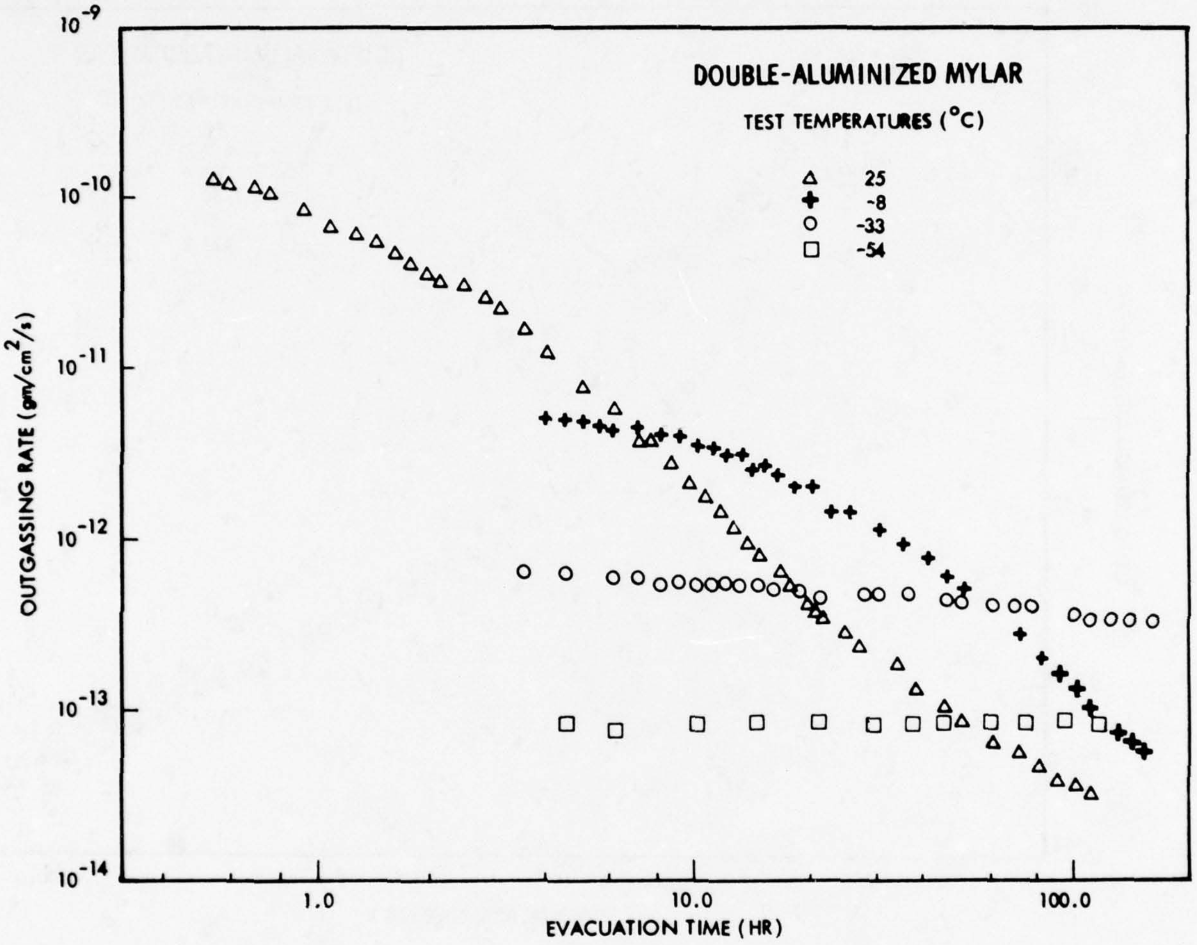

FIGURE 4 - OUTGASSING RATE OF DOUBLE-ALUMINIZED MYLAR FOR TEMPERATURES OF 25°C AND BELOW

mechanisms were present. Instead, the outgassing rates at times over 50 hours seem to vary little with increasing temperature, indicating the progressively increasing significance of previously minor outgas mechanisms with presumably higher activation energies.

Two short additional tests were conducted on double-aluminized Mylar to assess the effectiveness of bakeout on the outgassing rate. In these tests the samples were heated in vacuum to 45°C and 100°C, respectively, for 24 hours, after which they were cooled to 25°C, and their outgassing rates measured for another 24 hours. Preconditioning in this manner at 45°C and 100°C reduced the outgassing rate at 48 hours by factors of ten and two hundred, respectively, compared with the unpreconditioned 25°C data.

2.6.3 Dacron Net

This material has been tested at five temperatures. The maximum temperature range was selected according to the same criteria as were described in Section 2.6.2. The data are presented in Figure 5. For most of the temperature range the isotherms are displaced upwards as the temperature is increased. This slope, and the associated temperature dependence, is characteristic of diffusion in a heterogeneous system, i.e., system in which there could be variations in either diffusion flow path length or activation energy for diffusion, or both. The (-1) slope is obtained when the diffusion time constant, which can depend on flow path length and activation energy, and the amount of absorbed gas with a given time constant have an inverse linear relationship. At longer evacuation times or higher temperatures this type of relationship eventually produces an exponential relationship which is evident in the early portion of the 126°C data. The outgassing rate at later times for 126°C has a -1 slope, and is probably due to the onset of outgassing a different species. This conclusion is supported by QCM warm-up data which indicate that for tests at 25°C and below the outgas species is at least 99.5 per cent H_2O, in common with the other materials. At 57°C, however, other species appear in small amounts, while at 126°C

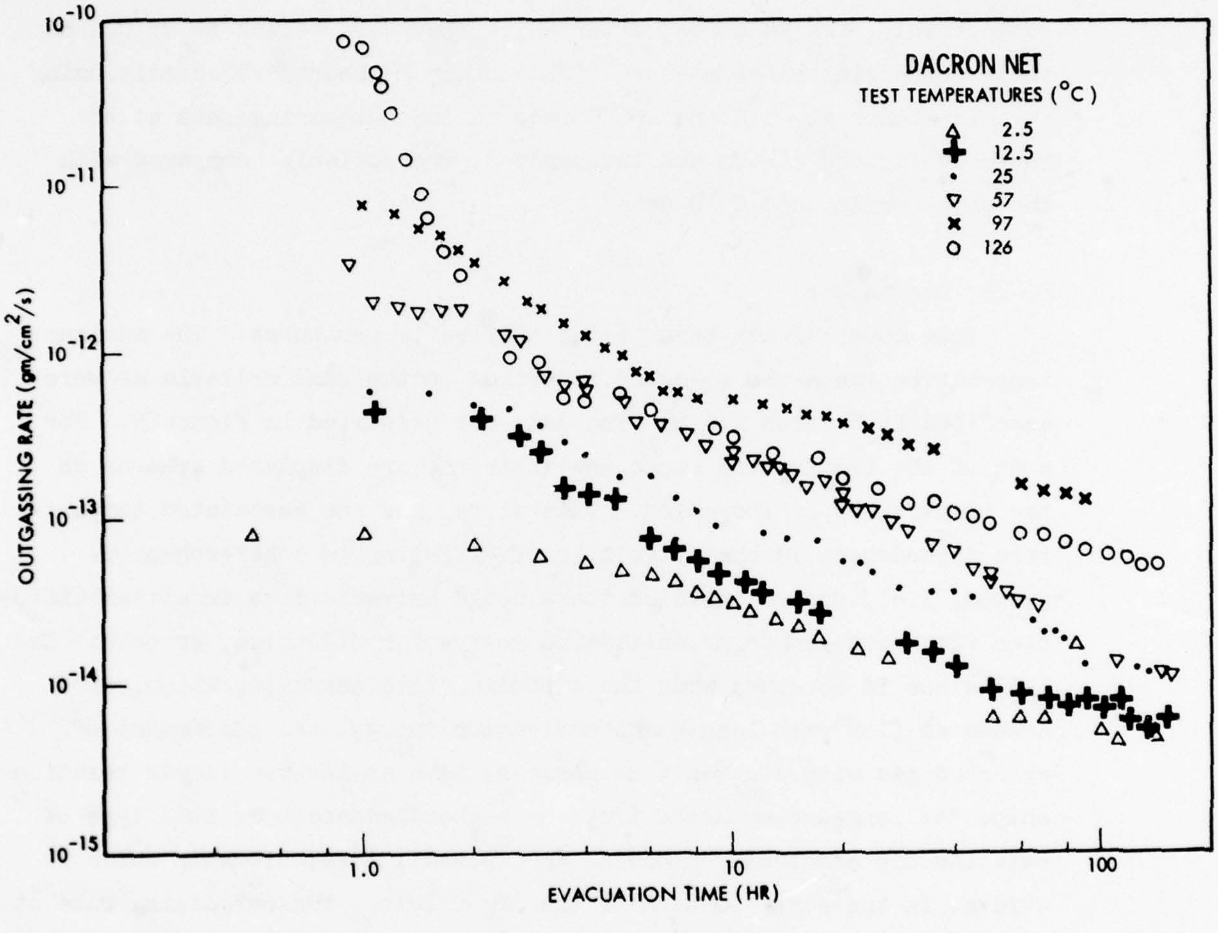

FIGURE 5 - OUTGASSING RATE OF DACRON NET FOR A RANGE OF TEMPERATURES

two distinct species other than H_2O were found in very significant proportions.

The QCM warm-up data indicate that at 126°C the proportions of H_2O and the two other species are approximately 54, 16 and 30 per cent respectively, in order of decreasing volatility. At 57°C the two less volatile species were difficult to separate by QCM warm-up, and amounted to less than 10 per cent of the total outgas product (the remaining 90 per cent being H_2O). For both isotherms the volatities of these two additional species were difficult to estimate accurately because of the small deposits obtained on the QCM. However, it is estimated that the 16 per cent component would be totally condensible at -90°C, and non-condensible on a -45°C surface. Similar figures for the 30 per cent component are 0°C and 40°C, respectively.

3.0 ANALYTICAL MODELLING

3.1 General Observations

Although analytical models based on time physical outgas-controlling mechanisms are unquestionably more desirable for predicting outgassing rate than empirical models, development of such models is probably impractical if the sole aim is to solve specific and immediate program problems. This is because it is necessary to generate a very large data base from which to develop the models, while these data may be more than sufficient themselves to satisfy the program need. Further, if analytical representations of the data are desired, it will be acceptable in many cases, as well as being simpler, to use empirical expressions instead of such models to represent the experimental data. However, insight into these outgas controlling mechanisms can only be obtained by developing expressions in terms of relevant physical parameters, and this is the ultimate goal of the present work.

The two main processes controlling outgassing are bulk diffusion and surface desorption. Theoretical expressions for these processes are readily available, but are difficult to apply to MLI materials. These materials characteristically have very small dimensions from bulk center to surface, which tends to blur the distinction between bulk processes and surface processes. In the case of the nets and glass fiber papers normal variations in fiber diameter, and the micropore structure of their surfaces can be of the same order of magnitude as the nominal diameter itself. The same considerations apply to the Mylar and Kapton shield materials, but with the added influence of the metallic film. In the nominal thickness range of 500 Å to 1000 Å the film is not continuous, but is based on an island structure which grows into a film by bridging between islands. In the case of aluminum an oxide film is formed on this structure. The metallic film complicates the situation by providing an added diffusion resistance for material diffusing out from the interior of the substrate, while providing a complex microstructured surface for physical adsorption and possibly weak chemisorption in the oxide film. The net effect on both spacers and shields is to complicate the diffusion and desorption processes by introducing distributions of activation energies and characteristic dimensions.

3.2 Analysis of Double-Aluminized Mylar Data

A first attempt at analytical representations was made on data for double-aluminized Mylar. Figure 4 shows that for temperatures of 25°C and below, processes of longer time constants appear to have been suppressed sufficiently such that a single mechanism dominates outgassing for the -54°C and -34°C isotherms and for the early part of the -80°C and 25°C isotherms. This portion of the data was therefore selected for the initial analytical study.

3.2.1 Empirical Equation

Before attempting to develop a physical model the early data of Figure 4 were fitted empirically, as follows

$$\dot{Q} = \left((4.76 \times 10^{-7})/t_c \right) \exp(-t/t_c) \text{ gms/cm}^2\text{/sec} \quad (1)$$

where

$$t_c = 2.8 \times 10^{-6} \exp(12600/RT) \text{ secs} \quad (2)$$

This equation gives the outgassing rate of the subject data with an accuracy of about ± 25 per cent.

3.2.2 Physical Models

As noted in Section 3.1 the basic outgassing mechanisms of diffusion and desorption are confused in the case of MLI by the possibility of variable activation energies and material geometry. Because of this situation it is relatively difficult to predict in advance which physical models are more likely. Hence a succession of physical models have been examined in order of increasing complexity.

3.2.2.1 Simple Desorption. This process is the evaporation of adsorbed molecules from surface sites with uniform energy. It can be shown(5) that the outgassing rate by this process, $\dot{Q}$, can be represented by

$$\dot{Q} = \frac{C_o}{\tau} \exp(-t/\tau) \text{ gm/cm}^2\text{/sec} \quad (3)$$

where

$$\tau \sim 1.6 \times 10^{-13} \exp(E_a/RT) \text{ secs} \quad (4)$$

C_o is the initial of adsorbed gas surface concentration, gms/cm^2 and E_a is the activation energy for desorption. These equations are clearly similar in form to the empirical equations (1) and (2). However, the experimentally measured time constant, t_c, is very much larger than

5. de Boer, J. H., The Dynamical Character of Adsorption, Clarendon Press (Oxford), 1953, Chapters 3 and 4.

the theoretical time constant, τ. Consequently, the simple desorption model would predict a far too rapidly decaying rate.

3.2.2.2 Multi-Energied Desorption. This model is similar to simple desorption, except that the activation energy is allowed to vary with surface coverage. It has been widely reported in the literature that in many situations activation energy varies linearly with coverage. This situation can be expressed by the following expressions

$$E(\theta) = E_1 + (E_2 - E_1)\theta \tag{5}$$

$$\dot{Q}(\theta)d\theta = \frac{C_o\, d\theta}{\tau(\theta)} \cdot \exp(-t/\tau(\theta)) \tag{6}$$

$$\tau(\theta) = 1.6\text{x}.10^{-13}\exp(E(\theta)/RT) \tag{7}$$

$$\dot{Q}_T = \int_o^1 \dot{Q}(\theta)d\theta \tag{8}$$

Equation (5) expresses the linear variation of the activation energy, E, with normalized coverage distribution function θ between minimum and maximum energies of E_1 and E_2. Equation (6) is the desorption rate of molecules at time t from sites of activation energy $E(\theta)$, with initial surface concentration C_o gms/cm^2 and residence time $\tau(\theta)$. Equation (7) relates $\tau(\theta)$ to activation energy. Equation (8) states that the total outgassing rate, $\dot{Q}_T$, is the integral of $\dot{Q}(\theta)$ with respect to the distribution function. A good fit was obtained to the 25°C isotherm using C_o equal to 10^{-6} gms/cm^2, and E_1 and E_2 equal to 21750 and 24000 cals/mole, respectively. These energies are considered to be improbably high for physical adsorption, but could indicate weak chemisorption. However, when the model was used to predict the outgassing rate for the lower temperature isotherms the correct curve shapes were obtained, but the magnitude of the reduction in rate with temperature was far too great - by as much as three orders of magnitude for the -54°C case. This large change is due to the energy values being too high.

The model was modified to account for the possibility of surface mobility of adsorbed gas. As molecules are desorbed from the surface sites some high energy sites will become vacant before all the low energy sites have been emptied. It is conceivable that molecules still adsorbed in lower energy sites could migrate across the surface to these vacated higher energy sites. This effect would tend to reduce the outgassing rate and extend the process for given values of E_1 and E_2, and should therefore permit a curve fit to be obtained for the 25°C data with lower values for E_1 and E_2. This modification was made to the model and the new values obtained for E_1 and E_2 were 21,500 and 23,500 cals/mole, respectively. As expected, this model did predict a smaller reduction in outgas rate with lowered temperature than the previous model, but the difference was insignificantly small. Since no further simple reasonable modifications to the adsorption model were apparent it was concluded at this point that the outgassing process was not surface-force controlled.

3.2.2.3 Simple Diffusion. It is possible that the outgassing mechanism under study could be due to diffusion through the Mylar and the metallic film of molecules originating in the Mylar or to diffusion of molecules sorbed in the oxide film, as has been suggested by Dayton.(6) In either case, if the diffusion process has a uniform activation energy, and if the material through which the gas diffuses is an infinitive plane with constant thickness, 2L, the outgas rate is given by

$$\dot{Q} = \frac{\pi}{8} \frac{C_o L}{\tau} \sum_{m=o} \exp \left[- \frac{\pi^3}{64\tau} \cdot (2m+1)^2 \, t) \right] \qquad (9)$$

---

6. Dayton, B. B., Outgassing Rate of Contaminated Metal Surfaces, Transactions of the Eighth National Vacuum Symposium, (1961), Pergaman Press, New York, (1962), pp 42-57.

where

$$\tau = \frac{\pi L^2}{16D} \tag{10}$$

Here C_o is the initial concentration of outgas species, gms/cm^3, and D is the diffusion constant, given by

$$D = D_o \exp\,(-E_d/RT) \quad \text{cm}^2/\text{sec} \tag{11}$$

where D_o is a constant and E_d is the activation energy for diffusion. Equation (9) expresses an outgassing/time characteristic whose initial segment shows $\ell n\dot{Q} = (-\frac{1}{2}\ \ell n\ (\text{time}) + (\text{constant}))$ while for long evacuation times $\ell n\dot{Q} \sim (\text{time})^{-1}$. For simple diffusion, cooling the sample will reduce the outgassing rate and extend the duration of the $(-\frac{1}{2})$ power dependency regime, but under no circumstances can the characteristic have a slope of less than $(-\frac{1}{2})$. It is clear from Figure 4 that as the temperature is reduced the slope of the data approches zero and hence they cannot possibly be representable by a simple diffusion model.

3.2.2.4 Complex Diffusion. The foregoing process of elimination has led the authors to believe that the correct model is some form of the diffusion equation (9), modified to include some combination of nonuniform activation energy, and/or nonuniform material thickness. Three possible scenarios exist: diffusion of gas originating only in the Mylar with and without significant diffusion resistance from the metallic film, and diffusion of gas originating only in the metallic oxide film micropore structure (Dayton's model). Analysis of these situation is in progress at the time of writing. The basic approach being used is to rewrite equations (9) and (11) to include a variable value of E_d, either as a function of location, or of the instantaneous value of local concentration. Variations in the predicted outgassing rate can be effected by manipulating the form of the variation of E_d, or by varying D_o. It has been found that such manipulations do permit curves to be obtained with the same slopes as the data and also having the correct relationship between isotherms although some difficulty has been encountered in predicting the correct absolute value of outgassing rate. It has been concluded that the extent of the manipulations of E_d and D_o required to obtain this qualitative agreement excludes the possibility of the outgassing originating only from the oxide film, and hence excludes the Dayton model. Work will now be concentrated on further exploring the possibilities of the single medium model - Mylar alone - as well as extending the model to include two media - Mylar and aluminum film - in series.

4.0 CONCLUSIONS

The work performed to date has led to two very clear cut conclusions. On the one hand the QCM-based apparatus has proven to be very accurate, reproducible, reliable in generation of outgassing data and economical in personnel time to operate. It has been in continuous operation for six months without failure. On the other hand, only limited success has been achieved so far in identifying a viable analytical model for predicting the outgassing isotherms of even one portion of the data for one material. Although the effort involved is, indeed, generating insight into fundamental mechanisms, there is a little doubt that, given the excellent performance of the experimental apparatus, the most economical method of determining the dependence of outgassing behavior of a material on time and temperature is still to measure it directly.

5.0 ACKNOWLEDGEMENTS

This work was performed as part of a Lockheed Independent Research Program.

6.0 REFERENCES

1. Keller, C. W., High-Performance Thermal Protection Systems," Rept. LMSC A-964947, Dec. 1969, Lockheed Missiles & Space Co., Sunnyvale, Ca., pp 4.1 - 4.26.

2. Glassford, A. P. M., Outgassing Behavior of Multilayer Insulation Materials, J. Spacecraft and Rockets, Vol. 7, No. 12, Dec. 1970, pp 1464-1468.
3. Parmley, R. T., Smith, F. J., Glassford, A. P. M., Coleman, J., and Stevenson, D. R., Effect of Environment on Insulation Materials - Vols. 1 and 2, NASA-CR 120978 and 120979 (1973), Final Report, Contract NAS 3-14342, Lockheed Missiles & Space Co., Inc.
4. Glassford, A. P. M., Analysis of the Accuracy of a Commercial Quartz Crystal Microbalance, Progress in Astronautics and Aeronautics, Volume 56, Allie M. Smith, Ed., American Institute of Aeronautics and Astronautics, New York, (1977).
5. de Boer, J. H., The Dynamical Character of Adsorption, Clarendon Press (Oxford), 1953, Chapters 3 and 4.
6. Dayton, B. B., Outgassing Rate of Contaminated Metal Surfaces, Transactions of the Eighth National Vacuum Symposium, (1961), Pergaman Press, New York, (1962), pp 42-57.

APPLICABILITY OF THERMOGRAVIMETRIC[+] ANALYSIS TO SPACE CONTAMINATION

J.A. Muscari, Martin Marietta
R.O. Rantanen, Martin Marietta
N.J. Pugel, Denver University

1.0 INTRODUCTION

Contamination source kinetics is far from the stage of simply stating a few general laws to explain the entire process. However, there are common aspects in all source outgassing that lend to general classification and semiquantitative interpretation. Many investigators have measured outgassing rates of nonmetallic materials and have devised equations to approximate the rates at other temperatures and time durations other than those tested.[1,2] The spacecraft materials screening test[3] measuring the Total Mass Loss (TML) and the Collected Volatile Condensible Materials (CVCM) has become a standard method (ASTM E595) to quantitatively measure the outgassing of materials and their condensables in a vacuum environment. While this is an appropriate screening procedure to categorize materials, it does not provide enough source rate kinetic parameters to assess detail contamination problems. The need for higher temperature data resulting from laser radiation impingement has reinforced the need for a test method to obtain source parameters over a wide temperature range. Isothermal thermogravimetry, as a test method, appears to be too time costly taking from at least several days to several weeks. Dynamic thermogravimetry provides all the needed parameters within a few hours and appears to be a valid test technique.

Current contamination modeling theory has postulated applying kinetic rate theory to predict source outgassing characteristics. Once the source parameters are known, source rates are combined with mass transport equations, deposition rates, and finally reemission rates to assess the degree of deposition that will degrade spacecraft surfaces. The nature of the kinetic process is of the form

$$-\frac{dz}{dt} = \Theta\, f(z) \tag{1}$$

where Θ = the empirical rate constant and
$f(z)$ = a specific form which depends on reaction order, geometry of the sample and holder, heating rate, etc.

Applying this directly to polymeric source kinetics, results in the following expression for mass loss rate

---

[+] This work was primarily funded by AFML, WPAFB under contract F33615-76-C-5212.

[1] J.J. Scialdone, NASA TN D-8294, August 1976.

[2] T.M. Heslin, NASA TN D-8471, May 1977.

[3] R.F. Miraca and J.S. Whittick, Stanford Research Institute N67 40270, September 1967.

$$\dot{m}_s(t,T) = -k_s(T)m_s^n \quad (2)$$

where $\dot{m}_s$ = mass loss rate,
$k_s(T)$ = rate constant,
m_s = active mass remaining in the source, and
n = order of reaction.

The rate constant can be related to the temperature using the Arrhenius equation given by

$$k_s(T) = Ae^{-E/(RT)} \quad (3)$$

where A = frequency factor (independent of temperature),
E = activation energy of the process,
R = molar gas constant, 1.986 $\text{cal}\cdot\text{mole}^{-1}\cdot\text{K}^{-1}$, and
T = absolute temperature, K.

In general, a low activation energy means a reaction whose rate is only slightly affected by changing temperature and a high E means a large change with temperature. Most nonmetallic spacecraft materials exhibit a mass loss characteristic of a first order reaction. The mass loss rate is dependent on the first power of the mass remaining that is available for outgassing. The volatile mass remaining at any temperature can be determined by raising the temperature high enough to exhaust all of the volatile component and taking the difference in mass. Thus

$$k_s(T) = \frac{\dot{x}}{(a_o - x)} \quad (4)$$

where $\dot{x}$ = mass loss rate at temperature T,
a_o = total mass available for outgassing, and
x = mass loss at temperature T.

Notice that the quantity (a_o-x) is the active mass remaining, m_s, of equation (2).

2.0 DYNAMIC THERMOGRAVIMETRY

Dynamic thermogravimetry is a continuous process that involves the measurement of sample weight as the temperature is increased by means of a programmed rate of heating. The output from a typical thermogravimetric analyzer consists of weight loss (TGA), expanded TGA (ten times), derviative of TGA (DTG), temperature, test chamber pressure, and residual gas analysis (RGA). The derivative thermogravimetry transforms electronically the weight data into a rate of weight change. Figure 1 shows a typical thermogravimetric data output for RTV-566 silicone adhesive. For our Mettler I system, in the dynamic mode, the temperature rate can be set

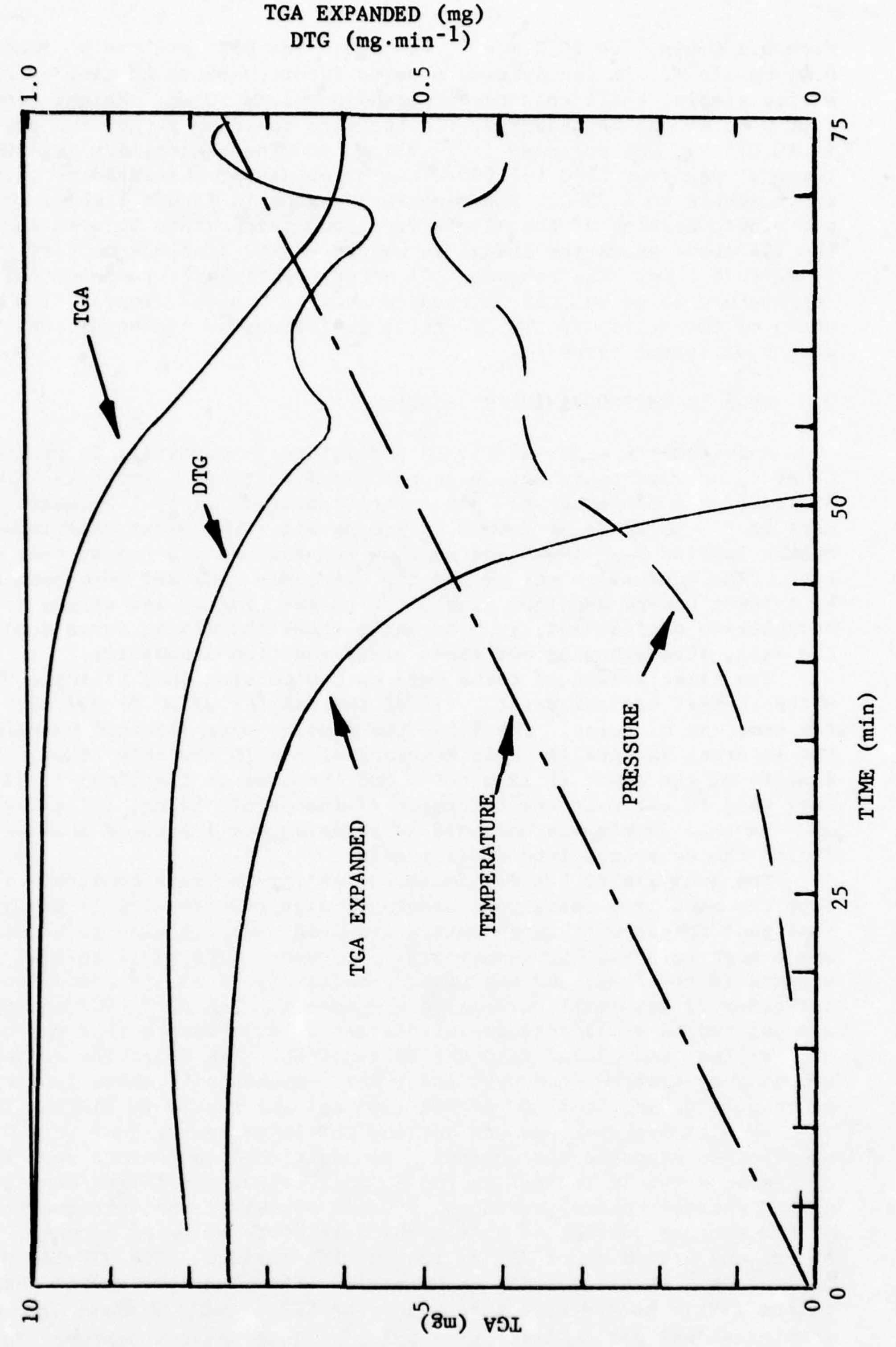

Figure 1 Thermogravimetric Data Output For RTV-566

from $0.2^{\circ}C \cdot min^{-1}$ to $25^{\circ}C \cdot min^{-1}$, at $\pm 4^{\circ}C$. The DTG data can be read to $0.01\ mg \cdot min^{-1}$. In the dynamic mode to insure uniform heating of the entire sample, small amounts are used, normally 10 mg. Weight losses from 0 to 1g can be measured. In the zero to 10 mg range; the precision is ±0.015 mg, the accuracy is ±0.03 mg, and the readability is 0.005 mg. Temperatures from $25^{\circ}C$ to $1600^{\circ}C$ can be obtained; regulated to $\pm 1.5^{\circ}C$ and readable to $1.25^{\circ}C$. The temperature ramp in Figure 1 shows the $10^{\circ}C$ per minute heating of the sample from room temperature to over $700^{\circ}C$. The TGA curve shows the change in weight of the sample from just under 10 mg to 6.1 mg. The expanded TGA output continues throughout the full temperature range but was omitted to avoid a crowded figure. The presence of two maxima in the DTG curve indicates two components which outgas at different rates.

3.0 DYNAMIC THERMOGRAVIMETRY RESULTS

A systematic study of the TG parameters is currently in progress; however, numerous tests have been performed which illustrate the applicability of the technique to space contamination. Table 1 presents a summary of the TG tests performed, assuming all first order reactions. The column labeled T_{max} shows the maximum temperature reached by that specific test. The activation energy and the frequency constant were both obtained by a least square straight line fit from the plot of lnk versus T^{-1}. The correlation coefficient, r, near unity shows the linear curve does fit the data, strengthening our first order reaction assumption.

The first series of tests were on Dow Corning (DC) Silicone 92-007 white thermal control paint. All of the samples of DC 92-007 were from the same can of paint. The first two samples were obtained by painting the internal surface (a conic section) of the TG crucible liner. The density of the paint ($1.19\ g \cdot cm^{-3}$) and the area of the liner ($1.01\ cm^2$) were used to estimate the thickness of the paint, 55 nm, 147 nm, and 325 nm. Another sample was obtained by scraping off a painted surface and dicing the scrapings into small pieces.

The analysis of the developed values for the rate constants showed that the mass loss rates were orders of magnitude too low to explain typical past spacecraft contamination problems. What seemed to be missing was a high volatile low temperature component. The small initial sample weights (6 to 17 mg) and the basic sensitivity of the TG prevented the detection of any small percentage components. The DC 92-007 material was painted on a clean glass surface and a large sample (657 mg) was peeled off, rolled, and placed into the TG crucible. The detection of two low temperature (weight loss 0.6% and 1.0%) components is shown in Table 1. Another large sample of DC 92-007 (583 mg) was tested by filling the TG chamber with nitrogen gas and cooling the paint sample down to $5^{\circ}C$ before starting to evacuate the chamber. No additional components were found.

Also shown in Table 1 is the TG data output for flight configured Ag/FEP thermal control surfaces, RTV-566 adhesive, and Astroquartz. The Ag/FEP sources consist of a film which is 20 to 40 nm of inconel, 100 nm of Ag, and 0.0508 mm of FEP as the outside surface. The RTV-566 was painted on a metallic surface and peeled off. The Astroquartz sample was silica fabric bonded to aluminum foil by FEP. Table 2 shows the prominant residual gas analyzer mass peaks at selected temperatures for RTV-566.

TABLE 1 SUMMARY OF TGA TESTS

SAMPLE	CONFIGURATION	CURE	AREA (cm^2)	INITIAL WEIGHT (mg)	ACTIVE WEIGHT (mg)	WEIGHT LOSS (%)	T_M (°K)	E (Kcal·Mole^{-1})	A (min^{-1})	r
DC 92-007-1	Painted Liner Thickness 55 nm	48 Hours Room Temp. 48 Hours 124°C	1.01	6.25	2.88	46.1	764	40.4	1.2×10^{11}	0.997
DC 92-007-2	Painted Liner Thickness 147 nm	48 Hours Room Temp. 48 Hours 124°C	1.01	16.78	8.76	52.2	765	51.1	1.7×10^{14}	0.997
DC 92-007-3	Diced DC A-4094	48 Hours Room Temp. 48 Hours 124°C	-	9.01	4.05	45.0	780	31.1	1.3×10^{8}	0.999
DC 92-007-4	Diced	48 Hours Room Temp. 48 Hours 124°C	-	9.72	4.42	45.5	788	52.8	1.8×10^{14}	0.996
DC 92-007-5	Rolled Strip 3.05 x 12.7 cm 0.143 mm Thick	None	77.4	656.7	3.94 8.54	0.6 1.3	394 487	15.9 13.4	4.1×10^{8} 3.0×10^{5}	0.998 0.998
DC 92-007-6	Rolled Strip 3.05 x 12.7 cm	Cooled Sample In N_2 Atm to 5°C then Evacuated	77.4	582.77	4.68 5.83	0.8 1.0	387 477	19.0 6.5	5.5×10^{10} 163	0.996 0.994
DC 92-007-8	Painted Liner Thickness 324 nm		1.01	36.98	0.33 8.14	0.9 22.0	430 788	6.5 52.4	156 1.2×10^{14}	0.994 0.999
DC 92-007-9	Painted Liner Thickness 325 nm		1.01	37.18	0.63 19.74	1.7 53.1	433 790	7.8 56.2	407 1.9×10^{15}	0.999 0.933
Ag-FEP-2	Diced 100 nm Ag 0.0508 nm FEP 20-40 nm Inconel 0.0508 3M-467	24 Hours 23°C & 45% R.H.	-	9.65	3.29 2.62 3.22	34.0 27.0 33.0	665 809 876			
Ag-FEP-3	0.4 cm Squares 100 nm Ag 0.0508 nm FEP 20-40 nm Inconel	24 Hours 24°C & 45% R.H.	-	9.89	2.58 6.94	26.1 70.2	816 901	71.4 92.1	7.3×10^{18} 2.0×10^{22}	0.998 0.996
Ag-FEP-4	Rolled Strip Ag/FEP/Inconel	24 Hours 24°C & 45% R.H.	-	1644.64	0.47	0.028	523	8.0	382	0.9998
RTV-566-2	Peeled from Disc	Over 7 Days Room Temp.	-	10.08	3.29 0.72	33.0 7.0	836 966	28.5 56.3	4.9×10^{6} 1.8×10^{12}	0.999 0.998
RTV-566-3	Peeled from Disc	Over 7 Days Room Temp.	-	500.69	7.01	1.4	487	21.3	2.3×10^{9}	0.997
RTV-566-8	Peeled and Diced		-	191.7	0.36 0.35	0.19 0.18	373 473	15.1 14.9	2.7×10^{8} 2.1×10^{8}	
RTV-566-9	Peeled and Diced			8.29	1.72 1.38	20.8 16.7	843 963	34.2 78.5	1.23×10^{8} 3.70×10^{17}	
Astroquartz	Diced Silica Fabric Bonded to FEP	None	-	11.39	0.52 1.11	4.6 9.7	808 879	73.8 909	9.0×10^{17} 1.3×10^{21}	

Table 2 Residual Gas Analysis For RTV-566 Showing Major Peak Mass Number And Relative Peak Intensity At Selected Temperatures From 298 K to 1048 K

m/e	BKGD	298 K	398 K	873 K	959 K	1048 K	m/e	873 K	959 K	1048 K	m/e	873 K	959 K	1048 K
12				352	844	2494	45	1802	8198		133	5429	4991	
13					1298	1168	50		1250	3317	147	1910	9017	
14		618	509	1743	4014	3568	53		1323	1602	148		1495	
15		883	717	5808	15260	12544	55		3682	7636	177	1653		
16		9801	7633	8783	19853	25448	56		2586	7072	191	3923	2323	
17		19561	15287	11293	13410	21278	57		2757	4039	193	2251	2117	
18	284	36180	27513	18668	20205	33169	59	1497	7894		208	33786	16792	998
25				435	1003	1070	66		1152		209	6744	3322	
26				2698	5322	5844	67			1077	210	4537	2108	
27				1930	5354	8667	69		1450	3754				
28	739	7390	6686	11725	18034	44937	70		1651	4181				
29				1378	4637	5845	73	15724	52795	1424				
31					1512		74	1465	4611					
32		1350	1134	799	936		75	1879	4138					
36						2668	76			2910				
37						1110	78	1167						
38						2255	83			1398				
39				693	2671	7430	84			1462				
40	102	613	592	1098	2262	3501	96	8066	4437					
41				787	4803	12692	103	1327	1270	2945				
42					2952	4810	119	1502	1109					
43				797	8371	6769								
44		564	551	1282	4099	17185								

Table 3 presents the best estimate of the source kinetics parameters for the four sources tested, assuming first order reactions.

Table 3 Best Estimates For Source Kinetic Parameters Using Dynamic TG

MATERIAL	E ($kcal \cdot mole^{-1}$)	A (s^{-1})	WEIGHT LOSS (%)
DC 92-007	17.5	4.6×10^{8}	0.7
	6.9	4.0	1.2
	52.1	2.6×10^{12}	48.9
Ag/FEP	8.0	6.4	0.028
	71.4	1.2×10^{17}	26.1
	92.1	3.3×10^{20}	70.2
RTV-566	21.3	3.8×10^{7}	1.4
	28.5	8.2×10^{4}	32.6
	56.3	3.0×10^{10}	7.9
Silica/FEP/Al	73.8	9.0×10^{17}	4.6
	90.0	1.3×10^{21}	9.7

4.0 ISOTHERMAL THERMOGRAVIMETRY

The Mettler 1 TG instrument had been used previously to perform isothermal TG tests on Dow Corning Silicone 6-1106, Viton A, Shell Epon 828 epoxy, Choseal silicone, and glass-filled diallyl phthalate.[5] These tests have shown that TGA can accurately predict isothermal kinetics at some 500°C lower temperatures than observed during dynamic TG testing. For the low outgassing materials, a single isothermal run would take up to 30 days to complete. For these tests the high volatile component was not isolated.

Isothermal mass loss for DC 92-007 and RTV-566 were recently measured. A 2.54 cm diameter disc painted with primer DC A-4094 and DC 92-007 was heated to 115°C and held at that temperature. However, the outgassing rate for this sample (initial weight 44.31 mg) was too low to be detected. The temperature was then elevated to 293°C. Integrating equation (2) to obtain the time dependent form of the mass loss rate and then differentiating the result gives

$$\dot{m}_s = a_o k e^{-kt}. \tag{5}$$

---

[5] H.A. Papazian, J.Appl. Polym. Sci., <u>16</u>, 2503 (1972).

Plotting ln $\dot{m}_s$ versus t and using a least square linear fit gives a value of $k = 5.93\mathrm{x}10^{-4}$ min^{-1} for T = 566 K, a_o = 44.2%, and a correlation coefficient of r = 0.7276. Using the kinetic parameters for DC 92-007 from Table 2 allows a comparison between dynamic and isothermal TGA; Figure 2 presents a plot of ln $\dot{m}_s$ versus t for these two methods. The values are quite close considering that the dynamic parameters are for the paint only and do not include the primer, DC A-4094.

The very low outgassing rate of RTV-566 led to performing the isothermal test using a 61.07 mg sample diced up to release the full active components. The RTV-566 was heated to 125°C for 5451 min (90.85 hrs). The mass loss rate was too low for the DTG sensitivity and the rate was determined from the slope of the expanded TGA output. Table 4 presents the test results and the calculated values using the dynamic parameters for RTV-566 from Table 3.

Table 4 RTV-566 Isothermal Mass Loss Rates At 125°C And Mass Loss Rates Using Dynamic TG Parameters

TIME	ISOTHERMAL MASS LOSS RATE	TGA DERIVED MASS LOSS RATES EACH COMPONENT		
(min)	(mg·min^{-1})	(mg·min^{-1})	(mg·min^{-1})	(mg·min^{-1})
1626	$2.6\mathrm{x}10^{-5}$	$2.49\mathrm{x}10^{-6}$	$2.15\mathrm{x}10^{-8}$	$1.01\mathrm{x}10^{-18}$
2586	$5.7\mathrm{x}10^{-5}$	$3.26\mathrm{x}10^{-8}$	$2.15\mathrm{x}10^{-8}$	0
3546	$5.7\mathrm{x}10^{-5}$	$4.29\mathrm{x}10^{-10}$	$2.15\mathrm{x}10^{-8}$	0

As Table 4 shows, the dynamic TG derived mass loss rate is several orders of magnitude lower than the measured isothermal mass loss rate. The TML for this test for the first 24 hours is 0.49% which is much higher than the NASA Goddard values ranging from 0.14 to 0.25%. The difference could be explained by the fact that the samples tested were in flight configuration with a primer of SS-4155 as the undercoating. Thus, the dynamic TGA values can vary from the isothermal based on the amount of primer that is scraped off for each sample.

5.0 HIGHER ORDER REACTION THEORY

The first order reaction theory applied to TG used the method of Freeman and Carroll.[6] The method of Reich and co-workers[7] uses the position of the TGA inflection point to determine not only the rate constant, k, but the order of the reaction, n. Differentiating the general rate equation (2) with respect to T and setting the result equal to zero gives

$$n = (E/R)\,\frac{m_M \dot{T}}{-\dot{m}_M T_M^2} \qquad (5)$$

[6] E.S. Freeman and B. Carroll, J.Phys.Chem., 62, 394 (1958).

[7] L. Reich, H.T. Lee and D.W. Levi, J.Polym.Sci., B1, 535 (1963).

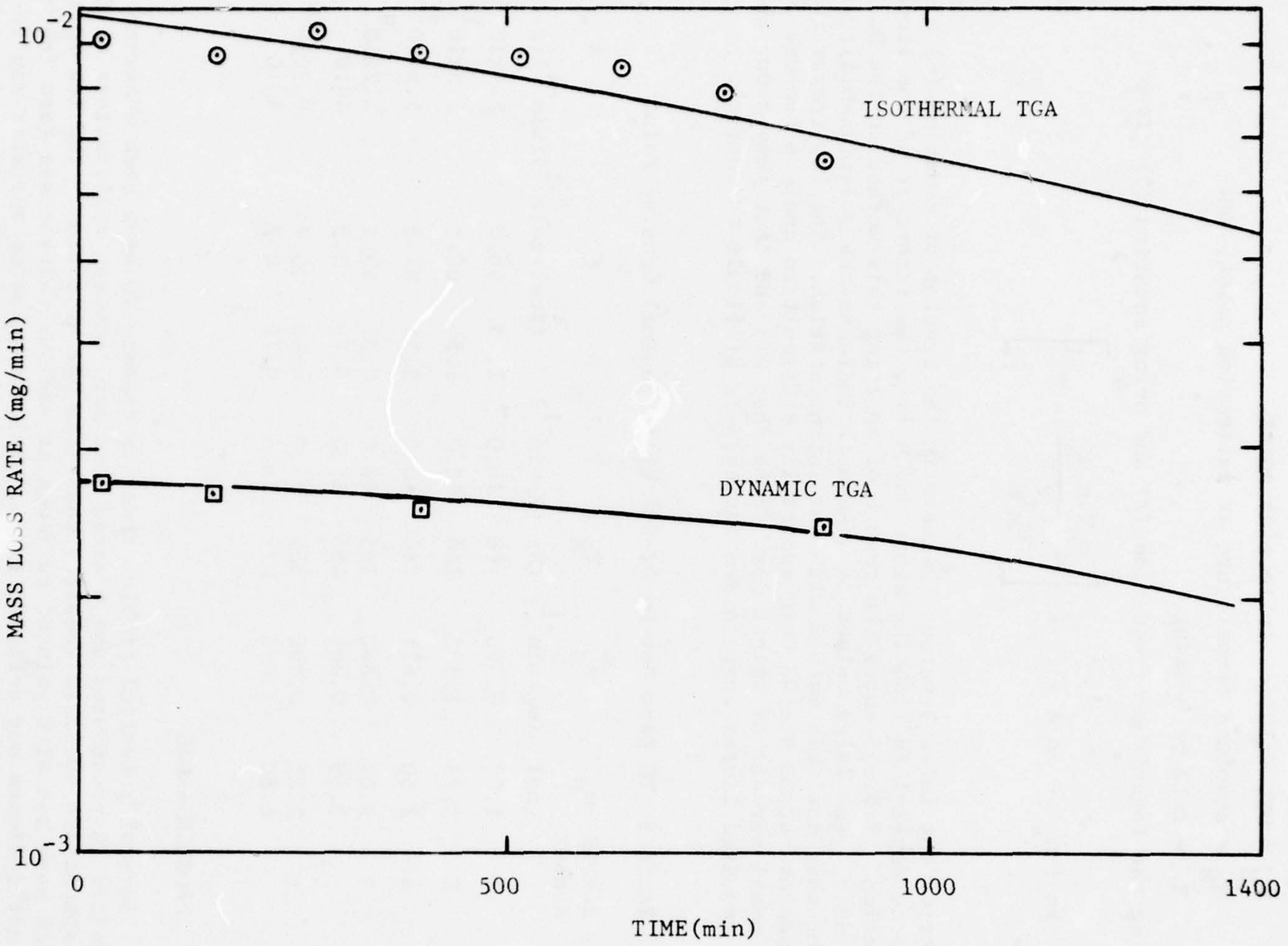

Figure 2 Isothermal TGA Mass Loss Rate for DC 92-007 at 293°C with Comparison Curve Using Parameters Obtained from Dynamic TGA

where m_M = weight of active material remaining at inflection point,

$\dot{m}_M$ = DTG value at inflection point,

T_M = absolute temperature at inflection point, and

$\dot{T}$ = rate of heating.

Taking the logarithm of equation (2) and using equation (5) gives

$$\ln(-\dot{m}_s) = \ln A + (E/R)\left[\frac{m_M \dot{T} \ln m_s}{-\dot{m}_M T_M^2} - T^{-1}\right] \qquad (6)$$

Plotting the $\ln(-\dot{m}_s)$ versus the term in the bracket of equation (6) allows E to be determined from the slope and A from the intercept of the linear relation. Table 5 shows the result of applying this method to the DC 92-007 data. The large values of n seem to indicate the questionability of using this analysis method with our intrumentation. The low temperature components of DC 92-007 were especially difficult to analyze because of the small percent of weight loss (less than 2%) and that they occur where the required linear temperature increase is difficult to control.

Table 5 TG Data For DC 92-007 White Thermal Control Paint

SAMPLE NUMBER	m_M (mg)	$\dot{m}_M$ ($\mathrm{mg \cdot min^{-1}}$)	T_M (K)	$\dot{T}$ ($\mathrm{K \cdot min^{-1}}$)	n	E ($\mathrm{Kcal \cdot mole^{-1}}$)	A ($\mathrm{(min^{-1})(g \cdot cm^{-2})^{1-n}}$)
1	1.03	0.350	768	10.0	1.15	46.0	5.4×10^{12}
2	3.73	1.302	766	10.0	1.54	62.5	1.5×10^{17}
4	2.60	0.675	788	10.0	2.55	81.8	5.6×10^{21}
5	2.04	0.860	398	18.4	2.51	18.1	1.2×10^{9}
	3.99	0.865	498	15.0	0.79	5.6	44.0
6	2.21	0.900	385	21.0	4.46	25.7	9.3×10^{12}
	4.80	1.075	477	16.6	0.78	4.7	53.0

6.0 PROBLEM AREAS

Several potential problem areas in dynamic TG have been observed. Standard TG procedures use a diced specimen, however applications of TGA to spacecraft surfaces requires mass loss per unit area. The few TG tests which were run with painted surfaces at various thicknesses (see Table 1) do not indicate any definite trend. Thick outgassing surfaces may require additional diffusion terms in the kinetic equations to adequately describe the release of mass.

Another potential problem is the extrapolation of dynamic TG parameters to low temperatures. Low temperature components may be very dependent on handling and the environment history of the sample material.

For spacecraft surfaces, temperatures are usually low and thus the solvent (this term encompasses highly volatile components, unreacted plasticizers, curing agents, etc.) may be the dominant weight loss component.

Estimation of a_o is difficult in most kinetic calculations. For reactions with a single component, a_o is the total weight loss. However, multi-steps in the basic sigmoidal TGA curve requires judgment in locating each portion of the weight loss participating in each step. There are several techniques proposed in TG literature reviewed, but none of which appears to have any better physical basis. Slight variations in a_o does not effect greatly the calculated value for E but it does vary A, the frequency constant.

Some of the advantages of dynamic TG over isothermal are as follows:

1. Short test time, about one hour compared to periods of at least 24 hours at each (at least three) different temperatures;
2. Significantly less data to process and analyze;
3. Continuous measurement of weight loss at each increment of temperature captures all kinetic features;
4. Single sample avoids variations due to source preparation; and
5. Fulfills need for screening materials at laser induced temperatures.

Some disadvantages of dynamic TG are:

1. Necessity of precise control of the temperature rate;
2. Low sensitivity for small percentage active components;
3. Difficulty in maintaining uniform temperature rate to detect low temperature components; and
4. Necessity that diffusion barriers be negligible.

OUTGASSING MEASUREMENTS ON MATERIALS IN VACUUM USING A VACUUM BALANCE AND QUARTZ CRYSTAL BALANCES

by

A. Zwaal

Product Assurance Division

ESTEC, Noordwijk, The Netherlands

ABSTRACT

For the prediction of cleanliness levels around spacecraft and on critical spacecraft surfaces, one needs - apart from a mathematical model - a number of outgassing characteristics of spacecraft materials. What is required are the time and temperature dependent data such as total outgassing rates, condensation rates of contaminants produced onto surfaces and re-evaporation rates.

As the Micro-VCM outgassing data are of limited value in the prediction of spacecraft contamination, ESTEC developed two outgassing systems using vacuum and quartz crystal balances. The idea behind this development was the desire to obtain Arrhenius-type outgassing equations in which the outgassing is a function of temperature, activation energy and time.

This paper describes the two outgassing systems developed at ESTEC together with some of the results that have been obtained. Also described is a theoretical approach to spacecraft contamination.

1. INTRODUCTION

As spacecraft become more sophisticated and the duration of missions is extended, the need for more stringent control of spacecraft cleanliness is becoming more and more apparent. For experiments which are contamination-sensitive, one requires a prediction of contaminant levels (ref. 1 - 7). However, to predict these levels, one needs not only a mathematical model, but also realistic input data of the outgassing of materials and the condensation and re-evaporation of spacecraft contaminants. It is due to a lack of proper measuring equipment that, so far, not much information in this respect is available.

Lately, however, the situation has changed and significant progress has been made owing to the introduction of quartz crystal microbalances (QCM's) which enable measurement of condensation and re-evaporation of contaminants down to cryogenic temperatures (ref. 8 - 12). Earlier outgassing measurements were based on pressure measurements (ref. 13) and vacuum balance measurements (ref. 14). Mass spectrometers were never widely employed for quantitative outgassing measurements of polymers because of the complexity of outgassing products and calibration problems. In view of the lack of realistic outgassing data, information obtained by application of the well-known Micro-VCM method has been used for a theoretical approach to the Kinetics of outgassing (ref. 15).

An attempt has been made to also calculate theoretical outgassing figures on the basis of the Langmuir evaporation theory (ref. 16 & 17), but the results obtained are of rather limited value since they are only valid for pure materials such as oils, greases, etc.

Considering that the outgassing products of polymers consist, in general, of limited quantities of many different components and that outgassing and contamination are controlled by some 10 different parameters, it is quite obvious that a theoretical prediction of outgassing and contamination by polymers is almost impossible (ref. 18). On these grounds, it will be clear that the most one can do is to perform practical tests; to define the limitations on the basis of the results; to find out whether or not a specific theory fits the results and - if possible - how the test can be improved. Naturally, it would be ideal if we could achieve some form of standard test method for the measuring of outgassing, condensation and re-evaporation rates.

2. TEST SYSTEMS

The equipment constructed to perform the outgassing measurements incorporates the advantages offered by combining QCM's with a conventional vacuum balance.

A. Vacuum Balance - Quartz Crystal System I (VBQC-I)

This system (see Fig. 1) consists of a Sartorius 4201 vacuum balance which is provided with a magnetically suspended sample hanger. The balance has a sensitivity of 1×10^{-5} grammes, but due to vibrations as well as temperature and humidity variations in the TQC laboratory, the accuracy is limited to 10^{-4} grammes. The maximum load of the balance is 25 grammes and sample temperature is controlled by an oven around the sample.

The system contains three Celesco 700A quartz crystal microbalances (QCM's) which can measure the amount of material condensed on the exposed crystal down to a few times 10^{-8} $g.cm^{-2}$ (sensitivity: 8.9×10^{-9} $g.cm^{-2}$ per mV output). The three QCM's can be cooled down to liquid nitrogen temperatures and are generally controlled at -75, -25 and +25°C respectively.

The removable condenser plate with holes in front of the QCM's is also controlled at -75°C as lowest QCM temperature and has a diameter of 146 mm ($\equiv$ 177 cm^2 area).

The pumping system is a Varian VT-102 ion pumping system, equipped with a Varian-250 quadruple mass spectrometer permitting analysis of outgassing products which do not condense on the condenser plate, i.e. mainly water, solvents and atmospheric gases. Also forming part of the system are metal gaskets and pressures down to a few times 10^{-9} torr can be obtained.

B. Vacuum Balance - Quartz Crystal System II (VBQC-II)

The second system (see Fig. 2) consists of a Sartorius 4433 vacuum balance which is mounted completely inside the system. Its sensitivity is 1×10^{-7} grammes and the maximum sample load is 3 grammes. Basically, this system is identical to the VBQC-I. The condenser plate has a diameter of 200 mm ($\equiv$ 314 cm^2 area).

The mass spectrometer is capable of analyzing all outgassing products from the sample through a hole in the condenser plate.

FIG.1 VBQC - I OUTGASSING SYSTEM

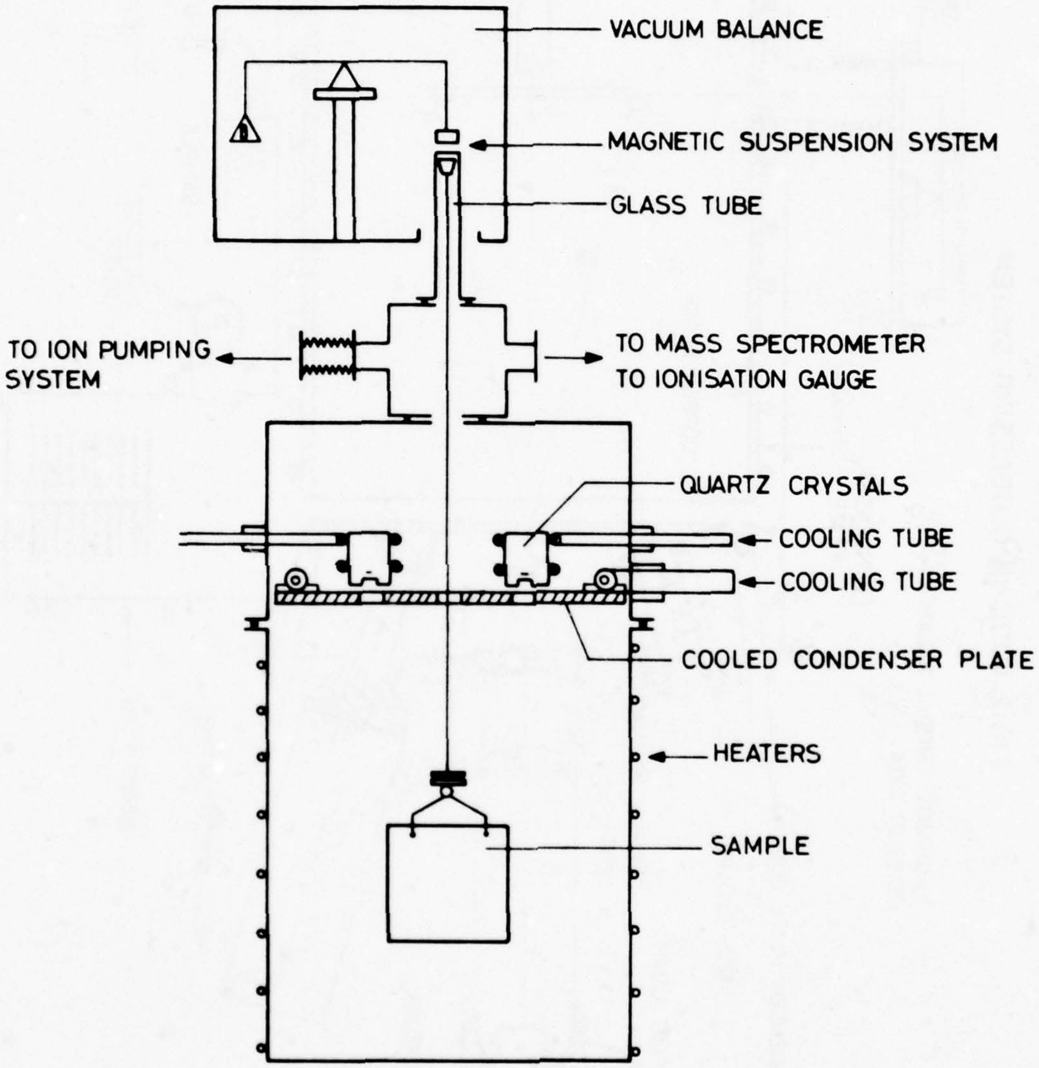

FIG 2 VBQC-II OUTGASSING SYSTEM

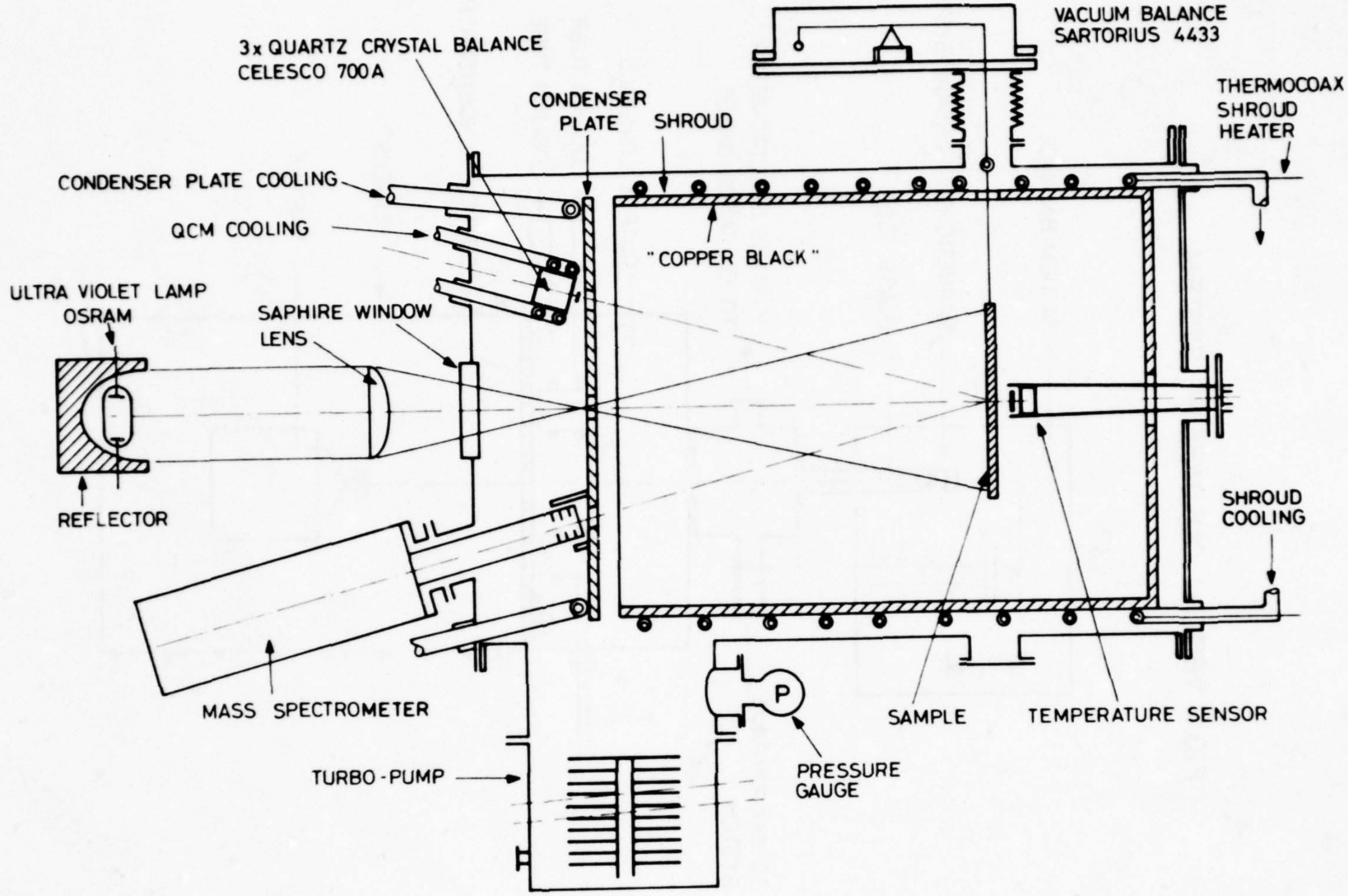

An additional feature is the sapphire window through which the sample can be irradiated by ultra-violet light. The sample can be heated either by radiation from the outside through this window or by radiation from the surrounding shroud.

The latter can be cooled down to liquid nitrogen temperature or heated to around 300°C.

The system is furthermore equipped with a Balzers turbopump and metal gaskets. The ultimate pressure is in the order of a few times 10^{-9} torr.

3. OUTGASSING MEASUREMENTS ON SPACELAB THERMAL BLANKET

A. Test Method

Three vacuum balance tests (VBQC tests), using the VBQC-I system described under 2A, were performed on the same thermal blanket sample at temperatures of respectively 80, 80 and 125°C so as to simulate successive SPACELAB flights. Prior to each test, the sample was conditioned at 20°C and 65% relative humidity over a period of at least one week. From the recorded mass versus time curves, the following outgassing data were obtained:

- Total mass loss (% TML). The "buoyancy effect" was assumed to be 20 mg on this sample of 20 grammes.
- Total mass loss rate.

Immediately after the vacuum test, the water vapour regain (% WVR) was measured at 20°C and 65% RH over a period of 24 hours, using a normal balance under atmospheric conditions.

The three quartz crystal balances were controlled at temperatures of respectively -75, -25 and +25°C while the condenser plate was controlled at -75°C.

From the measurements of the frequency of the quartz crystals, the following outgassing data as a function of time were obtained:

- Collected Volatile Condensable Material (% CVCM),
- Outgassing rate of condensable material.

To obtain the total of condensable material, the data from the quartz crystals ($1 \text{ Hz} \equiv 4.4 \times 10^{-9} \text{ g.cm}^{-2}$) were multiplied by a factor of 177 (the condenser plate's surface area in cm^2).

B. Material Description

The thermal blanket sample of 6.5 x 30.5 cm (= 198 cm^2 area) had a mass of 19.9621 grammes ($\equiv$ 101 $mg.cm^{-2}$). The materials used for this blanket were, according to the manufacturer (Aeritalia):

HPI material : 19 layers of 0.3 mil Kapton, goldized on both sides (Specification SP-AIT-0035);
Spacing material : 20 layers of Dacron net. Specification SP-AIT-0033;
Inner protective layers : Goldized Kapton 0.5 mil reinforced with Nomex net. Specification SP-AI-0030;
Outer protective layers : Teflon-coated fibreglass cloth (Beta cloth). Specification SP-AI-0038;
Goldized Kapton tape : Silicone pressure-sensitive adhesive. Specification SP-AI-0034;
Goldized Kapton tape : Reinforced with glass fibre, pressure-sensitive adhesive;
Vents : Fibre glass Narmco 506/181;
Thread : Nomex. Specification MIL-T-43636, Type I, size ff;
Fasteners : AMOCO Torlon 4203;
Bonding material : RTV-566 silicone adhesive.

C. Results

The final results of the three successive VBQC tests on the same thermal blanket are listed in Table 1 hereunder.

TABLE 1 - VBQC OUTGASSING DATA OF SPACELAB THERMAL BLANKET

Test	% TML	% CVCM -75°C	% CVCM -25°C	% CVCM +25°C
VBQC-021 at 80°C/170 h.	0.804	0.0133 (1)	0.0080	≤ 0.0003
VBQC-022 at 80°C/107 h.	0.900	0.0015	0.0006	≤ 0.0001
VBQC-24 at 125°C/165 h.	0.822	0.0104 (2)	0.0077	0.0004

Notes

(1) The recuperated contaminants from the condenser plate, after

the VBQC-21 test, amounted to 2.98 mg which corresponds to a percentage of 0.0149%. This is in good agreement with the value obtained from the quartz crystal balance at -75° C. The infra-red spectrum of the recuperated contaminants indicated hydrocarbons, phthalate esters and methyl silicones.

(2) The recuperated contaminants from the condenser plate, after the VBQC-024 test, amounted to only 1.1 mg ($\equiv$ 0.0055%). This lower value can be partly attributed to a condense cooling failure at the end of the test, resulting in a partial re-evaporation of the collected contaminants. The infra-red spectrum of the "stripped" screen contaminants indicated many more silicones than the spectrum of test VBQC-021.

The water vapour regain (WVR) by the thermal blanket after exposure to 65% RH at 20° C after 24 hours is listed in Table 2 hereunder.

TABLE 2 - WATER VAPOUR REGAIN OF THERMAL BLANKET

Test	%WVR
VBQC - 021	0.88
VBQC - 022	0.73
VBQC - 024	0.67
Average	0.76

The outgassing rates derived from the thermal blanket during the three VBQC tests are given in Figures 3, 4 and 5*.

* Conversion from $\%.S^{-1}$ to $g.cm^{-2}.S^{-1}$, multiply by 1×10^{-3}.
Conversion from $\%.S^{-1}$ to $torr.l.cm^{-2}.S^{-1}$, multiply by 0.95 (M = 18).

D. Conclusions drawn from Thermal Blanket Outgassing Tests

- The total mass loss after 7 days is 0.85% (average value), i.e. approximately the same percentage as the water vapour regain after the tests (0.76%).

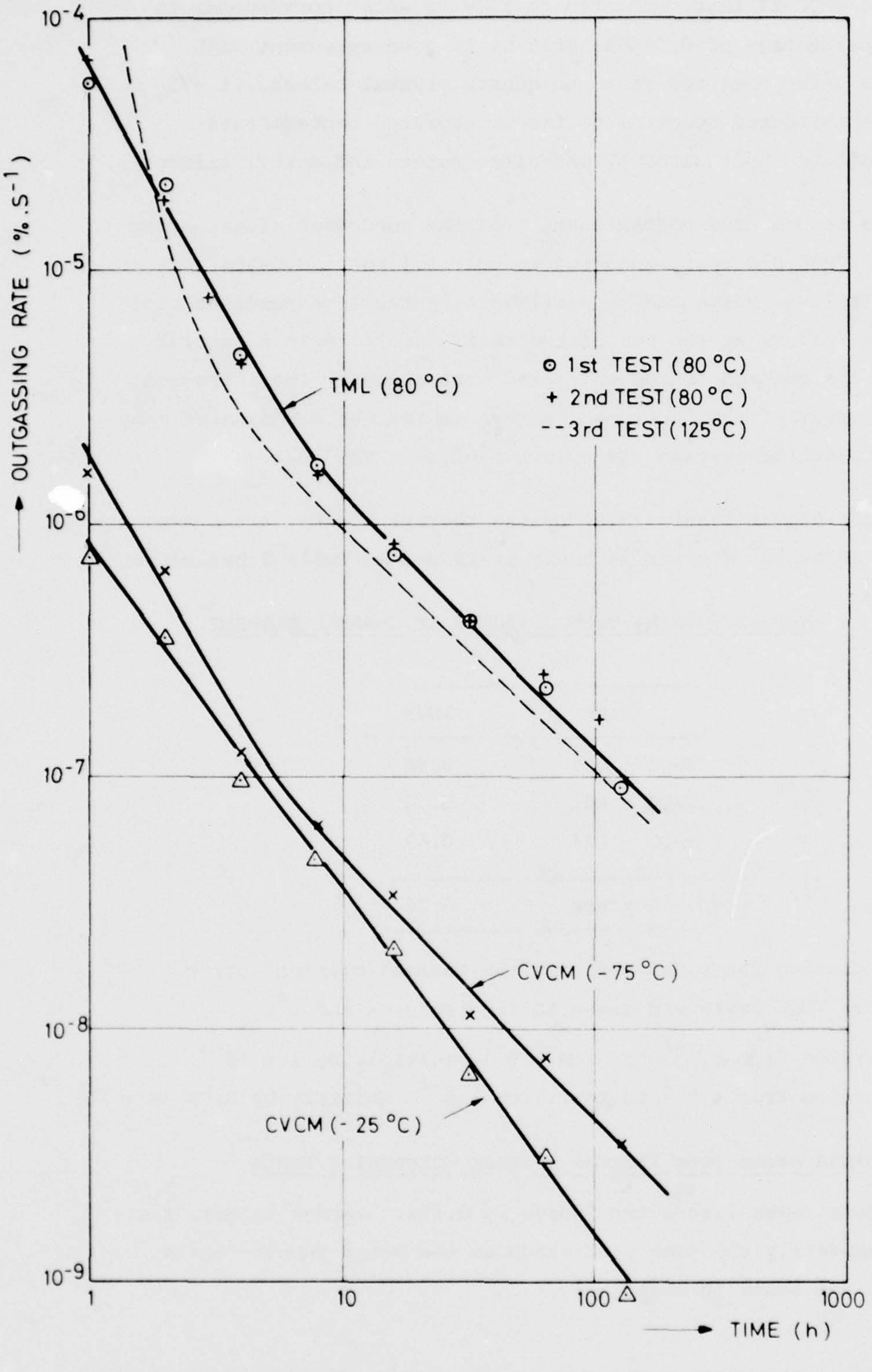

FIG.3 OUTGASSING RATE OF SPACELAB THERMAL BLANKET
(mass = 20 g , area 200 cm^2)

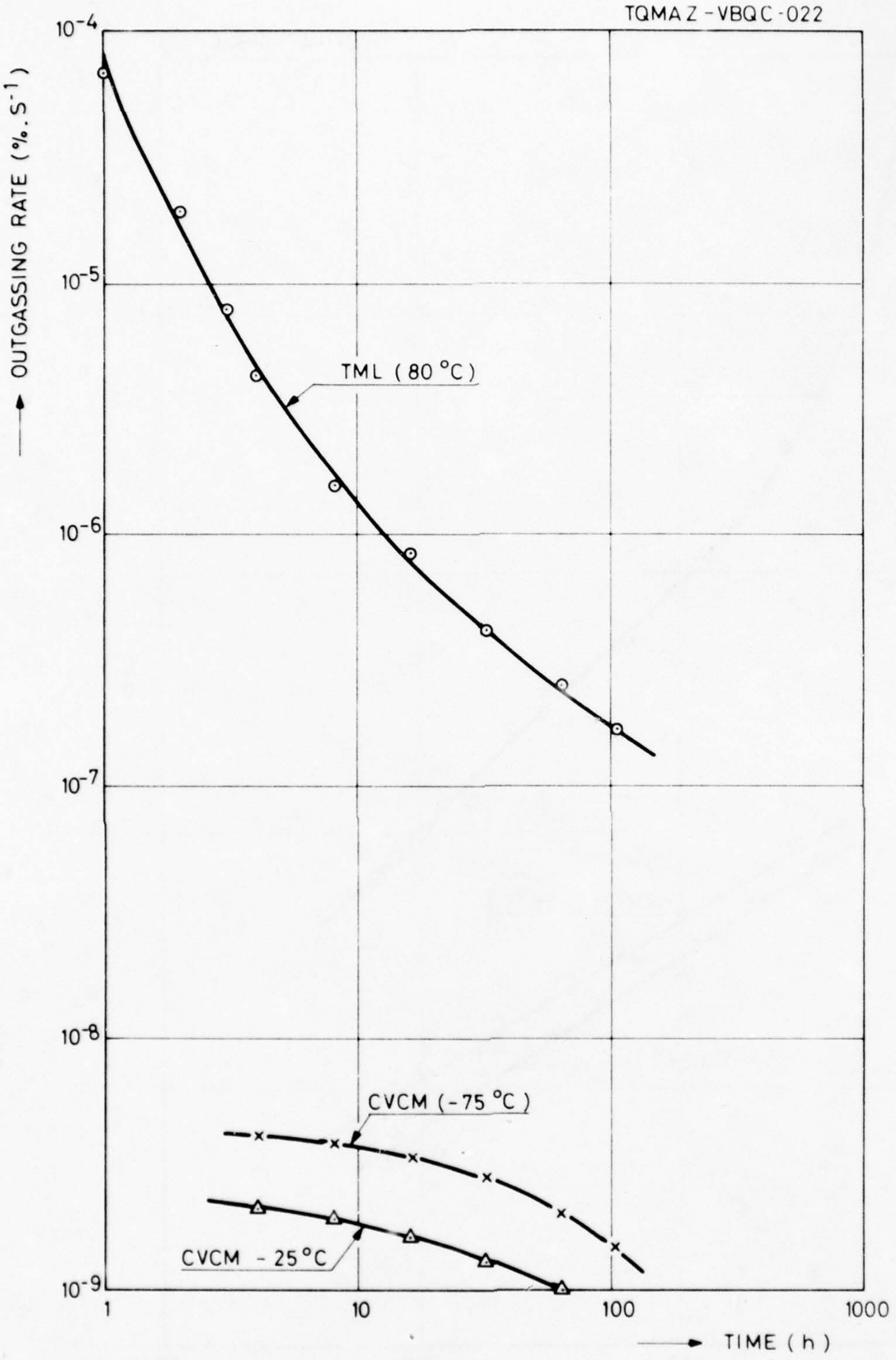

FIG.4 OUTGASSING RATE OF SPACELAB THERMAL BLANKET (2nd TEST)

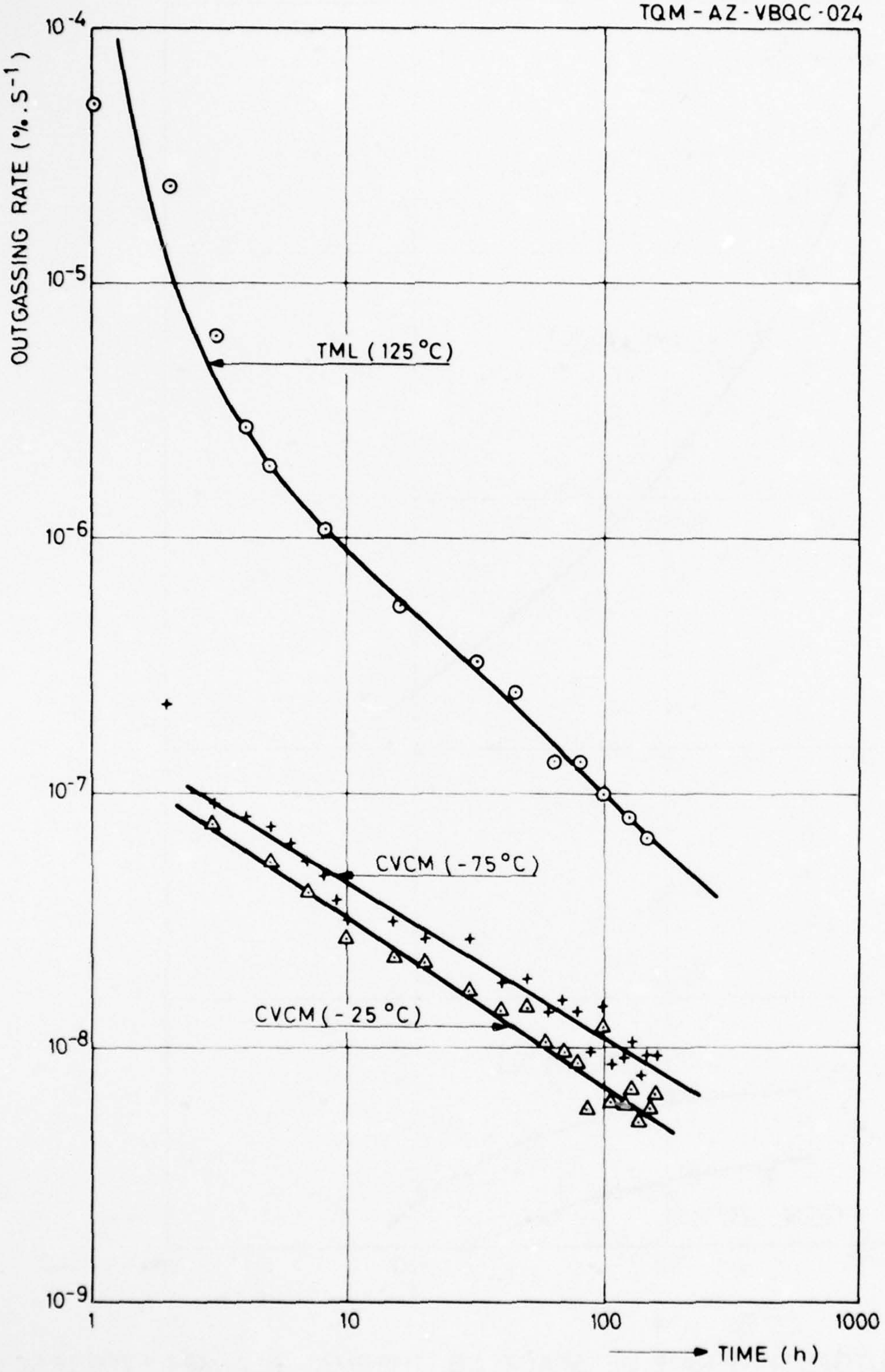

FIG.5 OUTGASSING RATE OF SPACELAB THERMAL BLANKET (3rd TEST)

- The total outgassing rate is almost independent of the temperature. This corresponds to a low "desorption"-activation energy.
- The amount of condensable material collected during the second test at 80° C was only 10% of the amount collected during the first test. (A vacuum bake proves to be an efficient way of releasing volatile condensable contaminants).

  The CVCM outgassing rate during the second test was roughly the same as that at the end of the first test.
- From the initial outgassing rates of the condensable materials during the third test at 125° C and the final outgassing rates during the second test at 80° C, the activation energies for condensable outgassing can be calculated according to Arrhenius's law:-

$$\boxed{\frac{V1}{V2} = e - (E/R\ (\frac{1}{T1} - \frac{1}{T2})}$$

TABLE 3 - ACTIVATION ENERGIES OF CONSENABLE MATERIAL

	V1/80° C	V2/125° C	Activation Energy
CVCM - 75° C	1.5×10^{-9}	9.1×10^{-8}	25,600 calmol^{-1}
CVCM - 25° C	8×10^{-10}	7.2×10^{-8}	28,100 calmol^{-1}

From the fact that the condensable outgassing rates tend to drop below the 10^{-8} $\%.S^{-1}$ at the end of the test at 125° C, it may be concluded that the outgassing of the condensable material is unlikely to be caused by thermal degradation because no steady state outgassing level is reached!

4. OTHER OUTGASSING DATA FROM VBQC-I TESTS

The final results of a number of VBQC-I tests are listed in Table 4 hereunder and partly plotted in Figure 6 to give an impression of the effect of temperature on condensable materials.

TABLE 4 - VBQC-I OUTGASSING DATA

Material	Test	Time/Temp.	% TML	% RML	% CVCM -75° C	% CVCM -25° C	% CVCM +25° C
Chemglaze Z 202	001	160h/125°C	2.42	-	0.082	0.033	$\leq$ 0.0002
Araldite AW 106	005	24h/125°C	2.43	-	0.173	0.0565	$\leq$ 0.007
Solithane 113	007	24h/125°C	0.26	-	0.025	0.014	$\leq$ 0.001
Honeycomb OTS	009	36h/100°C	0.293	0.073	0.0026	0.0010	0.0001
Honeycomb + RTV-560	010	18h/100°C	0.370	0.088	0.0250	0.0055	0.0001
Chemglaze II A-276	019	160h/125°C	2.07	1.45	0.232	0.064	0.028
Araldite AV 100	026	112h/125°C	1.70	0.87	0.060	0.045	0.025
Super Koropon *	027	142h/125°C	4.53	3.44	0.134	0.077	-

* After vacuum post cure 320h/80° C.

The curves drawn through the three points in Figure 6 give the impression that the CVCM at intermediate temperatures can be found easily. However, a theoretical contamination curve for ethylhexylphthalate indicates a sudden re-evaporation around 0° C. None of the practical curves is similar to the theoretical curve, which may be explained by the fact that the condensable material consists of several components, e.g. gaschromatograph mass spectrometer analyses of the material condensed at -75° C, originating from a honeycomb panel with RTV-560 adhesive on top, indicated some 20 different components (ref. 19).

5. THEORETICAL CONTAMINATION EQUATIONS

Contamination of a surface by outgassing products, originating from an outgassing source, can be expressed by the following equation:-

$$\boxed{Q_S = Q_C - Q_L} \qquad (\%.S^{-1})\ * \qquad \underline{\text{EQUATION 1}}$$

where:-

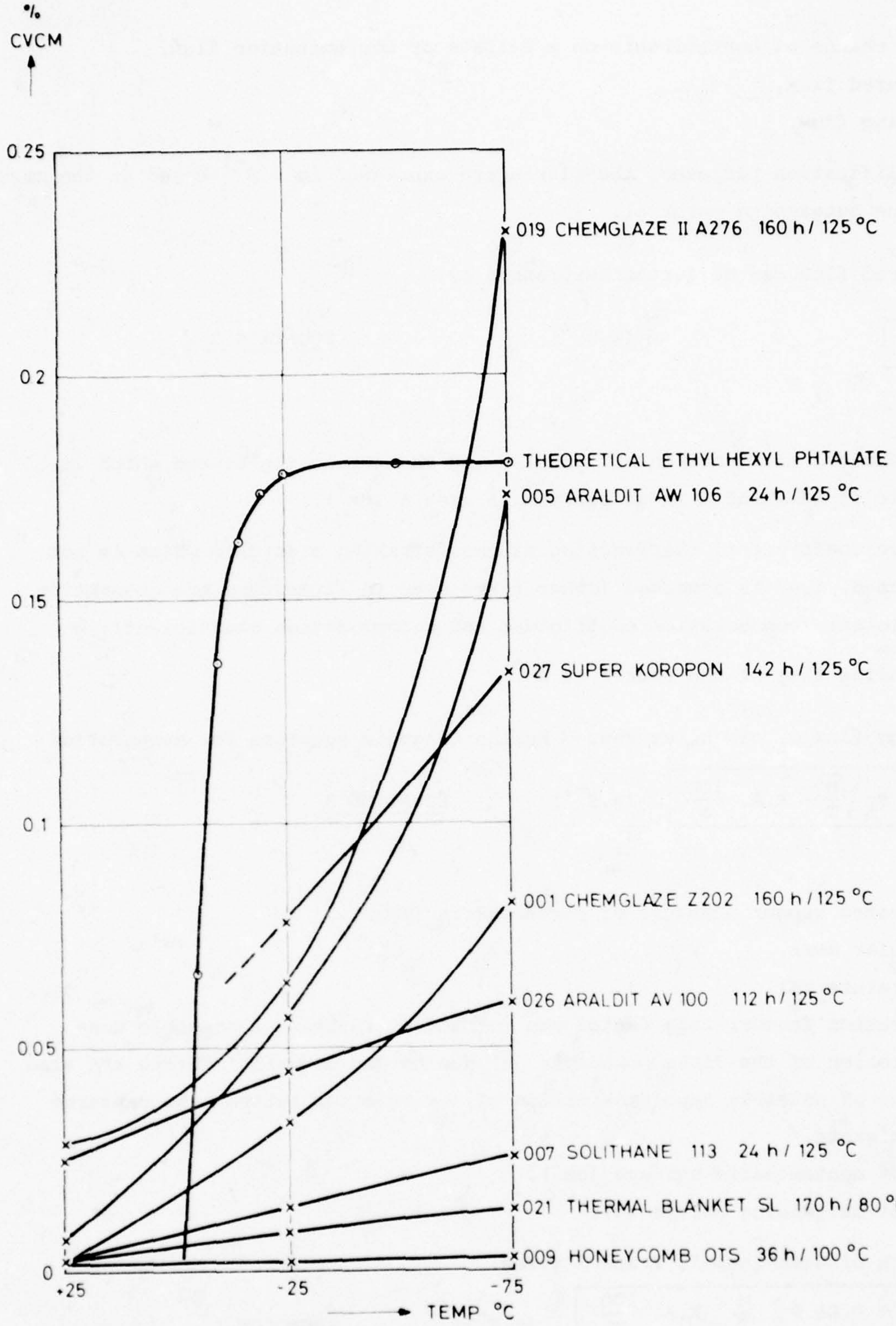

FIG.6 CONDENSIBLE MATERIAL AT DIFFERENT CONDENSER TEMPERATURES
(VBQC - TESTS)

Q_S = mass change of contaminents on a surface or contamination flux,
Q_C = captured flux,
Q_L = leaving flux.

*For simplification purposes, the fluxes are expressed in $\%.S^{-1}$ based on the mass (M) of the outgassing material.

The captured flux can be further expressed by:

$$\boxed{Q_C = F\sigma Q_o} \qquad (\%.S^{-1}) \qquad \underline{\text{EQUATION 2}}$$

where:

F = view factor, the fraction of mass leaving the outgassing source which is capable of striking a known surface of area A (cm^2),

σ = capture coefficient, the fraction of mass striking a surface which is not reflected, i.e. is absorbed (other terms used in literature are absorption coefficient, condensation coefficient and accommodation coefficient),

Q_o= outgassing flux of the source ($\%.S^{-1}$).

The leaving flux Q_L can be expressed by the Langmuir equation for evaporation:

$$\boxed{Q_L = 0.06\ P_S \sqrt{\frac{M}{T}} \cdot k.A. \frac{100}{m}} \qquad (\%.S^{-1}) \qquad \underline{\text{EQUATION 3}}$$

where:

P_S = saturated vapour pressure of contaminants (Torr),
M = molecular mass,
T = temperature (K),
k = evaporation factor; this factor was introduced in view of possible non-evaporation of the first monolayer (s) due to Van de Waals' forces and also in view of possible repolymerization of, or reaction between the captured contaminants,
A = area of contaminated surface (cm^2),
m = mass of outgassing source (g).

Combination of equations 1, 2 and 3 gives:

$$\boxed{Q_S = F\sigma Q_o - 0.06\ P_S\ \frac{M}{T} \cdot k.A. \frac{100}{m}} \qquad (\%.S^{-1}) \qquad \underline{\text{EQUATION 4}}$$

or, simplified:

$$\boxed{Q_S = F\sigma Q_o - Q_L} \qquad (\%.S^{-1})$$

EQUATION 5

A. CALCULATION OF EXPECTED SPACECRAFT CONTAMINATION BASED ON MEASURED CONTAMINATION FLUXES

Expected condensable contamination in a given application can be evaluated from equation 6 which is based on an assumed linear relationship between contamination flux (Q_S) and view factor F:

$$\boxed{Q_{S2} = \frac{F2}{F1} \; Q_{S1}} \qquad (\%.S^{-1})$$

EQUATION 6

where:

Q_{S2} = expected contamination flux ($\%.S^{-1}$),
F_2 = realistic view factor,
F_1 = view factor of VBQC test,
Q_{S1} = contamination flux during VBQC test ($\%.S^{-1}$).

B. CALCULATION OF EXPECTED SPACECRAFT CONTAMINATION USING THE STICKING COEFFICIENT

Certain contamination models use the sticking coefficient:

S = fraction of impinging flux (FQ_o), which sticks permanently onto the surface, or

$$\boxed{S = \frac{Q_S}{FQ_o}}$$

EQUATION 7

Expected spacecraft contamination can be calculated using equation 7 for a given application, where:

F_2 = view factor and
Q_{S2} = the expected contamination level.

$$\boxed{Q_{S2} = S\; F_2 Q_o} \qquad (\%.S^{-1})$$

EQUATION 8

The sticking coefficient has to be measured from tests. The VBQC tests give Q_S and Q_o data, so that - using equation 7, we obtain:

$$\boxed{S = \frac{Q_{S1}}{F_1 Q_o}}$$

EQUATION 9

Combination of equations 8 and 9 gives:

$$\boxed{Q_{S2} = \frac{F_2}{F_1} \cdot Q_{S1}} \qquad (\%.S^{-1}). \qquad \underline{\text{EQUATION 10}}$$

Via determination of the sticking coefficient using the VBQC test, we arrive at the same equation 6 as in paragraph 5, which is not surprising. The sticking coefficient "S" may be expressed also as the capture coefficient "σ" minus the ratio of leaving flux Q_L to impinging flux FQ_O by the combination of equations 5 and 7:

$$S = \sigma - \frac{Q_L}{FQ_O} \qquad \underline{\text{EQUATION 11}}$$

This equation demonstrates that the sticking coefficient changes with the impinging flux FQ_O because the leaving flux Q_L (i.e. the evaporated flux) is constant for a given temperature of the condenser and "σ" is supposed to vary only slightly with temperature.

The sticking coefficients of the thermal blanket contaminants, calculated on the basis of equation 7, from Q_S and Q_O fluxes which were obtained from VBQC tests (paragraph 3) are certainly not constant, as can be seen from Table 5 hereunder.

TABLE 5 - STICKING COEFFICIENTS OF THERMAL BLANKET CONTAMINANTS

Test	Sticking coefficient at -25°C			Sticking coefficient at -75°C		
	1 hour	10 hours	100 hours	1 hour	10 hours	100 hours
1st at 80°C	1.3×10^{-2}	2.6×10^{-2}	1.2×10^{-2}	2.9×10^{-2}	3.6×10^{-2}	3.2×10^{-2}
2nd at 80°C	3.0×10^{-5}	1.3×10^{-3}	4.7×10^{-3}	5.6×10^{-5}	2.6×10^{-3}	8.8×10^{-3}
3rd at 125°C	1.5×10^{-3}	3.4×10^{-2}	7.0×10^{-2}	1.9×10^{-3}	4.9×10^{-2}	1.1×10^{-1}

The fact that the sticking coefficients shown in Table 5 are not constants can be explained by considering equation 7. As will be seen, "S" is the ratio of Q_S (contamination flux consisting of high molecular weight components: hydrocarbons, esters and silicones) and the impinging flux FQ_O (i.e. mainly water). Thus, the outgassing of completely different components is being compared.

The method used to predict spacecraft contamination by means of equation 8 (the sticking coefficient method) is much more complicated than prediction according to equation 6 because Q_o and "S" both change with time and the second method does not even consider Q_o. The final results are, however, the same; both methods suffer from the same error of the non-proportional function of Q_L with FQ_o in equation 11.

The prediction of spacecraft contamination according to the two above methods is only absolute if the test conditions are the same as the actual conditions, i.e. if the amount of captured contaminants per unit condenser area is the same. In other words, the same configuration factor "K" must be used in equation. Should the predicted factor "K" be lower than the "K" factor of the VBQC test, then the predicted contamination level may be too high because the ratio $\frac{QL}{FQ_o}$ will probably increase (equation 11).

7. IDEAL OUTGASSING MEASUREMENTS

As mentioned in the preceding paragraph, ideal measurements are those that relate to "configuration" type samples. In practice, however, they are difficult to perform by means of vacuum balances due to accuracy and mass limitations. An alternative method consists of performing a standard test and measuring all required parameters. This will enable the prediction of absolute levels instead of pessimistic ones. The parameters required are those mentioned in equation 5, viz.:

$$\boxed{Q_S = F\sigma Q_o - Q_L} \qquad (\%.s^{-1}). \qquad \text{EQUATION 12}$$

The contamination flux Q_S and the total outgassing flux Q_o can be measured using the VBQC systems. The view factors are known and the unknown "σ" = capture coefficient and the Q_L = leaving flux according to the Langmuir evaporation equation can be measured by shielding the contaminant sensors (QCM's) from the outgassing source. This means that the view factor "F" becomes zero, so that Q_S becomes Q_L. In practice, this implies that the contaminant level will decrease as a result of re-evaporation of the contaminants on the QCM. Once Q_L is known, "σ" may be calculated from equation 5.

To obtain accurate data, it is important that Q_o does not change too much during the shielding period. This period should be, therefore, as short as possible.

A practical means of measuring Q_L is given in Figure 7.

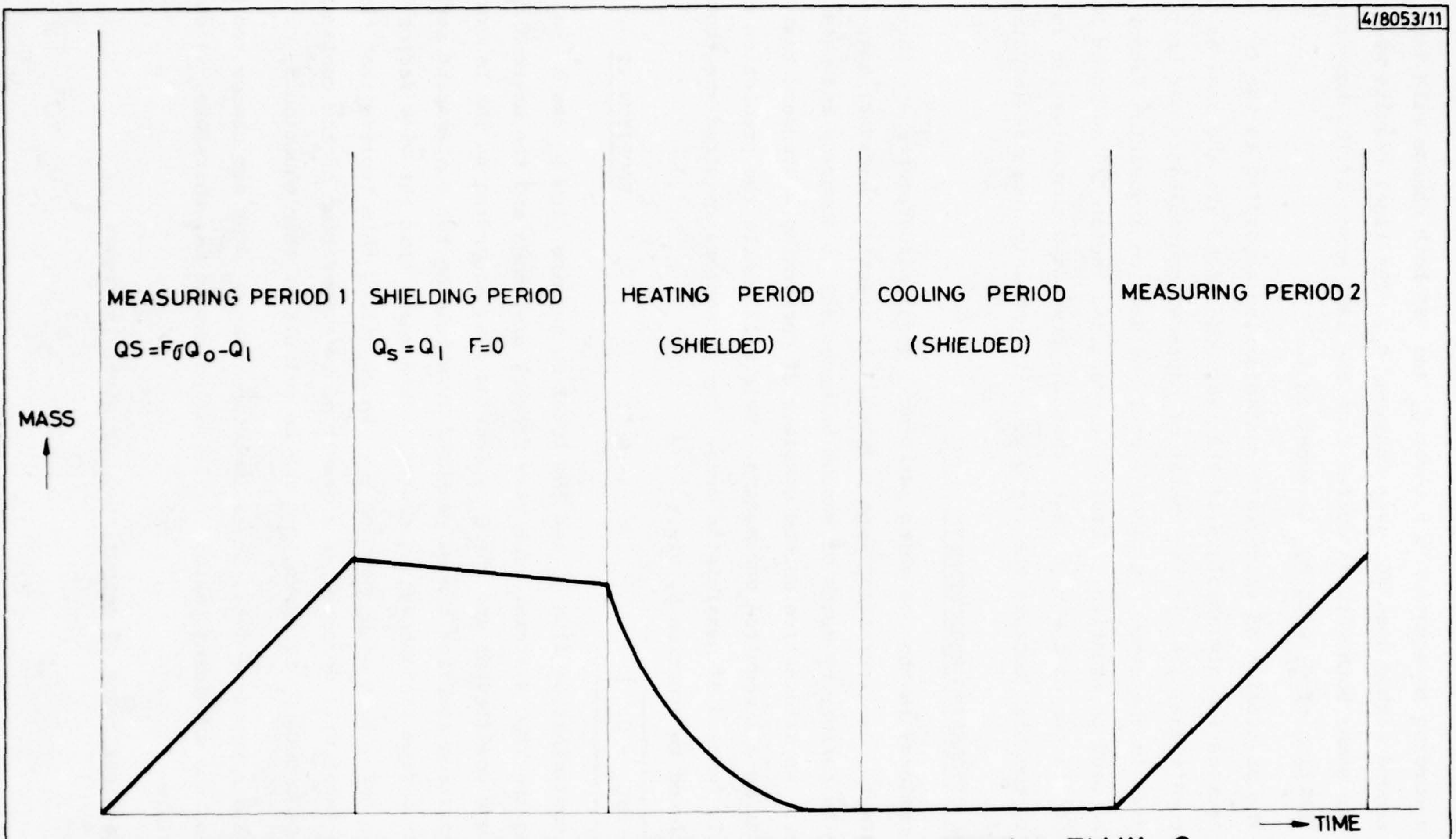

FIG.7 MEASURING OF CONTAMINATION FLUX Q_S LEAVING FLUX Q_l ACCORDING TO $\boxed{Q_S = F\sigma Q_o - Q_L}$

This type of test can produce curves of Q_S, Q_O, Q_L and "σ" as a function of time and temperature.

8. RE-EVAPORATION OF CONTINUOUSLY COLLECTED CONTAMINANTS AT THE END OF A TEST

The standard VBQC test method involves the collection of all contaminants on the QCM's during the test and their subsequent re-evaporation at the end of the test by heating the QCM's. This method of continuous collection may result in incorrect contamination fluxes (Q_S), especially when these fluxes drop by some order of magnitude during a test. An example, based on the Q_S curve (CVCM - 75°C) in Figure 3 shows how it is possible to obtain such incorrect contamination fluxes:

The initially measured contamination flux of 2×10^{-6} %.S^{-1} is supposed to have a leaving flux Q_L of 1×10^{-8} %.S^{-1}.

After 100 hours, the measured flux dropped to 4×10^{-9} %.S^{-1}. Supposing that the leaving flux at that time is still the same as during the initial period, i.e. 1×10^{-8} %.S^{-1}, then the real contamination flux, after 100 hours, should be 1.4×10^{-8} %.S^{-1} instead of the measured 4×10^{-9} %.S^{-1}.

The theoretical error is not verified in this case because the initial contamination flux Q_S, measured with a clean QCM during the second test on the thermal blanket, is close to the final Q_S during the first test, respectively 4×10^{-9} %.S^{-1} and 3×10^{-9} %.S^{-1} (see Figures 3 and 4).

Re-evaporation of contaminants at the end of a test by heating the QCM's results in re-evaporation rates as a function of time and temperature. Derived from these re-evaporation rates can be the effective vapour pressure $\boxed{P_S^{\,1} = P_S \sqrt{\frac{M}{T}} \cdot k.}$ (torr) at different temperatures. (See equation 12).

From the above measurements, the relation between effective vapour pressures and composition of the collected contaminants may be calculated (see Figure 8). Conversion of these effective vapour pressures, obtained at different temperatures, to effective vapour pressures at any temperature is possible by interpolation and extrapolation as shown in Figure 11.

From the curve of effective vapour pressure versus composition of collected contaminants at constant temperature (similar in appearance to Figure 9), the amount of contaminants which will re-evaporate in the predicted model can be

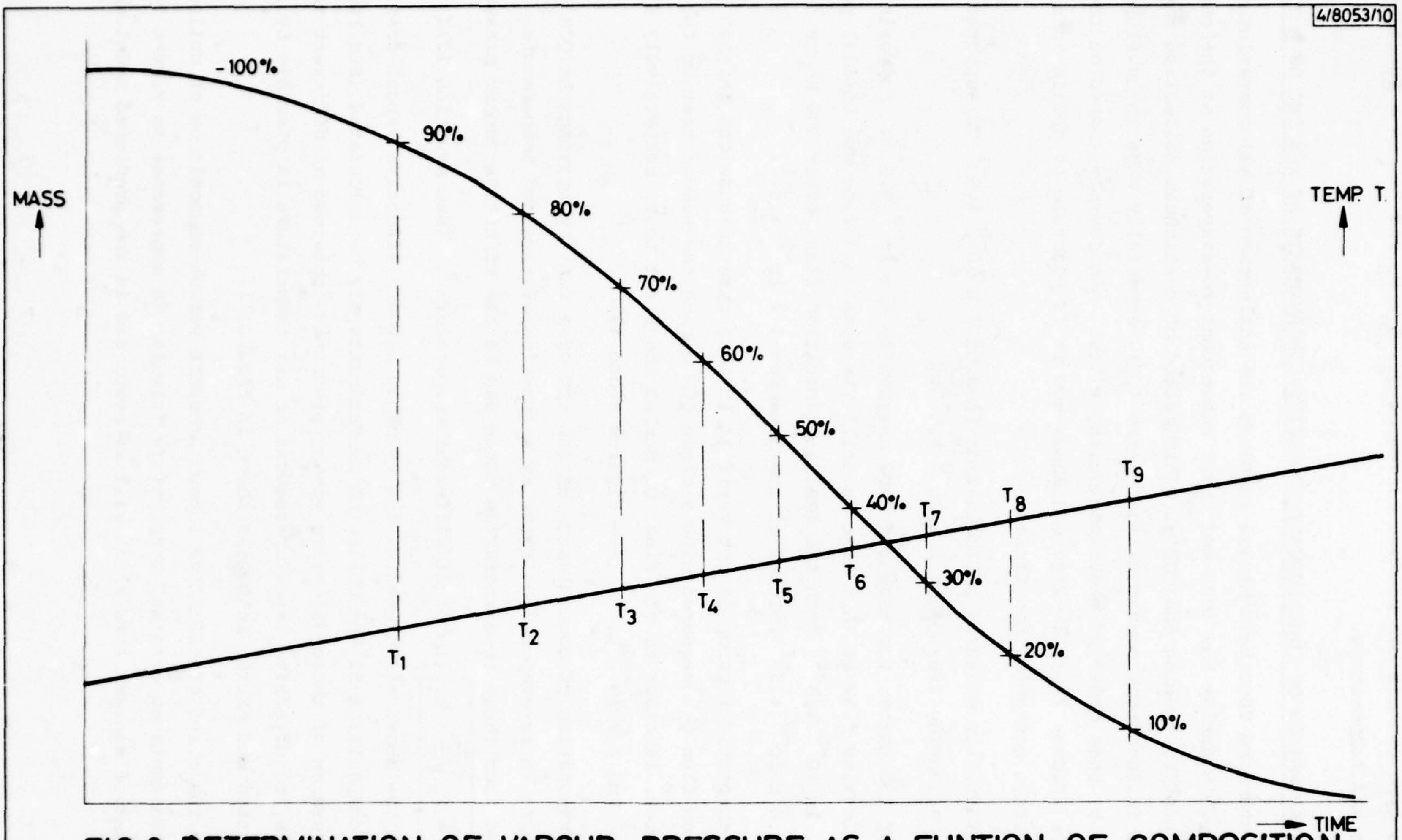

FIG.8 DETERMINATION OF VAPOUR PRESSURE AS A FUNTION OF COMPOSITION FROM RE-EVAPORATION RATES OF CONDENSED CONTAMINANTS

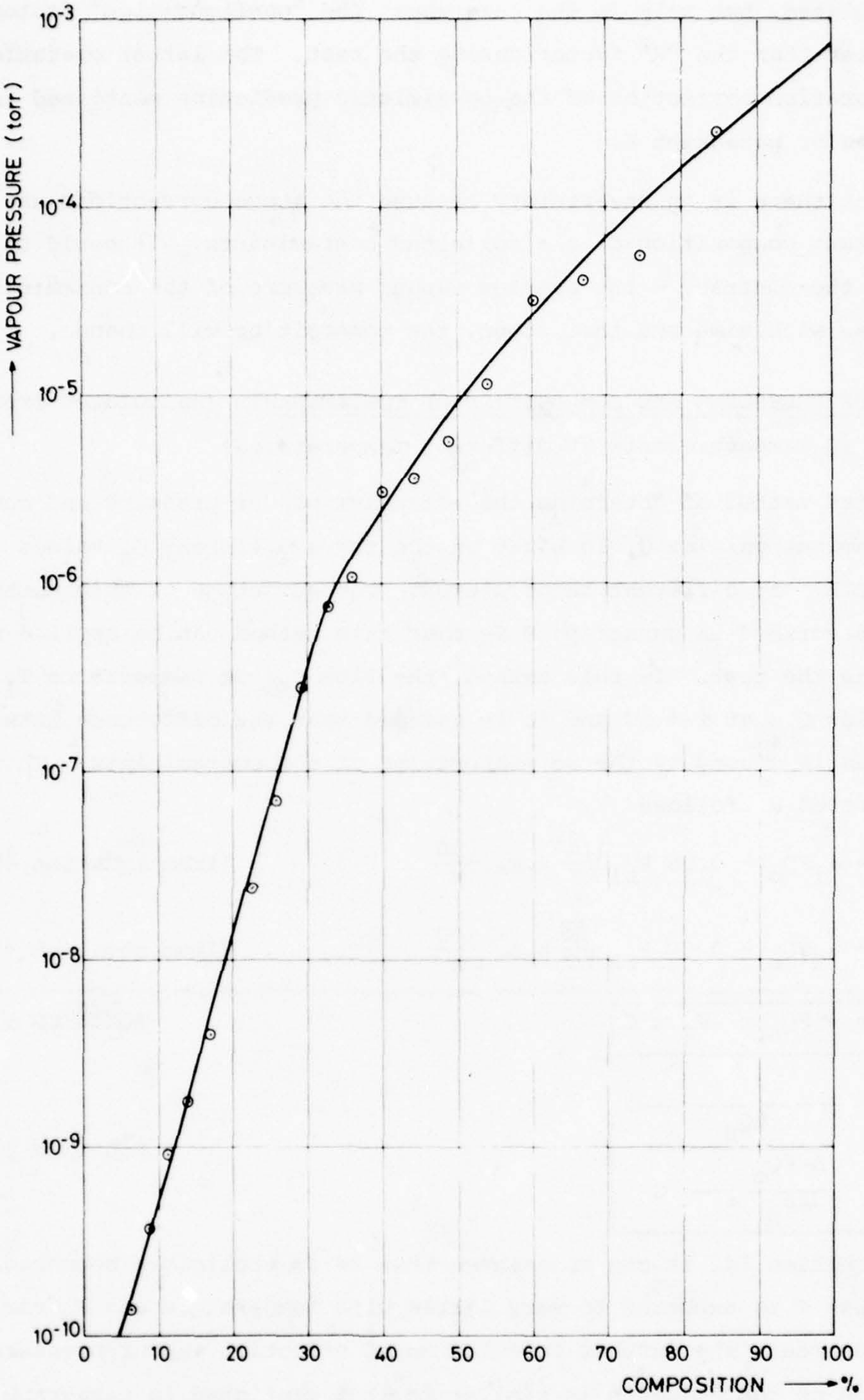

FIG.9 VAPOUR PRESSURE AT 25 °C OF MATERIAL CONDENSED AT -75 °C ORIGINATING FROM ARALDIT AW 106 AS A FUNCTION OF COMPOSITION (REF. VBQC-005)

calculated, but only in the case where the "configuration" factor "K" is smaller than the "K" factor during the test. The latter operation is a re-evaporation correction of the pessimistic prediction mentioned in the last alinea of paragraph 6.

Again, there is an uncertainty because the above corrections are based on a constant composition of the collected contaminants. It could be imagined that - to the contrary - the average vapour pressure of the contaminants will decrease with time and that, thus, the composition will change.

9. VAPOUR PRESSURES AND COMPOSITION OF CONTAMINANTS (calculated from contamination flux (Q_S) measurements at different temperatures)

A third method of obtaining the effective vapour pressure and composition of contamination flux Q_S is based on the three different Q_S values obtained with the QCM's at different temperatures. The advantage of this method over the one described in paragraph 8 is that this method can be applied at any time during the test. In this method, the flux Q_{S1} at temperature T_1 is compared to flux Q_{S2} at $T + \Delta T$ and it is assumed that the difference between these two fluxes is caused by the re-evaporation of the contaminants. This can be expressed as follows:

$$Q_{S1} = \sigma_1 F Q_o - 0.06\ P_{S1} \sqrt{\frac{M}{T}}\ k.a.\ \frac{100}{m} \qquad \text{(from equation 4)}$$

$$Q_{S2} = \sigma_2 F Q_o - 0.06\ P_{S2} \sqrt{\frac{M}{T}}\ k.a.\ \frac{100}{m} \qquad \text{(from equation 4)}$$

$$\boxed{\Delta Q_S = \sigma F Q_o - P_S \times C} \qquad \text{EQUATION 13}$$

or

$$\boxed{\Delta P_S = \cfrac{\Delta Q_S}{\cfrac{\Delta \sigma F Q_o}{\Delta P_S} - C}} \qquad \text{EQUATION 14}$$

In equation 14, it can be assumed that $\Delta\sigma$ is negligible compared to ΔP_S because σ is expected to vary little with temperature and P_S varies some 20% per degree! The further calculation of effective vapour pressures and composition of contaminants is similar to that mentioned in paragraph 8. The results of this approach on an Araldite AW 106 outgassing test are shown in Figure 9.

One of the problems of determination of vapour pressures of condensable contaminants as a function of temperature by measuring the re-evaporation rates from the QCM's is the accuracy of the temperature measurement of the QCM. Our present QCM's - in principle two quartz crystals between which a platinum resistor measures the average temperature of the two crystals; one crystal is shielded and the other exposed to the outgassing flux to be measured - indicated an error in temperature measurement of ∿20°C during a thermal cycling test of a solar array. The QCM temperature reading during that test was -150°C, the exposed crystal facing the solar array at +55°C indicated at that moment a water re-evaporation rate which corresponded to a temperature of -130°C (reference 22).

10. IDEAL CASE OF NO SURFACE CONTAMINATION

Theoretically, one can avoid surface contamination as can be seen from equation 4 hereunder:

$$\boxed{Q_S = F\sigma Q_o - 0.06\ P_S\ \frac{M}{T} \cdot k.A.\ \frac{100}{m}} \qquad \text{(EQUATION 4)}$$

No surface contamination means $Q_S = 0$ or in formulation:

$$\boxed{F\ Q_o = 0.06\ P_S\ \frac{M}{T}\ k.A. \frac{100}{m}} \quad (\%.S^{-1}) \qquad \text{(EQUATION 15)}$$

Introduction of the configuration factor "K" which can be expressed as:

$$\boxed{K = \frac{F\sigma m}{6A}} \qquad \text{(EQUATION 16)}$$

and combination of equations 12, 15 and 16 gives the relation between the effective vapour pressure $P_S{}^1$ and the total outgassing flux:

$$P_S{}^1 = KQ_o \text{ (torr).} \qquad \text{(EQUATION 17)}$$

This means that a contaminating component of which the outgassing flux is Q_o and the effective vapour pressure above the one calculated from equation 16 will not contaminate a surface under the conditions fixed by "configuration" factor "K."

In most cases, it will be difficult to realize no surface contamination, but in practice one can go at least some way towards achieving this goal by:

1) reduction of view factor "F" by shielding the critical surface;
2) reduction of capture coefficient "σ" (main problem is how?);
3) reduction of Q_o. In practice, this means the Q_S at the temperature of the critical element by:

(a) selection of proper materials,

(b) reduction in temperature of outgassing source,

(c) application of a shutter, so that the critical surface does not see the outgassing source until after a certain time when the outgassing has dropped below a certain level;

(d) covering the outgassing source by a low outgassing material of low permeability;

(e) pre-degassing of materials;

4) application of the lowest material mass possible;

5) augmentation of vapour pressure by increasing the critical surface temperature.

If the above actions cannot prevent surface contamination, then a periodical de-contamination of the critical surface is possible, e.g. by heating. The configuration factor "K" for the three outgassing systems at ESTEC has been calculated from equations 15 and 16 assuming that the capture coefficient = 1. The relevant data are given in Table 6 and the function of "K" with vapour pressure and outgassing flux is plotted in Figure 10.

TABLE 6 - CONFIGURATION FACTOR "K" FOR OUTGASSING SYSTEMS

System	m g	A cm^2	K
Micro-VCM	0.2	7	5×10^{-3}
VBQC-I	20	176	2×10^{-2}
VBQC-II	1	314	5×10^{-4}

An outgassing flux of 1×10^{-6} %.S^{-1} corresponding to 0.1% CVCM according to the micro-VCM test during 24 hours will just re-evaporate if the vapour pressure of the material is 5×10^{-9} torr. This vapour pressure at 25°C corresponds to the vapour pressure of triacontaan $C_{30}H_{62}$ (see Figure 11, curve 30). This means that the micro-VCM condensable material has a vapour pressure below that of triacontaan. The lowest vapour pressure of a contaminant at 125°C, which still gives a total mass loss of 0.1%, is 2.5×10^{-7} torr; this vapour pressure corresponds to that of heptatriacontaan $C_{37}H_{76}$.

Table 7 shows the equivalent hydrocarbons which will not pass the 0.1 CVCM limits of the micro-VCM test operating at different condenser temperatures.

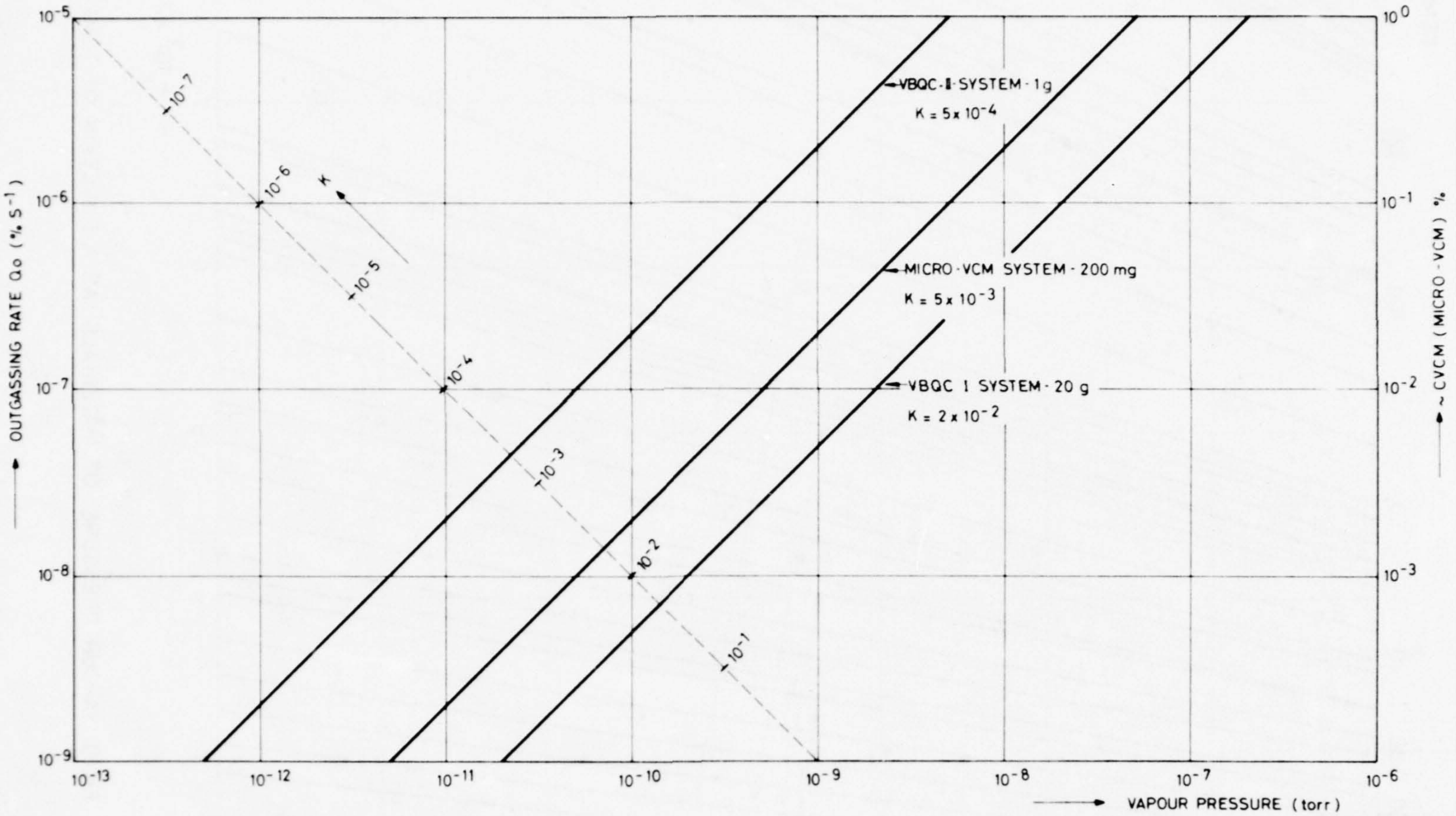

FIG.10 VAPOUR PRESSURE OF CONTAMINANTS WHICH JUST EVAPORATE AS A FUNCTION OF OUTGASSING RATE $P_S = k.Q_O$

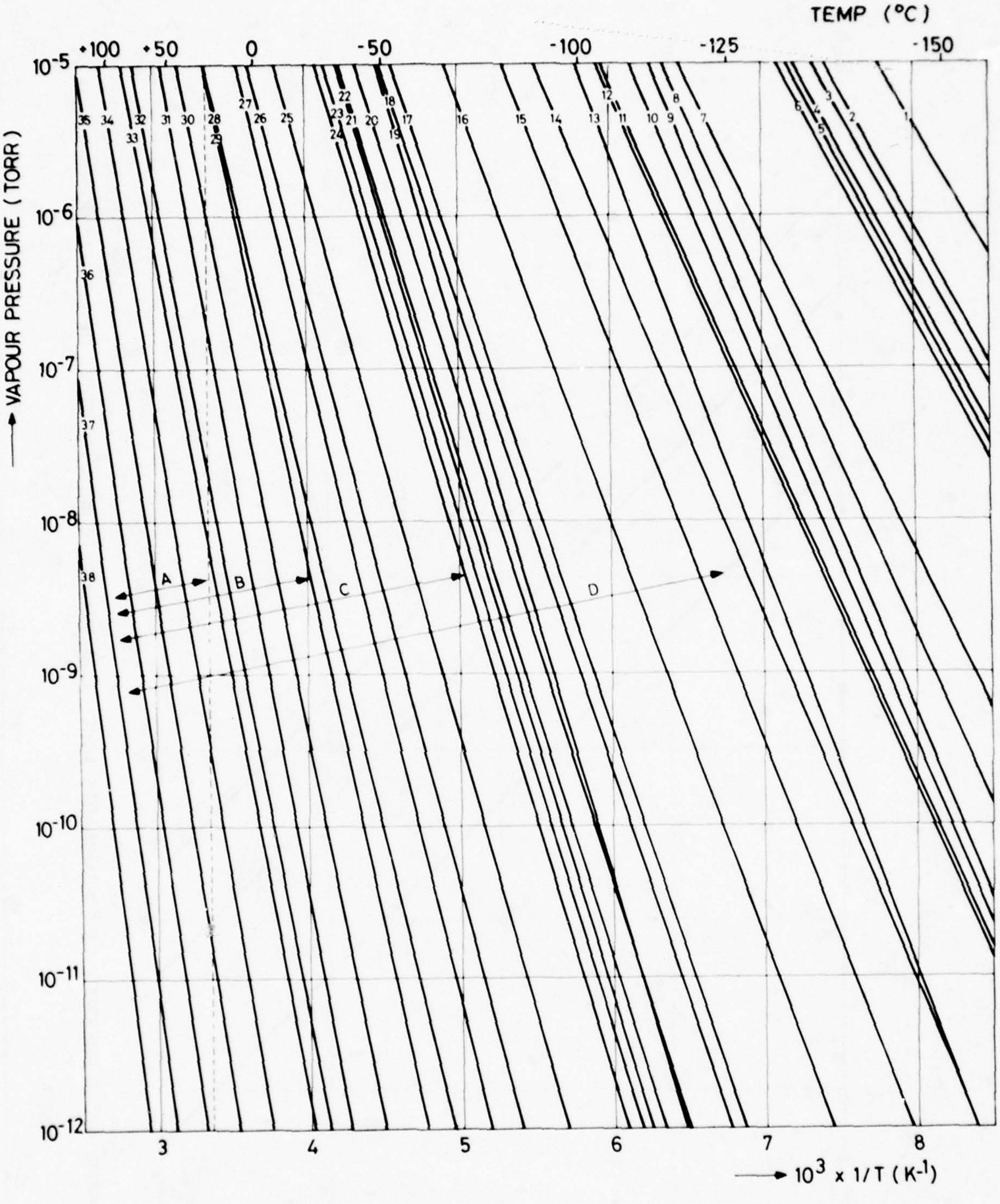

FIG.11 VAPOUR PRESSURE OF MATERIALS AS A FUNCTION OF TEMPERATURE

TABLE 7

Condenser Temp. °C	Equivalent hydrocarbons which will not pass the micro-VCM limits of 0.1% CVCM	Covering lines in Fig. 11
+ 25°C	$C_{37}H_{76}$ - $C_{30}H_{62}$	A
- 25°C	$C_{37}H_{76}$ - $C_{24}H_{50}$	B
- 75°C	$C_{37}H_{76}$ - $C_{16}H_{36}$	C
-125°C	$C_{37}H_{76}$ - $C_{10}H_{20}$	D

The flux of 1×10^{-6} %.S^{-1}, which was mentioned earlier and which will just re-evaporate in the micro-VCM system if the vapour pressure is 5×10^{-9} torr, will just evaporate in the VBQC-II system (having a "K" value of 5×10^{-4}) when the vapour pressure is 5×10^{-10} torr. This means that the materials of which the outgassing flux is 10^{-6}% and the vapour pressure between 5×10^{-10} torr - 5×10^{-9} torr are measured as CVCM with the micro-VCM system and not with the VBQC-II system at the same condenser temperature.

11. CONCLUSION

A standard test method for measuring the total outgassing rate and the condensible outgassing rates of spacecraft materials can give very useful information for material selection and spacecraft contamination prediction. If the predicted levels are not acceptable, the necessary corrective actions can be taken at the early design phase. The outgassing characteristics of materials can best be studied only when the fluxes are easily measurable. In general, this means that a high configuration factor "K" is required. On the other hand, for critical spacecraft surfaces, where contamination should be as low as possible, the design to be incorporated should be such that the lowest possible "K" factor is obtained.

In practice, the prediction of spacecraft contamination requires extrapolation of the VBQC test contamination data down to realistic spacecraft contamination levels in which the "K" factor is generally much lower than the "K" factor in the VBQC test. The linear extrapolation method and the sticking coefficient method both result in "worst case" figures because the re-evaporation of condensable contaminants is not completely taken into account.

The correction method for re-evaporation of contaminants required the vapour pressure to be expressed as a function of concentration for the condensable contaminants. These vapour pressure data may be obtained from the three methods given in this paper.

At the present time, no tests are being performed to correlate data pertaining to these three methods.

A problem in the determination of vapour pressures of condensable contaminants as a function of temperature by measuring the re-evaporation rates from the QCM's is the temperature measurement of the QCM's in our systems. Recent improvements on temperature stability of QCM's have been achieved by the use of double oscillating quartz crystals (ref. 20), even simultaneous mass and temperature determination on a QCM is possible by use of the electrode - tab configuration (ref. 21).

APPENDIX: VAPOUR PRESSURES OF SOME SPACECRAFT CONTAMINANTS

The vapour pressure/temperature function of typical spacecraft contaminants such as solvents, water, methyl siloxanes, phthalate esters, phenyl-methyl siloxanes, and alkanes (hydrocarbons) is in general not known below 1 torr. Knowledge of vapour pressures down to 10^{-12} torr and the corresponding temperatures is interesting for above mentioned types of contaminants because of possible spacecraft contamination of critical surfaces.

Also interesting is the selection of materials which can be used for calibration purposes of outgassing systems and for contamination experiments.

The vapour pressures of 1, resp. 10 torr and the corresponding temperatures given in the Handbook of Chemistry and Physics (D-185) have been used for the calculation of the constants A and B in the Clapeyron equation:

$$\boxed{\log P = A - \frac{B}{T}}$$

In the above equation P, the vapour pressure in torr and T is the absolute temperature in K.

The A and B constants for the methyl-phenyl silicones DC705, resp. DC705 were obtained from the manufacturers data sheets.

As no better data were available, the Clapeyron equation has been used for extrapolation of the vapour pressures down to 10^{-12} torr.

The A and B constants of the 38 materials are given in attached table and the corresponding pressure/temperature functions have been plotted in attached figure.

An interesting point of the plotted vapour pressure/temperature functions is that all the lines seem to come from one point. This means that any vapour pressure of an unknown material measured at certain temperature can easily be extrapolated to a vapour pressure at another temperature.

TABLE: VAPOUR PRESSURE EQUATION ACCORDING TO CLAPEYRON

$\log P = A - \frac{B}{T}$

P=vapour pressure (torr) T= temperature

NO.	CHEM.FORM.	M	NAME	A	B
1	$C_2Cl_3F_3$	188	Trichloro-trifluoro-ethane	8.408	1725
2	C_3H_6O	58	Acetone	8.555	1829
3	$CHCl_3$	120	Trichloro-methane	8.604	1852
4	C_6H_{14}	86	Hexane	8.588	1883
5	$C\ Cl_4$	154	Carbontetrachloride	8.342	1862
6	C_4H_8O	72	2-Butanone (MEK)	8.349	1878
7	C_7H_8	92	Toluene	8.447	2082
8	C_2H_6O	46	Ethanol	9.341	2260
9	C_6H_6	78	Benzene	10.385	2456
10	C_3H_8O	60	2-Propanol (IPA)	9.670	2390
11	C_8H_{10}	106	3-Xylene	8.565	2281
12	$C_6H_{18}O_3Si_3$	222	Hexamethylcyclotrisiloxane	8.458	2272
13	H_2O	18	Water	10.482	2681
14	$C_{10}H_{20}$	140	Decane	8.391	2431
15	$C_8H_{24}O_4Si_4$	296	Octamethylcyclotetrasiloxane	8.906	2626
16	$C_{10}H_{30}O_5Si_5$	370	Decamethylcyclopentasiloxane	8.766	2791
17	$C_{12}H_{36}O_6Si_6$	444	Dodecamethylcyclohexasiloxane	8.974	3056
18	$C_{14}H_{42}O_5Si_6$	458	Tetradecamethylhexasiloxane	8.902	3088
19	$C_{10}H_8$	128	Naphtalene	10.812	3523
20	$C_{14}H_{42}O_7Si_7$	518	Tetradecamethylcycloheptasiloxane	8.954	3219
21	$C_{16}H_{48}O_6Si_7$	532	Hexadecamethyl heptasiloxane	9.088	3330
22	$C_{15}H_{32}$	212	Pentadecane	9.328	3403
23	$C_{16}H_{48}O_8Si_8$	592	Hexadecamethylcyclo octasiloxane	9.015	3396
24	$C_{18}H_{54}O_7Si_8$	604	Octadecamethyloctasiloxane	9.148	3468
25	$C_{19}H_{40}$	269	Nonadecane	9.077	3690
26	$C_{16}H_{22}O_4$	278	Dibutyl phthalate	9.428	3973
27	$C_{20}H_{60}O_8Si_9$	680	Eicosamethylnonasiloxane	10.271	4285
28	$C_{24}H_{50}$	339	Tetracosane	9.494	4339
29	$C_{22}H_{56}O_9Si_{10}$	744	Docasamethyldecasiloxane	11.200	4855
30	$C_{24}H_{72}O_{10}Si_{11}$	828	Tetracosamethylhendecasiloxane	11.805	5293
31	$C_{16}H_{22}O_4$	278	Ethylhexyl phthalate	12.779	5814
32	?	484	DC-704-Methyl Phenyl trisiloxane	11.025	5570
33	$C_{30}H_{62}$	423	Triacontane	10.977	5705
34	?	?	DC-705 Methylphenyltrisiloxane	12.118	6424
35	$C_{34}H_{70}$	479	Tetratriacontane	12.178	6861
36	$C_{36}H_{74}$	507	Hexatriacontane	12.772	7473
37	$C_{38}H_{78}$	535	Octatriacontane	13.435	8152
38	$C_{40}H_{80}$	563	Tetracontane	14.067	8841

1.	J. J. SCIALDONE	Prediction Spacecraft Self-Contamination in Space and in a Test Chamber. Space Simulation Conf. 1972 - NASA-SP-298.
2.	D. EDLEY	GEOS Outgassing Calculation and Ion Production. Study note BA-4J-324 (1975) Britsch Aircraft Corp - England.
3.	W. WILKENS a.o.	Experimental Study on the Contamination Degradation Effects on the Optical and Thermo-Optical Performances of Critical Parts of the METEOSAT-Radiometer in Orbit. Prepared under ESA-Contract No. 2234/74/09 by DFVLR - West Germany (1976)
4.	E. A. ZEINER	AESC Multinodal Free Molecular Contamination Transport Model. Space Sim. Conf. 1975 - NASA-SP-379.
5.	L. E. BAREISS E. B. RESS R. O. RANTANEN L. J. LEGER	Preliminary Evaluation of the Contaminant Induced Environment for the Space Shuttle Orbiter. Space Simulation Conf. 1975 - NASA-SP-379.
6.	R. L. HARVEY	Spacecraft Neutral Self-Contamination by Molecular Outgassing. J, Spacecraft Vol 13-No. 5-May 1976.
7.	L. E. BAREISS M. A. HETRICK E. B. RESS	Spacelab Contamination Assessment MCR-77-105 - September 1977 - Contract MAS8-31547. Exhibit B.
8.	D. A. WALLACE	Use of the Quartz Crystal Microbalance for Outgassing and Optical Contamination Measurements. Journal of Vacuum Science and Technology 1972/Vol 9/1.
9.	D. McKEOWN W. E. CORBIN R. J. NAUMANN	Thermoelectrically-Cooled Quartz Crystal Microbalance. Space Simulation Conf. 1973 - NASA-SP-336.
10.	J. T. VISENTINE R. G. RICHMOND	Molecular Outgassing Measurements for an Element of the Shuttle Thermal Protection System. AIAA No. 76-446, 11th Thermophysics Conf., July 1976.
11.	R. S. PASSAMANECK J. E. CHIRIVELLA	Small Monopropellant Thruster Contamination Measurement in a High-Vacuum Low Temperature Facility. J. Spacecraft Vol 14 - July 1977.
12.	R. W. PHILLIPS L. U. TOLENTINO S. FEUERSTEIN	Spacecraft Contamination under Simulated Orbital Environment. J. Spacecraft Vol 14 - August 1977.
13.	R. P. HENRY	Mesure de taux de dégazage he Vide Novembre-Décembre 1969.
14.	W. WILKENS H. BENTLAGE	Outgassing Measurements using Vacuum Balances published in "Progress in Vacuum Microbalance Techniques" Vol 2-1973.
15.	J. J. SCIALDONE	An Equivalent Energy for the Outgassing of Space Materials. NASA-TN-D-8294.
16.	I. LANGMUIR	The Evaporation Condensation, and Reflection of Molecules and the Mechanism of Absorption. Phys. Rev. Ser 2, Vol 8, August 1916.

17. T. M. HESLIN — An Equation that Describes Material Outgassing for Contamination Modelling. NASA-TN-D-8471, May 1977.

18. J. DAUPHIN a.o.
A. ZWAAL — The Outgassing of Space Materials and its Measurement. ESRO-TN-124. February 1975.

19. A. ZWAAL — Contamination Analyses of OTS Radiator Panels. Internal Publication TQMAZ-7702 (1977).

20. J. Ph. TERMEULEN
F. J. Van EMPEL — The Use of Double Oscillating Quartz Crystals in Mass Determination. Progress in Vacuum Mibrobalance Techniques Vol 1-1972.

21. E. C. Van BALLEGOOYEN
F. BOERSMA
C. v.d. STEEN — Application of a Quartz Crystal with Electrodetab Configuration for Simultaneous Mass and Temperature Determination. Journal of Acoustic Society of America, March 1978.

22. G. GOURMELON
A. ZWAAL — Contamination Measurements on METEOSAT Solar Array using QCM's. ESA-EWP-1012, May 1976.

SESSION II

CONTAMINATION MODELING/SPACECRAFT

SPACELAB INDUCED ENVIRONMENT TECHNICAL OVERVIEW[†]

L. E. Bareiss
Martin Marietta Aerospace
Box 179
Denver, Colorado 80201

1. INTRODUCTION

Much has been written in recent years on the subject of the Space Transportation System (STS) Space Shuttle Orbiter induced contaminant environment and its ultimate impacts upon scientific instrumentation and sensitive systems flown as payloads within the Orbiter payload bay[1-3]. Equally as important is the induced environment of the STS Spacelab vehicle being designed and developed by the European Space Agency as a prime Shuttle payload. This will be additive to the environment of the Shuttle Orbiter and must be considered as a primary design parameter in the Spacelab development. Proper contamination control of the Spacelab vehicle is potentially even more critical than for the Shuttle Orbiter due to its inherent close proximity to scientific instrumentation within the payload bay. The National Aeronautics and Space Administration's Marshall Space Flight Center recognized this area of concern early in the Spacelab Program and funded several Spacelab contamination modeling and analysis studies to predict the Spacelab induced contaminant environment, determine its compliance with program contamination control criteria and establish recommended contamination abatement procedures and on-orbit operations.

This paper presents a compilation of the results of a systems level contamination analysis and related computer modeling activities conducted by Martin Marietta Aerospace, Denver Division under contract NAS8-31574. It depicts our current technical assessment of the contamination problems anticipated during the Spacelab program and presents recommendations for contamination abatement designs and operational procedures based upon experience gained in the field of contamination analysis and assessment dating back to the pre-Skylab era.

The impact of the induced contaminant environment of space vehicles has become extremely important as a basic design parameter for the multi use/variable configured Spacelab carrier and it numerous ultrasensitive payloads. The degree of efficiency to which the Spacelab design meets the contamination control criteria as dictated by the Spacelab payload user

---

[†] Work sponsored by the NASA, Marshall Space Flight Center, Alabama under contract NAS8-31574

community will determine the ultimate utility of the Spacelab to provide this community with the platform from which to conduct desired investigations with assurance that the induced environment will not compromise payload objectives.

2. SPACELAB MODELING AND ANALYSIS

2.1 Major Model Parametric Considerations - A primary design goal for the various Spacelab configurations is to insure that the operation of Spacelab/Orbiter systems and the mission objectives of scientific instruments are not compromised by the induced molecular and particulate contaminant environment emanating from the Spacelab carrier. To accomplish this, a rigorous computer modeling and analysis study has been conducted over the past 3½ years to establish the predicted on-orbit contaminant environment levels under variable orbital conditions as well as to determine Spacelab contamination related design and operational requirements necessary to meet the maximum allowable induced environment levels or criteria as set forth in Volume X of JSC 00770[4]. These criteria have also been recommended for application as a design goal for Spacelab by the European Space Agency (ESA) in ECR 00049[5]. The criteria state that it is a design and operational goal for Spacelab to control:

a. in an instrument field-of-view particles of 5 microns in size to one event per orbit;

b. induced water vapor column density to 10^{12} molecules$\cdot$cm^{-2} or less;

c. return flux to 10^{12} molecules$\cdot$cm^{-2} s^{-1};

d. continuous emissions or scattering to not exceed 20th magnitude$\cdot$s^{-2} in the UV range; and

e. to control to 1% the absorption of UV, visible, and IR radiation by condensibles on optical surfaces.

This set of criteria is compatible with the contamination control criteria imposed upon the Orbiter[4] and has been utilized as the baseline from which to make Spacelab design and development decisions throughout this paper. These criteria have been used as a basis in the modeling activities to establish a compatible model output format which facilitates the understanding of the criteria implications and aids in the performance of contamination evaluation studies.

Because of the dependence of the current model format upon the above contamination control criteria, it is important to note the additional assumptions and interpretations that are required to make the abbreviated criteria statements more applicable and useful in design and development evaluations. These interpretations will demonstrate the reasoning behind certain modeling decisions and approaches discussed in ensuing sections of this paper. In his memo of May 24, 1976[6], R. Naumann of the Marshall Space Flight Center (MSFC), chairman of the Contamination Requirements Definition Group (CRDG) presented the necessary additional interpretations of these criteria that were established by the cognizant scientific user community. These interpretations are discussed in detail in Section 4 herein.

The primary analytical tool utilized in this study was the Shuttle/Payload Contamination Evaluation Program (SPACE) which was developed to mathematically synthesize the contaminant sources, susceptible surfaces and transport mechanisms and to establish the predicted induced contaminant environments of the Spacelab carriers modeled. The general modeling considerations and approaches employed herein are discussed in Reference 7. In the subsections that follow, brief descriptions of the current Spacelab modeled configurations, contaminant sources and major SPACE Program input parameters and assumptions are presented.

2.1.1 Modeled Spacelab Configurations - The current SPACE Program developed primarily for static design and development analysis consists of three unique Spacelab configurations deemed representative of the assorted module and pallet hardware combinations that will be utilized throughout the Spacelab Program. The current Spacelab configurations modeled include: 1) the long module/one pallet (LMOP); 2) the short module/three pallet (SMTP); and 3) the five pallet (FIVP) configurations. Geometrical data utilized in establishing the necessary model input parameters for these configurations was obtained from Reference 8. Figure 1 illustrates the basic LMOP configuration elements utilized in the geometrical modeling. Note that the axis system and station numbers (X_o, Y_o, Z_o) presented are consistent with those of the Shuttle Orbiter coordinant system which is a baseline for this paper. The primary purposes for developing the geometrical configurations are to establish the spatial relationships between all Spacelab contaminant sources and surfaces and to obtain mass transport factors (MTF). The MTF represents the percentage of mass leaving a Lambertian source or surface capable of reaching another point or surface based upon geometry and surface shadowing between sources and receivers. When input into SPACE, the MTFs formulate the basis for describing the Spacelab induced contaminant environment.

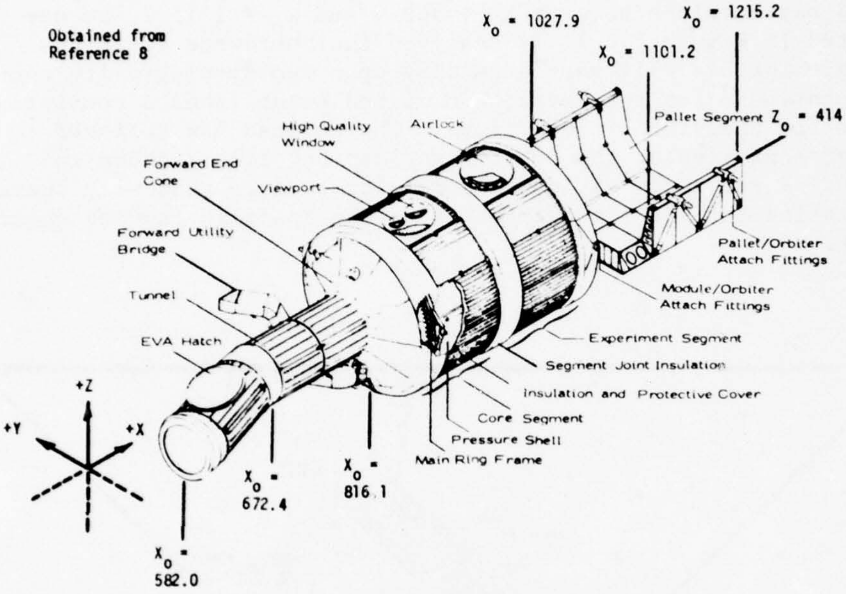
Obtained from
Reference 8

Figure 1. Baseline Long Module/One Pallet Reference Spacelab Configuration (LMOP)

The three modeled Spacelab configurations were segmented nodally and displayed graphically by the computer as depicted in Figure 2. The nodal breakdown of each configuration is used as the prime reference system between the configuration and contaminant source parametric data such as the materials mass loss characteristics and surface temperature profiles discussed later. A specially modified Martin Marietta Thermal Radiation Analysis System (TRASYS-II)[9] is utilized to establish the necessary geometrical relationship input data to the SPACE Program, however, almost any properly modified configuration model could probably be used in its place. Once the required relationships are established, this segment of the model is no longer needed.

However, any changes in geometrical relationships between surfaces and sources, require new relationships to be established from the TRASYS II program.

In order to establish consistency between the three modeled configurations, they were each located within the Orbiter payload bay envelope between $X_o = 582.0$ and $X_o = 1215.2$, as depicted in Figure 2. It is realized that hardware locations within the bay will vary depending upon center-of-gravity considerations, but the envelope utilized establishes a consistent base for analytical comparisons. The payload bay surfaces (representative of the Orbiter payload bay liner) shown in Figure 2 are included in the model for surface shadowing characteristics but are not chargeable to the Spacelab induced environment.

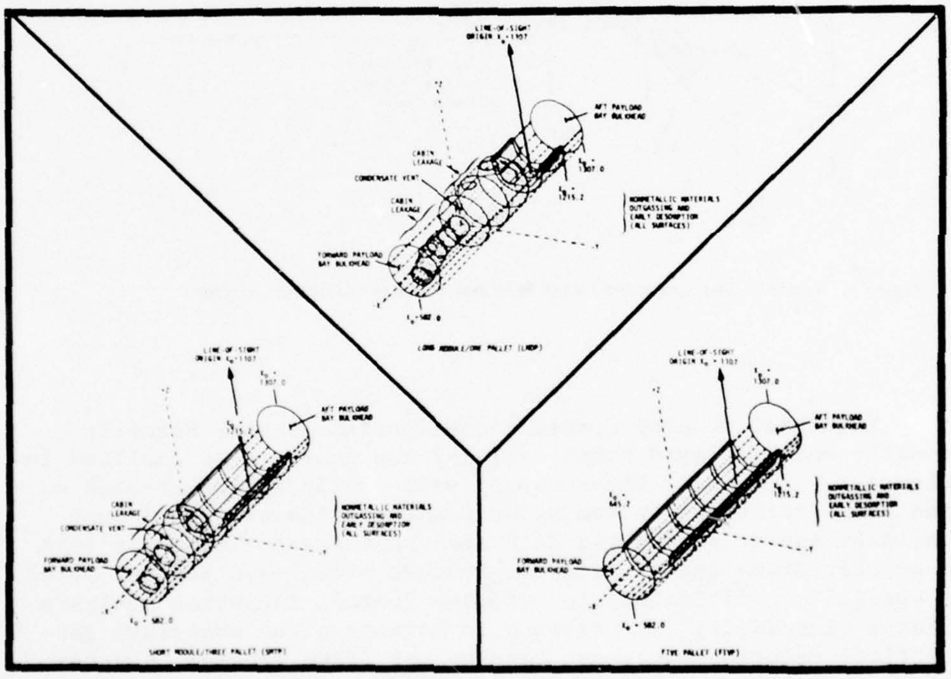

Figure 2. Modeled Spacelab Configurations and Contaminant Sources

The SPACE Program not only considers contaminant transport directly between a source and a receiving surface but also evaluates the physics of the contaminant cloud in the near vicinity of the Spacelab. The major items included therein are the phenomena of the column density or "thickness" of the induced environment through which a payload must view and the return flux (or backscatter) of released contaminant molecules to a surface of interest resulting from molecular collisions with the ambient atmosphere or with other contaminant molecules (self-scattering). To evaluate these phenomena, seventeen (17) lines-of-sight for each Spacelab configuration have been geometrically modeled. Along each of these lines-of-sight which originate at $X_o = 1107$, $Y_o = 0$ and $Z_o = 507$ (Figure 2), a series of pseudo surfaces were input to the model as point contaminant receivers. The point of origination is consistent with the Prime Measuring Point (PMP) advocated by the CRDG at MSFC for contamination control criteria evaluation. The lines-of-sight currently modeled were selected to uniformly encompass a 120 degree conical viewing volume around the +Z axis above the Spacelab configurations as illustrated in Figure 3 for the SMTP. This is also consistent with the CRDG interpretation of the contamination control criteria and encompasses the majority of viewing requirements of Spacelab payloads to be flown.

2.1.2 Spacelab Contaminant Sources - The modeled Spacelab carrier configurations currently have four major contaminant sources identified which have been evaluated in detail. These include: 1) external nonmetallic materials outgassing (i.e.; the long term mass loss of the material upon exposure to space vacuum); 2) early desorption from external surfaces (i.e.; the initial high mass loss of adsorbed and absorbed volatiles, gases and liquids); 3) cabin atmosphere leakage from pressurized tunnel and module segments; and 4) the Spacelab Condensate Vent (SCV). Figure 2 should be consulted for the locations of the modeled contaminant sources for each of the three Spacelab configurations.

These sources are treated as closed form mathematical expressions which physically approximate the contaminant emission processes involved. A parametric summary of the methodology and assumptions utilized in the modeling of these sources and the primary considerations involved in determining the major expressions and relationships are presented in the following

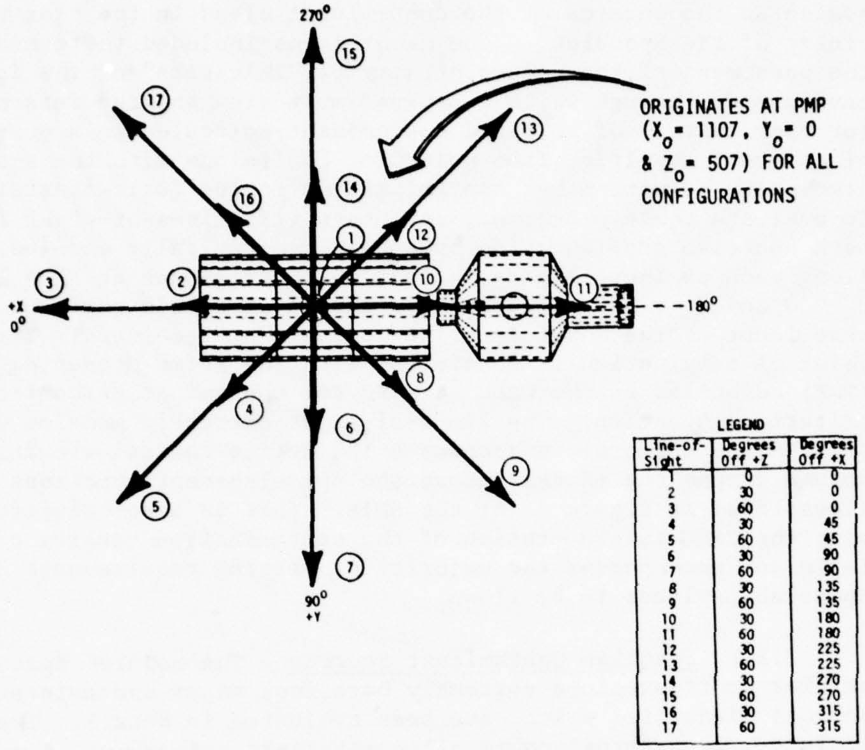

LEGEND

Line-of-Sight	Degrees Off +Z	Degrees Off +X
1	0	0
2	30	0
3	60	0
4	30	45
5	60	45
6	30	90
7	60	90
8	30	135
9	60	135
10	30	180
11	60	180
12	30	225
13	60	225
14	30	270
15	60	270
16	30	315
17	60	315

Figure 3. Modeled Spacelab Lines-of-Sight

paragraphs. It should be noted that it was determined through the modeling activities, that the major contaminant transport mechanism of concern to Spacelab and its payloads will be the phenomena of return flux through ambient interaction since most Spacelab/payload sensitive surfaces will not have direct lines-of-sight to the contaminant sources.

2.1.2 a. Outgassing - Nonmetallic materials outgassing is modeled as a continuous Lambertian contaminant source with an emission rate that is a direct function of surface temperature and time of exposure to the vacuum of space. The ESA design of the external Spacelab thermal control system has apparently been finalized and isothermal total mass loss/volatile condensible material (TML/VCM) test data on the chosen nonmetallic materials has been supplied by ESA. The current Spacelab passive thermal control system design incorporates Chemglaze II A-276 white paint (Hughson Chemical Company, Erie, Pennsylvania) as the thermal control coating for all internal and external pallet surfaces and multilayer insulation (MLI) manufactured by Aeritalia as the thermal blanket for the module and tunnel sections of Spacelab.

ESA thermal vacuum test data on these materials is contained in References 10 and 11, respectively. Figure 4 depicts the variation of Chemglaze and MLI TML rates and outgassing rates as a function of vacuum exposure time at a test temperature of 80°C. Outgassing rates for these materials were determined from the % VCM data for a -75°C Quartz Crystal Microbalance (QCM) deposition monitor by assuming that the sticking coefficient of the large molecular weight outgassing species was unity at that temperature. Chemglaze II % VCM data [10] was presented as total % VCM for the entire 165 hour test, therefore, only the average outgassing rate could be determined. In contrast, % VCM data on the MLI[11] was presented in terms of % VCM $\cdot$ s^{-1} and the MLI outgassing decay curve could be established.

The average outgassing rates at 125°C (OGR_{125}) derived from the ESA supplied test data in $g \cdot cm^{-2} \cdot s^{-1}$ were 1.33×10^{-11} for Chemglaze II and 1.29×10^{-9} for the module MLI. Outgassing rates are input to the SPACE Program at the 125°C reference temperature and are then adjusted internally to the model for individual nodal surface temperatures. The analytical expression developed to describe this temperature dependence for each material is presented below:

$$OGR_T = OGR_{125} \bullet EXP\ (T-125)/K, \qquad (1)$$

where, T = source temperature (°C) and

K = material characteristic constant which

= 20 for Chemglaze and

= 11 for MLI.

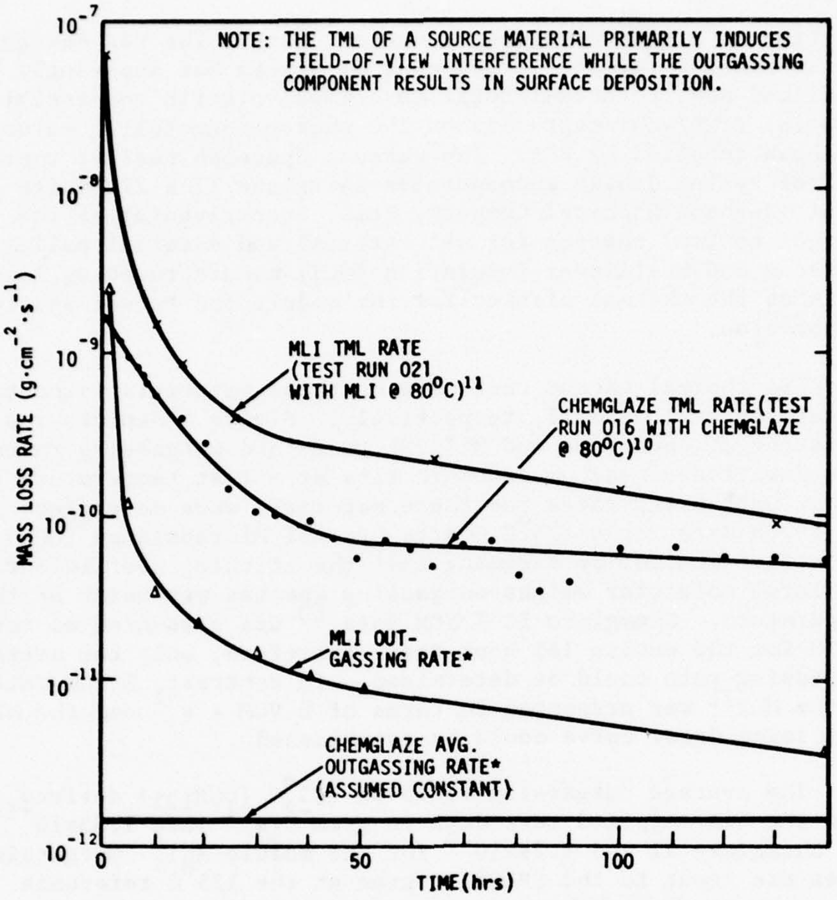

*BASED UPON %VCM TEST DATA AT -75°C COLLECTOR TEMP. AND 80°C SOURCE

Figure 4. MLI and Chemglaze II Mass Loss Rate Variation with Time

By utilizing the ESA obtained % VCM data at differing QCM temperatures, the outgassing component sticking coefficient variation with temperature was approximated for the MLI and Chemglaze II coatings. Again by assuming that the sticking coefficient approaches unity at -75°C, sticking coefficients at other temperatures are simply the ratios of the % VCM at temperature T_c over the % VCM at -75°C. Figure 5 presents the sticking coefficient variation with collector temperature, T_c, for MLI and Chemglaze II held at $T_s = 80^oC$. Superimposed on Figure 5 is the Skylab derived sticking coefficient relationship used in previous analyses for comparison.

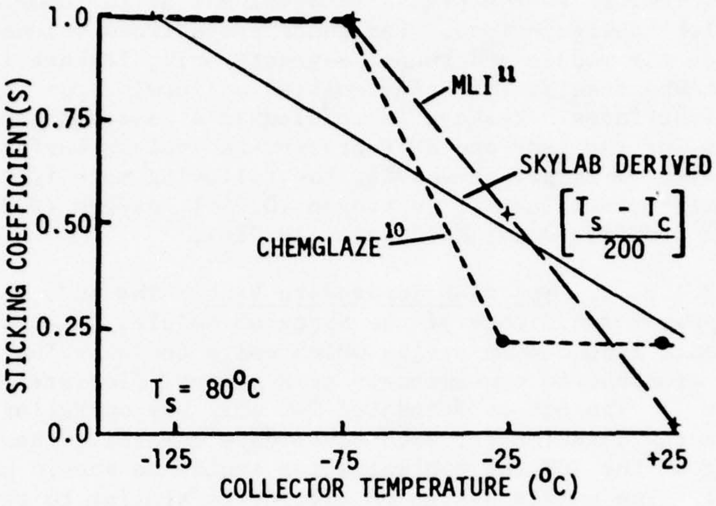

Figure 5. MLI and Chemglaze II Sticking Coefficient Relationships

2.1.2 b. Early Desorption - A similar approach is utilized in modeling the phenomena of early desorption, however, in contrast to outgassing; the early desorption rate tends to decay more rapidly upon initial exposure to space vacuum. The ESA test data depicted in Figure 4 was again used to establish the required SPACE Program model input parameters. Primary constituents of early desorption and their mole fractions include: water (0.57), nitrogen (0.23), carbon dioxide (0.12) and oxygen (0.08). The results presented later in this paper are based upon the early desorption rates at 10 hours into the decay curve. The 10 point was selected to obtain worst case predictions for payloads at the point in a mission when activation of susceptible instruments might be expected to commence. The modeled early desorption rates at 100^oC (EDR_{100}) in $g \cdot cm^{-2} \cdot s^{-1}$ were 1.29×10^{-9} for Chemglaze II and 4.43×10^{-9} for MLI at 10 hours with their temperature dependence modeled as

$$EDR_T = EDR_{100} \bullet EXP \ \frac{E}{R} \left[\frac{1}{373} - \frac{1}{T} \right], \qquad (2)$$

where, T = source temperature (^{o}K) and

E = source activation energy (7500 cal·mole^{-1} assumed).

2.1.2 c. Cabin Atmosphere Leakage - Cabin atmosphere leakage is limited to the pressurized volumes of the LMOP and SMTP Spacelab configurations. For those pressurized volumes, which include the module and tunnel segments only, leakage is modeled as a Lambertian source being emitted uniformly from their external surfaces. Leakage is modeled as a constant steady state source for the LMOP and SMTP pressurized volume surfaces at a rate of 1.35 kg per day having the following mole fractions of molecular constituents: nitrogen (0.758), oxygen (0.219), carbon dioxide (0.007) and water (0.016).

2.1.2 d. Spacelab Condensate Vent - The SCV, located on the upper forward cone of the Spacelab module, is a controllable overboard liquid dump system which emits condensed water and trace atmospheric contaminants at a nominal flowrate of 4.5 kg·min^{-1}. The SCV is scheduled for only one operation of 7 to 17 minutes duration for each seven days on-orbit, therefore, timelining of the SCV for contamination avoidance should not be difficult. The nozzle design of the SCV is similar to that of the Skylab contingency condensate vent employing a double-tapered exit orifice 2.45 mm in diameter and a heater system to inhibit nozzle freeze-up.

The SCV will produce copious amounts of ice/water particles and water vapor (approximately 15% by weight) during operation. The primary contamination concern other than proper timelining is the potential frost layer/snowcone buildup on Orbiter and Spacelab structural surfaces resulting from SCV plume impingement. This would result in an additional unpredictable contaminant source which would be impossible to control. Dornier Systems small vacuum chamber test data on the SCV illustrated in Figure 6 indicates that plume impingement on the Orbiter payload bay forward bulkhead has been minimized but not totally eliminated for the most forward Spacelab module positions within the bay. The main core and lower density region of the SCV plume will be confined to approximately a 22° conical half angle, however, the over expanded vapor region of the plume distribution pictured may have been restricted by the confines of the small (0.4 m diameter) test chamber employed. This should present negligible problems although, as a precaution, it might

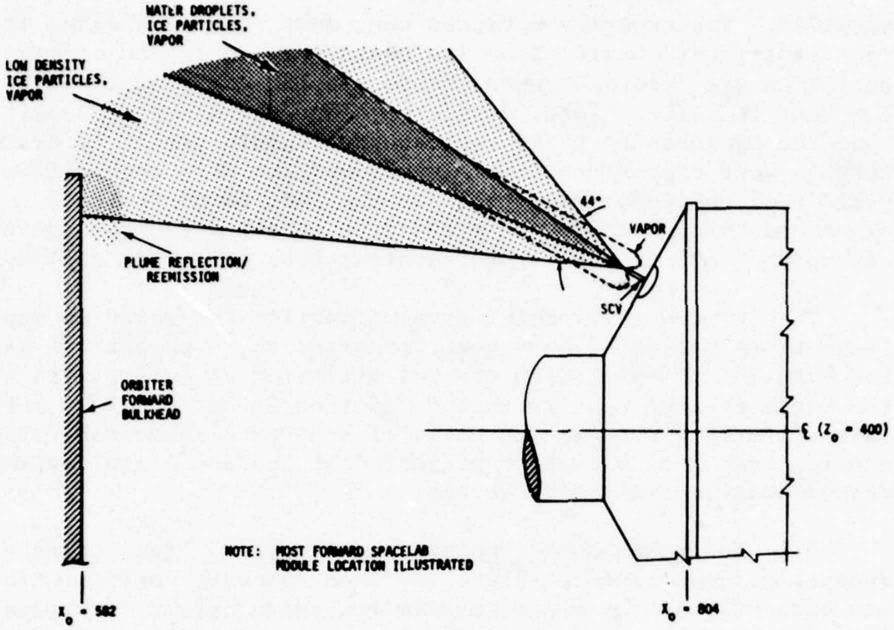

Figure 6. Spacelab Condensate Vent Plume Definition

be advisable to allow the payload bay area to heat soak under solar exposure during venting to minimize condensation.

3. SPACELAB MOLECULAR INDUCED ENVIRONMENT PREDICTIONS

Through the use of the SPACE Program, molecular induced environment predictions were established for the three modeled Spacelab configurations (i.e.; long module/one pallet-LMOP, short module/three pallet-SMTP and five pallet-FIVP) and for the contaminant sources described in subsection 2.1.2. The contaminant sources evaluated in detail in this section include nonmetallic materials outgassing, early desorption at 10 hours of vacuum exposure and cabin atmosphere leakage. The Spacelab condensate vent has been evaluated in detail in Reference 13 and is not specifically reiterated herein since plume structural impingement has been minimized and due to the condensate system's capability of holding condensate for up to seven days which will facilitate vent timelining. Although the experiment vacuum vent has been identified as an additional major contaminant source, sufficient supplemental design/test data is not yet available, and consequently the evaluation of this source has not been extended. The experiment vacuum vent must be evaluated on a "per experiment" basis since its contamination source characteristics are dependent upon the particular experiment using the vent facility. Interference with the operation of sensitive Spacelab payloads by these vent sources should easily be avoided through vent expulsion timelining around the data acquisition periods of payloads susceptible to the induced contaminant cloud and through employing protective measures such as operable covers and ambient drag vector avoidance by cryogenic payloads.

The induced environment predictions for the Spacelab configurations presented have been formatted to be compatible with the baseline contamination control criteria[4] as interpreted by the Contamination Requirements Definition Group (CRDG) at MSFC[6]. This criteria serves as the basis of the Spacelab contamination control criteria evaluation presented in Section 4 and for the recommendations included therein.

3.1 Molecular Number Column Density (NCD) Predictions - Seventeen fixed lines-of-sight for each Spacelab configuration are currently in the SPACE Program for which current NCD predictions have been made. These lines-of-sight (illustrated for the SMTP in Figure 3) encompass the 120° conical viewing volume centered around the +Z axis above the Spacelab vehicle originating at the CRDG Prime Measurement Point (PMP) at $X_o = 1107$, $Y_o = 0$ and $Z_o = 507$. These predictions are presented in Table I for the three modeled Spacelab configurations. Nonmetallic surface material mass loss predictions are based upon the maximum hot case Spacelab thermal profile data contained in Reference 14 and the ESA materials test data previously discussed.

The primary concern of the NCD parameter is its propensity to scatter, emit or absorb radiant energy thus interferring with the data acquisition ability of sensitive optical experiments. The corresponding contaminant pressures in the proximity of high voltage power systems can also induce such phenomena as corona arc-over damage and multipacting of transmitting systems. The predicted NCD levels for outgassing and leakage will remain relatively constant throughout a Spacelab mission, however, the early desorption NCD levels will decrease rapidly as the early desorption rate decays with time of vacuum exposure. The primary contamination threats from early desorption will, therefore, be limited to the initial on-orbit phases of a given mission.

Table I. Spacelab Molecular Number Column Density Predictions

SOURCE/ CONFIG. / LINE-OF-SIGHT	NUMBER COLUMN DENSITY (molecules·cm^{-2})							
	OUTGASSING			EARLY DESORPTION			LEAKAGE	
	LMOP	SMTP	FIVP	LMOP	SMTP	FIVP	LMOP	SMTP
1	1.9E8*	2.8E8	1.3E8	3.7E12	1.8E12	2.1E11	2.6E12	1.4E12
2	1.6E8	2.4E8	1.2E8	3.0E12	1.5E12	1.9E11	2.2E12	1.1E12
3	1.6E8	2.2E8	1.1E8	2.7E12	1.4E12	1.7E11	1.9E12	9.9E11
4	1.7E8	2.5E8	1.3E8	3.3E12	1.6E12	2.0E11	2.3E12	1.2E12
5	1.6E10	1.5E9	1.2E8	3.4E12	1.5E12	1.8E11	2.1E12	1.0E12
6	1.3E9	5.2E8	1.3E8	3.9E12	1.8E12	2.1E11	2.6E12	1.4E12
7	3.4E10	3.9E9	1.2E8	5.1E12	2.0E12	1.8E11	2.6E12	1.3E12
8	7.2E8	6.6E8	1.4E8	4,8E12	2.3E12	2.2E11	3.1E12	1.7E12
9	3.7E10	7.4E9	1.5E8	7.5E12	3.4E12	2.3E11	3.7E12	2.2E12
10	1.1E9	9.6E8	1.5E8	5.1E12	2.6E12	2.3E11	3.3E12	1.9E12
11	1.1E10	2.7E9	1.7E8	8.4E12	4.4E12	2.7E11	4.5E12	3.3E12
12	6.9E8	6.5E8	1.4E8	4.4E12	2.2E12	2.2E11	3.1E12	1.7E12
13	3.7E10	7.3E9	1.4E8	6.4E12	3.0E12	2.2E11	3.7E12	2.2E12
14	1.3E9	5.1E8	1.3E8	3.5E12	1.7E12	2.0E11	2.6E12	1.4E12
15	3.4E10	3.9E9	1.1E8	4.4E12	1.7E12	1.7E11	2.6E12	1.3E12
16	1.6E8	2.4E8	1.2E8	3.1E12	1.5E12	1.9E11	2.3E12	1.2E12
17	1.6E10	1.5E9	1.1E8	3.1E12	1.4E12	1.7E11	2.1E12	1.0E12

*1.9E8 = $1.9\text{x}10^{8}$

3.2 Molecular Return Flux Predictions - For most Spacelab payloads, the primary transport mechanism of the major contaminant sources will be the return flux resulting from contaminant molecular collisions with the ambient atmosphere flux. Direct line-of-sight and self-scattering return flux transport were evaluated and deemed negligible under the major Spacelab source conditions. All major Spacelab sources were evaluated for maximum return flux (i.e.; ambient drag vector perpendicular to surface of interest) to a 2π steradian field-of-view surface located at the PMP. The worst case orbital altitudes were considered for each source modeled (i.e., early desorption and leakage at 200 km and outgassing at 250 km) and medium solar activity was assumed. The resulting predictions are presented in Table II.

The main threat of molecular return flux is its ability to accommodate or stick to surfaces upon which it impinges thus absorbing radiant energy which scientific instruments are attempting to detect or modifying the thermal characteristics of surfaces to which it adheres. The constituents of early desorption and cabin leakage return flux will demonstrate negligible dwell times on all surfaces other than those that are cryogenic. In contrast, outgassing species can condense on surfaces with temperatures of 25^{o}C or warmer.

Table II. Spacelab Molecular Return Flux Predictions

SOURCE/ ALTITUDE CONFIGURATION	MAXIMUM RETURN FLUX-2π sr SURFACE (molecules$\cdot$cm$^{-2}\cdot$s^{-1})		
	OUTGASSING AT 250 km	EARLY DESORPTION AT 200 km	LEAKAGE AT 200 km
LMOP	8.7E11	5.0E14	4.1E14
SMTP	1.6E11	2.4E14	2.1E14
FIVP	1.4E10	2.4E13	——

The optimum approach to decreasing the impacts of return flux upon sensitive surfaces is to minimize surface impingement or reduce its ability to stick. Impingement can be minimized through proper selection of materials with low early desorption rates, flying in attitudes where major contributing surfaces are cool, flying in attitudes where return flux is minimized, by the payloads supplying their own operable protective covers or in some cases by providing an inert gas purge system.

3.3 <u>Deposition Predictions</u> - Spacelab deposition predictions calculated by the SPACE Program were based upon the mission dependent parameters set forth in the CRDG interpretations[6] of the existing Spacelab contamination control criteria[5]. These parameters include condensible deposition on a 0.1 steradian surface at 300°K (27°C) located at the PMP subject to a random drag vector orientation for a seven day mission. Sticking coefficient data employed in the modeling was based upon the ESA TML/VCM test data discussed in subsection 2.1.2. Materials outgassing is the only identified Spacelab contaminant source that will accumulate in measurable quantities on a surface at 27°C, therefore, the deposition predictions which are presented in Table III result from that source alone. Although the predicted levels of outgassing deposition resulting from Spacelab carrier sources equate to less than one angstrom in thickness for a 0.1 steradian surface at the PMP at 300°K, deposition will still be of concern for certain payloads with differing configurations and temperature profiles.

Table III. Spacelab Molecular Deposition Predictions

PARAMETER / CONFIGURATION	DEPOSITION (0.1 sr surface, 250 km, 27°C)		
	RATE	ACCUMULATIVE - 7 DAY MISSION	
	(molecules·cm^{-2}·s^{-1})	(molecules·cm^{-2})	Å
LMOP	8.61×10^{7}	1.26×10^{13}	0.21
SMTP	1.69×10^{8}	2.47×10^{13}	0.41
FIVP	1.33×10^{8}	1.94×10^{13}	0.32

4. SPACELAB CONTAMINATION CONTROL CRITERIA EVALUATION

The induced environment predictions presented in the previous subsection in conjunction with supplemental analysis were utilized to determine the ability of the various Spacelab configurations to meet the existing contamination control criteria imposed upon Spacelab[4] and to establish Spacelab design and development requirements to insure that the criteria are satisfied. To accomplish this, each major Spacelab contaminant source was evaluated against the five criteria statements based upon the interpretations and assumptions sanctioned by the CRDG in Reference 6. In the ensuing subsections, each main criteria statement is presented as depicted in Reference 4. Each is then followed by the applicable CRDG interpretations and finally a detailed analysis of the Spacelab contaminant sources.

4.1 Induced Particulate Environment - *It is a design and operational goal for Spacelab to control in an instrument field-of-view particles of 5 microns in size to one event per orbit.* This assumes a field-of-view of 1.5×10^{-5} steradian and is restricted to particles within 5 km of the spacecraft.

In determining the induced particulate environment of a manned spacecraft such as the Spacelab carrier, known defined particulate sources like the Spacelab condensate vent (SCV) can be parametrically analyzed in a closed mathematical form by knowing the primary vent system characteristics (based upon existing system test data or detailed stream tube vent plume and freezing analysis) and integrating these into an appropriate particle trajectory analysis program. This was conducted for the SCV and the acquired results indicate that this criteria statement can be exceeded during and for up to a minimum time increment of 17 minutes after SCV operation. Under this condition, the intent of the criteria can be met through timelining of the SCV overboard dump around operations of payloads that have been determined susceptible to particles in their field-of-view. Current planning is for the SCV to be operated only once per each seven days on orbit, therefore, noninterference timelining should create minimal problems.

In contrast to well defined controllable particulate sources such as the SCV, intermittent particulate sources (i.e., unpredictable surface/source random particle emission) present a more difficult analytical problem. This phenomena, too, was evaluated and it suffices to state that the current contamination control criteria as applied to random particulate emissions may be very difficult for the Spacelab carrier to meet based upon limited particle sighting data obtained during the Skylab Program by the S052 White Light Coronagraph experiment.

4.2 Molecular Column Density - *It is a design and operational goal for Spacelab to control induced water vapor column density to* 10^{12} *molecules*$\cdot$*cm*$^{-2}$ *or less.* This is measured along any vector within 60 degrees of the +Z axis originating at the Prime Measurement Point (PMP) ($X_o = 1107$, $Y_o = 0$ and $Z_o = 507$). It is further assumed that this represents the worst case situation.

The modeled sources which are of concern to meet the NCD criteria include the SCV, early desorption of externally exposed Spacelab surfaces and the leakage of cabin atmosphere from the pressurized Spacelab module/tunnel segments. No control is required for outgassing materials as stated by this criteria since this source is considered to contain no water constituents (i.e., the outgassing contaminant sources meet the NCD criteria statement).

The SCV exceeds the NCD criteria by over 3 orders of magnitude during its operation and must be timelined around the operation of those payloads deemed susceptible to water column densities greater than 10^{12} molecules$\cdot$cm^{-2} in order that the intent of the criteria be met. Since this overboard dump is currently planned to occur only once each seven days on orbit, interference with payload operations should be minimal if properly timelined.

In the evaluation of the leakage contaminant source, the worst case line-of-sight prediction within 60 degrees of the +Z axis is for the LMOP line-of-sight 11 where the total NCD = 4.46×10^{12} molecules$\cdot$cm^{-2} and the water vapor NCD = 7.14×10^{10} molecules$\cdot$cm^{-2} (see Table I). This value is well within the criteria limits and, therefore, leakage is in compliance.

The final contaminant source, early desorption, demonstrates a maximum total NCD of 8.4×10^{12} molecules$\cdot$cm^{-2} for the LMOP line-of-sight 11 at 10 hours into a mission. This equates to a 4.1×10^{12} molecules$\cdot$cm^{-2} NCD for water vapor which exceeds the criteria limit. In order to meet the intent of the NCD criteria for early desorption, it will be necessary for the external Spacelab surfaces to demonstrate an average early desorption rate (EDR) of less than 2.1×10^{-8} g$\cdot$cm$^{-2}\cdot$s^{-1} at 100°C. This can be accomplished through selection of external materials having an EDR less than this value, through decreasing the total area of coverage of high early desorbing materials or by delaying data acquisition by susceptible instruments until the NCD levels for water vapor have decayed to less than 10^{12} molecules$\cdot$cm^{-2}. Based upon the ESA supplied materials test data, this delay time could be as high as 24 hours. This is highly dependent upon the thermal history of surfaces during that period, however, it is assumed that an average delay time of 24 hours will bring the early desorption NCD levels into compliance with the criteria.

4.3 Molecular Return Flux - *It is a design and operational goal for Spacelab to control return flux to 10^{12} molecules$\cdot$cm$^{-2}\cdot$s^{-1}.* This refers to the total flux on an unshielded surface (2π steradian acceptance) oriented in the +Z direction at the PMP under worst case situations.

The stated criteria applies to the summation of return flux from all contaminant sources with no specific stipulations on the separate constituent levels allowable. However, the ensuing evaluation accounts for the acceptable source levels to meet the criteria on an individual basis. It is realized that from a practical viewpoint that each source should be allowed only a budgeted percentage of the total. This same consideration should also be applied to the Orbiter sources (which are not accounted for herein) to budget between Spacelab and Orbiter source levels. However, for the basic Spacelab design and development analytical approach which has been previously acceptable, it is assumed that each source may have an allowable return flux level of 10^{12} molecules$\cdot$cm$^{-2}\cdot$s^{-1} or less. It should be noted that if the design and operational recommendations in the ensuing paragraphs are followed, that the 10^{12} molecules$\cdot$cm$^{-2}\cdot$s^{-1} total return flux criteria will inherently be met.

The molecular return flux levels experienced during SCV operation significantly exceed the stated criteria limits (i.e. 1.4×10^{17} molecules$\cdot$cm$^{-2}\cdot$s^{-1}). Sensitive surfaces should be protected from return flux possibly by utilizing operable covers, if practical, while SCV dumps are in progress. Return flux could also be minimized through vehicle attitude selection which is not conducive to return flux during SCV operation. Ideally, such an attitude would place the ambient drag vector continually in the Spacelab +Z direction, thus reducing return flux to the PMP to almost zero.

The worst case Spacelab configuration for both outgassing and early desorption return flux to a 2π steradian surface at the PMP is the LMOP during the maximum temperature profile attitude (see Table II). The outgassing return flux prediction for the Spacelab LMOP under maximum ambient drag vector orientation is 8.7×10^{11} molecules$\cdot$cm$^{-2}\cdot$s^{-1} at 250 km altitude. The LMOP return flux prediction therefore meets the criteria.

Utilizing a similar approach for early desorption, it was determined that the maximum LMOP return flux rate would be 5.0×10^{14} molecules$\cdot$cm$^{-2}\cdot$s^{-1} based upon the 200 km altitude predictions. To meet the return flux criteria for early desorption, the EDR would have to be less than 9.22×10^{-11} g$\cdot$cm$^{-2}\cdot$s^{-1} at 100°C assuming that all external Spacelab surfaces contribute. As in the case of early desorption compliance with the NCD criteria statement, the intent of the return flux criteria can be met for susceptible payloads if the exposure of their sensitive surfaces is delayed until such time that the early desorption return flux rate has decayed through vacuum exposure to an acceptable level (approximately 35 hours). If practical, susceptible surfaces should provide their own protective devices such as operable covers and the maximum ram vehicle attitudes should be avoided during the Spacelab early mass loss period. Selection of orbital altitudes above approximately 600 km would also reduce the return flux to an acceptable level.

Meeting the intent of the return flux criteria for cabin atmosphere leakage may be more difficult to achieve due to its continuous, uncontrollable characteristics. Predictions for the worst case Spacelab leakage configuration, LMOP, indicate a return flux to a 2π steradian surface at the PMP of 4.1×10^{14} molecules$\cdot$cm$^{-2}\cdot$s^{-1} at 200 km altitude which exceeds the criteria. Decreasing the allowable design leak rate of the Spacelab vehicles could be extremely costly to the program and such an approach is somewhat impractical in that only 3.29 g$\cdot$day^{-1} could be allowed to leak to insure criteria compliance. Realistically, leakage return flux should not impact any exposed surfaces other than possibly such cryogenic systems as the LHe Infrared Telescope which will have an acceptance angle much less than 2π steradian (closer to 0.1 steradian). However, as stated, the return flux criteria is exceeded. The levels for leakage return flux can be decreased by utilizing previously suggested methods of surface protection, attitude and orbital altitude selection (above 600 km).

4.4 Background Brightness - *It is a design and operational goal for Spacelab to control continuous emissions or scattering to not exceed 20th magnitude$\cdot$s^{-2} in the UV range.* This is equivalent to $10^{-12} B_\odot$ at a wavelength of 360 nonometers ($B_\odot$ = solar brightness).

Background brightness induced by the scattering or emission of radiant energy can result from the presence of either contaminant particles or molecules within the field-of-view of a sensitive optical instrument. For the modeled Spacelab molecular contaminant sources, the primary phenomena of concern in this regard is the scattering of solar energy from the irradiated contaminant molecules. Analyses of this phenomena for outgassing, early desorption and cabin leakage have indicated that all will be well within the criteria as stated.

Although approximately 15% of the vent effluents from the SCV will be emitted in the form of water molecules, the greater concern of this source with regard to the background brightness criteria will be the scattering and emission from the generated ice particles. Due to its potential production of many particles in the submicron region where the scattering level can be significant, exceeding this criteria during vent operations is highly probable. For this reason, the SCV overboard dumps should be timelined to avoid interference with sensitive Spacelab payload data acquisition.

4.5 Absorption Due to Condensible Deposition - *It is a design and operational goal for Spacelab to control to 1% the absorption of UV, visible and IR radiation by condensibles on optical surfaces.* This refers to the objective of an optical system that would typically have a dielectric surface at ambient temperature (approximately 300°K) that is located at the PMP, is oriented along the +Z axis and has an acceptable of 0.1 steradian. It is also assumed that this is for a 7 day mission with random orientation of the ambient drag vector.

Evaluation of this criteria statement indicates that the only major modeled Spacelab contaminant source presenting a concern for absorption by condensibles under the above stated assumptions is the outgassing of Spacelab external nonmetallic materials. This is due to the fact that negligible amounts of the other evaluated source constituents will stick to a surface at 300°K for any measurable time period. To analyze the phenomena of outgassing deposition, a systematic approach was taken utilizing the predictions contained in Table III which are based upon the above stated assumptions. Since this criteria statement is based upon the contaminant effect rather than a specific contaminant level, a more comprehensive evaluation is necessary to determine the compliance of the model predictions with the criteria limits.

The results of this evaluation indicate that the maximum absorption due to condensibles will be induced by the SMTP Spacelab configuration. By assuming that the sensitive surface would be a reflective optic detecting at 1500Å wavelength, the maximum absorption due to outgassing deposition would be 0.16% under the conditions evaluated. This is well within the criteria limits and consequently the Spacelab design as modeled is in compliance.

4.6 Evaluation Summary - To facilitate the interpretation of the preceding criteria evaluation, with respect to Spacelab design/development control, the major results and conclusions are summarized herein. From this, certain program overview design and development directions can be made concerning the major modeled Spacelab contaminant sources and preliminary design/operational requirements. These include:

a. The contaminant source of outgassing meets all of the CRDG Spacelab design criteria statements evaluated as based upon the supplied test data from ESA.

b. The most restrictive criteria statement for Spacelab early desorption is that for return flux. An early desorption rate of less than $9.2\text{x}10^{-11}\ \text{g}\cdot\text{cm}^{-2}\cdot\text{s}^{-1}$ at 100°C will result in compliance with the criteria. If materials control to this level proves impractical from a design viewpoint, activation and/or exposure of payloads sensitive to the early desorption induced environment should be delayed up to 35 hours until early desorption has decayed to an acceptable level.

c. Cabin atmosphere leakage cannot from a practical point of view be controlled to a satisfactory level of compliance with the return flux criteria through Spacelab design alone. For Spacelab missions on which instruments that are sensitive to this phenomena are to be flown, the impact of leakage can be minimized through proper selection of orbital altitude, attitude and sensitive surface protective devices such as operable covers. For a vast majority of proposed Spacelab payloads, other than those operating at cryogenic temperatures, the impact of the predicted levels of return flux of cabin atmosphere leakage will be negligible.

d. During its operation, the SCV will exceed all of the criteria statements with the exception of the 1% absorption due to condensibles. This source cannot be controlled through design without major system modifications such as storing the condensate rather than expelling it overboard. The logical approach to complying with the intent of the criteria statements by the SCV would be to timeline venting to avoid interference with sensitive payload data acquisition and protect sensitive surfaces during vent operations.

In a general overview it can be stated that the current Spacelab design is acceptable from a contamination view point if the users of Spacelab are aware of the environment to which they will be exposed and the constraints/precautions necessary to insure that contamination does not compromise their instruments. It should also be noted that the conclusions presented herein have been based solely upon the Spacelab design and that the additional Orbiter sources must also be considered by any STS/Spacelab user.

5. ACKNOWLEDGEMENTS

The author would like to express his appreciation to M. A. Hetrick and D. A. Strange for their technical support and computer modeling activities and to C. M. Davis, NASA Marshall Space Flight Center, for his technical guidance.

6. REFERENCES

1) Bareiss, L. E., Rantanen, R. O., Ress, E. B. and Leger, L. J.: "Preliminary Evaluation of the Contaminant Environment of the Space Shuttle Orbiter," NASA SP-379, Paper No. 25, 8th Space Simulation Conference, Silver Springs, Md., November 1975.

2) Ress, E. B., Rantanen, R. O. and Bareiss, L. E.: "Preliminary Shuttle Payload Contamination Assessment," AAS Paper No. 75-228, August 1975.

3) Leger, L., Jacobs, S. and Ehlers, H. K. F.: "Space Shuttle Contamination Overview," Proceedings - Institute of Environmental Sciences, 1978.

4) JSC 07700, Vol. X and XIV, Revision C, "Space Shuttle Program Space Shuttle System Payload Accommodations" July 3, 1974, Lyndon B. Johnson Space Center.

5) ECR 00049, European Space Agency, "Goals for Spacelab External Contamination Requirements."

6) Memo: ES31 from R. Naumann to NA01/Manager Spacelab Program Office, Subject: Withdrawal of ECR EL 52-0032R1, May 24, 1976.

7) Bareiss, L. E., Hetrick, M. A., Strange-Jensen, D. A. and Ress, E. B.: "Shuttle/Payload Contamination Evaluation Program - The SPACE Computer Program," MSFC NAS8-31574 Exhibit B, MCR-77-104, April 1977, Martin Marietta Aerospace, Denver Division.

8) SLP/2104, "Spacelab Payload Accommodations Handbook," Preliminary Issue, May 1976, European Space Agency.

9) MCR-73-105, Rev. 1, "Thermal Radiation Analysis System (TRASYS)," NAS9-14318, May 1975, Martin Marietta Aerospace, Denver Division.

10) Telex LS/HM/885 and LS/HM/887 from H. Martinides - ESTEC to A. Galzerano - NASA MSFC, subject: "Outgassing of Chemglaze II A-276," dated May 25, 1977.

11) Zwaal, A.: "Outgassing of Spacelab Thermal Blanket," TQMAZ-77-06, August 1977, ESTEC.

12) Bareiss, L. E., Hetrick, M. A., Ress, E. B. and Strange, D. A.: "Payload/Orbiter Contamination Control Requirement Study - Spacelab Configuration Contamination Model," MSFC NAS8-31574 Exhibit A, MCR-76-387, September 1976, Martin Marietta Aerospace, Denver Division.

13) Bareiss, L. E., Hooper, V. W., Rantanen, R. O. and Ress, E. B.: "Payload/Orbiter Contamination Control Requirement Study," MSFC NAS8-30755 Exhibit A, MCR-74-474, December 1974, Martin Marietta Aerospace, Denver Division.

14) Technical Letter ESD-EP45-22788 from Thermodynamics Branch, Teledyne Brown Engineering to J. W. Littles, Chief Life Support and Environmental Branch, MSFC, Subject: "JSC/ESA Integrated Orbiter/Spacelab Thermal Model Temperature Data for Spacelab Extreme Design Conditions," April 12, 1976.

INFRARED RADIATION FROM THE SPACE SHUTTLE CONTAMINANT ENVIRONMENT

J. P. Simpson* and F. C. Witteborn

Space Science Division

NASA Ames Research Center, Moffett Field, CA 94035

Abstract. The Space Shuttle contaminant environment consists of molecules and particles originating on the Shuttle. The molecules come from outgassing, cabin leakage, flash evaporators and other man-controlled vents, and rocket exhaust. Particles are thought to come from abrasion, ablation of surfaces, dust trapped in cracks, dust from vents and cabin leaks, ice particles from improper venting, and droplets of unburned fuel. Simpson and Witteborn (1977, Applied Optics 16, 2051-2073) have discussed the effect of the infrared radiation from molecules and particles from 4 µm to 200 µm on a sensitive infrared telescope. (This paper also discusses non-Shuttle infrared sources such as the atmosphere of the earth and the interplanetary dust/zodiacal light.) They conclude that the radiation from the contaminant environment is tolerable only when it is at its minimum, when there are no rocket firings and the flash evaporators and the manually controlled vents are not being used. This report extends the predicted infrared spectrum from the molecular contaminants H_2O and CO_2 down to 2 µm. It also discusses the sighting frequency and infrared spectrum of particles caused by spallation of the surfaces of the Shuttle tiles by micrometeoroid impact.

H_2O and CO_2 are the most important infrared active molecules that come from outgassing, cabin leakage, or evaporators. It is assumed that

---

*Ames Associate under Contract NAS2-9636.

the initial populations of the molecular levels are given by thermodynamic equilibrium (TE). In a vacuum the molecules radiate until they come into equilibrium with the radiation field of the earth and sun. The time it takes depends on the Einstein transition probability. Meanwhile the molecules move away from the Shuttle; only the nearby ones are detected by Shuttle-borne experiments. Consequently, the radiation from transitions with small transition probabilities (long lifetimes) is given by the TE formulae (such as the 15-μm band of CO_2 and the 6.3-μm band of H_2O). Bands with large transition probabilities (such as the 4.3-μm band of CO_2 and the 2.7-μm band of H_2O are in equilibrium with the radiation field of the sun or earth (the latter is very weak). Since the Shuttle is actually moving through the earth's upper atmosphere, the H_2O bands are also excited by collisions with oxygen atoms. This results in additional radiation. For CO_2 this excitation is almost negligible.

The surface of the Shuttle tiles is coated with borosilicate glass. Hypervelocity impacts of micrometeoroids make small craters, from which particles are ejected at high velocities (other particles are ejected at low velocities). The shocked or even melted particles have much higher temperatures than the surface; they cool to ambient within a few seconds. However, because of the high velocities, most of the particles that pass through the 15 arcmin field of view of a 1-m diameter telescope do so almost immediately after ejection. The spectrum of the 1 to 20-μm particles is that of a silicate, with emission peaks at 10 μm and 20 μm and emissivities that decrease rapidly at longer wavelengths.

Estimates of radiation from the sources discussed here do not change the authors' earlier conclusion that the Shuttle environment would be suitable for sensitive infrared astronomical observations with appropriate constraints on Shuttle observations. The nature of the expected sources, however, should be considered in the design of instruments planned for use in the Shuttle environment.

1. INTRODUCTION

The performance of cooled infrared telescopes observing from the Space Shuttle Orbiter will be limited by the background radiation from zodiacal particles and, to some extent, from the contaminant atmosphere of the Orbiter itself. Simpson and Witteborn[1] have estimated the infrared background in the 4 to 300 μm range for the expected contaminant environment. They found that with adequate operational constraints, the Orbiter can provide a suitable environment for a cooled infrared telescope. The evaluation was made using a molecular contaminant atmosphere determined by Rantanen and Ress[2] and design parameters from the Shuttle Infrared Telescope Facility (SIRTF), a 1.2-m diameter telescope with 10K - 20K optics.[3] The potential use of such an instrument on important problems which may have their solutions in the near infrared, coupled with the minimum in natural background near 3 μm, has brought to light the importance of evaluating the contaminant induced infrared background from 2 to 4 μm. This is done for water vapor and CO_2 considering both radiative and collisional effects at an altitude of 350 km.

While the particulate environment of the Shuttle Orbiter remains much less predictable than the molecular environment, a potentially important particle production mechanism, namely spallation by micrometeoroids incident upon the tiled surface of the Orbiter, has been proposed by Barengoltz.[4] The particle sighting rates resulting from this mechanism are examined here. The spectrum of the ejected particles is predicted for various sizes of particles of the composition of the tiles. The particle sighting rates determined for this mechanism may be high enough to require that the most sensitive SIRTF instruments incorporate particle sighting discrimination procedures or hardware. They are, however, discrete events and thus do not produce a continuously elevated background. The absence of a continuously elevated background due to spacecraft corona around Skylab was reported by Schuerman and Weinberg.[5]

We will discuss here the infrared spectrum of H_2O and CO_2 at fairly high resolution and the spectrum and sighting frequency of particles spalled by micrometeoroids. Units will be kept general so that the results can be applied to any instrument operating in that wavelength range.

2. MOLECULAR CONTAMINANTS

In this section we will discuss the infrared spectrum of molecular H_2O and CO_2 that is offgassed, outgassed, purposefully evaporated, or leaked from the Orbiter cabin. The temperature of the vapor is low, ranging from 201K for certain parts of the Shuttle facing cold space, to 366K for the radiators when they are facing the sun. We will consider here only the temperature 296K because that is the temperature appropriate for cabin leakage. However, as will be seen, the molecules are not in equilibrium, and the radiation shortward of 5 μm does not depend on the initial temperature.

Bareiss et al.[6] have predicted column densities of H_2O and CO_2 for these sources. Column densities of H_2O for offgassing range from 10^{11} molecules/cm^2 for the minimum temperatures to greater than 10^{13} molecules/cm^2 for maximum temperatures and certain lines of sight. Column densities for the flash evaporators (when operating) range from a few times 10^{11} to a few times 10^{12} molecules/cm^2, depending on the line of sight. Both H_2O and CO_2 are leaked from the Orbiter cabin; the column densities are 1 to $5x10^{11}$ molecules/cm^2, depending on the line of sight. In addition the RCS Vernier thrusters produce the following infrared emitting contaminant molecules: CO, CO_2, H_2O, NO, and OH. The column densities range from 10^{12} to 10^{14} molecules/cm^2 depending on the thruster location. However, the temperature of the exhaust gas is so high that the infrared radiation from the gas is much more intense than that from any other source. Consequently, we will not consider the vernier thruster exhaust because it would not be worthwhile for sensitive infrared telescopes to take data while the thruster exhaust is in the field of view. The gaseous exhaust products dissipate in a few seconds so the lost observing time is negligible, provided that the interval between firings is large.

In this paper we will not consider the spectra of other molecules besides H_2O and CO_2. Such molecules might be the outgassed products of epoxy, teflon, paint, insulation, etc. We will also assume there are no leaks in the fuel, hydraulic, and coolant systems. Finally, we will not consider the gases that might be leaked from or used to purge other experiments.

When the H_2O and CO_2 molecules leave the Shuttle, they move into the radiation field of the earth and sun. We assumed that all the molecules move with the most probable velocity for the temperature 296K. Rantanen and Ress[2] have predicted the density of the molecules as functions of distance from the Shuttle and line of sight. From this we can calculate the number of molecules in the line of sight that fall into each time increment. Half the column density is reached by 21.3 m for H_2O and by 13.1 m for CO_2; the corresponding travel times for the molecules are 0.041 sec and 0.039 sec, respectively. It was assumed that the instrument's entrance aperture projects 3 m beyond the skinline of the Orbiter. The radiation field of the sun is approximately a blackbody at 5850K diluted by the solid angle of the sun divided by 4 π ster. The radiation field of the earth is given by a blackbody function at different temperatures subtending 2 π ster. (The actual solid angle is slightly smaller and varies with altitude.) The different temperatures are the brightness temperatures of the earth at different wavelengths given by Smith.[7] The brightness temperature is as low as 218K where the earth's atmosphere is optically thick, but 288K where the atmosphere is optically thin and one can see all the way to the surface of the earth from space. Because of the short time required for the molecules to disperse out of the field of view, the vibration-rotation bands could be divided into three groups. 1) Those with transition probabilities A greater than about 80 sec^{-1}, such as the 4.3-μm band of CO_2 and the 2.7-μm band of H_2O come into equilibrium almost immediately, as $(1-e^{-At})$. 2) Bands with A less than a few sec^{-1} do not substantially change their initial intensities in the few tenths of a second that it takes before they are dispersed out of the field of view. 3) Intermediate cases fall between. We did a molecular excitation and decay calculation for those vibrational levels from which bands in groups 1 and 3 arise. All vibration-rotation bands connecting these levels were considered. There were 7 vibrational levels in the calculation for H_2O and 11 for CO_2 (more because of the extra degeneracy in the linear CO_2). The initial populations of the rotational levels in each vibrational level were given by the Boltzmann equation for 296K. The level populations were then followed for 0.27 sec, at which time the column density has fallen to less than a tenth of the total value. The line list by McClatchey et al.[8] was used for the energy levels and transition probabilities. The spectrum at each increment of 0.01 sec was multiplied by the fraction of the column density in that time increment and summed. All transitions not included in this calculation (all of group 2) were added with their initial small intensities.

The spectrum for a column density of 10^{12} molecules/cm^2 of H_2O is given in Fig. 1, and the spectrum for 10^{11} molecules/cm^2 of CO_2 is given in Fig. 2. These are probably close to the minimum column densities

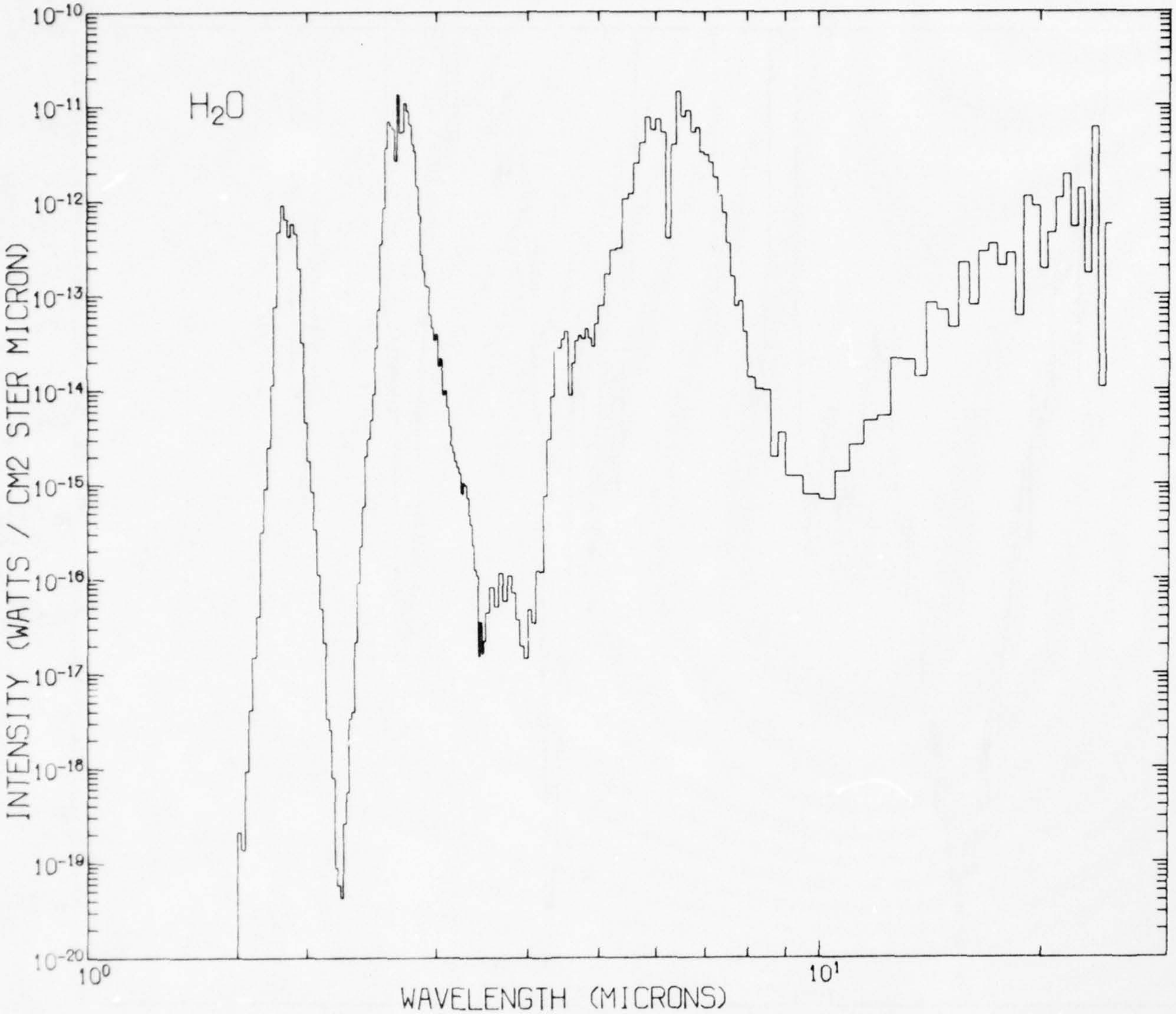

FIGURE 1 The intensity spectrum of 10^{12} molecules/cm^2 of H^{2}O is plotted from 1.6 to 25 μm. The molecules had an initial excitation temperature of 296K, but the energy level populations decay or are excited by the radiation from the earth and sun as the

AD-A070 386 AIR FORCE MATERIALS LAB WRIGHT-PATTERSON AFB OH F/G 22/2
PROCEEDINGS OF THE USAF/NASA INTERNATIONAL SPACECRAFT CONTAMINA--ETC(U)
1978 J M JEMIOLA
UNCLASSIFIED AFML-TR-78-190 NL

3 OF 13
AD
A070386

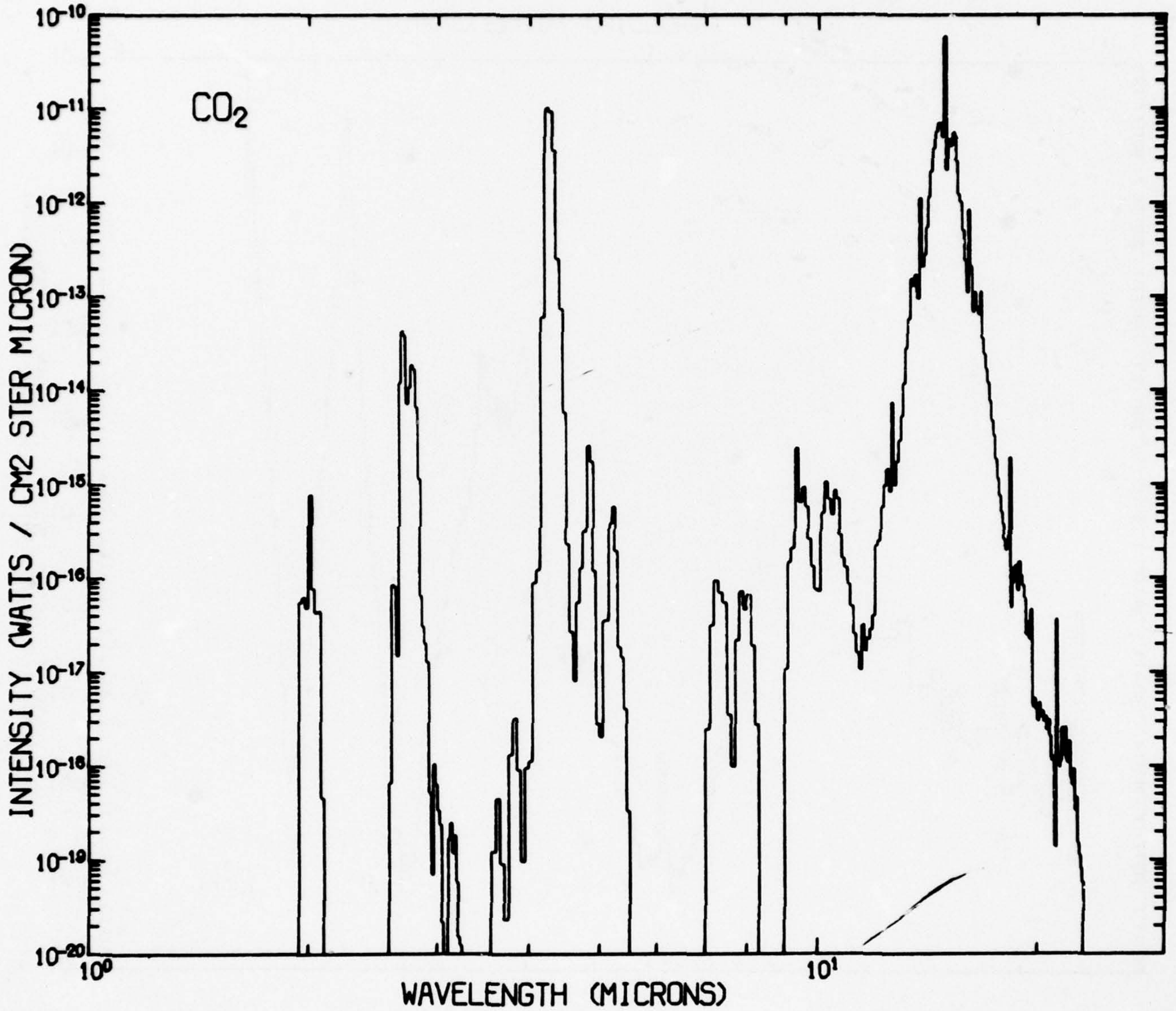

FIGURE 2 The intensity spectrum of 10^{11} molecules/cm^2 of CO_2 is plotted from 1.9 μm to infinity. The CO_2 molecules have the same excitation conditions as the H_2O in Figure 1.

achievable on the Space Shuttle, as discussed above. The spectra are somewhat different from those calculated previously for pure ${}^{1}H_2{}^{16}O$ and ${}^{12}C^{16}O_2$ with only radiative excitation from the ground state considered. For H_2O, the region at 4.5 μm is excited through fluorescence, and the minimum at 3.7 μm is partially filled in by HDO. ${}^{12}C^{16}O^{18}O$ adds extra bands in the 7-μm region.

The H_2O and CO_2 molecules are also excited by collisions with the ambient atmosphere. Because the mean free path through the atmosphere is so long (∿ kilometers), most molecules do not collide until they have already radiated down to the ground state. They are seen at all only because the probability of excitation is very large, due to the 7.7 km/sec velocity difference. Consequently, we can discuss the collisional excitation separately from the radiative excitation and add the two components of the spectrum together only at the very end. We chose an altitude of 350 km for the calculation; the average density at that altitude is 9.1×10^{-15} g/cm³.[9] The atmosphere is predominantly atomic oxygen at this altitude. The average number density of oxygen atoms is 3.1×10^{8} atoms/cm³. Since the intensity in the spectrum scales approximately as the density of the colliding oxygen atoms, the results can be scaled for other altitudes or nonaverage conditions.

An expression for the intensity of the radiation from collisionally excited molecules was derived by Simpson and Witteborn.[1] We rewrite it as

$$I = \frac{W}{\pi R^2 \Omega_{fov}} = \frac{h\nu}{4\pi} \frac{A}{v_{CM}} \frac{EP}{4\pi} \left\langle \frac{1}{d} \right\rangle \frac{N}{N_*} \tag{1}$$

where W is the power on a detector from one line, R is the radius of the telescope, Ω_{fov} is the solid angle of the field of view, A is the transition probability for the line, h is Planck's constant, ν is the frequency, v_{CM} is the velocity of the center of mass of the colliding oxygen atom and the emitted H_2O or CO_2 molecule, E is the emission rate of the molecules over the whole Shuttle, P is the excitation probability, $\langle\frac{1}{d}\rangle^{-1}$ is the weighted average distance of the molecule when it radiates into the field of view, and $\frac{N}{N_*}$ is the fraction of the excited molecules that still have not decayed when they pass through the field of view. $\langle\frac{1}{d}\rangle$ and $\frac{N}{N_*}$ are integrals over the velocity distribution of functions that depend on the hard sphere cross section, the atmospheric density, and the transition probability. The cross sections for collisional excitation of H_2O by O and CO_2 by N_2 have been measured only at much lower energies, and for the 010 and 001 fundamentals only. We extrapolated the excitation of the 010 band of H_2O by oxygen (6.3 μm) measured by Dunn et al.[10] Rieger et al.[11] extrapolated the excitation of the 001 bands of H_2O (2.7 μm) and CO_2 (4.3 μm) by oxygen, using theoretical considerations that the cross section for excitation of CO_2 by O should be much larger than that for excitation by N_2. Elgin and Kolb[12] did the same for the 010 band of CO_2 (15 μm). Kolb et al.[13] and Kolb and Elgin[14] have calculated the pure rotational excitation of H_2O after collision with oxygen atoms. The earlier paper gives better agreement with experiment. No calculations are available for the rotational levels of an excited vibrational state, but Elgin and Kolb[12] suggest that 5% of the center of mass energy goes into rotational excitation for CO_2. We used the same expression for H_2O. Although ad hoc, this does demonstrate that the bands will be greatly broadened, as though excited to a much higher temperature.

Because of the large uncertainties, we have calculated the collisionally excited spectrum at a much lower resolution than the radiatively excited spectrum. The results are given in Fig. 3 for $E = 2\times10^{20}$ molecules/sec of H_2O and in Fig. 4 for $E = 5\times10^{18}$ molecules/sec of CO_2. These emission rates correspond to column densities of $\sim10^{12}$ molecules/cm^2 of H_2O and $\sim10^{11}$ molecules/cm^2 of CO_2, with the emission plume geometry used by Rantanen and Ress.[2] Since the CO_2 comes from cabin leakage out the single walled bulkhead between the cabin and bay, a lower relative emission rate can produce the same column density looking straight out the bay than for outgassed H_2O. However, the expression for collisionally excited intensity was derived with the assumption that E/2 molecules/sec are emitted in the forward direction; therefore changing the Shuttle attitude will change the effective $E(CO_2)$ and hence $I(CO_2)$.

3. PARTICULATE CONTAMINANTS

A general discussion of spacecraft contaminant particles, their trajectories near the Orbiter and their infrared radiation is given by Simpson and Witteborn.[1] Particulate sightings from previous spacecraft have usually been associated with formation of ice particles near water vents or particle ejection associated with leaks or deliberate venting. The Orbiter is supposed to vent its fuel cell water in molecular form

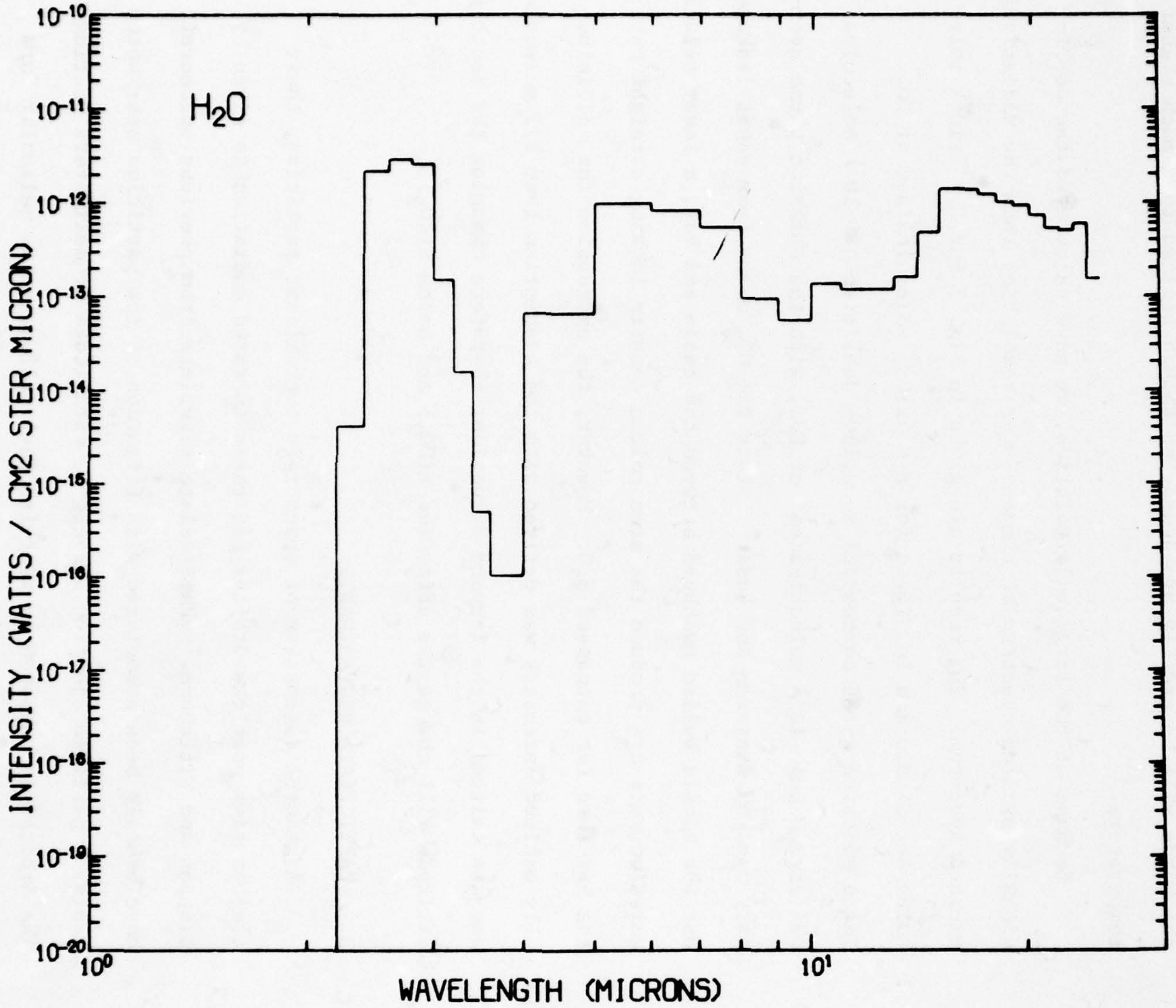

FIGURE 3 The intensity of the 2.7-μm and 6.3-μm fundamentals and pure rotation lines out to 25 μm is plotted for collisionally excited H_2O. The average atmospheric density for 350 km altitude was assumed. The emission rate of molecules from the Shuttle corresponds approximately to a column density of 10^{12} molecules/cm^2.

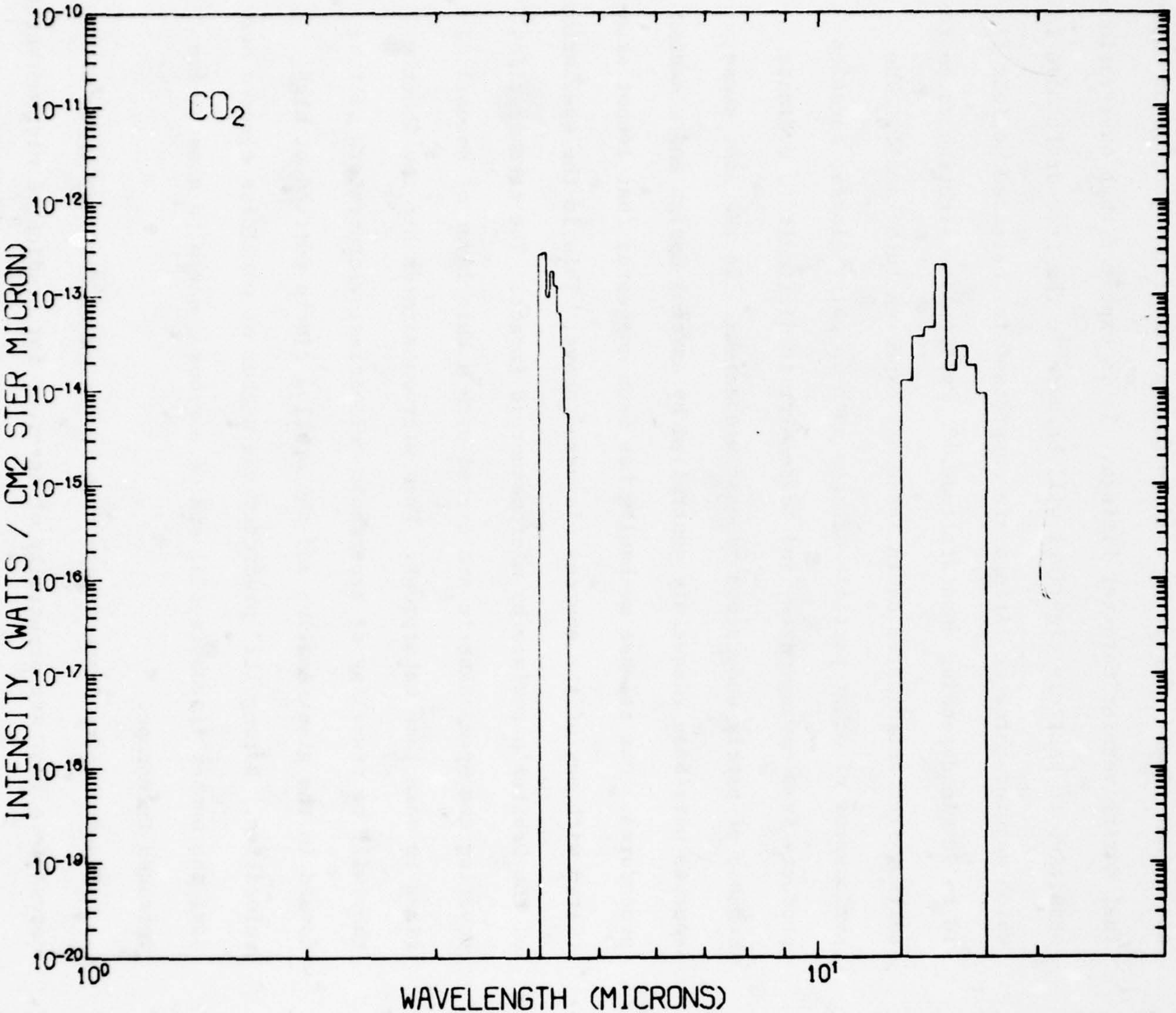

FIGURE 4 The intensity of the 4.3-μm and 15-μm fundamentals of collisionally excited CO_2 is plotted. (CO_2 has no pure rotation lines.) The average atmospheric density for 350 km altitude was assumed. The emission rate of CO_2 molecules used is based on the design specification limit of the leakage rate for the Shuttle cabin.

except when rapid venting is chosen. Other vents are manually controlled so that particulate sightings resulting from them could be limited to convenient times. Particles will be formed also from ejection of unburned fuel during vernier thruster firings. It is expected that observations sensitive to particle sightings will be made in the free-drift mode in which vernier thruster firings are suppressed for extended periods from 10 to 90 min depending upon attitude.[15] Particulate sighting rates resulting from anticipated cabin leaks are expected to be small. The seriousness of other particle sources such as paint flakes, abrasion products from moving parts, and loose dirt is difficult to evaluate because of poorly understood release mechanisms. In the past these sources have been adequately controlled by careful design and cleaning procedures. One release mechanism has been suggested that is not associated with any of the sources discussed above. This is the spallation of the Orbiter's surface by micrometeoroid impact. The ceramic tiles covering the Space Shuttle are coated with a thin layer of borosilicate glass to make them waterproof. When micrometeoroids hit the Shuttle they will be traveling at hypersonic velocities; microcraters will be formed in the glass coating and the spalled ejecta emitted at high velocities. Barengoltz[4] predicted the number of particles ejected per day; the number is substantial and of serious concern to a sensitive infrared telescope.

Hypervelocity craters have been investigated for many types of materials. They are especially of interest for studies of micrometeoroid craters on lunar rocks. In these studies particles of ~1 μm in size are accelerated to 5 to 15 km/sec velocity and shot at different target materials. Vedder and his coworkers in particular have used glass targets. They then make electron micrographs of each resulting crater. An example is shown in Fig. 5. We are probably concerned with larger micrometeoroids at higher velocities and hence larger craters, but the features should be similar. The craters consist of a deep central pit with a splash rim of melted glass. The glass particles from the pit probably all reached high enough temperatures to melt; the area around some of the craters includes submicron size droplets of melted glass. We will assume that some of the smallest particles were still molten when ejected from the central pit of the crater. Goldstein[16] gave temperatures of 1400-1800K for the melting temperature of the borosilicate glass coating.

When the impacting particle has a higher velocity, the crater rim is also spalled off along with other chips of glass from around the outside of the rim. All this material has been shocked by the hypervelocity impact. Gault and Heitowit[17] estimated that about half of the kinetic energy (KE) of the micrometeoroid goes into kinetic energy of the ejecta and about 0.2 goes to increasing the internal energy of the shocked mass. Thus if we let the mass of ejecta $M_e = \alpha \frac{\rho}{S} KE$ where $\alpha \sim 0.5$ and S is the yield strength of the material[4] and $\Delta E = \beta\, KE = M_e\, C\, \Delta T$ where $\beta \sim 0.2$ and C is the specific heat, we find $\Delta T \sim 80K$. However Mandeville and Vedder[18] found a smaller mass of the ejecta which leads to $\Delta T = 200\text{-}350K$ for $\beta \sim 0.2$. This is an average temperature. The

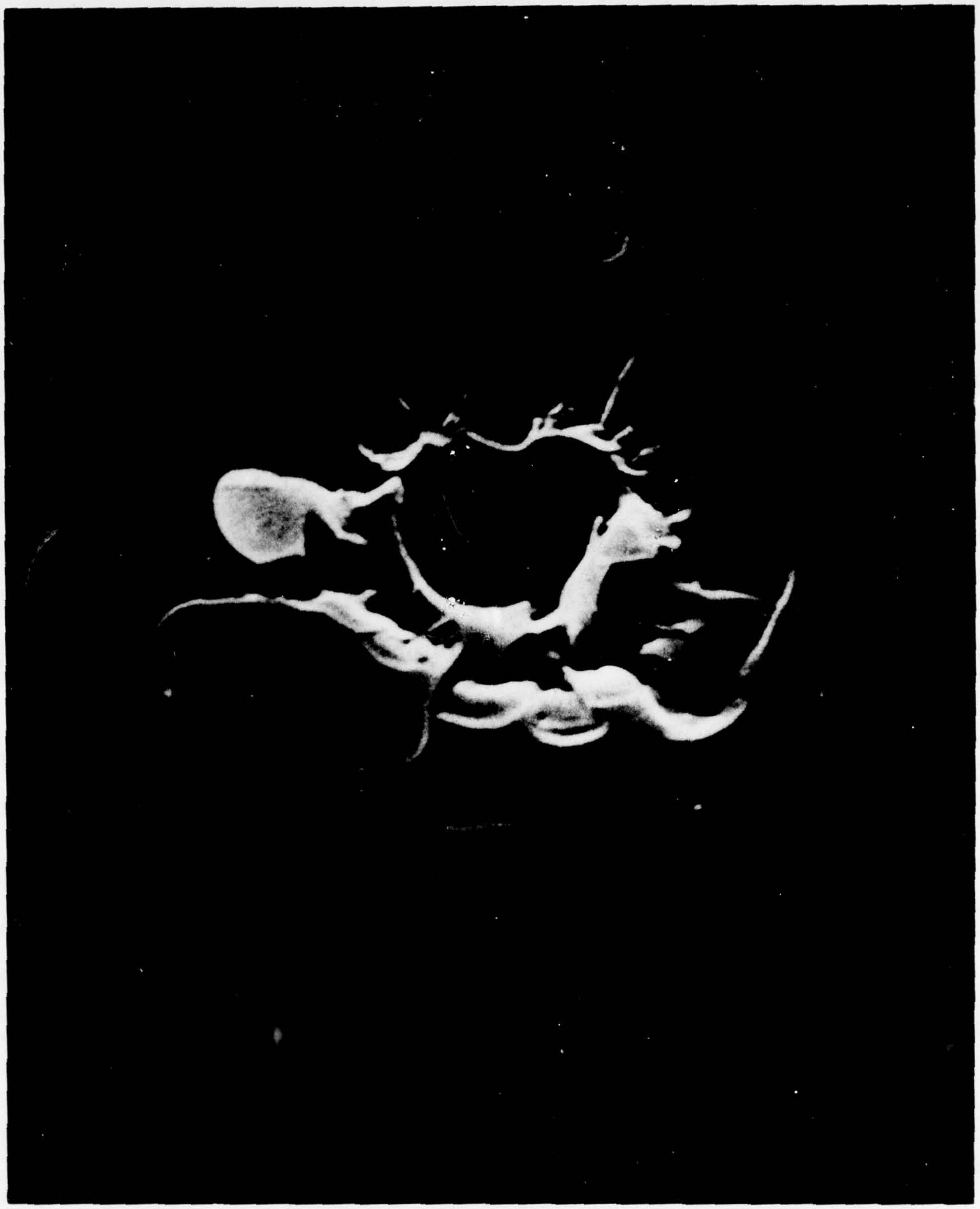

FIGURE 5 An electron micrograph of a crater on SiO_2 glass is shown. The impacting SiO_2 particle had a diameter of 3 μm and a velocity of 4 km/sec. The line going through the crater has a total length of 16μm.

temperature increase for the chips of glass from the rim could be lower if ejecta from the pit are hotter. With these uncertainties, we arbitrarily chose to plot spectra for $\Delta T = 150K$, or $T = 450K$ if a starting temperature of 300K was chosen. The final equilibrium temperature is also close to 300K.

To calculate the spectra of the particles we first assume that all particles are spherical. The diameters chosen ranged from 1 to 20 μm. We used the complete Mie theory for scattering and absorption by spheres. The equations are found in many books, such as van de Hulst[19] and Wickramasinghe.[20] The input parameters to a Mie scattering calculation are the size parameter x (the ratio of the particle circumference to the wavelength), the complex index of refraction $m = n - ik$, and the array of scattering angles. The output is the extinction efficiency $Q_{ext}(=\sigma_{ext}/\pi a^2$, where σ_{ext} is the extinction cross section and a is the particle radius), $Q_{sca}(=\sigma_{sca}/\pi a^2)$, and the angular dependencies. The emissivity ϵ equals the absorption efficiency $Q_{abs} = Q_{ext} - Q_{sca}$. The scattering and absorption properties of a particle with x near unity are very curious because the particle can influence much more of the incoming wavefront than its geometrical size. There can be very sharp fluctuations due to resonances (particularly if $k << 1$) and Q_{sca} and even Q_{abs} can be much larger than 1. That is, the particle can emit more than a blackbody at wavelengths where $Q_{abs} > 1$. These effects can be seen in the image brightness plots discussed below.

The next problem is the choice of the complex index of refraction m. In the infrared, m has been measured for similar materials (i.e., silicates) such as quartz and terrestrial and lunar rocks. Pollack et al.[21] have measured m for terrestrial obsidian, basalt, basaltic glass, and andesite. Since the optical constants n and k for basaltic glass generally fall in between the other materials, we used it for our first sample material for calculations of spectra between 2 μm and 50 μm. Beyond 50 μm, constants for fused quartz as given by Randall and Rawcliffe[22] were used.

The emissivities of the spalled particles were calculated from λ = 2 μm to 200 μm. The image of a nearby particle in the field of view will be out of focus; the size of the image is given by D/d where D is the diameter of the telescope and d is the distance to the particle. Then the power on a detector is given by $W_\lambda = \varepsilon \pi a^2 B_\lambda \Omega$, excluding the losses of a less than perfectly efficient system. We define the image brightness to be $I'_\lambda = W_\lambda/\Omega$, where Ω is the solid angle of the field of view ($\Omega = \pi\beta^2/4$ where β *is the diameter of the field of view*). Note that W_λ and I'_λ have no dependence on the diameter of the telescope so long as the particle is closer than $d = D/\beta$ (for a 1 m telescope with β = 1 arcmin, $d \leq$ 3.44 km but for a 15 cm telescope with a one degree fov, $d \leq$ 8.7 m). For distances greater than $d = D/\beta$,

$$W_\lambda = \frac{\pi^2 D^2}{4} B_\lambda \frac{a^2}{d^2} \qquad (2)$$

We have plotted the image brightness for 4 particle sizes in Fig. 6 for temperatures of 300K, 450K, and 1400K. A 300K blackbody is included for comparison. It is interesting to see that the famous 10-μm and 20-μm

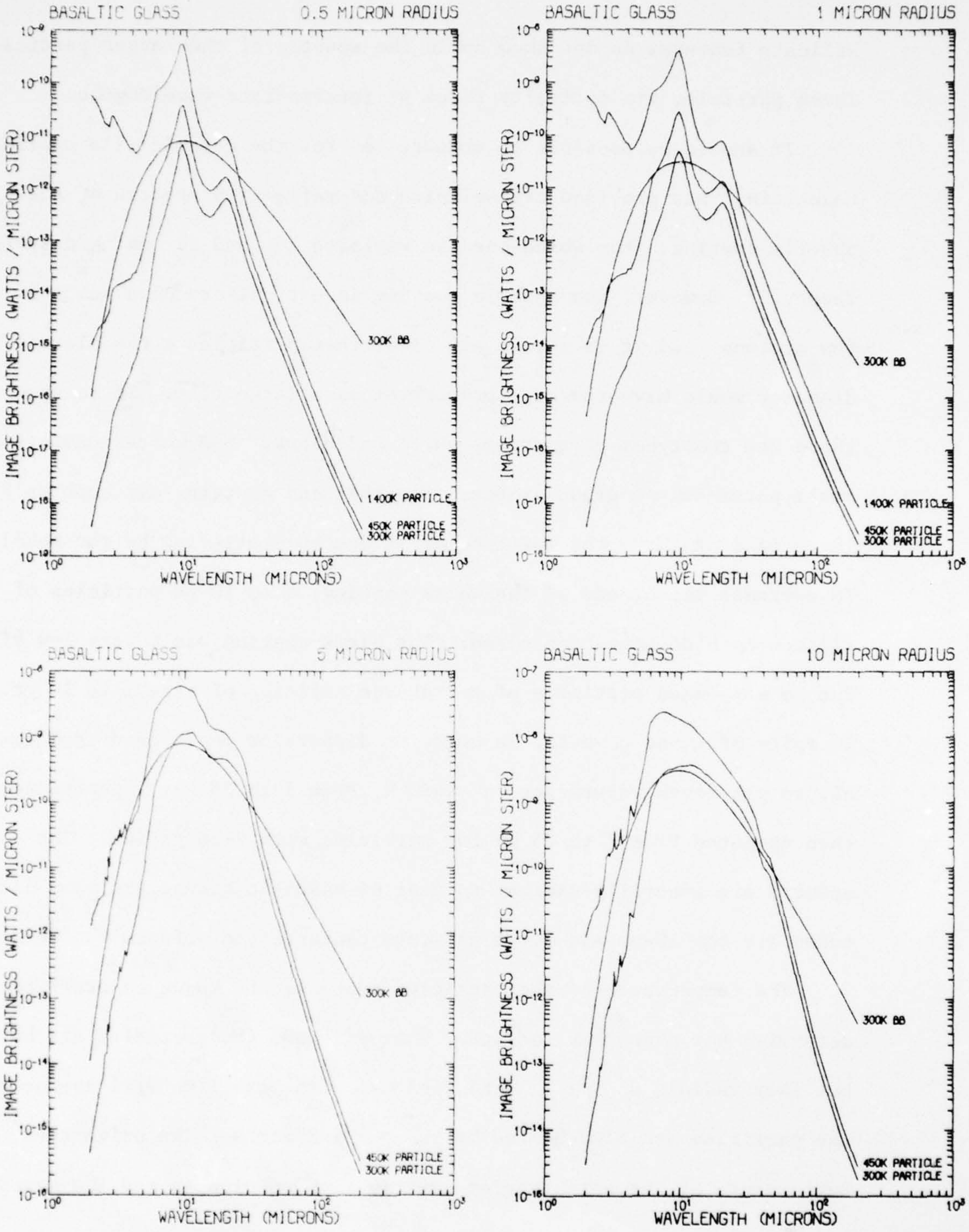

FIGURE 6 The image brightnesses for four sizes of particles of basaltic glass are plotted versus wavelength. The particles have temperatures of 300K, 450K, and 1400K. A 300K blackbody is plotted for comparison.

silicate features do not show up in the spectra of the larger particles. These particles are optically thick at intermediate wavelengths.

It should be possible to measure m for the ceramic tile coating. Goldstein[16] has provided transmission and reflection spectra of the black Shuttle coating, from which one can estimate n and k using dispersion theory.[21] However, the Shuttle coating is not uniform on a scale of a few microns, and it is not at all clear that particles a few microns in diameter would have the same properties as a large tile. To be specific, there are two types of coating, white and black. The white consists of small particles of glass sintered together and contains air bubbles 8 to 10 μm in diameter. The white color is due to scattering by the bubbles. To decrease the albedo of the white coating, 8 to 10 μm particles of silicon carbide have been added. The black coating has a very low albedo due to suspended particles of tetraboron silicide of size 1 to 10 μm.[16] In spite of these caveats, we used the dispersion analysis of Pollack et al. to get rough values for n and k from 7 to 25 μm. Spectra were then computed from 7 to 25 μm for particles with 2-μm radius. The spectra are generally similar to that of basaltic glass; the main features are the 10-μm and 20-μm silicate features and effects due to size.

The temperature of the particles must also be known in order to determine how much they radiate. When emitted, the particles are hot, but they radiate as $\bar{\epsilon} \sigma T^4$ and cool off with time. We will assume that the particles are also heated by the sun and earth. The brightness temperature of the earth varies greatly with wavelength and the season of the subearth point, ranging from ~216K in the depths of the H_2O and CO_2 bands where the atmosphere is optically thick to >300K at visible wavelengths over a hot desert. Since the particles have their largest Q_{abs} around 10 and 20 μm where the atmosphere is relatively optically thin, we will choose a relatively hot earth, $T_\oplus = 280K$. Then the energy equation is

$$\frac{dE}{dt} = \frac{4}{3}\pi r^3 \rho C \frac{dT}{dt} = -4\pi r^2 \bar{\epsilon}\sigma T^4 + \alpha_{vis}\, \pi r^2 \Omega_\odot \frac{\sigma}{\pi} T_\odot^4 + \alpha_{IR}\, \pi r^2\, 2\pi \frac{\sigma}{\pi} T_\oplus^4 \quad (3)$$

where $C = 0.3$ calories/g °C and $\rho = 2.4$ g/cm^3 and $\Omega_\odot \frac{\sigma}{\pi} T_\odot^4 = 1.360\text{x}10^6$ erg/cm^{2}sec. α is the absorbtivity. $\bar{\epsilon}$ is the temperature weighted emissivity $\bar{\epsilon} = \int_0^\infty \epsilon_\lambda\, B_\lambda\, d\lambda / \int_0^\infty B_\lambda\, d\lambda$. The spectra for basaltic glass were computed using values of $\bar{\epsilon}$ calculated for different particle sizes and temperatures. Linear interpolation was used to obtain intermediate values. We assumed $\alpha_{IR} = \bar{\epsilon}$ (280K). For α_{vis} we do not have a good value. Goldstein[16] gave $\alpha_{vis} = 0.3$ for the white Shuttle coating and $\alpha_{vis} = 0.9$ for the black. However these are bulk properties and include the bubbles and the silicon carbide or tetraboron silicide. That is, the material is effectively homogeneous. However the small spallation particles may or may not include the impurities, which are the main determinant of α_{vis}. Pure glass is much more transparent in the visible and, depending on particle size, can have α_{vis} very close to zero. Assuming that $\alpha_{vis} = 0.3$ or 0.9, we calculated $T(t)$ from the above equation for $T(t = 0) = 450K$. The particles cool very rapidly but more slowly for larger particles. The larger particles eventually come to a lower temperature because of their larger values of $\bar{\epsilon}$. However, at 0.1 sec, which is when most of the particles in Barengoltz's model pass in front of a telescope, the particles are near their original temperatures. The temperature as a function of time for $T(t = 0) = 450K$ and $\alpha_{vis} = 0.3$ is given in Fig. 7. We have ignored the solid angle of the Shuttle itself in the above calculation. Since the Shuttle is slightly warmer than the earth, the effect of the solid angle of the Shuttle is that the particles will cool more slowly. The length of time that this effect is important depends on the velocity of the particles. Particles with $v \lesssim 10$ m/sec are still close to the Shuttle at $t = 1$ sec (these are the larger particles which cool more slowly anyway), but particles with $v \gtrsim 10^3$ m/sec (the smaller particles) have already moved sufficiently far away by $t = 0.1$ sec to no longer feel any effect. All particles have moved far enough away after a few seconds that the final particle temperatures are as shown in Fig. 7.

We can also make predictions of the particle sighting rates due to spallation of the Shuttle tiles by micrometeoroids. (Other particle sources, such as dust and ices, are far less predictable.) The number of particles produced per day from the Shuttle by spallation were predicted by Barengoltz.[4] We will use his distribution function for velocity and particle size, which are ad hoc and need to be measured, but will scale the mass of the particles produced to agree with the measurements of the mass ejected from glass bombarded by hypervelocity particles by Mandeville and Vedder.[18] For particles with $E < 1\ \mu J$, Mandeville and

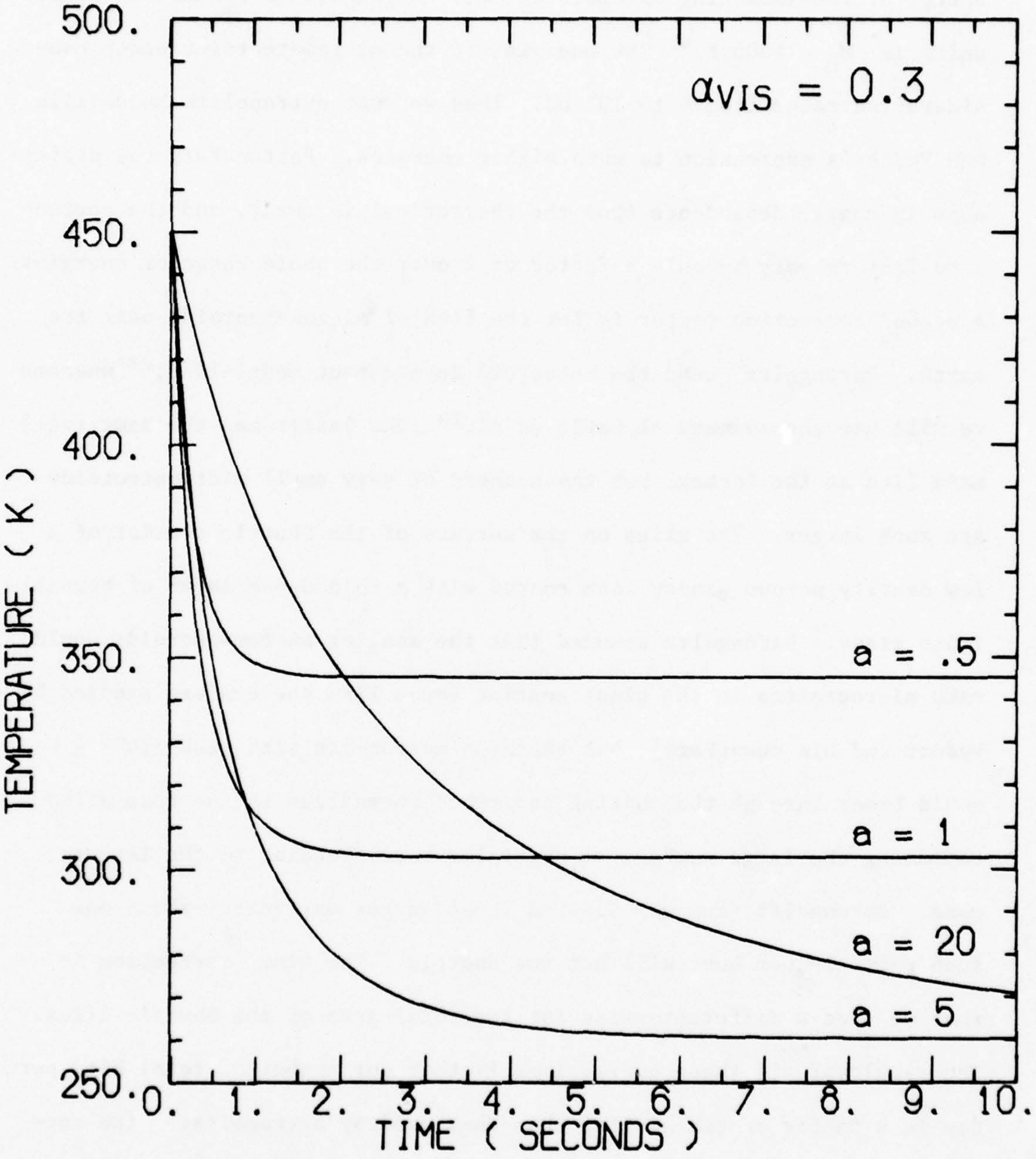

FIGURE 7 Particle temperatures as a function of time are plotted for particles with different radius a. The efficiency for visual absorption α equals 0.3.

Vedder found that $M_E = 230\ E^{1.1}$, where M_E is the mass of the ejecta from a single hypervelocity impact in picograms, and E is the kinetic energy of the impacting particle in μJ. Barengoltz's formula in these units is $M_E = 4000\ E$.[4] The energies of the micrometeoroids under consideration range from 4 to 10^4 μJ. Thus we must extrapolate Mandeville and Vedder's expression to much higher energies. Fortunately the difference in energy dependence from the theoretical is small, and the correction factors vary by only a factor of 2 over the whole range of energies. A second correction factor is for the flux of micrometeoroids near the earth. Barengoltz[4] used the Meteoroid Environment Model-1970;[23] whereas we will use the summary of Gault et al.[24] The latter has the same total mass flux as the former, but the numbers of very small micrometeoroids are much larger. The tiles on the surface of the Shuttle consist of a low density porous glassy foam coated with a thin dense layer of borosilicate glass. Barengoltz assumed that the smaller micrometeoroids would make microcraters in the glass coating (much like the craters studied by Vedder and his coworkers), but that the meteoroids with mass $\geq 10^{-6}$ g would break through the coating and embed themselves in the foam without releasing the large numbers of particles corresponding to the larger mass. Barengoltz (and we) ignored these larger particles; about one such particle per hour will hit the Shuttle. The final correction is that we used a different value for the total area of the Shuttle tiles. The result of all these corrections is that our number of total hits per day is a factor of ten smaller than that used by Barengoltz.[4] (He corrects his area to our value at the end of his paper.)

To calculate the fraction of particles that pass through the field of view, we first had to make several assumptions about the geometry of the situation. We assumed that particles are emitted randomly over the entire surface, then are swept back by the atmosphere and go into orbit around the earth. We assumed the atmosphere has the average density for 350 km altitude. The ejected particles can be divided into 2 classes depending on when they are sighted: 1) those that pass in front of the telescope immediately before atmospheric or orbital effects change the initial straight line trajectory, and 2) those that pass in front much later. For case 1, the important parameters are the diameter of the telescope and the distance it projects from the skin of the Shuttle. Of all particles emitted from the Shuttle, 0.2% fall into case 1 for a one m telescope projecting 3 m beyond the Shuttle. If the initial velocity of ejection is larger than a few m/sec, all the particles that pass in front of the telescope in case 2 are so far away that their out of focus images are smaller than the field of view. The fraction in this case is 0.5 x the field of view ÷ 2π. Thus, for a 15 arcmin fov the total fraction that passes through the field of view is 0.0026; for a 1 arcmin fov the fraction is 0.002.

We have run Monte Carlo calculations to determine the average energy deposited by a particle in the field of view as a function of particle size and initial velocity. These average brightnesses were then integrated over Barengoltz's size and velocity distributions to determine the fraction of particles in each brightness decade. These fractions, the number of sightings per day, and the time interval between sightings are all given in Table 1. We have assumed that each detector has a 1 arcmin fov, but that there is a 15x15 array of detectors. The brightness given is that seen by any one detector, but the sighting could be on any part of the array. For all but the last entry it was assumed that the particles radiate like 300K blackbodies. However, some of the very smallest particles will be melted glass from the centers of the craters and will be much hotter. The last entry gives particles that would be too small to detect at 200K, but would be detectable if they were much

Table 1. Particle sighting rates for a 1 m telescope with a 1 arcmin fov (in spectral band near 10 μm).

Fraction that put < 10^{-17} Joules/10 μm on detector	.97
Number of sightings per day	$2x10^4$
Time between sightings	2 sec
Fraction with 10^{-16} > Joules/10 μm > 10^{-17}	$2x10^{-2}$
Number of sightings per day	$8x10^2$
Time between sightings	2 min
Fraction with 10^{-15} > Joules/10 μm > 10^{-16}	$4x10^{-3}$
Number of sightings per day	$1x10^2$
Time between sightings	10 min
Fraction with 10^{-14} > Joules/10 μm > 10^{-15}	$6x10^{-4}$
Number of sightings per day	$2x10^1$
Time between sightings	1 hr
Fraction with > 10^{-14} Joules/10 μm	$4x10^{-5}$
Number of sightings per day	$1x10^0$
Time between sightings	1 day
Fraction of additional small hot particles	$2x10^{-2}$
Number of sightings per day	$5x10^2$
Time between sightings	2 min

warmer and were seen within the first fraction of a sec after being emitted. All integration times are one sec. However, most of the very fast particles pass through the field of view in 0.1 sec or 0.01 sec or even less. The spectral bandwidth is 5 to 15 μm in all cases.

4. CONCLUDING REMARKS

The total background intensity expected from H_2O and CO_2 in the constrained (no thruster firings, liquid vents off, 40 h or more in space) Orbiter environment at 350 km is given by the sum of the intensities in Figs. 1, 2, 3 and 4. This total is less than 2×10^{-11} W $cm^{-2} ster^{-1} \mu m^{-1}$ throughout the 2 to 20 μm range except for a narrow peak several times higher at 15 μm. A cryogenically cooled telescope like SIRTF, having a one m unobscured aperture with a one arcmin diameter field of view, would see a background spectral flux of about 1×10^{-14} W μm^{-1} or less in this range. Examples of background and random noise under the above conditions are summarized for three cases in Table 2.

The field of view and bandwidth chosen in these examples are both near the largest expected for a single detector in astronomical

Table 2. Backgrounds due to contamination

Band (μm)	Power (W)	Photons (sec^{-1})	Noise from photon fluctuations (W $Hz^{-1/2}$)
2.1-3.1	1.7×10^{-15}	2.2×10^{4}	1.1×10^{-17}
3.1-4.1	4.1×10^{-17}	6.4×10^{2}	1.6×10^{-18}
6.0-7.0	3.6×10^{-15}	1.2×10^{5}	1.1×10^{-17}

applications shortward of 20 μm. Yet the random noise from H_2O and CO_2 emission is less than that in state-of-art detectors. Thus, the infrared emission from the expected molecular contaminant atmosphere of the Orbiter is not expected to be a serious limitation on the use of a sensitive infrared telescope, provided that thruster firings and water ventings are inhibited.

The particle sighting rates and resultant energy received by a 1 m telescope in a 1 arcmin field of view and 10 μm band (centered near 10 μm) have been estimated for the spallation products formed by impacting micrometeoroids. This is the most copious source of particles anticipated for the Orbiter environment when the thrusters are not firing and when the water vents are closed. Most instruments that have been suggested for SIRTF[25] operate in much narrower bands than the 10 μm used in Table 1 or else at longer wavelengths where the intensity of radiation from particles is lower (Fig. 6). Such instruments would be affected at intervals comparable to or longer than the longest expected integration time (20 min). One instrument under consideration, a sensitive broadband photometer, would be affected by particle sightings more frequently and would have to incorporate discrimination devices or logic for rejecting transient signals. Thus the particle environment also appears to be satisfactory for infrared astronomy, provided appropriate safeguards are taken in the design of sensitive, broadband instruments. However, the particle production rate and velocity distribution are very poorly understood. More work is needed to predict sources of particulates, release mechanisms, and velocity distributions. Continuing efforts are needed to identify contaminants from payload materials as these are specified. Further tests are needed on the flash evaporators for the Orbiter to see if they really do emit water in molecular form only, with no ice particles.

5. ACKNOWLEDGMENT

We thank J. Vedder for permission to publish his electron micrograph of the crater in the glass target.

6. REFERENCES

1. Simpson, J. P. and Witteborn, F. C., Effect of the shuttle contaminant environment on a sensitive infrared telescope, Appl. Optics, 16:2051-2073 (1977).
2. Rantanen, R. O. and Ress, E. B., Payload/Orbiter Contamination Control Assessment Support, MCR 75-13, Martin Marietta Aerospace, Denver (1975).
3. Witteborn, F. C. and Young, L. S., Spacelab infrared telescope facility (SIRTF), J. Spacecraft and Rockets, 13:667-674 (1976).
4. Barengoltz, J. B., An Estimate of Particulates in the Vicinity of a Space Shuttle Orbiter due to Meteoroid Impact, Jet Propulsion Laboratory Report 900-793 (1977).
5. Schuerman, D. W. and Weinberg, J. L., Preliminary Study of Contaminant Particulates Around Skylab, NASA CR-2759, Available from National Technical Information Service, Springfield, Virginia 22161 (Oct. 1976).
6. Bareiss, L. E., Rantanen, R. O., and Ress, E. B., Payload/Orbiter Contamination Control Requirement Study, MCR 74-93, Martin Marietta Aerospace, Denver (1974).
7. Smith, R. E. ed., Space and Planetary Environment Criteria Guidelines for Use in Space Vehicle Development 1971 Revision, NASA TMX-64627 (1971).

8. McClatchey, R. A., Benedict, W. S., Clough, S. A., Burch, D. E., Calfee, R. F., Fox, K., Rothman, L. S., and Garing, J. S., AFCRL Atmospheric Absorption Line Parameter Compilation, AFCRL-TR-73-0096, Bedford, Mass. (1973).

9. CIRA 1972, COSPAR International Reference Atmosphere 1972, Akademie-Verlag, Berlin (1972).

10. Dunn, M. G., Skinner, G. T., and Treanor, C. E., Infrared radiation from H_2O, CO_2, or NH_3 collisionally excited by N_2, O, or Ar, AIAA J. 13:803-812 (1975).

11. Rieger, T. J., Tait, K. S., and Baum, H. R., Atmospheric interaction radiation from high altitude rocket exhausts, J. Quant. Spectrosc. Radiat. Transfer, 15:1117-1124 (1975).

12. Elgin, J. B. and Kolb, C. E., Extensions of Plume Interference Prediction Capabilities, Final Technical Report, ARI RR-104, Aerodyne Research, Inc., Bedford, Mass. (1977).

13. Kolb, C. E., Baum, H. R., and Tait, K. S., Classical calculations of H_2O rotational excitation in energetic atom-molecule collisions, J. Chem. Phys., 57:3409-3416 (1972).

14. Kolb, C. E. and Elgin, J. B., Classical calculations of NH_3 and H_2O rotational excitation in energetic collisions with atomic oxygen, J. Chem. Phys., 66:119-124 (1977).

15. Rockwell International Corporation, Study to Analyze Integration of Shuttle Infrared Telescope Facility (SIRTF) and the Biomedical Experiments Satellite Facility (BESS) Into the Space Transportation System, Final Report, SD77-SR-0003, Vol. 1 (1977).

16. Goldstein, Howard (1977) private communication.

17. Gault, D. E. and Heitowit, E. D., The partition of energy for hypervelocity impact craters formed in rock, in Proc. Sixth Hypervelocity Impact Symposium, Vol. 2, pp. 419-456 (1963).

18. Mandeville, J. C. and Vedder, J. E., Microcraters formed in glass by projectiles of various densities, Earth and Planet. Sci. Lett., 11:297-306 (1971).

19. van de Hulst, H. C., Light Scattering by Small Particles, John Wiley & Sons, Inc., New York (1957).

20. Wickramasinghe, N. C., Interstellar Grains, Chapman and Hall Ltd., London (1967).

21. Pollack, J. B., Toon, O. B., and Khare, B. N., Optical properties of some terrestrial rocks and glasses, Icarus, 19:372-389 (1973).

22. Randall, C. M. and Rawcliffe, R. D., Refractive indices of germanium, silicon, and fused quartz in the far infrared, Appl. Optics, 6:1889-1895 (1967).

23. Meteoroid Environment Model 1970 (Interplanetary and Planetary), NASA SP-8038 (1970).

24. Gault, D. E., Horz, F., Brownlee, D. E., and Hartung, J. B., Mixing of the lunar regolith, Geochim. Cosmochim. Acta (Suppl 5), 5:2365-2386 (1974).

25. McCreight, C. R., Walker, R. G., and Witteborn, F. C., IRAS and SIRTF: Implications of scientific objectives on focal plane sensitivity requirements, paper 132-12 given at the Society of Photo-Optical Instrumentation Engineers (SPIE) Technical Symposium, Vol. 132. Utilization of Infrared Detectors (Jan. 1978).

SPACECRAFT CONTAMINATION
MODEL DEVELOPMENT

J. M. Millard and C. R. Maag

AEROJET ELECTROSYSTEMS COMPANY
AZUSA, CALIFORNIA

ABSTRACT

The development and use of a contamination mathematical computer model that has application to any on-orbit spacecraft system is defined. The model is modular, consisting of several major subroutines. These routines consider outgassing, venting and leakage, and thruster engines and point sources. The heart of the model, an integration program, has three major elements that are integrated into concise sets of equations. The basic elements are source kinetics, transport mechanisms, and reemission kinetics. Results of computer modeling activities and a related systems level contamination and analysis conducted by Aerojet ElectroSystems Company are presented. A correlation of the analysis with observed radiator degradation of a geosynchronous altitude satellite is presented to show the merit of the modeling approach.

1.0 INTRODUCTION

Radiators for passively cooled satellite systems require low values of solar absorptance (α_s) and high values of infrared emittance (ε_h). However, these thermal properties are subject to the effects of the space/satellite environment which can cause an increase in the α_s/ε_h ratio resulting in degradation of system thermal performance. This degradation may be caused by radiation damage to thermal control surfaces and/or contamination deposition of particulate or outgassed materials.

Analysis of the long-term temperature data of a geosynchronous satellite has shown a definite warning trend of the passively cooled systems. Thermal analyses performed with the tempature data indicated the solar absorptance of radiator surfaces was increasing with time. Solar absorptance "maps" of the absorptance trends were compiled for the radiators and are presented in Figure 1. However, a thorough understanding of causes and effects relating to this absorptance increase were subject to conjecture due to the limited information temperature data could provide. Therefore, means of providing additional required information for investigating the cause of the warming trends were initiated.

The warming trend highlighted the need for a contamination model that could identify the causes of the increase in temperature with time, and determine the effects of any design changes. Because of the many facets to such a mathematical model, the computer program to predict mass deposition (contamination) was structured so that it is assembled in modular fashion (Figure 2). The program is arranged in subroutines and concise algorithmic blocks within subroutines which control the many facets of data manipulation and solution techniques necessary to manage a complex model form efficiently. The modeling of spacecraft contamination involves many phases of manufacture and

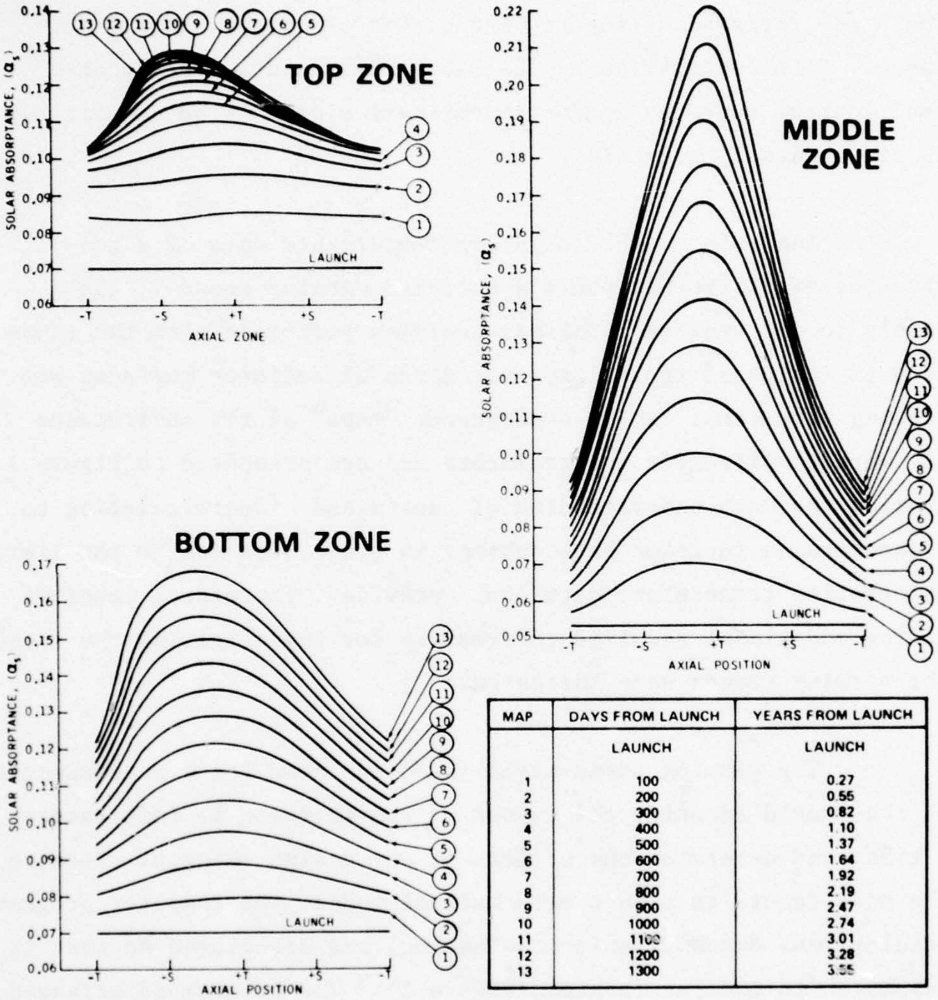

MAP	DAYS FROM LAUNCH	YEARS FROM LAUNCH
	LAUNCH	LAUNCH
1	100	0.27
2	200	0.55
3	300	0.82
4	400	1.10
5	500	1.37
6	600	1.64
7	700	1.92
8	800	2.19
9	900	2.47
10	1000	2.74
11	1100	3.01
12	1200	3.28
13	1300	3.55

FIGURE 1. TRENDS OF SOLAR ABSORPTANCE AS A FUNCTION OF TIME ON-ORBIT FOR THE RADIATOR OF AN OPERATIONAL SATELLITE

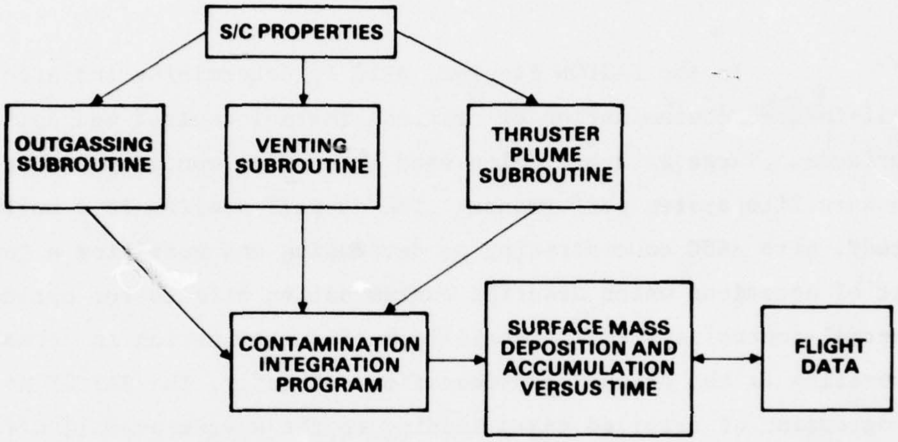

FIGURE 2. PROGRAM CONSTRUCTED IN MODULAR FASHION

ground handling, the launch environment, and orbital conditions. The modeling effort considered in this development deals only with the on-orbit environment (free molecular flow) experienced by the spacecraft. Results of related computer modeling activities at AESC are contained elsewhere in these proceedings.

2.0 DISCUSSION

The basic model is derived from the methods developed on the Satellite Contamination Program (SATCON).

In the SATCON Program, AESC is determining the effects of self-induced contamination of critical thermal control and optical surfaces. These data are being used to predict contamination effects on satellite system performance. The overall program is a multisystem study, with AESC concentrating on developing and verifying a general set of equations which describe contamination effects for optical and thermal-control systems. Satellite self-contamination in normal operation is the primary consideration. Briefly, the SATCON study is a progression of detailed tasks leading to the system overall effects evaluation as follows: (a) possible contamination source materials and target receptors are selected from candidate satellite surface materials; (b) for these materials, a theory of contamination mechanism and a set of equations are developed; (c) measurements of material emission kinetics are made under space conditions--a vacuum microbalance and a particle analyzer are used to determine particle composition and dynamics; (d) the transport mechanism is measured to validate the theory; (e) the thermal and optical effects of contamination are measured; and (f) testing is performed to verify the equations. The equations developed under this program provide the basic methodology for the mathematical model development.

The model presented in this paper is the composite of a data bank consisting of blocks of complex data formulated and formatted for efficient solution of the theoretical mathematical treatment developed under the SATCON program. An executive computer program was designed to effectively manage model data and solve for contaminant deposition rates by numerical solution of the governing theoretical differential equations.

Particular attention has been devoted to the development of a model with capacity applicable to large multinodal systems such as the external surface of entire spacecrafts and be within the realm of practical computer capability and use.

3.0 MODEL DEVELOPMENT

The Aerojet Mass Analyzer Program (AMAP) is designed to determine the contaminant source emission and reemission mass deposition rates on the surfaces of a vehicle in a space environment using line-of-sight theory and diffuse emission behavior. This program accounts for the deviation from these assumptions for surfaces such as thrusters with special shape factor input parameters.

The model presented in this paper is valid only for the free-molecular flow regime such as the vacuum space environment of an on-orbit satellite may provide. The development of the complete set of governing theoretical equations are presented by E. A. Zeiner in these proceedings.[1,2] The model presented in this paper is the result of general application technique and solution of this in-depth mathematical treatment as it applies to enclosure problems internal or external where space is the enclosing node.

While equally accurate for small nodal models, the model presented has been developed for practical solution capability of large multinodal enclosure problems of a general nature where free-molecular flow regimes are valid.

In-depth theoretical background and mathematical treatment development will not be presented in this paper as the comprehensive development is given elsewhere in these proceedings.[1,2] Equations programmed will be presented, however, without detailed description as that information is readily available.

The model presented assumes diffuse surface source emission and reemission, allowing for internodal distribution of contaminants incident to be described by geometric configuration factors (black body shape factors; F_{ij}) as are used in thermal radiation analysis. Capture coefficients (σ) are used to define the quantity of incident mass sticking and accommodated, thus being available for subsequent reemission consideration. Shape factors defining internodal distributions are a function of geometry and therefore apply to the system independent of temperature level or contaminant considered. Capture coefficients are a function of not only the contaminant type considered but also the temperatures of both the emitting and accommodating surfaces.

The initial distribution of mass emanating from vents and thrusters is defined by a set of shape factors which are defined as the mass rate initially incident on a surface divided by the total mass rate emanating from the vent or thruster (both are called vent nodes). This distribution is complex to determine and is a function of geometry, temperature, pressure, and contaminant. For some vent surfaces, the diffuse emission assumption may be adequate. For thrusters, plume analysis programs such as CONTAM II may be used. Defining these shape factors allows vent nodes to be handled in a convenient and similar fashion to other types of nodes and helps to prevent an unwieldy amount of input data.

The mass contamination model is concerned with VCM (volatile condensible materials) only. The governing set of differential equations appear in matrix form as follows for a one-contaminant, diffuse-source emission, and first-order diffuse re-emission:

$$\{\dot{m}d\} = \begin{bmatrix} A \end{bmatrix} \{md\} - \dot{m}s \ \{B\} \qquad (1)$$

where:

$$\begin{bmatrix} A \end{bmatrix} = \begin{bmatrix} GF^{-1}S - \delta_{ij} \end{bmatrix} \begin{bmatrix} \diagdown & & \\ & k & \\ & & \diagdown \end{bmatrix} \qquad (2)$$

where:

n : number of nodes in problem

$\begin{bmatrix} \diagdown & & \\ & k & \\ & & \diagdown \end{bmatrix}$: (n,n) diagonal matrix of nodal rate constants k_{ij} (sec^{-1})

$\{md\}$: (n) vector whose elements are the deposited mass surface density of each node (gm/cm^2)

$\begin{bmatrix} G \end{bmatrix}$: (n^2,n) matrix operator composed of F_{ij} functions.

$\begin{bmatrix} F \end{bmatrix}$: (n^2,n^2) matrix operator composed of algebraic functions of F_{ij} and σ_{ij}

$\begin{bmatrix} S \end{bmatrix}$: (n,n^2) matrix operator whose elements are functions of σ_{ij}

δ_{ij} : dirac (Kronecker) delta $\begin{matrix} i = j, \ \delta = 1 \\ i \neq j, \ \delta = 0 \end{matrix}$

$\{\dot{m}d\}$: (n) vector whose elements are the net mass rate deposited ($\text{gm/cm}^2\text{-sec}$)

$\dot{m}s$: scalar mass loss rate from source which is a function of elapsed time in space (gm/cm^2-sec)

$\{B\}$: (n) vector whose elements are functions of F_{is} and σ_{si}; where "s" denotes source,

$$\left\{ F_{is}\ \sigma_{si} \quad F_{2s}\ \sigma_{s2} \cdots F_{ns}\ \sigma_{sn} \right\}^T$$

Equation (1) represents a set of n first order non-homogenous linear differential equations which apply to a constant temperature profile throughout the nodal enclosure. The $\left[F\right]$ matrix becomes essentially a unity matrix when there are many nodes (F_{ij} values become small; << 1.0) and values for σ_{ij} are large (≈0.9, which is true in reality). With this assumption, inversion of the $\left[F\right]$ matrix is not necessary and it can be assumed to be unity. This simplification eliminates much computer core for solution routines and allows quick solution capability and computer capacity for large nodal models.

With these assumptions, the $\left[A\right]$ operator matrix reduces to the following form:

$$\left[A\right] = \left\{ \begin{array}{lll} K_1(F_1,\ \sigma_1,\ -1) & K_2\ (\sigma_{21}F_{12}) & \cdots\ K_n(\sigma_{n1}F_{1n}) \\ K_1\ (\sigma_{12}\ F_{21}) & K_2\ (F_{22}\ \sigma_{22}\ -1) & \cdots K_n(\sigma_{n2}\ F_{2n}) \\ \vdots & \vdots & \\ K_1\ (\sigma_{1n}\ F_{n1}) & K_2\ (\sigma_{2n}\ F_{n2}) & \cdots\ K_n(F_{nn}\ \sigma_{nn}\ -1) \end{array} \right\}$$

Source emmission is defined by the Arrhenius expression:

$$m_s = -k_s M_o^{-k_s t} \qquad (3)$$

where:

M_o : mass surface density of VCM contaminant on a surface (gm/cm^2)

t : time elapsed in space (sec)

K_s : source contaminant rate constant (sec^{-1})

First-order reemission from a surface is defined as follows:

$$\dot{m}_e = -k_e m_d \tag{4}$$

where:

k_e : contaminant rate constant (sec^{-1})

Rate constants are functions of contaminant type and temperature of emitting surface while capture coefficients are functions of contaminant type and temperatures of both emitting and accommodating surfaces.

The program is capable of analyzing the contaminant mass distribution and subsequent degradation effects for problems with up to 130 nodes and 40 different source and deposited contaminants. Such a solution is found by computing a separate solution for each contaminant and superimposing these solutions for the complete solution. It is assumed that there is no chemical interaction or alteration of contaminants due to multiple contaminants on a surface. It is also assumed that the small quantity of mass (percentage-wise) which is elastically reflected and is not accommodated on any surface is lost to space.

With the assumptions made, equation (1) represents a set of differential equations which have applicability to any vacuum enclosure problem. As an example, the exterior of a spacecraft may be considered as an enclosure with space forming the enclosing node, having $\dot{m}_e$ values of zero. The model presented and programmed thus represents an accurate, concise, and efficient approach to the solution of vacuum contamination deposition problems with a generalized approach.

A topical flow diagram of the program is shown in Figure 3. The model computes mass deposition rates for multiple surfaces and multiple contaminants for a point in time. The solution is performed for a set of nodal temperatures and specified elapsed time in space (or vacuum). If a transient solution is desired, the program must be run for a successive number of cases, each being a stable amount of time between each other. In other words, a transient solution is found by running several successive cases and time stepping through the solution period; the elapsed time and nodal temperatures changing for each case. This time interval (stable time) is a period of time over which the deposition rates computed may be assumed constant. This time interval is a program input, and the program uses this time interval to compute the changes in source and deposited mass for each node for each contaminant present, thus preparing the nodal contaminant data for the next case to be run.

4.0 INPUT DATA REQUIREMENTS

The complete model consists of seven blocks of data. A tape of the basic model is read in (all or part of the seven blocks), then overriding cards may be read in to edit the tape model or add to it. This gives the program multiple case, multiple start capability. The blocks of input data are as follows:

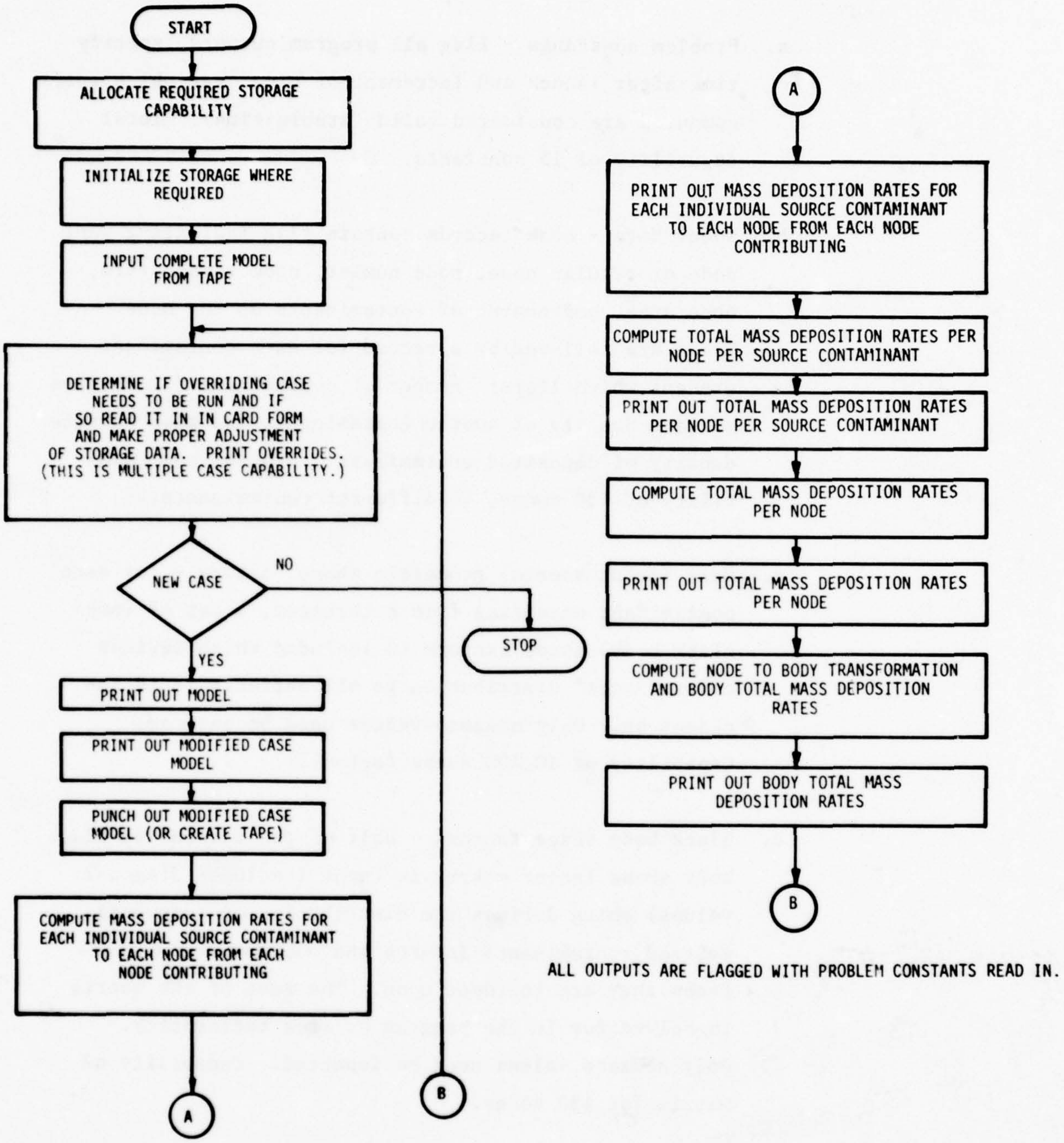

FIGURE 3. TYPICAL FLOW DIAGRAM OF PROGRAM

a. Problem constants - flag all program outputs, specify time after launch and increment of time over which rates computed are considered valid (stable time). Total capability of 15 constants.

b. Nodal data - node records contain flag indicating vent node or regular node, node number, node temperature, node area, and number of contaminants on the node. These are followed by a record for each contaminant present which lists: number of contaminant (ID #),mass surface density of source contaminant, and mass surface density of deposited contaminant. Program has capability of 130 nodes, 40 different contaminants.

c. Vent (point source) geometric shape factors - for each contaminant emanating from a thruster, a set of (non-black body) shape factors is included which defines contaminants' distribution to all surfaces it is incident on. Only nonzero values need be entered. Capability of 10,400 shape factors.

d. Black body shape factors - half of the internodal black body shape factor matrix is input (includes diagonal values) which defines the distribution of (nonvent) emitted contaminants (source and reemission) to surfaces they are incident upon. The rest of the matrix is solved for in the program by area reciprocity. Only nonzero values need be inputted. Capability of matrix for 130 nodes.

e. Tabulation of capture coefficients - table of capture coefficients (accommodation coefficients) as a function of temperature difference between emitting and receiving nodes must be inputted for each contaminant. Capability of 40 tables.

f. Tabulation of rate constants - table of rate constants as a function of temperature of emitting nodes must be inputted for each contaminant. Capability of 40 tables.

g. Node to body descriptions - block of data which lumps groups of nodes into bodies for determination of total mass source emission and deposition rates for bodies. Capability of 20 bodies each containing 20 nodes.

5.0 PROGRAM ROUTINES

The program is modular in nature being composed of several subroutines and algorithmic blocks within subroutines. Such a structure provides for improved program efficiency, reduced core usage and ease of editing for future improvements and modifications. The following subroutines are currently in service:

Main:	Allocates required program storage, prints program header, controls program and terminates it.
Zero:	Initializes storage where required.
Input:	Reads in model tape and inputs model into storage.
Case:	Reads in and prints out overriding cases (in card form) and adjusts model storage for case to be run. This routine gives the program multiple case (restart) capability.

Imprint:	Prints out the basic tape model (if flagged) and prints and/or punches (if flagged) the models for individual cases run.
Stick:	Linearly interpolates in tables of capture coefficients.
Rate:	Linearly interpolates in tables of rate constants.
Comp:	Sets up solution equations and solves them for all the various mass deposition rates and source emission rates for the printout options. All model inputs are required here for setting up the mass deposition rate differential equations. Changes in mass deposition for deposited and source contaminants over the time interval (stable time) are also computed here.
PCNDR:	Prints out (if flagged) individual nodal exchange mass deposition rates between nodes for each contaminant.
PTCNDR:	Prints out (if flagged) the total mass deposition rate and source emission rate for each node for each contaminant.
PTNDR:	Prints out the total mass deposition rate and source emission rate for each node.
PTBDR:	Prints out the total mass deposition rate and source emission rate for each body.

PBLK2: Computes a new block of nodal contaminant data based upon changes in mass rates computed in routine COMP over the stable time increment specified. It also prints and/or punches (if flagged) out this block of data for evaluation or use in another case.

6.0 PROGRAM OUTPUT

All outputs must be flagged by nonzero problem constants in order to be printed and/or punched. This prevents accidental output of unwanted data making user conscious of output. Output can be extensive and user must beware. Should errors be made and certain groups of constants not flagged, the program will terminate.

The following outputs and problems constants are available:

Constant	Control Feature
(1)	Print entire tape model.
(2)	Print entire model with individual case changes.
(3)	Punch out entire model with case changes.
(4)	Print mass deposition rates for each node from each node for each contaminant contributing.
(5)	Print total mass deposition rate and source emission rate for each node for each contaminant.
(6)	Print total mass deposition rate and source emission rate for each node.
(7)	Print total mass deposition rate and source emission rate for each body.
(8)	Time increment for interval over which rates assumed valid (stable time).

PBLK2: Computes a new block of nodal contaminant data based upon changes in mass rates computed in routine COMP over the stable time increment specified. It also prints and/or punches (if flagged) out this block of data for evaluation or use in another case.

6.0 PROGRAM OUTPUT

All outputs must be flagged by nonzero problem constants in order to be printed and/or punched. This prevents accidental output of unwanted data making user conscious of output. Output can be extensive and user must beware. Should errors be made and certain groups of constants not flagged, the program will terminate.

The following outputs and problems constants are available:

Constant	Control Feature
(1)	Print entire tape model.
(2)	Print entire model with individual case changes.
(3)	Punch out entire model with case changes.
(4)	Print mass deposition rates for each node from each node for each contaminant contributing.
(5)	Print total mass deposition rate and source emission rate for each node for each contaminant.
(6)	Print total mass deposition rate and source emission rate for each node.
(7)	Print total mass deposition rate and source emission rate for each body.
(8)	Time increment for interval over which rates assumed valid (stable time).

(9) Time after launch or start of source emission.

(10) Punch out new block of nodal data as a result of mass exchanges occurring over time increment (problem constant 8).

Constants 12 through 15 currently not used.

7.0 MODEL PREDICTION

A contamination assessment was performed for a synchronous altitude spacecraft to determine if the mass distribution would be similar to that of the solar absorptance degradation experienced on the radiators. This spacecraft was used to check out the contamination analysis program because of the large amount of thermal performance flight data available. The specific input parameters for this model consisted of: (a) 95 surface nodes, (b) 33 source materials, (c) normal operation hydrazine thruster profile, and (d) an 18-month prediction time. Two cases were considered when inputting data. The first case used the temperature data recorded at the end of 18 months on orbit. The second case used the initial stabilized on-orbit temperatures. The mass distribution and the major contributing sources were predicted for the 95-node model. These results were compared with the observed performance (α increase) after 18 months. This comparison was limited to two different radiator solar absorptance maps derived from temperature data in previous studies. Results of the analysis are shown in Figures 4 through 6.

Figure 4 shows the predicted contamination on the primary radiators for 18 months on orbit (18-month temperatures used). As can be seen, a preferential component of mass buildup exists near the center of the radiator. Figure 5 shows the preferential shape of the radiator degradation after 18 months on orbit. Normalizing the curves and superimposing Figures 4 and 5 yields Figure 6. It is clear

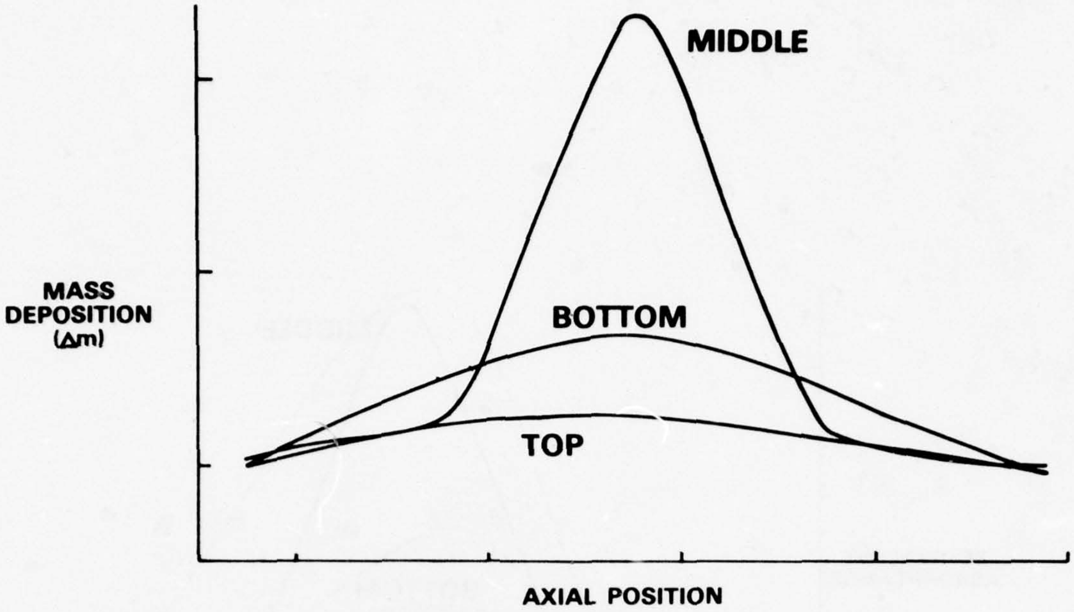

FIGURE 4. PREDICTED CONTAMINATION ON PRIMARY RADIATOR FOR 18 MONTHS IN ORBIT

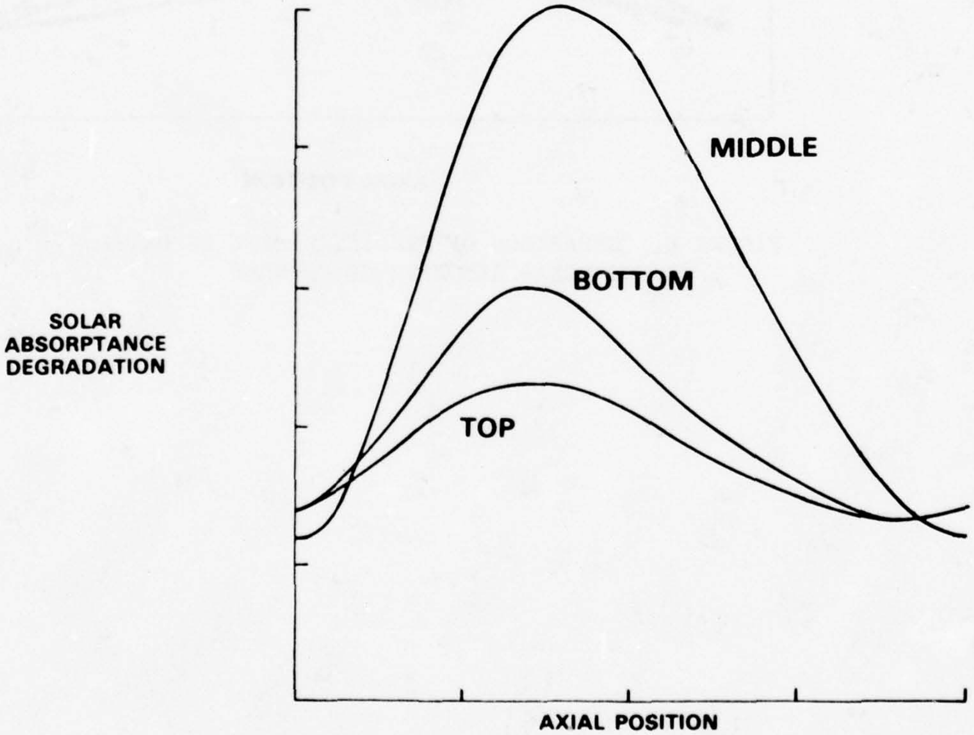

FIGURE 5. PRIMARY RADIATOR DEGRADATION AFTER 18 MONTHS (FLIGHT DATA)

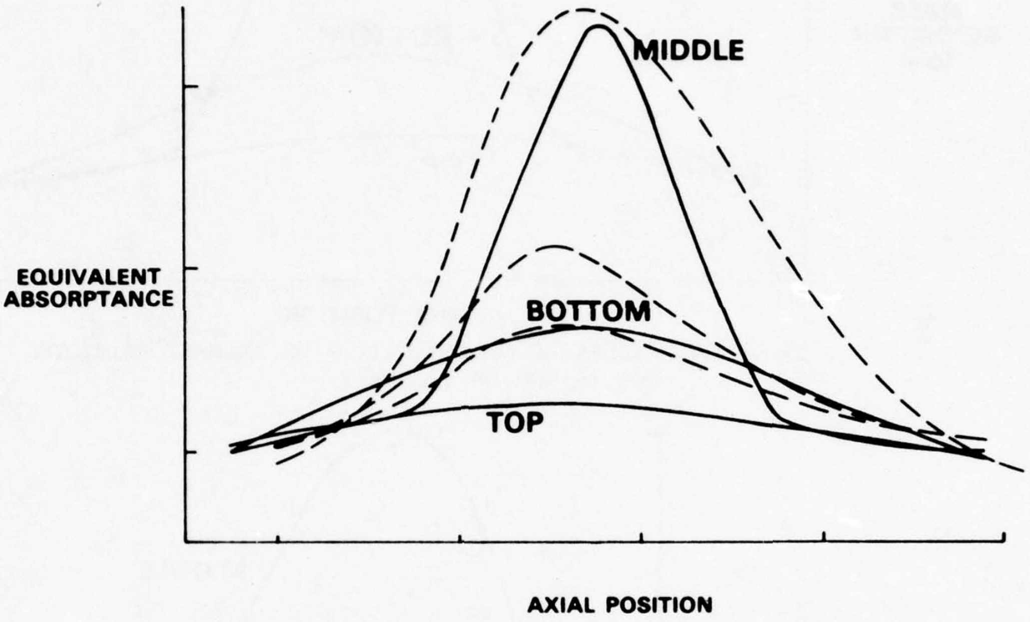

FIGURE 6. COMPARISON OF PREDICTED MASS DEPOSITION TO SOLAR ABSORPTANCE CHANGES

that the mass distribution on the primary radiator closely resembles the solar absorptance degradation distribution.

8.0 RESULTS AND CONCLUSIONS

The results show the major sources of contamination to be venting of the electronics enclosure and thruster plume effluents. A list of sources of contamination to the satellite radiators is presented in Table 1.

TABLE 1 SOURCES OF CONTAMINATION TO RADIATORS

Sources	Percentage
Electronics enclosure venting	68
Thruster plume effluents	28
Reaction wheel oil	1.0
Others	3.0

A second case that used the stabilized initial orbital temperatures was run. The results show the shape of the curves to be identical with those of the first case; however, there was a 10 to 12 percent increase in the mass deposited over the primary radiator when the initial orbital temperatures were used. These results suggest the model is a good representation of the mass transport mechanism and the model results are not strongly dependent upon the temperature distribution.

Continuing studies are being conducted at the time this paper is written which confirm the value and utility of the model and provide improved verification of the model as being representative of the mass transport mechanism. The model provides an efficient, comprehensive and concise generalized approach to solving the mass deposition contamination problem in a free-molecular flow environment.

To date there is insufficient experimental data available to positively correlate mass deposition with solar absorptance increase in a comprehensive fashion. However, with the mass deposition predictive technique developed, potential contamination problems on new spacecraft are being avoided or minimized in the design phase and improved detection and evaluation of optical and thermal problems on existing designs have become a reality.

ACKNOWLEDGMENTS

The authors are indebted to K. Powers and S. Rumbold for their assistance and support, to E. Zeiner for his outstanding technical input and to R. Scott for his many helpful suggestions during the development of this model. This work was supported in part by the Space And Missiles Systems Organization (SAMSO) under Contract F04701-76-C-0220.

REFERENCES

1. Zeiner, E. A., "A multinodal model for surface contamination based upon the Boltzman equation of transport," Proceedings of USAF/NASA International Spacecraft Contamination Conference, March 1978.

2. Zeiner E. A., "Measurements of the kinetics and transport properties of contaminants released from polymeric sources in space and the effects on collecting surfaces," Proceedings of USAF/NASA International Spacecraft Contamination Conference, March 1978.

An Improved Analytic Technique to Predict Space System Contamination

By

R. R. Hale

Aerojet ElectroSystems Company
Azusa, California

A new mathematical model to predict diffusion mass transport among surfaces is described which accounts for inter-molecular collisional behavior. The mathematical characterization utilizes dynamic thermal history behavior for the surfaces of interest. It evaluates the instantaneous local atmospheric pressure prior to and during ascent to calculate molecular collision probabilities. Adsorption coefficients for various temperatures are evaluated for each surface in a manner which simulates their mission temperature cycles. The input data for this portion of the contamination model is developed from thermal models, and a "sojourn" time and accommodation coefficient description is applied to surface behavior.

The model has been used to predict net contamination conditions at insertion for a geosynchronous satellite launched on a Titan 34D vehicle. Output data from that analysis is presented and further applications to alternative launch techniques are reviewed. A description of the parametric index which allows selection of either the diffusion or the line-of-sight contamination transport calculations, as appropriate to the mission instantaneous environment, is also given.

1.0 INTRODUCTION

In the analysis and mathematical characterization of contamination processes related to space missions, two separate mass transport regimes can be defined. Heretofore, the more widely investigated of these two regimes has been line-of-sight behavior in which molecules or particles can travel over significant distances before colliding with other bodies. This condition prevails in deep space and is characterized by relatively low population densities of molecular species in the local environment. Typical molecular concentrations, for example, are in the order of 10^{10} molecules per cubic centimeter or less. The corresponding mean free path is of the order 10^4 centimeters (10^2 meters) or longer. Such conditions characterize the orbital environment of most spacecraft with reasonable accuracy. Under these "line-of-sight" transport conditions, it is convenient to express the mass transport behavior of materials in terms of a "view-factor" analysis which describes the geometric relationships of source and target pairs. The view factor contamination prediction is valid if one assumes that external forces acting on the molecules or particles are negligibly small, that intermediate collisions essentially do not occur, and that the source material particles are emitted with a mathematically defined directional characteristic. (Possible forces include electrostatic, magnetic, and gravitational ones.) Other investigators have reviewed spacecraft contamination behavior under "line-of-sight" assumptions with various degrees of rigor in recent literature.

The mass transport ("contamination") behavior which occurs prior to insertion of the spacecraft in deep space vacuum, however, has not been prominently treated in the literature. The essential difference is that a nonnegligible probability of interactions, or collisions, exists due to the higher concentration of ambient molecules. At normal atmospheric pressure, for example, the molecular concentration is of the order 10^{19} molecules per cubic centimeter. The corresponding mean free path is less than 10^{-5} centimeters (10^{-7} meters). The effect of repetitive collisions is to randomize the direction of molecule (particle) motion, thereby giving rise to gaseous diffusion mass transport which is omnidirectional. In addition, since this diffusion transport behavior is not restricted to straight line travel, it is not subject to shadowing influences. Therefore, material transport by diffusion departs significantly from line-of-sight concepts and effects. This transport mode requires, then, a different mathematical and conceptual approach for application to pre-orbital spacecraft contamination studies. The value of such an analytical tool for space vehicles which are increasingly contaminant-sensitive, particularly for long-lived missions, appears to warrant developmental effort. This paper summarizes the results of Aerojet's recent activities in the mathematical and computer modeling of gaseous diffusion-transport contamination, and reviews a simple preliminary model which was applied to a particular launch and ascent sequence for a geosynchronous satellite mission.

2.0 BACKGROUND AND DEFINITIONS

In the field of space system contamination, mass transport can be characterized in three distinct modes.

2.1 Mode 1: Diffusion mass transport, typified by highly populous ambient molecules, generally gaseous. An example is the redistribution of material caused by molecular concentration gradients with respect to both time and distance.

2.2 Mode 2: Line-of-sight mass transport, characterized by the relative absence of ambient intermolecular collisions. An example is "backstreaming" of pump fluids under certain conditions in vacuum pumping.

2.3 Transition and Special Effects Modes: Mass transport by mechanisms not described accurately by either Mode 1 or Mode 2. Examples are intermediate molecular concentration regimes with combined viscous and non-viscous flow, particulates, and active forces, such as rocket exhausts, electrostatic and gravitational forces, and the like.

This paper will address the Mode 1 mass transport only. It is obviously appropriate to consider all three modes for total space system contamination control. Figure 1 summarizes the approximate time interval in a spacecraft's life cycle during which the respective contamination transport mechanisms are active. The total life cycle time during which contamination can occur begins with manufacture of the space component or system and ends at the termination of its useful life. Mode 1 contamination extends only through the launch and ascent phases.

3.0 MATHEMATICAL APPROACH

The classical kinetic theory of gases is based on the assumptions that matter is made up of molecules, and that the molecules have a velocity which is related to the temperature of the gas. This yields certain well-known mathematical relationships concerning the kinetic energy of the various molecules. These values of kinetic energy depend on the molecular mass and on the velocity as:

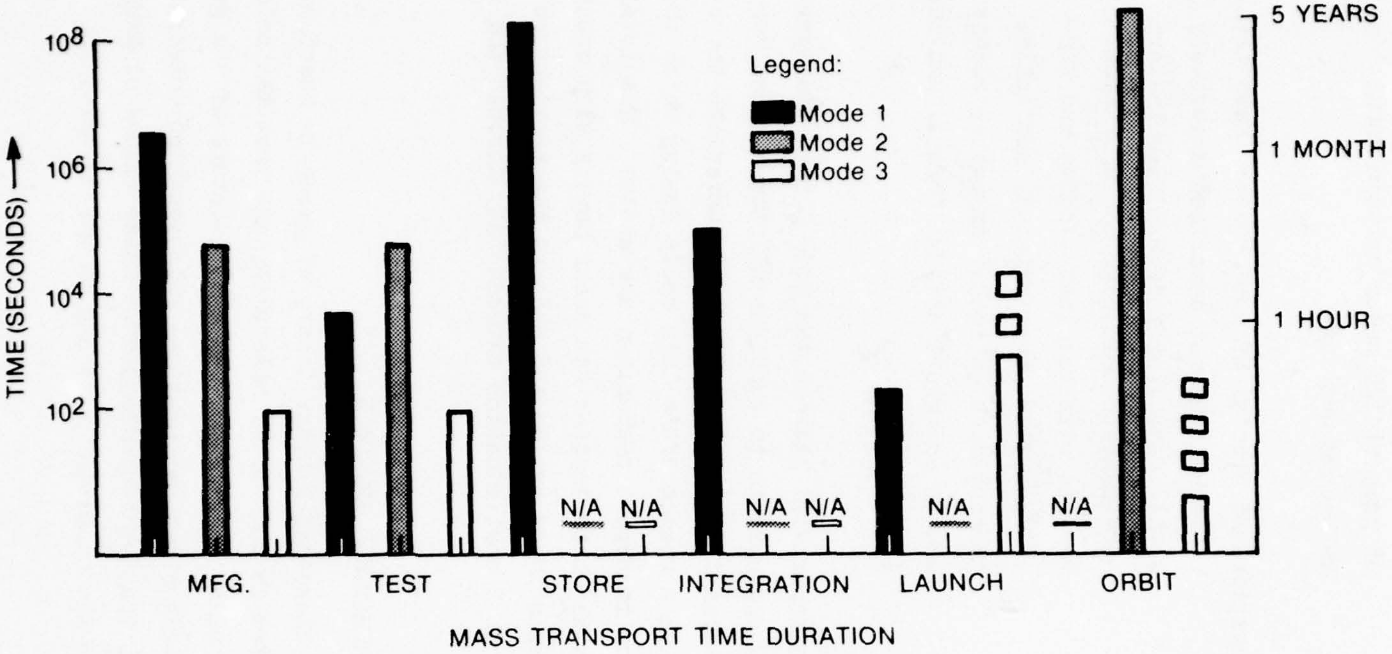

Figure 1 Contamination modes and durations during spacecraft life cycle

$$E = \frac{1}{2} m_s v_s^2 \tag{1}$$

where

E is the translational kinetic energy

m_s is the mass for the characteristic molecular species

v_s is the velocity of the molecule

It was determined by Maxwell and Boltzman that a velocity distribution function could be expressed to characterize the range of variation of the molecular velocity. This is of the form:

$$\frac{1}{n}\frac{dn}{dv} = f_v = \frac{4}{\pi^{\frac{1}{2}}} \left(\frac{m}{2KT}\right)^{3/2} v^2 \exp\left(\frac{-mv^2}{2KT}\right) \tag{2}$$

where

f_v is the fractional number of molecules whose velocity ranges between v and (v + dv)

For this function, the value of f_v is zero for $v = 0$ and for $v = \infty$; f_v has its maximum value at:

$$\underline{v_p = (2KT/m)^{1/2}}, \tag{3}$$

as can be seen by differentiating f_v with respect to v and setting the result equal to zero. V_p is the most probable velocity.

Application of Equation (2) to mathematically describe the properties of molecules in motion can yield different values of velocity, depending on the nature of the integration performed on the velocity distribution function. For example, if molecular kinetic energy exchange is to be calculated, the significant term is the mean square of velocity, which yields

$$\bar{v}^2 = \int_0^\infty v^2 f_v \, dv \Big/ \int_0^\infty f_v \, dv = 3KT/m \qquad (4)$$

from which, therefore,

$$v_2 = \left[\bar{v}_2\right]^{1/2} = (3KT/m)^{1/2} = 1.225 \, v_p \qquad (5)$$

If, however, it is desired to evaluate bulk transport of gas, the appropriate velocity is

$$v_{avg} = \int_0^\infty v \, f_v \, dv \Big/ \int_0^\infty f_v \, dv = \frac{2}{\pi^{\frac{1}{2}}} (2KT/m)^{1/2} \qquad (6)$$

therefore

$$v_{avg} = 1.128 \, v_p \qquad (7)$$

It is erroneous to apply the value of Equation (3) indiscriminately in mathematical modeling work, and, moreover, it is preferable to express the velocity distribution and to perform integrations over the appropriate range of molecular velocities. Figure 2 illustrates the various values of velocity and the function of Equation (2). For net molecular transport, then Equation (6) will be used.

An extension of the classical kinetic theory which assumes perfectly elastic intermolecular and surface collisions gives rise to the so-called ideal gas relations. This is commonly expressed mathematically as

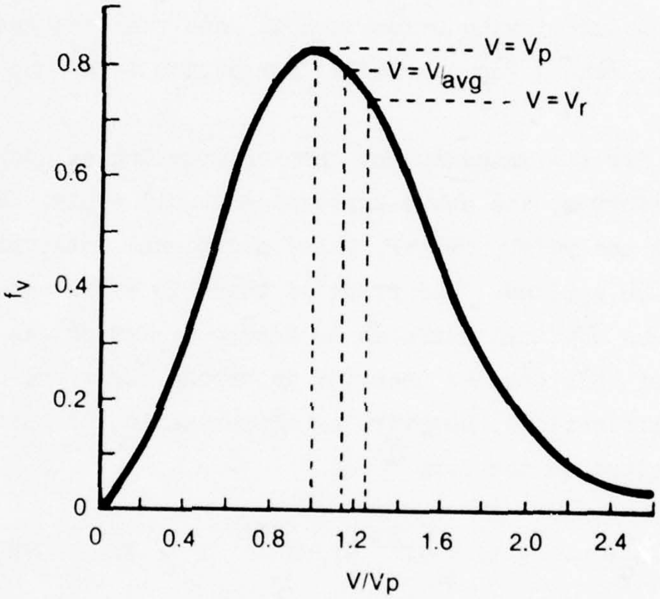

Figure 2 Maxwell-Boltzmann molecular velocity distribution function

$$PV = n R_o T \qquad (8)$$

where

P = the gas pressure

V = the volume occupied by the gas

n = the number of moles of gas in the volume V

R_o is a constant defined by the measurement system of units

T is the absolute temperature of the gas in the closed volume, V.

A simplifying assumption is made that the gases do not change state, making Van der Waals' correction terms unnecessary.

For the mathematical case of modeling an ideal closed system at equilibrium, the above expressions would apply. For the ascent transient analysis, however, three additional mathematical descriptors must be applied. The first of these is a characterization of the various physical surfaces to adsorb or desorb gas. A rigorous analysis of this complex behavior is beyond the scope of this paper. With simplifications, however, an approximation of this behavior can be described in the form①:

$$N_o \theta = 3.51 \times 10^{22} \left[P/MT\right]^{1/2} f\ t' \exp\left[E_D/R_o T_s\right] (1 - \theta) \qquad (9)$$

where

T is the temperature of the gas

T_s is the temperature of the surface

t' is the period of oscillation of the molecule normal to the surface (approximately 10^{-13} seconds)

E_D is the energy for desorption.

---

1. Roth, A., Vacuum Technology, North Holland Publishing Company, New York (1976), p. 175.

f is the sticking coefficient

P is the pressure

θ is the covered area, which is desorbing

$1-\theta$ is the uncovered area, which is adsorbing

N_o is the total number of molecules required to form one monolayer.

Equation (9) is only valid for less than a complete monolayer but is used here due to its relative simplicity. More complex equations can be used to describe the multilayer absorption case.

The second characteristic which must be described mathematically is the "pump-down" of the payload compartment which results from the reduction of local exterior atmospheric pressure with altitude. As the launch vehicle ascends, gas outflow from its interior volumes occurs in response to this pressure difference. Scialdone ② has presented a method for analytically evaluating internal chamber pressures, given vent path parameters, outgassing characteristics of the spacecraft materials, and the exterior pressure dynamic conditions. His computation method essentially requires simultaneous solution of flow equations, using parametric isothermal materials outgassing functions. In a typical mission, the altitude-time interrelationship during ascent will be predetermined by the launch vehicle and payload characteristics. For example, typical time versus altitude characteristics are indicated in Columns 1 and 2 of Table I. Handbook data ③ can readily be used to establish the external pressure as a function of altitude. This, in turn, provides a pressure versus time function, as illustrated by Columns 3 and 4 of Table I. Figure 3 graphically depicts

---

2. Scialdone, J. J., Internal Pressures of a Spacecraft or Other System of Compartments, Connected in Various Ways and Including Outgassing Materials, in a Time-Varying Pressure Environment, X-327-69-524, GSFC (1969).

3. U.S. Standard Atmosphere, 1976. NOAA, NASA, USAF. NOAA-S/T 76-1562, USGPO, Washington, D.C., (1976).

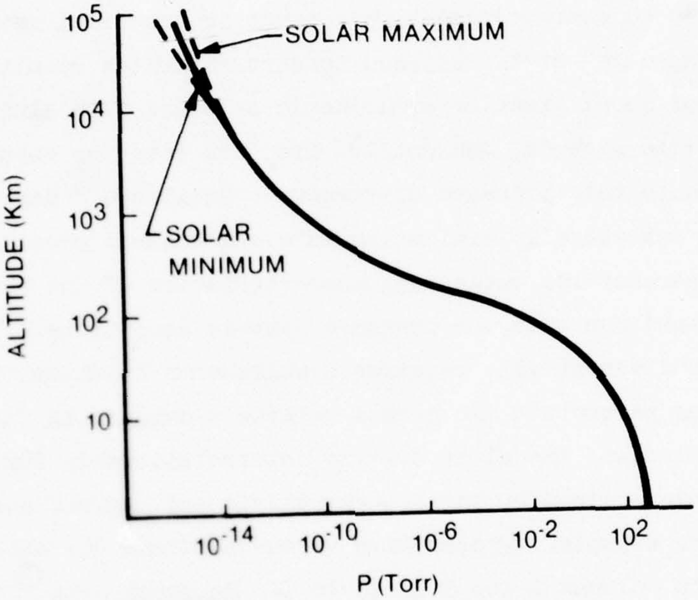

Figure 3 Altitude - pressure relationship

the interrelationship of altitude and pressure. For this actual model analysis, the time increment resolution was taken arbitrarily as 10 seconds, rather than 50 as shown in the abbreviated table. Obviously, any appropriate time interval may be chosen, depending on the requirements of precision for the particular analytical model.

TABLE I

LAUNCH MISSION ALTITUDE AND PRESSURE DYNAMIC CHARACTERISTICS

Time from Launch (seconds)	Altitude (10^3 m)	Pressure (Torr)	Pressure (Pascal)
0	0	7.6×10^2	1.0×10^5
50	6.7	3.2×10^2	4.3×10^4
100	34	4.8	6.4×10^2
150	61	1.3×10^{-1}	1.7×10^1
200	87	2.3×10^{-3}	3.1×10^{-1}
250	110	5.3×10^{-5}	7.1×10^{-3}
300	131	8.8×10^{-6}	1.2×10^{-3}
350	144	4.5×10^{-6}	6.0×10^{-4}
400	151	3.3×10^{-6}	4.4×10^{-4}

The third dynamic characteristic which must be defined to apply this model is surface temperature behavior. Equation (9) requires the use of specific surface temperatures to evaluate the quasi-equilibrium adsorbed gas state. During the actual vehicle ascent, the surface temperatures are changing with time; in fact, various surfaces have different temperature change rates because of their thermal and mass properties and their design configuration interrelationships. Using a thermal model of the spacecraft, the effect of different payload fairing temperature histories on key contamination-sensitive surface temperatures was analytically investigated. For two such conditions, which are characterized by the curves designated "maximum fairing temperature" and "minimum fairing temperature," the temperature of one thermal control surface can vary during ascent as shown in Figure 4. The curves indicate the predicted thermal control surface temperatures for "worst case" and "best case" payload fairing temperature conditions. The computed temperature difference is approximately 40 F degrees 300 seconds after launch. This results, of course, in significantly different desorption rates for the two launch cases. Further, it strongly suggests that some control is possible over launch phase intersurface mass transport by applying similar analyses and thermal design to optimize surface temperature histories.

A means for describing the net transport behavior of contaminant gases within the spacecraft environment is necessary. Whereas a net gas outflow occurs during ascent due to gross pressure changes as described above, gas composition gradients also change with time. The combination of theoretical energy and mass flux vector parameters and their driving forces are presented in Table II.

TABLE II

FORCES AND FLUXES (FROM IRREVERSIBLE THERMODYNAMICS)

Flux	Temperature Gradients	Composition Gradients, Pressure Gradients, Body Forces
Energy Flux, ϵ_i.	Fourier's Law	Diffusion thermo (Dufour effect)
Mass Flux j_{mi}.	Thermal Diffusion (Soret effect)	Fick's Law and extension

The energy flux caused by a composition gradient was discovered by Dufour in 1873; it is known as the Dufour effect and also as the diffusion-thermo effect. On the other hand, Soret established that

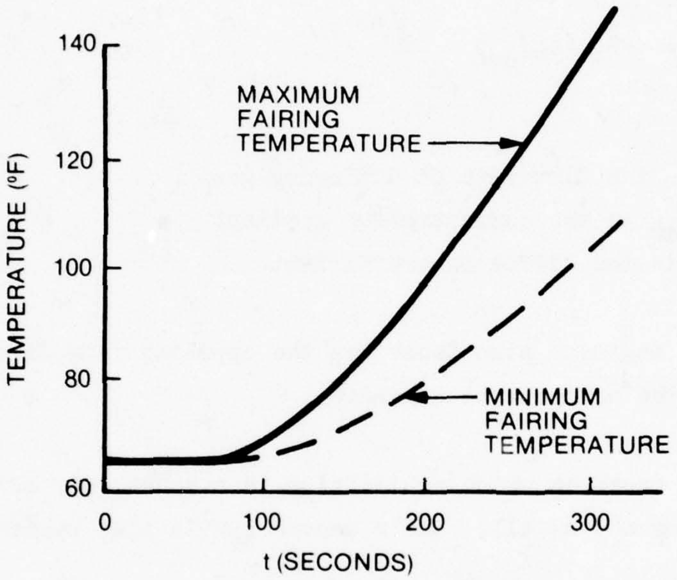

Figure 4 Predicted surface temperature vs. time after launch

mass fluxes can also be created by temperature gradients. Since the thermal diffusion and diffusion-thermo effects are typically[4] of a smaller order of magnitude, they have been excluded for initial analytic work. The predominant force considered, then, is Fick's Law diffusion. With this condition, a material composition gradient causes mass transport in the direction of the lower concentration region. Fick's first law is expressed:

$$Q = -D_1 (dc/_{dx}) \tag{10}$$

where

Q is the flow rate of diffusing gas

$dc/_{dx}$ is the concentration gradient

D_1 is the diffusion coefficient.

The negative sign describes the opposite flow direction with respect to the concentration gradient.

For cases in which equilibrium is reached only after long time periods or not at all, Fick's second law is also necessary.

$$D_1 \frac{d^2c}{dx^2} = \frac{dc}{dt} \tag{11}$$

Meyer[5] has established that, for two gases, the coefficient of interdiffusion is given by:

$$D_{12} = \frac{1}{3} \left[\lambda_1 V_{av_1} N_2 + \lambda_2 V_{av_2} N_1\right] \Big/ (n_1 + n_2) \tag{12}$$

---

[4] W. M. Kays, Convective Heat and Mass Transfer, McGraw Hill, N.Y. (1966).

[5] Meyer, D. E., Journal of Vacuum Science and Technology, 11, 168 (1974).

For the situation in which the concentration of one of the gases is rather small, as is the case for contaminant vapors, then Equation (12) reduces to⑥:

$$D_{12} = \frac{1}{3} \lambda_2 V_{av} = \frac{2}{3 \xi^2 P} \left(\frac{k^3 T^3}{\pi^3 m} \right)^{\frac{1}{2}} \qquad (13)$$

in which

m is the mass of the predominant molecule
T is the temperature, °K
k is Bolzmann's constant
ξ is the molecular diameter
P is the pressure.

An excellent literature review with tables of values for binary gas pair diffusion coefficients has been done by Marrero and Mason⑦. The value for air-water at temperatures of concern in this analysis is 0.29 cm^2/s ⑧. For this simplified comparative modeling to date, the binary air-water gas system is assumed. The order of magnitude of displacements resulting from gaseous diffusion can be readily approximated. It was shown by Einstein that

$$\bar{X}^2 = 2\,Dt \qquad (14)$$

where:

$\bar{X}$ is the distance executed by a particle
t is the time duration
D is the diffusion coefficient of the medium.

---

6. Roth, A., Vacuum Technology, North Holland Publishing Company, New York (1976).

7. Marrero, T. R., and Mason, E. A., J. Phys. Chem. Ref. Data, 1:3-118 (1972).

8. Sherwood, Thomas K.; Pigford, Robert L.; and Wilke, Charles R., Mass Transfer, McGraw Hill, N. Y., p. 23 (1975).

Since the diffusion coefficient values are typically a few tenths cm^2 per second at normal temperatures and pressures, the displacement is in the order of 1 cm per second. For the D value of 0.29 and a time of one second, we have, from Equation (14),

$$\bar{X}^2 = 2\,(.29)(1)$$

from which

$$\bar{X} = 7.6 \text{ mm in one second.}$$

A parameter is necessary to define the limit case in which gaseous diffusion is no longer significant. This situation occurs when the local molecular concentrations become sufficiently low that line-of-sight transport behavior occurs; that is, the molecules impinge on surfaces without intermolecular collisions. Strictly speaking, there occurs a transition concentration range during which some molecules statistically do not experience molecular collisions and some do. Detailed treatment of this transition regime is somewhat complex and should be separately addressed. However, for practical spacecraft contamination modeling, it is obviously important to address Mode 2 mass transport as well as Mode 1. A convenient parameter which can be routinely calculated and used as the program control variable is the mean free path. The expression for mean free path follows from Equations (6) and (8); it is commonly expressed as

$$\lambda = 2.33 \times 10^{-20} \frac{T}{\xi^2 P} \text{ (centimeters)} \qquad (15)$$

Since the transport distance of interest in contamination analysis is typically in the order of a meter (10^2 cm), a convenient limit value for λ is thereby defined. Then, for $\lambda \le 10^2$ cm, Mode 1 diffusion transport is stated to occur. Conversely, for $\lambda > 10^2$ cm, line of sight (Mode 2) mass transport is indicated. A parameter which is interrelated with λ is also available. The molecular incidence rate is the number of molecules striking a surface element per unit time, which can be shown to be

$$\phi = 3.513 \times 10^{22} \left[P/(MT)^{1/2} \right] \ \text{molecules}/\text{cm}^2\ \text{s}. \qquad (16)$$

The interrelationship of the values for ϕ and λ for air at 25°C is shown in Figure 5.

Together with the mission ascent parameters, Equations (9), (10), (11), (13), and (15) form the basis for an iterative calculation model which describes the dynamic contamination transport behavior for the physical spacecraft system. It is necessary, of course, to construct a math model of the surfaces of interest, including their relative areas and the separation distances for all surface pairs. However, it is not necessary to establish "view factors," as would be done for radiation heat transfer or Mode 2 modeling. Since this modeling work is new, simplifications have been used initially. These include the binary gas assumptions and only two interacting surfaces. Superposition can be used to extend the model to describe other contaminants; this would involve separate analysis of individual contaminants, each of which would form an air-contaminant binary gas pair. The matrices and the computations become more complex when multiple surfaces are analyzed, but this is not a formidable problem. A further refinement of this model would substitute more complex adsorption-desorption expressions [9] for Equation (9).

---

9. Redheed, P. A., Hobson, J. P., and Kornelson, E. V., The Physical Basis of Ultra-High Vacuum, Chapman and Hall, London (1968).

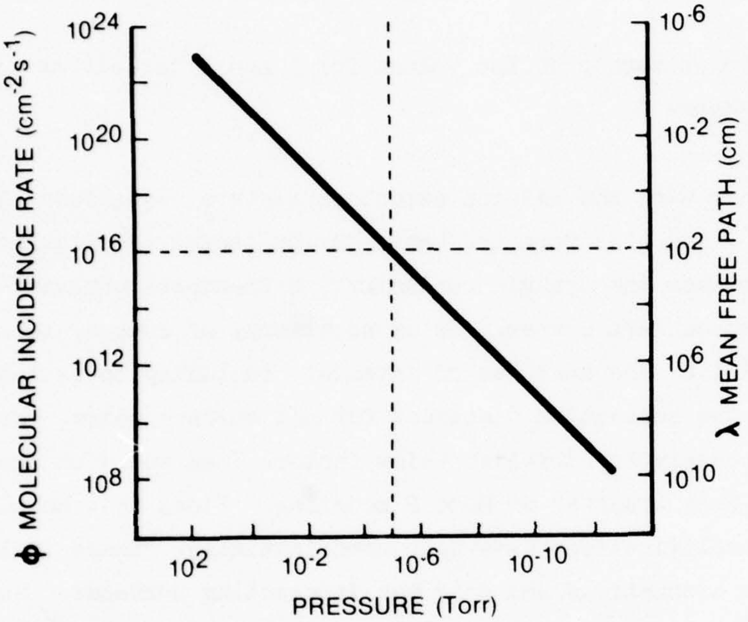

Figure 5 λ and φ vs. pressure for air at 25°C

4.0 APPLICATIONS

The model approach presented herein has a considerable amount of generality. Some analytic uses which suggest themselves include:

4.1 Prediction of contamination during storage.

4.2 "Self-contamination" analysis.

4.3 Contamination protection assessments.

4.4 Cyclic contamination evaluation (STS Orbiter).

4.5 Thermal-contamination interaction effects.

5.0 ACKNOWLEDGMENTS

The author graciously acknowledges the support of the Air Force program, F04701-77-C-0010, under which portions of this model were developed. Additional thanks are extended to Forrest Cleveland, Thomas Loverich, and other members of Aerojet ElectroSystems' Thermal Engineering group for their contributions to the thermal analysis.

SHUTTLE FLOW FIELD ANALYSIS USING THE DIRECT SIMULATION MONTE CARLO TECHNIQUE

J. E. Hueser and F. J. Brock

Old Dominion University
Norfolk, VA 23508

Paper presented at the
USAF/NASA International Spacecraft Contamination Conference
7-9 March 1978 US Air Force Academy, Colorado

1. INTRODUCTION

The theoretical evaluation of the performance of a molecular shield(1) requires a detail description of the flow field properties in the immediate vicinity of the Shuttle. Knowledge of the flow field properties is essential in determining the molecular shield-to-Shuttle separation distance; the orientation of the shield deployment boom with respect to the Shuttle axis; and the influence on shield performance due to molecular scattering, due to molecular reflection from the Shuttle surface, due to outgassing from the Shuttle surface, and due to Shuttle related gas sources such as leaks, vents, dumps and attitude control rockets. Optimization of the shield performance requires the investigation of the flow field properties for a range of Shuttle orbital attitudes and orbit heights.

From an investigation of analytical and numerical techniques which are capable of analyzing three-dimensional, external, rarified gas flow the Direct Simulation Monte Carlo Technique(2) was selected as the most useful in solving the Shuttle flow field problem.

Bird(2) has shown that the Direct Simulation Monte Carlo technique yields the numerical equivalent of a solution for the time dependent Boltzmann transport equation with boundary conditions. This is a

---

(1) Melfi, L. T., Characteristics and potential applications of orbiting ultrahigh vacuum facilities, Acta Astronautica 4:801-811 (1977).

(2) Bird, G. A., Molecular Gas Dynamics, Oxford University Press (London) 1976.

self-consistent technique which honors all the conservation laws applicable to real gas flow. The technique has the capability of analyzing three-dimensional flow with internal and external boundary conditions; transient flow phenomena by ensenble averaging; and steady state phenomena by time averaging.

Molecular modeling equations are used to obtain the modeled molecule cross section and the molecular collision frequency density. The modeled cross section σ is obtained from

$$\sigma = \frac{1}{\sqrt{2}\lambda n} , \tag{1}$$

where λ is the mean free path and n is the modeled density. The molecular collision frequency density is obtained from (for a single species gas)

$$N_c = \frac{1}{2} n^2 \sigma \bar{v}_r , \tag{2}$$

where N_c is the modeled molecular collision frequency per unit volume and $\bar{v}_r$ is the mean relative speed. The assumption is made that the molecular motion process and the molecular collision process may be treated as uncoupled provided the molecular motion time increment Δt_m is small compared to the mean time between molecular collisions. The validity of this assumption has been demonstrated(2) theoretically and experimentally. Molecular trajectories are calculated using the classical laws of motion and molecular collisions are calculated using classical collision dynamics.

2. COMPUTATIONAL PROCEDURE

A scale drawing of the Shuttle is shown in Figure 1. A close approximation of the Shuttle geometrical configuration has been written into the Shuttle flow field analysis program code.(3) The Shuttle surface is divided into 38 surface elements as shown in Figure 2 which are also written into the program code. Either of two options may be selected at execution time, payload bay doors open or closed. Figure 3 gives the flow field geometry and the location of the Shuttle within the flow field. The flow field is divided into seven blocks, each of which is subdivided into many computational cells. The location of the flow field boundaries, the location of the block boundaries, and number of computational cells in each block are selected at execution time. The flow field volume is typically of the order of $10^6 m^3$. The number of cells in the flow field typically ranges between 500 and 700. The Shuttle midplane is a plane of symmetry. The angle of attack α (angle between the free stream velocity and + x) is selected at execution time.

The molecular flux density incident on the flow field boundaries from the outside is calculated (internally) from the drifting

---

(3) Bird, G. A., Flow field simulation for the space Shuttle orbital vehicle, Proc. 10th Int. Symp. Rarefied Gas Dynamics (1976).

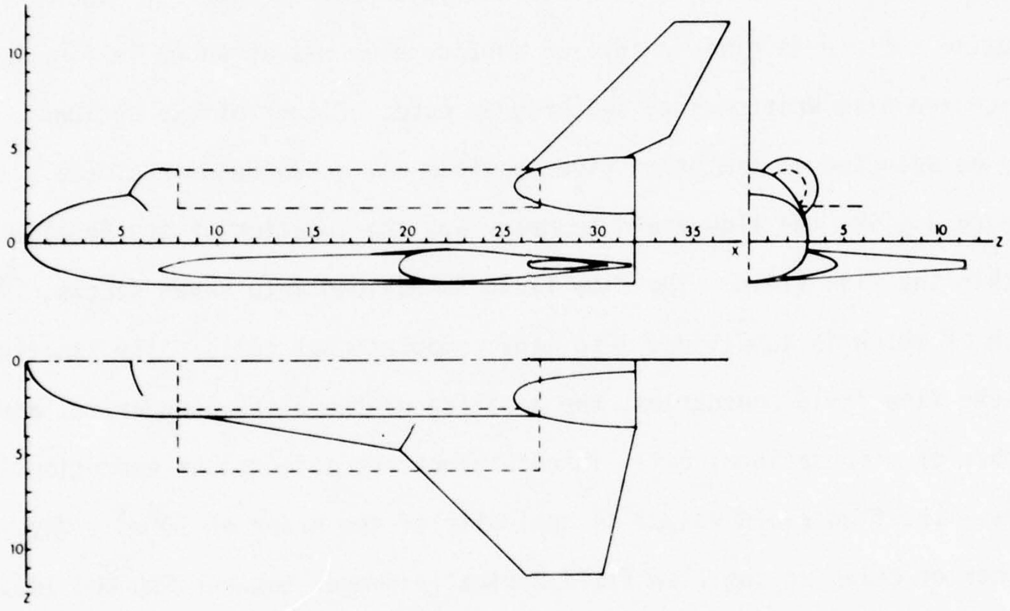

Fig. 1. Shuttle geometry (dimensions in meters). The midplane (z=0) is a plane of symmetry. A close approximation of the actual Shuttle geometry is written into the flow field analysis program code.

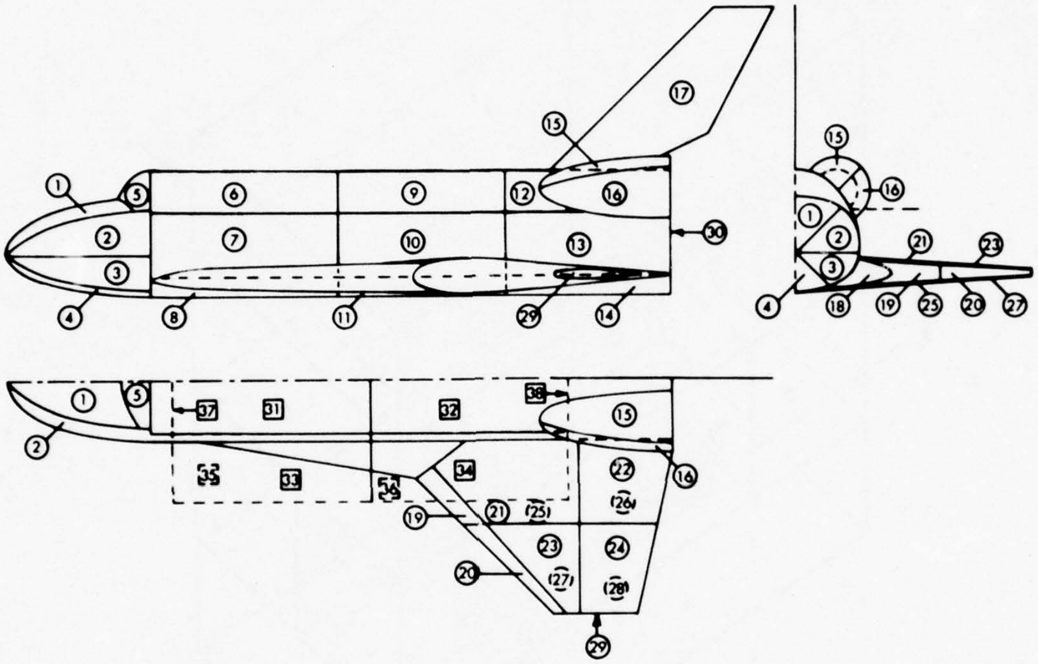

Fig. 2. The geometrical configuration of the Shuttle surface elements written into the flow field analysis program code. The numbers in solid symbols refer to surface elements in direct view, the numbers in dashed symbols refer to elements on the opposite side of the surface. The square symbols refer to the doors-open configuration only.

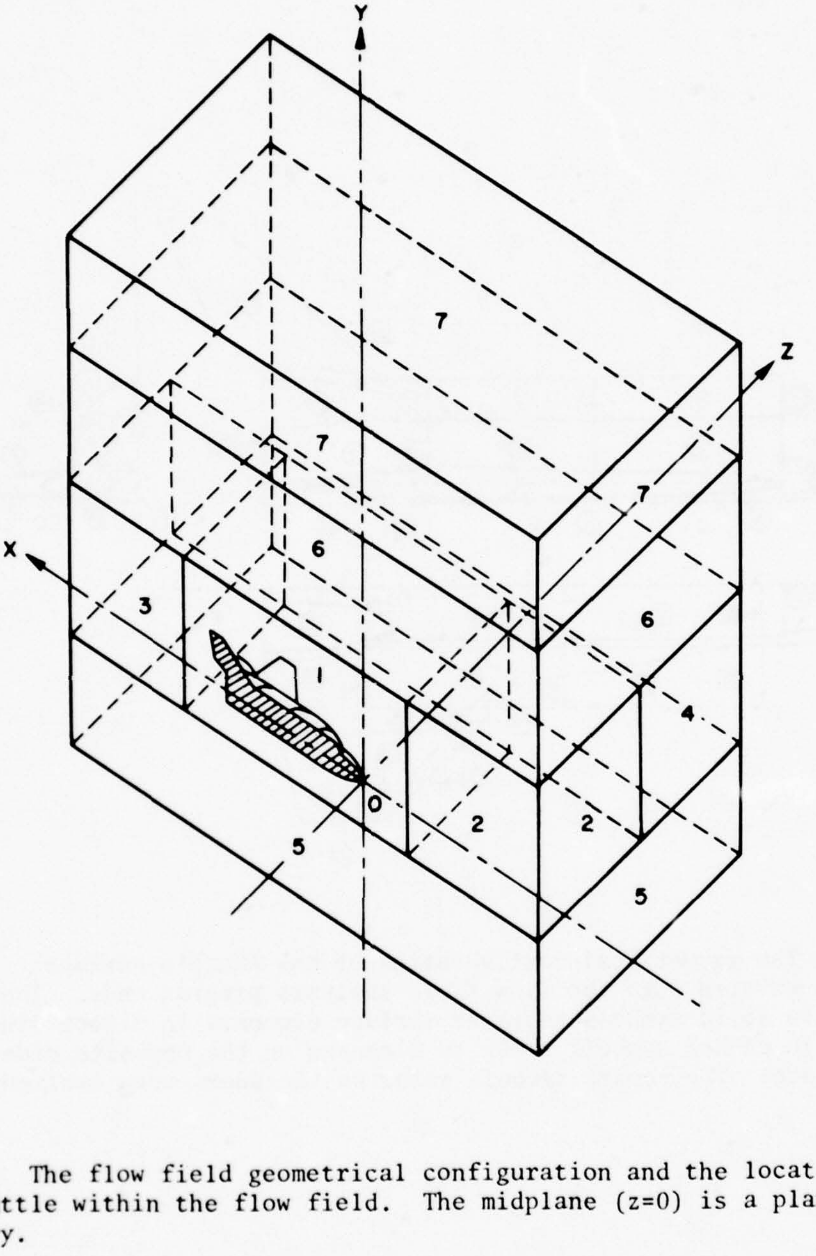

Fig. 3. The flow field geometrical configuration and the location of the Shuttle within the flow field. The midplane (z=0) is a plane of symmetry.

Maxwellian gas properties of the free stream. The stream drift velocity, the mean free path, and the mean thermal speed are specified at execution time (the free stream density is a modeled parameter). The molecular flux entering the flow field from the Shuttle surface (outgassing) is randomly distributed over each surface element and is assumed to be in thermal equilibrium with the surface at emission. The molecular emission angular distribution is assumed to obey the cosine law. Molecules which are incident on the Shuttle surface are assumed to equilibrate to the surface temperature before reflection. These reflected molecules are also assumed to obey the cosine law. The outgassing flux density is specified at execution time. Molecular fluxes may enter the flow field from a prescribed number of discrete sources located on or near the Shuttle. The location, emission direction, molecular velocity distribution, angular distribtuion, and emission flux of these discrete sources are specified at execution time.

The Shuttle flow field analysis program keeps continuous and separate account of five types of molecules: type 1, free stream molecules; type 2, free stream molecules which have been reflected from the Shuttle surface; type 3, free stream molecules which have experienced a molecular collision with other molecular types (excluding type 1); type 4, Shuttle outgassing molecules; and type 5, Shuttle discrete gas source molecules (such as leaks, vents, dumps, and attitude control rockets). There are two options for the molecular cross section, hard sphere or inverse ninth power, one of which is selected at execution time.

A schematic flow diagram of the Monte Carlo program is shown in Figure 4. The program maintains the position and velocity components current for each modeled molecule from the time it enters the flow field until it exits. The main program loop starts at 103, the flow field properties sampling loop starts at 112, and the incremental flow analysis loop starts at 111. At 116 molecular trajectory increments corresponding to Δt_m are calculated, including Shuttle surface collisions, block and field boundary interactions, etc. At 117 molecules enter the flow field from all sources and then molecular collisions are calculated.

The value of Δt_m is typically between 1 and 10 ms, NIS is typically between 1 and 5 and NSP is typically between 10 and 100. The number of passes through loop 103 depends largely on the problem, the resolution desired, the statistical fluctuation considered acceptable, and the kind of averaging required by the problem (ensemble or time). Depending on these same parameters, execution time may range between 0.5 and 20 hours in a Cyber 175.

3. DISCUSSION OF RESULTS

A number of Shuttle flow field configurations are presently under analysis and results from one of these is presented in the following

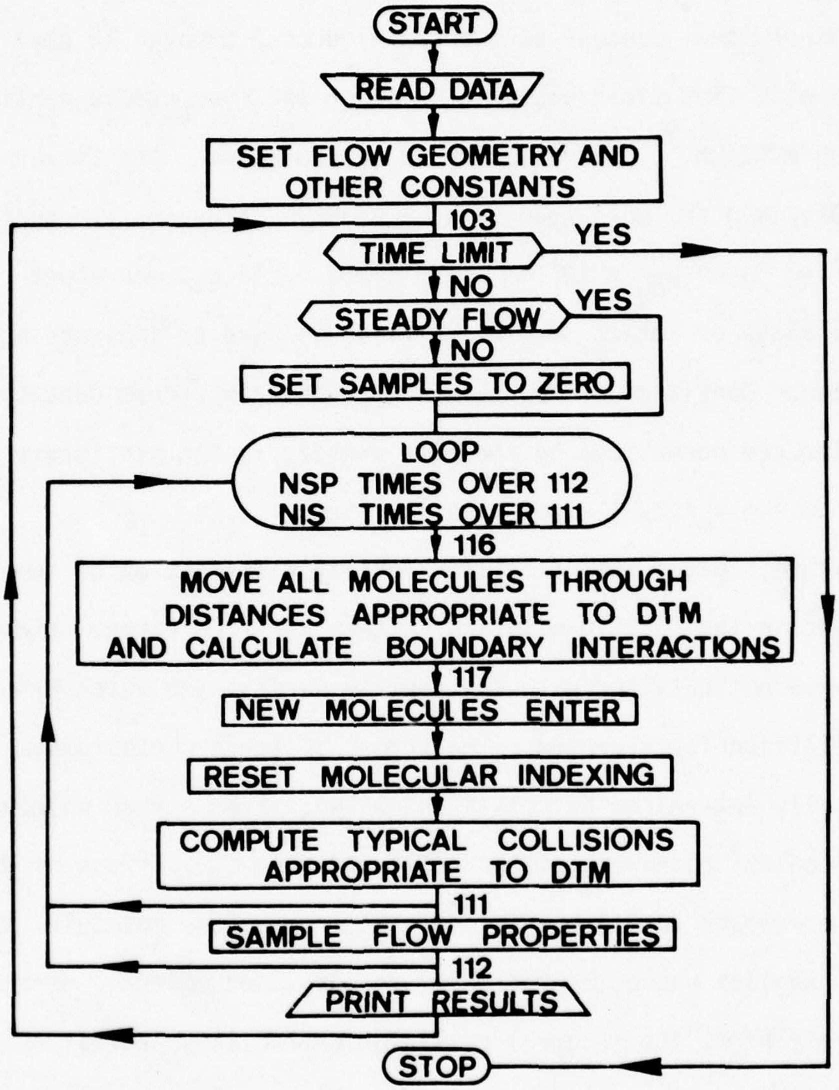

Fig. 4. Schematic flow diagram of the Monte Carlo, Shuttle flow field analysis program.

figures. To minimize the complexity of the illustrations only data in the Shuttle midplane are presented. Thus, the two-dimensional contour curves presented are the result of making a midplane cut through three-dimensional contour surfaces. Figures 5 through 12 give the results of a flow field analysis in which the free stream density $n = 8.33 \times 10^9 \mathrm{cm}^{-3}$, the velocity $u = 7790$ m/sec, the temperature $T = 855\mathrm{K}$, and the mean free path $\lambda = 386$ m. The Shuttle surface outgassing rate $\nu_{og} = 10^{15} \mathrm{cm}^{-2} \mathrm{sec}^{-1}$, the surface temperature $T_s = 300\mathrm{K}$, and the angle of attack $\alpha = 0$. A tilda is used to indicate a normalized parameter. Densities are normalized by the free stream density and flux densities are normalized by the flux density in the stationary free stream $\nu = n\, v_m/(2\sqrt{\pi}) = 2.2 \times 10^{14} \mathrm{cm}^{-2} \mathrm{sec}^{-1}$.

Figure 5 gives the normalized density distribution of type 1 molecules in the Shuttle midplane. These are free stream molecules which have not collided with the Shuttle surface and which have not been collisionally affected. The shapes of these contours are principally determined by collisions between free stream molecules and molecules which were either reflected from the surface or emitted from the surface due to outgassing. As free stream molecules pass through regions where the reflected or outgassed molecule density is relatively high, the integral collision probability increases. This implies that an increasing fraction of the type 1 molecules are converted to type 3 as a result of collisions with reflected and outgassed molecules, and the type 1 density decreases. Thus, the type 1

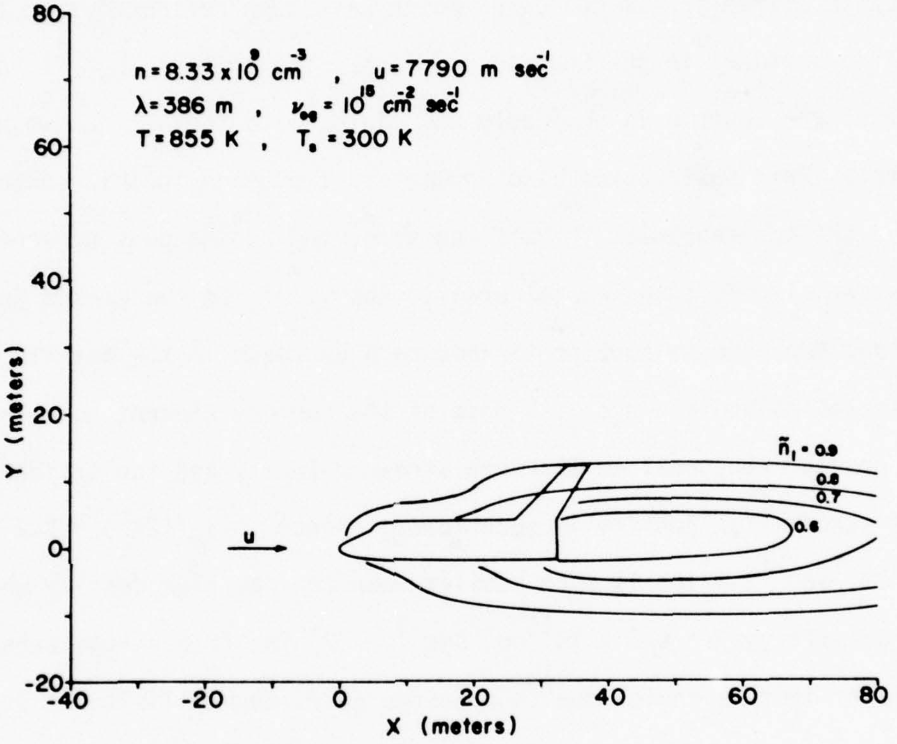

Fig. 5. The density distribution of freestream molecules (type 1) in the Shuttle midplane, normalized by the undisturbed freestream density $n=8.33 \times 10^9$ cm^{-3}. The freestream velocity $u=7790$ m sec^{-1}, the temperature T=855 K, and the mean free path $\lambda=386$ m. The Shuttle surface temperature $T_s=300$ K, and the surface outgassing rate $\nu_{og}=10^{15}$ cm^{-2} sec^{-1}.

contours ($\tilde{n}_1 < 1$) expand in the transverse direction as they are followed in the longitudinal direction (aft). Well aft of the Shuttle, the entire process is reversed and the contours collapse.

Figure 6 gives the normalized density distribution of type 2 molecules (free stream molecules which have been reflected from the Shuttle surface) in the Shuttle midplane. The contour $\tilde{n}_2 = 1$ near the nose of the Shuttle is obviously associated with the well known ram effect. This observation also applies to the bulge in this contour above the fuselage near the aft end since the engine pods present a substantial effective frontal area to the flow. In the center fuselage region, two effects combine to produce a decrease in the density of reflected molecules $\tilde{n}_2$: (1) Most of the surface element normals are nearly orthogonal to the free stream velocity and the incident free stream flux density is much lower, since $n\, v_m/(2\sqrt{\pi}) = 2.2 \times 10^{14} cm^{-2} sec^{-1}$ which is much smaller than the ram flux density which is approximately $n\, u = 6.5 \times 10^{15} cm^{-2} sec^{-1}$. (2) The free stream density is lower in this region due to upstream (previous) collisions. It may be observed that $\tilde{n}_2$ decreases more rapidly in the transverse direction than $1/y^2$ but that in the forward longitudinal direction $\tilde{n}_2$ decreases less rapidly than $1/x^2$. This is due to the difference in reflected flux density discussed above and to momentum transfer from the free stream to reflected molecules during collisions.

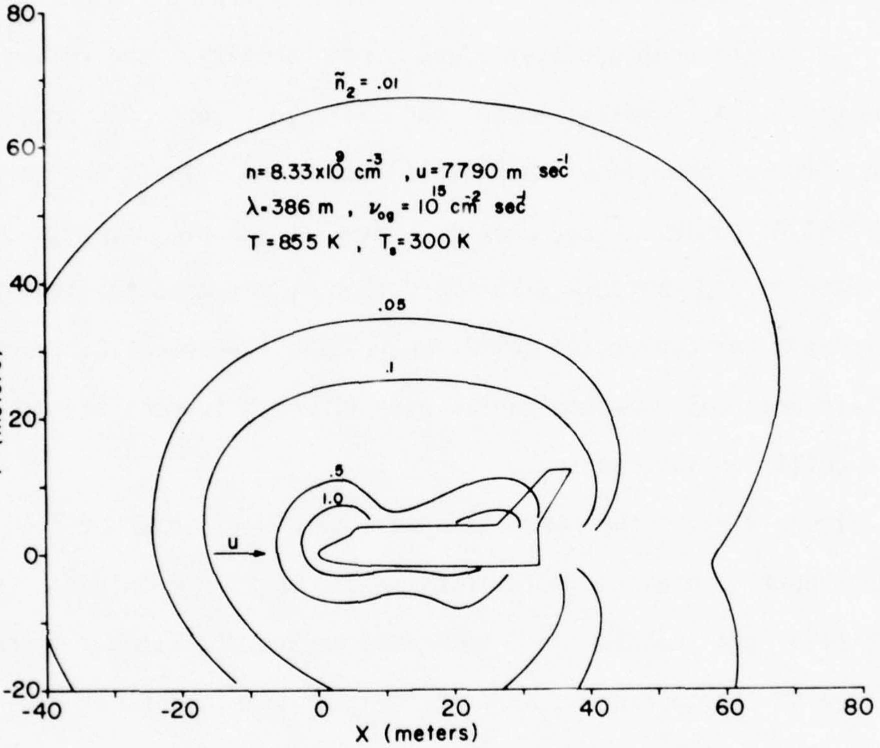

Fig. 6. The density distribution of reflected freestream molecules (type 2) in the Shuttle midplane, normalized by the undisturbed freestream density $n=8.33 \times 10^9$ cm^{-3}. The freestream velocity $u=7790$ m sec^{-1}, the temperature $T=855$ K and the mean free path $\lambda=386$ m. The Shuttle surface temperature $T_S=300$ K, and the surface outgassing rate $\nu_{og}=10^{15}$ cm^{-2} sec^{-1}.

Figure 7 gives the normalized density distribution of type 3 molecules (free stream molecules which have been collisionally affected by reflected or outgassed molecules) in the Shuttle midplane. $\tilde{n}_3$ increases moving aft due to the increasing integral probability of collisional conversion of type 1 molecules to type 3 and due to the increase in the combined type 2 and type 4 density. The relatively low value of $\tilde{n}_3$ is consistent with the relatively long mean free path in the free stream since the Shuttle outgassing rate is not sufficiently high that it dominates the mean free path in the flow field. The shape of the contours also imply that in the mean the type 3 molecules after conversion collision, retain a substantial fraction of their original momentum (while type 1) which is consistent with a first collision interaction.

Figure 8 gives the normalized density distribution of type 4 molecules (Shuttle outgassed molecules) in the Shuttle midplane. In the vicinity of the Shuttle, $\tilde{n}_4$ increases moving aft since a larger fraction of the surface area is aft (engine pods, vertical fin, wings). In this flow field analysis the outgassing flux density is uniform over the surface of the Shuttle. Over much of the volume near the Shuttle, the density of outgassing molecules $\tilde{n}_4$ exceeds the density of reflected molecules $\tilde{n}_2$. This confirms the conclusion that much of the type 1 scattering is due to collisions with type 4. It also explains the similarity in shape of the $\tilde{n}_3$ and $\tilde{n}_4$ contours near the Shuttle.

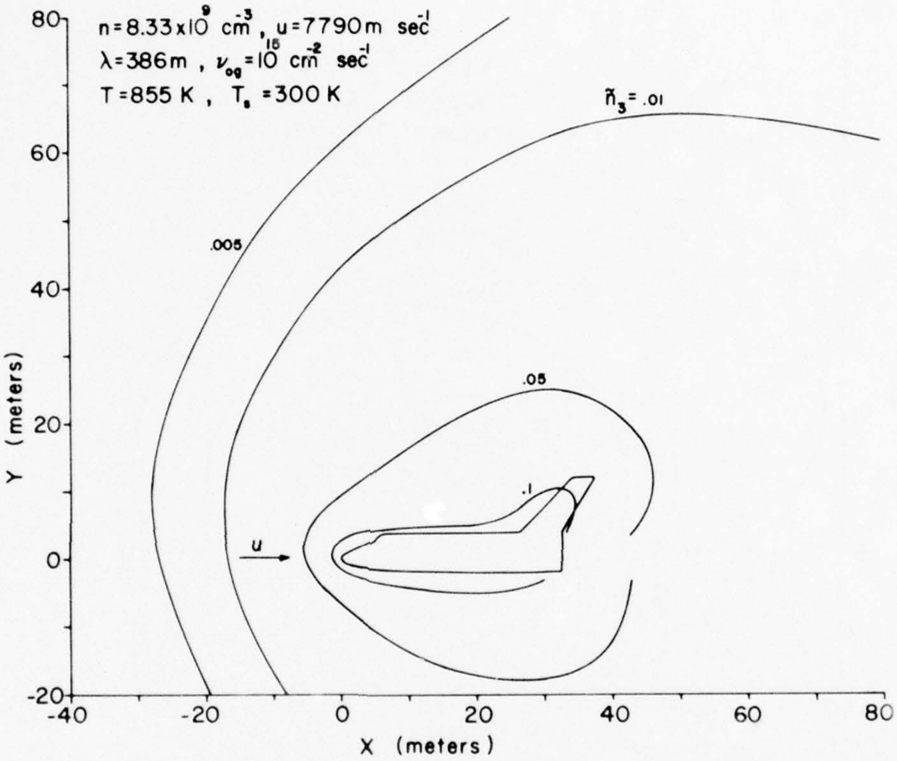

Fig. 7. The density distribution of collisionally affected freestream molecules (type 3) in the Shuttle midplane, normalized by the undisturbed freestream density $n=8.33 \times 10^{9}$ cm^{-3}. The freestream velocity u=7790 m sec^{-1}, the temperature T=855 K, and the mean free path λ=386 m. The Shuttle surface temperature T_S=300 K and the surface outgassing rate $\nu_{og}=10^{15}$ cm^{-2} sec^{-1}.

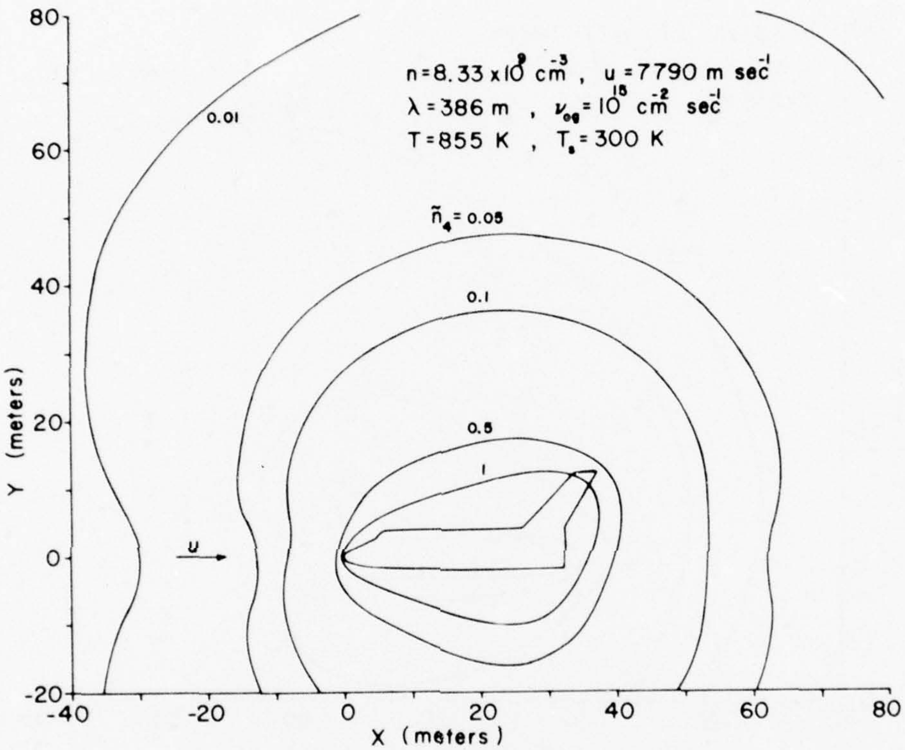

Fig. 8. The density distribution of Shuttle outgassed molecules (type 4) in the Shuttle midplane, normalized by the undisturbed freestream density $n=8.33 \times 10^9$ cm^{-3}. The freestream velocity $u=7790$ m sec^{-1}, the temperature T=855 K, and the mean free path $\lambda=386$ m. The Shuttle surface temperature $T_S=300$ K and the surface outgassing rate $\nu_{og}=10^{15}$ cm^{-2} sec^{-1}.

Figure 9 gives the total density distribution (summed over all molecule types) in the Shuttle midplane. Close to the Shuttle, the principal contribution to the total density is from outgassed molecules and reflected molecules. At distances larger than one Shuttle length away the principal contribution to the total density is from free stream molecules. It may be observed that the total density differs from the free stream density by less than 10 percent for distances greater than two Shuttle lengths away from the Shuttle.

Figure 10 gives the normalized upstream flux density distribution in the Shuttle midplane (summed over all molecule types). Near the Shuttle the upstream flux is principally due to emission of outgassing molecules with an upstream velocity component and secondarily to reflected molecules which were emitted with an upstream component. However, at several Shuttle lengths away and especially aft of the Shuttle substantially all the upstream flux is due to molecules which have experienced multiple collisions while in the flow field or to molecules which entered the flow field such that the angle between their trajectory and the free stream velocity is relatively large. The data in Figure 10 imply that experiments in a molecular shield deployed on a 75 m boom and oriented 45° aft of vertical would experience 0.1 percent surface coverage in approximately 10 hours. Immediately above the payload bay $\tilde{\nu}_{-x} = 3$ which implies that considerable attention must be given to protecting any sensitive experiment during deployment.

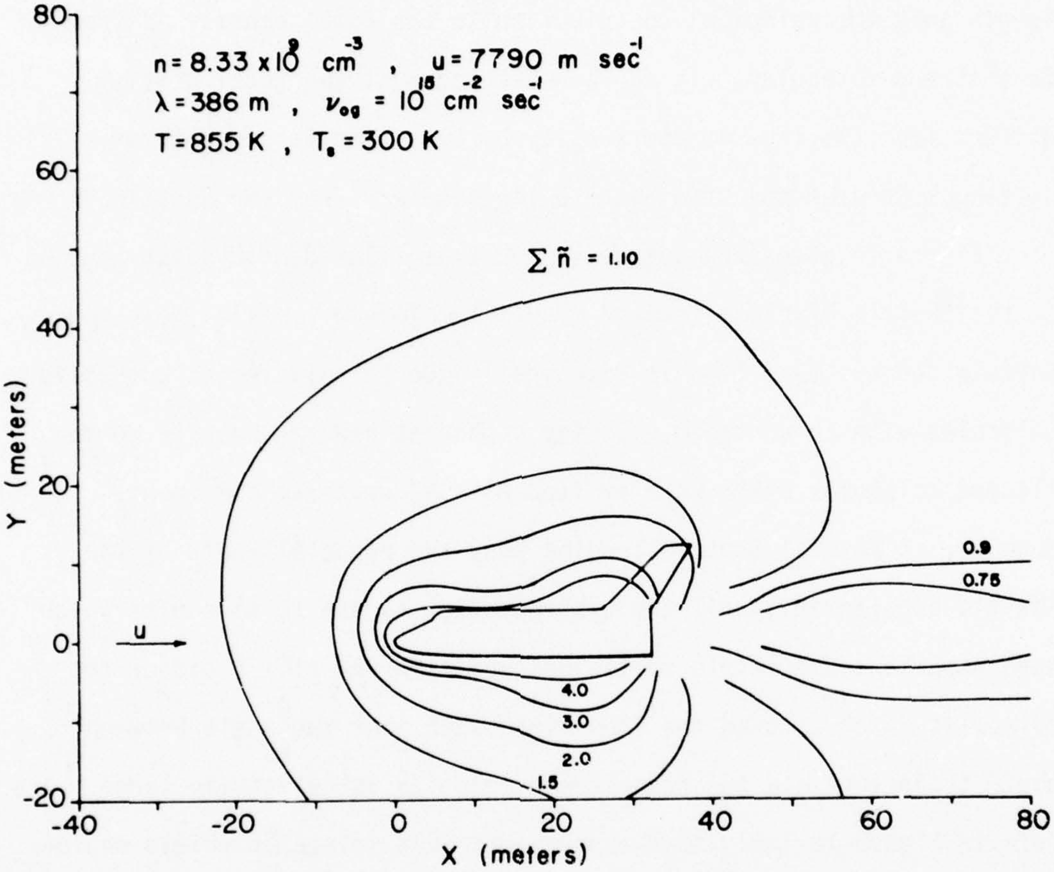

Fig. 9. The total density distribution in the Shuttle midplane, normalized by the undisturbed freestream density $n=8.33 \times 10^9$ cm^{-3}. The freestream velocity $u=7790$ m sec^{-1}, the temperature T=855 K, and the mean free path $\lambda=386$ m. The Shuttle surface temperature $T_s=300$ K and the surface outgassing rate $\nu_{og}=10^{15}$ cm^{-2} sec^{-1}.

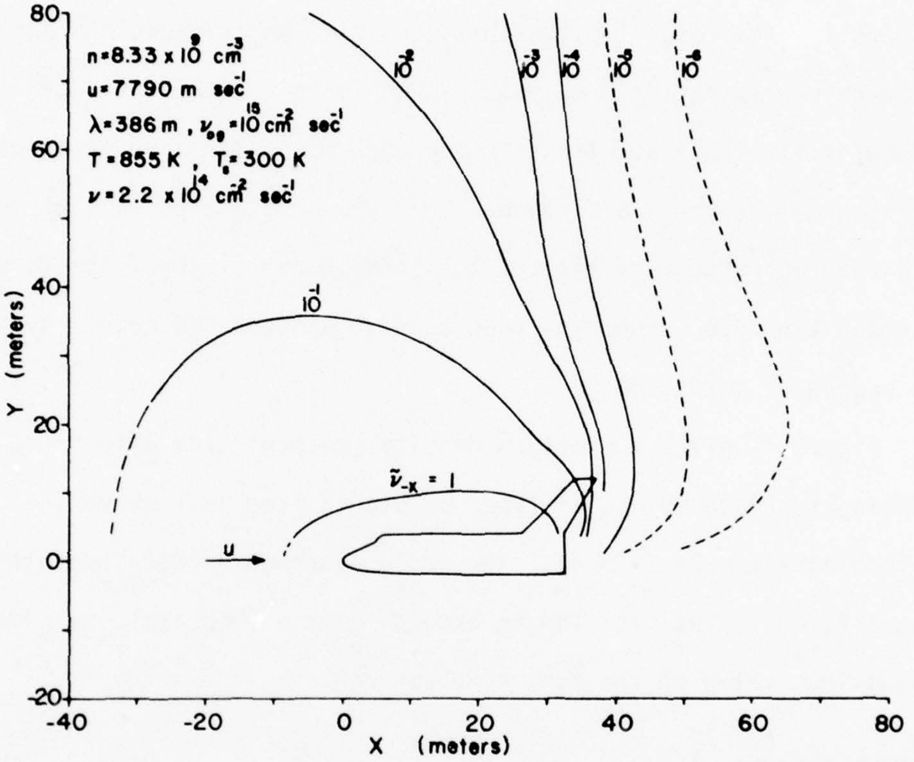

Fig. 10. The upstream flowing flux density distribution (summed over all molecular types) in the Shuttle midplane, normalized by the flux density in the stationary freestream $nv_m/2\sqrt{\pi})=\nu=2.2 \times 10^{14}$ cm^{-2} sec^{-1}. The freestream density $n=8.33 \times 10^{9}$ cm^{-3}, the velocity $u=7790$ m sec^{-1}, the temperature $T=855$ K, and the mean free path $\lambda=386$ m. The Shuttle surface temperature $T_s=300$ K and the surface outgassing rate $\nu_{og}=10^{15}$ cm^{-2} sec^{-1}.

Figure 11a gives the molecular flux density incident on typical surface elements near the Shuttle midplane for each molecular type. For surface elements near the aft end of the payload bay, the normalized incident flux density of type 4 molecules (outgassing) exceeds 1. This also implies that sensitive experiments may encounter a severe contamination problem. Figure 11b gives the incident molecular flux relative fraction for each molecular type, averaged over the entire Shuttle surface. The type 4 molecules account for more than 20 percent of the total, although over much of the forward fuselage the type 1 incident flux density exceeds the type 4 by about two orders of magnitude.

Figure 12 gives the column density (molecules/cm^2) in the Shuttle midplane for each molecular type, as viewed from just above the payload bay ($x = 24$, $y = 4$). The angle increment indicated on the figure is 20°. The path length extends to the flow field boundary. The maximum value of the type 4 column density is 5×10^{13}cm^{-2}.

ACKNOWLEDGEMENT

This work was supported by NASA Langley Research Center Grant NSG-1271 through Old Dominion University Research Foundation.

REFERENCES

1. Melfi, L. T., Characteristics and potential applications of orbiting ultrahigh vacuum facilities, Acta Astronautica 4:801-811 (1977).

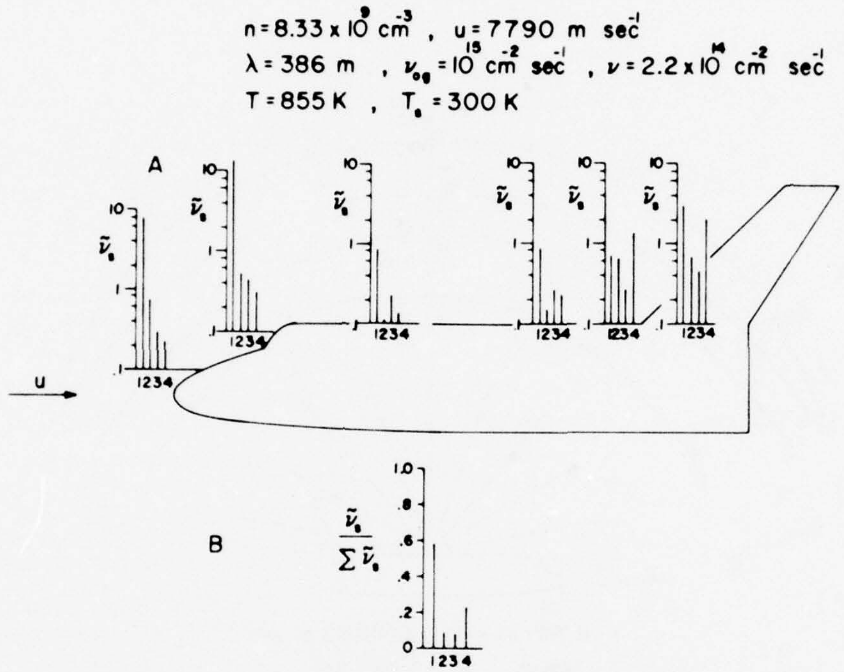

Fig. 11. (a) The molecular flux density incident on several surface elements of the Shuttle near the midplane, normalized by the flux density in the stationary freestream $nv_m/(2\sqrt{\pi})=\nu=2.2 \times 10^{14}$ cm^{-2} sec^{-1}. The incident flux density is given for each molecular type at each location (exponential ordinate). (b) The relative incident flux density for each molecular type averaged over the entire surface of the Shuttle. The freestream density $n=8.33 \times 10^9$ cm^{-3}, the velocity $u=7790$ m sec^{-1}, the temperature T=855 K, and the mean free path $\lambda=386$ m. The Shuttle surface temperature $T_s=300$ K and the surface outgassing rate $\nu_{og}=10^{15}$ cm^{-2} sec^{-1}.

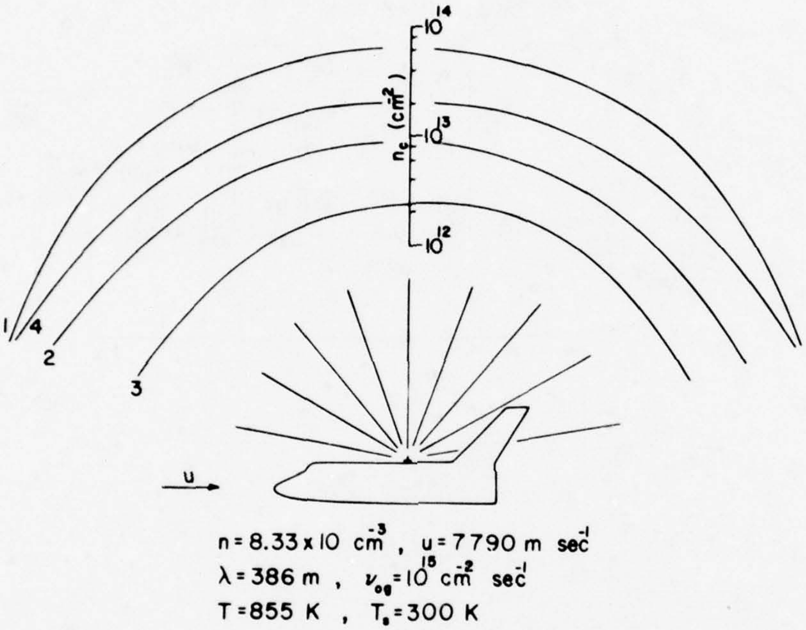

Fig. 12. The midplane column density for each molecular type as viewed from the top of the payload bay (x=24 m, y=4 m), given in molecules per cm^2. The freestream density $n=8.33 \times 10^9\ cm^{-3}$, the velocity $u=7790\ m\ sec^{-1}$, the temperature T=855 K, and the mean free path $\lambda=386$ m. The Shuttle surface temperature $T_S=300$ K and the surface outgassing rate $\nu_{og}=10^{15}\ cm^{-2}\ sec^{-1}$.

2. Bird, G. A., Molecular Gas Dynamics, Oxford University Press (London) 1976.

3. Bird, G. A., Flow field simulation for the space Shuttle orbital vehicle, Proc. 10th Int. Symp. Rarefied Gas Dynamics (1976).

NASA TECHNICAL MEMORANDUM

NASA TM-73889

NASA TM-73889

NASA CHARGING ANALYZER PROGRAM - A COMPUTER TOOL THAT CAN EVALUATE ELECTROSTATIC CONTAMINATION

by N. John Stevens, James C. Roche and Myron J. Mandell
Lewis Research Center
Cleveland, Ohio 44135

TECHNICAL PAPER to be presented at the
International Spacecraft Contamination Conference
cosponsored by the United States Air Force and
the National Aeronautics and Space Administration
Colorado Springs, Colorado, March 7-9, 1978

NASA CHARGING ANALYZER PROGRAM - A COMPUTER TOOL THAT CAN EVALUATE ELECTROSTATIC CONTAMINATION

by N. John Stevens, James C. Roche and Myron J. Mandell[*]

Lewis Research Center
Cleveland, Ohio 44135

E-9526

ABSTRACT

A computer code, the NASA Charging Analyzer Program (NASCAP), has been developed to study the surface charging of bodies subjected to geomagnetic substorm conditions. This program will treat the material properties of a surface in a self-consistent manner and calculate the electric fields in space due to the surface charge. Trajectories of charged particles in this electric field can be computed to determine if these particles enhance surface contamination. A preliminary model of the Spacecraft Charging At The High Altitudes (SCATHA) satellite has been developed in the NASCAP code and subjected to a geomagnetic substorm environment to investigate the possibility of electrostatic contamination. The results indicate that differential voltages will exist between the spacecraft ground surfaces and the insulator surfaces. The electric fields from this differential charging can enhance the contamination of spacecraft surfaces.

1.0 INTRODUCTION

In the past there has been concern over the possibility of spacecraft being contaminated by outgassing products.[1] Thermal control paints, thermal blankets, solar panels and adhesives are known to outgas for extended periods in space. It is believed that these molecular outgassing products can deposit on spacecraft and contaminate sensitive surfaces.

Normally, it was assumed that all spacecraft surfaces would not be charged more than a few volts above or below the space plasma potential. Accordingly, there was little concern for possible charged particle contamination since the fields around the spacecraft would not be sufficient to ionize neutral molecules.

---

[*] Systems, Science and Software, LaJolla, California 92038

STAR Category 18

The data from ATS-5 and -6 Auroral Particles Experiments have shown, however, that the environment at geosynchronous orbit can charge spacecraft surfaces to appreciable negative values.[2,3,4] The data indicates that the satellite structure can be charged to potentials as large as -19 KV during eclipse periods and to -2 KV during sunlight environmental charging occurrences.[5] The phenomenon, known as "spacecraft charging", is believed to be caused by the satellite encounter with kilovolt energy particle clouds (geomagnetic substorms). Furthermore, other satellites are believed to have encountered such substorms and to have experienced anomalous electronic switching events.[6]

If a spacecraft structure can be charged to such levels (even when sunlit), then it is conceivable that the insulator surfaces of a satellite could be charged to similar levels. A shadowed insulator could be charged to a voltage level substantially different from the structure or from another insulator that was illuminated. Hence, it is possible that large differential voltages could develop on a satellite experiencing a geomagnetic substorm.

With large negative differential voltages on satellites, the electrical stresses within an insulator could exceed the breakdown conditions and arcing can occur. Laboratory experiments have shown that arcing is possible under conditions likely to be experienced by satellites in substorms[7] and that arcing can be accompanied by low energy charged particle emission and loss of material.[8] The electrostatic fields, generated by the surface potentials, can attract charged particles back to the satellite, enchancing contamination.

It is also possible for other processes to occur when spacecraft surfaces are charged. An electrostatic precipitation effect could occur. Neutral molecules could be polarized by the electric field and be returned to the spacecraft surfaces by gradients in the field. Another process that could occur due to fields generated by the charged surfaces is acceleration of the charged particles in space, increasing the probability of molecular ionization by collisions. The resulting ions could return to spacecraft surfaces.

This possible enhanced contamination of spacecraft surface by environmental charging of surfaces is of concern. The first attempt to evaluate this contamination in a space environment will be conducted on the Spacecraft Charging At The High Altitudes (SCATHA) satellite by the Spacecraft Charging/Contamination Experiment.[9,10]

An analytical tool that will predict surface charging on any spacecraft surface due to the environment is required to study this electrostatic contamination. This tool should have the capability of computing the voltage distribution on the surface and into the environment and of determining particle trajectories. Such a tool has been developed as part of the joint AF/NASA Spacecraft Charging Investigation.[11] This tool is called NASCAP, an acroynm standing for NASA Charging Analyzer Program.

As an example of the use of the program to study electrostatic contamination, a preliminary model of the SCATHA satellite was developed and its charging studied. Results of this study will be presented in this report along with a description of NASCAP and its capabilities.

2.0 DESCRIPTION OF NASCAP

2.1 Introduction

The NASA Charging Analyzer Program (NASCAP) has been developed as an engineering tool to determine the environmental impact on spacecraft surfaces and systems. It is capable of analyzing the charging of a 3-dimensional, complex body as a function of time for given space environmental conditions. The material properties of the surfaces are included in the computations. The surface potentials, low energy sheath, potential distribution in space and particle trajectories are calculated. Therefore, this program is adaptable to the study of electrostatic contamination of any satellite in the space environment.

NASCAP is a quasi-static computational program, i.e. it assumes that all processes are in equilibrium at each time step. This is a reasonable assumption since charging times are long compared to the time steps.

In the following paragraphs the program elements will be briefly discussed. A detailed description can be found in the literature.[12] The program is currently operational on UNIVAC 1100 computers and a User's Manual is available.[13]

2.2 Program Elements

The NASCAP flow diagram outlining the sequence of elements of the program is shown in figure 1.

a. Program Set-up. - The computer model is set-up in an embedded mesh, 3-dimensional network (see fig. 2). The spacecraft is described in the inner mesh region which is currently limited to 17 x 17 x n points where n can be any number up to 33.

The space surrounding the spacecraft model is defined in a series of cascading outer mesh regions. Each outer region is double the size of the adjacent inner region. This cascading is to reduce computational

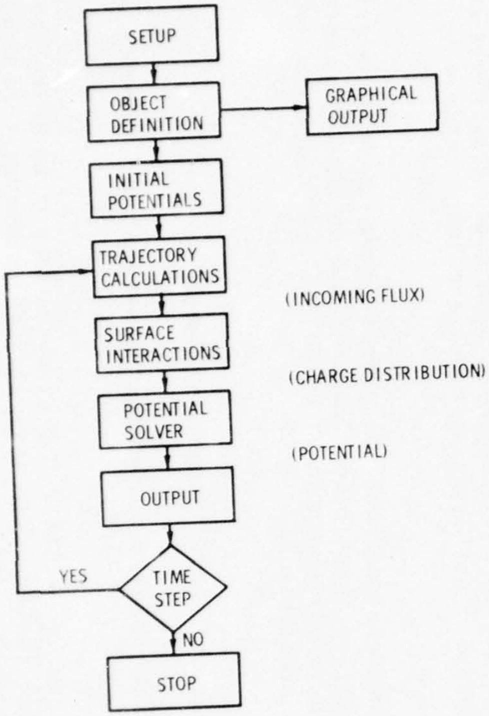

Figure 1. - NASCAP flow diagram.

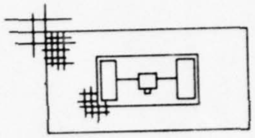

Figure 2. - Cross-section (y-z plane) of grid, showing first three embedded meshes.

AD-A070 386 AIR FORCE MATERIALS LAB WRIGHT-PATTERSON AFB OH F/G 22/2
PROCEEDINGS OF THE USAF/NASA INTERNATIONAL SPACECRAFT CONTAMINA--ETC(U)
1978 J M JEMIOLA
UNCLASSIFIED AFML-TR-78-190 NL

4 OF 13
AD
A070386

time. At the outermost boundary, undisturbed environmental parameters are specified. The environment can include solar inputs as well as particle fluxes.

b. Object Definition. - The spacecraft object must be defined in terms of rectangular parallelipiped or sections of parallelipiped. Curved surfaces are not allowed, but can be approximated by sections of parallelipipeds.

The surface can be bare or covered by a thin dielectric film. At present the material properties of aluminum and magnesium for structure and teflon, kapton and quartz for dielectric coverings are stored in the program. Other materials can be used but their material properties (secondary emission, backscatter, photoemission and resistivity) must be specified as a function of energy and angle of the incident particles.

Since a spacecraft can be a complex shape and errors in describing the model in terms of the program limitations can arise, a graphical output of the spacecraft model can be generated by the computer. Any set of axes or rotation angle can be specified for viewing the object. The computer will also remove all hidden lines. Therefore, it is possible to obtain 3-dimensional object definitions or projections in specified planes. As an example of the graphical output, the NASCAP model of the ATS-6 is shown in figure 3. This model has been generated within the 17 x 17 x 33 point size limitation and with sections of parallelipipeds. It is recognizable.

Finally, the graphical output will identify the specified surface materials of each cell. Hence, it is possible to determine that the computer model is the desired representation of the spacecraft prior to running the computational portions of the program.

c. Computational Elements. - The initial potentials on each spacecraft model node must be specified. These potentials can be set to zero if it is desired to obtain a time dependence on the charging. Specified values can also be used if the charging conditions from a given potential are to be determined. A program restart can use this capability.

The trajectory calculations are conducted to determine the incoming flux of particles. There are two basic operational modes for these calculations: particle pushing and Maxwellian approximations. In the particle pushing mode, the trajectories are traced backward from the surface, matching them to the specified environment distribution function at the outer boundary. There is available within the program six days of ATS-5 environmental data ranging from quiet to severe substorm conditions. In addition, other data can be used, if cast into the proper format. This mode of operation is computationally slow. If the environmental

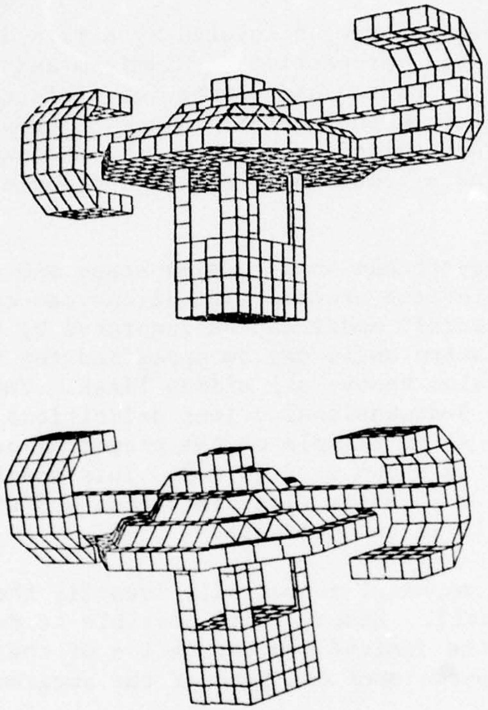

FIGURE 3 - NASCAP GRAPHICAL OUTPUT ATS-6 MODEL

conditions can be approximated by a Maxwellian distribution, then this can be used for faster computations. The Maxwellian approximation to substorm conditions does not appear to be unreasonable.[15]

The surface interactions are computed in order to determine the charge distributions on the spacecraft surface. The processes considered are secondary emission, backscatter, photoemission and leakage through the material. Surface conduction between adjacent cells is not presently considered. The program will compute space charge due to secondary and photoemitted electrons in the region adjacent to the spacecraft only.

A conjugate gradient technique is used to determine the surface potential distribution as well as the potential distribution in space. The program assumes that there are no space charge effects other than those adjacent to the spacecraft model.

The program will iterate on these computational elements until a self-consistent solution is obtained. It has been found that from 5 to 20 iterations are sufficient to obtain a valid potential distribution for a time step. A valid potential distribution is one that does not change significantly as the iterations are continued.

d. Output. - For each time step (if desired), a printout can be obtained of the charge or potential throughout the embedded mesh network. If desired, graphical outputs of the potential contours and particle trajectories in the plane of any axes combination can be requested.

3.0 PRELIMINARY SCATHA MODEL

3.1 Model Description

As an example of how NASCAP functions and what its capabilities are, a simplified model of the Spacecraft Charging At The High Altitudes (SCATHA) spacecraft was developed.[14,15] This spacecraft is shown in figure 4. For the NASCAP model only the cylindrical portion of the spacecraft was considered.

The NASCAP model is a quasi-cylinder 1.7 m diameter by 1.8 m long. The top and bottom of this cylinder is covered with aluminum and grounded to the structure. The cylindrical sides are primarily solar cells (quartz cover slides). There is a center band of aluminum which is grounded to the structure. Three 0.3m square patches of kapton are on the spacecraft to simulate one of the experiments, Spacecraft Surface Potential Monitors (SSPM). Two of these patches are on the cylindrical sides, 180° apart, while the third is on the top surface. This model is shown in figure 5. Note that the materials for each node have been coded to provide a visual display of the various surfaces. Each node represents a 10 cm by 10 cm area of the spacecraft.

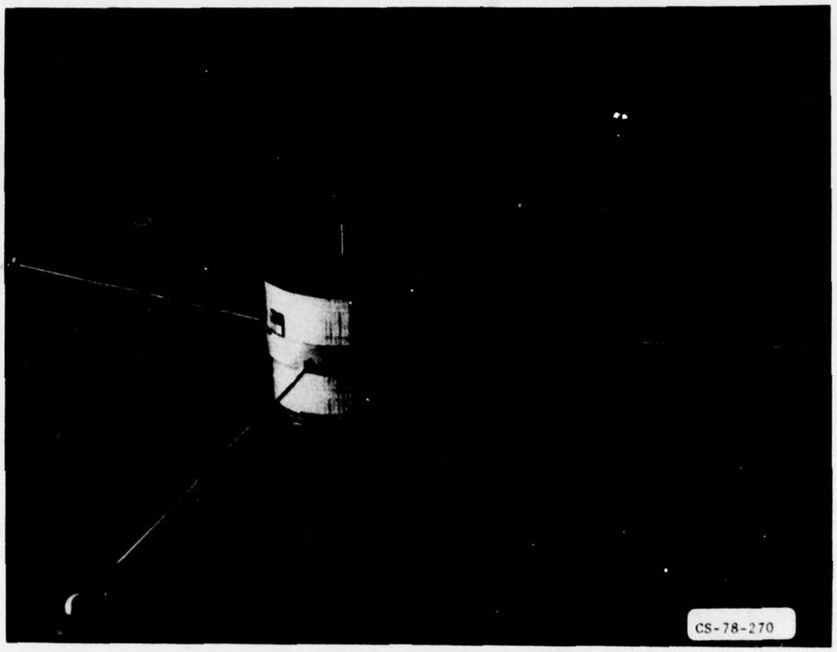

Figure 4. - Scatha Satelite.

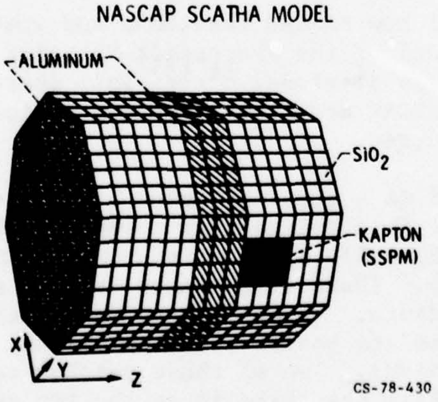

Figure 5. - NASCAP scatha model.

3.2 Environmental Conditions

The environment used in this model evaluations corresponds to the substorm conditions of October 16, 1969.[3] This substorm, incidentally, was one of those used in the original reports on the spacecraft charging phenomenon. The conditions are:

Electron Temperature	5000 volts
Electron Density	0.5 e/cm^3
Proton Temperature	10,000 volts
Proton Density	1 p/cm^3

The Maxwellian approximation for the particle energies is used. This environment is considered to be constant throughout the computational period. No sunlight is considered.

This model, then, simulates an uncharged satellite in eclipse experiencing a constant substorm for a period of one hour. No attempt is made to determine the effect of a charging environmental flux nor in determining how the surfaces would be discharged.

It is recognized that satellites can also be charged while some surfaces are sunlit. This case is also of interest for electrostatic charging. While NASCAP can handle these conditions (i.e. geomagnetic substorm environment in sunlight), the subroutines have not yet been verified. The effects of sunlight as well as changing flux will be considered in future work.

3.3 NASCAP Results

Computer runs were started with all nodes at 0 volts. The substorm environment then charged the surfaces to their equilibrium potentials which were dependent upon the surface material properties. The charging of typical surfaces on the spacecraft is shown in figure 6.

Within seconds after the initial influx of substorm particles, the aluminum surfaces (representing the spacecraft electrical ground) reached their equilibrium potentials (about -4000 volts). All insulating surfaces followed this change to the same potential. The potential distribution around the satellite, at this time, is very uniform as shown in figure 7.

As the substorm continues, the insulator surfaces slowly moved towards equilibrium potentials. This process took about 20 minutes. This differential charging time is in agreement with predictions given in the literature.[16,17] Since the insulator surfaces have higher secondary yields, these surfaces became less negative than the aluminum.

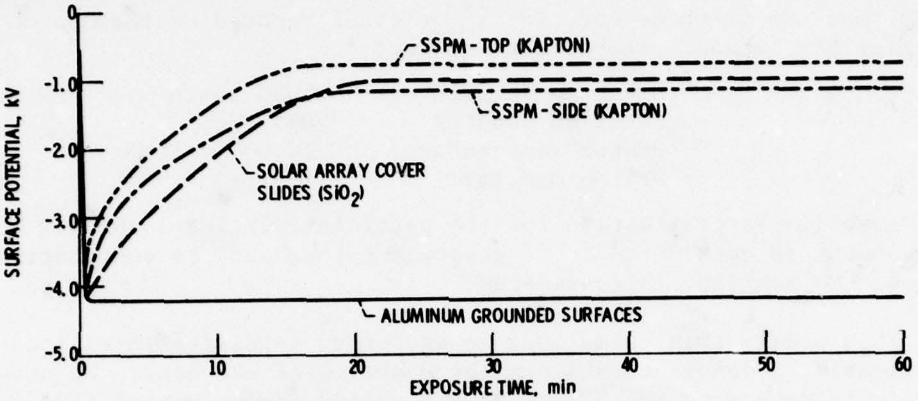

Figure 6. - Differential charging in substorm environment. Eclipse conditions. Scatha model.

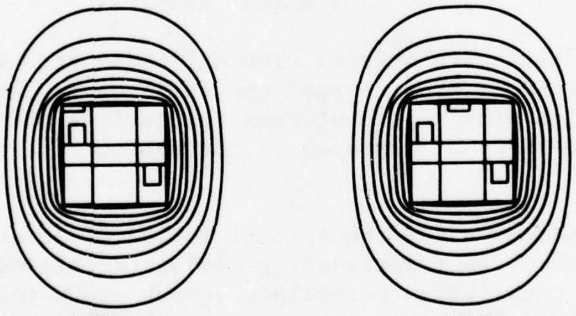
X-Z PLANE

Y-Z PLANE

Figure 7. - Potential distribution around satellite after 1 minute in charging environment.

Hence, differential charging developed around the spacecraft. The potential contours around the spacecraft at this time are shown in figure 8. Note the strong potential gradients that exist at regions where insulators and conductors come together.

It must be stressed that the potentials computed here are strongly dependent upon the material properties of the surfaces. While the most reasonable values from the literature have been incorporated in the program, they may be in error in this application. This error would influence the absolute magnitude of the surface potentials only. Differential voltages would still exist and would be similar to those shown in figure 8.

It is possible that the electric field arising from this differential charging of spacecraft surfaces might ionize the outgassing molecules and enhance contamination. In the SCATHA contamination experiment there is concern for molecule ionization when there is a few volt differential between the spacecraft and the space potential.[10] With this spacecraft model, there are voltage differences of kilovolts within 10 cm. Low energy particles will move more readily in the strong fields around the satellite and could increase contamination.

The NASCAP model was used to search for particle trajectories. Typical examples are shown in figure 9 for particles flowing from the aluminum center band and from the solar array cover slide. Areas in each region were arbitrarily selected as the starting points for the trajectory computations. The results indicate that electrons will escape from the satellite. The ions, however, will return to the structure. If these returning ions stay on the surfaces, then contamination will be significantly enhanced.

4.0 CONCLUDING REMARKS

The NASA Charging Analyzer Program (NASCAP) has been developed to determine the surface charging of spacecraft when encountering geomagnetic substorm conditions. Once a model of a spacecraft has been developed in the NASCAP code, the surface charging can be computed for any environmental input flux. With the surface charging available, charged particle trajectories can be computed to determine if it is possible for a particle to return to a satellite surface.

A preliminary model of the SCATHA spacecraft was developed and subjected to a one hour geomagnetic substorm condition without sunlight. It was found that, for these conditions, the grounded surfaces and insulators rose to the conductor equilibrium potential (-4 KV) within seconds. Then, the insulator surfaces each moved towards their less negative equilibrium potentials. This differential voltage distribution

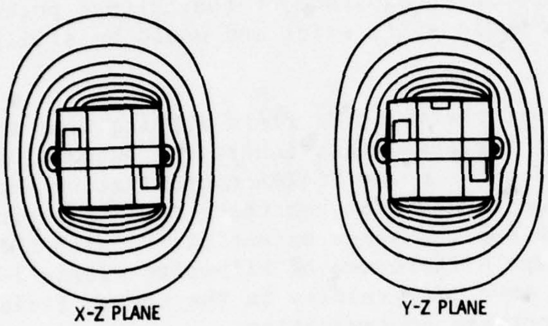

Figure 8. - Potential distribution around satellite after 1 hour in charging environment.

PARTICLE TRAJECTORIES FROM ALUMINUM CENTER BAND

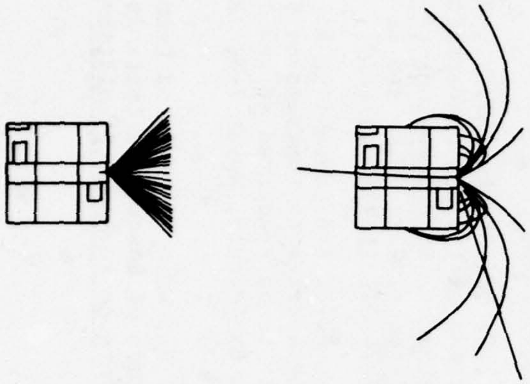

(a)

Figure 9. - Typical particle trajectories.

PARTICLE TRAJECTORIES FROM SOLAR CELL COVER GLASS

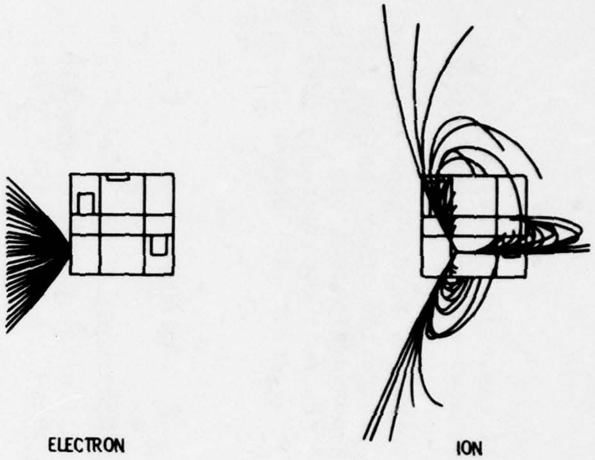

(b)

Figure 9. - Concluded.

around the spacecraft will cause low energy particles to be attracted back to the spacecraft surfaces enhancing contamination.

These computer runs with the NASCAP code represent the first attempts to use a self-consistent program to study the behavior of spacecraft surfaces experiencing a geomagnetic substorm condition. While the results are enlightening, there is considerably more that must be done in order to understand the interactions between the spacecraft surfaces and the environment.

REFERENCES

1. Eighth Conference on Space Simulation, NASA SP-379 (1975).
2. DeForest, S. E. and McIllwain, C. E., Plasma Clouds in the Magnetosphere, J. Geophys. Res., 76: 3587-3611 (1974).
3. DeForest, Sherman E., Spacecraft Charging at Synchronous Orbits, J. Geophys. Res., 77: 651-659 (1972).
4. Rosen, A., Spacecraft Charging-Environment Induced Anonalies, AIAA Paper 75-91 (1975).
5. Olsen, R. C., Whipple, E. C., and Purvis, C. K., Active Modification of ATS-5 and ATS-6 Spacecraft Potentials, Paper to be presented at NRL Conference, Jan. 24-26, 1978, Washington, D.C.
6. Fredricks, R. W. and Scarf, F. L., Observation of Spacecraft Charging Effects in Energetic Plasma Regions, in Photon and Particle Interactions with Surfaces in Space, R. J. Grard, Ed., D. Reidel Publishing Co., Dordrecht (1973), 277-308.
7. **Stevens, N. John, Berkopec, F. D., Staskus, J. V., Blech, R. A., and Narcisco, S. J., Testing of Typical Spacecraft Materials in a Simulated Substorm Environment, in Proceedings of the Spacecraft Charging Technology Conference, C. P. Pike and R. R. Lovell, Ed., NASA TM X-73537/AFGL TR-77-0051 (1977), 431-457.**
8. Yadlowsky, E. J., Hazelton, R. C. and Churchill, R. J.: Puncture Discharges in Surface Dielectrics as Contaminant Sources in Spacecraft Environments, Paper to be Presented at the International Spacecraft Contamination Conference, March 7-9, 1978, Colorado Springs, Colorado.
9. **Hall, David F., Borson, E. N., Winn, R. A., and Lehn, W. L.: Experiment to Measure Enhancement of Spacecraft Contamination by Spacecraft Charging, in Eighth Conference on Space Simulation, NASA SP-379 (1975), 89-107.**

10. Hall, David F.: Spacecraft Charging/Contamination Experiment on SCATHA, in Proceedings of the Spacecraft Charging Technology Conference, C. P. Pike and R. R. Lovell, Eds., NASA TM X-73537/ AFGL TR-77-0051 (1977), Abstract p. 699.

11. Lovell, R. R., Stevens, N. J., Schober, W., Pike, C. P., and Lehn, W. L., Spacecraft Charging Investigation: A Joint Research and Technology Program, in Spacecraft Charging by Magnetospheric Plasmas, Alan Rosen, Ed., Progress in Astronautics and Aeronautics, Vol. 47, AIAA (1976), 3-14.

12. Katz, I., Parks, D. E., Mandell, M. J., Harvey, J. M., Brownell, D. H., Jr., Wang, S. S., and Rotenberg, M., A Three Dimensional Dynamic Study of Electrostatic Charging in Materials, NASA CR-135256 (1977).

13. Mandell, M. J., Harvey, J. M., and Katz, I., NASCAP User's Manual, NASA CR-135259 (1977).

14. McPherson, D. A., and Schober, W. R., Spacecraft Charging at High Altitudes: The Scatha Satellite Program, in Spacecraft Charging by Magnetospheric Plasmas, A. Rosen, Ed., Progress in Astronautics and Aeronautics, Vol. 47, AIAA (1976), 15-30.

15. Katz, I., Parks, D. E., Mandell, M. J., Harvey, J. M., Wang, S. S., and Roche, J. C., NASCAP, A Three-Dimensional Charging Analyzer Program for Complex Spacecraft, IEEE Trans. Nucl. Sci., NS-24(No. 6): 2276-2280 (1977).

16. DeForest, S. E., Electrostatic Potentials Developed by ATS-5, in Photon and Particle Interactions with Surfaces in Space, R. J. Grard, Ed., D. Reidel Publishing Co., Dordrecht-Holland (1973), pp. 263-276.

17. Purvis, Carolyn K., Stevens, N. John, and Olgebay, Jon C., Charging Characteristics of Materials: Comparison of Experimental Results with Simple Analytical Models, in Proceedings of the Spacecraft Charging Technology Conference, C. P. Pike and R. R. Lovell, Eds., NASA TM X-73537/AFGL TR-77-0051 (1977), 459-486.

NASA TECHNICAL NOTE

NASA TN D-8438

NASA TN D-8438

CORRELATION OF SELF-CONTAMINATION EXPERIMENTS IN ORBIT AND SCATTERING RETURN FLUX CALCULATIONS

John J. Scialdone

Goddard Space Flight Center
Greenbelt, Md. 20771

NATIONAL AERONAUTICS AND SPACE ADMINISTRATION • WASHINGTON, D. C. • MARCH 1977

1. Report No. NASA TN D-8438	**2. Government Accession No.**	**3. Recipient's Catalog No.**
4. Title and Subtitle Correlation of Self-Contamination Experiments in Orbit and Scattering Return Flux Calculations		**5. Report Date** March 1977 **6. Performing Organization Code** 726
7. Author(s) John J. Scialdone		**8. Performing Organization Report No.** G-7702
9. Performing Organization Name and Address Goddard Space Flight Center Greenbelt, Maryland 20771		**10. Work Unit No.** 356-78-01 **11. Contract or Grant No.** **13. Type of Report and Period Covered**
12. Sponsoring Agency Name and Address National Aeronautics and Space Administration Washington, D.C. 20546		Technical Note **14. Sponsoring Agency Code**

15. Supplementary Notes

16. Abstract

Gaseous emissions from a spacecraft modify the orbital environment and degrade the observations of distant radiation sources. These emissions also provide contamination fluxes induced by self-scattering and scattering with ambient particles. These objectionable effects are especially important for a spacecraft with many large gaseous sources, orbiting at low altitudes and with surfaces which are critically affected by contamination (for example, the Space Transportation System).

Experiments were carried out on the orbiting Atmospheric Explorer-D satellite (AE-D) to verify the calculated return fluxes of a neon source. Known rates of neon were emitted in the direction of the velocity vector on command to the Molecular Return Measurement Unit (MRMU). At 250 km, the neutral mass spectrometer indicated a total neon return flux of 2.46×10^{-2} times the emitted flux. The calculated fraction was 1.23×10^{-2}, including 9.14×10^{-3} for the ambient scatter and 3.54×10^{-3} for the altitude independent self-scatter. The pressure gages indicated return pressures less than 9.33×10^{-4} Pa (7×10^{-6} torr) at altitudes from 161 to 210 km. The maximum return pressure for 161-km orbit was calculated as 7.3×10^{-7} including a self scattering contribution of 2.4×10^{-6} Pa (1.8×10^{-8} torr).

17. Key Words (Selected by Author(s)) Shuttle contamination, Molecular scattering, Rarefied flow	**18. Distribution Statement** Unclassified—Unlimited

19. Security Classif. (of this report)	**20. Security Classif. (of this page)**	**21. No. of Pages**	**22. Price***
Unclassified	Unclassified	17	$3.50

*For sale by the National Technical Information Service, Springfield, Virginia 22161

This document makes use of international metric units according to the Systeme International d'Unites (SI). In certain cases, utility requires the retention of other systems of units in addition to the SI units. The conventional units stated in parentheses following the computed SI equivalents are the basis of the measurements and calculations reported.

CONTENTS

CORRELATION OF SELF-CONTAMINATION EXPERIMENTS IN ORBIT AND SCATTERING RETURN FLUX CALCULATIONS

John J. Scialdone
Goddard Space Flight Center
Greenbelt, Maryland

INTRODUCTION

The outgassing of protective materials, the leakage of cabins and systems, the venting and flashing of coolant fluids, and the gases from the propulsion system and chemical reactions modify the ambient atmosphere surrounding a spacecraft. These gases adsorb and condense on critical surfaces, changing the surfaces' optical and thermal characteristics. The gases create clouds which radiate with higher intensities than celestial objects and which absorb radiations from sources being observed. The column densities characterizing these clouds increase with the scattering of the emitted gases from ambient particles and among themselves. The evaluation of these two forms of scattering provides estimates on the number of molecules which return to the spacecraft. These return molecules add to the contamination of surfaces and increase the densities in the field of view of instruments. Several theoretical analyses have been made of the ambient scattering, and methods of calculation have been developed (References 1 through 6). The calculations are quite similar to each other. A graphical representation of this return flux as a function of both orbit altitude and size of the spacecraft is shown in figure 1 (Reference 1). Approximate relationships for the self-scattering have also been developed (References 4 and 7), giving conservative estimates of this parameter. Neither of these estimates, however, has ever been validated experimentally in either a chamber or in space. The scattered molecules cannot be differentiated from both the emitted and the chamber-reflected molecules during a test in a limited-size space chamber (References 8 and 9).

This paper reports on tests carried on the Atmospheric Explorer-D satellite (AE-D) that were designed to measure (with mass spectrometers) the scattering of a neon source emitted on command from the satellite. The Molecular Return Measurement Unit (MRMU) simulated a gas emission such as the outgassing of materials, the venting of a gas, or a propulsion jet issuing from the spacecraft. The return flux of this source due to ambient molecular scattering and intermolecular self-scattering was to be measured at various orbit altitudes and for various angular directions with respect to the orbit-velocity vector. The energies

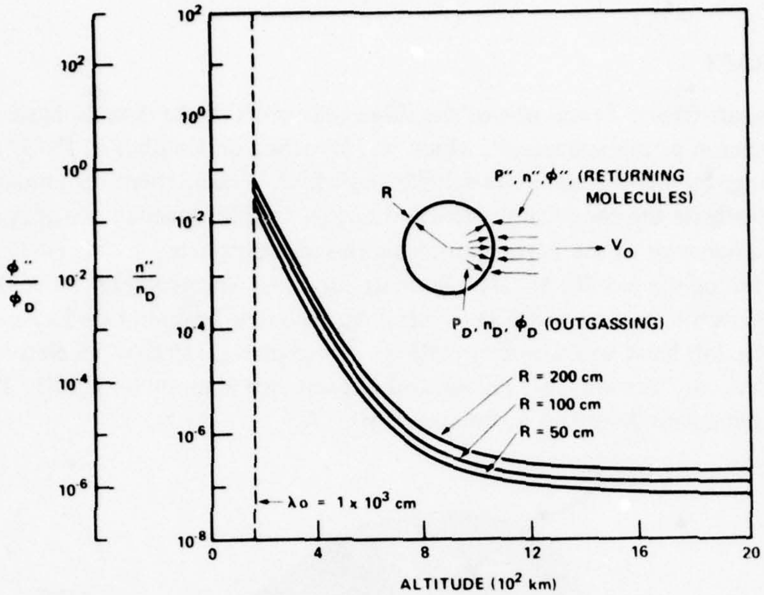

Figure 1. Density, pressure, and flux ratios at the spacecraft surface, produced by outgassed molecules returning to the satellite (for $\lambda_0 > 21$ R).

of the return molecules were also to be measured for both types of scattering. Unfortunately the premature failure of the spacecraft permitted only one test measurement at an altitude of 250 km and some exploratory tests at lower orbits. At 250 km, the Neutral Atmosphere Composition Experiment (NACE) mass spectrometer registered the density of the returned neon and indicated that the return flux amounted to 2.46×10^{-2} of the emitted molecules. This closely agrees with theoretical calculations indicating 1.26×10^{-2} for the total return fraction. The total ratio included 9.14×10^{-3} for the ambient scatter (as shown in figure 1) and 3.54×10^{-3} for the quasi-unchanging self-scatter. The ion gage, Pressure Sensor-A (PSA), and the capacitance manometer (PSB) used for exploratory tests indicated that the pressures resulting from the neon at altitudes varying from 161 to 210 km were, in all cases, less than 9.33×10^{-4} Pa (7×10^{-6} torr). The pressure calculated for 161 km should have been about 9.7×10^{-5} Pa (7.3×10^{-7} torr), including a self-scattering pressure of about 2.4×10^{-6} Pa (1.8×10^{-8} torr). These results give some assurance that the theoretical calculations can be used to estimate these parameters with a degree of confidence.

This document describes the AE-D spacecraft; the NACE spectrometer; the MRMU configuration and source characteristics; and the results of the experiment at 250 km. The experimental results are then compared with the expected theoretical results, followed by a summary with recommendations.

AE-D SPACECRAFT

The AE-D spacecraft (figure 2) was one of the three spacecraft of the Atmospheric Explorer program. The mission of this spacecraft, which was launched on October 6, 1975 from the Western Test Range by a two-stage Delta vehicle and which became silent on January 29, 1976, was to investigate the chemical process and energy transfer mechanisms that control the structure and behavior of the Earth's atmosphere and ionosphere. It carried 12 scientific instruments, including the NACE, MRMU, Bennett Ion Mass Spectrometer (BIMS), Open Source Neutral Mass Spectrometer (OSS), Neutral Atmosphere Temperature Experiment (NATE), Magnetic Ion Mass Spectrometer (MIMS), Atmospheric Density Accelerometer (MESA), Cold Cathode Pressure Gage (PSA), and Capacitance Manometer (PSB). These and other instruments are described in Reference 10.

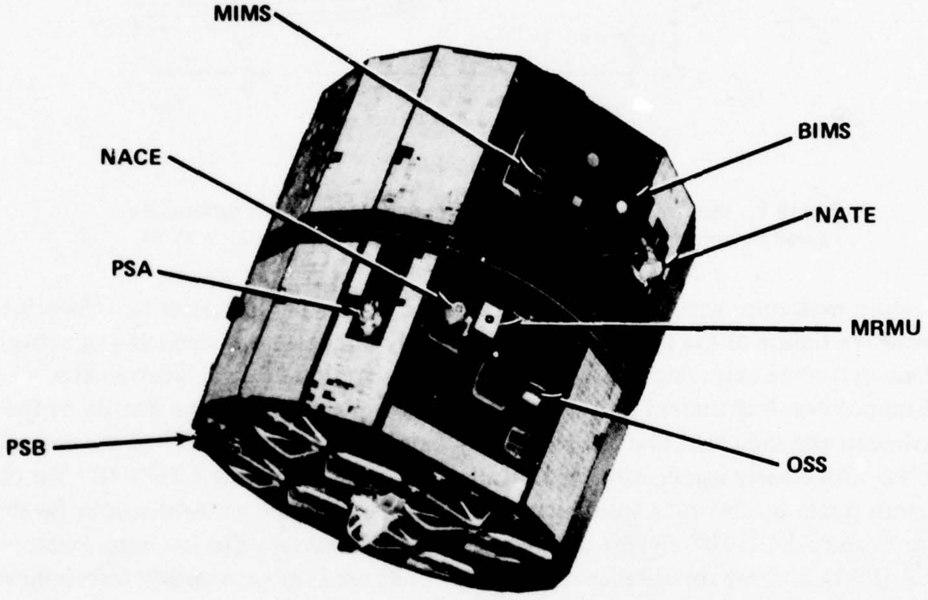

Figure 2. The AE-D spacecraft.

The AE-D spacecraft was a short 16-sided polyhedron approximating a right cylinder of 136 cm in outside diameter, 114 cm high, and weighing 679 kg. Its initial orbit had a perigee of 154.3 km and an apogee of 3804 km with an inclination of 90.1 degrees. As in the other AE spacecraft, the AE-D orbit-adjust propulsion system consisted of three hydrazine thrusters that provided the means to adjust the perigee and apogee altitudes, and the circularization of the orbit. The spacecraft could be operated in the despin and spin mode.

NEUTRAL ATMOSPHERE COMPOSITION EXPERIMENT (NACE)

The sensor that measured the return neon was the closed-source neutral mass spectrometer described in Reference 10 that was used for the Neutral Atmosphere Composition Experiment (NACE). It was designed to obtain *in situ* measurements of the neutral thermosphere composition and was carried on all of the Atmospheric Explorer satellites. The mass-spectrometer sensor included a gold-plated thermalizing chamber and an ion source, a hyperbolic-rod quadrupole analyzer, and an off-axis electron multiplier. The automatic ion-source sensitivity control and the pulse-counting techniques provided density-measurement capability for an altitude of approximately 125 to 1000 km. The normal operating mode included measurements at all masses in the range of from 1 to 44 amu with emphasis on helium, oxygen, nitrogen, and argon. Additional operational modes could be optimized for studies of minor constituents of any gas in this mass range. The measurements made by this instrument have been correlated with measurements made by other spectrometers, spectrophotometers, and accelerometers on the AE. The knife-edge orifice of the NACE, which was exposed after the breaking of the cover by pyrotechnic actuators, was 14.35 cm away from the exit port of the MRMU. The orifice was about 1.9 cm away from the spacecraft panel; the MRMU port protruded 1.27 cm from the same panel. The spectrometer was not calibrated for neon, and therefore its sensitivity was estimated from cross-section ratios and calibrated sensitivities for neon and argon.*

MOLECULAR RETURN MEASUREMENT UNIT (MRMU) NEON SOURCE

The neon source and metering system of the MRMU experiment is shown schematically and pictorially in figure 3. It consisted of a gas-filling valve, a 1.24-ℓ neon pressure tank, two pressure transducers, two series-redundant on-off valves, a porous metering plug located at the valves' exit, a 92-cm long section of 0.635-cm Teflon tubing, and a 0.476-cm ID stainless steel tube outlet that protruded from the spacecraft surface. Two temperature sensors measured the tank and tube exit temperatures. The total weight, including brackets and mounting hardware, was about 3.2 kg.

The neon source, based on a compromise which took into account restrictions on the space available on the spacecraft, the maximum allowable pressure, the availability of parts and other needs for a long blowdown time for extended operation, and large fluxes for high-altitude return-flux measurements, was designed to operate at an initial pressure of 37.19×10^5 Pa (36.7 atm). The flow-controlling porous leak used for the flight unit provided a neon flow of 4333 std cm^3/min that corresponded to a mass flow rate of 6.56×10^{-2} g/s and a molecular flow rate of 1.97×10^{21} s^{-1} for a neon density of 8.99×10^{-4} g/cm^3. The pressure-versus-time test of the unit is shown in figure 4. The pressure, the mass-flow rate, and the mass decay linearly with time in the high-pressure region. They have a time constant of about 830 s. The quantity of neon remaining after 3600 s of operation

---

*Personal communication, A. E. Hedin, March 3, 1976.

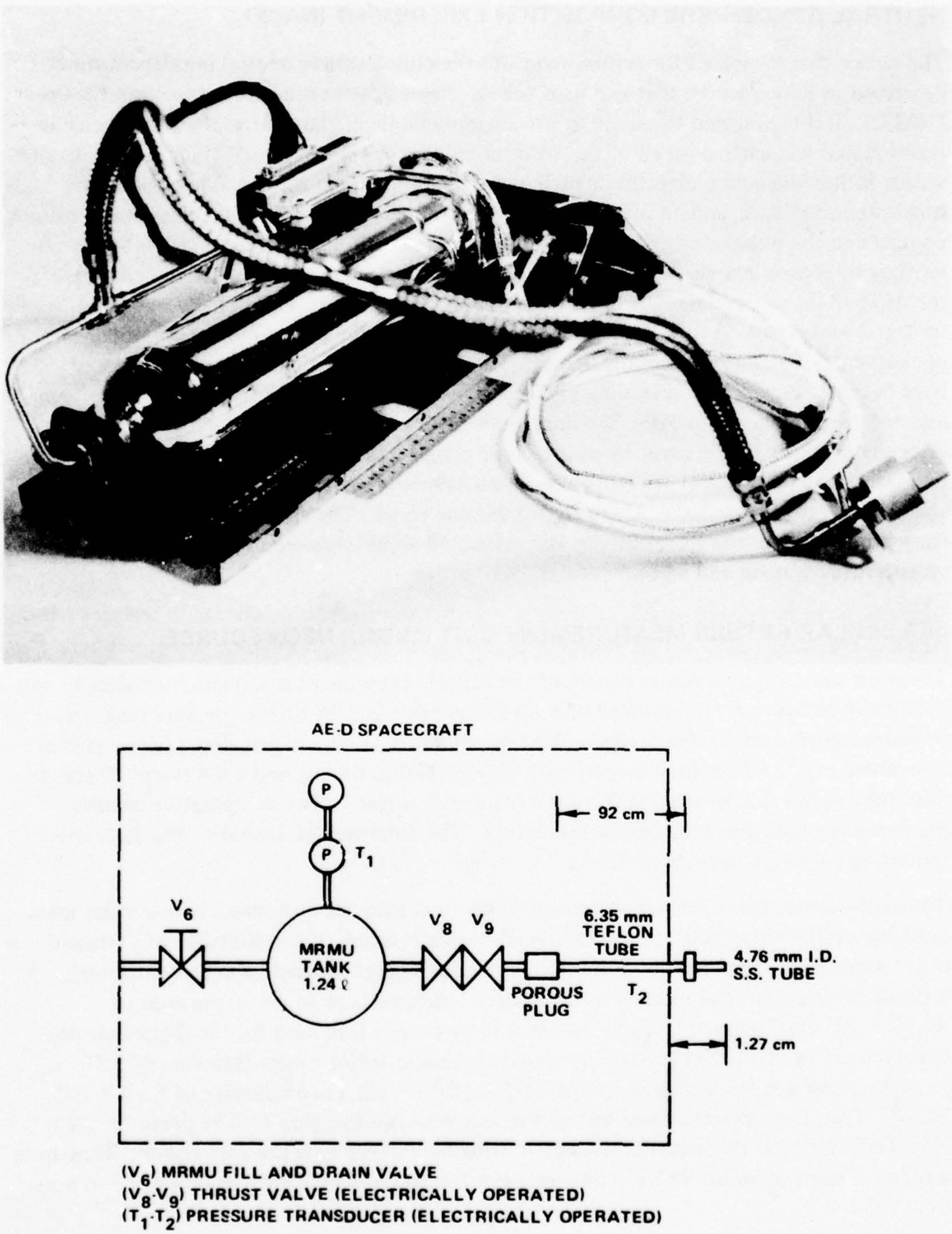

Figure 3. The MRMU gas-flow schematic diagram; photograph of the MRMU.

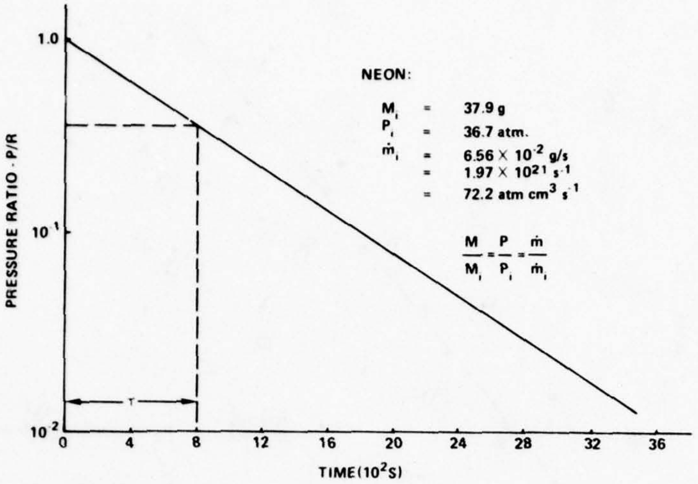

Figure 4. MRMU neon pressure, mass, and flow rate versus time.

is approximately 1 percent of the initial 37.9 g. The flow and pressure are at the same percentage after that time of operation.

Figure 5 shows the results of tests in a 3.65- by 4.57-m vacuum chamber to determine what were the pressures in the Teflon tubing at about 12 cm from the porous plug as a function of the upstream tank pressures. The pressure in this tubing is about 6.4×10^3 Pa (48 torr) for 36.48×10^5 Pa (36-atm) tank pressure. Another characteristic of this blowdown system is shown in figure 6. This shows the flux distribution as a function of the angle from the centerline of the exit port. The flow distribution was measured at 5.1 cm from the exit with a capacitance manometer rotating about the center of the exit port. The pressure in the tubing was held at 33.33×10^2 Pa (25 torr), corresponding to about 18×10^5 Pa (250 psig) (18 atm) in the tank. The reference pressure of the manometer was that of the large vacuum chamber that always remained below 1.33×10^{-2} Pa (10^{-4} torr). The curve shows that a 50-percent value of the flux (or pressure) corresponds to approximately a 47-degree half angle. The flow-distribution curve fitted a cosine function to the n = 1.75 power. Further, integrating this distribution flux over the hemisphere and equating it to the mass rate $\dot{m}$ gives the flux distribution as a function of distance r and angle θ,

$$\phi = \frac{n+1}{2\pi r^2} \dot{m} \cos^n \theta \qquad (1)$$

This indicates that at the edge of the spacecraft projected area (R = 68 cm) at a distance of 8.86×10^4 cm from the spacecraft corresponding to the mean-free path of the ambient atmosphere at 250-km altitude, the flux would be only 1 percent less than that at the center of the projected area.

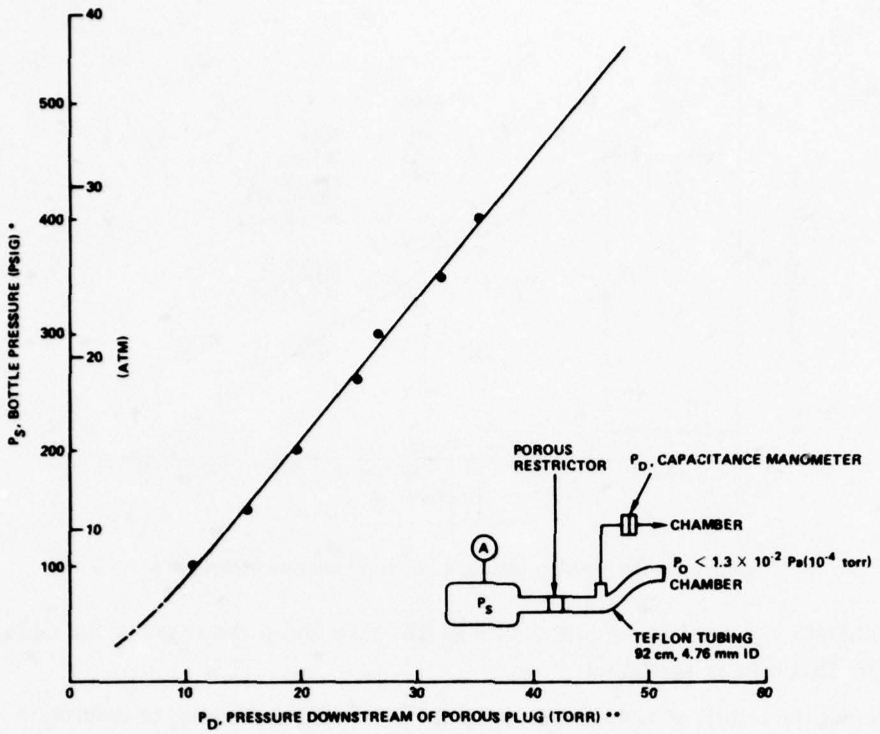

* PSIG = 6894.757 newtons/meter ^{2} (pascals)
** torr = 133.32 newtons/meter ^{2} (pascals)

Figure 5. MRMU exit pressure versus tank pressure.

The critical velocity produced at the exit port is

$$C = \left(\frac{2\gamma}{\gamma + 1} \quad \frac{\mathcal{R}T}{M}\right)^{1/2} = 3.87 \times 10^4 \text{ cm s}^{-1} \qquad (2)$$

where $\gamma = 1.66$, T = 290 K, M = 20 g mole, $\mathcal{R}$ is the gas constant. The adiabatic isoentropic velocity produced beyond the exit port can be estimated to be

$$V_E = \left(\frac{2\gamma}{\gamma - 1} \quad \frac{\mathcal{R}T}{M}\right)^{1/2} = 7.78 \times 10^4 \text{ cm s}^{-1} \qquad (3)$$

This velocity, superposed to the spacecraft velocity of 8.5 km, would allow the neon molecule to collide with a stationary ambient particle in about 0.1 s when the ambient particle is at a distance of 8.86 × 10^4 cm, which is the ambient mean free path at 250 km (Reference 11). The collided neon could be reacquired by the spacecraft in approximately 10 ms. The operation of the MRMU, with the mass spectrometer (MS) scanning for neon, consisted of enabling

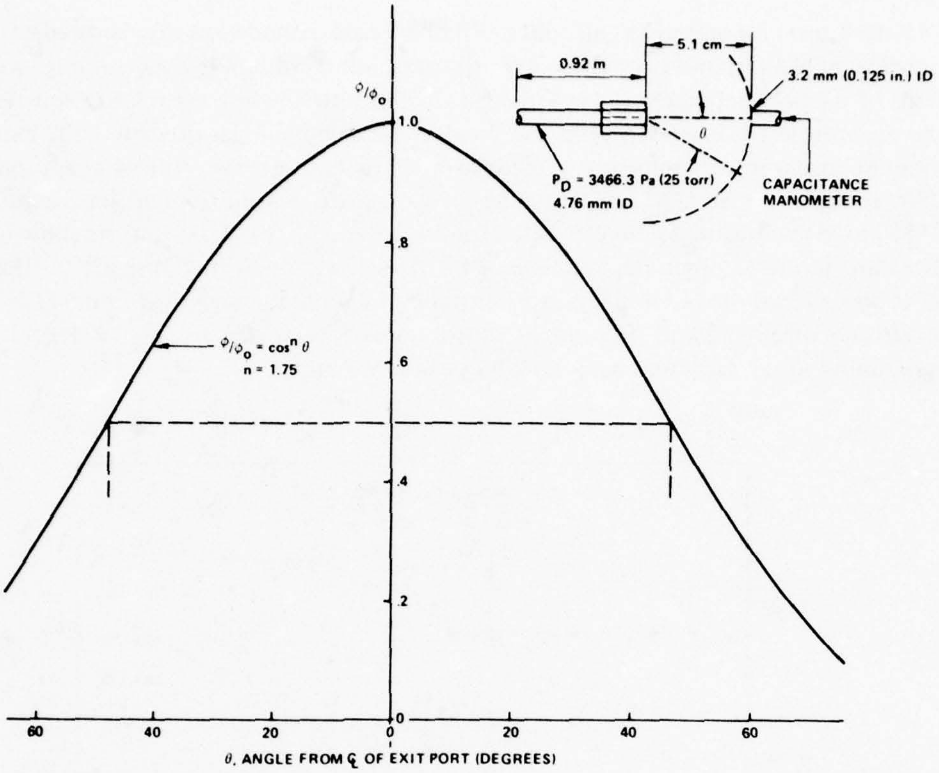

Figure 6. MRMU exit flow distribution at 5.1 cm.

the system, reading the initial pressure and temperature, and opening the valve. At completion of the experiment, the valve was commanded to close, and to read the final pressure and temperature. The minimum open and close cycle was 4 s.

THE EXPERIMENTS

Neon gas emissions were carried out at altitudes between 161 to 210 km previous to the 250-km experiment with the mass spectrometer. These exploratory tests were to ensure that densities around the spacecraft resulting from the neon emission would not be detrimental to other experiments. The PSA ion gage and the PSB capacitance manometer detected the neon and confirmed that the resulting densities would not pose a problem to other experiments.* They indicated that the response to the MRMU on-off was essentially instantaneous and proportional to the ambient pressure. The PSB manometer, limited in its low-pressure detection, indicated that the pressure produced by the neon was less than 9.33×10^{-4} Pa

---

*Personal communication, C. J. Rice, September 11, 1975.

(7×10^{-6} torr) for any of the altitudes. The PSA cold cathode ion gage showed the proportionality of the responses with ambient pressures, but it could not give unambiguous indications of the pressure increases because of its inability to separate the relative contribution to the signal from the increased neon and the decreased ambient gas pressure. The experiment, using the mass spectrometer as a detector, was carried out during orbit 94 at approximately 250 km while the AE-D was approaching the perigee of 150 km from an apogee altitude of 3755 km. *The measured source densities for 20, 28, and 32 (total oxygen) are shown in figure 7.* The date, latitude, longitude, and time of the test are also indicated in figure 7. The MRMU valve was opened on 54376.687 s at an altitude of 256.92 km and closed on 54348.687 s at an altitude of 251.22 km. The rate of emission was 5.24×10^{-2} g/s (1.58×10^{21} s^{-1}), corresponding to the measured neon tank pressure (29.3 atm).

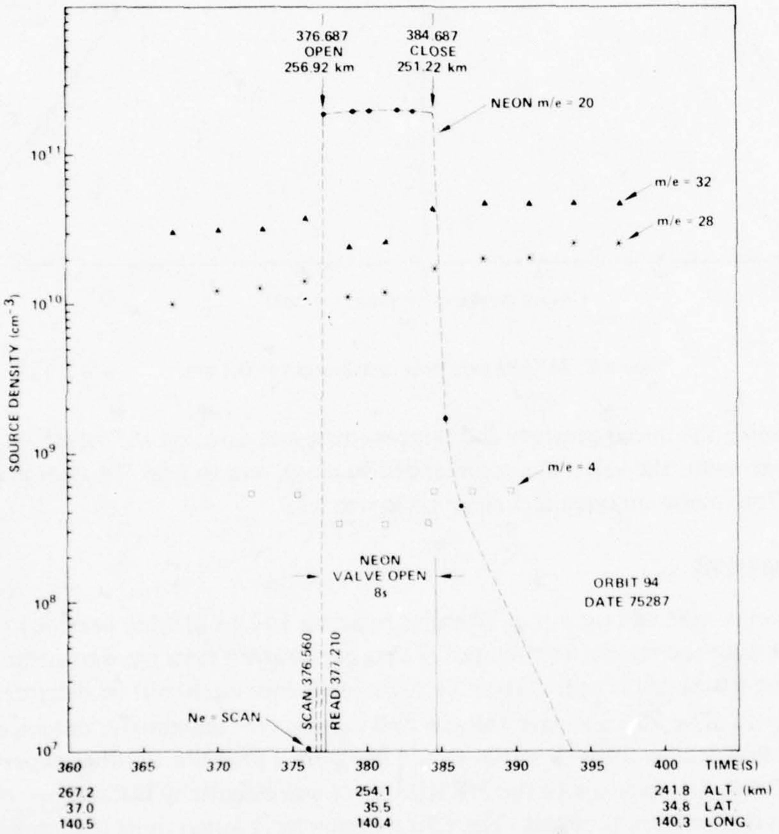

Figure 7. Source density versus time and altitude.

The corrected source densities for N_2, O_2, and A during the emission are also shown on this plot. It shows the neon density buildup and decay and that the maximum read neon density in the mass spectrometer was 1.92×10^{11} cm^{-3}.

ANALYSIS OF THE TEST RESULTS

Neon Detection Time and Density Drop

At t = 54376.2 s, before the neon emission, the mass spectrometer confirmed that there was no neon among the sources, as expected. The first reading of the neon occurred on t = 54377.210 s while the neon valve had opened 0.523 s earlier on 54376.687 s. The neon could not have been read earlier than 0.523 s because the mass spectrometer could scan neon at a rate of 0.650 per neon reading. It had begun to scan the various masses at 54376.560 s, that is, 376.687-376.560 = 0.127 s before the valve was open. The data, therefore, indicate that the neon was in the mass spectrometer within less than 0.523 s of its emission. From a previous discussion, the earliest time for neon capture, based on mean free path and gas velocity, could have been about 0.01 s after emission. PSA data during the 17 monitored neon tests confirm that the neon capture was within the 0.06 s time resolution of the instrument.*

In regard to the neon density drop following shut-off of neon at 54384.687 s, the first measurement was at 54385.167, 0.580 s later, and the density had dropped from 1.92×10^{11} to 1.71×10^{9} cm^{-3}. The density became 4.45×10^{8} and the noise level, 3.21×10^{6}, 1.515 s and 10.523 s, respectively, after valve closure.

Source Densities

As indicated in figure 7, the maximum neon source density was 1.92×10^{11} cm^{-3}, and it appears to be relatively constant as if the mass spectrometer were saturated. Also the density of mass 32 (really 0) dropped 35 percent, mass 28, 21.5 percent, and mass 4, 35 percent, during neon acquisition. However, the following observations** argue against the assumption that the instrument was saturated and suggest that the decrease in densities at mass 32, 28, and 4 resulted from the neon cloud reducing the flux of ambient molecules by scattering them away from the spacecraft. The total nominal density as measured was not unusually high and the ion-source voltage and current monitors showed no change at the time of neon burst. Contaminant gases generated within the source (masses 18 and 44) did not suffer same decrease. At the neon peak, the telemetry counts did show some fluctuations and the multiplier gain was normal. In addition, the PSA and PSB instruments confirmed that the neon density was well below the level needed to saturate the mass spectrometer.

---

*Personal communication, C. J. Rice, September 11, 1975.

**Personal communication, A. E. Hedin, March 3, 1976.

Neon Return Flux, Density, Pressure, and Column Density

The neon flux entering the spectrometer under equilibrium conditions is balanced by the thermalized neon flux which leaves the mass spectrometer through the same port, so that the return flux is

$$\phi_R = \frac{1}{4} n_i V = \frac{1}{4} n_i \left(\frac{8 \mathcal{R} T}{\pi M} \right)^{1/2} = 1.40 \times 10^4 \, n_i = 2.69 \times 10^{15} \text{ cm}^{-2} \text{ s}^{-1} \qquad (4)$$

where $n_i = 1.92 \times 10^{11}$ cm^{-3} is the measured neon density; V, the average neon velocity obtained using the gas constant $\mathcal{R} = 8.134 \times 10^7$ erg/K/g mole; M = 20 g mole; and T = 297 K, the temperature of the neon in the thermalizing chamber. The emitted flux for $\dot{m} = 1.58 \times 10^{21}$ s^{-1} and R = 68 cm at the time of the experiment was

$$\phi_E = \frac{\dot{m}}{\pi R^2} = 1.09 \times 10^{17} \text{ cm}^{-2} \text{ s}^{-1}. \qquad (5)$$

Therefore, the ratio of the return flux to the emitted flux is

$$\frac{\phi_R}{\phi_E} = 2.46 \times 10^{-2} \qquad (6)$$

The density at the surface of the spacecraft was approximately

$$n_R = \frac{\phi_R}{V_S} = 3.16 \times 10^9 \text{ cm}^{-3} \qquad (7)$$

where $V_s = 8.5 \times 10^5$ cms^{-1} is the orbit velocity at 250 km. The equivalent pressure of this density, assuming a gas temperature of T = 293 K, was

$$P_R = n_R KT = 1.28 \times 10^{-5} \text{ Pa } (9.65 \times 10^{-8} \text{ torr}) \qquad (8)$$

where $K = 1.38 \times 10^{-23}$ J K^{-1} (1.04×10^{-22} torr ℓ K^{-1}) is the Boltzmann constant. The column density neon can be calculated, as shown later, to be

$$N_C = \frac{\lambda_0}{V_s} \phi_R = \lambda_0 n_R = 2.8 \times 10^{14} \text{ cm}^{-2} \qquad (9)$$

where $\lambda_0 = 8.86 \times 10^4$ cm is the mean free path at that altitude.

THEORY

Ambient Scatter

The analysis estimating the return flux due to ambient scattering (Reference 1) considers molecules radially leaving a spherical spacecraft of radius R being scattered and reacquired by the emitting surface. Molecules scattered out of the idealized emitted beam columns are disregarded under the assumption that they are replaced by molecules scattered in from other columns. With these assumptions, the return flux is given by

$$\phi_R = \phi_E \frac{R}{\lambda_0}\left(\frac{V_s}{V_E} + 1\right) \qquad (10)$$

where λ_0 is the ambient mean free path, V_s, the spacecraft velocity, and V_E, the velocity of the emitted flux, ϕ_E. A more precise analysis, taking into account the contribution from other beams, should increase the return over the above results. Other authors, References 3 through 7, have studied the same problem and obtained expressions giving practically the same result. The above theoretical expression, applied to the condition of this test, for $\phi_E = 1.09 \times 10^{17}$ $cm^{-2}\ s^{-1}$, $R = 68$ cm, $\lambda_0 = 8.86 \times 10^4$ cm, $V_s = 8.5$ km/s, and for emission velocity $V_E = 7.78 \times 10^4$ cm/s, gives

$$\frac{\phi_R}{\phi_E} = 9.14 \times 10^{-3} \qquad (11)$$

for the return ratio so that the return flux due to ambient scattering is

$$\phi_R = 1.0 \times 10^{15}\ cm^{-2}\ s^{-1} \qquad (12)$$

According to Reference 1, one can estimate the density and pressure of this scatter from $n_R = \phi_R/v_s = 1.18 \times 10^9\ cm^{-3}$ by assuming that the return velocity is the spacecraft velocity.

Self-Scattering

In addition to ambient scatter, the self-scattering in the emitted flux should be considered. This scattering can be considerable and predominant at high altitudes, especially for large fluxes, as in the present experiment where a relatively dense beam of neon was ejected. Several investigators have provided estimates of the self-scattering. The most complete analysis has been provided by Robertson in Reference 7. This estimate employs a Krook model for self-scattering. This assumes a Maxwellian distribution superimposed on the radial component of the velocity. The following expression for the self-scattering is obtained using our present nomenclature:

$$\frac{\phi_S}{\phi_E} = 1.78 \times 10^{-2} \frac{\sigma R}{V_E} \phi_E \qquad (13)$$

where σ is the molecular cross section, R the radius of the spherical spacecraft, and V_E the gas velocity. This expression, with a numerical coefficient about 4.68 to 6.42 times larger, can be obtained from a simple analysis (Reference 4 and author unpublished work).

Substituting the values given previously for R, V_E, and ϕ_E, and using $\sigma = \pi d^2 = \pi (2.59 \times 10^{-8})^2 = 2.10 \times 10^{-15}$ cm^2 for the neon cross section, one obtains

$$\frac{\phi_S}{\phi_E} = 3.23 \times 10^{-20} \phi_E = 3.54 \times 10^{-3} \tag{14}$$

for the fraction scattered and the scattered flux to be

$$\phi_S = 3.54 \times 10^{-3} \phi_E = 3.88 \times 10^{14} \text{ cm}^{-2} \text{ s}^{-1} \tag{15}$$

This indicates that the calculated self-scattering flux, which increases with the square of the emitted flux and is not a function of the altitude, was about 14 percent of the measured return or 38 percent of the ambient calculated return.

The density due to the scattering was about

$$n_S = \frac{\phi_S}{V_E} \approx 4.56 \times 10^8 \text{ cm}^{-3}$$

Ambient and Self-Scattering Return Flux

Ignoring the flux depletion due to scattering, we may add the ambient scattered flux obtained from equation 10 and the self-scattered flux from equation 13, so that the total expected return flux is

$$\begin{aligned} \phi_R &= \phi_E \left[\frac{R}{\lambda_0} \left(\frac{V_S}{V_E} + 1 \right) + 1.78 \times 10^{-2} \frac{\sigma R}{V_E} \phi_E \right] \\ &= 1.26 \times 10^{-2} \phi_E = 1.38 \times 10^{15} \text{ cm}^{-2} \text{ s}^{-1} \end{aligned} \tag{16}$$

This calculated total flux is 51 percent of that which was measured. The total density of these return molecules is 1.62×10^9 cm^{-3}.

As mentioned above, the ion gage and capacitance manometer indicated a pressure less than 9.33×10^{-4} Pa (7×10^{-6} torr) during exploratory tests at altitudes between 161 and 210 km. This is in agreement with theoretical calculations. In fact, using equation 10 with $\lambda_0 = 5.59 \times 10^3$ cm for the mean free path at 161 km (Reference 11) and an emitted flux $\phi_E = 1.35 \times 10^{17}$ cm^{-2} s^{-1} corresponding to the maximum initial neon pressure, the ambient return ratio is $\phi_R / \phi_E = 0.145$ and the ambient return flux $\phi_R = 1.96 \times 10^{16}$ cm^{-2} s^{-1}. This flux is equivalent to a density of 2.31×10^{10} cm^{-3} and a pressure of 9.52×10^{-5} Pa (7.14×10^{-7} torr). The self-scattering ratio is from equation 13, $\phi_s / \phi_E = 4.42 \times 10^{-3}$ and the scatter flux $\phi_S = 6 \times 10^{14}$ cm^{-2} s^{-1}. This corresponds to a density of 7.06×10^8 cm^{-3} and a pressure of 2.9×10^{-6} Pa (2.18×10^{-8} torr). These calculations show that under maximum flux and lowest altitude, the total pressure could have been about 9.87×10^{-5} Pa (7.4×10^{-7} torr) in agreement with the reported pressure of less than 9.33×10^{-4} Pa (7×10^{-6} torr).

Column Density

The column density is the integrated value of the density from the surface of the spacecraft sphere of radius, R to infinity. Its value for $\lambda >> R$ is as shown, in Reference 1 and for the parameters at 250 km.

$$N = \frac{\dot{m}}{4\pi V_E} \frac{1}{R} = \phi_E \frac{R}{V_E} = 9.56 \times 10^{13} \text{ cm}^{-2} \qquad (17)$$

The second expression has been obtained by replacing $\dot{m} = 4\pi R^2 \phi_E$. The column density can be also expressed in terms of the return flux by replacing ϕ_E from equation 10. For the calculated ambient return, one gets $N \sim (\lambda_0/v_s)\phi_R \sim 1.04 \times 10^{14}$ cm^{-2} and for the total return, $N \sim 1.44 \times 10^{14}$ cm^{-2}.

COMPARISON OF THE EXPERIMENT RESULTS AND THEORY

The results of the experiment at an altitude of 250 km indicated a total neon return flux which was about two times the flux predicted by theoretical estimates. The ratio of the total measured return flux to the emitted flux was 2.46×10^{-2}. The same ratio from the calculations was 1.26×10^{-2}. If the self-scattering had not been included, the ratio of ambient scattering return flux to the emitted would have been estimated at 9.14×10^{-3}. The single experiment at 250 km did not allow separate measurements of the self-scattered and of the ambient-scattered return flux. The conservative analytical estimate of the self-scatter return indicates that this was 3.54×10^{-3} of the emitted flux or about 28 percent of the total scattered return for that altitude. With this magnitude, the self-scattered return would have been the major return contributor at altitudes above 300 to 350 km. On the other hand, at an altitude of 150 km, the self-scattering portion would have been only 1.4 percent of the ambient scattered flux. Table 1 shows the comparison between calculated and measured fluxes, densities, and column densities.

SUMMARY AND RECOMMENDATIONS

The MRMU experiment aboard the AE-D spacecraft did perform as intended; however, only a single measurement of neon scattering was made with a mass spectrometer and several exploratory measurements were made with pressure gages. The measurements which had been planned were: the scattering at various spacecraft altitudes, with the neon source pointed in various directions with respect to the orbit velocity vector; the ejection of neon while the spacecraft was spinning; the separation of scattering due to ambient and self-scattering; energy of the return flux; and finally, a complete validation of the theoretical calculations used to estimate the return fluxes of diffused and pointed gas sources from a spacecraft.

Table 1
AE-D Spacecraft, MRMU Neon Scattering Experiment: Comparison Between Calculated and Measured Results For 250-km Altitude

	Ambient Scattering		Self-Scattering		Total Scattering		Column Density (cm^{-2})		
	ϕ_R ($cm^{-2}\ s^{-1}$)	n_R (cm^{-3})	ϕ_S ($cm^{-2}\ s^{-1}$)	$n_{S'}$ (cm^{-3})	ϕ_R ($cm^{-2}\ s^{-1}$)	n_R (cm^{-3})	Ambient	Scattering	Total
Calculated Values	1.0×10^{15}	1.18×10^{9}	3.88×10^{14}	4.56×10^{8}	1.38×10^{15}	1.62×10^{14}	1.04×10^{14}		1.44×10^{14}
Measured Values	--	--	--	--	2.69×10^{15}	3.16×10^{9}	--	--	2.8×10^{14}
Ratio of Scattered to Emitted (Calculation)	9.14×10^{3}	--	3.54×10^{-3}	--	1.26×10^{-2}	--	--	--	--
Ratio of Scattered to Emitted (Measured)	--	--	--	--	2.46×10^{-2}	--	--	--	--
Ratio of Calculated to Measured	--	--	--	--	5.12×10^{-1}	5.12×10^{-1}	--	--	5.1×10^{-1}

Notes

Orbit Velocity V_s = 8.5 km/s @ 250 km altitude
MFP λ_0 = 8.86×10^{4} cm @ 250 km altitude
ϕ_F = emitted flux = 1.09×10^{17} $cm^{-2}\ s^{-1}$ (1.58×10^{21} s^{-1})
V_F = emitted term velocity = 7.78×10^{4} cm/s
· = test time = 8 s
σ = *cross section neon* = 2.1×10^{15} cm^2
R = equivalent radius spacecraft = 68 cm

The experiment measured and detected the return flux of neon ejected in the direction of the velocity vector at a spacecraft altitude of 250 km. The results compare well with the predicted values and give some assurance that the theoretical calculations can be used for estimation of these parameters.

The measured fraction of the total return flux to the emitted was 2.46 × 10^{-2}, and the total calculated percent was 1.26 × 10^{-2}. A conservative estimation, based on the calculations, is that 28 percent of the total return flux was due to self-scatter in the neon plume. In the absence of measurements taken at very high altitudes, this cannot be confirmed, but the magnitude of the measured return fraction of the flux (2.46 × 10^{-2}), when compared with the fraction calculated for the ambient scatter (9.147 × 10^{-3}) and with the self-scattering (3.54 × 10^{-3}), appears to give credibility to this estimate. The self-scattered portion, which does not change with altitude, could have been the predominant return at altitudes over 350 km, but only 1.4 percent of the total scatter at 150 km. This implies that for high-altitude flights, the self-scattering may be the highest contributor to the return, especially for sources such as engines and ventings. The experiment has also indicated that the maximum return flux was detected within 0.5 s of the start of emission and that it dropped two orders of magnitude in less than 0.58 s and three orders 1.5 s after valve closure.

Tests at altitudes between 161 and 210 km using pressure gages as detectors gave additional validity to the theoretical calculations. The tests indicated pressures due to neon return of less than 9.33 × 10^{-4} Pa (7 × 10^{-6} torr). This agrees with calculations that showed that the pressure at the lowest altitude of 161 km and for the maximum neon emission should be about 9.87 × 10^{-5} Pa (7.4 × 10^{-7} torr).

Because of the importance of these parameters in the evaluation of the contamination and the environment of a spacecraft, it is recommended that the same or similar experiments be carried out in the future. They should confirm the theoretical calculations for other altitudes and directions of emission, obtain energy of the return molecules, and establish the effect of the gas molecular mass on the return fraction. Further, the return of ions injected in ambient plasma, in neutral atmosphere, and in electric and magnetic fields should be investigated.

ACKNOWLEDGMENTS

The author thanks J. Rogers, R. Kruger, B. Paxson, A. Retzler, and N. Mandell for their help in the design and construction of the MRMU; W. Hoggard for coordinating the experiment; Drs. A. Hedin and C. Rice for advice on the measurement and use of their instruments; and D. Grimes and Dr. N. Spencer, the AE Project Manager and the Project Scientist, respectively, for their support.

Goddard Space Flight Center
National Aeronautics and Space Administration
Greenbelt, Maryland February 1977

REFERENCES

1. Scialdone, J. J., "Self Contamination and Environment of an Orbiting Spacecraft," the *Journal of Vacuum Science and Technology*, **9** (2), pp. 1007-1015, January 1972, also NASA TN D-6645, May 1972.
2. Scialdone, J. J., *Predicting Spacecraft Self-Contamination in Space and in a Test Chamber*, NASA TN D-6682, May 1972.
3. Robertson, S. J., "Back Flow of Outgas Contamination onto Orbiting Spacecraft as a Result of Intermolecular Collision," LMSC-HREC TR-D306000, Lockheed Missile and Space Co., June 1972.
4. Naumann, R. J., *Contamination Assessment and Control in Scientific Satellites*, NASA TN D-7433, October 1973.
5. Scialdone, J. J., "Environment of a Spacecraft Produced by Its Own Outgassing," Proceedings of International Conference on Evaluation of Space Environment on Materials, International Conference, Centre National d'Etudes Spatiales, Toulouse France, June 1974, pp. 329-346.
6. Harvey, R. L., "Spacecraft Self-Contamination by Molecular Outgassing," *J. Spacecraft*, **13** (5), May 1976, also Tech. Note 1975-1, Lincoln Lab. M. I. T., Cambridge, Mass., June 1975, pp. 301-305.
7. Robertson, S. J., *Spacecraft Self-Contamination due to Backscattering of Outgas Products*, LMSC-HREC TR D-496676, Lockheed Missile and Space Co., January 1976.
8. Scialdone, J. J., *Gas Flow Analysis during Thermal Vacuum Test of a Spacecraft*, NASA TN D-7492, January 1974.
9. Scialdone, J. J., *Time Dependent Polar Distribution of Outgassing from a Spacecraft*, NASA TN D-7597, April 1974.
10. "Atmospheric Explorer Experiments," *Journal of the U. S. National Committee, International Union of Radio Science*, published by the American Geophysical Union **8** (4), April 1973, pp. 261-406.
11. *The 1976 U. S. Standard Atmosphere*, NOAA, NASA and USAF, Washington, D. C. 1976.

NASA-Langley, 1977

QUESTION/ANSWER SESSION (7 MARCH 1978)

Capt. Jemiola (Air Force Materials Laboratory): Does anyone have any questions we can address to the presenters of the various papers in the first session? And then we'll do the same thing for the second session. I don't see any volunteers. Gene, could I get you to head this portion of the question/answer session.

E. Zeiner (Aerojet Electro-Systems): First, we'll have questions directed to the authors of the first session. I'll read the titles of the papers and their authors. The first one was by Tom Hughes from McDonnell-Douglas, "Outgassing of Materials in Space Environment: A Thermokinetics Approach." The second paper was by E. Zeiner from Aerojet on our analytical model of satellite contamination. The third paper was by Pete Glassford and C.K. Liu from Lockheed "Outgassing Rate Data for Multilayer Insulation Materials". The fourth paper was from Martin-Marietta given by Nancy Pugel, "Applications of Thermogravimetric Analysis to Space Contamination" and the last paper in the morning session by Mr. Zwaal, on "Outgassing Measurements of Materials in Vacuum Using a Vacuum Balance and Quartz Crystal Microbalances." To start this session off, I have a question I would like to ask Nancy. When you had compared the isothermal data to the dynamic TGA data, the dynamic TGA seemed to consistently follow the shape of the isothermal gravimetric data but it showed a lower outgassing rate. Did you have any idea why that displacement was there?

Nancy Pugel (Martin-Marietta): We have had several ideas about this. It's been a major problem area and today I've talked with a few people who had some ideas concerning it. Originally we thought the difference might be caused by early outgassing that is detectable through QCM/isothermal methods but is not detectable through dynamic TGA due to the latters inherent lower sensitivity. These early outgassings might be water molecules absorbed on the surface or whatnot that migrated there, possibly because of preparation procedures. This could account for the difference in the outgassing because dynamic TGA cannot detect water while isothermal can. But it was pointed out that this difference in outgassing should then just occur at the lower temperature levels but should not continue occurring at higher temperatures, as the two curves indicated in our paper, where the two curves had pretty much the same curve structure. It's a big problem. Joe, do you have anything to add?

Joe Muscari (Martin-Marietta): In the paper, Gene, there's a reference to some previous work at isothermal temperatures. What they did was look at the high temperature component of some polymers isothermally at lower temperatures. They ran data for over a period of a month, at several temperatures, and showed there was a direct correlation between the dynamic TGA and the isothermal. Again, I think the keypoint is that the high temperature components are not the component we generally see in space materials, because we are at such a low temperature we don't get a significant amount of it coming off. What we show with our isothermal tests, which is in the paper, is an attempt to look at the high volatile, low temperature component and compare that to a low temperature isothermal TG test. And, frankly, we just don't know why there is a difference between the two techniques. But in the two or three materials that we've run, it is consistent and we do always get lower outgassing rates using dynamic TGA by a factor of two to two orders of magnitude. We hope that in future work, we will be able to pin the reasons down.

E. Zeiner: Are there any questions to any of the authors? To Mr. Hughes, myself. Doctor .... Yes, go ahead Dave.

Dave Hall (Aerospace): This is a question, I guess, for all the authors. I'm wondering to what extent there are disagreements about the physics of outgassing. We've heard about 3 or 4 modeling approaches, at Hughes, at Martin, at Lockheed and at McDonnell-Douglas. Are there some fundamental physics disagreements among these models or is it just a matter what's the best way to do the modeling on each particular computer?

E. Zeiner: I think we'll have to form a truth committee and get back to you or something. I don't know how to handle that. I would say this, and I could be corrected by any of the other authors; the first order kinetics, I think we all touched on that. The Aerojet model is a diffusion model which has first order kinetics as one end of the spectrum and diffusion limitation as the other. And as far as I recall, the first order or at least the rate order of processes are fairly ammenable to easy testing or fairly conventional testing techniques which makes them very attractive. Tom, would you like to say anything more about that?

Tom Hughes (McDonnell-Douglas): It might be partly a matter of semantics. What we measure or think of as diffusion may indeed be evaporation and only you call it evaporation and I call it diffusion. It's partly a matter of opinion. Until we are able to isolate the difference between evaporation and diffusion down more firmly, I'm not sure anyone of us can say we are right and the other fellow is wrong. I certainly don't bear any such feelings. I'm not absolutely married to my concept. You've got to remember very often there are two paths to reach the same goal. Very often the mathematics are very different but you are each going to reach the same end point eventually. For instance, I had one curve up there showing the effect of temperature on outgassing rate. Now John Scialdone, in a paper he presented at an International Conference, I think, in Paris a year or two, or three years ago. His data is identical to mine, his equation is identical but he got it from a different approach. The one I used can usually be adapted to using data from TGA. The one John had, I think is from basic physics using monomolecular layers, individual sites and expected outgassing. So it's partly a matter semantics, it's partly different approaches but I think by the time we all get our data together, we're going to be at the same end point.

E. Zeiner: I might mention that in some of the experimental work Aerojet did under an Air Force sponsored space contamination program, we found that a material (we worked with a typical white paint DC92007) at roughly ambient temperatures. The outgassing process was strongly a diffusion-limited process obeying the very simple classical diffusion model at room temperature. When that coating was heated to about 125°C, it started exhibiting first order kinetics. So the same material, at least in our preliminary experiment, showed a change in its outgassing kinetics from one mode to another. It may be that materials can exhibit both diffusion-limitedor first-order kinetics depending on the source temperature.

F.J. Brock (Old Dominion University): I don't think it's quite right to say that one material can exhibit different modes of behavior under different circumstances. That seems to assume the material is complex and that one component of it is doing something at one temperature while another component is doing something else at another temperature. I would agree that semantics are important and we ought to be a little more cautious about how we use the term material. I think a material is unique and it's behavior is unique under any conditions. One of the problems is that for the first time people are investigating what happens around room temperature concerning outgassing. That's a very different problem, both experimentally and theoretically. Like Pete Glassford was saying earlier in the day, which I'm sure most people misunderstood, the external structure of the multi-layered insulation has nothing to do, in the end with the rate at which outgassing products escape. With that I agree, in the sense in which he said it. But it wasn't clear in what sense he meant that. I think part of the answer is we are not careful enough with how we say things.

A.P.M. Glassford (Lockheed): I think I understood that outgassing is the result of the material. I don't know what I was going to write there, I didn't get this thing, half of it. But anyway, since this is still on the board, outgassing is caused by some molecular species in the interior of a material which will diffuse to the outside. At the outside it will be released according to this equation here. I think that it's extremely easy to plot results on log-linear paper and draw lines and say that's an exponential and say that it has a slope and that slope is somehow related to an energy. I think if we permit people to do that we are going to get tied up in semantics. I feel that all outgassing should be described in terms of interior flow according to Fick's law or desorption from the exterior according to this law. And when I want to say that equation put down, I want that quantity torr, we all know what that is, put there and there. I don't want a plain exponential put there for this slope and have someone call that some energy, because that seems to sort of disguise ignorance. Now that's kind of a strong opinion but that's my opinion.

Lubert Leger (NASA/Johnson Space Center): Gene, I'd like to comment on that. I think regardless of approach we use, a kinetic approach that we talked about this morning or a diffusional approach - the result is the same. All we are doing is empirically fitting a curve to a set of very similar equations. We don't understand what occurs in outgassing. Obviously there must be some surface effects and some bulk effects. From real materials and the way we deal with them, there are multiple components coming off. Probably by diffusion. But if you have to start dealing with that from an analytical standpoint it becomes kind of unwieldly even with the approach you talked about this morning. If you have to deal with all the major components coming off, all the molecular weights, it become impossible to model. And it's senseless to do so, because you don't understand anything about the basic physics of the process by doing so. And you already have the data after you have done the test so why try to fit it to any sophisticated equation. The only reason you'd want to model it anyway is to incorporate it into some computer program. So why not take a simple approach, make a simple empirical fit to it, and use it in that particular format.

I think in most of the cases that we've been addressing, we're not worried about outgassing that necessarily occurs early in the vacuum exposure but the rates that occur in long time exposures. Terms of 100 hours or so. For that particular range, there is no predictive tool available. You just have to get the data and you have to use rates in whatever model you have. We're not understanding anything about the basic physics. That's the way we need to attack the problem rather than from a modeling approach.

A.P.M. Glassford: It's hard to get across what you are trying to say if you try to say too much in the short period of time we have here. One thing that struck me was that it was very easy to get all this outgassing data. And after you've gotten it, you could answer the program questions. All I'm doing in trying to fit these curves to this data is to try and get some insight and we're getting this insight, but who needs it if the program problem is solved. I agree 100% with what Lubert says.

Lubert Leger: Let me make one more comment, now on TGA. I've argued with people about TGA. We have a very complex problem in that we have multiple components coming off the material as a function of time. Isothermal TG data gives you a good description of the evolution of these components as a function of time. If you do a TGA type measurement, all you're doing is adding another parameter that you don't really know how to interpret -- the varying temperature. All TGA data is done as a function of increasing temperature. It seems to me, that if we can understand anything about the basic physics, we need to look at the isothermal data rather than the TGA data. TGA are high-temperature, chemical-decomposition based measurements, not isothermal at low temperature.

(Much background discussion)

Joe Muscari: Let me answer that and be a little long winded about it because I think it's important. First, let me take the offensive in that isothermogravimetric measurements are normally done with a QCM facing a sample. I think that this is an incorrect technique. It gives you incorrect data and you don't really understand that specific technique. Let me get into that and then I'll get into isothermal TGA done with a vacuum microbalance. The problem that you face with a quartz crystal microbalance, which is the standard way people measure isothermal TG, is the problem that the QCM is sensitive to temperature. You're dealing with an instrument that is not measuring the mass loss, it is measuring the CVCM. It is also measuring the re-emission at the same time. It has its own problems with frequency variation as a function of temperature, not only its own temperature but the temperature of the source that it's facing. All those problems cascade upon it, plus the fact that it's looking at a material that can be giving out two components between which it cannot decipher at any specific temperature. To unfold all that is an extremely difficult job. Now to look at the other aspect. Using a vacuum microbalance to look at isothermal

TG you have another problem and it's a very similar problem. You don't have the sensitivity. You're looking at materials that outgas at very low rates at the temperatures that we experience below 125°C. You have to monitor for very long periods of time, periods of weeks and months before you can interpret the data. When trying to use that data, you run into the same type of problems that you do with the QCM. You're actually measuring the parameter you are trying to determine, which is the mass loss and that's an advantage. Now, there are equal things against dynamic TGA and again Lubert called one out specifically. The fact that you can't precisely control the temperature ramp at low temperatures is a problem. A problem that needs to be solved. I think we're still in an exploration stage where we are trying to not only develop the correct model to interpret the data and to assess it, we are also trying to find accurate techniques of measurement.

Lubert Leger: First of all when I say isothermal TGA, it is vacuum microbalance TGA. It represents the condition the component sees on exposure to vacuum. That's precisely what we're trying to model. That's the data you want. You want the outgassing rate at 100 hours. You want the rate at 10 hours. You'd like to know, as a second step to that, how much of the total mass loss is condensing on a given surface. I agree with you, that's a difficult measurement to make. The only way we can make it is with QCMs right now. From the TGA standpoint, I don't think it's a matter of accuracy of controlling the temperature ramp that is the problem. It's a problem of unravelling another parameter, the varying temperature with all the other varying parameters that we have in here in the basic material.

John Scialdone (NASA/Goddard Space Flight Center): Why not use the old methods used by B. B. Dayton and many others to obtain outgassing data which employ the conductance and the rate of pressure increase methods? What's wrong with their presentation of the data prepared 20 or so years ago giving the outgassing rate over the sample at 25°C as a function of time and expressed in torr-liter per second per square centimeter? That's one question.

E. Zeiner: Was that a question or a statement - I'm not sure.

John Scialdone: I am interested more in the second portion of the argument over here -- the transport equation. These are the sources of the disagreement, the calculation of the rates of deposition and impingement on the surfaces you are using in your program. I'll rephrase. I am confused about the difference between the computer program which you are proposing, you and several other people (Aerojet). I don't know the mathematical differences between your program and the one from Martin-Marietta.

Robert Moss (Ford Aerospace): We are not going to end up with a philosopher stone. There is no single answer to outgassing and contamination and what we have to bear in mind is that there are different techniques and different answers for different problems. There are circumstances, for example, where I really don't care what it is that comes off; everything that comes off in some circumstances, is going to be disastrous and there are other circumstances where anything that comes off below 300°C is of no interest to me. It depends entirely on the mission, on the experiment, on what you have put into the spacecraft, and on the spacecraft configuration. For example, if we talk about desorption of water, one of the things that is important is the surface area. If you have a long thin film with a monolayer of water on it, you get entirely different water desorption than if you have the same mass of material in a single lump. So you have to look at the entire system and the application. If you have the same film and it was internal to the spacecraft, it was enclosed and had a labyrinth path to the outside, you'd have a different situation than if it was on the outside and all the water boiled off in the first 30 or 40 minutes of orbit. So, there are a lot of different ways to handle the problem.

General McCartney mentioned things like not turning on equipment for a certain number of hours, allowing things to outgas and water vapor to come off and that's a perfectly valid way of handling the problem. Another way to handle the problem is to coat everything with Parylene, which we are doing too. Another way to handle the problem is to make everything out of metal, not to use any organic compounds at all. Yes, I know, but there are places where you can make material substitutions. And so rather than try to knitpick whether this model or that model is good, bad or indifferent, I think we have to consider the actual application, the material involved, temperature profiles of what's coming off and where its going to deposit. That's the only time you can select whether you want to go TGA or micro-balance or weigh it, or whatever. If you don't look at the entire system, you're just kidding yourself.

Gene Zeiner: I think one thing is apparent. We are just beginning to learn what we hope will turn an art into technology. The difference of opinions are certainly very healthy and I know I've got a lot of things to go back and think about. I'd love to go on with this but I think in all fairness, I ought to let the second session have a shot. Thank you very much for your comments.

Ernie Ress (Martin-Marietta): OK, we'll open up round two on modeling. There were a number of papers on that. We did have some questions in a couple of areas and we want to open it up for more specifics on some of the modeling applications that were presented.

Tak Sugimura (TRW Inc.): I would like a very simple explanation without equations, on just the physics of modeling efforts at Martin-Marietta and

Aerojet. Just some of the basic physical assumptions that are made and some of the things you're trying to get out of this modeling. A five minute review would certainly be sufficient.

Ernie Ress: OK, I'll try to go over it as best as I can. Fundamentally, we develop a geometry for any system that we analyze using a basic thermo-type program. Within our company we call that program TRASYS. The computer system has a capability of going to a thousand nodes down to surfaces sizes of centimeters in subdivision and nodal structure depending on how you want to work it. The program provides us, from a geometry standpoint the ability to get surface shadowing as you build your geometries. We can put in any surface shapes we want, depending on the resolution you need. Of course, the computational time goes up as the function of the number of surfaces you're dealing with. The TRASYS type program will allow you to develop form factors or view factors between surfaces, giving you the geometric considerations of how much of one surface sees another. Using this, then you can also take those types of sources which are considered surface sources such as offgassing, outgassing or what have you. And you can allowthe program then to establish those view factors to treat that kind of source. Then you take the next component, once you've got your geometry established, and you set up your sources. The sources and the geometry sometimes go hand in hand. The sources for outgassing, which are surface sources, kind of dictate the types of nodes you want. Where they are, how big they are, and of course, depending on the resolution of the analysis you want. You can also subdivide these nodes from a geometry standpoint to increase your resolution. (A short contamination gate gap) We generally treat point sources as an area, a circular area. A nozzle for an engine, or something like that is generally treated as a circular area. But its really a point source and within the TRASYS program, we develop r(s) and thetas which are the distance and angular relationships for all the surfaces.

Once we take a point-type source, like an engine or a vent, and we know its plume characteristics, then we can calculate the mass flow based on the distance and the angular relationships for these point sources. For engines, we've developed a series of close formed equations. We break up the flow characteristics in three regions depending on the physics of the engine. I guess that basically takes care of the sources. The point sources are close formed analytical solutions developed in r(s) and theta characteristics which we use in the basic configuration model to provide us the geometry. The next thing is to work the transport. Once you've got surfaces, once you've got sources, then you've got to work transport. There are a number of things you can do. Our program allows us, depending on how you set it up to go line-of-sight or reflection off surfaces. You can go singular reflection or multiple reflections depending on how complex you want to get in the geometry world. Also in the transport mechanism, we treat the contaminants leaving the spacecraft and interacting with the ambient environment. These contaminants can be scattered back to the spacecraft which is the terminology return flux which you've had here. We also have the capability in the program to treat self scattering within the plume. The program sets up a matrix above the spacecraft or anywhere around the spacecraft depending on what you want. For the shuttle orbiter we set up a matrix above the spacecraft based on a series of lines-of-sight out of the payload bay. We can calculate along this matrix of points, a line-of-sight, the mass column density of contaminants. We can translate the line-of-sight anywhere with respect to the spacecraft within the accuracy of the field that we set up.

At each matrix point we collect the contaminants that reach that point, whether the contaminants are from a surface source coming out in a Lambertian distribution a certain distance away and at a certain angular consideration or whether the contaminants are a point source from the engine. We take into account, summing by constituents over whatever comes out of the RCS engines (shuttle) or whatever comes out by leakage, H_2O, CO_2, things like this. We keep count of the constituents. And we sum them all into mass column densities. We treat these with respect to return flux and we can accumulate the deposition on a surface with respect to return flux. Deposition can also come from a straight line-of-sight interaction or from surface to surface or from body to body.

We account for that too.

Also I might point out, we input thermal data to keep track of all the sources because the surface sources are thermal dependent and also the sticking coefficients or the accommodation coefficients of the contaminants on the surface are temperature dependent. So we have to keep track of all the temperatures of the surfaces and then you can run that in time slices or however you want for a mission relationship. We have the velocity vector relationship, the contaminants, on a mission basis and so then you can take return fluxes with varying attitudes -- a variety of conditions in that nature from a mission orientation standpoint. And then the next element is putting it into effects. We generally try to work in the world of defining an environment. The basic space program talks in terms in environment, in terms of deposition levels and mass column densities and the number of constituents involved in all these components. But we also have the capability to take the deposition and translate that into transmission/reflection based on the spectral wavelength and the thickness of the contaminants. We have the capability to take things like particles and run them in trajectories with respect to a spacecraft and follow them from orbit with respect to the spacecraft. We have the capability in our effects area to take particles, such as ice particles and run their sublimation characteristics with time on orbit so that you can get an idea of dissipation time/sublimation time on orbit for ice. We have the capability to calculate scattering and absorption based on the mass column densities of contaminants and the constituents of contaminants in the effects world. We also have the capability to look at the absorptance changes in some of the areas as a function of deposition thickness and the majority of all the data in the effects area is the accumulation of information that's been gained from all the test program and flight programs and the things that have been available where we can get that kind of data that we have plugged in it to provide us with some type of validation. Now that's basically a talking overview of the program and you saw the paper that Lyle Bareiss presented. He presented the Space Lab contaminant environment. And he showed the three Space Lab configurations. We also have the shuttle orbiter. We have a number of military-type satellite systems and you can inter-play them. You can take instruments, put them on a pallet, look at the cross-talk with respect to contamination between the instruments on a given pallet, you can take the pallet and put it in a payload bay -- treat those two independently, put the bay in the shuttle orbiter, treat that as a whole system. So you have the kind of capability in a overlay fashion with the model. That's just kind of a wordy overview on it. I don't know if that answers your question. (Too far distant to hear) There are obviously three areas where additional testing of data base have to be improved and I think possibly of verifications of the models. But the three main areas are obviously the ones that, I think, that have been kicked around here to some degree. One is in the source characteristics. How do you really treat the contamination effects of outgassing? How do you represent what goes on? And I think the camps that were kind of being drawn here in the discussion, were one of looking at the complexity and knowing all minute physics of what's going on versus one of trying to get really a bulk effect, and I'll use that term loosely. A bulk effect encompasses everything that really goes on in a total process or in a summation process. And this is only the level we should really be looking at this point in time in evaluation. So, I think that there still have to be work done in the sources area but I'm not too sure how much. I think the transport area is an area where there's a lot of work that has to be done and I think the key area is the one with engines. Whether it's a solid engine or a bi-prop or a mono-prop type engine. I think that's the key area where the transport mechanisms have to be better understood. And then from the effects area, I think there's a whole lot of information that has to be generated in the effects area to really tie the thing down. And what I mean by a whole lot of information, there has been so many spot tests or things that have been done that you can get very little correlatable information. People will put witness samples in a given test and will take the samples out and say there were so many particles on it but will never tell you the thickness, or there was a certain type of contaminant on it but you never know what the thickness was. You never get a chance to understand how the thickness relates to the effect. I think there needs to be test programs that have continuity end to end so that you're measuring a series of variables that you have control over throughout the test -- the thickness, the source characterisitcs, the effects and all the parameters that go with it. Whether it's transmission, reflection or scattering off the surfaces. If I were to really relate all these areas from a standpoint of importance, I guess I'd look at the effects being a key area. I think there's a lot of work that has to be done in the transport area -- especially the engines. I just don't know how we're going to get there without doing some flight measurements in that area. So I think that's pretty hard -- it's important, but it's going to be hard to get there. And I'd rate maybe the sources area next.

(Too distant to hear)

<u>Carl Maag (Aeroject Electrosystems Corp):</u> I have a simple answer for that. I guess I should demand equal time but I won't. In addition to all of the above, if you want a comparison between programs. Ours is essentially the same in that is uses a view factor model (different than TRASYS) and it uses the same type of blocks. But in addition, we get deeper into what Ernie would call the bulk. We get into the physics of the situation and Gene may want to jump in here and (And I'm sorry to say at this moment we ran out of time).

SESSION III

ROCKETS AND PLUMES

BACKFLOW CONTAMINATION
FROM SOLID ROCKET MOTORS

C. R. MAAG

AEROJET ELECTROSYSTEMS COMPANY
AZUSA, CALIFORNIA

ABSTRACT

Contamination from plumes of solid rocket motors have been suspect for the anomalous temperature behavior of many spacecraft systems and sub-systems. In an effort to find supporting evidence for this phenomena a number of spacecraft experimenters and designers, along with solid rocket motor (SRM) experts, were surveyed. The survey was limited to those experimenters and designers whose systems or sub-systems might have been subjected to SRM plume effluents (e.g., apogee kick motors). The results of the survey are presented. These findings will be particularly meaningful to those concerned with modeling the effects of solid rocket motors on critical spacecraft surfaces or on scientific experiments that could be directly or indirectly affected by molecular or particulate contamination.

1.0 INTRODUCTION

The Department of Defense (DOD) and the National Aeronautics and Space Administration (NASA) have a requirement for a booster system to transfer their spacecraft from low earth orbit (after deployment from the space shuttle) into high or geosynchronous altitudes. An Inertial Upper Stage (IUS) will provide the capability to deliver spacecraft beyond an orbiter's operating regime, including plane change and higher-energy orbits. The IUS system consists of two or more of two different sizes of solid rocket motors (SRM) incorporated into a family of vehicle configurations.

The potential contamination problems from solid rocket motor plumes have been known for many years. Borson and Landsbaum(1) performed a very detailed analysis of all the available experimental and flight data through 1968 on the contamination of spacecraft subsystems from all classes of rocket exhausts. At that time they indicated that the contamination from SRMs should be similar to that from steady-state bipropellant liquid engines except for additional contamination due to solid particles. Martinkovic(2) has since shown that bipropellant attitude control rockets eject contamination outside of the primary gas flow (backflow region). Borson(3) has more recently indicated that the contaminants contained in the plumes of SRMs would more than likely be carried by the plume gases in the direction opposite to the motor exhaust (180° to the thrust vector).

The prediction of the contamination of a surface exposed to the effluent of a motor requires the knowledge of the contaminant flux arriving at a surface. There are approximate methods for determining flow fields and the subsequent transportation of plume-borne contaminants extending hundreds of nozzle-exit radii downstream from a nozzle exhausting into a vacuum. The majority of existing plume prediction methods fail to give a satisfactory account of exhaust products upstream (back flow region). The plume expansion is limited in these mathematical models by the Prandtl-Meyer angle at the exit Mach number.

In an effort to find supporting evidence for this phenomena a number of spacecraft experimenters and designers, along with recognized authorities in the solid motor field were surveyed. The survey was limited to those experimenters and designers whose systems or subsystems might have been subjected to the effluents of solid propellant motors. Table 1 is a list of those satellites and test facilities acquired from organizations willing to discuss and share their data.

TABLE 1 SRM CONTAMINATION SURVEY

- LABORATORY DATA
  - -MOLESINK (JPL)
  - -AEDC Test Firing Pictures
- FLIGHT EVIDENCE
  - -NATO III
  - -BLOCK 5D
  - -NTS
  - -IUE
  - -AIMP-E
  - -LES 8/9
  - -ATS-1

2.0 DISCUSSION

2.1 Ground Testing

The operation of a SRM in a vacuum chamber results in conditions that are different from those found when it is fired in space. Ground test chambers have limited pumping capabilities. Chamber walls will in most cases cause recirculation of gases and/or molecular scattering. Solid motor tests in vacuum chambers are generally performed to verify performance under vacuum conditions. Plume dynamics are not usually included. Facilities such as the T-3 test cell at

AEDC* provide a satisfactory vacuum for such motor performance evaluations. Solid motor firings in the T-3 test cell have shown evidence of contamination buildup in the plume backflow region(4). Figure 1 shows the prefire and postfire condition of a TE-M-604-4 motor fired in the T-3 test cell. The thermal insulation blankets are extremely contaminated in the postfire still photo. Motion pictures of this test firing showed that molecular species began to buildup (thick enough to show interference phenomena) in less than 3 seconds after ignition and continued to do so until shutdown, at which time the pressure differential caused a severe contamination cloud (typical test condition) to occur. However, because of the facility limitations, it was not possible to perform measurements that would give meaningful results on contamination deposition or distribution.

Chirivella and Simon(5) conducted a series of tests at JPL to measure the mass flux in the far flow field of a nozzle plume in a high vacuum with emphasis on the back flow region. CO_2 and nitrogen gases were selected as representative gases, and quartz crystal microbalances (QCMs) were used to measure the mass flux of the plume. The results showed significant mass flux in the plume back flow region (140° to the thrust vector). Figure 2 shows a comparison between the theoretical approximation and measured data. This set of data is one of the most comprehensive ever obtained. It provides estimates of fluxes in those regions of a plume that depart more than 90° from the centerline.

2.2 Flight Evidence

The NATO III satellite recently experienced base shield temperatures in excess of design temperatures shortly after orbit

---

* Arnold Engineering Development Center

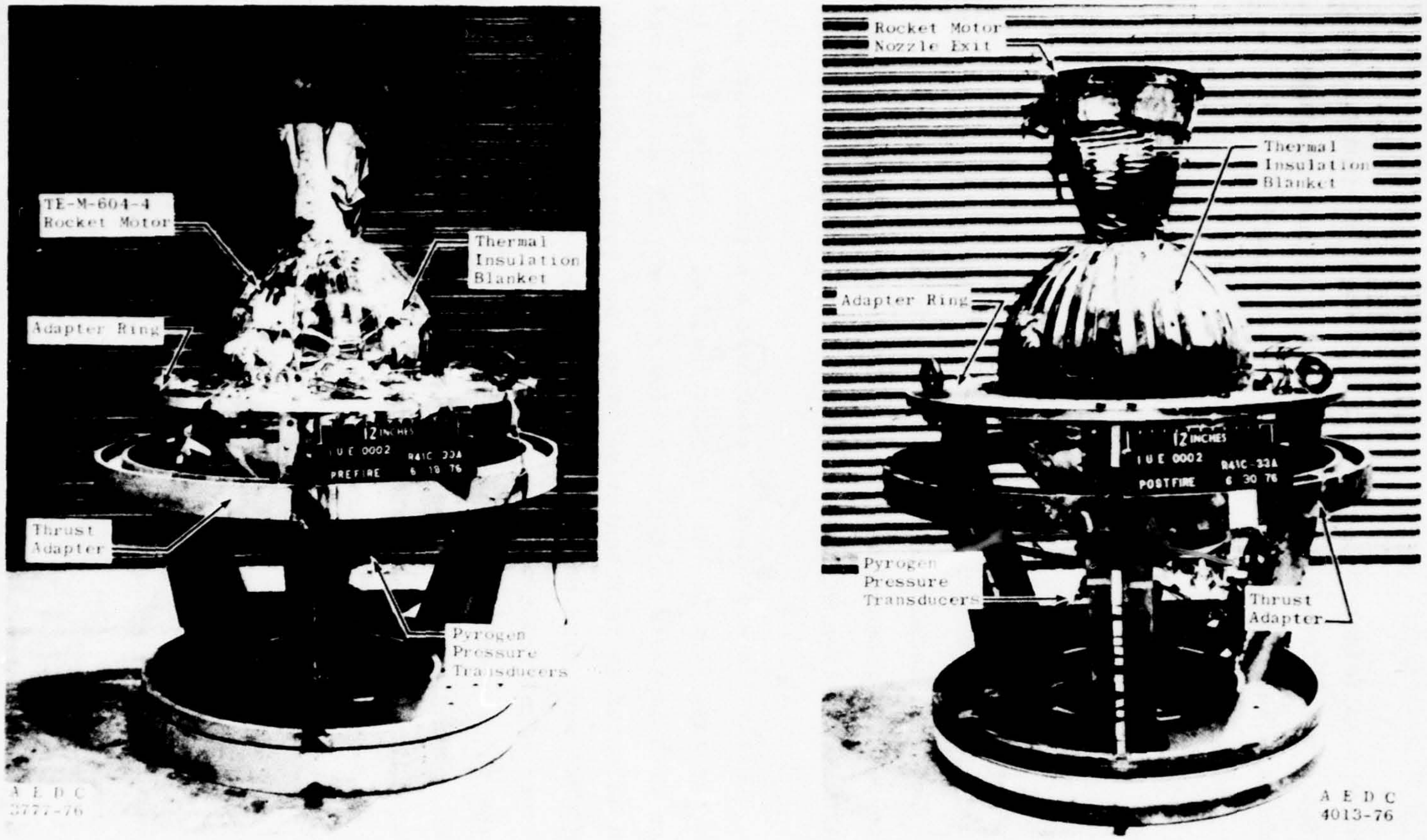

FIGURE 1. PREFIRE AND POSTFIRE PHOTOS OF A TE-M-604-4 MOTOR FIRED IN THE T3 TEST CELL

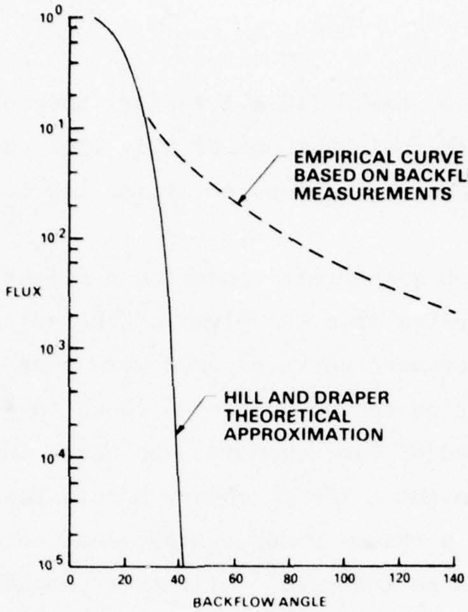

FIGURE 2. COMPARISON OF THEORETICAL AND MEASURED MASS FLUX FROM A PLUME IN HIGH VACUUM (JPL/MOLESINK)

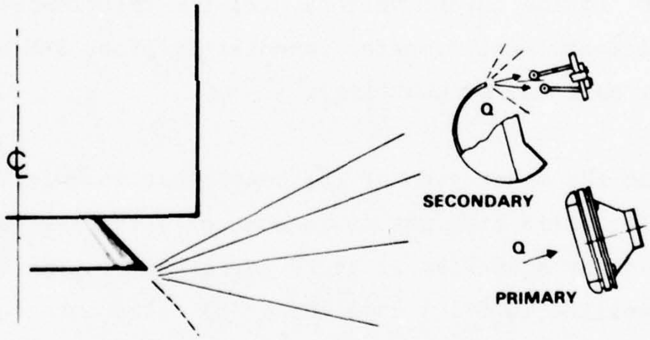

- UNEQUAL HEATING OF PRIMARY CALORIMETERS CAUSED BY ASYMMETRIES IN PLUME FLOW FIELD
- SECONDARY MODULE RECEIVED HEAT TRANSFER RATES HIGHER THAN PREDICTED, SUGGESTING BROADSIDE FLOW
- CALORIMETERS APPEARED TO HAVE ADDITIONAL HEAT TRANSFER AT SHUT DOWN

FIGURE 3. BLOCK 5D FLIGHT EVIDENCE

insertion (6). The base shield (10 mil Fep/Ag) showed a solar absorptance change ($\Delta\alpha_s$) in the neighborhood of 0.1. The cause has been attributed to the exhaust plume from the solid kick motor (SVM-6).

The Block 5D spacecraft conducted a flight experiment to measure heat transfer rates from the plume of the solid kick motor (TEM-364-15). The instrument packages used were slug-type calorimeters. Their approximate location to the nozzle is shown in Figure 3. The primary module consisted of two segments, one black anodized aluminum, the other polished aluminum. The secondary module consisted of three sensors located behind a chrome oxide coated plume shield. The experimental results seem to indicate (7) (a) that unequal heating of the two primary module calorimeters were caused by asymmetries in the plume flow field, (b) the secondary module received significantly higher heat transfer rates than predicted suggesting that the flow was somewhat broadside (100° to the thrust vector), (c) the calorimeters appeared to have some additional heat transfer immediately after SRM burnout (possible blow back and/or chuffing).

One the other side of the contamination coin, two (2) spacecraft using solid kick motors in concert with plume shields have not experienced any anomalies in their performance. The Navigation Technology Satellite (NTS-1.) used three (3) solid motors to achieve proper orbit and orientation. The exhaust characteristic of the perigee kick motor (PKM), the spin motor, and the apogee kick motor (AKM) were studied extensively. Figure 4 shows a cutaway view of plume profiles for AKM, PKM, and spin motor of the NTS payload transfer system. The iso-Mach lines were used in calculating the plume impingement heating rates of the payload transfer system. The configuration employed protection shields for avoiding possible contamination of the spacecraft thermal

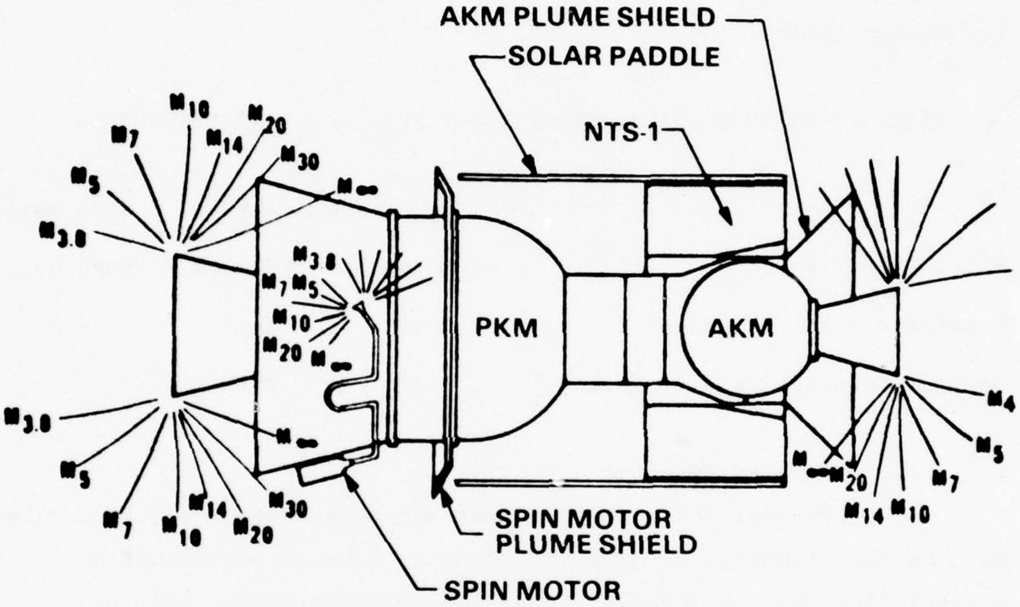

● PROTECTION SHIELDS USED TO PREVENT CONTAMINATION

FIGURE 4. NTS-1 FLIGHT CONFIGURATION

control surfaces from the solid motors (8). The exhaust characteristics of PKM, AKM, and spin motor are shown in Table 2. This spacecraft performed well within specifications.

The International Ultraviolet Explorer (IUE) launched in late January 1978 also utilized a solid propellant kick motor (TEM 604-4) with a plume shield to protect critical surfaces. As of this date, no anomalies have been seen. The system appears to be operating within its design limits.

TABLE 2 EXHAUST CHARACTERISTICS OF PKM, AKM, AND SPIN MOTOR

	PKM	AKM	Spin Motor
Solid Motor Type	TEM 364-4	TEM-604	MARC 67A2
Expansion Ratio (Nozzle)	3.10	36.3	16.0
Maximum Turning Angle (Degrees)	163°	161°	125°

2.3 Related Evidence

Perhaps the most pertinent and quantitative piece of flight data is that reported by Sheehy(9) from an onboard contamination monitor flown on the Anchored Interplanetary Monitoring Platform (AIMP-E). The need for this instrument was established by flight results obtained from the AIMP-D spacecraft. The spacecraft battery exceeded it's upper temperature limit of +60°C after a short time in final orbit and was shut off. It was postulated that the top surface of the spacecraft had been severely contaminated from the fourth stage (braking) SRM used to place the spacecraft into lunar orbit. A decision to fly a contamination monitor on the next flight (AIMP-E) was made. The reflectance of an aluminum front surface mirror was monitored before, during, and after the fourth stage motor firing.

The data as shown in Figure 5 shows a correlation of the contaminant deposition, optical properties and motor temperature increase followed by a gradual re-emission and stabilization after motor shutdown.

The LES 8/9 spacecraft has a quartz crystal microbalance (QCM) located on the payload dispenser rack during launch. The QCM recorded a significant mass deposition (420 μg) during the firing of the Titan second stage retro rockets(10,11). Although the three (3) retro rockets were firing toward the payloads, the QCM and payloads were shielded from line-of-sight impingement. It must be concluded that the contamination recorded must have been either small particles (0.5 μm or less) or large molecules otherwise they would not have been carried along in the plume. In addition, the optics of two scatterometers in the same payload were also significantly contaminated.

ATS-1 (Applications Technology Satellite) is a synchronous altitude satellite in a near equatorial orbit. It was launched on an Atlas/Agena and injected into orbit by a solid propellant apogee kick motor. One of the eight scientific experiments on board was a thermal coatings experiment. This experiment, even after ten years in orbit, still stands as the benchmark of thermal coatings experiments. Reichard and Triolo(12) indicated that there existed a discrepancy between the measured values of solar absorptance/hemispherical emittance ratio in the laboratory and the initial flight values measured 48 hours after launch. This data is illustrated in Figure 6. The experiment was located on the main body of the spacecraft, as shown in Figure 6 by the small rectangle above the bellyband. Careful examination of the data indicates that except for an isolated case a trend exists. The low α/ε coatings (colder surface temperatures) have degraded more percentagewise than the higher α/ε coatings. This trend

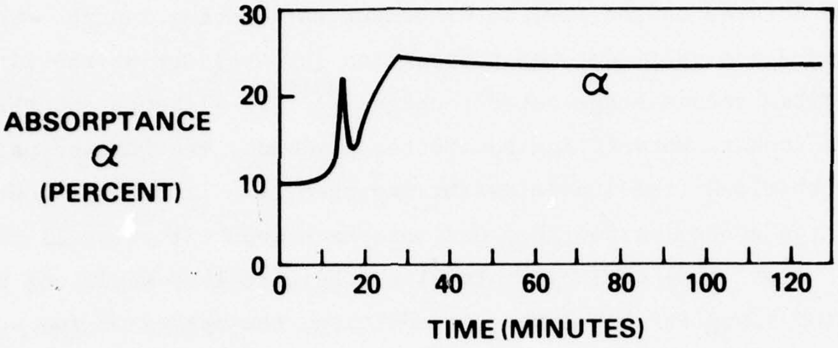

- UNEXPLAINED LOSS OF AIMP-D LED TO USE OF CONTAMINATION MONITOR
- REFLECTANCE OF MIRROR MONITORED DURING FOURTH STAGE SRM FIRING
- CONTAMINATION INDICATED

FIGURE 5. AIMP-E FLIGHT EVIDENCE

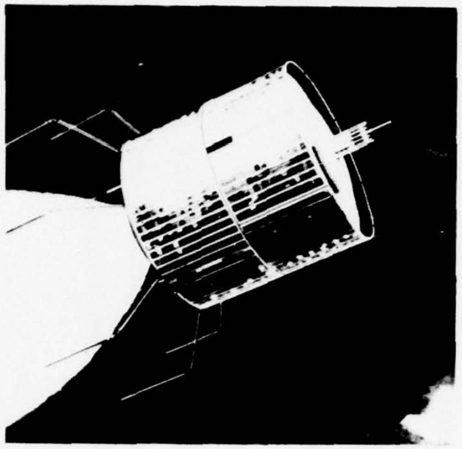

α_s/ϵ RESULTS OF FLIGHT AND LABORATORY MEASUREMENTS

CUP SURFACES	LAB	FLIGHT
RAZOR BLADE	1.04	1.03
AgBeCu	2.92	3.20
Al_2O_3/Al	0.54	0.59
TiO_2/MS	0.22	0.32
S-13	0.21	0.27
ZnO/KS	0.20	0.24
TiO_2/MS	0.20	0.23
Al_2O_3/KS	0.14	0.21
SiO_x/Al	0.48	0.49

FIGURE 6. ATS-1 FLIGHT EVIDENCE

is quite reasonable since the lower surface temperatures would tend to accomadate more contaminants than the coatings with high surface temperatures.

The same basic thermal coatings experiment, but carrying different coatings, was recently launched on the Navigation Technology Satellite (NTS-2). Unlike NTS-1, the spacecraft did not have apogee kick motor or spin motor plume shields. Triolo (13) indicated that all of the coatings were running much hotter than the predicted insertion temperatures. In fact, the temperatures of all the coatings were the same as the higher than predicted temperature of the radiator panel to which the experiment was coupled. Adjacent to the thermal coatings experiment on NTS-2 was a solar cell experiment conducted by NRL. Statler(14) has indicated that his experiment showed no apparent signs of contamination. The short circuit current (I_{sc}) of the solar cells as measured on orbit were within one percent of the lab values. Statler also indicated that although he saw no electrical output changes, the temperature of the experiment has climbed, ironically, to the equilibrium temperature of the thermal coatings experiment and the radiator (93°C). With an α/ε near unity the solar cell experiment turn on temperature was 60°C - sufficiently high enough not to accomodate contaminants.

With the evidence mounting to consider solid propellant motors as a possible contamination source, the author is offering a plausible reason for these discrepancies. Solid rocket motor contamination.

3.0 CONCLUSIONS

This review of the current status of solid rocket motor contamination effects reveals the scarceness of data available. Some concrete data exists. If advanced spacecraft systems are to be launched with solid propellant motors, it may be wise to consider using protective covers over the spacecraft. A more obvious solution, based on the successes of NTS-1 and IUE, would be to develop a plume skirt for the solid kick motor system.

The most striking conclusion of this study is that more research is needed to fully understand the mechanisms and processes of return flow from solid propellant motors. Additional programs are required to better understand the mechanisms of solid motor plumes so that existing computer codes can be adjusted to consider return flow. In addition, dedicated piggyback flight experiments are urgently needed to develop a data base to predict contamination from SRMs.

ACKNOWLEDGMENTS

I am indebted to those experimenters and designers who were willing to share their data through long tedious discussions. This work was supported in part by the Space And Missiles Systems Organization (SAMSO) under Contract F04701-77-C-0010.

REFERENCES

1. Borson, E. N. and Landsbaum, E. M., A Review of Available Contamination Results, TR-0200 (4250-20), SAMSO TR-69-82, AD-850122L, Dec. 15, 1968, Aerospace Corp., El Segundo, CA.

2. Martinkovic, P. J. Bipropellant Attitude - Control Rocket (ACR) Plume Contamination Investigation, AFRPL-TR-69-251, October 1969, AFRPL, Edwards, CA.

3. Borson, E. N., (Aerospace Corp.) Private Communication, August 1977.

4. Skladany, J., (NASA/GSFC) Still Photos and Motion Pictures of the IUE TEM-604-4 Solid Propellant Rocket Motor Firing, June 1976.

5. Chirivella, J. E. and Simon, W., Molecular Flux Measurements in the Back Flow Region of a Nozzle Plume.

6. Krueger, R., (NASA/GSFC) Private Communication, August 1977.

7. Leising, C. J., (JPL), Private Communication, November 1977.

8. Hwangbo, H., et al, Thermal Control Design and Analysis of Navigation Technology Satellite 1, AIAA Paper, No. 75-678, AIAA 10th Thermophysics Conference, Denver, Colorado, May 1975.

9. Sheehy, R. N., Contamination Monitor, NASA/GSFC X-713-68-134, January 1968.

10. Lynch, J. T., Quartz Crystal Microbalance Monitor of Contamination for LES 8/9, Project Report SC-33, MIT Lincoln Laboratory, June 1976.

11. Pearce, B. E., Postflight P74-1 Contamination Estimates, TOR-0077 (2506-01)-1, The Aerospace Corp., March 1977.

12. Reichard, P. J. and Triolo, J. J., Preflight Testing of the ATS-1 Thermal Coatings Experiment, AIAA Paper No. 67-333, AIAA Thermophysics, Specialist Conference, New Orleans, LA., April 1967.

13. Triolo, J. J., (NASA/GSFC) Private Communication, March 1978.

14. Statler, R., (NRL) Private Communication, August 1978.

CONTAMINATION MECHANISMS
OF
SOLID ROCKET MOTOR PLUMES

M. K. Barsh
J. A. Jeffery
P. Brestyanszky
K. J. Adams

Aerojet ElectroSystems Company
Azusa, California

Contamination Mechanisms of Solid Rocket Motor Plumes

M. K. Barsh, J. A. Jeffery,
P. Brestyanszky, and K. J. Adams

Aerojet ElectroSystems Company
Azusa, California

A new generation of space satellites require freedom from contamination upon insertion into final operational orbits. There is concern that the combustion plume from solid rocket motors (SRMs) such as the Inertial Upper Stage (IUS) units, which will be employed to deliver payloads into space after deployment from the STS shuttle craft, may be a source of significant contamination.

Although the payloads are located forward of the SRMs, evidence has been uncovered that suggests that recirculation of nominally trivial amounts of plume products flowing 180° to the direction the rocket exhaust occurs during the rocket firing and, further, that these recirculated products can and will deposit on sensitive thermal control surfaces of the payloads to degenerate their effectiveness.

In order to assess this phenomenon, several mechanisms were postulated which might explain how the recirculation could occur. These are:

1. Charge separation - the plume products assume a charge opposite to the SRM and/or payload structures by virtue of triboelectric effects or thermal ionization.
2. Intra-plume collision - some faster moving species collide with slower moving ones, resulting in a vector velocity counter to the plume direction.
3. Nozzle boundary layer effects - exhaust product flow at the nozzle wall-plume interface results in a boundary layer that conforms to the nozzle surface and ultimately flows in direction counter to the plume direction.

Preliminary analytical computer models describing those mechanisms have been developed and experimental verification of the phenomena has been explored.

1.0 INTRODUCTION AND SUMMARY

The NASA Space Transportation System (STS) which consists of the shuttle stage and the solid rocket motor (SRM) Inertial Upper State (IUS), will carry some payloads whose performance can be compromised by the accumulation of thermo-optically contaminating deposits. Whereas significant efforts to evaluate the contamination potential of the shuttle system have been made, no concern for the contamination potential of the SRM firings of the IUS have been explored. It has generally been assumed that since the payloads will reside well forward of the exit nozzle of the IUS systems that no rocket plume products could find their way to the critical areas of the payloads.

Aerojet ElectroSystems Company (AESC) elected to investigate the possibility of contamination from the IUS motor firings since prior studies of some of their payload systems slated for STS launchings had established that a homogeneous deposit of as little as 0.1 gm of material on some critical areas ($<1.0 \times 10^{-6}$ gm/cm^2) could degrade the system performance unacceptably. Since the first stage IUS propulsion products will weigh approximately 10,000 Kg, a deposit of 1 part in 100,000,000 derived from the SRM's could constitute a serious problem.

A survey was made of SRM launches in the past and a number of cases were uncovered which clearly suggested that "recirculation" contamination was a reality.[1] The nature of the evidence ranged from the increase in the optical absorptance (α) of thermal control surfaces to the presence of "convective" base heating caused by phenomena other than plume

---

[1] Maag, Carl R., Backflow Contamination For Solid Rocket Motors, presented at the USAF/NASA International Spacecraft Contamination Conference, Colorado Springs, Colorado (1978).

radiation upon SRM firings. The conclusion, deduced from the evidence that strongly points to exhaust products migrating forward and adhering to the payload sites, is counter-intuitive in view of the opposite velocity vectors of the main mass of the burn products. Yet this concept or related ancillary phenomena have received superficial consideration by other investigators. Thus, for example, Boynton[2] recognized that the exhaust gases occurring at the large turning angles of a rocket engine at high altitudes, have density distributions far different from those of the far field plume. This has been supported by the work of Simons[3] and Pearce[4]. Further, in discussing the possible effects of the nozzle boundary layer on plume expansion, Arnold[5] stated that some flow can expand around the nozzle exit and flow back up the outside of the nozzle. Suebold[6] confirms that subsonic flow next to the nozzle wall is capable of making a complete 180-degree turn and head back upstream. Martinkovic[7] expressed the same idea. Apparently, however, no attempts to quantize the mass fluxes resulting from such backflow were made.* Nor were any possible explanatory physical mechanisms formulated. Recently,

2. Boynton, F.P., Exhaust Plumes From Nozzles With Wall Boundary Layers, Journal of Spacecraft & Rockets, 5:1143-1147 (1968).

3. Simons, G.A., Effect of Nozzle Boundary Layers in Rocket Exhaust Plumes, AIAA Journal, 10:1534-1535 (1972).

4. Pearce, Blain E., An Approximate Distribution of Mass Flux In A High Altitude Solid Propellant Rocket Plume, AIAA Journal, 12:718-720 (1974).

5. Arnold, F., An Experimental Method For Locating Stream Tubes in A Free Jet Expansion to Near Vacuum, AEDC-TR-69.17.

6. Seubold, Jason G., Edwards, R.H., A Simple Method For Calculating Expansion of A Rocket Engine Nozzle Boundary Layer Into A Vacuum, Hughes Co.

7. Martinkovic, P.J., Bipropellant Attitude Control Rocket (ACR) Plume Contamination Investigation AFRPL-TR-69-261.

Chirivella[8] has reported experimental mass flux data in nitrogen and carbon dioxide from a series of five conical nozzles for angles extending beyond 100° relative to the nozzle centerline. Results indicated significant mass flux in the backflow region. Calia and Brook[9] supported these findings by confirming in their tests, substantial mass flux levels in the neighborhood and beyond the limiting Prandtl-Meyer characteristic. These flux levels were several orders of magnitude larger than predictions from inviscid flow theory.

In order to attempt to resolve the question of recirculation contamination from the IUS SRM's, an analytical model study was initiated. Three independent mechanisms were postulated for the steady-state burn and were studied using available literature data. An attempt has been made to predict, with the aid of these preliminary analytical models, the recirculation of potential contaminants forward to the site of a typical payload from SRM-1 (the larger of the two IUS motors). The modeling studies and the results and conclusions are described below.

2.0 BACKGROUND

Solid rocket motor firings have been studied and the following observations are pertinent. At start-up, the SRM generates a small amount of unburned products for a very short time until the SRM chamber pressure builds up. The major portion of the burn, steady-state, occurs at high temperature and pressure and essentially complete combustion is achieved (for stoichiometric propellant compositions). At shut-down, significant amounts of partially burned products are evolved as the pressure and

[8] Chirivella, Jose E., Molecular Flux Measurements In The Backflow Regions Of A Nozzle Plume, Tech memo 33-620, 1973, JPL.

[9] Calia, U.S., and Brook, J.W., Measurements Of A Simulated Rocket Exhaust Plume Near The Prandtl-Meyer Limiting Angle, <u>Journal Spacecraft and Rockets</u>, 12(No. 4): 205-208 (1975).

temperature decay. However, since most of the propellant combustion products occur during the steady-state phase and since this phase was most amenable for analysis, the analytical efforts were directed at the steady-state-burn plume products.

Three mechanisms analyzed for the recirculation of contamination from the SRM plumes of the IUS were:

1. Charge separation
2. Collisional
3. Boundary flow

For purposes of expediency in simplifying the mathematical derivations and computer programs, it was assumed that the three mechanisms were independent and that the results would be additive. It is, of course, evident that if the three mechanisms are viable, they must be operative concomitantly and that eventually they will have to be integrated to provide a more realistic prediction of the contamination potential. The more remote, (from targets of interest) but larger of the two IUS motors (SRM-1) was selected for study because it represented a conservative case.

The "charge separation" mechanism was conceived as the consequence of two separate phenomena: (1) triboelectric effects developed by the very high velocity particles ejected from the nozzle and (2) thermal ionization of the ejected species by virtue of the high temperatures of the burning propellant. Illustrative of the former phenomenon are references to potentials estimated up to a half million volts[10, 11] and

---

[10] Fristrom, R.M., Oyhus, F.A., and Albrecht, G.H., Charge Buildup on Solid Rockets As a Frame Burst Mechanism, ARS Journal, 32:1729-1730 (1962).

[11] Nanevicz, J.E., and Hilbers, G.R., Titan Vehicle Electrostatic Environment, Technical Report AFAL-TR073-170, July 1973.

average member of electrons in the plume of 10^{10} e/cm^3 [12]. With reference to the latter phenomena, thermodynamic predictions of the thermal ionization of species such as

$$Al_2O_3 \rightleftharpoons Al_2O_2^+ + O^- \quad (1)$$

$$+$$

$$HOH \rightleftharpoons H^+ + OH^- \quad (2)$$

etc.

support the premise. If it is assumed that the net results of the phenomena is to provide a charge separation effect, then the plume might be envisioned as taking on one charge and the spacecraft (and payload) the opposite charge. This, then, could provide one driving mechanism for the recirculation of some of the plume products (see Figure 1A).

The collisional mechanisms were an outgrowth of a microcosmic consideration of the burn history of a typical SRM. First, it is clear that when combustion occurs at the solid combustion plume interface, explosion and ejection from the surface of various sized burning propellant pieces occur. As these are subsequently ejected out of the nozzle, they continue burning and are ultimately consumed. Yet, some of the larger particles have been observed to still be burning even after they have left the nozzle. This indicates a distribution of velocities and sizes of ejected species in the plume. This then suggests the possibility of larger, slower moving particles in the plume being impacted by smaller, faster moving particles which can then rebound and provide a source of

---

12. Smith, Felix T., and Gatz, Carole R., Chemistry of Ionization in Rocket Exhausts, Paper presented at the ARS Ions in Flows and Rocket Exhausts Conference, Palm Springs, CA. (1962).

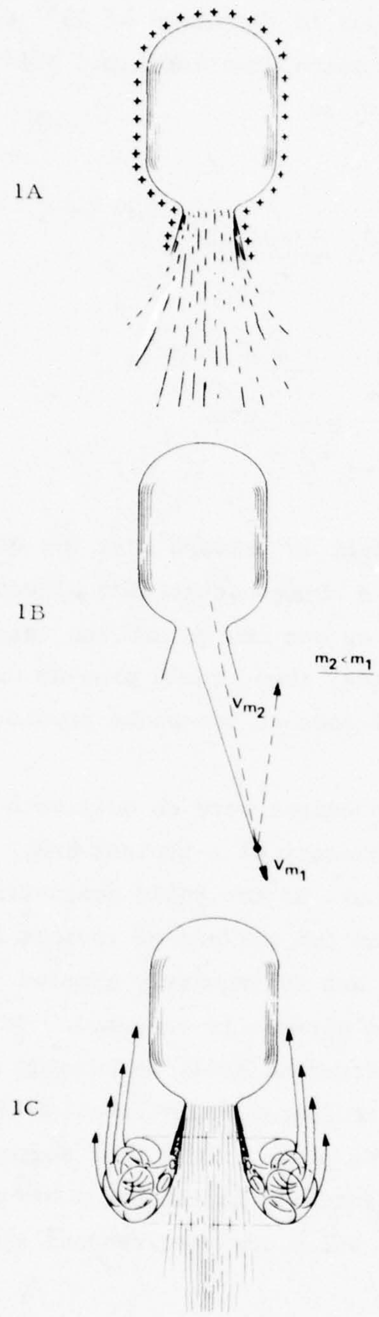

FIGURE 1 CONTAMINATION RECIRCULATION MODELS

recirculation contamination (see Figure 1B). It is noteworthy that the classical inviscid flow Prandtl-Meyer expansion of a plume into a vacuum has been studied and has been able to predict plume products up to as far as 120° from the axis of the rocket. But, attempts to analyze the plume rigorously were unsuccessful even though theoretical considerations clearly state that a 180° recirculation was possible[14]. An alternate approach involving a statistical approach was subsequently selected and is described in the analytical sections.

The "boundary flow" mechanism was postulated because of the recognition that the nozzle wall boundary turbulence was at once a possible explanation for slower moving species in the plume and for a way in which the species could "turn the corner." Previous work at Lockheed Aerospace Corporation[15] gave some insight into how these phenomena could occur but the analysis was only carried to indicate species up to approximately 120° from the axis of the rocket. Since an explanation for recirculation in the 120° to 180° range was sought, an approach was invoked which identified three possible sources of rearward flowing material which could be formulated analytically. First, the presence of a shock wave and the related base-flow, boundary layer separation was assumed per Weinbaum et al.[13] Next, the effect of the nozzle turbulent boundary-layer on mass fluxes beyond the theoretical limiting angle was considered. Finally, the existence, in the vicinity of the nozzle exit, throughout the firing period, of a torus or vortex ring of particles experiencing high rotations, was formulated. The subsequent dissipation of this "doughnut" of particles then gave rise to a vector distribution of particle velocities some of which were oriented so as to provide a continuous source of material for recirculation contamination (see Figure 1C).

13. Weinbaum, Sheldon and Weiss, Robert F., Hypersonic Boundary Layer Separation and the Base Flow Problem, AIAA Journal, 4 No 8: 1321-1330 (1966)

14. Grimson, J., Advanced Fluid Dynamics and Heat Transfer, McGraw Hill, 1971.

15. Private communication with M. Fong et al, Lockheed Missiles and Space Division, Sunnyvale, CA.

In the following section, a more detailed description is provided of the way in which the three mechanisms were formulated. The description will include an identification of the analysis flowcharts utilized to make the recirculation contamination predictions. The input data used for these models is summarized in Figures 2, 3, and 4.

3.0 ANALYTICAL MODELS

3.1 Charge Separation

The objective of the charge separation model is to predict recirculation flux of particles from the solid rocket plume due to electric fields. These electric fields have been studied extensively and arise from charging effects due to thermal ionization and triboelectric processes.[11,12,16,17] The charge builds up on the spacecraft surface and exerts a force on any charged particles in the plume. The force can be substantial enough to explain a significant return flux of particles which impinge on sensitive satellite surfaces.

In order to model the process, some assumptions had to be made. The return flux is obviously dependent on several of the parameters in question. For instance, the greater the velocity of the particle, the greater its probability of escaping the pull of the electric fields, but the greater the charge on the particle the greater its probability of

16. Cole, B.N., Baum, M.R., Mobbs, F.R., An Investigation Of Electrostatic Charging Effects in High-Speed Gas-Solids Pipe Flows, Proceedings of The Institute of Mechanical Engineers, 184 (pt. 3C): 77-83 (1969).

17. Maise, George, and Sabadell, Alberto J., Electrostatic Probe Measurements In Solid Propellant Rocket Exhaust, AIAA Journal, 8 (No. 5): 895-901 (1970).

INPUT DATA

Engine Specifications:

	Max. Propellant Weight	21,400 lbs
	Expended Inerts	214 lbs
	Total Impulse	6,266,000 lbs
	I_{sp} (effective)	292.35 sec.
	Burn Duration	156 sec.
	Chamber Pressure	P_c = 600 psi
Nozzle	Throat Diam.	6.25 in.
	Exit Diam.	56.5 in.

$\gamma = 1.12$

Exit Mach No. M = 4

FIGURE 2

Fuel Composition	% Wt
NH_4ClO_4	68%
Al	18%
$C_{11}H_{26.6}O_{.2}$ (Binder)	12.94%
$C_{22}H_{42}O_4$ (Cat.)	1.06%

FIGURE 3

INPUT DATA (Continued)

Constituent	Wt %
Al_2O_3	34.02
CO	26.27
CO_2	3.01
Cl	.001
H	.0001
HCl	21.11
H_2	2.76
H_2O	4.72
N_2	8.11

FIGURE 4 PRODUCTS OF COMBUSTION

recirculating. Greater particle mass also increases escape probability, and other factors influence this probability to a lesser extent. In light of this it is seen that recirculation is very sensitive to particle parameters. Thus an effort must be made to determine accurately the distribution of all these parameters, and fit Gaussian distributions to them for use in a random number computer subprogram. It was found that the particle size distribution in the plume could be described by a dual Gaussian distribution with peaks about the means of .1μ and .3μ.[18] The .3μ peak had 80% of the amplitude of the .1μ peak and their standard deviations were .1μ. In order to simulate this curve in the computer program five particles were chosen from the .1μ distribution for every four particles chosen from the .3μ distribution. The velocity of the particles was calculated to be normally distributed about an average of 3688 meters/second with a standard deviation of 1000 meters/second and normally distributed in a mean direction of 0° with respect to the longitudinal axis and a sigma of 16°.[19,20] The charges on the particles were chosen to be normally distributed about an average of 10 electrons and a standard deviation of 10 electrons.[12] The final distribution describes the radial position at which the particle leaves the nozzle. When preliminary computer runs revealed that the return flux was relatively insensitive to choice of radial position, a radial position distribution was selected as an initial working value. This distribution described more particles as originating at the center of the nozzle with less emanating closer to the nozzle wall. Thus the distribution was chosen to have an

---

[18] Personal communication with E. Borson, Aerospace Corp., Nov. 1977.

[19] Kliegel, James R., Gas Particle Nozzle Flows, Chemical Reactions and Phase Changes in Supersonic Flow.

[20] Hoffman, R.J. et al, Plume Contamination Effects Prediction: The CONTAM Computer Program Version II, AFRPL-TR-73-46 (1973) Final Report, Contracts F04611-70-C-0076 and F04611-72-C-0037, McDonald Douglas Astronautics Corp.

average radial position of zero and a standard deviation numerically equal to the nozzle radius, .72 meters. Other assumptions in the computer analysis are that the rocket is in steady state operation, the charge distribution over the spacecraft is uniform and the spacecraft is modeled as 6 cylinders atop one another representing different segments of the entire spacecraft (Figures 5, 6). In order to keep the model as conservative as possible, Al_2O_3 was chosen from the thermodynamically calculated table of combustion products (Figure 4) to represent the contaminants. Although it is realized that some unidentifiable condensates must also be present in the exhaust products contamination, it was felt that the high density of Al_2O_3 would keep our results conservative. It was also felt that most of the gaseous products would not adhere to satellite surfaces, even at low temperatures, whereas Al_2O_3 particles, once they adhered, would tend not to re-emit. For these reasons, Al_2O_3 particles were chosen as representative of the return flux and contaminants.

The modeling approach was to randomly choose a particle according to the distributions above and then step the particle through a series of time increments in order to trace its trajectory. The particle is never allowed to travel more than one meter before its position, velocity, and the force acting upon it are recomputed. Thus the entire trajectory of the particle relative to the rocket is described and its impingement location recorded. The masses of the impinging particles are summed to give the total mass contamination on the surfaces of the satellite and the rocket. These numbers are further divided by the areas of the sensor and rocket respectively to give the density of contamination in g/cm^2. In order to save computation time the escape energy divided by the charge was used to predict, a priori, what particles would not return and these were rejected from consideration and not calculated. In terms of the Gaussian distributions, the following relation was derived from the equation of motion:

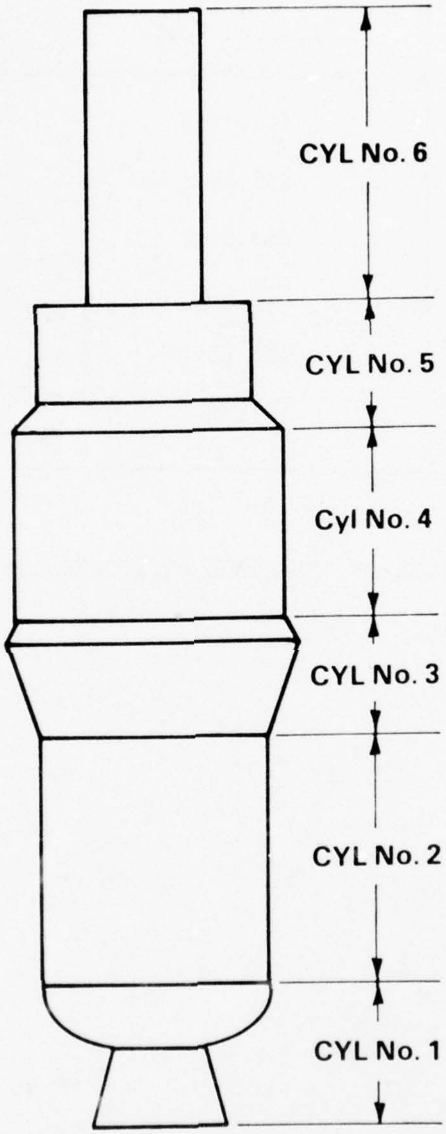

FIGURE 5 SPACECRAFT MODEL

Cylinder No.	Diameter (cm)	Length (cm)
1	213.36	149.86
2	231.14	251.46
3	289.56	119.38
4	277.88	203.20
5	218.95	114.30
6	114.30	304.80

FIGURE 6 DIMENSIONS OF IDEALIZED CYLINDRICAL SURFACES

$$\frac{mv^2}{Q} \leq \frac{4}{3} \pi \frac{(r-\sigma_r)^3 \; (v-\sigma_v)^2}{Q + \sigma_q} \tag{3}$$

where the σ_x's are the standard deviations of the distributions of their subscripts (r refers to particle radius, v to velocity, and q to charge). Thus only particles satisfying this relationship would be calculated by the iterative approximation of the trajectory described above. The analysis flowchart is indicated in Figure 7.

The trajectories and impingement locations were printed by the computer for every particle, and it was observed that most particles with high charge tended to recombine in the plume while particles of large mass because of their energy (the force being charge dependent and not mass dependent) tended to escape, as was the case of particles with large velocity. Thus particles with low mass and velocity and low average charge tended to recirculate (sometimes in rather large arcs) to impinge on the modeled surfaces. More generally tended to impinge on the surfaces closer to the nozzle, the probable explanation being their proximity to the plume and its greater charge due to its larger area (the surface charge distribution being assumed to be constant as a first approximation). The impingement results are summarized in Figure 10 in terms of gm/cm^2.

The model is limited, of course, by its calculation of finite elements of the trajectory and the input data and assumptions. The assumption that the electrical effects act independently of the vortex turbulence and collisional processes is the most obvious one that will have to be eliminated in further contamination studies. The model will have to couple the effects of all three in order to give an accurate

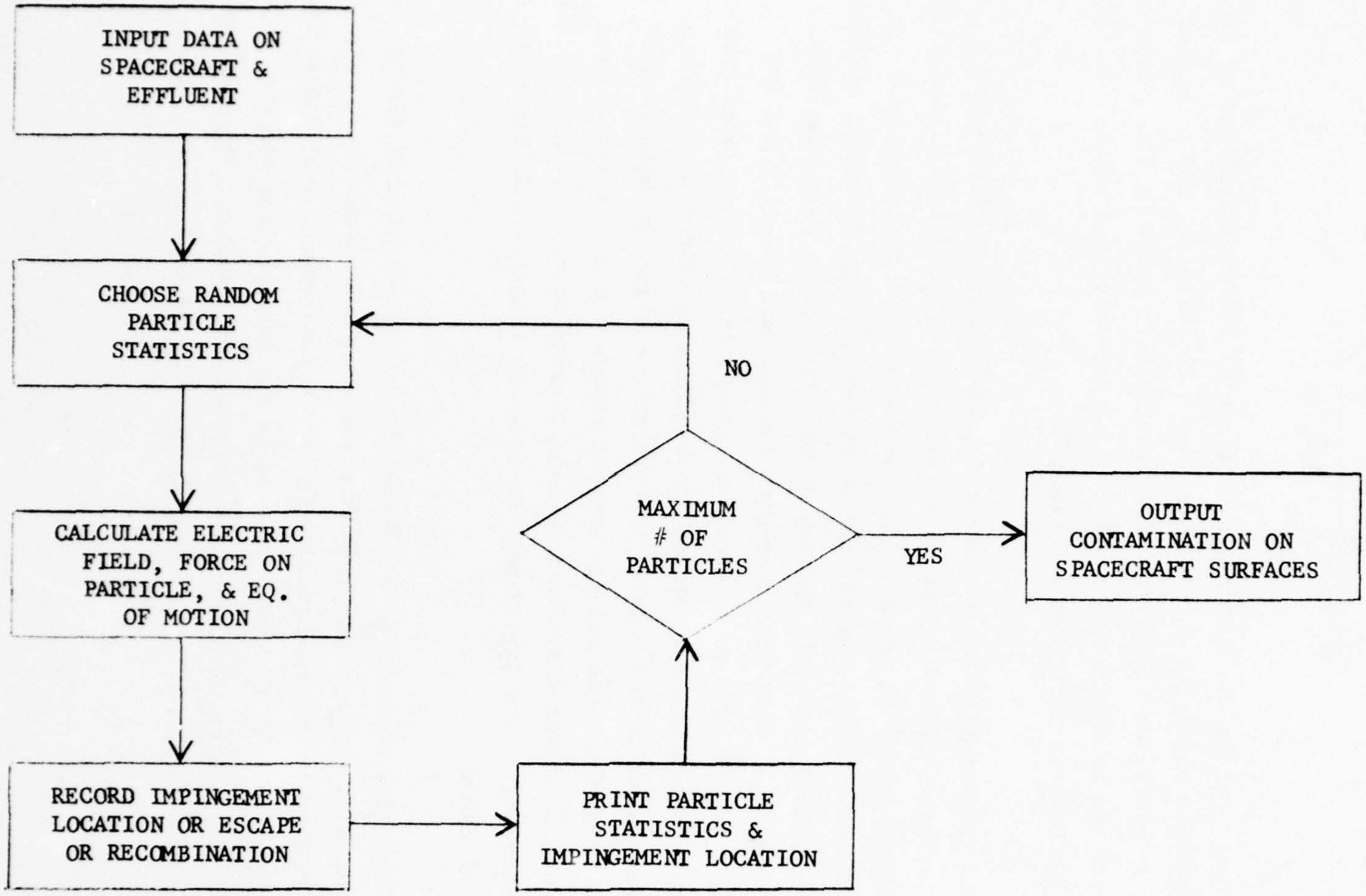

FIGURE 7 CHARGE SEPARATION ANALYSIS FLOW CHART

account of what is going on in the plume. Better distributions for particle velocities, charges, and densities will be obtained as the engine is tested and experiments are done. Better data on the effluents and the magnitude of the engines' charging effects will also be obtained and included in future modeling efforts.

3.2 COLLISIONAL

Of primary interest in the dynamics of Rocket Plumes is the manner in which the intermolecular and interparticle collisions influence the flow fields. Collisional processes were postulated to be a possible mechanism by which recirculation occurs. In order to facilitate the calculations involved in such a model, some plausible assumptions had to be made. The first of these involved the particle size distributions and were based upon calculations done as part of plume impingement studies at NASA MSFC[21]. A bimodal Gaussian size distribution was assumed with a mass fraction of .55 for submicron particles with an average size of .178μ and a mass fraction of .45 for micron particles with an average size of 1.78μ. The geometry of the spacecraft was modeled as six cylinders atop one another representing the different segments. Start-up and shut-down transients were ignored and only steady state operation was investigated. The particle density in the plume was assumed to have a $1/r^2$ dependence in distance from the nozzle and be limited by the 16° maximum cone angle calculated in the CONTAM computer code[19]. The assumption was made that the plume interparticle collision frequency could be described by the classical statistical Boltzmann approach using densities, mean free paths, and collisional cross sections. Probably the least valid assumption was that the collisional processes were independent of the electrical forces or turbulent vortices. This is obviously not true, but as a first rough approximation, to be

---

[21] Personal communication with Ron Kessler, NASA, MSFC, Oct. 1977

improved by later integration of the three models in a more rigorous model, it was judged expedient in order to permit solution of the independent models.

The approach was essentially statistical in nature. A Lambertian distribution of rebound directions was used to predict the impingement location. The location of the collision was given in cylindrical coordinates as (r_1, θ_1, z_1) and the particle rebounded at the classical velocity given by a totally elastic collision to a position (r_2, θ_2, z_2). An integral was derived which gave the deposition expected at Point 2 resulting from collisions at all Points 1 incorporating all the assumptions of the model. This equation is:

$$M = \int_0^t dt \int_{z_2'}^{z_2''} dz_2 \int_{M_{MIN}}^{1/10\, M_{MAX}} dM_1 \int_{M_1}^{M_{MAX}} dM_2 \int_{v_{MIN}}^{1/2\, v_{MAX}} dv_2 \int_{2v_2}^{v_{MAX}} dv_1 \int_0^{r_1'} dr_1 \int_{r_N}^{r_N + r_1 \mathrm{TAN}\, \varphi} dz_1$$

$$\times \left(\frac{8kT}{\pi \mu} \right)^{1/2} \left(\frac{\pi (d_1 + d_2)^2}{4} \right) \frac{N(M_1)\, N(M_2)}{\pi^2 (r_N + z_1 \mathrm{TAN}\, \varphi)^4 v_1 v_2 t^2}$$

$$\times\ G(v_1, v_2) \quad V(r_1, \theta_1, z_1, r_2, \theta_2, z_2) \tag{4}$$

where

t = time

(r_1, θ_1, z_1) = collision location

(r_2, θ_2, z_2) = impingement location

r_N = nozzle radius

m_1 = mass of smaller particle

m_2 = mass of larger particle
m_{min} = minimum mass of particles
m_{max} = maximum mass of particles
v_1 = velocity of smaller particle
v_2 = velocity of larger particle
v_{min} = minimum velocity of particles
v_{max} = maximum velocity of particles
k = Boltzmann constant
T = temperature
d_1 = diameter of smaller particle
d_2 = diameter of larger particle
$N\ (m)$ = number of particles of mass m
φ = maximum angle of particle effluents
μ = reduced mass of two particles
$G(v_1\ v_2)$ = bimodal Gaussian for particle velocities
$V(r_1,\theta_1, z_1,r_2,\theta_2, z_2)$ = Vector quantity dependent on Geometry

The computer analysis flow chart is indicated in Figure 8. This integration resulted in the total mass impingement on the spacecraft surfaces. The results as summarized in Figure 10 show no expected contamination from collisional processes.

This model is fundamentally limited by its assumption, but all attempts were made to keep it conservative. It is, however, a valid first approximation, being a conservative approach that was at the same time based upon realistic parameter values. Further refinements will include more exact modeling of the spacecraft and better data on adhesion. However, by far, the most important refinement of the model will be the integration of the three mechanisms; collisional, charge separation, and boundary flow effects to give a more realistic coupled mechanism which should predict the contamination more exactly.

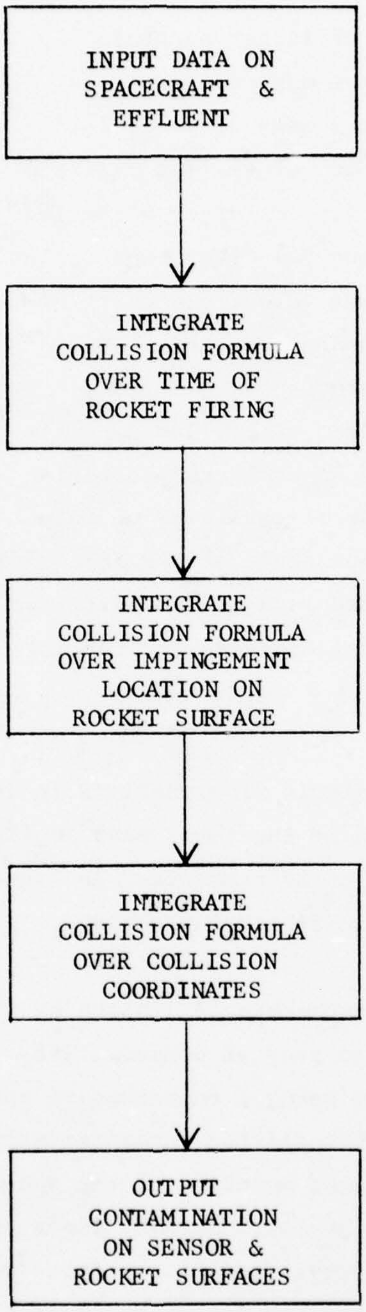

FIGURE 8 ANALYSIS FLOW CHART

3.3 Boundary Flow

The boundary-flow model consists of two parts. First a number of different mechanisms are invoked to explain migration of material to regions surrounding the upstream portion of a vehicle. The mechanisms are examined to determine how this material is directed towards the critical surfaces.

A number of assumptions and simplifying postulates were made to permit development of this model. They are summarized below:

A vacuum environment of 10^{-8} Torr $< P_{ambient} < 10^{-6}$ Torr was assumed and all possible influences from ultra-violet or other radiation were ignored. The surfaces were treated as if they were at uniform surface temperatures and all materials which collided with the critical surfaces were assumed to remain. For simplicity, the targets were treated in the same manner as the previous models; ideal cylindrical surfaces in accordance with the dimensions in Figures 5, 6 (cylinder No. 1 being closest to the SRM nozzle). Of the products of combustion, only Al_2O_3, considered as despositing. All other gaseous products are neglected. It was further assumed that the contaminant deposits are homogeneous and their distribution is uniform on any given idealized cylinder. The deposit density was taken as that of alumina and is in the range 3.5 to 3.9 gm/cm^3 [22].

In addition, the following conditions were postulated: Flow is turbulent in the boundary layer and the fluid is compressible, viscous, and exhibits slightly non-Newtonian properties. Particles were assumed spherical of a maximum size of 3μ[23]. This general size

---

22. Goldsmith, A. and Waterman, T.E., Thermophysical Properties of Solid Materials, Armour Research Foundation WADC-TR-58-475 (1958).

23. Schorr, Morton, Solid Rocket Technology, Wiley (1972).

differs from that selected for the previously described mechanisms because of the manner in which they are generated by the exhaust*. All collisions were treated as elastic. Only the steady-state condition was considered. The engine chamber pressure-time curve during firing was assumed constant over the steady state burn phase. The nozzle was assumed (for simplicity) to be conical instead of contoured and the nozzle half angle was taken as 15^o. From the propellant weight and firing time it was estimated that the resulting average mass flow $\bar{\dot{w}}$ = 137.18 lb/sec.

Starting with a clean nozzle, deposits are postulated to build up quickly on the nozzle walls up to a limiting thickness. This is supported both by experimental evidence and analysis as reported by Colucci[24]. It is believed that the phenomenon is the result of a steady-state condition established by virtue of the deposition of new materials and the simultaneous removal of already deposited material by the flow at the wall. This activity which takes place within the boundary layer where the velocities are relatively low, develops a mass fraction, constituted of relatively large particles, which is a combination of the masses normally present from the exhaust products plus the contributions being made by the material removed from the surface. The flow subsequently becomes fully turbulent[25,26,27] at the nozzle walls with a boundary layer thickness described by the following equation.

*See discussion Pg. 25 on constitution of boundary layer.

[24] Colcucci, S.E., 5th Symposia on Ballistic Missile and Space Technology.

[25] Skelland, A.H.P., Non Newtonian Flow and Heat Transfer, Wiley (1967).

[26] Davies, J.T., Turbulence Phenomena, Academic Press (1972).

[27] Marseille, Gordon, The Mechanics of Turbulence, International Symposium of The National Scientific Research Center, (1961).

$$\delta_T = \left\{ \frac{(\beta n+1)\Omega}{\psi} \left[8^{n-1} \left(\frac{3n+1}{4n} \right)^n \right]^\beta \left(N^o_{Re,x} \right)^{-\beta} \right\}^{\frac{1}{\beta n+1}} \qquad (5)$$

The terms of this equation are defined by the following

$$\Omega = \frac{\alpha(0.817)^{2-\beta(2-n)}}{Z^{\beta n+1}}$$

$$\psi = \frac{2-\beta(2-n)}{2(1-\beta+\beta n)} - \frac{2-\beta(2-n)}{2-2\beta+3\beta n}$$

$N^o_{Re,x} = \frac{x^n u_o^{2-n} \rho}{K}$ (a form of Reynolds number for Non-Newtonian fluids)

for a Newtonian fluid $n=1$ and $K=y$

and $N_{Re,x} = \frac{\rho u x}{y}$

where u = velocity

n is a "flow behavior index" for a non-Newtonian flud where $0 \leq n < 1$

K is a "consistency" index analogous to viscosity

x - distance along the surface

f (friction factor in turbulent flow thru smooth tubes)

$$f = \frac{\alpha \gamma_1^\beta}{D^{\beta n} V^{\beta(2-n)} \rho^\beta}$$

$$\gamma_1 = 8^{n-1}K\left(\frac{3n+1}{4}\right)^n$$

α & β are defined as functions of n

D = tube diameter

V = mean linear velocity

If the nozzle is considered as a very thin plate, the subsonic flow in the boundary layer (with a low γ of 1.13-1.3)[27] exhausts into a very high vacuum, under which conditions, compressible flow theory allows a turning angle for the flow of up to 180°. Associated with the back flowing material is a distribution of various combustion products with a total mass, mole fraction and consequent number of particles exhausting at a given instant. If the instantaneous mass flowing through the boundary layer thickness at the nozzle exit plane is summed over the total firing time, the total recirculated mass due to this mechanism results.

In addition, since the fluid is in reality not inviscid[9], there will exist a transition fluid layer between the turbulent flow boundary layer and the free stream. In this transition region, particles will be experiencing high rotation,[12,29,30] resulting in the creation of a

---

28. Thompson, Philip A., Compressible Fluid Dynamics, McGraw Hill (1974).

29. Hoglund, Richard F., Recent Advances in Gas Particle Nozzle Flows, ARS Journal, 32:662-671 (1962).

30. Tchernov, Alexander, Izvestiyn Akademii Nauk Kazakhskoi (SSR), Scriga Energetich, #8 (1955).

torus or vortex ring at the nozzle exit plane[31,32]. This grows to a certain size and provides a contamination source via one of two possible mechanisms: (1) the toroid separates from the main stream and migrates upstream, where it dissipates and forms a contaminant cloud,--these toroids are periodically formed during the entire firing time; (2) the toroid spalls off materials tangentially as it is being continuously fed by the exhaust products--some of the material having the appropriate vector velocity constitute the back flow contamination potential. For purposes of this study the former (migrating toroid) mechanism runs was invoked in evaluating the model. If the instantaneous masses in the toroids are summed over the firing time, total mass attributable to this mechanism results. Subsequent studies will deal with a steady -state torus expelling material into the backflow region.

Several additional phenomena may come into play to augment the back flow of the potential contaminants. For example, the effects of the high velocities, the step geometries at the nozzle edge, and the density distributions can generate severe curving shock waves in this regime.[13] These shock waves may act to direct the effluents in the reverse flow direction. Also, recent experimental and analytical evidence indicates that significantly greater mass fluxes than heretofore suspected exist at the Prandtl-Meyer limiting stream line of the plume[8,9].

For the model under investigation, here, the mass contributed by this mechanism is derived as follows: a gas density distribution function is given by

$$f(\theta) = f(\theta_o)\, e^{-\beta(\theta-\theta_o)} \tag{6}$$

---

31. Prandtl, Ludwig and Tietjens, O.G., Fundamentals of Hydro and Aerodynamics, Dover (1957).

32. McCormack, Percival D., Vortex Ring and the Plate Jet, AIAA Journal, (April 1969).

where it is assumed that the streamline at the edge of the boundary layer turns through some angle θ_o. The equation is valid for $\theta > \theta_o$. For $0 < \theta < \theta_o$ a cosine law was proposed and is given by

$$f(\theta) = \cos^{\left(\frac{2}{\gamma-1}\right)} [(\pi/2)(\theta/\theta_\infty)] \tag{7}$$

where

θ_∞ is the value of the limiting angle, θ_ℓ, for inviscid supersonic flow

β and θ_o are functions of the nozzle exit condition and are given by

$$\beta = A[\gamma+1)/(\gamma-1)]^{\frac{1}{2}} (2\,\bar{U}_\ell/U_\ell)(R_e/2\delta)^{\frac{\gamma-1}{\gamma+1}} \tag{8}$$

where A is a constant and corresponds to a normalization factor for plume density given by:

$$A = \frac{U^*/2U_\ell}{\int_o^{\theta_\ell} f(\theta \sin\theta \, d\theta}$$

in which U^* is the sonic velocity, U_ℓ is the limiting velocity of the gas defined by

$$U_\ell = [(\gamma+1)/(\gamma-1)]^{\frac{1}{2}} U^*$$

and θ_ℓ is the limiting turning angle of gas at the nozzle exit.

θ_o is approximated by

$$\theta_\infty \left[1 - (2/\pi(2\delta/R_e)^{\frac{\gamma-1}{\gamma+1}}\right]$$

AD-A070 386 AIR FORCE MATERIALS LAB WRIGHT-PATTERSON AFB OH F/G 22/2
PROCEEDINGS OF THE USAF/NASA INTERNATIONAL SPACECRAFT CONTAMINA--ETC(U)
1978 J M JEMIOLA
UNCLASSIFIED AFML-TR-78-190 NL

5 OF 13
AD
A070386

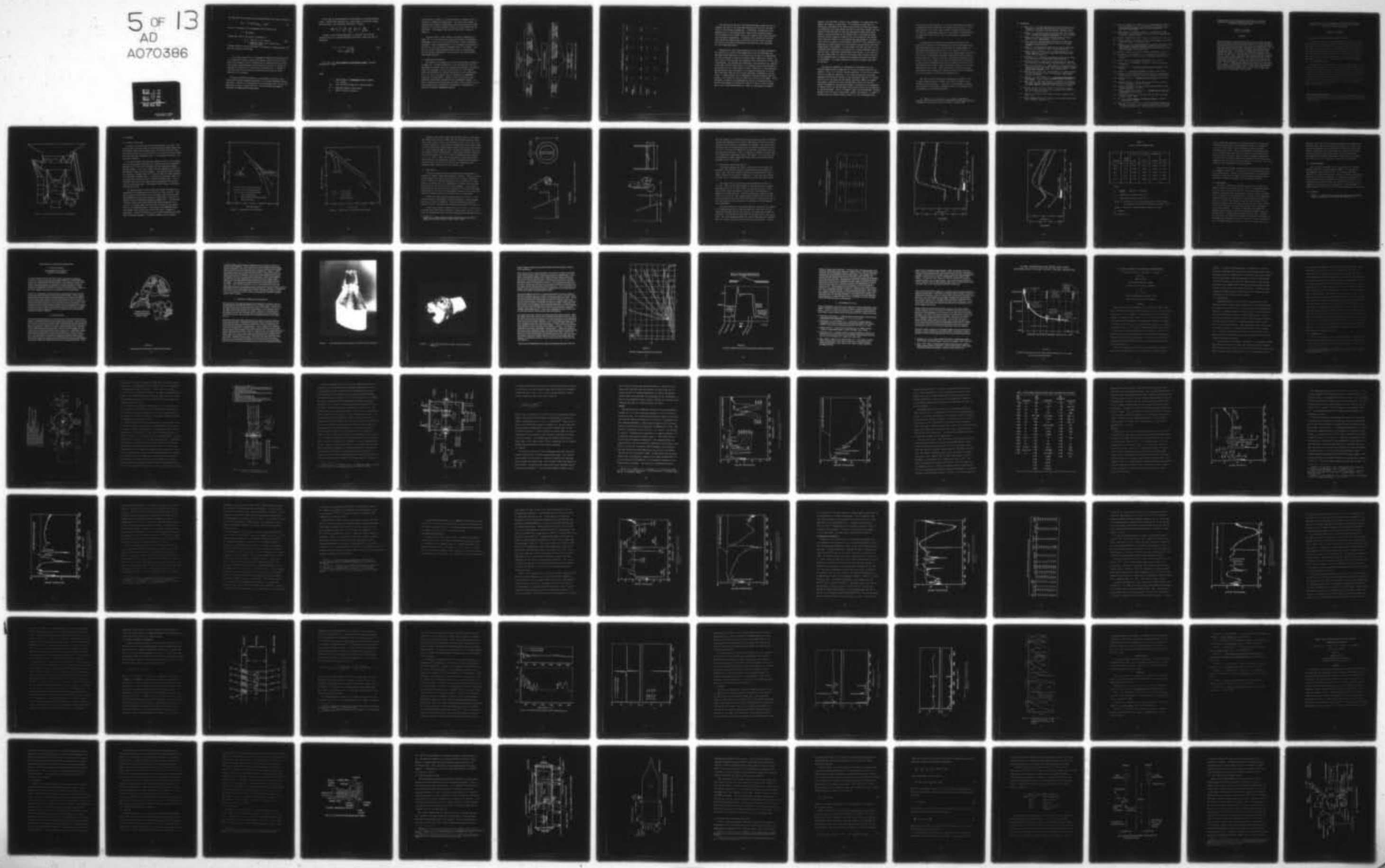

The mass flow in the portion of the plume defined by the above is given by

$$dm = -2\pi R_e (\rho U/\rho_e U_e)_{B.L.} \rho_e U_e dy \tag{9}$$

where y is location of the streamline from the nozzle wall

ρ = gas density

whereas mass flow in the plume is expressed by

$$dm = \rho(\bar{U}/U_\ell)U_\ell \, 2\pi r^2 \sin\theta \, d\theta \tag{10}$$

r = spherical radius from a point source with the nozzle

The mass backflow from this mechanism is evaluated by summing Equation (9) over the <u>y</u> and the firing time.

Since fluxes described by the exponential density distribution occur in the plume far-field at stream angles greater than 90° from the flow axis, their presence yields a rearward flow of material which interacts with already rearward moving existing material (see above), thereby increasing the potential for recirculation contamination. It should be noted that the above postulated mechanisms hold only during vacuum operation of the engines.

The basic analytical procedure is to determine the number of particles resulting in the masses generated by the various mechanisms identified above. Portions of the particles in each mechanism will fly off into space and not affect vehicle surfaces. Other particles will deposit according to mechanisms described below.

One of the driving mechanisms is the influence of existing electric fields. Soo[33] derives equations for a large number of uniformly charged solid particles. For a particle initially at radius R

$$v \frac{dv}{dr} = \frac{1}{\epsilon_o} \left(\frac{q}{m}\right)^2 \frac{M_R}{4\pi r^2} - \frac{12}{\rho_p \epsilon_o} \frac{\epsilon_r - 1}{\epsilon_r + 2} \left(\frac{q}{m}\right)^2 \frac{M_R^2}{(4\pi)^2 r^5} \tag{11}$$

Another of the driving mechanisms is collisions with existing products built up by toroidal migrations for which a mean free path is calculated:

$$\lambda_B = \frac{1}{\pi \sum_C n_C d_{BC} \sqrt{1 + \frac{m_B}{m_C}}} \tag{12}$$

where

n - number density of appropriate exhaust product i.e., specie C

d_{BC} - avge. molecular diameter of combined product

m - molecular weight of each specie

λ_B - mean free path for specie B

---

[33] Soo, S.L., Fluid Dynamics of Multiphase Systems, Blaisdell Publishing Co. (1967).

From the point of impact, a particle/molecule is assumed to be reflected in a Lambertian distribution. The return flux through a 2 steradian solid angle is determined by calculating molecular column densities in a series of annular volumes at various radii from the spacecraft. The boundary flow Analysis Flow Chart is shown in Figure 9.

From the results of the boundary flow model, summarized in Figure 10, it can be seen that a significant amount of contaminant impingement can occur on the various surfaces. These calculations represent a severe understatement of the contamination potential in view of the very conservative assumptions made in the model. As in the case of the charge separation model, the true contamination picture requires integration of all the models and would probably yield higher deposits.

4.0 RESULTS AND DISCUSSION

The summary of the results of the analytical model is presented in Figure 10. If simple additivity of the contributions from the mechanisms is assumed, the total contribution deposited on cylinder 6 (which can represent a critical payload area) 16 x 10^{-7} gm/cm^2, would be unacceptable for systems as described in the introduction. It is, of course, recognized that the assumption of homogeneous deposition is questionable. However, there are both space and laboratory experimental indications that condensable products as well as superfine particulates may constitute a fair fraction of the recirculated product and thereby both behave as condensables to provide a relatively homogeneous deposit.

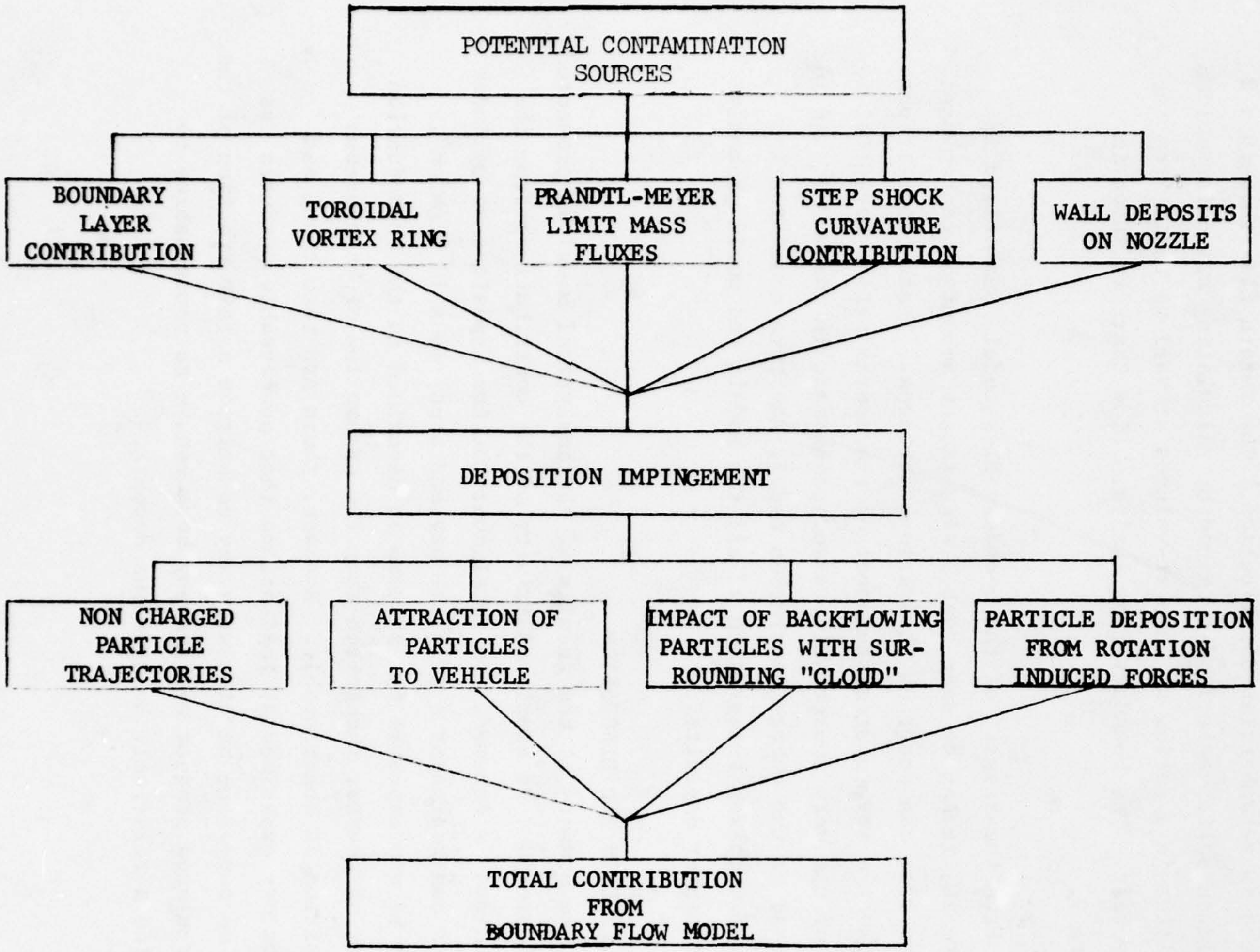

FIGURE 9 BOUNDARY FLOW ANALYSIS FLOW CHART

	IMPINGEMENT ($gm/cm^2\ 10^{-7}$)					
MODEL	CYL. 1	CYL. 2	CYL. 3	CYL. 4	CYL. 5	CYL. 6
Charge Separation	62	45	28	17	9	5
Collisional	negl.	negl.	negl.	negl.	negl.	negl.
Boundary Flow	150	150	140	107	71	11
TOTAL	212	195	168	124	80	16

FIGURE 10 ACCUMULATIVE IMPINGEMENT

The conservative nature of the approach becomes evident when it is realized that none of the individual mechanisms account for the possibility of recirculated condensables. Furthermore, integration of the mechanisms into a consolidated model (rather than an additive model) would introduce cross coupled terms in the equation which would increase the calculated contamination. In addition, the contribution from the start-up and shut-down phases of the SRM burn would further increase the actual recirculation contamination potential over that estimated for the steady-state phase.

Questions have been raised regarding the rate of charge dissipation on a particle in a rocket plume plasma and it has been mentioned that particles would indeed have to recirculate on the order of a millisecond in order to impinge on sensitive surfaces before losing their charge. In fact, times of recirculation have generally been calculated to be less than a millisecond. The question has subsequently been postulated that prohibitively high velocities would have to be attained in order for particles to recirculate in such a short period of time. Velocities of that magnitude and much greater were calculated in the computer program and it is felt that these high velocities are in fact physically attainable by the particles. A plasma sheath due to atmospheric ionizing collisions with the surface of the spacecraft was not taken into account in this model. At the altitudes of interest this phenomenon may not be a substantial effect. Further investigation is warranted to see if in fact it will be present and, if so, to determine whether its effect is substantial or minimal.

However, the first SRM is fired in the ionosphere in a region where the ambient ion density is quite high. It is therefore likely that if a charge were to develop on the rocket surface that the field lines would be terminated on the ions present and that the particles emitted from the exhaust of the SRM would not even be influenced by these field lines. However, the effectiveness of the ambient ions in shielding the plume from the surface charge is related to the total voltage on the surface. From literature research it is estimated that the voltage on the spacecraft could be as much as a half million volts.[10,11] With voltages of this magnitude the Debye lengths are on the order of several meters and could indeed affect recirculation. Further models will take the effect of the ionosphere more rigorously into account but in this preliminary study it was felt that it would not substantially alter results. It is also true that the second rocket is fired at sufficiently high altitude to be out of the ionosphere and thus greater recirculation from electrical forces is anticipated. Its closer proximity to sensitive surfaces will also be a factor.

The question regarding the likelihood of the adherence of the aluminum oxide particles impacting the critical surfaces should be considered. First, it is obvious that the particles, if they do recirculate, will be hot from the combustion in the rocket and may have sufficient thermally-derived kinetic energy so that collisions would not be "sticky." Whether or not the particles can radiate sufficient energy in transport from plume to satellite so that sticking would occur is not evident without refinement of the analytical models. Alternately, the assumption of charge effects and van der Waals forces could account for the adherence of the particulates. Also a "fly-paper" effect from contaminants initially present on the critical surfaces might augment the adhesion. It might be expected that cold target surfaces could retain the contaminants more effectively than warm surfaces so that the accumulative recirculation contamination effects might only be observed on the former. In the last analysis, since space flight evidence strongly indicates that recirculation contamination does occur, some effect or combination of the described effects must account for the observed contamination phenomena.

Preliminary joint efforts by the Aerospace Corporation and Aerojet were carried out to experimentally verify recirculation with both small SRMs and the full scale IUS motor in vacuum chambers at Arnold Engineering Development Center. The results,[34] while inconclusive, did demonstrate the presence of aluminum oxide, carbon and other, as yet, unidentified apparently condensable products forward of the nozzle end. However, questions concerning the validity of the results in the test chamber led to the conclusions that the question of recirculation contamination potential of SRMs will have to be resolved either with further refined laboratory testing or in an actual instrumented space flight. These possibilities are being actively pursued and further preliminary laboratory testing will be considered for the development of appropriate instrumentation.

The authors wish to graciously acknowledge the support of the Air Force program F04701-77-C-0010, under which portions of this information were developed. In addition, special thanks are given to E. Borson of the Aerospace Corporation for his contributions and participation in the program described.

34. Maag, Carl R., and Scott, R.R., Ground Contamination Monitoring Methods, presented at the USAF/NASA International Spacecraft Contamination Conference, Colorado Springs, Colorado (1978).

5.0 REFERENCES

1. Maag, Carl R., Backflow Contamination For Solid Rocket Motors, presented at the USAF/NASA International Spacecraft Contamination Conference, Colorado Springs, Colorado (1978).
2. Boynton, F.P., Exhaust Plumes From Nozzles With Wall Boundary Layers, *Journal of Spacecraft & Rockets*, 5:1143-1147 (1968).
3. Simons, G.A., Effect of Nozzle Boundary Layers in Rocket Exhaust Plumes, *AIAA Journal*, 12:718-720 (1974).
4. Pearce, Blain E., An Approximate Distribution of Mass Flux in a High Altitude Solid Propellant Rocket Plume, *AIAA Journal*, 12:718-720 (1974).
5. Arnold, F., An Experimental Method For Locating Stream Tubes In A Free Jet Expansion to Near Vacuum, AEDC-TR-69.17.
6. Seubold, Jason G., Edwards, R.H., A Simple Method For Calculating Expansion Of A Rocket Engine Nozzle Boundary Layer Into A Vacuum, Hughes Co.
7. Martinkovic, P.J., Bipropellant Attitude Control Rocket (ACR) Plume Contamination Investigation AFRPL-TR-69-261.
8. Chirivella, Jose E., Molecular Flux Measurements In The Backflow Regions Of A Nozzle Plume, Tech memo 33-620, 1973, JPL.
9. Calia, U.S. and Brook, J.W., Measurements Of A Simulated Rocket Exhaust Plume Near The Prandtl Meyer Limiting Angle, *Journal Spacecraft and Rockets*, 12(No. 4): 205-208 (1975).
10. Fristrom, R.M., Oyhus, F.A., and Albrecht, G.H., Charge Buildup on Solid Rockets As A Flame Burst Mechanism, *ARS Journal*. 32:1729-1730 (1962).
11. Nanevicz, J.E., and Hilbers, G.R., *Titan Vehicle Electrostatic Environment*, Technical Report AFAL-TR-73-170, July 1973.
12. Smith, Felix T., and Gatz, Carole R., Chemistry of Ionization In Rocket Exhausts, Paper presented at the ARS Ions In Flows And Rocket Exhausts Conference, Palm Springs, CA. (1962).
13. Weinbaum, Sheldon and Weiss, Robert F., Hypersonic Boundary Layer Separation and The Base Flow Problem, AIAA Journal, 4 (No. 8): 1321-1330 (1966).
14. Grimson, J., Advanced Fluid Dynamics and Heat Transfer, McGraw Hill, 1971.
15. Private communication with M. Fong et al, Lockheed Missiles and Space Division, Sunnyvale, CA.

16. Cole, B.N., Baum, M.R., Mobbs, F.R., An Investigation of Electrostatic Charging Effects In High-Speed Gas-Solids Pipe Flows, Proceedings of The Institute of Mechanical Engineers, 184 (pt. 3C): 77-83 (1969).

17. Maise, George, and Sabadell, Albert J., Electrostatic Probe Measurements In Solid Propellant Rocket Exhaust, AIAA Journal. 8 (No. 5): 895-901 (1970).

18. Personal communication with E. Borson, Aerospace Corp., Nov. 1977.

19. Kliegel, James R., Gas Particle Nozzle Flows, Chemical Reactions and Phase Changes in Supersonic Flow.

20. Hoffman, R.J. et al, Plume Contamination Effects Prediction: The CONTAM Computer Program Version II, AFRPL-TR-73-46 (1973) Final Report, Contracts F04611-70-C-0076 and F04611-72-C-0037, McDonald Douglas Astronautics Corp.

21. Personal communication with Ron Kessler, NASA/MSFC, October 77.

22. Goldsmith, A. and Waterman, T.E., Thermophysical Properties of Solid Materials, Armour Research Foundation, WADC-TR-58-475 (1958).

23. Schorr, Morton, Solid Rocket Technology, Wiley (1972).

24. Colucci, S.E., 5th Symposia and Ballistic Missiles and Space Technology.

25. Skelland, A.H.P., Non Newtonian Flow and Heat Transfer, Wiley (1967).

26. Davies, J.T., Turbulence Phenomena, Academic Press (1972).

27. Marseille, Gordon, The Mechanics of Turbulence, International Symposium of The National Scientific Research Center (1961).

28. Thompson, Philip A., Compressible Fluid Dynamics, McGraw Hill (1974).

29. Hoglund, Richard F., Recent Advances In Gas Particle Nozzle Flows, ARS Journal, 32:662-671 (1962).

30. Tchernov, Alexander, Izvestiyn Akademii Nauk Kazekhskoi (SSR), Scriga Energetich, #8 (1955).

31. Prandtl, Ludwig and Tietjens, O.G., Fundamentals of Hydro and Aerodynamics, Dover (1957).

32. McCormack, Percival D., Vortex Ring and the Plate Jet, AIAA Journal, (April 1969).

33. Soo, S.L., Fluid Dynamics of Multiphase Systems, Blaisdell Publishing Co. (1967).

34. Maag, Carl R. and Scott, R.R., Ground Contamination Monitoring Methods, presented at the USAF/NASA International Spacecraft Contamination Conference, Colorado Springs, Colorado (1978).

CONTAMINATION AND HEAT TRANSFER PROBLEMS RESULTING FROM HIGH EXPANSION OF THE SUBSONIC BOUNDARY LAYER FLOW IN THE VOYAGER TE-M-364-4 SOLID ROCKET MOTOR*

Charles J. Leising
Morris L. Greenfield

ABSTRACT

Mass and volumetric constraints dictated that the Voyager Spacecraft science instrument package be located within 40 cm of the TE-M-364-4 Solid Motor exit plane. Although the science was located 100 degrees away from the nozzle centerline, there was still concern about the flow from the subsonic boundary layer overheating and contaminating the instrument surfaces. Preliminary estimates indicated that plume shields would have to be employed, but additional information was required for design. One of the more difficult problems was how to estimate the mass flux. Standard Method of Characteristic solutions are not valid at larger angles and scaled MOLSINK test data seemed to indicate unacceptably high levels. The buildup of flow along the plume shield surface and the amount that would flow around the edge of the shield and impinge on the instruments also had to be calculated. For this latter problem TRW was contracted to use their Monte Carlo program. Confirmation was then obtained with plume instrumentation during the first Block V launch. This paper discusses the plume model, applicable MOLSINK test results, the TRW predictions and the Block V and Voyager flight results.

CONTAMINATION AND HEAT TRANSFER PROBLEMS RESULTING FROM HIGH EXPANSION OF THE SUBSONIC BOUNDARY LAYER FLOW IN THE VOYAGER TE-M-364-4 SOLID ROCKET MOTOR*

Charles J. Leising
Morris L. Greenfield

1.0 DESCRIPTION OF VOYAGER PLUME IMPINGEMENT PROBLEM

To reduce structural mass and remain within a specified envelope inside the Centaur Shroud, the Voyager TE-M-364-4 75.6 kN thrust solid rocket motor was positioned with its exit plane within 40 centimeters of the science instrument package. Even though the science was located 100 degrees away from the nozzle centerline there was still concern that flow from the low velocity boundary layer in the nozzle would expand around the lip, flow backward and overheat or contaminate the instrument surfaces (Fig. 1). The Prandtl Meyer angle for low mach number flow can exceed 150 degrees.

Techniques have been developed to account for the expansion of the supersonic boundary layer but very little has been done to characterize the adjacent subsonic portion. One reason is the lack of valid analytical tools. Streamtube or Monte Carlo techniques could have been used to evaluate the Voyager configuration but no software was available. Hand calculations would have been too tedious and costly, and full scale test data was out of the question because of the cost of the solid rocket motors and the high vacuum requirements. In addition, no applicable flight data could be located.

---

*This paper presents the results of one phase of research carried out at the Jet Propulsion Laboratory, California Institute of Technology, under Contract No. NAS 7-100, sponsored by the National Aeronautics and Space Administration.

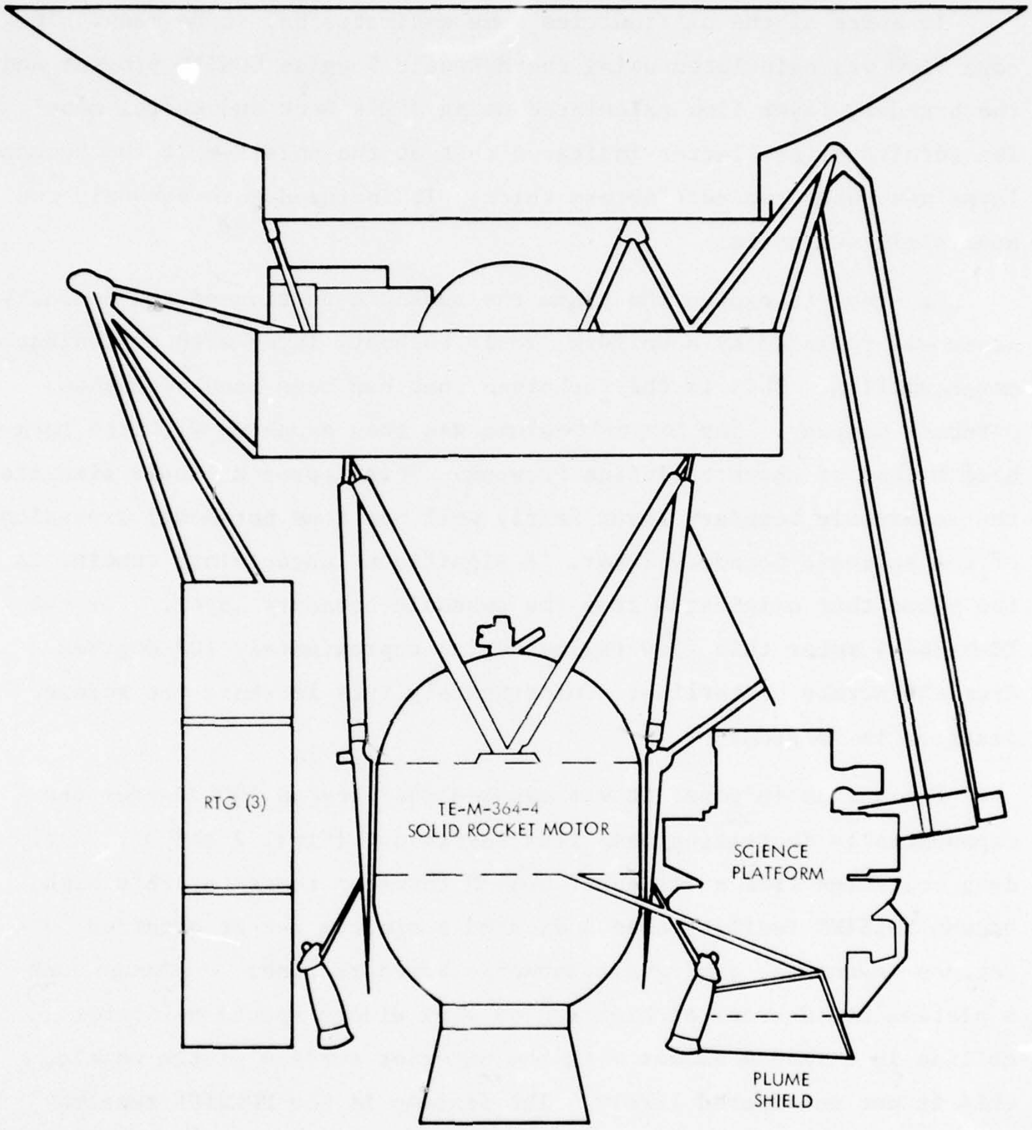

Figure 1. Voyager Spacecraft Prior to Deployment

2.0 APPROACH

2.1 Original Predictions

In spite of the difficulties some estimates had to be made. The core flow was calculated using the McDonald Douglas CONTAM program and the boundary layer flow calculated using JPL's Back and Cuffel model. The results of the latter indicated that at the nozzle exit the boundary layer was about two centimeters thick. It included both subsonic and supersonic sublayers.

In order to expand the plume the subsonic portion of the boundary layer was replaced by a uniform, sonic boundary layer with equivalent momentum flux. This is the technique that has been used by Hughes Aircraft Company. The composite plume was then expanded with the Lockheed Method of Characteristics Program. This approach should simulate the supersonic boundary layer fairly well but does not model expansion of the subsonic boundary layer. A significant uncertainty remains in the plume that originates from the subsonic boundary layer. For the TE-M-364-4 motor this flow regime begins approximately 100 degrees from the nozzle centerline. Unfortunately this is where the science platform is located.

For design purposes it was assumed that beyond 100 degrees the exponentially decreasing mass flux levels out (Figs. 2 and 3). Early data collected from a series of 0.44 N thruster tests in JPL's high vacuum MOLSINK facility also indicated a plateau but it occurred 30 degrees beyond the supersonic-subsonic boundary line. Although such a plateau could occur at high angles when widely spaced molecules collide in a random manner with the exterior surface of the nozzle, this is not considered likely. The plateau in the MOLSINK results was probably due to reflection off the cell walls. Because of uncertainty in how to interpret the test results estimates were made with a 100 degree plateau, a 130 degree plateau, and no plateau.

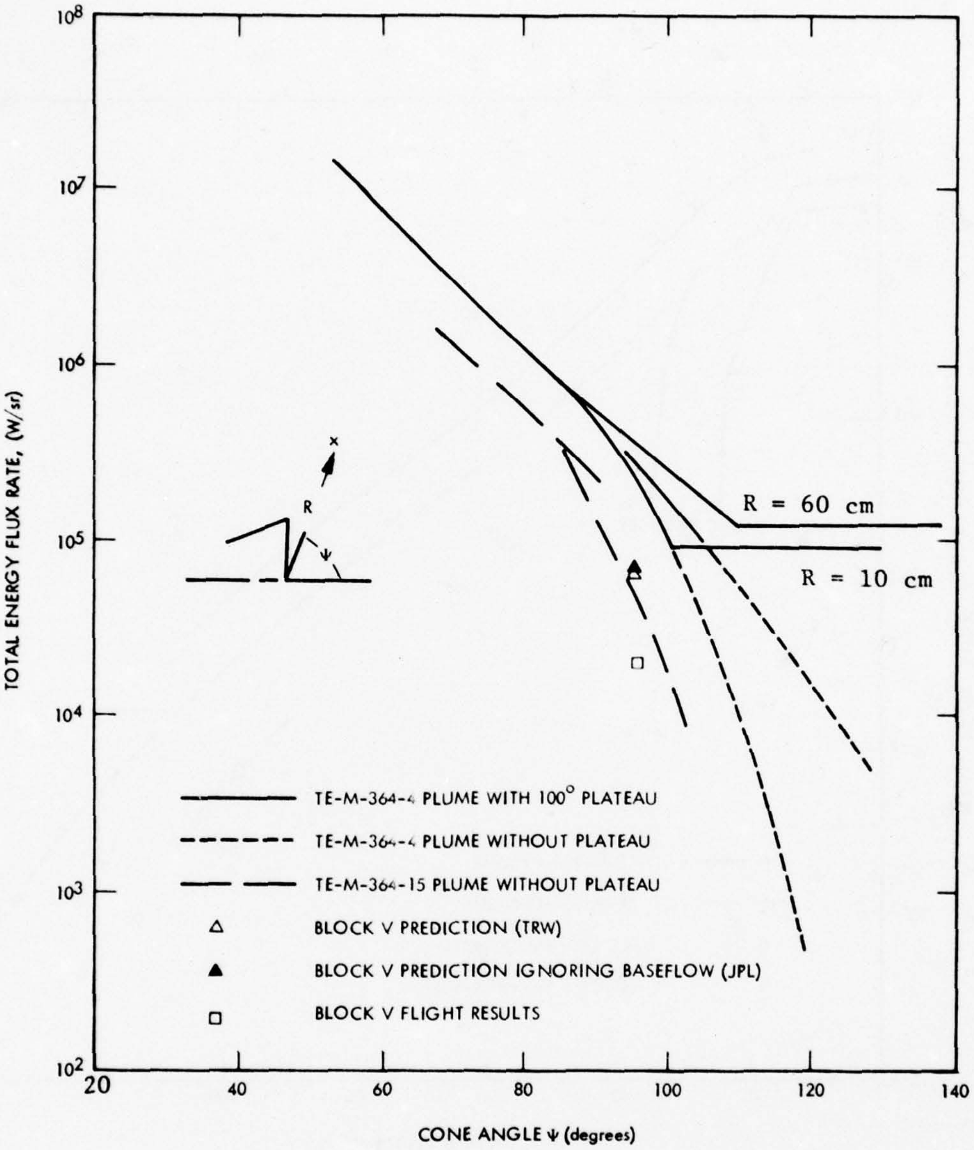

Figure 2. Energy Flux vs. Cone Angle

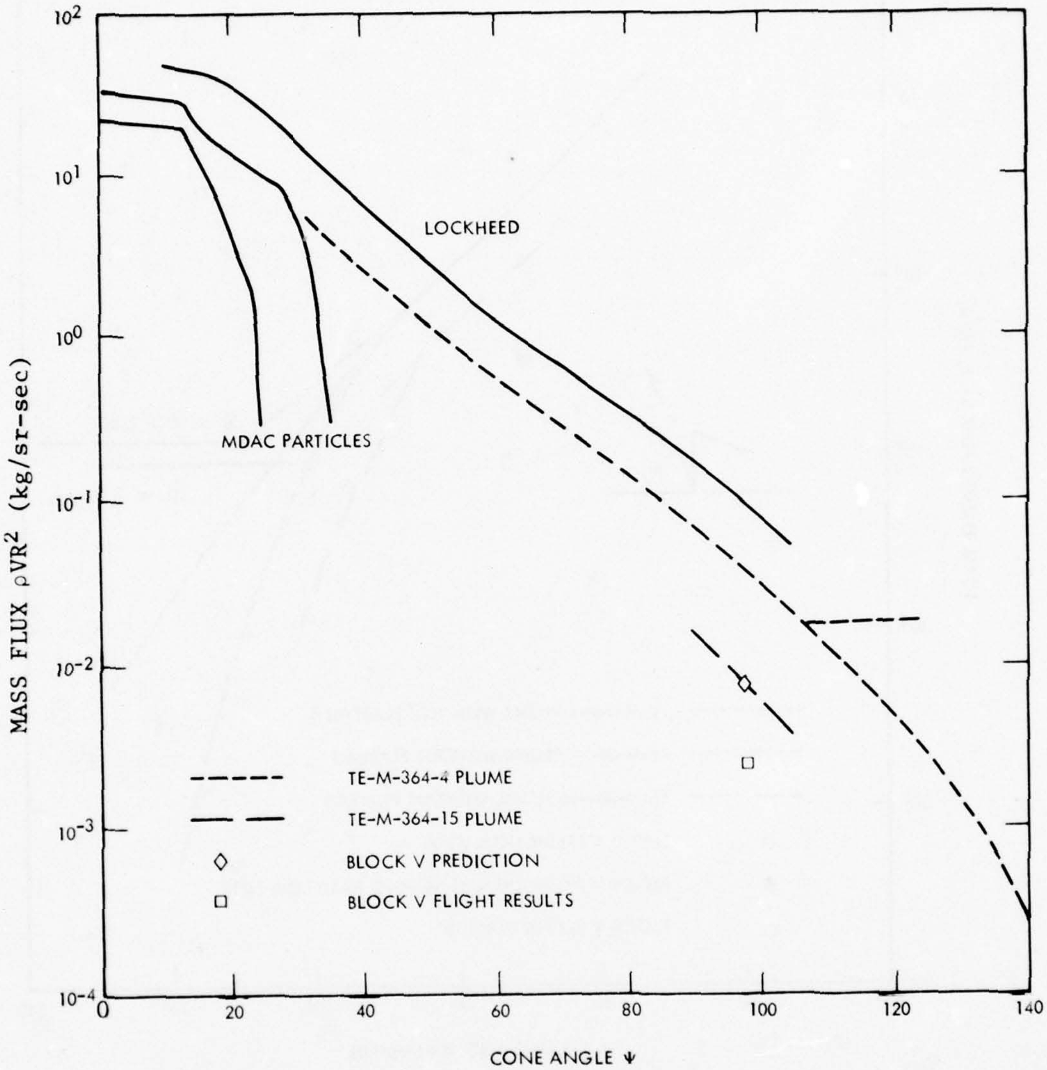

Figure 3. Mass Flux as a Function of Cone Angle

Figures 2 and 3 depict mass flux and energy flux vs. cone angle. The results indicated that energy flux on the Voyager science instrument package would approach 11.4 W/cm^2 which was far in excess of the .23 W/cm^2 allowable. Since energy flux represents only an upper limit to heat transfer more detailed heat transfer calculations were performed. Corrections were made for slip flow since the Knudsen number was calculated to equal approximately 1. The results indicated convective heat transfer rates of 1.1 to 4.5 W/cm^2 and radiative heat transfer of .11 - 1.1 W/cm^2. Mass flux was predicted to vary between 0.003 - 0.006 g/cm^2 sec. No significant particle contamination was expected since the particles would not be able to turn through the high expansion angles experienced by the boundary layer.

2.2 Plume Shield

To protect against potential overheating and contamination it appeared as though a plume shield would be required. However, it soon became apparent that this would be difficult to design. Additional data was required to specify thickness, location and degree of wraparound. The shield had to be lightweight, fit within the shroud and not inhibit the science boom from later deployment. It also had to withstand the plume and prevent any significant flow around the edges. The buildup of flow along the plume shield surface and the amount that would flow around the edge of the shield had to be calculated.

The most difficult problem was calculating the buildup of flow along the shield. Approximate techniques indicated a large boundary layer 8 cm or more in thickness. This slow moving gas could turn around the edge of the shield and impinge on the science instruments.

To solve this problem a contract was let with TRW to simulate the flow with their Monte Carlo program.[1] To verify these analyses calorimeters were incorporated into two plume instruments and installed next to

---

[1] Sugimura, T., Monte Carlo Flowfield Calculations for the MJS-77 Plume, Final Report, Contract 945381, TRW, (1977).

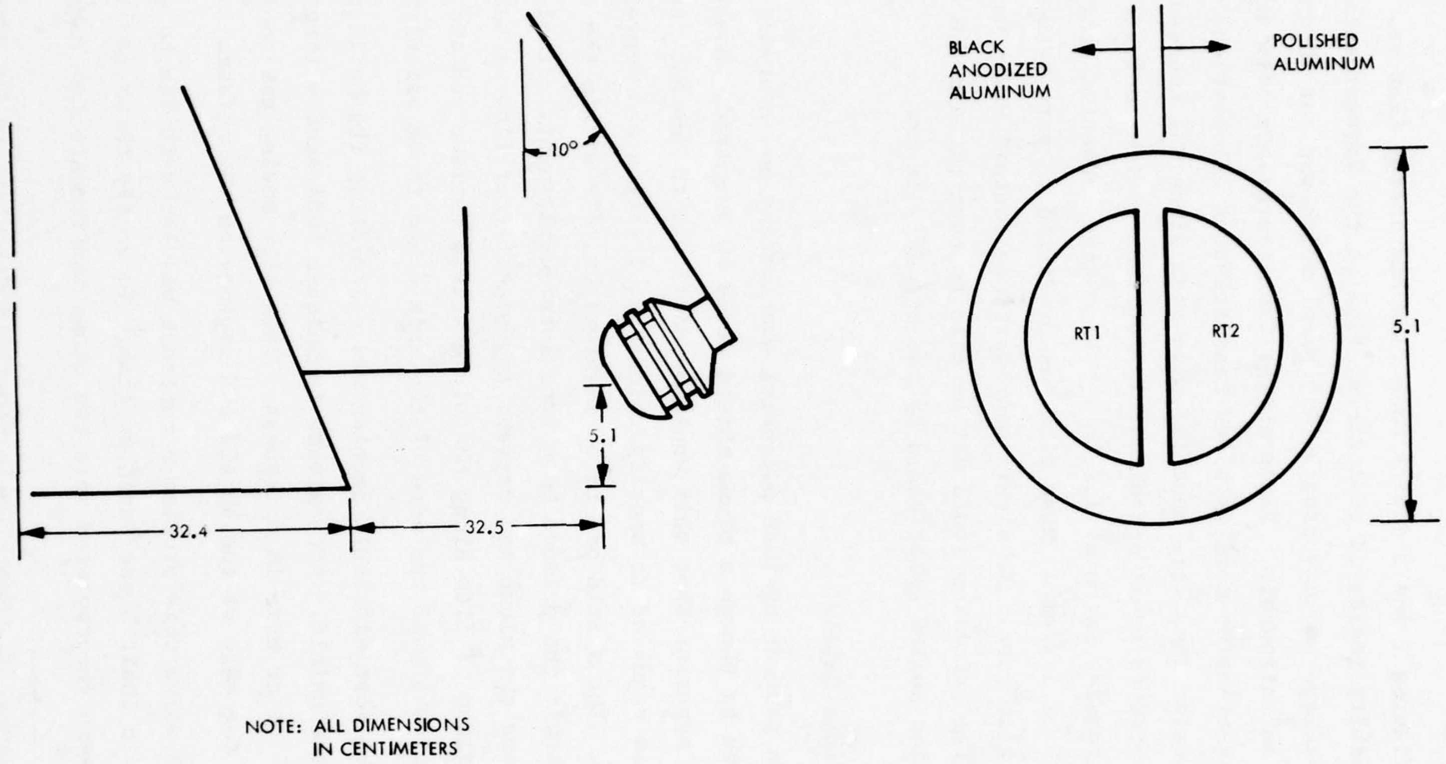

Figure 4. Primary Flow Block V Plume Instrument

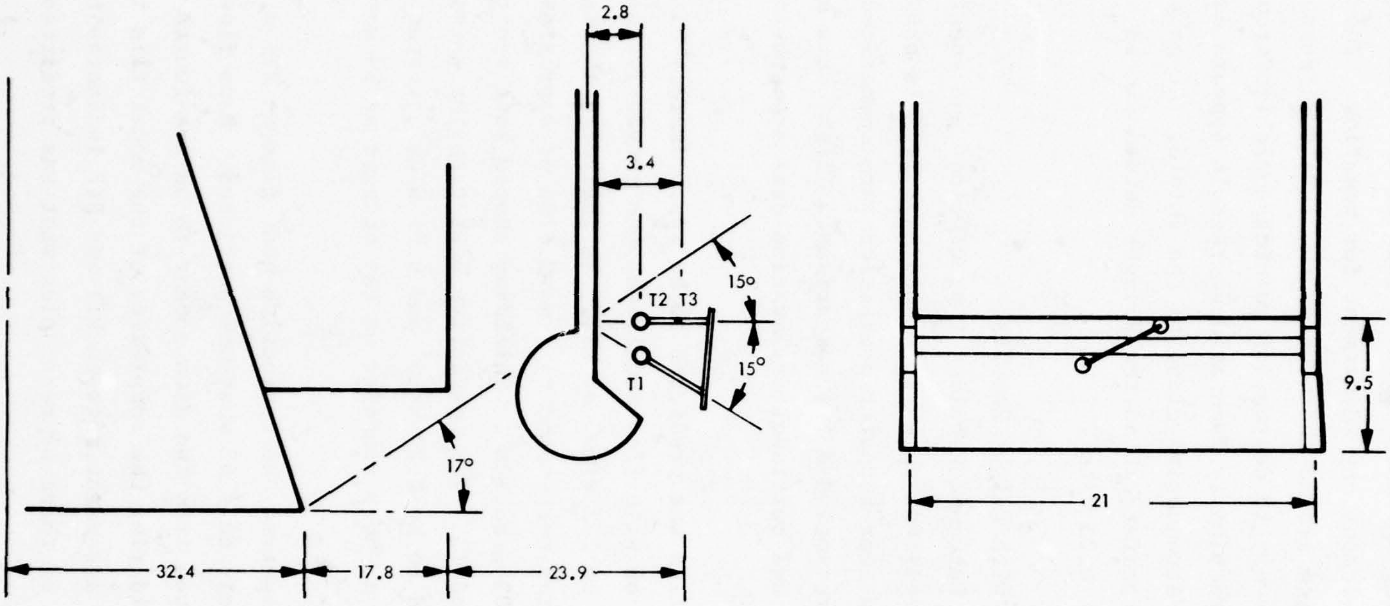

NOTE: ALL DIMENSIONS
IN CENTIMETERS

Figure 5. Secondary Flow Block V Plume Instrument

the heat transfer to the shield, the flow around the edges of the shield and the flow impinging on the Block V instruments could all be calculated fairly well without any adjustment for baseflow. The results also indicated that flow around the edge of the shield decreased by a factor of 2.5 to 3 for every 10 degrees of turning angle (referenced from the upstream flow direction). Even at 0 degrees it appears as though there is a significant attenuation close to the shield. At no point did the predicted heat transfer behind the Voyager shield exceed the maximum allowable rate of 0.23 W/cm^2.

2.5 Correlation with Flight Results

Correlation between the Block V predictions and the flight data was good. The predicted energy flux and mass flux is presented in Figs. 2 and 3 and heat transfer predictions are summarized in Table 1. Flight results are included for comparison. Flight data are plotted in Figs. 6 and 7 and pertinent calibration data are provided in Table 2.

The energy flux was predicted to be approximately 81 W/sr or 17 W/cm^2. Based on slip flow conditions the convective heat transfer was predicted to be 2.3 W/cm^2 at RT2. As indicated in Fig. 3 these heat transfer rates correspond to a mass flux of approximately 73 kg/sec-sr or 0.003 g/sec-cm^2. Shielding should have reduced the mass flux at T1, T2 and T3. The convective heat transfer rates at T2 and T1 were predicted to be 0.23 W/cm^2 and 0.05 W/cm^2, respectively. Due to the flow direction, heat transfer on the stinger at T3 was expected to be negligible.

As can be observed the convective heat flux on RT1 and RT2 appears to be approximately half of what was predicted. Mass flow rate and energy flux derived from the data appear to be one-fourth of what was predicted. Considering the complexity of the model this is good agreement. The close agreement between RT1 and RT2 indicates that radiation must be a factor of three or more below what was predicted. If there

TABLE 1

COMPARISON BETWEEN MEASURED AND PREDICTED HEAT TRANSFER TO BLOCK V PLUME INSTRUMENTS

Location	Actual W/cm^2	Predicted W/cm^2
RT 1	1.08	3.0
RT 2	1.25	2.3
T 1	0.049	0.05
T 2	0.044	0.2
T 3	0.033	0.0

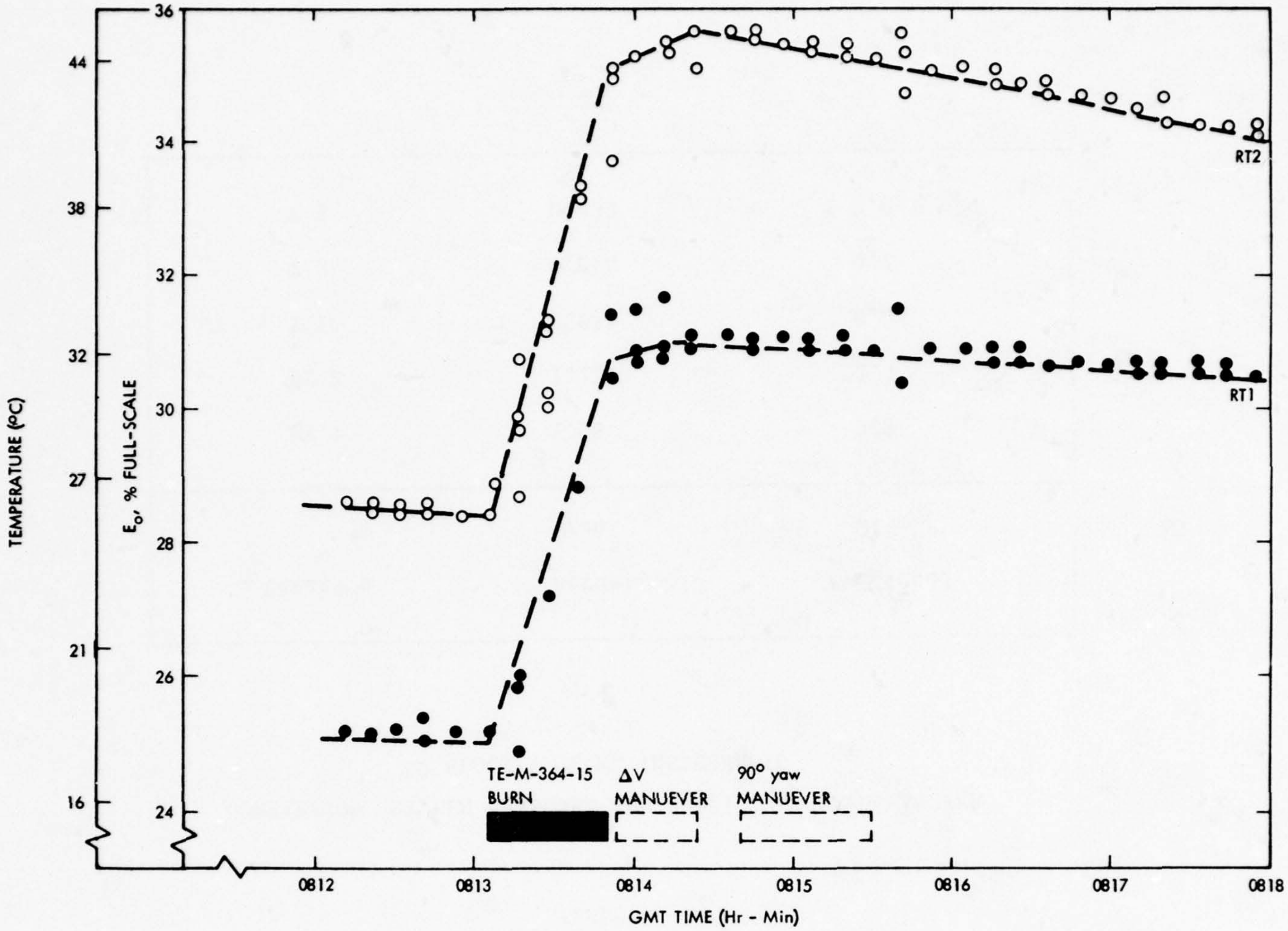

Figure 6. Block V Primary Flow Plume Instrument Data

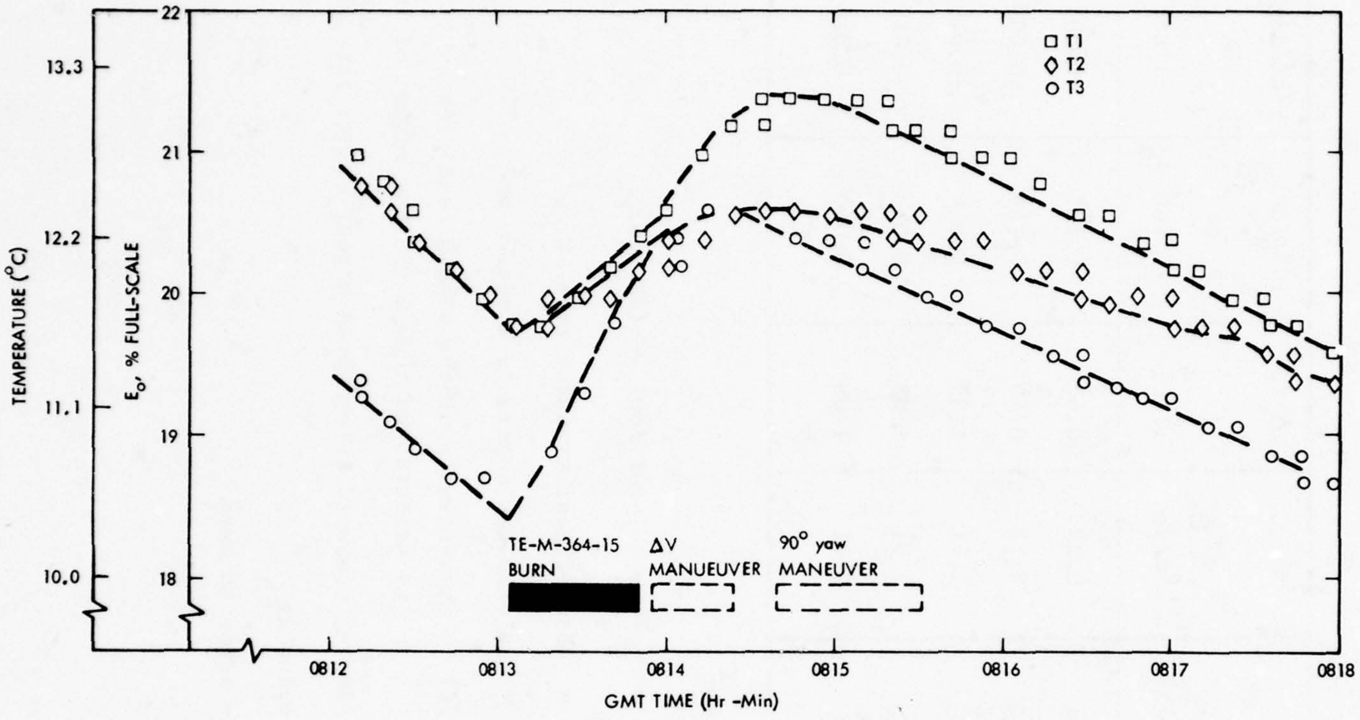

Figure 7. Block V Secondary Flow Plume Instrument Data

TABLE 2

BLOCK V PLUME INSTRUMENT DATA

Location	C $\frac{W/cm^2}{^oC/sec}$	dE_o/dT (1^oC)	$(dE_o/d\theta)_B$ (1/sec)	$(dE/d\theta)_{PB}$ (1/sec)	q W/cm^2
RT 1	3.23	0.40	0.129	-0.003	1.08
RT 2	3.23	0.40	0.149	-0.003	1.25
T 1	1.51	1.08	0.016	-0.019	0.049
T 2	1.51	1.08	0.013	-0.019	0.044
T 3	0.61	1.08	0.040	-0.018	0.033

Notes:

$$q = \frac{C}{dE_o/dT} \quad (dE_o/d\theta)_B - (dE_o/d\theta)_{PB} \qquad (1)$$

q = deduced heat transfer rate, W/cm^2

C = calorimeter constant, W $sec/^oC\ cm^2$

dE_o/dT = sensitivity of the signal conditioning circuit output to temperature change (in the region of interest), $1/^oC$

$dE_o/d\theta$ = measured telemetered signal change rate, 1/sec

B - during

PB - prior to burn

was any significant radiation RT1 would have measured a higher heat transfer rate than RT2, the black anodized surface of RT1 having an absorptance about three to six times greater than the polished aluminum surface on RT2. Finally the magnitude of the measurements of T1, T2 and T3 again indicate a mass flow rate approximately four times less than predicted. However, there is evidence (temperature rise rate of T3) that the flow was not aligned with the stinger axis, suggesting that there was mixing or turbulence in the flow. This could perhaps be from impingement on the instruments.

Results later obtained on Voyager confirmed that the predictions were somewhat conservative. Temperatures on the plume shield rose at only moderate rates. Because of the configuration of the temperature sensors it is difficult to assess these measurements quantitatively. No anomalous behavior or damage to the science was observed.

3.0 CONCLUSIONS

The Block V flight data indicates that there is a significant amount of mass flow at angles as large as 90^o. Calorimeters mounted 20 to 30 cm away from the TE-M-364-15, 44.5 kN Solid Rocket Motor measured a convective heat transfer rate of about 1 W/cm^2 corresponding to a mass flux of 0.00075 g/cm^2-sec. To predict these magnitudes, classical boundary layer and method of characteristic solutions can be used. On Block V the measured convection was only half of that predicted, whereas energy flux and mass flow rate were about a fourth of what was predicted. At these large angles, this is considered fairly good agreement. The largest uncertainty is probably the boundary layer thickness. Beyond the supersonic boundary layer flow regime, there is a significant uncertainty in mass flux. Although new analytical tools should be developed, it is probably acceptable in the meantime to assume that mass flux continues to decay exponentially until 30 degrees beyond the supersonic-subsonic boundary layer point.

Nothing in the flight data or analysis disapproves the existence of plateau at high angles; but both seem to indicate that there is no significant buildup of flow along the Block V base or Voyager plume shield. The efficacy of a plume shield is confirmed by the Monte Carlo analysis, the Block V experiment and by the satisfactory performance of the Voyager plume shield. Mass flux can be reduced by a factor of 2.5 to 3 for every 10 degrees of turning angle.

4.0 ACKNOWLEDGEMENTS

Appreciation is expressed to Dr. Jason Seubold, Dr. Takashi Sugimura (TRW) and Lt. William Kosman (SAMSO). Dr. Seubold was instrumental in the overall effort. He constructed the models, generated the plume predictions and assisted in defining the configuration of the Block V instruments. Dr. Sugimura was responsible for the outstanding results obtained in the Monte Carlo analysis. Lt. Kosman was JPL's prime interface with the Block V Project. He also supplied the raw flight data. Appreciation is also expressed to SAMSO, RCA and the Block V Project for their cooperation and assistance.

5.0 REFERENCE

Sugimura, T., Monte Carlo Flowfield Calculations for the MJS-77 Plume, Final Report, Contract 945381, TRW. (1977)

SPACE SHUTTLE PLUME CONTAMINATION

R. CARL STECHMAN

THE MARQUARDT COMPANY
VAN NUYS, CALIFORNIA

The Space Shuttle Orbiter uses earth storable bipropellant propulsion systems for attitude control and orbit change maneuvers. This propulsion system has a demonstrated high performance and realiability, but the rocket engine combustion products are much more complex than the products of hydrazine monopropellent decomposition or cold gas propulsion. These products of combustion can deposit or condense on surfaces in the vicinity of the rocket engine, and can cause a degredation in system efficiency.

Studies were conducted to identify the plume contamination potential for the primary and vernier thrusters of the Space Shuttle Orbiter. These studies indicate that plume transported contamination does not impinge or condense on the surfaces of the Orbiter, but some potential does exist for the flow of fuel film contaminant down the wall of the exhaust nozzle and off of the nozzle lip when short pulse widths and cold combuster walls are encountered. Contamination of Space Shuttle deployed payloads will be negligible since only the vernier thrusters are operated during this portion of the mission. The high performance of these engines will result in negligible plume contamination regardless of their orientation.

1. INTRODUCTION

The Space Shuttle Orbiter has two reaction control subsystems that perform a number of operations within the Space Shuttle mission profile. Figure 1 shows the location of the forward reaction control engines mounted in the surfaces on the sides of the nose section of the Orbiter, and on the top surface ahead of the pilot's compartment, and the aft reaction controls mounted on the extensions of the orbital maneuvering system pods. The forward RCS engines are primarily used in conjunction with the aft RCS engines for exoatmospheric flight maneuvering commencing with external tank separation. They can also be used in the atmosphere for external tank separation during return to launch site, and mission abort maneuvers in conjunction with the aft RCS engines. The aft RCS system, in addition to the RTLS function mentioned, also provides the primary control for transulation from orbit to conventional flight. There

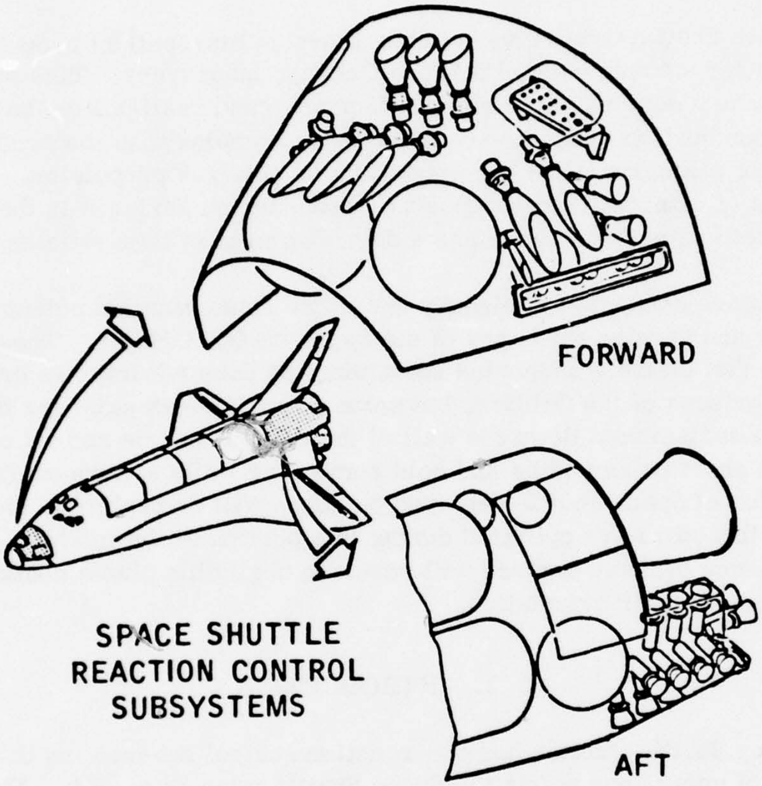

FIGURE 1

SPACE SHUTTLE REACTION CONTROL SUBSYSTEMS are thirty-eight primary thrusters which generate 870 pounds of thrust at nominal inlet conditions. These thrusters are not presently operated during payload deployment. There are also six RCS vernier thrusters of 25 pounds thrust which are operated during the payload deployment. Figures 2 and 3 show photographs of two versions of these thrusters. Studies have been conducted to determine the influence of the rocket exhaust plumes on the spacecraft shuttle surfaces and on the deployed payloads. Initial results indicate that little or no orbiter contamination will result from the firing of these engines due to the high efficiency and minimum injector manifold volume of the engines. The payloads are deployed when the primary engines are not operating. Future shuttle missions, however, may incorporate spacecraft deployment manuevers and auxiliary power systems which may be exposed to the exhaust plumes of both the primary and vernier thrusters. Therefore, a discussion of the nature of the rocket engine plume and the contamination that can result from it are important if one is to prevent contamination of sensitive surfaces on these future systems.

2. THRUSTER DESIGN CHARACTERISTICS

The nature of rocket engine plume and the concentration, velocity, and location of potential contaminants, whether they are solids, liquids or gases, are strongly influenced by the characteristics of the rocket engine. The areas of the engine design which influence the rocket plume are the volumes between the valve seats and the injector face (dribble volume), the propellent flow distribution over the face of the injector, the temperature of the propellent and engine hardware, and the shape of the combustion chamber and exhaust nozzle.

Pulsing operation and steady state operation are known to produce different plume characteristics. During the steady state firings, combustion is relatively efficient and the major plume constituents are those predicted from equilibrium thermodynamic considerations. Even at steady state conditions, most rocket engines have a variable mixture ratio distribution because of the injector pattern, film cooling and dynamic consideration. The composition of the rocket exhaust plume therefore varies as a function of radial distance from the plume center line. Some rocket engine injection patterns are asymmetrical and the plume composition thus varies with angular position around the engine center line. With film cooled engines, such as the Space Shuttle primary thruster, the outer regions of the plume are relatively rich in the propellent used as the film coolant (monomethylhydrazine) and its decomposition products.

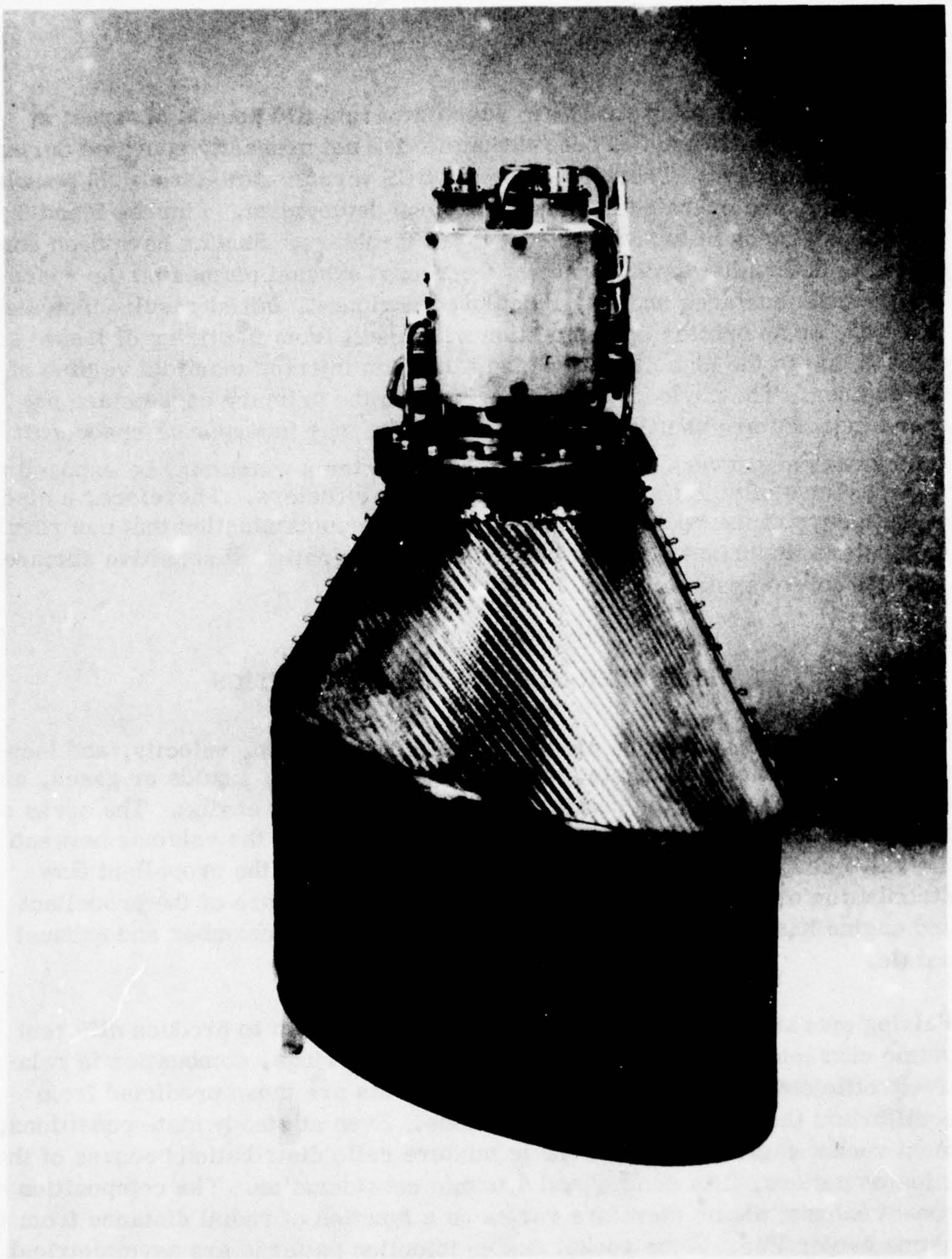

FIGURE 2 SPACE SHUTTLE REACTION CONTROL SUBSYSTEM PRIMARY THRUSTER

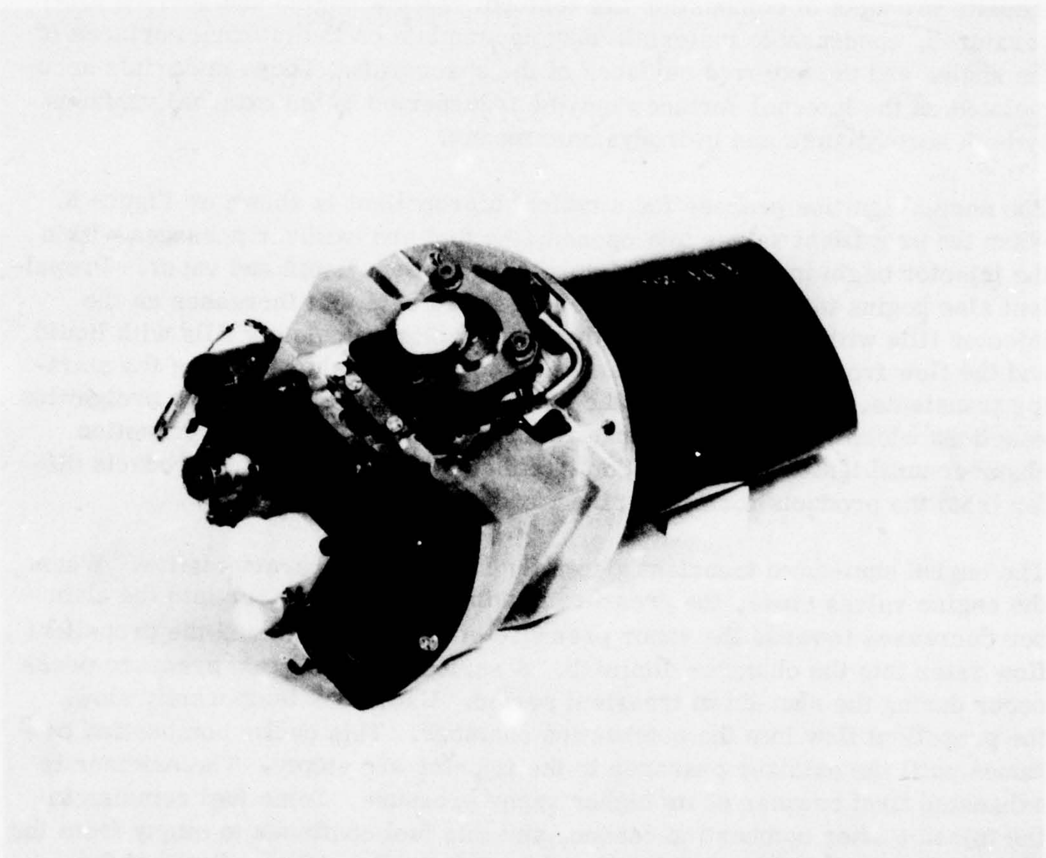

FIGURE 3 SPACE SHUTTLE REACTION CONTROL SUBSYSTEM VERNIER THRUSTER

Figure 4 shows a typical exhaust plume profile with superimposed mixture ratio distribution.

Pulse firing of rocket engines introduces special factors which are probably of the most importance in the consideration of plume contamination. Performance at short pulse widths is lower than steady state values because the start-up and tail-off transients are a releatively large fraction of the total pulse time. During these transients, unreacted fuel and oxidizer and intermediate products of combustion are formed. At low engine and surface temperatures, condensable materials may accumulate on the internal surfaces of the engine and the external surfaces of the spacecraft. Those materials accumulated on the internal surfaces may be transported to the external surfaces by both aerodynamic and hydrodynamic means.

The normal ignition process for a typical bipropellent is shown on Figure 5. When the propellent valves are opened, the fuel and oxidizer passages within the injector begin to fill with a mixture of propellent liquid and vapor. Propellent also begins to flow from the injector with a rate that increases as the injector fills with liquid. Eventually, the injector completely fills with liquid and the flow from the injector reaches its maximum value. During the starting transients, the propellent in the combustion chamber enter into preignition reactions which raise the temperature and pressure within the combustion chamber until ignition occurs. Some of the preignition reaction products differ from the products formed during steady state ignition.

The engine shut-down transient also influences plume characteristics. When the engine valves close, the pressure driving fuel and oxidizer into the chamber decreases towards the vapor pressure of the propellent and the propellent flow rates into the chamber diminish. A series of combustion pressure peaks occur during the shut-down transient period. Each peak temporarily slows the propellent flow into the combustion chamber. This cyclic combustion continues until the oxidizer passages in the injector are empty. The oxidizer is exhausted first because of its higher vapor pressure. Some fuel remains in the injector after combustion ceases, and this fuel continues to empty from the injector for many milliseconds after the oxidizer flow stops. Some of the shut-down fuel leaves the engine directly through the nozzle while some deposits on the combustion chamber walls and later leaves the engine under the influence of evaporation, gravity, surface tension, and shear from the combustion gases.

The processes taking place in the engine during pulsing operation cause the

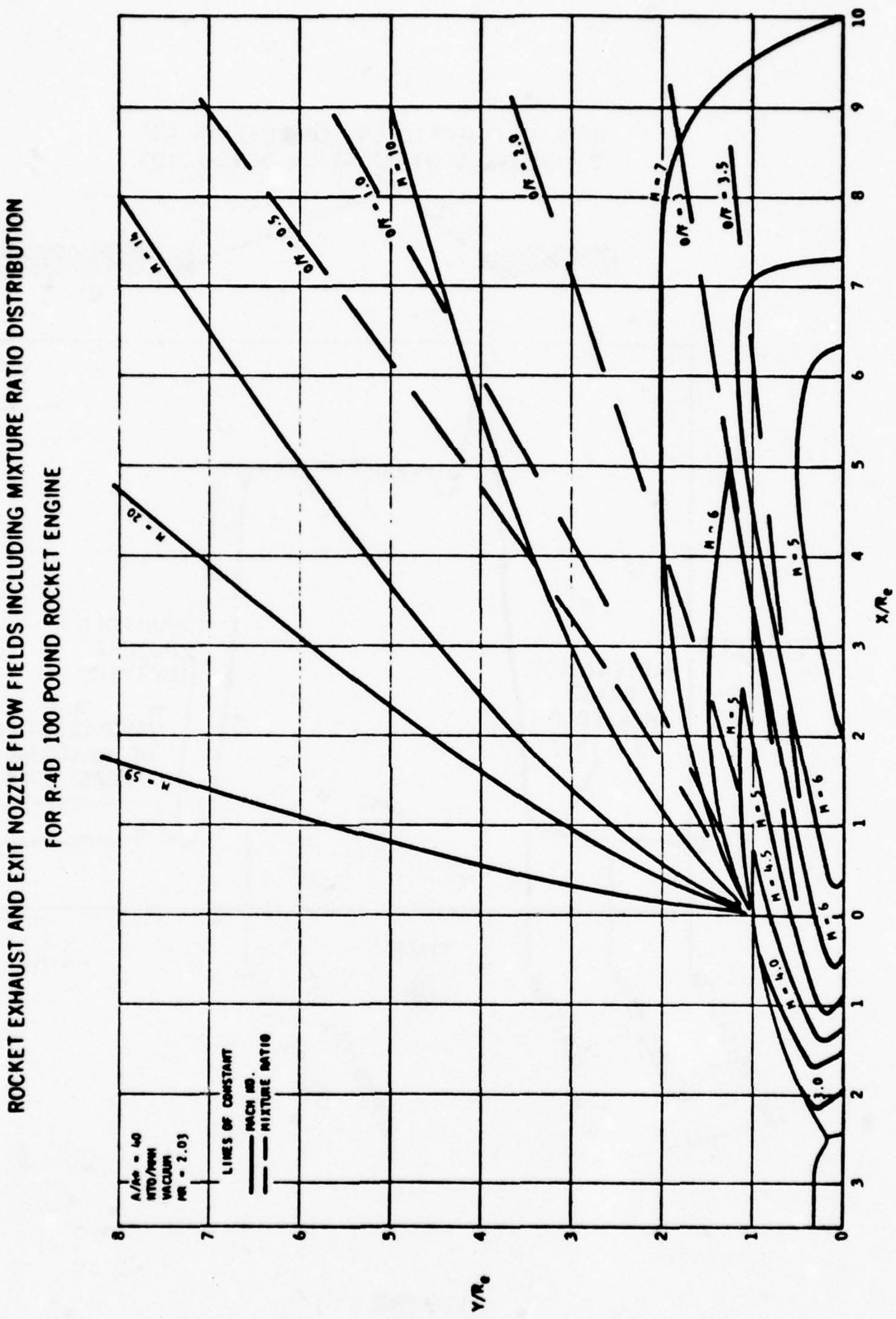

FIGURE 4

ROCKET ENGINE EXHAUST FLOW FIELD

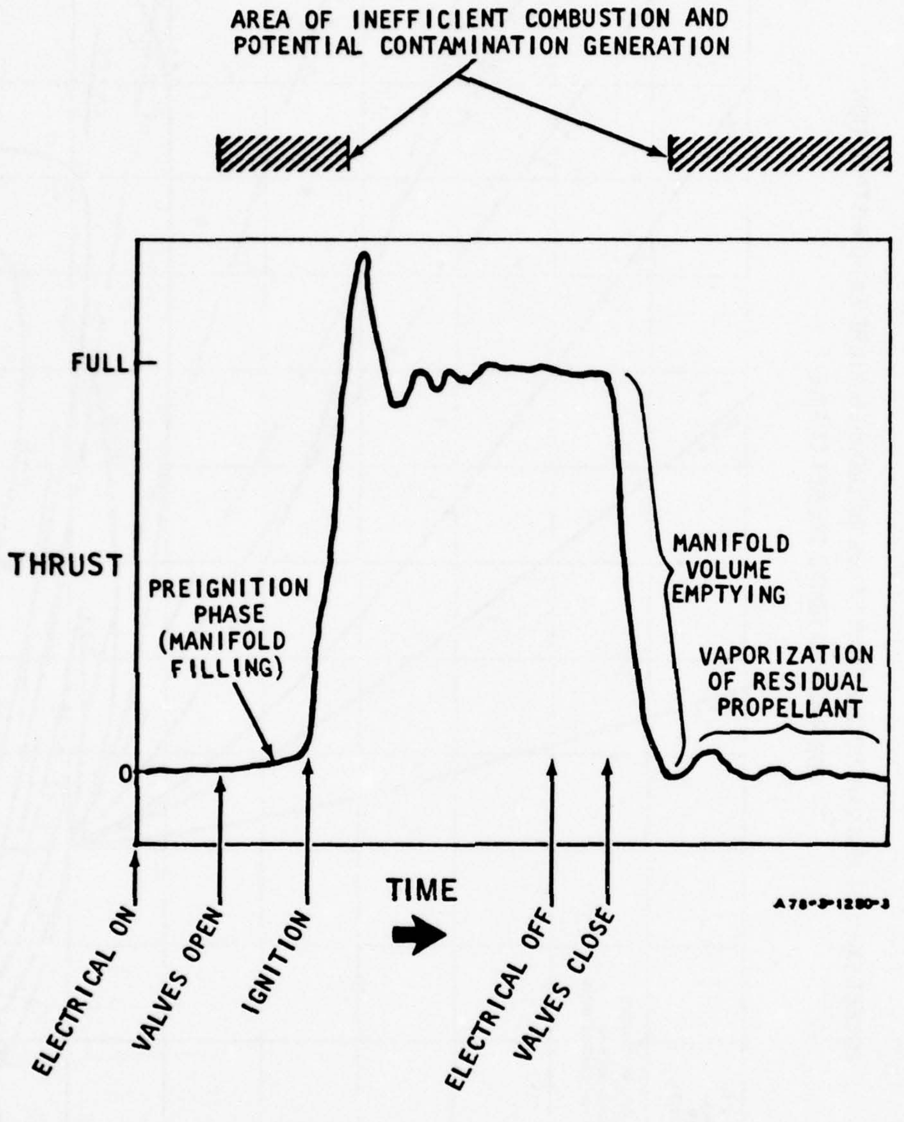

FIGURE 5

TYPICAL THRUST TRACE FOR REACTION CONTROL THRUSTER plume to change rapidly with time. During portions of the pulsing duty cycle, the plume can consist almost entirely of oxidizer vapor, while at other times it may be rich in combustion products or fuel vapor. The designs of the 870 pound thrust primary thruster and 25 pound thrust vernier thruster are oriented towards minimization of plume contamination during both the pulsing and steady state operation. Minimization of the plume contamination during steady state operation is accomplished through a high performance injector. This injector assures that a maximum amount of the propellents are combusted, leaving little or no unreacted propellents to exit out through the exhaust nozzle. During pulsing operation the minimization of plume contamination is accomplished through a design of a minimum dribble volume injector. These two design criteria, (1) high combustion efficiency, and (2) minimum dribble volume, provide the basis for the minimization of plume contamination under all operating conditions. Experimental data and analytical calculations have verified that these criteria establish a basis for an engine design with minimum plume contamination.

3. EXPERIMENTAL DATA

Plume contamination tests have been conducted on various bipropellent rocket engines, ranging in thrust of less than 1 pound up to greater than 300 pounds thrust. (Ref 1-5) A majority of the tests were conducted on Marquardt's 25 pound thrust Vernier engine and the 100 pound thrust R-4D engine used on the

1. Etheridge and Boudreau, "Attitude Control Rocket Exhaust Plume Effects" Journal Spacecraft and Rockets, Vol 7, No 1, Jan 1970.
2. Stechman, R.C., and Thonet, T.A., "The Effect of Rocket Exhaust Impingement on Spacecraft Surfaces during Pulsing Engine Duty Cycles", JANNAF 12th Liquid Propulsion Meeting CPIA No. 201, Oct., 1970.
3. Arnett, Gary M., "Lunar Excursion Module R.C.S. Engine Vacuum Chamber Contamination Study", NASA TM 53859, July 8, 1969.
4. Yanizeski, G.M., "Thermal Control Coating Degradation by the Service Module Reaction Central System Rocket Exhaust During Skylab Missions" TM-1022-12, Bellcomm Inc., August 1970; Sept 1970.
5. Jack, John R., Spisz, E.W. and Cassidy, J.F., "The Effect of Rocket Plume Contamination on the Optical Properties of Transmitting and Reflecting Materials", AIAA Paper 72-56, 10th Aerospace Sciences Meeting, Jan 1972.

Apollo Service Module and Lunar Module. These two engines represent a large variation in engine dribble volume and the results of the tests indicate a definite correlation between engine dribble volume and plume contamination potential. Figure 6 shows a plot of contamination versus engine dribble volume. Also plotted on this Figure are data for Marquardt's 5 pound bipropellant engine, and a 1 pound engine. This correlation while qualitive in nature, indicates that once the electrical pulse width to dribble volume ratio is greater than 5, the contamination potential becomes nil.

The R-40 primary thruster engine has a dribble volume equivalent of approximately 10 milliseconds. Operating at a minimum electrical pulse width of 40 milliseconds results in a ratio of 4, which would indicate that the engine would generate a very small amount of contaminant during its pulsing operation. The vernier thruster, with a dribble volume equivalent of approximately ~~8~~ 3 milliseconds, operating at a 40 millisecond pulse width, would have a ratio of nearly 15, which again would indicate that the plume contamination caused by this engine would be nil.

Studies conducted by McDonnell Douglas in support of the Space Shuttle Orbiter Program (Ref 6, 7), using the CONTAM Program indicate that the potential for contamination is very small and verify the analysis previously discussed. The CONTAM Program provides an excellent basic analysis for determining the plume contamination potential. This analysis, however, uses a simplified combustion (TCC) model. The primary and vernier thrusters utilize film cooling and mixture ratio stratification which can not be effectively analyzed using the methodology of the program. Modifications of the CONTAM Program to include these effects are now being accomplished under Air Force Rocket Propulsion Laboratory funding.

Results of studies conducted by McDonnell Douglas and Marquardt indicate that there is some potential for contamination due to migration of liquids along the exit nozzle and around the lips of the nozzle during cold thruster

---

6. Oeding, R.C., et al, "Space Shuttle RCS Plume Contamination Study", MDC G5250, McDonnell Douglas Astronautics Company--west, July 1974.
7. Anon, "DOD Space Transportation System Payload Interface Support Study, Interim Report, Appendix C--Contamination Study", MDC G6367, McDonnell Douglas Astronautics Company--west, March 1976.

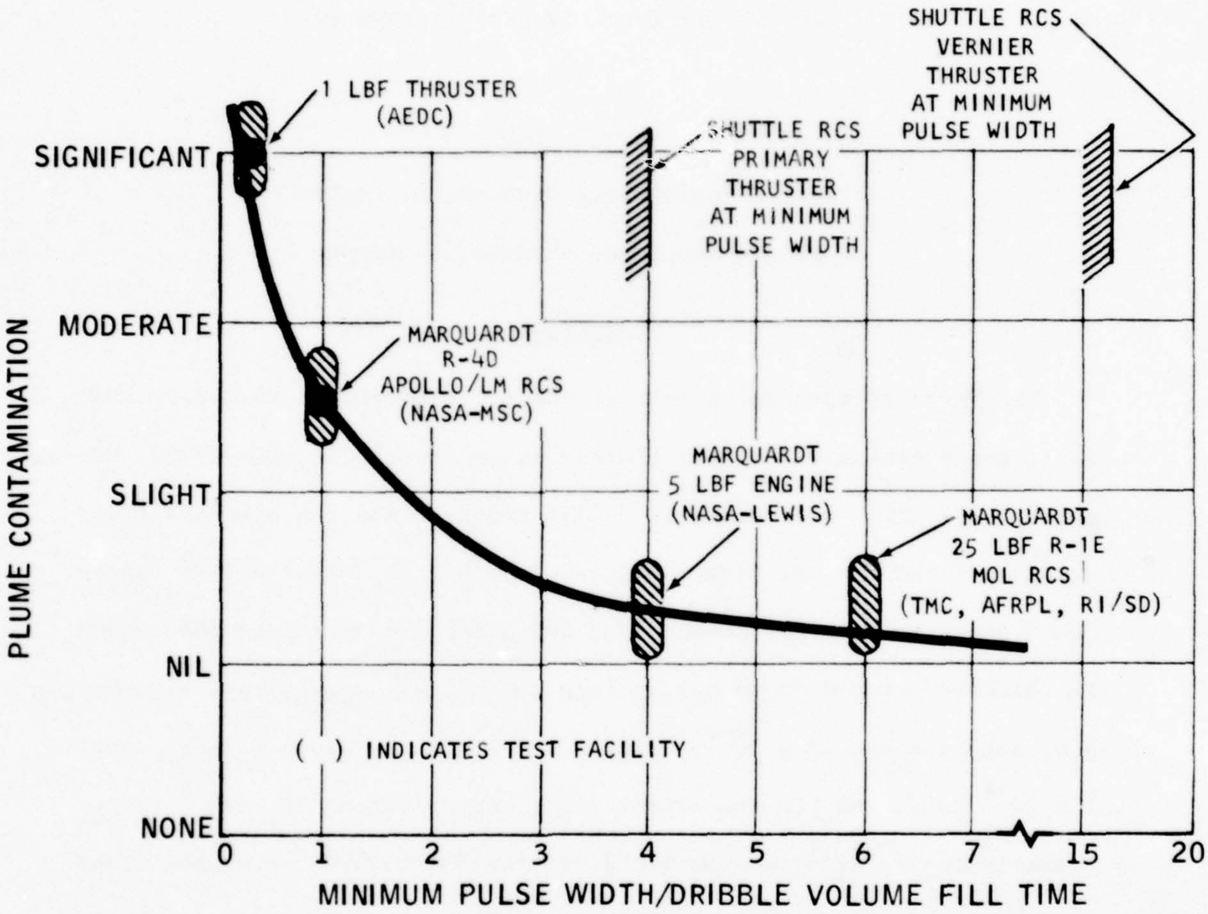

PLUME CONTAMINATION RESULTING FROM BIPROPELLANT NTO/MMH ROCKET ENGINE OPERATION

FIGURE 6

PLUME CONTAMINATION RESULTING FROM BIPROPELLANT NTO/MMH ROCKET ENGINE OPERATION

IR OPTICAL PROPERTIES OF BIPROPELLANT CRYOCONTAMINANTS

J. A. Roux, B. E. Wood, A. M. Smith, J. G. Pipes

ARO, Inc.

AEDC Division

A Sverdrup Corporation Company

Arnold Air Force Station, Tennessee

and

H. E. Scott

Arnold Engineering Development Center

Arnold Air Force Station, Tennessee

ABSTRACT

The infrared spectral transmittance of cryodeposits formed by MMH, N_2O_4, and a simulated exhaust plume mixture (N_2--50.3%, CO--17.2%, CO--10%, and H_2O--22.5%) was measured. Also measured was the spectral transmission of the exhaust plume products from a 5 lb_f bipropellant engine. These deposits were cryopumped on a 20K germanium substrate and ranged in thickness from 0.25 to 6.7 μm; the deposition pressure for the MMH and N_2O_4 deposits was $\approx 5 \times 10^{-8}$ torr, for the simulated plume mixture about 1×10^{-6} torr, and for the bipropellant contamination $\approx 2 \times 10^{-6}$ torr. Transmission spectra were obtained for the 500 to 3700 wavenumber range using a Fourier transform spectrometer. These spectra are valuable for contaminant species identification and for species deposition temperature determination.

The optical properties (n,k) of such cryodeposits are essential for predicting the degradation of plume contaminated cryocooled optical

surfaces. Values of the complex index of refraction ($\bar{n}$ = n-ik) for the above cryodeposits were derived from the experimental data using an analytical model in conjunction with a non-linear least squares method. The analytical model treats the germanium as a thick non-interfering film and the deposit as a thin film. Results from the least squares method were also compared with a substractive Kramers-Kronig determination of the real part of the index of refraction. A quartz crystal microbalance (QCM) along with the dual beam laser technique was used to measure the cryofilm thickness and density.

1.0 INTRODUCTION

Contamination which can result from the exhaust plume of small thrusters used for attitude control maneuvers can pose severe problems for long-life satellite systems. It has been found that engine exhaust products can contaminate sensitive optical surfaces located upstream of the nozzle exit plane (referred to as the backflow region). Sensor systems, which require cryogenic cooling to achieve maximum sensitivity, are particularly susceptible to cryopumping engine exhaust products which reach the backflow region. The contaminants which reach the backflow region are thought to originate from the engine nozzle boundary layer. Gases in the boundary layer travel at low velocities and are therefore able to expand through very large turning angles and flow upstream of the nozzle exit plane.

To better identify the possible contaminants for a bipropellant (MMH/N_2O_4) engine the IR spectra of MMH, N_2O_4, and a simulated ideal exhaust plume mixture (N_2--50.3%, CO_2--17.2%, CO--10%, and H_2O--22.5%) were investigated, then the actual contaminants from a 5 lb_f bipropellant engine exhaust plume were measured. For the bipropellant engine the cryocontamination was collected at an angle of 90 deg from the plume axis centerline and at a distance of 3 feet along the nozzle exit plane. Normal absolute transmission spectra were measured using ≈20K germanium as a substrate material. Germanium was chosen as a substrate since it has the desirable qualities of an absorption edge at 1.5 μm, a flat transmission of 47% (300K) between 2 and 10 μm, and lattice absorption bands between 10 and 20 μm. Furthermore it is one of the most commonly employed substrates for cryocooled optical components because of its higher thermal conductivity as compared to pure dielectrics, the Itrans, or poly-crystals. Complete experimental details are given elsewhere;[1] thus only a basic outline of the apparatus is presented here. A theoretical model of substrate plus film transmission is derived and is subsequently employed with the experimental results to determine the complex refractive index ($\bar{n} = n-ik$) of each of the above mentioned contaminants. The substractive Kramers-Kronig treatment for calculation of the film refractive index has also been employed, and results are compared to those of the least square determination. In addition, the density and thickness of the above contaminants were determined through use of the dual beam laser technique[1] and a QCM.

2.0 INSTRUMENTATION

A plan view schematic of the experimental apparatus, showing the IR interferometer (Digilab Model FTS-14), the high vacuum chamber containing the cryocooled window, and the IR source location is given in Fig. 1;

---

[1] Pipes, J. G., Roux, J. A., Smith, A. M., and Scott, H. E., Transmission of infrared materials and condensed gases at cryogenic temperatures, AEDC-TR-77-71 (1977).

1. Pyroelectric detector and collection optics.
2. Stainless steel high vacuum chamber, 85 cm tall by 70 cm in diameter (33.5 in. by 27.5 in. in diameter).
3. Cryogenically cooled infrared window; germanium, 4 mm thick by 70 mm square (0.158 in. by 2.76 in.) and QCM.
4. Helium-neon laser (0.6328 μm) beam (one of two shown) employed to measure cryofilm thickness.
5. Infrared beam, 38 mm in diameter (1.5 in.).
6. 2-mw He-Ne laser.
7. Michelson interferometer.
8. Infrared source and collimator mirror.

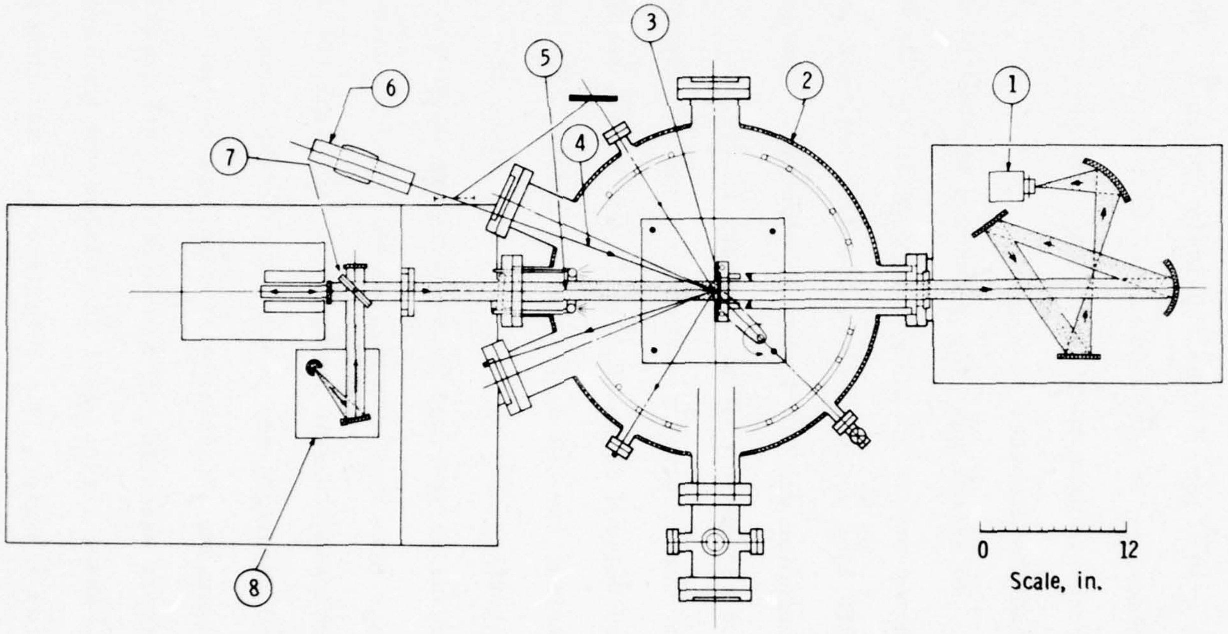

Figure 1 Plan view schematic of the Infrared Optical Transmission Chamber (IROTC) with FTS-14 interferometer-spectrometer.

this chamber was used for obtaining the MMH, N_2O_4, and simulated plume mixture data. The chamber is an all-stainless-steel cell equipped with a liquid-nitrogen (LN_2)-cooled liner. A water vapor free vacuum of $\approx 4 \times 10^{-8}$ torr can be routinely obtained. The aluminum germanium window holder can be actively cooled with either LN_2 (80K) or gaseous He (20K). Three platinum resistors located on the window holder gave temperature readouts accurate to 0.5K.

To assure that the germanium window did not act as an optical stop in any manner a stop was located in the "back-of-window" gas baffle. This stop was 1.50 inches in diameter, and the clear aperture of the germanium was 2.0 inches in diameter. The germanium window was mounted for cryogenic cooling as shown in Fig. 2.

The spectral resolution of the interferometer system could be selected between 16 and 0.5 cm^{-1}, but 4 cm^{-1} resolution was found to be sufficient for all work reported herein. The wavelength accuracy of the interferometer is near 0.02 cm^{-1} since the interferogram sampling interval is governed by an auxiliary He-Ne laser interferometer. Transmission data were recorded in the 500-3700 wavenumber region. Transmission measurements were performed by rotating the germanium out of the beam and recording and storing a reference power spectrum. Up to 16 interferograms (36 for the bipropellant engine data) were generally co-added before execution of the Fourier transform thereby improving the signal-to-noise ratio. Next the window was rotated into the beam and the process repeated. The reference file was then divided into the sample file and plotted by a digital incremental plotter, producing the final data record on a linear ordinate scale of zero- to 100-percent transmission.

1. Infrared beam, 38-mm-diameter (1.5.).
2. Optical stop required to underfill cryocooled window with infrared beam. Also, this stop is supported by a 3-in.-ID pipe that prevents gas added to chamber from cryopumping on rear of window.
3. Aluminum holder with cryogenic passageways.
4. Germanium window heat sunk with an indium gasket to the aluminum holder.
5. Cover plate.
6. Gaseous helium or liquid nitrogen inlet.
7. Gaseous helium or liquid nitrogen outlet.
8. Crosshatched area illustrates area of window heat sunk to holder. Clear diameter is 50.7 mm (2 in.) while infrared beam diameter is 38 mm (1.5 in.).
9. QCM heat sunk with indium gasket to aluminum holder.

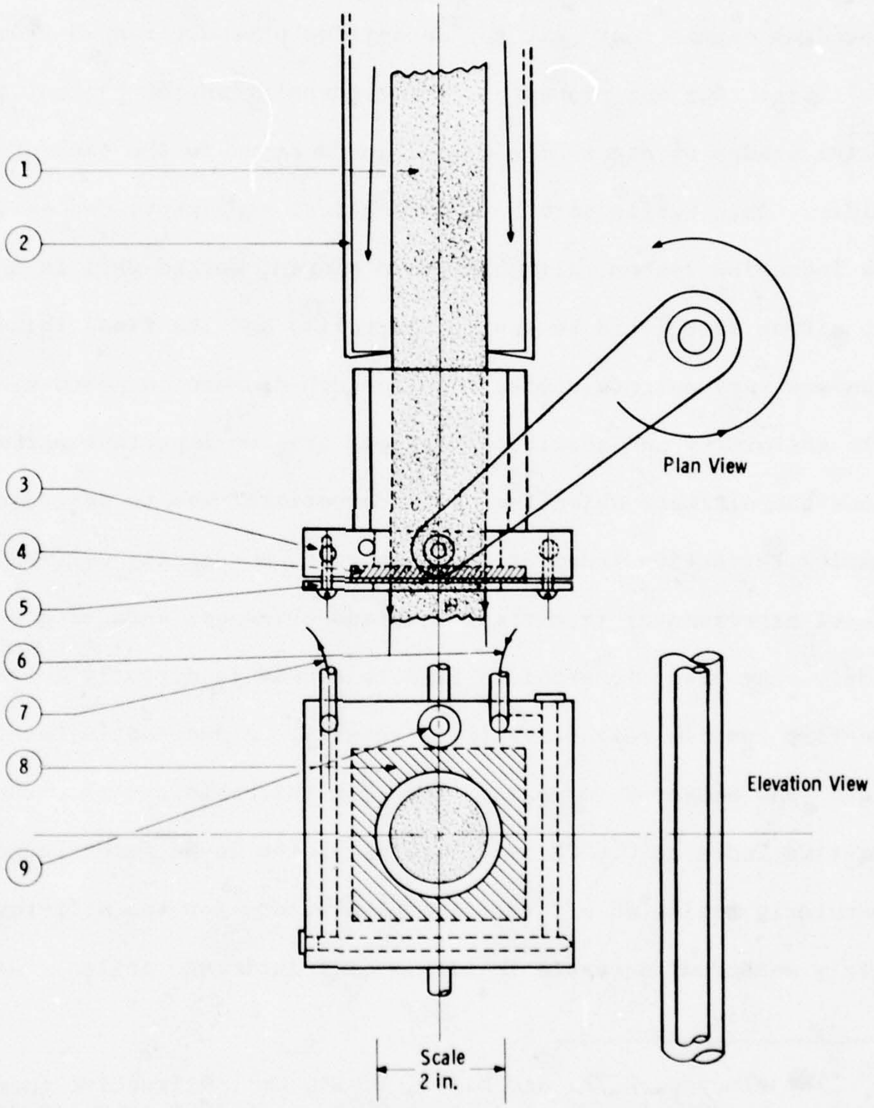

Figure 2 Plan and elevation views of cryogenically cooled window holder.

Controlled contamination of the cryocooled germanium window was accomplished with the gas induction system shown schematically in Fig. 3. A toroidal-shaped header with thirty-six 1/16-inch-diameter orifices spaced 10 degrees apart directed the gas toward the germanium window. The upstream pressure, typically 0.5 torr, was regulated by the variable leak valve and measured with an MKS Baratron capacitance manometer. Depending on the test gas, the deposition pressure ranged from 10^{-8} to 10^{-6} torr. Gas was prevented from condensing on the back of the germanium window by a gas baffle positioned close to the back of the window holder. This baffle also held the optical stop mentioned earlier. The gas induction system, although quite simple, worked well in that the deposition rate could be easily controlled and the final thin-film thickness was very uniform across the two-inch-diameter exposed window area. Film uniformity and absolute thickness are two important parameters since the ultimate objective of the experiment was to determine the complex refractive index of the thin film, a quantity derived by comparison of experimental transmission versus thickness data with a theoretical model. Any error in absolute film thickness is directly introduced into the film complex refractive index results. A dual-angle laser beam technique[2] was employed to measure the film thickness and also the film refractive index at 0.6328 μm. Basically, two He-Ne laser beams are specularly reflected off the germanium window for two different and accurately measured (accurate to within .1°) incidence angles. As the gas

---

[2] Tempelmeyer, K. E. and Mills, D. W., Jr., Refractive index of carbon dioxide cryodeposit, J. of Applied Optics, 16:2968-2969 (1968).

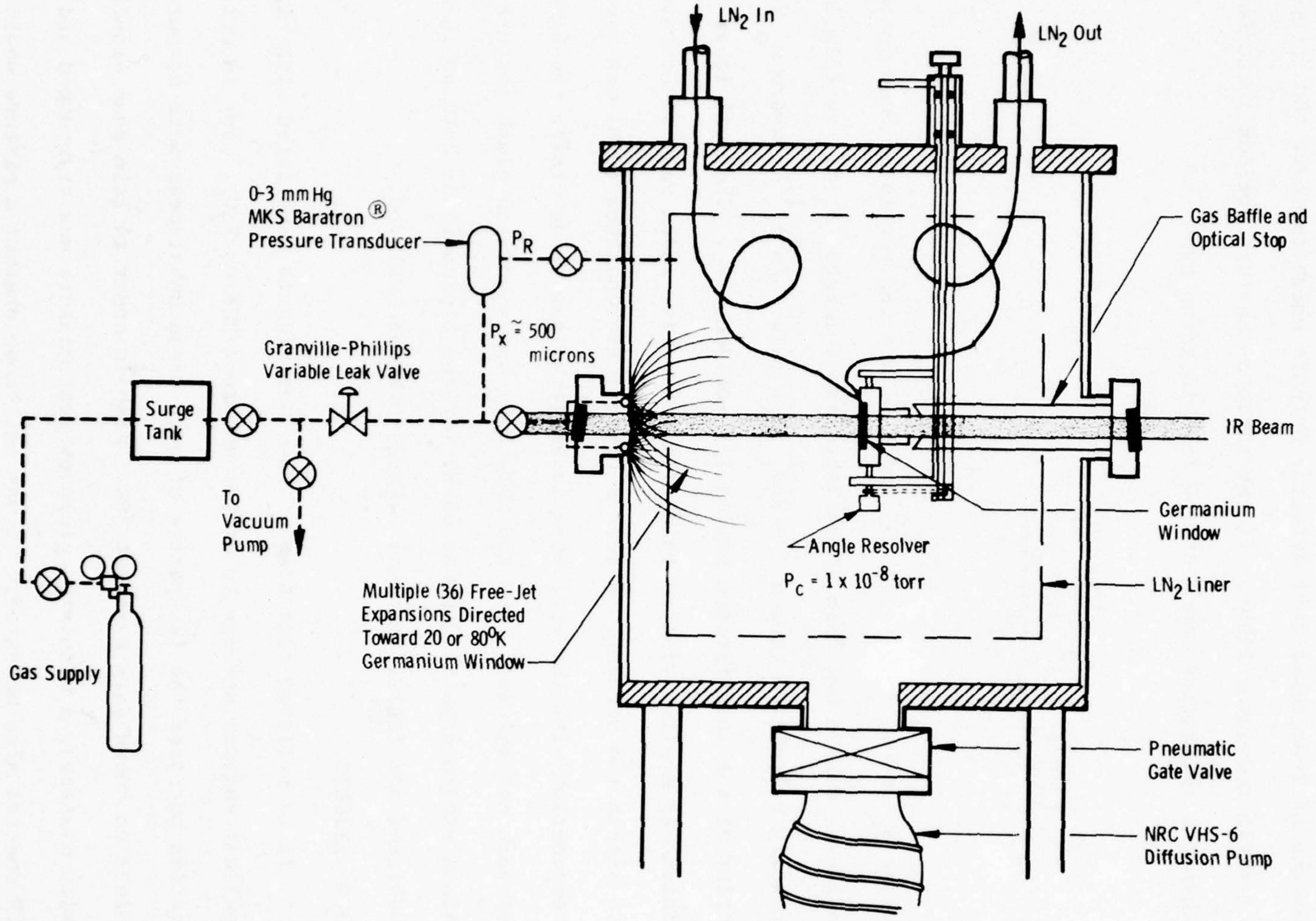

Figure 3 Gas Induction System.

is condensed two interference patterns of different periods are observed on the silicon solar cell detector outputs which indicate the intensity of reflected laser light. If the ratio of pattern periods is termed β then the refractive index of the film is given by

$$n = \frac{[\sin^2\theta_b - \beta^2 \sin^2\theta_a]^{1/2}}{1 - \beta^2} \qquad (1)$$

where θ_a and θ_b (typically 19° and 68°) are the two laser beam incidence angles. Once n has been established the thickness d_1 of the film is readily calculated from $m_a\lambda = 2nd_1\ [1 - (\sin^2\theta_a/n^2)]^{1/2}$, where m_a is the order of the interference maxima for incidence θ_a. The dual laser beam thickness monitor yielded thin-film refractive index values accurate to within two percent. A quartz crystal microbalance (QCM) was used in conjunction with the dual beam laser technique to determine the density of each contaminant. For the MMH, N_2O_4 and simulated plume mixture a Sloan single crystal QCM was used; for the bipropellant data an in-house designed and fabricated dual crystal QCM was employed.

3.0 RESULTS

It is believed that some of the contaminants associated with bipropellant engines are due to either unburned MMH or N_2O_4. For identification purposes the IR spectra of both these substances were measured since no known data exist at 20K. Also in order to gain some experience with mixtures, a simulated plume exhaust mixture was cryopumped and the IR spectra also measured. It was not known whether a mixture would be more or less scattering than the pure substances. Along with the IR spectra the refractive index was measured at 0.6328 μm and also in conjunction with the thickness measurement the density was measured. Finally, these same properties were determined for the contamination from a 5 lb_f bipropellant engine located at 90 deg from the nozzle axis centerline and about 3 ft along the nozzle exit plane.

20K MMH

Transmission spectra of MMH were obtained for several thicknesses varying from .23 μm (one interference pattern) to 3.17 μm (14 interference patterns). At the helium-neon wavelength (.6328 μm) the refractive index was measured and found to be 1.39 ±.02; in conjunction with the thickness measurement, a QCM measured the mass per unit area and a density of 0.82 gm/cm^3 was calculated for the MMH deposit at 20K. This yields a Lorentz-Lorenz value ($n^2-1/n^2+2 \cdot 1/\rho$) equal to .294 $cm^3/gram$ at .6328 μm. Transmission data obtained for the largest thickness, 3.17 μm deposited on germanium are shown in Fig. 4. (The dashed curve is for the bare 20K germanium transmission.) The absorption bands are listed in Table 1 and the vibrational assignments of Durig, Harris, and Wertz[3] are listed for comparison; their[3] assignments were associated with data obtained from liquid MMH whereas the spectra in the present case were for thin solid films of MMH. The MMH spectra show two wavenumber areas of considerable absorption--the region from 900-1700 cm^{-1} and the region from 2700-3300 cm^{-1}. No noticeable absorption is seen between these two regions. The broad dip in transmission centered

---

[3] Durig, J. R., Harris, W. C., and Wertz, D. W., Infrared and Raman spectra of substituted hydrazines. I. methylhydrazine, J. of Chem. Phys., 50: No. 3, 1449-1461, (1969).

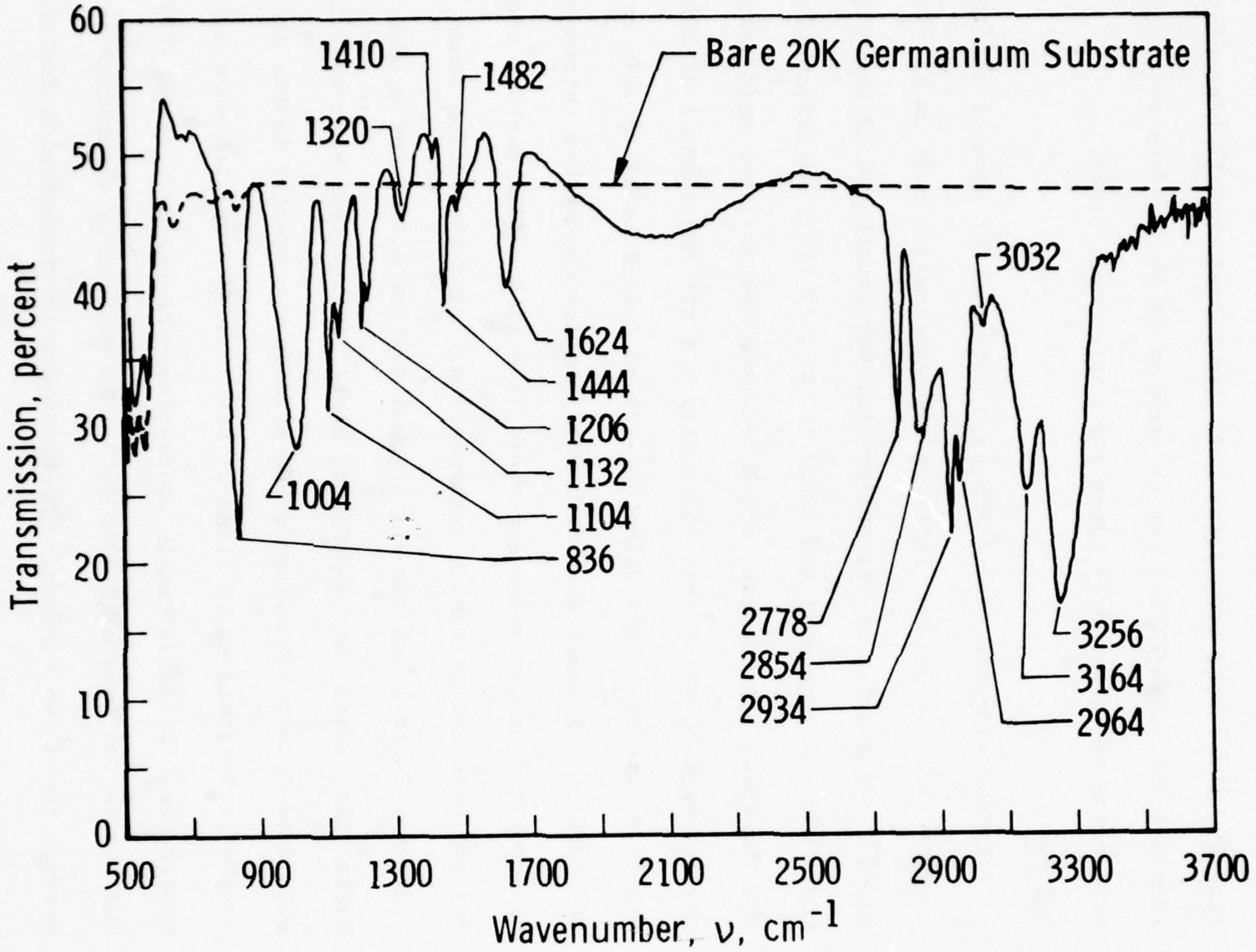

Figure 4 Transmission of 3.17-μm-thick solid MMH on 20K germanium.

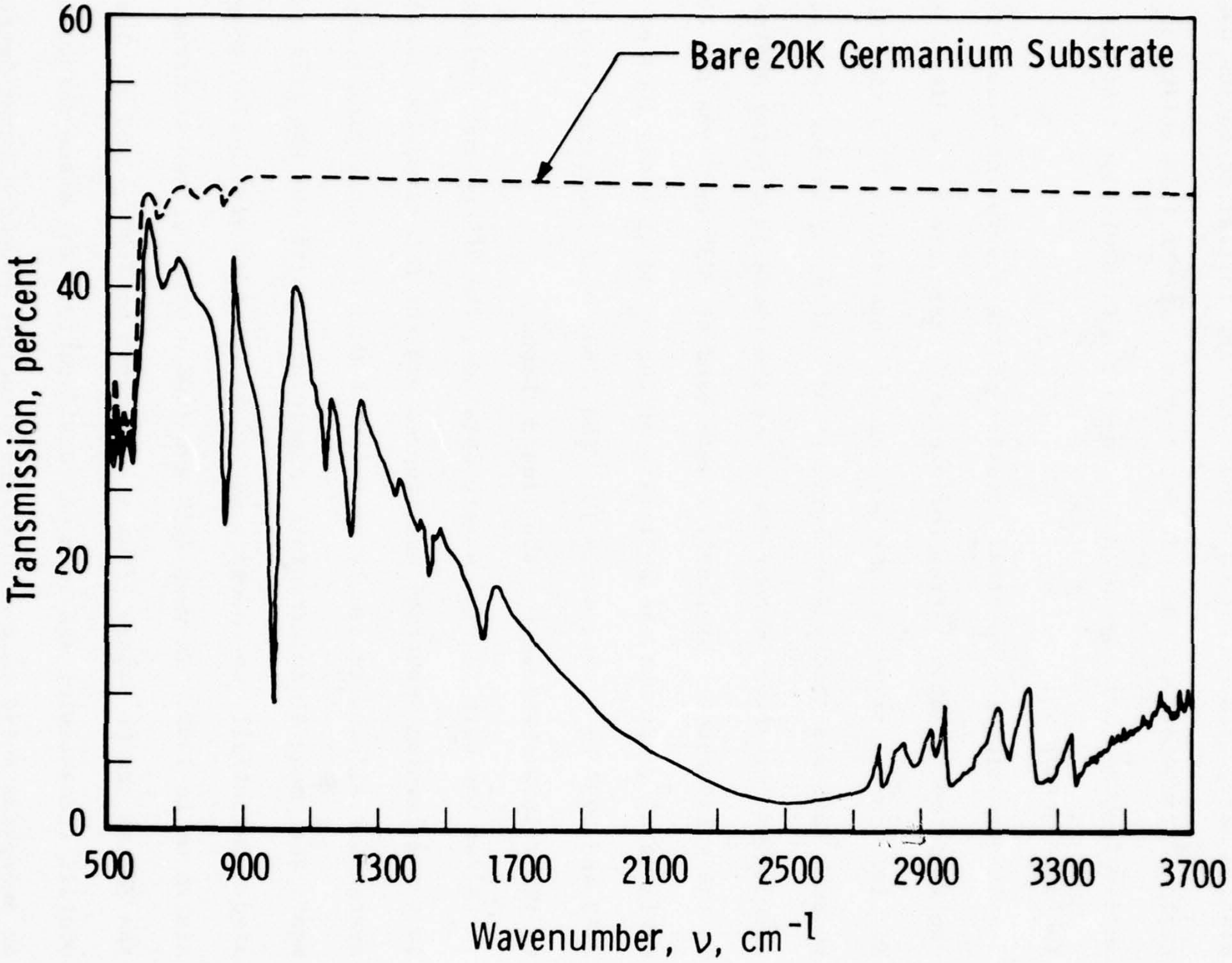

Figure 5 Transmission of 3.17-μm-thick solid MMH after warmup of germanium substrate from 20K to 160K.

between 1900 and 2100 cm^{-1} is actually an interference minima and is a part of the channel spectra. As can be observed some of the transmission curve lies at values higher than the initial germanium base surface transmission. This is due to the thin MMH film acting as an anti-reflection coating which increases the transmission over that of the bare germanium.

In comparing the spectral location of the absorption bands with those listed in Table 1 from Durig et al[3] there are a few discrepancies. In Fig. 4 a relatively strong band can be observed at 3155 cm^{-1} whereas no such band was observed by Durig et al[3]; this may be due to a lack of resolution for their measurements[3] or the bands just being sharper in the solid phase. Similarly a weak band at 3025 cm^{-1} was not observed by Durig et al[3], nor was the splitting of the ν_4 and ν_5 bands located at 2963 and 2937 cm^{-1}, respectively. The other band locations were nearer to the values obtained for the liquid phase.

After the data in Fig. 4 were obtained, the 20K gaseous helium flow to the germanium substrate was stopped and the MMH-germanium surface system was allowed to slowly warm up. Spectral transmission measurements were made at intermediate temperatures until the MMH film evaporated. Essentially no change occurred in the transmission for temperatures up to 145K. Between 145K and 160K a phase change occurred in the MMH as can be deduced from a comparison of Figs. 4 and 5. The overall transmission was reduced considerably. The phase change from an amorphous solid to a crystalline structure caused a large increase in the scattered radiation thereby reducing the transmission of radiation through the MMH-germanium composite. Visually at this time the MMH film

Table 1. Infrared Spectra of NH_2NHCH_3 (MMH), N_2O_4, and Bipropellant Contamination

20°K MMH ν	Assignment	20°K N_2O_4 ν	Assignment	20°K Bipropellant ν	Assignment
836	ν_{18}	750	ν_{12}	665	CO_2
1,004	ν_{16}	785	$\nu_{12}+R$	800	N_2O_4, H_2O
1,104	ν_{15}	820	ν_2	1,275	ν_{11} N_2O_4
1,132	ν_{13}	850	ν_2+R	1,310	N_2O_4
1,206	ν_{12}	940 - 1,060	$\nu_4+\nu_6$ N_2O_3	1,600	NO_2 - ν_3
1,320	ν_{11}	1,050	ν_1 NO_3^-	1,645	N_2O_3 - ν_2
1,410	ν_{10}	1,260	ν_{11}	1,745	N_2O_4 - ν_9
1,444	ν_9	1,305	$\nu_{11}+R$ & ν_3 NO_3^-	1,765	NO
1,482	ν_8	1,450	$2\nu_7+R$	1,840	N_2O_3
1,624	ν_7	1,595	ν_3 NO_2	1,880	N_2O_4
2,778	ν_6	1,618	ν_2 N_2O_3	1,910	NO
2,854	$\nu_9+\nu_{10}$	1,720	ν_5	1,980	N_2O_3
2,934	ν_5	1,745	ν_9	2,100	?
2,964	ν_4	1,765	ν_9+R	2,150	CO
3,032	$\nu_7+\nu_{10}$?	1,880	$\nu_4+\nu_5$	2,240	N_2O
3,164	$\nu_3+\nu_{11}-\nu_{10}$?	1,980	ν_1+R N_2O_3?	2,285	$C^{13}O_2$
3,256	ν_3	2,135	$\nu_2+\nu_3$ NO_3^-?	2,345	CO_2 ν_3
		2,235	ν_3 N_2O	3,300	H_2O
		2,345	ν_3 CO_2		
		2,970	$\nu_5+\nu_{11}$		
		3,115	$2\nu_7+\nu_9$		
		3,155	$2\nu_7+\nu_9+R$		

appeared translucent or milky. The absorption band locations, where detectable, were not shifted appreciably. The ν_{18} band located at 840 cm^{-1} before the phase change split into two bands located at 845 and 960 cm^{-1}. The band located at 1005 cm^{-1} before the phase change shifted to 985 cm^{-1} afterwards which now agrees with the location of the ν_{16} band of Durig et al.[3] Slight variations were seen in the shape and location of the other bands. In general, the shape of the bands were much sharper after the phase change. This was especially true in the 700-1700 cm^{-1} region. After the phase change, the temperature of the germanium substrate was allowed to increase until the MMH had completely evaporated which occurred between 175 and 180K. The chamber pressure at this time was approximately 5 x 10^{-6} torr.

20K N_2O_4

Shown in Fig. 6 is the IR transmission spectrum of a 1.45 μm thick (6 interference maxima) N_2O_4 film deposited on the 20K germanium window. As opposed to the MMH, the N_2O_4 exhibits strong absorption only at the lower wavenumber (700-2300 cm^{-1}). The refractive index at .6328 μm and density were measured and found to be 1.56 ±.02 and 1.84 gm/cm^3 respectively at 20K. This yields a Lorentz-Lorenz value of 0.175 cm^3/gram. During deposition the N_2O_4 films fractured or changed phase abruptly after a film thickness of about 3 μm was reached. This phenomenon was exhibited by a sudden change (within 5 seconds) from a clear transparent film to a highly diffuse-scattering film with the result that thin film interference patterns could no longer be observed. Channel spectra (interference patterns) in the infrared spectra also were destroyed at this time.

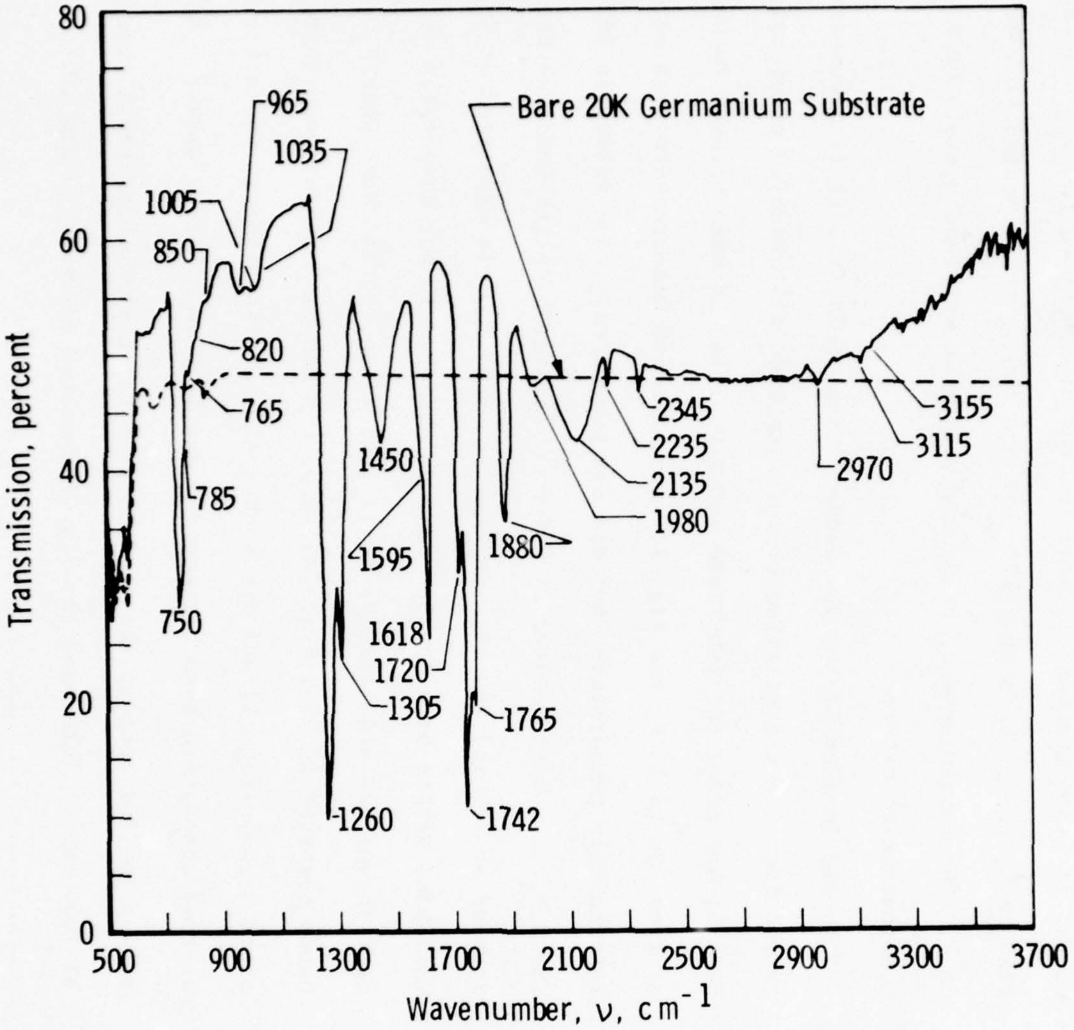

Figure 6 Transmission of 1.45-μm-thick solid N_2O_4 on 20K germanium.

The identifiable N_2O_4 and other bands are listed in Table 1. These data were compared with 77K N_2O_4 measurements of Wiener and Nixon[4] and for gaseous N_2O_4, the measurements of Bibart and Ewing;[5] band assignments follow those of Weiner and Nixon[4] unless indicated otherwise. The major vibration bands are the ν_{12} band located at 750 cm^{-1}, the ν_{11} band at 1260 cm^{-1}, the ν_5 band at $\simeq$1720 cm^{-1} and the ν_9 band located at 1742 cm^{-1}. The remaining N_2O_4 bands are either weaker fundamentals or a combination of others.

To aid in identifying the bands listed in Table 1 it is necessary to consider the transmission of the same N_2O_4 film studied previously, Fig. 6, but after the substrate and N_2O_4 film had been allowed to warm up from 20K to 153K, see Fig. 7. Transmission measurements were made at intermediate temperatures but are not presented. Upon warmup to 153K the N_2O_4 ν_{12} band located at 750 cm^{-1} in Fig. 6 splits into two bands[6] located at 745 and 765 cm^{-1} in Fig. 7. When N_2O_4 is deposited at 77K, this band exists as a doublet[6] as was observed in our data taken at 77K (not shown) and also seen by Weiner and Nixon.[4] The three weak N_2O_4 bands observed in Fig. 6 at 785, 820, and 850 cm^{-1} became much sharper after warmup (Fig. 7) and are much easier distinguished. There is a broad absorption band between 940 and 1060 cm^{-1} before warmup. After warmup to 153K most of the band is gone but a sharp band still remains at 1050 cm^{-1}. This band finally disappeared between 200 and 207K. The

---

[4] Weiner, R. N. and Nixon, E. R., Infrared spectrum of dinitrogen tetroxide, J. of Chem. Phys., 50:No. 4, 906-908, (1957).

[5] Bibart, C. H. and Ewing, G. E., Vibrational spectrum, torsional potential, and bonding of gaseous N_2O_4, J. of Chem. Phys., 61:No. 4, 1284-1292 (1974).

[6] Snyder, R. G. and Hisatsune, I. C., Infrared spectrum of dinitrogen tetroxide, J. of Mol. Spectros., 1:139-150 (1957).

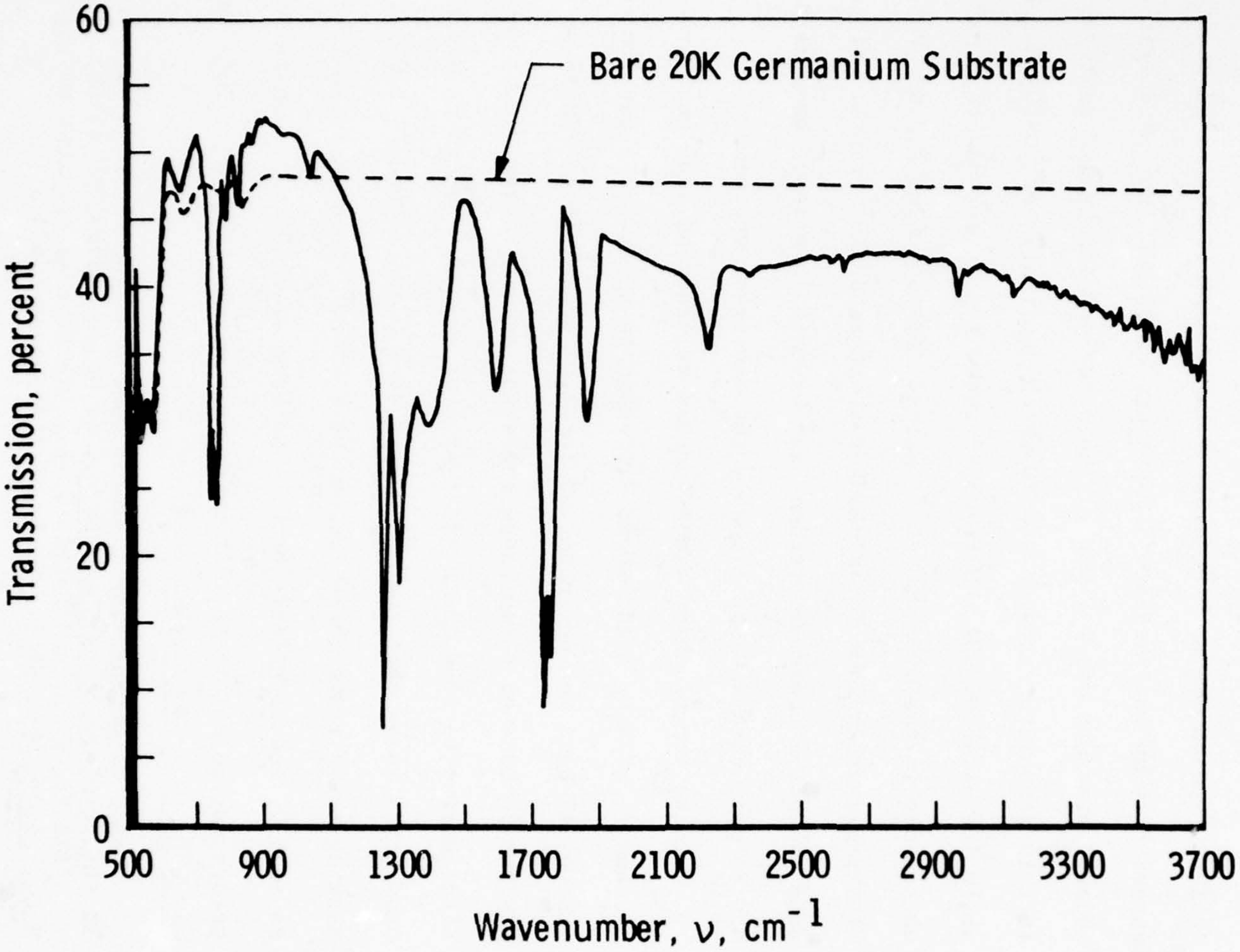

Figure 7 Transmission of 1.45-μm-thick solid N_2O_4 after warmup of germanium substrate from 20K to 153K.

sharp band located at 1050 cm^{-1} is believed to be some form of nitrate[7] (NO_3^-) as it remained on the surface after most of the other film had sublimed. Most of the band initially between 940 and 1060 cm^{-1} is believed[8] to be due to N_2O_3 since a large part of the broad band disappeared at an intermediate temperature of 80-90K (not shown) at a chamber pressure of 10^{-6} torr. The other possible gases that sublimate in this temperature region are NO which sublimates at 60-70K and N_2O which leaves at 80-90K. Neither of these two gases, however, exhibit absorption in the 940-1060 cm^{-1} region. (Note: N_2O_4 and NO_2 sublimate at approximately 150K for a chamber pressure of 10^{-6} torr). Since N_2O_3 does exhibit a broad absorption band at this location,[8] whereas NO and N_2O do not, then N_2O_3 is probably the source of the band.

The two strong sharp bands located at 1260 and 1305 cm^{-1} are the ν_{11} and ν_{11}+R N_2O_4 bands where R represents a torsional lattice mode. (The ν_{11}+R band was not observed for N_2O_4 deposited at 77K in our studies.) Both of these bands are still present after warmup to 153K. After warmup to 153K the band is seen at 1390 cm^{-1} which is a nitrate band, this means that the ν_{11}+R band of N_2O_4 at 1305 cm^{-1} (20K) is also masking the nitrate band. Hence the 1305 cm^{-1} band in Table 1 is listed as an N_2O_4 and ν_3 nitrate band. The band at 1450 cm^{-1} seen in Fig. 6 before warmup shifts to 1385 cm^{-1} after warmup (Fig. 7). This band

---

[7] Kato, R. and Rolfe, J., Vibrational frequencies of NO_2^- and NO_3^- ions in KBr crystals, J. of Chem. Phys., 47:No. 6, 1901-1910 (1967).

[8] Bibart, C. H. and Ewing, G. E., Vibrational spectrum of gaseous N_2O_3, J. of Chem. Phys., 61:No. 4, 1293-1299 (1974).

apparently is the N_2O_4-$2\nu_7$ band which shifts to the lower frequency due to a reduction in the torsional lattice vibrations. In Fig. 6 a sharp band is seen at 1618 cm^{-1} with a side lobe labeled at 1595 cm^{-1}. In the warmup data between 20 and 90K these bands become quite distinct with the disappearance of the 1618 cm^{-1} band at 90K. It is therefore felt that the 1618 cm^{-1} band is the ν_2 band[8] of N_2O_3. After warmup to 153K the band at approximately 1595 cm^{-1} is now quite distinct and is probably the NO_2-ν_3 band.

In the region of 1700 cm^{-1}, Fig. 6, there are three distinct bands seen at 1720, 1745 and 1765 cm^{-1} which are assigned[4] to be the ν_5, ν_9 and ν_9+R N_2O_4 bands, respectively. Upon warmup to 153K the band at 1720 cm^{-1} gradually disappears as seen in Fig. 7. The 1880 cm^{-1} band is the N_2O_4 $\nu_4+\nu_5$ combination band and shifts to 1860 cm^{-1} upon warmup to 153K. The 1980 cm^{-1} broad band seen in Fig. 6 disappears upon warmup to about 90K and is not seen in Fig. 7. Since it disappears at the same temperature as the 940-1060 cm^{-1} band, and the 1618 cm^{-1} band, it also is believed to be due to N_2O_3 even though this band is located some 50 cm^{-1} from that observed for N_2O_3 gas by Bibart and Ewing.[8] The band labeled 2135 cm^{-1} in Fig. 6 was very temperature-dependent, shifting some 85 cm^{-1} to its location of 2220 cm^{-1} in Fig. 7 at 153K. Further temperature increase caused the band to finally be located at 2260 cm^{-1} at 180K. At this temperature the N_2O_4 and NO_2 had already sublimated leaving only a deep blue film on the substrate. This band is believed to be a nitrate, NO_3^-, combination band, possibly $\nu_2+\nu_3$, which could result from the ν_2 and ν_3 bands as recorded by Kato and Rolfe.[7] Further indication that the film remaining at this temperature is a nitrate is that a relatively strong absorption band remains at approximately 1340 cm^{-1} and a weaker one at 1050 cm^{-1} corresponding to NO_3^- fundamentals ν_3 and ν_1, respectively.[7,9,10,11] The film had completely evaporated when a temperature of 207K was reached.

Other bands seen in Fig. 6 are two sharp bands located at 2235 and 2345 cm^{-1}. These two bands were eliminated when the warmup temperature reached 90K (not shown). The band at 2235 cm^{-1} was found to be the N_2O ν_3 fundamental band which is the strongest N_2O fundamental. The 2345 cm^{-1} band was found to be the CO_2 ν_3 band and is the strongest CO_2 fundamental. Only a trace amount of N_2O and CO_2 is required to enable these bands to show up. The other very weak bands marked in Fig. 6 between 2900 and 3200 are attributed to N_2O_4 and are the $\nu_5+\nu_{11}$ band at 2970 cm^{-1}, the $2\nu_7+\nu_9$ band at 3115 cm^{-1} and the $2\nu_7+\nu_9+R$ band at 3155 cm^{-1}. Although these bands appear very weak in Fig. 6, but they are more prominent when N_2O_4 is deposited on a 77K surface.

---

[9] Herzberg, G. Molecular Spectra and Molecular Structure -- II. Infrared and Raman Spectra of Polyatomic Molecules, Van Nostrand Co., Inc. (1945).

[10] Devlin, J. P. and Pollard, G., ATR infrared spectra of uniaxial nitrate crystals, J. of Chem. Phys., 53:No. 11, 4147-4151 (1970).

[11] McGraw, G. E., Bernitt, D. L., Hisatsune, I. C., Vibrational spectra of isotopic nitric acids, J. of Chem. Phys.,42:No. 1, 237-244 (1965).

It should be mentioned that the ν_7 fundamental band which is located at 685 cm^{-1} in the gas was not observed in the solid films studied here. This band, as was pointed out,[4] is considerably weaker in the solid phase as contrasted to that observed in the gaseous phase.

20K Simulated Plume Mixture

To prepare for an actual engine firing, a simulated plume mixture of gases was prepared. The mixture approximated stoichometric combustion conditions for an MMH/N_2O_4 engine not considering hydrogen. The mixture ratio was 50.3% N_2, 22.5% H_2O, 17.2% CO_2, and 10% CO. The refractive index for this mixture formed at 20K was 1.26 ±0.02 at .6328 μm, and the density was .77 gms/cm^3. The transmission spectra of the simulated plume mixture is shown in Fig. 8 for a deposit thickness of 6.72 μm (25 interference patterns). This deposit was very clear and could not be visibly detected with the eye. In the visible (scattering was negligible in the IR) the mixtures exhibited less scattering than the pure gases studied individually. In Fig. 8 the H_2O, CO, and CO_2 bands are clearly identifiable. The CO band shows up at 2142 cm^{-1}, and the ν_2 and ν_3 CO_2 bands show up at 660 and at 2346 cm^{-1}, respectively. The carbon 13 isotope $C^{13}O_2$ ν_3 band appears at 2282 cm^{-1} and the weaker $2\nu_2+\nu_3$ CO_2 band occurs at 3604 cm^{-1}. H_2O absorption bands are observed also with the ν_2 band located at approximately 1610 cm^{-1} with a weaker side band occurring at 1630 cm^{-1}. The ν_1 and ν_3 bands are observed at 3690 and 3715 cm^{-1}, respectively. These bands observed in the mixture are much sharper than were observed for a pure water film at 20K. For the pure water films, a very broad shallow band occurred in the vicinity of 1500-1700 cm^{-1} and a very strong broad band was observed from about 2900-3600 cm^{-1} and centered at approximately 3280 cm^{-1}. The ν_1 and ν_3 bands were not observed. Weaker broad absorption bands were observed for H_2O in the 700-900 cm^{-1} and 2100-2400 cm^{-1} regions but are not observed in Fig. 8.

In Fig. 9 the transmission of the film after warmup to 96K is shown. Notice the overall shape of the curve has been altered considerably but the presence of the CO_2 bands at 640 cm^{-1} and in the 2280-2380 cm^{-1} region are still easily seen. The double band of H_2O near 1620 cm^{-1} has now changed to a broader single band centered at 1640 cm^{-1} and the previously unseen broad band centered at approximately 3180 cm^{-1} is now very pronounced. The overall reduction in transmission is attributed

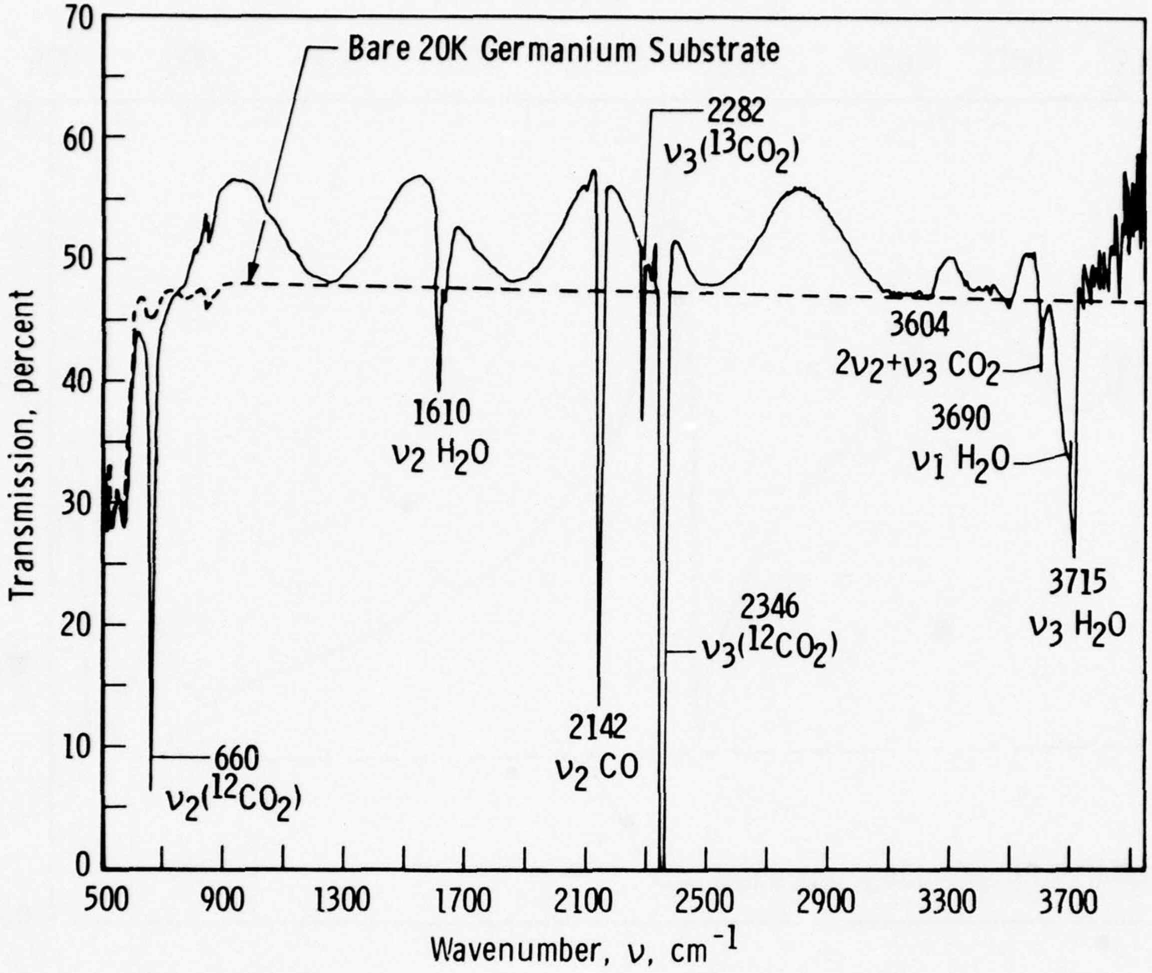

Figure 8 Transmission of 6.72-μm-thick solid simulated plume mixture I on 20K germanium.

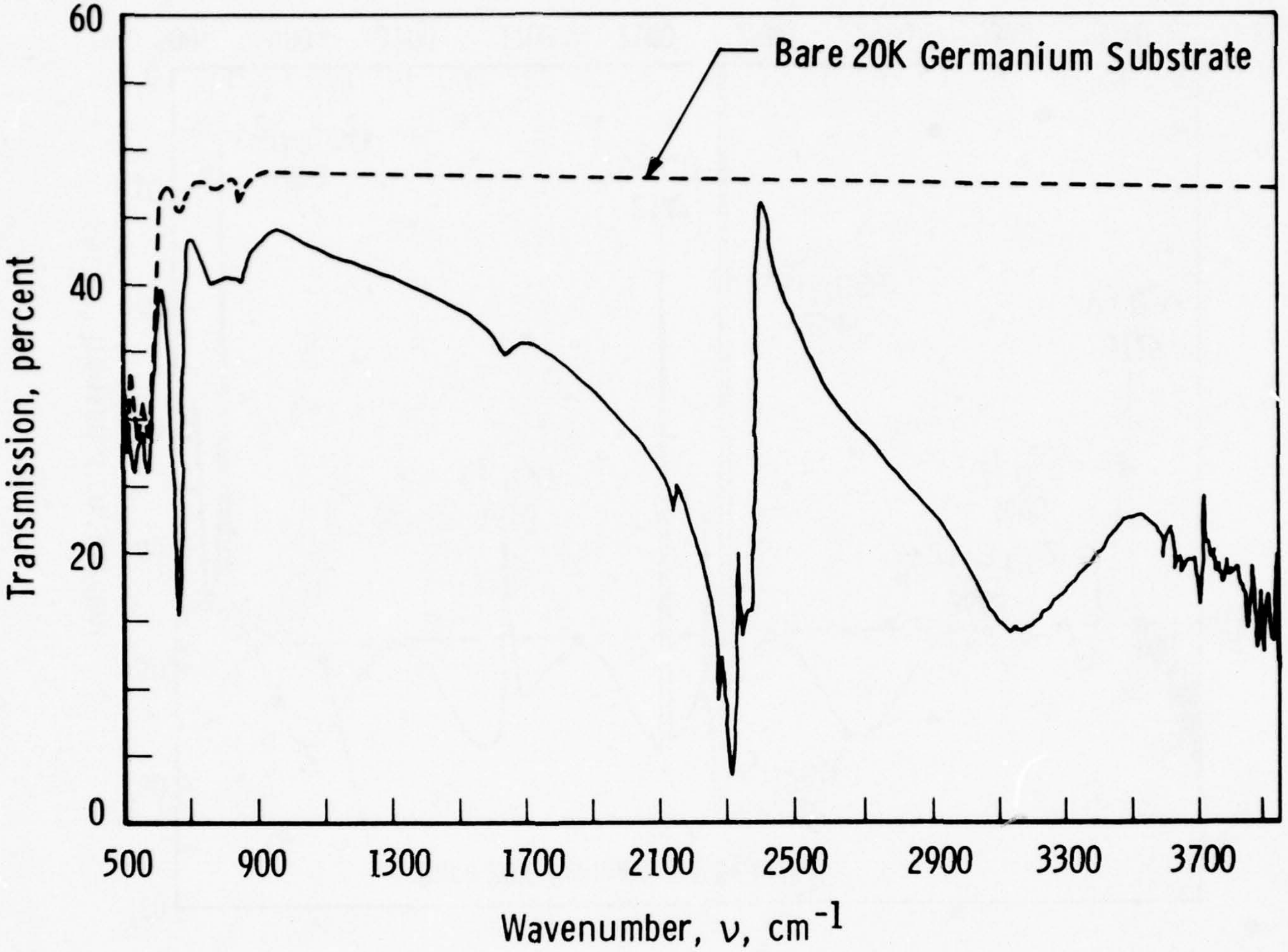

Figure 9 Transmission of 6.72-μm-thick solid simulated plume mixture after warmup of germanium from 20K to 96K.

to an increase in scattering caused by the phase change (crystallization) or N_2 sublimation (at 30-40K) during warmup. Further warmup to 110K (not shown) resulted in the evaporation of CO_2 with only a trace amount observable in the transmission spectra. Similarly the H_2O bands at 3690 and 3715 cm^{-1} disappeared but the broad band centered at 3180 cm^{-1} became even more prominent. The center of this band varied somewhat in other experiments occurring anywhere between 3180 and 3300 cm^{-1}.

Bipropellant Contamination

Shown in Fig. 10 are the results of transmission measurements made for cryopumped exhaust products from a 5 lb_f thrust bipropellant engine--the fuel being monomethylhydrazine (MMH) and the oxidizer nitrogen tetroxide (N_2O_4). Exhaust products were cryopumped at 20K on a germanium substrate located at 90 deg from the nozzle centerline at the nozzle exit plane. The deposit thickness for the data presented in Fig. 10 was 3.62 μm. Table 2 shows the refractive index (.6328 μm) and density of the contaminant for various oxidizer-fuel (O/F) ratios and pulse widths; the refractive index average was 1.34 and the average density was 0.77 gms/cm^3. The primary contaminants were H_2O, CO_2, N_2 and N_2O_4 and possibly trace amounts of CO, NO, N_2O, and N_2O_3. The bands corresponding to the various species in Fig. 10 are identified in Table 1. At 665 cm^{-1} is seen the CO_2 ν_2 band. A relatively broad band is seen between about 700-860 cm^{-1} with it centered at 800 cm^{-1}. This band is due to two species--H_2O and N_2O_4. The N_2O_4 ν_{12} band is located at 750 cm^{-1} and the H_2O absorption band has been observed to peak at approximately 780 cm^{-1} at 20K but it is a relatively broad band (770-820 cm^{-1}). The next discernible band is located at $\simeq$1275 cm^{-1} and is the N_2O_4 ν_{11} band. A band located

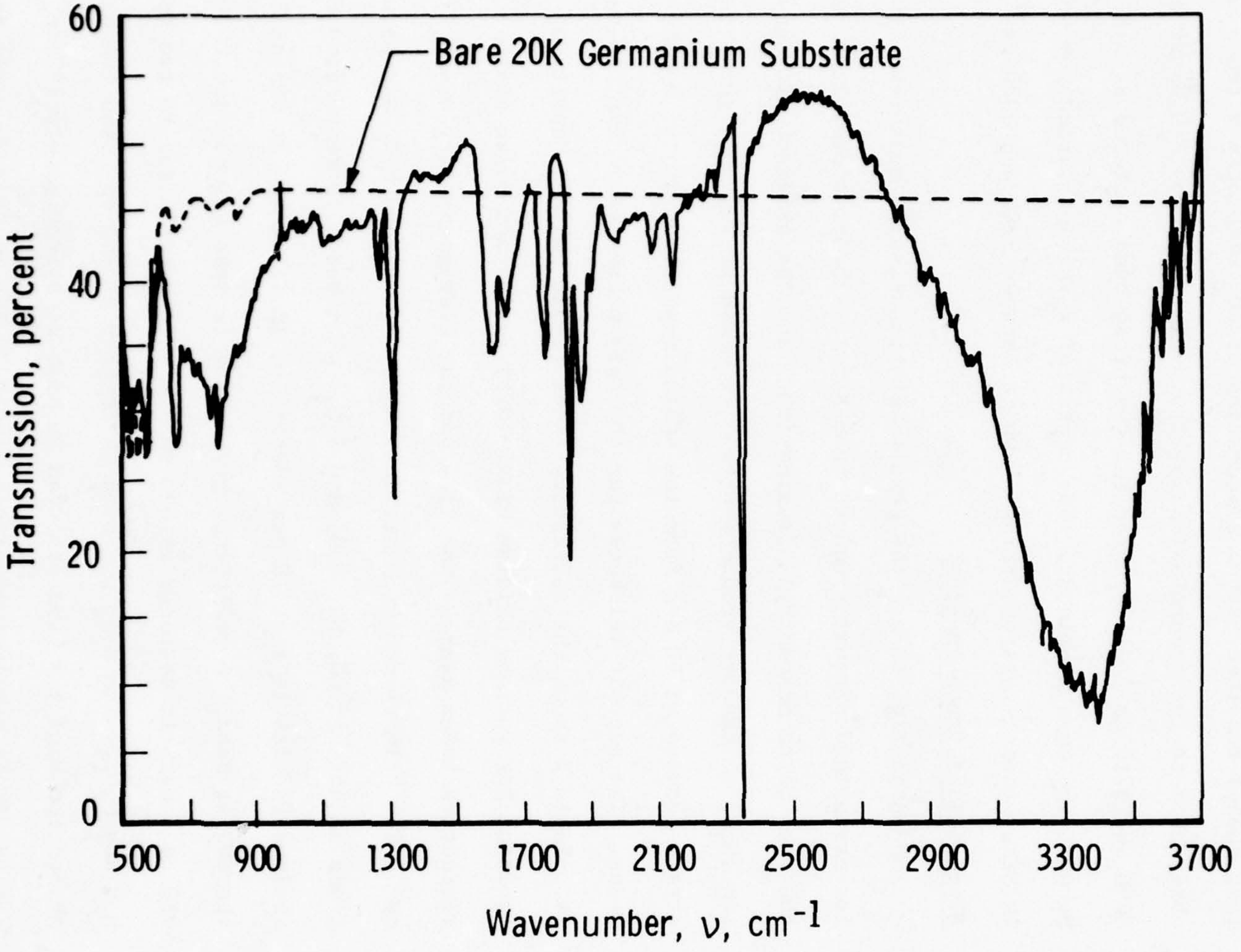

Figure 10 Transmission of 3.62-μm-thick solid bipropellant contamination on 20K germanium.

Table 2. Deposition Characteristics of Bipropellant Plume Contamination

Pulse Time, msec	No. of Pulses	O/F Ratio	Ge Surface Temp., ^oK	n	ρ, gm/cm^3	Lorentz Constant	Hz per Pulse	Thickness(Å) per Pulse	Mass (μg) per (cm^2 · pulse)	Thickness(Å) per sec of Firing	Mass (μg) per (cm^2 · sec of Firing)	Film Total Thickness, μm
50	315	1.6	26	1.3473	0.747	0.2859	8.2	19.8	0.233	396	4.66	0.624
100	180	1.6	26	1.349	0.811	0.2646	14.8	32.7	0.420	327	4.20	0.589
100	170	1.4	26	1.3344	0.761	0.2713	13.6	33.3	0.400	333	4.00	0.566
100	200	1.4	26	1.3454	0.737	0.2885	12.2	29.7	0.345	297	3.45	0.594
100	139	1.8	26	1.3388	0.785	0.2664	16.5	37.2	0.460	372	4.60	0.517
100	239	1.8	26	1.329	0.783	0.2599	12.4	29.0	0.357	290	3.57	0.692
100	1,332	1.6	75	1.417	1.010	0.2491	7.15	12.8	0.127	128	1.27	1.710
100	280	1.6	100	1.346	0.850	0.2506	7.47	15.6	0.132	156	1.32	0.436
100	475	1.6	140	1.368	0.850	0.2648	5.07	10.6	0.0897	106	0.897	0.501
100	570	1.6	140	1.340	0.837	0.2506	4.89	10.4	0.0866	104	0.866	0.591

at 1310 cm^{-1} is attributed to N_2O_4 and is the (ν_{11}+R) band of Wiener and Nixon.[4] The intensities of the 1275 cm^{-1} and 1310 cm^{-1} bands are decidedly different from that observed for N_2O_4 in Fig. 6. Upon warmup of the germanium and contaminant film to 105K (see Fig. 11) the absorption of both bands increase but much more dramatically for the 1275 cm^{-1} band. Both bands were still present after warmup to 165K for a chamber pressure of 4 torr.

The next two distinct bands are located at approximately 1600 cm^{-1} and 1645 cm^{-1}. The 1600 cm^{-1} band is the ν_3 band of NO_2 and the 1645 cm^{-1} band is believed to be the ν_2 band of N_2O_3 which is listed as 1646-1658 cm^{-1} by Bibart and Ewing.[8] As can be seen in the warmup data of Fig. 11, this band is almost gone at a temperature of 105K. Again only N_2O_3, N_2O and NO evaporate at this low temperature and N_2O_3 is the only one of the three which shows an absorption band in this wavenumber region.

The next two bands seen in Figs. 10 and 11 are those located at 1745 and 1765 cm^{-1}. These two bands almost appear as one in Fig. 10 but warmup data at intermediate temperatures (not shown) indicated the two distinct bands. The band at 1765 cm^{-1} disappeared on warmup to approximately 80K and appears to be an NO fundamental band. The 1745 cm^{-1} band remains after warmup until a temperature of approximately 190K was reached (for a chamber pressure of 1.5 mm). This band is the N_2O_4 ν_9 band.

The next three bands seen in Fig. 10 are those located at 1840, 1880, and 1910 cm^{-1}. The 1880 cm^{-1} band is an N_2O_4 which remains during warmup of the surface until the film evaporates at about 190K. This band was also observed in Fig. 6 for the N_2O_4 data. The 1840 cm^{-1} and the 1910 cm^{-1} bands are believed to be due to N_2O_3 and NO, respectively. A portion

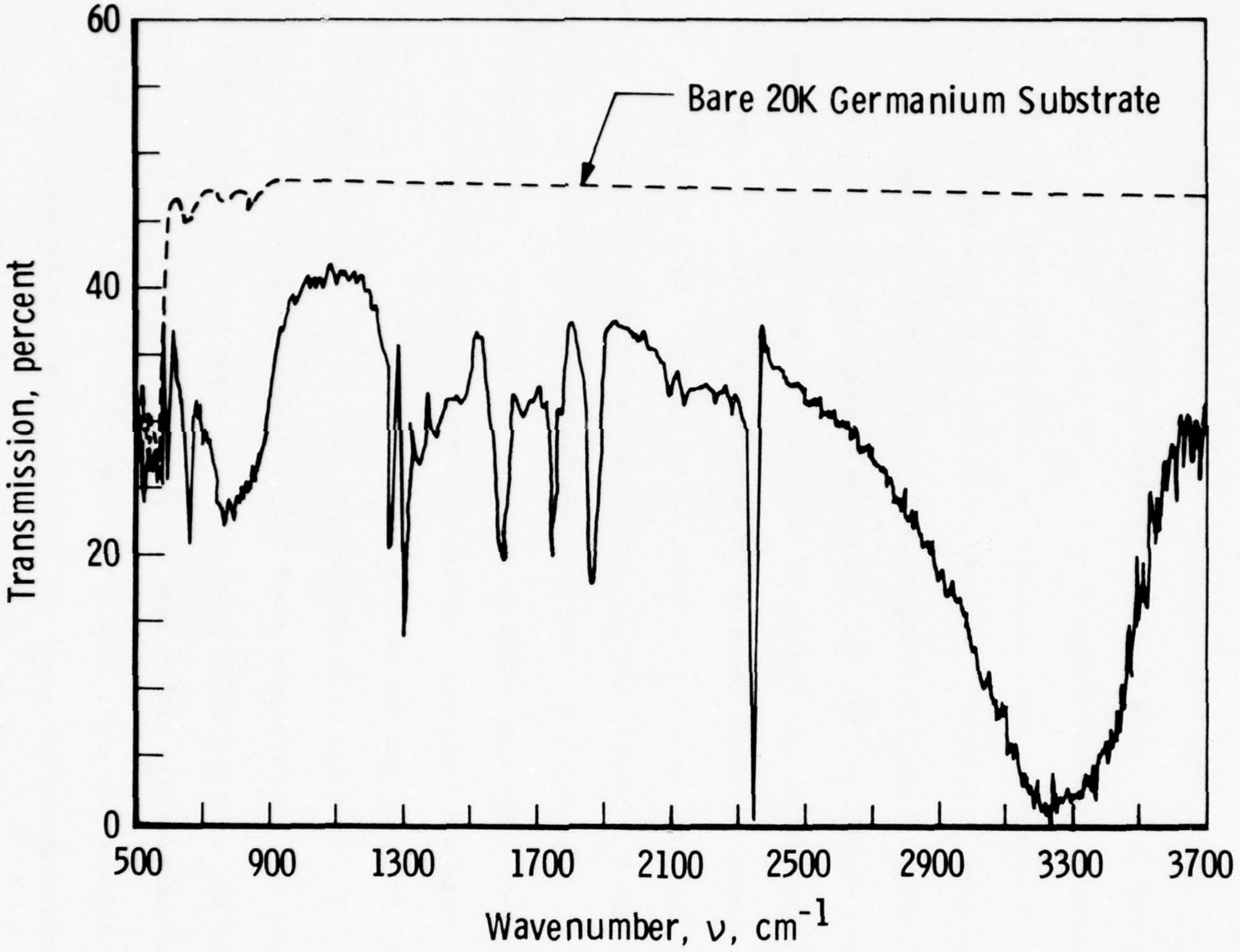

Figure 11 Transmission of 3.62-μm-thick solid bipropellant contamination after warmup of germanium from 20K to 105K.

of the 1840 cm^{-1} band could also be due to NO. Both of these bands are gone upon warmup to 105K (see Fig. 11) and were seen to disappear at a temperature of about 90K which further indicates them to be due to either N_2O_3 or NO. Similarly arguments can be made for the weak band observed at 1980 cm^{-1}. This band was observed in the N_2O_4 data (Fig. 6) and it likewise disappeared upon warmup to 90K and is believed due to N_2O_3.

A series of weak bands occur at 2100, 2150, 2240, and 2285 cm^{-1}. The band at 2150 cm^{-1} is believed to be the CO 2138 cm^{-1} band even though normally CO would have sublimated at 30-40K and the band is still barely seen at 105K in Fig. 11. This is believed to be due to the CO being trapped in the matrix. In studies of mixtures involving CO we have seen CO to be contained by other gases up to temperatures of 70K. The band observed at 2240 cm^{-1} is due to a trace amount of N_2O. This band is the strongest of all N_2O bands. Another weak band seen at 2285 cm^{-1} is due to the $C^{13}O_2$ band which has been observed previously. This leaves only the 2100 cm^{-1} of these four which is yet to be identified. Most of the source of this band sublimated during warmup at temperatures between 105 and 139K but is still unknown at this time.

The last two bands observed in Fig. 10 are the CO_2 ν_3 band located at 2345 cm^{-1} and the very broad H_2O band observed in the vicinity of 3300 cm^{-1}. The CO_2 band was still visible after warmup to about 165K (not shown) which is considerably higher than the temperature at which CO_2 would normally sublimate (at about 115K for a pressure of 1×10^{-2} torr). This is another indication of how gases are trapped within a frozen matrix of other constituents. Similarly, most of the H_2O sublimated during the temperature warmup range of 195-200K although weak abosrption was observed in the

2500-3400 cm^{-1} range up to a warmup temperature of 225K. The absorption bands for H_2O in Figs. 10 and 11 were considerably different from that seen in other measurements involving gas mixtues in which H_2O was only one of the constitutents. In this case the bands were much sharper as can be observed from the simulated plume mixture in Figs. 8 and 9. The sharp H_2O fundamentals seen in the simulated plume mixture, ν_1 at 3652 cm^{-1}, ν_2 at 1595 cm^{-1} and ν_3 at 3756 (see Herzberg[9]), were not observed for the H_2O contribution in the data in Fig. 10. However, after warmup of the simulated plume mixture the broad absorption around 3300 cm^{-1} was very similar to that observed in Fig. 10 for the bipropellant engine firings.

Although several of the bands seen in Figs. 10 and 11 were identified as N_2O_4 some of the bands that were seen in the N_2O_4 data were not observed in Figs. 10 and 11 and the relative intensities of the bands were not consistent with those observed for the measurements on N_2O_4 in the research cell. Also no MMH bands were observed in the bipropellant data of Fig. 10 indicating that no excess fuel was seen but excess oxidizer (N_2O_4) was observed. A very small amount of CO was observed in the spectra of Fig. 10 but this band is considerably less intense than was expected. Indications have been that 5-6% of the exhaust products from an MMH/N_2O_4 engine is CO and this percentage is comparable to that used in the simulated plume mixture which shows a very strong CO band at 2140 cm^{-1}. The first question to be considered is: was the germanium window cold enough to pump CO? It was firmly established that N_2 was pumped at this temperature which required a lower temperature ($\simeq$27K) for condensation than does CO (28-29K). Therefore, the surface was cold enough to pump CO. The alternative explanation is that most of the CO was contained in the central core of the plume exhaust and was cryopumped downstream of the germanium test surface which was located in the backflow region.

4.0 OPTICAL CONSTANTS OF CONTAMINANTS

In order to determine the complex refractive index ($\bar{n} = n - ik$) of the thin solid film on a thick germanium window from the transmission versus thickness data for wavenumbers between 700 and 3700 cm^{-1}, an analytical model of film plus window transmission was derived. It was assumed that the germanium window was a thick film and thus there was no phase coherence between multiple internal reflected rays. Moreover, the real part of the germanium complex index, n_g, was known and given by[1]

$$n_g = A + BL + CL^2 + D\lambda^2 + E\lambda^4 \qquad (2)$$

where $L = (\lambda^2 - 0.028)^{-1}$, A = 3.99931, B = 0.391707, C = 0.163492, D = -0.000006, E = 0.00000053. The geometry describing the transmission is shown in Fig. 12. For convenience the different layers have been subscripted 0, 1, 2, and 3, where subscripts 0 and 3 are vacuum and 1 and 2 are the thin contamination film and the thick germanium substrate, respectively. The model employed to fit the experimental results is for normal incidence only. As shown in Fig. 12, E_0^+ is the amplitude of the incident radiation which undergoes an infinite number of multiple reflections after passing into the thin film. Following multiple reflection the total amplitude of reflected and transmitted radiation is given by B1 and E_2^+, respectively. E_2^+ internally reflects from and transmits through the back of the germanium window, becomes A1 and C1, and again

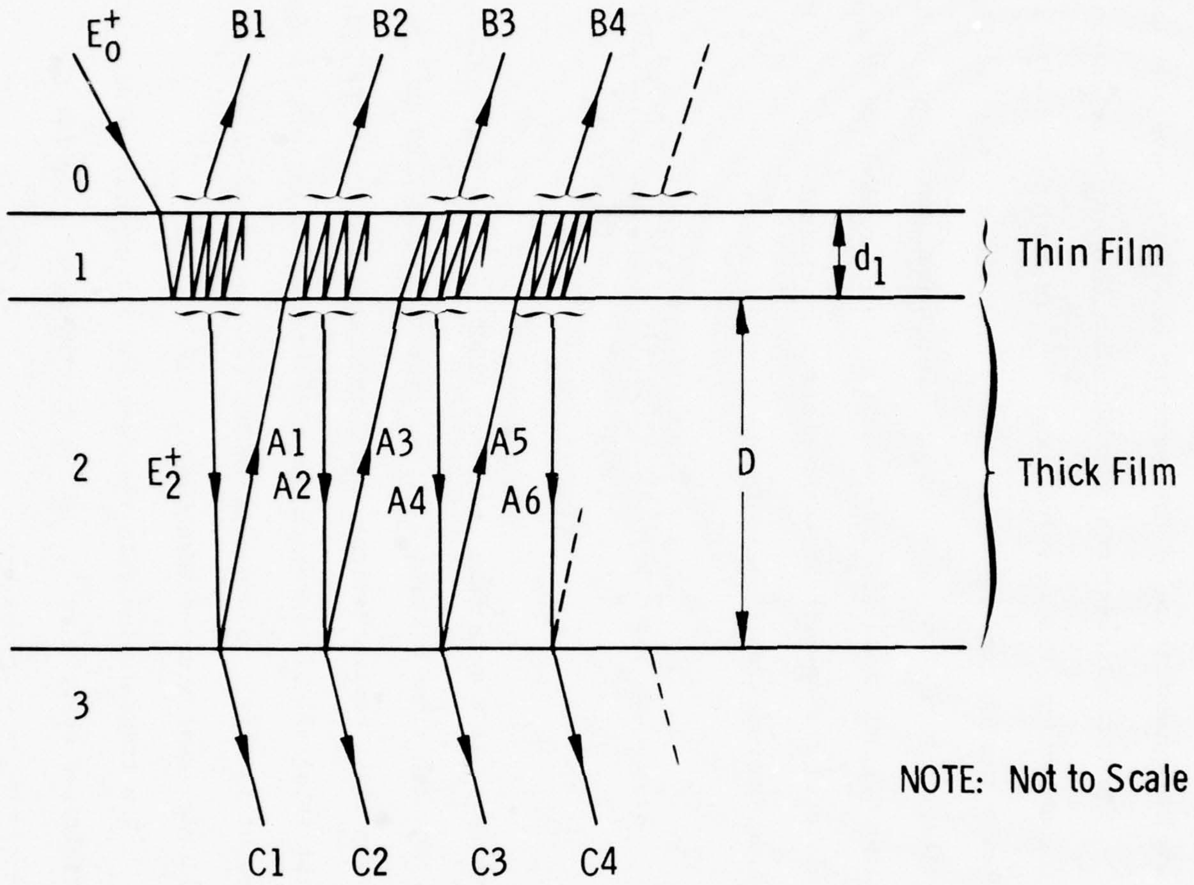

NOTE: Not to Scale

Figure 12 Geometry depicting analytical model for a thin film formed upon a thick film.

undergoes thin-film multiple reflection in medium 1. This results in the rays B2 and A2, and so on. Analytically the relationships describing the transmission of the geometry in Fig. 12 have been derived.[12,13]

The optical constants of the cryocontaminants were determined by using the analytical transmission model[12,13] in conjunction with a non-linear least squares convergence routine. Also the subtractive Kramers-Kronig relation between n and k was used in conjunction with (for N_2O_4 and bipropellant data) and in comparison with (for MMH and simulated plume mixture) the non-linear least squares determination of n. The subtractive Kramers-Kronig[1] relation is given by

$$n(v) = n(v_m) + \frac{2}{\pi} P \int_o^\infty \left(\frac{k(v')v' - k(v)v}{(v)^2 - v^2} = \frac{k(v')v' - k(v_m)v_m}{(v')^2 - v_m^2} \right) dv' \qquad (3)$$

where v_m is a reference frequency (2500 cm^{-1} for MMH, 2000 cm^{-1} for the simulated plume mixture, 2500 cm^{-1} for N_2O_4, and 2180 cm^{-1} for the bipropellant contamination), and P indicates the Cauchy principal value of the integral. Integration was performed using the simple trapezoidal rule; the k(v') values used in Eq. (3) were those determined by the non-linear least squares technique.

The transmission data recorded for all deposits discussed here were digitized every 2 cm^{-1}. In the determination of $\bar{n}$ for MMH 15 thicknesses

---

[12] Vasicek, A. Optics, of Thin Films, North Holland Publishing Company, Interscience Publishers, Inc., New York (1960).

[13] Heavens, O. S., Optical Properties of Thin Films, Dover Publications Inc., New York (1965).

(0 to 3.26 μm) were used and for the simulated plume mixture 16 thicknesses (0 to 5.38 μm) were used. Shown in Figs. 13 and 14 are optical constants for these two deposits. These optical properties were determined solely by use of the analytical model with the non-linear least square convergence technique; the Kramers-Kronig is shown only for comparison purposes. As seen the two techniques were in excellent agreement with one another, thus demonstrating the Kramers-Kronig to yield highly reliable results.

For the N_2O_4 8 thicknesses (0 to 1.45 μm) and for the bipropellant contamination 11 thicknesses (0 to 2.35 μm) were used in determining the optical properties. For N_2O_4 the cryodeposit fractured during the formation of the 9th thickness; for the bipropellant data, the test schedule only permitted time for the formation of 11 thicknesses. Usually a minimum of 15 thicknesses is desired in order for the analytical model to converge upon a well defined value of n. The n value appears to be primarily defined by the period of the transmission versus thickness curve at each wavenumber. When only a few thicknesses are obtained, the transmission versus thickness (for each wavenumber) curve is not well defined. It was found that for the high wavenumbers (2100 cm^{-1}) the analytical model had no problem in defining n; however, at the lower wavenumbers a neighborhood (range) of n values seemed to equally satisfy the transmission data. The k value which is primarily determined by the magnitude of the transmission did not have this difficulty and was well defined over the whole spectral region (700 to 3700 cm^{-1}). Thus to determine n, the k values were used with the subtractive Kramers-Kronig technique to compute n; these new n values were then used in the analytical model

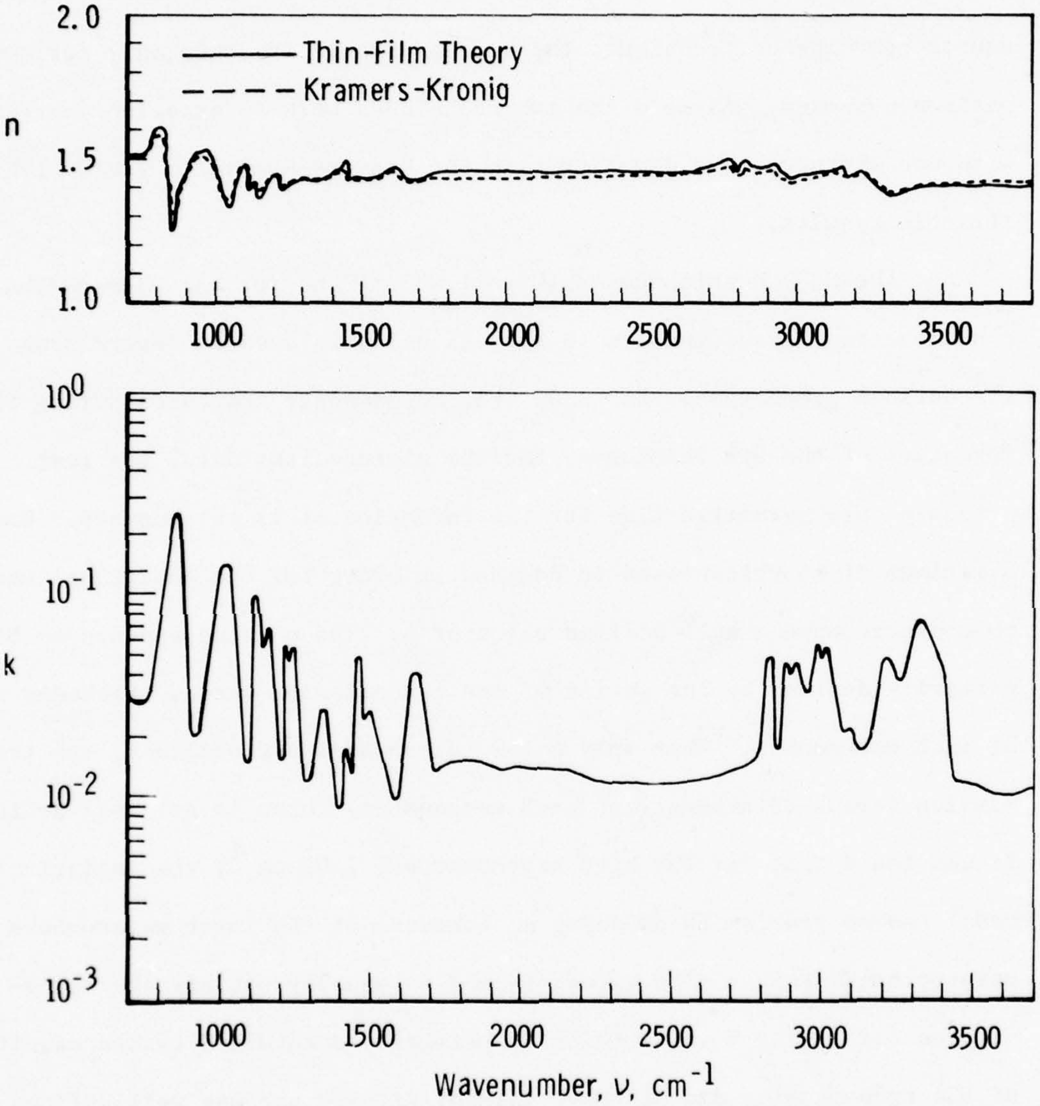

Figure 13 Complex refractive index for MMH on 20K germanium.

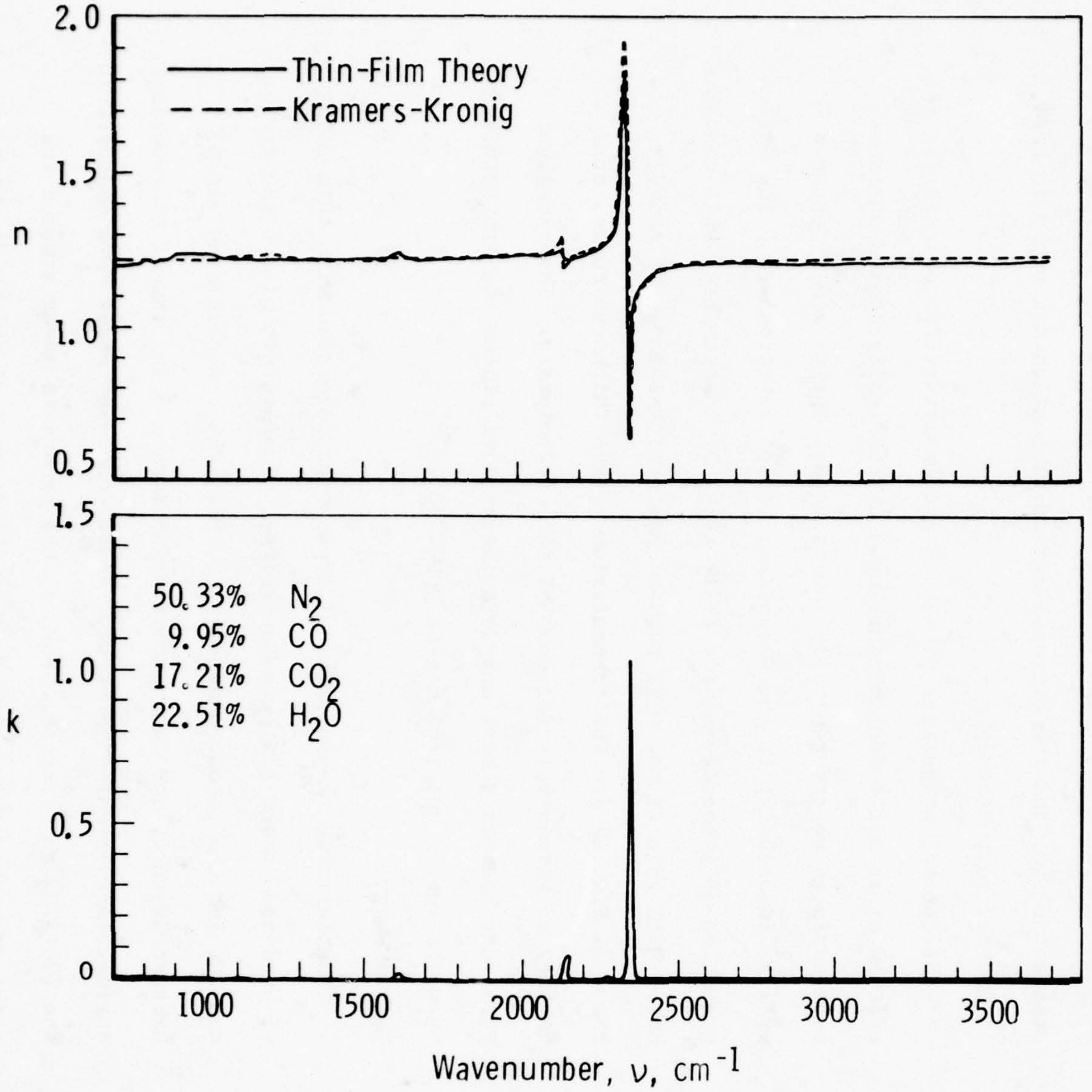

Figure 14 Complex refractive index for the simulated plume mixture on 20K Ge.

(along with the k values) to see if good agreement occurred with the transmission data. For all wavenumbers the Kramers-Kronig n's along with the least-squares k's yielded excellent agreement when the analytical model and transmission data were compared. The optical constants for N_2O_4 and the bipropellant contamination are shown in Figs. 15 and 16, respectively.

The optical properties presented are important for calculating the effects of possible contaminants upon cryogenically cooled surfaces. Such surfaces as cryogenically cooled sensor optics and telescopes will be functioning in the wavenumber region investigated. The interpretation of information from these types of instruments, when contaminated with thin films, will require spectral knowledge of n and k. Shown in Fig. 17 are the transmission versus thickness curves at a variety of wavenumbers for each of the contaminants. The excellent agreement between theory and data is typical of the results obtained over the entire spectral region 700-3700 cm^{-1}.

5.0 SUMMARY

The infrared transmission of cryocooled germanium with thin films of condensed gases has been determined. Temperature of the substrate was 20K and the gases condensed were MMH, N_2O_4, a simulated plume exhaust mixture, and the contamination from a 5 lb_f thrust bipropellant engine. The infrared spectra of these condensed gases were measured in the 700-3700 cm^{-1} region. For all the condensed gases studied the infrared spectrum was determined as a function of thickness which was measured by a two angle laser technique. At the He-Ne line the refractive index of each film was measured and in conjunction with a QCM

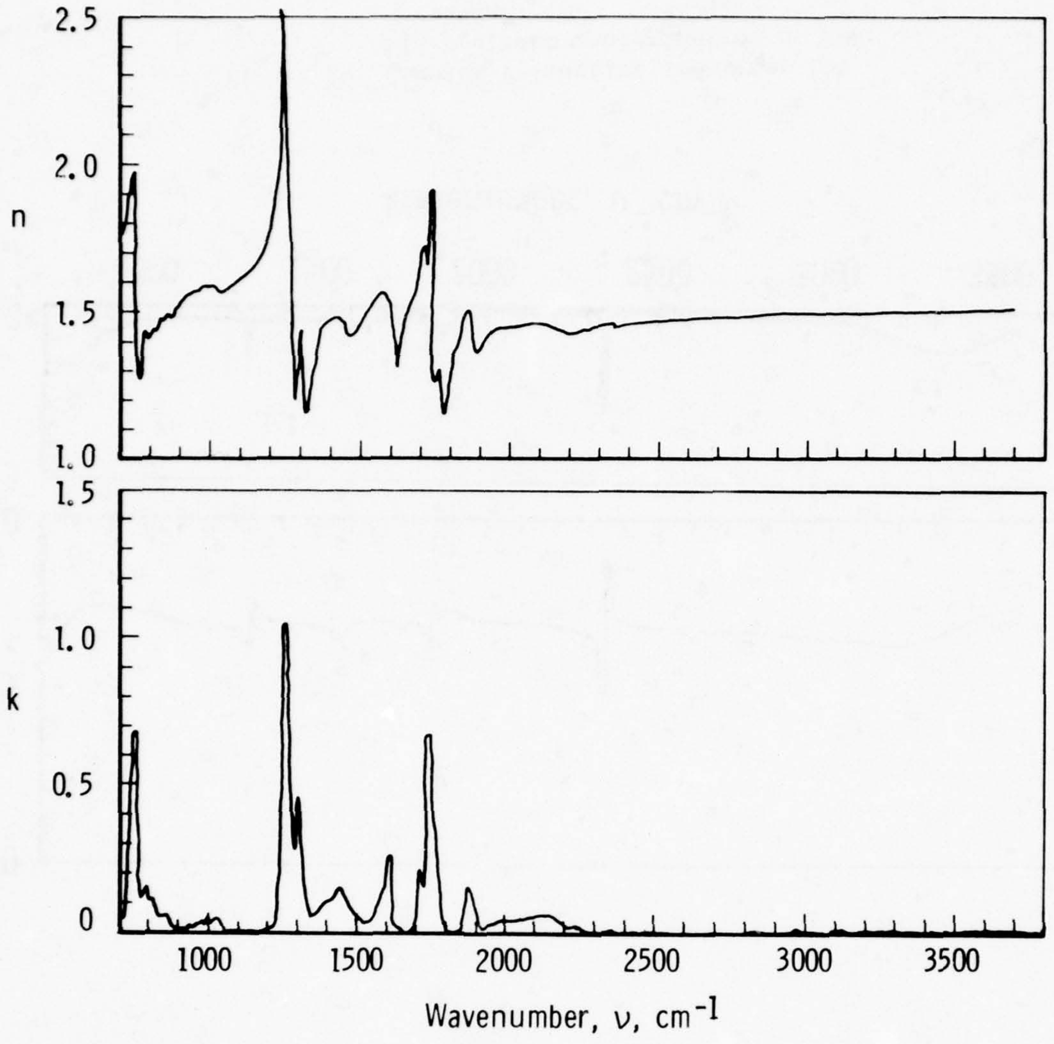

Figure 15 Complex refractive index for N_2O_4 on 20K Germanium.

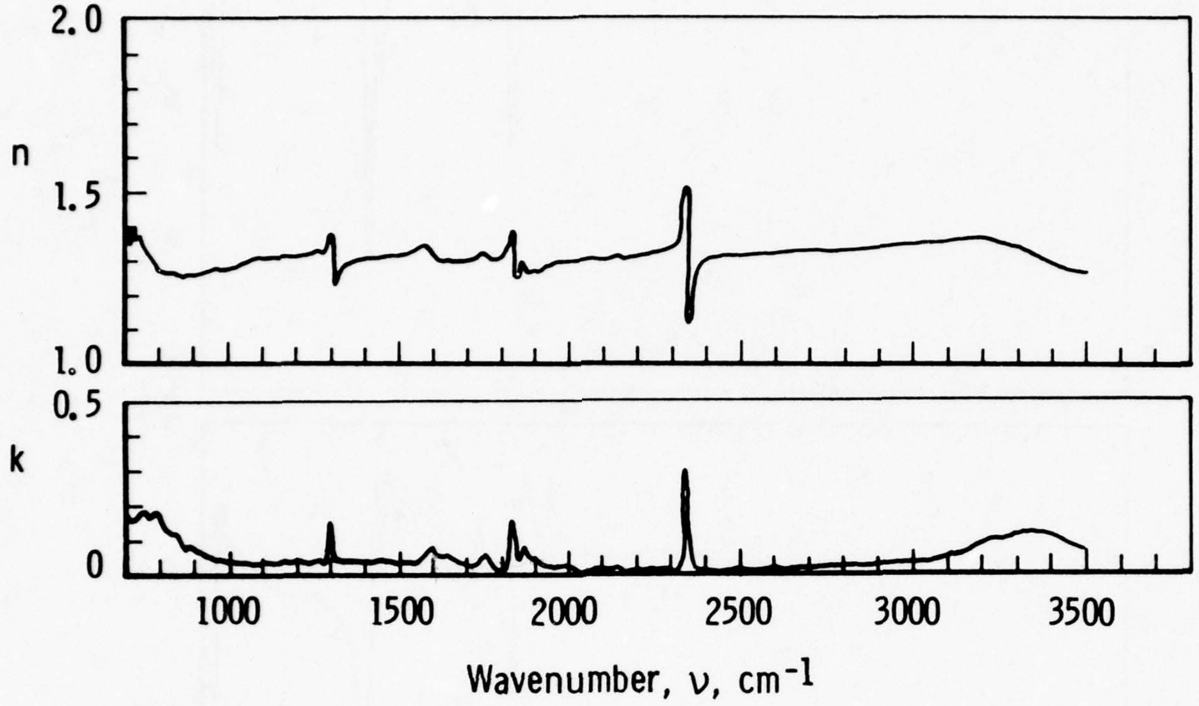

Figure 16 Complex refractive index for the bipropellant contamination on 20K Germanium.

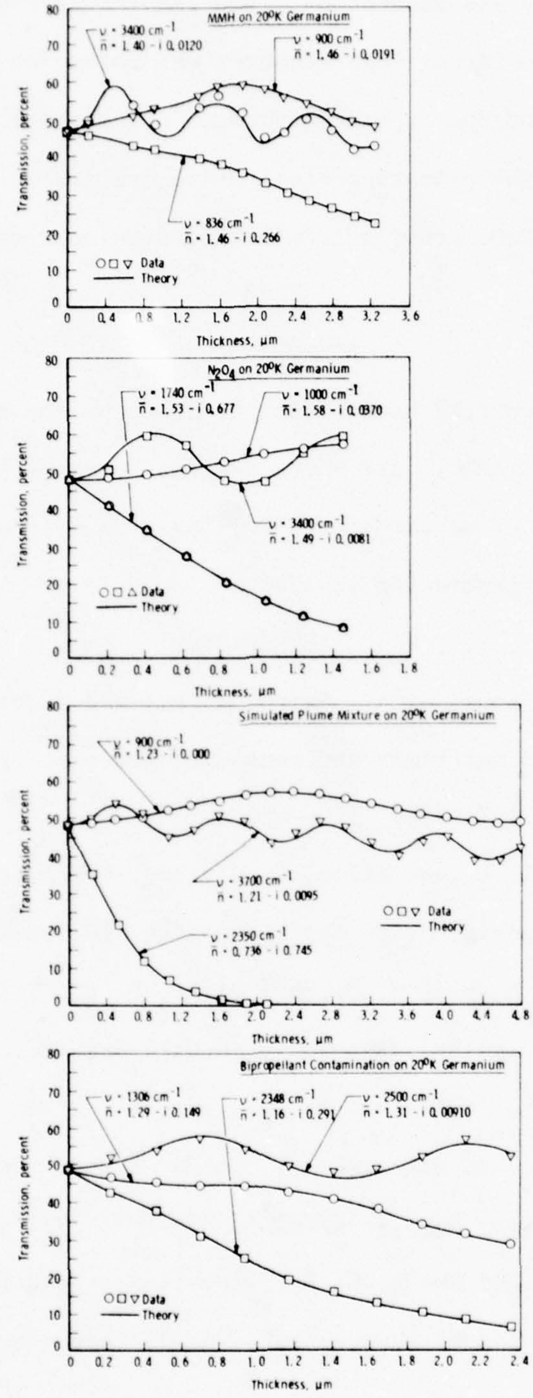

Figure 17 Comparison of theory and data for various contaminants on 20K germanium for different wavenumbers.

the deposit density was determined. The complex refractive index was determined by a non-linear least squares determination from a derived analytical model and the experimental data. For the 5 lb_f thrust bipropellant engine the primary contamination species were found to be N_2O_4, CO_2, N_2 and H_2O; minor contamination species were found to be CO, NO, N_2O, an N_2O_3.

ACKNOWLEDGEMENT

The research reported herein was performed by the Arnold Engineering Development Center (AEDC), Air Force Systems Command (AFSC). Work and analysis were done by personnel of ARO, Inc., a Sverdrup Corporation company, operating contractor of AEDC.

REFERENCES

[1] Pipes, J. G., Roux, J. A., Smith, A. M., and Scott, H. E., Transmission of infrared materials and condensed gases at cryogenic temperatures, AEDC-TR-77-71 (1977).

[2] Tempelmeyer, K. E. and Mills, D. W., Jr., Refractive index of carbon dioxide cryodeposit, J. of Applied Optics, 16:2968-2969 (1968).

[3] Durig, J. R., Harris, W. C., and Wertz, D. W., Infrared and Raman spectra of substituted hydrazines. I. methylhydrazine, J. of Chem. Phys., 50: No. 3, 1449-1461 (1969).

[4] Weiner, R. N. and Nixon, E. R., Infrared spectrum of dinitrogen tetroxide, J. of Chem. Phys., 50:No. 4, 906-908 (1957).

[5] Bibart, C. H. and Ewing, G. E., Vibrational spectrum, torsional potential, and bonding of gaseous N_2O_4, J. of Chem. Phys., 61:No. 4, 1284-1292 (1974).

[6] Snyder, R. G. and Hisatsune, I. C., Infrared spectrum of dinitrogen tetroxide, J. of Mol. Spectros., 1:139-150 (1957).

[7] Kato, R. and Rolfe, J., Vibrational frequencies of NO_2^- and NO_3^- ions in KBr crystals, J. of Chem. Phys., 47:No. 6, 1901-1910 (1967).

[8] Bibart, C. H. and Ewing, G. E., Vibrational spectrum of gaseous N_2O_3, J. of Chem. Phys., 61:No. 4, 1293-1299 (1974).

[9] Herzberg, G. Molecular Spectra and Molecular Structure-- II. Infrared and Raman Spectra of Polyatomic Molecules, Van Nostrand Co., Inc. (1945).

[10] Devlin, J. P. and Pollard, G., ATR infrared spectra of uniaxial nitrate crystals, J. of Chem. Phys., 53:No. 11, 4147-4151 (1970).

[11] McGraw, G. E., Bernitt, D. L., Hisatsune, I. C., Vibrational spectra of isotopic nitric acids, J. of Chem. Phys., 42:No. 1, 237-244 (1965).

[12] Vasicek, A. Optics of Thin Films, North Holland Publishing Company, Interscience Publishers, Inc., New York (1960).

[13] Heavens, O. S., Optical Properites of Thin Films, Dover Publications, Inc., New York (1965).

EXHAUST PLUME CONTAMINANTS FROM AN AGED HYDRAZINE MONOPROPELLANT THRUSTER

T. D. McCay, D. P. Weaver, W. D. Williams, H. M. Powell,

and J. W. L. Lewis

ARO, Inc.

AEDC Division
A Sverdrup Corporation Company
Arnold Air Force Station, Tennessee

ABSTRACT

An experimental study of the exhaust plume of an aged (200,000 pulses) 0.44 N hydrazine monopropellant thruster has been performed with the goal of characterizing both the gas dynamic and contamination properties of the exhaust. The thruster was operated over a thrust range of 0.44 to 1.10 N with a nominal 0.14 sec on/10.0 sec off duty cycle using initial catalyst bed (Shell 405) temperatures of 367, 478 and 589 K. Exhaust diagnostic systems employed included a mass spectrometer probe, a quartz crystal microbalance (QCM), a laser-Raman/Rayleigh system, an electron beam which permitted fluorescence measurements and flow visualization, and a particle collector. Plume species number densities and rotational temperatures were determined along with mass deposition rates at various QCM cryogenic surface temperatures. Traditional engine performance parameters were also determined in order to relate performance and exhaust properties. This paper concentrates on contamination measurements made using the mass spectrometer probe and QCM. The results show the variation of species mole fractions and deposition rates with pulse number and operating condition along with the associated engine performance values. A significant increase in hydrazine concentrations in the plume was observed to occur at a point in time without significant loss of engine performance. This phenomenon was investigated in detail and the results are discussed.

1.0 INTRODUCTION

The use of monopropellant thrusters as attitude control systems and for station keeping functions has stimulated interest over the past several years in the contamination characteristics of their plume exhausts. The tendency for present-day satellites and spacecraft is to have a large number of cryogenic temperature surfaces, one effect of which increases the importance of knowing the types and quantities of possible contaminating elements in the propulsion devices' exhausts. The contamination characteristics of a thruster include the mass flux of particulate, condensate and raw fuel, for both the forward-flow and back-flow regions of the exhaust; and the applications of such knowledge are obvious. This particular study has concentrated its investigations in the forward-flow region and had as its goal the measurements of not only the contaminant mass flux but also the gas dynamic properties of the plume exhaust to verify and quantitatively determine the relationship between the gas dynamic properties and the contamination level and nature of its source.

To accomplish these tasks use was made of an aged monopropellant hydrazine engine of nominal 0.44 N thrust level which was operated in the pulsed mode. In addition to the usual engine properties of combustion chamber pressure, catalyst bed wall temperature and fuel mass flow rate, measurements were performed to determine the gas dynamic properties (species densities and temperature) at both the engine exit plane and in the forward-flow expansion region, the contaminant mass flux, and the nature of the solid and/or liquid particulate in the exhaust. Particular emphasis was placed on the detection and identification of catalyst-bed particles.

This paper presents a description of the experimental techniques employed to accomplish these goals, exemplary gas dynamic data and a detailed presentation of the contaminant measurements obtained using the mass spectrometer probe and QCM. Additionally, a description of a catastrophic increase in plume contaminants that occurred during the thruster study will be presented along with a documentation of thruster performance changes after this occurrence. A total of 18 test periods of two days duration each were necessary to complete the experimental study.

2.0 EXPERIMENTAL APPARATUS AND PROCEDURES

2.1 Thruster

The thruster studied is a single injector monopropellant hydrazine device which contains Shell 405 catalyst material. The thruster is designed to provide 0.44 N thrust and a specific impulse of 2099 N-sec/kg at a steady-state chamber pressure of 5.93×10^5 Pa. The exhaust was provided by a conical nozzle with 0.76 mm throat diameter and an exit area ratio of 55. Prior to the measurements of the exhaust properties, engine performance levels were determined by measuring the thruster combustion chamber pressure and fuel mass flow rate for several values of valve inlet pressure. The results compare well with previous measurements performed by the engine manufacturer, as well as previous investigators.[1] The prepulse catalyst bed temperature was systematically varied over the range of 366.5 to 477.6 K using an external heater, and fuel temperature was nominally room temperature (285 K). The external lower wall temperature of the combustion chamber and the nozzle throat temperature were measured throughout this work. Chemical analysis of the hydrazine fuel was performed to determine its chemical purity, and all specifications were satisfied (Mil-P-26536C). The engine was operated in a pulsed mode, and the chamber pressure was varied from 5.86 to 14.1×10^5 Pa. The pulse width, as determined from engine solenoid valve current traces, was nominally 140 msec. A schematic of the thruster is shown as Fig. 1. The radiation heat shield shown in the figure was removed prior to operating the thruster at AEDC.

2.2 Vacuum Chamber

The engine was contained within a cryogenically-pumped research vacuum chamber with a diameter and length of 1.2 m and 5.2 m, respectively. Liquid N_2, gaseous He at 20 K and liquid He were used for cryogenic pumping of the plume exhaust products, and for the highest engine thrust condition studied the chamber background pressure was less than

---

[1] Baerwald, R. K. and Passamaneck, R. S., Monopropellant Thruster Exhaust Plume Contamination Measurements, AFRPL-TR-77-44 (1977).

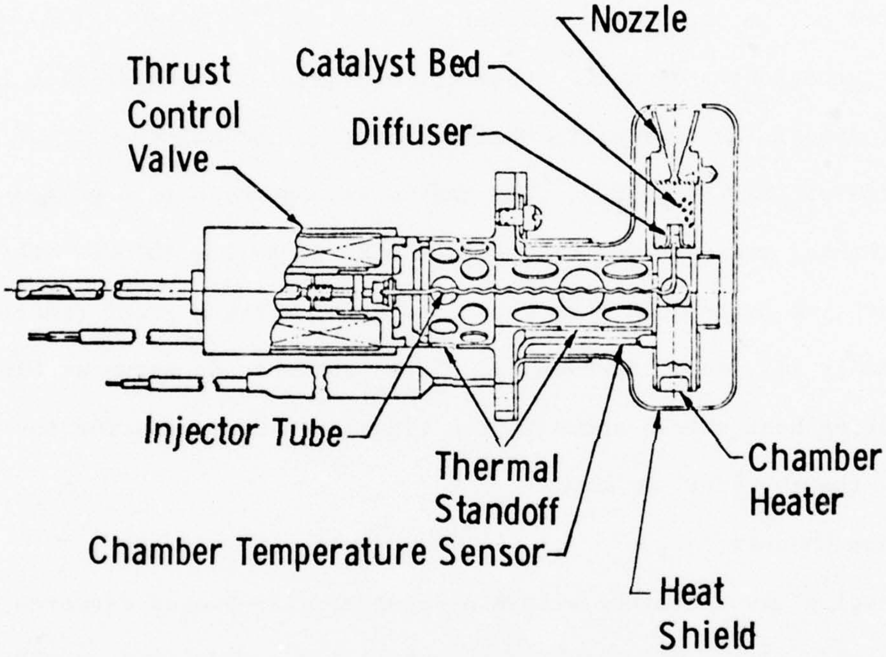

Fig. 1 0.1-lbf-Thrust Monopropellant Engine

9.3×10^{-2} Pa, corresponding to a simulated altitude of approximately 94 km. The engine was mounted on a traversing mechanism with three linear degrees of freedom which allowed all flowfield instrumentation to be stationary; Fig. 2 shows the location of the engine within the vacuum chamber. A description of the vacuum chamber and thruster is contained in a previous paper.[2]

2.3 Mass Spectrometer Probe

The cryogenically pumped mass spectrometer probe used in this investigation has been described in detail in a previous publication[3]. The gaseous helium-cooled probe, shown in Fig. 3, was located on the thrust axis and centerline of the thruster plume with the skimmer tip located at axial positions $450 \leq \hat{x} \leq 650$. The probe was fabricated in two thermally-insulated sections; the front section was cooled to 12-20 K for pumping purposes, and the aft section, containing the electronics, was uncooled. Since the 12 K probe temperature would not cryopump (adsorb) the plume hydrogen, CO_2 was periodically injected into the probe to permit H_2 pumping by absorption into the resultant CO_2 frost.

The probe functions under the same principle as a molecular beam system. In effect, the probe serves as the last stage of a two-stage miniature molecular beam-mass spectrometer system. For free jets (plumes exhausting to vacuum) with little condensation, this gives practically an

---

[2] Williams, W. D., McCay, T. D., Powell, H. M.., Weaver, D. P., Price, L. L. and Lewis, J. W. L., Experimental Study of Monopropellant Hydrazine Thruster Exhaust. JANNAF 10th Plume Technology Meeting, San Diego, CA. (1977).

[3] McCay, T. D., Powell, H. M. and Busby, M. R., Direct Mass Spectromeric Measurements in a Highly Expanded Rocket Exhaust Plume, AIAA Paper 77-154 (1977).

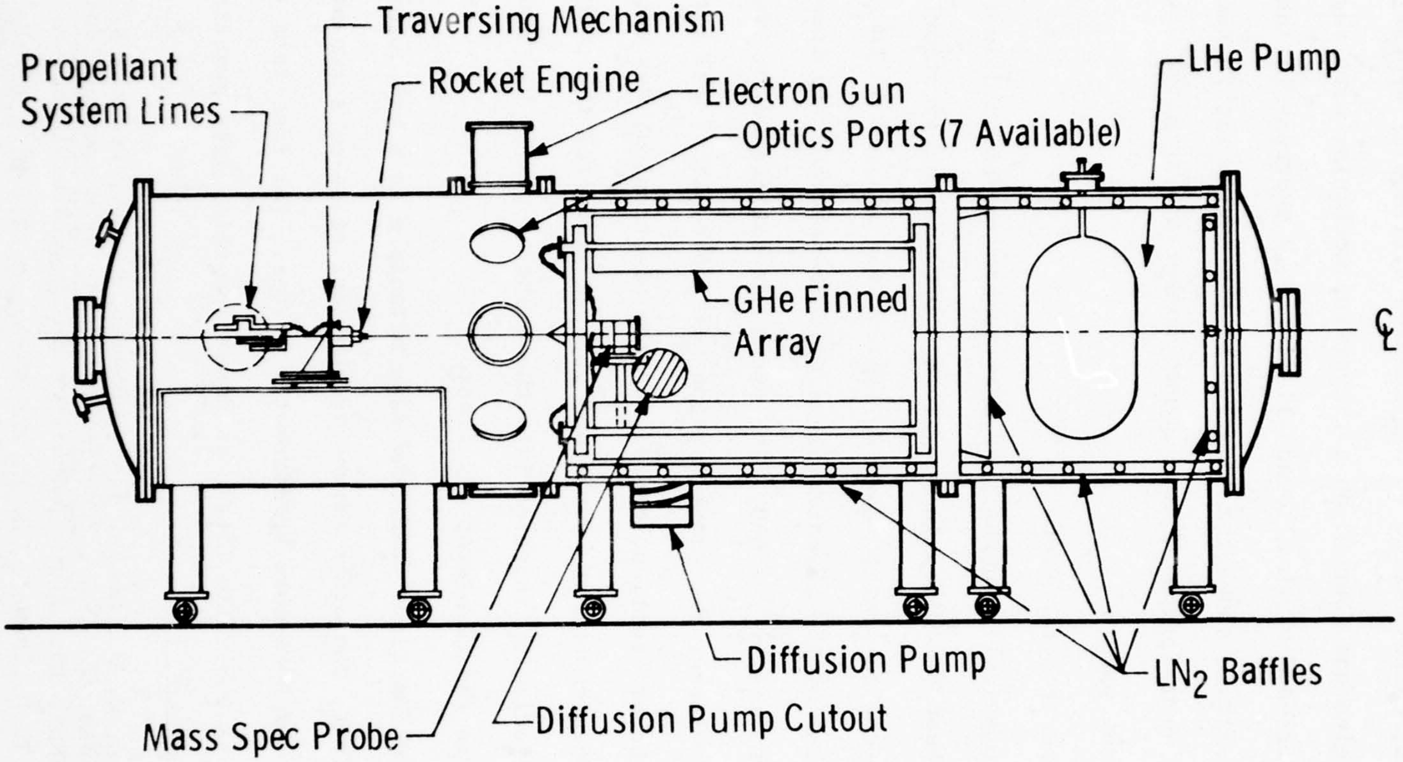

Fig. 2 Engine Installation in 4- by 10-ft Chamber

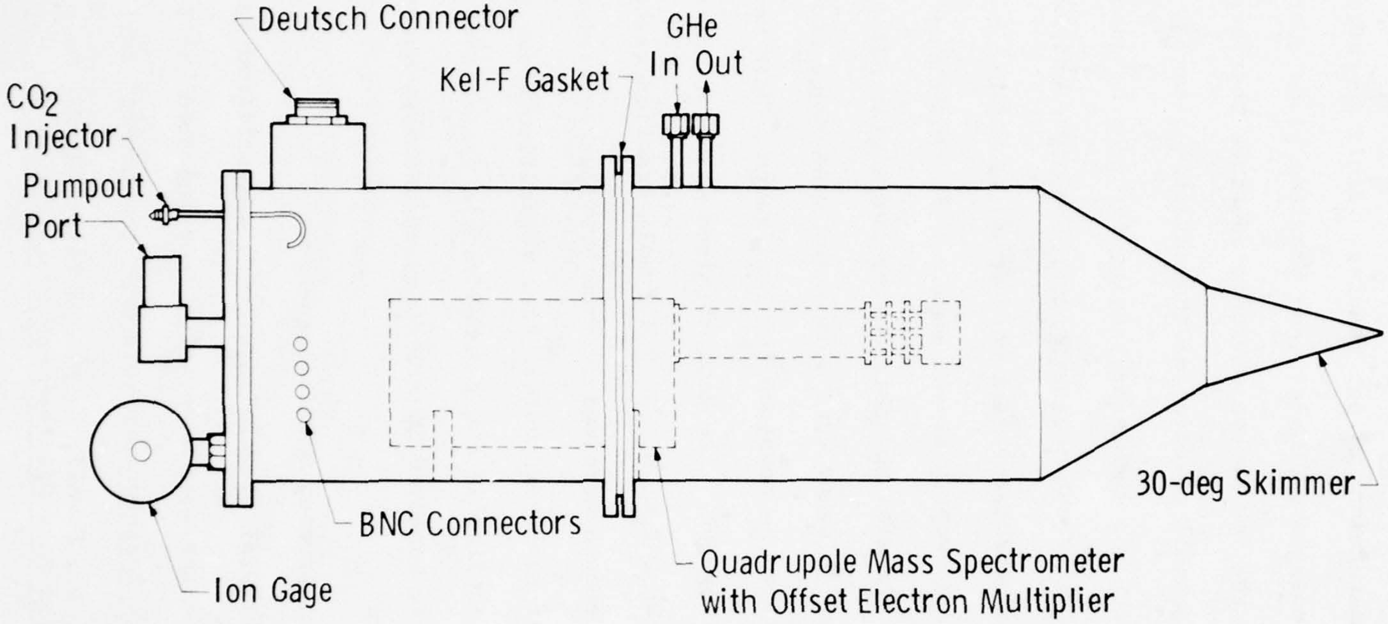

Fig. 3 Schematic of Mass Spectrometer Probe

unperturbed measurement of jet species. Basic operation consists of the probe skimming a molecular beam from the plume centerline which is directed onto the ion source entrance aperture that serves as a collimator. Only a small fraction of the entering gases is ionized in the ion source, with the remainder passing through the quadrupole section and paraxial multiplier and impinging upon the probe endplate.

The mass spectrometer data were taken in two basic modes, either the spectrometer was swept over the entire 0-55 atomic mass unit (amu) mass range as many times as possible during the engine pulse, or a limited sweep was employed which swept over a four-amu mass range and permitted detailed intrapulse data to be obtained for that range. Data were output on a Visicorder® oscillograph. The data obtained were for the primary species of interest, H_2, NH_3, H_2O, N_2 and N_2H_4; mole fraction rather than absolute number density measurements were made. From previous investigations[4] it has been determined that published values[5] for ionization cross sections and cracking patterns were applicable for the quadrupole system used in the probe. Therefore, these were employed in reduction of the mass spectrometer data.

2.4 The Quartz Crystal Microbalance System

A quartz crystal microbalance (QCM) was utilized in this study for measurements of the mass deposition rate and total mass deposition in the exhaust plume. Measurements were made for crystal surface temperatures

---

[4] McCay, T. D., Powell, H. M. and Busby, M. R., Development of a Cryogenically Pumped Mass Spectrometer Probe for Rocket Plume Studies, AEDC-TR-76-55.

[5] Cornu, A. and Massot, R., Compilation of Mass Spectral Data, 2nd ed., Vol. I, Heydon, New York (1975).

in the range 90 to 200 K at a variety of radial and axial positions in the forward flow region of the thruster for a wide range of engine operating conditions.

The QCM consists of a quartz crystal, an electronic oscillator, and a data processing/recording system. The piezoelectric effect of the quartz crystal is used to stabilize the resonance frequency of the oscillator. This resonance frequency, which depends upon the angle of the crysta cut, is found to be a function of the mass deposited on the crystal surface and the crystal surface temperature. The relation for the change in frequency, Δf, that results when the crystal experiences a mass change, ΔM, and temperature change, ΔT, is given by

$$\Delta f = C_m \Delta M + C_T \Delta T \tag{1}$$

where C_m is the mass coefficient and C_T is the temperature coefficient of the quartz crystal.

Since a measurement of the variation of QCM frequency with deposited mass was required, care was taken to minimize the influence of temperature on the observed frequency. For this reason a QCM of the temperature compensating variety developed by JPL[1] was utilized. For this type of QCM a doublet crystal is cut and electrodes suitably arranged such that two independent crystal oscillators are obtained. For the two crystals,

$$\Delta f_1 = C_{m_1} \Delta M_1 + C_{T_1} \Delta T_2 \quad \text{and} \quad \Delta f_2 = C_{m_2} \Delta M_2 + C_{T_2} \Delta T_2 \; . \tag{2}$$

Since two crystals are of identical piezoelectric properties and are constrained to identical temperature environments,

$$C_{m_1} = C_{m_2} , C_{T_1} = C_{T_2} , \text{ and } \Delta T_1 = \Delta T_2 ,$$

and the following relation results:

$$\Delta f = \Delta f_1 - \Delta f_2 = C_{m_1} (\Delta M_1 - \Delta M_2) \tag{3}$$

When one of the crystal surfaces is shielded from mass deposition, the beat frequency shift of the two crystals is given by the following simple relation:

$$\Delta f = C_{m_1} \Delta M_1 \tag{4}$$

An evaluation of the mass coefficient, C_m, yields the desired mass deposition rate expression utilized for this study:

$$\frac{dM}{dt} = 1.524 \times 10^{-8} \frac{df}{dt} \tag{5}$$

where the mass deposition rate per unit area, dM/dt, is given in grams/cm^2-sec when df/dt is given in Hz/sec.

The QCM utilized in this study was supplied by the Jet Propulsion Laboratory and had an AT crystal cut of $35^{\circ}10'$. This cut, which gives a small temperature coefficient in the temperature range 125 K and above, when coupled with the JPL doublet crystal design, provides effective temperature compensation in the range over which measurements were made.

The QCM unit was cooled by thermal contact via a metal conduction path attached to the 4 x 10 chamber gaseous helium supply system. Resistance heaters, controlled by the thermocouple at the crystal surface, maintained the unit operating temperature. The ability to vary the crystal surface temperature allowed a gross distinction of the contaminating species. Expected condensate for a given QCM temperature is listed in Table 1 for reference.

Table 1 Expected QCM Condensate

QCM Temperature	Expected Condensate
200 K	Trace Impurities
172 K	Hydrazine
144 K	Hydrazine and water
100 K	Hydrazine, water, ammonia

The experimental configuration of the QCM system for the two phases of the thruster study is depicted in Fig. 4. In test phase I, the QCM crystal surface was located at an angle of 30 deg relative to the chamber centerline and 38.75 cm from the center of the thruster exit plane for the thruster axis centered on the chamber centerline and the thruster cart in the forward-most position. For test phase II, the QCM crystal surface was positioned on the (thruster) chamber centerline at a distance of 113.35

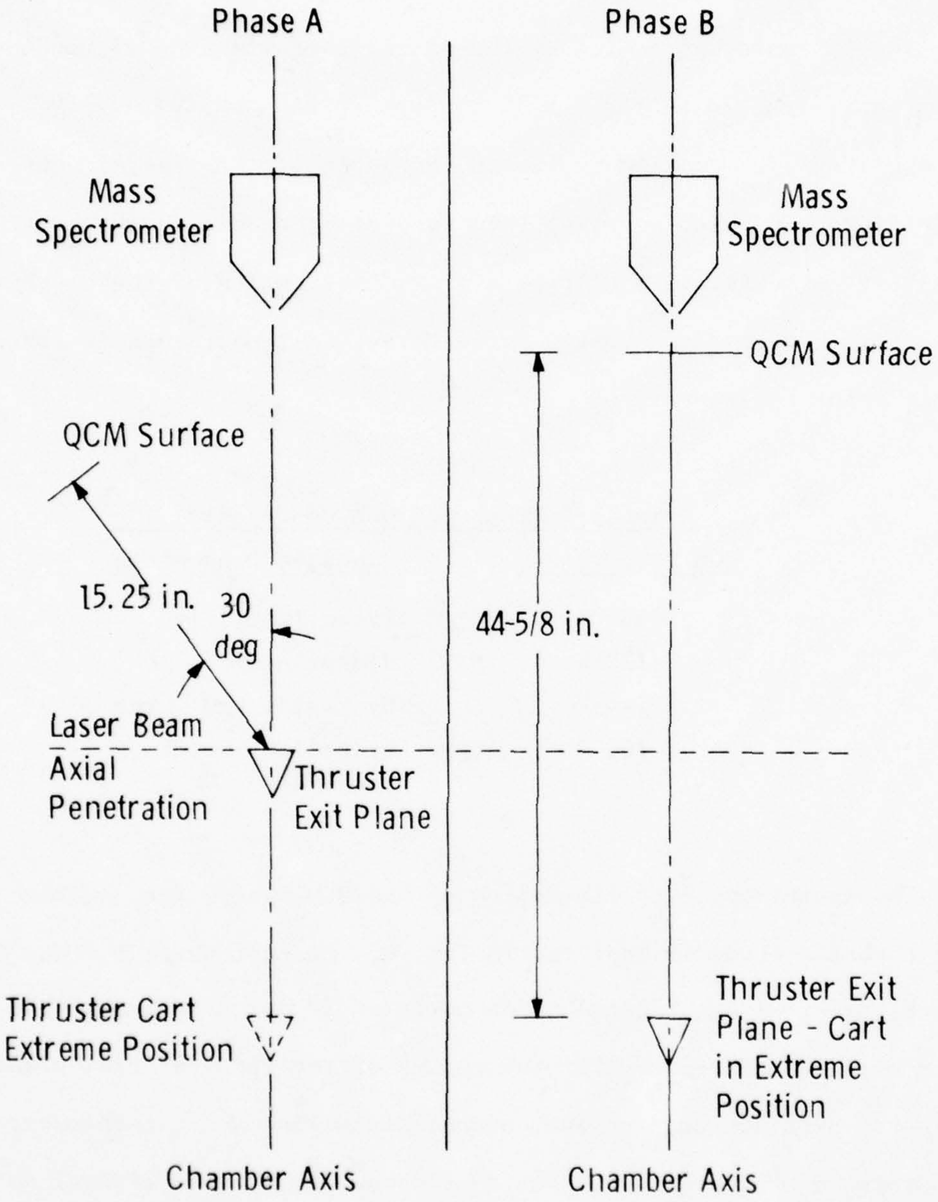

Fig. 4 QCM-Mass Spectrometer Configuration for Test Phase A and B

cm from the thruster exit plane with the thruster cart in the forward most position. For both experimental configurations, QCM position and surface angle with respect to the thruster exit plane was referenced in terms of an axial position from thruster exit and a radial distance perpendicular to the thruster axial centerline.

2.5 Laser Raman and Rayleigh/Mie System

Raman scattering[6] measurements were performed 0.5 and 1.3 cm downstream from the engine exit plane to determine the species number densities of N_2, NH_3 and H_2 and the rotational temperature (T_R) of H_2, which , because of sufficiently high gas density, is equal to the gas kinetic temperature. Such data were acquired for combustion chamber pressures covering the range 5.86 to 14.1×10^5 Pa. A Holobeam 600 series pulsed ruby laser system was utilized to provide excitation for the Raman and Rayleigh/Mie scattering. The 6 x 3/8-inch ruby rod was oriented to provide a horizontally polarized beam, and the laser was operated in the conventional mode which provided a pulse width of 1 ms and an energy of 35 J per pulse at 6943 Å. The laser beam energy was injected into the chamber via appropriate focusing optics, and the observed cylindrical focal volume, which was located on the thruster axial centerline, had the approximate dimensions of 1 mm diameter by 2.77 mm length. Figure 5 shows the experimental configuration for the Raman and Rayleigh/Mie systems as well as that for the electron beam system described in 2.6. A partial, synthetic spectrum for Raman scattering from a simulated plume exhaust is shown in Fig. 6. This spectrum

---

[6] Lewis, J. W. L. and Williams, W. D., <u>Measurement of Temperature and Number Density in Hypersonic Flow Fields Using Laser Raman Spectroscopy</u>, AIAA Paper No. 75-175, presented at the 13th AIAA Aerospace Sciences Meeting, Pasadena, CA, Jan. 20-22, 1975.

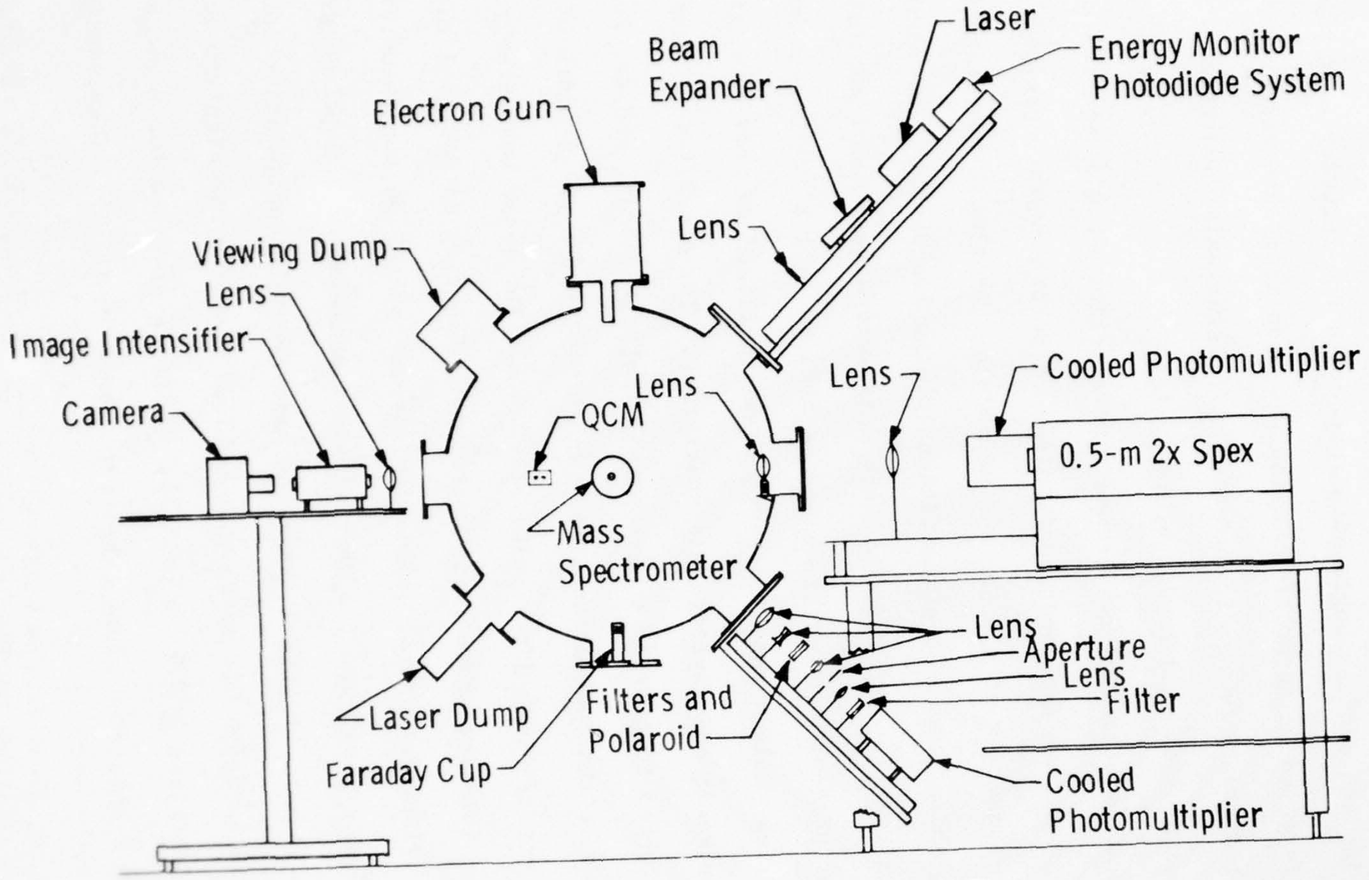

Fig. 5 Experimental Arrangement

AD-A070 386 AIR FORCE MATERIALS LAB WRIGHT-PATTERSON AFB OH F/G 22/2
PROCEEDINGS OF THE USAF/NASA INTERNATIONAL SPACECRAFT CONTAMINA--ETC(U)
1978 J M JEMIOLA
UNCLASSIFIED AFML-TR-78-190 NL

6 OF 13
AD
A070386

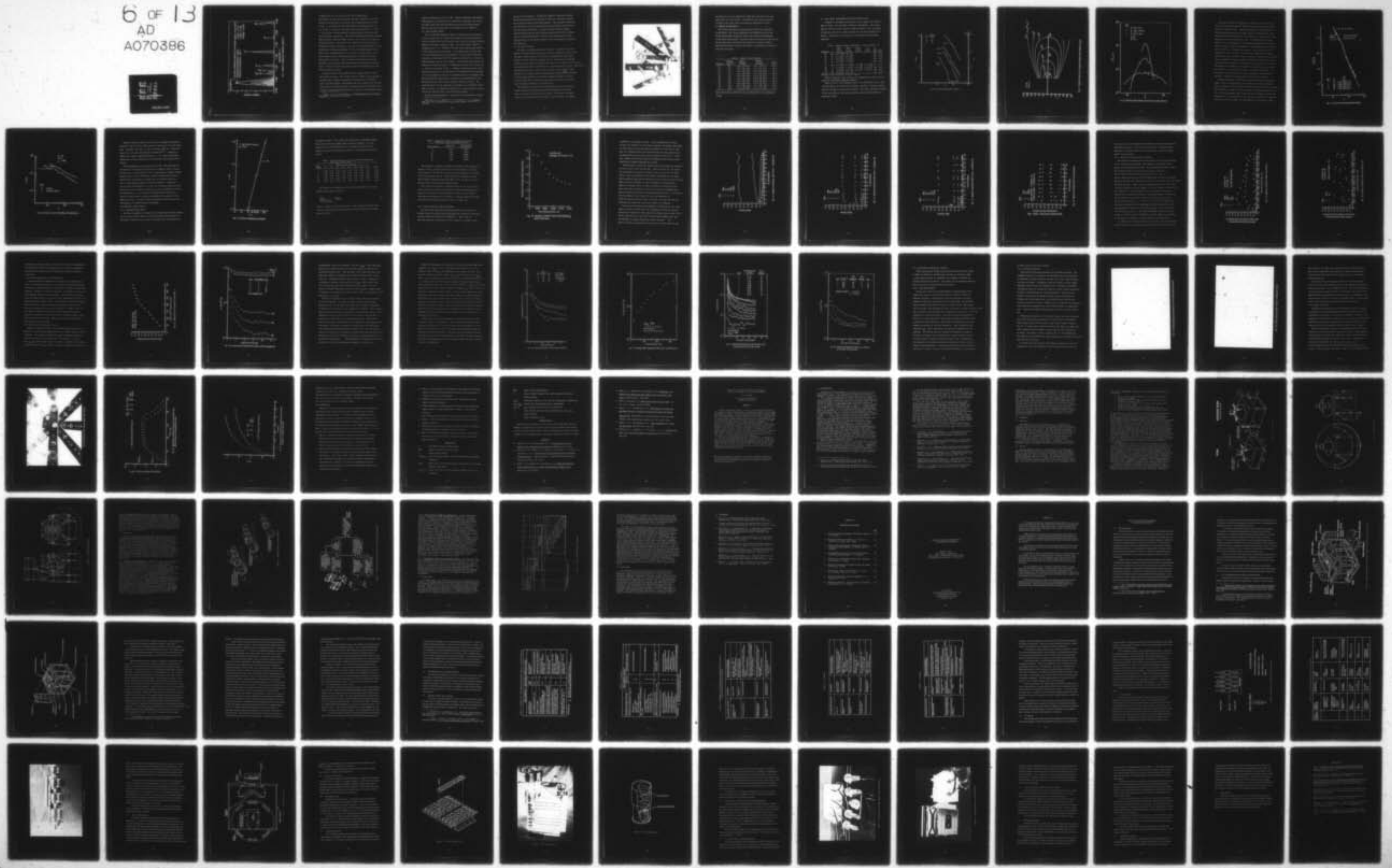

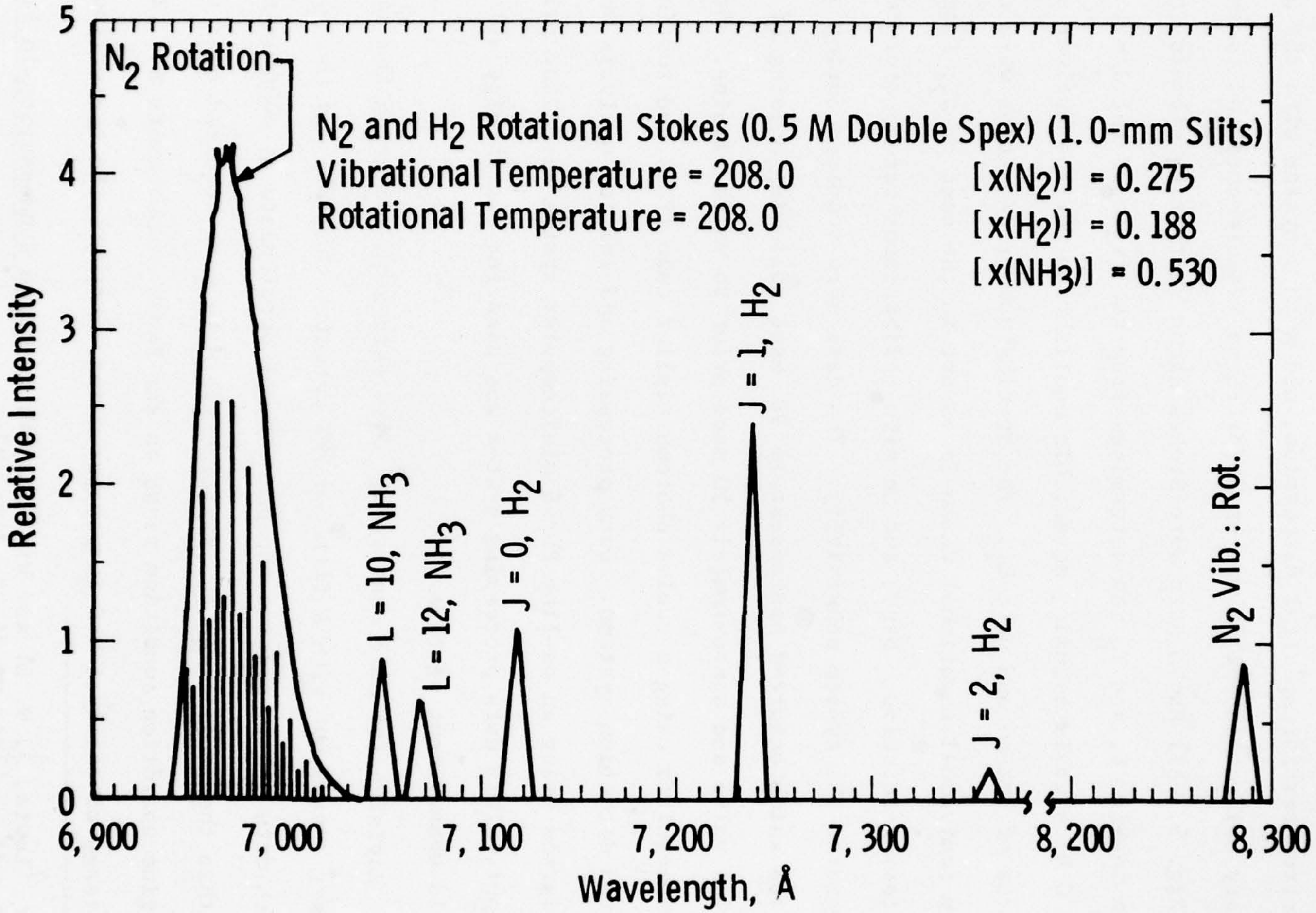

Fig. 6 Raman Scattering Synthetic Spectrum

is appropriate for the use of a 0.5-m focal length double spectrometer for spectral dispersion, and such a system with the necessary collection optics was used for these measurements and is shown in Fig. 5. All Raman data were Stokes Raman scattering signals, as seen in Fig. 6, and T_R was determined from the ratio of the J = 1 and J = 0 H_2 signals assuming metastable equilibrium for the nuclear spin states of ortho- and para-H_2. The species number densities were obtained from individual rotational Raman lines or, in the case of N_2, from the vibration-rotation band, and in situ calibrations were performed to determine the system sensitivity. The data were acquired during a 1 msec period which occurred approximately 90 msec following opening of the engine valve and approximately 50 msec prior to valve closing. Data were acquired using a cooled photomultiplier tube (PMT) and routine photon detection systems. Data processing and initial analysis were performed using an on-line PDP-8 minicomputer system with line printer output. This data processing system was used for essentially all flow-field measurement systems.

Rayleigh (or Mie) scattering[7] data were acquired using the same laser system but with a filtered PMT detector channel, and the purpose of such data was to observe the presence of particulate or condensate within the plume exhaust. Rayleigh/Mie data were acquired over the same engine operation condition range as the Raman measurements and also for a range of catalyst bed temperatures and, further, the centerline spatial

---

[7] Lewis, J. W. L. and Williams, W. D. Argon Condensation in Free-Jet Expandions, AEDC-TR-74-32, July 1974.

region investigated was $20 \lesssim \hat{x} \lesssim 300$. During a subsequent experimental investigation a calibration will be performed to determine the scattering signal level from only the gaseous species in the plume exhaust, and the existence of particulate or condensate will be inferred.

2.6 Electron Beam System

For the flowfield expansion region for which the species density is too low to permit the use of Raman scattering, the electron beam fluorescence technique[8] was used to measure local values of N_2 number density, $n(N_2)$, and rotational temperature (T_R). The axial distance region investigated was $78 \lesssim \hat{x} \lesssim 300$, and at selected axial points, radial profiles of both $n(N_2)$ and T_R were measured. To accomplish this, use was made of a 30 keV electron beam of approximately 1 mA beam current which was produced by an RCA model VC2126 V4 electron gun mounted in a stainless steel housing at the top of the chamber. The beam was injected into the chamber and flowfield through a 1.0-mm-diameter orifice and collected by a Faraday cup as shown in Fig. 5. Magnetic focusing provided a small diameter beam source at the centerline of the chamber, and the directing of the beam through the orifice was accomplished with an alignment yoke. Flow visualization capability was provided by a sweep-deflection coil located below the orifice and by associated control circuitry. The stationary beam could be deflected at any angle up to 30 degrees either side of vertical, or repetitively swept with a constant angular velocity through any angle and about any mean deflection angle.

No flow field perturbation is expected for the measurement of $n(N_2)$

---

[8] Williams, W. D., Hornkohl, J. O. and Lewis, J. W. L. Electron Beam Probe for a Low Density Hypersonic Wind Tunnel, AEDC-TR-71-61, July 1971.

and T_R by this technique. The N_2^+ first negative fluorescent emission system and specifically the R-branch of the (0,1) vibrational band of this system was used for these measurements. The fluorescent radiation was collected by the 0.5-m spectrometer and processed by the detection and data acquisition systems. T_R was determined using the dipole excitation model and the usual Boltzmann analysis of the line intensities of the measured R-branch. Finally, data acquisition was accomplished during a 5 msec period located at the same temporal location of the Raman data.

2.7 Particle Collector

The sample collecting system shown in Fig. 7 consisted of two components, an aluminum housing and the collectors themselves. The housing was made of eight strips of one-inch-wide aluminum bolted and welded together to form a web with one open end. The collectors were standard *scanning electron microscope* (SEM) disks mounted to the housing and consisted of aluminum stubs with vacuum-deposited, copper-coated glass covers. The actual sampling surfaces were of three types: the bare copper itself; beeswax melted onto the copper surface; and SEM quality Microstick® glue dripped onto the copper substrate and spread by moving the disks to and fro. A total of 84 disks, 9 with wax, 16 with glue and 59 with bare copper were distributed throughout the aluminum web.

The sampling was carried out by installing the web in the vacuum chamber such that the engine nozzle exit was located in the center and in the plane of the open end of the web. The axis of the engine nozzle was located along the centerline of the web length. The engine

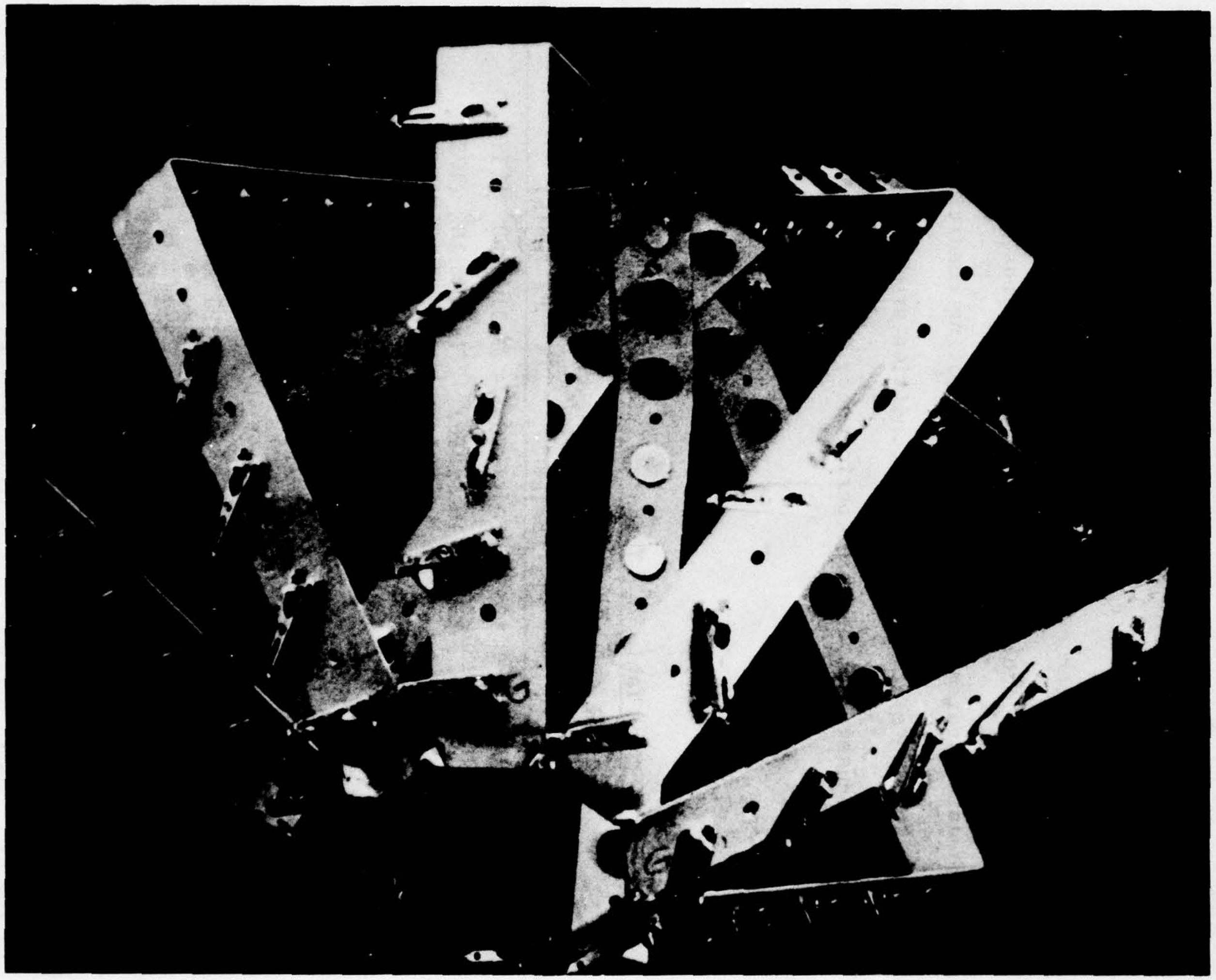

Fig. 7 Particle Collector

was pulsed into the web approximately 1000 times, and then the web was removed from the vacuum system. The SEM disks were removed and placed on stands in dust-free boxes from subsequent viewing with the SEM.

3.0 RESULTS AND DISCUSSION

The thruster was operated during 18 test periods over a duration of nine months. The thruster performance was determined prior to any exhaust measurements, during two interim test periods, and subsequent to the exhaust measurements. The basic operating conditions of the thruster and the nomenclature attached to each condition are shown in Table 2. Additional discussion of thruster performance is presented in a subsequent section of this paper.

Table 2 Thruster Test Conditions

Condition	Initial Catalyst Temp., K	Inlet Pressure Pa (psia)	Chamber Pressure Pa (psia)	Chamber Temp.
1A	367	1.59×10^6 (230)	9.31×10^5 (135)	665 K
1B	367	2.04×10^6 (296)	1.21×10^6 (175)	695 K
1C	367	2.41×10^6 (349)	1.41×10^6 (205)	715 K
2A	478	1.58×10^6 (230)	9.31×10^5 (135)	700 K
2B	478	2.04×10^6 (296)	1.21×10^6 (175)	730 K
2C	478	2.41×10^6 (349)	1.41×10^6 (205)	745 K
2S	478	1.00×10^6 (145)	5.86×10^5 (85)	650 K
3A	589	1.59×10^6 (230)	9.31×10^5 (135)	735 K
3B	589	2.04×10^6 (296)	1.21×10^6 (175)	760 K
3C	589	2.41×10^6 (349)	1.41×10^6 (205)	775 K

Duty cycle: 0.138 sec on/10.0 sec off as determined by valve opening and closing

3.1 Laser Raman, Rayleigh/Mie and Electron Beam Results

A summary of the Raman scattering data from a single test period is shown in Table 3 for the engine conditions investigated. The results show the absolute values of species number densities of N_2, H_2 and NH_3 as well as T_R for the two axial positions for the various engine conditions. Also shown are the values of the sum (n_T) of these number densities.

Table 3 Summary of Raman Measurements - Test Period No. 11

Condition	$\hat{x}$	$n(N_2)$ (cm^{-3})	$n(H_2)$ (cm^{-3})	$n(NH_3)$ (cm^{-3})	n_T (cm^{-3})	T_R (K)	T_R/T_o
2A	18.5	$4.9 \times 10^{16*}$	5.5×10^{16}			183	0.26
2B	↓	5.4×10^{16}	6.8×10^{16}			148	0.20
2C		7.2×10^{16}	7.3×10^{16}			185	0.25
2S		2.9×10^{16}	3.6×10^{16}			177	0.27
2A	28.5	2.3×10^{16}	3.3×10^{16}	2.4×10^{16}	8.1×10^{16}	121	0.17
2B	↓	2.2×10^{16}	3.5×10^{16}	3.8×10^{16}	9.6×10^{16}	119	0.16
2C		3.1×10^{16}	3.8×10^{16}	3.0×10^{16}	9.9×10^{16}	106	0.14
2S		1.4×10^{16}	2.3×10^{16}			99	0.15

*Average of test period No. 6 and 14 results.

Figure 8 shows the axial variation of the Rayleigh (or Mie) scattered signal for the engine conditions studied.

Shown in Fig. 9 as an exemplary result is an isodensity map for $n(N_2)$ as determined by the electron beam technique, and Fig. 10 shows the radial profiles of $n(N_2)$ at three axial positions. Both axial and radial profiles of not only $n(N_2)$ but also T_R were obtained and will be published in a subsequent report.

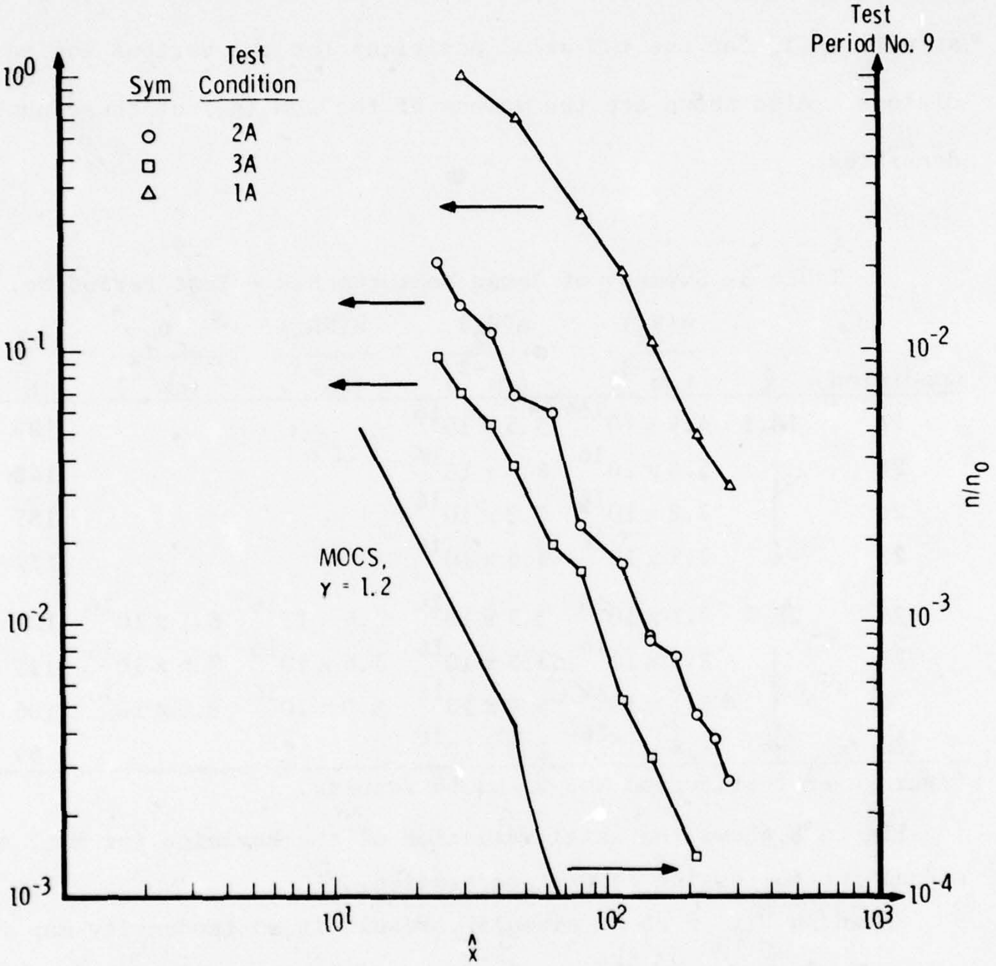

Fig. 8 Axial Variation of Rayleigh/MIE Scattering

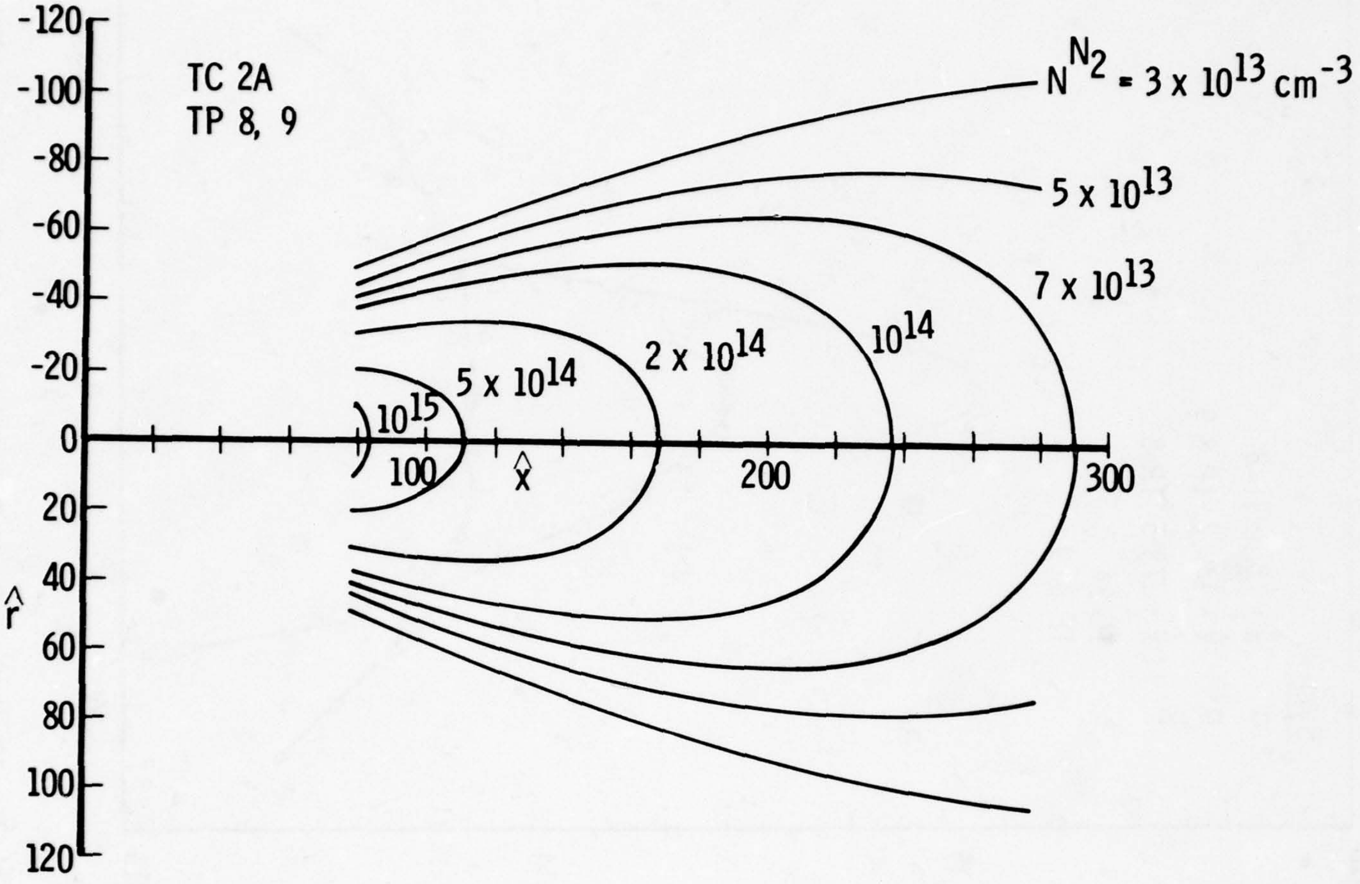

Fig. 9 Electron Beam N_2 Isodensity Map from Radial Survey

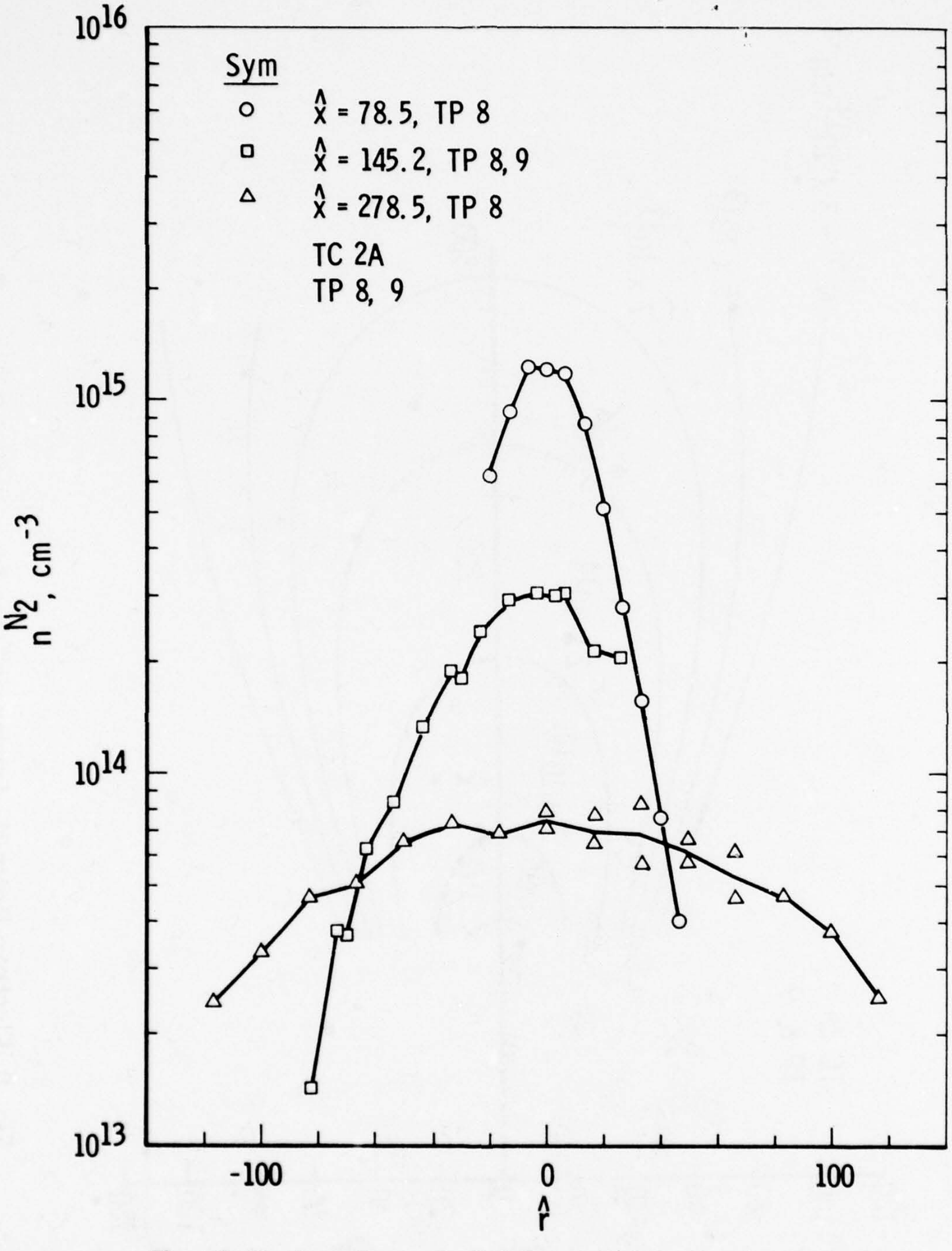

Fig. 10 Electron Beam Radial Survey of N_2 Number Density

The axial variation of $n(N_2)/n_o(N_2)$ is shown in Fig. 11, and it is to be noted that the Raman data represent an average of the last 20-25 pulses of a 30-pulse train. That these results are representative of the steady-state portion of the pulse train was verified by mass spectrometric and electron beam data. The values of n_o used for Fig. 11 are estimated to have an inaccuracy of ±10%. A significant result shown by Fig. 11 is the discrepancy of the measured and predicted axial variations of $n(N_2)$. Further improvements in the boundary layer corrections are not expected to remove the discrepancy. This discrepancy can be attributed, at least in part, to an inaccurate composition and mixture specific heat ratio (γ) used for the calculation. Similarly, the validity of the assumption of frozen chemistry, although most likely true for the freestream, is not certain for the region of flow interior to the nozzle. The possibility of vibrational relaxation of NH_3, which will also affect the value of γ, should also be included for accurate predictions. No conclusions can be offered at this time regarding the possibility of systematic variations in $n(N_2)/n_o(N_2)$ with engine inlet pressure.

Conclusions similar to those for the axial variation of the species density values of $n(N_2)/n_o(N_2)$ can be given for the axial variation of T_R/T_o, as shown in Fig. 12. Both electron beam and Raman data for a single test condition are shown in Fig 12, and while the Raman measurement at $\hat{x}$ = 18.5 is in good agreement with calculation, the discrepancy worsens with increasing $\hat{x}$. It is important to note that the temperature is lower than predicted, which will enhance the condensation of such species as NH_3.

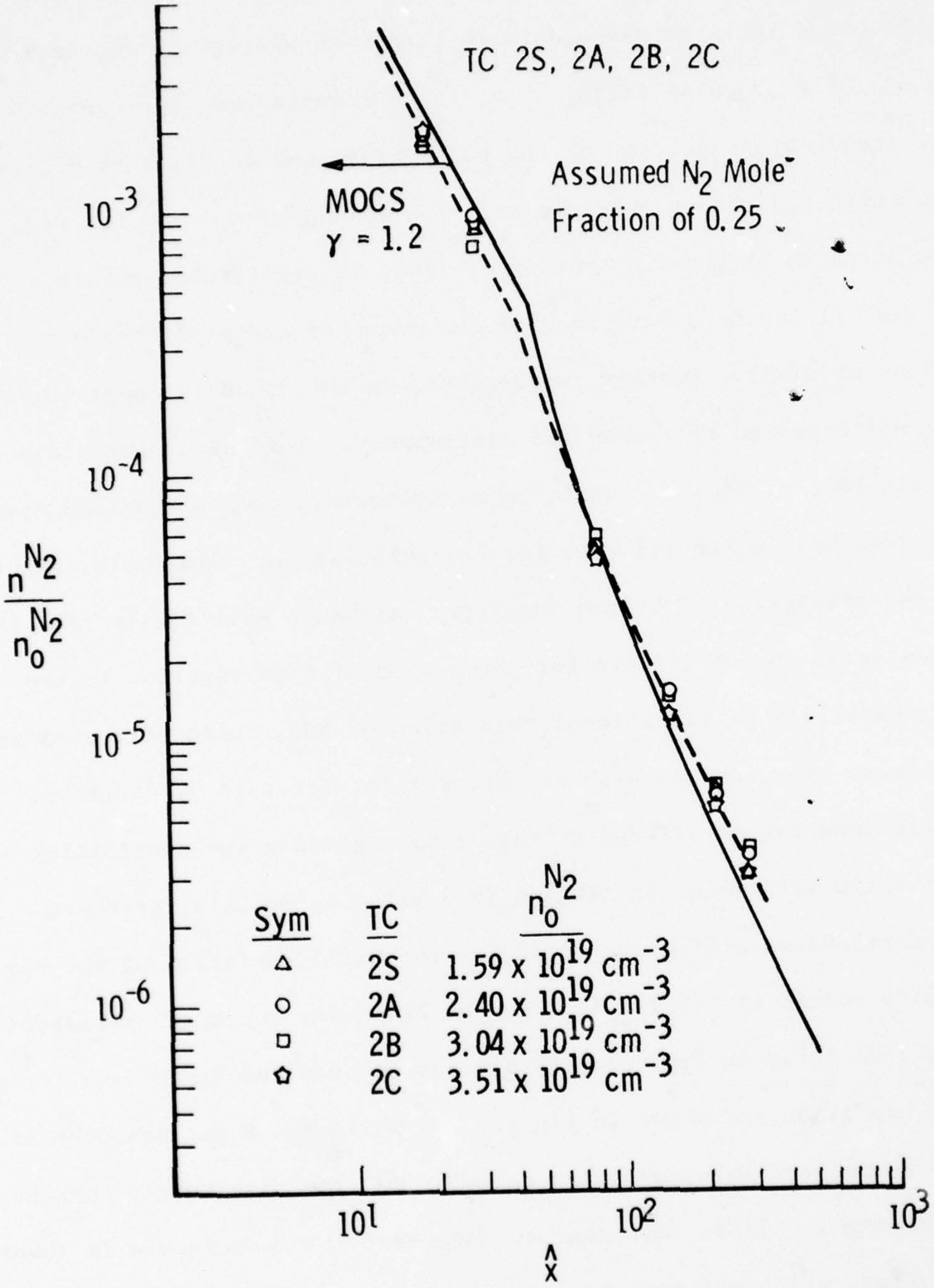

Fig. 11 Axial Survey of N_2 Number Density

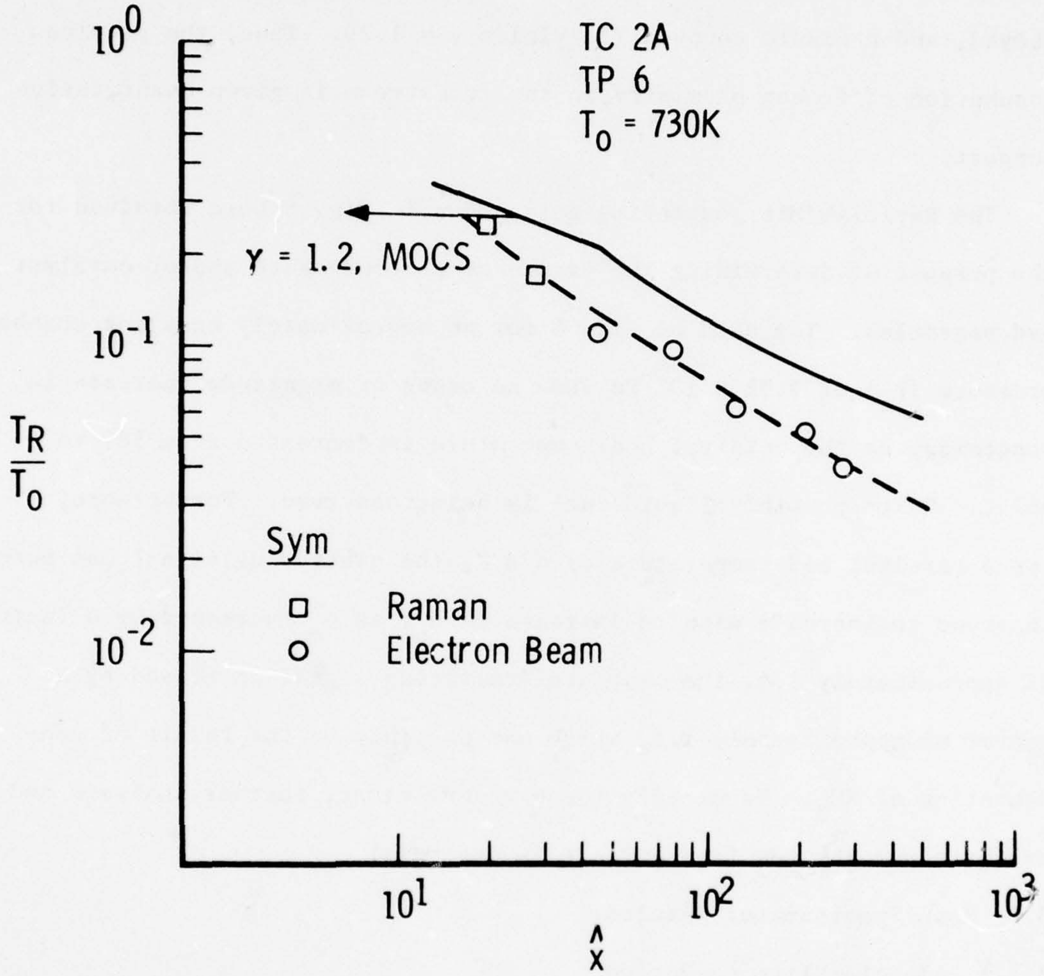

Fig. 12 Axial Survey of Rotational Temperature

Using the results of Figs. 11 and 12, one can compute and generate a graphical variation of the static pressure P with T_R(or T) for the expansion. The result from Figs. 11 and 12 is shown in Fig. 13. From this figure it is seen that the isentropic relation $PT^{\gamma/1-\gamma}$ = constant is obeyed, and a simple computation yields $\gamma = 1.29$. Thus, the previous assumption of frozen chemistry in the freestream is given quantitative support.

The Rayleigh/Mie scattering data shown in Fig. 8 were obtained for the purpose of determining the existence of condensate and/or catalyst bed particles. The data of Fig. 8 for an approximately constant chamber pressure (P_c) of 9.31×10^5 Pa show an order of magnitude increase in scattering as the catalyst bed temperature is decreased from 589 to 367 K. Quite possibly liquid fuel is being observed. Furthermore, for a catalyst bed temperature of 478 K, the scattering signal has been observed to increase with an increase in n_o; as n_o increased by a factor of approximately 1.4, the absolute scattering signal increased by a factor of approxiamtely 1.6, which may possibly be the result of condensation of NH_3. To clarify these observations, further analysis and calibrations are required and are in progress.

3.2 Mass Spectrometer Results

3.2.1 Ammonia/Nitrogen Ratios

The ratio of ammonia to nitrogen mole fractions was monitored throughout the test periods in which the mass spectrometer was installed and operating. Tabulated results which are averaged over test periods 6-11

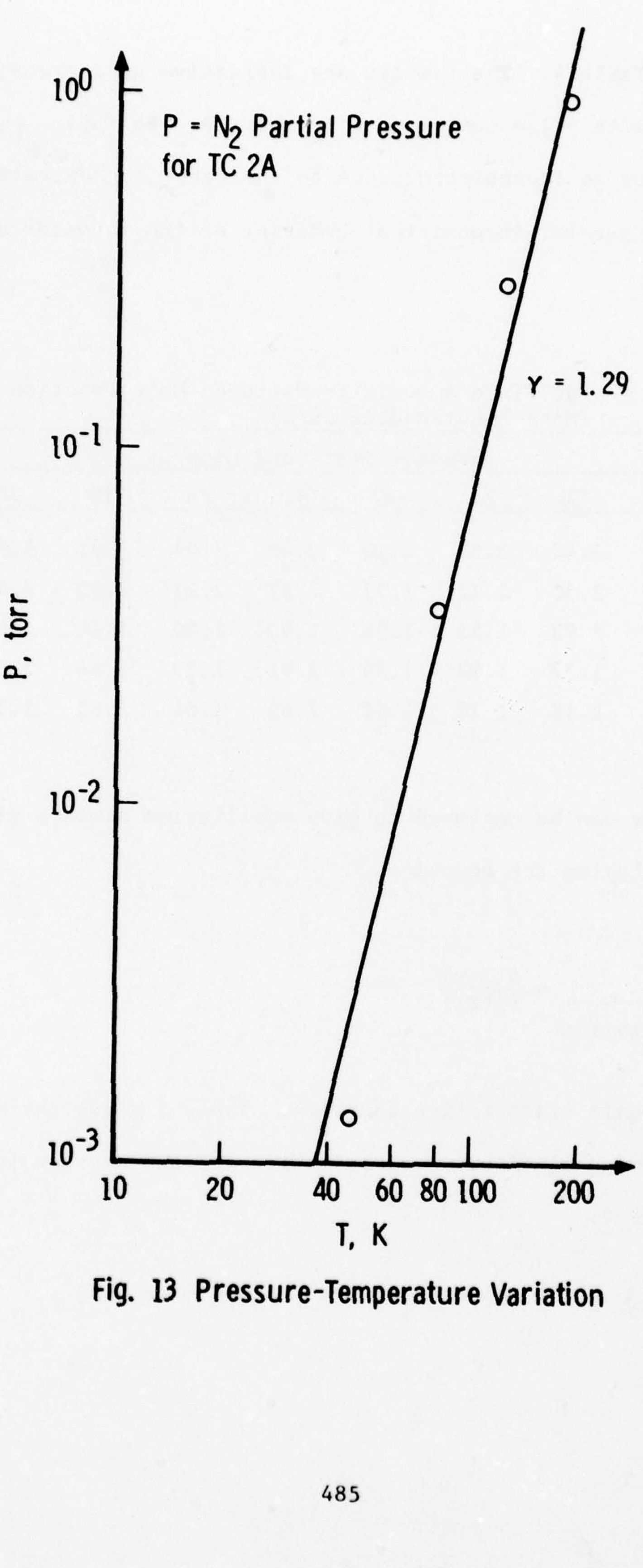

Fig. 13 Pressure-Temperature Variation

are shown in Table 4. The results are indicative of increasing ammonia dissociation with pulse number (due to thruster heating). The first pulse data show an inconsistency due to the large concentrations of hydrazine and general inconsistent behavior of the thruster during first pulses.

Table 4 Far Field Ammonia to Nitrogen Mole Fraction Ratios (Mass Spectrometer Data)

Pulse Number	Thruster Test Condition								Avg.
	2S	1A	2A	3A	1B	2B	3B	2C	
1	3.40	3.42	3.58	3.10	3.43	2.64	2.97	3.35	3.24
5	2.08	2.36	2.17	1.72	2.57	2.21	2.03	2.43	2.20
10	1.94	1.93	1.91	1.58	1.90	1.80	1.64	1.66	1.80
15	2.02	1.77	1.82	1.74	1.91	1.73	1.64	1.65	1.79
25	1.82	1.58	1.78	1.61	1.65	1.64	1.63	1.73	1.68

The ratios can be employed to give equilibrium ammonia dissociation levels by employing the equation

$$\frac{[NH_3]}{[N_2]_{\text{equilibrium}}} = \frac{4(1-x)}{(1+2x)} \tag{6}$$

where x = ammonia dissociation fraction. Table 5 gives the dissociation fraction assuming equilibrium dissociation and the average pulse values given in Table 4.

Table 5 Equilibrium Values of Ammonia Dissociation Fractions - Mass Spectrometer Results

Pulse Number	$[NH_3]/[N_2]$	Corresponding Equilibrium x
1	3.24	0.072
5	2.20	0.214
10	1.80	0.289
15	1.79	0.292
25	1.68	0.299

The intrapulse variation of ammonia to nitrogen was not monitored in general; however, limited data were taken in anticipation of possible future interest. The results for pulses 11-25 (average) for test condition 2A are shown in Fig. 14. These results are consistent with the data in Table 4 which were taken at 0.090 sec into the pulse to correspond to the laser and electron beam data gate.

Due to the lack of detailed calibration data for the mass spectrometer system and the large variations due to engine (and possibly spectrometer) fluctuations, no good evaluation of the error in the mass spectrometer measurements can be offered. A cursory analysis does indicate that the variations in species ratios are within 20%.

3.2.2 Species Variation with Pulse Number

During the mass spectrometer testing periods the five species of primary interest (N_2, NH_3, H_2O, N_2 and N_2H_4) were monitored as functions of pulse number for several test conditions. These types of data were employed in determination of the ammonia to nitrogen ratios

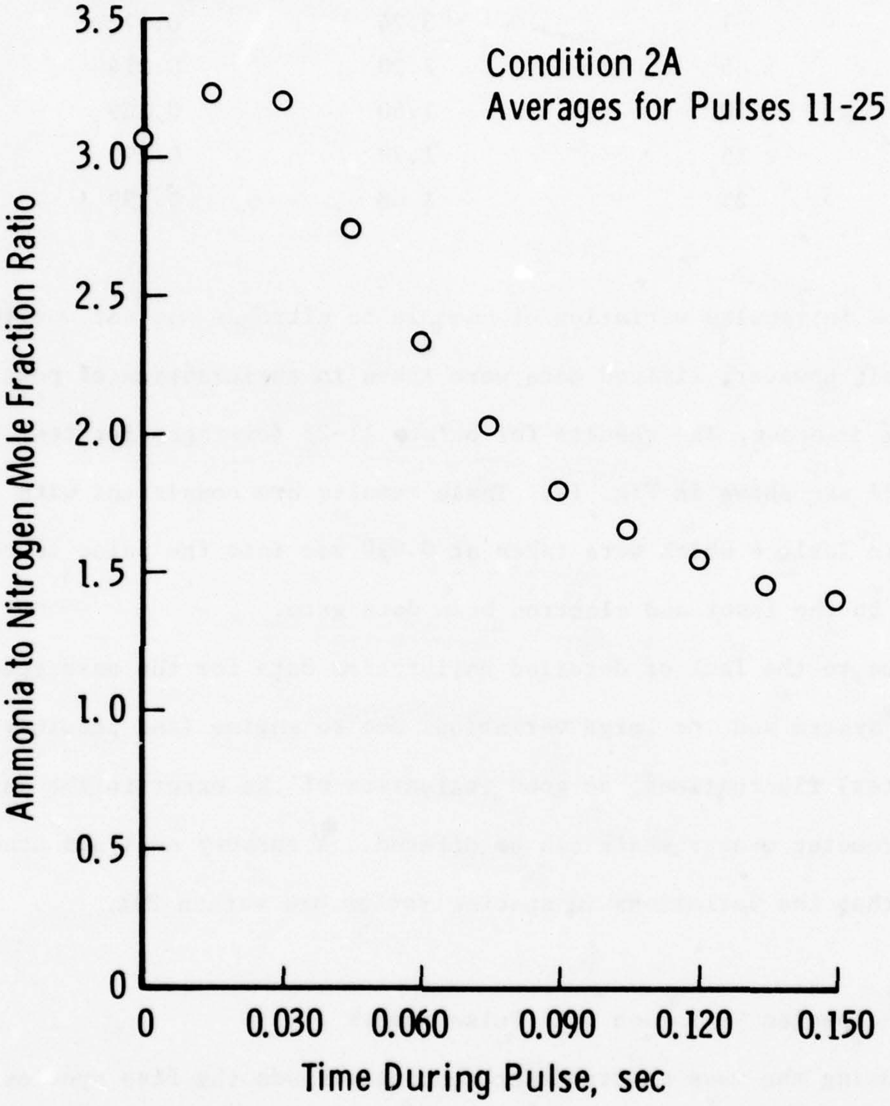

Fig. 14 Variation of Mole Fraction Ratio $[NH_3/N_2]$ within the Pulse

presented in the previous section. In most instances, all of these species were monitored, but in several instances the hydrogen peak signal to noise ratio was quite poor, and the hydrogen data could not be used. This high background noise was associated with the large quantities of H_2 absorbed into the CO_2 frost used for pumping in the probe. In addition, ammonia and hydrazine contributed daughter peaks of mass 2 which significantly degraded hydrogen data quality.

Several cases for which five species data were obtained are presented in this section as mole fraction data. Mole fractions for each species for conditions 2A, 2B and 2C are shown in Figs. 15, 16 and 17, respectively. The most noteworthy of the species' properties are the large mole fractions of N_2H_4 present during pulse one of each case and the small number of pulses necessary to reduce the N_2H_4 value significantly. Ammonia to nitrogen ratios for these cases may not necessarily agree with those from the previous section, since these are individual runs and the previous section data represented averaged results. It is obvious from the exemplary data in Figs. 15 to 17 that hydrazine is primarily present during the first few pulses of a train and that the percentage increases with thrust level, which is as expected.

Data for two additional test conditions are shown in Fig. 18. This figure also gives an opportunity for examining the effects of initial catalyst bed temperature. These data are consistent with the data of the previous figures but are presented as ratios since hydrogen data were not available to permit calculation of mole fractions. The initial catalyst bed temperature is seen to have a major effect on the

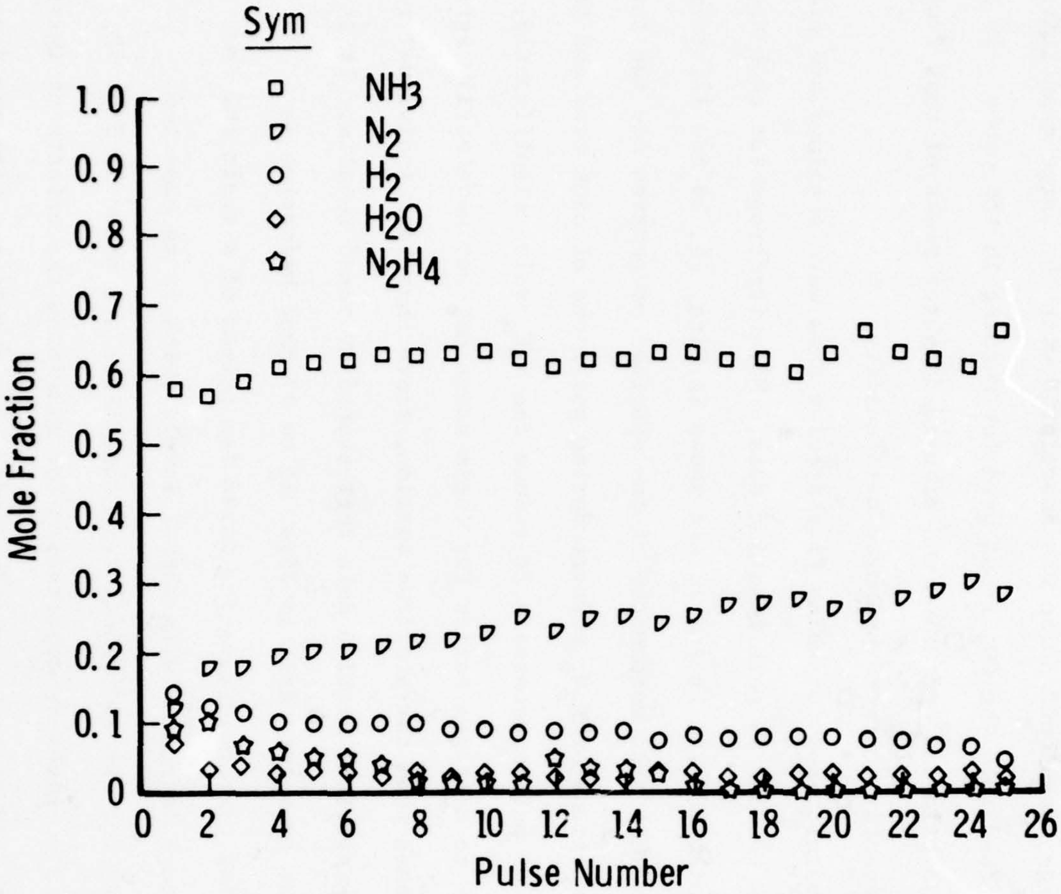

Fig. 15 Species Variation with Pulse - Condition 2A

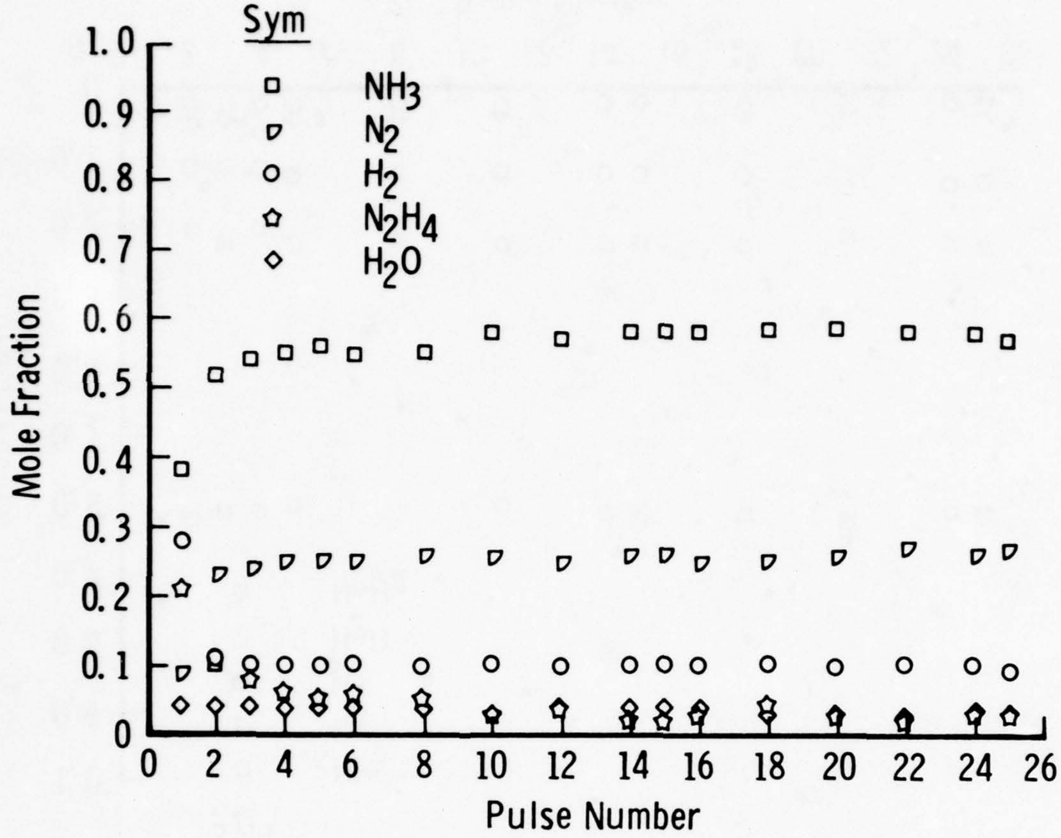

Fig. 16 Species Variation with Pulse - Condition 2B

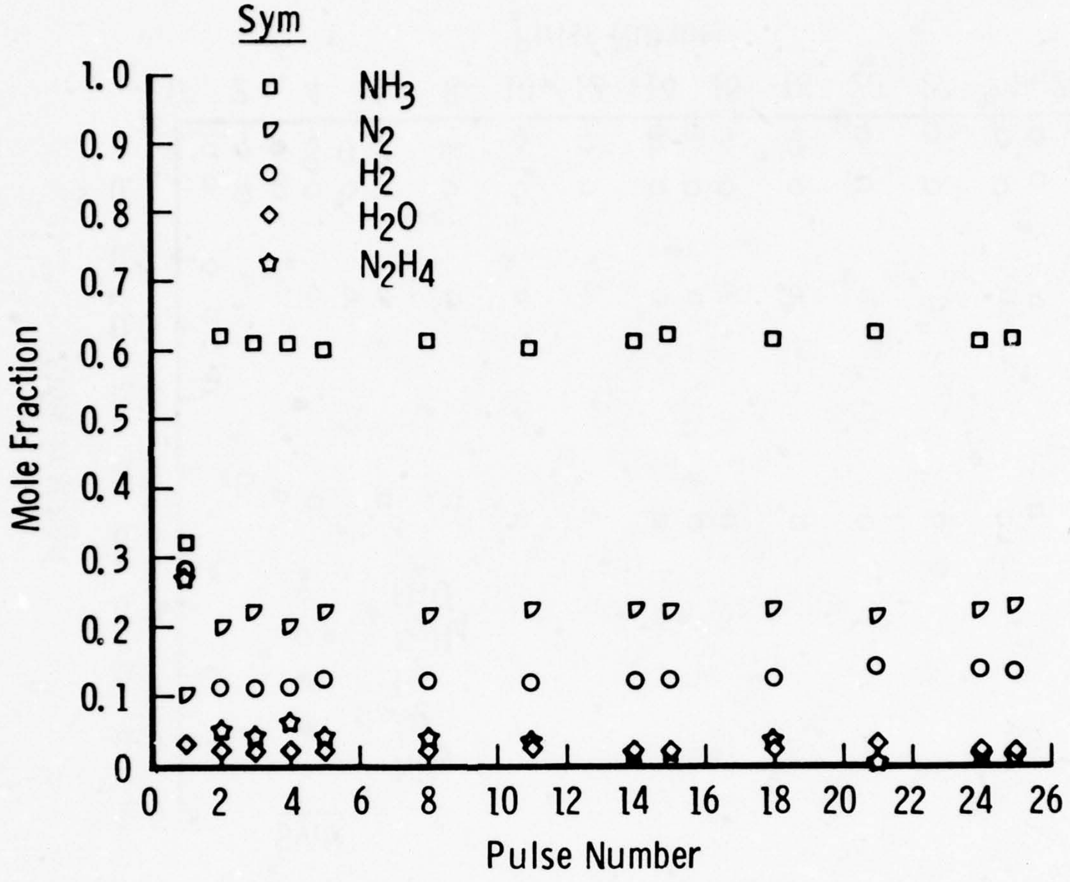

Fig. 17 Species Variation with Pulse - Condition 2C

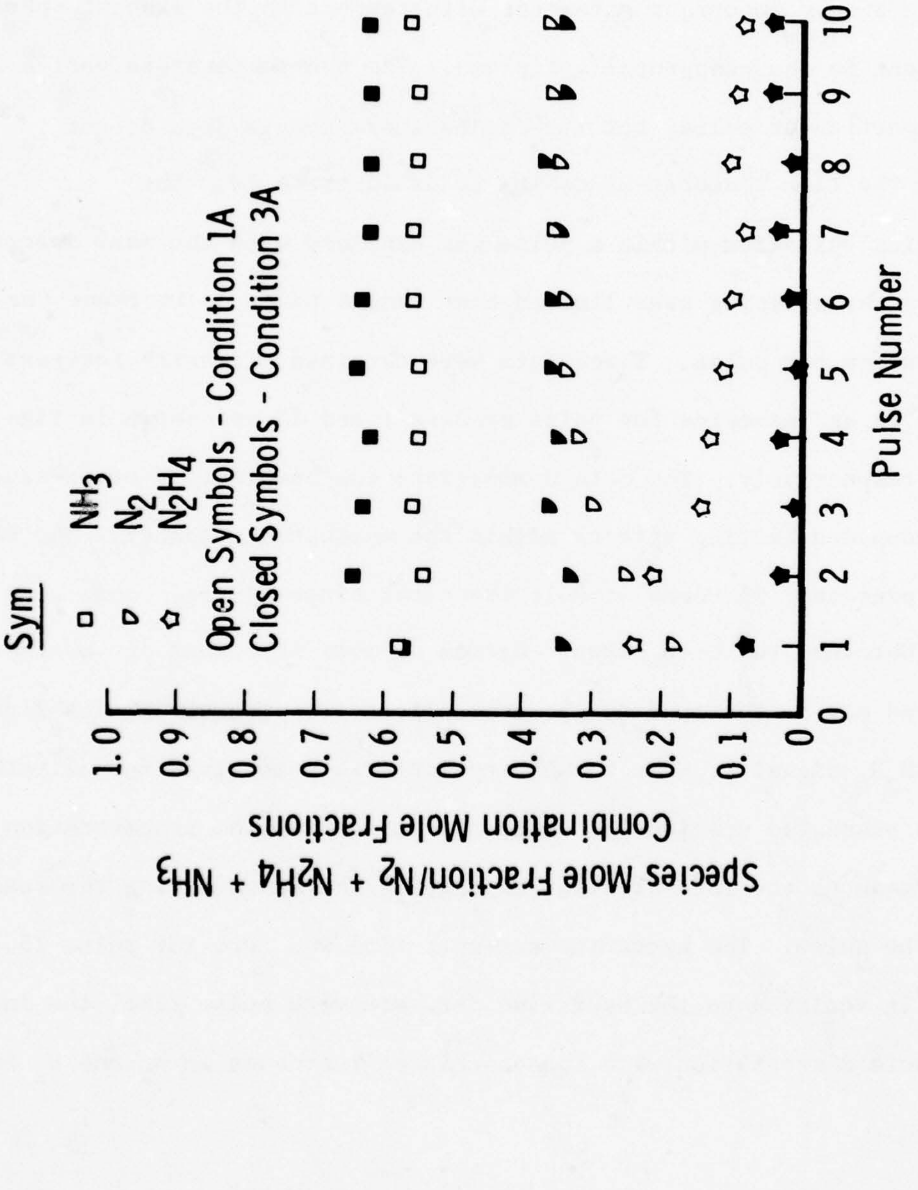

Fig. 18 Species Variation with Pulse Number

first pulse; that is, the hydrazine concentration is greatly reduced with increased temperature. After the first few pulses a consistent major difference in thruster behavior is not observed as a result of higher initial bed temperature.

3.2.3 Intrapulse Exhaust Species Variations

The catalyst bed temperature has been shown in the last two sections to be a very important parameter with respect to the exhaust species present in the monopropellant plume. The bed temperature varies during any particular pulse, but the engine thermocouple data do not have the time response necessary to demonstrate it. The species variation within a pulse was examined with the mass spectrometer system by sweeping over limited mass ranges so as to increase the total number of sweeps per pulse. These data were obtained primarily for test condition 2A, and examples for pulse numbers 1 and 25 are shown in Figs. 19 and 20, respectively. The data demonstrate the combination of pressure buildup and heating effects within the combustion chamber. The data are not presented in terms of mole fractions since hydrogen data were not obtained for both cases. Ratios of mole fractions of species presented may be obtained by the appropriate division of species' signals. The N_2H_4 signal is seen to be very large in pulse 1 as for all other data presented previously. Note that the hydrazine concentration does decrease as the interstitial temperature increases during the remainder of the pulse. The hydrazine concentration was zero for pulse 25.

In addition to the hydrazine decrease with pulse time, the increased ammonia dissociation with the associated increases in N_2 and H_2 is also

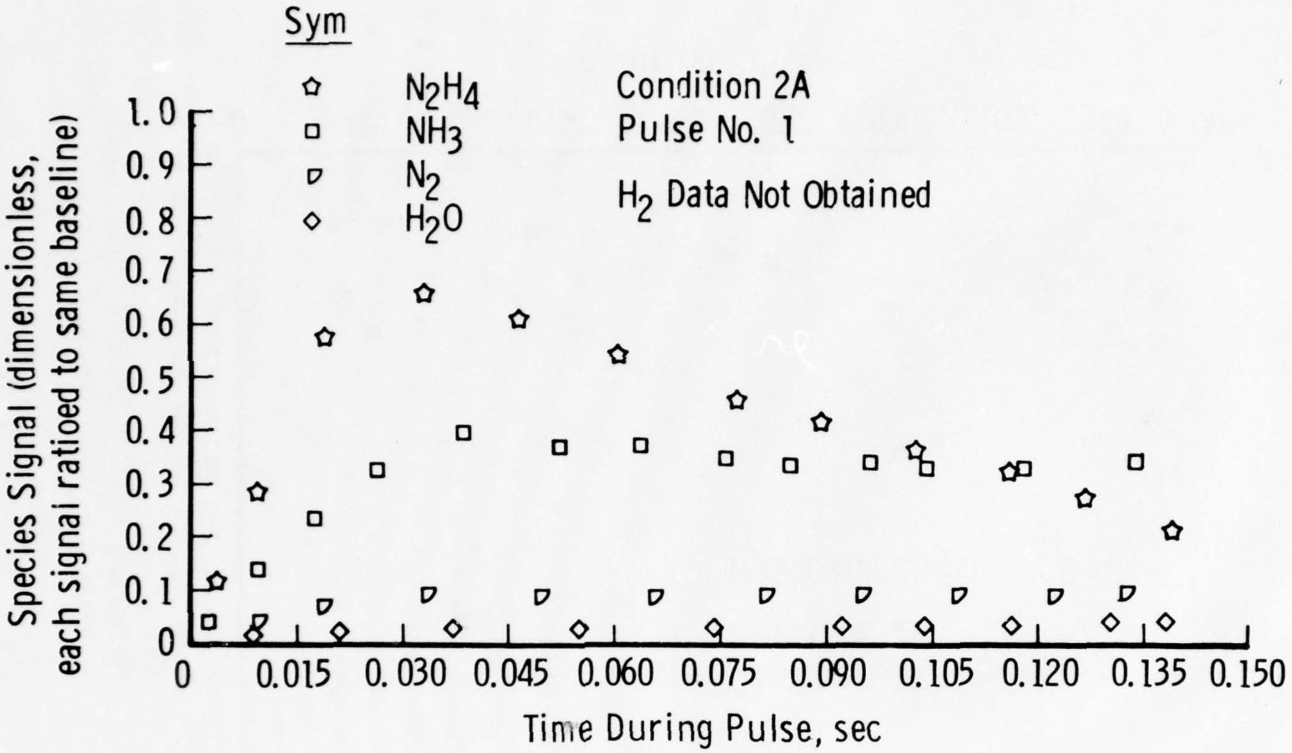

Fig. 19 Species Variation within Pulse No. 1

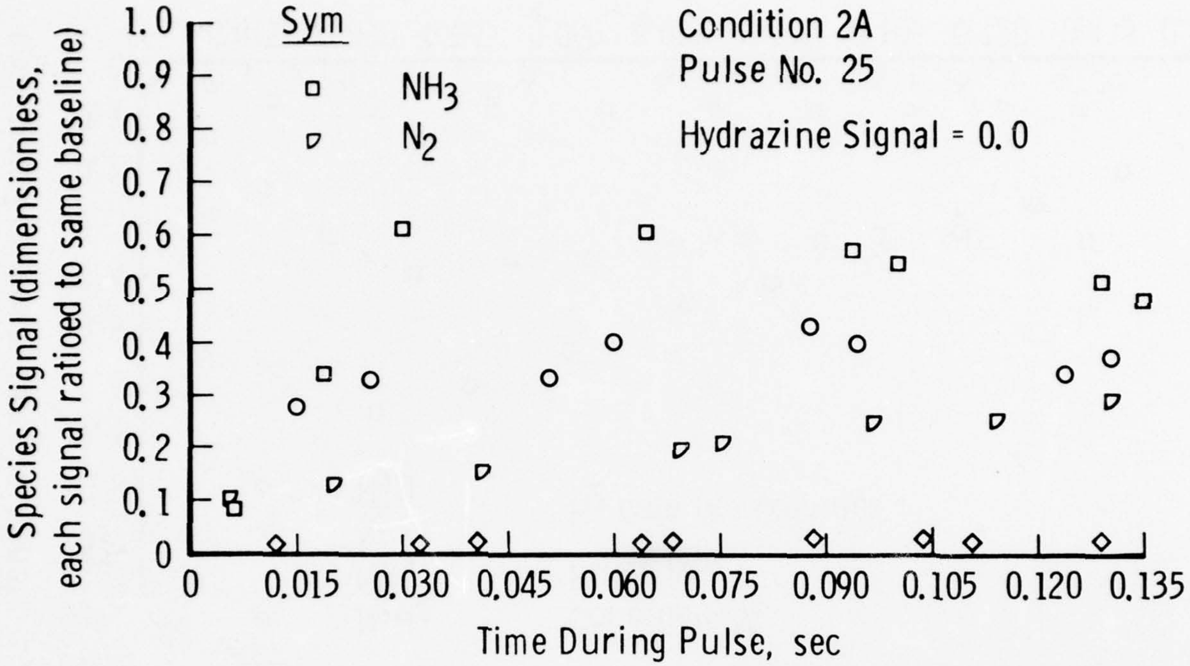

Fig. 20 Species Variation within Pulse No. 25

detectable by inspecting Figs. 19 and 20. Since a direct experimental determination of interstitial temperature was not made, no attempt at correlating the species data with temperature and pressure data was carried out.

3.2.4 Pressure Dependence of Plume Hydrazine

Since the amount of hydrazine in the plume was of significant interest, a calibration sequence was run in which the amount of hydrazine (at 0.090 secs into the pulse) was recorded as a function of valve inlet pressure. Regardless of the inlet pressure, the hydrazine concentration was negligible after the first few pulses. For the first pulse, however, the amount of N_2H_4 in the plume varied significantly with the inlet pressure (and hence thrust level). For an initial catalyst bed temperature of 478 K the relative variation of hydrazine in the plume as a function of pressure measured at the valve inlet is shown in Fig. 21. The change in slope of the apparently linear variation with inlet pressure was observed for more than the one calibration sequence shown, but no explanation is offered. Similar data for other catalyst bed temperatures were not obtained.

3.3 Quartz Crystal Microbalance Results

Figure 22 shows the variation of the mass flux ($\dot{m}$) detected by the QCM for a range of surface temperatures and at a single engine operating condition. The ordinate and abscissa display the deposited mass flux and thruster pulse number, respectively. The variation of $\dot{m}$ with both T_{QCM} and thruster pulse number is obvious. Operation of the QCM at various temperatures (T_{QCM}) enabled a qualitative characterization of the

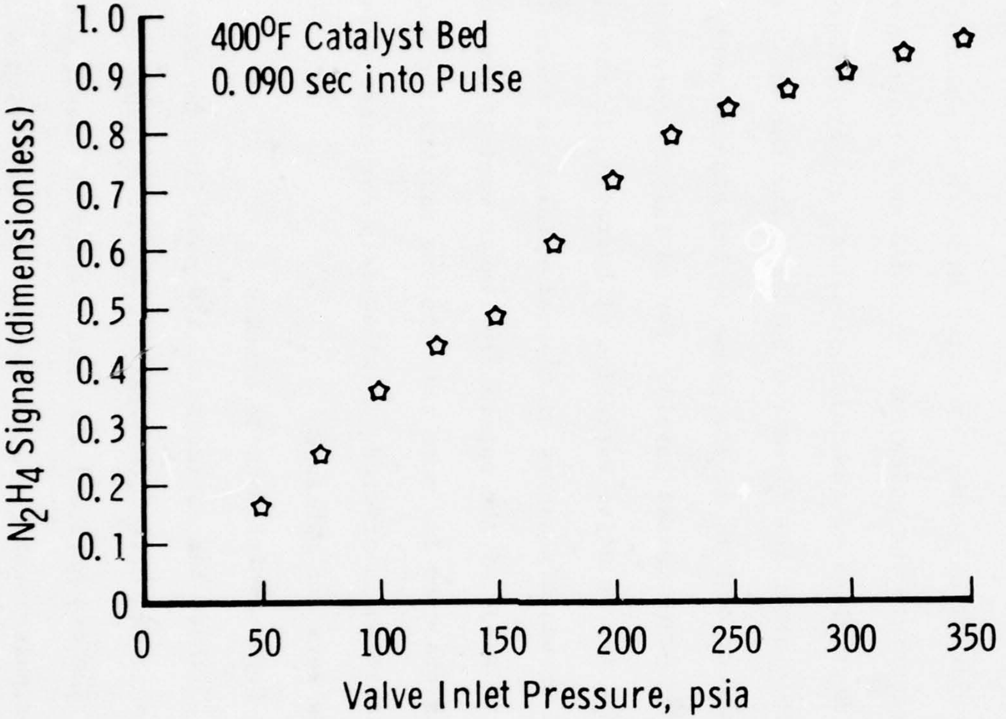

Fig. 21 Hydrazine in Plume for Pulse No. 1

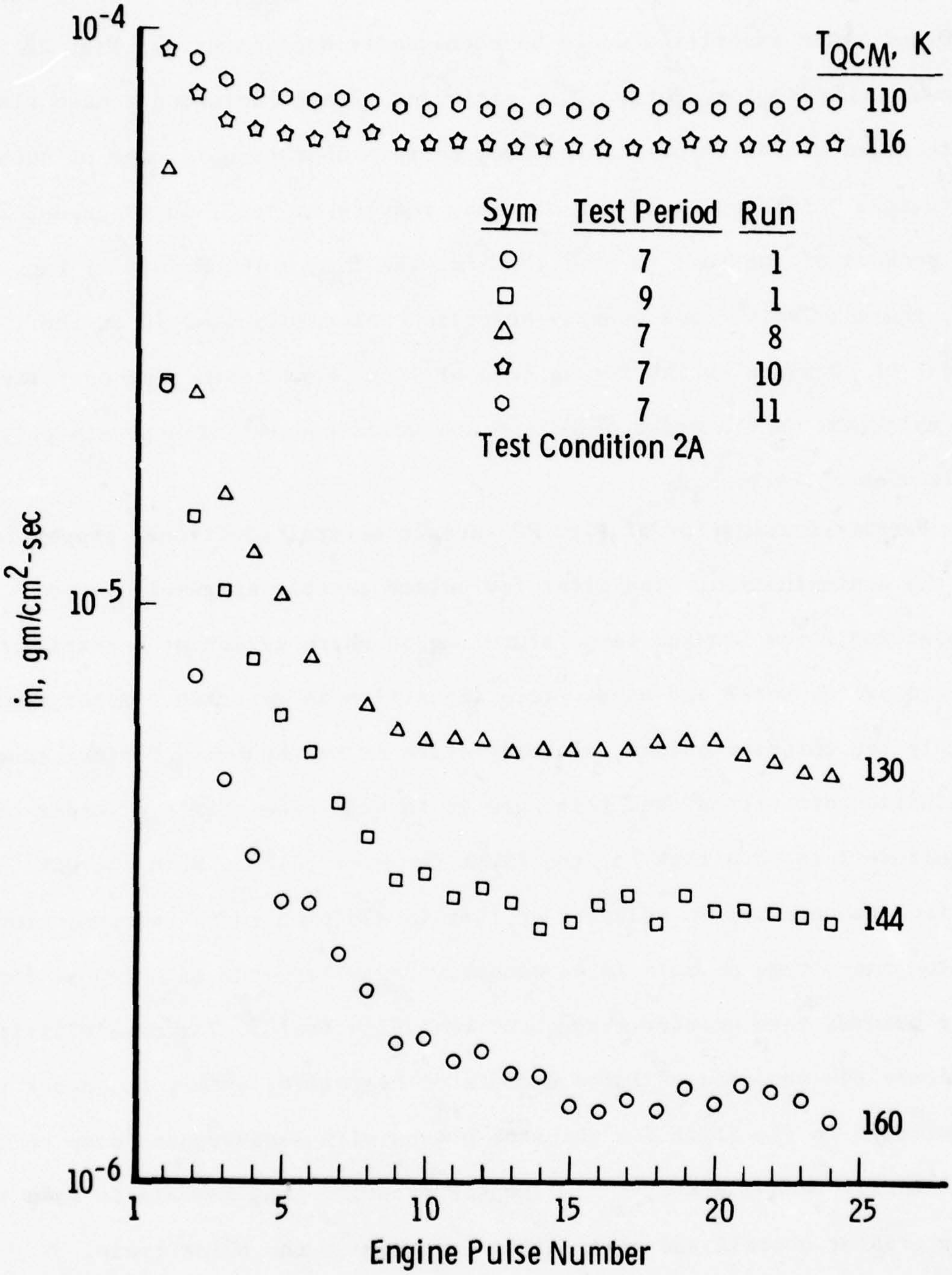

Fig. 22 ṁ versus Pulse Number for Various QCM Temperatures

contamination species in the deposit. For $144 \leq T_{QCM} \leq 160$ K only N_2H_4, H_2O and trace impurities would be permanently deposited, and Fig. 22 shows such exemplary data. This variation of the contaminant mass flux with pulse number is of interest for certain operational modes of such thrusters. Although analysis of these results is still in progress, it is perhaps of interest to note that for the $T_{QCM} = 160$ K data of Fig. 22, the cumulative mass density deposited after 20 pulses is on the order of 70 $\mu g/cm^2$ which, for an area of 1 cm^2, represents a deposit layer of thickness on the order of 0.1 μm and would consist of approximately 10^{17} molecules of, say, N_2H_4.

Further examination of Fig. 22 reveals several additional properties of the contamination. The first few pulses exhibit extremely large deposition rates for the temperature region where permanent deposition of hydrazine, water and other trace impurities is expected. After approximately ten thruster pulses, a steady-state is reached with respect to contamination deposition, and this rate is in each case nearly an order of magnitude less than that for the first thruster pulse. When the QCM surface temperature is adjusted so that in addition to the abovementioned contaminants some ammonia is permanently deposited, the main deposition rate becomes more uniform throughout the pulse train. The data clearly indicate the presence of large amounts of hydrazine, water, and other trace impurities in the first few thruster pulses with a subsequent drop to an essentially steady state. The contribution from ammonia is seen to be much greater overall and more uniform throughout the pulse train.

Figure 23 demonstrates the variation of the mass flux with engine test condition for a T_{QCM} = 161 K at the engine axial position of 1.25 cm. Similarly, Fig. 24 depicts the variation of the average mass flux, $\langle \dot{m} \rangle_n$, with the engine inlet valve pressure, P_{inlet} (thrust level), for a T_{QCM} = 130 K. Here the average of the mass flux level is performed over the last n = 5 thruster pulses. The nearly two-orders-of-magnitude increase in $\dot{m}$ with engine pulse number for a range of inlet pressures at T_{QCM} = 130 K is presented in Fig. 25, and the large increase in $\dot{m}$ with P_{inlet} can be viewed as a function of individual thruster pulses. Figure 25 again demonstrates large deposition rates for the first few thruster pulses at a surface temperature where hydrazine, water and other trace impurities are expected to deposit. However, the difference between this rate for the first thruster pulse and that when the thruster reaches a steady deposition rate is seen to increase dramatically with the inlet pressure. Additionally, the number of pulses required to reach the steady deposition rate is seen to increase with increasing inlet pressure.

Finally, Fig. 26 shows the variation of $\dot{m}$ with thruster pulse number for three catalyst bed temperatures. For these data, the thruster inlet pressure was maintained at 230 psia and the surface temperature at 143 K. Here the deposition rate is seen to increase with decreasing catalyst bed temperature throughout the pulse train, with the most striking difference occurring in the first few thruster pulses. The number of pulses required to reach a steady deposition rate is also seen to decrease with increasing catalyst bed temperature.

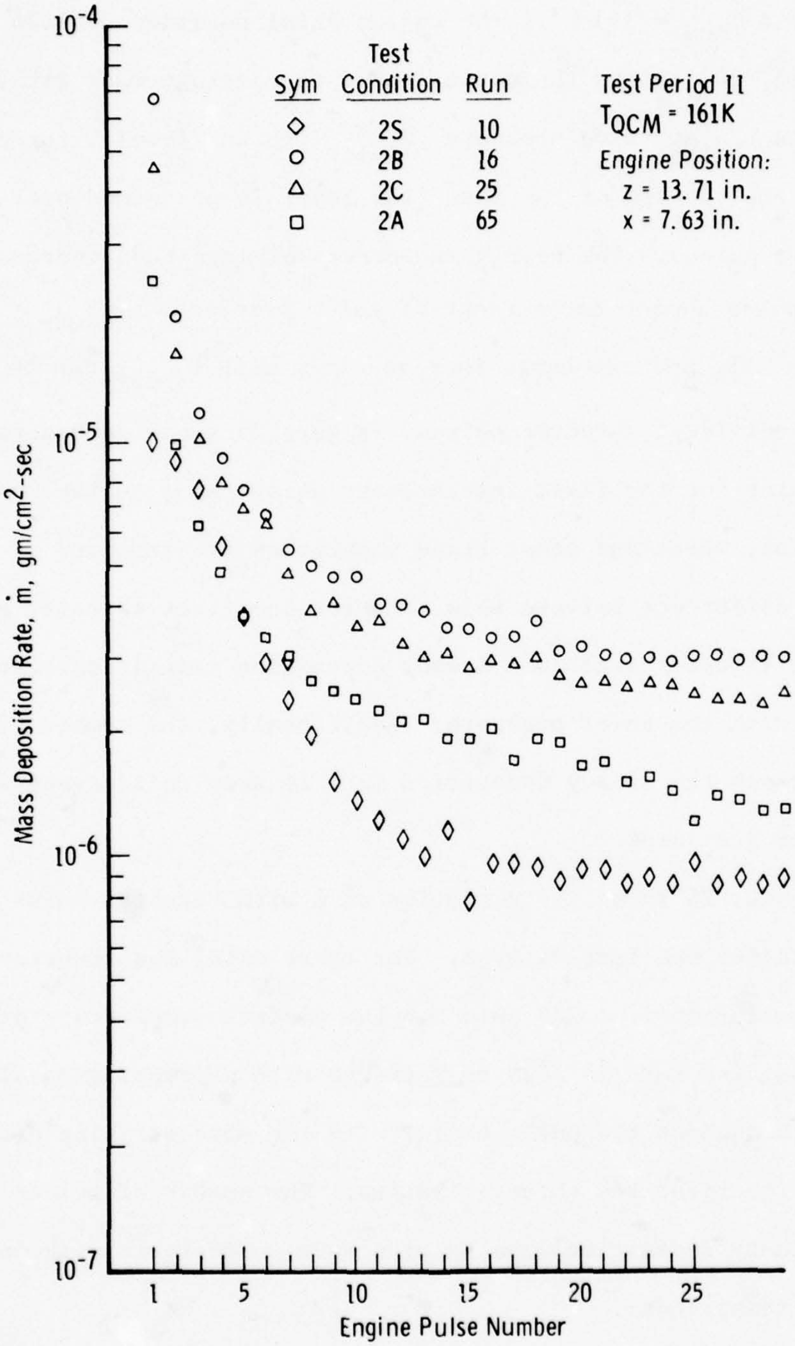

Fig. 23 ṁ Versus Pulse Number for Several Engine Conditions

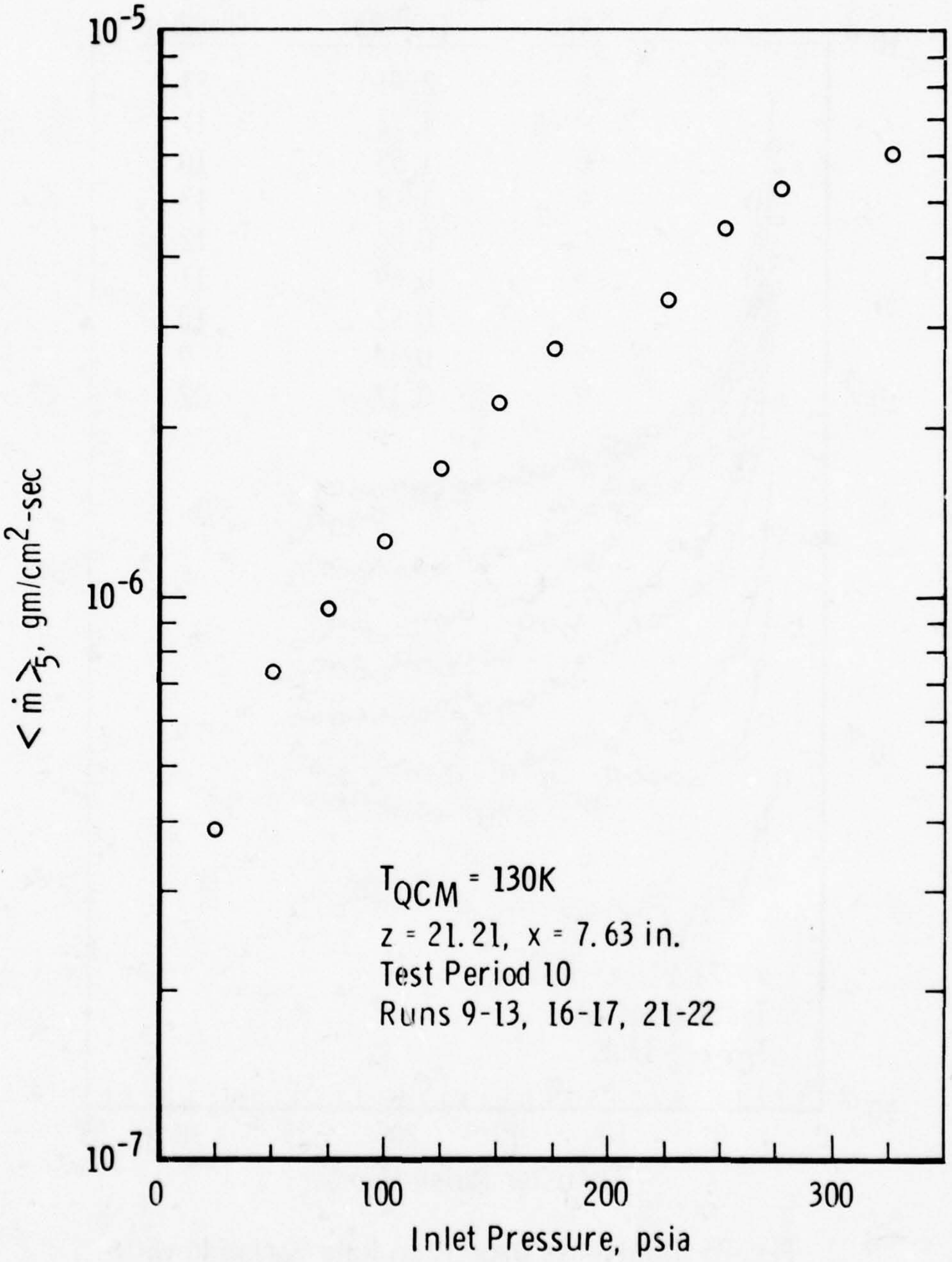

Fig. 24 Average Mass Deposition Rate versus Inlet Pressure

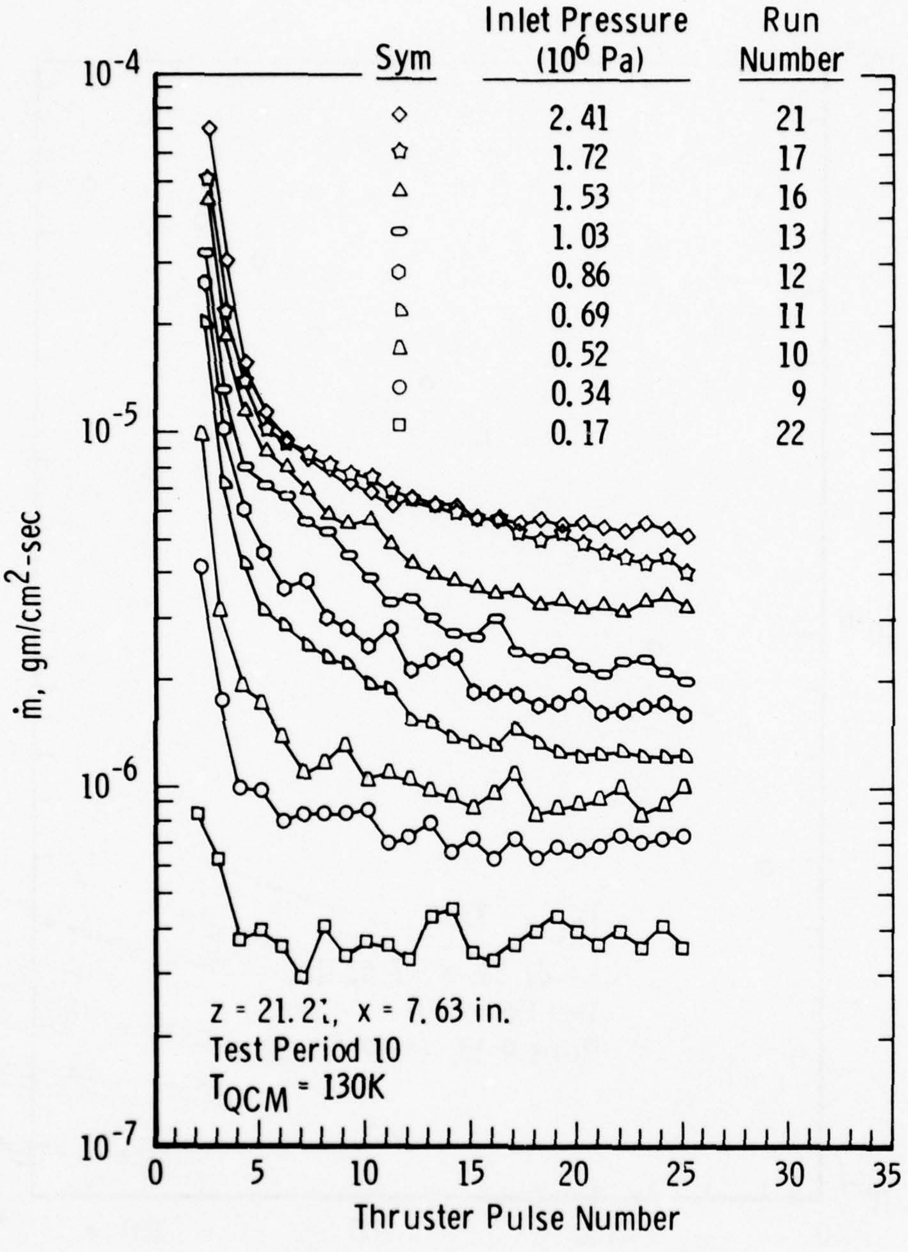

Fig. 25 QCM Mass Deposition Rate Variation with Inlet Pressure and Pulse Number

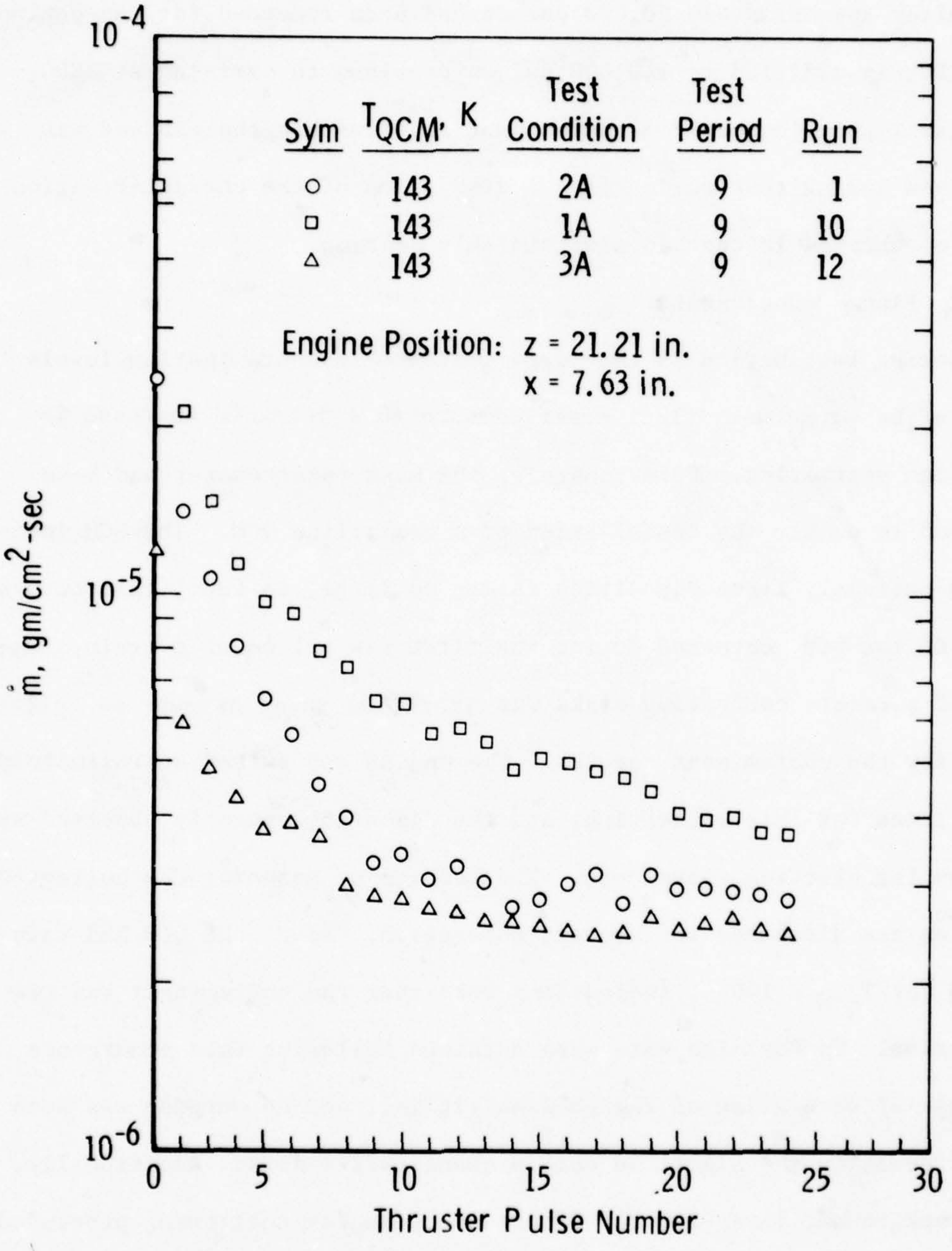

Fig. 26 QCM Mass Deposition Rate as a Function of Thruster Pulse Number

3.4 Catastrophic Contamination Increase

After approximately 60,000 pulses had been recorded for the engine at AEDC, in addition to 140,000 pulses previous to arriving at AEDC, a catastrophic increase in contaminant level within the exhaust was observed during test period 13. A discussion of the characterization of this occurrence is contained within this section.

3.4.1 Plume Measurements.

During test period 13 the large increase in contamination levels within the plume were first observed through a dramatic increase in Rayleigh scattering. Unfortunately, the mass spectrometer had been removed to enable the installation of a centerline QCM. The QCM indicated extremely large deposition rates; so large, in fact, that saturation of the QCM occurred during the first few pulses of a train. Therefore, the web of particle collecting disks was installed in an attempt to collect and identify the contaminant species. The engine was pulsed approximately 1000 times for this collection, and the disks subsequently observed with a scanning electron microscope. The results of scanning the collected samples are discussed in the next subsection. Since the QCM had saturated for $T_{QCM} \approx 160$ K, indications were that the contaminant was raw hydrazine. No Rayleigh data were obtained following this occurrence because of saturation of the photomultiplier, and no purpose was seen in attenuating the signal to obtain quantitative data. Additionally, the background, laser-induced fluorescence and/or scattering precluded further Raman measurements. Further electron beam data were acquired to determine the changes, if any, in the flowfield parameters, but analysis of these results is still in progress.

3.4.2 Particle Collection

The particle collection experiment was previously described. The attempted collection of particles was successful with large quantities of submicron and larger particles captured on all three types of disks, wax, glue and copper. In addition, there was evidence of fuel droplet impingement upon the particle sampling disks. Discussions with AFRPL revealed that proof of catalyst bed particle capture required the identification of iridium among the collected particles. Extensive x-ray analysis of the collected samples failed to reveal the presence of iridium, and it was assumed that no particulate matter from the bed itself was actually collected. However, the x-ray analysis in conjunction with microscopic examination did reveal alumina spheres in large quantities. Based on the AFRPL information, these were not from the catalyst bed.

Microscopic examination of the disks did reveal that near the centerline of the plume copious quantities of liquid droplets had impinged. These droplets badly etched the pure copper surface disks, as shown in Fig. 27. A control disk obtained by spraying pure N_2H_4 on a copper disk with a nebulizer revealed patterns very similar to those obtained in the plume. An example of this is shown in Fig. 28. The similarities were sufficient to establish that large quantities of hydrazine were present near the plume centerline.

The disks near the centerline were obviously subjected to high heat loads, and the collectors without wax were blackened and those with wax

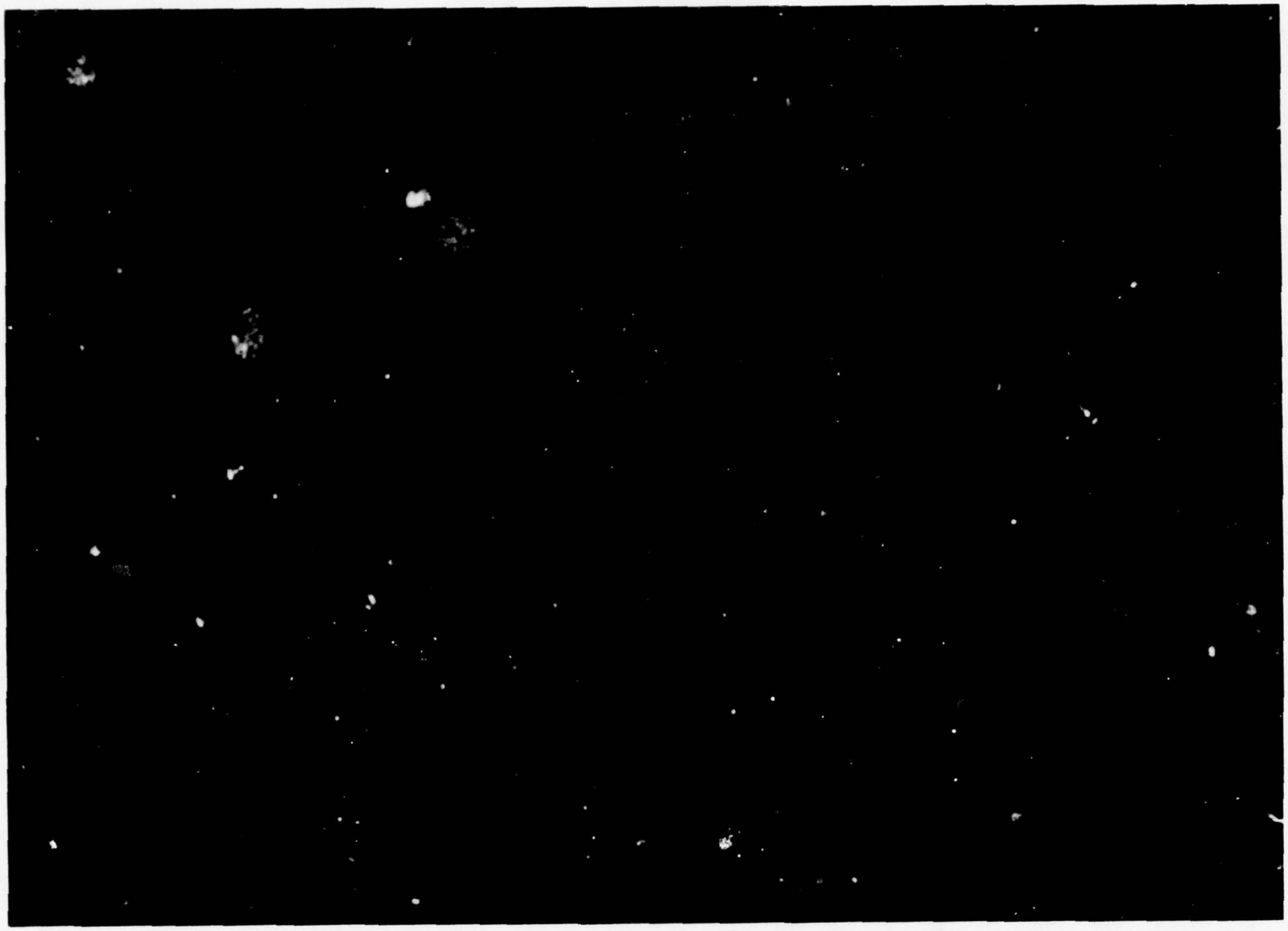

Fig. 27 SEM Sampling Disk Placed in Thruster Exhaust Plume

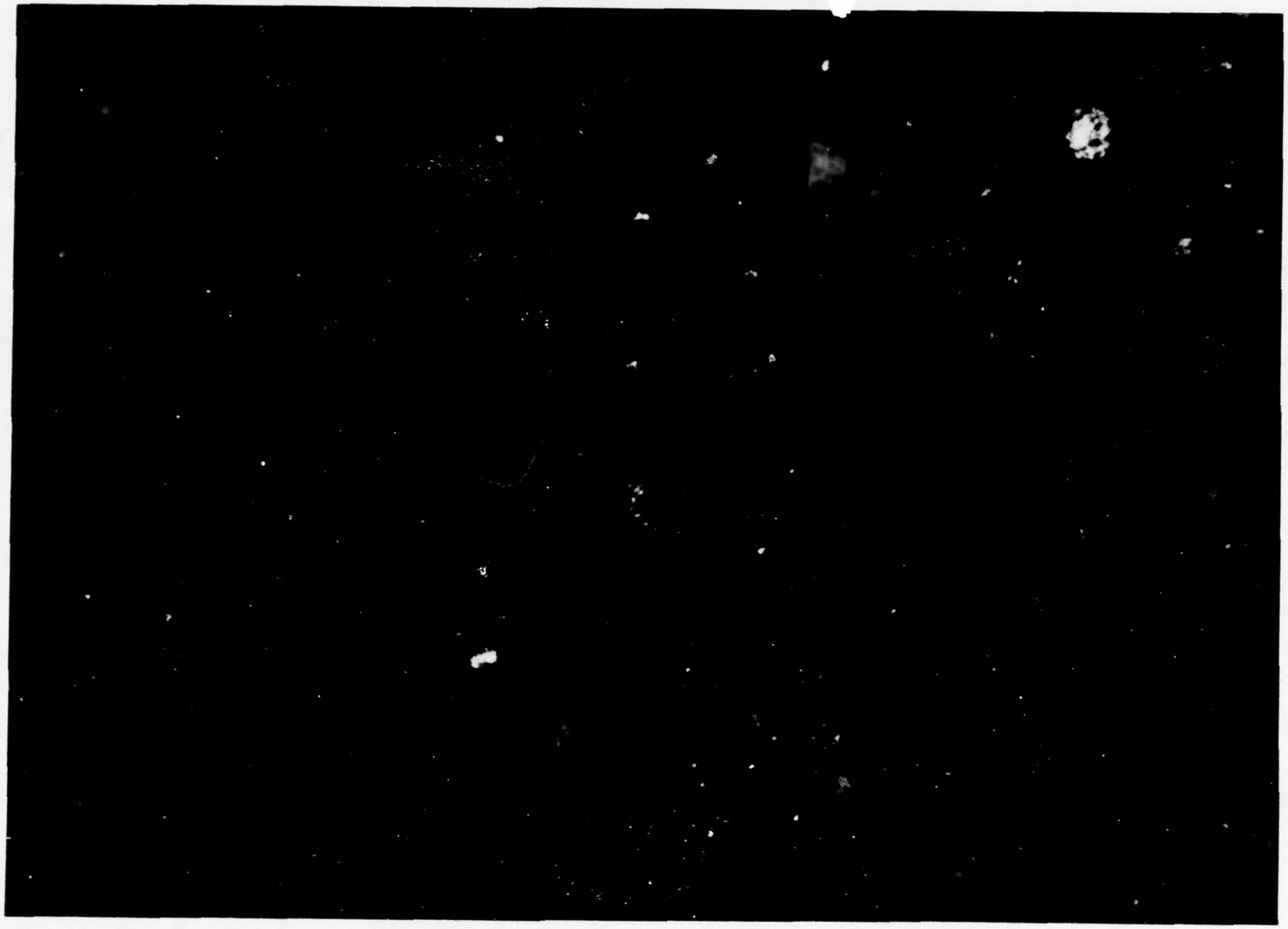

Fig. 28 SEM Sampling Disk Placed in Nebulizer Mist

were whitened. The disks just outside the direct impingement area showed the etching effects just discussed. These effects were obscured for the disks nearest the centerline because of the intense stagnation heating.

In addition to the observations reported in the preceding discussion, an interesting shadowing effect on the sampling disk mounting device was observed. This is shown in Fig. 29. The areas shielded from the plume by being behind the disks are very dark. The surfaces that appear dark but were underneath disks were noted to correspond to disks which were not pressed flat against the mounting device. A good explanation of the shadowing has not been devised at the present.

3.4.3 Engine Performance

Following the observation of the catastrophic increase in exhaust contamination levels,the performance degradation of the thruster was investigated by repeating the calibration experiments conducted at the beginning of and during the research work. It could not be investigated simultaneous to the other measurements since proper operation of the thruster dictates the combustion chamber pressure tap be plugged.

The post-catastrophe mass flow rate (measured for 60-sec firings) was found to be about 10% higher than pre-catastrophe. The combustion chamber pressure and lower wall temperature changes, before and after, are demonstrated in Figs. 30 and 31, respectively. Although both pressure and temperature were different for the early and late test periods, both were still within operating limits for the thruster. The temperature drop shown in Fig. 31 is as expected for poor

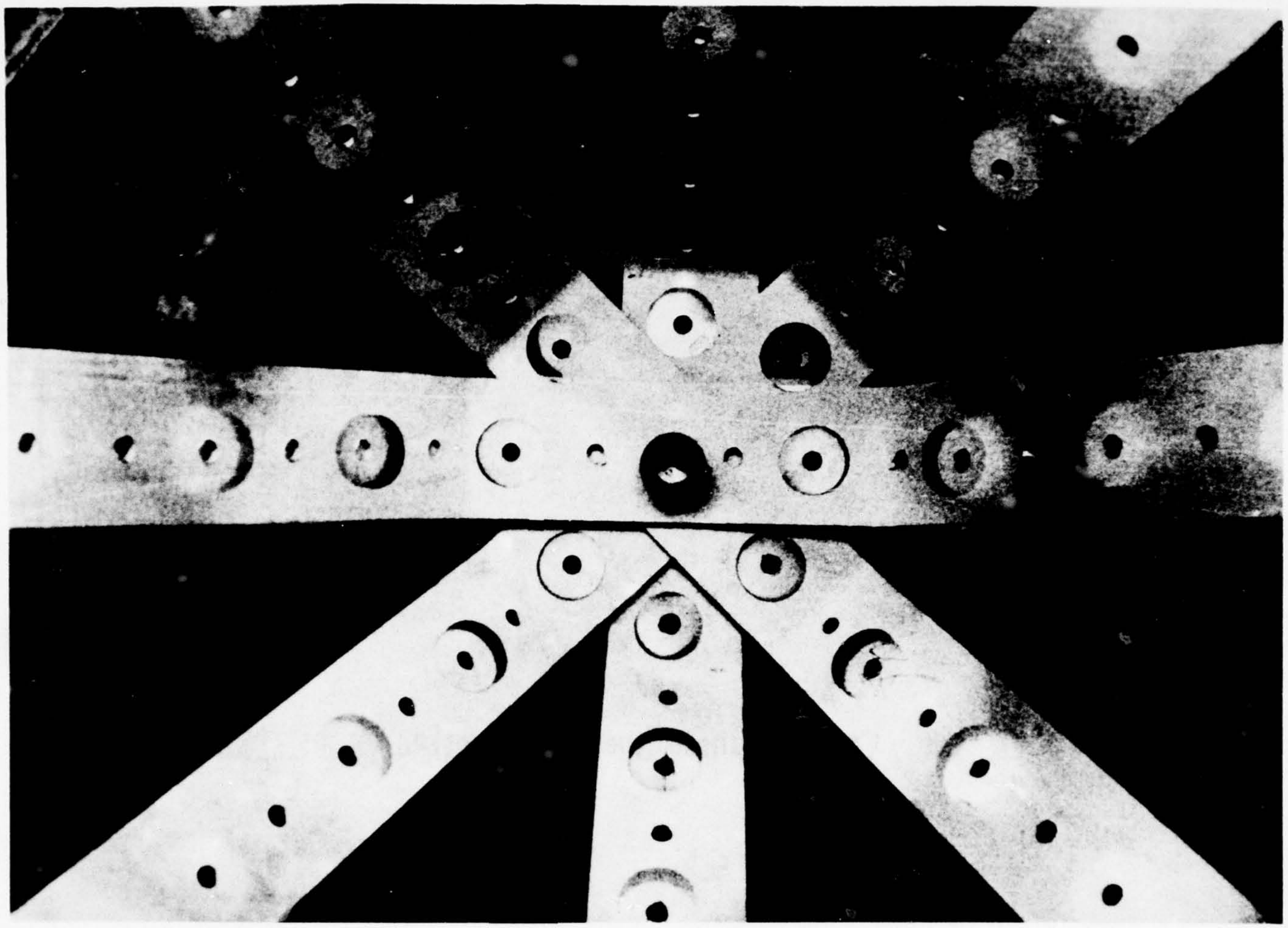

Fig. 29 Aluminum Disk Sample Holder After Testing

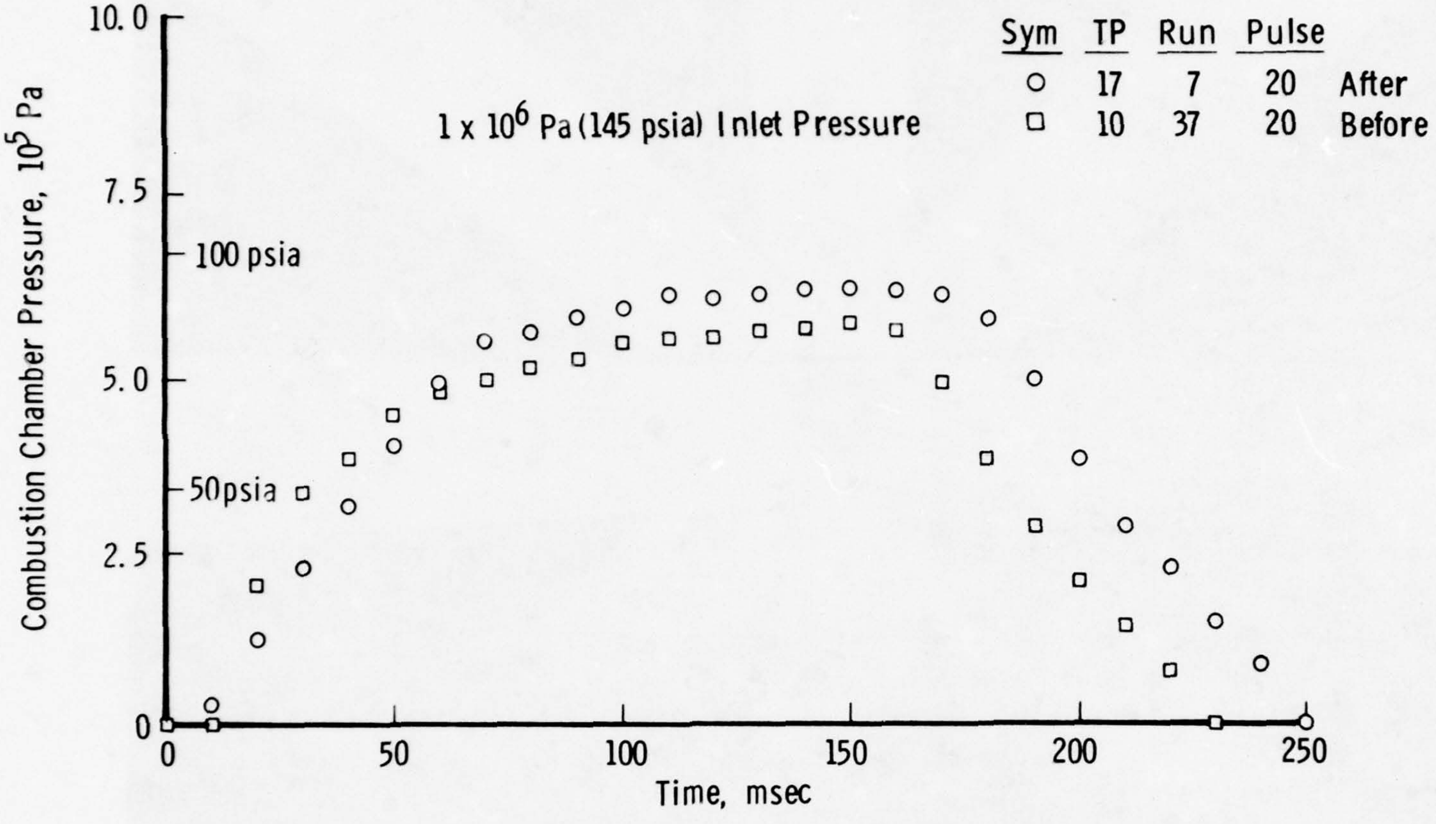

Fig. 30 Combustion Chamber Pressure Pulse before and after Increase in Contamination Level

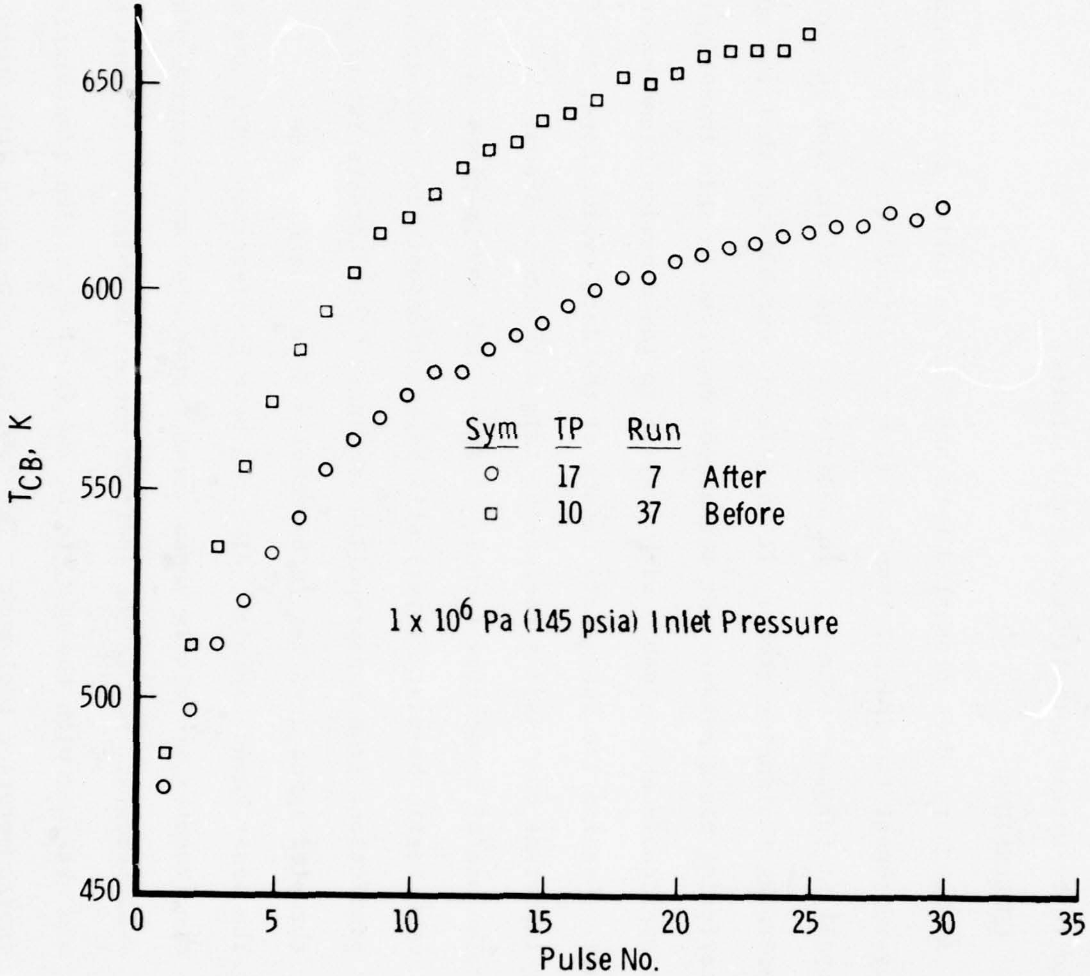

Fig. 31 T_{CB} versus Thruster Pulse Number before and after Increase in Contamination Level combustion, but it is interesting to note that the pressure increased as did the mass flow rate. Additional analysis of the existing data will be necessary to properly interpret engine performance, but sufficient data have been scrutinized to establish the performance to be within normally acceptable limits.

4.0 CONCLUSIONS

Although the data presented here and its evaluation are preliminary, they represent the initial benefits from a detailed study of a monopropellant thruster exhaust. In addition to the information obtained concerning the engine itself, it was clearly established that the non-interfering plume measurement techniques employed in this investigation are applicable and valuable with respect to gas dynamics plume measurements. Despite the incomplete nature of the data evaluations, the following important conclusions concerning this work can be drawn:

1. The use of predictive techniques which lack nozzle-plume chemistry (also nozzle boundary layer) will be insufficient for contaminant predictions from monopropellant engines. The characteristics of thruster aging have yet to be modeled into a usable code.
2. The laser Raman-Rayleigh, electron beam fluorescence, QCM, and mass spectrometer are viable measurement systems for small engine plume measurements. Due to the indirect manner in which plume properties are obtained with the QCM, it is the least effective quantitative instrumentation implement. The data base obtainable with these systems is directly applicable to interpreting engine behavior and contamination production.

3. There are large quantities of hydrazine in the forward flow exhaust region for all operating conditions during the first few pulses of a pulse train from an aged thruster.
4. Condensate levels within the exhaust plume are high for certain engine operating conditions.
5. Copious quantities of hydrazine may be present in the forward flow region without a serious degradation or washout of the thruster occurring.

The following recommendations are obvious extensions of this work:

1. Conduct a similar investigation for the same type thruster with an unaged catalyst bed.
2. Investigate other thruster designs in similar fashion to determine if aging phenomena are consistent for such designs.
3. With the soon-to-be-established data base, evaluate in detail the present predictive capabilities, establish the discrepancies and make improvements.

NOMENCLATURE

$\dot{m}$	mass deposition rate on QCM surface
MOCS	method of characteristics solution
n	species number density
$(n/n_o)_{eff}$	effective number density ratio determined from Rayleigh/Mie scattering
n_T, n_o	plume total species number density and reservoir total number density, respectively
P_{inlet}, P_c	engine inlet pressure and combustion chamber pressure, respectively

QCM	quartz crystal microbalance
$\hat{r}$	ratio of radial distance from axial centerline to nozzle throat diameter
T_R, T_o	rotational temperature and reservoir temperature, respectively
T_{CB}, T_{QCM}	catalyst bed and QCM temperature, respectively
TC, TP	test condition and test period, respectively
$\hat{x}$	ratio of axial distance from nozzle throat to the nozzle throat diameter
γ	ratio of specific heats

ACKNOWLEDGMENT

This work was sponsored by the Air Force Rocket Propulsion Laboratory (AFRPL) and performed by the Arnold Engineering Development Center (AEDC), Air Force Systems Command (AFSC). Work and analysis were done by personnel of ARO, Inc., a Sverdrup Corporation company, operating contractor of AEDC.

REFERENCES

1. Baerwald, R. K. and Passamaneck, R. S., Monopropellant Thruster Exhaust Plume Contamination Measurements, AFRPL-TR-77-44 (1977)
2. Williams, W. D., McCay, T. D., Powell, H. M., Weaver, D. P., Price, L. L. and Lewis, J. W. L., Experimental Study of Monopropellant Hydrazine Thruster Exhaust. Paper presented at JANNAF 10th Plume Technology Meeting, San Diego, CA. (1977).
3. McCay, T. D., Powell, H. M. and Busby, M. R., Direct Mass Spectrometric Measurements in a Highly Expanded Rocket Exhaust Plume, AIAA Paper 77-154 (1977).

4. McCay, T. D., Powell, H. M. and Busby, M. R., Development of a Cryogenically Pumped Mass Spectrometer Probe for Rocket Plume Studies, AEDC-TR-76-55, June 1976.

5. Cornu, A. and Massot, R., Compilation of Mass Spectral Data, 2nd ed., Vol. I, Heydon, New York (1975).

6. Lewis, J. W. L. and Williams, W. D., Measurement of Temperature and Number Density in Hypersonic Flow Fields Using Laser Raman Spectroscopy, AIAA Paper No. 75-175, presented at the 13th AIAA Aerospace Scienced Meeting, Pasadena, CA, Jan. 20-22, 1975.

7. Lewis, J. W. L. and Williams, W. D. Argon Condensation in Free-Jet Expansions, AEDC-TR-74-32, July 1974.

8. Williams, W. D., Hornkohl, J. O. and Lewis, J. W. L., Electron Beam Probe for a Low Density Hypersonic Wind Tunnel, AEDC-TR-71-61, July 1971.

Design of a Propulsion System Test Facility to Study Rocket Plumes in the Space Environment

L. F. Molinari

Jet Propulsion Laboratory
Pasadena, California

ABSTRACT

NASA has initiated a project at JPL for the design and fabrication of a facility to test various types of propulsion systems in the vacuum environment of space. The Propulsion Contamination Effects Module (PCEM) Spaceflight Experiment is being designed for installation in the payload bay of the Space Shuttle Orbiter. The objectives of the experiments are to measure exhaust plume characteristics and surface impingement effects from high-thrust chemical and low-thrust electric thrusters. The PCEM facility will include sensors for measuring several parameters. Included as instruments are temperature-controlled quartz crystal microbalances and a mass spectrometer. The experimental data will be used to demonstrate the ability of analytical models to predict forces, heat fluxes, surface charging effects, and levels of contamination which might be encountered by a spacecraft employing these thrusters. Measurement emphasis will be placed upon the backflow region of the plume. This area is of primary concern to the spacecraft designer, and yet it represents an area of maximum theoretical ambiguity.

The initial PCEM configuration will be designed to accommodate a 110 N (25 lb_f) monopropellant hydrazine propulsion system. Design modification kits will enable the PCEM to accommodate other propulsion systems, including a 3870 N (870 lb_f) N_2O_4/MMH liquid bipropellant rocket engine, 4.4×10^{-3} N (1×10^{-3} lb_f) and 1.3×10^{-1} N (3×10^{-2} lb_f) ion drive engines, a 4450 N (1000 lb_f) solid rocket motor, and a 110 N (25 lb_f) O_2/H_2 gaseous bipropellant system.

This paper presents the results of one phase of research carried out at the Jet Propulsion Laboratory, California Institute of Technology under Contract No. NAS7-100, sponsored by the National Aeronautics and Space Administration.

1.0 INTRODUCTION

The need for the development of a capability for providing basic experimental data to verify plume models utilized in the design of spacecraft is evident. The necessity exists because of the limitations inherent in existing experimental facilities and analytical models.

The problems resulting from the effects of rocket engine plumes and plume contaminants on spacecraft systems and instruments have long been recognized by NASA, and studies have been initiated to define and resolve the problem. A NASA (GSFC) Nimbus study was authorized in 1970, and one conclusion from the report (Ref. 1) was: ". . . space simulation chambers will not achieve vacuums even remotely resembling those which occur in space. Yet, it is precisely this very high vacuum which enables the phenomenon to occur which we are undertaking to study. . . . This consideration leads us to the most accurate investigation, namely, a flight experiment. Here, we need not worry about environment since it is there. . . . Our overall conclusion is that further work is needed. . . . We feel that some work in the analytical direction and some work in the experimental direction both are needed." The propulsion technology group of the OAST Space Technology Workshop (Summer Workshop) held at Harrisonburg, Va., in August 1975 recognized thruster-induced backflow contamination as a Justification Category I problem. This category specifies "space environment essential" for resolution. The JANNAF and the Workshop Steering Committees have sponsored plume technology conferences in which the results of many investigations were evaluated. Consequently, there has been an evolution in the advancement of plume technology. However, modeling data for spacecraft design is considered to be limited and the extrapolation of empirical data from mini-thrusters [$\leq$0.9 N (0.2 lb_f)] tested in vacuum chambers to larger thrust engines [>200 N (50 lb_f)] in space is considered highly questionable, at best.

Numerous plume-associated anomalies have been observed on such NASA spacecraft as Nimbus, ISCE, ATS, Landsat-C, and Voyager. Voyager experienced the most recent problem as was reported in Ref. 2. Significant cost and performance impacts resulted from these problems. NASA and the Air Force are supporting investigations in the field of propulsion plume technology, and the Workshop Steering Committee priority area entitled "Payload Environments" includes work related to plume technology.

---

1. Lyon, W. C., "Thruster Exhaust Effects Upon Spacecraft," NASA-TM-X-65427, Goddard Spaceflight Center (Oct. 1970), p 23.

2. "Voyager Controllers Grappling with Maneuverability Problem," Aviation Week and Space Technology, 107 (No. 14):41 (Oct. 3, 1977).

JPL has conducted studies and experiments for both NASA and the Air Force in the plume technology field. In the studies of Refs. 3, 4, 5, and 6 the JPL Molsink facility was utilized. This is an ultrahigh vacuum facility with an operating pressure range of 1.3×10^{-7} to 1.3×10^{-3} Pa (10^{-9} to 10^{-5} torr), although 1.3×10^{-4} Pa (10^{-6} torr) is a more typical background pressure when testing a 0.9 N (0.2 lb_f) monopropellant hydrazine thruster in the pulse mode (Ref. 6).

In an Air Force report (Ref. 7) on an attitude control rocket [98 N(22 lb_f)] exhaust plume experiment, Boudreaux and Etheridge investigated the effects of exhaust gases on spacecraft surfaces and spaceborne equipment. They reported that the Air Force facility utilized for the tests was capable of simulating an altitude of 53 km (174,000 ft) and with the engine firing, a steady-state altitude of 46.3 km (152,000 ft) was demonstrated. The authors noted the limitations of the facility and in their conclusions recommended: "An in-flight experiment be undertaken to complete the technology development initiated in the first two phases of the program. Primary data gains are expected from the use of a space exhaust plume since impingement would include both normal and oblique flow without mantle compaction, and is not able to be simulated in the laboratory. . . ."

Other studies (e.g., Ref. 8) express concern for plume effects and have indicated a need for space testing. The Propulsion Contamination Effects Module (PCEM) Spaceflight Experiments will fulfill the

---

3. Chirivella, J. E., and Moynihan, P. I., "Hydrazine Rocket Engine Plume Deposits Measured with Quartz Crystal Microbalances," Seventh JANNAF Plume Technology Conference, Huntsville, Ala. (April 1973), pp 691-706.

4. Chirivella, J. E., "Molecular Flux Measurements in the Back Flow Region of a Nozzle Plume," TM33-620, Jet Propulsion Laboratory, Pasadena, California (July 1973).

5. Chirivella, J. E., "Hydrazine Engine Plume Contamination Mapping," TR-75-16, Air Force Rocket Propulsion Laboratory (Oct. 1975).

6. Baerwald, R. K., and Passamanek, R. S., "Monopropellant Thruster Exhaust Plume Contamination Measurements," Publication 77-61, Jet Propulsion Laboratory, Pasadena, California (Sept. 1977).

7. Boudreaux, R. A., and Etheridge, F. A., "Attitude Control Rocket Exhaust Plume Experiment Final Report - Phases 1 and 2," AFRPL-TR-67-3, Air Force Rocket Propulsion Laboratory (Feb. 1967).

8. Boynton, F. P., "Exhaust Plumes from Nozzles with Wall Boundary Layers," J. Spacecraft, 5 (No. 10): 1143-1147 (Oct. 1968).

requirements for space experiments as suggested in the above references and by various NASA Centers. PCEM is designated as a NASA payload category AE/SA-B (attached experiment/space available, class B) experiment facility. The primary design objective is to fly the PCEM system (i.e., facility with propulsion system) in the Shuttle bay, conduct the experiment, and safely return it to earth. Orbits, dependent upon inclination and cargo weight, will tentatively be on the order of 280-460 km (150-250 NM). The facility will have the capability of testing rocket propulsion systems at steady state thrust levels of up to 4450 N (1000 lbf). Operations related to the propulsion system test will be essentially automatic and, in the event the automatic sequencing malfunctions, the system will shut down safely and will be returned for problem evaluation, repair, and reflight on another mission. The PCEM should thus provide an excellent addition and extension to the capabilities of existing ground test facilities.

2.0 DISCUSSION

2.1 Objectives

The prime objective of the PCEM Project is to determine the effects of plumes from various types of thrusters under actual space conditions and to utilize the data thus obtained to build a predictative capability covering these effects. The PCEM instrument measurement systems will be used to measure core flow and backflow efflux (mass and constituents), electrical charge buildup, and impingement forces and heating rates. The recorded experimental data will be added to the existing data base to determine the ability of analytical models to predict these same effects. These models will then be updated.

A secondary serendipitous objective is to characterize the propulsion system in the space environment. The PCEM will accommodate propulsion systems instrumented for performance characterization data.

2.2 Systems

The major hardware systems to be integrated for the PCEM experiments are the PCEM facility with associated ground support equipment (GSE), the rocket propulsion system and its GSE, and the Space Shuttle/Spacelab pallet and associated systems. The rocket propulsion systems include subsystems such as the thruster, the propellant feed system, the instrumentation system (i.e., pressure, flow, and temperature instruments for performance characterization), and the related support equipment. The rocket propulsion systems which are to be accommodated by the

PCEM for the experiments, along with the responsible NASA Centers, are as follows:

1. N_2H_4, 110 N (25 lb_f) monopropellant system, Marshall Space Flight Center (MSFC).
2. N_2O_4/MMH, 3870 N (870 lb_f) liquid bipropellant system, Jet Propulsion Laboratory (JPL).
3. 4.5×10^{-3} N (1×10^{-3} lb_f/8 cm) Ion drive engine system, Lewis Research Center (LeRC).
4. Solid rocket motor (SRM), 4448 N (1000 lb_f), JPL.
5. O_2/H_2, 110 N (25 lb_f) gaseous bipropellant system, LeRC.
6. 1.3×10^{-1} N (3×10^{-2} lb_f/30 cm) Ion drive engine system, LeRC.

The monopropellant system is currently completing the development phase at MSFC. This propulsion system will be provided by MSFC and will include the propellant tank, feed system, and instrumentation system. The N_2O_4/MMH propulsion system was developed for the Space Shuttle Orbiter, Reaction Control Subsystem (RCS). This system will be incorporated into a modified package by JPL for the PCEM experiment and will include instrumentation for engine performance characterization. The 4.5×10^{-3} N (1×10^{-3} lb_f/8 cm) and 1.3×10^{-1} N (3×10^{-2} lb_f/30 cm) Ion drive engines are currently under development at LeRC. Each of these systems will be provided by LeRC as a package which will include the thruster, the propellant system, the power system, and instrumentation required for engine performance characterization. The solid rocket motor package will be prepared for PCEM installation by JPL and will include instrumentation for recording performance parameters. The O_2/H_2, 110 N (25 lb_f) gaseous bipropellant system is being developed by LeRC. This propulsion system will be provided by LeRC as a package which will include the thruster, propellant feed systems, tankage, and instrumentation required for engine performance characterization.

The PCEM facility consists of the structure assembly, the basic science instrumentation system, the control system, the electrical system, and the mechanical systems. The structure assembly provides mounting provisions for the propulsion system package, including the adapter and thrust alignment subsystem and possibly an elevating mechanism. One concept is depicted in Fig. 1. Figures 2 and 3 show two preliminary types of structural concepts. The structure also houses the control subsystem, the mechanical and electrical subsystems, and the basic science instrument subsystems, including associated refrigeration and controls. The initial PCEM facility will be designed to accommodate the MSFC monopropellant propulsion system. Subsequently, the facility will be refurbished with kits specifically designed to accommodate the other propulsion systems.

The basic instrument measurement systems considered for plume measurement during the space experiments are the temperature controlled quartz crystal microbalances, the mass spectrometer, the plume profile temperature and pressure probes, and surface collectors. The quartz

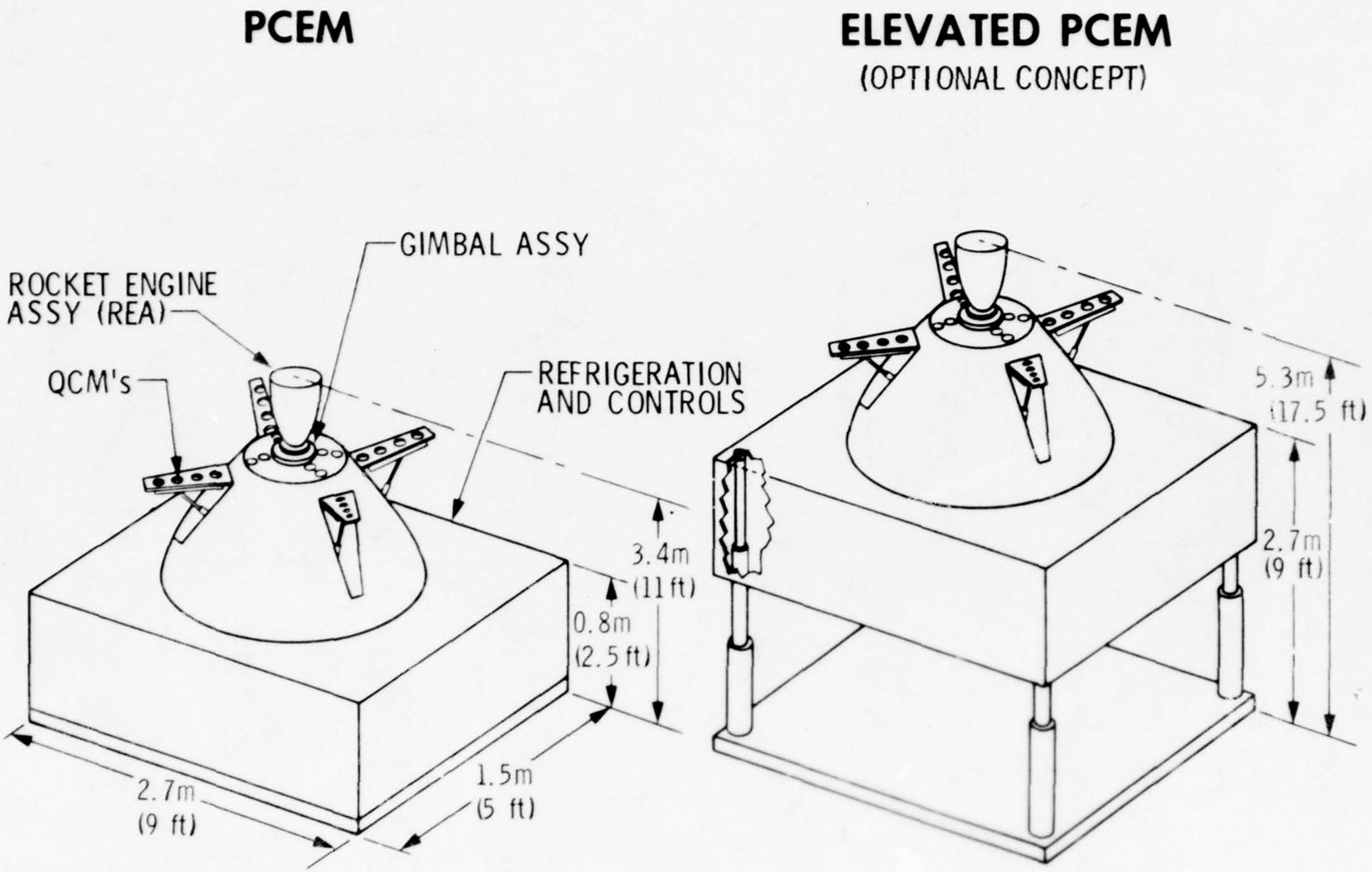

Figure 1. A PCEM Concept

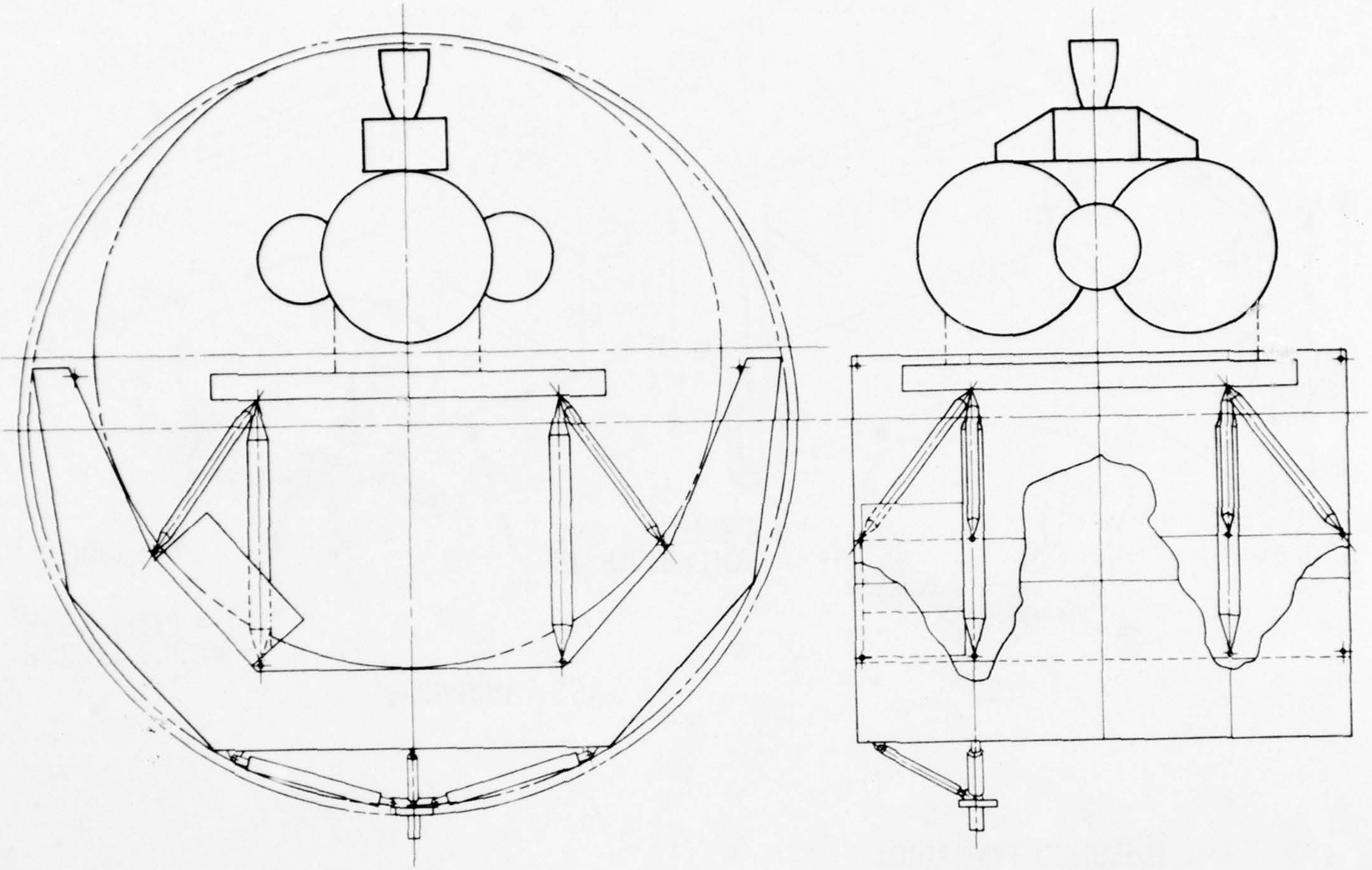

Figure 2. Fixed Structure

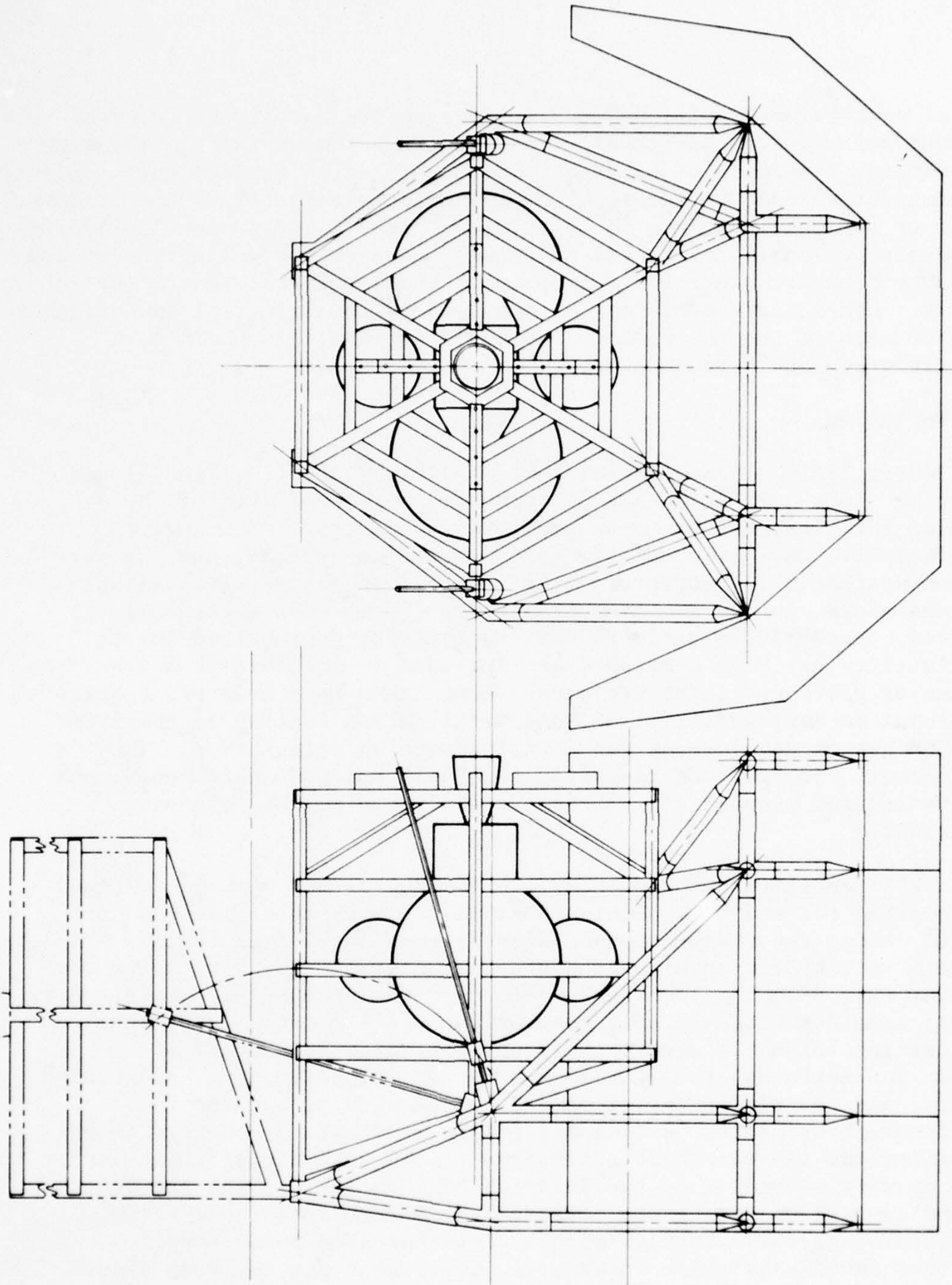

Figure 3. Deployable Structure

crystal microbalances will be used to measure the deposition rates of incident molecules at different crystal surface temperatures. The mass spectrometer system is to be used to measure flux of various gas species. The temperature and pressure probes will measure temperature and pressure levels at various locations in the plume profile. The surface collectors are passive units (i.e., tiles) which will be used for collection of contaminants deposited during the experiment and later analyzed in the laboratory. Other instruments may be supplied by the Principal Investigator (PI) for each of the experiments and could include, for example, a Langmuir probe and Faraday cups.

2.3 Technology

Testing in the space environment aboard Shuttle (see Fig. 4) and acquiring plume definition and performance characterization data, as proposed for PCEM, has not been previously conducted. However, the PCEM facility, the basic science instrumentation systems, and the propulsion systems all incorporate elements that are currently available and, therefore, no new advancements in the "state-of-the-art" are required. Much of the hardware and instrumentation required for the PCEM facility has been developed and included in one form or another on current or previous flight projects. Some items may, however, require additional design, modification, and verification testing to complete the PCEM system development for Shuttle/Spacelab integration. The requirements for the PCEM facility, the basic science instruments, and the prepackaged propulsion systems are described in the following paragraphs.

2.3.1 PCEM Facility Requirements. The PCEM facility will be designed for mounting to, and will utilize 80-100% of, a Shuttle/Spacelab pallet. Among the design tradeoffs to be considered (see Fig. 5) is the necessity for an elevating propulsion system mount to raise the thruster exit plane beyond the mold line of the Orbiter bay doors. Some primary considerations in this tradeoff are the electro-mechanical complexities, plume interaction effects with Shuttle mechanical systems and surfaces, the Shuttle contamination environment, solar wind effects, and Shuttle center of mass location with respect to the experiment thrust axis. Additional design areas which have yet to be worked include the data acquisition interfaces with Shuttle/Spacelab for test data recording by the Shuttle/Spacelab system, and the sequencing and control of the tests. Others are Shuttle/Spacelab TV-Film data recording, the interface with Shuttle/Spacelab power supplies, and other Shuttle/Spacelab interfaces, i.e., cold plates, dump system, and others as needed. The weighting factors attached to these design considerations will be dependent upon the definitions and requirements established by the PIs for the experiment science and the PCEM Design Team for structural and mechanical considerations. The GSE will be acquired primarily from existing sources.

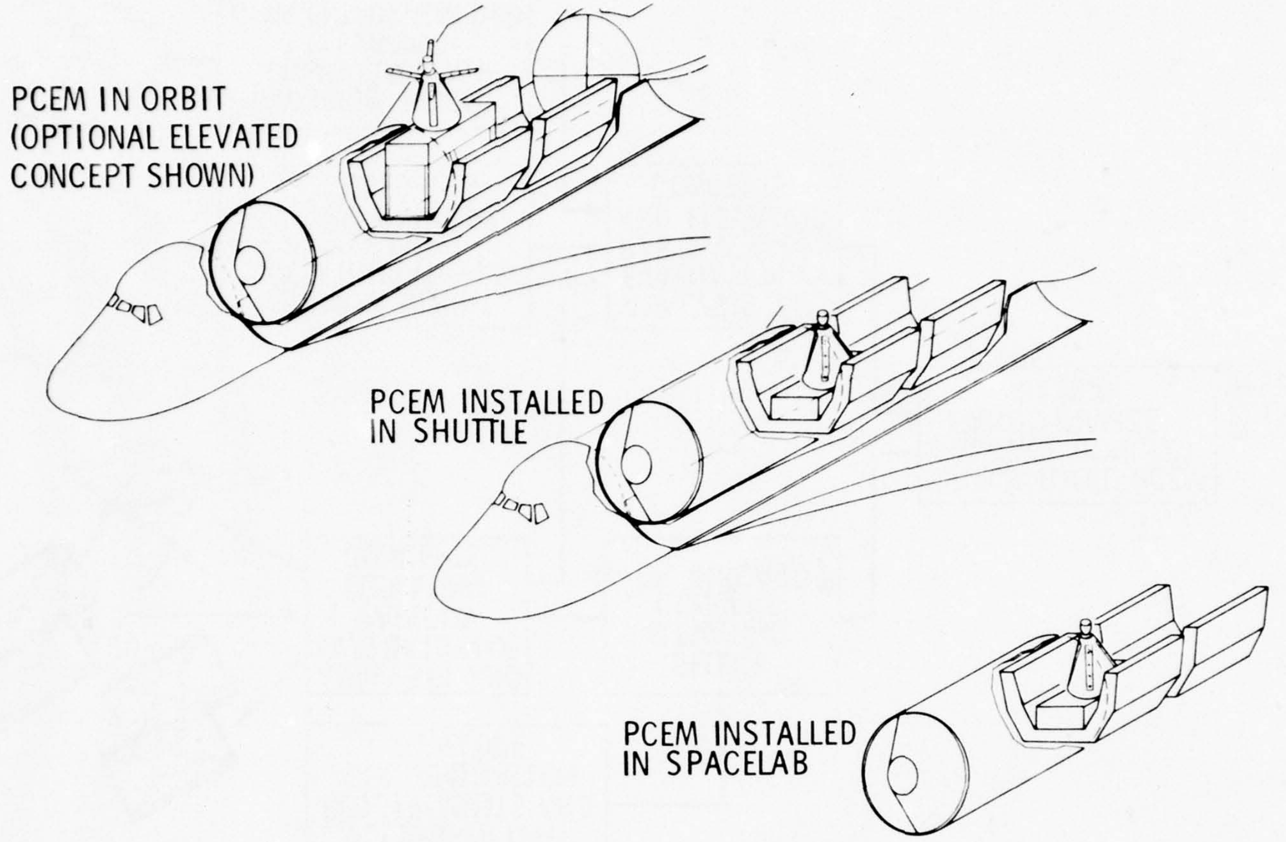

Figure 4. PCEM Experiment in Space Shuttle

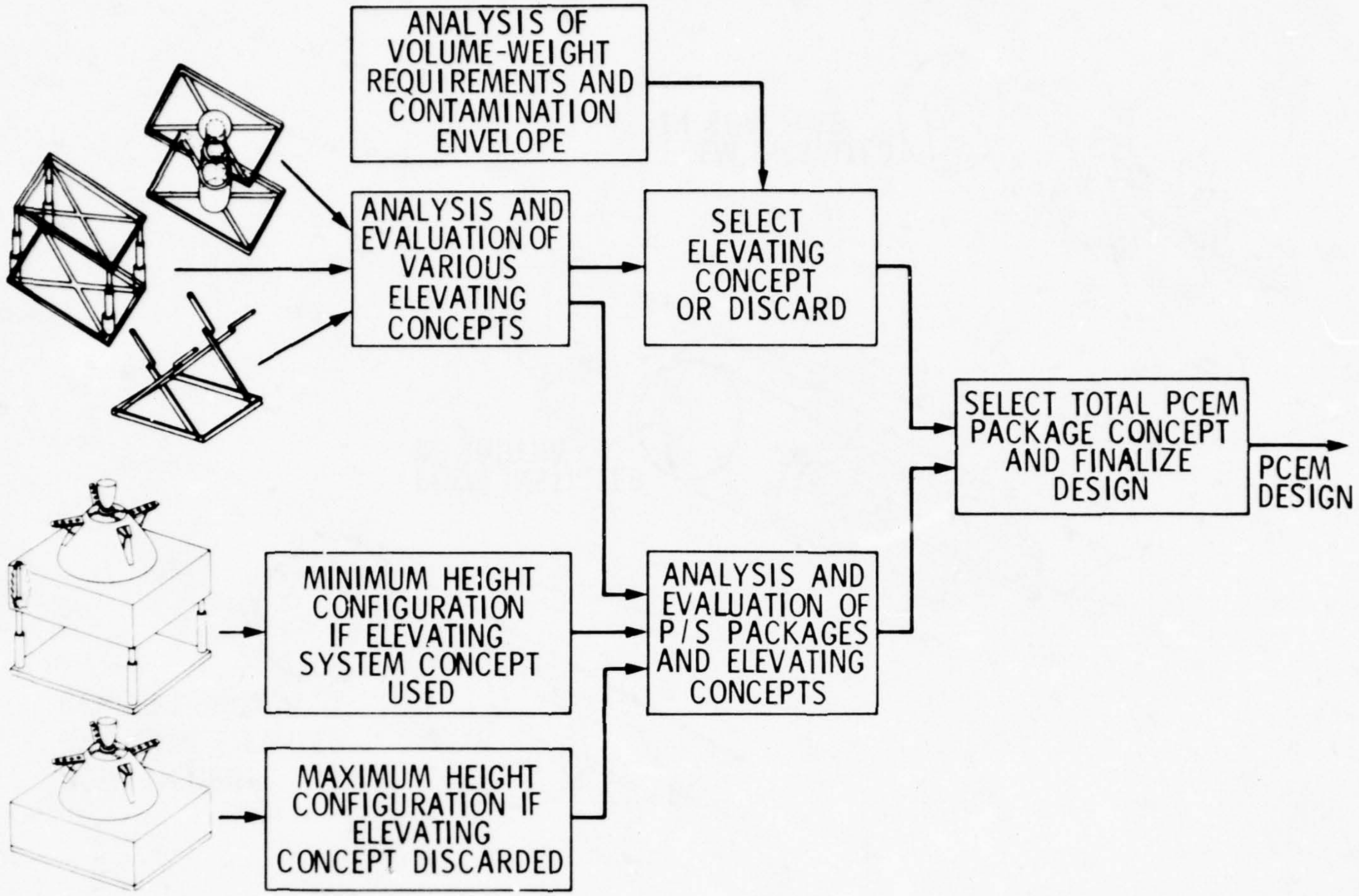

Figure 5. PCEM Concept Selection (Fixed or Elevating Configuration)

2.3.2 Basic Science Instruments Requirements. A basic complement of science instruments for plume measurements will be part of the PCEM facility. The quartz crystal microbalances (QCMs) with a refrigeration unit for temperature control requires some design, modification, and verification testing of currently or soon to be available off-the-shelf hardware. MSFC will use temperature controlled QCMs in the Induced Environment Contamination Monitor (IECM) for the initial Space Shuttle flights. These instruments are available from commercial instrument manufacturers. Options for refrigeration units include Stirling, Split Stirling, Vuilleumier, and Joule-Thompson refrigeration systems which have been used on various aircraft and spacecraft, and some are available from commercial manufacturers. The mass spectrometer also will require some design, modification, and verification testing of currently available hardware. Options for the mass spectrometer include the adaptation of the instrument which is included in the MSFC-IECM package, an instrument which is currently in the development test phase by Langley Research Center (LaRC), or some commercially available units. The temperature and pressure probes and the surface collectors will utilize currently available hardware which is to be adapted to the PCEM facility. The actual design details will be dependent upon the requirements established by the Principal Investigators for the experiment science from each NASA Center and by the PCEM Design Team for structural and mechanical considerations. However, the design, fabrication, and installation of these basic PCEM instrument units present no anticipated problems.

2.3.3 Prepackaged Propulsion Systems Requirements. The propulsion systems, as previously stated, are currently in development or in use. They will be modified and repackaged for mounting and operation in the PCEM facility. The Propulsion Section of each NASA Center will be responsible for providing the rocket engine systems. This responsibility also entails establishing the definition and requirements necessary for designing the propulsion system packages and establishing the interfaces for the installation and operation in the PCEM facility. The hardware is currently available, and no impacts on schedule or delivery are contemplated.

2.4 Flight Phase

The flight phase of the PCEM project will include a minimum of five flights. This minimum would be achieved with the successful installation and sequenced operation of the two ion drive engines [4.5×10^{-3} N (1×10^{-3} lb_f) and 1.3×10^{-1} N (3×10^{-2} lb_f)] into one package installed in the PCEM facility. Should this prove unfeasible, the systems would be designed for separate installations and flights. A preliminary schedule for the facility and the flights is shown in Fig. 6. Flights in excess of those required for the assigned propulsion systems would be reflights for a

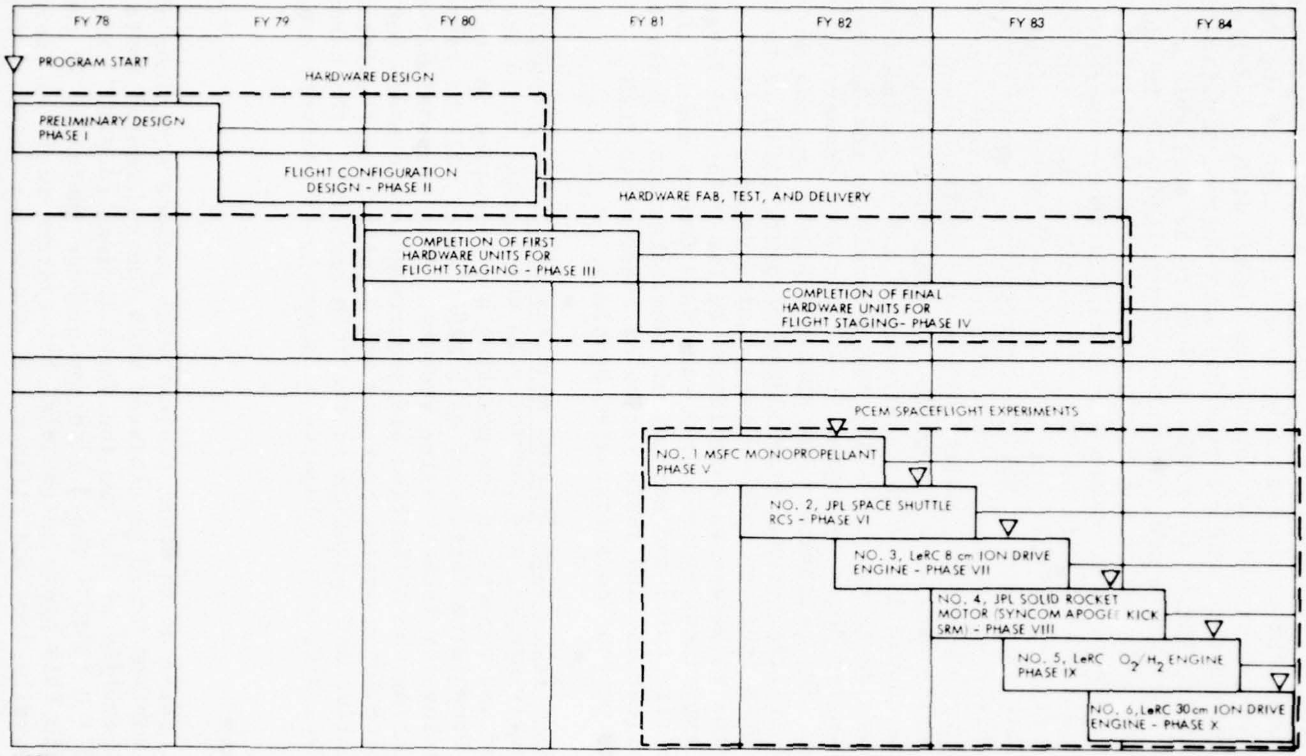

NOTES:
▽ INDICATES "READY FOR FLIGHT"
FLIGHT EXPERIMENTS ARE ON "SPACE AVAILABLE" BASIS, SCHEDULE SHOWN IS MINIMUM WHICH CAN BE ACCOMMODATED

Figure 6. Summary PCEM and Flight Schedules

propulsion system which was returned for repair or modification following a flight malfunction, or flights for different types of propulsion systems. The PCEM-Shuttle/Spacelab flight operations include the flight staging operations, the Shuttle/Spacelab Level IV integration operation, the Shuttle/Spacelab Level III through Level I preflight operations, the flight and experiment, and the post flight operations.

The flight staging operations commence with the delivery of the flight hardware (i.e., PCEM Facility, Propulsion System, Ground Support Equipment, and Modification-Refurbishment Kits as required) to the flight staging area of JPL. This operation includes the integrating of the flight PCEM facility and Propulsion system, the checks and verification tests, the safety review, and flight acceptance. Subsequently, the integrated PCEM system would be delivered to the Shuttle flight integration site for Level IV integration operations. The Level III through Level I Shuttle/Spacelab operations will then be performed, culminating in the Shuttle/Spacelab flight to earth orbit. The spaceflight experiment tests in the Shuttle/Spacelab will be under the cognizance of the PI for the specific propulsion system assigned to the flight (i.e., each NASA Center with thruster experiment responsibility will have its own PI). The PCEM facility design will be such that the operation of the propulsion system and data acquisition will be essentially automatic with very little operational activity required on the part of the Payload Specialist at the PCEM control panel. The Specialist aboard the Shuttle will be in contact with the Payload Operations Control Center (POCC) for any special operating instructions from the PI. Upon return to earth and subsequent de-integration, the PCEM hardware will be depositioned after disassembly and it will then be returned to the responsible NASA Center. The data package will be forwarded to the PI for data reduction, analysis, and report.

3.0 CONCLUSIONS

The impingement of rocket exhaust gases on spacecraft surfaces may be the cause for many problems encountered on spacecraft and satellites. Among these are contamination of critical optical and mechanical components, disturbance forces and torques, high heat fluxes, and surface charging. Analytical or numerical models are utilized for the prediction of these effects, and the accuracy of these models must be ascertained by comparison with test data. The requirement for much of this data is for portions of the exhaust plume where the pressure level may be below the simulation capabilities of most ground test facilities. The PCEM facility will allow an investigator to test a propulsion system in the space environment, obtain the data needed for correlation with existing models, and update or revise these models as required. This facility is thus visualized as a valuable extension of present experimental capabilities into the real environment of space.

4.0 REFERENCES

1. Lyon, W. C., "Thruster Exhaust Effects Upon Spacecraft," NASA-TM-X-65427, Goddard Spaceflight Center (Oct. 1970), p 23.

2. "Voyager Controllers Grappling with Maneuverability Problem," Aviation Week and Space Technology, 107 (No. 14): 41 (Oct. 3, 1977).

3. Chirivella, J.E., and Moynihan, P. I., "Hydrazine Rocket Engine Plume Deposits Measured with Quartz Crystal Microbalances," Seventh JANNAF Plume Technology Conference, Huntsville, Ala. (April 1973), pp 691-706.

4. Chirivella, J.E., "Molecular Flux Measurements in the Back Flow Region of a Nozzle Plume," TM33-620, Jet Propulsion Laboratory, Pasadena, California (July 1973).

5. Chirivella, J.E., "Hydrazine Engine Plume Contamination Mapping," TR-75-16, Air Force Rocket Propulsion Laboratory (Oct. 1975).

6. Baerwald, R. K., and Passamanek, R. S., "Monopropellant Thruster Exhaust Plume Contamination Measurements," Publication 77-61, Jet Propulsion Laboratory, Pasadena, California (Sept. 1977).

7. Boudreaux, R. A., and Etheridge, F. A., "Attitude Control Rocket Exhaust Plume Experiment Final Report - Phases 1 and 2," AFRPL-TR-67-3, Air Force Rocket Propulsion Laboratory (Feb. 1967).

8. Boynton, F. P., "Exhaust Plumes from Nozzles with Wall Boundary Layers," J. Spacecraft, 5 (No. 10): 1143-1147 (Oct. 1968).

SESSION IV

CONTAMINATION MONITORING

SHUTTLE INDUCED ENVIRONMENT CONTAMINATION MONITOR

Edgar R. Miller
Space Sciences Laboratory
NASA/George C. Marshall Space Flight Center
Marshall Space Flight Center, Alabama 35812

Presented at
USAF/NASA International Spacecraft
Contamination Conference
Colorado Springs, Colorado
March 7-9, 1978

ABSTRACT

The Induced Environment Contamination Monitor (IECM) is a set of ten instruments integrated into a self-contained unit. The IECM is scheduled to fly as part of the Demonstration Flight Instrumentation (DFI) on Shuttle Orbital Flight Tests 1 through 6 and on Spacelabs 1 and 2 as part of the Verification Flight Instrumentation (VFI).

NASA began strong manned mission contamination control efforts for the Skylab mission and, recognizing the possible limiting effects induced contamination might have on sophisticated observational programs planned for the 1980's, committed to an effort to insure that the induced environment would not be a problem.

The purpose of the IECM is to measure the actual environment to determine whether the strict controls placed on the Shuttle system have solved the contamination problem.

The IECM will operate during prelaunch, ascent, on-orbit, descent, and post-landing. The on-orbit measurements are molecular return flux, background spectral intensity, molecular deposition, and optical surface effects. During the other mission phases dew point, humidity, aerosol content, and trace gas will be measured as well as optical surface effects and molecular deposition.

The ten instruments are: Dewpointer, Humidity Monitor, Cascade Impactor, Optical Effects Module, Passive Sample Array, Temperature-Controlled Quartz Crystal Microbalance, Air Sampler, Mass Spectrometer, Camera/Photometer, and Cryogenic Quartz Crystal Microbalance. Each instrument is briefly described, and its measurement limitations are compared to the contamination control requirements.

Efforts are being made to operate the IECM using the Shuttle Remote Manipulator System to directly measure off- and outgassants as well as column densities. This would be accomplished by actually picking up the IECM and moving it about the Shuttle for various measurements.

SHUTTLE INDUCED ENVIRONMENT CONTAMINATION MONITOR

1.0 INTRODUCTION

When the decision was made to develop the Space Transportation System (STS) as a universal carrier for manned space science experiments, there was much concern from the scientific community, particularly the astronomers, as to whether the induced particles and gases environment would place limitations on the measurement programs envisioned for the 1980's.[1,2] This concern stimulated a number of activities which include the identification of potential contamination problems, the establishment of upper limits of induced environment tolerable to experimenters, studies to assess the induced environment from current STS design, and recommended changes to achieve the desired background.

Similar concerns were identified during the development of the Skylab Program and prompted a significant research effort to develop an understanding of the various mechanisms by which experiments could be compromised and to establish the technology of contamination abatement through vehicle design and operational procedures. These efforts contributed to the successful operation of most of the Skylab and Apollo Telescope Mount (ATM) experiments. Some measurements of the molecular deposition and scattered light background were made on Skylab which confirmed that many of the precautions taken were

---

1. Anon., Final Report of the Space Shuttle Payload Planning Working Groups, Astronomy Volume 1, NASA/Goddard Space Flight Center, Greenbelt, Maryland (May 1973).

2. Space Science Board, Scientific Uses of the Space Shuttle, National Academy of Sciences, Washington, D.C. (1974).

necessary. These measurements and related laboratory work indicate there is still much to be learned concerning the interactions between the spacecraft, the induced atmosphere, and the ambient atmosphere.

As a result of concerns for possible contamination from the induced environment, the Contamination Requirements Definition Group (CRDG), chaired by R. J. Naumann of NASA's Marshall Space Flight Center, set goals for the control of particles and gases that would be emitted by the Space Shuttle.[3] To assure that the goals have been met, the Induced Environment Contamination Monitor (IECM) (Figure 1) was designed to provide verification of particles and gases measurements during ground operation, ascent, on-orbit, descent, and post-landing. These verification measurements are planned for all six Orbiter Flight Tests (OFT's) and for Spacelabs 1 and 2.

Spacelab 1 will provide the opportunity to obtain contamination data from a short-module-plus-pallet configuration. Spacelab 2, which is planned as a pallet-only setup, will provide a comparison between these two basic configurations.

A smaller version of the IECM will be flown on the Long Duration Exposure Facility (LDEF) satellite to obtain contamination data on deployment and retrieval as well as ground handling of large satellite payloads (Figure 2).

2.0 STS CONTAMINATION CONTROL REQUIREMENTS

Contamination control requirements were incorporated into the Space Shuttle Flight and Ground Systems Specification, Volume X,[4] by the Particles

---

[3] Payload Contamination Control Requirements for Shuttle Transportation System (STS) Induced Environment, STS Payload Contamination Requirements Definition Group Report, NASA/Marshall Space Flight Center, Alabama (July 1975).

[4] Space Shuttle Program Level II Program Definition and Requirements, NASA/JSC-07700 Flight and Ground Systems Specification, Volume X, Revision B (August 1975). (This specification will be cited as "Volume X" throughout the remainder of this paper.)

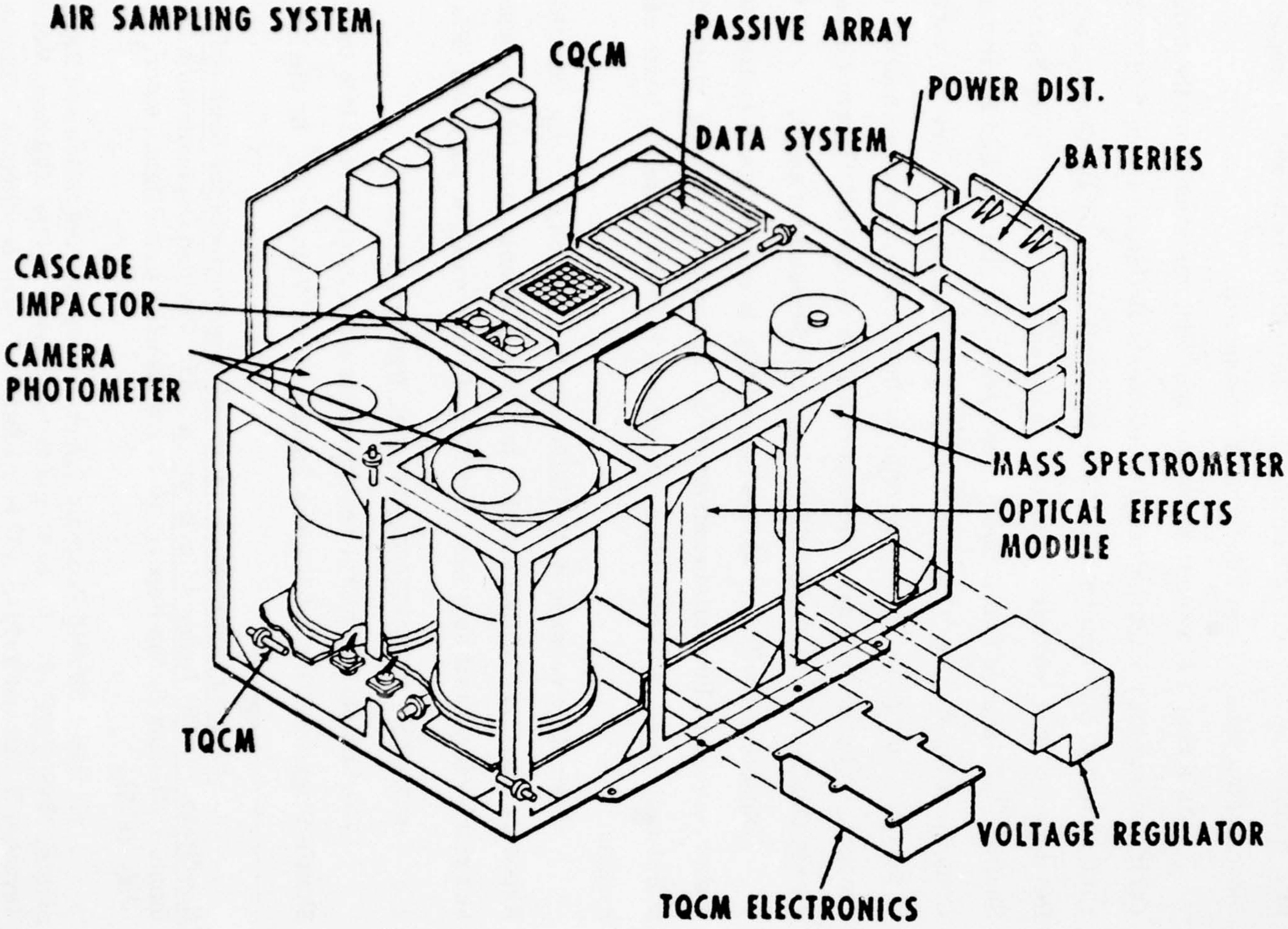

Figure 1. Induced Environment Contamination Monitor, OFT/DFI and Spacelab VFI Unit.

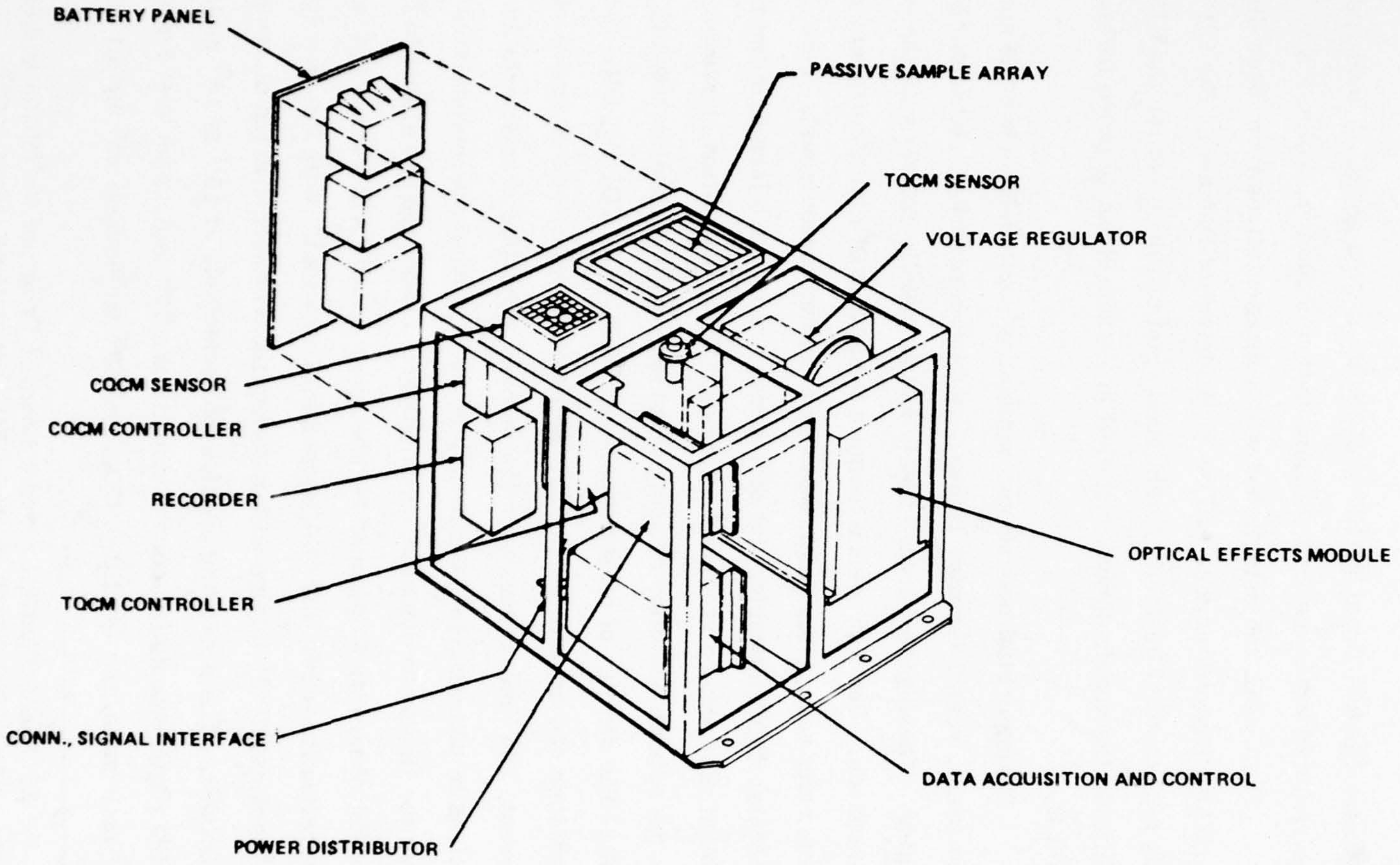

Figure 2. Induced Environment Contamination Monitor — LDEF.

and Gases Control Panel (PGCP) as Shuttle design goals. These specifications were restated in the payload accommodation document, Volume XIV.[5]

The CRDG was established with representatives from user disciplines, each NASA payload center, and the Department of Defense. The CRDG in-depth study for potential payloads established a net requirement for the STS that is similar to the requirements specified in Volume X but is more inclusive and definitive.[3]

During orbital operations, molecules continually leave the spacecraft from leaks, vents, thruster firings, surface desorption, and material outgassing. These gases expand freely and eventually collide with the ambient atmosphere. Their presence forms a tenuous artificial atmosphere around the spacecraft, sometimes referred to as a contamination cloud. This cloud has a molecular column density that on the average is much less than the residual ambient atmosphere at orbital altitudes. The composition, however, is such that the column densities of some species greatly exceed the natural environment. The species of most concern are H_2O, CO_2, CO, H_2, OH, and a variety of silicone and organic polymers. Some of these molecules are of astrophysical interest, and their presence in the induced atmosphere in detectable concentrations is undesirable. Other molecules may have absorption lines that could mask the line to be detected. The spectral resolution to be used in the astronomical observations planned for the Space Shuttle will permit the detection of absorption lines with 0.001 A equivalent line width. With this resolution, a 10^{10} molecule/cm^2 column with a strong transition line in the ultraviolet will be detectable. The preceding species are detectable at 10^{11} to 10^{12} molecules/cm^2. The CRDG requirements for column density are 10^{13} molecules/cm^2 for $N_2 + O_2$, 10^{11} molecules/cm^2 for $H_2O + CO_2$, and 10^{10} molecules/cm^2 for all other

---

[5] Space Shuttle Program Level II Program Definition and Requirements, NASA/JSC-07700, Volume XIV, Revision E (July 1977).

species. The requirement stated in Volume X for H_2O is 10^{12} molecules/cm^2.

Another concern is the deposition of the heavier molecules, particularly the silicones, on optical surfaces. Such molecules become polymerized by the presence of energetic radiation and form a permanent brown film. A thickness of only a few monolayers ($\sim 10^{-7}$ gm/cm^2) is sufficient to begin to cause significant optical degradation in the vacuum ultraviolet, whereas a film of up to 10^{-5} gm/cm^2 is tolerable on infrared optics or on thermal control surfaces.

Most critical optical surfaces must of necessity be shadowed from any portion of the STS by light baffles. Such baffles provide excellent protection against direct line-of-sight transport of molecules leaving an outgassing surface that might otherwise deposit on the critical surface. Some molecules can arrive at a surface protected in this manner by making one or more collisions with other molecules in the contamination cloud or by colliding with an ambient atmospheric molecule. For the expected number densities associated with the STS, collisions with atmospheric molecules will be the dominant return mechanism. For surfaces at ambient temperature (~ 300°K) the CRDG requirement specifies that no more than 10^{-5} gm/cm^2 of material shall deposit during a 30-day mission on an unprotected surface (2 arc sec steradian acceptance) and no more than 10^{-7} gm/cm^2 shall deposit on a surface with 0.1 steradian acceptance angle during a 30-day mission. A layer of 10^{-7} gm/cm^2 should produce less than 1 percent degradation for the expected contaminants over most wavelengths from the far ultraviolet to the far infrared. For cryogenic surfaces there is an additional concern stemming from the large amounts of H_2O in the induced environment which will condense at cryogenic temperatures. The CRDG requirement specifies that such a surface with a 0.1 steradian acceptance angle shall accumulate no more than 10^{-5} gm/cm^2 in a 30-day mission. This requirement is expressed in Volume X in terms of a limit of 10^{12} molecules/cm^2/sec backscatter flux. This flux would result in a total molecular deposition of 4.1×10^{-6} gm/cm^2 after 30 days, assuming a unity sticking fraction.

The presence of particulate matter in the vicinity of the spacecraft has been observed on all manned space missions. Also, many unmanned spacecraft have observed "false stars" which turned out to be particles that came from the spacecraft. The concern from the potential scientific users is twofold: the occasional large particle that moves through the field of view and produces an unwanted signal, and the possible production of a cloud of extremely fine particles that scatter sunlight and increase the background brightness.

Infrared astronomy is one of the disciplines most troubled by the sporadic particles. The 1.5-meter cryogenic infrared telescope can detect the blackbody radiation from a slow moving 5-micron particle at a distance of several kilometers. An occasional particle can be identified and removed from the data, but the process is time consuming and results in a partial data loss. If such occurrences were frequent, the data loss could become significant. The CRDG criterion calls for fewer than one such particle entering a 1.5×10^{-5} steradian field of view per orbit.

The CRDG requirement limiting the production of unresolved particles is based on the rationale that the background brightness from scattered light should be no more than 10 percent of the natural sky background from wavelengths of 155 nm to 1000 nm. The natural background was measured in the ultraviolet through the visible by Witt and Lillie and is approximately equivalent to 10^{-13} $B_\odot$ in the ultraviolet and 6×10^{-14} $B_\odot$ in the visible. Therefore, the required background brightness is 10^{-14} $B_\odot$ in the ultraviolet and 6×10^{-15} $B_\odot$ in the visible. This is stated in Volume X as "a 20th magnitude star per square arc second in the ultraviolet region." This is equivalent to 10^{-12} $B_\odot$.

To limit the number of particles carried into orbit from ground operations, cleanliness precautions in the form of HEPA filtered purge gas and controlled work discipline are exercised during ground activities. Volume X requires that payload surfaces be kept visibly clean during this operation. The CRDG requested the additional requirement that a 100K or better environment be maintained at all times and purge gas be used to produce no more than 10^{-6} gm/cm^2 nonvolatile residue (NVR) on the surfaces. The preceding contamination control requirements are summarized in Table 1. An excellent summary review of Space Shuttle-induced contamination concerns as well as specific effects of this environment on a sensitive infrared telescope has been given by Simpson and Witteborn.[6] Leger, Jacobs, and Ehlers have discussed Space Shuttle contamination analysis and control.[7]

3.0 DESCRIPTION OF IECM INSTRUMENTS

The IECM instrumentation was chosen or developed by the Space Sciences Laboratory, Marshall Space Flight Center, to meet the contamination level measurement requirements previously outlined. With the exception of infrared background radiation, which requires a cryogenically cooled infrared radiometer, the IECM instrumentation has the capability to verify the Space Shuttle specified contamination levels. Table 2 summarizes instrument performance specifications.

3.1 Humidity Monitor and Dewpointer

Two types of humidity detectors are used. One is a bulk detector called a Brady Array developed by Thunder Scientific. It responds to the presence of H_2O molecules in a specially prepared crystalline lattice with interstitial spaces through which these molecules can drift freely. The Brady Array can be

---

[6] Simpson, J. P. and Witteborn, F.C., Effect of the Shuttle contaminant environment on a sensitive infrared telescope, Applied Optics 16 (No. 8): 2051-2073 (1977).

[7] Leger, L.; Jacobs, S.; and Ehlers, H.K.F., Space Shuttle contamination overview, Proc. Institute of Environmental Sciences (February 1978).

TABLE 1. SUMMARY OF CONTAMINATION SPECIFICATIONS AND MEASUREMENTS

REQUIREMENTS PRELAUNCH THROUGH ASCENT		
CONTAMINATION SPECIFICATION	SPEC. REF.	MEASUREMENT REQUIRED
AIR TEMPERATURE $70^o + 5^oF$	A, B	TEMPERATURE AND HUMIDITY
HUMIDITY 30–50%	A, B	TEMPERATURE AND HUMIDITY
PURGE GAS CLASS 100, GUARANTEED CLASS 5000, LESS THAN 15 PPM HYDROCARBONS	A, B	TRACE GAS ANALYSIS AEROSOL COUNT AND SIZE DISTRIBUTION
PURGE GAS PRODUCE LESS THAN 10^{-6} gm/cm^2 CONDENSIBLES ON SURFACES	B	NON–VOLATILE RESIDUE (NVR) DEPOSITION
CONTROL WORK DISCIPLINE TO MAINTAIN SURFACE CLEANLINESS AT LEVEL 300 A (VISIBLY CLEAN WITH LESS THAN 10^{-6} gm/cm^2 NVR)	A, B	AEROSOL COUNT AND SIZE DISTRIBUTION DUST FALL MEASUREMENTS NON–VOLATILE RESIDUE NVR DEPOSITION
MAINTAIN PARTICLE COUNT LESS THAN 100K IN VICINITY OF P/L	B	AEROSOL COUNT AND SIZE DISTRIBUTION

REFERENCES:
A. JSC 07700, VOL. X, PARAGRAPHS 3.6.12.2.4.1–.5
B. CRDG REQUIREMENTS DOCUMENT, PARAGRAPHS 4.1.2–.10

TABLE 1. (Concluded)

REQUIREMENTS ON ORBIT		
CONTAMINATION SPECIFICATIONS	SPEC REF.	MEASUREMENT REQUIRED
MOLECULAR COLUMN DENSITY LESS THAN		
10^{12} H_2O/cm^2	A	MOLECULAR COLUMN DENSITY
10^{11} $H_2O + CO_2/cm^2$	B	
10^{13} $N_2 + O_2/cm^2$	B	
10^{10} OTHER MOLECULES/cm^2		
SCATTERED/EMISSION LIGHT BACKGROUND LESS THAN		
$m_u = 20$ STAR/SEC^2 (10^{-12} BO IN U.V.)	A	BACKGROUND SPECTRAL INTENSITY
$10^{-14.2}$ BO IN VISIBLE	B	
$10^{-14.0}$ BO IN ULTRAVIOLET	B	
10^{-11} WATTS/m^2/sr/nm $\lambda < 30\ \mu$	B	
10^{-10} WATTS/m^2/sr^1/nm $\lambda > 30\ \mu$	B	
FEWER THAN ONE 5 μ PARTICLE PER ORBIT IN 1.5 X 10^{-5} STERADIAN FIELD–OF–VIEW	A, B	PARTICLE SIZE AND VELOCITY DISTRIBUTION
MOLECULAR RETURN FLUX SUCH THAT:		
$H_2O < 10^{12}$ MOLECULES/cm^2/sec	A	MOLECULAR RETURN FLUX
DEPOSITION 10^{-7} gm/cm^2 30 DAYS 0.2 sr ON 300°K SURFACE	B	MOLECULAR DEPOSITION ON AN AMBIENT SURFACE
DEPOSITION 10^{-5} gm/cm^2/30 DAYS 2 π sr ON 300°K SURFACE	B	MOLECULAR DEPOSITION ON AN AMBIENT SURFACE
DEPOSITION 10^{-5} gm/cm^2/30 DAYS 0.1 sr ON 20°K SURFACE	B	MOLECULAR DEPOSITION ON A CRYOGENIC SURFACE
DEGRADATION OF OPTICS 1%	A	DEGRADATION OF OPTICAL SURFACES

REFERENCES:
A. JSC 07700, VOL. X, PARAGRAPH 3.6.12.2.4.6
B. CRDG REQUIREMENTS DOCUMENT, PARAGRAPH 4.2

TABLE 2. SUMMARY OF MEASUREMENT REQUIREMENTS AND IECM INSTRUMENTATION PERFORMANCE

MEASUREMENT REQUIRED	INSTRUMENT	REQUIRED PERFORMANCE (PREDICTED PERFORMANCE)
TEMPERATURE AND HUMIDITY	BRADY ARRAY	MEASURE: R.H.,O. – 100% ± 2% AIR TEMP. 0-70°C ± 1°C (WILL MEET REQUIREMENT)
	DEWPOINTER	MEASURE D. P.,O.-40°C ± .5°C (WILL MEET REQUIREMENT)
TRACE GAS ANALYSIS	AIR SAMPLER SYSTEM	CONTINUOUS – DETECT & IDENTIFY TRACE CONTAMINANTS IN < 1 PPM FROM LARGE SAMPLE VOLUME (WILL MEET REQUIREMENT)
		GRAB–DETECT SPECIFIC REACTIVE CONTAMINANTS IN SMALL SAMPLE TAKEN AT REDUCED PRESSURE (WILL MEET REQUIREMENT)
AEROSOL COUNT AND SIZE DISTRIBUTION	CASCADE IMPACTOR	MEASURE AEROSOL CONTENT IN RANGES FROM 0.3 – 1; 1–5, 5 MICRONS IN CLASS 100–100K ENVIRONMENT (WILL MEET REQUIREMENT)
NON–VOLATILE RESIDUE DEPOSITION	CASCADE IMPACTOR (NVR DETECTOR)	DETECT MOLECULAR DEPOSITION WITH 10^{-7} gm/cm^2 RESOLUTION ($\sim 10^{-9}$ gm/cm^2)

TABLE 2. (Continued)

MEASUREMENT REQUIRED	INSTRUMENT	REQUIRED PERFORMANCE (PREDICTED PERFORMANCE)
DUST FALL	OPTICAL EFFECTS MODULE (OEM)	MEASUREMENT PRESENCE OF DUST AT LEVEL 300 SURFACE CLEANLINESS (WILL MEET REQUIREMENT)
MOLECULAR COLUMN DENSITY	COLLIMATED MASS SPECTROMETER	MEASURE $10^8 \cdot 10^{17}$ MOLECULES /cm^2/sec/.1 sr FROM 2–150 AMU ($10^8 \cdot 10^{15}$ MOLECULES/cm^2/sec/.1 sr FROM 2–150 AMU)
BACKGROUND SPECTRAL INTENSITY	CAMERA/PHOTOMETER	MEASURE TO $10^{-14.2}$BO IN VISIBLE AND NEAR U. V. (WILL MEET REQUIREMENT)
	NONE	MEASURE IN BACKGROUND 10^{-11} WATT/m^2/sr/nm,$\lambda < 30\ \mu$ 10^{-10} WATT/m^2/sr/nm,$\lambda > 30\ \mu$ (NONE)
PARTICLE SIZE AND VELOCITY DIST.	CAMERA/PHOTOMETER	DETECT AND MEASURE PARTICLES 5μ DIA. MOVING AT 1 m/sec. ($\sim 10\ \mu$ DIA. AT 1m/sec)
MOLECULAR RETURN FLUX	COLLIMATED MASS SPECTROMETER	MEASURE 10^{10} MOLECULES/cm^2/sec FROM 2 – 150 AMU (WILL MEET REQUIREMENT)

TABLE 2. (Concluded)

MEASUREMENT REQUIRED	INSTRUMENT	REQUIRED PERFORMANCE (PREDICTED PERFORMANCE)
MOLECULAR DEPOSITION ON AMBIENT SURFACE	CASCADE IMPACTOR (NVR) DETECTOR	MEASURE MOLECULAR DEPOSITION IN AMBIENT SURFACE WITH RESOLUTION OF 10^{-9} grams/cm^2
	TEMPERATURE–CONTROLLED QUARTZ CRYSTAL MICRO–BALANCE (TQCM)	PROVIDE +80°C TO –50°C ± 1°C CONTROL OF COLLECTING SURFACE. MEASURE MOLECULAR DEPOSITION WITH 10^{-9} gram/cm^2 RESOLUTION
	PASSIVE SAMPLE ARRAY (PSA)	MEASURE TOTAL DEPOSITION (ALL ABOVE WILL MEET REQUIREMENT)
MOLECULAR DEPOSITION AT CRYOGENIC TEMPERATURES	CRYOGENIC QUARTZ CRYSTAL MICRO–BALANCE (CQCM)	RADIATIVELY COOL COLLECTOR TO 130°K. DETECT DEPOSITION WITH 10^{-9} gm/cm^2 RESOLUTION (WILL MEET REQUIREMENT)
DEGRADATION OF OPTICAL SURFACES	OPTICAL EFFECT MODULE (OEM)	MEASURE CHANGE IN U. V. TRANSMISSION TO 1% AS FUNCTION OF TIME. MEASURE DIFFUSE REFLECTION CHANGE TO 1% AS A FUNCTION OF TIME.
	PASSIVE SAMPLE ARRAY (PSA)	MEASURE TOTAL CHANGE (ALL ABOVE WILL MEET REQUIREMENT)

exposed to extreme temperatures and vacuum environment without impairing its ability to sense water. There are no known interferences that are sensed as H_2O, and it appears to be resistant to all major contaminants.

A thermistor is contained in the array to provide temperature data and to convert the measurements to relative humidity. The instrument can sense a 0.1 percent change in humidity, but hysteresis and thermal compensation limit the overall accuracy to ±2 percent over the entire temperature range.

The second system is an EG&G Dewpointer that actually measures the dew-point temperature. This is accomplished by servo controlling a thermoelectrically cooled mirror to the dew point. The mirror is illuminated by a light-emitting diode, and the specular and scattered light components are measured by photodiodes. The difference signal from the two detectors is the error signal. In this manner, the mirror is always driven to the temperature of incipient condensation. The dew-point temperature is measured to an accuracy of $\pm 0.5^\circ C$, but the response time is 10 to 20 seconds.

The two instruments are complementary in that the dew-point measurement is inherently more accurate than the Brady Array and is better suited for static situations where little time resolution is necessary. On the other hand, the Brady Array is required to track the rapidly changing humidity associated with descent where it is important to know the moisture content as a function of altitude.

Both instruments are commercial items that have been fairly widely used. The Brady Array is primarily a laboratory- and field-use instrument. A small development effort was required to package the detector and associated electronics as a flight instrument. The EG&G Dewpointer was successfully flown on Skylab, and spare flight hardware is being used.

3.2 Air Sampler

Several approaches using mass spectrographs and gas chromatograph/mass spectrographs (GC/MS) with suitable inlet systems were considered for trace gas analysis. However, because of the cost and complexity of such flight systems, it was decided to sacrifice real-time readout capability and use post-flight analysis for this function.

The Air Sampler system, shown schematically in Figure 3, consists of five sampling bottles (one for ground operation, three for ascent, and one for descent) connected to a pumped manifold. Two positive displacement air pumps, shared with the Humidity Monitor and Dewpointer, are connected in parallel to the manifold. Bottle position one is used for ground operations to detect condensibles to 10 ppb or less. This bottle is manually uncapped and capped for operation and removal. Position one is also used for condensible collection during descent and post-landing. Condensibles during ascent are collected by the bottle in position two. Bottles in positions three and four are for detection of HCl combustion products during ascent using grab sampling (opening of evacuated bottle) and air pumping, respectively. Position five bottle is for sampling nitrogen compounds during descent. A summary of air sampling bottle operations, sensitivities, and adsorbers is given in Table 3.

Analysis of samples will be done in the laboratory using GC/MS techniques.

3.3 Cascade Impactor

The aerosol count in the ambient air will be measured by a Celesco Industries 3-stage cascade impactor (Figure 4) with special polymeric-coated quartz crystals serving as impactor plates. Ambient air is drawn in by a small pump at the rate of 250 ml/min, passed through a small orifice, and impinged against the measuring crystal. The special polymer serves to retain the particles on the surface and ensures that they are coupled with the vibrational motion of the quartz crystal. Viscous forces tend to entrain the particle in the air stream, and centrifugal forces tend to throw the particle onto the impactor surface. Depending on the air flow and spacing, particles larger

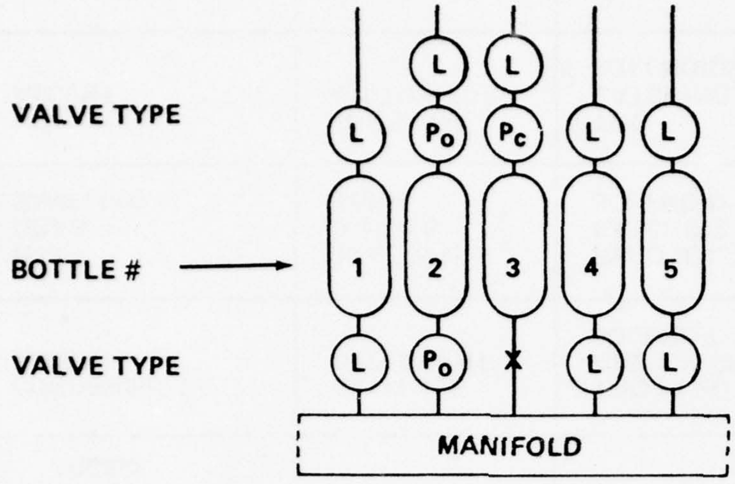

VALVE TYPE NUMBER	VALVE DESCRIPTION
L	LATCHING SOLENOID; VITON SEAL
P_o	SQUIB, NORMALLY OPEN
P_c	SQUIB, NORMALLY CLOSED
X	SEALED

Figure 3. Schematic of Air Sampler bottles and valves.

TABLE 3. AIR SAMPLING BOTTLE CHARACTERISTICS

BOTTLE LOCATION NUMBER**	PRIMARY SAMPLING FUNCTION	ESTIMATED SENSITIVITIES	VALVE TYPES USED	BOTTLE CONTENTS
1	A. CONDENSIBLES, GROUND OPERATIONS	10 PPB OR LESS	NONE (MANUALLY CAPPED)	TENAX GC, SPHEROCARB, 400 mg EACH IN TANDEM
	B. CONDENSIBLES, DESCENT AND POSTFLIGHT PRIOR TO ACCESS	ALTITUDE DEPENDENT 10 PPB TO PPM	LATCHING SOLENOID	TENAX GC, SPHEROCARB, ~ 75 mg EACH IN TANDEM
2.	CONDENSIBLES ASCENT	ALTITUDE DEPENDENT	TWO PYRO N. O. AND LATCHING SOLENOID	TENAX, GC, SPHEROCARB ~ 75 mg EACH IN TANDEM
3.	HC1, GRAB SAMPLING	10 ± 5 PPM @ 1 TO 5 TORR	PYRO N. C., LATCHING SOLENOID	$Ag_2 0$ COATED PLATLETS
4.	HC1, ASCENT	10 ± 5 PPM @ 1 TO 5 TORR	TWO LATCHING SOLENOIDS	$Ag_2 0$ COATED PLATLETS
5.	NITROGEN COMPOUNDS, DESCENT	10 + 5 PPM @ 1 TO 5 TORR	TWO LATCHING SOLENOIDS	RUTHENIUM COMPOUND COATED PLATLETS

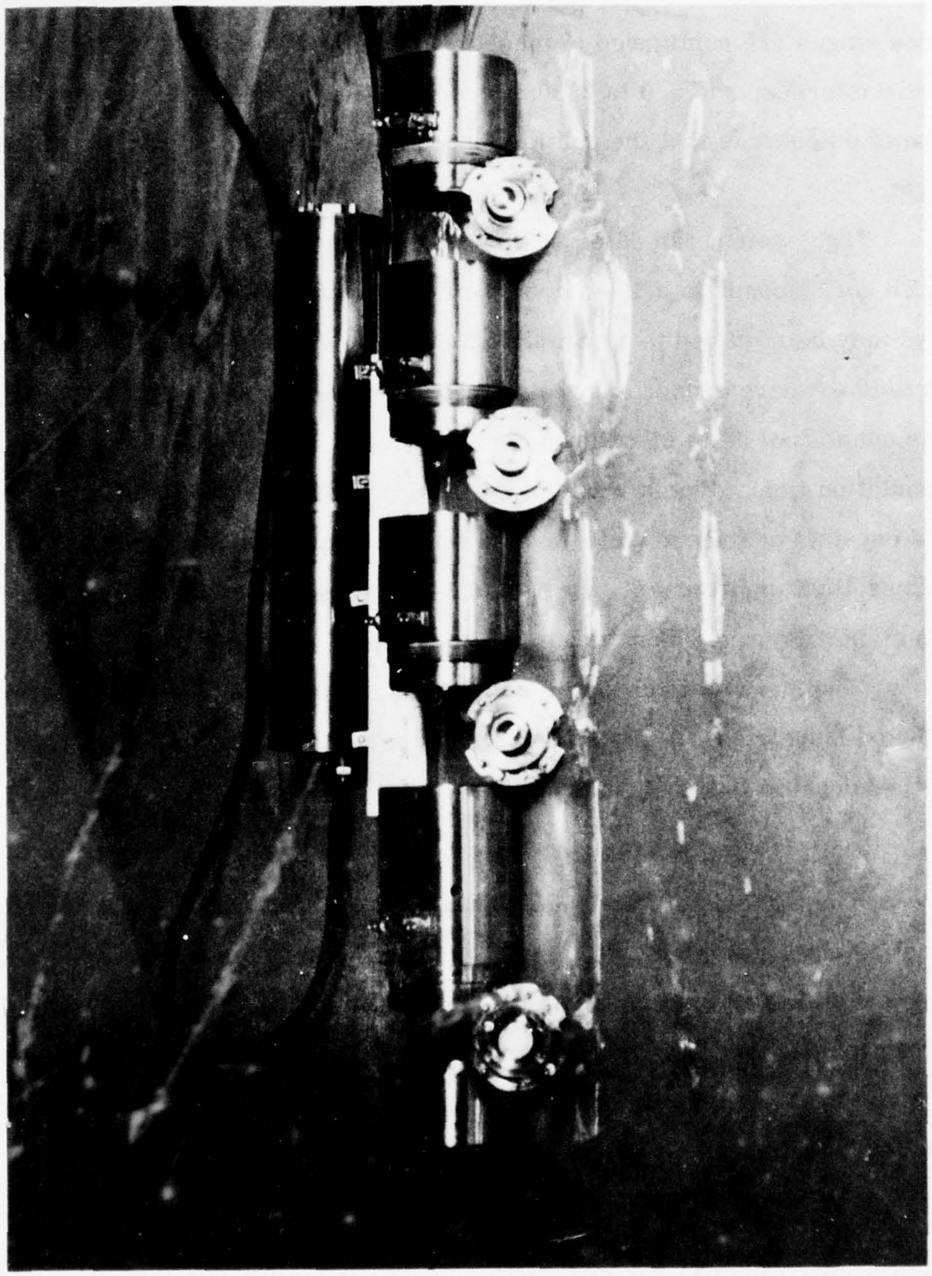

Figure 4. Cascade impactor.

than a certain radius will be imbedded in the polymeric coating on the crystal; their mass is measured by noting the change in oscillation frequency. The three stages are configured to measure particles from 0. 3 to 1. 0 micron, 1. 0 to 5. 0 microns, and 5. 0 to 25. 0 microns. One particular advantage of this type of detector is that the particles are retained and can be analyzed post-flight.

The system can detect a change on the order of 10^{-9} gram deposited, which corresponds to a 10-micron particle. In a class 100 environment, 2 days may be required to accumulate a detectable quantity of 0. 3- to 1. 0-micron particles, whereas approximately 3 hours are required to accumulate a detectable quantity of 5- to 25-micron particles. In a class 100K environment, accumulation times of only minutes are required to detect measurable changes. The crystals can accumulate several tens of micrograms before saturation. In a class 100K environment, the 5- to 25-micron section will collect 9 micrograms per day and will saturate in 2 to 4 days.

The cascade impactor is a variation of a commercial unit made by Celesco Industries. A flight prototype is being flown due to lack of funds to further develop this instrument.

3. 4 Optical Effects Module

The Optical Effects Module (OEM) (Figure 5) built by Advanced Kinetics, Inc., consists of a monochromatic (253. 65 nm light source, focussing and collecting optics, a rotatable sample carousel, and detectors. The OEM provides the IECM with the capability to monitor optical degradation of typical window materials due to both particulates and condensible molecular species. Six sample positions on the carousel allow three samples to be exposed at all times except for measurement. Two samples, plus an open position for calibration, remain inside the OEM housing for monitoring internal contamination. As the samples are periodically sequenced into the measurement

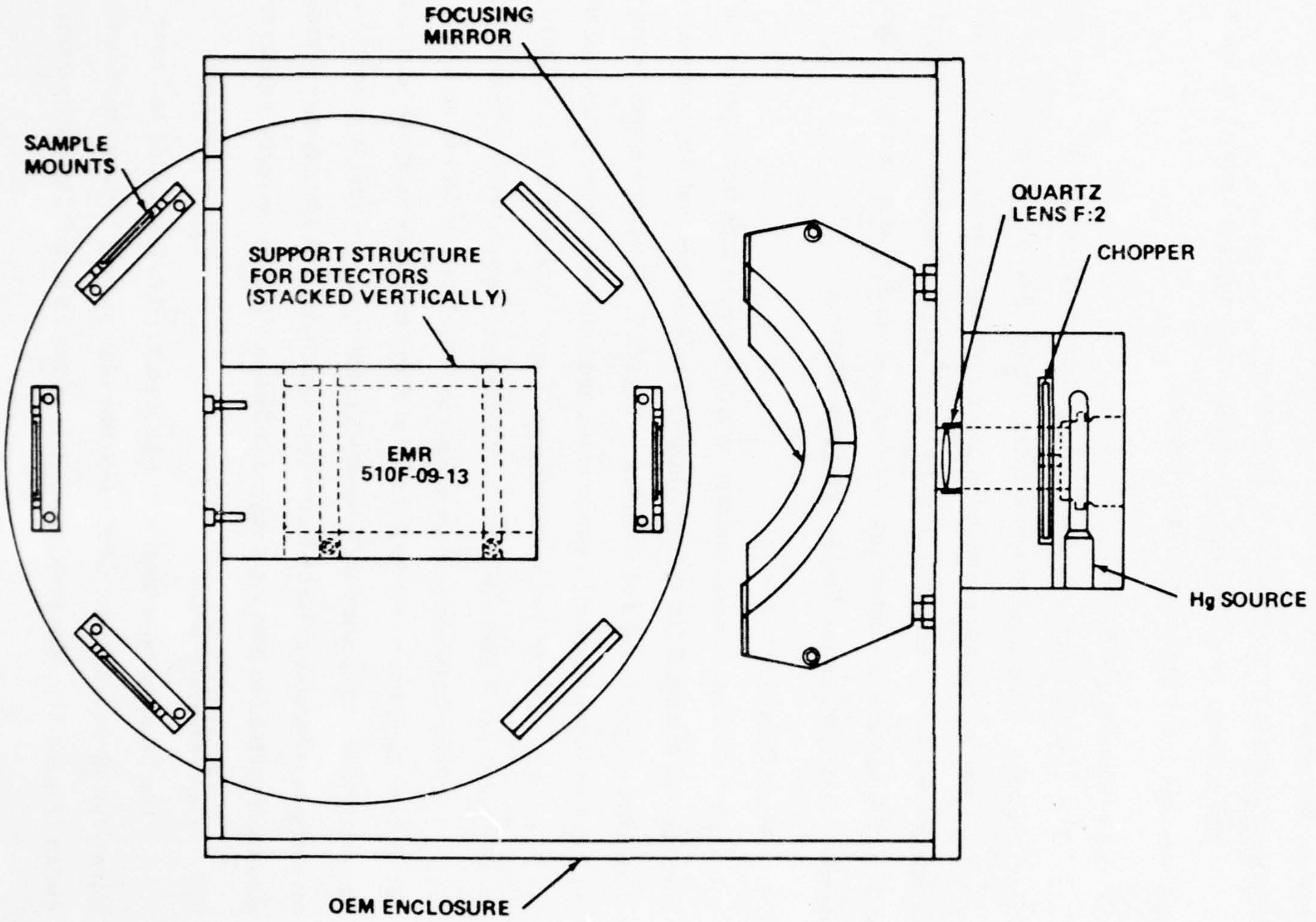

Figure 5. Optical Effects Module.

position, two photomultiplier detectors monitor specular transmittance and diffuse reflectance to a precision of 1 percent.

The nominal repetitive operation will allow approximately 7 minutes exposure and 1.3 minutes for measurements.

3.5 Passive Sample Array

The Passive Sample Array (PSA) consists of 8 sample trays containing 6 samples each, for a total of 48 samples (Figure 6). Each tray may be easily removed from its mounting, providing the capability of quick change out for laboratory analysis of changes of optical properties. The PSA was built at the Marshall Space Flight Center and is a modified version of a similar "witness" sample experiment on the Apollo Telescope Mount.

3.6 Mass Spectrometer

The IECM mass spectrometer is a quadrupole type developed by the University of Michigan for the Atmosphere Explorer Neutral Atmospheric Composition Experiment and is shown in Figure 7. It covers a mass range of 2 to 150 AMU with adjustable sweep rates and selectable mass range and stops. The flux range is 10^8 to 10^{15} molecules cm^{-2} sec^{-1} 0.1 sr^{-1} with a sensitivity of 2×10^{-3} count sec^{-1} $particle^{-1}$ cm^{-3} with adjacent peak contribution of 10^{-3}.

The instrument contains a gettering collimator system to provide a collection cone of 0.1 sr. The collimator and spectrometer head are sealed from atmospheric contamination until on-orbit conditions exist and is resealed for re-entry to minimize refurbishment between flights. A gas release system is also incorporated to provide a tagged collimated gas for on-orbit calibration.

3.7 Camera/Photometer

The background intensity will be measured in the visible and near ultraviolet by an automatic camera/photometer system built by Epsilon Corporation (Figure 8). The system consists of two 16 mm Bolex movie cameras

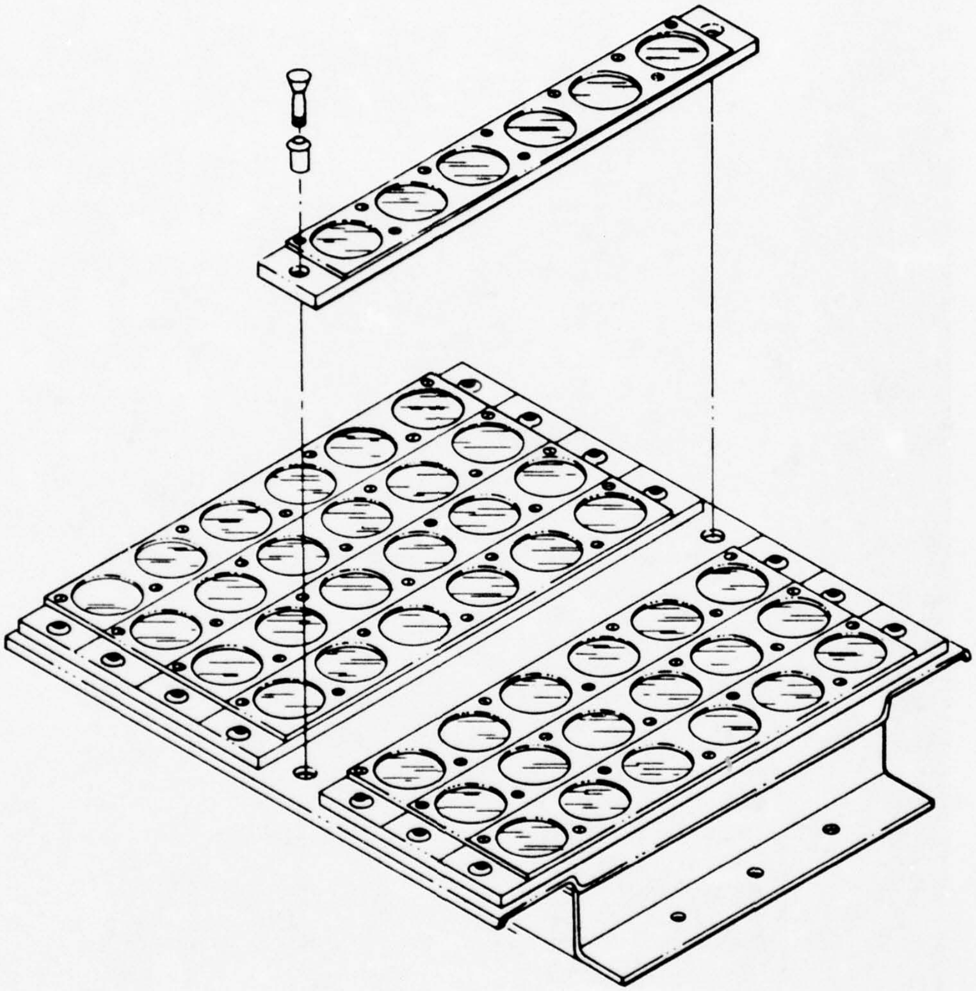

Figure 6. Passive Sample Array.

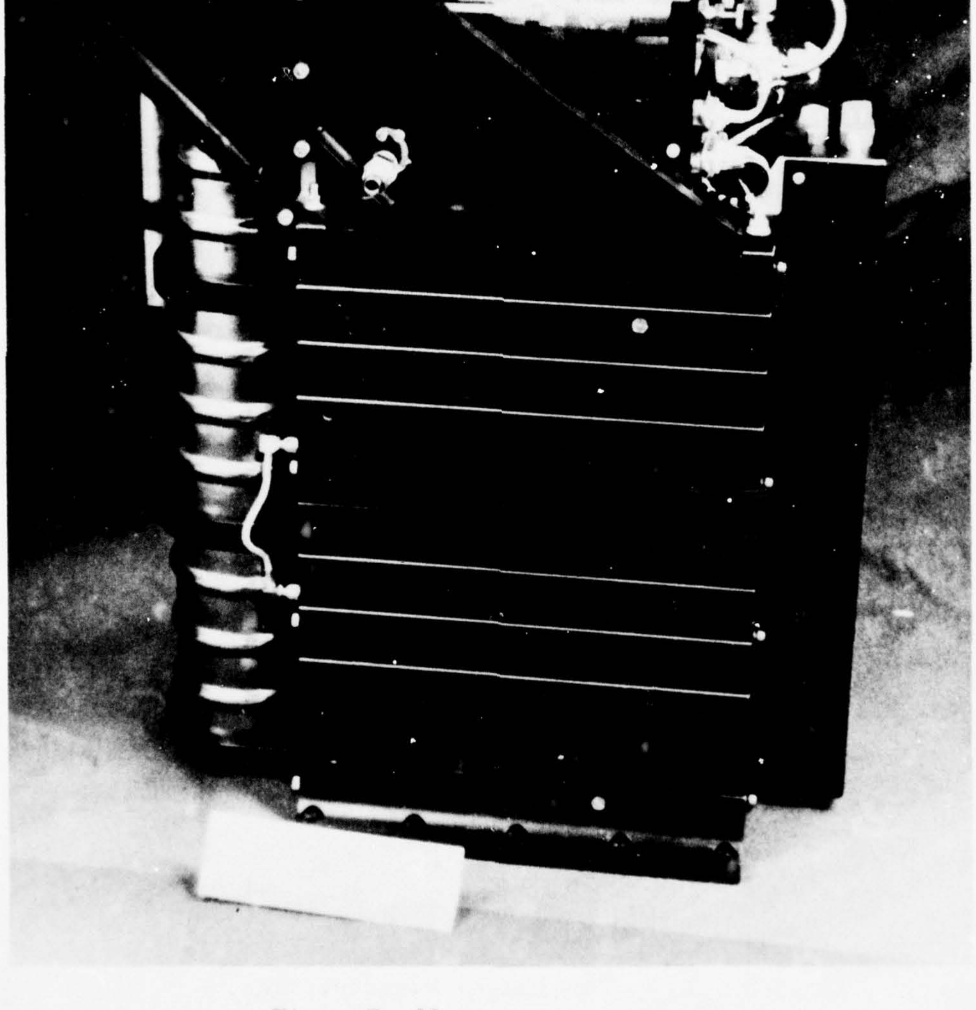

Figure 7. Mass spectrometer.

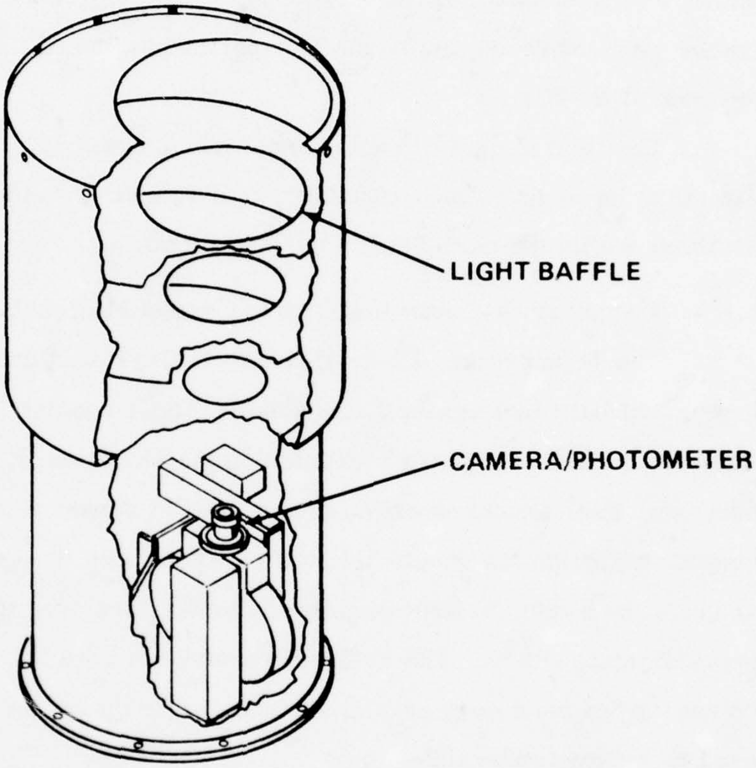

Figure 8. Camera/Photometer.

with 10 mm, f/1.9 Switar lenses and 4000 frame magazines. The film is advanced every 150 sec after a start command. The shutter is controlled by a photomultiplier photometer that integrates the incident light and closes the shutter when a predetermined exposure has been reached. This exposure value is chosen to give a film density just above the knee of the D-log E curve. This allows a measurement of the background without degradation of any particle tracks. The exposure time and the experiment elapsed time are annotated on the edge of the film.

The field of view of each camera/photometer is 20° in the vertical direction, providing stereo capability to define the velocity and direction of particles within the near field of the spacecraft.

3.8 Temperature-Controlled Quartz Crystal Microbalance

The Temperature-Controlled Quartz Crystal Microbalance (TQCM) instrument built by Faraday Laboratories, Inc., consists of a control unit with five sensor heads (Figure 9) mounted on the sides, ends, and top of the IECM package. Each sensor head consists of a QCM sensor and a two-stage bismuth-telluride thermoelectric device which uses the Peltier effect to heat and cool the sensor to the commanded temperature over the range of 80°C to approximately -60°C. The 80°C temperature is used for vaporization or "clean-up" of the quartz crystal surface, while the colder temperatures are used to collect condensibles.

*The sensors have a field of view of approximately 120° and the sensi*tivity to measure mass changes of approximately 1×10^{-9} gm up to a total mass of approximately 1×10^{-4} gm.

3.9 Cryogenic Quartz Crystal Microbalance

The Cryogenic Quartz Crystal Microbalance (CQCM) (Figure 10), also built by Faraday Laboratories, Inc., consists of two passive thermally controlled QCM sensors isolated from the IECM structure. During normal orbital

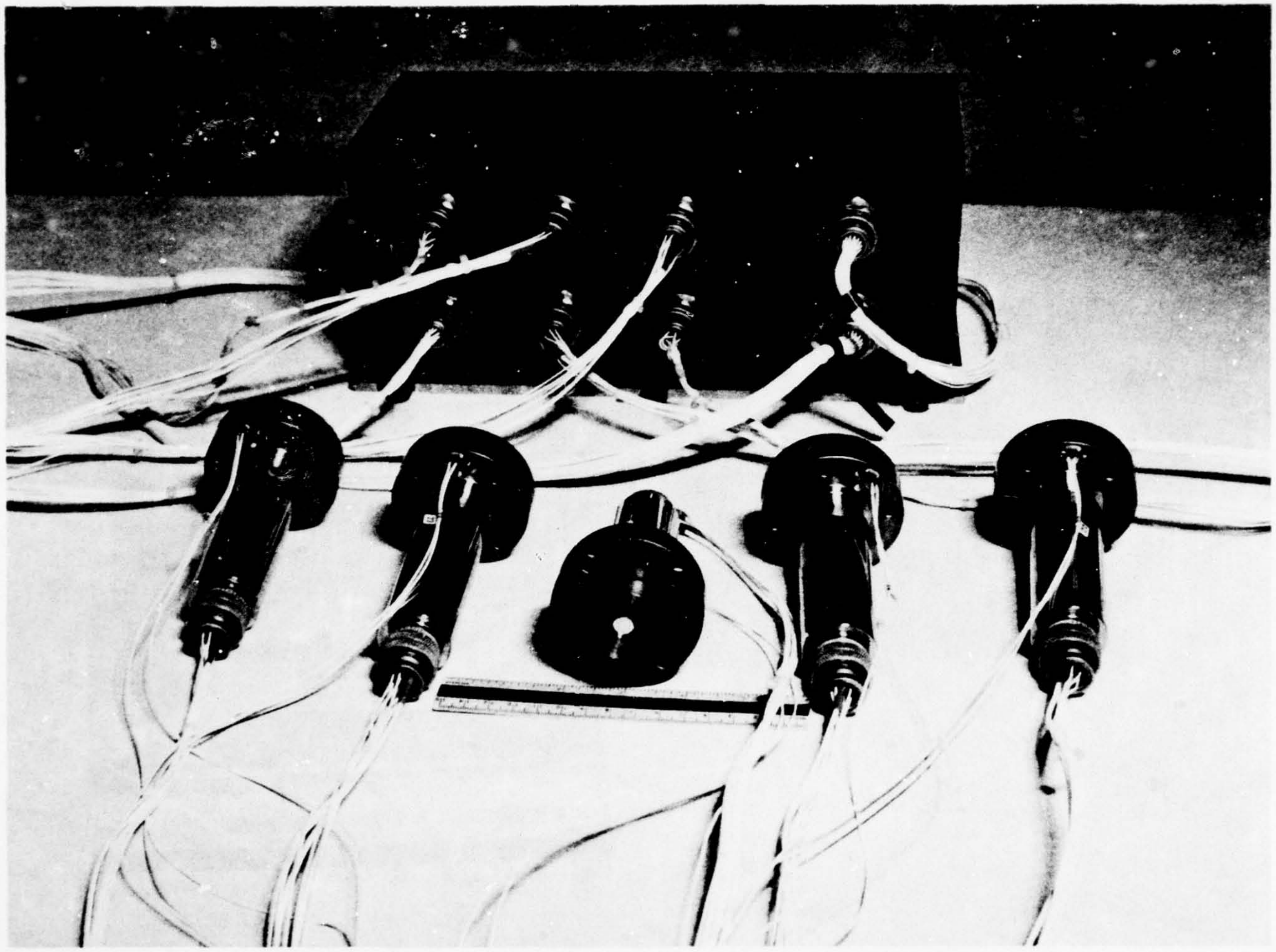

Figure 9. Temperature-Controlled Quartz Crystal Microbalance.

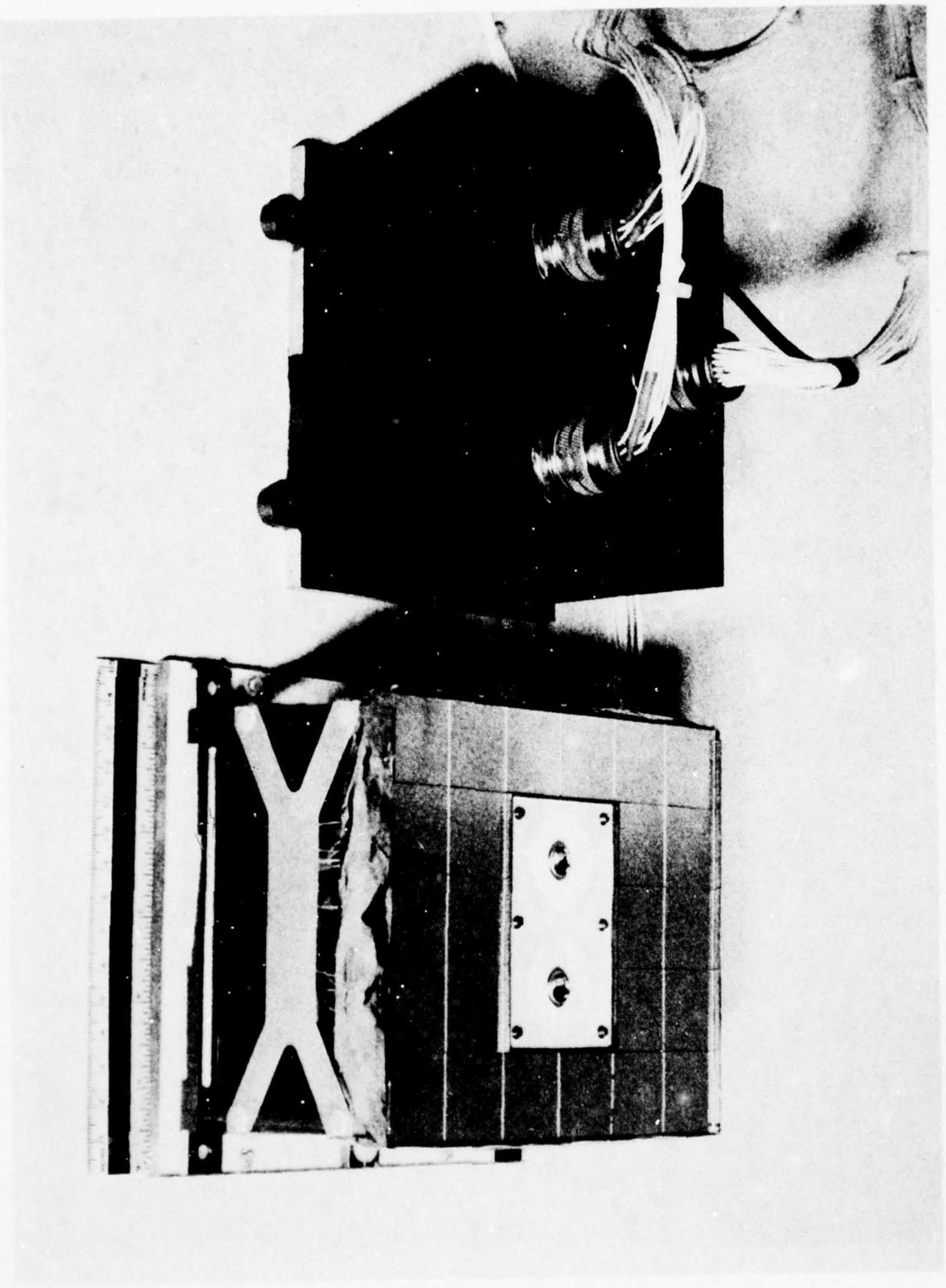

Figure 10. Cryogenic Quartz Crystal Microbalance.

modes the sensors nominally would be at a lower temperature than the IECM ambient. However, during "cold soak" portions of the Orbiter operations, the CQCM is designed to cool down to below -133°C where molecular water will begin to condense. The two sensors are designed to passively cool down and actively heat up at slightly different rates such that differential condensation and evaporation rates may be detected. A heater is incorporated to provide sensor cleaning capability.

4.0 LONG DURATION EXPOSURE FACILITY IECM

The LDEF satellite to be launched by Space Shuttle will carry a small version of the IECM primarily to gather contamination data on an off-line buildup of a Space Shuttle payload and on deployment operations.

The LDEF IECM (Figure 2) is instrumented with the Optical Effects Module, Passive Sample Array, Temperature-Controlled Quartz Crystal Microbalance with five sensors, and a Cryogenic Quartz Crystal Microbalance. Like the larger version, the LDEF IECM is self-contained. Batteries supply power for the instruments and data system for some 20 hours after deployment, although power is obtained from the Space Shuttle Orbiter before deployment.

The LDEF will be retrieved after approximately 9 months in space.

5.0 IECM OPERATIONS

The IECM will monitor contamination levels during prelaunch operations at Kennedy Space Center. At present, it is planned to obtain data in the Orbiter Processing Facility (OPF), the Vertical Assembly Building (VAB) once the Orbiter is mated with the mobile launch platform, and on the launch pad in the Payload Changeout Room (PCR).

The prime measurements during prelaunch operations will be temperature, humidity, aerosols, nonvolatile condensibles, and trace gases utilizing the Brady Array, Dewpointer, Cascade Impactor, Air Sampler, Optical

Effects Module, and Passive Sample Array (Table 1). These same instruments will be operating during ascent, descent, and post-landing, with the exception of the Optical Effects Module on ascent and with the addition of the Temperature-Controlled Quartz Crystal Microbalance and Cryogenic Quartz Crystal Microbalance.

The prime measurements during ascent and descent will be the same as prelaunch with the appropriate sampling rate and Air Sampler sequencing changes. For post-landing measurements the IECM will operate for approximately 1 hour on internal batteries, measuring effects of temperature heat-up from re-entry and the purge gas hookup which will occur approximately 15 minutes after landing.

The prime measurements on-orbit will be concerned with particulate and gaseous contaminants that will be continuously emitted from the spacecraft and will be interacting with the space environment. The Mass Spectrometer, Camera/Photometer, Optical Effects Module, Passive Sample Array, Temperature-Controlled Quartz Crystal Microbalance, and Cryogenic Quartz Crystal Microbalance will be operating.

A special maneuver has been requested on several OFT flights to scan the spacecraft from the wake to ram with respect to its velocity vector to provide data on molecular collisional cross sections, utilizing the mass spectrometer and its gas release system.

The IECM measurements are time-coded to allow correlation with various spacecraft events such as spacecraft maneuvering, "hot soaks," "cold soaks," venting, etc.

5.1 Contamination Mapping

The Space Shuttle Remote Manipulator System (RMS) presents the opportunity to maneuver the IECM around the spacecraft to directly measure emitted contamination. The Marshall Space Flight Center has designed a release/attach mechanism for the IECM such that the IECM can be both mechanically and electrically removed from the payload bay at the RMS. The mapping maneuver will involve placing the IECM in various positions above the spacecraft to monitor ambient outgassing and off-gassing, Vernier control systems, and evaporator contamination levels. When this is accomplished, an RCS engines plume flow field survey will be made by a pressure gauge incorporated in the IECM for this purpose. At the end of these maneuvers the IECM will be reattached mechanically and electrically to the spacecraft and will resume its normal on-orbit contamination monitoring operations.

6.0 CONCLUSION

The Shuttle Induced Environment Contamination Monitor provides a method to verify the contamination environment associated with Space Shuttle and to obtain data on the adequacy of controls that are now imposed. These data will be used to verify and revise models now being used to predict contamination levels on various Space Shuttle/Spacelab missions.

REFERENCES

1. Anon., Final Report of the Space Shuttle Payload Planning Working Groups, Astronomy Volume 1, NASA/Goddard Space Flight Center, Greenbelt, Maryland (May 1973).

2. Space Science Board, Scientific Uses of the Space Shuttle, National Academy of Sciences, Washington, D. C. (1974).

3. Payload Contamination Control Requirements for Shuttle Transportation System (STS) Induced Environment, STS Payload Contamination Requirements Definition Group Report, NASA/Marshall Space Flight Center (July 1975).

4. Space Shuttle Program Level II Program Definition and Requirements, NASA/JSC-07700 Flight and Ground Systems Specification, Volume X, Revision B (August 1975).

5. Space Shuttle Program Level II Program Definition and Requirements, NASA/JSC-07700, Volume XIV, Revision E (July 1977).

6. Simpson, J. P. and Witteborn, F. C., Effect of the Shuttle contaminant environment on a sensitive infrared telescope, Applied Optics 16 (No. 8): 2051-2073 (1977).

7. Leger, L.; Jacobs, S.; and Ehlers, H. K. F., Space Shuttle contamination overview, Proc. Institute of Environmental Sciences (February 1978).

AD-A070 386   AIR FORCE MATERIALS LAB WRIGHT-PATTERSON AFB OH   F/G 22/2
PROCEEDINGS OF THE USAF/NASA INTERNATIONAL SPACECRAFT CONTAMINA--ETC(U)
1978   J M JEMIOLA
UNCLASSIFIED   AFML-TR-78-190   NL

7 OF 13
AD
A070386

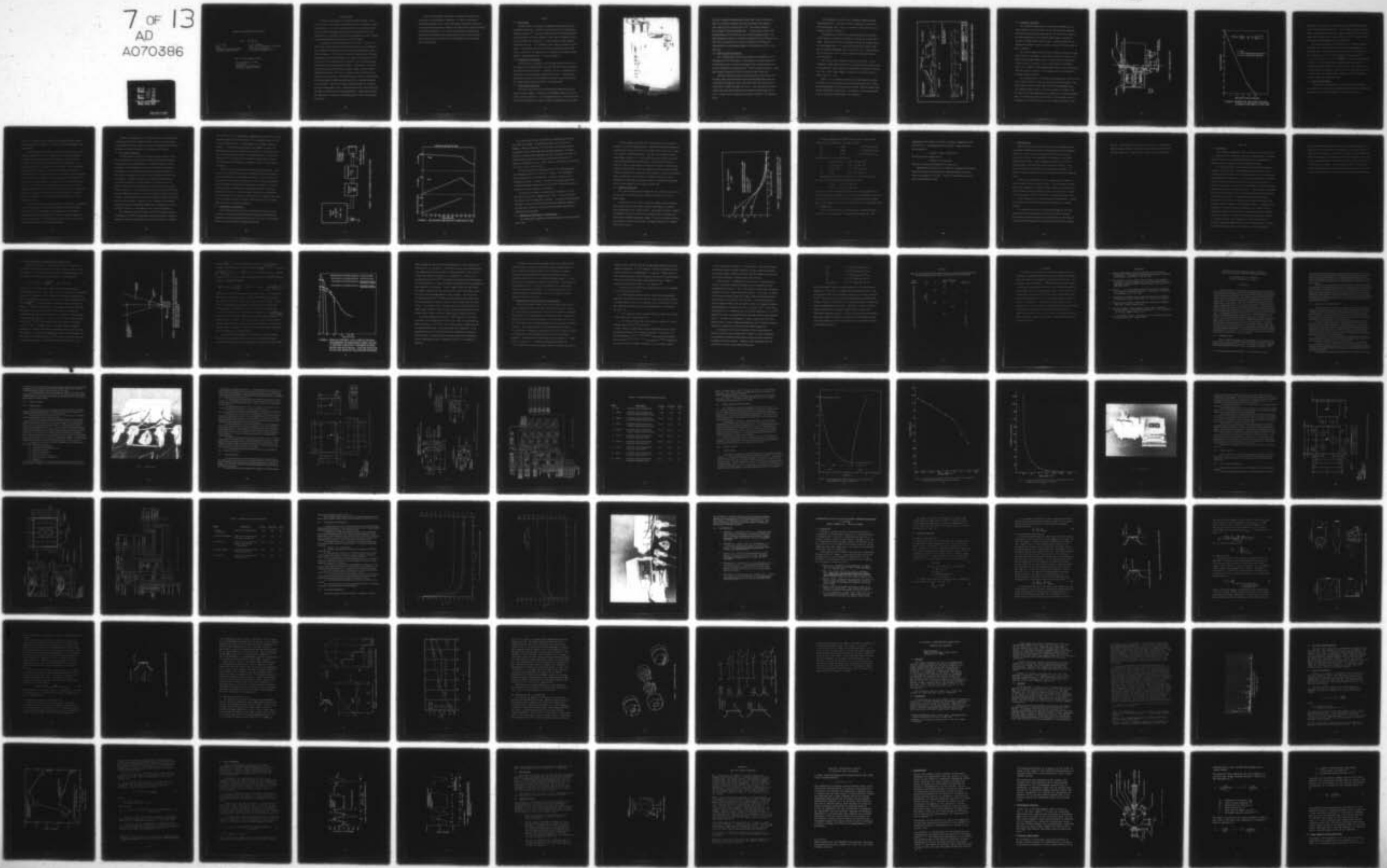

MASS SPECTROMETER FOR IECM

Part I - Description

R. C. Ruff
ES74
Marshall Space Flight Center
Huntsville, Alabama 35812

D. R. Taeusch
Space Physics Research Laboratory
University of Michigan
Ann Arbor, Michigan 48105

Part II - Measurement Concepts

W. A. Oran and T. Rathz
ES72/ES74
Marshall Space Flight Center
Huntsville, Alabama 35812

BACKGROUND

The Induced Environment Contamination Monitor (IECM) is to be flown on the first six Shuttle Orbital Flight Tests as Development Flight Instrumentation. The Mass Spectrometer (MS) is incorporated into the IECM to perform molecular column density and molecular return flux measurements as specified by the Shuttle Transportation System--Payload Contamination Requirements Definition Group(1) (CRDG).

The purpose of the MS measurements is two-fold. The first is to define what emitted molecules are being backscattered to the Shuttle bay for correlation with deposition type measurements being made by other IECM instruments. The second is to define the column density of the gas cloud (induced atmosphere) through which optical experiments must look. The sources of this emitted gas are from leaks, vents, thruster firings, and off-gassing and out-gassing of surfaces. These gases, as they flow away from the spacecraft at thermal speeds, collide with the ambient atmosphere molecules which have a relative velocity of 8 km/sec with respect to the spacecraft. This collision process causes a small fraction of the emitted gas to be deflected back into the 0.1 steradian collimated view of the MS. The MS will count all molecules from 2 to 150 atomic mass units (amu) which it sees. Interpretation of these counts depends on how much is known about the scattering process. A gas release calibration experiment to quantify the scattering process will be incorporated into the MS.

In Part I of this paper is presented a description of the MS and a discussion of its measurement capabilities. In Part II is presented a conceptual simulation of the in situ measurements and a discussion of how the expected backscattering is related to the column density and the kinematics of the scattering process. This is done to help define the relationship between the measurements and actual column density so that preferred vehicle maneuvers and attitudes can be established which will optimize the scientific results.

PART I

1.0 Introduction

The MS system, consisting of a quadrupole mass analyzer and its associated electronics, is similar to several which flew on Atmospheric Explorer satellites.(2) The basic modifications for the IECM application are the additions of an inlet collimator, a gas source calibration system, and a resealable valve mechanism. The MS system is being developed and built by the University of Michigan, Space Physics Research Laboratories. Two identical units will be delivered to Marshall Space Flight Center, Space Sciences Laboratory, for integration and operation aboard Shuttle. A photograph of unit 1 is shown in Figure 1.

2.0 Description of Instrument

The MS system is mounted in the IECM such that the center line of the conical view is perpendicular to the top of the IECM which is mounted parallel to the Shuttle bay floor. Therefore, the view is perpendicular to the long (X) axis of the Shuttle, parallel to the Z axis. The sequential operations of the MS are all controlled by the data system of the IECM. The specific subsystems of the MS are described below.

2.1 Mass Sensor Subsystem

The mass sensor consists of a thermalizing chamber and electron impact ionization source, a hyperbolic-rod quadrupole analyzer, and an off-axis electron multiplier. The quadrupole analyzer is tuned for flat top peaks and measurements are made by digitally stepping from peak to peak.

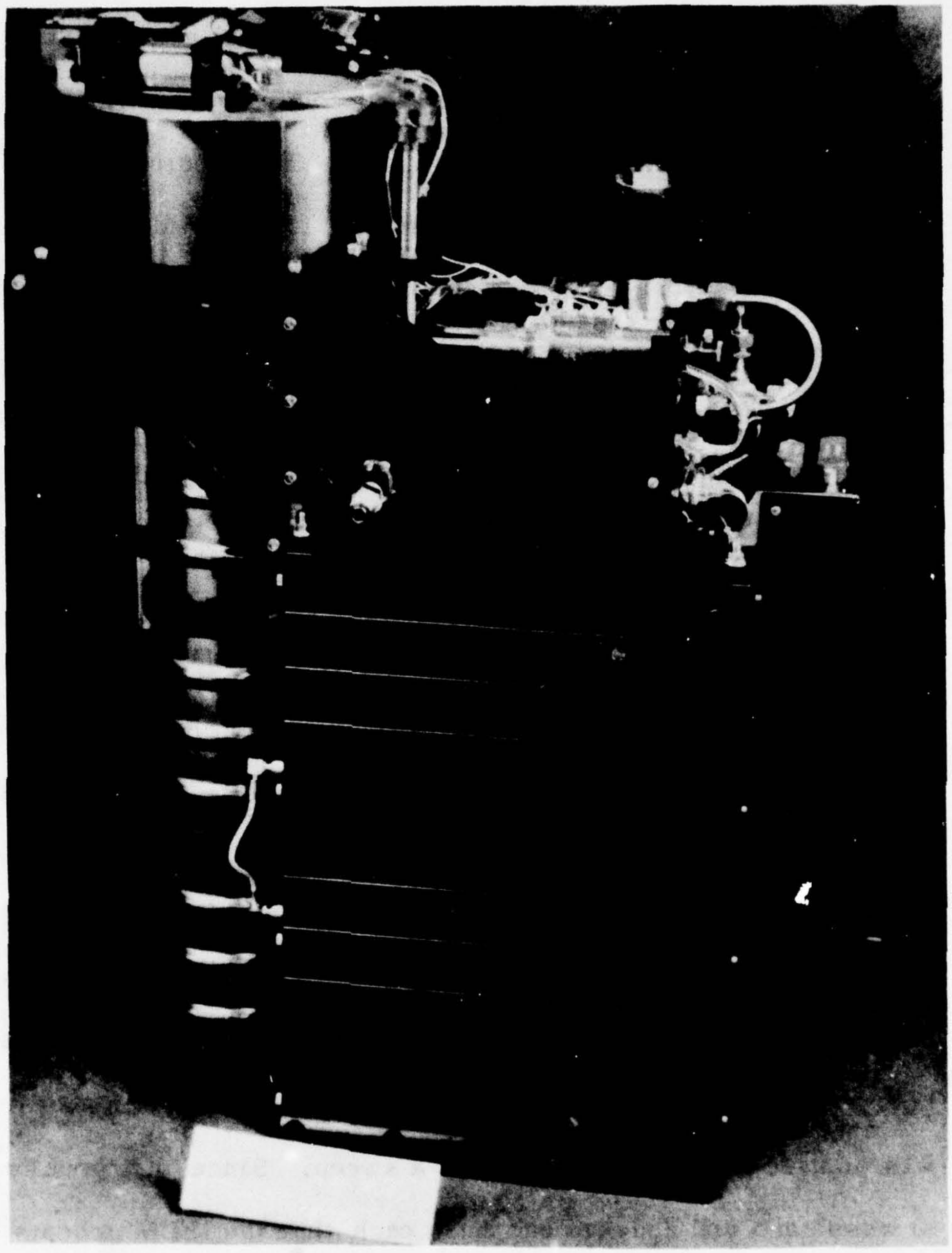

Figure 1. Mass Spectrometer for IECM, Unit 1

The MS is capable of monitoring molecules with a mass to charge ratio from 2 to 150 with a resolution such that contributions from adjacent mass peaks are less than one part in 10^3. The electron multiplier has 14 stages of electron multiplication. This provides a current pulse of approximately 10^6 electrons per ion to a pulse counting circuit. The pulse amplifier is limited to a maximum counting rate of 5×10^7 pulses/sec. The sensor subsystem has an overall sensitivity of 10^{-5} amps/torr which implies an internal number density of 500 molecules/cm^3 for every count/sec.

2.2 Data and Control Subsystem

The amplified pulses from the electrometer are supplied to a 24 bit accumulator (16,777,215 counts). A floating point converter compresses the data from 24 bits to 13 bits consisting of 9 bits of linear number and 4 bits of multiplier or decimal position. The 9 bits equal 512 counts, which give a digital resolution of 0.2% to 0.4% for all counts above 512.

Since the IECM data system is an 8 bit system, two 8 bit words will be given to the IECM processor every 2 seconds during slow sweep and every 200 MS during fast sweep. One of the 3 bits not used for counts will be used to "mark" the start of a sweep. Since the mass sweep starts at mass zero and indexes one mass each time the IECM accepts the 16 bits, no further data is required for automatic reduction of the measured mass.

The remaining 2 bits will be used to multiplex digitized analog housekeeping words. Four masses will be required to assemble one 8 bit housekeeping word. Thus, it is possible to have 38, 8 bit words during one scan of 150 masses.

Several functions of the MS are initiated and timed by the IECM control system. The IECM interrogates the MS for the two 8 bit data words. The intervals between interrogation control the integration time for accumulating counts. It is presently planned that the IECM would have two preset interrogation rates--a slow scan with 2 second integration and a fast scan with 0.2 second integration at each amu (atomic mass unit) peak.

The IECM has three additional controls over the MS. A "Gas Calibration" signal initiates release of an isotopically labeled gas mixture. A "Special Mass" signal requests an abbreviated sweep from 2 to 48 amu. The "Valve Close" signal triggers a mechanism to seal the orifice of the MS before re-entry.

Figure 2 is a pictorial description of the abbreviated sweep and the normal sweep which alternates between sweeping from 2 to 150 amu and 150 integrations of the water peak at 18 amu. Both the normal sweep and the abbreviated "Special Mass" sweep take 8 steps across amu 28 to act as a check on the operation of the instrument.

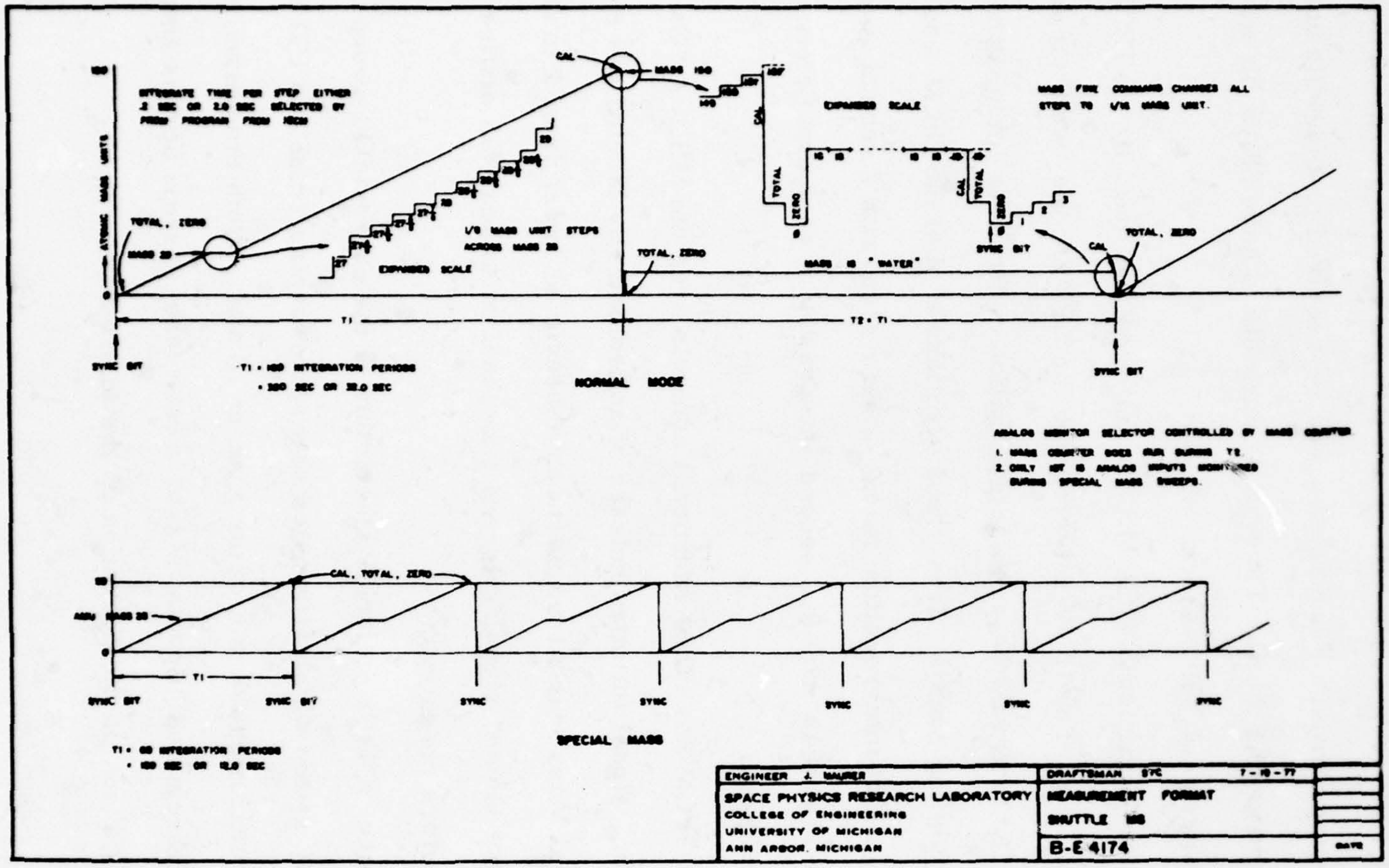

FIGURE 2. PICTORIAL DESCRIPTION OF NORMAL AND ABBREVIATED MASS SWEEPS

2.3 Collimator Subsystem

The collimator design consists of three chevron baffles plus an orifice (Figure 3) which separates the flow such that those molecules which enter the orifice at an angle greater than 10° from the normal to the orifice are directed into a chamber which contains a number of sintered zirconium powder "getter" pumps. The theoretical curve of normalized ion source response to angle of incidence of the flow field is given in Figure 4.

The size and amount of getter material required depends on the gas load for which it is designed. This should be minimized. However, the orifice must be large enough to allow an adequately short vacuum time constant for the internal gas. It was decided that a 3 mm diameter orifice was as small as seemed engineeringly feasible, gave an adequately short time constant, and gave a low enough gas load to be handled by a reasonable number of getters.

The conductance of a 3 mm diameter knife edge orifice is 850 cm^3/sec. The ion source volume to which the vacuum time constant applies is that volume behind the last chevron baffle in front of the quadrupole tube. The collimator volume itself is, of course, pumped by the getters and the volume of the quadrupole analyzer is pumped by a separate appendage pump. The conductance from the ion source to the analyzer section is estimated to be 70 cm^3/sec which is small compared to the inlet orifice

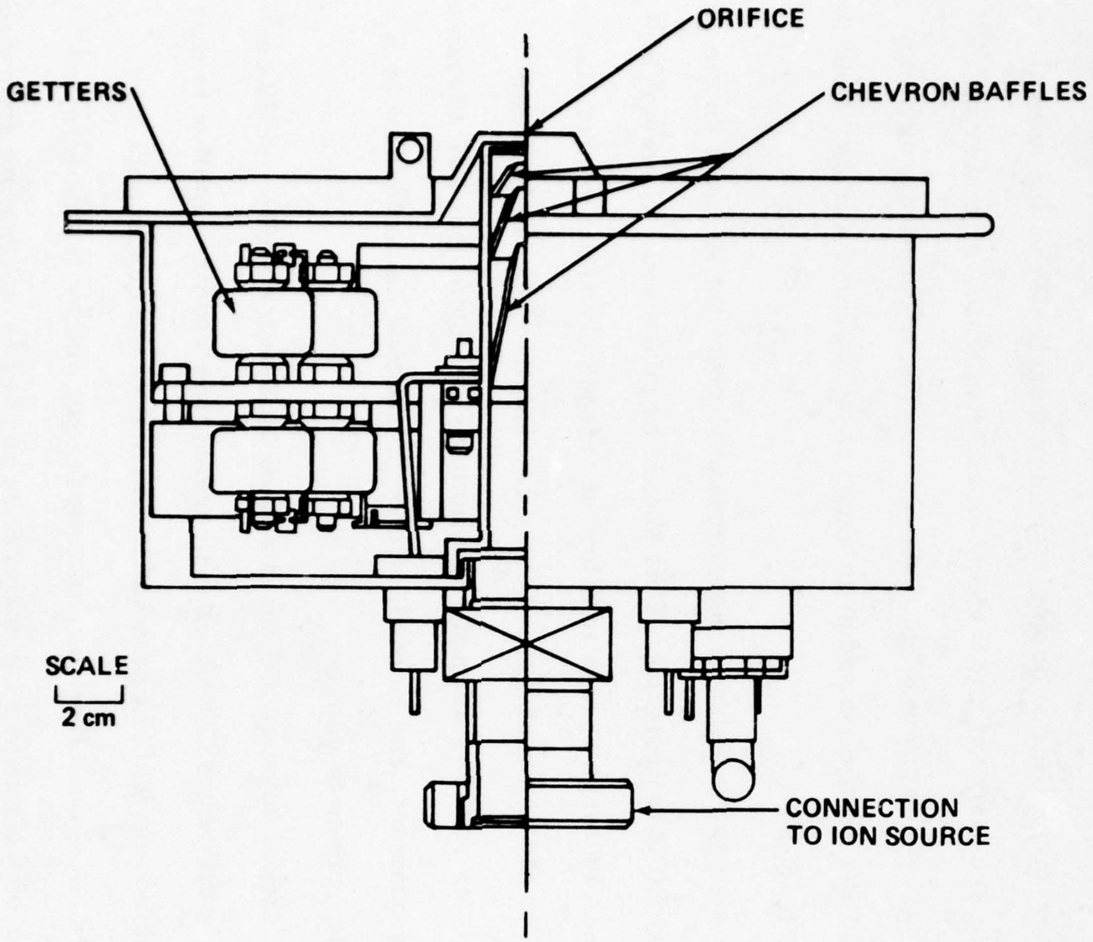

FIGURE 3. COLLIMATOR DESIGN

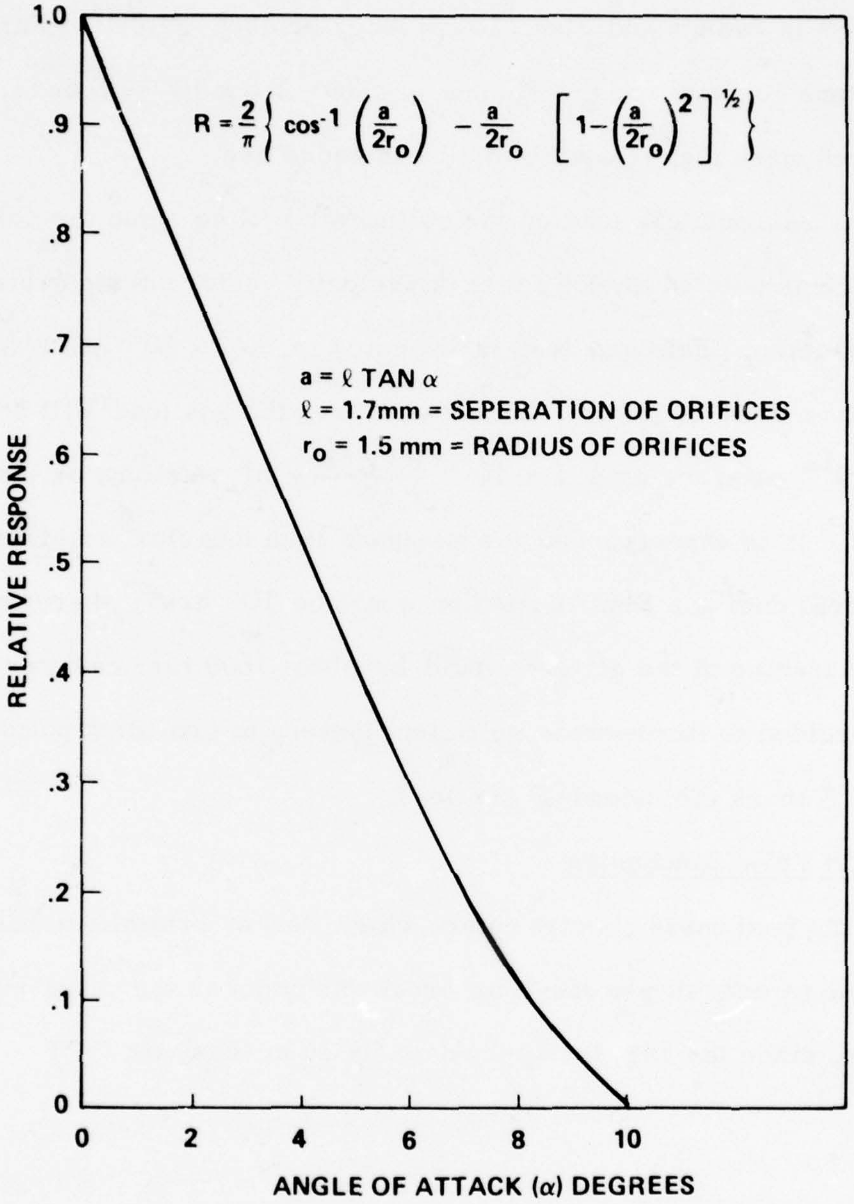

FIGURE 4. NORMALIZED ION SOURCE RESPONSE TO ANGLE OF INCIDENCE OF GAS FLOW

conductance. Therefore, the ion source density will respond primarily to the external changes in inlet flux. The ion source volume is a cylinder about 1 cm in radius and about 10 cm long, or about 31 cm^3. This gives a vacuum time constant for the volume of about 3.6×10^{-2} seconds, which is believed more than adequate for the intended use.

The maximum gas load on the collimator will be when the normal to the orifice is pointed directly into the velocity vector during orbit at 250 km altitude. This gas load is expected to be 2×10^{15} part/cm^2 sec. The orifice area is 7×10^{-2} cm^2; therefore, the gas load will be 1.41×10^{14} part/sec or 4.4×10^{-3} $\frac{\text{torr cm}^3}{\text{sec}}$ at a collimator temperature of 300°K. It is expected that the maximum time this flux would be encountered during a Shuttle mission would be 100 hrs.; therefore, the *maximum* loading of the getters would be about 1600 torr cm^3 per mission. It was decided to incorporate sufficient getters to provide a pumping speed of 5 times the incoming gas load.

2.4 Inlet Valve Mechanism

In the past mass spectrometers which flew on orbital satellites were able to use simple one-time break-off tubes as the valve mechanism. However, since the MS is expected to fly on at least six OFT missions, a mechanism was developed for resealing the orifice before re-entry to protect the getters, ion source, and electron multiplier from contamination.

The valve mechanism developed to meet the various mechanical and thermal requirements is shown in Figure 1. The valve for prelaunch sealing (called opening valve) must be bakeable to 350°C and must, therefore, utilize a metal sealing ring under high compression. This force is generated by a ceramic rod in compression. At the appropriate time after orbit is achieved, a solenoid is activated which releases a spring loaded arm. The momentum of this arm is used to break the ceramic rod. The metal cap holding the metal sealing ring is then released and swings away in a 180 degree arc to expose the mass spectrometer orifice to space. The closing valve does not need to be exposed to the 350°C bake and, therefore, utilizes a rubber 0-ring with much less compression force. Upon receipt of the proper signal from the IECM, a solenoid is again used to release the spring loaded arm which swings the 0-ring against the orifice.

It is expected that unless a large amount of contamination is enountered, the mass spectrometer will need minimal refurbishment between flights. This would consist of resealing the metal opening valve while under a nitrogen purge and then a simple bake to remove the large nitrogen gas load from the getters. The sealing mechanism used for this and all other vacuum bake operations is a copper pinch-off tube.

A major contamination of the instrument such as a valve malfunction or high pressure during a Shuttle bay door closing test would require a major refurbishment which involves cleaning or replacement of the electron multiplier or actual dismantling of the quadrupole for cleaning.

2.5 Gas Source Calibration

In order to better relate the measured ion-source densities in the mass spectrometer on the IECM to the effluent densities and resulting column densities of contaminant gases, an inflight calibration will be performed. The calibration will consist of activation of a gas release system which will emit a known flux of isotopically labeled water and neon into the collimated view of the MS, and the backscattered flux will be monitored. A sufficient quantity of the calibration gas mixture will be provided to enable a 45-minute calibration, during which time the angle of attack of the mass spectrometer pointing vector will be varied between 0 and 180°. The relationship between the backscattered flux and the known effluent flux density as a function of angle of attack will thus be obtained. This will provide the calibration needed to interpret the measurements of Shuttle effluents. Moreover, these calibration measurements provide the basis for evaluating the differential scattering cross sections for 8 km/s collisions, a measurement of basic physical importance.

The calibration source will utilize a 350 cm^3 vessel pressurized to 10 atmospheres of ^{22}Ne, with deuterated liquid water (D_2O) in sufficient quantity to maintain its vapor pressure (23.5 torr @ 25°C). A total flux of 3 x 10^{19} $cm^{-2}s^{-1}$ is maintained by regulating the pressure to 4.5 lb/in^2 and restricting the flow to 1000 torr cm^3/s to a capillary array of 1 cm^2 cross sectional exit area. A block diagram of the system is shown in Figure 5. The capillary array collimates the effluent to about a 10° half angle stream into the collimated view of the MS. Under these conditions the water flow rate would start at about 4 torr cm^3/s, increase to 100 torr cm^3/s at 45 minutes after initiation, and then drop to 30 torr cm^3/s when the Ne was depleted, if maintained at 25°C. This is shown in Figure 6.

The ^{22}Ne and D_2O gases were selected for several reasons. Since water is such a large component of the Shuttle effluent and since water is a major contaminant for many infrared observations, D_2O was chosen to elucidate the role of water in the ambient and self-scattering mechanisms while not actually being masked by natural H_2O contamination. Neon was chosen to provide a comparison scattering mechanism for a monoatomic gas near the same mass. These two gases should allow a determination of the scattering cross section as related to inelastic and elastic collisions. Later OFT flights probably will utilize $H_2{}^{18}O$ in place of D_2O to further study the inelastic scattering mechanism.

3.0 Operational Characteristics

Once the MS has been turned on in orbit and the orifice valve has been opened, the MS will automatically step through its preprogrammed sequence of mass peaks and provide the data to the IECM. It is presently planned to have three modes of operation for the MS.

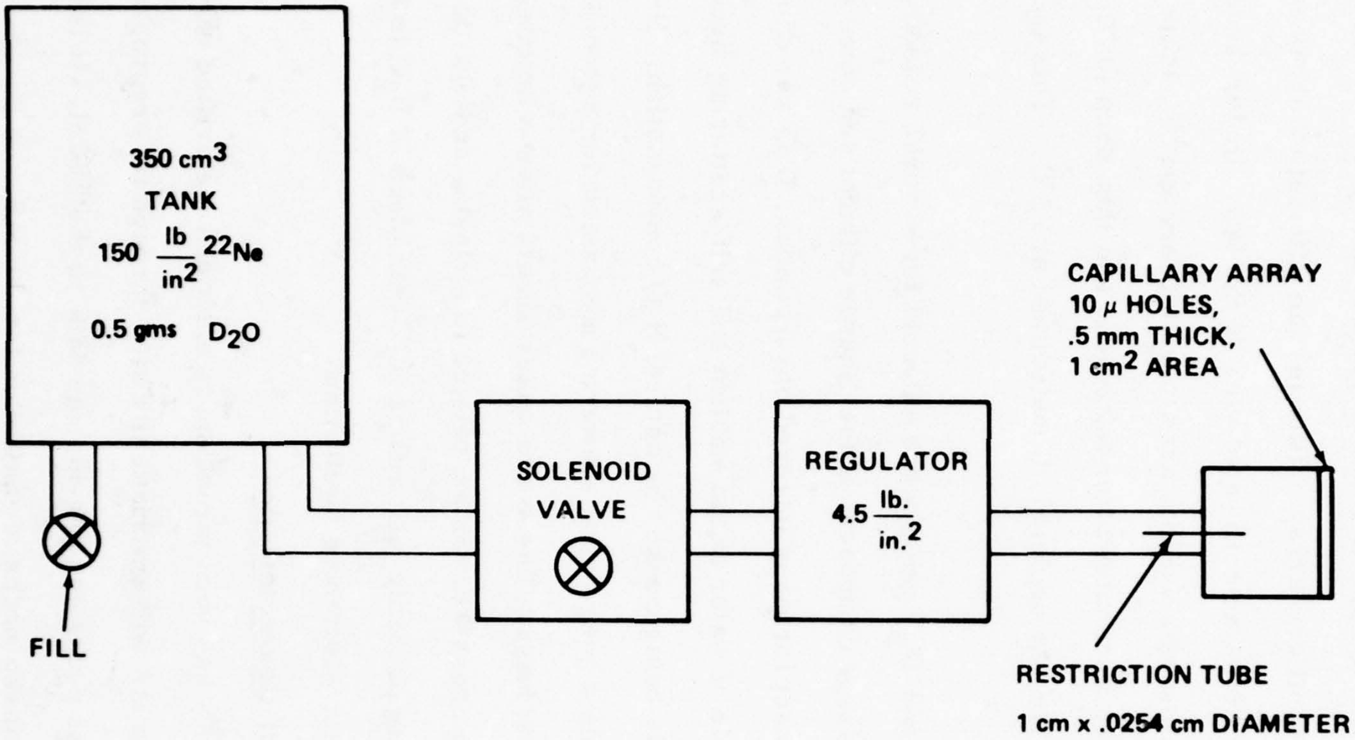

FIGURE 5. BLOCK DIAGRAM OF GAS RELEASE SYSTEM

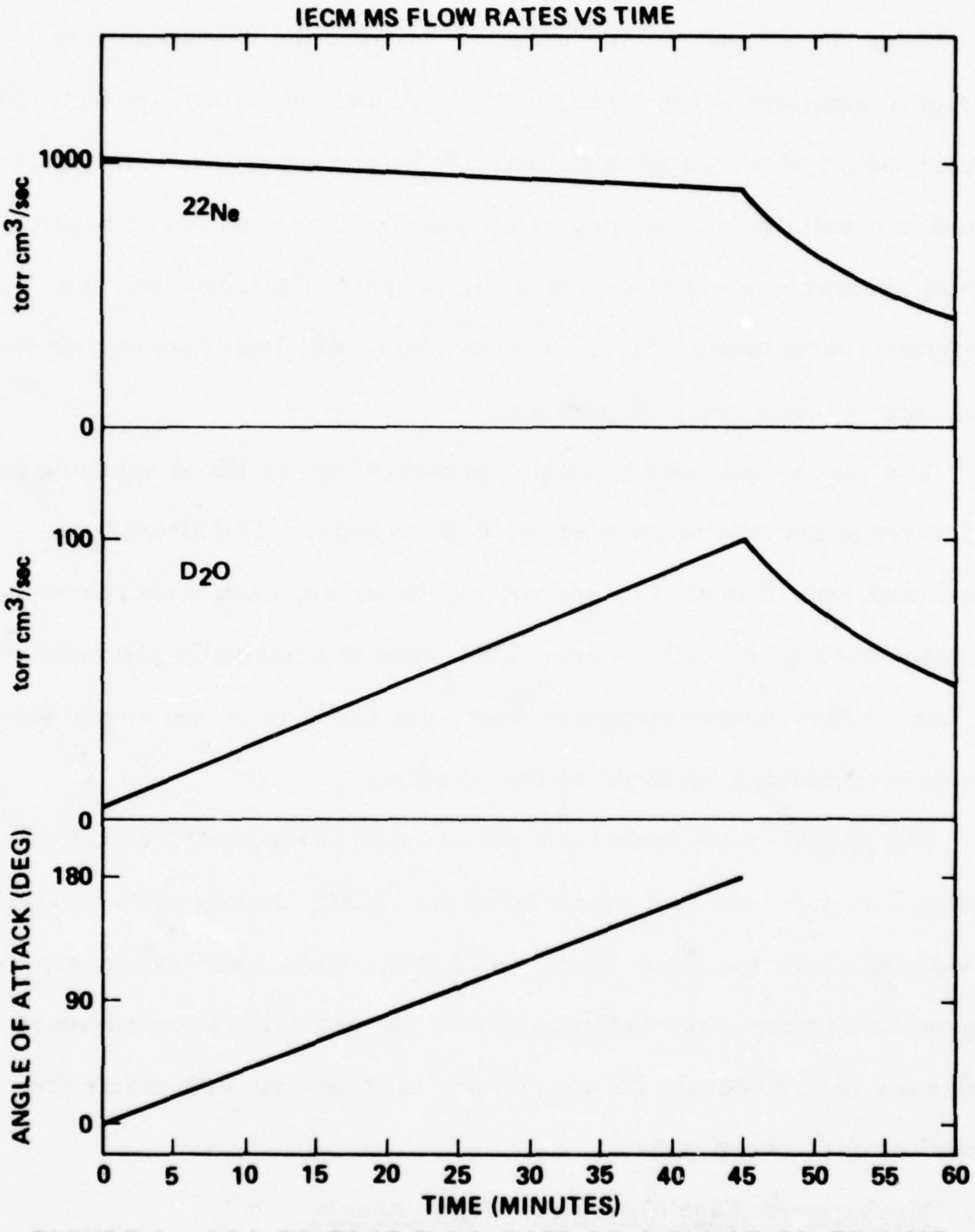

FIGURE 6. GAS RELEASE FLOW RATE AS A FUNCTION OF TIME

The normal mode will be for the IECM to interrogate the MS only once every two seconds. As described earlier, the MS would step through a complete sweep from 2 to 150 amu and then alternate with 150 measurements of the water peak (amu 18) before repeating. This mode provides a relatively long integration time for those masses with very low partial pressures while also measuring temporal fluctuations of the important contaminant, water. It does, however, limit data on masses other than water to once every 10 minutes.

The fast sweep mode is simply generated by the IECM speeding up its interrogation rate to once every 0.2 seconds. The alternating sweep with amu 18 is still in operation. However, each mass is now recorded once every 1.0 minute. This mode is principally planned for the Remote Manipulator operation where the IECM is picked up and moved around over various surfaces of the Shuttle.

The special mass mode is an abbreviated sweep mode. It can be activated at any time by a signal from the IECM. In this mode the MS only sweeps over the range from 2 to 48 amu. This mode was incorporated to provide a better time resolution during the gas calibration sequence. This mode can, however, be used at any time desired with either the normal or fast sweep mode.

4.0 Measurement Capabilities vs. Requirements

The measurement capabilities need to be analyzed at the two extremes of flow rate.

The flow regimes of interest are of two basic kinds, one being the directed stream flow superimposed on a Maxwell-Boltzmann distribution of thermal speeds which is due to the spacecraft vehicle velocity with respect to a stationary ambient atmosphere. This flow is of importance only at small angles of attack, i.e., small angles between the normal to the inlet orifice and the directed stream direction. The other flow of interest is that due to the scattered molecules which are the result of emitted spacecraft gas which collides with the free stream molecules and causes a small fraction of them and the ambient gas to be returned to the mass spectrometer inlet. This flow may be detectable at all angles of attack, and can be determined at small angles of attack as long as the molecule being looked at has a mass different from the ambient stream gas.

4.1 Directed Stream Flow

For a flux of known quantity through the inlet orifice we wish to know the flux which successfully passes through the collimator into the ion source region.

Calculations have been made to relate the angular spread of ambient gas velocities due to their thermal velocities superimposed on the flow velocity generated by the Shuttle velocity. The results are shown in Figure 7. The different s values were chosen in the range of expected ambient gas molecules and expected temperature range. It can be seen that the ambient gas molecules can reach the ion source at angles greater than 10 degrees to the velocity vector.

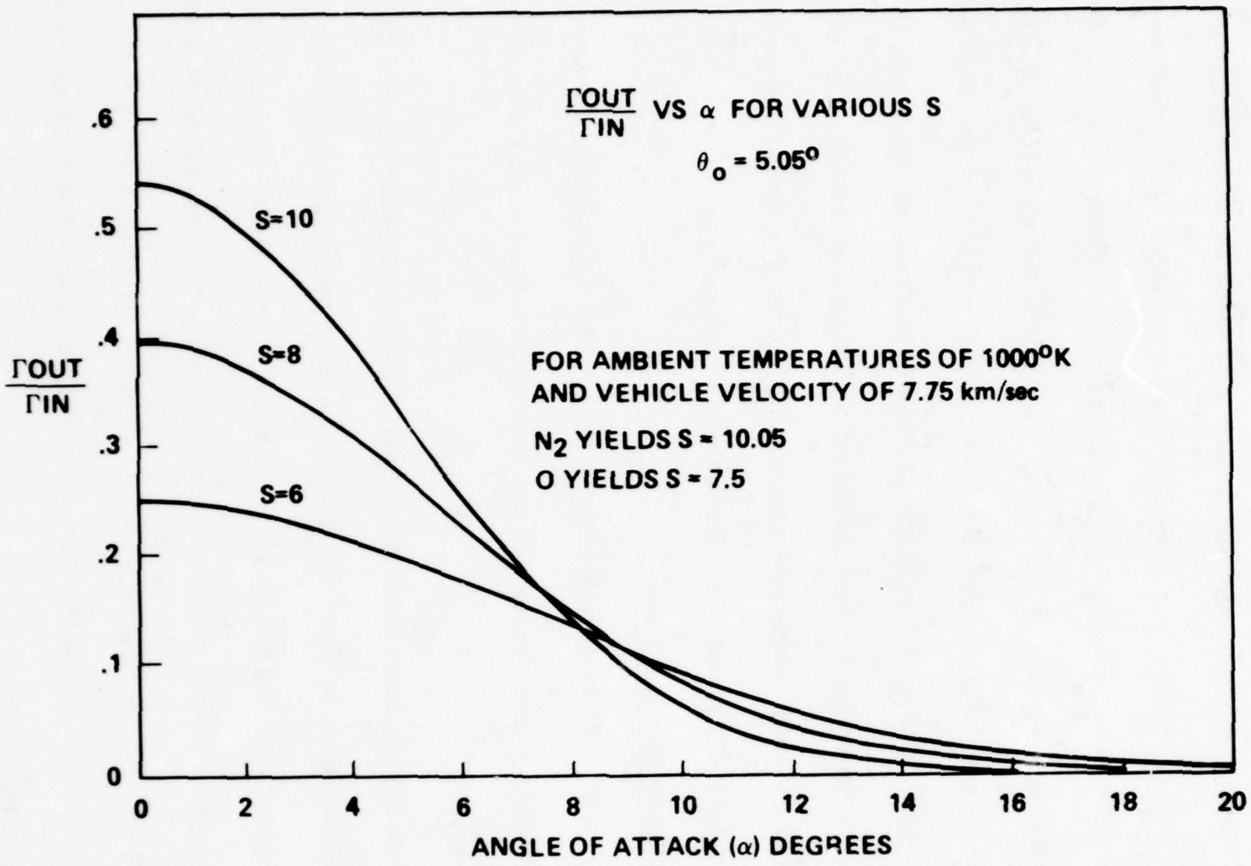

FIGURE 7. RATIO OF FLUX THROUGH INLET ORIFICE, Γ IN, TO FLUX WHICH REACHES ION SOURCE Γ OUT.

Using the appropriate Jacchia(3) values for density times stream velocity at 250 km altitude at zero angle of attack:

O_2	yields	1×10^{14} part/cm^2 sec
N_2	yields	7×10^{14} part/cm^2 sec
O	yields	1.2×10^{15} part/cm^2 sec

We get densities N_i in the ion source of

$N_i (O_2)$ due to O = 1.98×10^{10} part/cm^3

$N_i (O_2)$ due to O_2 = 5.34×10^{9} part/cm^3

or $N_i (O_2)$ total = 2.51×10^{10} part/cm^3

and $N_i (N_2)$ = 3.22×10^{10} part/cm^3

Recalling that the MS has a sensitivity of 1 count/sec for every 500 part/cm^3, we have the MS measurement rate N of

$N (O_2)$ = 5.02×10^7 counts/sec

$N (N_2)$ = 6.44×10^7 counts/sec

This rate is near the maximum rate for the pulse counting amplifier and above the maximum accumulator count for a 2-second integration. However, these numbers result only when the MS is looking directly at the ambient gas. Several degrees off this angle will drop the rate to a manageable value.

4.2 Random Flux

In the case of random fluxes of effluent gases being backscattered to the MS, we must determine the minimum detectable flux rate. The requirement of the CRDG is to be able to measure a random flux of 10^9 $cm^{-2}sec^{-1}sr^{-1}$. Assuming this flux to be water, we get a density in the ion source of

$$N_i(H_2O) = 2.86 \times 10^3 \text{ part/cm}^3.$$

The MS sensitivity reduces this to

$$N(H_2O) = 5.71 \text{ counts/sec}$$

which has a statistical uncertainty of 2.5 counts/sec.

Although this accuracy is low, it should be remembered that the data analysis can reduce the uncertainty by combining several successive sweeps to increase the sensitivity. Also, the normal data rate is for a two-second integration period.

5.0 Data Reduction

As has been shown in the previous section, the counting ratio will vary geratly depending on a variety of Shuttle operations and atmospheric conditions. For this reason, a large part of the past mission data reduction will consist of correlating MS measurements to the Shuttle maneuvers and attitude. Another important correlation will be to the Shuttle altitude to determine the ambient gas particle density. Using these correlations and an estimate of scattering cross sections, it is planned to calculate column densities for all masses which have significant counts.

In order to better identify sources of outgassing, it is planned to utilize the RMS to map the Shuttle surfaces. The IECM would be picked up out of the cargo bay by the RMS and maneuvered such that the MS and other instruments would be looking at certain critical surfaces. Again, it will be imperative to know where the MS is pointing at any given time.

These requirements for Shuttle attitude and altitude data as related to the IECM time clock have been requested and appear to be readily available.

It is expected that several weeks after each flight the necessary correlations will have been made and reduced data will be available. Identification of specific outgassing source materials may take longer (if at all possible) depending upon the complexity of mixtures and cracking patterns. (Some discussion of this is given in Part II.) Comparison of data from flight to flight is expected to give an indication if the Shuttle and Shuttle bay can be expected to get cleaner with continued flights.

PART II

1.0 Introduction

The two major contamination effects which the MS will measure are: (1) a column density of molecules above the instrument which can interfere with observations (e.g., infrared adsorption) and (2) scattering of the effluents into the instruments which can degrade the optics.

The overall philosophy in conducting these IECM MS measurements would be to do them in such a fashion that they can be used to predict contamination effects under other operational conditions. The best method of implementing this philosophy is to conduct the measurements in a manner that they assess the validity of and update models which describe the phenomena of interest. The IECM MS will measure the return flux of both outgassed products and a special gas release. Simple models are available by which the column density can be determined from the return flux (details will be presented later). The column density determined from these measurements would then be compared to that predicted from models and the models updated/modified in an appropriate fashion. A computer code prepared by the Martin Marietta Corporation is now "in hand" and can calculate the column densities around the Shuttle under a wide variety of conditions. However, the column density of particles around the vehicle is a complex function of the magnitude of several sources such as: (1) surface outgassing/offgassing, (2) cabin/Spacelab leakage, (3) exhaust from thruster firings, and (4) water dumps (e.g., flash evaporator).

Even if the measured and predicted values were in good agreement, one could never be certain whether this resulted from an accurate model or a lucky set of circumstances. Therefore, to utilize the data obtained from the MS measurements and confidently predict future results, there should be an in situ measurement of the sources in order to verify the expressions describing their magnitude. In the following sections we will discuss both the MS measurements of backscattering/column density and also the type of data that should be obtained when measuring the Shuttle emissions.

2.0 Mass Spectrometer Measurements of Column Density

In Figure 8 we depict in a simplified fashion the interaction of an unperturbed atmospheric particle with an emitted particle which is part of the column density above the MS with its highly collimated aperture. The flux of particles reaching the aperture (area A) is approximately$^{(4)}$

$$F \sim N_A(r) \quad N_o \left|\vec{V}_o - \vec{V}_A\right| \left(\frac{d\sigma}{dr}\right)^{\pi - \sigma}_{s/c} \quad \frac{A}{r^2} \quad (.1 \text{ str})\, r^2 dr \tag{1}$$

where $N_A(r)$ is the density of the emitted particles around the body, N_o is the atmospheric density, $\left|\vec{V}_o - \vec{V}_A\right| \sim V_o$ is the velocity of the atmosphere relative to the emissions, A/r^2 is roughly the solid angle subtended by the MS seen by a distance r away, $(.1 \text{ str})\, r^2 dr$ is the volume element above the MS, and $\left(\frac{d\sigma}{dr}\right)^{\pi - \sigma}_{s/c}$ is the probability that a particle will be scattered into angle $\pi - \sigma$ from the volume element. This equation assumes no additional scattering in the cloud above the MS which would tend to deflect the scattered particles away from the aperture. This limits the above equation to the regime where $\int \sigma n(r) dr = \sigma N_R \leq 1$ (σ is the cross section assumed to be $\sim 3 \times 10^{-15}$ cm^2), or the column density (N_R) above the instrument $\sim 3 \times 10^{14}/\text{cm}^2$. For larger values of the column density, equation 1 would have to be modified to account for additional scatters; however, this could be done in a relatively straightforward manner. For the purposes of this paper we will assume that $N_R \leq 10^{14}/\text{cm}^2$ which is also consistent with the upper limits of N_R (i.e., $\sim 10^{12}/\text{cm}^2$) requested by the CRDG. The

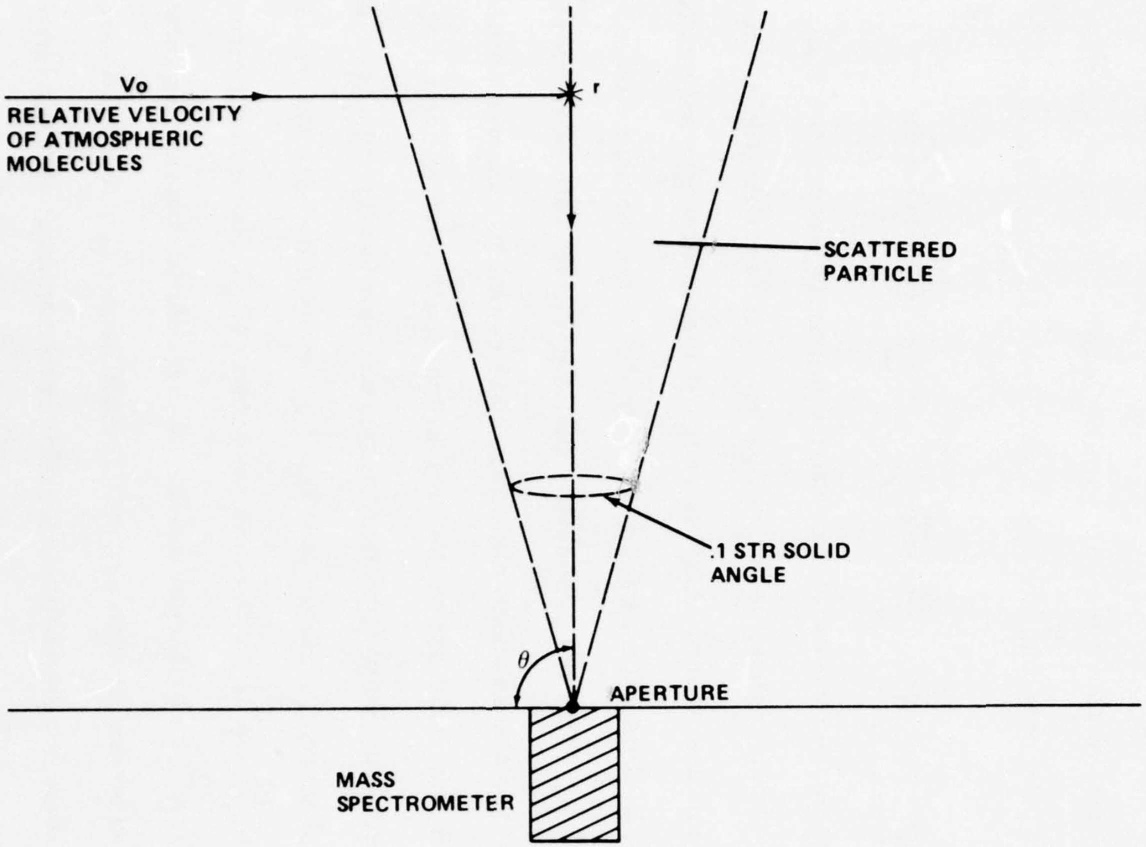

FIGURE 8. SIMPLIFIED PICTURE OF THE INTERACTION OF AN ATMOSPHERIC MOLECULE WITH A SPACECRAFT EMISSION AS SEEN BY THE MASS SPECTROMETER

function $\left(\frac{d\sigma}{dr}\right)_{s/c}^{\pi-\sigma}$ has been evaluated elsewhere for a collision which is isotropic in the center of mass (com) and equals $\frac{\sigma}{4\pi}\left(\sqrt{1-\beta^2\sin^2\sigma}+2\beta\cos\sigma+\frac{\beta^2\cos^2\sigma}{\sqrt{1-\beta^2\sin^2\sigma}}\right)$ where $\beta=\frac{V_{com}}{V'}$, σ = cross section, and V_{com} = velocity of the com, and V' is the velocity of the particle in the com after the collision. Equation 1, therefore, becomes

$$\frac{F(\sigma)}{A} \sim N_R N_o V_o \sigma\left(\frac{.1}{4\pi}\right)\left(\sqrt{1-\beta^2\sin^2\sigma}+2\beta\cos\sigma+\frac{\beta^2\cos^2\sigma}{\sqrt{1-\beta^2\sin^2\sigma}}\right) \quad (2)$$

Equation 2 needs some interpretation for the cases of $\beta \geq 1$. An example of this occurs in a partially inelastic collision where the particles scatter in the com with a velocity less than V_{com}; in these instances $\sigma \leq 90^\circ$. For the case of a completely inelastic collision ($\beta \rightarrow \infty$), then both the particles continue along a line defined by the direction of the incident particle or $\sigma \sim 0^\circ$. In Figure 9 we have plotted the relative flux (i.e., $\frac{F(\sigma)}{AN_R N_o V_o \sigma\left(\frac{.1}{4\pi}\right)}$) for the case of an atmospheric atomic oxygen colliding with a relatively stationary mass 22 particle. This was done for an elastic and an inelastic collision where 90% of the energy in the com is dissipated. As can be seen from this figure, the degree of inelasticity of the collision plays a dominant role in determining the scattering pattern.

One of the principal difficulties in calculating the return scattered fluxes (even if the column density is known) is inaccurate knowledge of the parameters characterizing the interaction of the atmosphere (principally

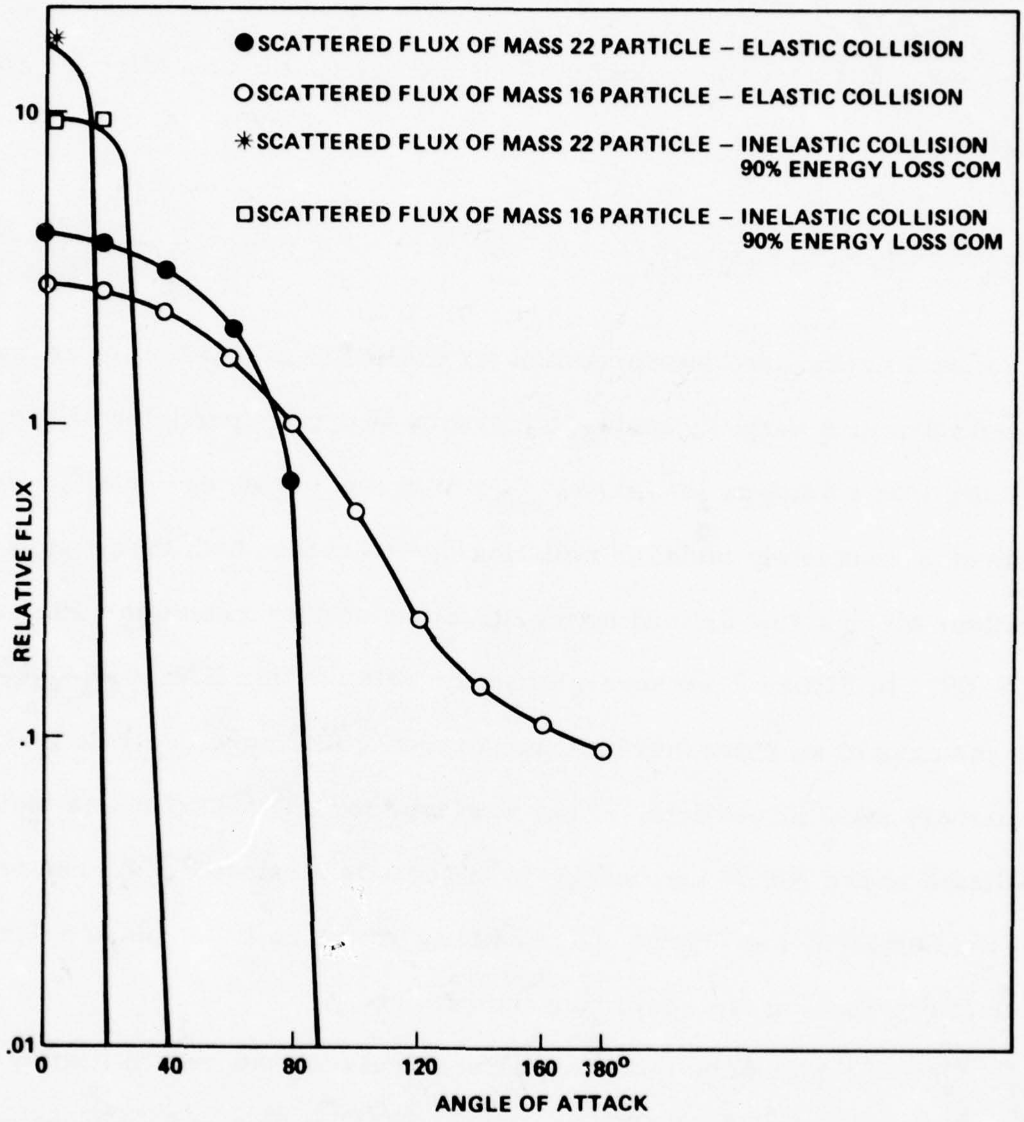

FIGURE 9. RELATIVE SCATTERED FLUX AS SEEN BY THE MASS SPECTROMETER. AN ATMOSPHERIC ATOMIC OXYGEN IS STRIKING A RELATIVELY STATIONARY (22 AMU) EMITTED ARTICLE AT 8km/sec. BOTH THE CASE OF AN ELASTIC AND INELASTIC COLLISION ARE PRESENTED.

atomic oxygen) with spacecraft emitted molecules at velocity differences of 8 km/sec (i.e., $V_o \sim 8$ km/sec). At this time one can only extrapolate from very fragmentary laboratory studies in defining parameters such as cross sections and degree of elasticity (i.e., parameter β). However, the controlled release of the Ne^{22}, D_2O gas cloud (mentioned previously) during the MS measurements can result in values being obtained for these parameters under actual in situ conditions. In fact, Figure 9 shows the type of data that might be expected from the release as both the MS and release system are slowly rotated through different angles of attack. The collision of the atomic oxygen and Ne^{22} should be basically elastic and the pattern for the scattered particles should be similar to that in Figure 9 for the elastic collision. On the other hand, one might expect the collision between the atomic oxygen and D_2O to excite various vibration/rotational levels and the patterns may be similar to those in Figure 9 for the inelastic collision.

Given the magnitude of the release $\sim 10^{19}$ molecules/sec and some assumptions of the geometry and velocity of the cloud, the anticipated N_R from the release is $\sim 10^{14}/cm^2$. This column density is sufficiently low that additional deflections in the cloud should not be significant. Using appropriate values for the MS aperture area, calibration constants and other constants, a curve fit of the in situ gas release data to equation 2 can give experimental values to parameters such as σ and degree of elasticity.

To define a column density of effluents above the Shuttle, the MS should be fixed in position and the Shuttle rotated in angle of attack so that a backscattered pattern similar to that of Figure 9 is obtained. Using the interaction parameters obtained from the gas release, a numerical value for the N_r can be obtained utilizing equation 2. For the case of H_2O the calculations should be fairly accurate. In the instance of other molecules (e.g., N_2 and O_2), one would have to assume that the interaction parameters are similar. This may not be the case, and it would be beneficial if additional gas release were conducted using a diatomic molecule instead of D_2O.

3.0 Measurements of Shuttle Emission Characteristics

As discussed before, to fully utilize the MS measurements and be able to confidently predict backscatter/column densities under a variety of in situ conditions, measurements must be made to validate the equations describing the in situ characteristics of Shuttle emissions. Fortunately, during part of the measurement program, a projected maneuver is to have the IECM picked up by the Remote Manipulator System and map the Shuttle emissions. This would allow an in situ characterizing of the sources. It is of interest to compare the magnitude of the various sources in order to establish their relative importance and priority for measurement purposes. The magnitude of cabin leakage has been specified at ~ 3 kgm/day or $\sim .03$ gms/sec. Assuming an average outgassing rate of $\sim 10^{-10}$ gm/cm^2 sec for the non-metallic surfaces of Shuttle and total top surface area of $\sim 600\ m^2$, then the average outgassing rate of the upper surfaces of Shuttle is $\sim 6 \times 10^{-4}$ gm/sec. The flash evaporator can eject H_2O at a rate of up to ~ 90 kgm/day or ~ 1 gm/sec. While in orbit we will assume that only the vernier thrusters will operate to control attitude, and at a rate of a 40 msec thrust every minute there are $\sim$ 2 gms of material ejected/40 msec thrust or $\sim$ .03 gms/sec.(5)

However, these very tentatively calculated rates have to be modified by the following considerations:

a. Both the flash evaporator and the vernier thrusters generally point down and away from the payload bay area, and the relative amount of material effectly "seen" by an experiment can be considerably less than that calculated depending upon how much impinges and is re-emitted by the wings, etc.

b. The 3 kgm/day of cabin leakage could be an upper limit, and the actual amount may be substantially less.

c. The desorption rate early in the mission is expected to be substantially greater than $10^{-10}\ gm/cm^2\ sec$.

It would, therefore, appear that at a first approximation all the sources are equally important, and all should be measured. In particular, the thermal dependence $\sim e^{+(T\ -\ 100^\circ C)/29^\circ C}$ of long-term outgassing and both the thermal $e^{E/R(1/373\ \cdot\ -1/T)}$ and temporal $e^{-t/18\ hrs}$ dependence of the early desorption should be verified (E is the activation energy

$\sim$12 K cal/mole for H_2O and R = 2 K cal/mole °K). The emission pattern of both the thrusters and flash evaporators should be checked, especially the rates for angles > 90° off nozzle axis since this portion of the emission can directly contribute to column densities above the bay.

Of the sources, it would appear that the species of emitted particles from the non-metallic surfaces would give the most complex (and least interpretable) MS spectra. This is due in part to the potential scavenging properties of atomic oxygen striking the surface. For example, at 250 km the environmental atomic oxygen will strike a surface orientated toward the ram direction at a flux rate of $\sim 10^{15}/cm^2$ sec. It is possible that the O will scavenge the atoms on the non-metallic surface as on metallic surfaces and be readmitted in molecular form (i.e., O_2, H_2O, CO).(6) In any event, assuming all the O is readmitted, the mass of these admissions is $\sim 3 \times 10^{-8}$ gms/cm^2 sec which is much greater than the surface emission rate mentioned earlier. Therefore, the impingement of atomic oxygen could well be the dominant effect of surface offgassing/outgassing, and the surface emissions should also be measured when exposed to the atomic oxygen flux.

To help assess the intrinsic capability of a mass spectrometer to detect the various species emitted from a surface, we have investigated the possibility of uniquely determining the species presently expected to be outgassed from the surface. Taking the early desorption from the teflon liner as typical we have the following rates:

H_2O	$\sim 5 \times 10^{13}$ molecules/cm^2 sec
N_2	$\sim 2 \times 10^{13}$ molecules/cm^2 sec
CO_2	$\sim 1 \times 10^{13}$ molecules/cm^2 sec
O_2	$\sim 3 \times 10^{12}$ molecules/cm^2 sec
$C_3H_{10}O_1Si_1$	$\sim 6 \times 10^{12}$ molecules/cm^2 sec

where the trimethyl silanol is assumed equivalent to the heavy molecule outgassing. Table I shows the relative fractionalization pattern as seen by the detector of the mass spectrometer based only on the above emission rates.(7) We can see by this characterizing example that, although some overlap is observed, the patterns of the individual molecules is sufficiently unique to unambiguously specify them. Therefore, it appears possible to uniquely determine the constituents outgassed from a surface for a "reasonable" grouping of species. We are also looking into the possibility of having a computerized search of several hundred compounds utilizing statistical techniques in order to analyze the mass spectrometer output in a more rigorous fashion.

TABLE I

Relative Intensities of Specific Masses Seen by a Mass Spectrometer after the Gas Molecules Have Been Fractionalized by the Ion Source

AMU Number	Imput Molecules				
	H_2O	N_2	CO_2	O_2	$C_3H_{10}O_1Si_1$
12			13		
13			2		
14		20			
15					8
16	9		19	6	
17	211				
18	1000				
19	5				
20	3	2			
28		400	16		4
29					
32				160	
33				1	
34					
43					5
44			200		
45					29
47					15
59					15
61					3
75					120
76					7
77					4

In Summary

The IECM mass spectrometer is basically a highly collimated version of an instrument which has flown on the Atmospheric Explorer series and which was developed by the University of Michigan. The sensitivity of the instrument is $\sim 10^9/\text{cm}^2$ sec for non-reactive gases. The principal measurements of the MS will be to measure directional backscattered rates and column densities due to Shuttle emissions. A controlled gas release of Ne^{22}, D_2O will allow a measurement of the interaction parameters (e.g., cross section and degree of elasticity) under in situ conditions. Utilizing the measured values of these parameters, one can then define the column density above the instrument. In addition, to be able to use this data and confidently predict the column densities under other in situ conditions, measurements must be made to verify the equations describing the strength of the sources of the Shuttle emissions.

References

1. Payload Contamination Control Requirements for STS Induced Environment, STS Payload Contamination Requirements Definition Group Report, NASA/MSFC, July 22, 1975.

2. Pelz, David G., Carl A. Reber, Alan E. Hedin, and George R. Carignan, "A Neutral Atmosphere Composition Experiment for the Atmospheric Explorer CDNE," Radio Science 8, No. 4, pp. 277-285, April 1973.

3. Jacchia, L. G., "Static Diffusion Models of the Upper Atmosphere with Empirical Temperature Profiles," Smithsonian Contributions to Astrophysics 8, No. 9, 1965.

4. Preliminary Assessment of the Vacuum Environment in the Wake of Large Space Vehicles, NASA TMX, W. Oran and R. Naumann.

5. From the User's Manual "Shuttle/Payload Contamination Program," April 1977, Martin Marietta Corp.

6. See, for example, "Atomic Oxygen--Metal Surface Studies as Applied to Mass Spectrometer Measurements," G. W. Sjolander, J. G. R. 81, August 1976, p. 3767.

7. See "Compilation of Mass Spectral Data," A. Cornu and R. Massot, Heyden and Son Ltd., London, 1966.

QUARTZ CRYSTAL MICROBALANCE SYSTEMS FOR SHUTTLE CONTAMINATION MEASUREMENTS *

D. McKeown and C.R. Claysmith
Faraday Laboratories, La Jolla, CA

ABSTRACT

The adsorption of contamination on a surface is highly temperature dependent. In order to conduct fundamental studies of contamination on Shuttle, surface temperatures must be controlled over a range common to the space environment. Two different types of temperature controlled quartz crystal microbalance systems using active and passive cooling have been developed to measure contamination as a function of temperature. The active system uses thermoelectric devices for automatic temperature control. Its purpose is to measure volatile and low-volatile contaminants, such as, lubricants and RTV's. The system consists of a controller and five remotely located 15-MHz optically-polished quartz crystal mass sensors. Each sensor can be set by ground command at five predetermined temperatures between -60 and +80°C ± 1°C or free run. The frequency change of each sensor is readout digitally to 1 Hz giving a contamination loading sensitivity of 1.56×10^{-9} g/cm^2. The passive system is radiatively cooled and operates at cryogenic temperatures. Its purpose is to measure high-volatile contaminants, such as, water vapor. It consists of a controller and sensor head. The sensor head contains two removable sensors. One sensor operates below the freezing point of water and monitors contamination including water vapor. The other sensor is heated above the freezing point of water and monitors the contamination background. The temperature of each sensor is monitored between -153 and +37°C ± 1°C. The mass sensitivity and frequency readout are the same as for the active system.

1.0 INTRODUCTION

When the Shuttle approaches orbital altitude, the atmospheric density will drop to low levels and the mean-free-path for gases will become larger than the dimension of the craft. At this point, a cloud of Volatile Condensable Material (VCM) will begin to envelope the Shuttle. This

---

* Work supported under NASA MSFC, AL Contract NAS 8-32110

cloud consists primarily of the outgassing of materials used on its construction, desorption of surface contamination, rocket exhaust and waste dumps. Most of the particles in this induced contamination cloud will stream off radially into space with no adverse affect on surfaces. A fraction of these particles, though, will strike and contaminate various sensitive surfaces.

Surfaces can be contaminated by direct line of sight to the source, by redirection of contamination particles, by particle-particle interactions with the upper atmosphere and by particles of contamination that leave the Shuttle and vaporize on exposure to the sun. Today, I would like to describe two types of quartz crystal microbalance systems that we have developed for the NASA Marshall Space Flight Center to measure surface contamination on Shuttle. One system is a Temperature-Controlled Quartz Crystal Microbalance (TQCM) and the other is a Cryogenic Quartz Crystal Microbalance (CQCM).

2.0 SURFACE CONTAMINATION

The contamination of surfaces in space is affected by many parameters. Some of these parameters are temperature, type of material, condition of surface, exposure to solar radiation, sputtering[1] by the upper atmosphere, angle of incidence and intensity of the contamination flux. At altitudes beyond the magnetosphere, charging of the surface and ionization of the contaminate flux by the solar plasma can lead to the enhancement of contamination by mutual attraction.

Of all the various parameters affecting contamination, the temperature of the surface is dominant. This can be seen by going to extremes. If the surface temperature is steadily increased, the contaminants sticking coefficients will decrease and the desorption rates will increase resulting in low-levels of contamination. If the temperature is steadily decreased to values below the freezing points of the contaminants, the sticking coefficient will increase and desorption will decrease resulting in high-levels of contamination.

For purposes of a QCM contamination experiment, it is useful to divide contaminants into three broad groups depending upon the contaminants desorption activation energy, E, (cal/g-mol).

The first group is the high-volatiles for which $E < 10{,}000$ and covers materials, such as, H_2O and CO_2. The temperature of a QCM must be steadily decreased below about -130°C to temperatures approaching liquid helium before these VCM's freeze out and make accurate measurements possible.

The second group are the volatiles for which $10{,}000 < E < 25{,}000$.

This range covers, for example, various types of lubricants and conformal coatings. Here, cooling of a QCM should start at about +30°C and be steadily decreased before measurements can be made.

The third group are the low-volatiles for which $E > 25,000$. This group covers, for example, epoxies, RTV's and rocket exhaust materials. A QCM operating at the ambient spacecraft temperature will usually give good results for these VCM's.

3.0 TQCM SYSTEM

3.1 TQCM Design

The TQCM System was developed to measure the flux of volatile and low-volatile contamination on Shuttle and is similar in design to the TQCM constructed for laboratory measurements[2].

The TQCM System is shown in Fig. 1. It consists of a controller and five electronics, sensors and heat sinks.

The mass sensors are instrumented with high-sensitive 15-MHz crystals with a mass sensitivity of 1.56×10^{-9} g/cm^2-Hz. These crystals are over two times more sensitive than 10-MHz crystals presently being used in Faraday Laboratories QCM's[3]. The frequency of each sensor is readout digitally to ± 1 Hz. The crystals are optically polished and coated with MgF_2 to simulate an optical surface. Each sensor can be set by ground command at five predetermined temperatures between −60 and +80°C ± 1°C or free run to obtain minimum operating temperature. The minimum temperature is 80°C below ambient. Maximum sensor loading is approximately 3×10^{-4} g/cm^2. If maximum loading is reached, the sensors can be cleaned by commanding the TQCM to +80°C. The operating temperatures of each sensor are monitored between −103 and +87°C.

By pointing the sensors in different directions, the following contamination studies can be made.

1) Temperature dependence
2) Adsorption and desorption rates
3) Spatial distribution
4) Time decay constants
5) Diurnal variations
6) Effects of solar irradiation
7) Upper atmosphere interactions
8) Sputtering

The spatial distribution with time and temperature will be defined by the output of the five separate TQCM sensors as the sensors are periodically

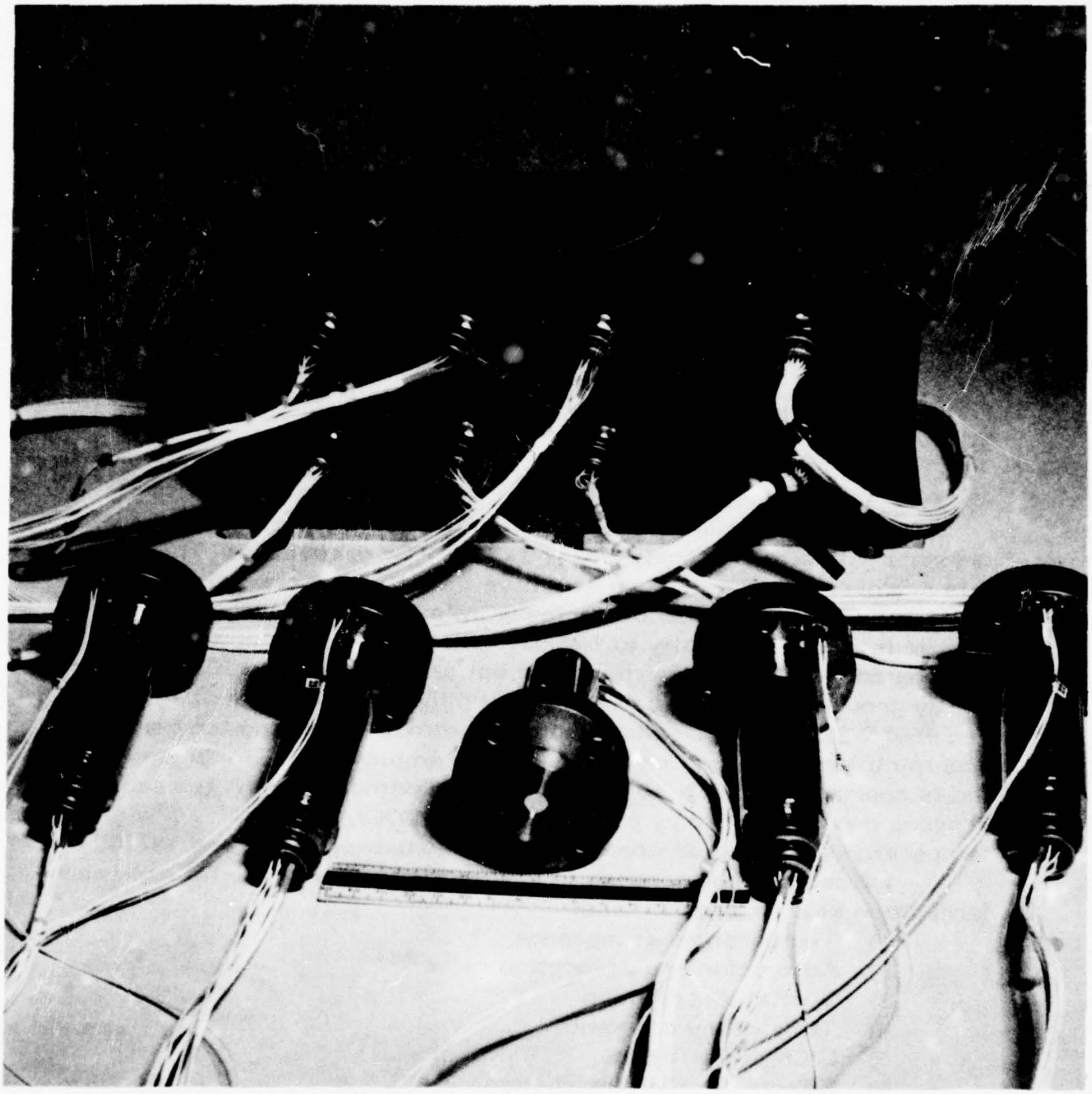

Fig. 1 TQCM System

commanded to various temperatures. At temperatures above +30°C, the low-volatile contaminants will be measured. Below +30°C, volatile materials will be measured. Computer programs will be written for "quick look" data reduction and for data analysis of the measurements to separate out the various contaminant species.

The mechanical specifications of the TQCM Controller are shown in Fig. 2. This drawing is taken from a large design print and the Controller dimensions are in inches (19.05 x 16.51 x 33.02 cm) to facilitate its machining.

The TQCM Electronics (3.18 by 11.75 cm), Heat Sink (6.35 by 1.9 cm) and Sensor (2.92 by 2.79 cm) are shown in Fig. 3.

The heat sink is gold plated aluminum for lightness. Its temperature is monitored by a Pt thermometer between -83 and +107°C ± 1°C.

The electronics makes use of new low-power integrated circuits[4]. Its power dissipation is only 15 mW as compared to 250 mW in earlier units and significantly reduces the power load to the heat sink. The electronics provides circuits to drive the mass sensor and a high-gain low-impedance output amplifier for remote operation.

The removable mass sensor is designed for ease of replacement by loosening the lock and set screws on the heat sink. The crystal set is also replaceable. The precision Pt thermometer provides temperature readout to 0.5%. A specially designed two-stage thermoelectric device cools the crystals. It operates at ± 7 Vdc for heating or cooling as compared to ± 1.5 Vdc for laboratory devices for improved power supply efficiency.

The TQCM Controller Block Diagram is shown in Fig. 4. Separate high and low-power DC/DC supplies provide power for the thermoelectric devices and temperature control and sensor electronics. The frequency counter reads out TQCM frequencies to 65,535 Hz to ± 1 Hz. By observing each time the counter resets itself, the full 300 kHz loading range of the crystal sensor can be attained.

The five remotely located sensor electronics are connected at J3-J7 and heat sinks at J8.

3.2 TQCM Operation

The TQCM commanded modes of operation are given in Table 1. The TQCM operates at +28 ± 4 Vdc. Minimum power is 1.85 W with all QCM's ON and sensors operating at ambient temperatures. Maximum power is 71.12 W with all QCM's and all thermoelectric devices ON for cooling of the sensors.

The TQCM Controller is designed to maintain any sensor opera-

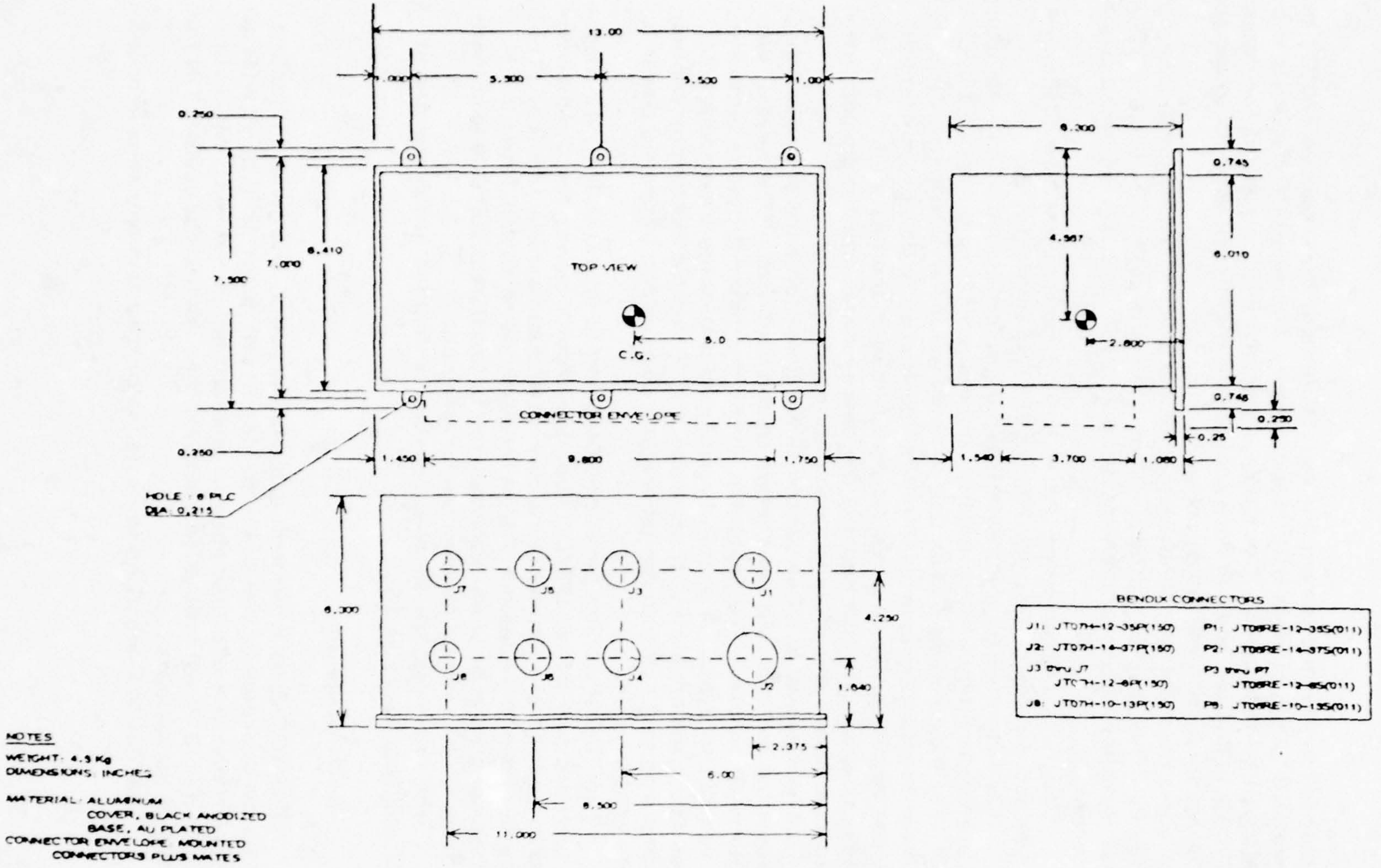

Fig. 2 TQCM Controller Mechanical Specifications

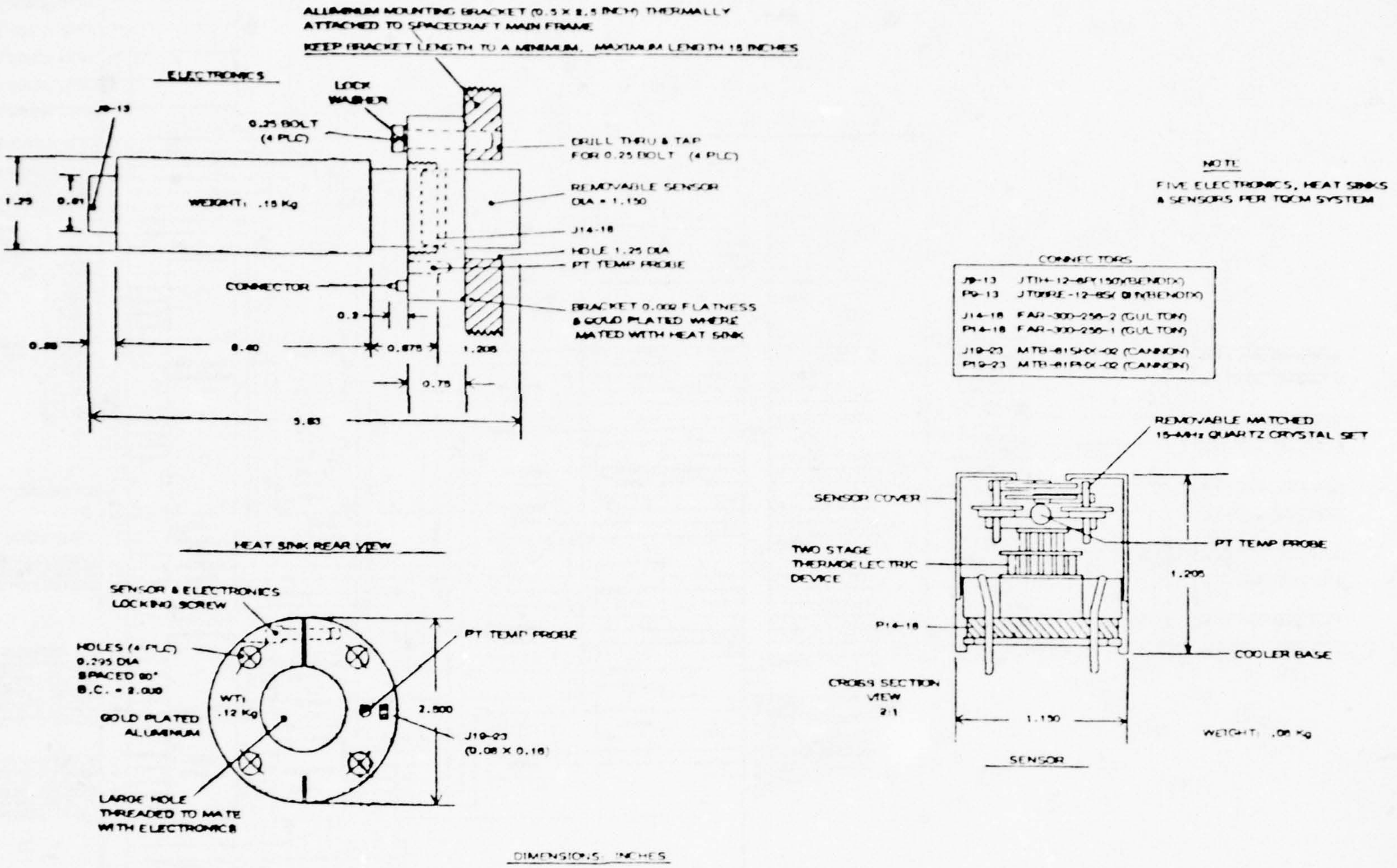

CONNECTORS

J9-13	JTIH-12-8P(150)(BENDIX)
P9-13	JT06RE-12-8S(DIN)(BENDIX)
J14-18	FAR-300-256-2 (GULTON)
P14-18	FAR-300-256-1 (GULTON)
J19-23	MTB-81SHX-02 (CANNON)
P19-23	MTB-81PHX-02 (CANNON)

Fig. 3 TQCM Electronics, Heat Sink and Sensor Specifications

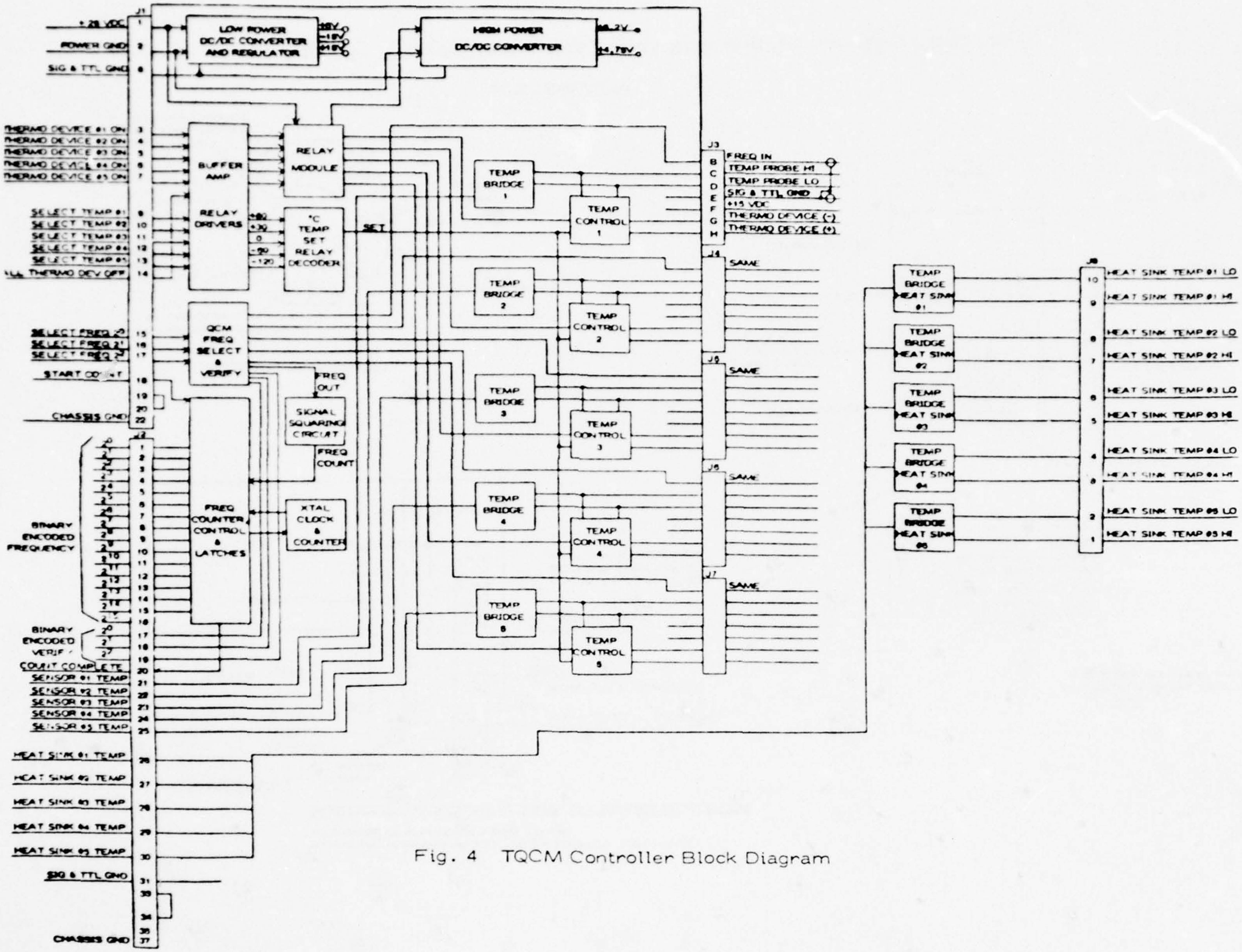

Fig. 4 TQCM Controller Block Diagram

Table 1 TQCM System Operating Powers

Mode		Description	Pwr In	Inst Pwr	Eff %
1.	ON	All QCM's and Controller ON	1.85	1.11	60
2.	Heat 1	All QCM's and Controller ON 1 Sensor heating maximum rate	5.44	2.72	50
3.	Heat 5	All QCM's and Controller ON 5 Sensor heating maximum rate	13.35	8.68	65
4.	Cool 1	All QCM's and Controller ON 1 Sensor cooling maximum rate	17.82	11.94	67
5.	Cool 5	All QCM's and Controller ON 5 Sensor cooling maximum rate	71.12	54.76	77
6.	Cool 5	All QCM's and Controller ON 5 Sensors stabilized −60°C	51.08	36.78	72
7.	Cool 5	All QCM's and Controller ON 5 Sensors stabilized −30°C	28.93	20.25	70
8.	Cool 5	All QCM's and Controller ON 5 Sensors stabilized 0°C	15.03	9.92	66
9.	Heat 5	All QCM's and Controller ON 5 Sensors stabilized +30°C	7.15	3.93	55
10.	Heat 5	All QCM's and Controller ON 5 Sensors stabilized +80°C	12.19	7.68	63

ting in a cooling mode at -30°C if there is a failure in the command data link. The -30°C mode was picked because of the relatively low power required to maintain cooling.

The TQCM response to temperature command is very rapid as is shown in Fig. 5. To cool a sensor from +80°C to -60°C requires 7 minutes and 3 minutes to return to +80°C.

3.3 TQCM Laboratory Measurements

The TQCM was tested in a laboratory vacuum chamber at 7 x 10^{-7} Torr by measuring the contamination of a surface by roughing pump oil. The adsorption and desorption of oil by an aluminum surface is shown in Fig. 6. Below -30°C absorption predominated and contamination built up. Above -30°C desorption predominated. The break in the curve at about -10°C resulted from a phase change in the contamination from solid to liquid.

The number of monolayers of contamination on the aluminum surface with temperature is shown in Fig. 7. The surface was first cleaned at +80°C and rapidly dropped to -20°C. The contamination loading was then allowed to reach equilibrium at various higher temperatures. From the figure, it can be seen that there was always oil contamination present below +30°C. It would be impossible to have made these measurements without a temperature-controlled QCM because there is no net mass change at equilibrium.

Data similar to Fig. 6 and 7 should be seen on Shuttle but of a much more complex nature because of the large variety of contaminants present. Solar radiation of the contaminated surface and upper atmospheric interactions will further complicate the analysis.

4.0 CQCM SYSTEM

4.1 CQCM Design

The CQCM is radiatively cooled and operates at cryogenic temperatures[5]. It is designed to monitor highly volatile contaminants. The CQCM, consisting of a Controller and Sensor Head, is shown in Fig. 8. Measurements are made with two removable 15-MHz mass sensors mounted in the radiant cooler. One sensor operates below the freezing point of water which is approximately -133°C (140°K) in vacuum. It monitors contamination including that of water vapor. The second sensor is heated above the freezing point of water and monitors the contamination background. It provides a

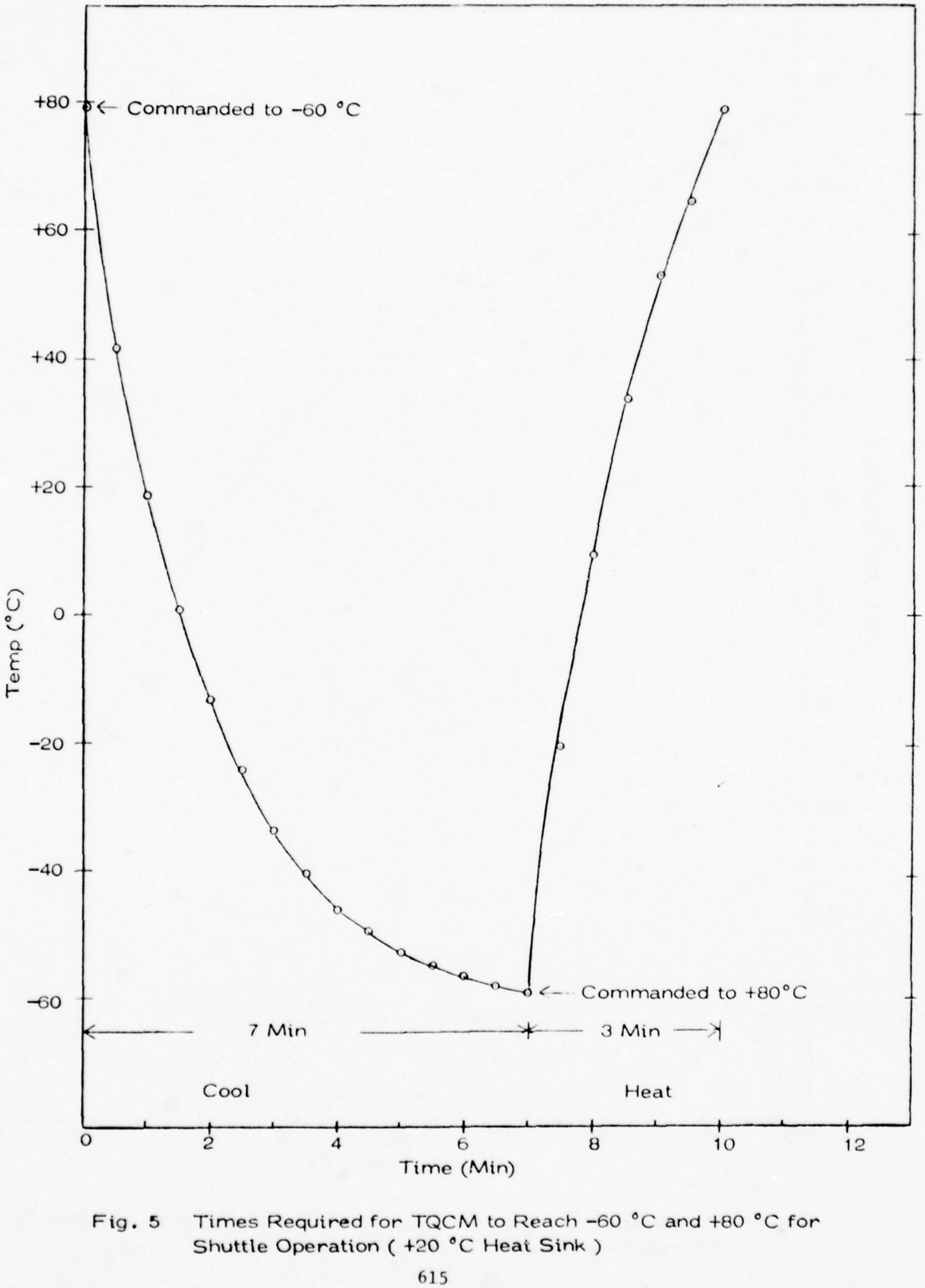

Fig. 5 Times Required for TQCM to Reach -60 °C and +80 °C for Shuttle Operation (+20 °C Heat Sink)

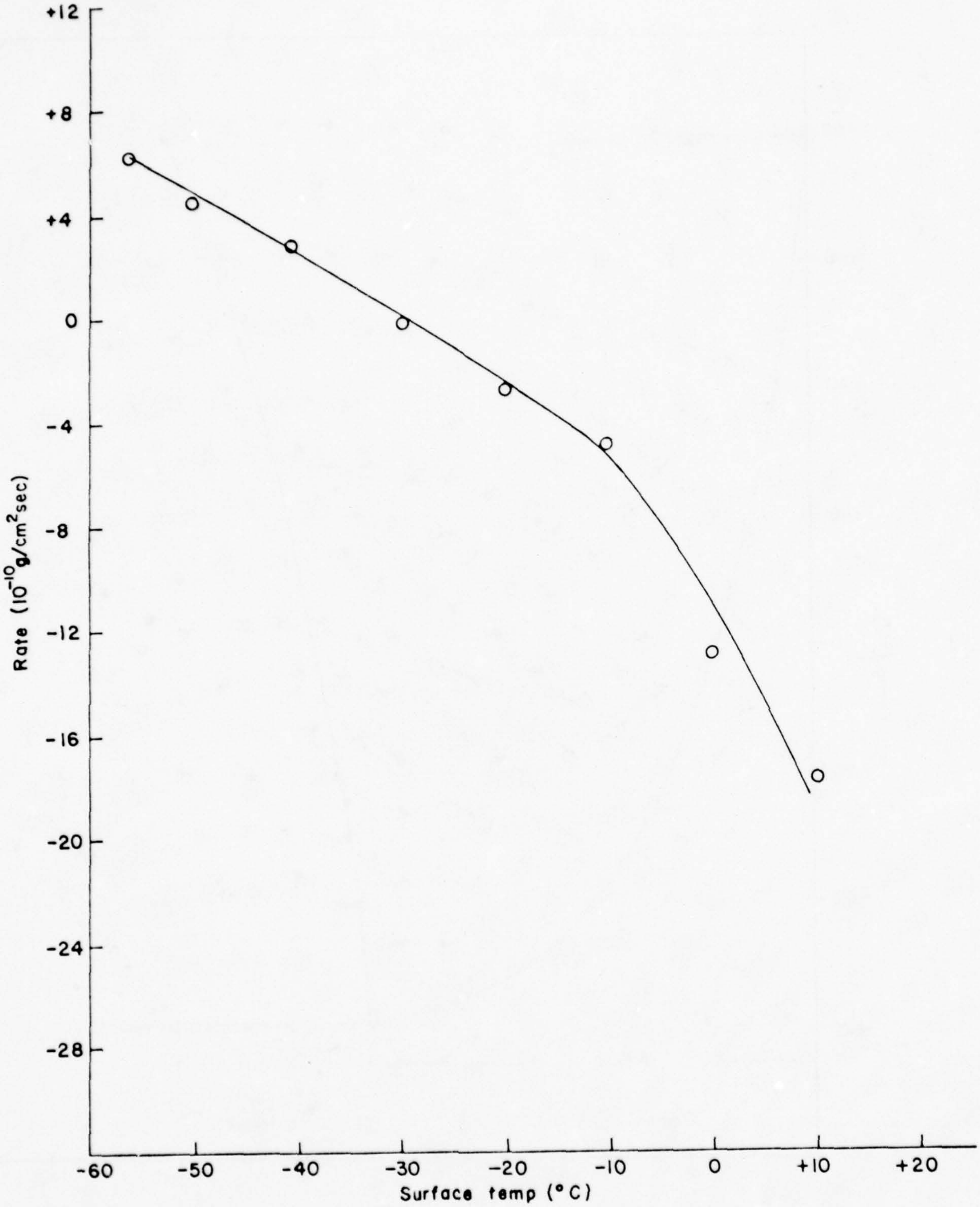

Fig. 6 Contamination adsorption and desorption rates with temperature for roughing pump oil on aluminum in vacuum

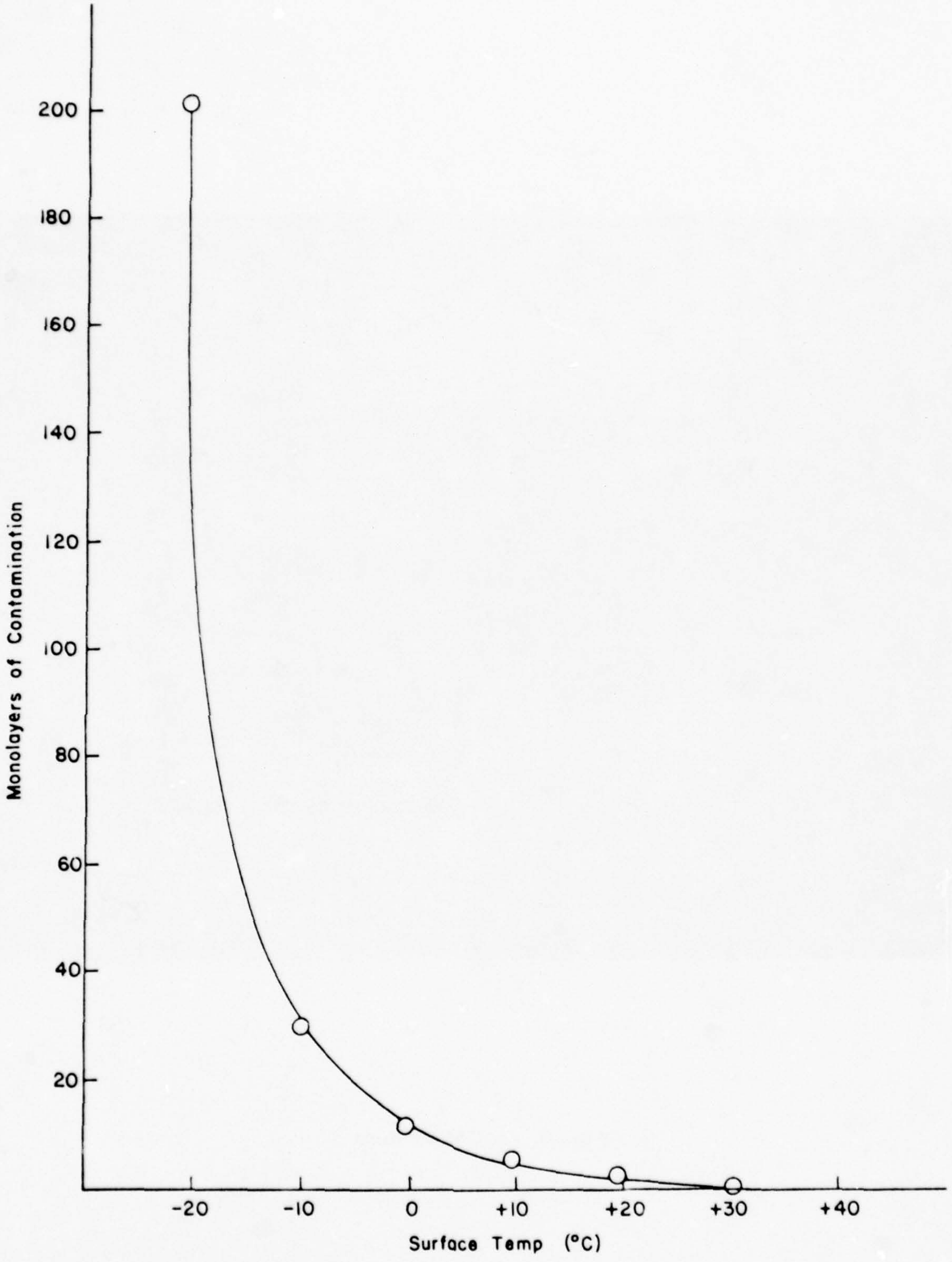

Fig. 7 Number of contamination monolayers of roughing pump oil on aluminum at equilibrium in vacuum

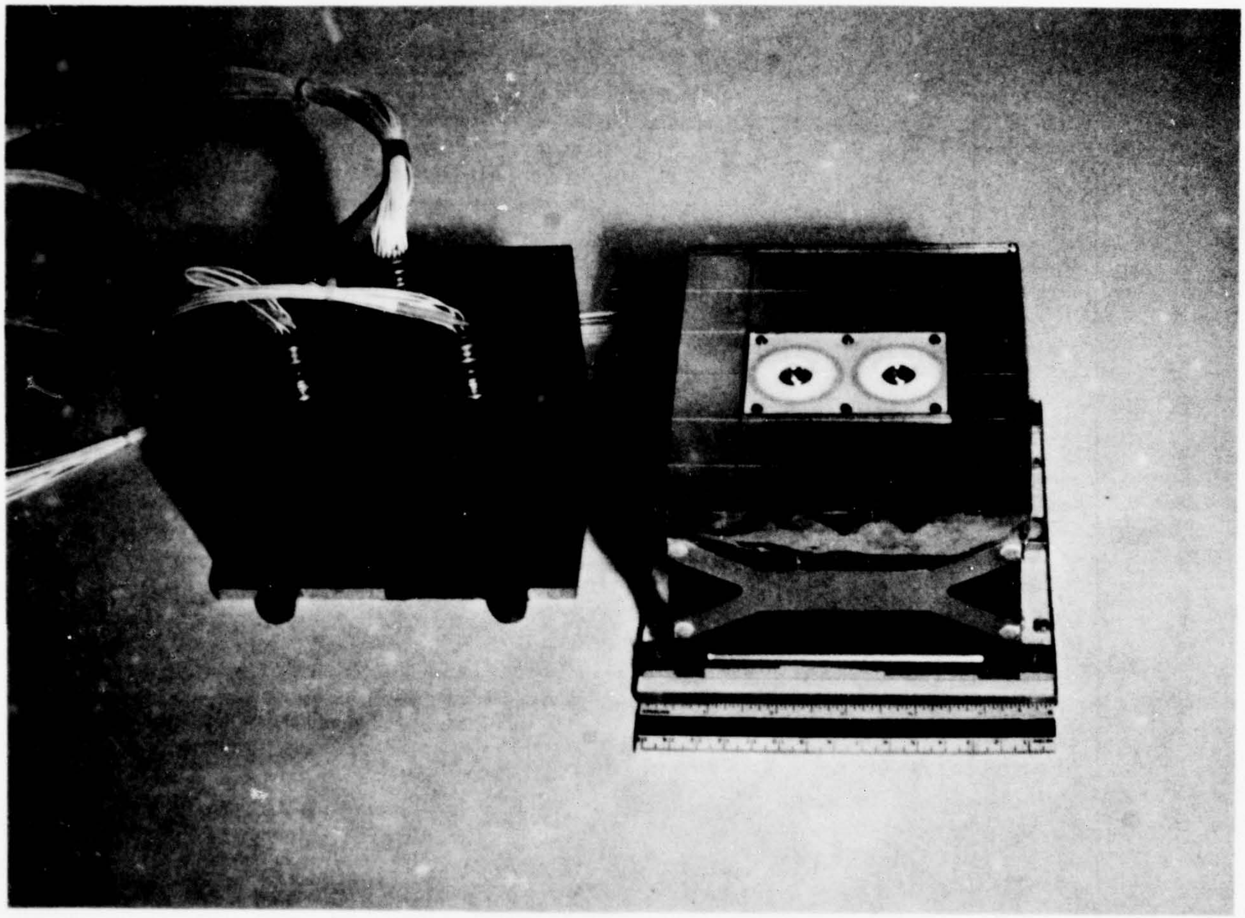

Fig. 8 CQCM System

reference from which the density of the water vapor cloud enveloping Shuttle can be determined. The mass measurement range of each sensor is the same as the TQCM. The temperature of each sensor is monitored between −153 and +37°C (120 and 310°K). The design incorporates a low-power electronics[4] and heaters for ice removal.

The CQCM Controller (13.21 x 14.99 x 8.41 cm) mechanical specifications are shown in Fig. 9.

The CQCM Sensor Head (15.24 x 16.15 x 8.41 cm) design is shown in Fig. 10. The Sensor Head contains the radiant cooler, two removable mass sensors, oscillators and output amplifiers.

The radiant cooler is a plane surface constructed from one piece of aluminum. The sensors are mounted in a well, machined in the radiator. Second-surface quartz/silver mirrors are attached to the radiator by an RTV. The mirrors have a solar absorptance of approximately 0.06 and a thermal emittance of approximately 0.80.

The radiator is attached to the base plate by four high-strength fiberglass-epoxy laminate standoffs. The two electronic units are connected to the mass sensors by stableohm leads to provide thermal isolation. Radiative heat exchange from spacecraft to the radiator is minimized using a stack of 20 multilayer superinsulation of gold plated Kapton.

The CQCM Controller Block Diagram is shown in Fig. 11. The Controller provides DC/DC isolated power to operate the CQCM. Frequency of each sensor is readout by command thru a 65,535 Hz ± 1 Hz capacity counter. Temperature bridges 1 and 2 readout the water vapor and reference sensor temperatures. Inputs are provided for turning ON the radiator and sensor heaters for ice removal.

The remotely located Sensor Head is connected to the Controller at J2 and 3.

4.2 CQCM Operation

The CQCM commanded modes of operation are shown in Table 2. It operates on +28 ± 4 Vdc. Minimum power is 1.33 W with only the QCM's ON. Maximum power of 3.08 W occurs with both QCM and all heaters ON.

4.3 CQCM Thermal Modeling

The operating temperatures were obtained by computer thermal modeling[5].

The calculated cool-down time of the CQCM with only the Refer-

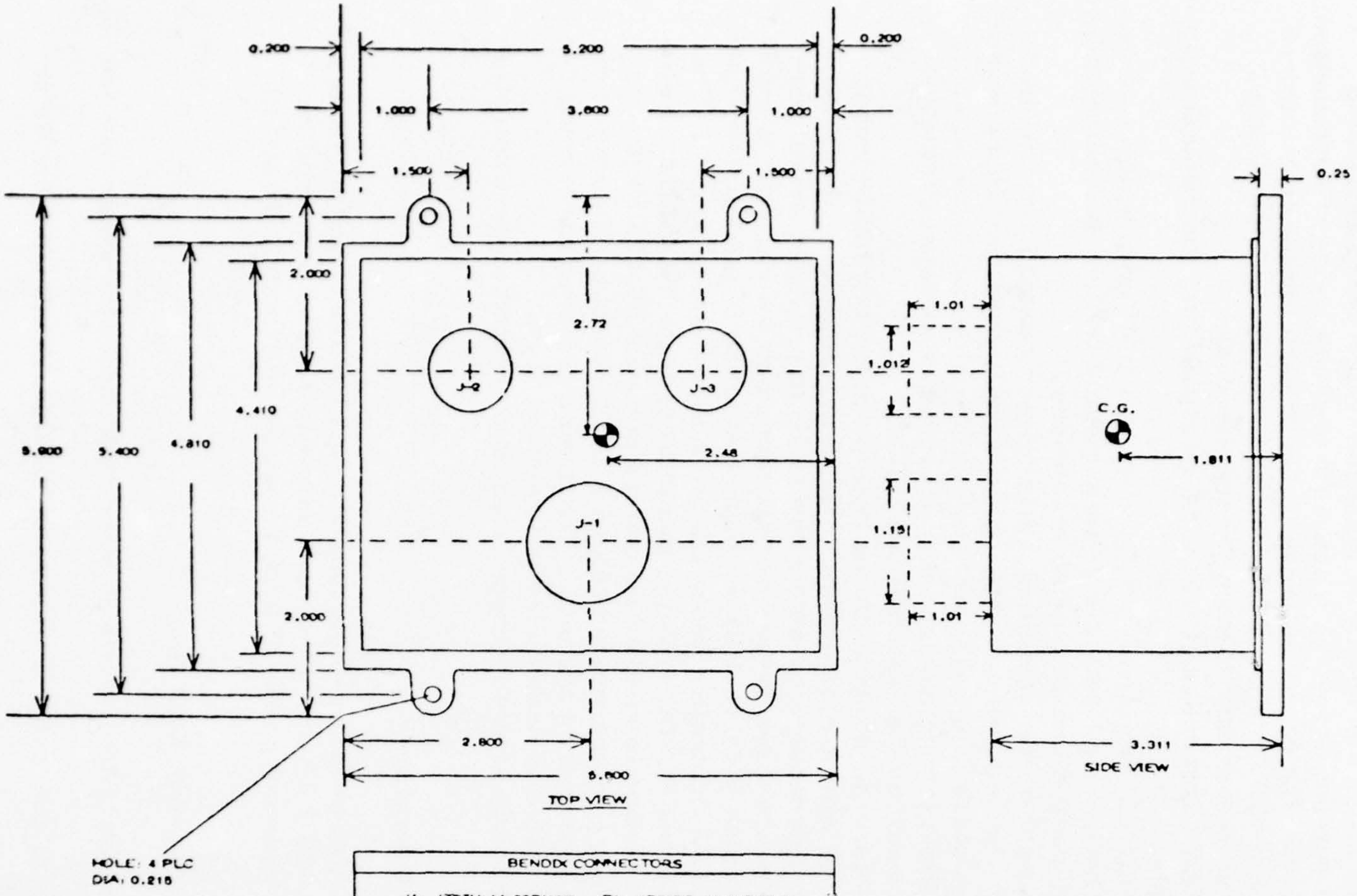

BENDIX CONNECTORS	
J1: JT07H-14-37P(150)	P1: JT06RE-14-37S(011)
J2, J3: JT07H-12-8P(150)	P2, P3: JT06RE-12-8S(011)

NOTES

WEIGHT: 0.89 Kg
DIMENSIONS: INCHES

MATERIAL: ALUMINUM
COVER, BLACK ANODIZED
BASE, AU PLATED
CONNECTOR ENVELOPE: MOUNTED
CONNECTOR PLUS MATE

Fig. 9 CQCM Controller Mechanical Specifications

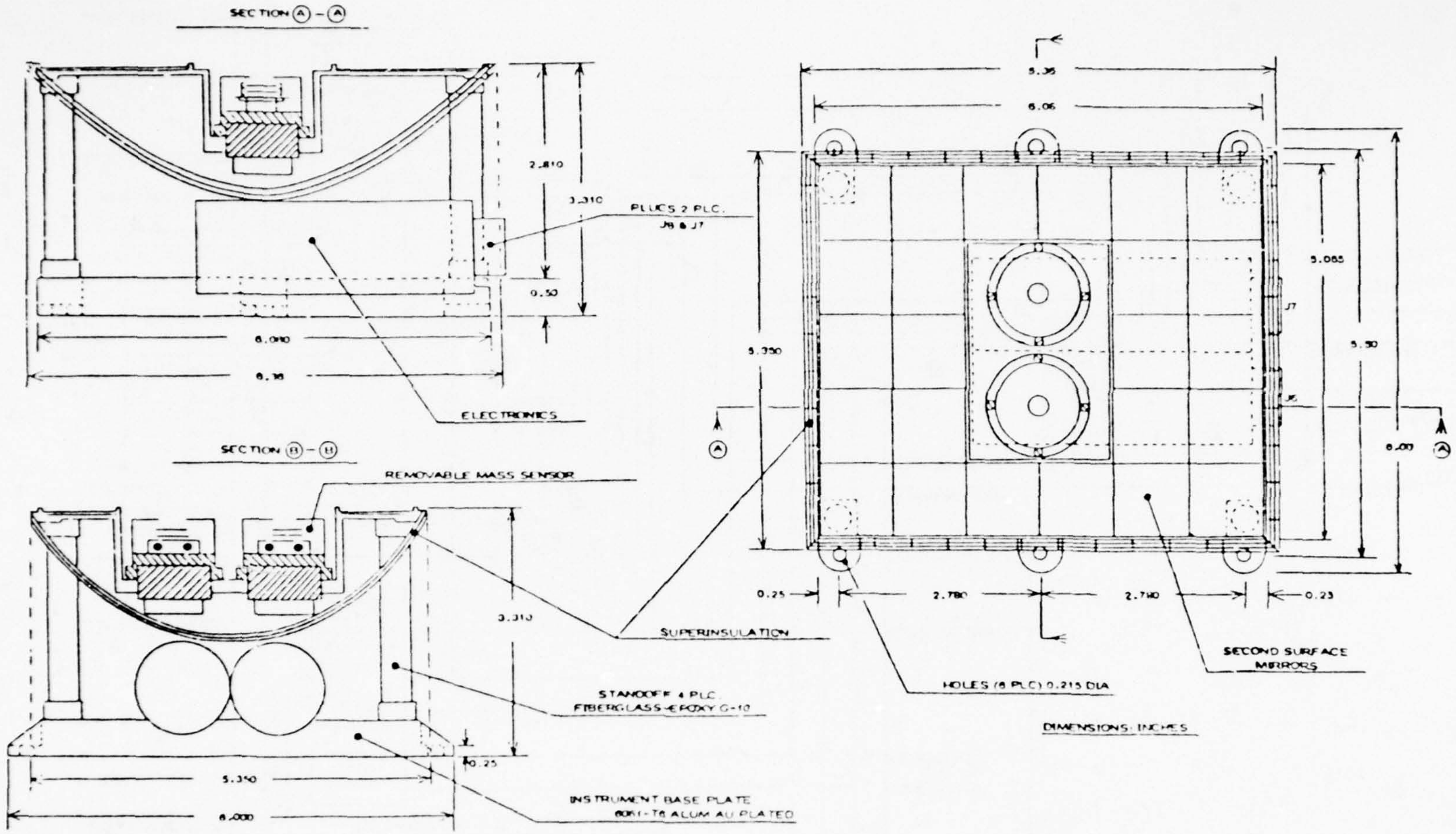

NOTES:

WEIGHT: 0.55 Kg

BENDIX CONNECTORS
J8 & J7, JT1H-12-8P(1N7)
Mates
P8 & P7, JT06RE-12-8P(011)

Fig. 10 CQCM Sensor Head Specifications

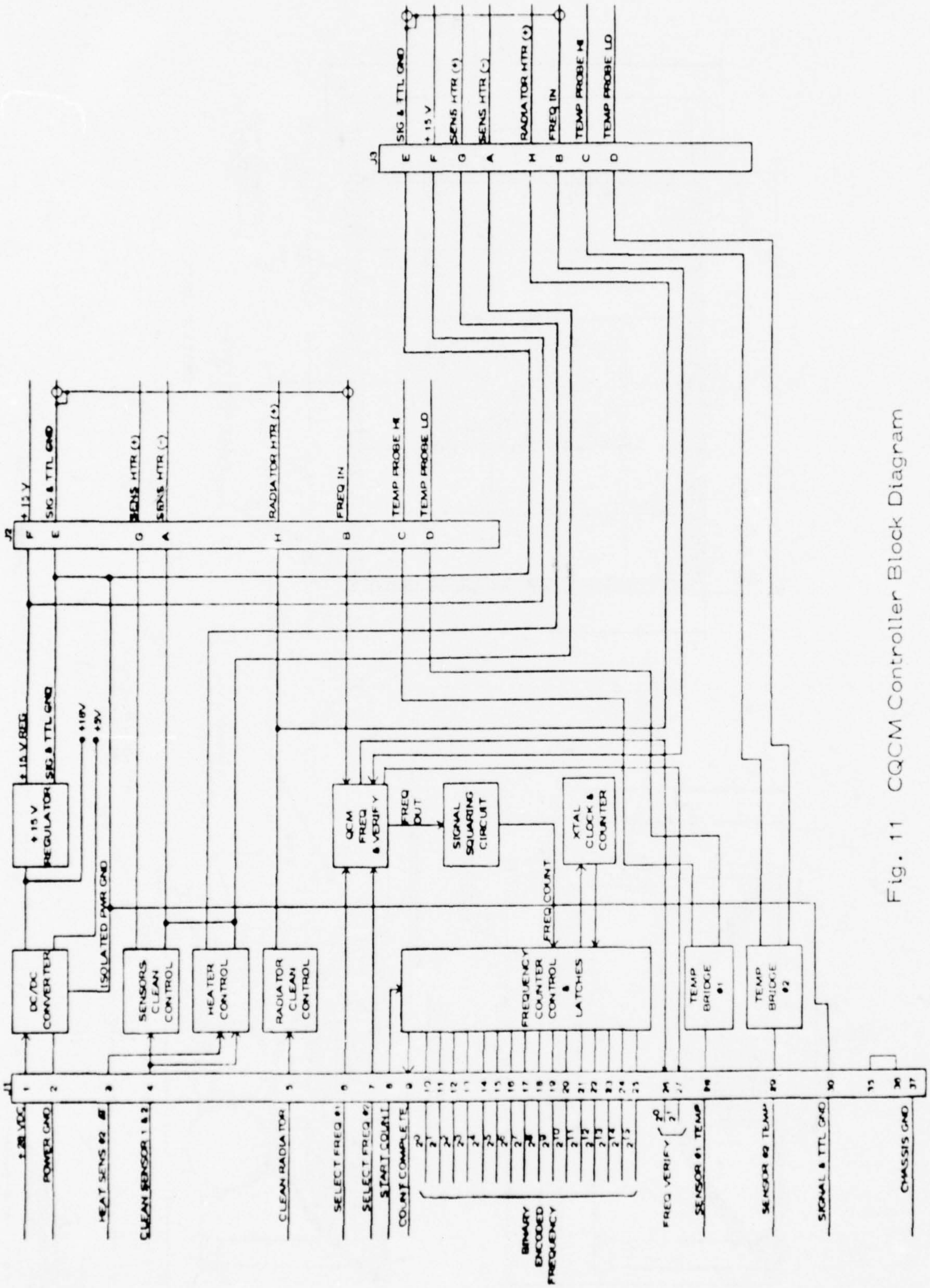

Fig. 11 CQCM Controller Block Diagram

Table 2 CQCM System Operating Powers

Mode	Description	Pwr In	Inst Pwr	Eff %
1. Static (minimum)	QCM's and Controller ON	1.33	.60	45
2. Normal Operation	QCM's and Controller ON Ref Sensor heater ON	1.84	.92	50
3. Clean 1 & 2	QCM's and Controller ON Water Vapor Sensor Heater ON	2.28	1.30	57
4. Clean radiator	QCM's and Controller ON Radiator Heater ON	2.04	1.14	56
5. Clean all	QCM's and Controller ON All Heaters ON	3.08	1.85	60

ence Sensor heated is shown in Fig. 12.

The calculated temperature rise of the CQCM with power to the water vapor monitor radiant cooler for ice removal is shown in Fig. 13.

5.0 SYSTEMS TEST MONITOR

A monitor has been built to functionally test the operation of the CQCM and TQCM System. The monitor is shown in Fig. 14 with CQCM and TQCM Systems in place for functional tests.

The Monitor provides a simple to operate, direct method for check-out and functional test of the TQCM or CQCM System. At the launch site, it will provide a rapid check of proper instrument functioning or a quick test of sensor operation after contaminated sensors are replaced without having to use the spacecraft telemetry system.

The Monitor has displays or switches for testing every active pin function on the TQCM or CQCM System. The Monitor specifications are

1) Power: 115 V, 2A (60 Hz)

2) Provides all required DC power for operating a TQCM or CQCM System.

3) The frequency output of any TQCM or CQCM mass sensor can be readout by selecting the proper binary coded panel switches. When switches are operated, lamps verify the commands.

4) The digital frequency meter displays output of any desired TQCM or CQCM mass sensor. A voltage analog of frequency is provided as an output for recording.

5) The digital temperature meter displays temperature of any desired TQCM Sensor or Heat Sink or CQCM Sensor temperature. A voltage analog of temperature is provided as an output for recording.

6) A ten position switch is used to set up a particular TQCM Sensor Temp (1 thru 5) or Heat Sink Temp (6 thru 10).

7) Total current meter allows various TQCM or CQCM operating modes to be monitored for possible deviation from design power values. An analog output is provided for recording current.

8) LED lamps indicate whether the TQCM or CQCM is being tested.

9) Command switches provide temperature inputs to the TQCM or CQCM to simulate Shuttle flight operations.

6.0 ACKNOWLEDGMENTS

The authors wish to thank Dr. Robert J. Naumann, David W.

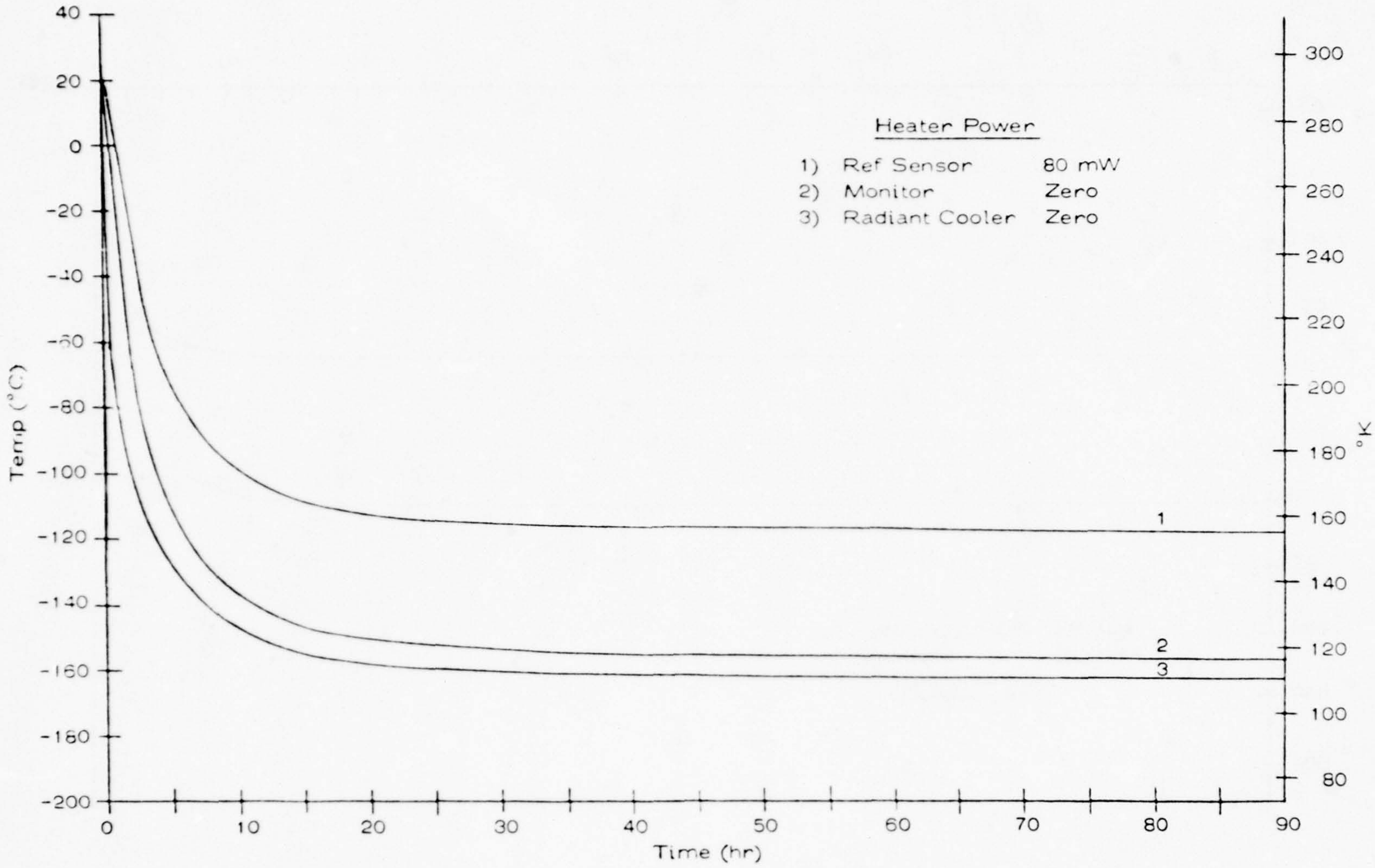

Fig. 12 Calculated CQCM Cool-Down with Power-On in Space

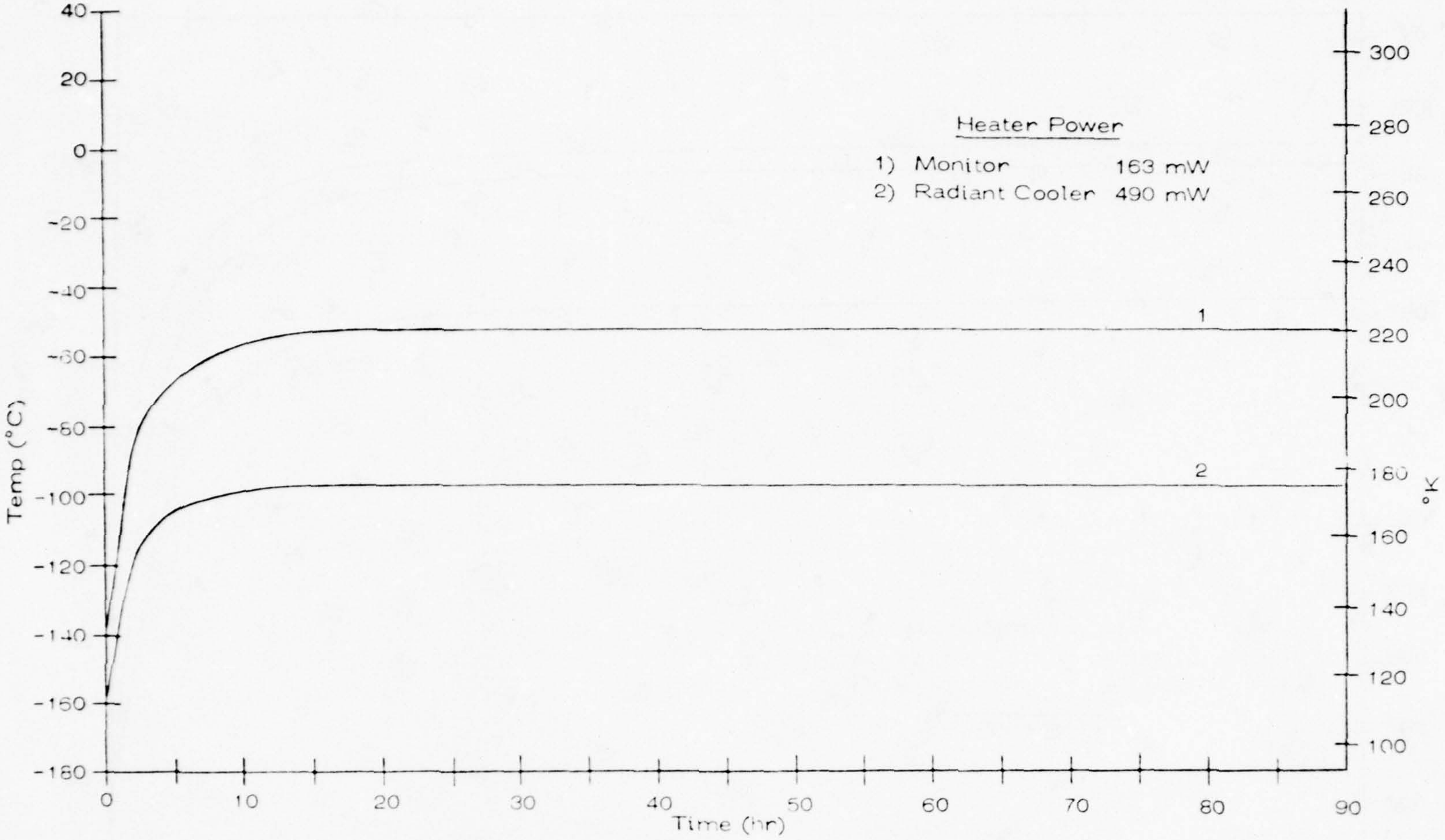

Fig. 13 Calculated CQCM Temperature in Space when Heaters are Operated for Ice Removal

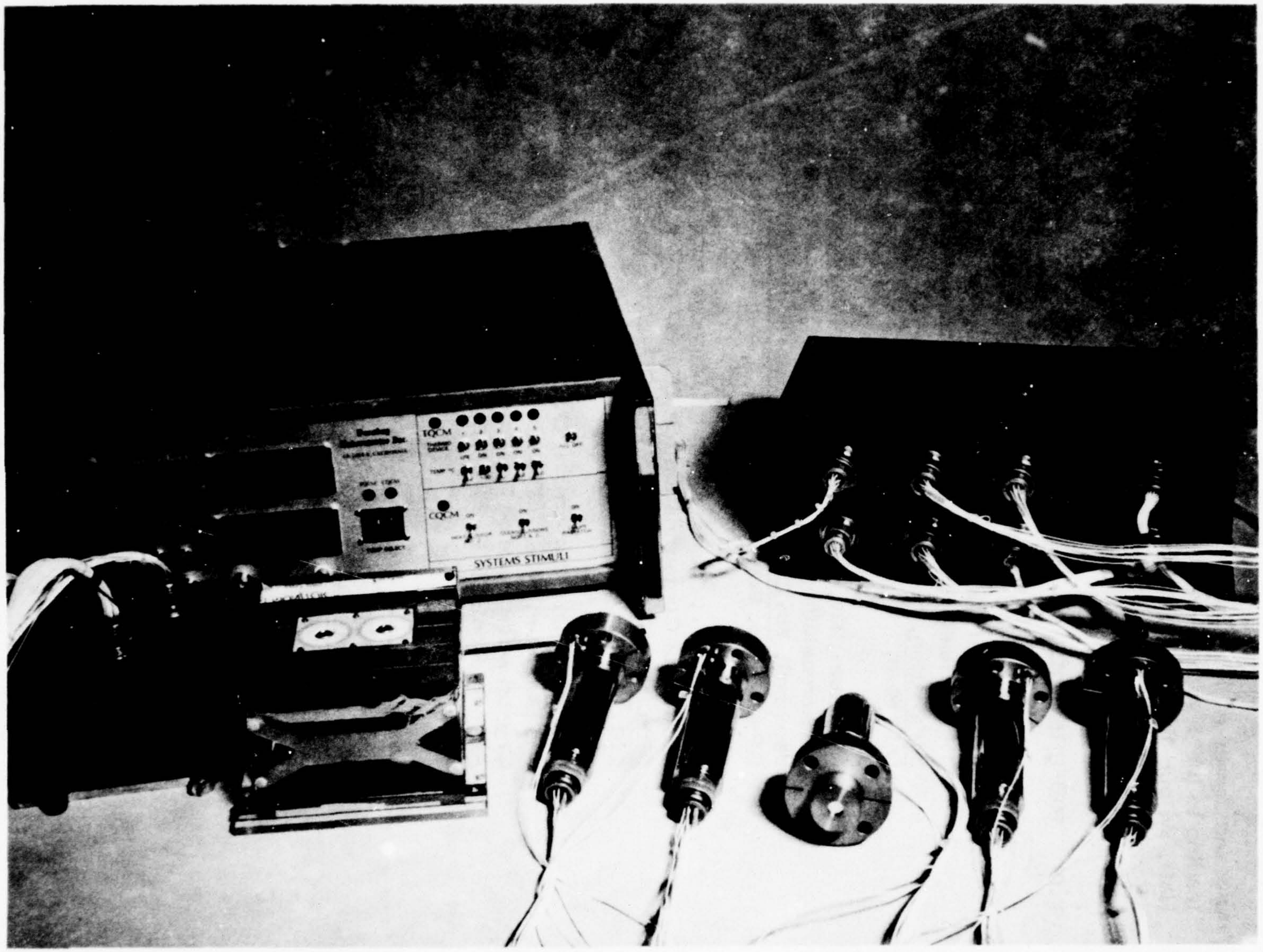

Fig. 14 Functional Tests of CQCM and TQCM Systems

Jex and James A. Fountain of MSFC for their helpful discussions leading to the development of the TQCM and CQCM and to John C. Hall, Wilbur T. Breckenridge, Richard S. Dummer and E. John Michel of Faraday Laboratories for their work in the design and construction of the flight systems.

7.0 REFERENCES

1. McKeown, D. and Corbin, W.E. Jr., "Space Measurements of the Contamination of Surfaces by OGO-6 and Their Cleaning by Sputtering and Desorption", Space Simulation, NBS, SP-336, pp. 113-127, Washington, DC (1970).

2. McKeown, D., Corbin, W.E. Jr. and Naumann, R.J., "Thermoelectrically-Cooled Quartz Crystal Microbalance", 7th Conference on Space Simulation, NASA SP-336, pp. 345-358 (1973).

3. Lynch, J.T., "Quartz Crystal Microbalance (QCM) Monitor of Contamination for LES-8/9", 9th Space Simulation Conference, NASA CP-2007, pp. 211-219 (1977).

4. McKeown, D., Claysmith, C.R., Breckenridge, W.T. Jr. and Dummer, R.S., "Temperature Controlled Quartz Crystal Microbalance System", AFML-TR-83, Final Report, Contract F33615-75-C-5171, Faraday Laboratories Inc. (1977).

5. McKeown, D., Sonnenschein, G., and Fox, M.G., "Cryogenic Quartz Crystal Microbalance", 8th Conference on Space Simulation, NASA SP-379, pp. 343-353 (1975).

CONSIDERATIONS IN THE USE OF QCMs FOR ACCURATE CONTAMINATION MEASUREMENT

D. A. WALLACE
BERKELEY CONTROLS INC. - IRVINE, CALIFORNIA

1.0 INTRODUCTION

Piezoelectric quartz, flat plate crystals have been used as microbalances for the measurement of mass flux in free molecule flow since Sauerbrey's[1] initial work in 1959 defined the nature of the crystal's frequency response to mass addition. The QCM, as this type of microbalance has come to be known, serves as the workhorse thickness monitor for thin film deposition processes as well as a tool for outgassing studies and, diagnostically, for molecular flux contaminant source identification on spacecraft.

In many applications of the QCM to date, qualitative measurements have been sufficient. However, in more analytical work such as that of Hughes, Allen, Linford and Bonham[2] or Glassford[3,4] or Liu and Glassford[5], an accurate determination of molecular flux is essential for confirmation of theoretical models.

[1] Sauerbrey, G., "Verwendung von Schwingquartzen zur Wagung dunner Schicten und vur Mikro Wagung", Zeit, fur Physik, Vol. 155: 206-222 (1959).

[2] Hughes, T.A., Allen, T.H., Linford, R.M.F., and Bonham, T.E., Investigation of Contamination Effects on Thermal Control Materials, AFML-TR-74-218 (1975) Final Technical Report, Contract F33615-73-C-5091, McDonnell Douglas Corp.

[3] Glassford, A.P.M., An analysis of the accuracy of a commercial quartz crystal microbalance. AIAA Paper No. 76-438, presented at AIAA 11th Thermophysics Conference, San Diego, Calif. (1976).

[4] Glassford, A.P.M., The response of a quartz crystal microbalance to a liquid deposit. Paper presented at the Space Simulation Conference, Los Angeles, California (1977).

[5] Liu, C.K., and Glassford, A.P.M., Kinetics data for diffusion of outgas species from RTV 560. Paper presented at the Space Simulation Conference, Los Angeles, Calif. (1977).

This paper will examine the flow equations involved in QCM molecular mass flux measurement, the effect of parameters such as crystal temperature, QCM entrance configuration and randomness of the flow and discuss the implications of these equations in measuring several materials' mass flux.

2.0 TECHNICAL DISCUSSION

2.1 Basic Crystal Mass Flux

The crystal's sensitivity to mass deposition is proportional to the amplitude of surface displacement for a crystal in thickness shear vibration. The value, S, obtained by integration over the active area of the crystal is usually used as the crystal mass sensitivity factor, assuming uniform deposition on the crystal. Within the deposition range for which frequency shift is linearly related to mass deposition, i.e. approximately $\Delta f < 0.01\ f_o$, the mass flux equation for a crystal exposed on one side to a condensing gas is

$$\frac{\mathring{m}}{A} = S\,\frac{\Delta f}{\Delta t} \qquad (1)$$

Where S = crystal mass sensitivity, g/cm^2-Hz

$\mathring{m}$ = mass flow, g/s

A = area, cm^2

Δf = frequency change, Hz

Δt = time interval, s

If, rather than incoming flow, a deposited mass is evaporating from the crystal into an infinite sink, then,

$$\left.\frac{\mathring{m}}{A}\right|_{evap} = -S\,\frac{\Delta f}{\Delta t} \qquad (2)$$

It is important to realize that in most situations both types of flow are occurring and the crystal frequency change with time relates to both the incoming flow and the crystal temperature dependent evaporating flow as,

$$\frac{\mathring{m}}{A} = S\,\frac{\Delta f}{\Delta t} + \left.\frac{\mathring{m}}{A}\right|_{evap} \tag{3}$$

2.2 Crystal Entrance Configuration

Obviously the determination of incoming mass flux using frequency change must include a consideration of the evaporating mass flux. The mass flux equation is further altered by the QCM entrance configuration. Figure 1, Case 1, shows a representative entrance section consisting of an entrance conical frustum (Station 0) and a cylindrical section leading to the crystal (Station X). The probability that an entering molecule will eventually reach the crystal and be captured is a function of the nature of the entering flux, i.e. diffuse or directed, the entrance configuration and the entrance wall temperature relative to the crystal temperature. If the flow is diffuse and the walls are warmer than the crystal (which is assumed to have unity sticking coefficient for the entering molecules) a conductance factor, K_{o-x}, can be determined. The evaporating molecules face a similar flow reduction in leaving the crystal since through wall collision some will return to the crystal, be recondensed and recycled back through the system. The evaporative flow conductance, K_{x-o}, is related through reciprocity to the entering flow conductance, K_{o-x}. The expression for this diffuse flow with warm entrance walls is,

$$\left.\frac{\mathring{m}}{A}\right|_{o} = \frac{A_x}{A_o}\,\frac{S}{K_{o-x}}\,\frac{\Delta f}{\Delta t} + \left.\frac{\mathring{m}}{A}\right|_{evap} \tag{4}$$

If the entrance walls are at the same or lower temperature as the crystal, Figure 1 Case II, the walls condense entering molecules which strike them and thus the entering and exiting flow conductance is altered from the previous warm wall case. The probability of a molecule passing directly through the frustrum without striking the

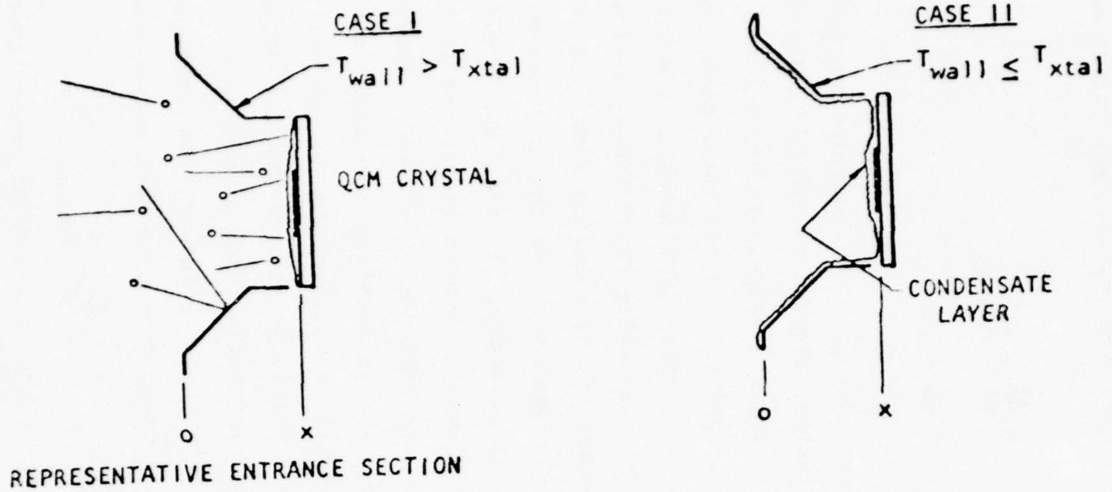

FIGURE 1 MASS FLUX MEASUREMENT WITH QCM ENTRANCE SECTION

wall and the further probability of the molecule reaching the crystal without collision, must be calculated i.e. $K_{o-x}\big|_{direct}$. An added element is added to the crystal mass flux by the evaporation of material from the walls which has a probability of striking the crystal before exiting the system, $K_{w-x}\big|_{direct}$. The expression for Case II is,

$$\left.\frac{\mathring{m}}{A}\right|_{o} = \frac{S\,\frac{A_x}{A_o}\,\frac{\Delta f}{\Delta t} + \left.\frac{\mathring{m}}{A}\right|_{evap}\left[\frac{A_x}{A_o} - \frac{A_w}{A_o}\,K_{w-x}\Big|_{direct}\right]}{K_{o-x}\Big|_{direct}} \tag{5}$$

For this case with evaporation only,

$$\left.\frac{\mathring{m}}{A}\right|_{e} = -\,\frac{S\,\frac{\Delta f}{\Delta t}}{1 - \frac{A_w}{A_x}\,K_{w-x}\Big|_{direct}} \tag{6}$$

2.3 Nature of Flow

Free molecule flow is often thought of as wholly diffuse i.e. Maxwellian, in nature with the further assumption of the existence of an isotropic pressure, whereas in many cases a much altered velocity distribution exists. This is especially true in cryopumped chambers, nozzle flows and spacecraft situations. The degree of directionality in a flow field is characterized by the speed ratio, $\bar{S}$, defined as the ratio of the directed velocity, u, to the gas mean thermal velocity, v_m,

$$\bar{S} = \frac{u}{v_m} = \frac{u}{\sqrt{\frac{2kT}{m}}} \tag{7}$$

Where T = gas temperature
k = Boltzmann constant
m = molecule mass

Several illustrative examples of random and directed flow are given in Figure 2. Random, diffuse flow conditions exist in the enclosure shown with walls at equal temperature. A crystal facing an infinite outgassing wall sees molecules emanating from the wall according to

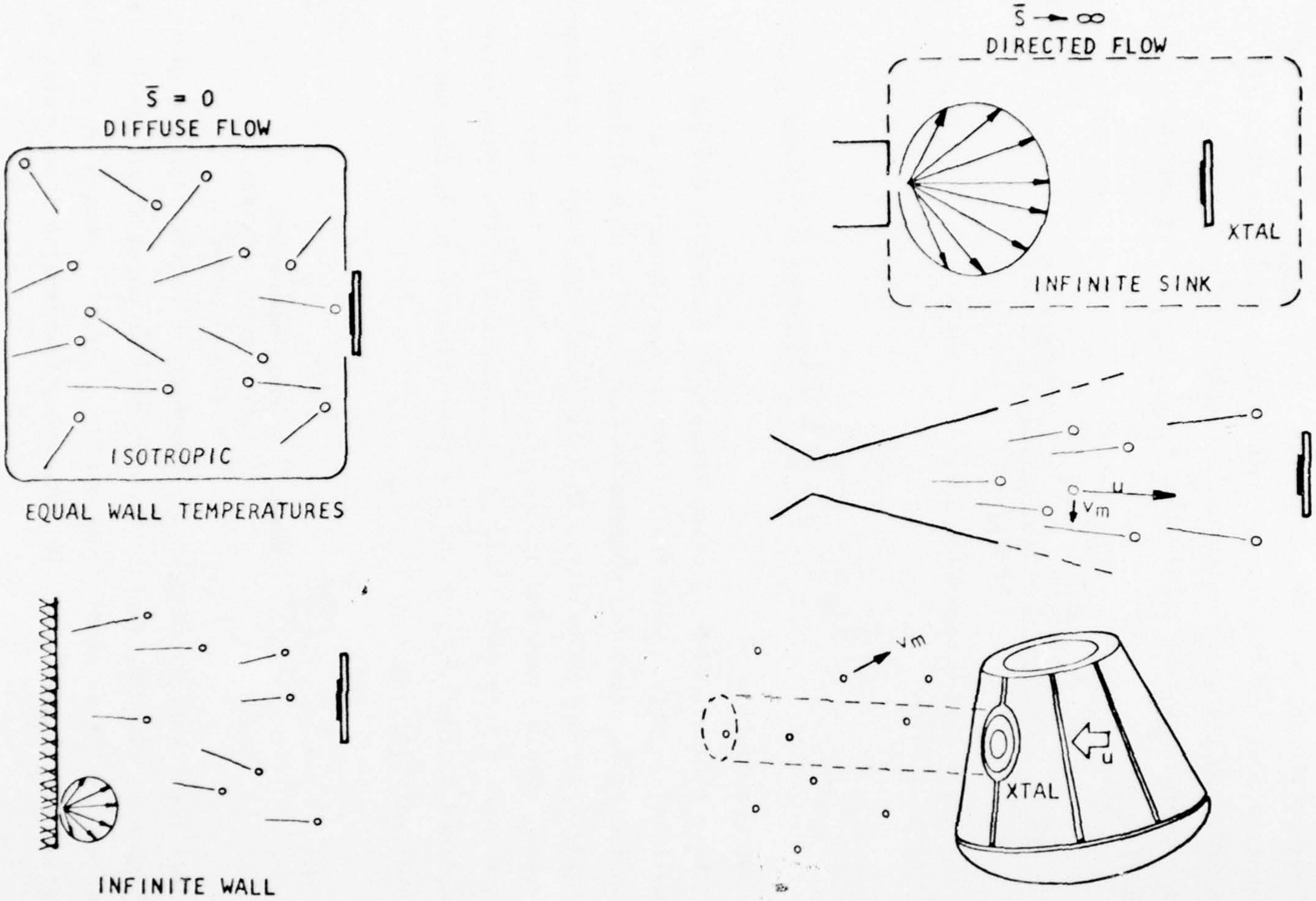

FIGURE 2 EFFECT OF DIRECTIONAL MASS MOTION VS DIFFUSE FLOW

the cosine law which, in the aggregate, results in diffuse flow at the crystal.

On the other hand, the Knudsen cell shown in the figure with cosine distribution emanation of molecules, results in highly directional flow at the crystal since the enclosure is assumed to be an infinite sink. Only molecules from the aperature of the cell within the solid angle intersecting the crystal arrive at the crystal. There is no chance of collisions producing randomness. To a lesser extent, the same is true of nozzle flow. The nozzle imparts a mass motion, u, on the gas yet to a degree it still acts as a gas at rest with thermal velocity, v_m. The spacecraft moving at high velocity, u, through the rarefied gas at rest with thermal velocity, v_m, essentially sees molecules with a very high speed ratio striking the vehicle.

If we treat the limiting case of directed flow, i.e. collimated flow, $\bar{S}=\infty$, shown in Figure 3, only the approaching flow within the envelope A_x can reach the crystal if the walls are considered to be condensing. Evaporation from the crystal and from the walls continues to be diffuse resulting in the expression for collimated mass flow to a cold wall QCM of,

$$\left.\frac{\mathring{m}}{A}\right|_{o} = S\,\frac{\Delta f}{\Delta t} + \frac{\mathring{m}}{A}_{evap}\left[1-\frac{A_w}{A_x}\,\left.K_{w-x}\right|_{direct}\right] \qquad (8)$$

Since evaporation is by nature diffuse it is independent of the nature of the entering flow. Thus equation (6) continues to apply for the case of evaporation only.

2.4 Measurement implications of Combined Flows

From the above equations it is evident that if an accurate determination of mass flux arriving at a QCM is to be deduced from crystal frequency shift information, the crystal temperature and to a certain extent the vapor pressure characteristics of the deposited material need to be known. An illustration of QCM response to

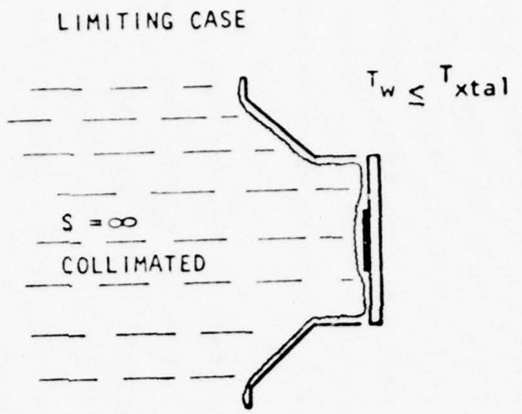

FIGURE 3 MASS FLUX MEASUREMENT WITH DIRECTED FLOW

crystal temperature change is shown in Figure 4(a). A case is shown for a cold wall QCM with constant entering mass flux, m_o, and changing evaporative mass flux, $\overset{\circ}{m}_e$, as a function of crystal temperature. For the low crystal temperature, ① , $\overset{\circ}{m}_e$ is low, $(\overset{\circ}{m}_o - \overset{\circ}{m}_e)$ equals approximately $\overset{\circ}{m}_o$ and the flow equations may be simplified accordingly. As the crystal temperature is increased to ② , $(\overset{\circ}{m}_o - \overset{\circ}{m}_e)$ decreases and thus $\frac{\Delta f}{\Delta t}$ decreases until at ③ $\overset{\circ}{m}_e$ equals $\overset{\circ}{m}_o$ and $\frac{\Delta f}{\Delta t}$ is zero. If the crystal temperature is increased beyond this point, the evaporative flux exceeds the entering flux and a negative $\frac{\Delta f}{\Delta t}$ is indicated.

The situation is further illustrated in Figure 4(b) where $\overset{\circ}{m}_o$ is still assumed to be constant and the crystal temperature is held constant for some time interval. The initial low crystal temperature, ① , results in low evaporation and rapid condensate buildup with reduced growth rate for temperature ② and no growth during the time the crystal is at temperature ③ . The temperature ④ period reduces the condensate until all material is removed at which point of course the frequency change rate returns to zero. Without knowledge of either this entire cycle or the crystal temperature, it would be difficult in this case to distinguish between an absolutely clean QCM with $\overset{\circ}{m}_o$ equal zero and a situation with a thick condensate and large entering and evaporating mass fluxes of equal magnitude. Both cases would produce zero frequency shift.

2.5 Vapor Pressure Characteristics

The importance of the earlier statements concerning combined flow of incoming and evaporating flows on QCMs becomes evident as we consider the measurement of flows of specific gases. Figure 5 shows the vapor pressure characteristics of water vapor, a family of polydimethylsiloxanes and DC 704 silicone oil vapor. Water vapor is a major outgassing component in most vacuum systems and as such may be the primary constituent of the system background pressure. If it is desirable to measure the water vapor flux in a chamber at

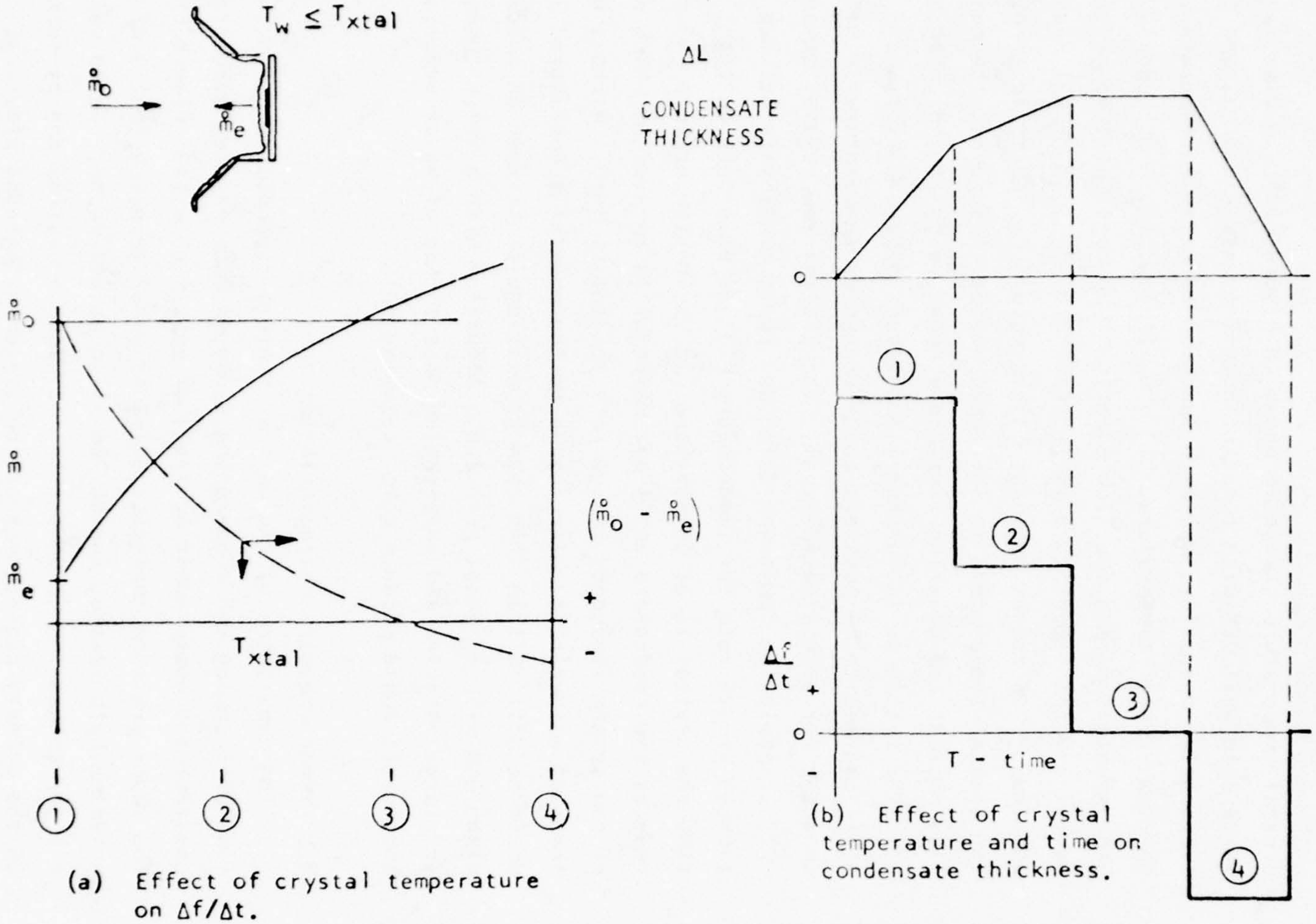

(a) Effect of crystal temperature on Δf/Δt.

(b) Effect of crystal temperature and time on condensate thickness.

FIGURE 4 ILLUSTRATIVE QCM RESPONSE AS FUNCTION OF CRYSTAL TEMPERATURE

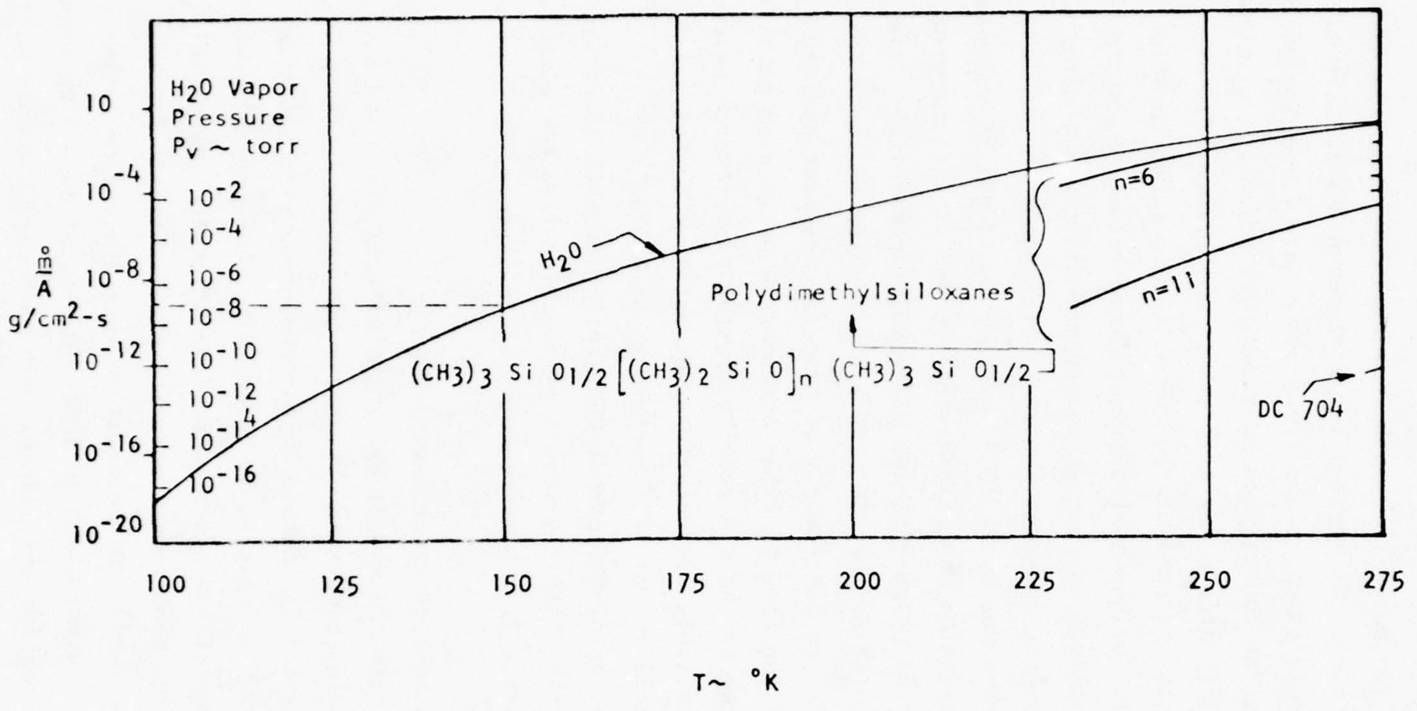

FIGURE 5 VAPOR PRESSURE, EVAPORATION RATE CHARACTERISTICS

10^{-7} torr for instance, the graph indicates QCM temperatures below 150°K must be used. At crystal temperatures above this level, evaporation would simply prevent the condensate formation on the crystal. This, of course, can be a definite advantage in situations where outgassing rates of materials such as various RTVs are to be measured without the complication of water vapor condensation. From the graph it is obvious that a crystal temperature of for instance -50°C, would collect the higher moleculer weight polydimethylsiloxanes with low reevaporation rates, whereas water vapor in the system would be at vapor pressures above 10^{-2} torr and would not be sensed by the QCM. The observation may be made that indeed at this temperature the QCM would not respond to any but a major ambient air leak in the immediate vicinity of the QCM. DC 704 oil vapor on the other hand is collected by the QCM readily at temperatures near ambient. Measurement of the flow of other atmospheric gases such as nitrogen, oxygen and argon by the QCM require crystal temperatures below 20°K to achieve acceptably low reevaporation rates while hydrogen's vapor pressure is still in the 10^{-7} torr range at 4.2°K.

Determination of the proper QCM sensing crystal temperature must consider then both the levels of incoming flux and evaporation rates, if accurate flux measurements are to be made.

2.6 Equations applied to an example QCM

To illustrate the magnitude of the effects discussed earlier, consider the Celesco/Berkeley cryogenic QCM sensor shown in Figure 6. The sensing crystal is mounted in a stress-free ring mount which allows the sensor to operate to below 20°K. The crystal temperature is sensed by a platinum resistance element located immediately behind the crystal. The performance accuracy of this sensor has been studied by Glassford[3]. Of interest to this discussion is the entrance section to the crystal which is shown in greater detail in Figure 7(a). The flow equations for this sensor with both warm and cold walls and

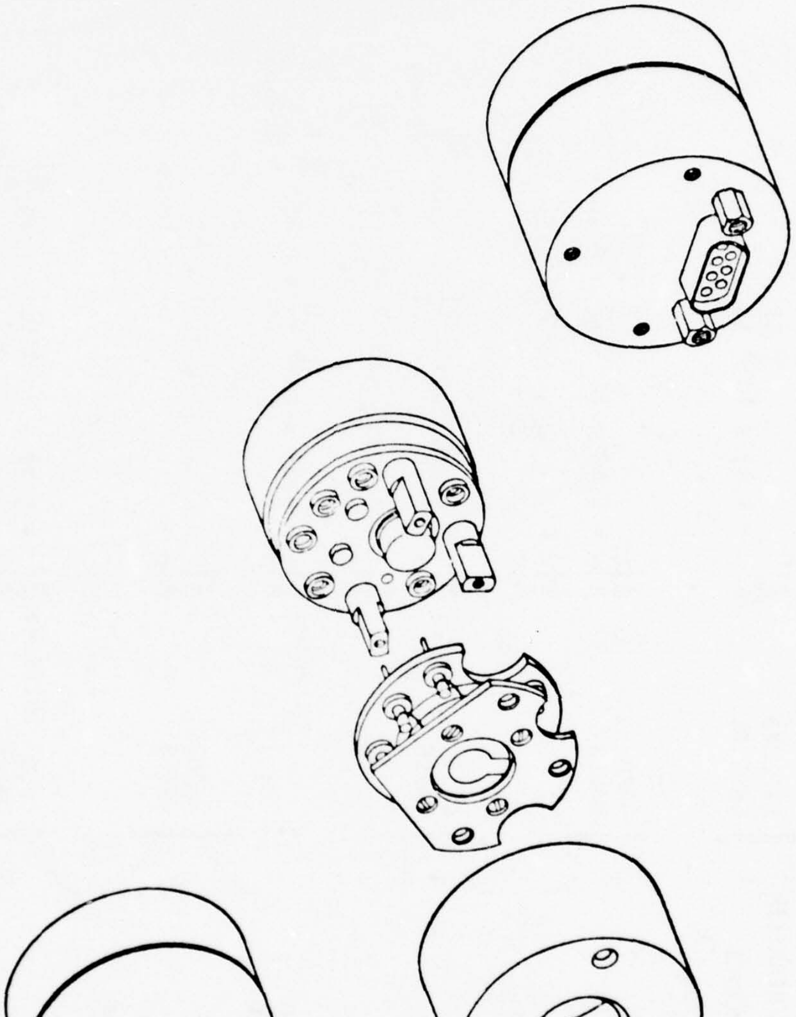

FIGURE 6 CELESCO/BERKELEY CRYOGENIC QCM

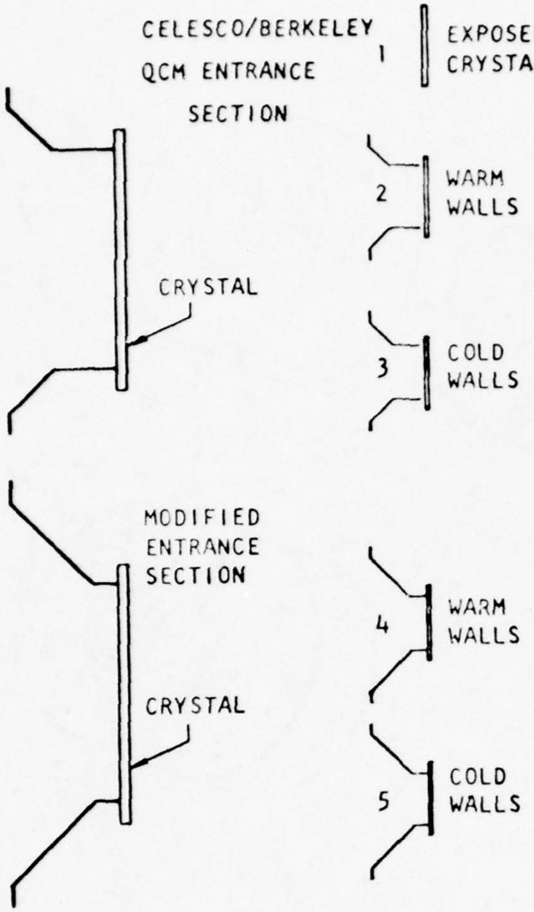

$$\left.\frac{\mathring{m}}{A}\right|_o = 4.43 \times 10^{-9} \frac{\Delta f}{\Delta t}$$

$$\left.\frac{\mathring{m}}{A}\right|_o = 5.63 \times 10^{-9} \frac{\Delta f}{\Delta t} + \left.\frac{\mathring{m}}{A}\right|_{evap}$$

$$\left.\frac{\mathring{m}}{A}\right|_e = - 5.63 \times 10^{-9} \frac{\Delta f}{\Delta t}, \left(\left.\frac{\mathring{m}}{A}\right|_o = 0\right)$$

Diffuse $\left.\frac{\mathring{m}}{A}\right|_o = 5.926 \times 10^{-9} \frac{\Delta f}{\Delta t} + 1.106 \left.\frac{\mathring{m}}{A}\right|_{evap}$

$$\left.\frac{\mathring{m}}{A}\right|_e = - 5.358 \times 10^{-9} \frac{\Delta f}{\Delta t}, \left(\left.\frac{\mathring{m}}{A}\right|_o = 0\right)$$

Directed $\left.\frac{\mathring{m}}{A}\right|_o = 4.43 \times 10^{-9} \frac{\Delta f}{\Delta t} + 0.827 \left.\frac{\mathring{m}}{A}\right|_{evap}$

$$\left.\frac{\mathring{m}}{A}\right|_o = 4.517 \times 10^{-9} \frac{\Delta f}{\Delta t} + \left.\frac{\mathring{m}}{A}\right|_{evap}$$

Diffuse $\left.\frac{\mathring{m}}{A}\right|_o = 5.78 \times 10^{-9} \frac{\Delta f}{\Delta t} + 1.19 \left.\frac{\mathring{m}}{A}\right|_{evap}$

$$\left.\frac{\mathring{m}}{A}\right|_e = - 4.86 \times 10^{-9} \frac{\Delta f}{\Delta t}, \left(\left.\frac{\mathring{m}}{A}\right|_o = 0\right)$$

Directed $\left.\frac{\mathring{m}}{A}\right|_o = 4.43 \times 10^{-9} \frac{\Delta f}{\Delta t} + 0.912 \left.\frac{\mathring{m}}{A}\right|_{evap}$

FIGURE 7 EFFECT OF MODIFIED ENTRANCE ON FLOW EQUATIONS diffuse and directed flows, are shown in this Figure in comparison to an ideal exposed 10 MHz crystal. The entrance section which intuitively would seem to expose the crystal quite openly, is seen in fact to alter the mass sensitivity by 21% in the case of warm walls and by 25% for cold walls which do exist on this sensor. Modifying the entrance section as shown in Figure 7(b) significantly increases the flow conductance, as indicated by the reduced values in the equations. The important point here is not the relative merits of one entrance section over another, but simply that the flow conductance must be correctly known and used in the flow equation rather than an assumed exposed crystal sensitivity value if accurate flow measurements are to be made with the QCM.

EVALUATING A CONTAMINATION HAZARD WITH A RESIDUAL GAS ANALYZER

Raymond Kruger
NASA, Goddard Space Flight Center
Greenbelt, MD 20771

1.0 ABSTRACT

This report describes the use of a residual gas analyzer (RGA) to monitor the partial pressure of a suspect contaminant material during the bake-out of a vacuum chamber and also during the following test operation which involved a sensitive spacecraft instrument. A method for estimating the RGA sensitivity to the contaminant is presented. The method is considered to be conservative from the standpoint of assessing the contamination hazard arising from the material in question. An analysis of the test data is presented; it indicates that gross contamination did not occur. A cold finger technique that provides a surface on which residual gases can condense is also described. Data from the cold finger is used to infer that the sensitive test item had not been contaminated.

The techniques used are shown to be viable and methods for improving upon them are suggested.

2.0 BACKGROUND

In preparing for the environmental test of a sensitive ultraviolet telescope planned for use aboard a spacecraft, a significant quantity of DC-704* diffusion pump fluid was detected using cold finger techniques**. This was an unusual occurrence; the chamber previously had been used for highly sensitive experiments and careful analyses had rarely detected even trace quantities of this fluid.

---

* A Dow Corning Corporation trade name; tetraphenyltetramethyltrisiloxane, molecular weight 484.

**Appendix A provides an explanation of the cold finger technique.

A cold finger test made six months before this test was scheduled showed less than 1 mg of residue with no DC-704 identified; a test conducted about one month earlier showed less than 1 mg of residue with no DC-704. However, a cold finger analysis conducted about three weeks before the telescope test was scheduled showed 76 mg of residue with DC-704 definitely identified. An analysis completed one week before the planned telescope test indicated 102 mg of residue and DC-704 appeared to be the major constituent.

A check of facility operating procedures uncovered a change that could result in the fluid being introduced into the test volume; the use of the new procedure was discontinued. However, the chamber was considered contaminated and unsuitable for conducting tests of sensitive items.

Because of schedules requiring that the test item undergo calibrations in the chamber at this point in time and other considerations, it was impossible to perform a thorough chamber cleaning; the need for fixturing, etc., made the use of other chambers impractical.

3.0 APPROACH

It was decided to conduct a short chamber bake-out and during the bake-out to monitor the level of DC-704 using an RGA. If one could assign a partial pressure to the RGA readings, then, knowing the vapor pressure characteristics of the DC-704, one could assess the hazard of its condensing on the sensitive surface of the test item. This would not preclude adsorption due to the surface forces but would provide an indication as to whether gross contamination would occur. The cold finger too could be used to assess chamber contamination.

A Granville Phillips Company, Spectra Scan 400 quadrupole RGA was used to monitor the partial pressure of the DC-704. A spectrum of DC-704 had been obtained with a similar spectrometer previously and a review of the spectrum, together with a review of previous chamber spectra, indicated that the peaks at mass to charge ratio (m/e) = 195 and 197 provided a good indicator for DC-704; they were significant in the DC-704 spectrum and were generally at a low level in scans made previously in various chambers in the laboratory.

Literature values for DC-704[1,2] also indicated that these mass numbers were appropriate. Peaks at m/e = 188 and 259 provided additional confirmation as to the identification of DC-704. Peaks above m/e = 300 were not usable because of the performance of the particular RGA; peaks below m/e = 188, while necessary to confirm the presence of DC-704, were present from many other sources. Peak height ratios among the selected peaks also confirmed the identification. The peak at m/e = 197 was chosen to be representative of the partial pressure of DC-704. Figure 1 is a portion of the RGA scan taken at time 91.7 hours during the test of the telescope.

Methods for establishing the relationship between the m/e = 197 peak height and the partial pressure of DC-704 were considered. A formal calibration of the RGA decided against because suitable facilities could not be made available in time. The use of literature values was considered but the corrections necessary to make them applicable to the particular RGA were considered subject to too many uncertainties. It was decided to use what was considered to be a conservative approach from the standpoint of contamination. The method simply assumed that the height of the m/e = 197 peak was equal to the saturation vapor pressure when the first reading, made as soon as possible after the beginning test, was taken. This pressure would be taken at the temperature of the chamber at that time (25°C). Two conservative factors were therefore involved. First, since the system was being dynamically pumped, the partial pressure would be less than the vapor pressure; by definition, the vapor pressure is an equilibrium value. Secondly, unless very large quantities of the oil existed in the chamber, the partial pressure could be expected to fall with time as the sources were depleted. Therefore, by the time the reading was taken, the partial pressure probably would have fallen by some amount.

Data on the vapor pressure of DC-704 was taken from the manufacturer's bulletin.[3]

---

[1] Wood, G.M. and Roenick, R.J., Jr., Tables of uncertified mass spectra of diffusion pump oils, J. Vac. Sci. & Tech., (1968)

[2] Colony, J.A., Mass Spectrometry of Aerospace Materials, NASA TN D-8261 (June 1976)

[3] Bulletin 22-054a, Information About Silicone Fluids, Dow Corning Corporation, Midland, Michigan, (January 1974)

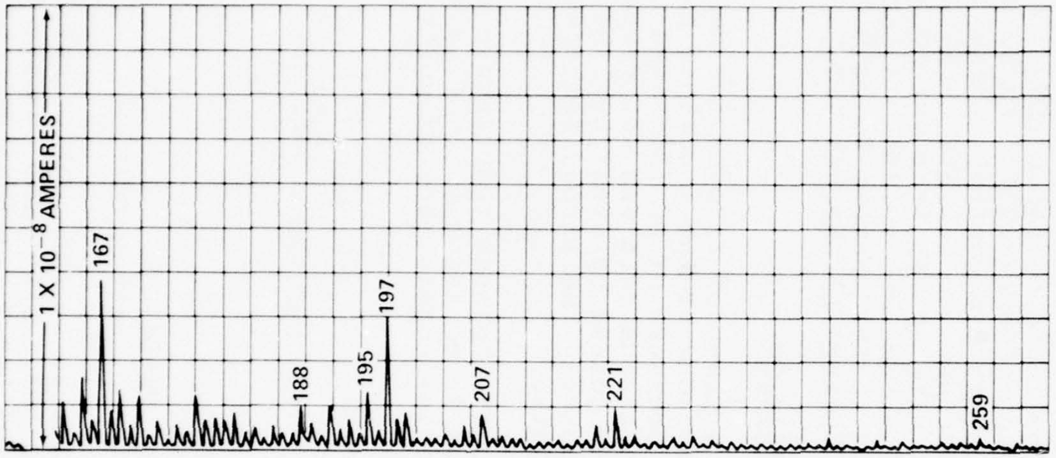

SCAN TAKEN AT TIME T = 37.25 HOURS

CHAMBER SHROUD TEMPERATURE 57° C

FIGURE 1 – RGA SCAN

4.0 FACILITY CHARACTERISTICS

The tests were conducted in Goddard Space Flight Center facility 238. The chamber is 3.7m (12 ft.) in diameter and 4.6m (15 ft.) high. An optically dense shroud provides thermal control with a capability of simulating the thermal sink of space with liquid nitrogen (LN_2). Gaseous nitrogen at -90°C(-130°F) to +100°C(+212°F) can be passed through the shroud for temperature control. Six 81 cm (32 in.) diffusion pumps are used to achieve hard vacuum. Each of these pumps is provided with an LN_2 trap but no isolation valve separates them from the test volume. A large LN_2 cooled plate was inserted in the chamber to provide additional pumping capacity during the chamber bake-out.

5.0 BAKE-OUT OPERATION

Figure 2 is a graph of information derived during the bake-out operation. One of the functions plotted is the saturation vapor pressure of DC-704 based on the shroud temperature. Continuous data was not recorded; the data points plotted are joined by straight line segments for presentation purposes. The shroud temperatures are noted near the data points.

The relationship between temperature and vapor pressure[5] is given in equation (1). (The equation is slightly modified for consistency of units within this report.)

$$P = \exp\left(30.279 - \frac{12825}{T+273}\right) \qquad (1)$$

where:

P = pressure, Pascal
T = temperature, degrees Celsius

The other data plotted is the peak height of $m/e = 197$ as determined by the RGA. Since the chamber temperature was 25°C at the time of the first reading, this reading (actually 4.4×10^{-9} amperes) made after a one-hour warm-up, was taken as being equal to the vapor pressure of DC-704 at 25°C, 2.88×10^{-6} Pa.

The first three data points indicate that the partial pressure of DC-704 was decreasing with time. The fourth

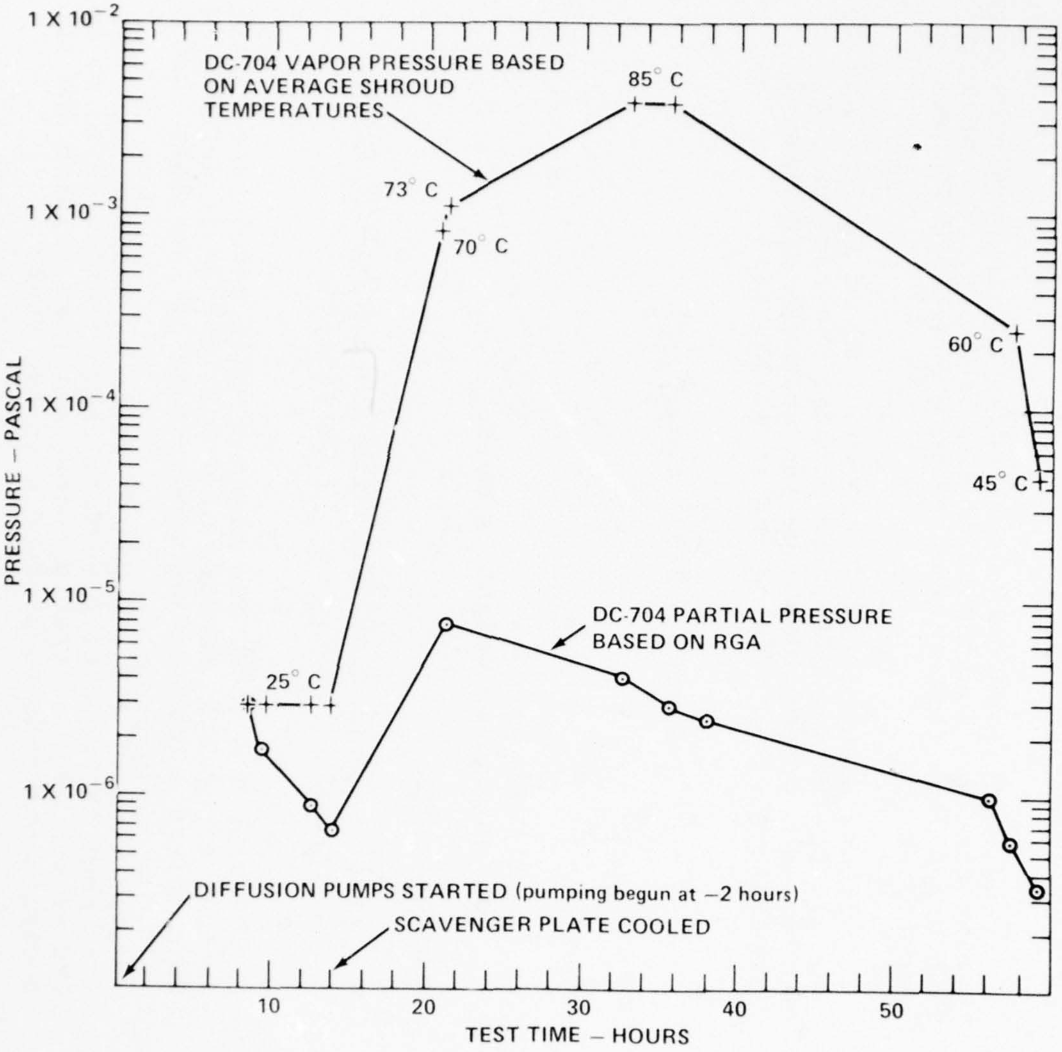

FIGURE 2 – BAKE-OUT PROFILE

data point was taken when the scavenger plate was being cooled and continues the downward trend. The points taken at 12.67 hours and 27 hours (73°C and 85°C) show that the RGA reading was decreasing in spite of an increasing wall temperature, a sign of a decreasing source since, with constant pumping speed, decreasing pressure is indicative of decreasing gas load.

The cold finger was operated at LN_2 temperatures only during the last four hours of the bake-out. The analysis indicated less than 1 mg of residue and no DC-704 was identified.

If one assumed that there was 1 mg of residue and it was all DC-704, an effective partial pressure can be estimated. One may describe the pressure in terms of temperature, flux, and molecular weight as:[4]

$$P = (T + 273)^{\frac{1}{2}} \left\{\frac{\phi}{7.78(M)^{\frac{1}{2}}}\right\} \tag{2}$$

where:

ϕ = flux, $g/cm^2 \cdot s$
M = molecular weight, g/mole.

Substituting,

$$P = (T + 273)^{\frac{1}{2}} \left\{\frac{1 \text{ X } 10^{-3} g/(182 \text{ cm}^2 \text{ X } 4 \text{ h X } 3600 \text{ s/h})}{7.78\ (484)^{\frac{1}{2}}}\right\} \tag{3}$$

Taking T = 85°C, the highest value during the entire period, a partial pressure of $4.2 \text{ X } 10^{-8}$ Pa is determined. This infers a condensation temperature of less than -1°C.

In view of all the conservative assumptions and the fact that the sensitive surface was not expected to go below 0°C it was decided that a reasonable risk existed and the decision was made to proceed with the test.

---

[4] Dushman, S. and Lafferty, J.M., Scientific Foundations of Vacuum Technology, John Wiley & Sons, Inc., New York (1962) p. 14

6.0 TEST OPERATIONS

Figure 3 presents data comparing the average temperature of the chamber shroud with that of the test item sensitive surface. Chamber pumpdown took place from time 0 to 5 hours at which time the pressure was 2.7 X 10^{-4} Pa. Return to ambient pressure took from time 308 hours (when the pressure was 2.7 X 10^{-5} Pa) to time 219 hours.

In Figure 4, the temperature of the test item sensitive surface has been converted to the corresponding saturation vapor pressure of DC-704; the RGA readings are in terms of partial pressure of DC-704. These transformations were accomplished as noted earlier under the section on bake-out operation. As before, a sensitivity of 655 Pa/A was used to convert the RGA electronic output to terms of pressure.

The wall temperatures were varied more slowly than usual to decrease the possibility of releasing quantities of contaminants into the chamber so rapidly that they could reach hazardous levels before the pumps could remove them.

In all cases, the partial pressure as indicated by the RGA is below the vapor pressure curve. From this we may infer that condensation did not take place. In one place, at time 37.3 hours, the RGA data point is only slightly below the vapor pressure curve. In view of the conservatism of the method, even this point was considered safe. (The minimum level of RGA capability is also noted in Figure 3.)

The cold finger analysis indicated a residue measuring 11.2 mg. DC-704 was identified. This, however, is not in itself an indication that the contamination hazard was too great. Using equation (2) and substituting, we find:

$$P = (T + 273)^{\frac{1}{2}} \left\{ \frac{11.2 \text{ mg}/(182 \text{ cm}^2 \text{ X } 303 \text{ h X } 3600 \text{ s/h}}{7.78\ (484)^{\frac{1}{2}}} \right\} \qquad (4)$$

$$P = (T + 273)^{\frac{1}{2}} \{3.3 \text{ X } 10^{-13}\}$$

At T = 63.5°C (the highest average shroud temperature) the pressure based on equation (4) is 6 X 10^{-12} Pa, a DC-704

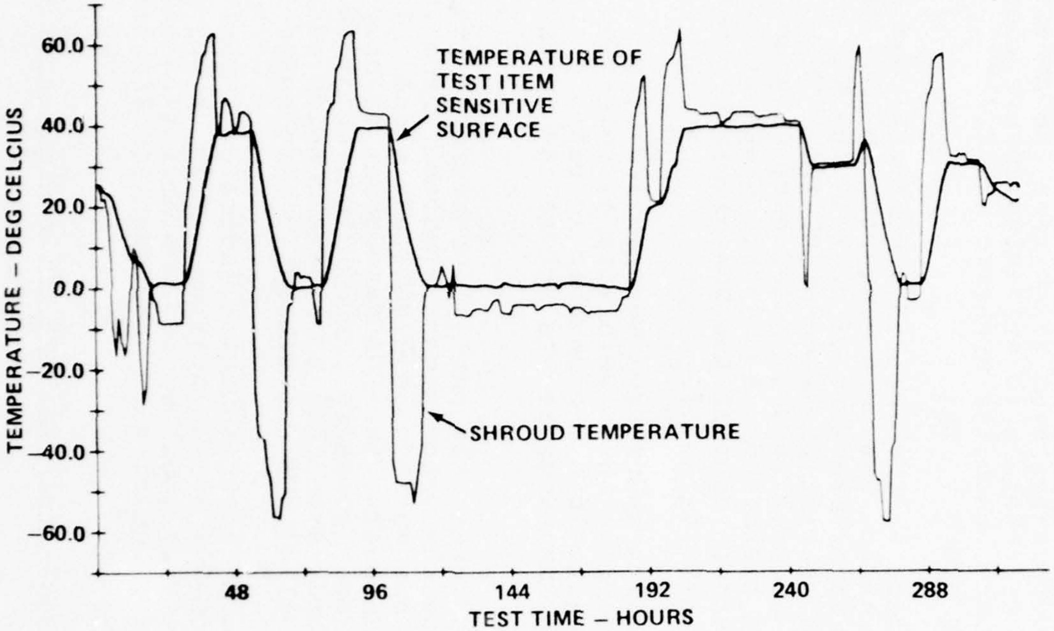

FIGURE 3 – TEST ITEM AND SHROUD TEMPERATURE PROFILE

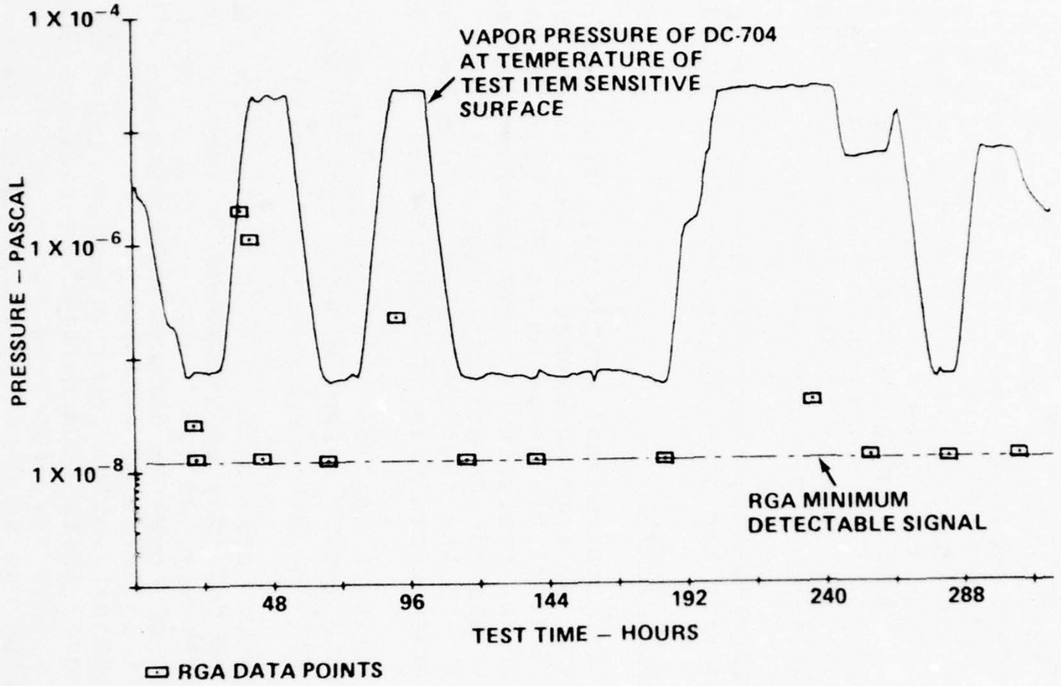

FIGURE 4 – COMPARISON OF RGA DATA WITH VAPOR PRESSURE OF DC-704 AT THE TEMPERATURE OF THE TEST ITEM SENSITIVE SURFACE.

vapor pressure which could correspond to a temperature of -44°C; no condensation on the test item is indicated.

7.0 CONCLUSIONS

The data taken during the bake-out and test operations pointed to the conclusion that the test had been conducted without condensing DC-704 diffusion pump oil on the test item. The RGA derived data indicated that the partial pressure in the chamber ambient remained below the saturation vapor pressure corresponding to the test item temperature. While the cold finger data do not provide conclusive proof that contamination did not occur, they provided no evidence that condensation would have taken place on the test item sensitive surfaces.

Most importantly, there were no test item indications that degradation had taken place because of DC-704.

8.0 RECOMMENDATIONS

The method for contaminant monitoring presented in this report depends on some knowledge of the contaminant, including identifiable peaks on an RGA scan, plus a knowledge of the contaminant vapor pressure characteristics. Based on the experience gained during this test, certain modifications to the test procedure would make the method easier and more certain in its application.

1. Maintain the RGA in a continuous scan mode. This would prevent missing data during critical periods.

2. Adjust scales on the RGA equipment so that the data may be displayed in terms of partial pressure. An additional refinement would be to process the data in real time and display it in terms of temperature corresponding to the saturation vapor pressure (taken as being equal to the RGA derived partial pressure). In this way, the temperature of the test item can be directly compared to the temperature at which condensation can occur.

3. Provide the chamber with a constant leak of a gas such as helium or neon using the partial pressure of this gas as a real time indicator of RGA performance.

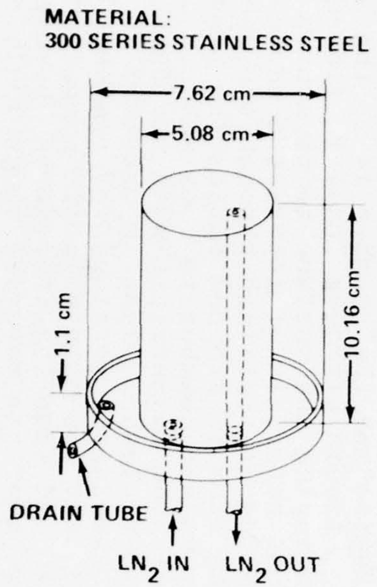

FIGURE A-1, COLD FINGER ASSEMBLY

APPENDIX A

THE COLD FINGER TECHNIQUE

The "cold finger" technique is a method used at the Goddard Space Flight Center to identify materials in the residual gases in vacuum systems. The technique employs a cold finger (see Figure A-1) which provides a surface on which these materials can deposit. The cold finger is located within the vacuum chamber test volume. The cold finger is washed with hot distilled water before the beginning of a test and then rinsed with isopropyl alcohol. The alcohol is poured over the assembly and allowed to run out through the drain tube into a container where it is retained for chemical analysis. This provides a pre-test sample.

When a test begins and the chamber is in the operating vacuum region, liquid nitrogen (LN_2) is flowed through the cold finger bringing the surface temperatures to near 80K. Species of most materials of interest condence on these cold surfaces and are retained through the course of the test. The LN_2 flow is stopped during the process of returning the vacuum chamber to room ambient and the cold finger is near room temperature when the chamber door is opened. Another alcohol rinse is obtained as quickly as possible and the sample retained for chemical analysis. It is recognized that the more volatile components are lost in this shut-down and sampling procedures, however, the process does retain much of the material which would constitute a contamination hazard.

Since approximately the same quantity of sample is taken each time (100 cm^3), a weighing of the residue provides some quantitative comparison of contaminant levels. The residue is chemically analyzed using infrared spectrophotometry plus, at times, gas-chromotography/mass-spectrometry.

If the post-test sample is shown to have low levels of contaminants, it is used as the pre-test baseline for the next test.

The total area on which material can condense and be later washed is a 234 cm^2; the area of the central cylinder (including its top) is 182 cm^2.

Molecular Contamination Studies by Molecular Beam Scattering

H. Nuss, Industrieanlagen-Betriebsgesellschaft mbH (IABG)
D-8012 Ottobrunn/Munich

ABSTRACT

The capability of molecular beam scattering from a solid surface for identification of molecular contamination of the surface was studied. The experimental approach using a thermal molecular beam source, a phase sensitive measuring technique and a vapor effusion source for defined contaminant application are described. The scattering distribution measured for a N_2 molecular beam interacting with a Platinum surface were measured for clean and those conditions contaminated by diffusion pump oil DC 705. An expression for the equilibrium of adsorption and desorption rate was derived. Comparing the measured dependency of the molecular beam intensity from surface temperature with the theoretically derived formula for the surface coverage offers a method to determine the desorption energy. The applied method allows to identify a surface coverage of DC 705 oil of approximately $2 \cdot 10^{-2}$ monolayers.

Paper presented at the USAF/NASA International Spacecraft Contamination Conference, March 7-9, 1978, U.S. Air Force Academy, Colorado

1. Introduction

Optical and thermal control surfaces of spacecraft components and experiments have been shown to be sensitive to the effects of contaminant deposition. Ultraviolet radiation can cause chemical reactions that result in changes of reflectivity and absorptance/emittance characteristics of the surfaces. For the studies of degradation effects by various organic films the influences during prelaunch testing in space simulation chambers and the effects of contamination during missions have to be considered. Limitations on performance of infrared telescopes operated on a Space Shuttle Orbiter or on Spacelab are imposed by the contaminant atmosphere of the spacecraft. To keep fluctuations in background radiation below the noise equivalent power of the best detectors anticipated for the 1980s a limit on the column density of infrared active molecules of approximately 10^{12} molecules cm^{-2} was recommended 1).

The purpose of this paper is to report the capability of molecular beam interaction with a solid surface for detecting molecular contamination of a surface by an organic film.

The influence of contamination on the scattering distributions of molecular beams was reported in different papers 2) 3). The theoretical description of the scattering distributions in the region of specularly directed scattering is in good agreement with the hard-cube-theory 4). The aspect of molecular beam interaction with a solid surface for satellite applications was studied, too 5).

The measuring principle to be applied in this study is based on the change of the scattering distribution of a molecular beam from a clean surface and from a contaminated surface.

The adsorption and desorption rates caused by the residual gas (clean surface) and by the deposited contaminant DC 705 (contaminated surface) will be estimated. An adsorption isobar will be derived which defines the relationship between surface coverage and surface temperature. By comparing the temperature dependence of the scattered beam intensity and of the surface coverage the desorption energy can be determined.

2. Experimental Approach

A plan view of the experimental setup is shown in Fig. 1. The work chamber 6) in which the scattering experiments were conducted was evacuated by adsorption pumps and an ion pump of 400 l/s pumping speed. To the main vacuum chamber a vapor effusion source is attached for the deposition of molecular contamination films. The work chamber assembly was furnished with a molecular beam source, sample holder adapter and heater, and a molecular beam detector and phase sensitive measuring setup 7).

2.1 Molecular Beam Source

The production for molecular beams characterized by almost complete freedom from intermolecular collisions is possible by producing a certain vapor pressure in an

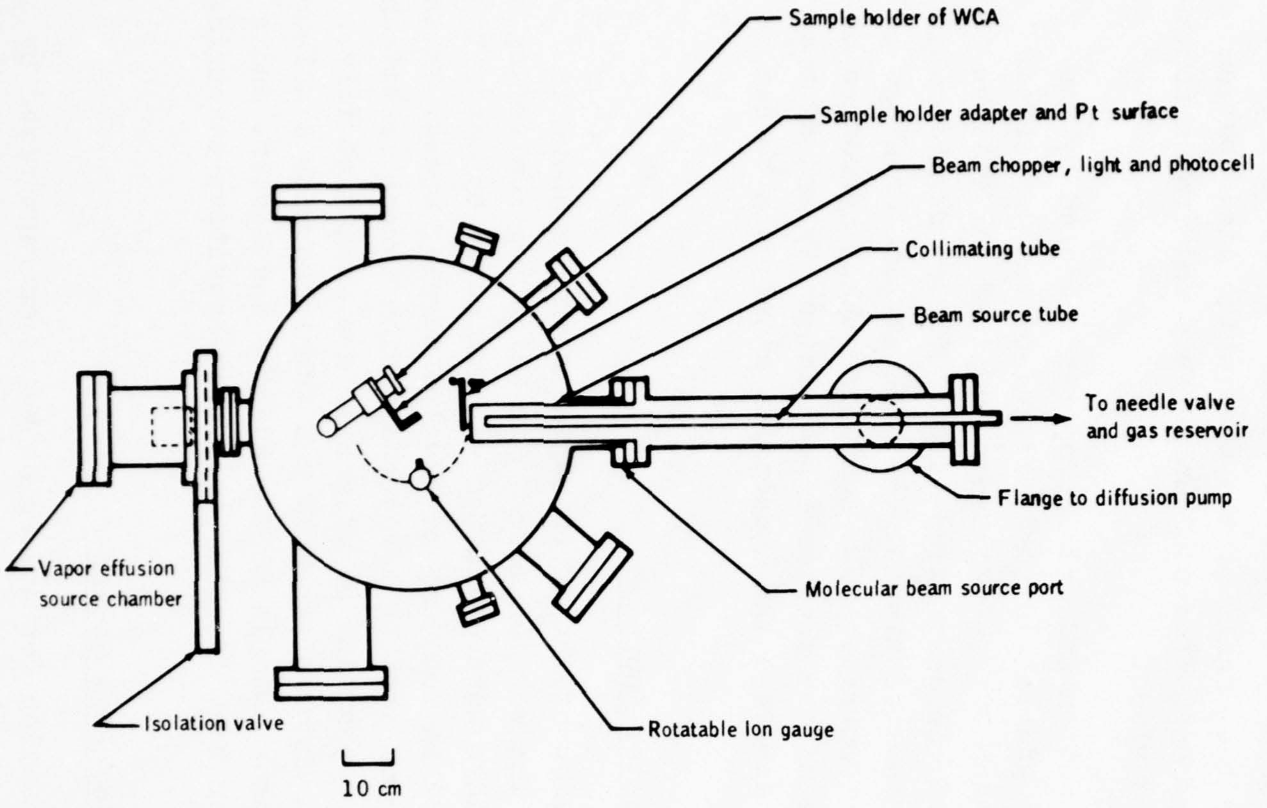

Fig. 1: Plan view of the experimental setup

enclosure with a well defined exit opening into a vacuum chamber.

For molecular flow conditions the total number N of particles per second escaping through an aperture of the enclosure is 8)

$$N = \frac{p_s A_s}{(2\pi m k T_s)^{1/2}} = 3.51 \cdot 10^{22} \frac{p_s A_s}{(M T_s)^{1/2}} \tag{1}$$

p_s : Pressure in enclosure, mbar
A_s : Area of ideal aperture, cm^2
T_s : Temperature in enclosure, K
m : Mass of particle, g
M : Molar mass of vapor, g $mole^{-1}$
k : Boltzmann constant, mbar cm^3 K^{-1}

The number of particles per second striking a target of unit area on the axis of the aperture at a distance r from the aperture is:

$$I(o) = \frac{n_s v_a A_s}{4\pi r^2} = 1.11 \cdot 10^{22} \frac{p_s A_s}{r^2 (M T_s)^{1/2}} \tag{2}$$

n_s : number of particles per unit volume in enclosure, molecules cm^{-3}

v_a : average molecular velocity, cm s^{-1}

Considering a cylindrical channel instead of an ideal aperture, the cylindrical channel being of length l and radius a the total number of particles per second given by equation (1) is reduced by the Clausing factor to N_1:

$$N_1 = \frac{8a}{3l} \frac{p_s A_s}{(2mkT_s)^{1/2}} \qquad (3)$$

The optimum orifice geometry for the delivery of the maximum fraction of effusing molecules onto a target is a long cylindrical aperture 9). This type of aperture was used for the molecular beam source which consists of the beam source tube and the collimating tube (Fig. 2). An oil diffusion pump system with a liquid nitrogen cooled cold trap and an optically dense water cooled baffle served as the pumping system for the beam source. The beam source tube was attached to a manifold with a variable needle valve and gas reservoir.

2.2 Phase Sensitive Measuring Setup

According to the equations (1) to (3) it can be estimated that for a pressure in the enclosure of $p_s = 10^{-1}$ mbar for a collimated beam of particles drawn from the

AD-A070 386 AIR FORCE MATERIALS LAB WRIGHT-PATTERSON AFB OH F/G 22/2
PROCEEDINGS OF THE USAF/NASA INTERNATIONAL SPACECRAFT CONTAMINA--ETC(U)
1978 J M JEMIOLA
UNCLASSIFIED AFML-TR-78-190 NL

8 OF 13
AD
A070386

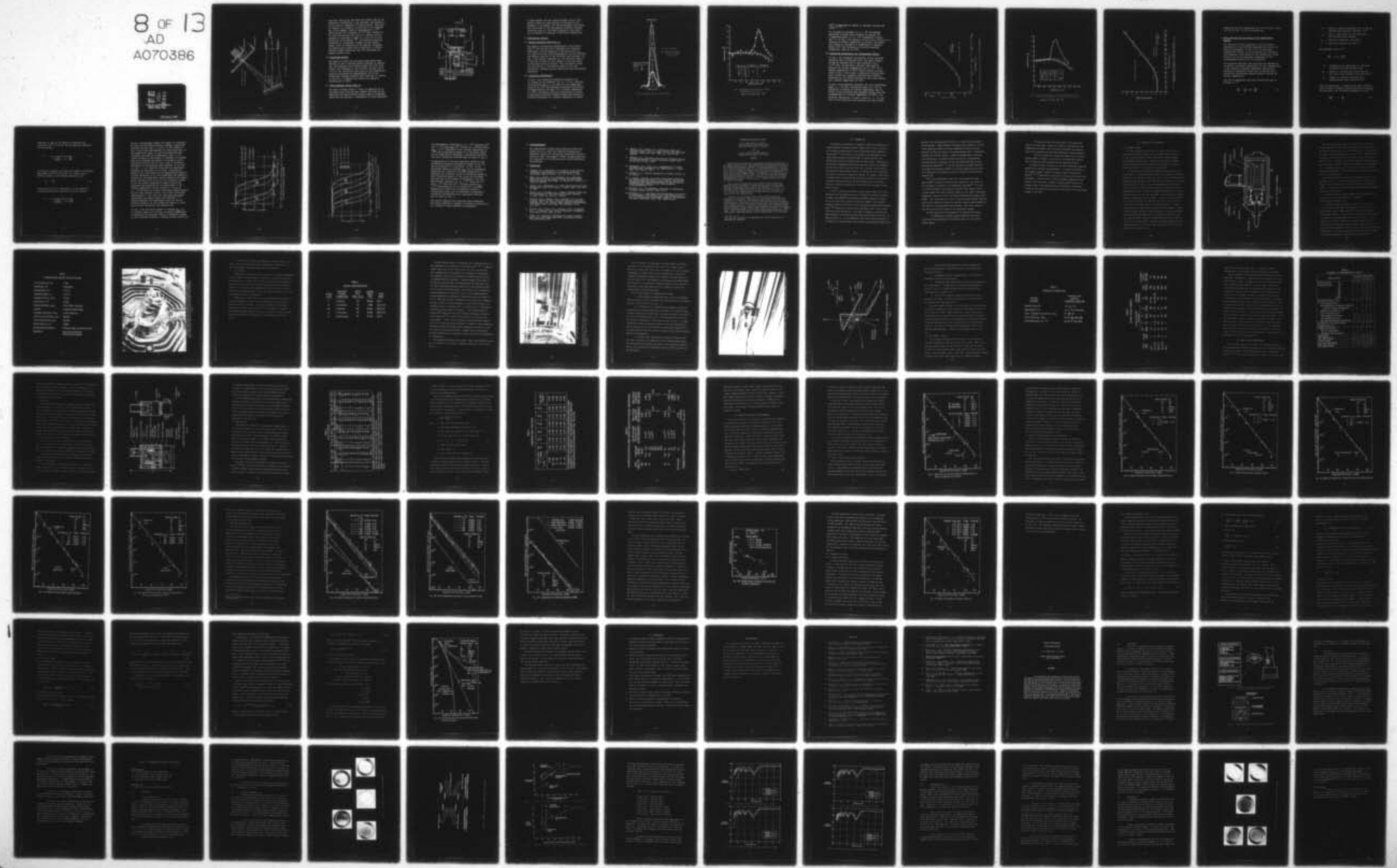

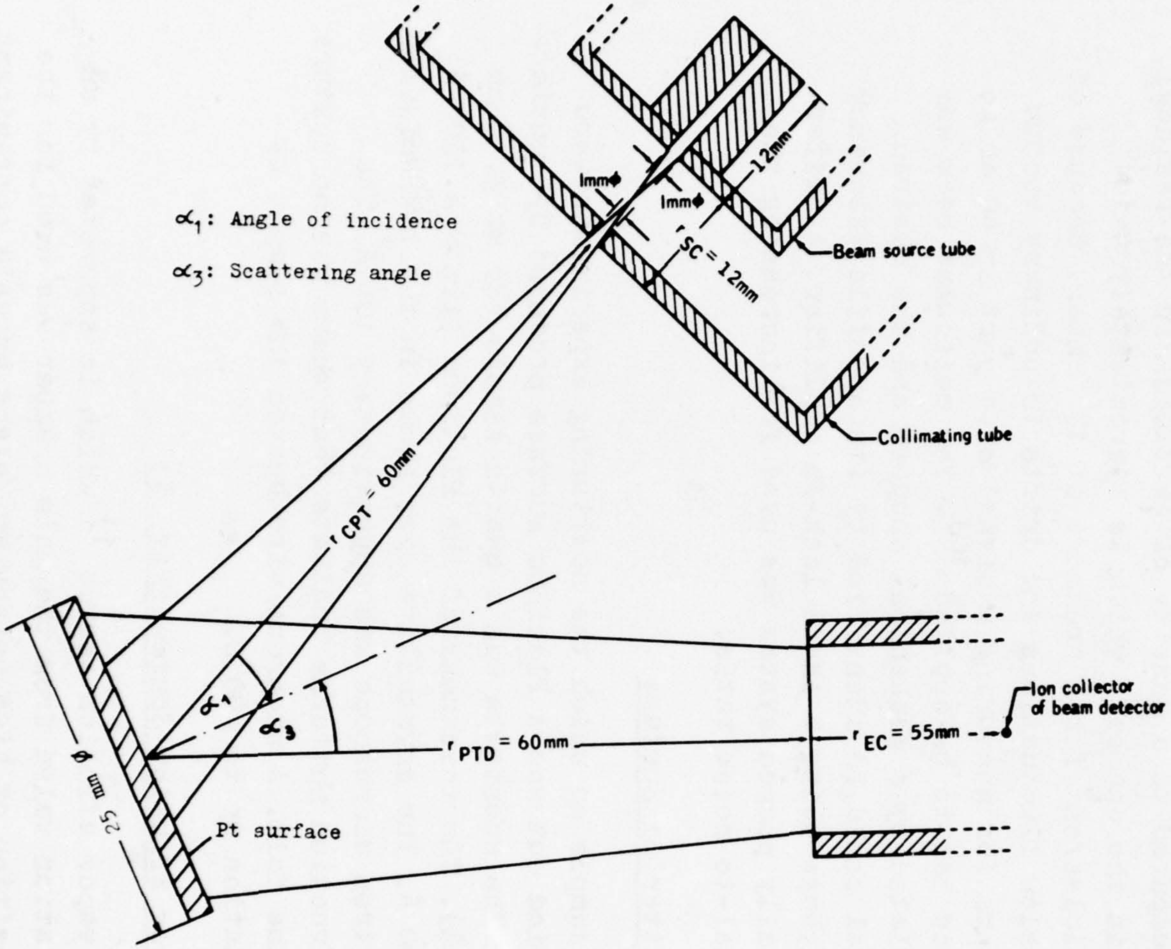

Fig. 2: Geometry of scattering experiment

molecular beam source and taken far enough away for an experiment conveniently to be conducted, the density is in the order of magnitude 10^9 particles/cm^3. This must be compared to a density of particles in the residual gas in the chamber, which is approximately $4 \cdot 10^{10}$ particles/cm^3 for a pressure of 10^{-6} mbar. Because of the slow fluctuations and drifts in ordinary vacuum systems for measuring a signal of 1 part in 40 an ac method has to be applied 10). The molecular beam was modulated by a mechanical chopper and the desired signal could be identified by its specific frequency and phase using a phase lock-in amplifier. A differentially pumped system was used for increasing the signal-to-noise ratio.

2.3 Scattering Surface

The sample on which the scattering experiments were carried out was a Platinum surface produced by sputtering. The substrate was a quartz sample (25 mm Ø, 6 mm thick). The thickness of the Platinum film was 1200 Å ± 200 Å. The crystallite size shown in the transmission electron microscope was approximately 100 Å. The diffraction patterns indicate that there was no texture in the foil. A nichrome wire heated the sample by radiation up to 400°C.

2.4 Vapor Effusion Source (Fig. 3)

The vapor effusion source 1) which is separated by an isolation valve from the main chamber was used for the deposition of high molecular weight organic contaminant films onto the surface. A combination of three apertures

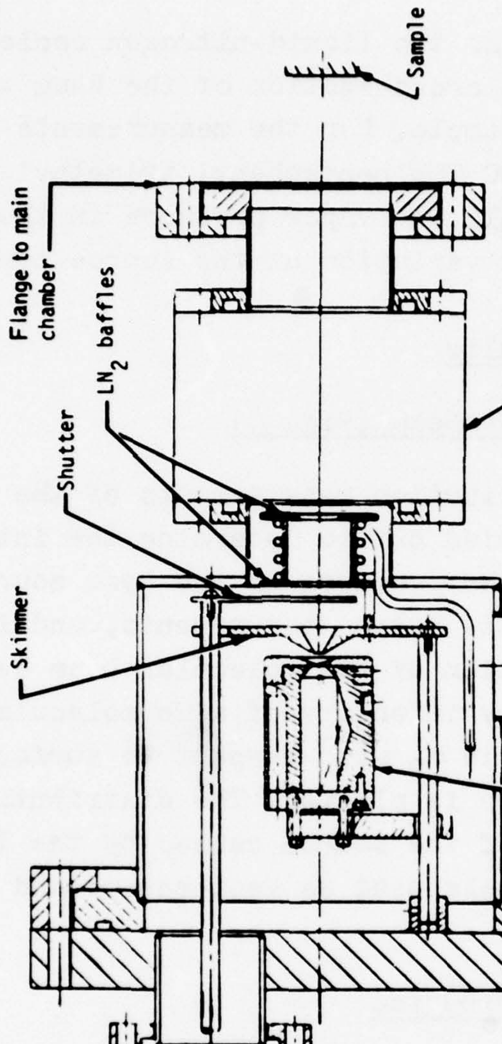

Fig. 3: Vapor effusion source chamber

(a beam skimmer and two liquid-nitrogen cooled collimators) limit the cross section of the beam to the diameter of the sample. For the measurements the source was filled with DC 705 pentaphenyl trimethyl siloxane diffusion pump oil. The vapor pressure in the source can be changed by variation of the source temperature.

3. Experimental Results

3.1 Primary Molecular Beam (Fig. 4)

The angular distribution measurements of the primary beam 7) were carried out to determine the intensity dependence from the pressure in the beam source p_s, for signal-to-noise ratio measurements, and for checking the angular solution of the molecular beam detector. In Fig. 4 the primary intensity of a He molecular beam as a function of angle α_2 with respect to surface normal of the beam source is plotted. The distribution shows the directivity of the source caused by the long cylindrical channels used as beam source and collimating apertures.

3.2 Scattering Distribution

In Fig. 5 the normalized scattered intensity I/I_o (I_o refers to the intensity for $\alpha_3 = 0$) as a function of scattering angle α_3 is shown. In the temperature range 39 to 129°C the measured scattering distribution is "approximately diffuse"; for a surface temperature of 210°C a specularly directed distribution is found. A reversible transition between diffuse and specularly directed scattering at a surface temperature of about

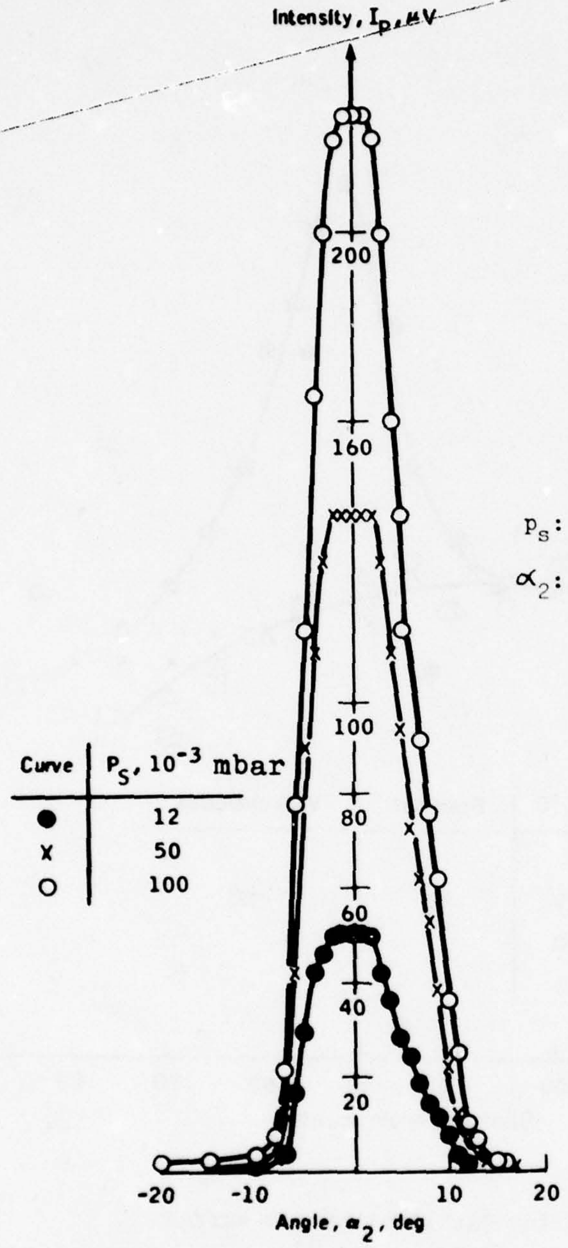

p_s: Source pressure

α_2: Angle with respect to surface normal of beam source

Fig. 4: Primary molecular beam intensity

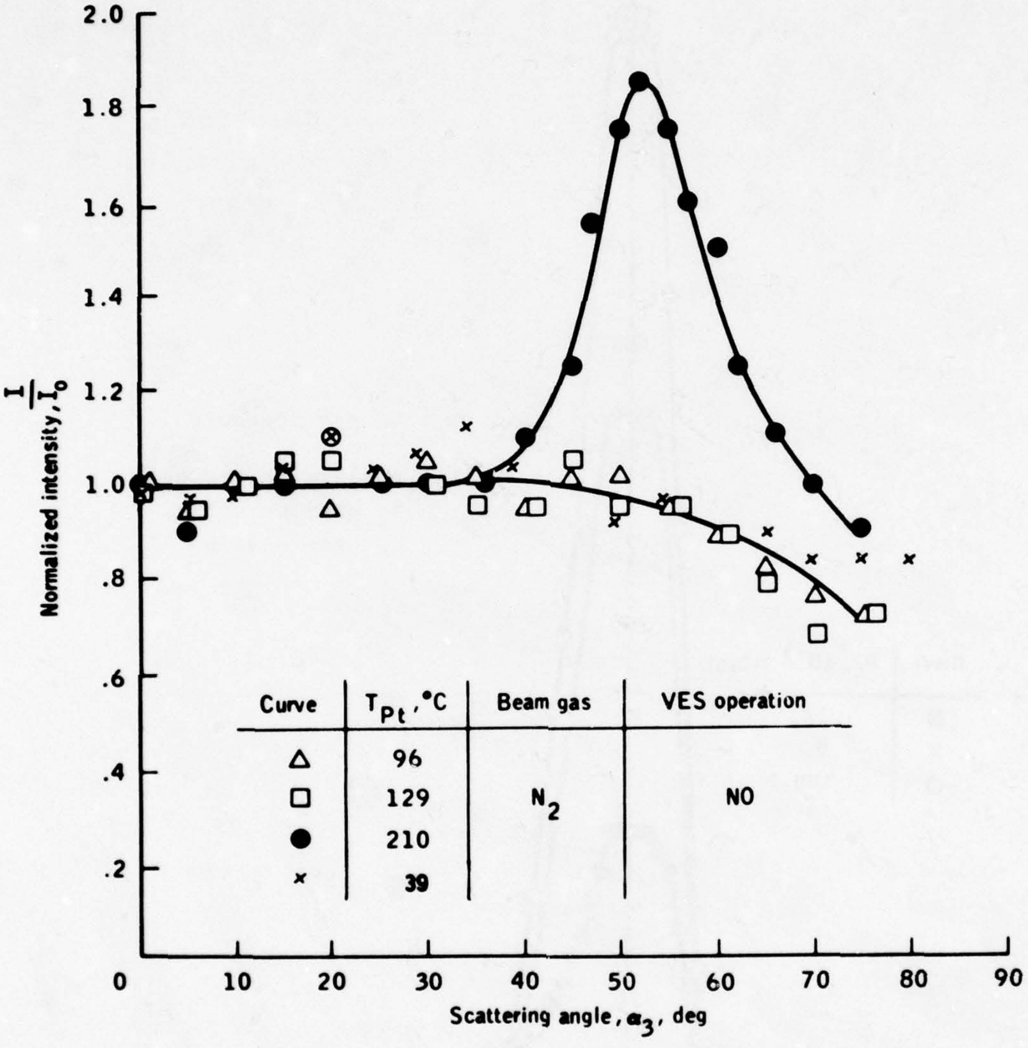

Fig. 5: Scattering distribution for surface temperatures 39 to 210 °C angle of incidence $\alpha_1 = 62^\circ$

$200^{o}C$ is explained by removal of adsorbed residual gas layers 2) 3).

For an angle of incidence of $\alpha_1 = 62^{o}$ the maximum specularly directed beam intensity is measured for a scattering angle of $\alpha_3 = 52^{o}$ (subspecular scattering 3)). In Fig. 6 the maximum scattered beam intensity as a function of surface temperature is plotted. The intensity starts to increase at a temperature of approximately $160^{o}C$ and increases in the entire measured temperature range up to $210^{o}C$.

3.3 Scattering Distribution for Contaminated Surface

In Fig. 7 the intensity distribution of the scattered molecular beam is displayed after the vapor effusion source was operated with a vapor pressure of $p_s = 5 \cdot 10^{-9}$ mbar. No specularly directed beam could be measured for surface temperatures up to $213^{o}C$. For a surface temperature of $360^{o}C$ similar results as indicated in Fig. 5 were found: A specularly directed beam with a width and a maximum scattered beam intensity comparable to the values measured for the clean surface for a surface temperature of $210^{o}C$.

In Fig. 8 the normalized intensity I/I_o for an incidence angle $\alpha_1 = 55^{o}$ and a scattering angle $\alpha_3 = 45^{o}$ is plotted as a function of surface temperature. The increase of the scattered beam intensity starts after the contamination at a surface temperature of $220^{o}C$. The necessary temperature to reach a value of 1.5 for the ratio of the scattered beam intensity for high surface

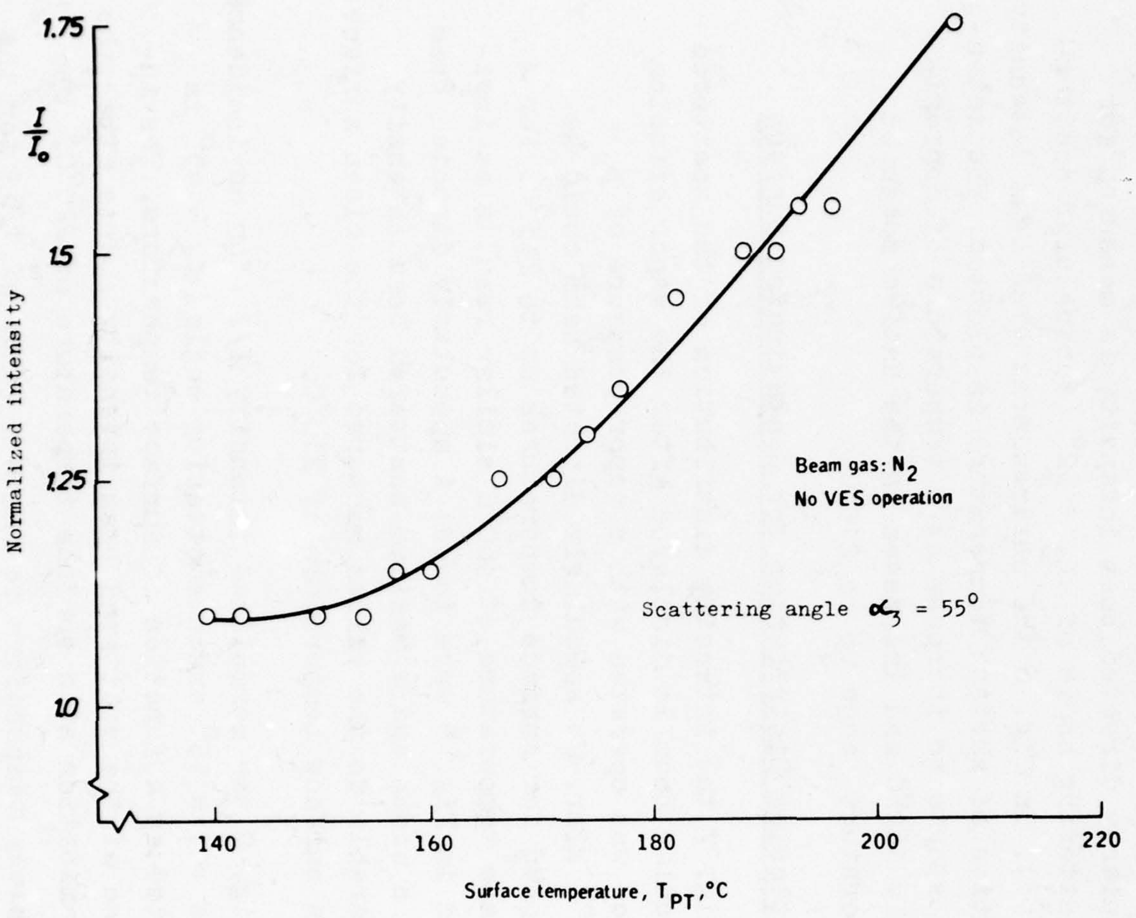

Fig. 6: Scattered beam intensity as a function of surface temperature

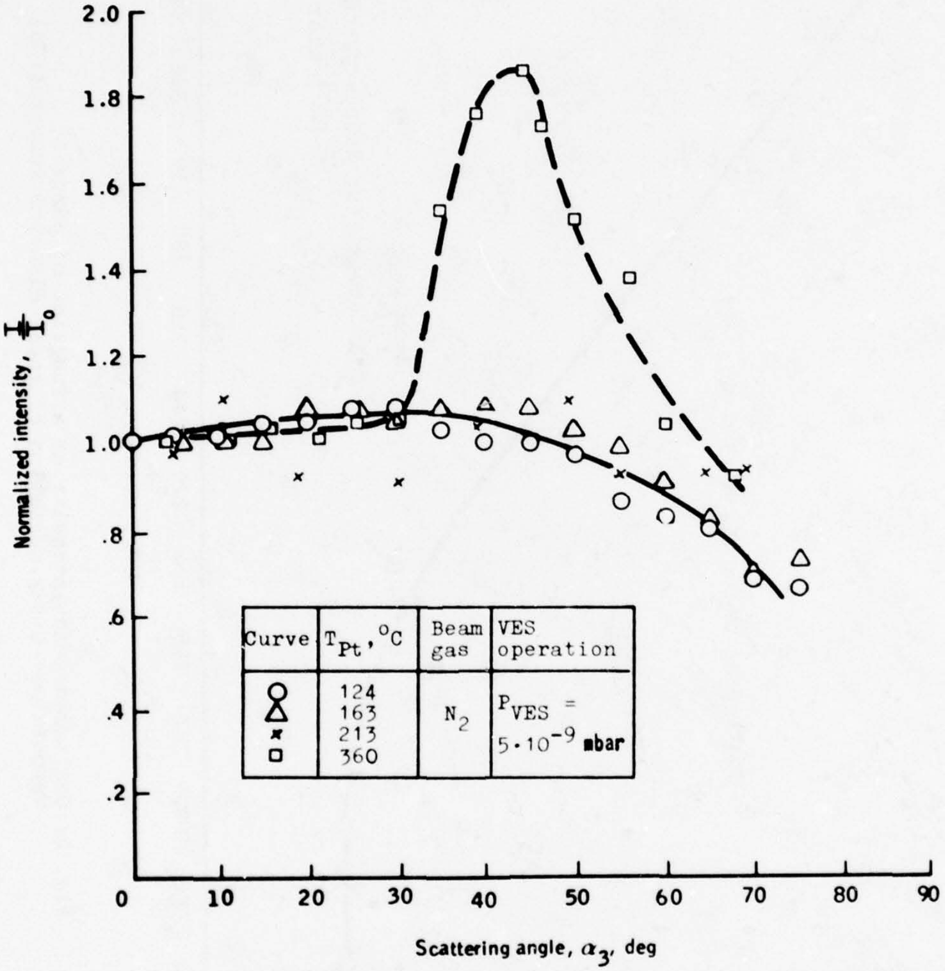

Fig. 7: Scattering distribution for surface temperatures 124 °C to 360 °C after operation of vapor effusion source (VES), angle of incidence $\alpha_1 = 55°$

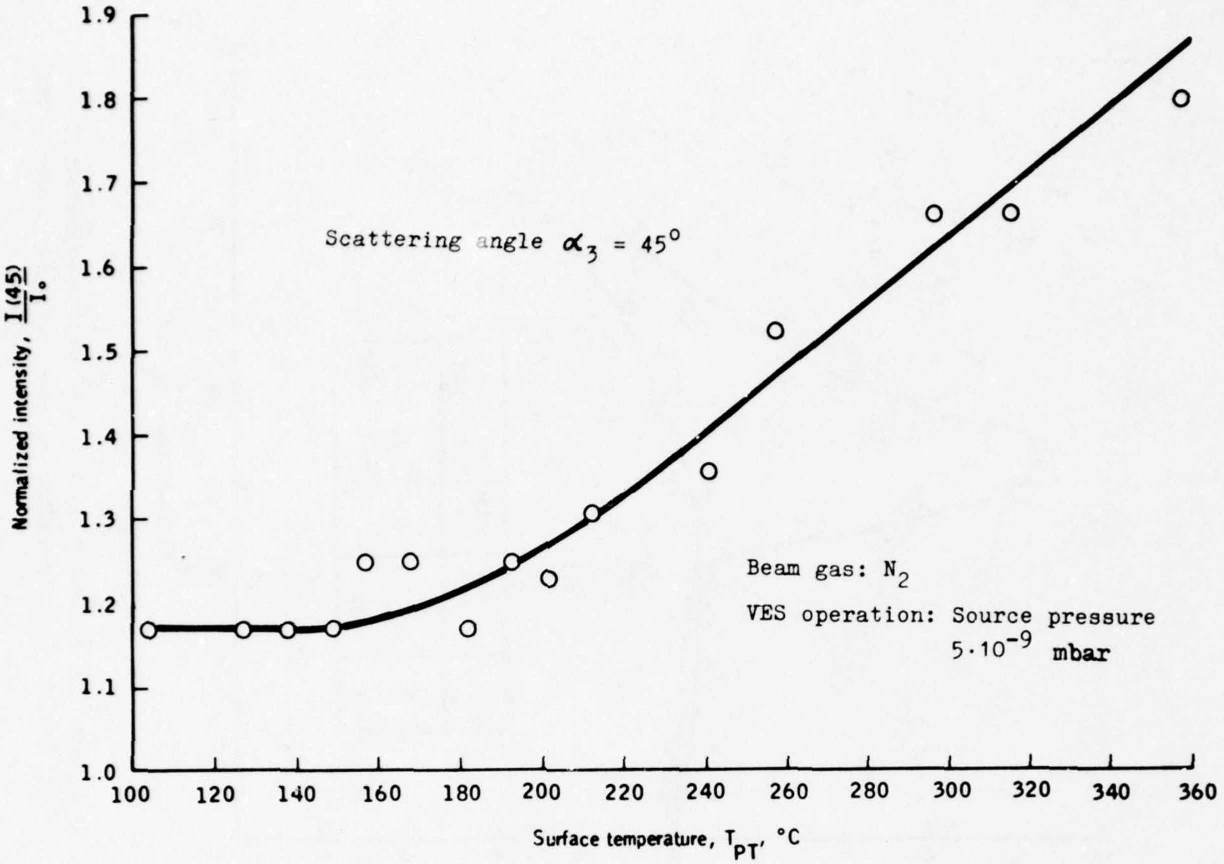

Fig. 8: Scattered beam intensity as a function of surface temperature after operation of vapor effusion source (VES)

temperature and low temperature was 210 °C before contamination and 360 ° C after contamination.

4. Interpretation and Discussion of the Experimental Results

The objective of this paragraph is the theoretical explanation of the different experimental results described in paragraph 3.2 and 3.3 for a clean and a contaminated surface. In the following the adsorption and desorption rates caused by the residual gas (clean surface) and by the deposited contaminant DC 705 (contaminated surface) will be estimated.

The scattered molecular beam intensity was measured as a function of surface temperature. For the determination of the scattered intensity dependence from surface coverage an adsorption isobar will be derived which defines the relationship between surface coverage and surface temperature.

The rate of desorption from unit surface area may be written as 11):

$$- \frac{d\sigma}{dt} = \frac{\sigma}{\tau_0} \exp\left(- \frac{E_A}{RT}\right) \qquad (4)$$

σ : Number of adsorbed molecules per cm^2 for not dissociating molecules, molecules cm^{-2}

τ_o : Time of oscillation of the molecules in the adsorbed state, seconds

E_A : Energy of adsorption, cal $mole^{-1}$

R : Molar gas constant, cal mole K^{-1}

The adsorption rate is [12)]

$$\frac{d\sigma}{dt} = \alpha N_A f\left(\frac{\sigma}{\sigma_0}\right) \qquad (5)$$

α : Probability for adsorption of a molecule hitting an uncovered surface area

N_A : Number of molecules per second and cm^2 arriving on the surface, molecules $cm^{-2}s^{-1}$

σ_o : Number of adsorbed molecules for a monomolecular layer, molecules cm^{-2}

With the assumption of Langmuir that every molecule, which strikes a molecule already adsorbed, returns to the gas phase, the following expression is valid [13)]:

$$f\left(\frac{\sigma}{\sigma_0}\right) = 1 - \frac{\sigma}{\sigma_0} \qquad (6)$$

Denoting $\Theta = \frac{\sigma}{\sigma_0}$ as the degree of covering from equations (4), (5) and (6) for equilibrium conditions can be written:

$$\Theta = \frac{1}{1 + \frac{\sigma_0}{\tau_0 \alpha N_A} \exp(-\frac{E_A}{RT})} \qquad (7)$$

According to kinetic gas theory the number of molecules per second and cm^2 N_A arriving on a surface for a particle density n and average velocity v_a is:

$$N_A = \frac{nv_a}{4} \qquad (8)$$

With equation (8) the expression for the degree of covering according to equation (7) is as follows:

$$\Theta = \frac{1}{1 + \frac{4\sigma_0}{\tau_0 \alpha n v_a} \exp(-\frac{E_A}{RT})} \qquad (9)$$

To get a relationship between the degree of covering θ and the scattered beam intensity showing a specularly directed portion (Fig. 5, 6 and 7, 8) the curves of Fig. 6 and 8 were approximated by linear functions. In the temperature range, in which the scattered beam intensity increases with temperature (Fig. 6, 8) a linear decrease of the degree of covering θ is assumed. With this procedure the degree of covering θ can be calculated from the data of Fig. 6 and 8. Plotting θ determined by the measured beam intensity in the form $\ln\left(\frac{1}{\theta} - 1\right)$ as a function of $\frac{1}{T}$ gives the adsorption energy E_A as the slope in this plot (according to equation (9)). This method is an approximation neglecting the dependence of E_A from temperature and degree of covering in the temperature range covered by the experiments. Evaluating the value for the adsorption energy E_A for the surface temperature range in which the scattered beam intensity $\frac{I}{I_0}$ is proportional to the surface temperature (Fig.6) results in a value of E_A = 23 kcal/mole for surface conditions without operating the vapor effusion source. This value corresponds approximately to the value for desorbing water vapor considering the tightly bound last monolayer 14). Having determined the approximate value for the adsorption energy E_A by this method the degree of covering θ can be calculated from equation (9).

In Fig. 9 the calculated degree of covering θ_{Res} due to residual gases as a function of surface temperature is displayed for different values of adsorption energy E_A and of particle density n. Taking the mean values for

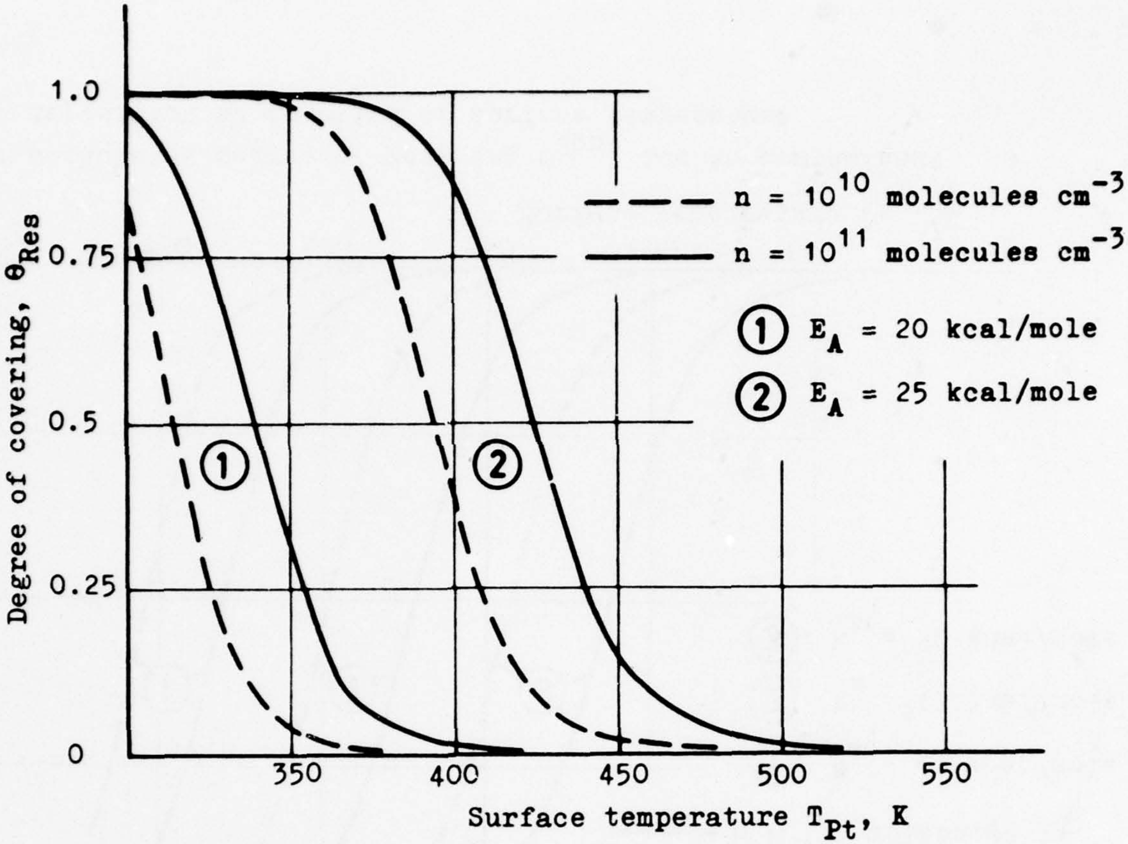

Fig. 9: Calculated degree of covering θ_{Res} due to residual gases as function of surface temperature

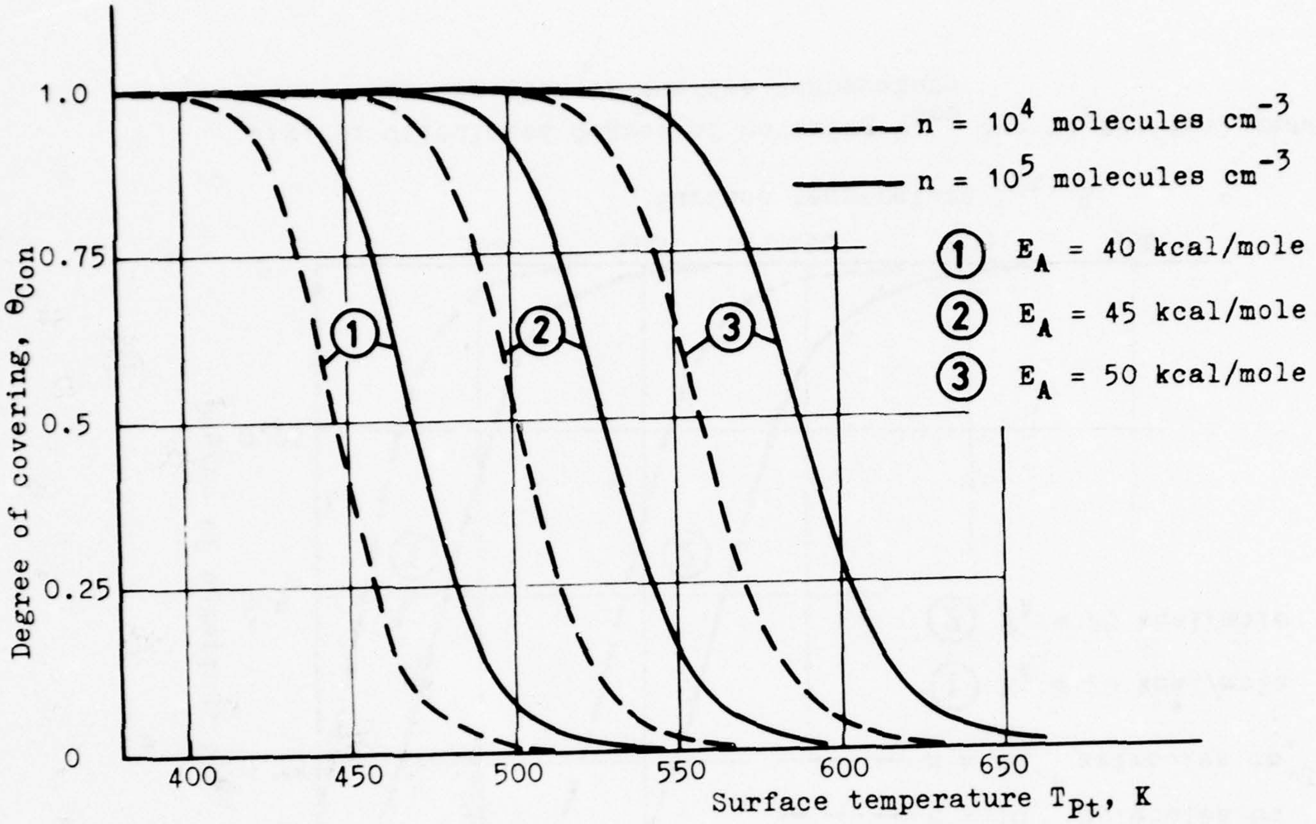

Fig. 10: Calculated degree of covering θ_{Cont} due to contaminant deposition as function of surface temperature

the experimental conditions of $\sigma_o = 10^{15}$ molecules cm^{-2} and $n = 10^{11}$ molecules cm^{-3} results in a covering degree $\Theta_{Res} = 3 \cdot 10^{-2}$ monolayers (for a surface temperature of 210°C and an adsorption energy of 25 kcal/mole) which can be identified by measuring a scattering distribution with a specularly directed beam as shown in Fig. 5.

By application of the above mentioned method for the contaminated surface an adsorption energy for DC 705 can be evaluated of 52 kcal/mole. In Fig. 10 the calculated degree of covering Θ_{Con} due to contaminant deposition as a function of surface temperature is displayed for different values of adsorption energy E_A and of particle density n. The latter was estimated with the aid of the formula of paragraph 2. For the experimental conditions of $\sigma_o = 10^{14}$ molecules cm^{-2} and $n = 10^{4}$ molecules cm^{-3} a covering degree $\Theta_{Con} = 2 \cdot 10^{-2}$ monolayers can be calculated (for a surface temperature of 360°C and an adsorption energy of 52 kcal/mole) which can be identified by measuring a scattering distribution with a specularly directed beam as shown in Fig. 7.

The results indicate that molecular beam scattering from solid surfaces is capable to identify contamination of a surface by some hundredth of monolayers.

5. Acknowledgement

The experimental studies were carried out while the author was on a leave from IABG and working as an ESRO/NASA fellow, the theoretical evaluation was performed at IABG. The support of ESRO is appreciated and the assistance of the Johnson Space Center gratefully acknowledged.

6. References

1. Simpson, J.P.; Witteborn, F.C; Effect of the Shuttle Contaminant Environment on a Sensitive Infrared Telescope, Applied Optics, Vol. 16, 1977, p. 2051

2. West, L.A.; Kozak, E.I.; Somorjai, G.A., Molecular Beam Scattering from Single Crystal Surfaces under Ultrahigh Vacuum Conditions, J. Vacuum Sci. Technol. 8, 1971, p. 430-436

3. Smith, J.N.; Saltsburg, H.: Atomic-Beam Scattering from Epitaxially Grown Gold Films, J. Chem. Physc. 40, 1964, p. 3585

4. Logan, R.M.; Stickney, R.E., Simple Classical Model for the Scattering of Gas Atoms from a Solid Surface, J. Chem. Phys. 44, 1966, p. 195-201

5. Evlanov, E.N.; Lebedev, Yu.V.; Leonas, V.B.: On the Possible Method of Gas- Satellite Surface Interaction Studies, Proc. 9th Intern. Symp. Rarefied Gas Dynamics, 1974 DFVLR Press, Porz-Wahn, West-Germany, 1974, p. E 16-1

6. Dillow, C.F.; Allen, T.H.; Linford, R.M.F.; Richmond R.G., A System for the Study of Molecular Contamination, NASA SP 379, 1975, p. 623

7. Nuss, H.E., Molecular Contamination Study by Interaction of a Molecular Beam with a Platinum Surface, NASA TMX-58169, 1976

8. Hughes, V.W.: Schulz, H.L. (Editors): Atomic and Electron Physics Part A, Atomic Sources and Detectors, Academic Press, New York, 1967, pp. 155-198 and 390-414

9. Freeman, R.D.: Molecular Flow and the Effusion Process in the Measurement of Vapor Pressures, Report ASD-TDR-63-754, Pt III, 1967

10. Brackmann, R.T.; Fite, W.L.: Condensation of Atomic and Molecular Hydrogen at Low Temperatures, J. Chem. Phys. 34, 1964, p. 1572

11. Redhead, P.A., Thermal Desorption of Gases, Vacuum 12, p. 203-211

12. D. Jaeger: Einfluss von an der Oberflaeche adsorbierten Gasteilchen und Einfluss von Struktur auf die Gas-Festkoerper-Wechselwirkung gemessen an der Molekularstrahlstreuung, Deutsche Luft- und Raumfahrt, Forschungsbericht 73-14

13. de Boer, J.H.: The Dynamical Character of Adsorption, Clarendon Press, Oxford, 1968, p. 54

14. Griffith, J.S.: Some Tests for the Increase in Friction of Mechanisms of the Mariner Mars 1969 Spacecraft in the JPL Molsink Space Simulation Chamber, AIAA/ASTM/IES 4tn Space Simulation Conf. 1969, Paper 69-996

BIPROPELLANT ENGINE PLUME STUDY[†]

H. E. Scott and D. F. Frazine
Arnold Engineering Development Center
Arnold Air Force Station, Tennessee

and

Lt E. G. Lund
Air Force Rocket Propulsion Laboratory
Edwards Air Force Base, California

ABSTRACT

Data from the first phase of an experimental program to characterize the exhaust properties of a liquid bipropellant engine under vacuum conditions are presented and discussed. Emphasis is placed on measurements of the mass flux in the plume backflow region of a 5 lb_f bipropellant thruster at angles up to 150° with respect to the plume centerline using temperature compensated quartz crystal microbalances (QCMs). The measurements were conducted in a high vacuum cryogenic chamber at AEDC. The addition of new GHe and LHe cryopanels provided a blank-off pressure in the 10^{-7} torr range and maintained the background pressure in the 10^{-5} torr range while pulse firing the motor (25-100 msec pulse width, 1-10% duty cycle). Chamber recovery time was a few tenths of a second.

Several engine configurations were tested at different operating conditions so as to characterize exhaust properties and to investigate potential contamination effects. Variations included: injector--0° and 45° splash plate; combustion chamber--2 inch cylindrical, 1.5 inch cylindrical, and 2 inch conical; nozzle area ratio--50:1 and 100:1; O/F--1.4, 1.6, and 1.8; chamber pressure--75, 100, and 125 psia; pulse duty cycle--1%, 5%, 10%, and continuous.

QCM data for the plume mass flux at 25° to 150° from the plume centerline are presented. Comparisons with plume models demonstrate the importance of treating the nozzle boundary layer expansion into the plume backflow region. These data are the only known data describing the boundary layer expansion of a hot rocket engine exhaust into a hard vacuum representative of space conditions. In addition to the QCMs, other diagnostic measurements were made to characterize the exhaust properties during the first phase of this experimental study. Some of these results are presented in a companion paper. During the second phase of testing electron beam fluorescence, mass spectrometric, additional QCM and scattering measurements will be performed.

[†] This work was initiated by the AFRPL/PACP and jointly sponsored by the AFRPL/PACP and AEDC/DOTR.

1.0 INTRODUCTION

The potential contamination of spacecraft surfaces and components by exhaust products from space thrusters, whether solid, liquid or electric, has received increased attention from the spacecraft design community in recent years[1-6]. This concern is attributed to the development of more sophisticated spacecraft systems designed to perform multiple, non-interferring missions for longer periods of time in space. Contamination and subsequent degradation of sensitive spacecraft surfaces and components, such as thermal control coatings, solar cells, antennas, optical devices, and especially cooled infrared sensors, can compromise mission objectives and lead to a reduction in spacecraft lifetime. For example, contamination of thermal control surfaces with low absorptivity-to-emissivity properties, required for passive control of spacecraft temperatures, can cause an increase in spacecraft temperature, thus affecting the spacecraft mission and/or lifetime.

In order to predict the effects of rocket exhaust plumes from liquid bipropellant and monopropellant engines on spacecraft surfaces of interest, a computer code (CONTAM)[7] was developed by McDonnell Douglas Corporation for the Air Force Rocket Propulsion Laboratory (AFRPL). Davis and Wax[8] conducted a partial verification of this code against monopropellant hydrazine data[9, 10] collected at the Jet Propulsion Laboratory (JPL). Their studies identified serious deficiencies in the code's treatment of the nozzle and plume expansion, particularly at large angles from the plume centerline. An additional deficiency in the CONTAM code, which has long been recognized, is the absence of a nozzle boundary layer treatment and subsequent boundary layer expansion into the plume backflow region (i.e., expansion angles greater than 90 degrees). Proper treatment of boundary layer processes is critical to the successful prediction of plume contamination effects since most spacecraft surfaces are located in the plume backflow region. Consequently, the AFRPL has initiated studies to improve the CONTAM code by correcting these deficiencies. An extensive plume data base for a monopropellant hydrazine thruster, along with cold flow and condensation data for pure and mixed gas expansions[12, 13], has been obtained at the AEDC[11] and JPL[9]. The purpose of the present program is to provide a quantitative data base for a representative bipropellant engine for further verification of the improved code.

Prior to this experimental study very little bipropellant plume data existed[14], and most of these data were qualitative. As a result of the development of improved in situ measurement techniques[16, 17,] as well as a high performance 5 lb_f bipropellant engine[15] small enough to test in a vacuum chamber under space simulation conditions, the subject measurements program was initiated at the Air Force Arnold Engineering Development Center (AEDC). The 5 lb_f thruster was fired in a space simulation chamber which had been suitably modified to provide the necessary cryogenic pumping capability, and various in situ measurements were performed. Here, we are reporting the results from the first phase of this experimental program.

The basic objectives of the program can be summarized as follows:

(1) demonstrate a cryogenic pumping capability sufficient to permit mass flux measurements in the backflow region of a 5 lb_f bipropellant engine;

(2) measure the mass flux distribution in the bipropellant plume over a wide range of angles with respect to the nozzle axis for CONTAM code verification; vary the engine configuration and operating conditions to determine any significant dependence on these parameters;

(3) fully characterize the engine by identifying all products (gaseous species, droplets, or particles) in the plume and by measurement of nozzle exit plane concentration and temperature profiles.

This paper provides an overview of the entire program and a detailed examination of the mass flux measurements. It includes discussions on the cryogenic chamber, diagnostic techniques, quartz crystal microbalance[9, 10, 18] (QCM) design and operation, and results of the mass flux measurements. Time and space limitations preclude a comprehensive discussion of all the results, although a companion paper[19] presents preliminary results of the condensed phase IR transmission measurements. A technical report describing the project in more detail will be published by AEDC in late 1978.

2.0 OVERVIEW OF THE EXPERIMENT

2.1 Cryogenic Chamber

The space simulation facility (Fig. 1) used for this study is a conventional cylindrical chamber 10 ft in diameter and 20 ft long. It is fully lined with liquid nitrogen (80°K) and refrigerated gaseous helium (20°K) cryogenic panels. Additional liquid helium cryopumps were installed both downstream and forward of the engine to pump H_2, a major constituent in the bipropellant exhaust plume.

The requirements which determine chamber performance criteria and design goals in a plume measurements program of this nature are frequently obvious but also difficult to quantify. Keep in mind the objective was to measure the mass flux distribution from the rocket engine and in this case to measure mass flux levels in the plume backflow region which are at least six orders of magnitude lower (unknown at the outset) than in the forward flow direction. Clearly the chamber background pressure must be kept sufficiently low that the plume shape is not significantly different than in an operational space environment. A careful flow field analysis is required to translate this statement into design criteria, yet no verified flow field model exists for the backflow region. A second requirement which is more easily converted into a design goal is simply a mean free path long enough to permit molecules to travel the distance from the nozzle to the QCMs with no intermolecular collisions. Mean free path calculations indicated a background pressure on the order of 10^{-5} torr or lower was needed. Hence the design goal adopted here was a chamber pressure of 1×10^{-5} torr under continuous firing of the 5 lb_f thruster for a period of 1 sec.

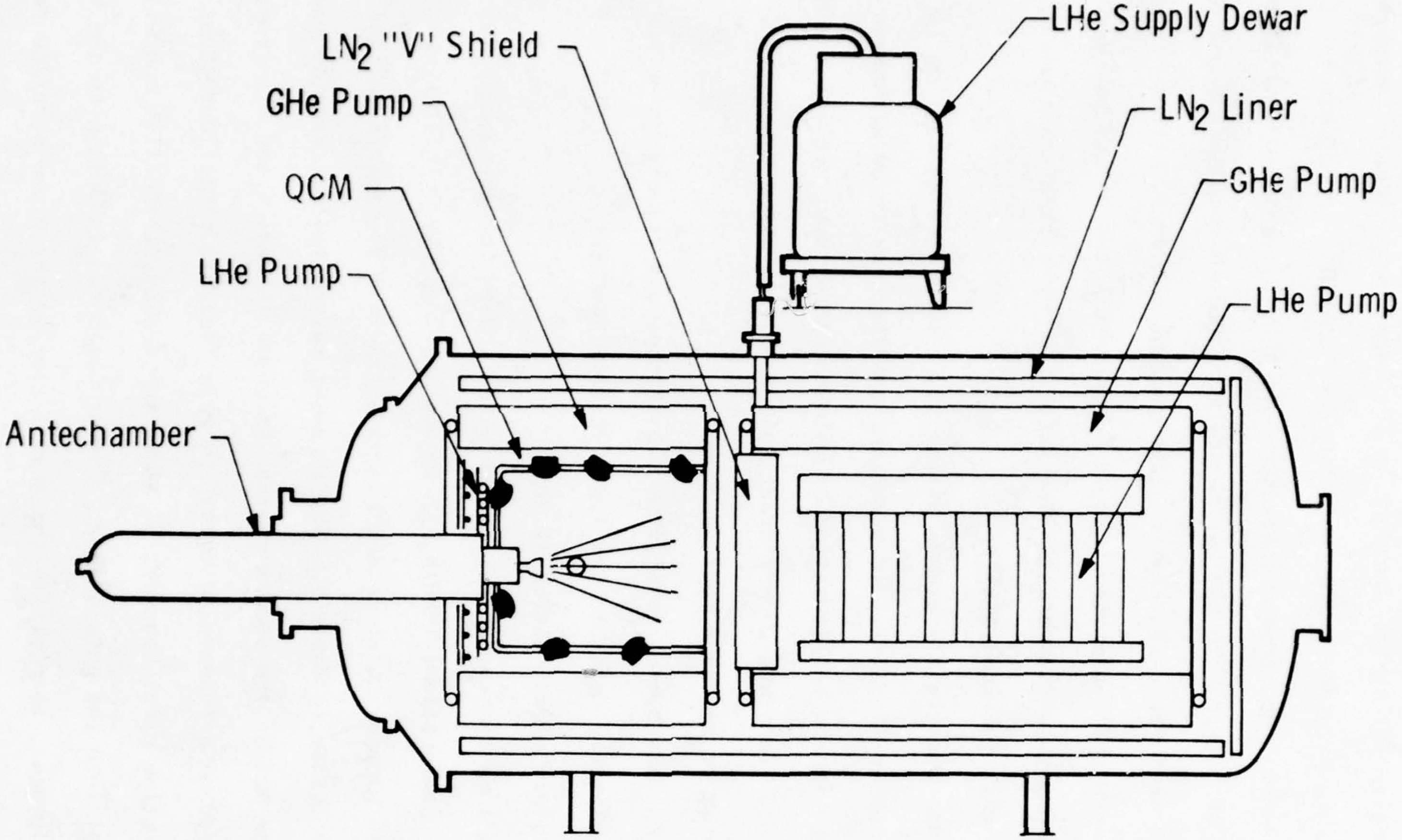

AEDC 10V CRYOGENIC CHAMBER
FIG. 1

The data presented here gives clear evidence that the chamber performed adequately for the backflow measurements. Typically during the engine firing the pressure in the backflow region, as measured by an ion gauge pointed toward the plume, was 3×10^{-5} torr. Between firings the chamber recovered quickly (in less than 0.1 sec) to a pressure of $4\text{-}8 \times 10^{-6}$ torr. To further verify that the chamber background pressure had no measurable systematic effect on the QCM data, helium was added to raise the chamber pressure to 10^{-3} torr where the effect on the QCM measurements was apparent. The details of this experiment are presented later with the QCM results.

One additional feature of the facility deserving mention is the antechamber (Fig. 1). It permitted the thruster to be withdrawn for changes in the configuration or maintenance without cycling the main chamber. This was a very practical capability since cycling the chamber required at least 24 hours.

For additional details on the chamber and its cryogenic pumping capabilities, refer to the AEDC Facility Handbook[20].

2.2 Bipropellant Engine (5 lb_f)

As mentioned earlier the thruster chosen for this study was a 5 lb_f bipropellant (MMH/N_2O_4) engine developed by Aerojet Liquid Rocket Company under an AFRPL contract[15] in 1973; specifications[21] are provided in Table 1. The thruster was installed, free to radiate, in one end of the vacuum chamber as shown in Figs. 1 and 2. It was mounted on a traversing mechanism with flexible propellant lines permitting axial translation along the chamber centerline and withdrawal into the antechamber. Effort was made, in designing the mounting arrangement, to minimize the obstruction in the plume backflow region for the QCM measurements at large angles from the nozzle axis.

TABLE 1

BIPROPELLANT ENGINE SPECIFICATIONS

Thrust (Vacuum), lb_f	5 max.
Propellants, O/F	N_2O_4/MMH
Mixture Ratio, O/F	1.4-1.8
Chamber Length, in.	1.5-2.0
Chamber Pressure, psia	75-150
Area Throat, $in.^2$	0.0186
Nozzle Area Ratio, A_e/A_t	50 and 100, Contoured
Injector	6-Element Splash Plate
Propellant Flow Rate, lb/sec	0.0167 (Nominal)
Inlet Pressure Oxidizer, psia	100-300
Inlet Pressure Fuel, psia	100-300
Dribble Volume, $in.^3$	0.0006
Nozzle/Chamber Material	Silicide-Coated, Columbium Alloy
Application	Space Propulsion/RCS Buried/Free to Radiate

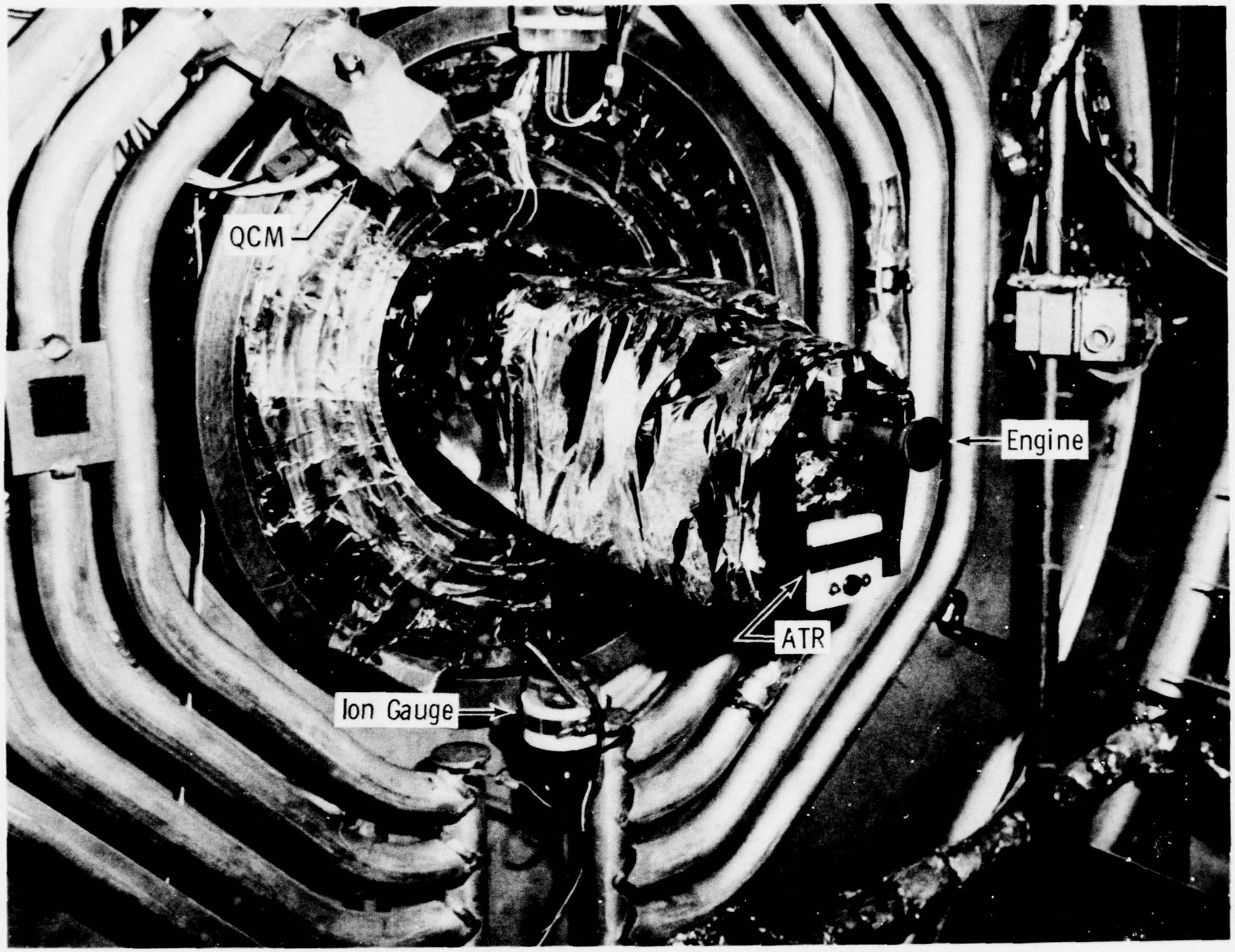

BIPROPELLANT ENGINE (5 lbf) INSTALLED IN CRYOGENIC CHAMBER.
QCMs, ION GAUGES, AND ATR CRYSTAL ARE INCLUDED IN BACKGROUND.
FIG. 2

A variety of five thruster configurations, listed in Table 2, were tested. The five configurations were assembled from two injectors and four interchangeable combustion chamber/nozzle combinations.

2.3 Test Rationale

Although this project falls loosely into the area of plume contamination, we are not dealing with contaminants as defined in the usual literal sense. The objective was to measure the mass flux distribution in the bipropellant exhaust plume over a wide range of angles and engine operating conditions. Therefore it must remain clear throughout this paper that we are concerned with mass flux measurements even if we loosely refer to the mass flux in the plume backflow region as contamination.

The QCMs used to measure the mass flux distribution had to operate at a very low temperature in order to collect (cryopump) as many bipropellant plume constituents as possible. By operating the QCMs at 25°K, based on known equilibrium vapor pressure curves[22], we could expect to cryopump all bipropellant exhaust species except H_2. The species actually collected at various QCM operating temperatures will be discussed later with the results.

TABLE 2

ENGINE CONFIGURATIONS

Config. Code	Combustion Chamber Length/Shape	Nozzle Area Ratio, A_e/A_t	Injector Splash Plate	Firing Dates
C	2 inch/cyl.	50	45 deg	Oct 5
A	1.5 inch/cyl.	50	0 deg	Oct 17-19
BL	2 inch/cyl.	100	45 deg	Nov 8-11
B	1.5 inch/cyl.	50	45 deg	Nov 21-23
D	2 inch/conical	50	45 deg	Dec 6

Another important aspect of the approach was a deliberate effort to take advantage of all available non-interference type[11, 16, 17] diagnostic methods rather than relying solely on one tool such as the QCM which would compromise the entire program if any problems were encountered. Each diagnostic technique was selected for a specific purpose and also to complement the other techniques. The best example of the latter is the manner in which the QCM, the condensed phase IR transmission, and the laser interference techniques combined to provide information which none in and by itself could produce. The two-angle laser interference technique measured the thickness of a thin film of condensed exhaust products pumped onto a cryogenically cooled optical substrate (shown in Fig. 3). When the thickness is combined with the mass of the cryodeposit measured by a QCM at the same temperature as the optical substrate, the cryodeposit density is obtained; this is a useful piece of information for identifying the constituents in the deposit. The condensed phase IR transmission[19] coupled with the laser thickness measurement yielded the optical properties[16] (n, index of refraction and k, absorption index) of the deposit. Finally, the IR transmission spectra permitted identification of all IR active species collected by the QCMs at a given temperature and helped to establish the QCM operating temperatures required to selectively collect the plume constituents. Together the three techniques provided significantly more information than the three working independently.

2.4 Measurements

The program was divided into two phases. Phase I was completed recently and is the subject of this paper; it addressed objectives 1 and 2 listed earlier.

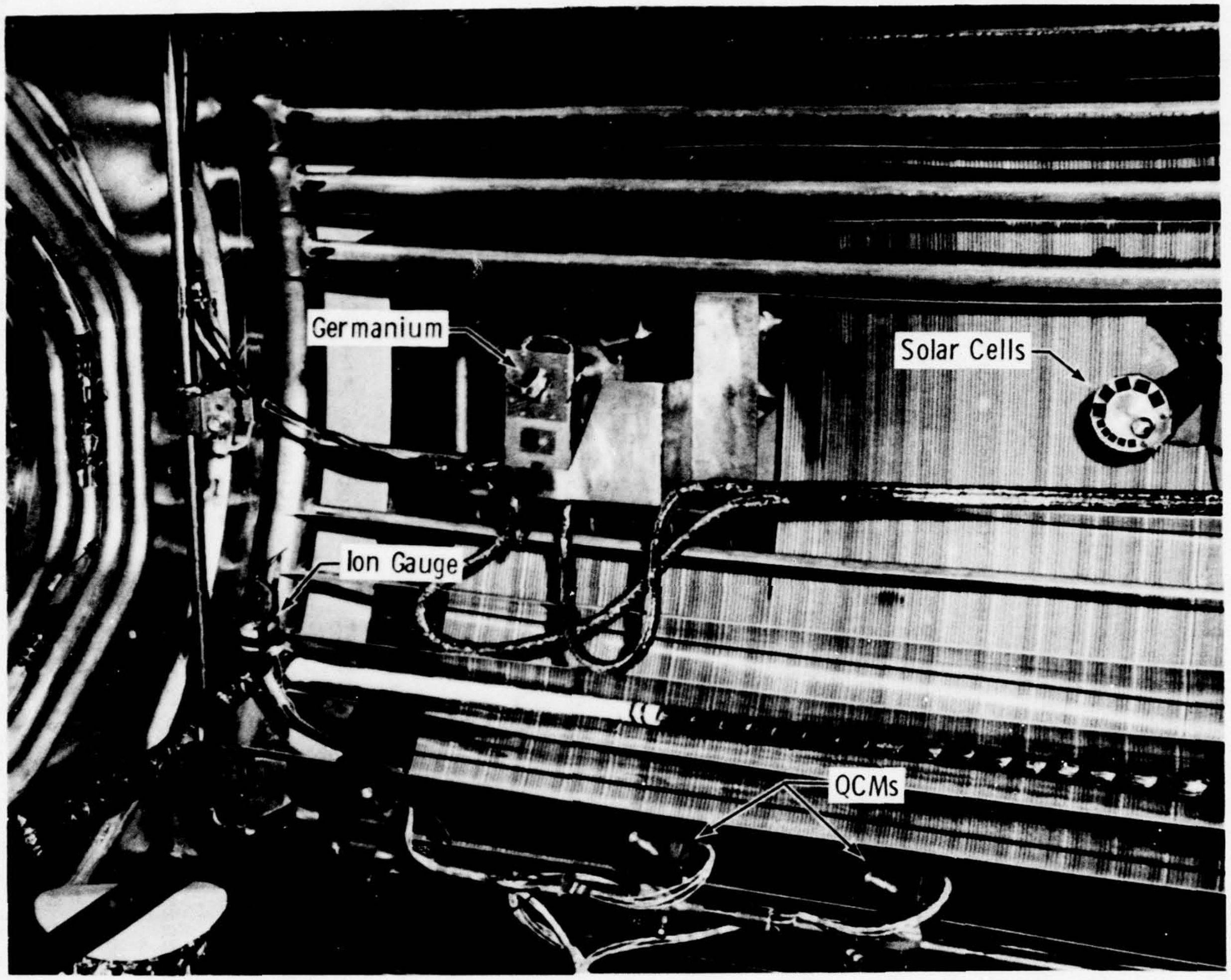

QCMs, SOLAR CELLS, AND GERMANIUM SUBSTRATE INSTALLED IN CRYOGENIC CHAMBER.
FIG. 3

QCMs INSTALLED IN CRYOGENIC CHAMBER. AT THE EXTREME RIGHT 10 SOLAR CELLS ARE MOUNTED IN A CIRCULAR PATTERN. THE GERMANIUM SUBSTRATE FOR THE IR TRANSMITTANCE MEASUREMENT IS SHOWN NEAR THE CENTER OF THE FRAME. NOTICE THE QCM LOCATED DIRECTLY BELOW THE GERMANIUM SUBSTRATE.

Until the thruster firings began, the actual chamber performance, especially in the plume backflow region, was still unknown, making it necessary to devote some of the Phase I measurements to assessing chamber performance. As shown in Figs. 2 and 3 ion gauges were distributed throughout the backflow region for this purpose. The gauge located at the left side of Fig. 3 was attached to a mechanical vacuum feed-through which allowed it to be rotated or translated parallel to the plume axis. In addition, a mass spectrometer was used to sample and analyze the residual gases in the backflow region.

Phase I plume diagnostic instrumentation included:

a. eleven temperature-compensated quartz crystal microbalances located at angles of 25 to 150 degrees from the plume centerline to measure the mass flux distribution; see Figs. 1 - 5.

b. IR transmission of condensed exhaust products collected on a cooled optical substrate (germanium) to provide in situ identification of species deposited on the QCMs and to determine the optical properties[16] (n, k) of the condensed exhaust gases. The germanium substrate for the IR transmission measurement is shown near the center of Fig. 3. The QCM found directly below the substrate was kept at the same temperature and used in conjunction with the IR and laser interference measurements[19] in the fashion described earlier to obtain the deposit density and the optimum QCM operating temperatures.

c. two-angle laser interference to measure the thickness and the index of refraction at 0.6328 micron of the condensed exhaust gases. The laser beams were incident on the center of the same optical substrate used for the IR transmission measurement and thus provided properties for the same deposit.

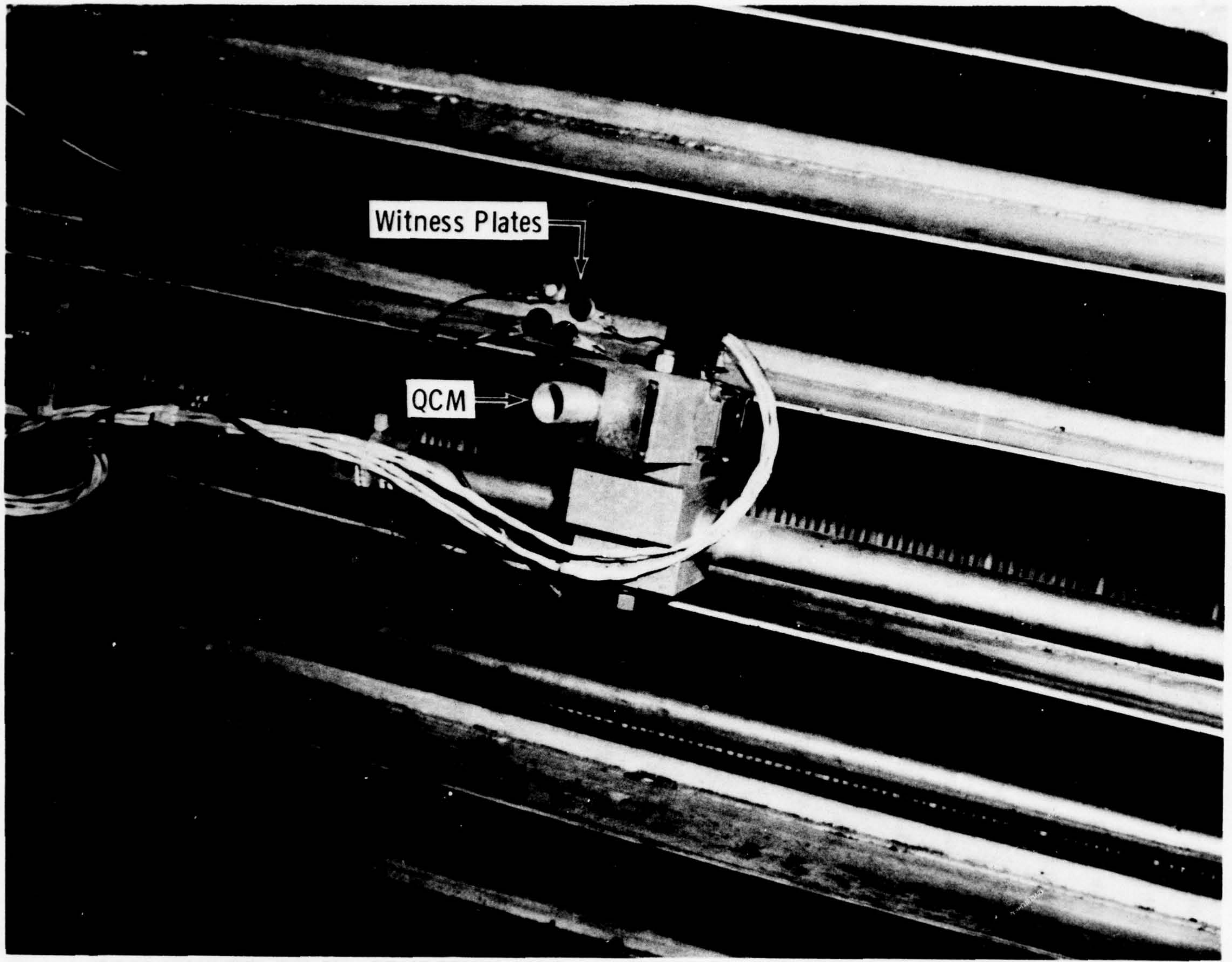

QCM MOUNTED ON GHe CRYOGENIC LINE. WITNESS PLATES ARE LOCATED ABOVE THE QCM.

FIG. 4

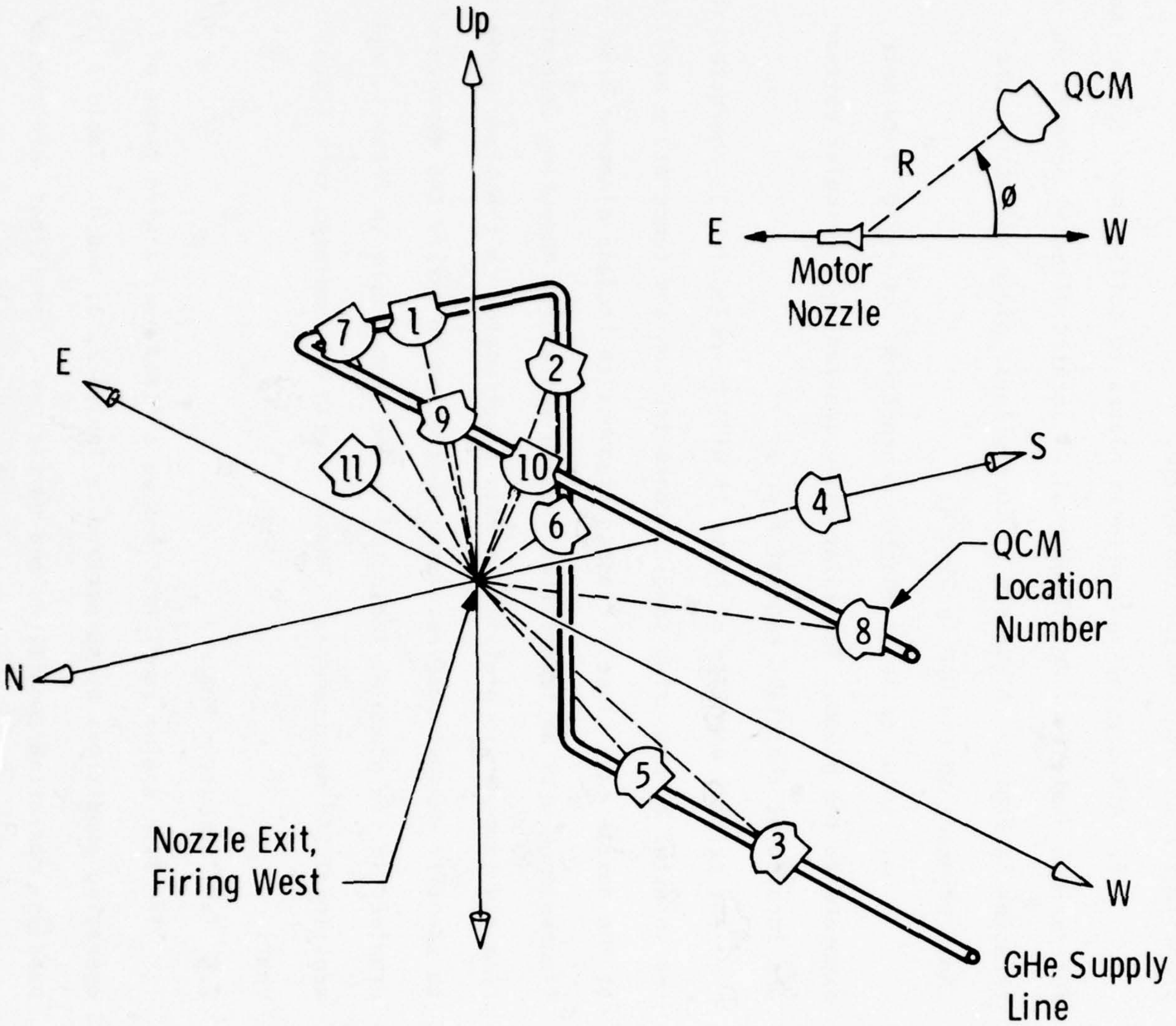

TYPICAL QCM LOCATIONS IN 10V CHAMBER

FIG. 5

d. electron beam fluorescence for flowfield visualization. The electron beam source is covered but visible in the extreme lower left corner of Fig. 3.

e. photography to detect sizeable droplets in the plume or a propellant film layer inside the nozzle.

f. ATR crystals and witness plates to collect hard contaminants for residue analysis. An ATR crystal is located directly beneath the thruster in Fig. 2. A variety of four witness plate collectors are shown adjacent to the QCM in Fig. 4.

g. solar cells to monitor degradation resulting from their exposure to the plume. Ten solar cells mounted in a circular pattern are located at the right edge of Fig. 3.

The primary emphasis of Phase II will be objective 3, characterizing the thruster by measuring species concentration and temperature profiles at the nozzle exit plane. Planned diagnostics include electron beam fluorescence with an intensified vidicon system for measuring concentration and temperature profiles, a mass spectrometer on the plume centerline to identify exhaust species, laser scattering to verify the absence of droplets in the plume as indicated by the photography in Phase I, and additional QCM measurements. Phase II will be completed this fiscal year.

2.5 Test Summary - Phase I

The five engine configurations were fired over a wide range of operating conditions as summarized in Tables 2, 3, and 4. Table 3 lists baseline operating conditions and variations. Conditions were chosen to reveal any effects these variables might have on the mass flux distribution or hard contaminant levels in the plume. Varied parameters included oxidizer to fuel ratio (O/F), duty cycle (δ), combustion chamber

TABLE 3

OPERATING CONDITIONS

Variable Parameter	Variations with Baseline Conditions Underlined
Oxidizer/Fuel (O/F)	1.4, $\underline{1.6}$, 1.8
Duty Cycle (δ), %	$\underline{1}$, 2, 5, 10, Continuous
Comb. Chamber Pressure (P_c), psia	75, $\underline{100}$, 125
Pulse Length (t_p), msec	25, 50, $\underline{100}$, 200, 1000
QCM Temperature (T_X), ^{o}K	$\underline{25}$, 40, 75, 140, $\geq$180

TABLE 4

ENGINE FIRING SUMMARY

Firing Date	Config. Code	Engine Parameter Variations				QCM Temp. Variations	Total Pulses	Cumulative Firing Time (sec)
		O/F Ratio	δ (%)	P_c (psia)	t_p (msec)	T_x (^oK)		
Oct 5	C	1.6	1	128	100	25 only	206	29
Oct 17-19	A	All	1, 10	All	All	25, 100, 160	3577	242
Nov 8-11	BL	All	All	All	All	All	4350	362
Nov 21-23	B	All	All	All	All	All	5024	387
Dec 6	D	1.6	2	100	100	All	1813	186

pressure (P_c), and pulse length (t_p). As indicated in Table 4, configurations A, BL (baseline), and B were tested most thoroughly.

Table 5 summarizes the measurements performed on each engine configuration. The QCM data is complete for all configurations, but somewhat limited on C and A. Coverage by the in situ IR transmission and laser interference measurements[19] was also thorough. Extensive IR transmission measurements were not attempted on configurations C and A because of intense interest in chamber and engine checkout at that point in time. Photography was done with a motorized 35 mm camera triggered by the firing sequencer through a microprocessor. Exposures were programmed to capture various portions of the firing pulse. The electron beam fluorescence species density measurement was limited to a proof-of-principle attempt in anticipation of extensive application in Phase II; it was successful. As discussed earlier the mass spectrometer was used in Phase I primarily for assessing chamber performance. It was not fast enough to obtain a complete scan over the mass number range of interest during a single pulse firing. Nevertheless some interesting partial scans were obtained, and extensive use of a mass spectrometer tailored for the plume measurement is planned in Phase II. Again the reader is referred to the project technical report, to be published, for complete results of all the measurements.

3.0 QUARTZ CRYSTAL MICROBALANCES

In the planning stage of this program, the intent was to use the QCM design which had performed successfully in the Jet Propulsion Laboratory (JPL) Molsink chamber for the monopropellant thruster contamination study[9, 10, 18]. After the JPL designs were reviewed, it was evident that

TABLE 5
SUMMARY OF MEASUREMENTS (PHASE I)

Measurement		Engine Configuration				
		C	A	BL	B	D
QCMs at Crystal Temperature (^{o}K)	25	X	X	X	X	X
	40			X	X	X
	75			X	X	X
	100		X	X	X	
	140			X	X	X
	180			X	X	
	≥ 200			X	X	
Condensed Phase In Situ						
— IR Transmission for						
• Identification of Species Collected by QCMs at Same Temperature				X	X	X
• Optical Constants (n, k)				X		
— Laser Interference for						
• Cryodeposit Thickness		X	X	X	X	X
• Cryodeposit Density		X	X	X	X	X
• Index of Refraction at 0.6328 μm		X	X	X	X	X
IR Spectra of Gas Phase During Chamber Warm-Up				X	X	
E-Beam Fluorescence						
• Flow Visualization			X			
• Species Density (demo)						X
Photography				X	X	
ATR Spectroscopy		X	X	X	X	X
Witness Plates		X	X	X	X	X
Solar Cell Degradation			X	X	X	X
Mass Spectroscopy				X	X	

extensive modifications would be necessary to adapt the "low temperature" units which had been used to measure "far field" contamination. To meet the requirements of this study additional QCMs of the "variable temperature" design used by JPL to measure the mass flux within 30 deg of plume centerline were needed.

3.1 QCM Design

To determine the necessary design changes, one of the JPL variable temperature QCMs was operated in a small cryogenic vacuum chamber. In the present AEDC version (Fig. 6) the electronics package was insulated from the mounting and independently temperature controlled at near room temperature. The crystal was mounted on a temperature controlled heat sink connected to the QCM mounting block by a thermal conductor sized to allow a 20°K to 300°K temperature cycling in one hour with a heater power of 10W. With these two modifications, the QCM could be clamped to a constant low temperature heat sink, the crystal temperature controlled anywhere between the heat sink temperature and 300°K, and the oscillator electronics maintained at room temperature.

Crystals from some original JPL units were used, and additional crystals were purchased from the same vendor. Three of the crystals were cut at $39^{\circ}49'$ for a low temperature coefficient in the 77°K range while the remaining nine were cut at $40^{\circ}28'$ for the range less than 40°K.

The oscillator and mixer circuit was modified only by adding an output stage with a gain of ten to improve the S/N when the QCMs are operated on long cables.

A field-of-view (fov) limiting aperture (see Figs. 4 and 6) was added to the cover plate on all QCMs, except one, to reduce the field-of-view to approximately $\frac{2\pi}{12}$ ster (48° full angle), and thereby to reduce

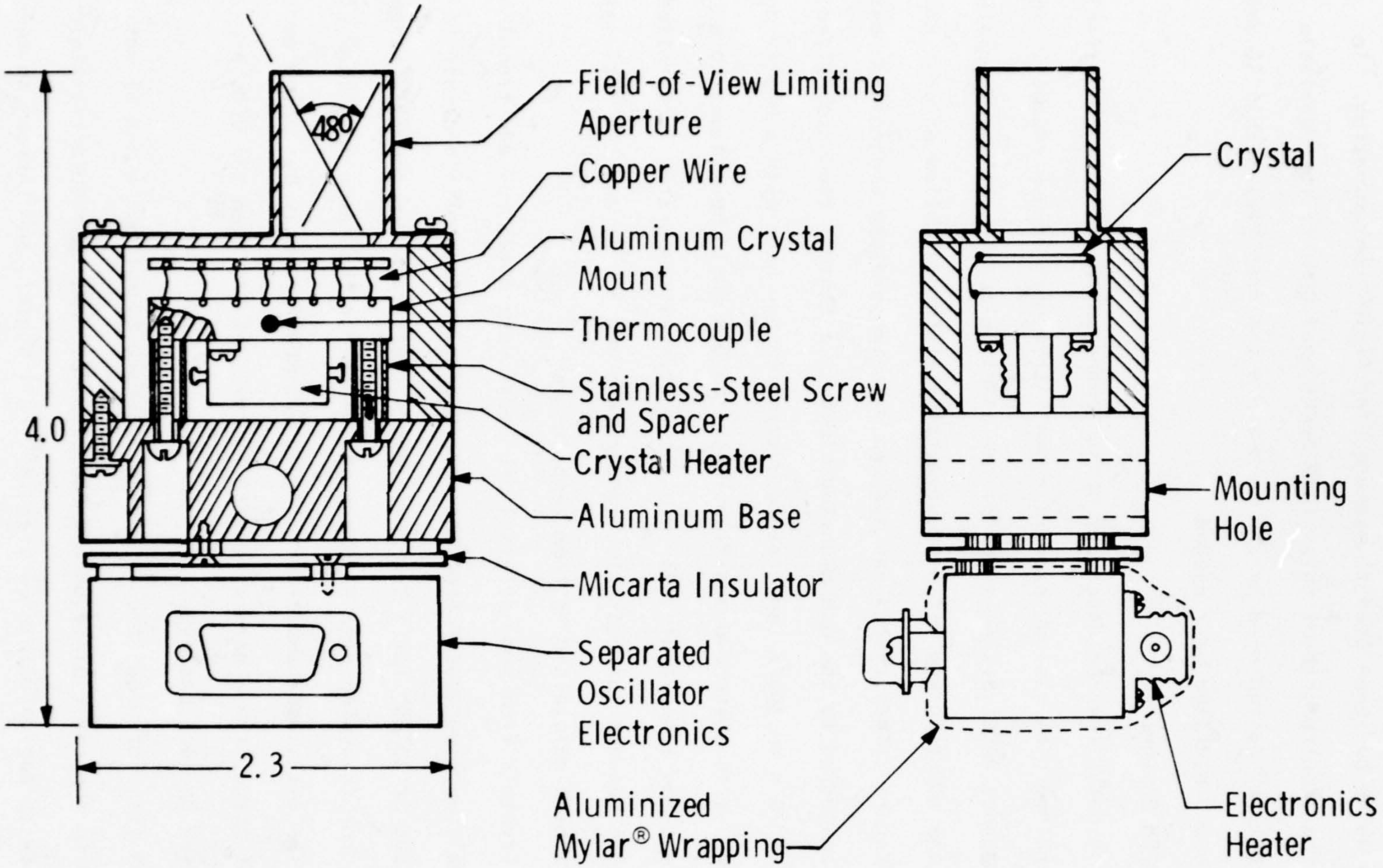

QUARTZ CRYSTAL MICROBALANCE

FIG. 6

the molecular flux reaching the crystal from directions other than the nozzle. The QCM without a fov limiting tube was located at 90° from plume centerline adjacent to the cooled germanium substrate and used in conjunction with the IR transmission measurements.

Crystal temperature was taken to be that measured by a thermocouple imbedded in the heat sink to which the crystal was mounted (Fig. 6). The temperature of the QCM surroundings was less than $80^{\circ}K$, excluding the thruster nozzle directly in the field-of-view, and as a result of radiation exchange between the QCM and its surroundings, the crystal temperature was calculated to be within $0.1^{\circ}K$ of the heat sink temperature in the worst case.

3.2 QCM Operation

Eleven QCMs were installed in the chamber by clamping them to a stainless steel cryogenic line at various locations (see Figs. 3, 4, and 5 and Table 6) to achieve the desired angles between the plume centerline and the QCMs. With two exceptions, the QCMs were always pointed at the nozzle; QCM No. 1 ($\phi = 118^{\circ}$) was pointed downstream parallel to the plume centerline, and QCM No. 9 ($\phi = 62^{\circ}$) was pointed downstream toward the center of the LN_2 shield (Fig. 1). Neither of these QCMs had a geometrical view of the nozzle, the purpose being to measure backscattered flux during firing from directions other than the nozzle or antechamber door and to determine if significant back scattering from the plume and the cryopanels occurred.

The cryogen line to which the QCMs were clamped was cooled with nominal $20^{\circ}K$ GHe, allowing the QCM crystal temperatures to be controlled from $25^{\circ}K$ to $300^{\circ}K$. Several operating temperatures above $25^{\circ}K$ were chosen in order to selectively collect particular plume species (refer

TABLE 6
QCM LOCATIONS

Location No.	Oct 5, 1977 Configuration - C			Oct 17-19, 1977 Configuration - A			Nov 8-11, 1977 Configuration - BL			Nov 21 - Dec 6, 1977 Configuration - B, D		
	QCM No.	R (cm)	ø (deg)	QCM No.	R (cm)	ø (deg)	QCM No.	R (cm)	ø (deg)	QCM No.	R (cm)	ø (deg)
1	1	157	30	1*	76.7	109	1*	81.3	118	1*	79.0	115
2	2	112	45	2	61.7	117	2	66.8	131	2	63.6	128
3	3	91	60	3	91.4	60	3	81.0	69	3	83.0	66
4	4**	81	90	4**	82.3	81	4**	83.8	90	4**	80.7	87
5	5	79	90	5	78.7	90	5	72.6	101	5	71.8	97
6	6	56	118	6	50.8	111	6	55.9	127	6	53.0	123
7	12	81	108	12	81.3	108	12	76.2	117	12	74.0	114
8	8	91	90	8	91.4	90	10	155.0	26	10	159.6	25
9	9	104	60	9	104.1	60	9*	92.9	62	9	94.0	62
10	10	127	45	10	127.0	45	7	112.0	49	7	115.4	47
11	11	172	32	11	73.7	104	11	39.4	147	11	35.3	143
	7	Spare		7	Spare		8	Spare		8	Spare	

* QCMs Nos. 1 and 9 were pointed downstream toward the far end of the chamber away from the motor with no direct line of sight to the nozzle.

** QCM No. 4 was located as close as possible to the germanium substrate for the IR transmittance measurement. It did not have a collimating tube to limit the fov like the other QCMs.

to Tables 7 and 8). Data were recorded at the highest temperature first to avoid evaporation of previously condensed species, and thereby to shorten the measurement sequence.

When all of the QCM crystals had stabilized at the desired temperature, a set of QCM frequencies and temperatures was recorded; this was usually about ten minutes prior to the beginning of a sequence of engine firings. A second set was recorded just prior to the engine firing and a third set just after the firing sequence. If the data sets are designated 1, 2, and 3, respectively, the measured mass flux I is

$$I = \frac{d\dot{m}}{d\Omega} = \frac{KR^2 \Delta f}{N\, t_p}, \text{ gm/sec-ster} \qquad (1)$$

where $\dot{m}$ = mass flux collected by QCM, gm/sec

Ω = solid angle subtended by the QCM fov, ster

K = QCM calibration constant[9] = 1.77×10^{-8} gm/cm^2 - Hz

R = distance from nozzle exit to QCM crystal, cm

$$\Delta f = (f_3 - f_2) - (f_2 - f_1)\frac{t_3 - t_2}{t_2 - t_1}, \text{ Hz} \qquad (2)$$

N = number of engine firing pulses

t_p = pulse length, sec

t_i = time at which data were recorded, sec

During the firing sequence, QCM frequencies were monitored with a frequency-to-voltage converter and a strip chart recorder. Those QCMs which could accumulate sufficient mass during the sequence to saturate the crystal and stop oscillation were sampled first on the recorder so their data would not be lost. Data consisted of thermocouple voltages,

TABLE 7

CONDENSED MASS FRACTIONS*

QCM - R(cm) - ø (deg) T_X (^oK)	155 26	112 49	81 69	73 101	56 127	67 131	Avg. Mass Fraction
$\geq$ 180	0.025	0.021	0.021	0.010	0.017	0.012	0.017
140 - 180	0.383	0.412	0.380	0.398	0.371	0.266	0.368
75 - 140	0.138	0.123	0.175	0.122	0.196	0.345	0.183
40 - 75	0.111	0.117	0.150	0.185	0.211	0.109	0.147
25 - 40	0.343	0.327	0.274	0.285	0.205	0.268	0.285

*For the baseline engine configuration at baseline operating conditions (except averaged for t_p = 25 and 100 msec). These tabulated values were obtained by subtracting and normalizing the data plotted in Figs. 12a and 12b.

TABLE 8
BIPROPELLANT EXHAUST CONSTITUENTS COLLECTED AT VARIOUS TEMPERATURES

QCM Temp. (^{0}K)	Cryopumped Species		Equilibrium Vapor Pressure* (torr) at QCM Temperature	Mass Fraction Measured at QCM Temperature		Mass Fraction Predicted for Major Species	
180	Nitrate			0.017			
140	Plus	H_2O	4×10^{-9}	0.360	0.54	0.222	0.54
75	Plus	CO_2	8×10^{-9}	0.179		0.320	
		N_2O	8×10^{-8}				
		N_2O_4					
		NO_2					
		N_2O_3					
40	Plus	NO	4×10^{-12}	0.144	0.42		0.44
25	Plus	N_2	8×10^{-8}	0.279		0.420	
		CO	9×10^{-10}			0.004	
		CH_4	8×10^{-13}			0.013	
Not Collected		H_2		0.021 (Calculated)		0.021	

---

*Compare to Chamber Pressure - 2×10^{-6} to 3×10^{-5} torr; Ref. 22

QCM output frequencies, sample number, sample time, and engine firing particulars such as pulse length, duty cycle, number of pulses in the sequence, combustion chamber pressure, and O/F ratio. When one or more QCMs stopped oscillating due to mass saturation, normally at frequencies between 50 and 100 kHz, the crystals were heated to 300°K, and the frequencies were monitored until no further monotonic frequency change was evident. This process of cleaning the QCM crystals required a maximum of one hour.

4.0 RESULTS OF QCM MASS FLUX MEASUREMENTS

In this section results are presented in the form of plots comparing the measured mass flux per unit solid angle I (gm/sec-ster) for the various engine configurations and operating conditions. The oxidizer to fuel ratio (O/F), pulse duty cycle (δ), combustion chamber pressure (P_c), firing pulse length (t_p), and QCM crystal temperature (T_x) are specified in each case. Since comparisons by inspection only are often difficult, least squares exponential curves have been computed to fit appropriate sets of data. The slopes and intercepts (in semilog representation) for these exponential curves are always listed for the varied parameter, but the fitted lines are not always shown in order to avoid confusion on already busy figures. Instead a so-called "reference line" is shown on most figures; this is simply the least squares exponential fit to the data for all engine configurations at baseline operating conditions and $T_x = 25^\circ$K. As indicated in Fig. 7 the equation for the reference line is

$$I = 9.49\ e^{-0.0752\phi\ (\mathrm{deg})} \qquad (3)$$

It serves as a point of reference on each figure and accentuates the effect of any departure from the baseline operating conditions. At the same time the slope/intercept values can be used to detect any systematic changes in the measured mass flux resulting from the varied parameters.

Also on most figures a few backscatter measurements are plotted. These measurements indicate mass flux levels collected from viewing directions other than the nozzle during engine firing. This flux is attributed to molecular backscattering from either the cryogenic panels or the plume itself. The QCMs making these backscatter measurements were pointed downstream toward the far end of the chamber and had no direct line of sight to the nozzle. For ease of comparison with the other QCM measurements, these backscatter data have been plotted as if the QCMs were directed at the nozzle and located at the same R, ϕ coordinates (Table 6); i.e., the data is displayed as mass flux per unit solid angle rather than mass flux per unit area.

This is also an appropriate time to point out that the QCM locations were staggered with about half mounted on each side of the chamber or nozzle centerline, yet the measured flux values show no evidence of asymmetry in the plume. Therefore the nozzle geometrical axis and the plume centerline are taken to be identical, and all QCM data is plotted at positive angles.

4.1 Effect of Varying Engine Configurations

Data was obtained on all five engine configurations operating at baseline conditions (see Tables 3 and 4), and the results are plotted in Fig. 7. Under these firing conditions the five configurations produced remarkably similar mass flux levels and angular distributions. These combined data for the five configurations, like all the QCM mass

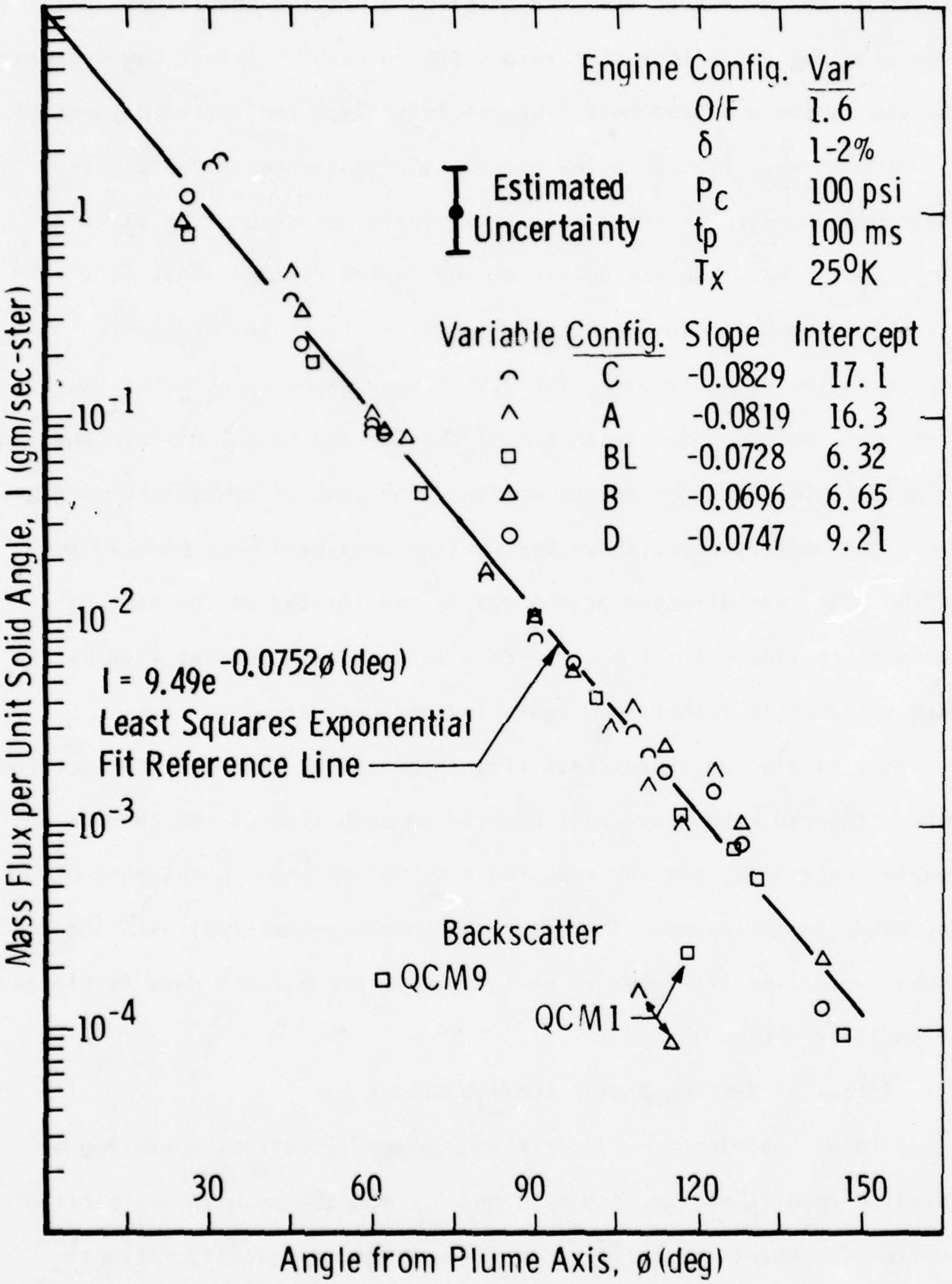

Fig. 7 Mass Flux for Various Engine Configurations at Baseline Operating Conditions

flux measurements obtained in this program, exhibit an exponential dependence on ϕ, the angle from the plume centerline. Nearly all measured values fall within a factor of two of the exponential line fitted to the combined data points, and thereby justify the use of exponential curve fitting. In addition to the curve fitted to the combined data, slopes and intercepts are listed in Fig. 7 for the exponential curves fitted to the data for each engine configuration. Although the slopes and intercepts are all very close, the manner in which C and A agree but differ from the remaining configurations is eye-catching because it correlates with the chronological sequence of relocating the QCMs (Table 6). In spite of this observation, the general conclusion drawn from Fig. 7 is that these measurements reveal no significant differences in the mass flux distributions for the five engine configurations tested.

4.2 Effect of Varying Engine Operating Conditions

Figs. 8, 9, and 10 show the results of varying the oxidizer to fuel ratio - 1.4 to 1.8, the duty cycle - 1 to 10%, and the combustion chamber pressure - 75 to 127 psia for the baseline engine configuration. No pronounced effects on the measured mass flux are apparent, except a hint in Fig. 10 that the flux at the low angles was slightly higher for higher P_c.

Figs. 11a and 11b illustrate the effect of varying the firing pulse length from 25 msec to 1 sec (there were also a few 2 sec firings) for two engine configurations. Inspection of either the listed slopes/intercepts or the plotted points reveals a consistent increase in the measured mass flux as the pulse length decreased. The increase is less than a factor of two but was quite reproducible for all engine configurations. The constant slope tells us the effect does not depend on angle.

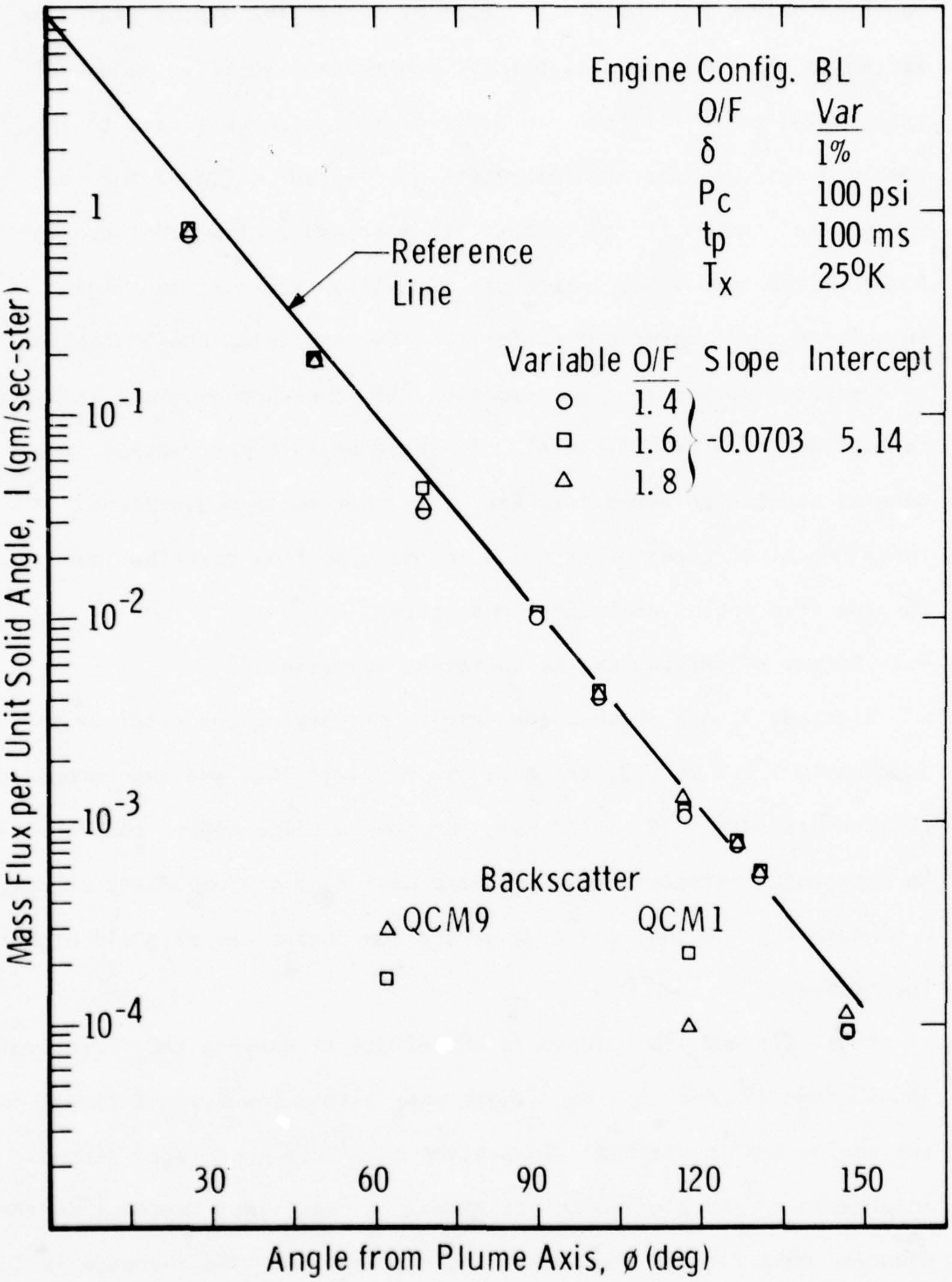

Fig. 8 Effect of Oxidizer to Fuel Ratio; Baseline Engine

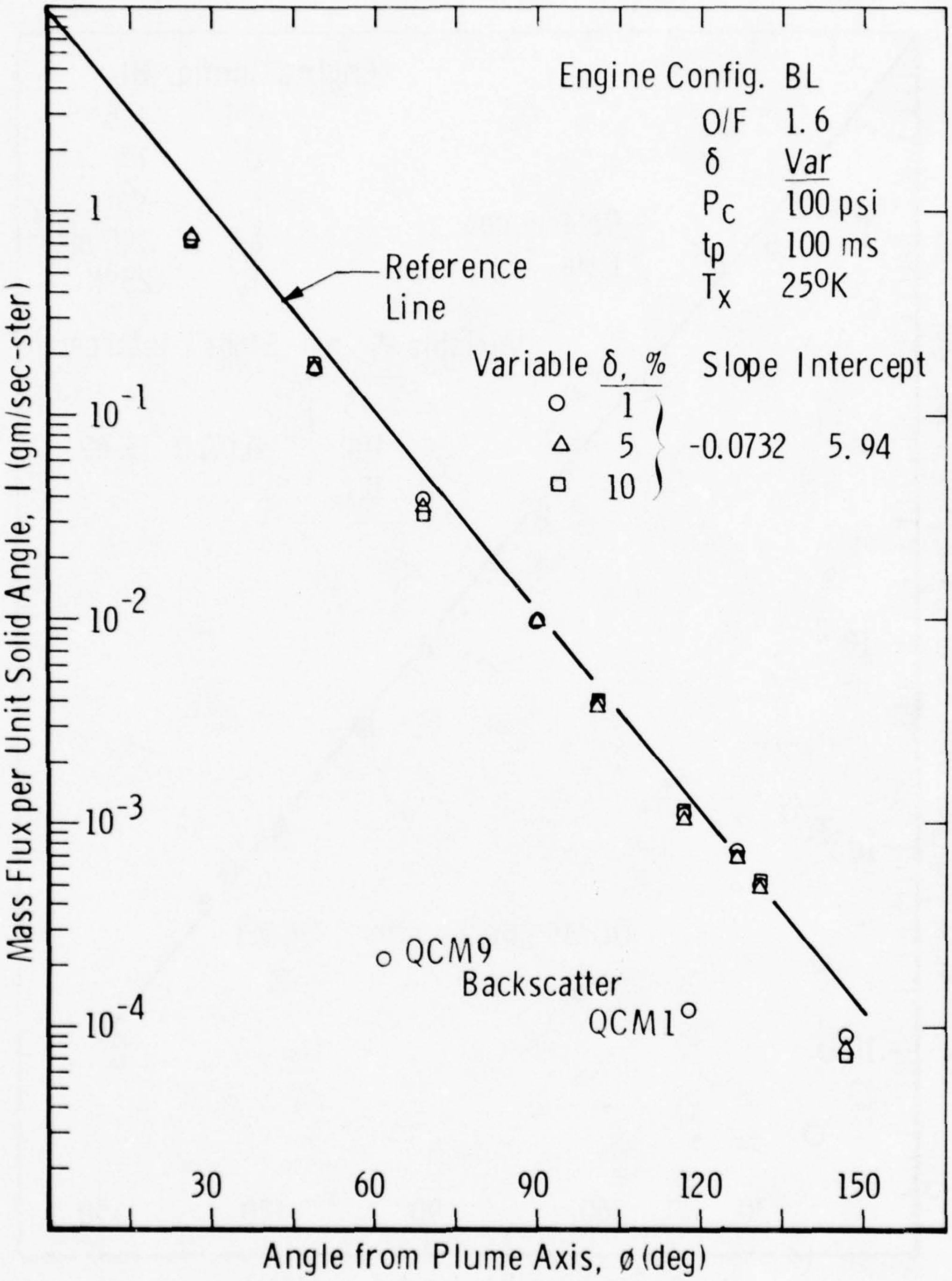

Fig. 9 Effect of Duty Cycle; Baseline Engine

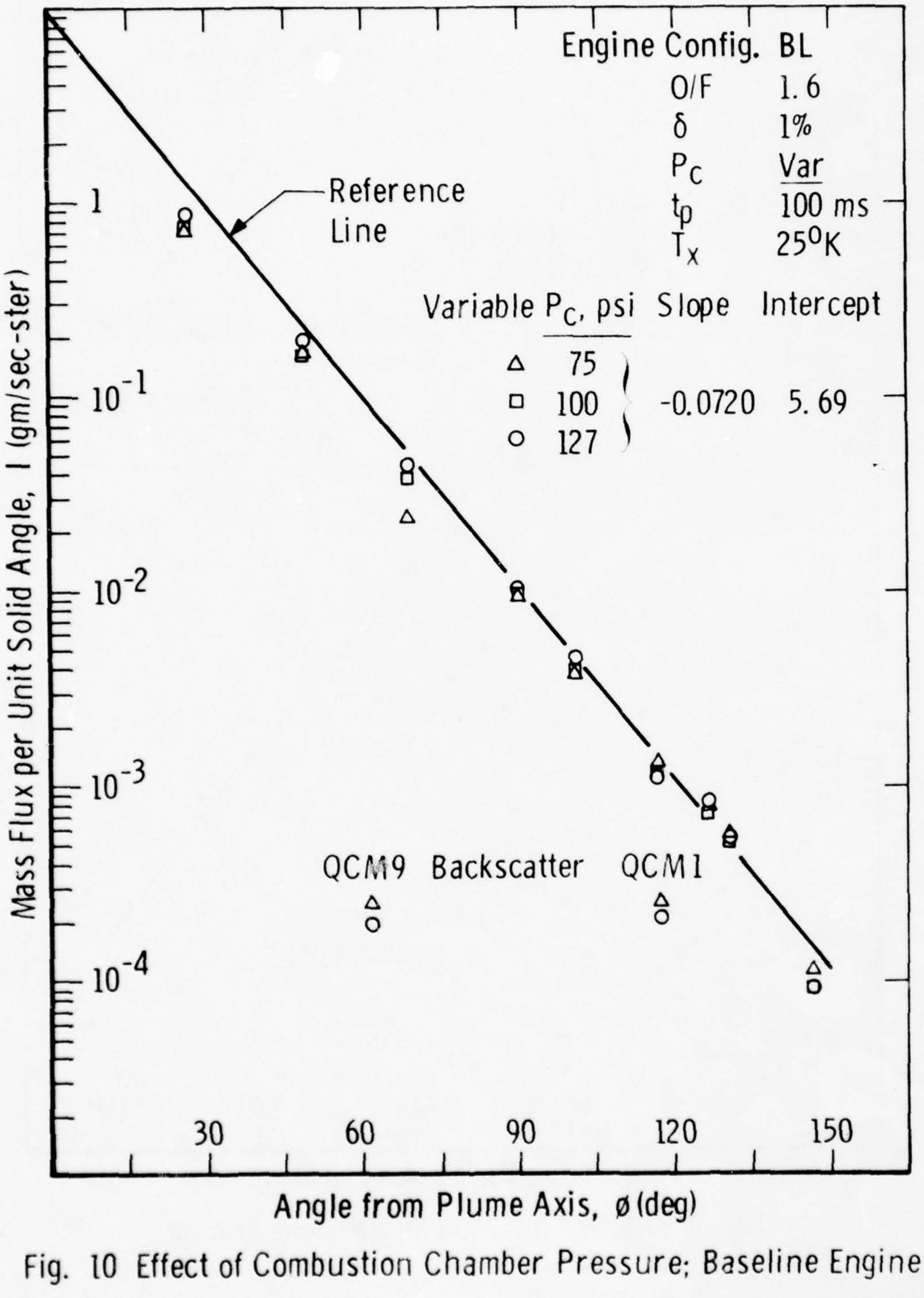

Fig. 10 Effect of Combustion Chamber Pressure; Baseline Engine

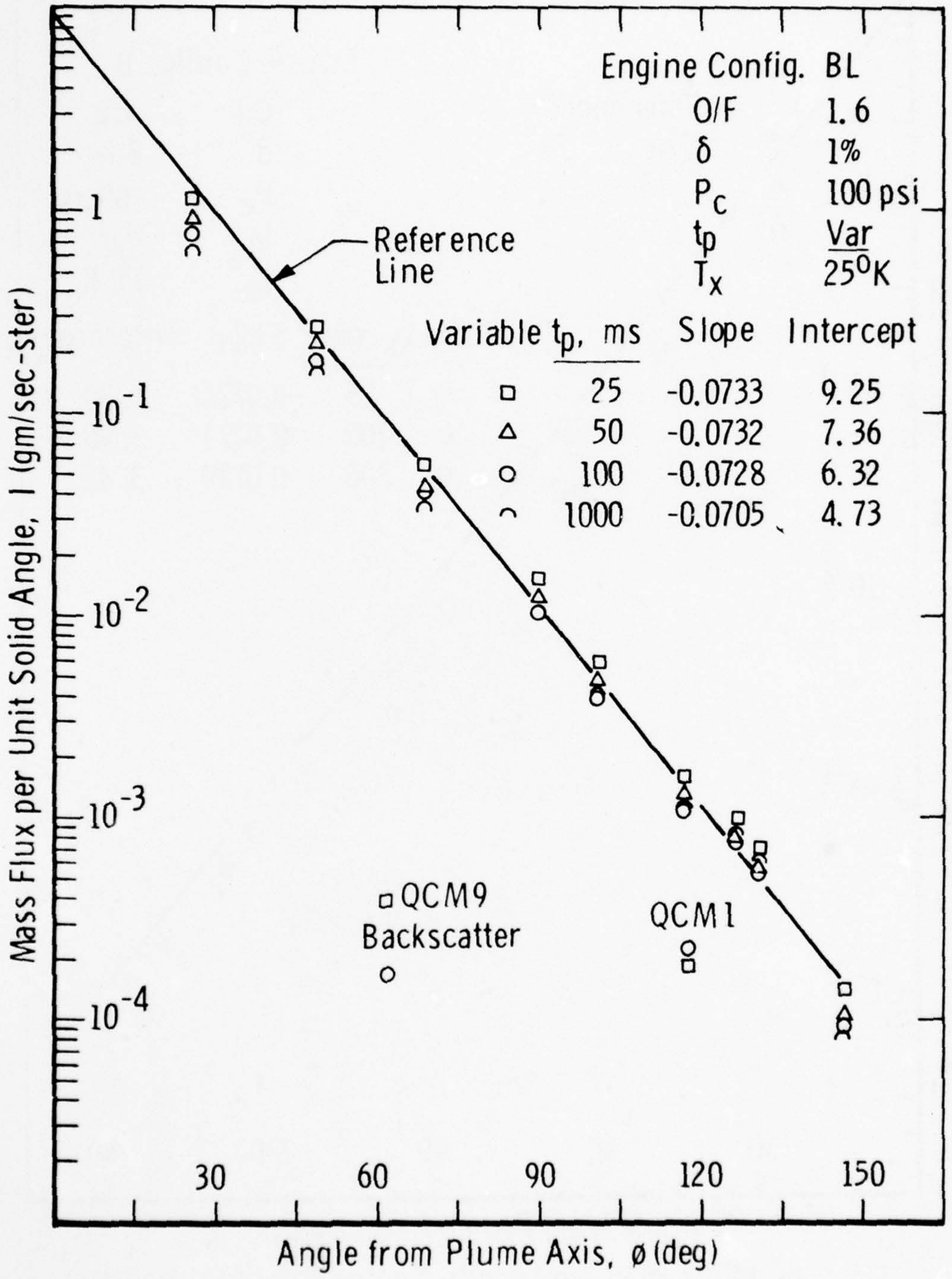

Engine Config.	BL
O/F	1.6
δ	1%
P_c	100 psi
t_p	Var
T_x	25^0K

Variable	t_p, ms	Slope	Intercept
□	25	-0.0733	9.25
△	50	-0.0732	7.36
○	100	-0.0728	6.32
⌒	1000	-0.0705	4.73

Fig. 11a Effect of Pulse Length; Baseline Engine

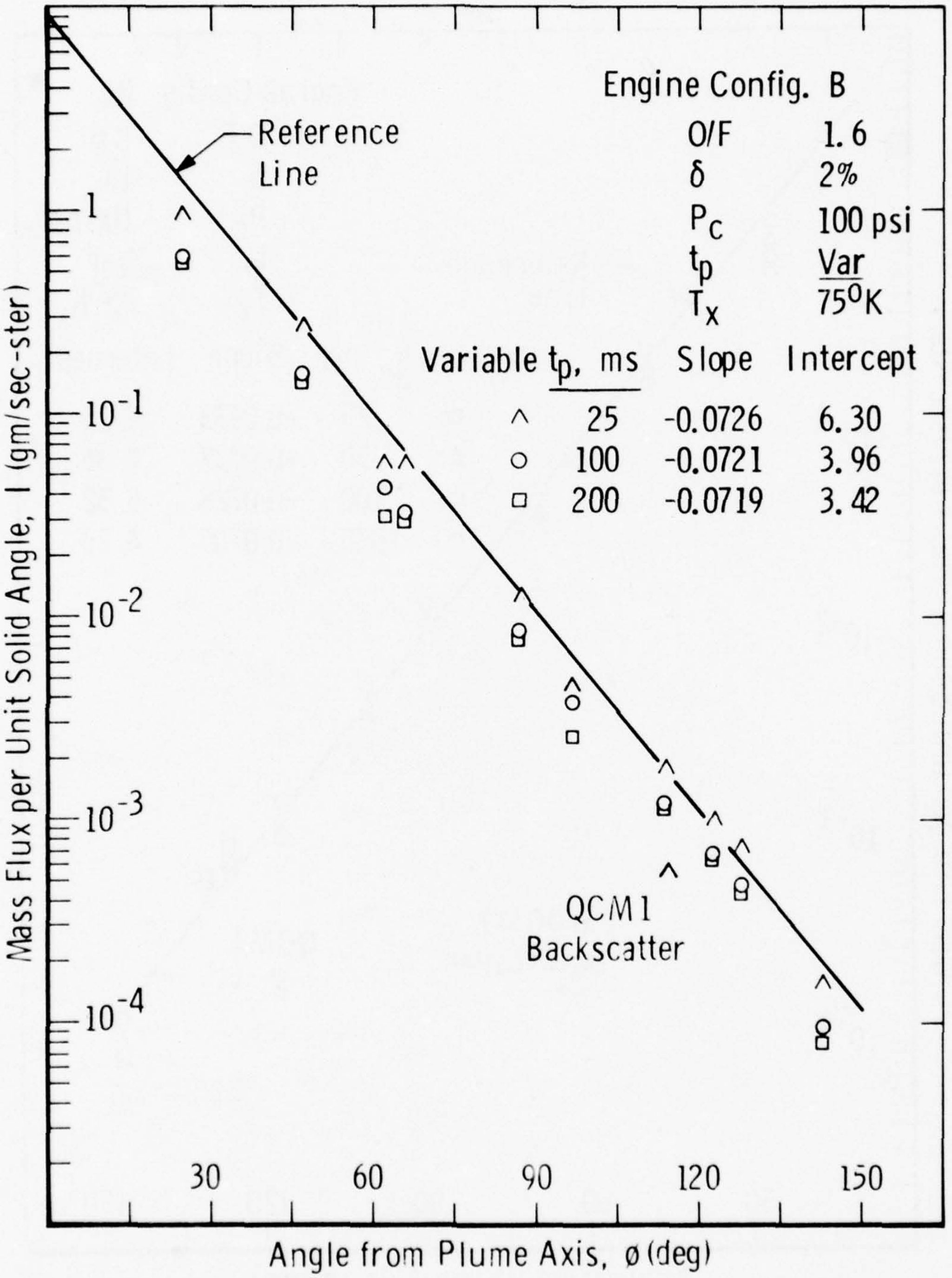

Fig. 11b Effect of Pulse Length; Engine Configuration B and Crystal Temperature 75°K

Moreover, the change in intercept is expected if higher mass flux levels are associated with engine ignition and shut down, in which case the mass flux from the thruster depends on the number of pulses making up the accumulated firing time.

4.3 QCM Temperature Variation

Figs. 12a, 12b, and 12c compare the mass flux collected at the various QCM operating temperatures. In these figures the fitted exponential lines are shown explicitly. The fitted line intercepts decrease in a well-behaved and predictable manner as the crystal temperature (T_x) increases, simply indicating that fewer exhaust species were cryopumped at the higher temperatures. Notice the sharp drop (about two orders of magnitude) in collected mass flux when the crystal temperature increases from 140 to 200°K. The species collected at $T_x > 180^{\circ}$K are more readily referred to as contaminants in the usual sense because no major bipropellant combustion products condense at such high temperatures. Fig. 12c confirms that the products collected at 200°K were coming from the thruster and were not temporarily trapped species which would evaporate in time. From present indications (IR spectra) these were nitrates and represent potential spacecraft contaminants. Witness plate samples will be used to verify this identification.

As mentioned earlier the in situ IR transmission measurement was carefully planned to help determine[†] the QCM operating temperatures and to identify the IR active species which were collected at each temperature. The identified exhaust species and the crystal temperatures chosen to selectively cryopump the major species are listed in Table 8; also the

---

[†] Along with equilibrium vapor curves which are frequently not available for plume species.

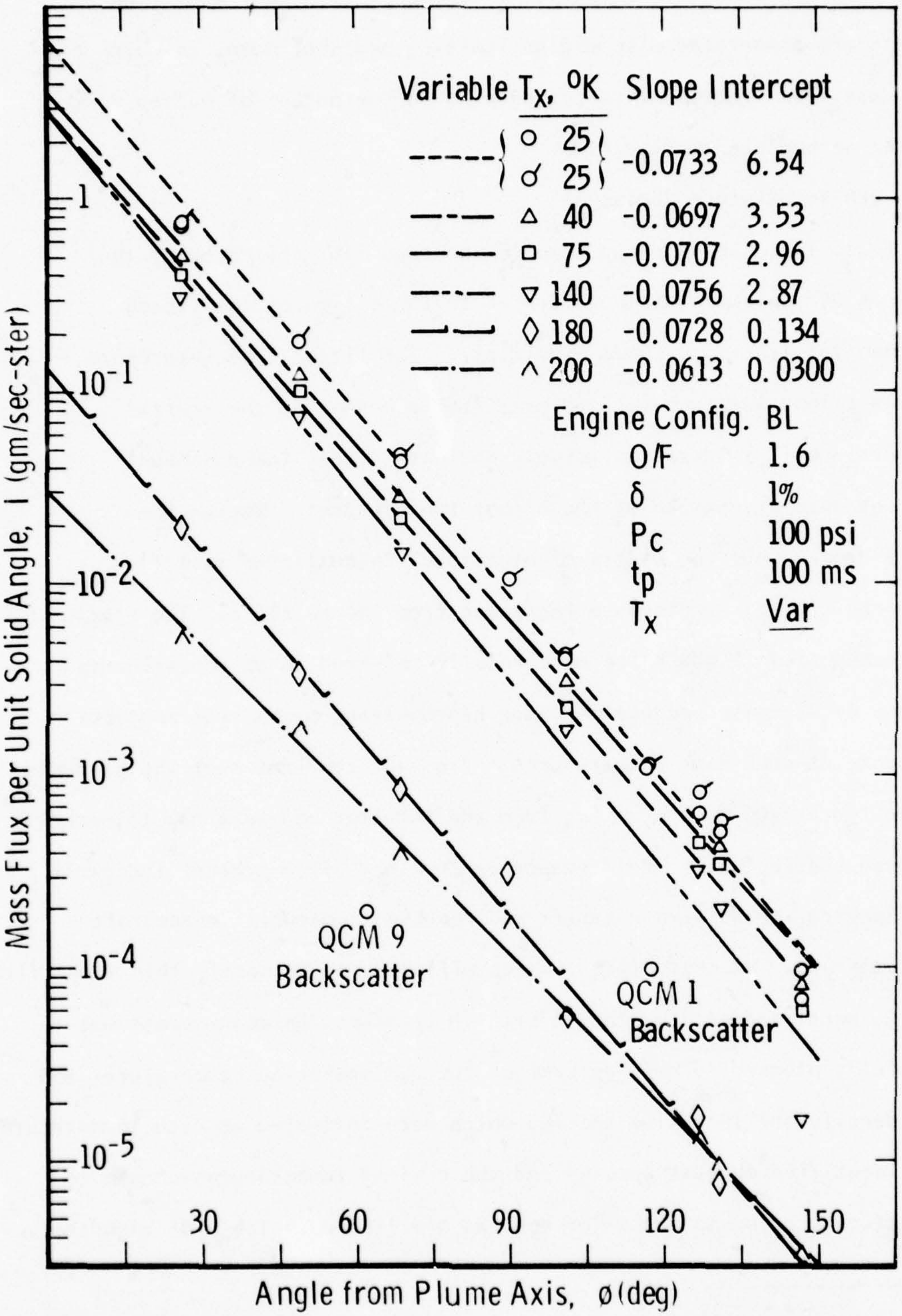

Fig. 12a QCM Temperature Variation; Baseline Engine

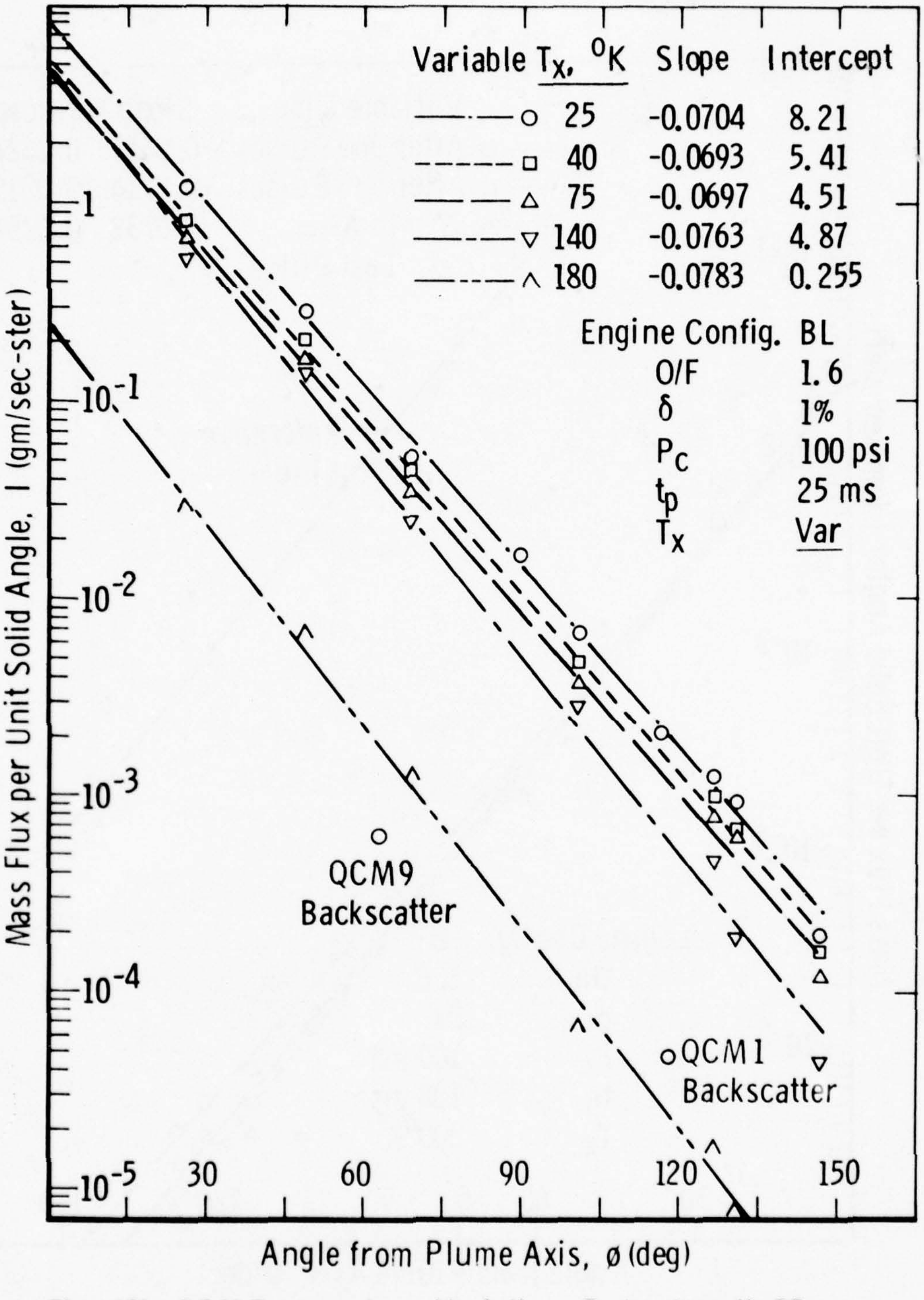

Fig. 12b QCM Temperature Variation; Pulse Length 25 msec

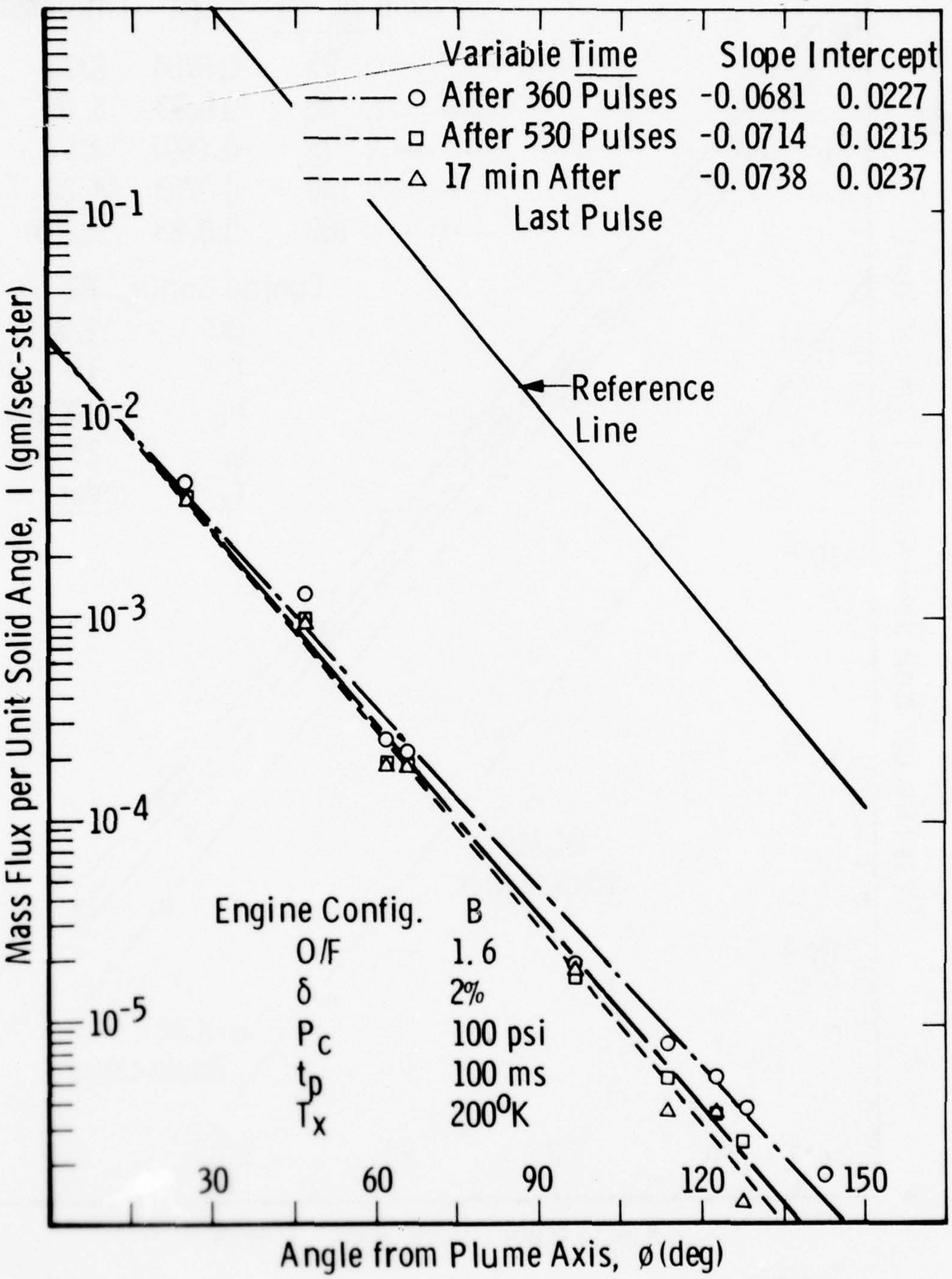

Fig. 12c Evaporation at Crystal Temperature 200°K

available equilibrium vapor pressures[22] are given. When only major constituents are considered, Table 8 indicates that H_2O is collected at 140°K, $H_2O + CO_2$ at 75°K, and $H_2O + CO_2 + N_2$ at 25°K. Then by subtracting and properly normalizing the mass flux collected by each QCM at this series of operating temperatures, one obtains the approximate mass fractions of major species found in the bipropellant exhaust plume.

The above approach was used to generate the condensed mass fractions given in Table 7 from the same data plotted in Figs. 12a and 12b. Of course the values listed in Table 7 do not include H_2 which does not condense at 25°K. From an equilibrium computation for very similar engine operating conditions, we obtained a predicted mole fraction for H_2 of 0.231 which converts to a mass fraction of 0.021. Then the average values listed in Table 7 were renormalized, assuming this mass fraction of uncollected H_2, to get the measured mass fractions listed in Table 8. Also, in Table 8, the remaining mass fractions predicted by the equilibrium computation are shown for comparison. Although the measured and predicted values at each QCM temperature do not agree well, there is general agreement for the total fractions collected above and below 75°K, as indicated by the braces in Table 8. The same "washed-out" temperature dependence is also illustrated in Fig. 12d where relative condensed mass fraction versus crystal temperature is plotted. There are sharp jumps as expected in the condensed mass at the temperatures where H_2O and N_2 condense, but there are no similar steps in the data between 60°K and 140°K, conspicuously not at 86°K where CO_2 should condense. In fact Fig. 12d shows that CO_2 and H_2O are not well separated. Most likely this observed smoothing is due to CO_2 cryosorption by H_2O cryodeposits.

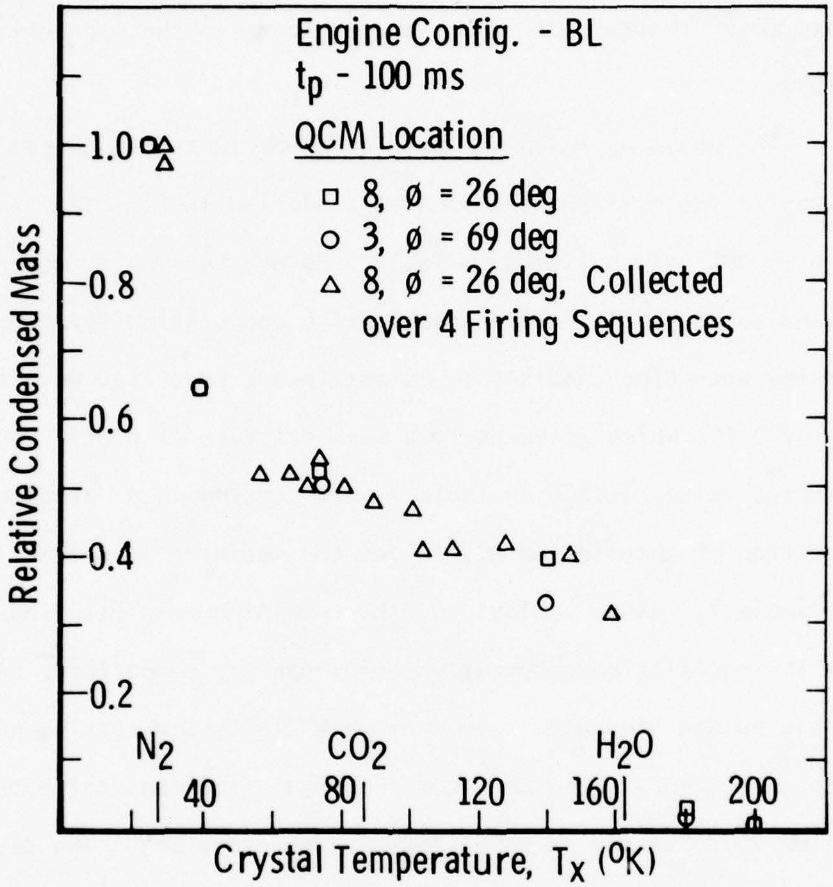

Fig. 12d Relative Mass Collected as Function of Crystal Temperature

One final observation is based on Figs. 12a and 12b. The slopes of the fitted lines for the mass flux collected at the intermediate crystal temperatures, 40°K and 75°K, are consistently lower than those for 25°K and 140°K. This suggests that the CO_2 and other species collected at the intermediate temperatures are relatively more abundant at higher angles than the N_2 and H_2O collected at 25°K and 140°K respectively. The point is more apparent in Table 7 where the condensed mass fractions for the 75 - 140°K range tail up at the higher angles. This effect could be explained by a higher concentration of CO_2 in the boundary layer. Hopefully an explanation, or at least some clarification, will be provided by nozzle exit plane concentration profiles obtained in Phase II.

4.4 Assessment of Results

4.4.1 Chamber Performance

As stated before, the importance of a sufficiently long mean free path to the measurement of mass flux in the plume backflow region was recognized. A reduced mean free path resulting from an increase in vacuum chamber pressure during a firing sequence would invalidate the measurements. To determine the effect on the QCM data, the chamber pressure was systematically increased by adding helium. The QCM data obtained while performing this stepwise increase in chamber pressure is presented in Fig. 13 where the tabulated pressures (P_{He}) take into account the gauge factors for hydrogen and helium. The lowest pressure listed was the case before the addition of helium began, and the residual gas was assumed to be mostly hydrogen. There was no significant change in the QCM data after adding the first increment of helium. Further increases in chamber pressure up to 8.4×10^{-4} torr, a factor of 200 times the lowest pressure, caused only a factor of three decrease in

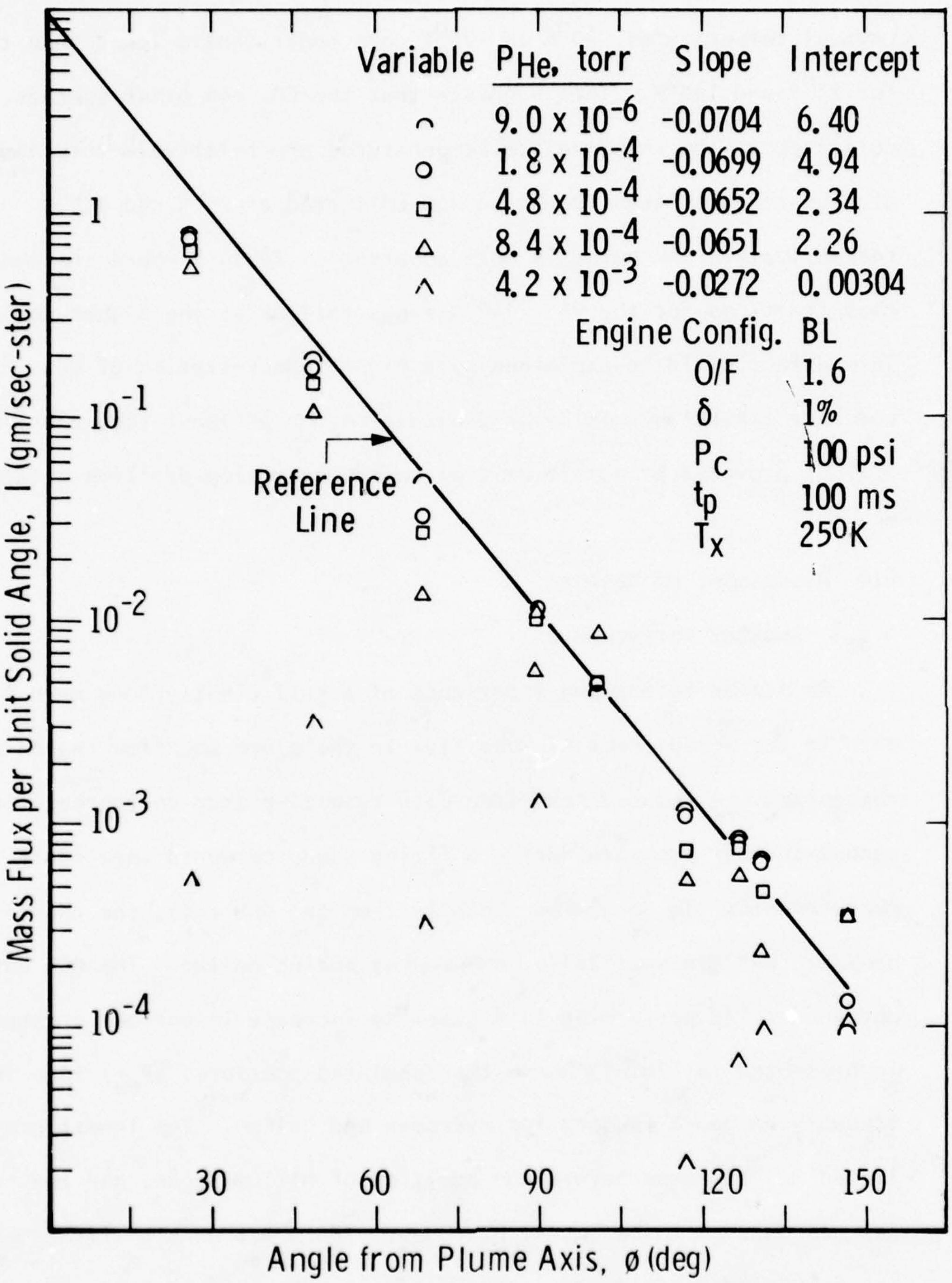

Fig. 13 Effect of Cryogenic Chamber Pressure

the collected mass flux. Finally, when the chamber pressure was increased to 4.2×10^{-3} torr, the results became very erratic. For comparison, the typical chamber pressure during a firing sequence was 3×10^{-5} torr. This experiment demonstrated that the cryogenic chamber performance was more than adequate and that the chamber had no measurable effect on the mass flux measurements.

4.4.2 Random and Systematic Error

One challenge associated with the mass flux measurements was to produce repeatable conditions for each engine configuration such that results might be meaningfully compared to one another and to theory. Such experimental realities introduced several sources of error into the mass flux measurements. These sources of error are discussed below.

Random error can be estimated from the data. Because there were insufficient data at identical test conditions to provide a meaningful statistical base, several sets of data which included variations in test conditions that did not strongly affect measured results were combined. Measurements on engine configuration A at six angles for five firing sequences were analyzed. Test conditions were

$T_x = 25^{\circ}K$, $t_p = 100$ msec, $0/F = 1.6$, $\delta = 1$ to 5%, $P_c = 75$ to 125 psia.

Relative standard deviation at each angle ranged from 5.9 to 10.4%. Similar data for engine configuration B was analyzed with relative standard deviations ranging from 4.8 to 15.1%. Thus, the random error in the QCM measurements is estimated at ± 10%.

Systemic error in the measured values of I can be estimated by differentiating the functional relationships between I and the measured parameters. These include Eq. (1) and the experimentally determined relation (Eq. (3). Quite generally for the purpose of error analysis

$$I = I(R, \phi, K, \Delta f, T_x, \Omega, N, t_p, 0/F, \delta, P_c) \tag{4}$$

where all symbols have been defined earlier. Treating these measured parameters in order:

R - distance from nozzle exit plane to QCM location

$$\frac{1}{I}\frac{\partial I}{\partial R}\Delta R = -\frac{2\,\Delta R}{R} = -\frac{2\text{ cm}}{40\text{ cm}} = -0.05 \qquad (5)$$

ϕ - angle from plume axis to QCM location

Using Eq. (3)

$$\frac{1}{I}\frac{\partial I}{\partial \phi}\Delta\phi = -0.0752\,\Delta\phi = -0.15 \qquad (6)$$

K - QCM calibration constant

$$\frac{1}{I}\frac{\partial I}{\partial K}\Delta K = 0.5 \qquad (7)$$

This estimate of uncertainty in K is based on our effort to calibrate the set of QCMs at 25°K in a molecular beam chamber with CO_2.

Δf - change in QCM frequency during engine firing sequence

Measured frequencies were probably within 1 Hz. However, jumps in crystal frequency as condensed mass accumulated could have caused errors. During initial checkout frequency jumps less than 200 Hz were observed in several QCMs. Large jumps of several kHz were also observed in a few QCMs, but in the data reduction these would have been recognized as bad points. Since most frequency changes measured during a firing sequence were less than 200 Hz, jumps usually appeared as questionable or obviously bad data; there were not a large number of these questionable data points.

At the higher angles and crystal temperatures the measured change in crystal frequency was only a few hertz. Resolution in the measurement of I was determined by a frequency resolution of 1 Hz and the firing time. Therefore, the noise equivalent mass flux per unit solid angle (NEI) for a typical 10 sec firing sequence is estimated to be

$$NEI = \frac{K\,R^2\,(\Delta f = 1)}{N\,t_p} = 2.75 \times 10^{-6} \text{ gm/sec-ster} \tag{8}$$

In practice, background mass flux prevented this NEI from being realized; the actual NEI was closer to 1×10^{-5} gm/sec-ster.

T_x - QCM crystal temperature

Condensed mass depends strongly on crystal temperature near those temperatures where major species have sufficiently high vapor pressure to evaporate (see Table 8). Since these temperatures were avoided, there should be little error associated with T_x. The one exception was the lowest temperature (25°K) which is close to the point at which N_2 evaporates. For an estimated fraction of N_2 not collected, we will use the difference between the predicted and measured mass fractions at 25°K from Table 8. Thus

$$\frac{1}{I}\frac{\partial I}{\partial T_x}\Delta T_x = -0.16 \tag{9}$$

Ω - QCM field-of-view

Measured values of I depended on the fov to some extent, more so at the higher angles where the absolute values approached the backscattered mass flux levels. During the firing of engine configurations B and D, QCM No. 9 at 62° had no fov limiting tube, yet the measured values shown in Fig. 11b were not perceptably greater. However, during the firing of engine configuration BL, when QCM No. 1 (118°) and No. 9 (62°) were pointed downstream with no line of sight to the nozzle, they measured 14% and 0.3% respectively (Fig. 8) of the flux they would have measured if pointed directly at the nozzle. Apparently there was flux from directions other than the nozzle., and at large angles the flux outside the fov exceeded that within the fov, when viewing the nozzle, by a factor of two. Nevertheless, since the objective was to measure I with identical fields-of-view at all angles, the small differences in the fields-of-view of the various QCMs and the small errors in pointing direction had a negligible effect on I.

t_p - firing pulse length

At a programmed pulse length of 25 msec, the actual firing time determined from records of P_c was about twice as long. At longer programmed pulse lengths (> 100 msec), the actual firing time matches the programmed length more closely. The actual firing time is considered a characteristic of the engine, and the appropriate error is associated with the programmed pulse length. For t_p = 25 msec and Δt_p = 0.002 msec

$$\frac{1}{I}\frac{\partial I}{\partial t_p}\Delta t_p = -\frac{0.002\ \text{msec}}{50\ \text{msec}} = -4 \times 10^{-5} \qquad (10)$$

P_c - combustion chamber pressure

From the measured values the change in I was less than 25% for a change in P_c from 75 to 125 psia. For ΔP_c = 5 psia,

$$\frac{1}{I}\frac{\partial I}{\partial P_c}\Delta P_c = \frac{0.25 \times 5\ \text{psia}}{50\ \text{psia}} = 0.025 \qquad (11)$$

The estimated uncertainty in N is zero, and changes on O/F and duty cycle (δ) had no significant effect on I. Finally then, the total systematic error in the mass flux measurements is obtained by combining the errors of unknown sign randomly and errors of known sign algebraically.

$$\frac{\Delta I}{I} = 0.16 \pm \left[\overset{T_x}{(0.05)^2} + \overset{R}{(0.15)^2} + \overset{\phi}{(0.5)^2} + \overset{K}{(4 \times 10^{-5})^2} + \overset{t_p}{} \overset{P_c}{(0.025)^2}\right]^{\frac{1}{2}} \tag{12}$$

Note that most of the systematic error is the result of uncertainty in the QCM calibration constant. The assigned uncertainty in K is based solely on our partially completed effort to calibrate the QCMs at 25°K. It does not seem reasonable to expect so much uncertainty in K for these QCMs.

The random error is insignificant compared to the systematic error, so the total error estimate is

$$\frac{\Delta I}{I} = \begin{cases} \pm\, 0.53 & \text{for } T_x \geq 40^{\circ}\text{K} \\ 0.16 \pm 0.53 & \text{for } T_x = 25^{\circ}\text{ K} \end{cases} \tag{13}$$

4.4.3 Comparison with Analytical Predictions

As pointed out in the introduction CONTAM does not incorporate a boundary layer model and, therefore, does not expand the flow field properly to predict mass flux in the backflow region. It would seem then the most worthwhile assessment for us to make here is to compare the experimental data to both an inviscid model and a boundary layer model. Such a comparison could be of value in providing direction to upcoming model improvement efforts. For the inviscid model prediction it is convenient to use the cosine law approximation[23, 24, 26] to the method of characteristics (MOC), and for the boundary layer model Simons[26] has developed simple closed-form expressions for Boynton's numerical treatment[25] of the supersonic portion of the nozzle boundary layer. It should be clearly understood at the outset that these are only first-order estimates for the purpose of comparison.

Boynton's work suggests that at large angles from the nozzle axis the plume gas density obeys an exponential decay law. Based on Boynton's results, Simons[26] assumed the cosine law is valid for angles less than some angle ϕ_o, and the exponential applies for angles greater than ϕ_o, where ϕ_o is the turning angle for the streamline at the edge of the boundary layer. Using this approach Simons obtained the following analytical forms for the gas density distribution:

$$f\,(\phi) = \cos^{2/(\gamma-1)}\left[(\pi/2)(\phi/\phi_\infty)\right] \text{ for } \phi < \phi_o \qquad (14)$$

where γ is the ratio of specific heats, and ϕ_∞ is the value of the limiting turning angle for an inviscid supersonic flow.

$$f(\phi) = f(\phi_o)\, e^{-\beta(\phi - \phi_o)} \text{ for } \phi > \phi_o \qquad (15)$$

where ϕ_o and β are functions[26] of the nozzle exit conditions. ϕ_o is related to the boundary layer thickness (δ_e) through

$$f(\phi_o) = (2\delta_e/R_e)^{2/(\gamma + 1)} \qquad (16)$$

where R_e is the nozzle exit radius.

For evaluating Simons' equations, the appropriate parameter values for the 5 lb_f thruster (baseline configuration) were determined to be:

Ratio of specific heats, $\gamma = 1.25$

Effective nozzle area ratio, $A_e/A_t = 84$

Exit Mach number, $M_e = 5.2$

Combustion chamber pressure, $P_c = 100$ psia

Combustion chamber temperature, $T_c = 2500^oK$

Then the numerical values of Simons' parameters are:

$\phi_o = 22.06^o$

$\phi_\infty = 75.8^o$

$f(\phi_o) = 0.42$

$\beta = 8.93$

$\delta_e/R_e = 0.188$

The resulting mass flux distributions predicted by the inviscid and boundary layer models are plotted in Fig. 14 with the experimental data, Eq. (3), for comparison. As expected the inviscid prediction falls off much too fast. Furthermore, the boundary layer prediction also decays

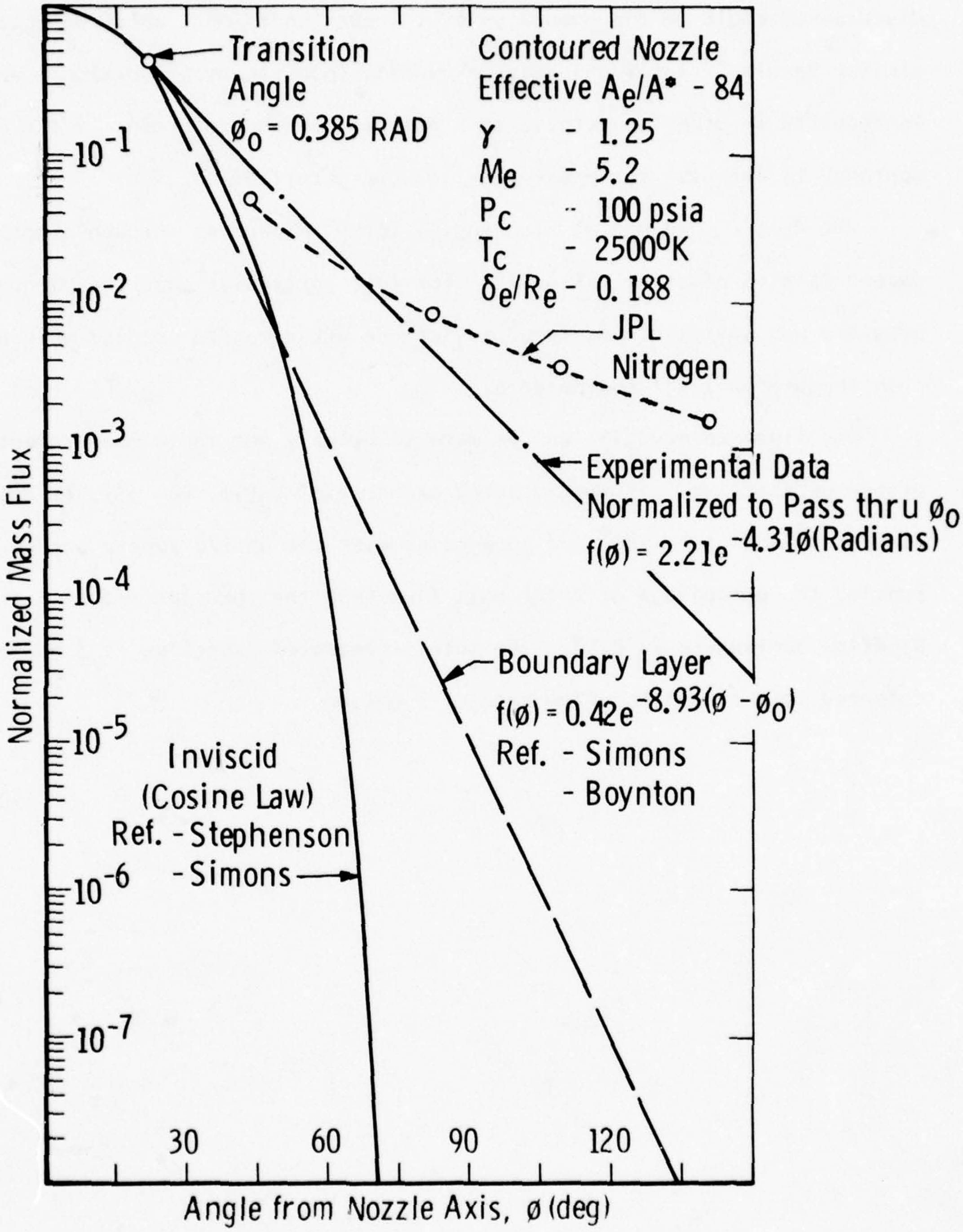

Fig. 14 Comparing Measured and Calculated Mass Flux Distributions

too rapidly. The slope $\beta = 8.93$ for the predicted exponential curve is a factor of two higher than that for the data. One possible source for this discrepancy could be the boundary layer input conditions which were taken from similar results[24] for ideal gases expanding into vacuum. Additional analysis is required in order to resolve this discrepancy and determine if the Simons approach is adequate for plume backflow characterization.

JPL data[10] obtained at high angles for N_2 expanding through a nozzle into vacuum is also plotted in Fig. 14. For this particular case the plenum pressure was 104 psia. At large angles the JPL data are considerably higher than the bipropellant engine data.

One final observation can be made to quickly put these measurements into proper perspective. If the measured exponential curve, Eq. (3), is extrapolated down to 0^{o} and up to 180^{o} and integrated over the entire sphere around the nozzle, the percentage of total mass flux from the thruster reaching the backflow hemisphere is 0.5%. The total integrated mass flux is 3 gm/sec compared to a propellant flow rate of 5 gm/sec.

5.0 CONCLUSIONS

1. The cryogenic chamber provided an adequate simulation of space operating conditions and had no significant effect on the plume flow field or the mass flux collected by the QCMs.
2. Variation of engine configuration had no measureable effect on the mass flux distribution.
3. Variation of engine operating conditions, with the exception of pulse length, had no significant effect on the mass flux distribution.
4. The QCM data show a smooth exponential mass flux distribution at angles greater than 30° from the plume axis. This strongly suggests that a proper treatment of the boundary layer is required to correctly predict mass flux in the backflow region.
5. At the higher QCM temperatures (greater than $180^{\circ}K$) where condensation of major exhaust species is not expected, approximately 1 - 2% of the total mass flux was collected throughout the exhaust plume. These constituents, generally identified as nitrates, represent potential contaminants for spacecraft surfaces.
6. The QCM design modifications (thermally separated electronics) permitted reliable operation to temperatures as low as $25^{\circ}K$.
7. By far the largest uncertainty in the QCM data is attributed to uncertainty in the calibration constant. QCMs must be calibrated over the entire temperature range of operation. Field-of-view effects should be investigated.

ACKNOWLEDGMENTS

This program was initiated by the AFRPL, conducted by the AEDC, and jointly funded by the AFRPL, SAMSO, and AEDC. In the two years since it was initiated, many individuals have contributed to its success. It is a pleasure to acknowledge: J. D. Stewart/AFRPL for initiating and defining the project, Maj M. Carpenter and Lt F. Manning/SAMSO for funding and support, J. A. Roux/AEDC for checking out the first QCM and determining the necessary modifications, W. B. Stephenson/AEDC for the analytic calculations and pretest experimental checkout of all the QCMs in the molecular beam chamber, and R. E. Alt/AEDC for the cryogenic chamber modifications and operation, thruster installation, and the firing matrix.

REFERENCES

1. Chirivella, J. E., "ATS-F Radiant Cooler Contamination Test in a Hydrazine Thruster Exhaust", JPL-TM-33-592 (1973).

2. Davis, L. P. and Witbracht, I. L., "Thruster Contamination Predictions for NATO III Satellite", AFRPL-TR-75-67 (1975).

3. Burch, B. A., "Effect of Contamination on Spacecraft Surfaces Exposed to Rocket Exhausts", AEDC-TR-68-23 (1968).

4. Bowman, R. L., et al, "Skylab Plume Contamination Experiments", NASA-TM-X-71474 (1973).

5. Lynch, J. T., "Quartz Crystal Microbalance (QCM) Monitor of Contamination for LES 8/9", Project Report SC-33, Lincoln Laboratory, Massachusetts Institute of Technology (1976).

6. Oeding, R. G., et al, "Space Shuttle RCS Plume Contamination Study", McDonnell Douglas Astronautics Co., MDE G5250 (1974).

7. Hoffman, R. J., et al, "Plume Contamination Effects Prediction - The CONTAM Computer Program, Version II", AFRPL-TR-73-46 (1973).

8. Davis, L. P. and Wax, S. G., "Verification of Contamination Predictions for Monopropellant Thrusters", AFRPL-TR-77-56 (1977).

9. Baerwald, R. K. and Passamaneck, R. W., "Monopropellant Exhaust Plume Contamination Measurements", AFRPL-TR-77-44 (1977).

10. Chirivella, J. E., "Hydrazine Engine Plume Contamination Mapping", AFRPL-TR-75-16 (1975).

11. Williams, W. D., et al, "Experimental Study of Monopropellant Hydrazine Thruster Exhaust", Proceedings of the 10th JANNAF Plume Technology Conference, San Diego, CA (1977).

12. Chirivella, J. E., "Molecular Flux Measurements in the Back Flow Region of a Nozzle Plume", JPL-TM-33-620 (1973).

13. Williams, W. D. and Lewis, J. W. L., "Condensation Scaling Laws for Reservoir and Nozzle Parameters and Gas Species as Determined by Laser Scattering Experiments", AFRPL-TR-76-67 (1976).

14. Spisz, E. W., et al, "Exhaust Plume and Contamination Characteristics of a Bipropellant RCS Thruster", Proceedings of the 7th JANNAF Plume Technology Conference, Huntsville, AL (1973).

15. Schoenman, L. and Schindler, R. C., "Five-Pound Bipropellant Engine", AFRPL-TR-74-51 (1974).

16. Pipes, J. G., et al, "Transmission of Infrared Materials and Condensed Gases at Cryogenic Temperatures", AEDC-TR-77-71 (1977).

17. Williams, W. D. and Lewis, J. W. L., "Rotational Temperature and Number Density Measurements of N_2, O_2, CO, and CO_2 in a Hypersonic Flow Field Using Laser-Raman Spectroscopy", AEDC-TR-75-37 (1975).

18. Stockbridge, C. D., in Vacuum Microbalance Techniques, K. H. Behrndt, ed. (Plenum Press, New York, 1966), Vol 5, p. 193.

19. Roux, J. A., et al, "IR Optical Properties of Bipropellant Cryocontaminants", paper presented at the USAF/NASA International Spacecraft Contamination Conference, USAF Academy, CO (1978).

20. AEDC Facilities Handbook (Tenth Edition), Arnold Engineering Development Center (1974).

21. Schoenman, L. and Lundgreen, R. B., "AJ10-181 5 lb_f Bipropellant Engine, Users Manual", Final Report, Contract PO TA1902G, Aerojet Liquid Rocket Company (1976).

22. Honig, R. E. and Hook, H. O., "Vapor Pressure Data for Some Common Gases", RCA Review, Vol XXI, 360 (September 1960).

23. Hill, J. A. F. and Draper, J. S., "Analytical Approximation for the Flow from a Nozzle into a Vacuum", J. Spacecraft Rockets 3, 1552 (1966).

24. Stephenson, W. B., et al, "Development of an Integrated Cryogenic Pumping System for Rocket Plume Studies", AEDC-TR-71-19 (1971).

25. Boynton, F. P., "Exhaust Plumes from Nozzles with Wall Boundary Layers", J. Spacecraft Rockets 5, 1143 (1968).

26. Simons, G. A., "Effect of Nozzle Boundary Layers on Rocket Exhaust Plumes", AIAA Journal 10, 1534 (1972).

GROUND CONTAMINATION
MONITORING METHODS

C. R. MAAG and R. R. SCOTT

AEROJET ELECTROSYSTEMS COMPANY
AZUSA, CALIFORNIA

ABSTRACT

Instrumentation and techniques for determining surface contamination on optical and thermal control surfaces are discussed. Two types of monitoring methods are described - Internal Reflection Spectroscopy and Front Surface Quarter Wave Coated Dielectric Mirrors. IRS measurements of a KRS-5 prism from 2.5 to 30 μm will allow determination of contamination film thickness, calculation of real and imaginary index of refraction, and general species identification via refractive index signature analysis. The $\lambda/4$ coated mirror accurately indicates the presence of thin contaminant films and any change in spectral reflectance from 0.25 to 2.5 μm. Changes in solar absorptance (α_s) and real index of refraction signature can be derived from the mirror measurements. A more detailed description of these measurement techniques, along with sample spectra of deposited contaminants from a solid rocket motor test firing is presented.

1.0 INTRODUCTION

Much effort is usually put into the selection of optical surfaces to be used on a Spacecraft or on flight instrument packages. Adhesives, potting compounds, lubricants, etc. are chosen for their low outgassing properties and compatability with the system. Thermal coatings and second surface mirrors are selected for their particular thermal radiative properties and subsequent stability in the space radiation environment. Every material on an instrument or spacecraft has a function and is so chosen to fulfill it.

The majority of these optical surfaces can, as Figure 1 shows, become contaminated from sources external to the payload during construction and/or testing. During testing there is a large risk of contaminating the payload from polymeric materials in the chamber and from backstreaming of vacuum pump oils. Optical and thermal control surfaces are particularly sensitive to the effects of contaminant deposition. The cleaning of surfaces contaminated during testing is often difficult and extremely expensive. In the case of optical instruments or sensors the contamination may render the payload useless or significantly decrease its lifetime in orbit.

As part of an on-going program at Aerojet to study contamination phenomena, a design concept has been identified, tested and is being recommended as a contamination monitor for ground environment application. These environment monitors (witness samples) would follow along with a spacecraft during all phases of handling (e.g., manufacturing, test, etc.) up to the launch phase. This practice would enable one to easily define the quantity and species of any contaminant and at what time it attached itself to the spacecraft. The utilization of these monitors would provide invaluable information in understanding during what phase of manufacture and test contamination is occurring,

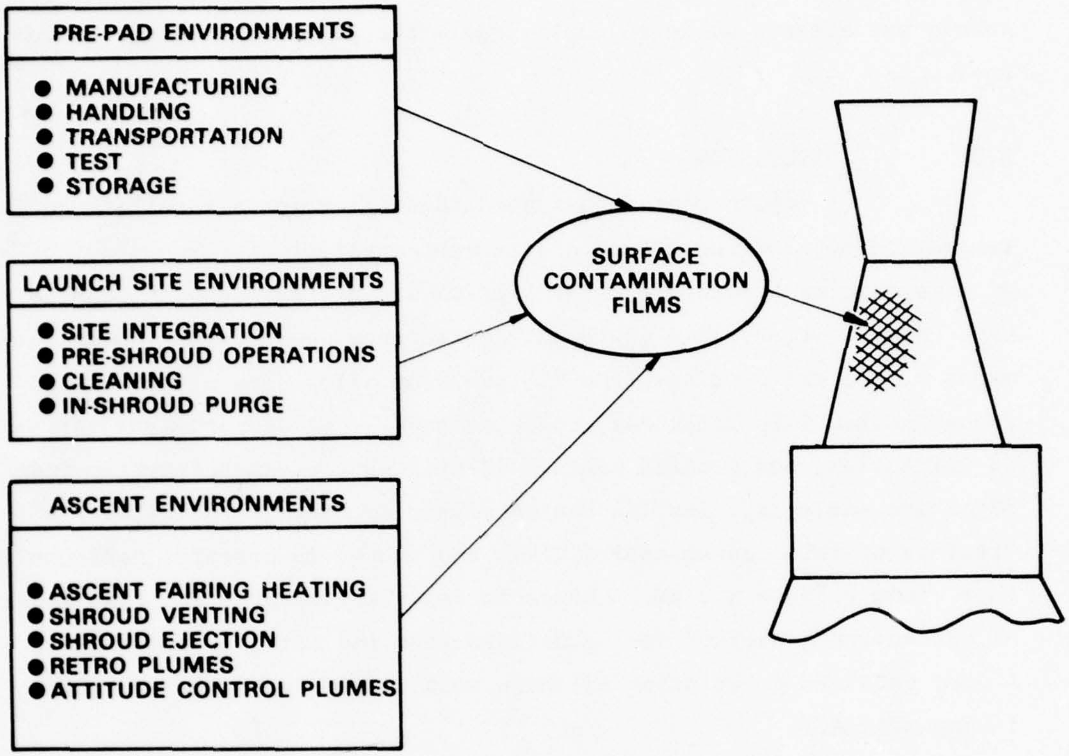

FIGURE 1. ENVIRONMENTS CAPABLE OF CONTAMINATING PAYLOAD CRITICAL SURFACES BEFORE ORBIT INSERTION

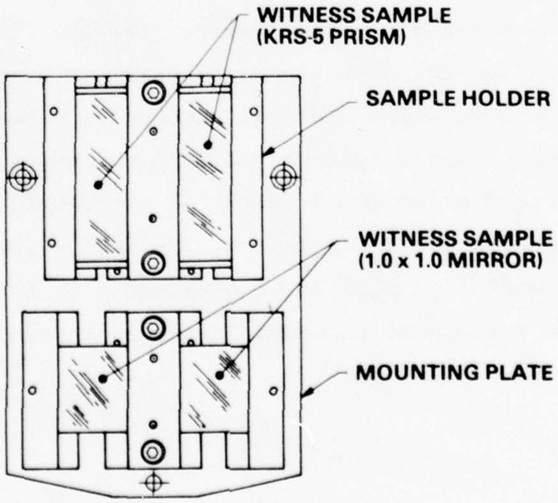

FIGURE 2. CONTAMINATION MONITOR WITNESS SAMPLE ASSEMBLY

how thick the contaminant is, if cleaning is required, and what the subsequent effects would be to the radiative properties of the spacecraft.

2.0 DISCUSSION

A design concept has been identified for a satellite contamination monitor for ground environment application. Two types of witness samples are used - A KRS-5 prism and a front surface quarter wave coated mirror. IRS (Internal Reflectance Spectroscopy) measurements of the KRS-5 prisms from 2.5 to 30 μm allow determination of contamination film thickness, calculation of real and imaginary index of refraction, and general species identification via refractive index signature analysis. The $\lambda/4$ coated mirror accurately indicates the presence of thin contamination films and change in spectral reflectance from 0.25 to 2.5 μm. Change in solar absorptance and real index of refraction signature can be derived from the mirror measurements. A more detailed description of these measurement techniques is given in Appendix A.

The contamination monitor witness sample assembly concept shown in Figure 2, consists of two mirror samples and two prism samples supported by a mounting plate and adapter bracket. This configuration was selected to allow one mirror and one prism to be removed at selected time events to evaluate effects of sequential exposure. The samples would be replaced by a new (clean) set when the exposed set is removed. The other mirror and prism would remain in place until the mounting plate is removed from the spacecraft at the last event time. This allows total accumulation data to be obtained. Thus the monitor configuration gives individual exposure environment data as well as total exposure data.

Table (1) indicates a recommended event timetable at which samples would be installed and removed. Contamination measurements for delta time periods would be obtained up to last spacecraft access before launch.

A set of monitor units is proposed to provide mapping of any spacecraft configuration and evaluation of any preferential contamination effects. All units would be of identical construction. The recommended location of the monitor assemblies is of course dependent upon payload configuration. The sample removal method envisioned is to remove the sample assembly from the payload to a convenient work table, remove one set of samples, install a new set of samples, and then replace the monitor assembly on the payload.

The mirror and prism samples removed would be returned for spectral measurement and data evaluation. Protective containers should be provided for clean sample storage and sample transportation.

All monitor units would be removed from the spacecraft at the launch site prior to fairing installation. In addition to the normal sample spectral measurements, one assembly total duration mirror (potentially the most contaminated) should be cleaned per an AESC mirror cleaning procedure,[1] measured at the center and edge, exposed to 300 equivalent sun hours of UV radiation in a vacuum facility, and remeasured at edge and center after UV exposure. This process will evaluate potential solar absorptance degradation effects on cleaned optical surfaces due to early flight UV exposure.

TABLE 1. RECOMMENDED MEASUREMENT EVENT SCHEDULE

MANUFACTURE/TEST

- Initial installation - first opportunity
- Remove and measure before thermal vacuum test
- Remove and measure after thermal vacuum test
- Remove and measure after transportation

At Launch Site

- Remove all units before fairing installation

3.0 EXPERIMENTAL

3.1 TE-344 Retromotor Test

An opportunity arose during the last quarter of calendar year 1977 that allowed AESC to both check out the ground contamination monitor concept and obtain needed information from solid rocket motor plumes. Through the efforts of Aerospace Corporation and AEDC* personnel, AESC quarter wave dielectric mirrors were exposed in two (2) separate solid motor tests. The first test was carried out as a piggy-back test during test firings of two TE-344 Titan II retromotors. The tests were conducted in the AEDC T-3 test cell on 17-18 November 1977.

AESC dielectric mirrors plus a host of other witness plates supplied by Aerospace and AEDC were placed at various locations in the test cell. All witness plates were placed outside of the predicted primary motor plume (broadside and backflow regions). Preliminary results show the presence of particles of aluminum oxide

*Arnold Engineering Development Center

(clusters) and carbon. Photographs of the resulting contamination on the dielectric mirrors are shown in Figure 3. High speed motion pictures showed ablation of the glass phenolic nozzle. The films also showed the reverse flow from the facility diffuser duct at motor shut down (burn out). As has been mentioned elsewhere in these proceedings, because of facility limitations, it is not possible to perform measurements that would give meaningful results on contamination, deposition or distribution.

The objectives of the test were met. The witness plates performed well enough to be considered as contamination monitors for the IUS validation test firing.

3.2 IUS Motor Validation Test

The experimental program was carried out in the AEDC J-5 test cell. For the experiment described herein, the IUS motor was fired for 145 seconds. The samples were each mounted in individual chambers so as to eliminate any motor start-up or shut down anomalies. The chambers were in reality 7-inch stainless steel vacuum slide valves with a blank-off flange for sample mounting. The chambers were each individually wrapped with multi-layer insulation (MLI) to eliminate adverse heating effects. The chamber/valves were sequentially opened and closed by computer to allow for different sample exposure periods.

A total of four dielectric mirror samples were exposed to the plume products. Each mirror along with other types of witness plates (supplied by different experimenters) were mounted in an individual chamber. Figure 4 shows the locations of the four sample valves relative to the diffuser inlet. Figures 5 and 6 show the positions of the four valves in side views. Two valves were located as shown in Figure 5, and the other two were located as shown in Figure 6.

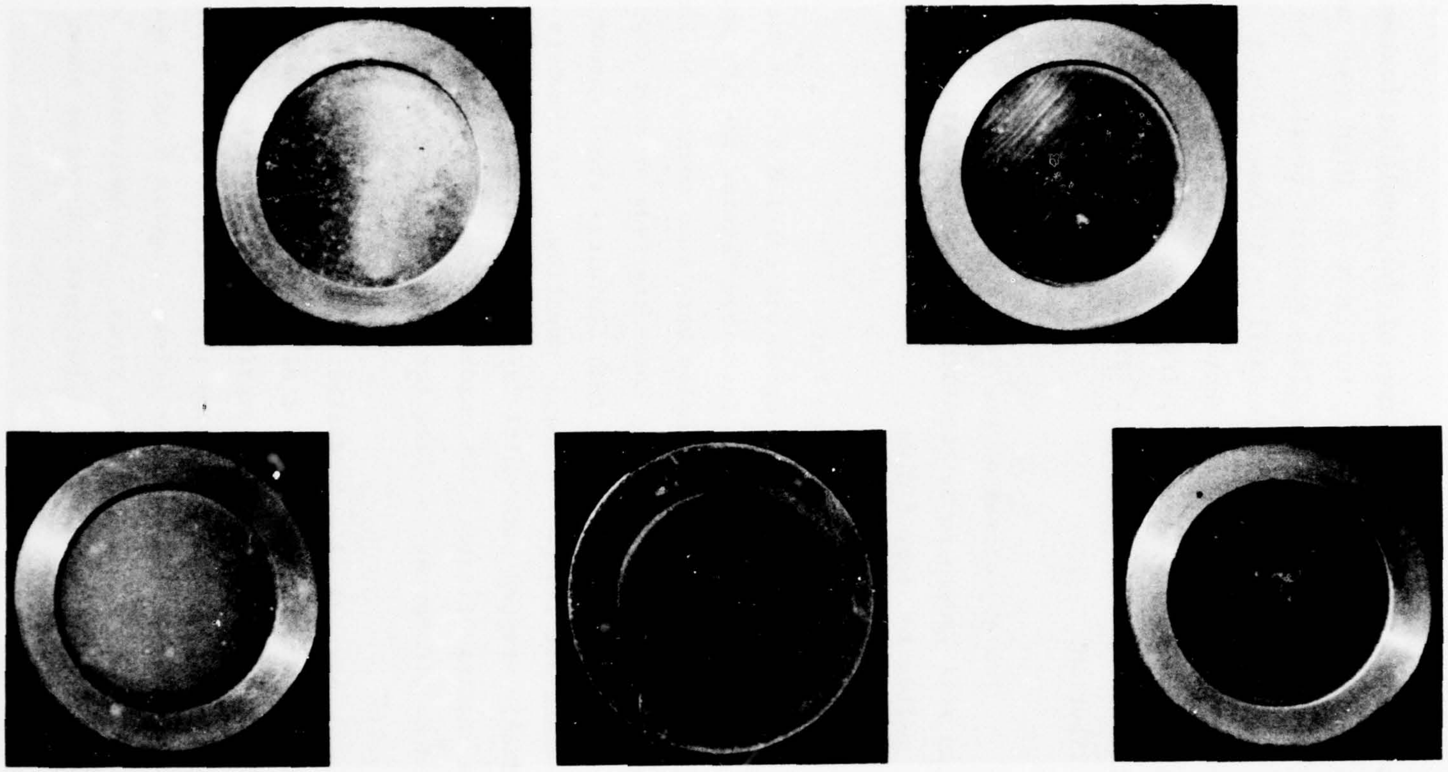

FIGURE 3. POST FIRE T3 TEST CELL DIELECTRIC MIRRORS

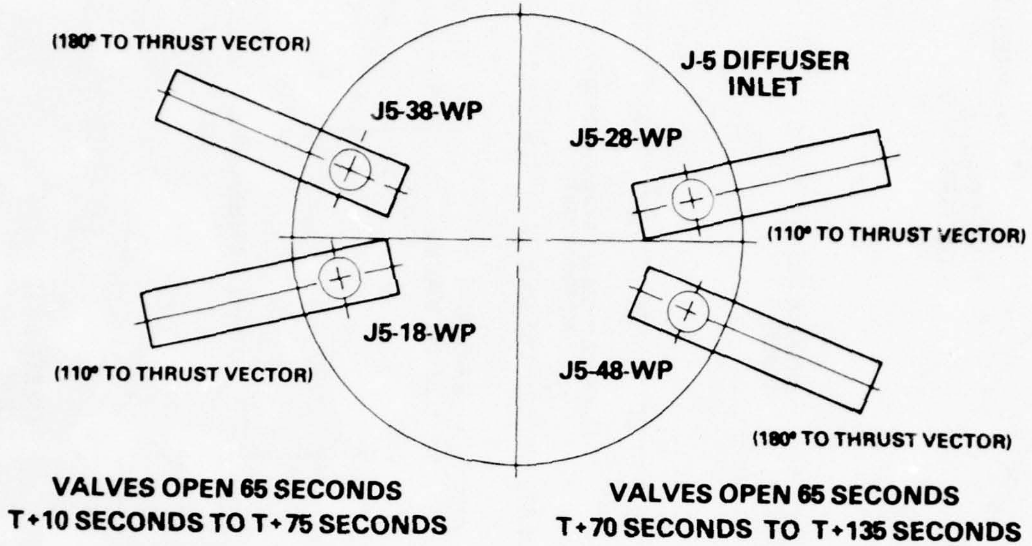

FIGURE 4. WITNESS PLATE VACUUM CHAMBER LOCATION - END VIEW

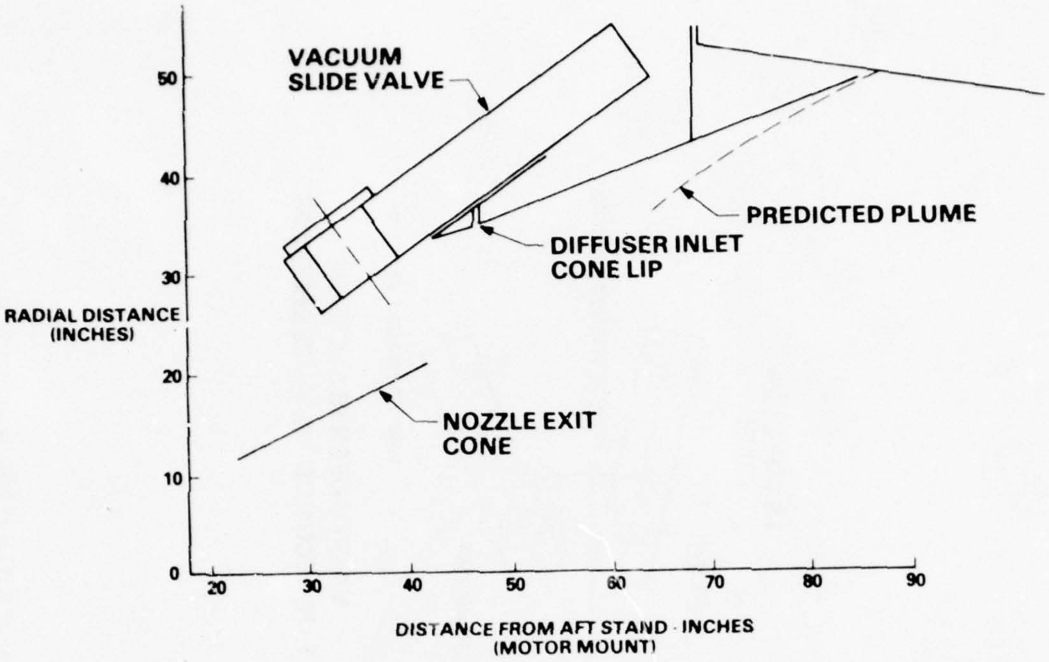

FIGURE 5. WITNESS PLATE VACUUM CHAMBER LOCATION - 110° TO THRUST VECTOR

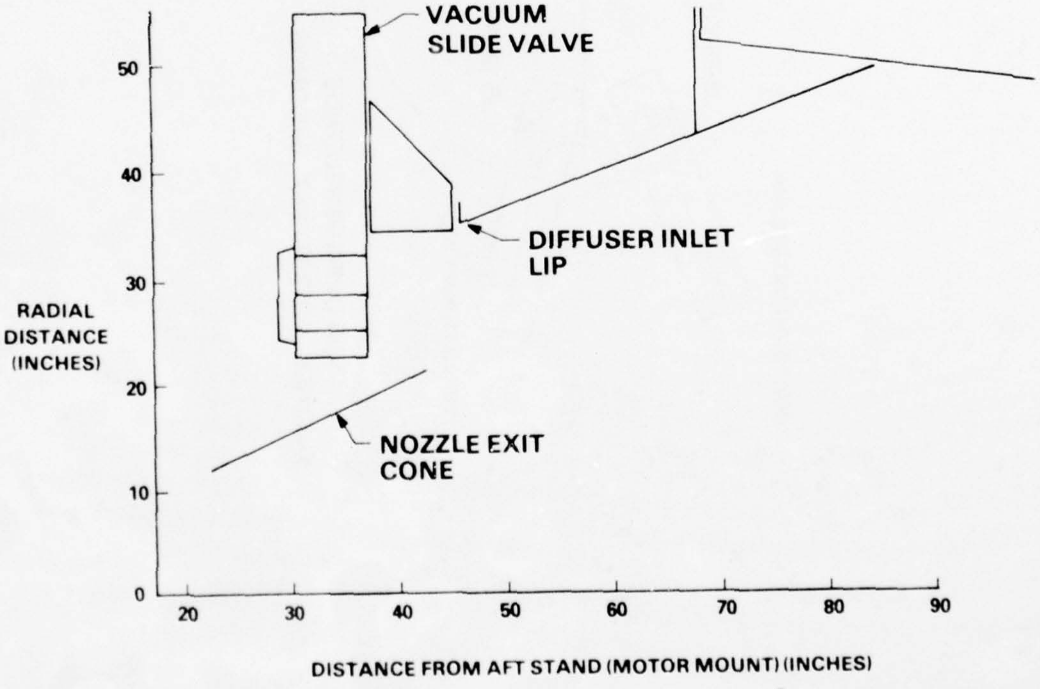

FIGURE 6. WITNESS PLATE VACUUM CHAMBER LOCATION - 180° TO THRUST VECTOR

The valves were opened and closed in pairs with each pair consisting of one each from Figure 5 and one each from Figure 6. One pair of valves was opened to expose all witness plates 10 seconds after motor ignition and closed after 75 seconds into the firing. The second pair of valves was opened 70 seconds after motor ignition and closed after 135 seconds into the firing (10 seconds before motor shut down). The second pair of valves were closed before the burnout transient pressure effects could occur. Table 2 summarizes the valve sequencing for the entire test. All valves were opened and closed by a computer sequencer.

TABLE 2 VALVE SEQUENCE FOR IUS MOTOR TEST

T Minus 10 min - Open All Valves
T Minus 2 min - Close All Valves
T Minus 30 sec - Open All Valves
T Minus 5 sec - Close All Valves
T Plus 10 sec - Open J5-38-WP, J5-18-WP
T Plus 70 sec - Open J5-28-WP, J5-48-WP
T Plus 75 sec - Close J5-38-WP, J5-18-WP
T Plus 135 sec - Close J5-28-WP, J5-48-WP

All mirror samples were stainless steel approximately 2.5 cm in diameter and 2 mm thick. They were coated as described in Appendix A. The samples were captured in stainless steel mounts with screw tops. Each was mounted flush on the inside of the blank-off flange. The samples were transported to and from AEDC in their own individual enclosure.

Spectral reflectance measurements were made both before and after exposure of the samples to the solid motor effluents and are shown in Figures 7 through 10. The after exposure measurements

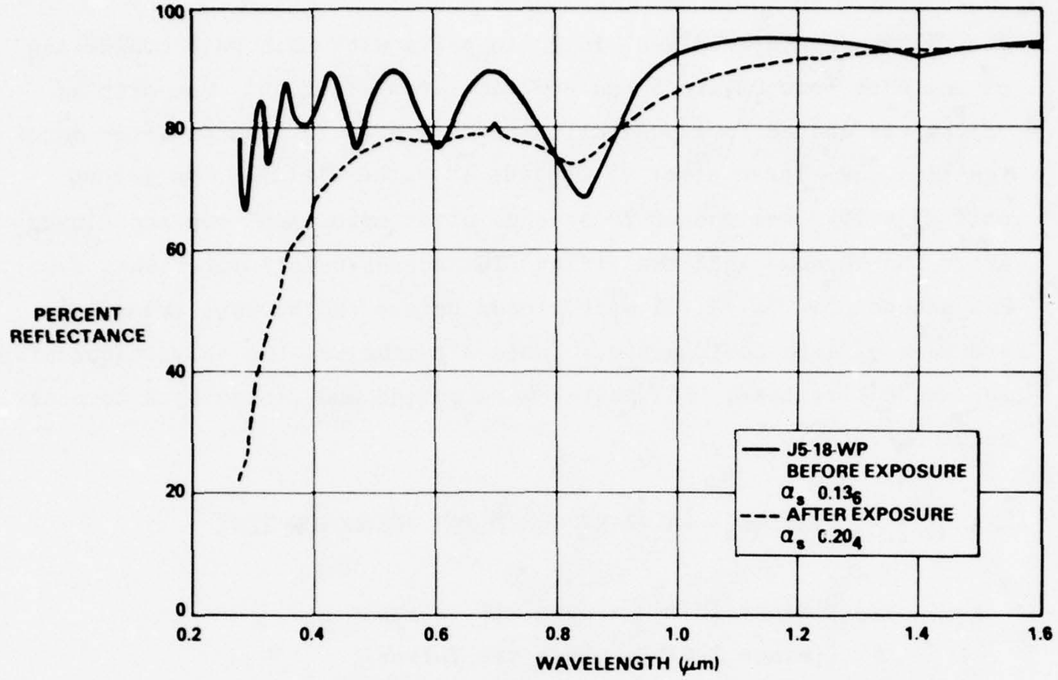

FIGURE 7. SPECTRAL REFLECTANCE OF FIRST OPENED 110° MIRROR

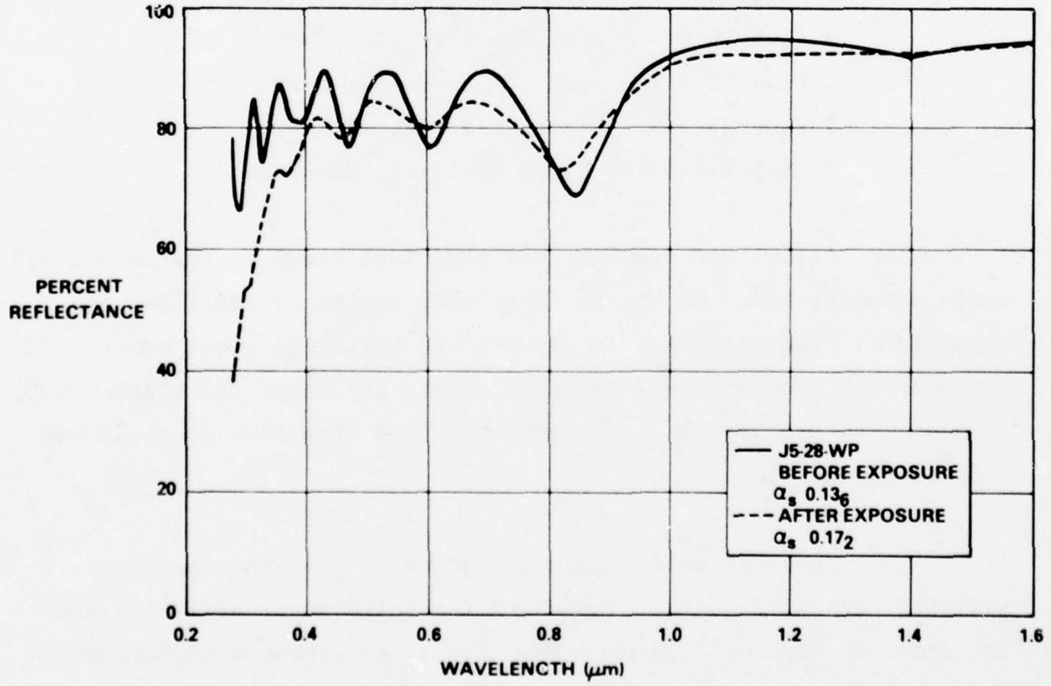

FIGURE 8. SPECTRAL REFLECTANCE OF SECOND OPENED 110° MIRROR

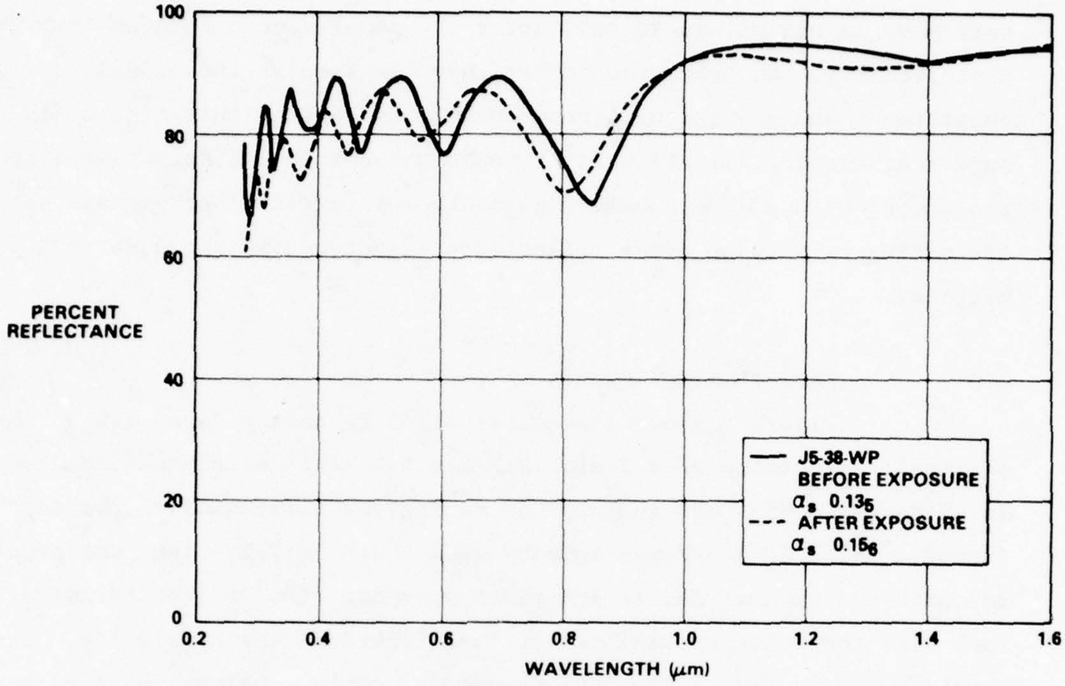

FIGURE 9. SPECTRAL REFLECTANCE OF FIRST OPENED 180° MIRROR

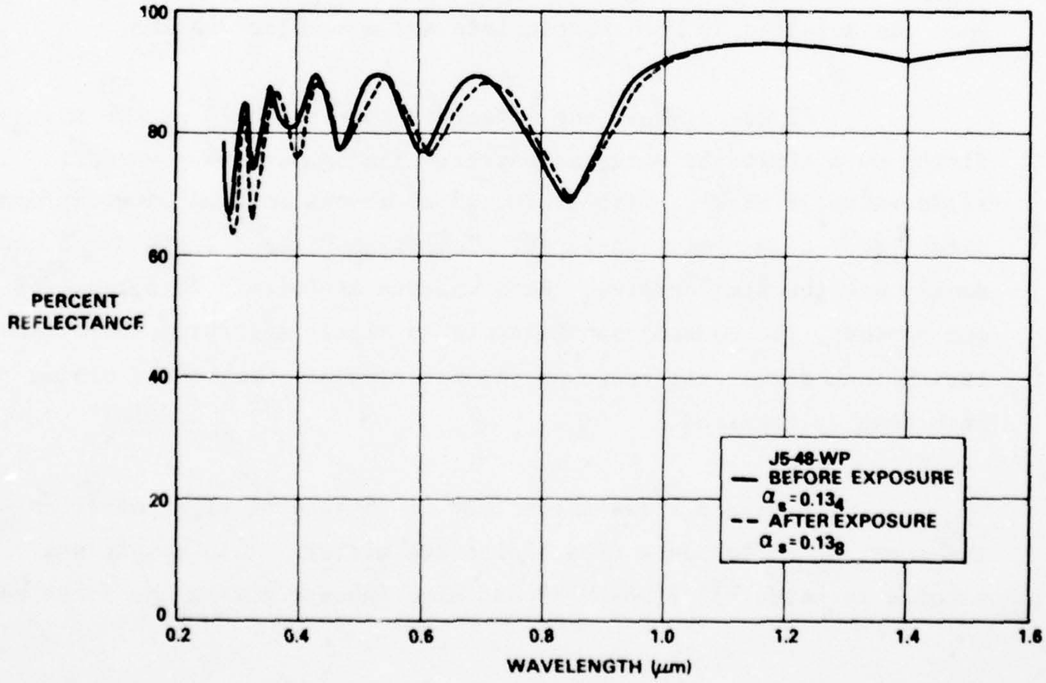

FIGURE 10. SPECTRAL REFLECTANCE OF SECOND OPENED 180° MIRROR

were made in air within 30 days after the samples were removed from the test facility. No precaution other than the samples individual storage compartment and dessicator storage were taken during this time to insure that the contamination layer would not change. A Cary 14 spectrophotometer with a Gier-Dunkle (MgO coated) integrating sphere was used for making ex-situ spectral reflectance measurements from 0.25 to 2.5 microns.

4.0 EXPERIMENTAL RESULTS

Figure 7 shows the effect of 65 seconds of exposure on the spectral reflectance of a dielectric mirror. This sample was mounted in slide valve J5-18-WP and exposed during the first half of the test firing. Valve J5-18-WP was mounted such that the valve face was parallel with the exhaust nozzle and plume boundary (110° to the thrust vector) also the valve opening center line looked at the nozzle lip. The sample exhibits severe spectral damage throughout the entire solar region. Examination of the sample after the test showed the mirror had been contaminated by both particulate and molecular species.

Figure 8 shows the effect of the last half of the test firing on a similarly situated mirror. The sample was mounted in slide valve J5-28-WP. Slide valve J5-28-WP was mounted directly opposite (180°) slide valve J5-18-WP. Comparing Figures 7 and 8 one can easily see the similarities. Both spectra are within 10 percent of one another, the contaminant layer is so highly absorbing and/or scattering that almost all trace of the interference maxima and minima have been obliterated.

Figure 9 shows the effect of 65 seconds of exposure on the spectral reflectance of a dielectric mirror. This sample was mounted in slide valve J5-38-WP and also exposed during the first half of the test firing. Valve J5-38-WP was mounted such that the valve face was normal to the nozzle exit plane and the diffuser inlet plane (180^o to the thrust vector). The sample exhibits moderate spectral changes mostly at the interference minima. Examination of the sample after the test showed a "visible" trace quantity of a molecular contaminant.

Figure 10 shows the effect of the last half of the test firing on a similarly situated mirror. The sample was mounted in slide valve J5-48-WP. Slide valve J5-48-WP was mounted directly opposite (180^o) slide valve J5-38-WP. Comparing Figures 9 and 10 one can again see a striking similarity. Both spectra are within a few percent of each other. In addition, they also show a considerable amount less absorption than seen in Figures 7 and 8.

Although it is not necessary to totally analyze the results of the test firing at this time, since it is self evident that all of the mirrors exposed exhibited contamination (in varying degrees), the more salient points should be mentioned. It has been generally theorized[2,3] and/or postulated that exhaust products would indeed turn and expand beyond the predicted plume shape. How far they would turn has been a point of conjecture. The IUS solid motor test firing has shown that contaminants can in fact find their way to the back flow region. The test has shown that a significant number of particles are carried out (broadside) of the predicted plume envelope. Few, if any, particles were observed in this test to return to the back flow region (180^o to the thrust vector).

One of the more interesting and also satisfying observations of data from this study was that similar oriented samples behaved exactly the same. Two important pieces of information are available from the test data. First, the change in reflectance values for the samples exposed during the first portion of the test are greater than those exposed during the latter portion. One might suspect that the motor had not yet achieved a stable burn at the time of initial valve openings. Secondly, both samples in the backflow region (180^{o} to the thrust vector) were subject to more molecular species than particulate buildup, whereas, just the opposite is true for "broadside" samples. Figure 11 shows the mass accumulation on the test specimens. The samples are arranged in the photograph as they were situated in the test chamber (see Figure 4). The sample in the center has not been exposed.

5.0 CONCLUSIONS

The prediction of mass accumulation (contamination) prior to launch of a payload is a formidable task. Simple, accurate contamination monitoring methods are needed for satellites with sensitive optical and thermal control surfaces during ground operations. The instrumentation and techniques have been defined to monitor and accurately measure effects of contamination deposits. Quarter-wave dielectric mirrors have been successfully used to measure backflow contamination from solid propellant motors demonstrating the usefullness of the concept.

Changes in spectral reflectance were found in some cases to be significant. Measured changes in reflectance were due to both the deposition of thin absorbing films and scattering effects. Chemical effects from HCL or erosion of mirror surfaces were not detected in any of the samples exposed.

It should be recognized that the conclusions drawn from this data are those of the authors and apply only to this specific test firing. The most obvious testing "error" was that of making the

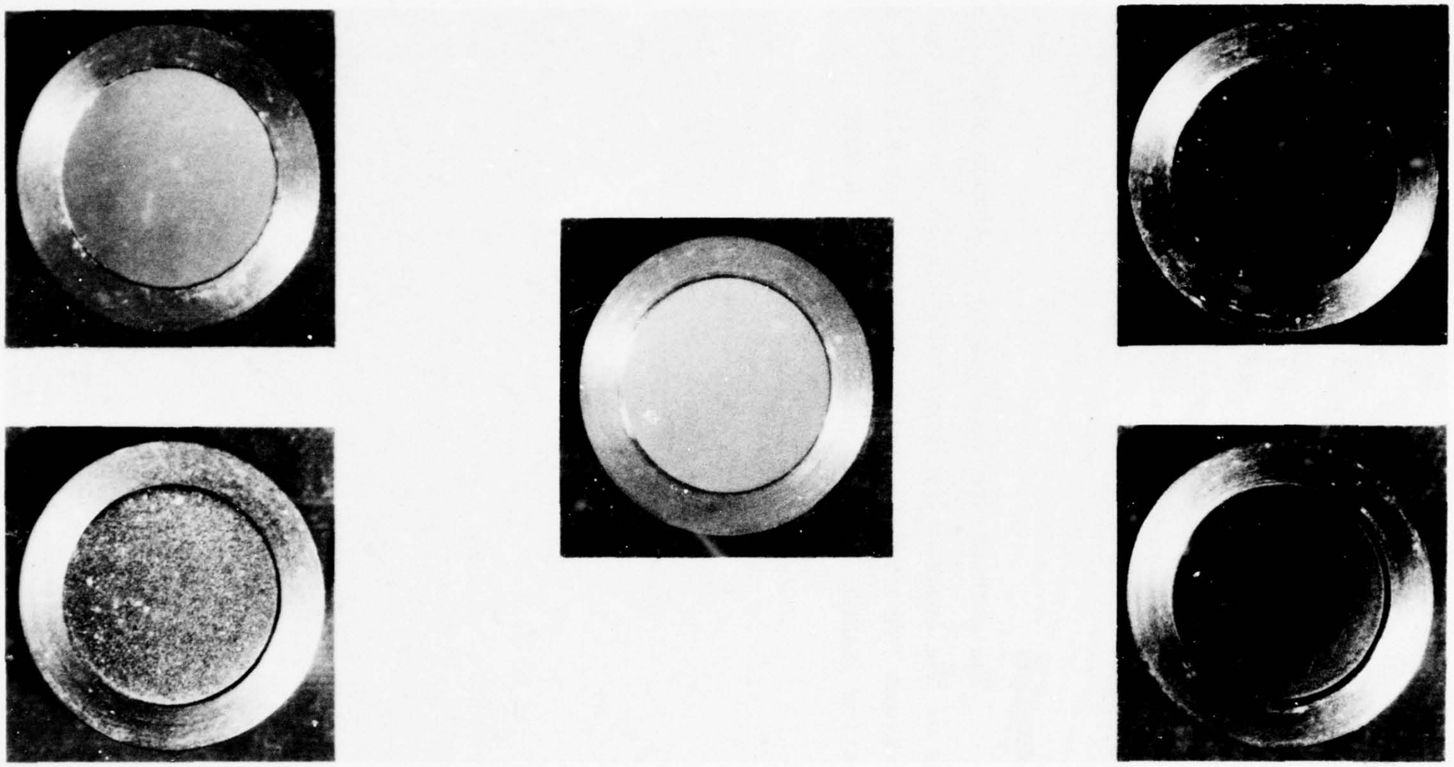

FIGURE 11. IUS VALIDATION TEST FIRING DIELECTRIC MIRRORS

reflectance measurements ex-situ. Unfortunately, the chamber at AEDC was not equipped for making in-situ reflectance measurements. The samples were carefully protected after removal from the chamber so as to avoid additional contamination. It is quite reasonable to consider the mirror degradation that occurred representative of that which would occur in space.

ACKNOWLEDGMENTS

The authors are indebted to E. Borson and H. Scott for allowing us the opportunity to participate in the AEDC test firings. This work was supported in part by the Space and Missiles Systems Organization (SAMSO) under Contract F04701-77-C-0010.

AD-A070 386 AIR FORCE MATERIALS LAB WRIGHT-PATTERSON AFB OH F/G 22/2
PROCEEDINGS OF THE USAF/NASA INTERNATIONAL SPACECRAFT CONTAMINA--ETC(U)
1978 J M JEMIOLA
UNCLASSIFIED AFML-TR-78-190 NL

9 OF 13
AD
A070386

REFERENCES

1. Barsh, M. K., Second Surface Mirror Cleaning and Verification, Proceedings of USAF/NASA International Spacecraft Contamination Conference, Colorado Springs, Colorado (1978)
2. Seubold, J. G. and Edwards, R. H., A Simple Method for Calculating Expansion of a Rocket Engine Nozzle Boundary Layer Into a Vacuum, Hughes Co.
3. Barsh, M. K., et al, Contamination Mechanisms of Solid Rocket Motor Plumes, Proceedings of USAF/NASA International Spacecraft Contamination Conference, Colorado Springs, Colorado (1978)

APPENDIX A

Description of Witness Sample Measurement Techniques

The practice of having witness samples carried along with a spacecraft during all phases of handling would enable one to easily define the quantity and species of any contaminant(s) that attached itself to a payload. Two different types of witness samples should be considered and are briefly discussed in the following paragraphs.

The first type of witness sample is what is termed a dielectric mirror. This monitor would consist of a highly polished substrate (such as stainless steel) evaporated with aluminum and subsequently overcoated with aluminum oxide ($A\ell_2O_3$)[a coating thickness in the neighborhood of 8λ/4 (eight quarter waves)]. This monitor would provide several important pieces of information. One would use conventional reflectance spectroscopy to observe any effects (changes) in spectral or total reflectance in the solar wavelength region (.25 to 2.5 μm) by observing shifts or amplitude changes in the reflectance maxima or minima (constructive and destructive interference); any change in refractive index (n) can be computed. If a change does occur, some thin absorbing layer of another substance has been deposited on the surface. Usually this thin surface layer is the contaminant of interest.

The reflectance values at the maxima have been observed to remain practically unchanged, while the reflectance at the minima shows a large decrease. This effect is easily explained[1] by the fact that at the reflectance maxima - the effective half-wave thickness - the standing waves in the layer have a node at the dielectric - contaminant boundary, so that the absorbing layer has little effect if it is thin enough. On the other hand, at the reflectance minima - the effective odd quarter-wave thickness - the standing wave has a loop at the surface which is strongly affected by a very thin absorbing layer, hence the reflectance at minima can be expected to change rapidly in comparison to the maxima as the thickness of the absorbing layer increases. In addition to "knowing" a contaminant existed, one could now irradiate this monitor with ultra-violet radiation (in-situ) and determine any photolysis effects. This monitor could be left as is or cleaned before UV exposure to determine if any residual contaminant is left behind.

The second type of witness sample is a KRS-5 prism. This prism is a transparent optical element [also known as an internal reflection element (IRE)] used in internal reflection spectroscopy for establishing the conditions necessary to obtain internal reflection spectra of materials (2.5 to 30 μm). Internal reflection spectroscopy (IRS) is the technique of recording the optical spectrum of a sample material (contaminant) that is in contact with an optically denser but transparent medium (KRS-5 prism), and then by measuring the wave-length dependence of the reflectivity of this interface by introducing light into the denser medium. In this technique the reflectivity is a measure of the interaction of the evanescent wave with the sample material. One of the most fundamental applications of IRS is in the measurement of optical constants of materials. It is also the most direct and sensitive way of recording optical constants at the present time. To determine the optical constants it is only necessary to make measurements of $R_{\perp}$ and $R_{\parallel}$ (perpendicular and parallel polarization) at a properly selected angle of incidence or, alternately by using light whose state of polarization is known, to measure the reflected intensity at two angles of incidence. Finally, knowing n and k it is easy to determine the effective thickness of any contaminant film from the first term of the series expansion of Fresnel's equations.[2]

The utilization of both types of monitors would provide invaluable information in understanding during what phase of manufacture and test contamination is occurring, how thick the contaminant is, and what the subsequent effects would be to the radiative properties of the payload.

REFERENCES

1. Hass, G. and Hunter, W. R., Applied Optics, 9, 2101 (1970)

2. Harrick, N. J., Internal Reflection Spectroscopy, Interscience, New York, 1967.

TITLE: ASSEMBLAGE ANALYSIS - IDENTIFICATION OF CONTAMINATION SOURCES

By: E. R. Crutcher
Boeing Aerospace Company
Quality Assurance Laboratories

ABSTRACT

It has been found that contamination samples of less than one milligram often contain a sufficient variety of particulate types to reconstruct a history of contamination exposure. This approach involves the use of analytical light microscopy, and related techniques, to identify source-characteristic assemblage of particulates. Sources are identified as belonging to one of four major categories: auto-generated, function-generated, facility-generated, or activity-generated. The first two indicate system reliability and design-operational environment compatibility. The last two involve production related problems of facility control or failure to properly isolate the part from externally generated contaminates.

Sources cannot generally be identified through the identification of a single particle species, but only through a combination of species in specific size ranges and present in "reasonable" proportions with respect to other members of the assemblage. This paper presents the basis for criteria used to identify an assemblage and the analytical support required to evaluate such a sample. Examples of common assemblages are given as well as precautions against conclusions based on too few members of an assemblage. A brief final statement is included regarding the benefits of this type of program support.

ASSEMBLAGE ANALYSIS - IDENTIFICATION OF CONTAMINATION SOURCES

1.0 INTRODUCTION

Contamination problems occasionally plague programs attempting to maintain the cleanliness levels required by increasingly sophisticated instrumentation. When such problems arise it is important to identify the source, or sources, of that contamination. The discovery of a source can lead to improvements in instrument or system design, improved clean room technology, or the identification of a need for tighter specification control and training. If the source is not identified, contamination problems can require very expensive rework and training in response to an ambiguous problem.

The heterogeneity and small sample size of most contamination samples preclude most customary analytical approaches. Assemblage analysis uses sample heterogeneity as an essential source labeling device and can easily be applied to clean room problems where the total sample size is less than one microgram.

Assemblage analysis has not completely removed the ambiguity from all contamination problems, but in many instances it has resulted in the unequivocable identification of a source, thus providing a quick and relatively inexpensive specific solution.

Assemblage analysis is a term borrowed from archeology where it refers to a technique used to monitor cultural development and change through time. Here it refers to a methodology used to identify sources of contamination through the recognition of different types of particulate assemblages characteristic of specific sources. A "source" can be a point of origin, a generation mechanism, a transport mechanism, or some combination of the three. There are five basic assumptions which underlie this technique:

1. A source generates more than one type of particulate or aerosol.
2. The particulate generated by a source reflects the mechanism of production, the material being acted upon, and the environmental conditions at the time and place of generation.
3. Once generated the particulate behaves in a predictable manner, subject to gravitation, filtration, and chemical or physical alteration.

4. Specific transport mechanisms deliver particulate which has specific physical parameters that reflect the method of transport, the distance of transport, and obstacles or scrubbing devices designed to clean the mobil phase in the transport system.

5. The method used to collect the sample and the subsequent analytical methods do not significantly distort the data.

These assumptions, and the experience of the analyst, combine to form the foundation of this technique.

2.0 DEFINITION OF ASSEMBLAGE TYPES

There are four main assemblage types: auto-generated, function generated, facility generated, and activity generated. Each of these types is characterized by the relationship between the assemblage and the system being contaminated.

2.1 Auto-generated Contaminates: non-wear derivatives of the system's structural materials.

Some materials are incompatible with their operational environment, or behave in a manner detrimental to the mission goals in specific environments. Two examples of these types of problems are the volatile-condensibles in some materials used early in the space program[1], and the particulate generation associated with the dielectric breakdown of FEP Teflon in synchronous earth orbit[2]. Many additional, more routine examples exist, such as gasket incompatibility with some hydraulic fluids, or corrosion problems. Discovery of this type of contaminate requires a modification of program goals or a redesign of parts for the system.

2.2 Function-generated Contaminates: wear or system operational derivatives of the systems' structural or fluid materials.

These contaminates consist of two subcategories: wear generated by moving parts; and polymer films produced by heat and pressure stresses on hydraulic or lubrication oils. This type of contaminate can always be found in systems with moving parts. They can be evaluated to generate system reliability data or to identify weaknesses in the system[3].

[1] Marmo, F. F. and J. Pressman, Definition Research Study, N73-30843, Final Report, Contract #NASW-2395, G.C.A. Corp. (1973)

[2] Fogdall, L. B., Cannaday, S. S., Wilkinson, M. C., Crutcher, E. R., and Wei, P.S.P., Combined Environmental Effects on Polymers, Eighth Space Simulation Symposium Proceedings (1976).

[3] Scott, D., Ferrography - An Advanced Design Aid for the 80's, Wear, 34:251-260 (1975).

2.3 Facility-generated Contaminates: particulate not related to the structural materials in the systems, or to the production or assembly cycle of the system.

This type of contamination generally indicates a source not anticipated in the design of the production flow diagram. Often this involves the failure of an air scrubbing system, process baths being used in unexpected ways, or some similar problem that was not foreseen in the selection of the facilities to be used during the production and assembly of the system. Examples include leaks in air systems that introduce contaminated air, surface films on parts as a result of using cleaning solutions as "stripping" baths, and rooms being "converted" into clean rooms unsuccessfully.

2.4 Activity-generated Contaminates: particulate can be explained in terms of the production cycle of the system.

The activities that are associated with the manufacture, assembly, and inspection of a part, or system, generate contaminates. The identification of these particulates can often pinpoint the time and place of contamination. Examples include plastic particulate from a swaging mandrel found in hydraulic tubing, or tooling residue in machined parts. Poor clean room technique is included in this category. Contamination consisting of epithelial cells, clothing fiber, and human hair in an otherwise clean system indicates a breach of clean room discipline.

3.0 ANALYTICAL APPROACH

3.1 The Relationship Between an Assemblage and a Source

The particulate in a contamination sample can generally be categorized into a general type with little difficulty. The task of the analyst is then to identify the source. The source identified must have relevance within the framework of the industrial environment. The identification of a diatom from a pre-cambrian silt may be interesting, but the breakdown of a filter containing diatomaceous earth is more relevant. This is a fanciful example of source analysis carried too far, but it points out the importance of communication between the analyst and the program involved. The "sources" which must be identified are those over which we have some control. The more the analyst knows about the system's construction materials and environment the easier the analysis becomes. Potential (relevant) sources suggest assemblages and minimum criteria required to determine the source. It is much more difficult to fully characterize assemblages and then look for relevant sources. As Figure 1 points out a source implies an assemblage; an assemblage suggests a source.

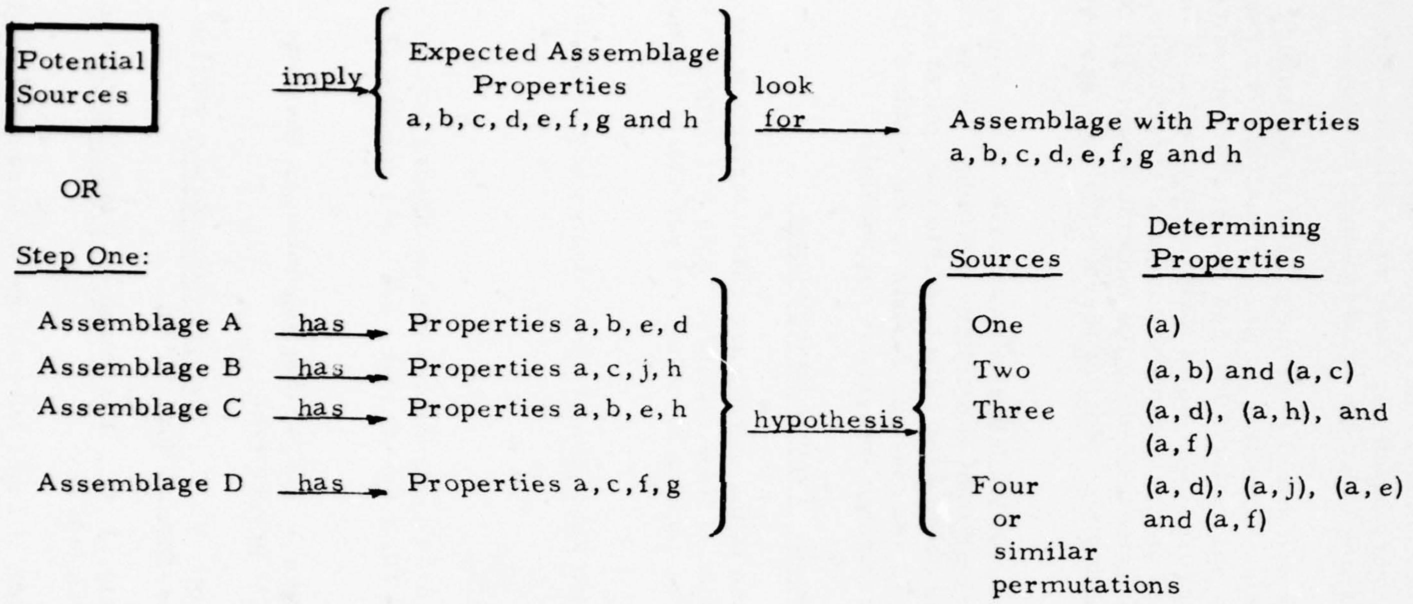

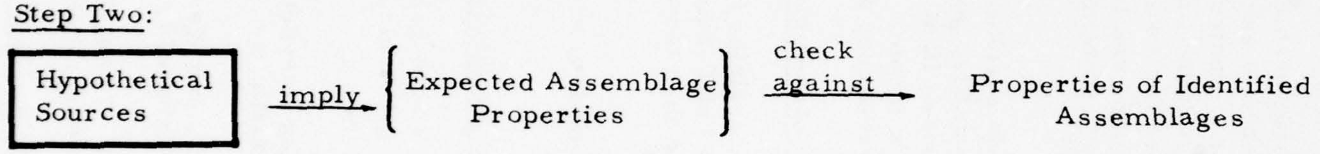

FIGURE 1: RELATIONSHIP BETWEEN ASSEMBLAGES AND SOURCES

3.2 Identification of Assemblages I: Analytical Approach

As with any other analytical scheme that is not of an in situ type, collection biases must be considered. Since the subject of this paper is not collection techniques, they have been presented only very briefly in Table #1. All are subject to some biases or limitations, the detailing of which would fill another paper.

Ideally, collection problems are minimal or the part is small enough to be brought to the laboratory for analysis. The first part of the analysis is a rapid overview of the part or collected sample using a low power stereoscopic microscope. Distribution gradients and gross size ranges involved are noted. The sample is then prepared for analysis on the analytical compound microscope. Microanalytical techniques are then used to identify the individual particles and to characterize the particulate distribution. Most of these techniques are described in the literature.[4,5,6]

The microscopic system used in this laboratory consists of a compound microscope using transmitted polarized light and oblique top light. Phase contrast is also used with polarized light and oblique top light to add to the optical data recoverable from a single mount. This microscopic system is the center of the total approach. Without microscopy assemblage analysis is not possible.

3.3 Identification of Assemblages II: Typical Assemblages

The individual particles found in the sample are characterized or identified and listed along with a brief indication of their quantity. This list suggests typical assemblages which are then tested by looking for other, as yet undetected members of these assemblages.

The following sections contain examples of contaminates that illustrate typical assemblages.

3.3.1 Auto-generated Assemblages

For convenience auto-generated assemblages can be divided into three subdivisions based on the mechanics of their generation. Each has specific characteristics.

1. Outgassing Assemblages - Outgassing assemblages have two characteristic chemical properties:

---

[4] Bowen, E. R. and Westcott, V. C., Wear Particle Atlas, N00156-74-C-1682, Final Report, Foxboro/Trans-Sonics, Inc. (1976).

[5] McCrone, W. C. and Delly, J. G., The Particle Atlas, Ed. II, Ann Arbor Science, Ann Arbor, Michigan (1973).

[6] Crutcher, E. R., The Role of Light Microscopy in Aerospace Analytical Laboratories, Ninth Space Simulation Symposium Proceedings (1977).

METHOD	DESCRIPTION	COMMENTS
1. Liquid Flush of Surface	A clean liquid flows over the test surface and collects particulate.	Effective provided liquid much cleaner than surface and liquid can be collected for testing.
2. Lift from Surface	Tape, collodion, cured rubber, treated filter, and similar materials can be used to lift particles from a surface.	Particulate is collected with its spatial distribution unchanged. Some methods form a cast of the surface area sampled. Some methods are limited as to the surfaces they may be used on.
3. Filtration	Known volume of gas or fluid is drawn through a membrane filter, preferably a cellulose acetate.	If the filter is cellulose acetate a high quality permanent mount can be made. Other types of filters generally require more preparation before analysis.
4. Other	Impaction, electrostatic precipitation, thermalphoresis, etc.	Techniques useful for collecting specific size ranges of particles.

TABLE #1: SOME METHODS OF COLLECTING PARTICULATE

3.3.1 1. a. The outgassing product from a single source does not significantly vary from particle to particle; and

b. the individual particles are small, their size being determined by nucleation, flocculation, and coagulation type effects.

They also have a characteristic distribution with respect to the source consisting of:

a. A concentration gradient with distance; and

b. a shaped distribution controlled by media flow, diffusion effects, electrical forces, surface properties, and other similar effects.

2. Corrosion Assemblages -

Corrosion assemblages can be complex, stable, metastable, and unstable compounds of the original structural materials and some other reactant and/or catalyst. The particulate tends to consist of aggregated crystallites if the corroding structural material is a metal. The crystallites often exhibit a variety of sizes, but a single morphological habit. The particles will often be stratified or banded and porous. Polyorganic materials may become crystalline, similar to the metals, or simply alter into a particulate of mulitple organic phases. The filler material is often useful in the corrosion of a polyorganic material as a tracer. Most inorganic fillers are not effected by the chemical alteration of the organic and can be identified by their optical crystallographic properties.

3. Other Auto-generated Assemblages -

FEP teflon particles and aerosols of associated materials from dielectric breakdown in some orbital environments are an example of this type of assemblage. These assemblages are generally produced by some force other than friction acting on the structural material. Vibration, radiation, electric charge, and heat or cold are common causes of this type of particulate assemblage.

3.3.2 Function-generated Assemblages

Function-generated, or wear assemblages, are usually very easy to identify or characterize. In most systems they consist of metal, gasket or seal material, and polymerized lubricant films. As a result of recent advances in diagnostic wear analysis there is a wealth of literature on typical, metal wear assemblages.[3,4] Wear polymers are not so well documented but most are easily identified by their characteristic structures.[7,8]

The motion of one surface against another produces a large number of submicrometer particles. Larger particles are also produced which can be used to diagnose more significant wear mechanisms. Break-in wear produces large numbers of elongated tablet shaped particles. Some cutting wear is usually generated as production abrasive-finishing particles work their way out of the metal during operational stress. The number of large wear particulate decreases after the break-in period and then begins to increase again as the system ages. The size, width/length ratio, length/thickness ratio, and diameter/thickness ratio are all related to the specific wear mechanisms active in the system. If the identification of the wear mechanism is not sufficient to identify the wearing part, individual particles can be selected for microprobe analysis. A comparison with the alloys in the system and the elemental analysis of specific particles will identify the alloy wearing and the wear mode. Similarly, the shape and quantity of friction polymers and gasket or sealant wear particulate can indicate the effectiveness of a given lubricant or the suitability of a gasket material or gasket configuration.

1. Wear Metal Assemblages

There are many types of characteristic assemblages. Most of these have a "typical" single morphology as a marker.

Bearing wear is marked by spherical metal particles 1-3 µm in diameter. These are produced in relatively small numbers compared to the exfoliated small flat tablets also produced by this type of wear. Spheres are only produced by bearing wear.[9]

---

[7] Reda, A. A., A Note on the Investigation of Friction Polymer Rolling Pin Formation, Wear, 32:115-116 (1975).

[8] Bose, A. C., Klaus, E. E., and Tewksbury, E. J., Evaluation of Wear Products Produced by Some Chemical Reactions in Boundary Lubrication, ASLE Transactions, 19; 4:287-292 (1975).

[9] Loy, B. and McCallum, R., Mode of Formation of Spherical Particles in Rolling Contact Fatigue, Wear, 24:219-228 (1973).

Cutting wear produces long, thin particles. These particles are often similar to those produced by a lathe. Their cross section is often an indication of the size of the piston or cylinder anomaly that is causing the problem.[10]

Gear wear is marked by long, thick particles characteristic of the shear-roll action between teeth in a system of gears.

Other typical metal wear assemblages are detailed in Bowen and Westcott (1976).[4]

2. Gasket and Seal Wear Assemblages

Gaskets and seals normally consist of a plastic or elastomer with a filler. The discovery of these materials in the system is indicative of their wear. Normally free filler, plastic or elastomer and filler, and just plastic or elastomer will be found as a result of gasket or seal wear. Tapered cylinders of these materials are the most typical wear morphology.

3. Friction Polymers

Ideally, metal never touches metal in a properly lubricated system. The metal is shielded by a thin film of lubricating material. This material is often a solid or very viscose liquid between the metal parts. During operation this material is worn away, resulting in the generation of particulate referred to as friction polymers. There are three main morphologies in this material. "Rolling pins" is a term used to describe tapered cylinders of the lubricating film.[7] The cylinders are produced by a shearing action that rolls small sections of the film into cylinders. Thin flat films are another common shaped friction polymer. These often contain spherulitic soap crystals. The last common structure is the result of a buildup of the friction film into relatively thick layers which then break free and float in the system.

As a final note on function generated assemblages, abrasive particles are common during the early operation of new machines. Production techniques involving the use of abrasives invariably result in some of the abrasive becoming embedded in the metal. With the expansion and contraction of operational stress these particles are released into the

---

[10] Dean, S. K. and Doyle, E. D., Significance of Grit Morphology in Fine Abrasion, Wear, 35:123-129 (1975).

system. If an analysis of the systems contaminates indicates abrasives as the only non-wear particulate present in any significant amount the abrasives should be considered part of the function generated particulate.

3.3.3 Facility-generated Assemblages

Facility-generated assemblages contain a very complex variety of particulate types. They include airborne particulate and aerosols from all kinds of sources, natural or industrial. They also include liquid suspensions of natural material, precipitates, or industrial material residues. These assemblages are so varied that no "typical" assemblage will be listed, instead Table #2 is offered as an example of common particulate types.

As with the assemblage types mentioned earlier, a facility-generated assemblage has properties of its own beyond the elemental composition of its members.

Size Distribution: As a rule of thumb, the smaller the size distribution, the further removed from the source. Air conditioning systems, even if inefficient, tend to deliver particulate under 10 µm. Materials brought in on clothing or through doors often exceeds that size.

Shape:

High Spherulite Content: Spherulites are small spheres of crystalline material. Their two most common sources are air agitated process solution with high soluble salt content, or flux condensation from welding or similar operation involving a temporary fluid state. A high concentration of these types of particulate can often aid in the discovery of the source.

Spheres in general indicate industrial or human activity and are useful in indicating possible sources.

Spatial Distribution: As with outgassing, a characteristic distribution of the particulate is often helpful in identifying the direction of the source. In this case the source can generally be considered to be at infinite distance with contamination density a function of surface curvative with respect to the source. In process solution contamination two types of distributions typically occur. The first is a film of very fine particulate which may be nucleated or precipitated by the surface of the part in the solution, be collected by the part as it passes through the surface of the solution, or be the product of air exposure to a liquid phase contaminate film. These mechanisms often result in the contaminate being found on only the upper or lower surface of a part. The second type is characterized by randomly distributed contaminates caused by discrete single liquid or solid suspensions in the process bath.

SOURCES	BIOLOGICAL PARTICULATES	INDICATION
Flowering Plants	Pollen, Plant Parts	Exposure to external environment, season
Molds, Fungus	Spores, Mycelium	Moist environment
Water Life	Diatoms, Algae	Unfiltered water, stagnant water
Animal and Insect	Insect Parts, Animal Hair	Insect or animal access open
SOURCES	FIBER PARTICULATES	INDICATION
Cloth	Synthetic & Natural, Colored, Colorless	Clothing, rags, rugs, etc. being used
Filters	Synthetic, Natural, Glass, Mineral	Startup or breakdown of filter
Insulation	Glass, Mineral	Exposed insulation
Reinforcing	Glass, Mineral, Graphite	Material failure
SOURCES	INDUSTRIAL RESIDUE PARTICULATES	INDICATION
Metal Forming	Tooling Particles, Weld Fume, Grinding Particles, Slags, Scale, Abrasives, Fluxes, etc.	Better cleaning required
Process Chemicals	Salt Spherulites, Reaction Residues, etc.	Better rinsing required
Construction	Cement Dust, Spray Paint, Plastics, Resins, etc.	Improved isolation required
Transportation	Wear Rubber, Asphalt, Flyash, etc.	More protection during transportation required

TABLE #2: TYPICAL FACILITY GENERATED PARTICULATE

3.3.4 Activity-generated Assemblages

Every activity in the production of a system, from forming to assembly, produces particulate. Metal working activities, tooling, grinding, cutting, welding, etc., produce particulate similar to operational metal wear. It can generally be distinguished by its larger size and tendency to be more highly oxidized at the surface. Process solutions and heat treating operations may leave residues behind. Inspection of a part may result in contamination with human hair, clothing fibers, and dried, exfoliated skin.

These assemblages are often cataloged for a given program since they do not change once a production sequence has been determined. A given welding operation produces the same type of contamination regardless of the part it's applied to. Once such an operation is cataloged it serves as a reference for most future applications.

3.4 Identification of the Source:

Particulate contamination from a single source is the result of a complex set of variables which determine the types of particulate possible. As Figure #1 suggested, the identification of a source is a decision made on the basis of reasonable probability. The more unique the properties of a source's particulate assemblage the more certainly that source can be quickly and easily identified. The fact that a completed system invariably contains more than one assemblage from multiple sources complicates the task of identifying the major source of contamination. Figure #2 demonstrates the relationship between one type of particulate, its assemblage, and its source. The best method of determining the source of contamination is to test the suspected source and compare the contamination assemblages with the assemblage from that source. Experience and a well stocked reference slide cabinet will increase the speed and the specificity of this type of analysis.

4.0 CONCLUSIONS

The identification of contamination sources using assemblage analysis has very definite economic advantages. No other analytical approach is capable of evaluating typically small, heterogeneous samples as completely or as quickly. Assemblage analysis is not a single instrument approach. Although an analytical microscope is essential many other instruments can be used to aid in the identification of specific substances. This technique offers an approach which synergistically combines different analytical capabilities to solve problems.

PARTICULATE	ASSEMBLAGE	SOURCE
Emery	Breakin wear metal Silicon carbide Emery dominant mineral species	Breakin Wear
	Silicon carbide Emery dominant mineral species Resin binder material may be present Metal and metal oxide spheres Large cutting type metal particles Fibers, Iron oxide	Production Activity Generated
	Silicon carbide Emery Quartz Feldspars Industrial residues Fibers Biologicals, Soot, Iron oxide, etc.	Exposure to General Industrial Environment
	Quartz Feldspars Pyroxenes Emery etc.	Natural Mineral Assemblage

FIGURE 2: THE RELATIONSHIP BETWEEN A CONTAMINANT, ITS SOURCE AND ITS ASSEMBLAGE

The economic benefits that can be derived from this approach begin in the early design phase of a program and follow the program through to routine production. In the early prototype, or materials testing portion of a program, assemblage analysis techniques can be used to detect contamination autogenerating mechanisms. Early detection of these mechanisms can cut weeks off a testing program that is doomed to failure and identify the problem before it damages effective parts of a prototype. Wear problems are also identified at a stage of development long before a failure occurs in the part. Both wear mechanisms and wearing surface are identified thus supplying specific direction to design modifications.

In the event of a system failure assemblage analysis can often identify the root cause. Material selection problems give rise to autogenerating mechanisms, design problems result in excessive wear, production quality control problems produce facility-generated contaminates, and production plan problems produce activity-generated contaminates.

These same techniques can be used to help solve problems that arise during a products working life. Different operational environments, a change in subcontractor, or a modification of the production sequence can give rise to unexpected, though often easily solved problems.

The economic benefits that can be derived as a result of this analytical approach are significant. This technique differs from most current approachs in that conclusions are based on the total sample rather than one compound or a collection of elemental data. This technique has produced very significant cost and product reliability benefits for us. Its future application will undoubtedly increase those benefits.

5.0 REFERENCES

1. Marmo, F. F. and J. Pressman, Definition Research Study, N73-30843, Final Report, Contract #NASW-2395, G.C.A. Corp. (1973).

2. Fogdall, L. B., S. S. Cannaday, M. C. Wilkinson, E. R. Crutcher and P.S.P. Wei, "Combined Environmental Effects on Polymers", Eighth Space Simulation Symposium Proceedings, (1976).

3. Scott, D., "Ferrography - An Advanced Design Aid for the 80's", Wear, 34:251-260, (1975).

4. Bowen, E. R. and V. C. Westcott, Wear Particle Atlas, N00156-74-C-1682, Final Report, Foxboro/Trans-Sonics, Inc. (1976).

5. McCrone, W. C. and J. G. Delly, The Particle Atlas, Ed. II, Ann Arbor Science, Ann Arbor, Michigan (1973).

6. Crutcher, E. R., "The Role of Light Microscopy in Aerospace Analytical Laboratories", Ninth Space Simulation Symposium Proceedings (1977).

7. Reda, A. A., "A Note on the Investigation of Friction Polymer Rolling Pin Formation, Wear, 32:115-116 (1975).

8. Bose, A. C., E. E. Klaus and E. J. Tewksbury, "Evaluation of Wear Products Produced by Some Chemical Reactions in Boundary Lubrication", ASLE Transactions 19; 4:287-292 (1975).

9. Loy, B. and R. McCallum, "Mode of Formation of Spherical Particles in Rolling Contact Fatigue, Wear, 24:219-228 (1973).

10. Dean, S. K. and E. D. Doyle, "Significance of Grit Morphology in Fine Abrasion", Wear, 35:123-129 (1975).

QUESTION AND ANSWER SESSION FOR

CONFERENCE SESSIONS III AND IV

Regrettably, microphone problems made the recordings of this question and answer session unintelligible.

SESSION V

CONTAMINATION PREVENTION AND CONTROL

SPACE GRADE CHEMICALLY FOAMED SILICONE ELASTOMERS

BY

Dr. Arnold A. Hiltz

General Electric Company

Re-entry and Environmental Systems Division

Room 2023, Bldg. 9
751 Fifth Avenue
King of Prussia, PA 19406

SUMMARY

Space grade chemically foamed elastomers are prepared by subjecting the foams prepared from conventional silicones to a thermal vacuum stripping exposure after the normal cure and postcure treatments. The resulting foams meet all the weight loss and volatile condensible materials criteria required for a space grade material. They are much more economical to prepare than would be the foams prepared from the space grade silicones as starting materials. They possess physical and thermal properties similar to or superior to those foams which have not been given the stripping treatment.

SPACE GRADE CHEMICALLY FOAMED SILICONE ELASTOMERS

1.0 INTRODUCTION

Chemically foamed silicone elastomers are available in a variety of densities and compositions and are widely used as insulation systems and/or insulators - ablators for various space and re-entry applications. The main advantages of the chemically foamed systems over the syntactically filled silicones are their lower modulus and higher elongations to failure. The resulting flexibility provides for ease of application of the foamed materials.

Normally, the chemically foamed materials are made in block form. The base Room Temperature Vulcanizing (RTV) silicone is blended with the foaming agent, the catalyst is then blended in and the mixture poured into a simple pan-type mold, where it is allowed to foam and cure at room temperature. The top skin is removed and the block is then subjected to the normal cure and post cure cycle. This is then slit on a conventional rubber slitting machine to the desired thickness. Normally, blocks measuring 30" x 30" are made in thicknesses ranging up to 6 or more inches. Sheets may then be skived at thicknesses ranging from a minimum of approximately 0.080" (depending on the density) to a maximum of 6" or more.

The flexibility of the sheets permits their application to many surfaces by a technique similar to that used in "wallpapering". In all cases, the surfaces must be cleaned thoroughly, degreased and primed with a silicone primer. After proper cure of the primer, the adhesive which is the unfoamed, base RTV silicone is applied to the surface. Normally, thicknesses of 10-15 mils of the adhesive are applied, and usually with a hard rubber roller, although it may be applied by spraying or by brushing. Then the sheets are applied and held in place with slight pressure, until the adhesive cures.

In addition to sheet stock applications, the material can be spray applied in thicknesses ranging from 3 - 5 mils up to 0.4". For complicated and/or inaccessible areas, molded-to-shape parts can be made and applied by adhesive bonding.

Although, as is shown later, the foamed silicones are excellent insulators, one of their main disadvantages arises from the fact that the silicones as normally prepared and cured, contain as much as 4 - 6% by wt. of volatile components, which will outgas in the low pressures encountered in space. In addition, the volatiles components may condense on colder or more polar surfaces, and cause undesirable fogging of windows, or undesirable contamination of other components.

2.0 VARIETIES OF FOAMED SILICONE ELASTOMERS

There are two distinct families of the foamed silicone elastomers. One was developed as an ablator/insulator material for lifting entry type applications. These are called the Elastomeric Shield Materials (ESM) and contain short length inorganic fibers to promote the formation of a hard char and to enhance char retention by the virgin material. Several types of ESM are currently in use. Some of these are fabricated in a honeycomb support for improved shear resistance capability. Table 1, lists the common ESM materials along with their densities and descriptions.

The members of the other family of foamed elastomers do not contain the inorganic fibers and are used essentially as insulations. These are designated PD 200 and are made in two different varieties, as shown in Table 2.

Table 1

TYPES OF ESM FOAMED SILICONE ELASTOMERS

Material	Density (p.c.f.)	Description
ESM 1004 X	16	Unsupported
ESM 1004 X (NS)	22	Nomex honeycomb support
ESM 1004 AP	34	Unsupported
ESM 1001 P(S)	42	Phenolic glass honeycomb support
ESM 1004 LP	50	Unsupported
ESM 1004 LP(S)	55	Phenolic glass honeycomb support

Table 2

TYPES OF PD200 FOAMED SILICONE ELASTOMERS

Material	Density (p. c. f.)
PD 200-16	16
PD 200-32	32

These may also be foamed in honeycomb supports if additional shear resistance is required. The absence of the inorganic fibers leads to lower moduli and higher elongations to failure. They are fabricated in the same manner as the ESM foams but the process is simplified since there is no requirement for milling the inorganic fibers into the base RTV silicone.

3.0 REDUCTION OF VOLATILE MATERIALS

There are two approaches for preparing silicone elastomeric foams which meet the requirements of a space grade material.

1. Use special, space-grade RTV silicones as starting materials. Both General Electric and Dow Chemical market space grade RTV silicones. However, such materials are very expensive ($395.00 / lb) when compared with the regular grades, and besides could become contaminated during processing.

2. Another approach is to prepare the foams from the normal starting materials, and after the normal cure and post cure treatments, to subject them to a thermal-vacuum stripping treatment. This latter procedure has been adopted for both the ESM and PD200 families of materials in the sheet stock form. Naturally, the lower the pressure, the higher the temperature, and the longer the time of treatment the cleaner will be the resulting foams. However, temperatures should be kept at below 400°F for extended exposures of 24 hours or more. In practice a temperature of 350°F for 48 hours at pressures of 10^{-6} torr or lower have been found to be effective.

4.0 VOLATILE DETERMINATIONS

Weight loss and volatile condensible measurements have been made on the materials that had been subjected to the normal cure as well as those that were vacuum stripped. Measurements have been made both for ESM and PD200 that had received both treatments. The measurements were made at 10^{-6} to 10^{-8} torr, and 250°F for twenty four hours. Samples were run by NASA-Goddard, Greenbelt, Maryland and by Ball Brothers Research Corporation (BBRC) Boulder, Colorado. The results of the determinations are summarized in Table 3.

Table 3

WEIGHT LOSS AND VOLATILE CONDENSIBLE MATERIAL DETERMINATIONS ON FOAMED SILICONE ELASTOMERS

Material	Treatment	Wt. Loss (%)	V. C. M. (%)	Determinations Made By
PD200-16	Normal cure & post cure	1.127	0.491	NASA-Goddard
PD200-16	Above & vacuum strip	0.033	0.025	NASA-Goddard
ESM1004X	Normal cure & post cure	4.26	1.12	NASA-Goddard
ESM1004X	Above & vacuum strip	0.17	0.0	NASA-Goddard
ESM1004AP	Normal cure & post cure	1.93	-----	BBRC
ESM1004AP	Above & vacuum strip	0.30	-----	BBRC
ESM1004LPS	Normal cure & post cure	1.41	-----	BBRC
ESM1004LPS	Above & vacuum strip	0.355	-----	BBRC

B. B. R. C. were not asked to determine the volatile condensible materials content. However, based on the experience with the NASA determinations it is safe to assume that the VCM content would be at least 0.1% for the non-stripped materials and would be less than 0.1% for the vacuum stripped materials.

It is evident that the vacuum stripping procedure provides material that meets the requirements for a space-grade material. Heated vacuum chambers have been used which permitted the simultaneous treatment of several blocks of material each 30" x 30" x 4" thick. Consequently, the large scale production of space grade material can be achieved.

The magnitude of the economies that can be realized by using the vacuum stripping procedure can be seen from a comparison of the raw material costs. The cost per pound for the space grade RTV silicone is $395.00 while the cost of the conventional material is not over $10.00 per pound. Since a large amount of foamed material can be treated in large, heated space simulators, the treatment costs per pound of material is of the order of $2 - $3 (for large batches of material). In addition, tests show very little difference in properties or behavior between the space grade foams prepared from conventional. Actually, as will be seen later the thermal conductivity and the ablation performance are both slightly improved as a result of the stripping procedure.

5.0 EFFECT OF VACUUM STRIPPING ON THERMAL & MECHANICAL PROPERTIES

5.1 Thermal Properties

Thermal conductivity, specific heat and TGA data have been obtained on various foams both in the virgin and in the vacuum stripped states.

1. Thermal Conductivity: Thermal conductivity measurements were made by the guarded hot plate both at atmospheric and at reduced pressures and at various temperatures. The results of typical measurements are illustrated in Figure 1 for ESM 1004AP. It is seen that in general, the thermal conductivity is highly dependent on the stripping treatment, being as much as 25% lower at 150°F for the stripped material than for the non-stripped material. Hence, there is an immense thermal insulation advantage in using the stripping process.

2. Specific Heat: The specific heats were measured by Differential Scanning Calorimetry. The data are plotted as specific heat for each material - in both conditions. It is seen from Figure 2 the data for a given material (ESM1J04LP) is the same whether it has been vacuum stripped or not.

3. Thermogravimetric Analyses (TGA) Characterization: Samples of both types of material were run in duplicate in 1 atm. nitrogen, 1 atm air, and at a pressure of 10^{-4} atm. in air. The results of the measurements for a typical material in both states are shown in Figure 3 & 4 as plots of residual weight fraction as a function of temperature.

FIGURE 1

THERMAL CONDUCTIVITY OF ESM 1004 AP

(1ATM. PRESSURE)

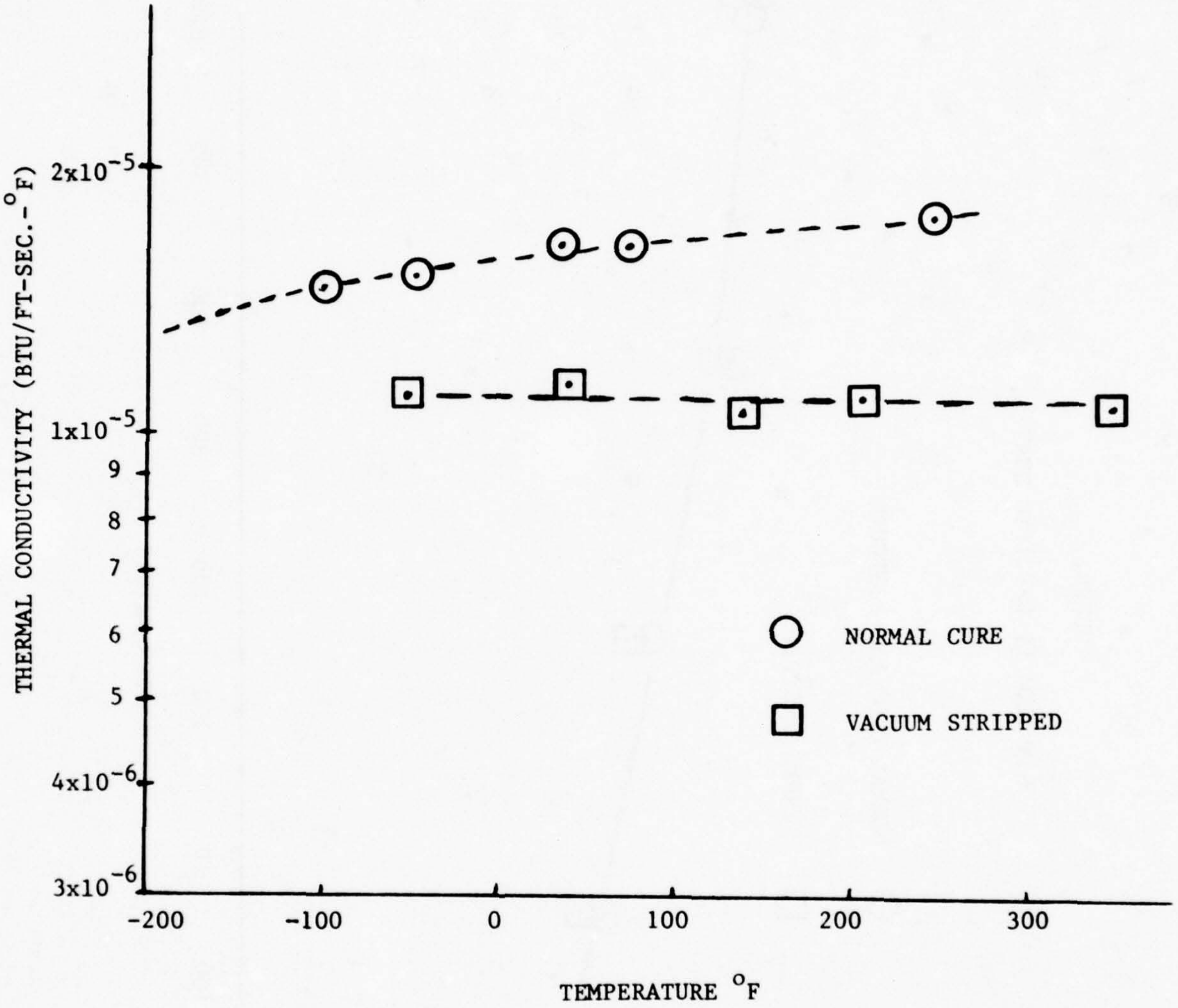

FIGURE 2

ESM 1004 LP SPECIFIC HEAT

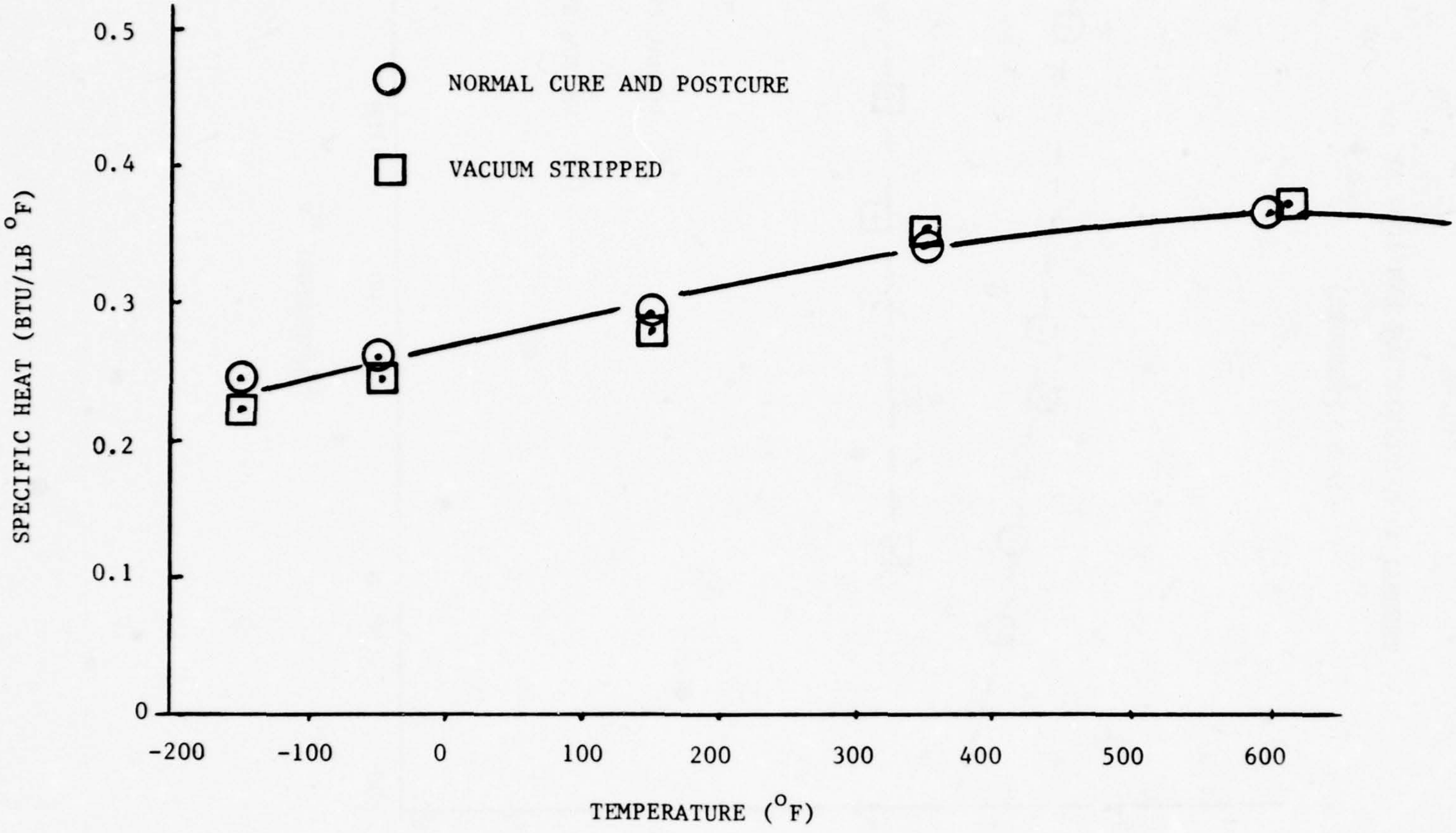

FIGURE 3

TGA OF ESM 1004 AP

NORMAL CURE AND POST CURE

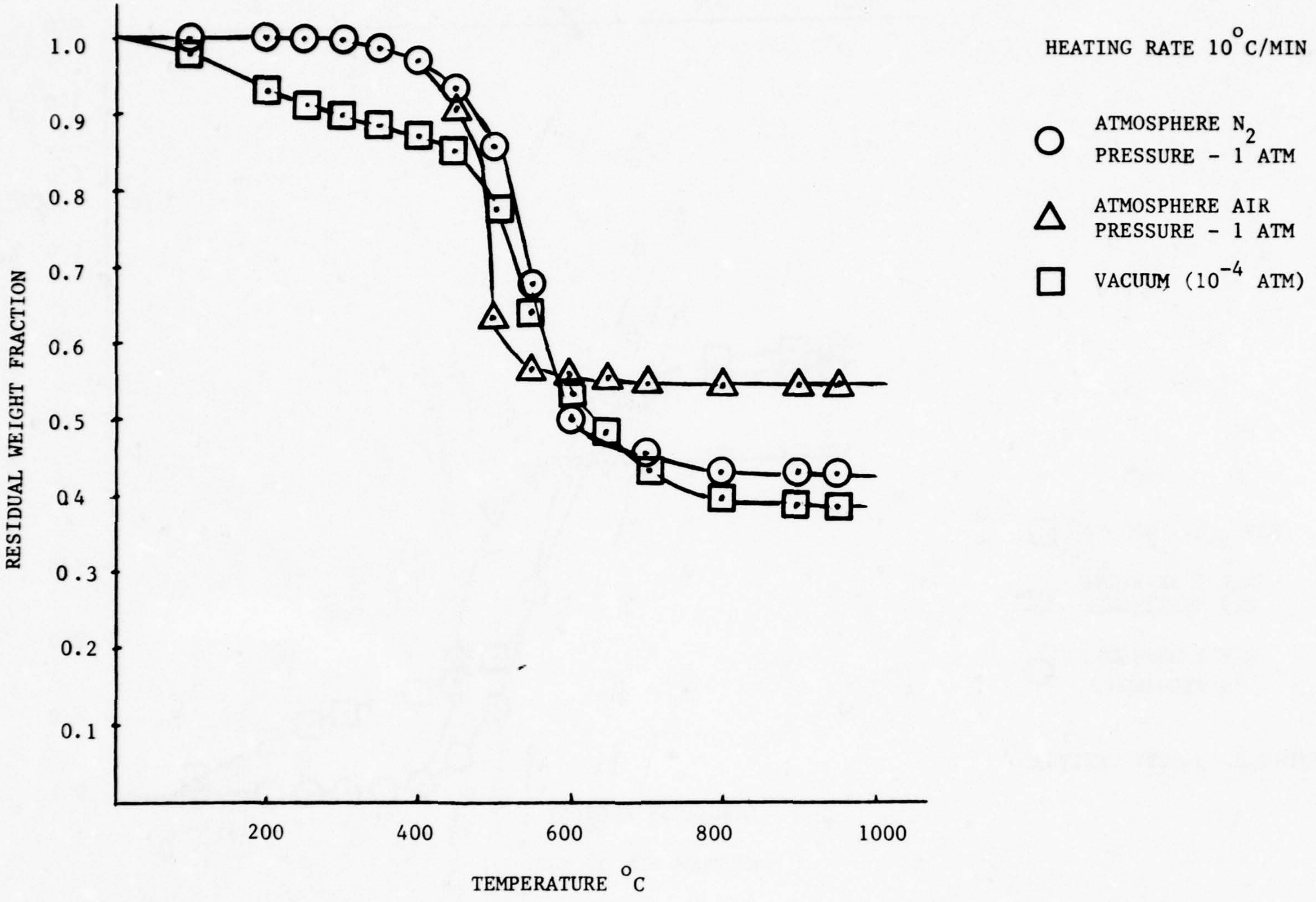

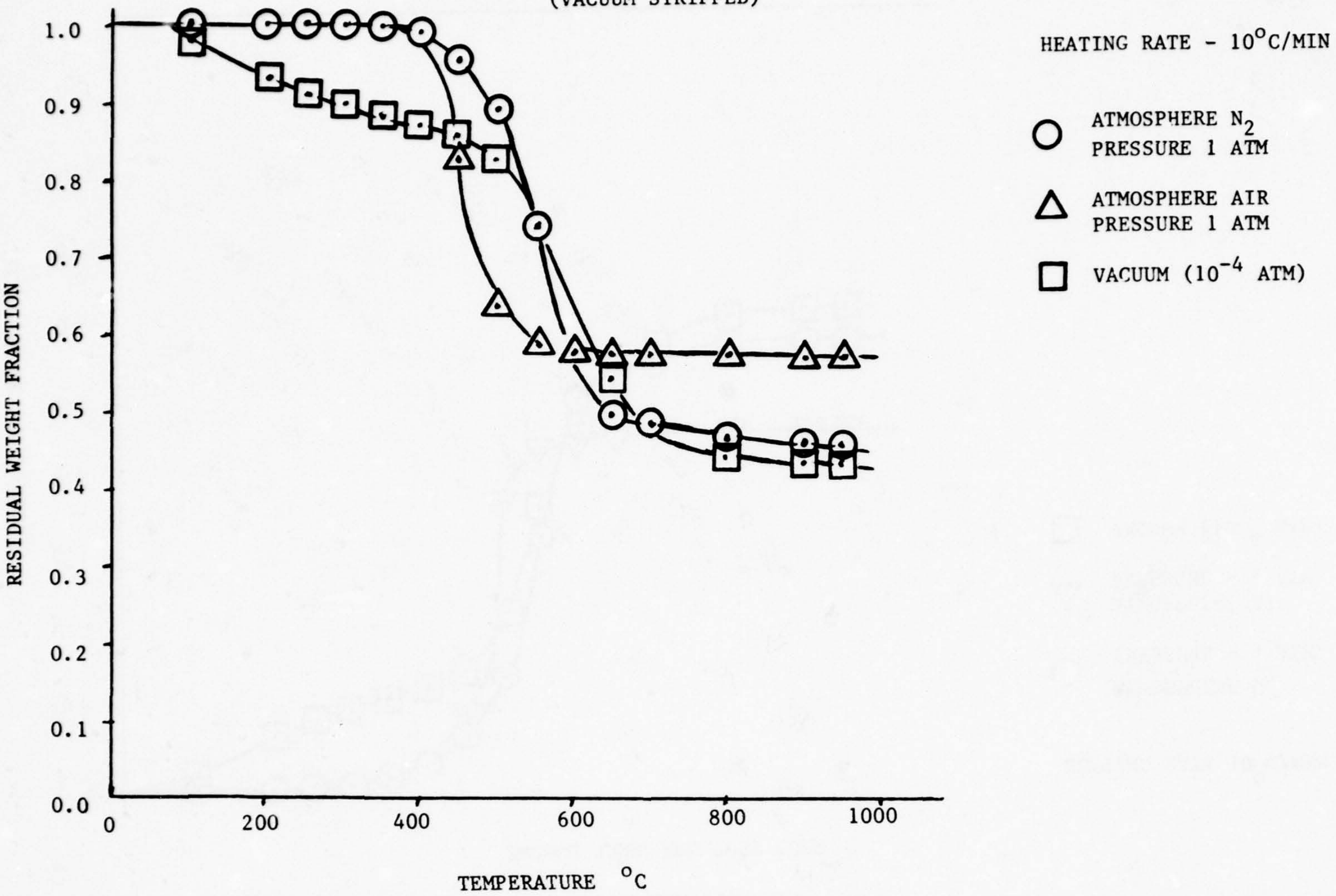
FIGURE 4

TGA OF ESM 1004 AP

(VACUUM STRIPPED)

In this analysis, the residual weight fraction at 900°C is used as a basis for comparison. Duplicate runs on the same material are all well within 2% with deviations of from 4-6% on specimens of the same type but from different lots. Greater initial weight losses were experienced in the order vacuum $>$ nitrogen $>$ air. The reason for the lower weight loss experienced in the degradation in air is the formation of non-volatile oxidation products.

The vacuum stripped specimens generally show slightly lower weight loss (ranging from 6 - 20%) than the virgin materials.

5.2 Physical Properties

In all cases, property measurements were made on the materials in two conditions, viz. virgin-as normally fabricated, and vacuum stripped.

Tensile, compression and thermal expansion data were obtained. Test specimen configurations and facilities use to obtain the data are summarized in Table 4 . All of the test techniques are considered as being standardized procedures and/or long standing use within GE/RESD.

1. Tensile Properties: The tensile property data are shown as functions of temperature in Figures 5, 6 and 7. The materials exhibited typical silicone behavior, i.e., a strong dependence of property on temperature including a two order of magnitude increase in modulus below the glass transition temperature.

2. Compressive Properties: Compressive secant modulus data are shown in Figure 8. The results show a slight increase in modulus with increasing temperature from 75°F to 600°F, which is typical silicone behavior. The vacuum stripping treatment appears to increase the stiffness of the silicone foams to a slight extent.

TABLE 4

ESM MECHANICAL PROPERTY CHARACTERIZATION TEST TECHNIQUES

TYPE OF TEST	PROPERTIES DETERMINED	TEST SPECIMEN GEOMETRY	TEST TECHNIQUE	TEST FACILITY
Tension	1. Ultimate Strength 2. Failure Strain 3. Initial Tangent Modulus (1) E 4. Poisson's Ratio (1)	"Dogbone" Tensile bar, ½ inch thick, 6 inches long, one inch wide reduced gage width.	Standard Tensile pull using pneumatic grips and two modified Instron strain gage extensometers to sense and record axial and transverse strains simultaneously	Instron Test Machine with environmental chamber: XYY recorder
Compression	Secant modulus at 5.0 percent strain	Rectangular parallelopiped (1 x 1 x 3 inches) loaded parallel to 3 inch direction.	Direction compressed between parallel platens in test machine; strain measured by crosshead displacement	Instron Test Machine with environmental chamber
Bond Shear	Mode of Failure (2) and shear stress at failure	Right circular cylinder, 3.0 in. O.D., 2.0 in. I.D., of ESM system/substrate bonded between two 3.0 in. O.D. Aluminum loading blocks.	Torsion of right circular cylinder about its axis	GE-RESD Torsion Test Machine with Environmental Chamber, XYY Recorder
Bond Flatwise Tension	Mode of Failure (2) and tensile stress at failure	One inch square ESM system/substrate bonded between aluminum loading blocks.	Tensile pull using Pin loading with clevice grips	Instron Test Machine with Environmental Chamber
Thermal Expansion	Thermal Strain vs. Temperature, $\Delta L/L_o$ vs. T	3/4 x 3/4 x 2.00 inches	Quartz Tube Dilatometry with continuous ΔL vs. T measurement using LVDT	GE-RESD low temperature dilatometer system

NOTES:

(1) E and μ to be determined by three non-destructive loadings of each specimen

(2) ESM anticipated to fail at lower stress than bond

FIGURE 5

TENSILE STRENGTH OF ESM 1004-AP

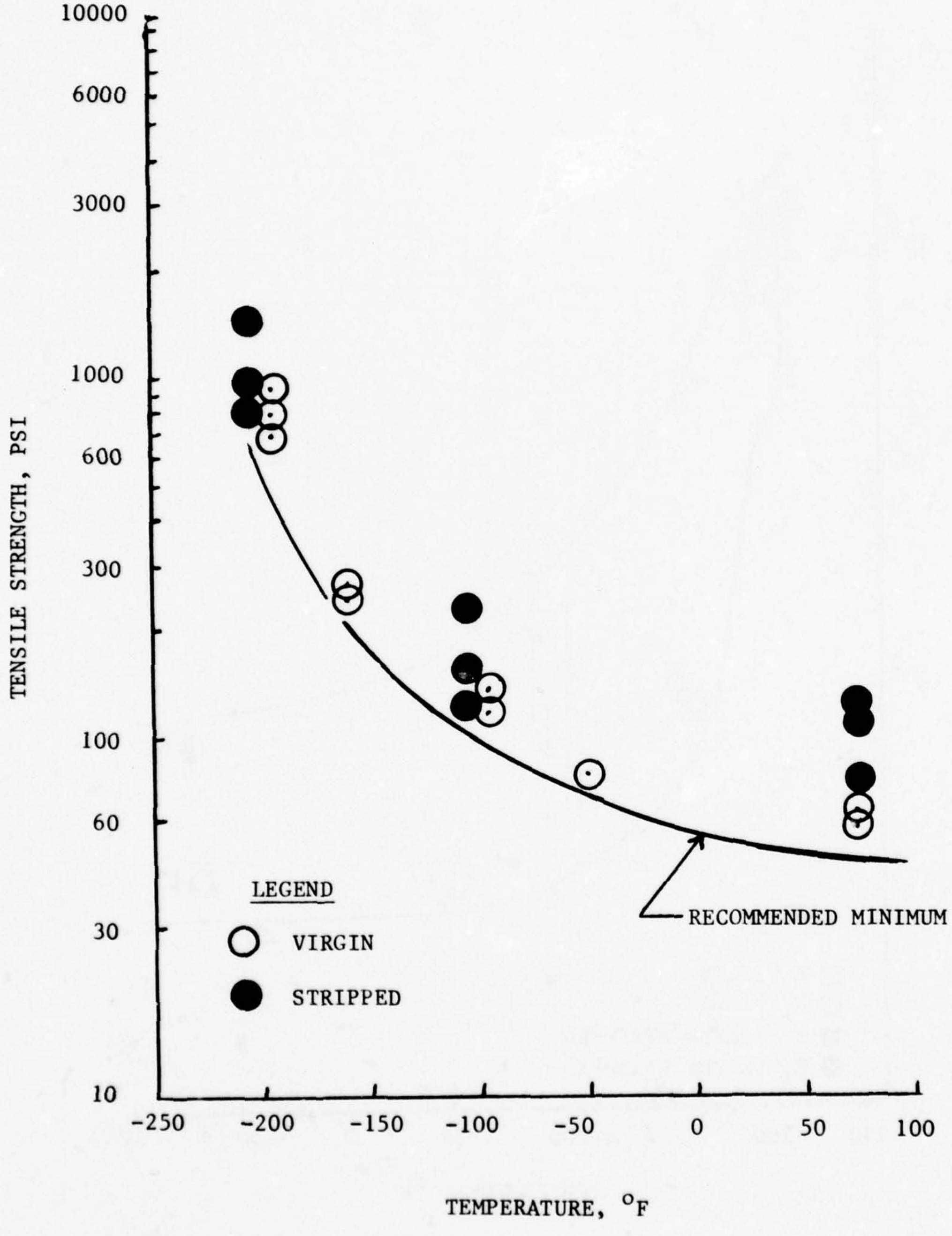

FIGURE 6

TENSILE MODULUS OF ESM 1004-AP

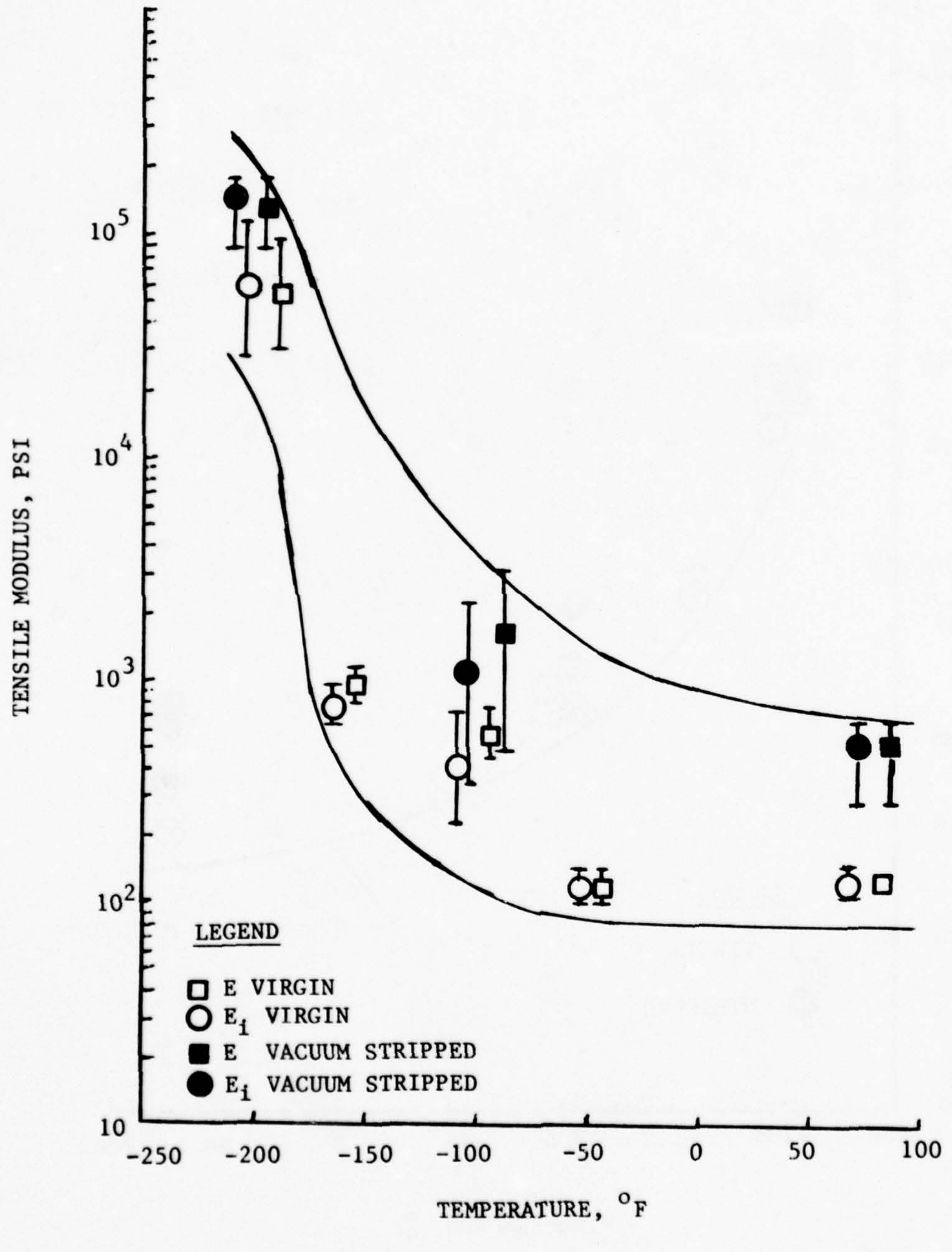

FIGURE 7

FAILURE STRAIN OF ESM 1004-AP

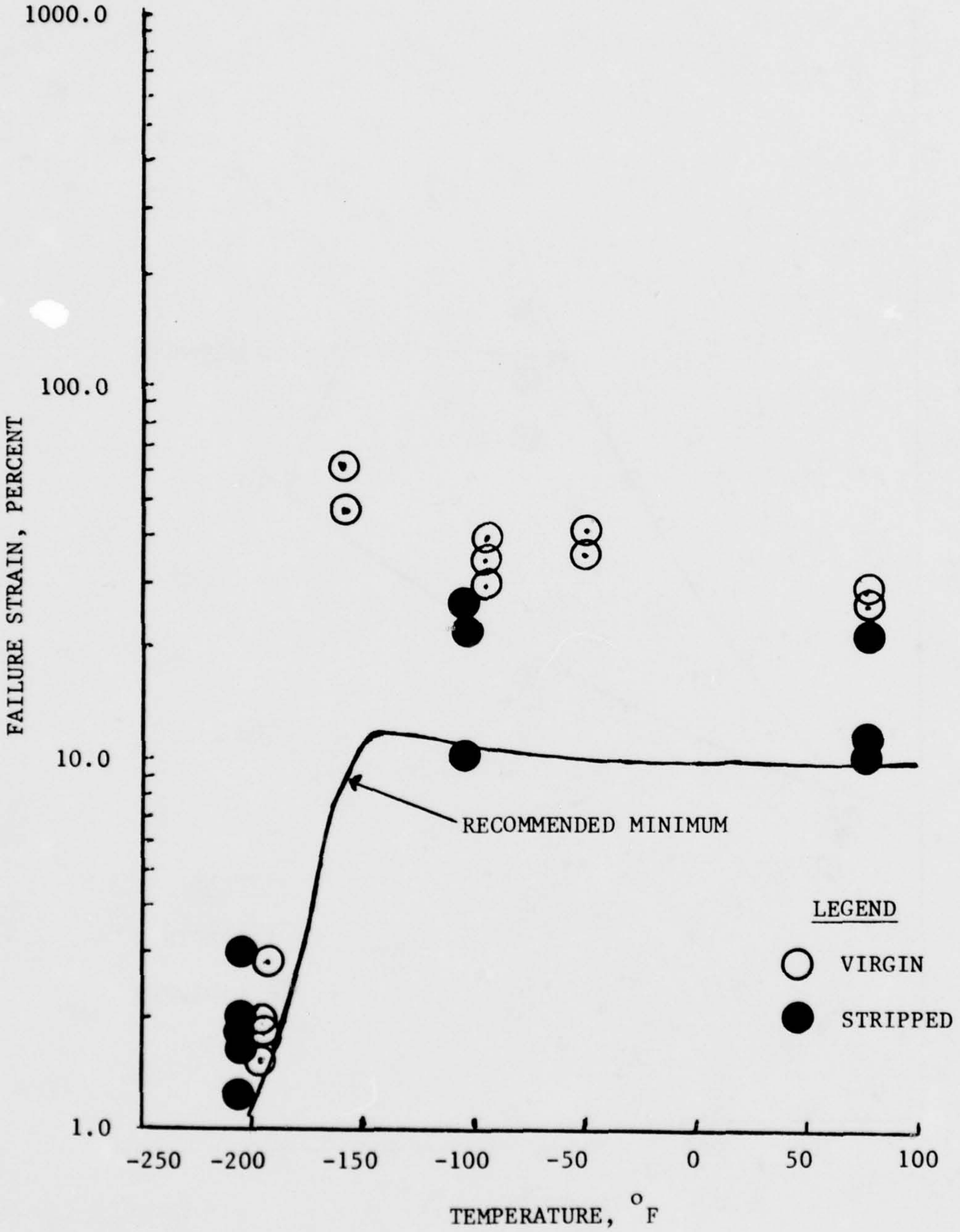

FIGURE 8

COMPRESSIVE SECANT MODULUS OF ESM 1004-AP

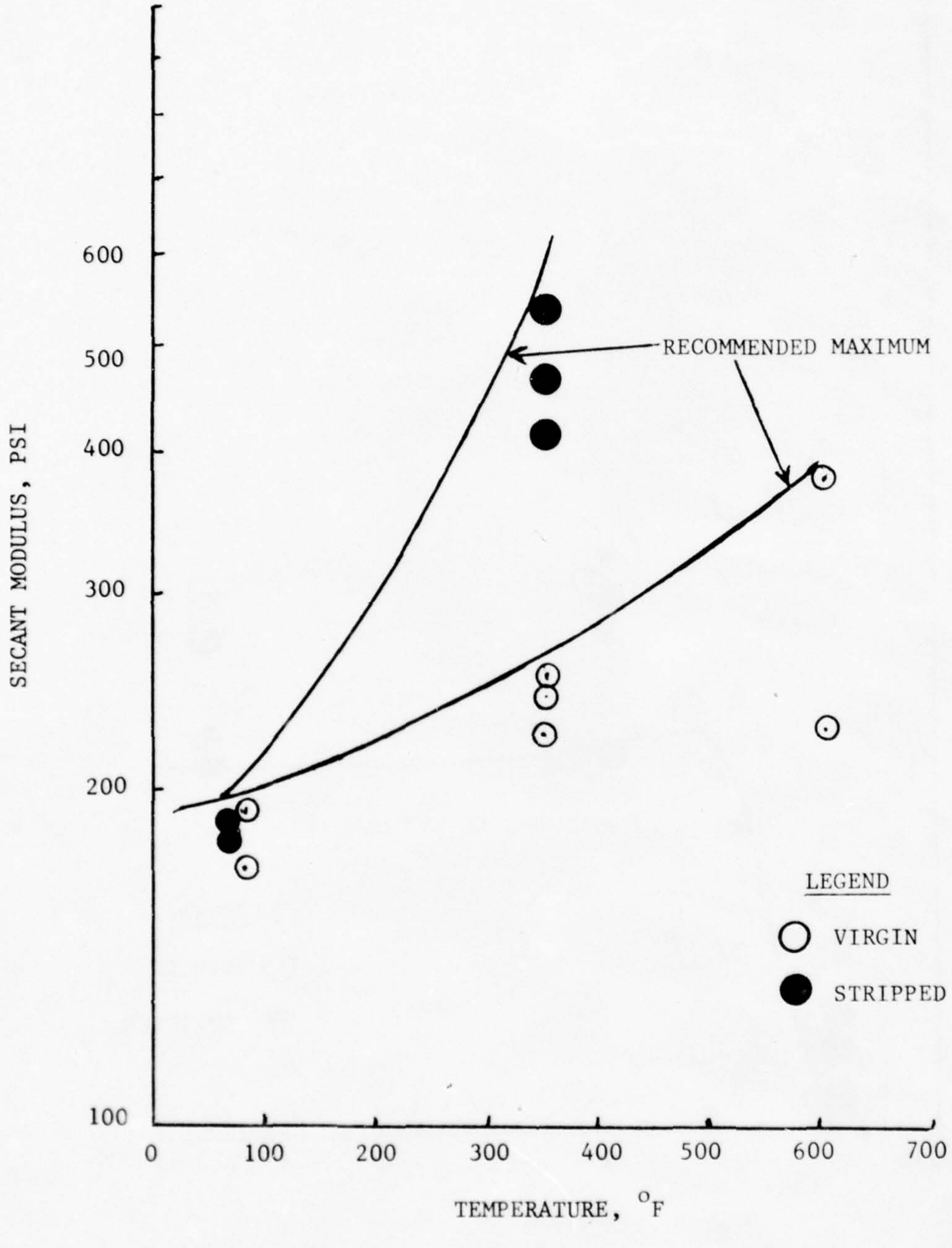

3. Thermal Expansion Properties: Results of thermal expansion measurements and recorded in Figures 9 and 10 as plots of $\Delta L/L$ as a function of temperature. Figure 11, which is included for reference, shows the thermal expansion behavior of the base RTV silicone. In general, the foamed silicones exhibit the typical silicone behavior: a high coefficient of expansion above the glass transition temperature and a significantly lower coefficient below. The transition occurs over a temperature range, which is normal, but is generally completed at around -175°F for materials based on this particular type of RTV silicone rubber.

The vacuum stripping treatment appears to have little or no effect on the thermal expansion behavior.

5.3 Bond Shear Tests

The bond shear test results are given in Table 5. Tests were also made on honeycomb supported material and it is seen that all these specimens (ESM1004LPS) exhibited cohesive failure in the RTV silicone bond line. This indicates that the full shear capability was developed and demonstrates the adequacy of the adhesive in a shear stress condition.

5.4 Bond Flatwise Tensile Tests

The adequacy of the adhesive bond was also evaluated by flatwise tensile testing. A sketch of the test specimen and a listing of its possible failure modes are given in Figure 12. Of these potential failure modes, only code "D", adhesive, RTV silicone/phenolic glass is indicative of a poor bond. Modes of failure "E" and "F" reflect problems associated with specimen preparation while modes of failure "A", "B", and "C" are all acceptable from the system standpoint.

FIGURE 9

THERMAL EXPANSION OF ESM 1004-AP

(VIRGIN MATERIAL)

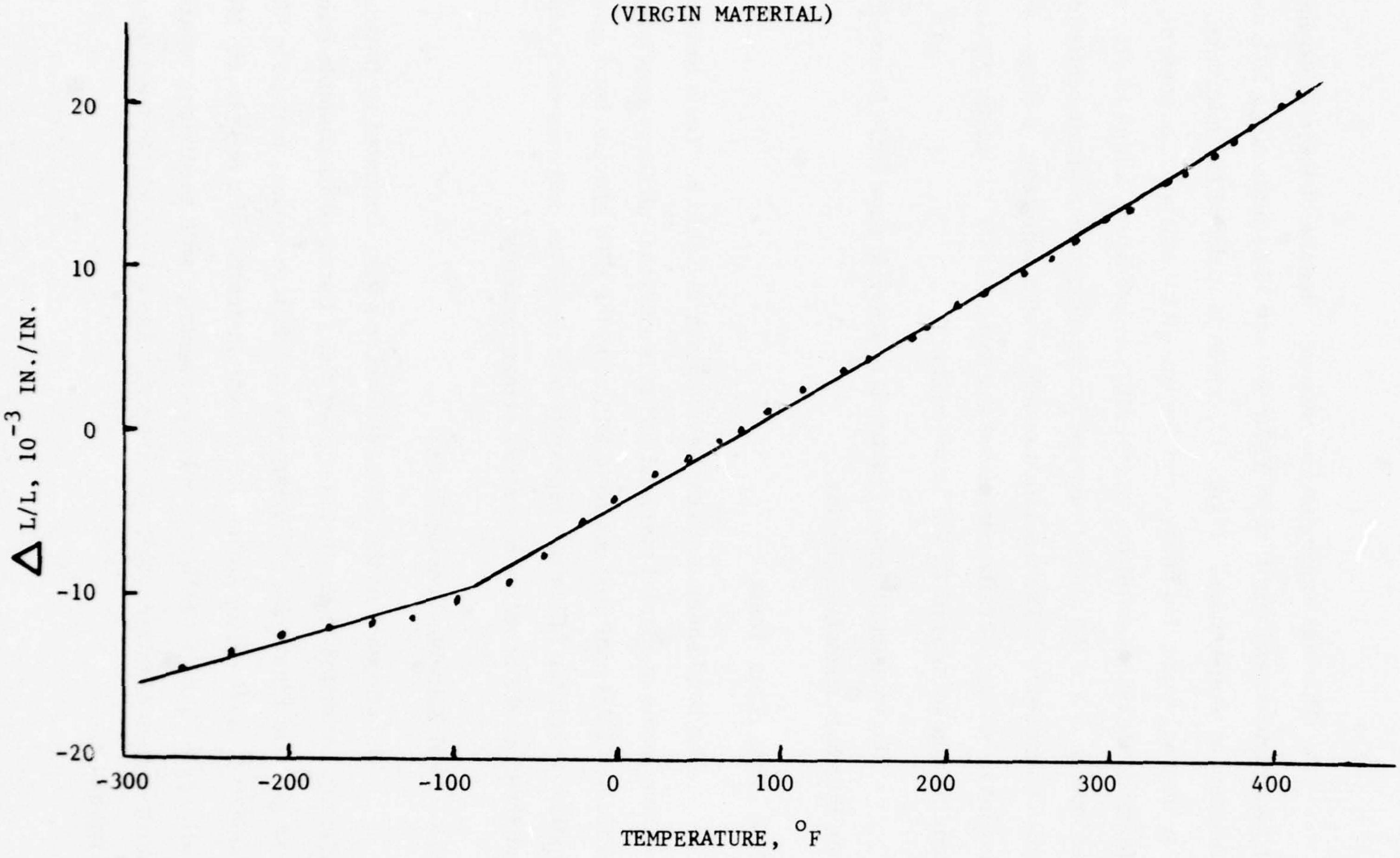

FIGURE 10

THERMAL EXPANSION OF ESM 1004-AP

(STRIPPED)

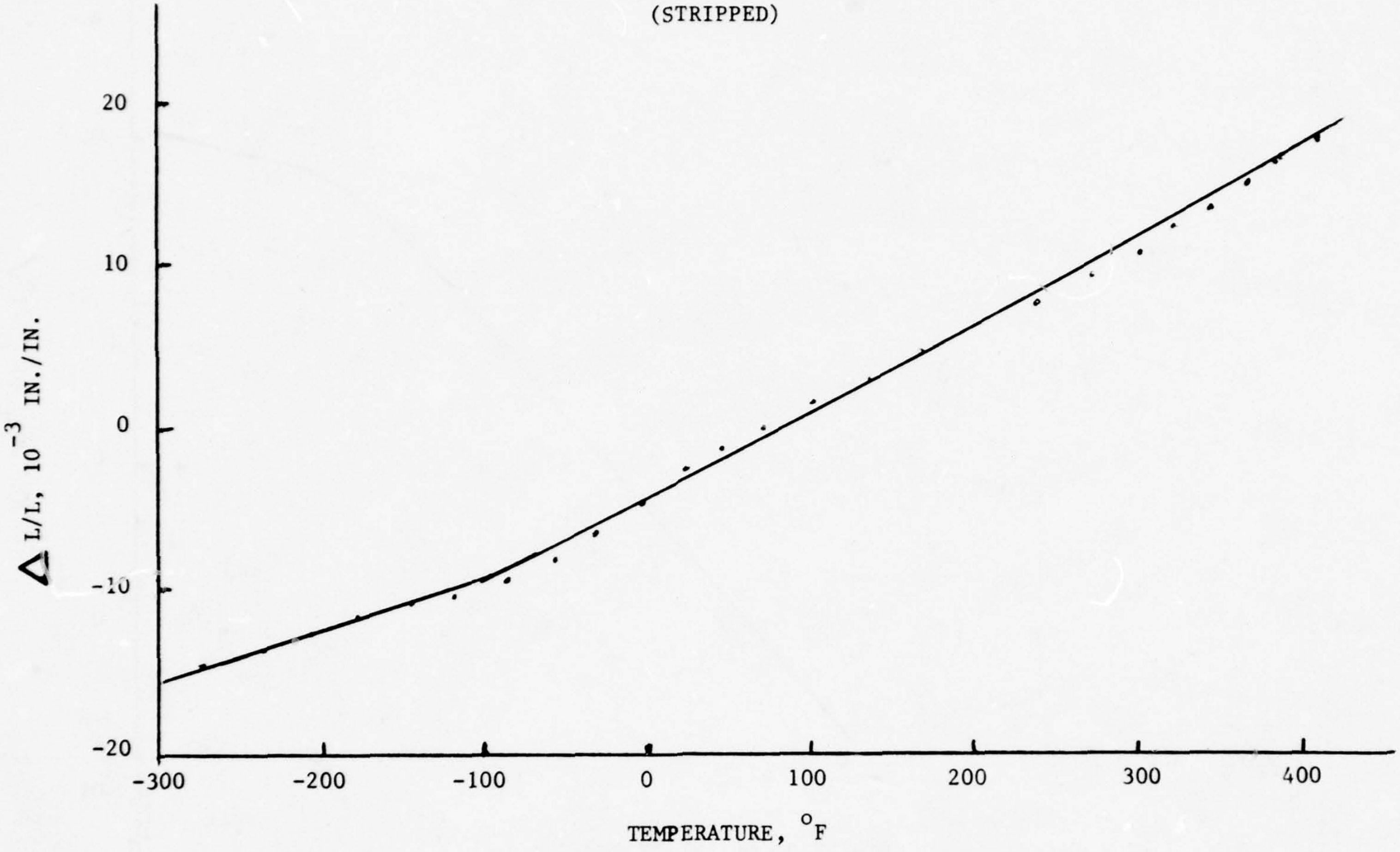

FIGURE 11

THERMAL EXPANSION OF RTV-560

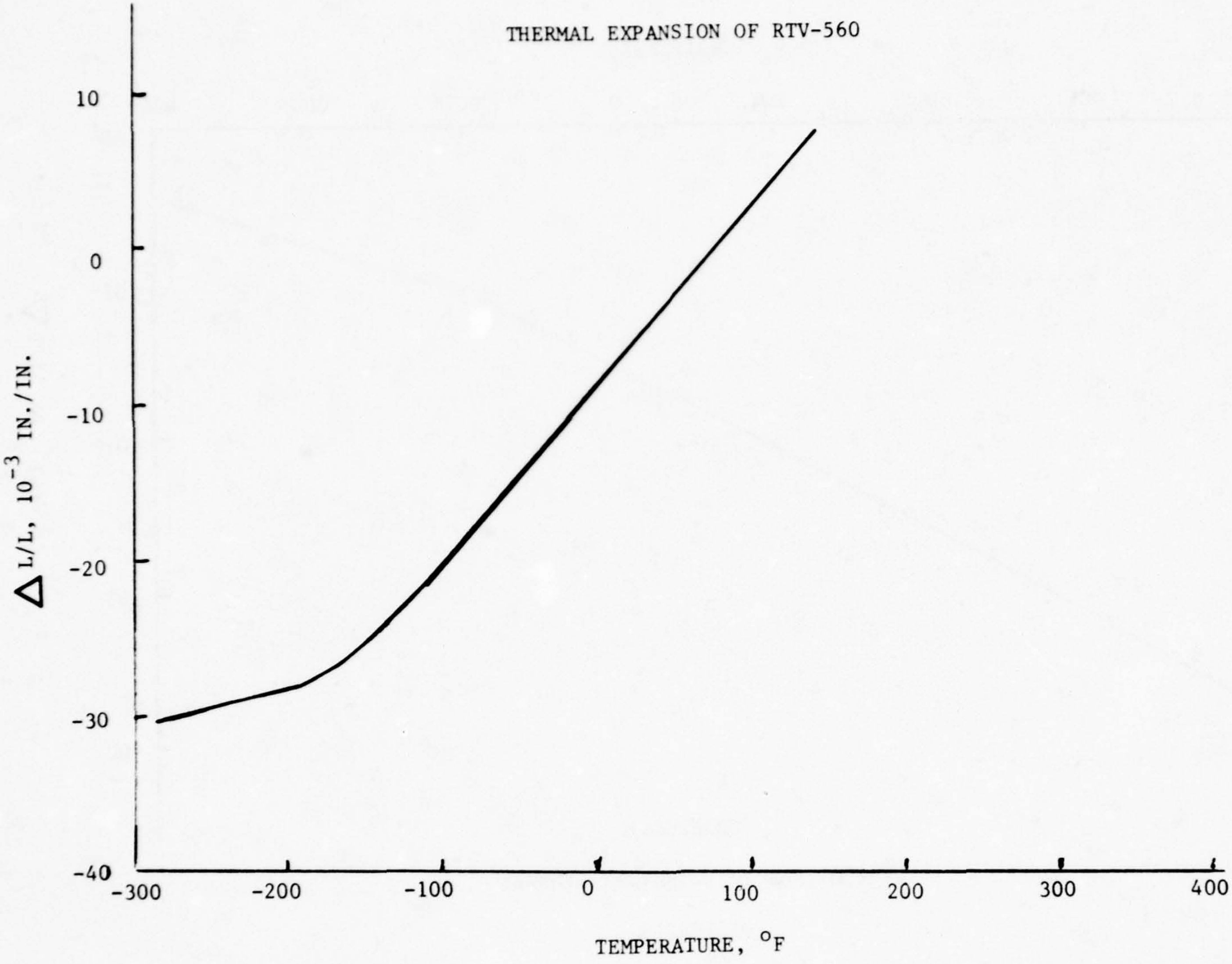

TABLE 5

BOND SHEAR (TORSION) TEST RESULTS

Temperature = $350^{\circ}F$

MATERIAL	SPECIMEN NUMBER	SHEAR STRENGTH (psi)	MODE OF FAILURE*			
			A	B	C	D
ESM 1004-LP (Virgin)	V-L-S-1-H	-				100
	-2	41.1			100	
	-3	16.4			100	
	-4	17.6			100	
	-5	25.4			100	
ESM 1004-LPS (Virgin)	V-PS-S-1-BB	105	100			
	-2	111	100			
	-3	118	100			
	-4	112	100			
	-5	111	100			
	$\overline{X}$	112				
ESM 1004-LPS (Pre-conditioned)	P-PS-S-1-EE	141	100			
	-2	54	50	50		
	-3	131	100			

* A: Cohesive in RTV-560 Bond
B: Adhesive to Aluminum
C: Adhesive to Phenolic Glass
D: Damaged in Processing

FIGURE 12

POSSIBLE FAILURE LOCATIONS FOR BOND FLATWISE TENSION TESTS

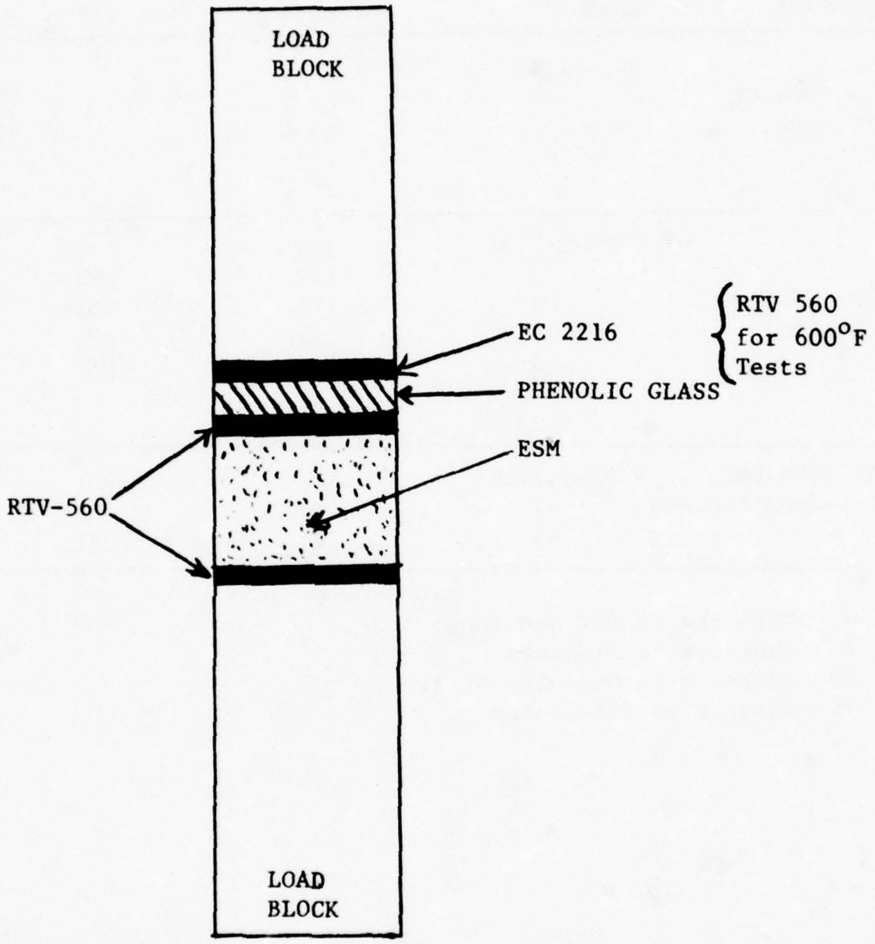

MODES OF FAILURE:

A. COHESIVE IN ESM
B. COHESIVE IN PHENOLIC GLASS
C. COHESIVE IN RTV-560
D. ADHESIVE RTV-560/PHENOLIC GLASS
E. ADHESIVE RTV-560/ALUMINUM

The bond flatwise tensile data are recorded in Tables 6 and 7. They are all considered to be acceptable, thus once again establishing the adequacy of the base RTV silicone bond.

A comparison of the strength values obtained for ESM 1004AP in these tests with the dogbone tensile data reveals generally good agreement, although the flatwise tensile strengths tend to be slightly lower. This is probably due to the presence of a small but significant degree of anisotropy which results from the foaming operation.

5.5 Thermostructural Capability

Panels of various foamed silicones measuring 12" x 12" x 1" thick were bonded with the base RTV silicone to panels of aluminum, titanium, stainless steel, and fiberglass. These were cycled over the temperature range of -300°F to +600°F at heating and cooling rates of 3°F/minute without failure.

5.6 Ground Ablation Tests

Numerous tests have been run under various heating conditions in the G.E. 5MW hyperthermal arc facility on the normal ESM formulations. In addition, several tests were recently run on the stripped material. Typical data are shown in Figure for the ESM 1004AP. In general, the stripping procedure significantly reduces the magnitude of recession due to ablation. No adverse effects of the stripping procedure were noted in any of the ablation tests.

6.0 ACKNOWLEDGEMENTS

The author gratefully acknowledges the assistance of all those who made the various measurements and who conducted the tests described in this paper. The process described in the paper was developed under General Electric funding.

TABLE 6

ESM 1004-AP BUTT TENSION TEST RESULTS (VIRGIN MATERIAL)

SPECIMEN NUMBER	TEST TEMPERATURE (°F)	FAILURE STRESS (psi)	MODE OF FAILURE (PERCENT)		
			A	B	C
V-A-F-11-Z	-200	995	100		
-12		844		100	
-13		903	100		
-14		1031	90	10	
-15		994	100		
$\bar{X}$		953			
V-A-F-6-Z	-100	122.4	100		
-7		83.8	100		
-8		110.1	100		
-9		104.0	100		
-10		106.5	100		
$\bar{X}$		105.4			
V-A-F-1-Z	75	61.0	100		
-2		62.8	100		
-3		69.6	100		
-4		69.0	100		
-5		66.7	100		
$\bar{X}$		65.8			
V-A-F-16-Z	350	52.3	100		
-17		45.5	100		
-18		44.1	100		
-19		53.5	100		
$\bar{X}$		48.8			
V-A-F-1-S	600	17.7	100		
-2		19.1	100		
-3		13.9	100		
-4		11.2	15		85
-5		19.1	100		
$\bar{X}$		16.2			

PM102

TABLE 7

ESM 1004 AP BUTT TENSION TEST RESULTS (PRECONDITIONED MATERIAL)

SPECIMEN NUMBER	TEST TEMPERATURE (^{o}F)	FAILURE STRESS (psi)
P-A-F-1-S	-200	805
-2		802
-3		490
$\overline{X}$		699
P-A-F-4-S	-100	93.0
-5		95.0
-6		92.0
$\overline{X}$		93.3
P-A-F-7-S	75	64.1
-8		63.1
-12		62.3
$\overline{X}$		63.2
P-A-F-9-S	350	40.3
-10		42.4
-11		43.8
$\overline{X}$		42.2
P-A-F-21-S	600	22.2
-22		24.4
-23		23.7
$\overline{X}$		23.4

NOTE: All specimens failed 100% cohesive in ESM

FIGURE 13

ESM 1004 AP VACUUM STRIPPED MATERIAL
RECESSION DATA

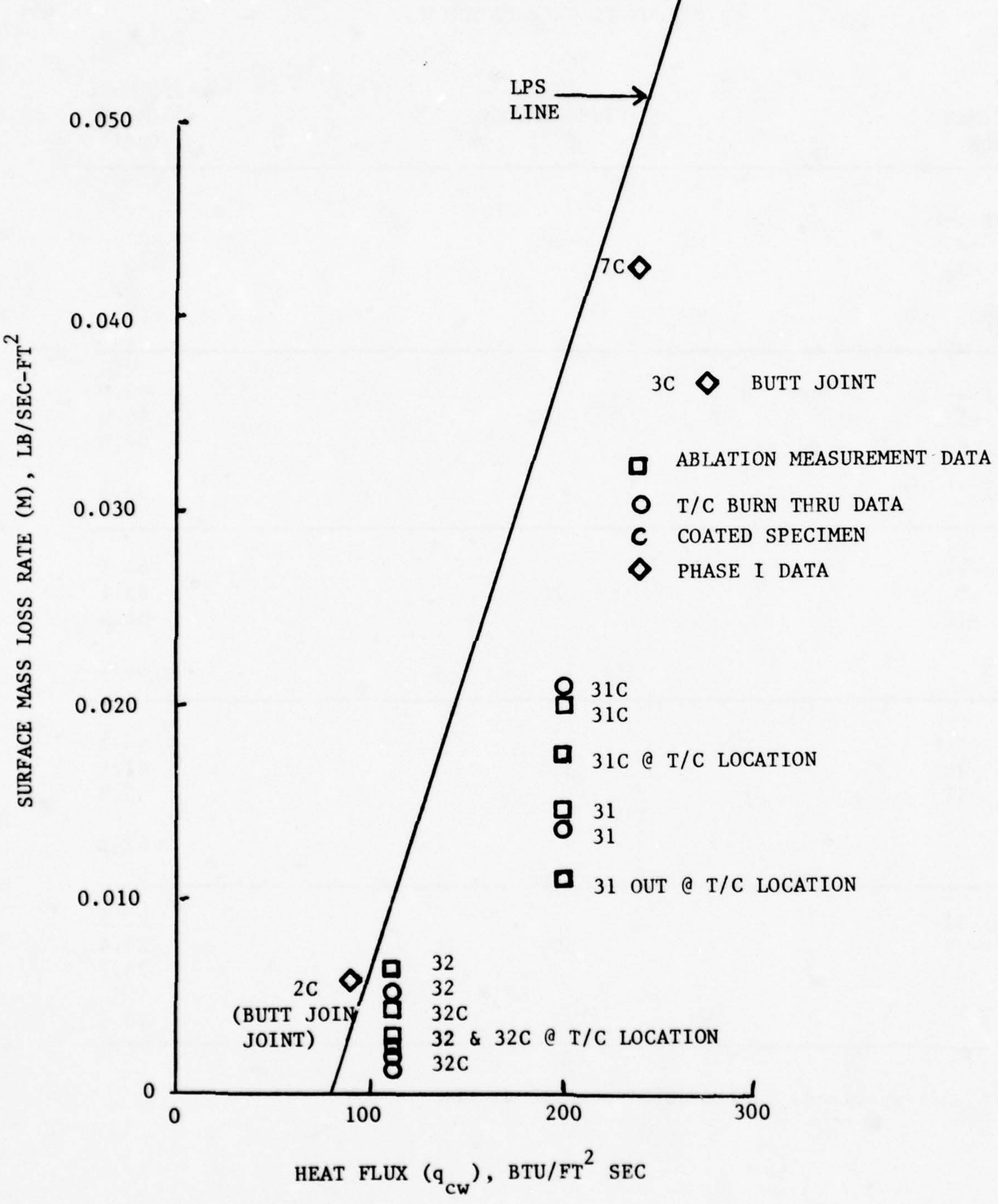

ALUMINUM OXIDE PARTICLES PRODUCED BY SOLID ROCKET MOTORS

R. Dawbarn
ARO, Inc.
A Sverdrup Corporation Company
Arnold Air Force Station, Tennessee

The candidate propellant for the Shuttle solid rocket motors contains approximately 16 percent aluminum powder. In this percentage range the aluminum can be considered as a significant portion of the fuel. However, it serves a dual purpose in that it also tends to stabilize the burning process. It has long been recognized that combustion instabilities in solid rocket motors can be alleviated by adding powdered metals to the fuel mix. There is therefore a considerable source of literature and data concerning metal oxide particles produced by solid propellant rocket motors. However, before embracing these data and applying them to environmental and contamination concerns posed by Shuttle operations one should be fully aware of the prime interest which prompted these previous studies.

1.0 DAMPING COMBUSTION INSTABILITIES

The combustion rate of solid propellants is pressure sensitive. Therefore, acoustic waves which may be generated within the combustion cavity can cause accelerated burning at the anti-nodes. If this accelerated burning feeds pressure pulses back into the acoustic field in a resonant mode then the resulting undamped system can lead to a violent failure of the rocket motor. It has been found that these instabilities can be damped by the inclusion of the metal oxide particles in the acoustic field in the combustion cavity. Figure 1 presents the curves showing attenuation $\alpha D/cm$ versus particle size for three frequencies as derived from the theory of Temkin and Dobbins and calculated by

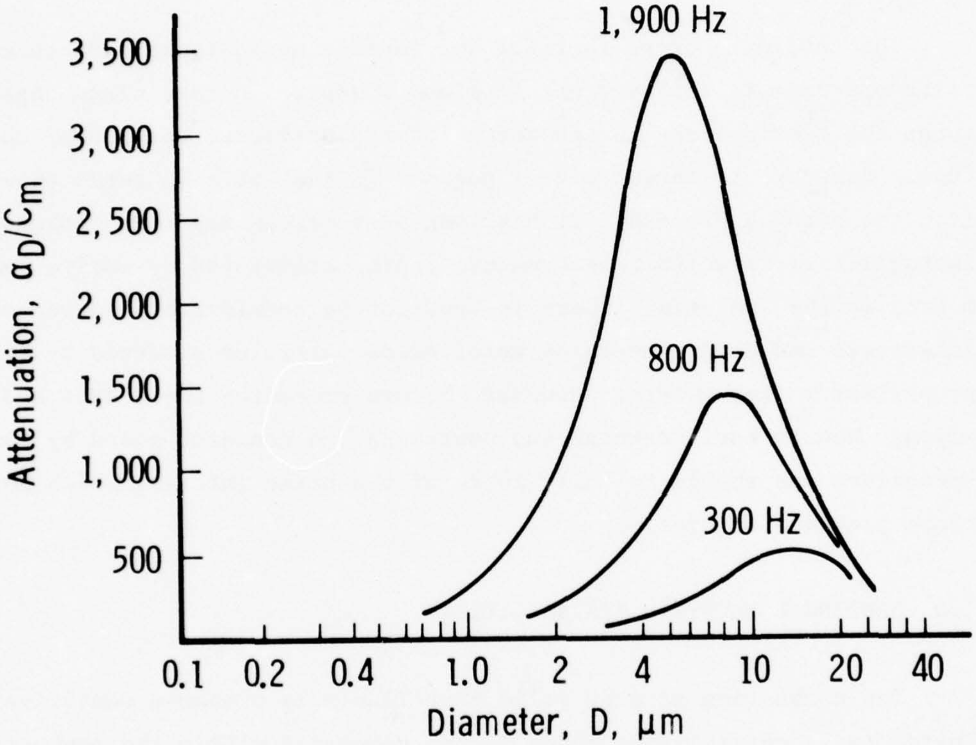

Fig. 1 Attenuation α_D/C_m versus Diameter (Ref. 1)
(Calculated for $C_m = 0.02$)

Dehority.[1] As can be seen, the range of particle size of interest is from 0.5 μm to 50 μm, with the bulk of the attenuation for low frequencies being produced by particles in the 2-20 μm range. However, while these larger particles are beneficial inside the combustion cavity, they are detrimental to rocket performance (specific impulse) as they are ejected along with the gases through the nozzle. With a requirement for a sufficient number of large dampers to maintain combustion stability, yet a need to limit the number of particles in the flowfield to an absolute minimum, the processes involved in the formation of the oxide particles are of great interest. Many experiments have been conducted and attempts made to collect samples of these oxide particles to determine their number and size distribution. Since the particle sizes of interest for damping and specific impulse loss have been from 2-50 μm, the majority of the collection techniques as well as the counting and sizing methods have been oriented toward this size range. Thus in many cases the submicron particles have been ignored.

1.1 Mean Diameters

In some instances it is convenient to refer to a particular size distribution of particles in terms of a mean particle diameter. The most commonly understood mean diameter is the linear mean, i.e.,

$$\bar{d}_{10} = \frac{\Sigma d dn}{\Sigma dn} \tag{1}$$

However, other mean diameters are also calculated and used depending on the particular field of application. In general the mean diameter can be of the form

---

[1] Dehority, G. L., "A Parametric Study of Particulate Damping Based on the Model of Temkin and Dobbins," NWC TP 5002, Sept. 1970.

$$\bar{d}_{qp}^{\,(q-p)} = \frac{\int_{d_o}^{d_{max}} d^q \frac{dn}{dx}\, dx}{\int_{d_o}^{d_{max}} d^p \frac{dn}{dx}\, dx} \tag{2}$$

where p can take integral values from 0 to 3 and q from 1 to 4. Each combination of p and q places a specific emphasis on a particular size range within the distribution. For example, the linear mean $\bar{d}_{10}$ heavily emphasizes a large number of small particles whereas a $\bar{d}_{43}$ mean, minimizes the contribution of the smaller particles. Since the larger particles are of prime concern in combustion stability and two-phase flow losses the $\bar{d}_{43}$ mean diameter is usually reported; i.e.,

$$\bar{d}_{43} = \frac{\Sigma d^4\ dn}{\Sigma d^3\ dn} \tag{3}$$

This method of summarizing the experimental data has led to a misconception of the total range of particle sizes produced by solid rocket motors and has fostered a false impression that there is a general consistency in the data collected from the various test programs. Figure 2 presents raw data in the form of bar graphs of particle size distributions obtained from Al_2O_3 samples taken from Titan IIIc firings. The samples were analyzed using the same methods but were collected using different techniques. As can be seen, the size distributions are radically different insofar as the number of small particles reported, whereas the calculated mean particle size from these two data sets are d_{43} = 11.4 μm and 12.6 μm. The mass weighted mean which would seem in reasonably good agreement is adequate for combustion studies. However, the data are inconsistent when one is concerned with the possible effects of contamination by smaller particles.

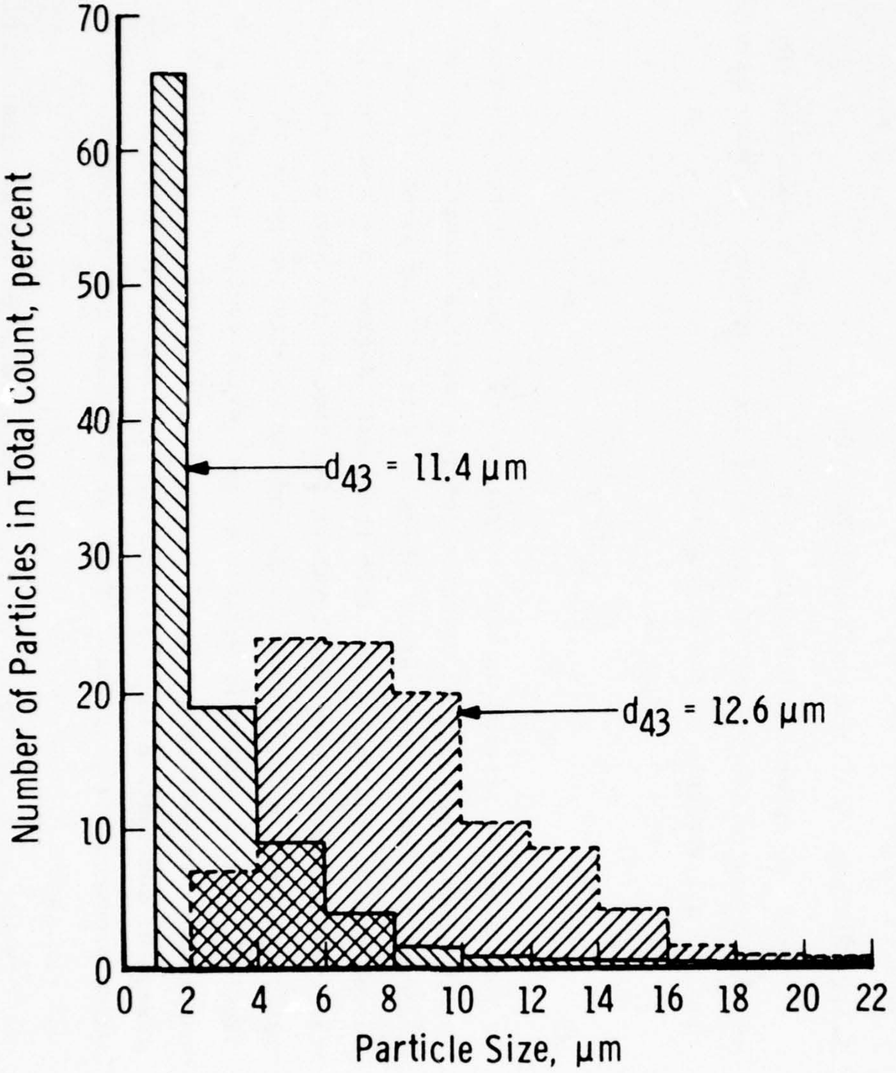

Fig. 2 Histogram from Titan IIIc Samples

1.3 Particle Size Distribution Functions

There are several ways of presenting particle size distributions. In addition to the histogram, there is a variety of distribution functions, and again one finds the format chosen, determined by the eventual use of the experimental data. In order to compare data from various sources, particle size information presented in this paper has been fitted to a distribution function.

1.3.1 Fitting Data to Distribution Function

There are several mathematical functions which have been used to provide a representation of particle size distributions. In many ways they are all variants of the expression

$$\frac{dN}{dD} = aD^p e^{-bD^n} \tag{4}$$

In some cases an attempt is made to relate one or more of the constants (a,p,b,n) to some physical parameter of the particle formation process. Nukiyama and Tanasawa[2] obtained extensive data of drop sizes in sprays formed by air atomization and from these data defined $p = 2$ and $n \approx 1$ for these sprays with b some undetermined function of the physical characteristics of the liquid, nozzle design and the relative velocity of the liquid and air. Similarly Worster et al.[3] using available data on Al_2O_3 particle sizes defined $p = 3$ and proposed a functional relationship between the constants a and b and the throat diameter of the rocket motor which produced the particles. Rosen et al.[4] used a semi-empirical

---

[2] Nukijama S. and Tanasawa, Y., "An Experiment on the Atomization of Liquid by Means of an Air Stream (1st report)," Trans. S.M.E. Japan, Vol. 4, No. 14 (Feb. 1938).

[3] Worster, B. W. and Kadamiya, R. H., "Rocket Exhaust Aluminum Oxide Particle Properties," ARI RR-30 (Aug. 1973).

[4] Rosin, P. and Rammler, E., "The Laws Governing the Fineness of Powdered Coal," Journal of the Inst. of Fuel, Vol. 7, 1933.

technique to derive a functional relationship between the constants to fit the equation to data obtained from grinding coal dust. In this case $p = n-4$ and $a = 6bn/\pi$, with b and n determined empirically.

It would appear that the possibility of defining the constants in terms of such fundamental physical properties as viscosity, surface tension, density, etc. of the particles and the force fields in which they are formed is very remote. However, the apparent universality of this function in its ability to fit the size distribution of particles formed by a variety of processes can be used to advantage in comparing data such as those obtained in collections of Al_2O_3 from rocket exhausts. It is particularly useful in that it predicts a finite number of small particles and defines a specific particle size where the distribution peaks. In many experimentally observed particle collections this peaking of the data is noted (Figs. 4 and 9). However, in some samples which are collected, due to the collection technique or the method of analysis, the data are truncated and the peak is missed. In the curves presented in this paper the data were used to obtain the best fitting distribution function and the resulting peaking of the distribution function is thus in some cases an "extrapolation" ofthe distribution below the observed particle size. All distributions have been normalized to this maximum peak or mode for ease of comparison.

The following method was used to choose the appropriate values of the constants a, b, n and p. The distribution function can be rewritten as

$$\log\left(\frac{1}{D^p}\frac{dN}{dD}\right) = \log a - b\, D^n \log e \tag{5}$$

Thus, the data were plotted as $\log\left(\frac{1}{D^p}\frac{dN}{dD}\right)$ against D^n for various values of n and p. The values of n and p were adjusted for the best straight line fit. For the majority of the data examined, values of n = .3 and p = 2 were satisfactory. The total range of values was n = (.3 → 1.0) and p = (1 → 3). From these data fits, values of a and b can be calculated from the slope and intercept. In order to obtain some uniformity in plotting the distribution functions they were normalized at their mode. The mode was determined by setting

$$\frac{d}{dD}\left(\frac{dN}{dD}\right) = 0 \tag{6}$$

and thus $D = n\sqrt{\frac{P}{bn}}$ for the maximum value of $\left(\frac{dN}{dD}\right)$.

2.0 COMPARISON OF Al_2O_3 PARTICLE SIZE DATA

Data obtained from many rocket motor firings, using a variety of collection techniques have been combined to support the hypothesis that the mean particle size produced by solid rocket motors is a function of the throat diameter of the rocket.

Samples of data used to obtain this correlation along with the empirical distribution function are presented in Figs. 3 and 4. As can be seen, the correlation does a fair job of accommodating the data, especially when one considers the orders of magnitude difference in the size rocket motors presented in these two examples. Confidence that such a correlation does indeed exist is greatly shaken, however, when one compares data presented in Fig. 5. These data all represent particle size distributions of particles from Titan III-C rocket motors, taken using different collection techniques. As can be quite readily seen, the data indicate a wide variety of size distribution functions. It is also of interest to note that the size distributions (curves 3 and 4) as determined by two separate laboratories analyzing the same sample are not in agreement. Thus it would appear that even with the same samples and using similar sizing techniques the results, while close, are not

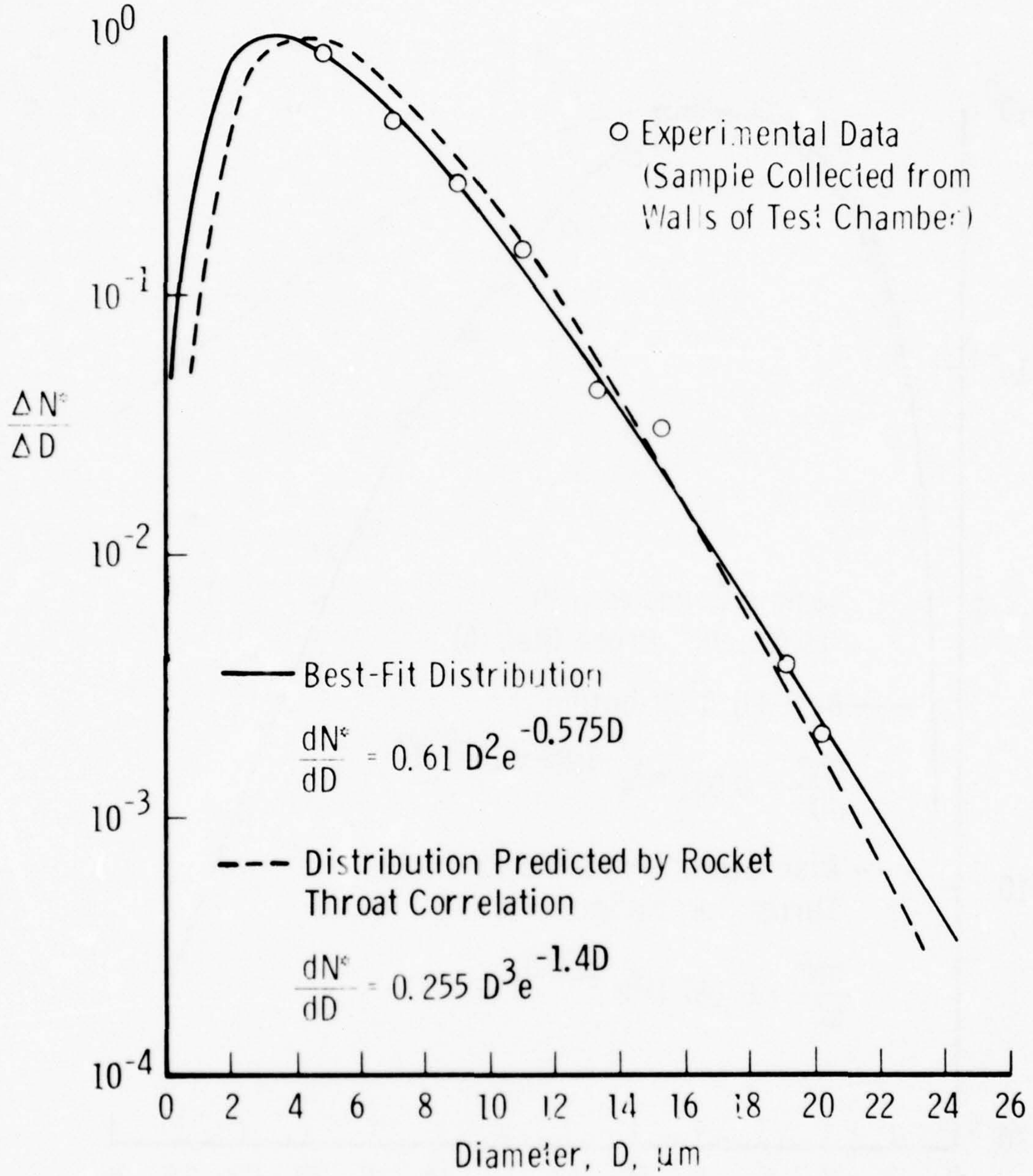

Fig. 3 Small Research Motor (0.85-in. Throat)

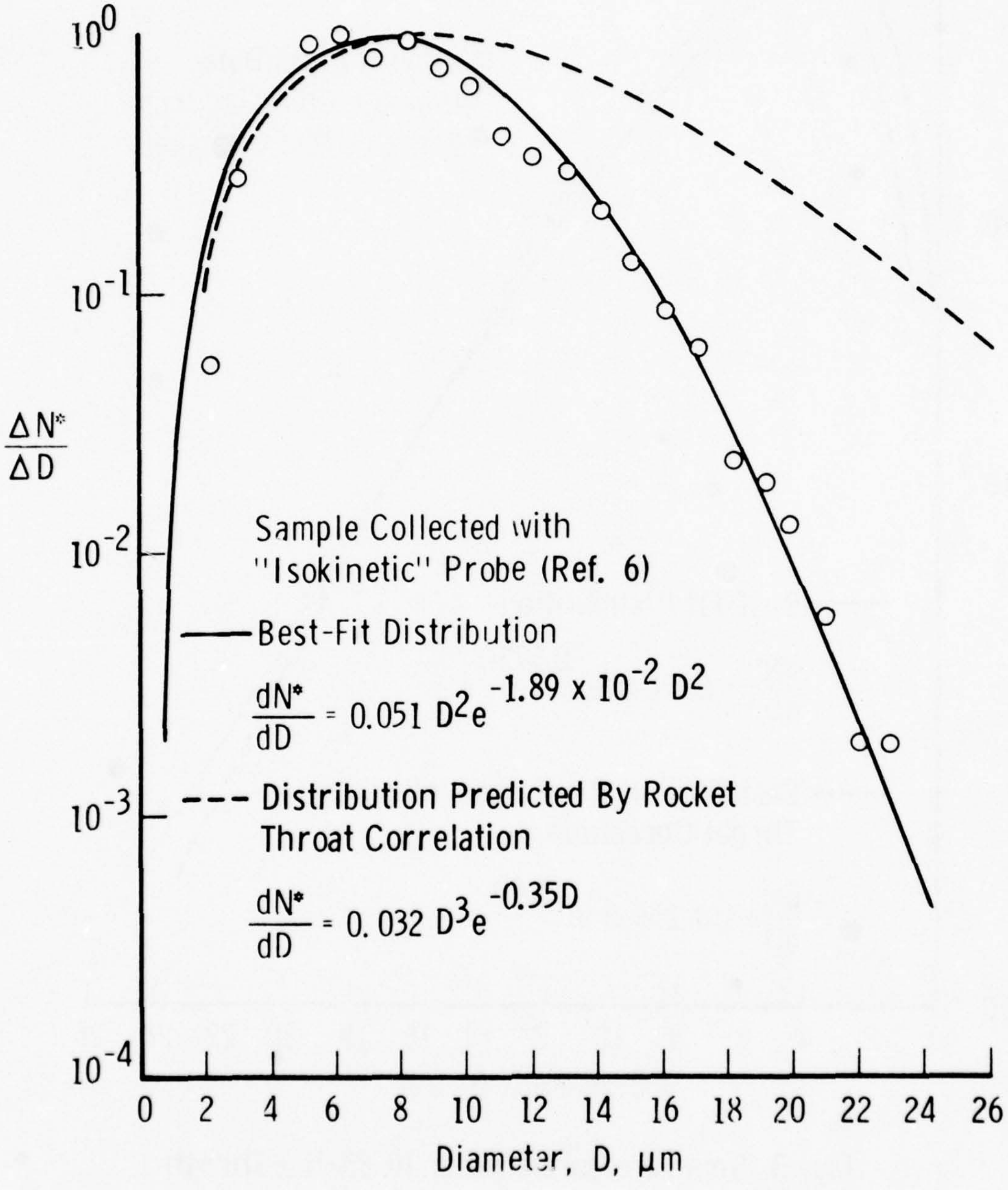

Fig. 4 Size Distribution from Titan IIIc (37.7-in Throat)

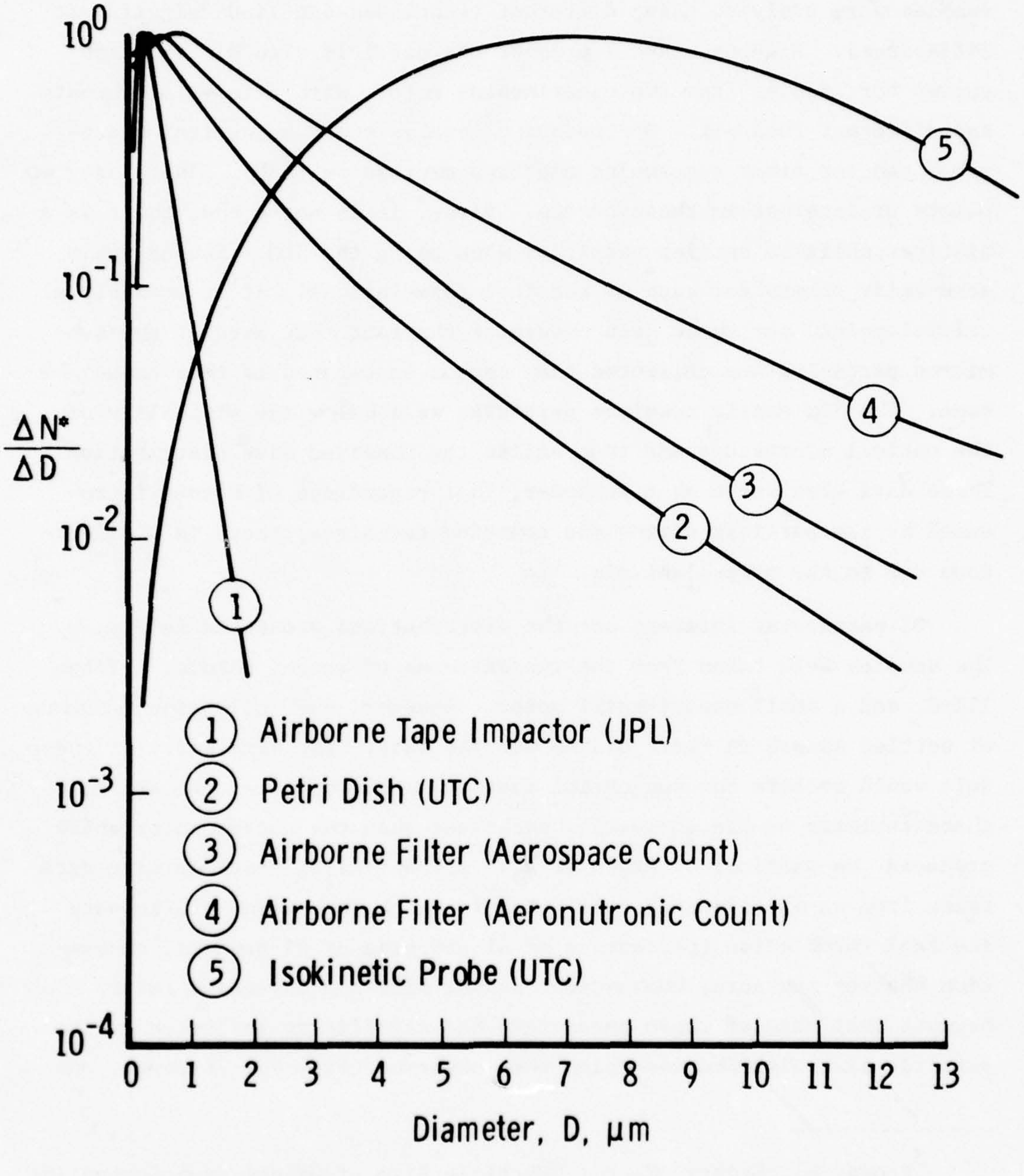

Fig. 5 Comparison of Data from Various Titan Plumes

reproducible. However, when one examines the results where the same samples were analyzed using different techniques one finds significant differences. Figures 6 and 7 present the particle size distribution curves for samples from two experimental motors with 2-in.-diam throats and different fuel mix. One method of analysis was an optical microscope and the other a scanning electron microscope (SEM). There are two points of interest in these curves. First, it is noted that there is a distinct shift to smaller particles when using the SEM. Second, this same shift occurs for each of the fuel formulations. It is possibly a trivial point, but these data emphasize the fact that even if the submicron particles are collected they cannot be counted if they cannot be seen. The SEM easily resolves particles well below the visibility of the optical microscope and thus shifts the observed size distribution. These data also serve as a reminder, that regardless of biases introduced by the particle sizing and counting technique, there is a difference due to the propellant mix.

Of particular interest are the distributions presented in Fig. 8. The samples were taken from the two extremes of rocket motors, a Titan III-C, and a small experimental motor. However, the collection technique of settled sample in Petri dishes was the same. The similarity of these data would confirm the suggestion that available data to date are more characteristic of the collection technique than the rocket motor which produced the particles. Brown et al.[5] present Al_2O_3 particle size data taken from an experimental test motor in which they were able to vary the fuel formulation (percentage of Al and size of Al powder), combustion chamber pressure, combustion chamber size and expansion ratio. They suggest that none of these parameters had significant influence on the particle size distribution which they observed (Fig. 9). However, one

---

[5] Brown, B., McArty, K. P., "Particle Size of Oxides from Combustion of Metalized Solid Propellants," 8th International Symposium on Combustion, C.I.T., Pasadena, CA, Aug.-Sept. 1960.

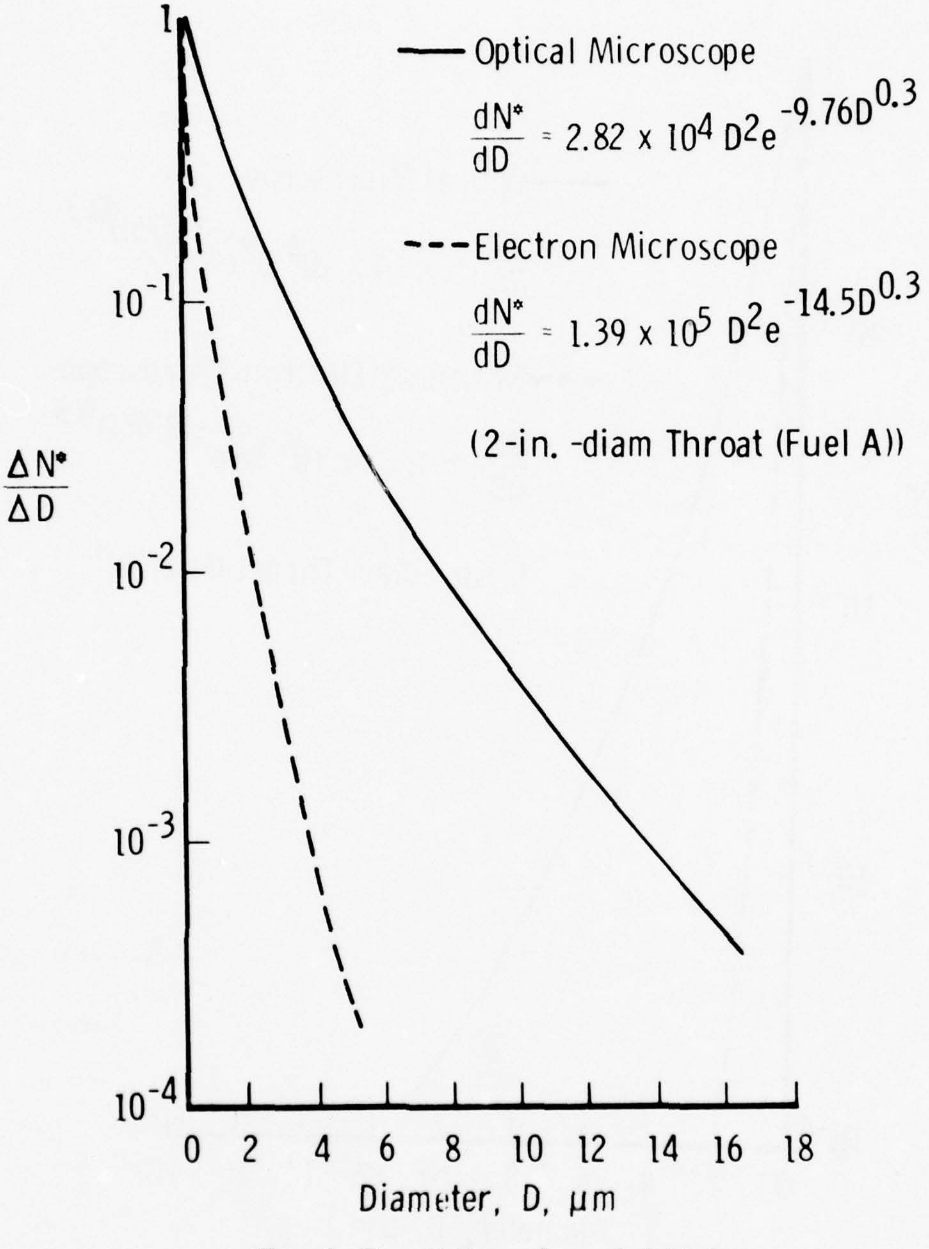

Fig. 6 Small Experimental Motor

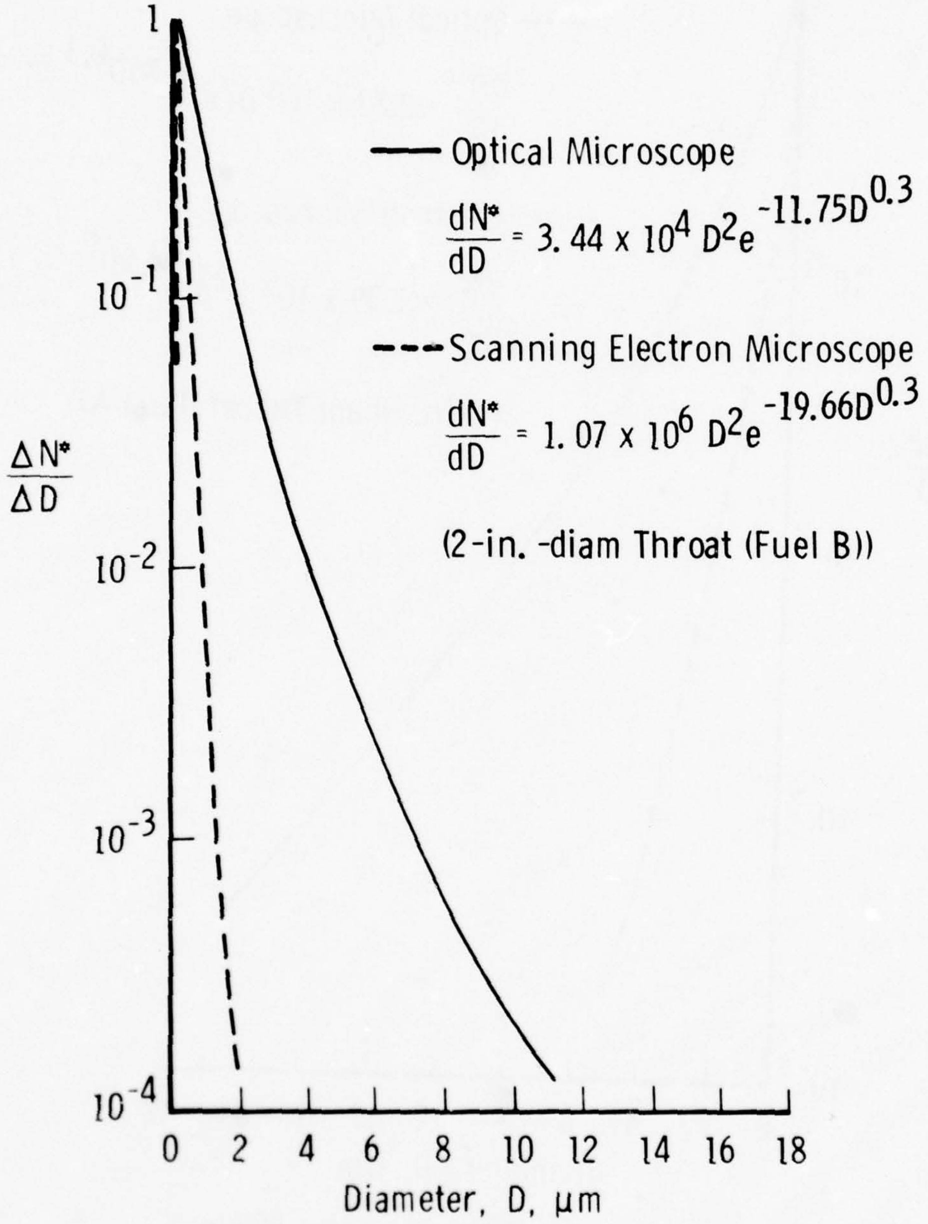

Fig. 7 Small Experimental Motor

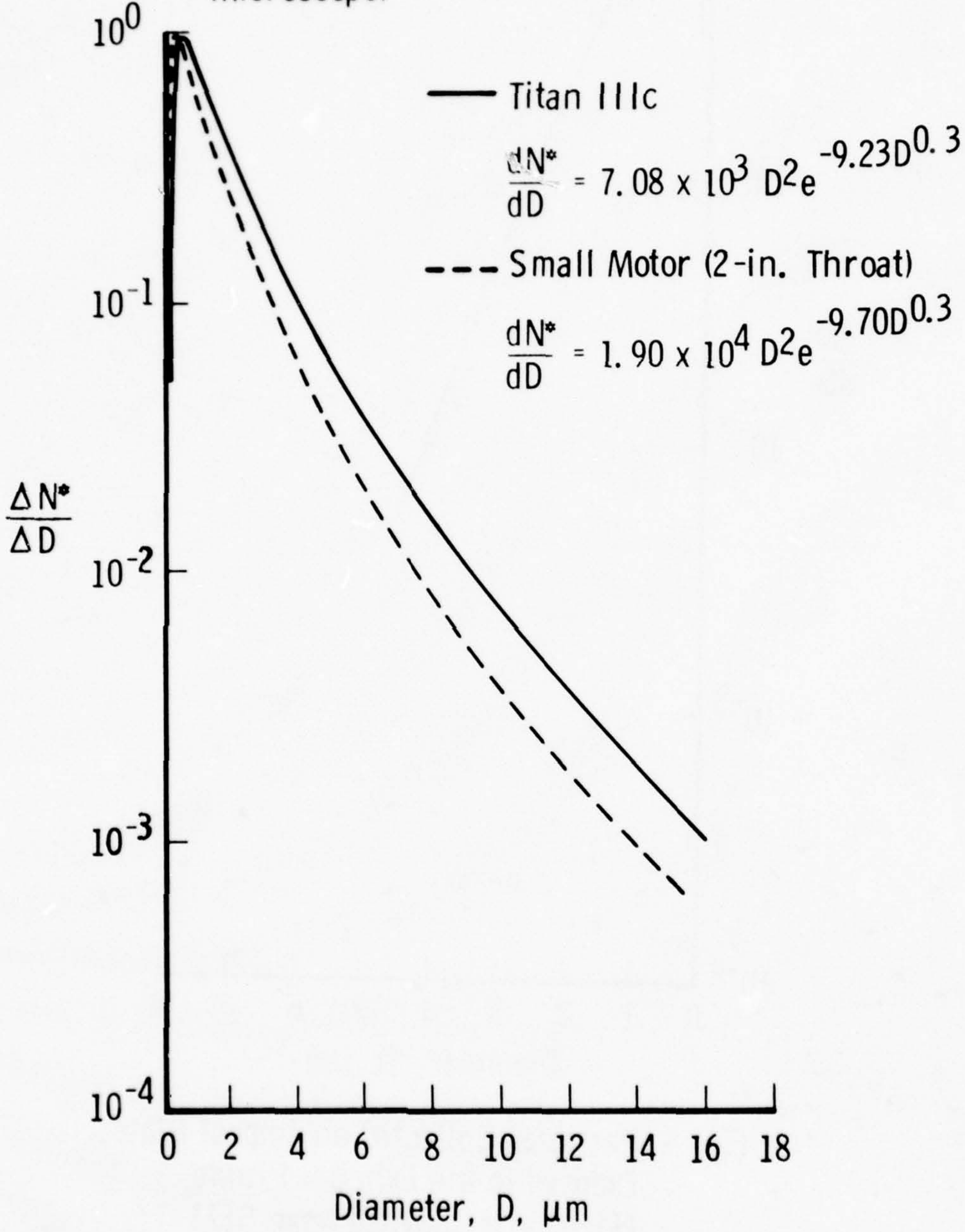

(Method of Collection and Analysis Identical, i.e., Petri Dish - Optical Microscope)

Fig. 8 Comparison of Titan and Small Motor

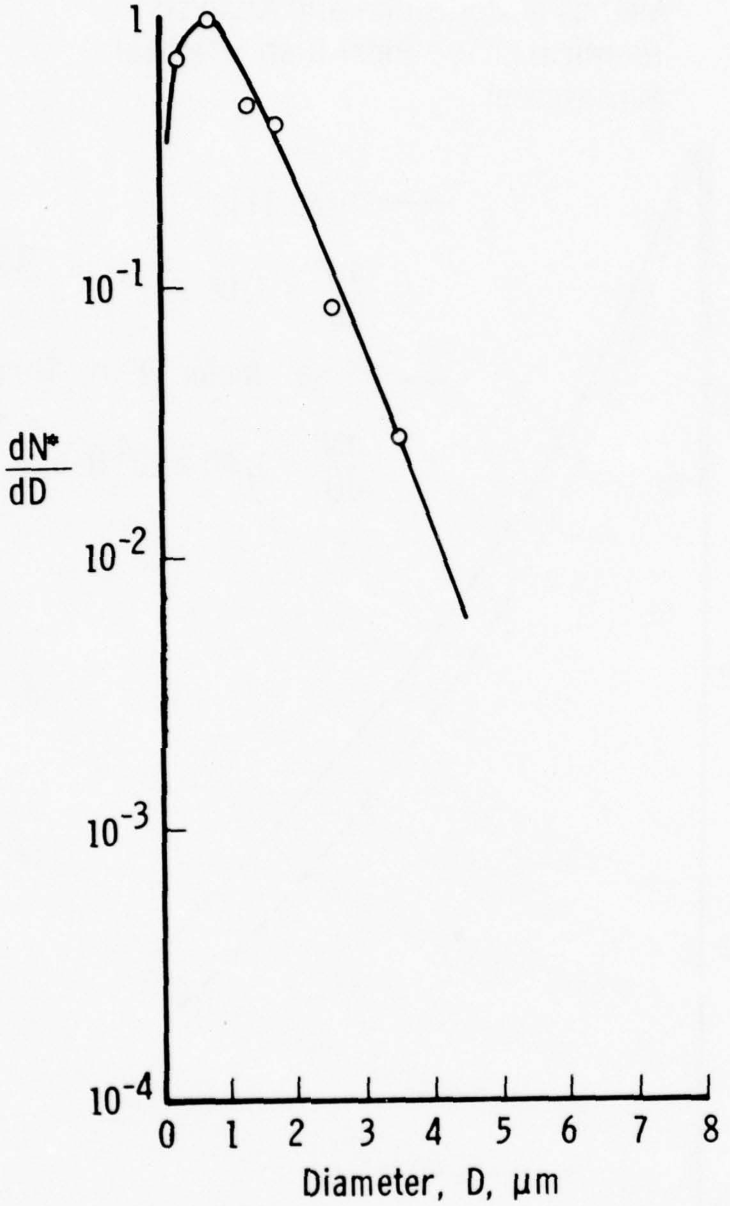

Fig. 9 Particles Collected on Impact Plates Exposed to the Exhaust Plume (Sized and Counted from SEM Photographs)

wonders if the collection technique which remained the same for all tests could possibly mask any subtle changes in the particle size distribution.

3.0 ALUMINUM OXIDE SAMPLING TECHNIQUES

The data presented thus far are representative of sampling techniques where the Al_2O_3 has been collected at a considerable distance from the rocket. Due to the obvious hostile environment close to the exhaust nozzle there are limits on where samples can be taken. A successful attempt to obtain Al_2O_3 particles on the launch platform of a Titan III-C was made by Willoughby[6] using an "isokinetic probe." This probe was aligned with the flowfield and was so constructed that the exhaust gases flowing around the probe produced a low pressure region at the base of the probe, thus drawing a sample of the rocket plume through the sampling section. Here the gases were allowed to decelerate and deposit the particles on a sampling surface.

Sampling methods may be classed as passive and active. The passive collectors include petrie dishes, polyethylene sheets, sticky tapes and even, in one case, rainwater accumulated on the roof of an automobile. The active collectors, consisting of filters and impactors (wire, flat disc, cascade, tape) where cloud samples are drawn through the collector, have been used at stationary ground points and also aboard aircraft flown through exhaust plumes.

Samples have been processed by a variety of methods to produce particle size distribution data. Where the collection technique has produced a reasonably dispersed monolayer of particles, the usual analysis has been by counting and sizing under an optical or scanning electron

---

[6] Willoughby, P. G., "Sampling and Size Determination of Particulates from the Titan III-C Exhaust Plume," United Technology, TR-33-74-U1, Feb. 1974.

microscope. In those instances where the sample was too dispersed (collected on large polyethylene sheets) or too closely packed, the sample was washed from the collector and then redistributed on an appropriate microscope slide. Usually this process involved using ultrasonic baths to try to avoid coagulation of the particles as the liquid carrier evaporated. Samples collected on filter papers have been analyzed in terms of mass loading by simply weighting the filter and also by ashing the filter and recovering the Al_2O_3 by repeated washing of the residue. An extreme pre-processing procedure is described as follows:

> "The ground sampling panels were cut into 3"-wide strips and scrubbed in 600 cc of water. The solids were filtered and the filter dried and ashed at 600°C in a porcelain crucible. The residue was treated with aqua regia and heated to just under boiling for 1/2 hour. The resulting material was cooled, diluted with water and filtered. The filter was dried and ashed at 600°C in a platinum crucible and the remaining material treated with 50 percent HF for 1/2 hour at a temperature just under boiling, the resulting material was filtered and ashed in a porcelain crucible. The Al_2O_3 particles were then sized and counted."

It can be quite easily seen from these comments on the techniques used to collect and analyze samples that there are several biases against the submicron particles.

Those samplers at ground level collecting the fallout from the exhaust, have an extremely effective atmospheric filter to remove the submicron particles. The "isokinetic probe" which removes this filter suffers from the fact that its sampling surface is an impaction collector and at the lower velocities in the probe the larger particles impact and the submicron particles flow around the surface. Devices flown through the exhaust cloud with some attempt to sample isokinetically would be expected to produce a more representative sample. Unfortunately, in most cases what is gained in the sampling is lost in the processing, since the filters and sticky tapes employed are either burned and/or washed to extract the sample from the collector.

4.0 RESULTS FROM THE MARSHALL SPACE FLIGHT CENTER (MSFC) SAMPLING TESTS

These tests consisted of a 6.4% scaled model of the space shuttle with two Tomahawk solid rocket motors used to simulate the solid strap on boosters. The model was mounted above a scaled version of the proposed shuttle launch pad and both the solid and the liquid engines were fired simultaneously. The basic test series was conducted to evaluate the acoustic coupling between the vehicle and the launch pad at lift off. The particle collection experiments were conducted as a peripheral test to evaluate some of the techniques used in previous field tests. The particle size distributions obtained from the MSFC scaled shuttle tests are presented in Figs. 10 and 11. As can be seen in Fig. 10, the various collection techniques do bias the size distribution. It is interesting to note that the "isokinetic" probe data from these tests are quite similar to those for the UTC Titan samples.[6] The distributions presented in Fig. 11 compare the particles from the Tomahawk to other rocket motors where the sample has been collected by fallout into Petrie dishes.

4.1 Titan III-D Plume Sampling (ETR 5-20-75)

These particular data have been singled out for emphasis, in that they would appear to be the least biased by sampling and counting techniques. The data were taken by JPL under the direction of Dr. Varsi.[7] The rocket plume was produced by a Titan III-D and was sampled at an altitude of 20 km approximately 10 minutes after launch. The sampling

---

[7] Varsi, G., "Proceedings of the NASA Atmospheric Effects Working Group Meeting," Vandenburg AFB, Oct. 27-28, 1976.

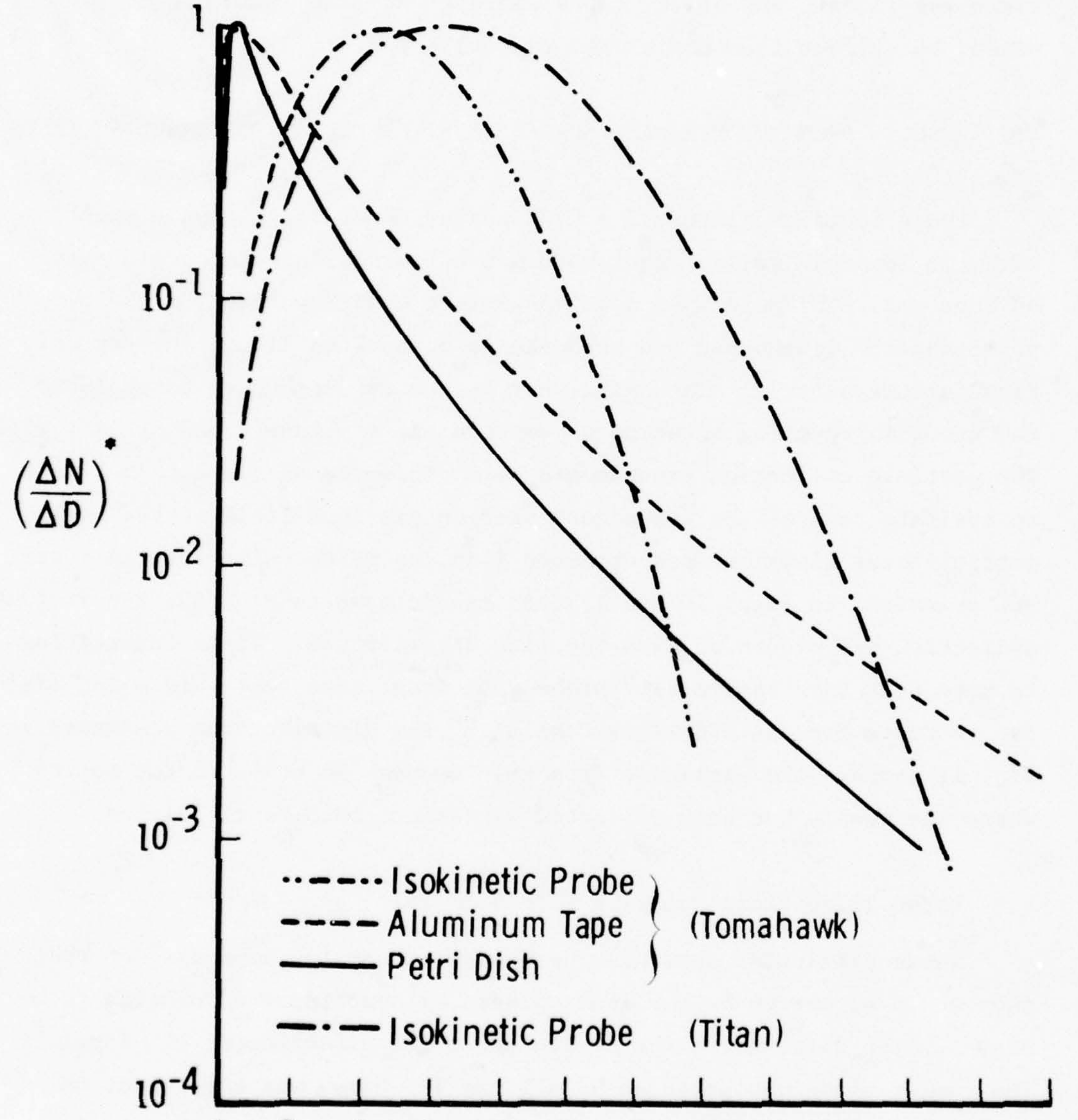

Fig. 10 Particle-Size Distributions (Tomahawk MSFC)

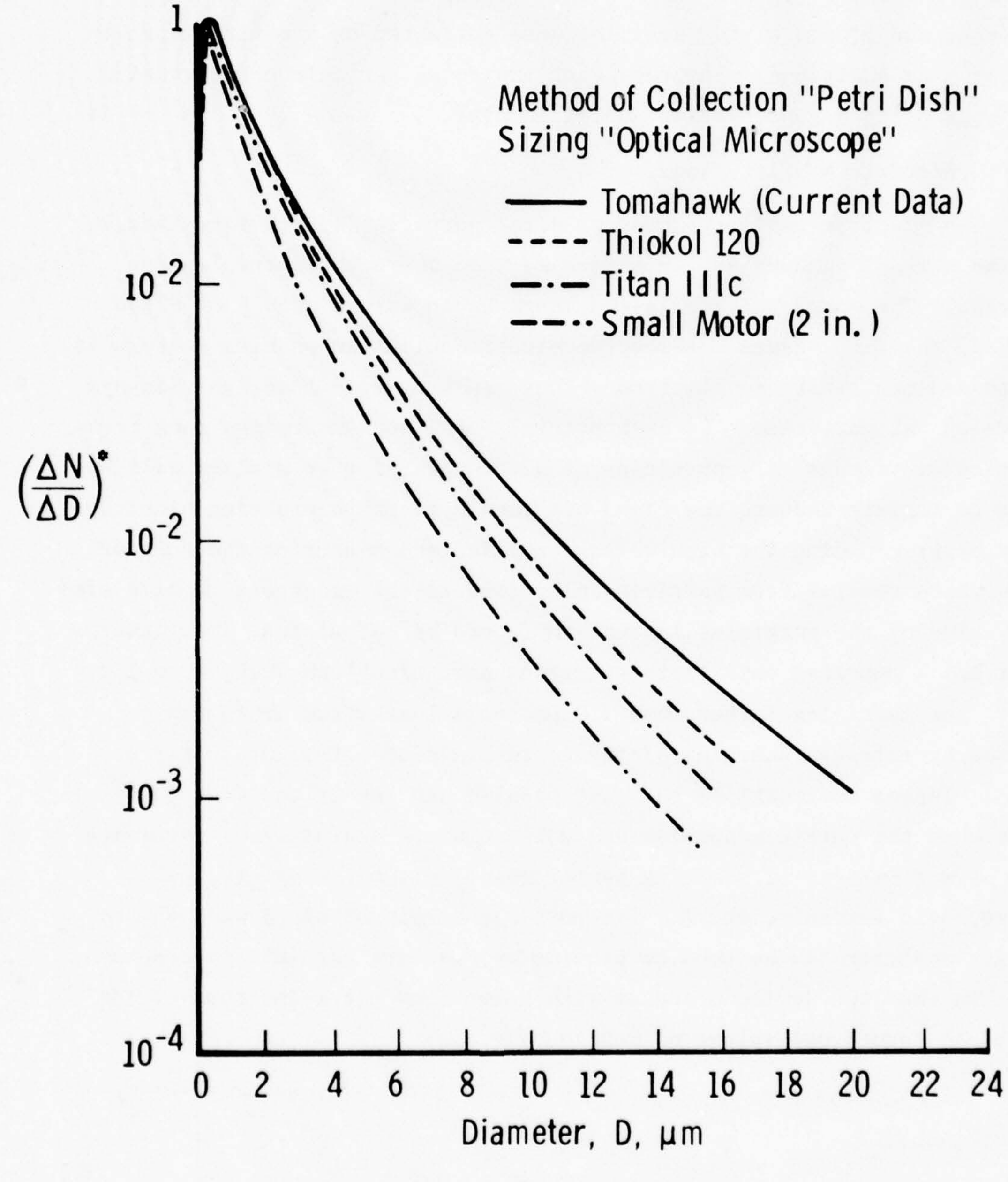

Fig. 11 Al_2O_3 Particle-Size Distributions for a Variety of Motors aircraft flew through the plume and collected the Al_2O_3 isokinetically. Submicron sized particles were analyzed using an electric mobility analyzer and micron sized particles were collected on a moving tape impactor. An additional measurement of the total particle concentration was made using a condensation nuclei counter.

4.1.1 Electric Mobility Analyzer

The electric mobility analyzer sizes particles by drawing a sample of the aerosol through an ionization section where the particles are charged. The sample stream is then surrounded with a sheath of clean air and the flow passes between two electrodes. A known high voltage is impressed between these electrodes thus applying an attractive sideways force on the particles. If each particle has the same charge then for a particular voltage only particles of a specific size or smaller will be able to migrate through the clean air sheath to the attracting electrode. Thus by programming the high voltage applied and measuring the current flow which results from particles migrating to the electrode, a size distribution of the particles in the sample can be calculated. The instrument has a reported capability of sizing particles from .005 μm to 1.0 μm.[8] For particles larger than 1.0 μm, wall losses and ambiguities caused by multiple charging of the particles render the data questionable. Indeed the multiple charging problem can render the data questionable when the particle species are unknown since a mixture of particles can have a variety of charging properties (i.e., oil droplets, soot, clays, acid aerosols, etc.). The particle sample obtained with the mobility analyzer can be used to provide an absolute particle concentration in that the device operates with known flow rates and thus yields particle counts per volume of sampled air.

---

[8] Liu, B. Y., Fine Particles Aerosol Generation, Measurement Sampling and Analysis Academic Press, Inc., New York, 1976.

4.1.2 Tape Impactor

The tape impactor collects particles on the sticky surface of a tape which is slowly moving past the sampling orifice. The particle laden air is drawn into the sampler and accelerated through a nozzle which faces the tape. Because of their momentum, large particles (>1.0 μm) impact on the surface and are captured. Some of the smaller particles can follow the airstream as it turns and flows aroung the tape and thus there is a gradual decrease in the collection efficiency for smaller particles. Correction factors are applied to the data to account for these losses. Since the tape is constantly moving it produces a well spaced collection of particles which can later be sized and counted. The size distribution measured by the tape impactor can, however, be distorted by loss of larger particles in the inlet and nozzle section and in addition it does require extreme care in the sizing and counting since the particles are not randomly distributed on the tape surface (i.e., due to shape of nozzle and direction of tape travel the particles will tend to distribute themselves according to size).

4.1.3 Aiken Nuclei Counter

An Aiken nuclei counter does not yield a size distribution, but can give an approximate value for the number density of particles. It operates by drawing a known volume of the air into a chamber saturated with water vapor. A piston or diaphragm is then released which results in an adiabatic expansion of the vapor mixture. In this supersaturated environment water vapor condenses on all the particles present and the resulting cloud of droplets is detected by an optical sensor. The optical measurement is a simple extinction measurement and is successfully converted to a number density because of two factors. First, the water droplets observed are much larger than the original particles and therefore the unknown indices of refraction of these particles are not important. Secondly, the growth process of the water drops is such that the smaller drop radius will increase at a much faster rate than the larger ones. Thus, the final cloud of droplets will all be close to the same size at the time of the extinction measurements. The instrument can therefore be calibrated with a known aerosol number density and be expected to hold this calibration for an unknown aerosol where the particle composition and size may be quite different.

4.1.4 Data Fitted to a Distribution Function

The particle counts per size interval from the mobility data were fitted to a distribution function as previously described. The curve was normalized to the mode and is presented in Fig. 12. The data from the tape impactor provides a second particle size distribution which partially overlaps the mobility data. However, the overlap is in a regime where the tape impactor data has large correction factors applied to allow for small particle losses. Thus a distribution function was fitted to the tape impactor data for particle sizes greater than 0.5 μm. Both sets of data indicate an inflection point around the 0.35 μm particle size and the tape impactor data was therefore scaled to match the mobility distribution at this point.

The resulting distribution is shown in Fig. 12 with data points from both instruments. The poor fit of the 0.1 μm data from the tape impactor can be accepted since in this range the instrument count has been corrected by a large and somewhat questionable loss factor. It is immediately obvious that this distribution is quite different from those presented previously. The most striking point is that its mode is in the submicron range. Since there is a delay between plume formation and sampling (T_0 + 10 minutes), then the first impulse is to suspect that the larger particles have settled out. However, calculating the settling rate of a 10 μm Al_2O_3 particle and considering the 10 minute interval the total distance fallen would be approximately 9 meters. It would thus seem that this settling would be insignificant insofar as skewing the size distribution, at least up to the 10 μm particle sizes. Similar

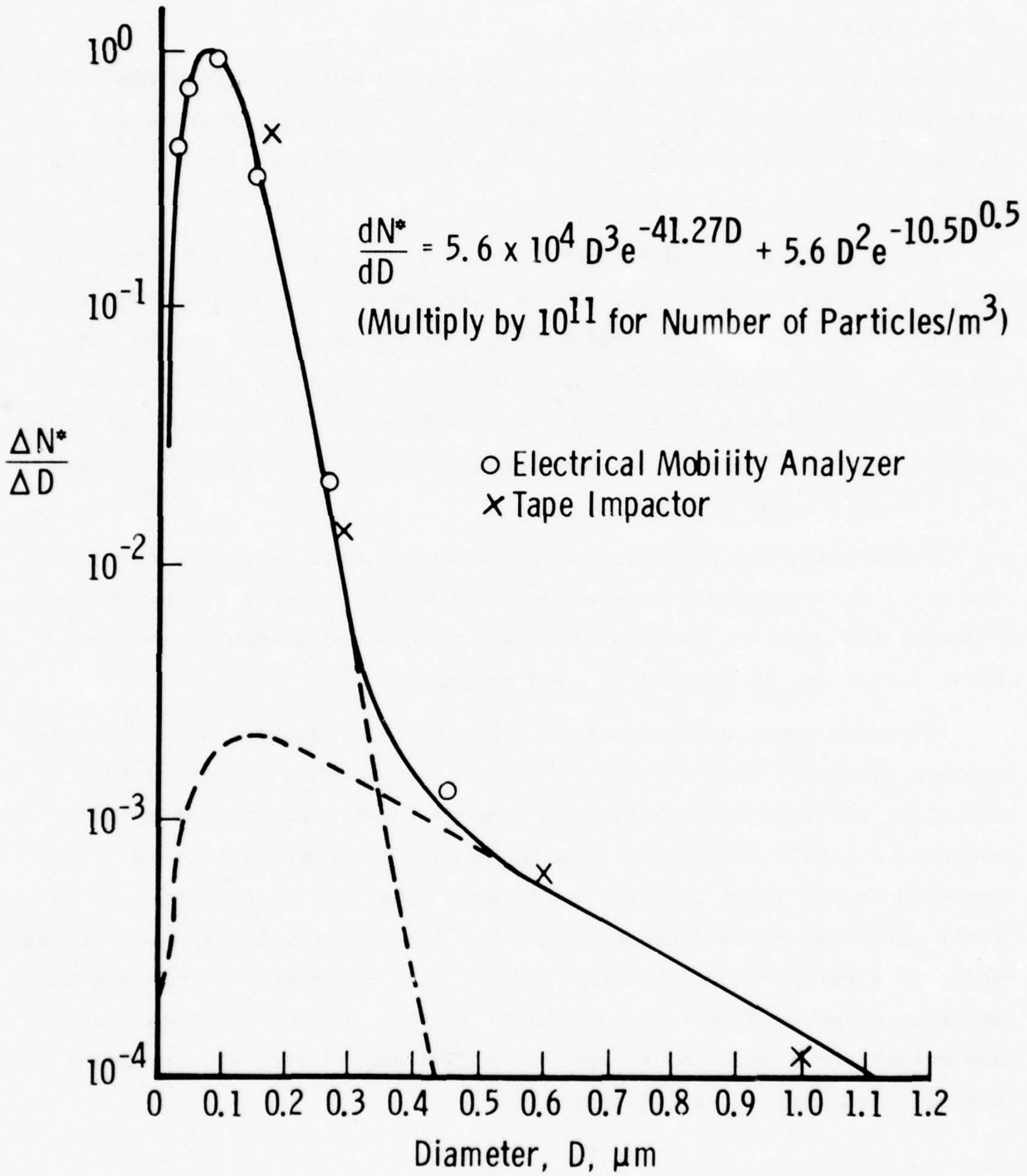

Fig. 12 Titan IIID Data Reported by Dr. Varsi (Ref. 7)

calculations for 100 μm particles suggest that they could be depleted due to gravitational settling.

The closure condition based on calculated emissions from the solid motors at 20 km altitude of 930 gms of Al_2O_3 per meter altitude and an estimated plume diameter of 2 km yields an average mass loading in the atmosphere of 2.9×10^{-4} gms/m^3.

Using the particle size distribution in Fig. 12 and adjusting the particle number density to match the value measured by the Aiken nuclei counter (i.e., 3×10^{10} particles/m^3), then the equations can be integrated to yield an atmospheric mass loading. These calculations indicate values of 5.24×10^{-5} gms/m^3 for particles sized from .025 to .525 μm and 4.78×10^{-5} gms/m^3 for particles from .525 to 6.0 μm or a total of 1.0×10^{-4} gms/m^3.

Considering the possible uncertainties of such values as the plume diameter, and the aluminum oxide deposition rate as well as the possible biases which might be included in the particle measurement techniques these values are in remarkably good agreement.

A second point of interest in these data is that the size distribution is bimodal. Kraeutle et al.[9] have observed this bimodal nature of the Al_2O_3 particle distribution in samples taken from smaller rocket motors. A size distribution from their data is shown in Fig. 13. When compared to the Titan III data it is noted that the distribution of the small particles is similar, however, the larger particles (>1 μm) are an order of magnitude more numerous. Using this distribution function and assuming a number density of 3×10^{10} particles/m^3 for the Titan plume one calculates a mass loading of 2.3×10^{-2} gms/m^3 with 10 percent of the mass in the submicron sized particles.

---

[9] Victor, A. C., Breil, S. H., "A Simple Method for Predicting Rocket Exhaust Smoke Visibility," Journal of Spacecraft and Rockets, August 1977.

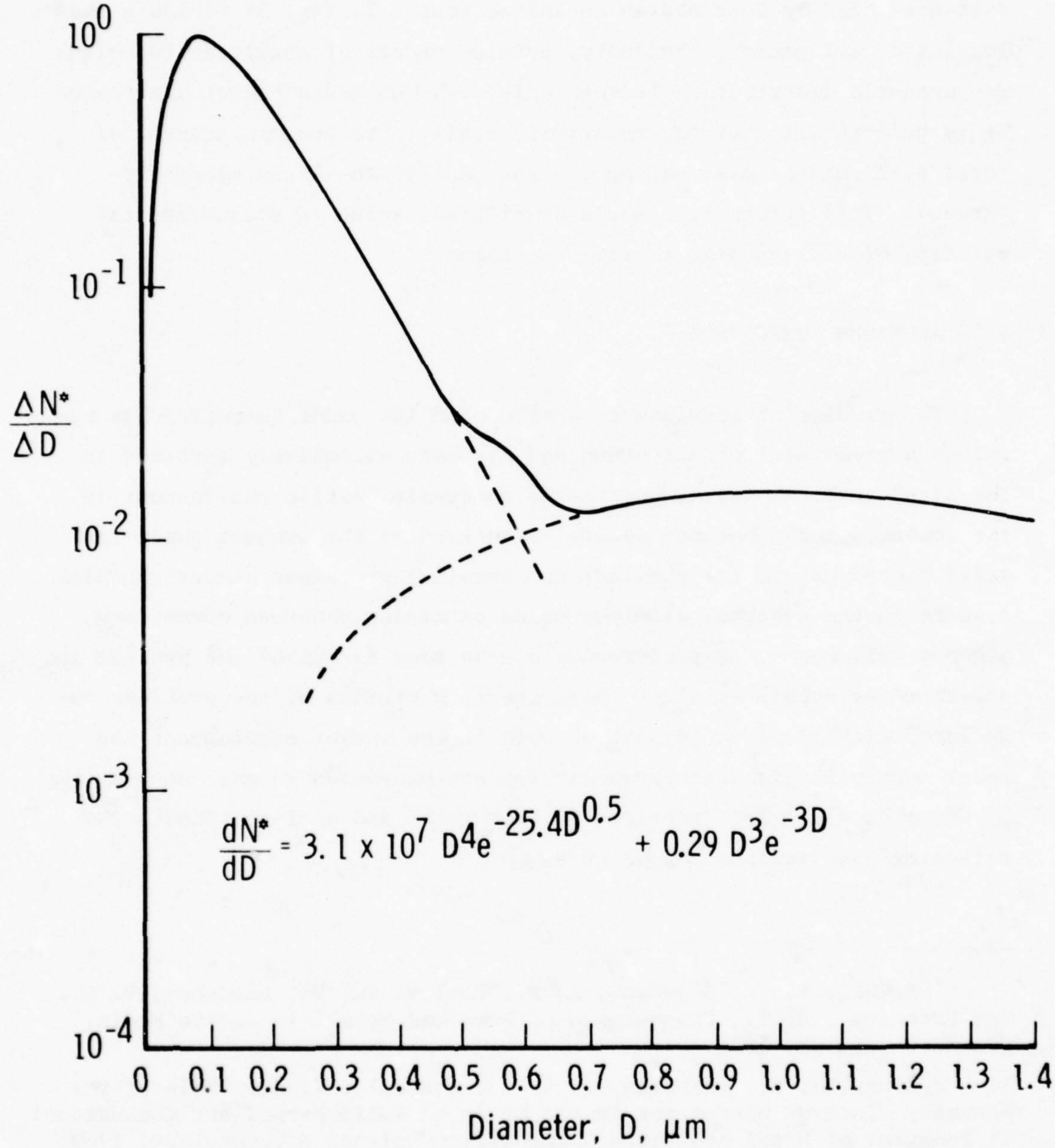

Fig. 13 Distribution Obtained by Kraeutle (Ref. 9)

Repeating this exercise with the distribution function derived from data collected by Petrie dish technique (curve 2, Fig. 5) yields a mass loading of 1.1 gms/m^3, obviously, a value orders of magnitude too high. The Kraeutle distribution is seemingly high but certainly within reason. It is unfortunate that the relatively easily obtained measurement of total particulate mass loading was not made on the Titan cloud fly-through. This information would be of great value in evaluating the validity of various distribution functions.

5.0 ALUMINUM COMBUSTION

The problem of aluminum combustion and its oxide formation has received a great deal of attention and has been extensively reported in the literature. However, due to the extremely hostile environment in the combustion chamber and nozzle expansions of the exhaust gases from solid rocket motors the physical and chemical processes occurring which results in the eventual aluminum oxide particles observed downstream, are not well known. A good review of the many facets of the problem is presented by Pokhil et al.[10] More specific studies of the problems associated with aluminum combustion both in the rocket environment and under controlled laboratory conditions are presented in work such as that by Crump et al.[11] and Prentice.[12] From these and similar studies the following observations can be made.

---

[10] Pokhil, P. F., Belyayev, A. F., Frolov, Yu, V., Logachev, V. S., and Korotkov., A. I., "Combustion of Powdered Metals in Active Media," FTD-MT-24-551-73, 1972.

[11] Crump, J. E., Prentice, J. L. and Kraeutle, K. J., "Role of the Scanning Electron Microscope in the Study of Solid Propellant Combustion: II Behavior of Metal Additives," Combustion Science & Technology, 1969, Vol. 1, pp. 205-223.

[12] Prentice, J. L., "Aluminum Droplet Combustion Rates and Mechanisms in Wet and Dry Oxidizers," NWC-TP-5569, April 1974.

1. The molten aluminum droplets in the combustion chamber are, in general, considerably larger than the particles of aluminum included in the fuel. It is noted that as the fuel surface recedes, the aluminum particles are exposed and tend to cluster. Rather than leave the surface immediately they melt and form a liquid Al and solid Al_2O_3 matrix before being swept into the gas stream. This process of agglomeration thus suggests that the final Al_2O_3 particle size cannot be directly related to the original size of metallic aluminum particles in the fuel. The degree of agglomeration is influenced by several factors which include, initial particle sizes of both fuel and oxidizer, uniformity of mixture, type of binder, rate of burning, pressure in combustion chamber and thickness of oxide coating on the metallic aluminum particles used in the fuel.[13]

2. During the melting and agglomeration process, the oxide coatings from the original aluminum particles crack open and accumulate on the surface of the droplets. As the heating process continues these shell fragments melt and form a visible lens cap like structure on the surface of the spherical molten aluminum.

3. Ignition appears to occur as the molten Al-Al_2O_3 droplet leaves the surface and enters the high temperature combustion zone. From high speed photographs it is observed that the flame stands off from the surface of the droplet thus indicating a gas phase reaction. Due to the continuum radiation produced from all the Al_2O_3 in the combustion chamber it is impossible to distinguish any spectra indicating the occurrence of the suboxides AlO and Al_2O. However, supplementing evidence from the ignition of aluminum filled flash bulbs does show emission lines of AlO.[10,14]

---

[13] Crump, J. E. (Editor), "Combustion of Solid Propellants and Low Frequency Combustion Instability," NOTS-TP-4244, June 1967.

[14] Herzberg, G., Molecular Spectra and Molecular Structure, Spectra of Diatomic Molecules, D Van Nostrand Co., Inc., New York, New York, 1950.

Porter et al.[15] studied the species vaporizing from an $Al-Al_2O_3$ mixture using a mass spectrometer. Their system was limited to temperatures of 1800°K, however, they identified Al and Al_2O as the prime gaseous constituents with a trace signal of AlO. Brewer et al.[16] conducted similar vaporization experiments and concluded that in the $Al-Al_2O_3$ mixture the basic sub-oxide is Al_2O whereas in the vaporization of Al_2O_3 alone AlO is the dominant gas species. It was also observed that when molten aluminum was in contact with the Al_2O_3 this increased the evaporation rate of the Al_2O_3 by two orders of magnitude.

Considering these comments and then returning to the observations of molten aluminum droplets with molten lens caps of Al_2O_3 surrounded by a reactive flame zone, it can be seen that the production of aluminum oxide particles in a rocket motor is a complex process. The sub-oxides are obviously formed in the reaction zone surrounding the burning droplet, with possible additions from the evaporation of Al_2O_3 at the $Al-Al_2O_3$ interface on the droplet. Adding to this complexity is the fact that the droplets and gases are swept from the surface of the burning propellant and are rapidly accelerated through the nozzle and into the expanding plume. However, from these observed processes one can speculate that there are at least two possible sources of Al_2O_3 particles, the liquid Al_2O_3 lens caps which remain as residue after the Al has evaporated and Al_2O_3 formed from the condensation of the gaseous sub-oxides.

---

[15] Porter, R. F., Schissel, P., Ingram, M. G., "A Mass Spectrometric Study of Gaseous Species in the $Al-Al_2O_3$ System," Journal of Chem. Phys., Vol. 23, No. 2, Feb. 1955.

[16] Brewer, L. and Searcy, A. W., "The Gaseous Species of the $Al-Al_2O_3$ System," Journal Am. Chem. Soc., Vol. 73, 1951.

5.1 Condensation of Gaseous Oxides

There is no experimental evidence that either of the sub-oxides can exist in the solid or liquid phase. Material identified by Hoch et al.[17] as solid Al_2O and AlO was later shown to be Al_4C_3 and $AlTaO_4$ by Yanagida.[18] Thus the condensation of gaseous AlO-Al_2O to Al_2O_3 is both a chemical and physical process. Hermsen[19] has applied the classical homogeneous nucleation theory as presented by Frenkle[20] to predict nucleation rates. To circumvent the problem of not being able to define a supersaturation of the AlO-Al_2O gas, he uses the ratio of the partial pressure of the Al gas to the equilibrium vapor pressure of Al gas in Al_2O_3 vaporization products. Regardless of the confidence one might have in this treatment of the problem, the predicted nucleation rates are of questionable value since they vary by a factor of 10^{16} over the temperature range of interest (i.e., 3000°K to 3500°K). It would thus seem that until the condensation process can be identified, it is premature to try to adapt existing condensation theories to predict nucleation rates. While the actual process involved in the condensation of the sub-oxides is not yet known it is not unreasonable to suggest that condensation is the source of the submicron particles observed in the rocket exhaust plume.

---

[17] Hoch, M. and Johnston, H. L. "Formation Stability and Crystal Structure of the Solid Aluminum Sub-oxides: Al_2O and AlO," Journ. Am. Ceramic Soc., Vol. 76, 1954.

[18] Yanagida, H., Kroger, F. A., "Condensed Phases in the System Al_2O_3-Al," Ceramic Bulletin, Vol. 23, 1955.

[19] Hermsen, R. W., Dunlap, R., "Nucleation and Growth of Oxide Particles in Metal Vapor Flames," Combustion & Flame, Vol. 13, No. 3, June 1969.

[20] Frenkle, J. Kinetic Theory of Liquids, Oxford University Press, London, 1946, p. 397.

5.2 Dispersion of Liquid Al_2O_3

It has been noted that due to an agglomeration process at the burning surface of the fuel, relatively large droplets of molten aluminum with attached Al_2O_3 lens caps, enter the gas flowfield. A typical histogram of these agglomerated droplet sizes as measured by Boggs et al.[14] is reconstructed in Fig. 14. From the scaled photographs of burning droplets as shown in Ref. 13, one can estimate that the volume of liquid Al_2O_3 in the lens cap is approximately 0.8 percent that of the molten aluminum droplet. The order of magnitude of this value is confirmed by the observation that the original aluminum powder (approx. 15 μm diam) has on the average a 75-Å-thick coating of Al_2O_3.[21] Assuming negligible evaporation or condensation of the liquid Al_2O_3 then one can predict a range of residual alumina droplets from 4 to 40 μm in diameter based on the agglomerated particle sizes shown in Fig. 14.

It is also observed that a considerable quantity of liquid Al_2O_3 accumulates on the nozzle walls and is shed due to the high velocity gases. Bartlett et al.[22] have used the droplet stability criteria of a critical Bond number to calculate the maximum size of a molten aluminum oxide droplet which could survive the aerodynamic forces in the rocket flowfield. In a similar manner one can postulate the maximum aerodynamic drag forces which might be encountered and equating these forces to the surface tension of liquid Al_2O_3[23] calculate that the minimum droplet size produced by this mechanism is on the order of 1 μm. It would thus appear that the agglomeration process at the burning surface and

---

[21] Price, E. W., "Summary Report on Workshop on Behavior of Aluminum in Solid Propellant Combustion," Proceedings of the 13th JANNAF Combustion Meeting, Nov. 1976.

[22] Bartlett, R. W., Delaney, L. J., "Effect of Liquid Surface Tension on Maximum Particle Size in Two Phase Flow," Pyrodynamics, Vol. 4, 1966.

[23] Kingery, W. D., "Surface Tension of Some Liquid Oxides and Their Temperature Coefficients," Journal of the American Ceramic Society, Vol. 42, No. 1, Jan. 1959.

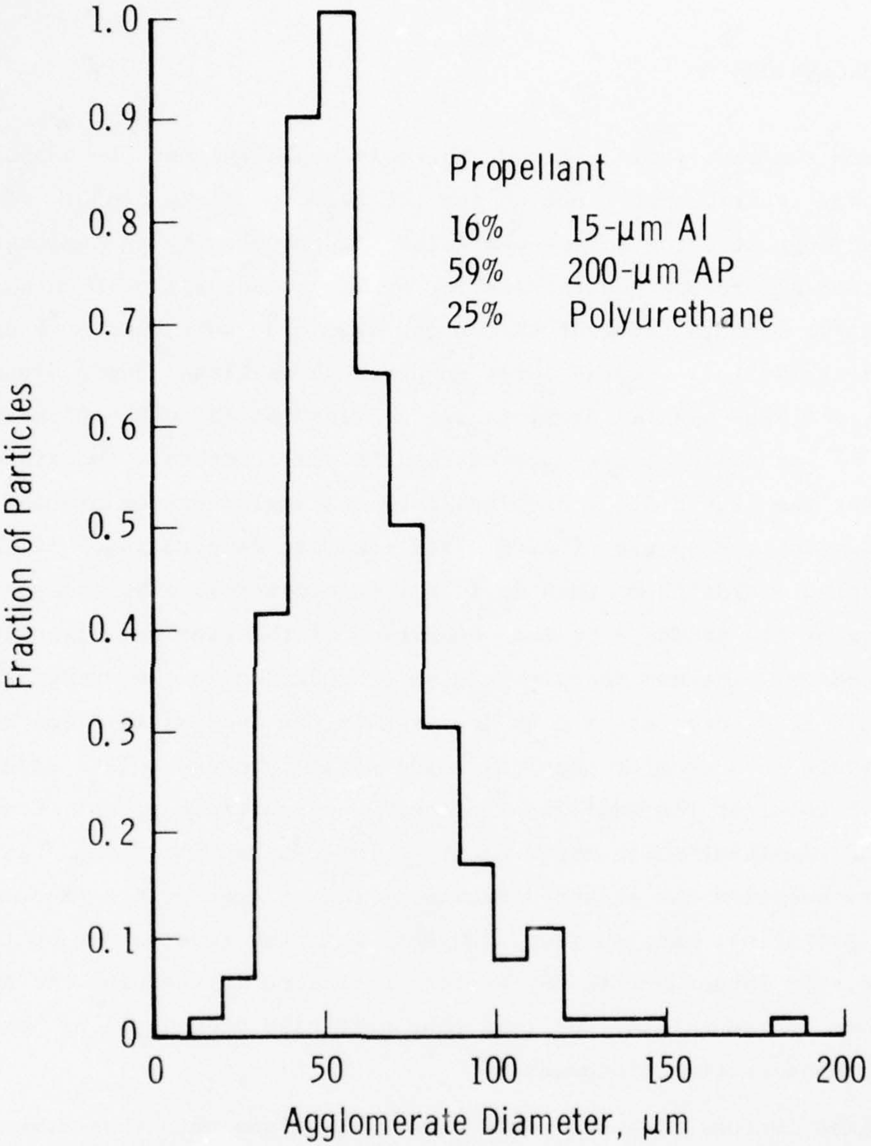

Fig. 14 Agglomerate Diameters in Aluminized Propellant (Ref. 14)

aerodynamic dispersal of liquid Al_2O_3 provide particles in the micron size range.

6.0 CONCLUSIONS

From the observations cited, there is ample evidence to support a multimodal distribution function for the Al_2O_3 particle sizes. If as has been suggested the larger particles are produced by an agglomeration and dispersal process and the smaller ones by condensation then an argument can be made in favor of the strong submicron particles mode of the Varsi distribution. In the large motors such as Titan, Super Hippo and Shuttle the agglomerated droplets are confined in the combustion zone ($\sim 3500^oK$) for a much longer period than in small motors. In this environment the liquid Al_2O_3 droplets from the agglomeration process are in a reducing atmosphere of Al gas and thus are evaporating. If this evaporation yields Al_2O, then it is not rate controlled by the partial pressure of AlO produced by the combustion of the aluminum directly in the oxidizer. The net result would be a depletion in the number and size of liquid Al_2O_3 droplets and an increase in the sub-oxides which would participate in a chemico-physical condensation process. This argument does not consider the additional processes of particle growth, coagulation and remelting which might occur in the exhaust flowfield. It does, however, question the accepted viewpoint that bigger motors produce bigger particles, and, in fact, suggests that the reverse may be true. That is, the larger motors may be more efficient in reducing the Al_2O_3 contained in the initial fuel and thus primarily produce Al_2O_3 particles through condensation processes.

These factors plus the noted bias in previous data thus argue in favor of the bimodal particle size distribution functions as derived from data by Varsi and Kraeutle with significant quantities of Al_2O_3 contained in the submicron particles.

It is unfortunate, but notwithstanding all the previous efforts to determine the particle size distribution of Al_2O_3 in rocket plumes, it appears that further measurements, preferably made within the exhaust cloud, are still needed. In order that the data can be checked for consistency, three types of measurements should be made. The first and possibly the easiest measurement is total mass loading in the cloud. This measurement can be made using absolute filters for average values or possibly QCM's in conjunction with a precipitator (electrostatic or inertial) for determining cloud profiles. The second measurement needed is a count of the total number of particles per unit volume. A condensation nuclei counter could yield this data. The third measurement is the particle size distribution. No one instrument can cover the size range of interest (.005 to 50 μm). The electric mobility analyzer would appear to be the most promising for the .005 to .5 μm size range. Inertial impactors can operate effectively over a range from .1 μm to 10 μm. A cascade impactor with QCM readout at each stage could give near real time readout and thus indicate the homogeneity of the cloud section sampled. The particles ranging from .5 μm to 50 μm can be detected by optical scattering and there is a variety of instruments available.

It should be noted that all of these measurements including the simple total mass determined from weighing collections on filters, will be compromised if there are significant numbers of condensed water or acid droplets in the cloud. This requires that the rocket cloud therefore be formed in a relatively dry atmosphere and thus adds an additional constraint to the problem of cloud sampling.

Additional studies of the basic mechanisms of Al_2O_3 particle formation would be worthwhile, since if the condensation and coagulation process is occurring to a significant extent outside the combustion chamber and nozzle, then the Al_2O_3 particles deposited in the stratosphere and space can be quite different from those observed at low altitude due to the significant differences in the plume expansion. This would especially be of concern in the operation of the solid rocket motor for the interim upper stage (IUS) of the space shuttle operations.

ACKNOWLEDGMENT

The work reported herein was sponsored by NASA Marshall Space Flight Center, and performed by the Arnold Engineering Development Center (AEDC), Air Force Systems Command (AFSC). Work and analysis were done by personnel of ARO, Inc., A Sverdrup Corporation Company, operating contractor of AEDC.

REFERENCES

1. Dehority, G. L., "A Parametric Study of Particulate Damping Based on the Model of Temkin andDobbins," NWC TP 5002 (Sept. 1970).
2. Nukijama, S. and Tanassawa, Y., "An Experiment on the Atomization of Liquid by Means of an Air Stream (1st report)," Trans. S.M.E. Japan, Vol. 4, No. 14 (Feb. 1938).
3. Worster, B. W. and Kadamiya, R. H., "Rocket Exhaust Aluminum Oxide Particle Properties," AR1 RR-30 (Aug. 1973).
4. Rosin, P. and Rammler, E., "The Laws Governing the Fineness of Powdered Coal," Journal of the Inst. of Fuel, Vol. 7 (1933).
5. Brown, B., McArty, K. P., "Particle Size of Oxides from Combustion of Metalized Solid Propellants," 8th International Symposium on Combustion, C.I.T., Pasadena, California (Aug.-Sept. 1960).
6. Willoughby, P. G., "Sampling and Size Determination of Particulates from the Titan III-C Exhaust Plume," United Technology, TR-33-74-U1 (Feb. 1974).
7. Varsi, G., "Proceedings of the NASA Atmospheric Effects Working Group Meeting," Vandenburg AFB (Oct. 27-28, 1976).
8. Liu, B. Y., Fine Particles Aerosol Generation, Measurement Sampling and Analysis, Academic Press, Inc., New York (1976).

9. Victor, A. C., Breil, S. H., "A Simple Method for Predicting Rocket Exhaust Smoke Visibility," Journal of Spacecraft and Rockets (Aug. 1977).

10. Pokhil, P. F., Belyayev, A. F., Frolov, Yu, V., Logachev, V. S., and Korotkov, A. I., "Combustion of Powdered Metals in Active Media," FTD-MT-24-551-73 (1972).

11. Crump, J. E., Prentice, J. L., and Kraeutle, K. J., "Role of the Scanning Electron Microscope in the Study of Solid Propellant Combustion: II Behavior of Metal Additives," Combustion Science & Technology (1969), Vol. 1, pp. 205-223.

12. Prentice, J. L., "Aluminum Droplet Combustion Rates and Mechanisms in Wet and Dry Oxidizers," NWC-TP-5569 (April 1974).

13. Crump, J. E. (Editor), "Combustion of Solid Propellants and Low Frequency Combustion Instability," NOTS-TP-4244 (June 1967).

14. Herzberg, G., Molecular Spectra and Molecular Structure, Spectra of Diatomic Molecules, D. Van Nostrand Co., Inc., New York, N. Y. (1950).

15. Porter, R. F., Schissel, P., Ingram, M. G., "A Mass Spectrometric Study of Gaseous Species in the Al-Al_2O_3 System," Journal of Chem. Phys., Vol. 23, No. 2 (Feb. 1955).

16. Brewer, L. and Searcy, A. W., "The Gaseous Species of the Al-Al_2O_3 System," Journal Am. Chem. Soc., Vol. 73 (1951).

17. Hoch, M. and Johnston, H. L., "Formation Stability and Crystal Structure of the Solid Aluminum Sub-oxides: Al_2O and AlO," Journ. Am. Ceramic Soc., Vol. 76 (1954).

18. Yanagida, H. and Kroger, F. A., "Condensed Phases in the System Al_2O_3-Al," Ceramic Bulletin, Vol. 23 (1955).

19. Hermsen, R. W. and Dunlap, R., "Nucleation and Growth of Oxide Particles in Metal Vapor Flames," Combustion & Flame, Vol. 13, No. 3 (June 1969).

20. Frenkle, J., Kinetic Theory of Liquids, Oxford University Press, London (1946), p. 397.

21. Price, E. W., "Summary Report on Workshop on Behavior of Aluminum in Solid Propellant Combustion," Proceedings of the 13th JANNAF Combustion Meeting (Nov. 1976).

22. Bartlett, R. W. and Delaney, L. J., "Effect of Liquid Surface Tension on Maximum Particle Size in Two Phase Flow," Pyrodynamics, Vol. 4 (1966).

23. Kingery, W. D., "Surface Tension of Some Liquid Oxides and Their Temperature Coefficients," Journal of the American Ceramic Society, Vol. 42, No. 1 (January 1959).

EFFECTIVENESS OF THE SHUTTLE ORBITER PAYLOAD BAY LINER AS A BARRIER TO MOLECULAR CONTAMINATION FROM HYDRAULIC FLUIDS

R. G. Richmond, NASA-Johnson Space Center, Houston, Texas
R. M. Kelso, NASA-Johnson Space Center, Houston, Texas

1.0 INTRODUCTION

Recent investigations have identified potential source locations of contamination on the Shuttle Orbiter during on-orbit operations.[1] These sources include outgassing, offgassing, flash evaporator effluents, vernier control system, cabin atmosphere leakage and return flux. The payload bay of the Shuttle Orbiter is designed to contain numerous experiments that are expected to be extremely sensitive to even slight amounts of molecular contamination. Although the effects of molecular contamination vary somewhat for different molecular species, high molecular-weight components such as oils and hydraulic fluids can result in significant impairment of operation or degradation of experiment performance. This is particularly true in the case of experiments utilizing optical surfaces where a single monolayer of a contaminant could compromise the experiment objectives.[2,3]

One method of controlling contamination in the payload bay is the Shuttle Orbiter payload bay liner. For those specific payloads which are highly sensitive to contamination, the lower half of the Shuttle Orbiter payload bay inboard cavity will have a liner consisting of a teflon-coated Beta glass. This liner was designed to prevent particulate contamination generated in the mid-fuselage section from entering the payload bay.

Incorporated into this payload bay liner is approximately 6-1/2 ft^2 of stainless-steel filter material. This filter material will be installed in four ports on each side of the payload bay liner to permit gas exchanges

---

[1] Rantanen, R. O.; Strange Jensen, D. A., Orbiter/Payload Contamination Control Assessment Support, Final Report

[2] Richmond, Robert G. and H. N. Harmon, "An Instrument for Real-Time Detection of Contamination in Space Environmental Test Chambers"

[3] Richmond, Robert G. and J. D. Hayes, "Development of Techniques for Advanced Optical Contamination Measurement with Internal Reflectance Spectroscopy,"

between the lower mid-fuselage area and the payload bay area. Air-flow patterns between these two areas could cause significant pressure differences across the liner due to repressurization/depressurization rate changes. This filter material, rated at 35 microns, is a twilled, double-dutch-weave (TDDW) pattern which forces the gas flow to change directions twice in passing through the filter.

In the Shuttle Orbiter configuration, hydraulic fluid systems are used to provide the power to actuate devices such as the elevons, main engine gimbal and control systems, landing gear, brakes, and steering mechanisms. The Shuttle Orbiter hydraulic subsystem is shown in figure 1. This power is derived from three, independent, hydraulic pumps, each driven by its own hydrazine-fueled auxiliary-power unit and cooled by its own water boiler. During on-orbit conditions these devices are not in operation, and the hydraulic fluid is kept warm by heat from the freon loop. The hydraulic pumps are located on the aft bulkhead of the Orbiter. Numerous fluid lines for these pumps are routed beneath the payload bay. Should leaks occur in these hydraulic fluid lines, hydraulic fluid could (1) saturate the payload bay liner and be emitted into the payload bay; and/or (2) transmit through the filter material where it could condense on sensitive payload experiments within the Orbiter's bay producing deleterious effects.

Recent investigations have been conducted to determine the effectiveness of the payload bay liner and filter material to serve as barriers to hydraulic fluids if spills or leaks occur in the hydraulic fluid lines. The specific objectives of these studies were as follows:

(1) Measure the transmission rate of the hydraulic fluid through representative samples of the payload bay liner and filter material. The hydraulic fluid used in this experiment is manufactured per specification MIL-H-83282A and consists of a blend of several different fluids. The average molecular weight is 421. Its specific heat and vapor pressure at 37.7°C are 0.50 BTU/LBM°F and 0.6 torr, respectively.

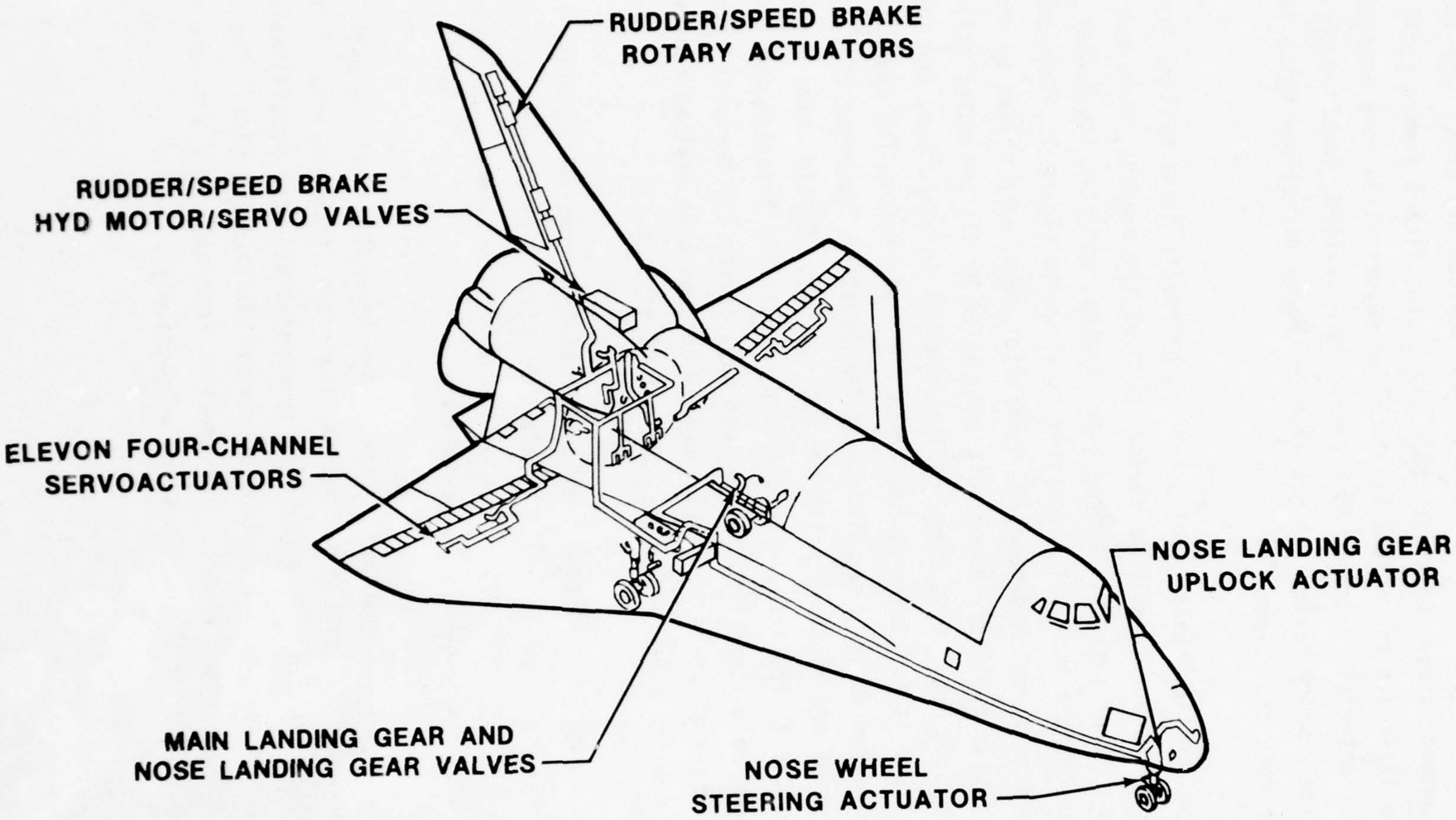

FIGURE 1.- SHUTTLE ORBITER HYDRAULIC SUBSYSTEM.

(2) Measure the relative condensation coefficient for the hydraulic fluid. The condensation coefficient is a dimensionless number that represents the ratio between the rate at which molecules actually condense on a surface and the rate at which they strike the surface.[4]

(3) Measure desorption rates for the hydraulic oil from contamination sensors. Since the hydraulic fluid is made of a combination of components, these components may condense at different collecting surface temperatures. Desorption rate measurements were performed to determine at what temperatures the condensed products would desorb from the quartz crystal microbalance.

2.0 EXPERIMENTAL APPROACH

The approach to this series of experiments was simple and straightforward - to simulate a hydraulic fluid leak and measure its transmission rate through single layers of the subject materials. To better understand the mechanisms of the molecule - surface interactions, and to assist in math modeling of the bay molecular contamination environment, the molecular condensation coefficient, and mass desorption rates were measured.

Since molecular contamination stemming from Shuttle Orbiter hydraulic fluid lines are considered leaks, a "molecular generator" to simulate an oil leak was designed and fabricated. Although we have designed and used molecular <u>beam</u> generators,[5,6] the use of a broader molecular source would more closely simulate an actual spill or leak. Total mass loss data of the oil (Bray Oil Co. #83282) at room temperature, 37.7°C, and 65°C at 10^{-5} torr suggests that mass flux rates from even small samples would

---

[4] Dushman, S. (ed.), <u>Scientific Foundations of Vacuum Techniques</u>

[5] Richmond, R. G., "Molecular Beam Generator"

[6] Nuss, H. E., "Molecular Contamination Studies by Interaction of a Molecular Beam with a Platinum Surface"

exceed 1 x 10^{-8} gm/cm^2.sec. These rates are measurable with the mass flux sensor (a thermoelectrically-cooled quartz crystal microbalance, TQCM) but cause some inconvenience because of saturation effects.[7,8] An incident mass flux rates of 1 x 10^{-9} gm/cm^2.sec. or less would be ideal in terms of TQCM saturation effects and still maintain reasonably good measurement statistics.

3.0 EXPERIMENT CONFIGURATION

The requirements discussed above led to the configuration shown schematically in figure 2. The experimental series was conducted in a small space environment simulation chamber. The dimensions of the chamber are 1.1 m diameter and 1.4 m long; its vacuum system consists of a mechanical roughing system and two 4100-liter/sec. oil diffusion pumps with liquid-nitrogen-cooled baffles to reduce backstreaming of hot oil molecules into the test region. A liquid-nitrogen-cooled shroud installed within the chamber serves as a heat sink and cryogenically pumps condensable gases such as carbon dioxide and water vapor. Other main elements, viz. the molecular generator, the samples, and the TQCM and data system are described below.

3.1 Molecular Generator

The molecular generator consisted of standard, off-the-shelf vacuum system components. The oil reservoir was simply a small 1.0" quartz viewport mated to a 2-3/4" vacuum flange. Two copper-constantan thermocouples, a small 50 watt thin-film heater and fiber glass tape insulation were used to measure and control oil temperature. The remainder of the system were four "drift tubes" 1.5" diameter with mating 2-3/4" vacuum flanges and a right-angle valve. Wrap-around heaters were used on all drift tubes and valve and maintained at least 30°C higher temperature than the oil to prevent condensation on the walls of the molecular generator.

---

[7] Visentine, J. T., R. G. Richmond, and R. M. Kelso, "Experiment to Measure Molecular Outgassing Rates from Shuttle Orbiter Flexible Reusable Surface Insulation (FRSI)"

[8] Dillow, C. F., T. H. Allen, R. M. F. Linford, and Robert G. Richmond, "A System for the Study of Molecular Contamination"

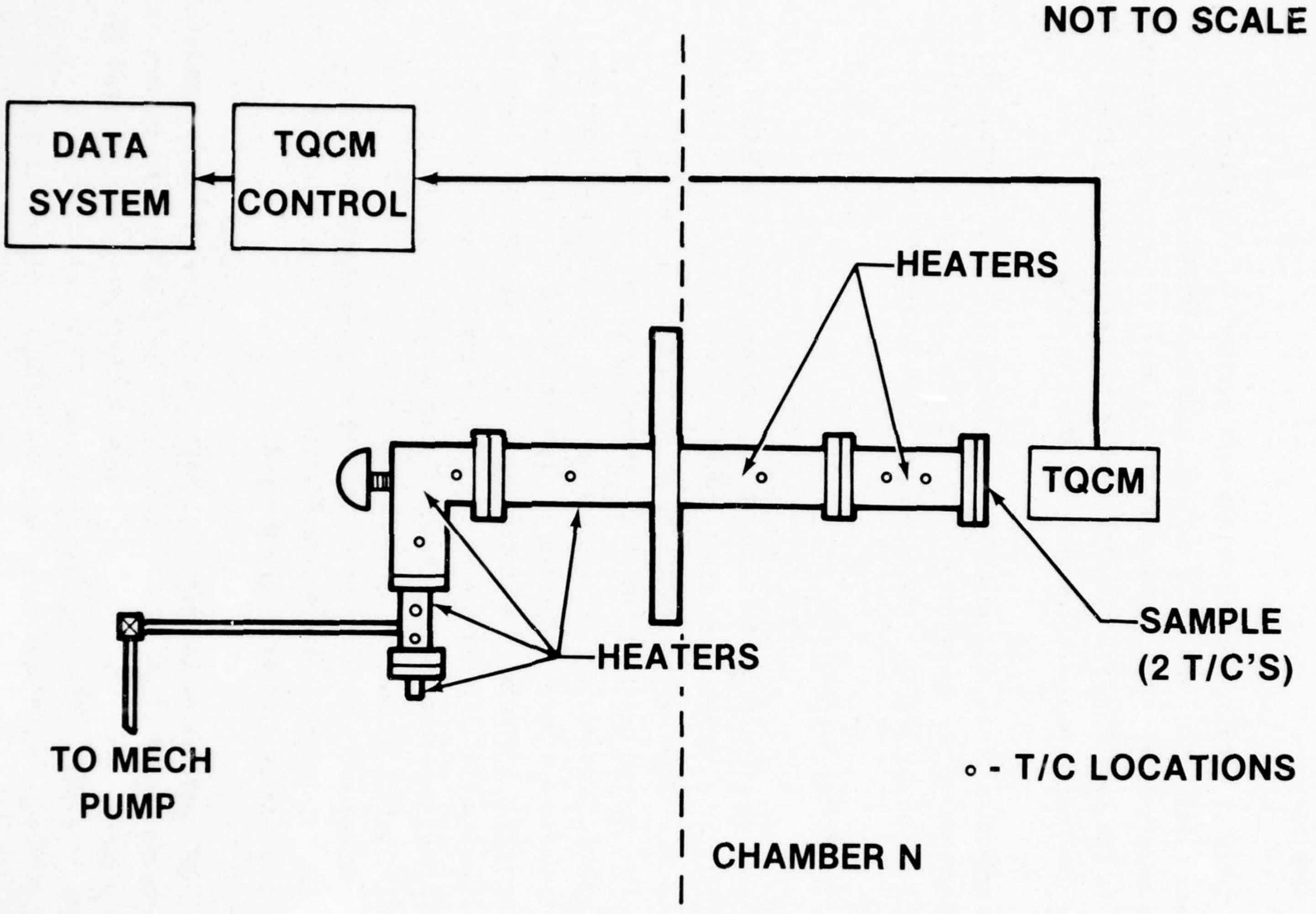

FIGURE 2.- EXPERIMENT CONFIGURATION.

3.2 The Samples

Two types of single-layer materials were evaluated: (1) a teflon-coated Beta glass cloth, and (2) a twilled, double-dutch-weave, TDDW stainless-steel filter. The teflon-coated Beta glass cloth, Dodge Industries, X-389-7, is the same 8 oz/yd^2 material used in the manufacture of space suits since the Apollo program. The samples are shown in figure 3.

The hydraulic fluid used in these experiments is Bray Oil Company No. 83282, manufactured per specification MIL-H-83282A and consists of a blend of several different fluids. The average molecular weight is 421.

3.3 Quartz Crystal Microbalance

The sensing element for this series of experiments was the TQCM. The TQCM consists of a sensor, heat sink, and electronics unit and is designed to operate in a space environment. The sensor consists of two 10-MHz piezoelectric quartz crystals, which are thermally controlled with a two-stage thermoelectric device. A precision platinum resistance thermometer is used to measure crystal temperature. The front crystal (sensing crystal) is located behind a window in a sensor cover. The second crystal (reference crystal) is situated directly behind the sensing crystal, which shields it from the molecular sources in the external environment. The heat sink is used to dissipate heat removed from the thermoelectric device when the crystals are cooled. The electronics unit generates voltages that drive the crystals to produce an audio beat frequency signal from which the condensing molecular flux rates are derived.

The TQCM operates on the principle that the quantity of mass accumulated on the sensing crystal, i.e. the incident molecular flux less the evaporating flux, is directly proportional to the changes in beat frequency produced by the electronics unit. The time rate of change of the beat frequency provides a measurement of the molecular flux as mass condenses on the sensing crystal. The sensitivity for the TQCM is typically 3.5×10^{-9} gm/cm^2-Hz, and when it is used with a data system capable of resolving frequency changes as small as 0.1 Hz, mass loadings as small as 3×10^{-10} and repro-

S- 78- 26271

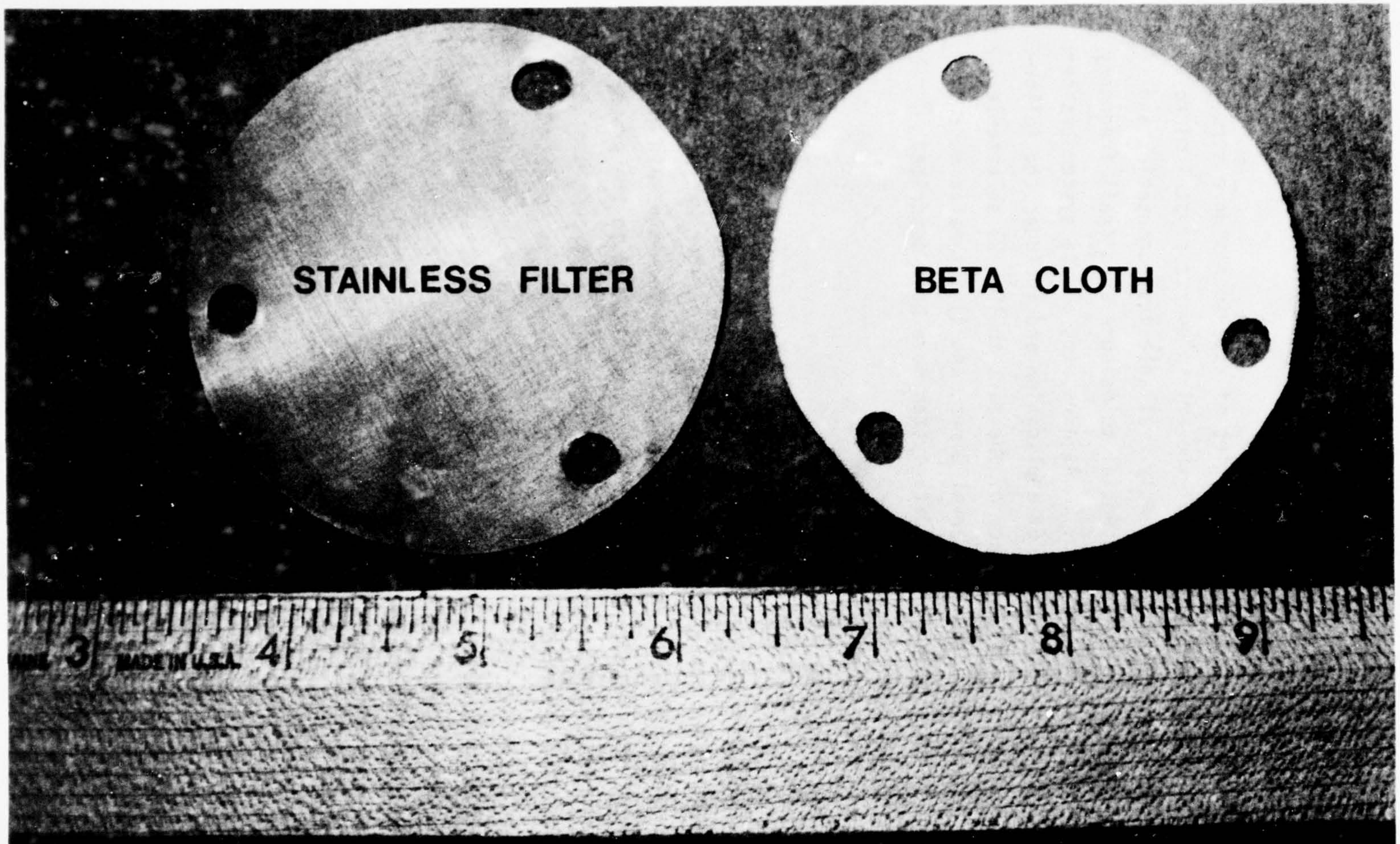

FIGURE 3.- SAMPLES OF PAYLOAD BAY LINER AND STAINLESS STEEL FILTER CLOTH.

ducible flux rates as low as 7 x 10^{-12} g/cm^2.sec. have been detected.[7] A diagram of the TQCM is shown in figure 4.

Data system requirements for this series of experiments were straightforward although they represent state-of-the-art in quartz crystal microbalance measurements. Review of currently available instrumentation and techniques has shown few with any potential to measure such small frequency changes (averages of 2 x 10^{-3} Hz/sec.). As a result, a data system has been designed specifically for this type of application and includes the following general capabilities: 1) accuracy of one part in 10^5, 2) selectable integration times, 3) selectable interval times, and 4) automatic mode of data recording. The details of this data system have been described elsewhere[9] and will not be included here.

4.0 EXPERIMENTAL PROCEDURE

The vacuum chamber was pumped to the 10^{-6} torr range with the liquid nitrogen coldwall fully operational. The molecular generator was heated (oil to 65°C, drift tubing to 95°C) but was valved off from the main chamber. The TQCM, mounted on a rotational feedthrough, was adjusted to the proper temperature and rotated out of the beam to measure any background contamination. The molecular generator was rough pumped a few minutes to eliminate the bulk of air present. The roughing valve was closed and the molecular generator was opened to the main chamber. The TQCM was rotated into the beam for measurements every half hour. Rotation of the TQCM out of the beam prevented saturation of the sensor crystal. This general approach, both with and without samples installed, was used throughout this experiment series.

---

7. Visentine, J. T., R. G. Richmond, and R. M. Kelso, "Experiment to Measure Molecular Outgassing Rates from Shuttle Orbiter Flexible Reusable Surface Insulation (FRSI)"

9. Richmond, R. G., "Instrumentation for Measuring Low-Level Currents/Voltages"

AD-A070 386 AIR FORCE MATERIALS LAB WRIGHT-PATTERSON AFB OH F/G 22/2
PROCEEDINGS OF THE USAF/NASA INTERNATIONAL SPACECRAFT CONTAMINA--ETC(U)
1978 J M JEMIOLA
UNCLASSIFIED AFML-TR-78-190 NL

10 OF 13
AD
A070386

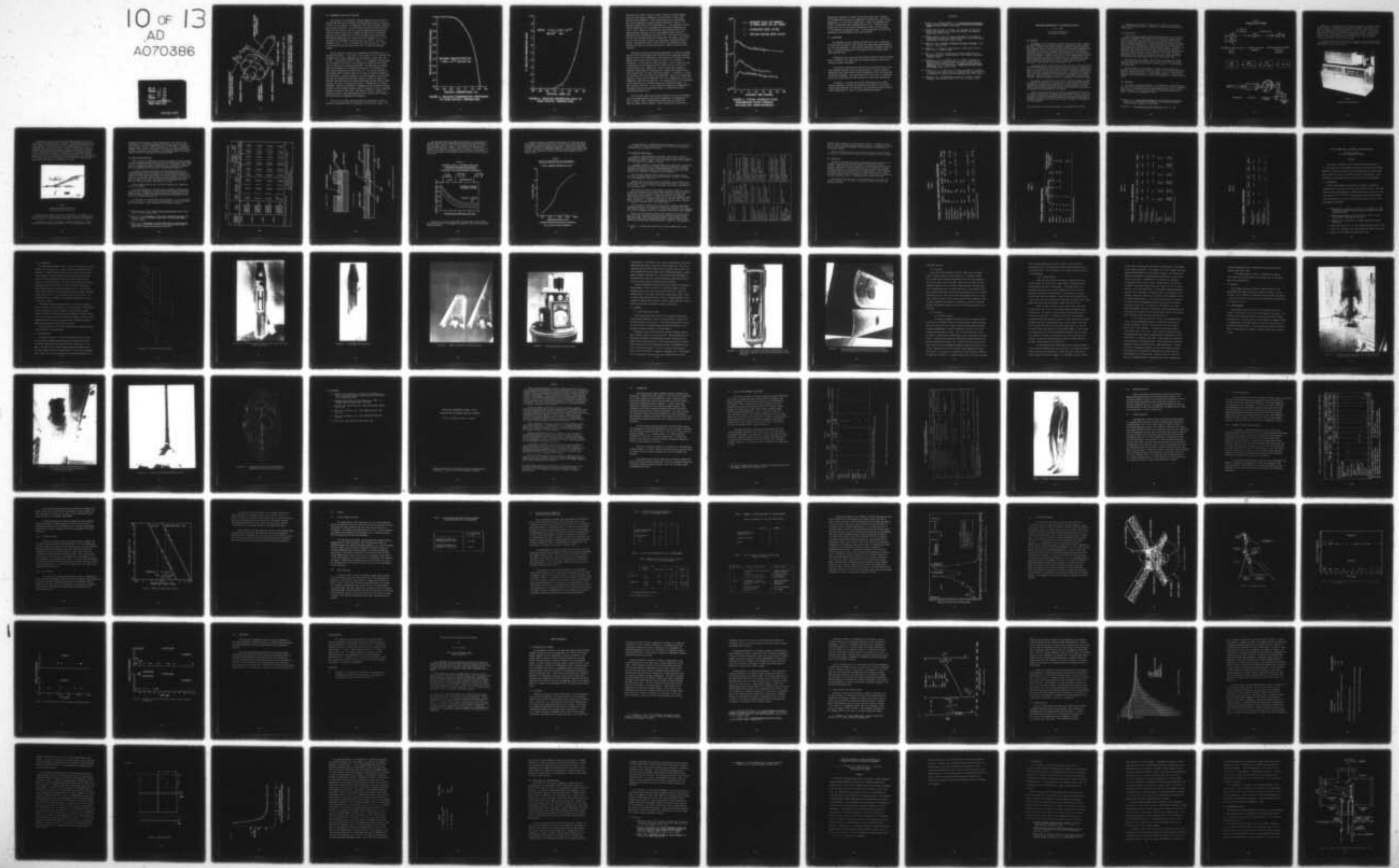

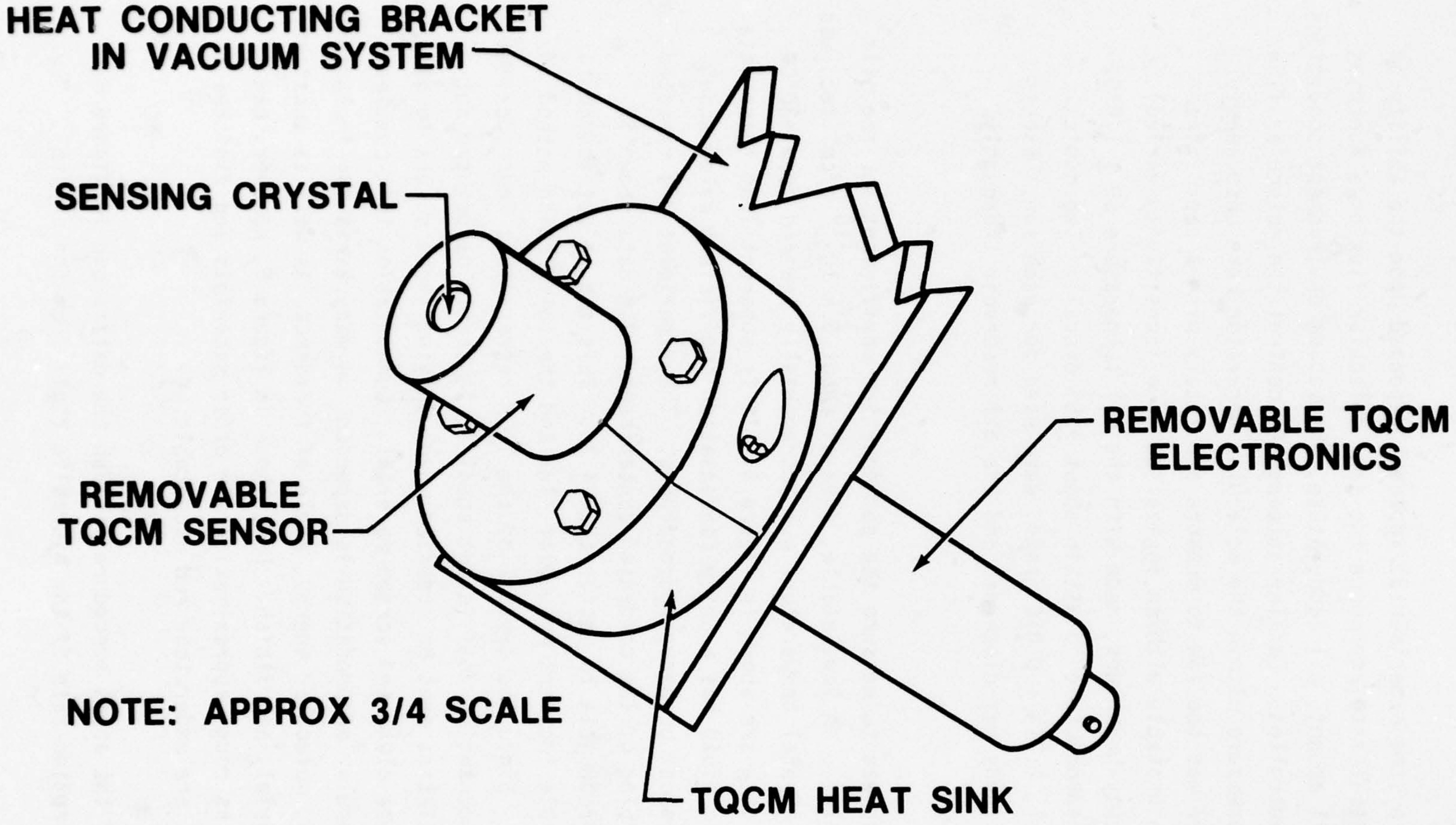

NOTE: APPROX 3/4 SCALE

TQCM SENSITIVITY: 4×10^{-9} g/cm^2 · Hz

FIGURE 4.- THERMOELECTRICALLY-COOLED QUARTZ CRYSTAL MICROBALANCE (TQCM).

5.0 EXPERIMENTAL RESULTS AND DISCUSSION

The success of the experimental approach depended upon the ability of the molecular generator to reproduce the same molecular flux as a function of time if the oil amount, oil temperature, and vacuum environment conditions were carefully controlled. Earlier attempts to control the molecular flux solely with the pressure within the molecular generator were unsuccessful since the pressure was too low to measure accurately with a capacitance manometer and too unstable with an ionization gage (sensitivity varied). Four separate twenty-hour runs, made with the oil temperature 65 ± 1.5°C, indicate a flux reproducible to within about ± 6% overall. Two cubic centimeters of oil, 1.713 ± 0.016 grams, were used for each run. Excess oil from previous runs was discarded and the oil reservoir thoroughly cleaned.

The next step was to measure the condensation coefficient for the oil (no sample installed). A low, stable, flux of about 5×10^{-10} g/cm^2.sec. was produced and the crystal temperature was incrementally lowered from +30°C to -40°C. These data are shown in figure 5. It is apparent from these data that the hydraulic fluid has a unity condensation coefficient below about -25°C, a value typical of heavy hydrocarbons. The experiment was repeated after rapid desorbing of the condensed contaminant. The data shown in figure 5 were reproducible to better than ± 3%. This can be attributed to the extremely stable incident molecular flux and the integration method of data acquisition. Since the crystal of the TQCM represents a "near perfect" substrate for condensation coefficient studies, it should be pointed out that some uncertainties must be expected when applying these values to other surfaces, e.g. Beta cloth and screen material. Condensation is a complex phenomenon. Molecular accomodation is dependent on many variables including molecular species, molecular energy, angle of incidence, as well as substrate temperature, material, and finish. Data shown in figure 5, however, can probably be used as rough approximation for other materials and finishes if the uncertainties are understood and acceptable.

A reverse of the above procedure yielded the data shown in figure 6, the relative desorption rate of the hydraulic fluid from the crystal. The

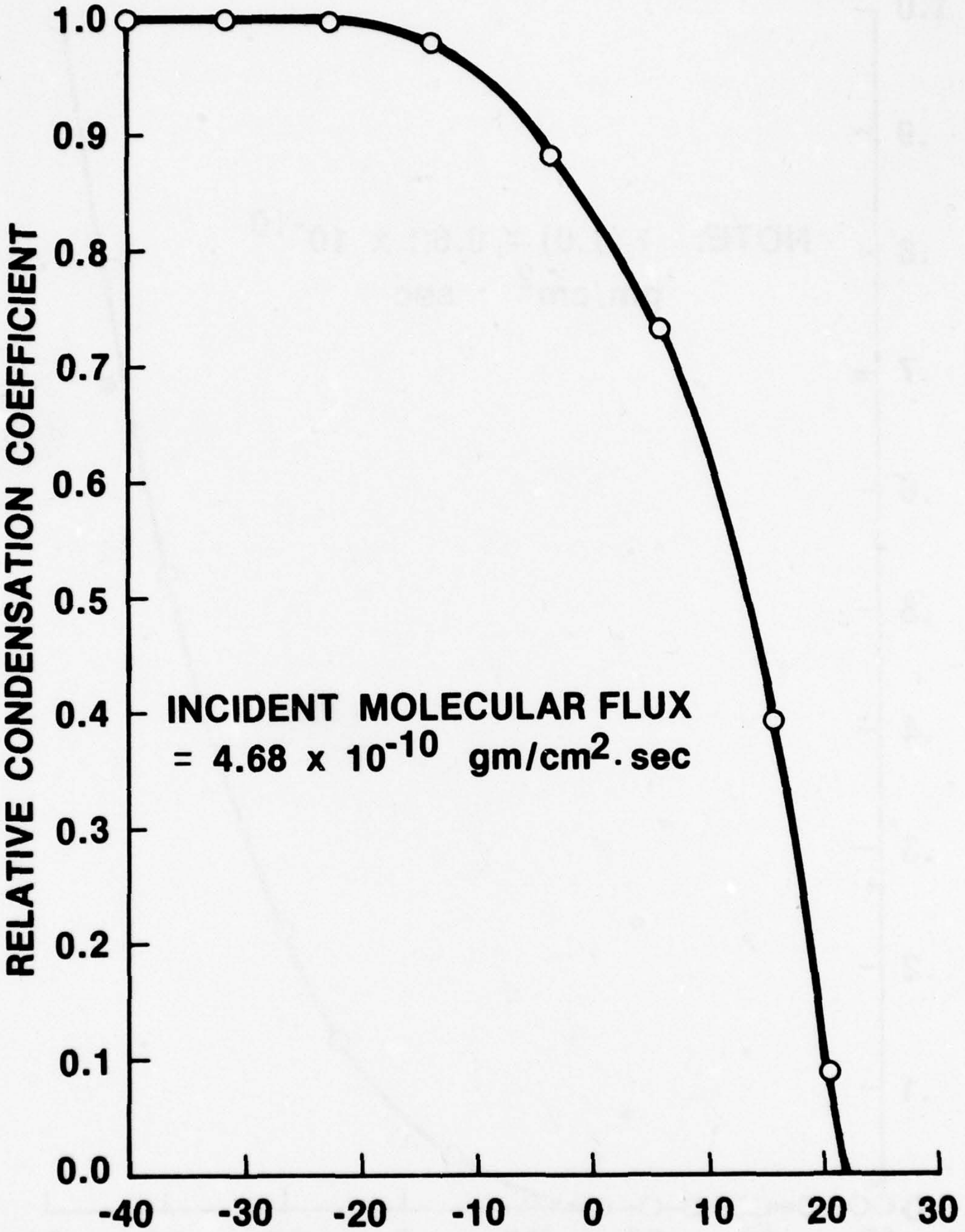

FIGURE 5.- RELATIVE CONDENSATION COEFFICIENT VS TQCM CRYSTAL TEMPERATURE.

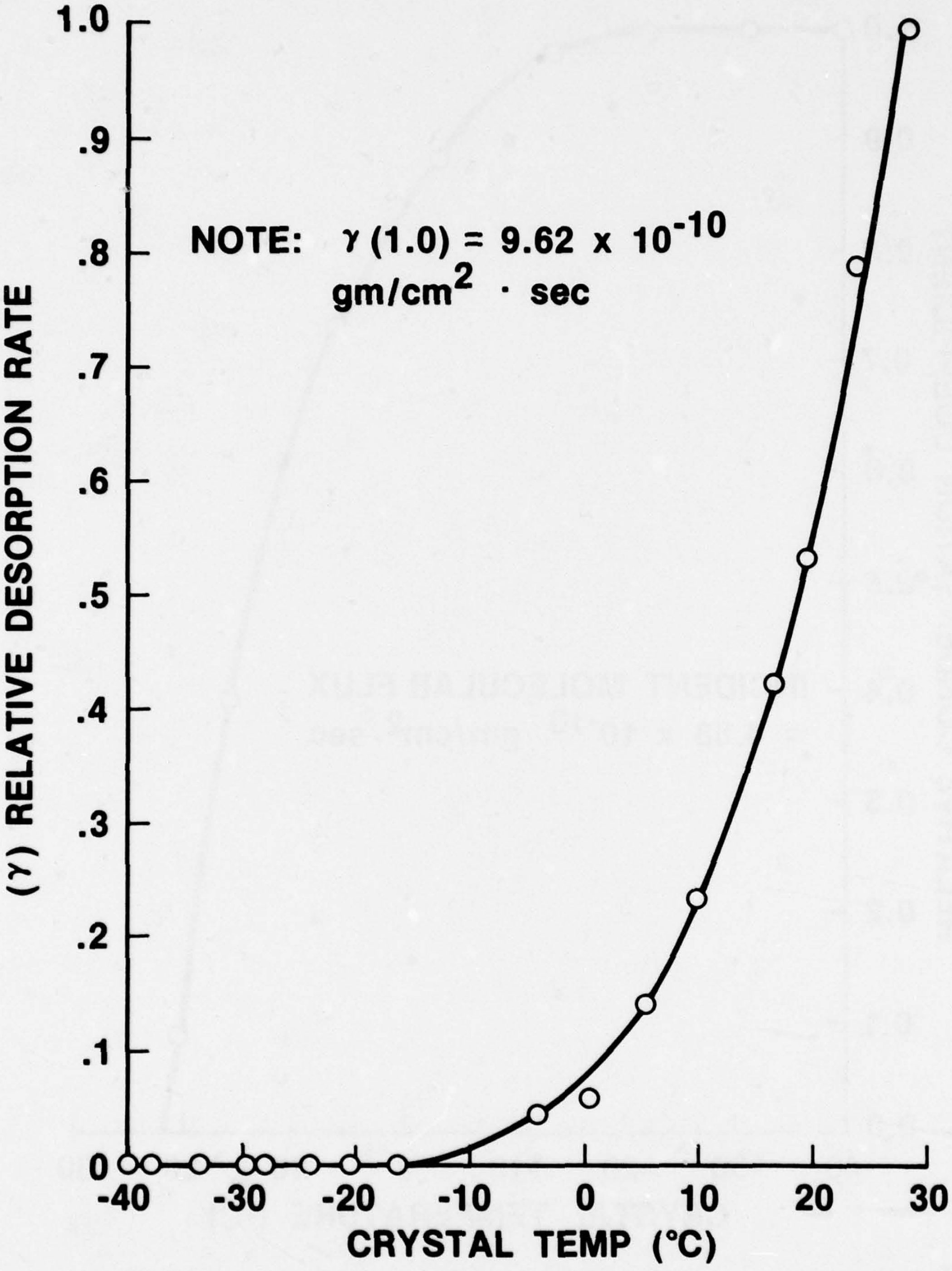

FIGURE 6.- RELATIVE DESORPTION RATE VS TQCM CRYSTAL TEMPERATURE.

desorption rates shown in figure 6 are not linear but increase exponentially with microbalance temperature, results typical of heavy (high molecular mass) compounds. It was stated earlier that the accumulated mass flux as measured by a quartz crystal microbalance is equal to the incident molecular flux less the evaporated flux. This experiment verified that the evaporated flux is negligible for microbalance temperatures of -25°C or less. Repeat of this experiment showed reproducibility of the measured values to average ± 8.7%, a value somewhat poorer than that measured for the condensation coefficient study. This can be attributed to the fact that adsorbed molecules can migrate over the surface, giving rise to collisions with other molecules, and aggregates of adsorbed molecules develop. Aggregates are bound to each other by the condensation energy. Uncertainties then can be caused by molecular "island" clustering on the substrate.

The molecular generator was operated sans sample to verify the incident molecular flux, and the samples were installed and the experiment repeated. Typical results of the transmission of the hydraulic oil through the screen material and the Beta cloth are shown as curves 2 and 3 of figure 7, respectively. As can easily be seen from figure 7, after 12 hours the rate of transmission of the hydraulic fluid is about 24.8% and 18.4% for the screen and Beta cloth, respectively. Both of these values represent a remarkable effectiveness in inhibiting fluid transmission considering the woven characteristics of these single-layer samples. In addition, it should be noted that, due to the nature of the experiment, none of the samples were operated at lower than room temperature 25 ± 3°C, a temperature in which the condensation coefficient is near zero. This suggests that all fluid molecules follow line-of-sight or scattered trajectories through the sample, i.e., none "saturate" the cloth. It was noted that increasing the temperature of the sample to 60°C had no measurable effect in increasing the rate of transmitted molecular flux.

One of the more significant on-orbit conditions could not be simulated by our experiment geometry, viz. when the hydraulic fluid temperature is near its nominal value. These conditions occur after the payload bay doors are opened, and the hydraulic fluid is kept warm by circulating it

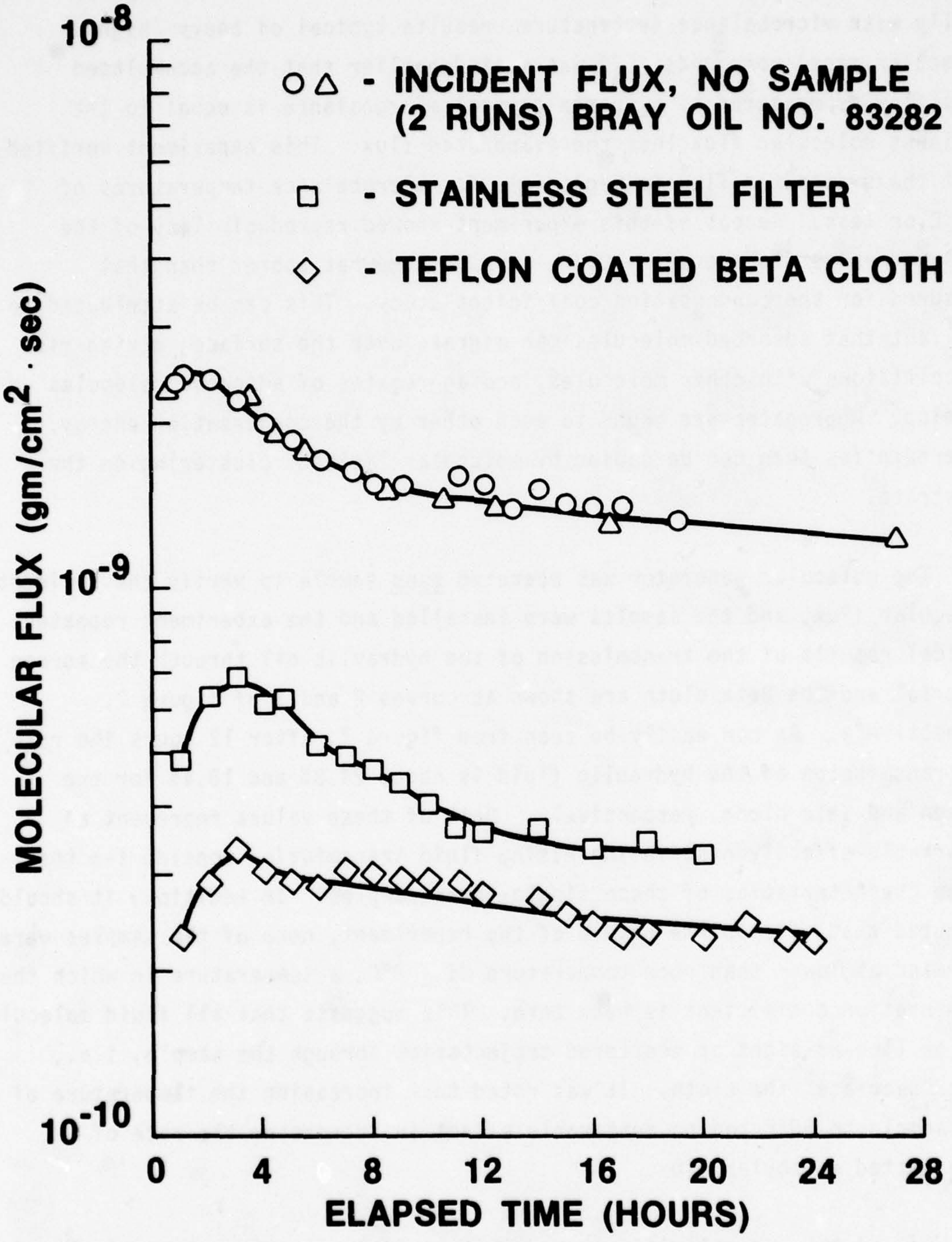

FIGURE 7.- TYPICAL HYDRAULIC FLUID TRANSMISSION RATES THROUGH PAYLOAD BAY LINER MATERIALS.

NASA-JSC

through heat exchangers to transfer heat from the freon loop. Hydraulic fluid temperatures and bay liner temperatures corresponding to this mission sequence are -1.1°C and -60°C, respectively. Lower fluid temperature will result in significatly lower incident molecular flux. In addition, the payload bay liner at -60°C should condense any incident flux and prevent it from reaching the experiment areas. The data generated by the described experiment can be considered as worst-case simulation.

6.0 CONCLUSIONS

An experiment has been conducted to measure the rate of transmission of Shuttle Orbiter hydraulic fluid through two single-layer sample materials for one fluid temperature. These materials demonstrate remarkable effectiveness in inhibiting transmission of the hydraulic fluid considering their woven characteristics.

Although one of the more significant Shuttle Orbiter on-orbit conditions was not simulated it was shown that the conducted experiment could be considered as a worst case example.

The effective condensation coefficient and the desorption rate of the Shuttle Orbiter hydraulic fluid has been measured, utilizing a sensitive thermoelectrically-cooled quartz crystal microbalance, TQCM, and unique data acquisition techniques. The values determined by this series of experiments are basically consistent with those measured for other heavy hydrocarbons.

In addition, it has been conclusively demonstrated that a simple molecular generator, designed and contructed from standard, off-the-shelf vacuum system components, can effectively and consistantly produce molecular fluxes simulating an oil leak in a space-simulated environment.

REFERENCES

1. Rantanen, R. O., Strange Jensen, D. A., Orbiter/Payload Contamination Control Assessment Support, Final Report, Martin Marietta Aerospace (1977).

2. Richmond, Robert G. and H. N. Harmon, "An Instrument for Real-Time Detection of Contamination in Space Environmental Test Chambers," NASA SP-298, (1972), p. 503.

3. Richmond, Robert G. and J. D. Hayes, "Development of Techniques for Advanced Optical Contamination Measurement with Internal Reflectance Spectroscopy," NASA SP-336, (1973), p. 609.

4. Dushman, S. (ed.), Scientific Foundations of Vacuum Techniques, Wiley, New York, (1962), p. 18.

5. Richmond, R. G., "Molecular Beam Generator," *NASA Technical Brief*, Vol. 1, No. 3, (1976), p. 380.

6. Nuss, H. E., "Molecular Contamination Studies by Interaction of a Molecular Beam with a Platinum Surface," NASA Technical Memorandum TMX-58169, (1976).

7. Visentine, J. T., R. G. Richmond, and R. M. Kelso, "Experiment to Measure Molecular Outgassing Rates from Shuttle Orbiter Flexible Reusable Surface Insulation (FRSI)," Progress in Astronautics and Aeronautics, Vol. 56, Thermophysics of Spacecraft and Outer Planet Entry Probes, AIAA, (1977), p. 197.

8. Dillow, C. F., T. H. Allen, R. M. F. Linford, and Robert G. Richmond, "A System for the Study of Molecular Contamination," presented at the 9th International Space Simulation Conference, NASA SP-379, (1975).

9. Richmond, R. G., "Instrumentation for Measuring Low-Level Currents/ Voltages," NASA Technical Brief, Vol. 1, No. 4, (1976), p. 534.

PARTICULATE CONTAMINATION - TIE-DOWN WITH PARYLENE C

W. E. Loeb*

Union Carbide Corporation
Electronics Division

1.0 Abstract

Entrainment of loose conductive particles within microcircuit packages has been documented as a persistent problem. Occasionally, small, usually microscopic, pieces of metal remain inside hermetically sealed devices despite strenuous efforts to assure cleanliness during manufacturing operations. The problem is of particular concern when hybrid circuits are employed on spacecraft, where stresses encountered during launch can cause previously undetected particles to migrate from innocuous positions to places resulting in electrical shorts. Measures taken, both to test packaged devices for the presence of these particles and to remove them, have included among other means radiographic examination and particle impact noise detection (PIND). Still, small particles can escape notice and non-conducting particles, especially in PIND testing, can cause part rejection.

A positive solution, employed successfully for NASA's Centaur electronics and under evaluation by military agencies, involves a plastic coating, Parylene C. At a thickness of 0.1 mil this material effectively encapsulates and seals (ties down) the offending particles in place, preventing further movement to positions causing electrical malfunction. Additionally, the parylene coats and, thus, insulates all surfaces inside the package so that larger particles, should they manage to break loose, cannot impair electrical performance. Additional process detail will be presented in this review paper.

In contrast to conventional liquid resins, parylene coatings are formed by pyrolysis of high purity di-p-xylylene in a vacuum environment followed by deposition and spontaneous polymerization on cool surfaces. The process resembles vacuum metallizing except that the parylene monomer molecules, while in the gas phase, surround the object to be coated and cause growth of the coating to occur uniformly on all surfaces.

Certain unique features make the parylene system suited for particle tie-down: the ability of the monomer gas to penetrate holes and, thus, coat the inside of microcircuit packages; the ability of the coating to conform precisely to convoluted surfaces including wire bonds and the underside of inverted chip devices; and its ability to cover thoroughly at thicknesses of 0.1 mil and below.

---

*The author now is with Gnostic Concepts, Inc., Menlo Park, CA 94025.

Compatibility of Parylene C coatings with active and most passive devices has been demonstrated. Documentation of these and the exceptions will be given.

2.0 Introduction

Despite exhaustive measures taken during manufacture, loose conductive particles occasionally remain trapped within hybrid microcircuit packages. Sources of contamination, inspection for it, and ease of removal after various fabrication stages have recently been reviewed[1] as part of an ongoing study being made under Air Force sponsorship. While debris generated prior to sealing can generally be observed and removed, solder balls and weld splatter can form during the sealing operation itself. Obviously, contamination of this nature cannot be removed without opening the device. Electrical tests alone do not always reveal the presence of such particles, which can lodge innocuously yet move under spacecraft launch stresses to places where they can cause electrical shorts. As a result, additional testing has become necessary in attempts to prevent contaminated hybrid microcircuits from being installed in critical application areas.

One widely used test regime, particle impact noise detection (PIND), involves vibrating sealed devices while they are acoustically monitored. Costs have been high, due especially to part rejection.[2] Other approaches are being sought.

One such approach is to immobilize trapped particles within device packages by coating them with plastics or resins. This procedure has become known as "particle tie-down" or "closed package" control. The remainder of this paper describes Parylene C, a vapor deposited plastic, used for this purpose. Silicone resins are also under investigation in the study referenced above.[1]

3.0 Parylene C

This family of polymers (Parylene C is one member) is formed by deposition from a low pressure gas directly on the object to be coated. The monomer gas, in turn, is generated from a corresponding high purity solid, called di-para-xylylene; in the case of Parylene C, dichloro-di-para-xylylene or DPX-C. The process is diagrammed in Figure 1.

(1) Malloy, G. T., Microcircuit Packages Free of Loose Metallic Particles; Quarterly Report IR-S13-6-(1); September, 1977; Air Force Contract F33615-76-C-5273; Hughes Aircraft Company.

(2) Miller, B., Aviation Week and Space Technology, April 11, 1977.

FIGURE 1

PARYLENE DEPOSITION PROCESS

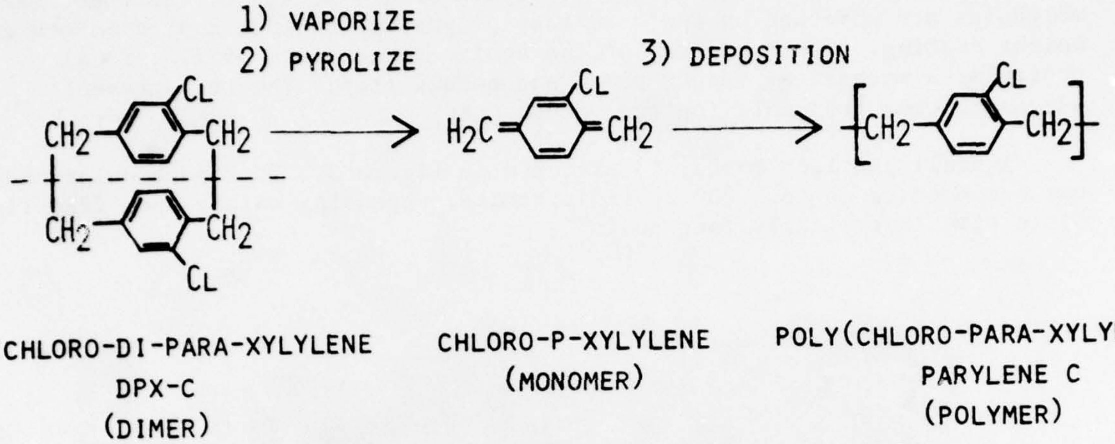

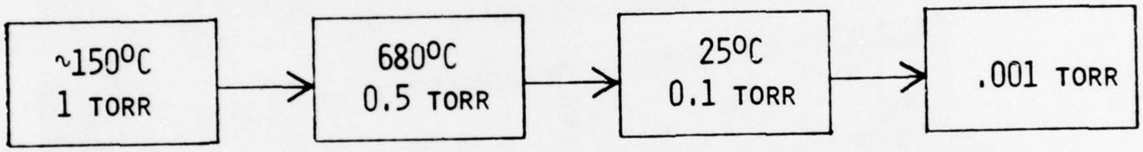

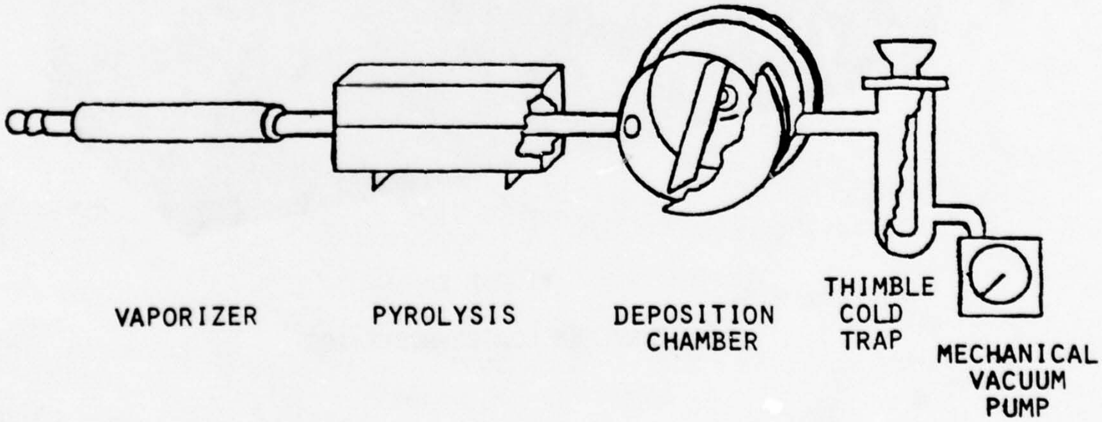

DPX-C, first vaporized at 150°C, 1 mm pressure, passes through a tubular furnace where it is quantitatively pyrolyzed to monomer. The monomer gas enters a chamber containing the substrate to be coated. Substrates remain near room temperature even though pyrolysis occurs at 680°C. As these gas molecules are absorbed on surfaces they polymerize to form a high molecular weight coating. The remainder of the equipment consists of electrical controls, a mechanical vacuum pump, and a cold trap. The trap prevents excess monomer from entering the vacuum pump.

A small parylene coater is pictured in Figure 2. This particular model can accommodate up to 2,000 hybrid circuits, depending mainly upon fixturing. Cycle time is typically four hours.

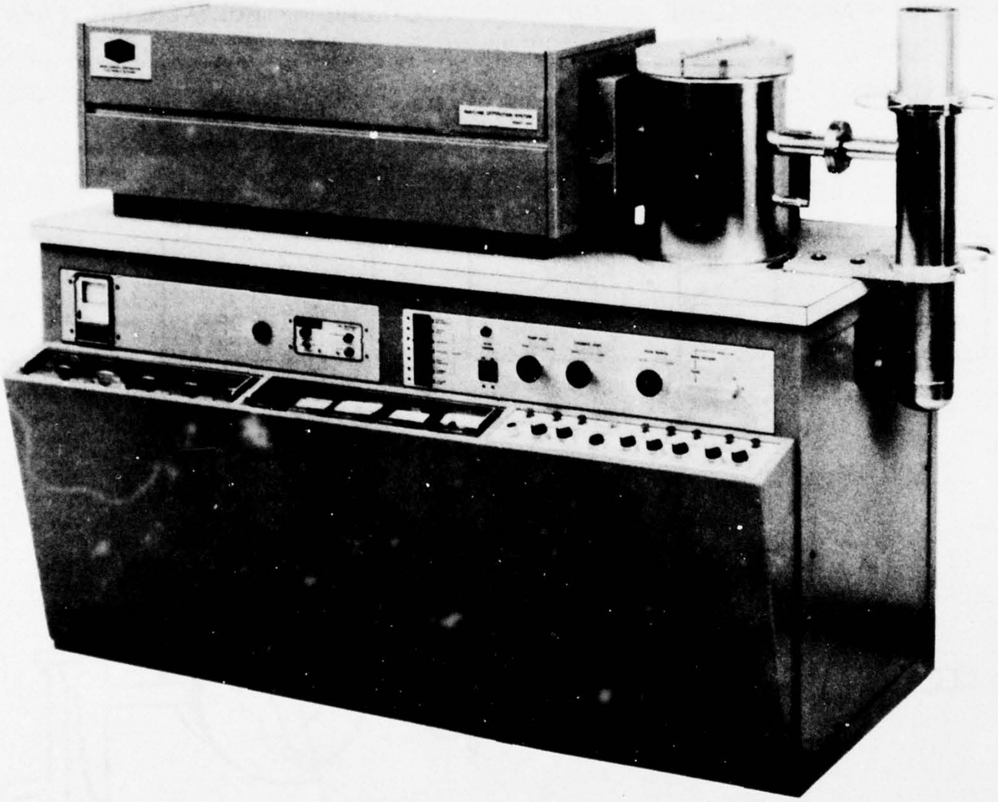

FIGURE 2

PARYLENE COATER-MODEL 10C

Regarding this process, note that spontaneous polymerization occurs on all substrate surfaces without catalysts. Polymerization catalysts are either ionic or free and radical in nature and can adversely affect electrical performance. Furthermore, there is no intermediate liquid state; therefore, post-cure is not required. Curing of liquid resins is usually accompanied by shrinkage with resulting exposure of edges and other stress points. Another feature enhancing the conformality of parylene coatings is the low monomer gas viscosity. Substrates are surrounded and monomer approach takes place at uniform rates from all directions. The process, in other words, has good throwing power and affords protection of areas difficult to access by other means. Conformality is illustrated in Figure 3 which shows a beam lead coated at a thickness of 0.5 mil.

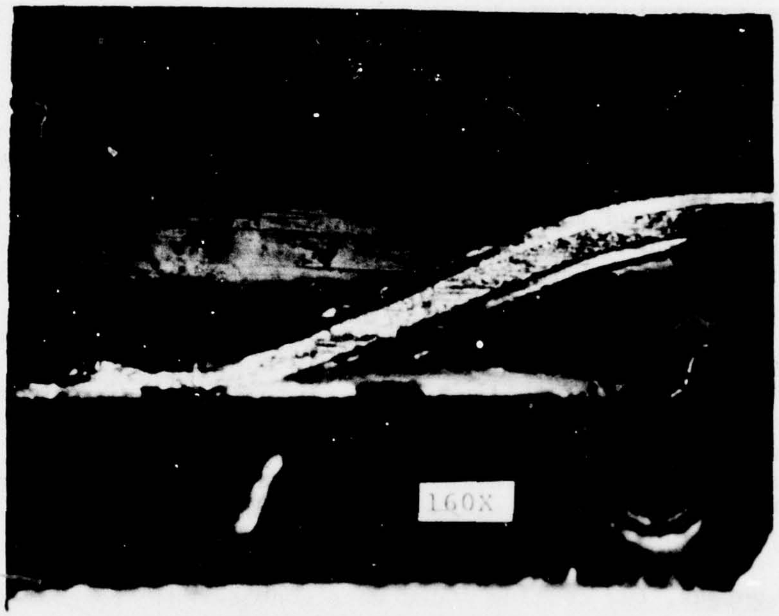

FIGURE 3

BEAM LEAD COATED WITH PARYLENE C
(Courtesy Northrop Electronics)

Parylene N, the parent hydrocarbon of this family of polymers, and parylene D, with two chlorine atoms per aromatic ring, have also been used in selected areas. Detailed property tabulations are given in Appendix A.

In addition to their conformality, the other unique feature of the parylenes is their freedom from pinholes. This is related both to their spontaneous polymerization without shrinkage and to the physics of the polymerization. Theoretical considerations indicate that chain growth occurs only in the outer 1,000Å surface of the bulk polymer. For application on hybrid circuits, typical thicknesses are 0.15 mils, equivalent to 38,000Å. Thus, growth of a Parylene C coating may be likened to multiple dipping and curing (an accepted means for eliminating pinholes with liquid resins) in which the operations are repeated 38 times.

4.0 Use on Hybrid Circuits

Use of parylene to immobilize particles encountered in hybrid packages was first studied by Hughes Aircraft Company for Goddard Space Flight Center in 1971.[3] Subsequently, work at Hughes Aircraft[4] for Marshall Space Flight Center established the debris holding ability as a function of thickness. Type of contamination and test results are reproduced in Table I.

Vibration and shock testing were conducted both before and after thermal exposure at 125°C for 1,000 hours. From these tests it was concluded that immobilization performance was satisfactory at thicknesses in excess of 0.15 mil and, in most cases, at 0.1 mil or above. In the case of lead shot, it was noted that these particles were substantially larger, 75 mils in diameter, than those encountered in hybrid packages and, being spherical with point contact, were difficult to hold.

Device compatibility was also reported by Hughes and is summarized later in this paper.

Most recently Parylene C has been used to eliminate problems caused by particulate contamination in hybrid microcircuits used on the Centaur launch vehicle. Teledyne Microelectronics Division[5] working jointly with NASA Lewis Research Center developed tooling for coating hybrid circuits up to 1 1/4 x 1 1/4 inches in size.

At the outset, two coating modes were considered: to coat the devices prior to lidding or to coat through a pretapped hole in the lid, followed by sealing the hole. These alternatives are depicted in Figure 4.

(3) Hughes Aircraft Company, Hybrid Parylene Coating Study, Report Reference No. C-7746/2, August 1972.

(4) Oberin, F. W., Development for Application of Parylene Coatings, NAS Contract 8-29940, Final Report, June 1974, NTIS N75-12208, Hughes Aircraft Company.

(5) Wylie, D. M., Development of Parylene Passivation for Centaur Hybrid Microcircuits, Final Report NASA CR 135071, Contract NAS 3-19144, August 1976, Teledyne Microelectronics Division.

TABLE I – RESULTS OF SHOCK AND VIBRATION TESTING OF DEBRIS SPECIMENS[4]

Coating Thickness (inches)	Debris Type	Shock	Vibration	Both	Shock		Vibration		Both	
		(Prior to Thermal Aging)			(After Thermal Aging 1000 Hours at 125°C)					
					N_2	N_2O_2	N_2	N_2O_2	N_2	N_2O_2
0.0001										
	Lead shot	F	–	–	–	–	–	–	–	–
	Tangsten	P	P	P	P	P	P	P	P	P
	Silicon chips	PF	P	PF	PF	PF	P	P	PF	PF
	Gold wire	P	P	P	P	P	P	P	P	P
0.00015										
	Lead shot	F	–	–	–	–	–	–	–	–
	Tungsten	P	P	P	P	P	P	P	P	P
	Silicon chips	P	P	P	P	P	P	P	P	P
	Gold wire	P	P	P	P	P	P	P	P	P
0.0002										
	Lead shot	F	–	–	–	–	–	–	–	–
	Tungsten	P	P	P	P	P	P	P	P	P
	Silicon chips	P	P	P	P	P	P	P	P	P
	Gold wire	P	P	P	P	P	P	P	P	P
0.0004										
	Lead shot	PF*	–	–	–	–	–	–	–	–
	Tungsten	P	P	P	P	P	P	P	P	P
	Silicon chips	P	P	P	P	P	P	P	P	P
	Gold wire	P	P	P	P	P	P	P	P	P

*1 out of 3 failed after six shocks.

P – Passed, PF – Partial Failure, F – Failed
N_2 – 99.9% Nitrogen
N_2O_2 – 98.5% N_2/1.5% O_2

A. Before Lidding

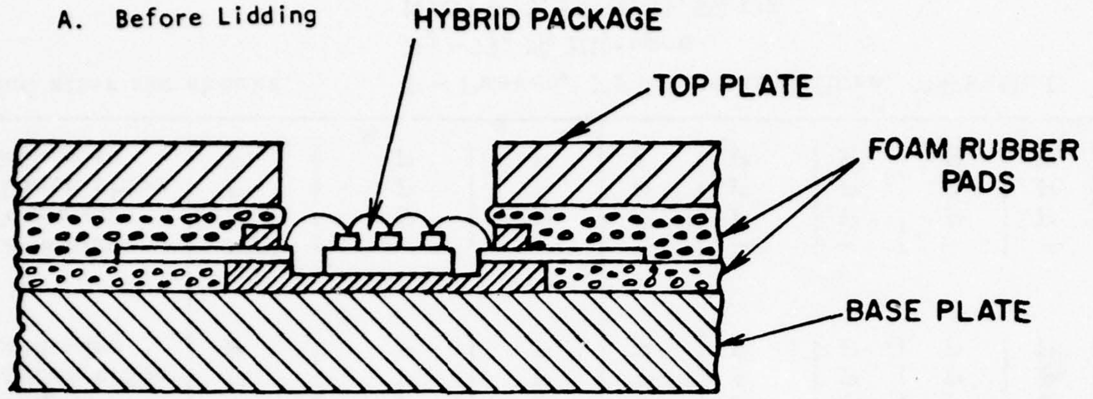

B. After Lidding

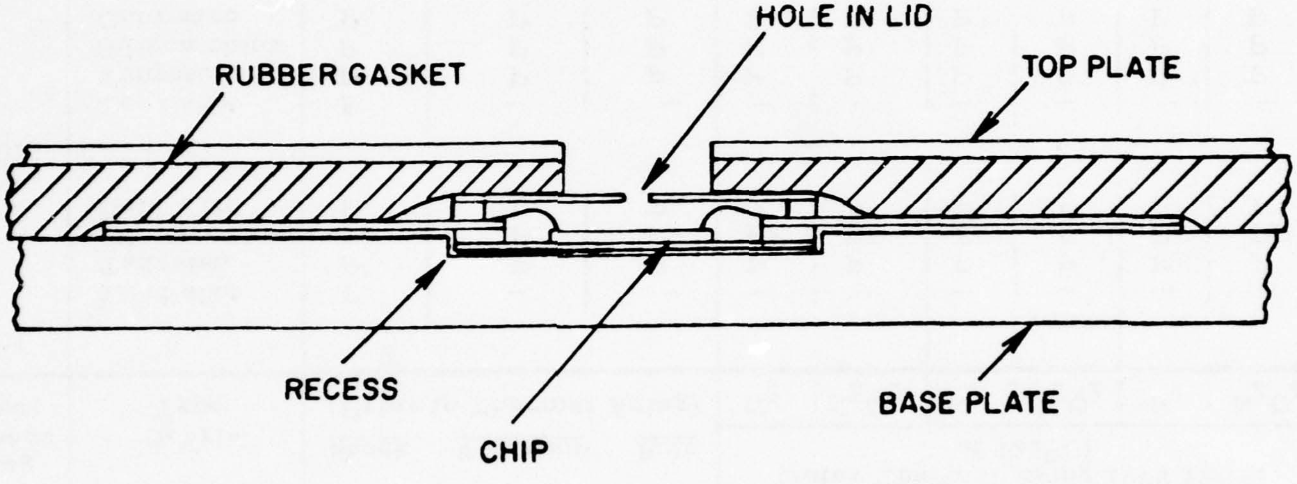

FIGURE 4

ALTERNATIVE MASKING AND HOLDING CONCEPTS

Masking requirements were deemed too extensive for coating prior to lidding; therefore, the through-hole method was chosen despite higher material usage. However, this selection required testing to assure uniform coverage within the package. Five package sizes and three hole diameters were evaluated. Results, given in Figure 5, showed that a centrally located hole, 31 mils diameter, would allow 0.1 mil coating of Parylene C throughout the package, provided the external coating thickness was 0.6 mil.

FIGURE 5

INTERNAL AREA vs INTERNAL PARYLENE THICKNESS FOR VARIOUS PACKAGES

(COURTESY TELEDYNE MICROELECTRONICS[5])

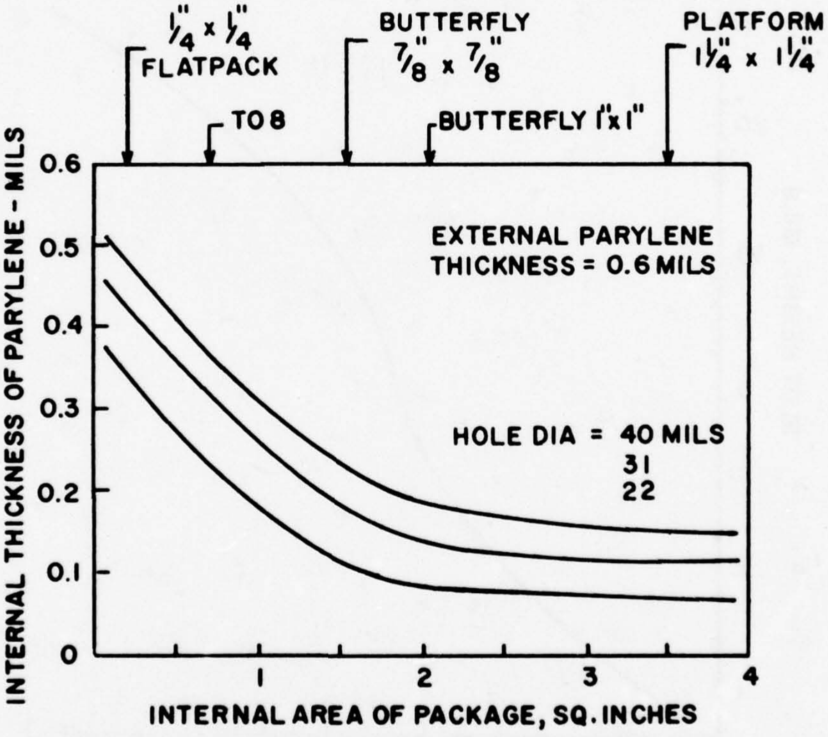

Tooling, in the form of book molds, was constructed which allowed only the hole area of the packages to be exposed. Thus, electrical leads remained uncoated.

Studies of penetration afforded by Parylene C have also been made at Union Carbide. Parallel glass plates, four inches on a side, were spaced at varying distances and sealed on three sides. These were exposed and internal Parylene C film thickness measured as a function of distance into the slot. The results, displayed in Figure 6, show the depth within given slots at which thickness is reduced to one-half that deposited on the external faces.

FIGURE 6

CREVICE PENETRATION OF PARYLENE C

(UNION CARBIDE CORPORATION DATA)

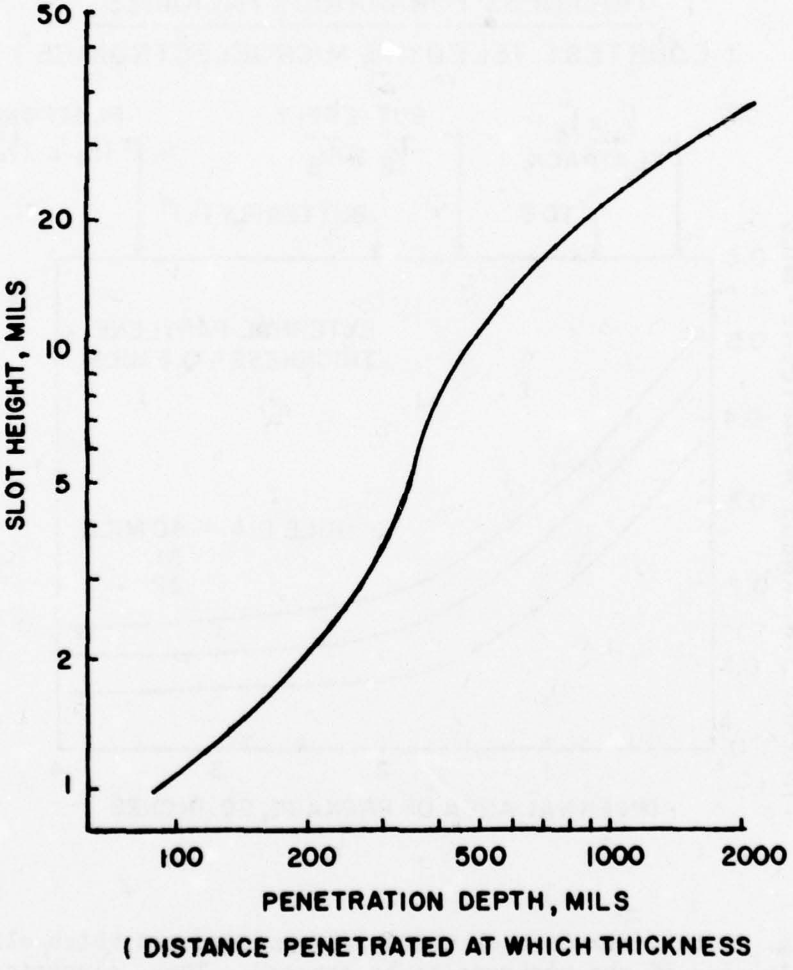

PENETRATION DEPTH, MILS

(DISTANCE PENETRATED AT WHICH THICKNESS IS $\frac{1}{2}$ THAT ON OUTER SURFACES)

In other words, at an external parylene thickness of 0.5 mil, and for a slot height of 10 mils, penetration would be 400 mils before internal thickness would be lowered to 0.25 mil.

5.0 Component Compatibility

As part of their evaluation of Parylene C for particle tie-down, Hughes Aircraft examined the effect of this product on all types of elements encountered in hybrid circuits. These are listed in Table II with respective measurements and a summary of results.

In general, Parylene C coatings either had no effect upon or benefited the insulation resistance and voltage breakdown performance of conductor patterns, strength of wire bonds, thermal dissipation of wires and beam lead devices, resistance values of thin film resistors, most thick film resistors, and electronic performance of semi-conductors.

The capacitance between conductor patterns was increased over the controls, as expected based on the higher dielectric constant of Parylene C, 3.1 as compared to 1.0 for air.

Thermal aging of coated microwave transmission lines resulted in increased line loss, 22% vs only 7% for the uncoated controls. The reasons are not known. Coated but unaged transmission lines showed improvement in loss characteristics.

Semi-conductor devices for the Hughes study were chosen on the basis of their known sensitivity to surface state conditions. Shifts in electrical behavior, within acceptable limits, were observed for both coated devices and uncoated controls. In general, these were attributed to characteristic sensitivity of the devices and to the test conditions rather than to Parylene C. A possible exception may be the PIN diode. Some PIN diodes treated prior to coating with an adhesion promoter did not recover to acceptable operating limits after HTRB testing.

Low resistivity, unglazed thick film resistors suffered unacceptable resistance increases upon coating with Parylene C, especially after long-term thermal exposure. Performance of coated glazed resistors was acceptable, as was that of unglazed devices with resistance values greater than 1000Ω/□.

While thin film nichrome resistors were unaffected by parylene treatment, it has been reported[6] that coating with Parylene C speeds reaction with water vapor. Thin film nichrome resistors, when exposed to water under bias, dissolve and open whether coated or uncoated. However, when resistors are fabricated on glazed substrates, coated, and then exposed to

---

(6) Eichel, S., Teledyne Microelectronics, private communication, June, 1977.

TABLE II

EFFECT OF PARYLENE C ON HYBRID CIRCUIT ELEMENTS[4]

Element	Measurements	Result Summary
Conductor Patterns	IR, ambient and after 1000 hrs. 150°C. VB, ambient and after 1000 hrs. 150°C. Capacitance ambient and after 1000 hrs. 150°C.	No effect. Coated patterns increased withstand voltage. Coatings increased capacitance 4-10%.
Wire Bond Strength	Pull strength, as coated and after thermal cycling -65° to +150°C.	As coated specimen strength increased 23-31%; cycled specimens retained strength better than uncoated.
Thermal Dissipation, Wires and Beam Lead Chips	Radiant energy emitted and burn-out current.	Coatings increased emissivity; burn-out current not changed or improved slightly.
Microwave ICs, Microstrip Transmission	Line loss, as coated and after 1000 hrs., 150°C.	As coated had lower loss than controls; aged samples had increased loss.
Thin Film Nichrome Resistors	Resistance, as coated and after 1000 hrs., 150°C.	No effect.
Thick Film Resistors, Glazed	" "	No effect; possible anomaly on 10 Ω/□ not caused by parylene.
Thick Film Resistors, Unglazed	" "	No appreciable effect except on 10Ω/□ where aging caused 23% increase.
Semiconductors PIN Diode NPN & PNP Trans. N-Channel MOSFET OP-AMP C-MOS Device	Leakage currents, HTRB	No adverse effects due to coating. Both coated and uncoated PIN diodes showed out-of-limit leakage on HTRB.

humidity, they corrode faster than uncoated controls. It should be noted that an adhesion promoter, standard practice except for through-hole coating, was not used and that non-adherent coatings generally are ineffective in preventing corrosion.

Other than this one instance, it can be stated that no adverse effect of Parylene C on hybrid circuit elements has been reported to Union Carbide.

6.0 Conclusion

Reliability problems encountered in packaging hybrid microcircuits are frequently approached using concepts adopted from the semi-conductor industry. These include careful selection of materials and control of manufacturing operations to assure strength as well as electrical performance, hermetic containers for environmental protection, and extensive screening of finished product to eliminate faulty or marginal units. While extremely low failure rates testify to the success of these methods in most cases, conformal coatings may offer supplementary means or even design alternatives. Cost effectiveness relative to other solutions is the key criterion.

Effectiveness and lower cost have been demonstrated in at least one instance, with the use of Parylene C coatings to resolve a particle contamination problem.

APPENDIX

TABLE I

TYPICAL PHYSICAL AND MECHANICAL PROPERTIES

	Parylene N	Parylene C	Parylene D	Epoxy	Silicone	Urethane
Tensile Strength, psi.	6,500	10,000	11,000	4,000 - 13,000	800 - 1,000	175 - 10,000
Yield Strength, psi.	6,100	8,000	9,000	–	–	–
Elongation to Break, %	30	200	10	3 - 6	100	100 - 1,000
Yield Elongation, %	2.5	2.9	3	–	–	–
Density, g./cm.^{3}	1.11	1.289	1.418	1.11 - 1.40	1.05 - 1.23	1.10 - 2.5
Coefficient of Friction						
Static	0.25	0.29	0.33	–	–	–
Dynamic	0.25	0.29	0.31	–	–	–
Water Absorption, 24 hours	0.06 (0.029″)	0.01 (0.019″)	–	0.08 - 0.15	0.12 (7 days)	0.02 - 1.5
Index of Refraction, n_D23°C.	1.661	1.639	1.669	1.55 - 1.61	1.43	1.50 - 1.60

Data recorded following appropriate ASTM method.

APPENDIX

TABLE II

TYPICAL BARRIER PROPERTIES

Polymer	Gas Permeability cm.^{3}-mil/100 in.^{2}-24 hours-atm. (23°C.) N_2	O_2	CO_2	H_2S	SO_2	Cl_2	Moisture Vapor Transmission, g.-mil/100 in.^{2}-24 hours, 37°C. - 90% RH
Parylene N	7.7	39.2	214	795	1,890	74	1.6
Parylene C	1.0	7.2	7.7	13	11	0.35	0.5
Parylene D	4.5	32	13	1.45	4.75	0.55	0.25
Epoxy	16	66	9	–	–	–	7
Silicone	15	22	45	–	–	–	290
Urethane	3	3	8	–	–	–	12

Data recorded following appropriate ASTM method.

APPENDIX

TABLE III

TYPICAL ELECTRICAL PROPERTIES

	Parylene N	Parylene C	Parylene D	Epoxy	Silicone	Urethane
Dielectric Strength, Short Time, volts/mil at 1 mil	7,000	5,600	5,500	2,300	2,000	3,500
Volume Resistivity, 23°C., 50% RH, ohm-cm.	1×10^{17}	6×10^{16}	2×10^{16}	1×10^{14}	1×10^{15}	2×10^{15}
Surface Resistivity, 23°C., 50% RH, ohms	10^{13}	10^{14}	5×10^{16}	5×10^{13}	3×10^{13}	6×10^{14}
Dielectric Constant						
60 Hz	2.65	3.15	2.84	4.2	2.6	3.5
10^3 Hz	2.65	3.10	2.82	3.9	2.6	3.4
10^6 Hz	2.65	2.95	2.80	3.4	2.6	3.2
Dissipation Factor						
60 Hz	0.0002	0.020	0.004	0.03	0.0005	0.01
10^3 Hz	0.0002	0.019	0.003	0.03	0.0004	0.01
10^6 Hz	0.0006	0.013	0.002	0.04	0.0008	0.01

Data recorded following appropriate ASTM method.

APPENDIX

TABLE IV

TYPICAL THERMAL PROPERTIES

	Parylene N	Parylene C	Parylene D	Epoxy	Silicone	Urethane
Melting or Heat Distortion Temperature, °C.	405	280	>350	up to 220	up to 300	170
Linear Coefficient of Expansion, $(10^{-5}/°C.)$	3.5	6.9	–	4.5 - 6.5	25 - 30	10 - 20
Thermal Conductivity, $(10^{-4}$ cal./sec./cm.^{2}·°C./cm.)	~ 3	–	–	4 - 5	3.5 - 7.5	5

Data recorded following appropriate ASTM method.

AFGL INFRARED SURVEY EXPERIMENTS CLEANING PROCEDURE

Charles V. Cunniff
Air Force Geophysics Laboratory

ABSTRACT

Space borne cryogenically cooled infrared telescope systems are optically sensitive to particulate contamination along the line-of-sight. Methods of cleaning and handling flight instrumentation have been developed at AFGL and used on the Infrared Celestial Survey program. These procedures are described in detail and flight results are presented.

1.0 INTRODUCTION

The Air Force Geophysics Laboratory is conducting a program of experiments to survey the sky in the infrared spectral region. The effect of particulate contamination upon infrared experiments in space has long been recognized (1,2,3,4,5,6) so payload design and handling techniques have been developed to minimize the possibility of dust and dirt in the experimental environment.

---

1. Blanchard, M.B., Farlow, N.H., Ferry, G.V. and Shade, H.D. 1967. Sixth Annual Technical Meeting, American Association for Contamination Control.
2. Blanchard, M.B., Ferry, G.V. and Farlow, N.H. 1968. J. Geophys. Research Space Physics, 73, 6343.
3. Blanchard, M.B. and Farlow, N.H. 1966, Contamination Control Vol. 5, 22.
4. Walker, R.G. and Price, S.D. 1975, AFCRL-TR-75-0373, ERP No. 522.
5. Price, S.D. and Walker, R.G. 1976, AFCRL-TR-76-0208, ERP No. 576.
6. Price, S.D. 1977, AFGL-TR-77-160, ERP No. 606.

2.0 THE EXPERIMENT

The experimental payload, Figure 1, consists of the nose cone, stellar tracker, stellar aspect sensor, a super critical helium-cooled infrared radiometer, instrument support section, attitude control system, and the recovery package. Aerobee sounding rockets are used as the propulsion vehicles for these experiments. After rocket burnout the payload and sustainer are separated by means of a Marmon clamp release and pre-loaded separation springs; sensor doors, nose tips and stellar aspect sensor doors are then ejected and the payload despun. Figure 2. The attitude-control-system captures the payload and points the star tracker, coaligned to the rocket roll-axis, to a pre-selected star near local zenith. The infrared sensor cap is lowered and the radiometer deployed to a specific zenith angle. Figure 3.

The payload is rotated about the roll-axis allowing the radiometer to scan a portion of the sky measuring the infrared sources. After completion of a 360 degree roll the radiometer is stepped through an angle slightly less than its field-of-view to permit mapping a contiguous sector of sky. At the conclusion of data taking the radiometer is returned to the stowed position and the recovery system actuated. Approximately 9000 to 10000 square degrees are scanned during each flight.

By precise selection of the launch window and site, mapping the entire celestial sphere can be accomplished.

3.0 PAYLOAD DESIGN

The nose tip, Figure 4, is built in two sections with an "O" ring seal to prevent particulate contamination after cleaning and mounting. The stellar aspect sensor port shown in Figure 5 contains two "O" ring seals. The outer seal is a dust safeguard between the rocket skin and the stellar aspect sensor port and the second is a seal for the ejectable door. Figure 2 is a view of the helium-cooled infrared radiometer in the

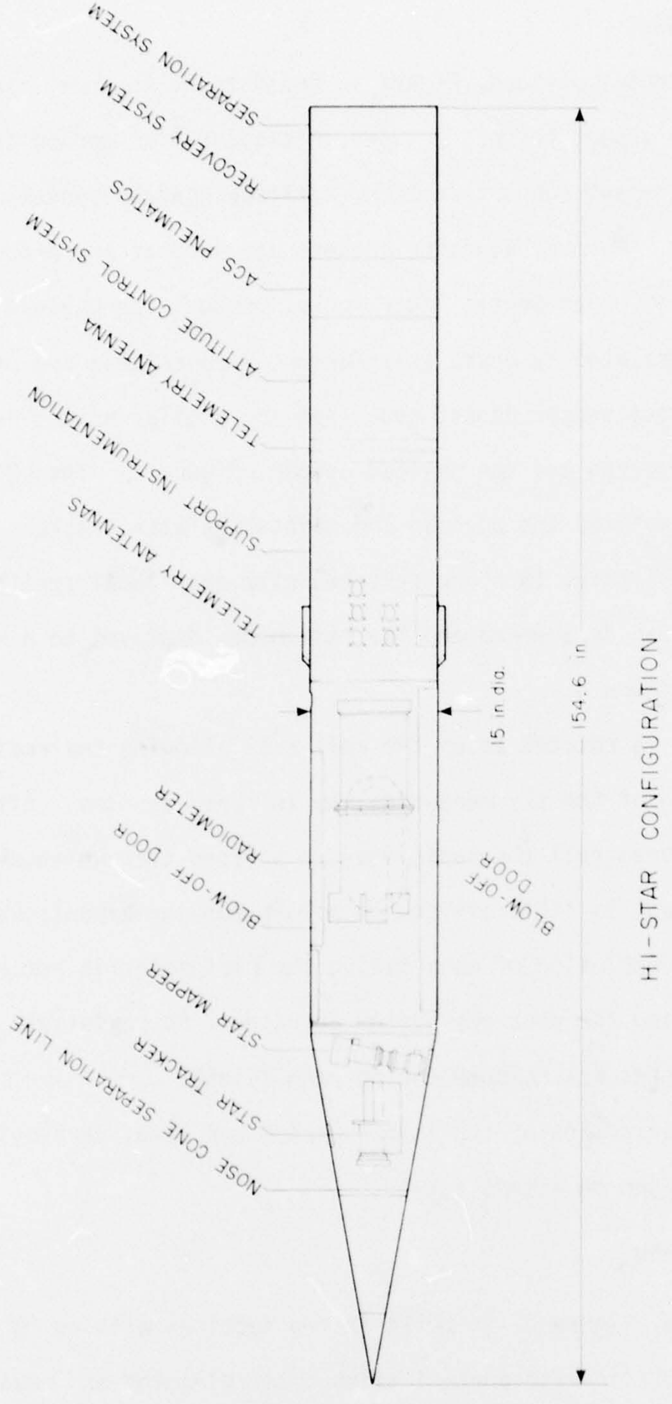

FIGURE 1 - HI STAR CONFIGURATION

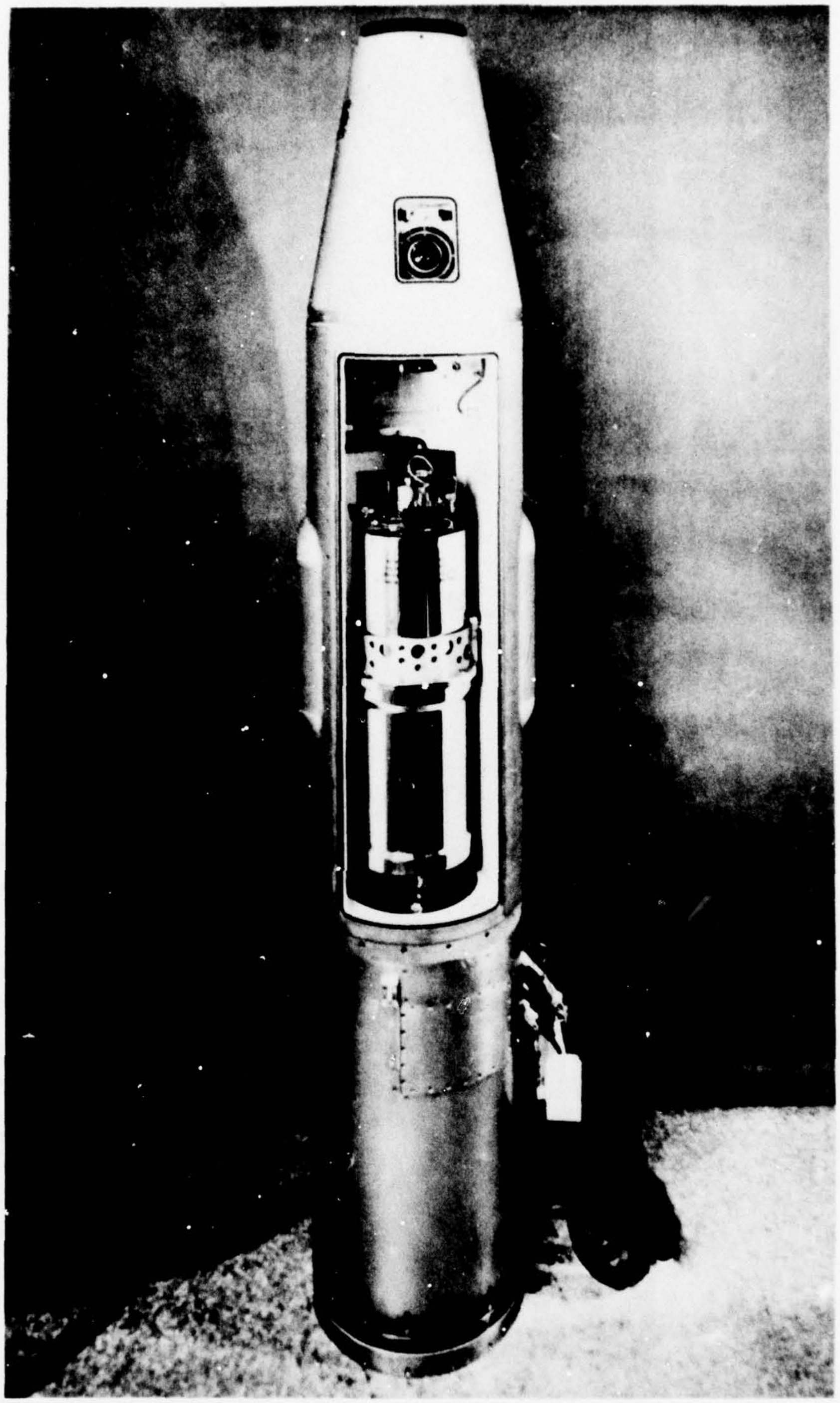

FIGURE 2 - PAYLOAD AFTER SEPARATION, NOSE TIPS AND DOOR EJECTION

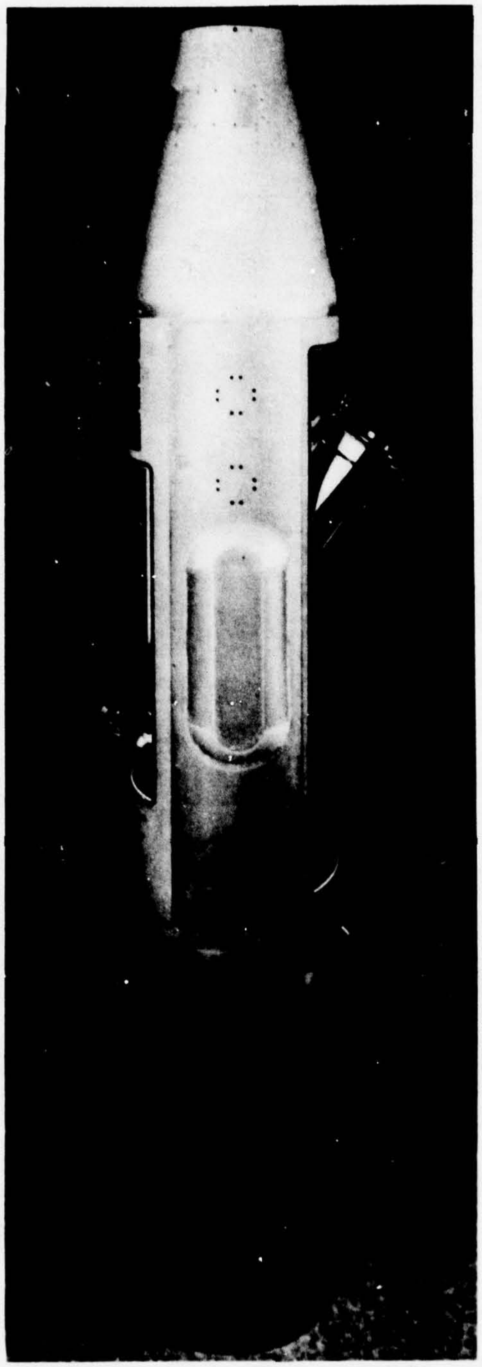

FIGURE 3 - RADIOMETER DEPLOYED

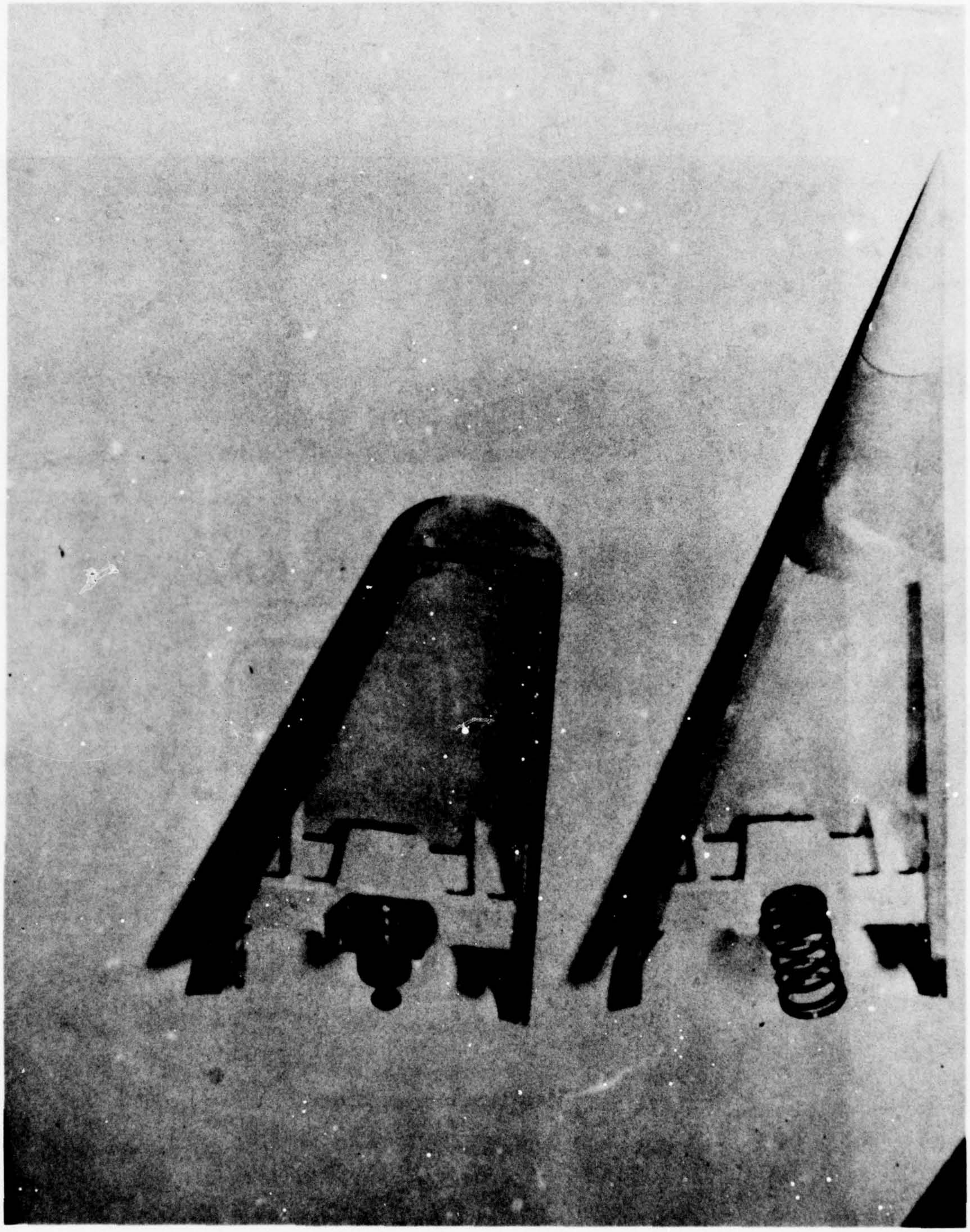

FIGURE 4 - NOSE TIP PRIOR TO INSTALLATION

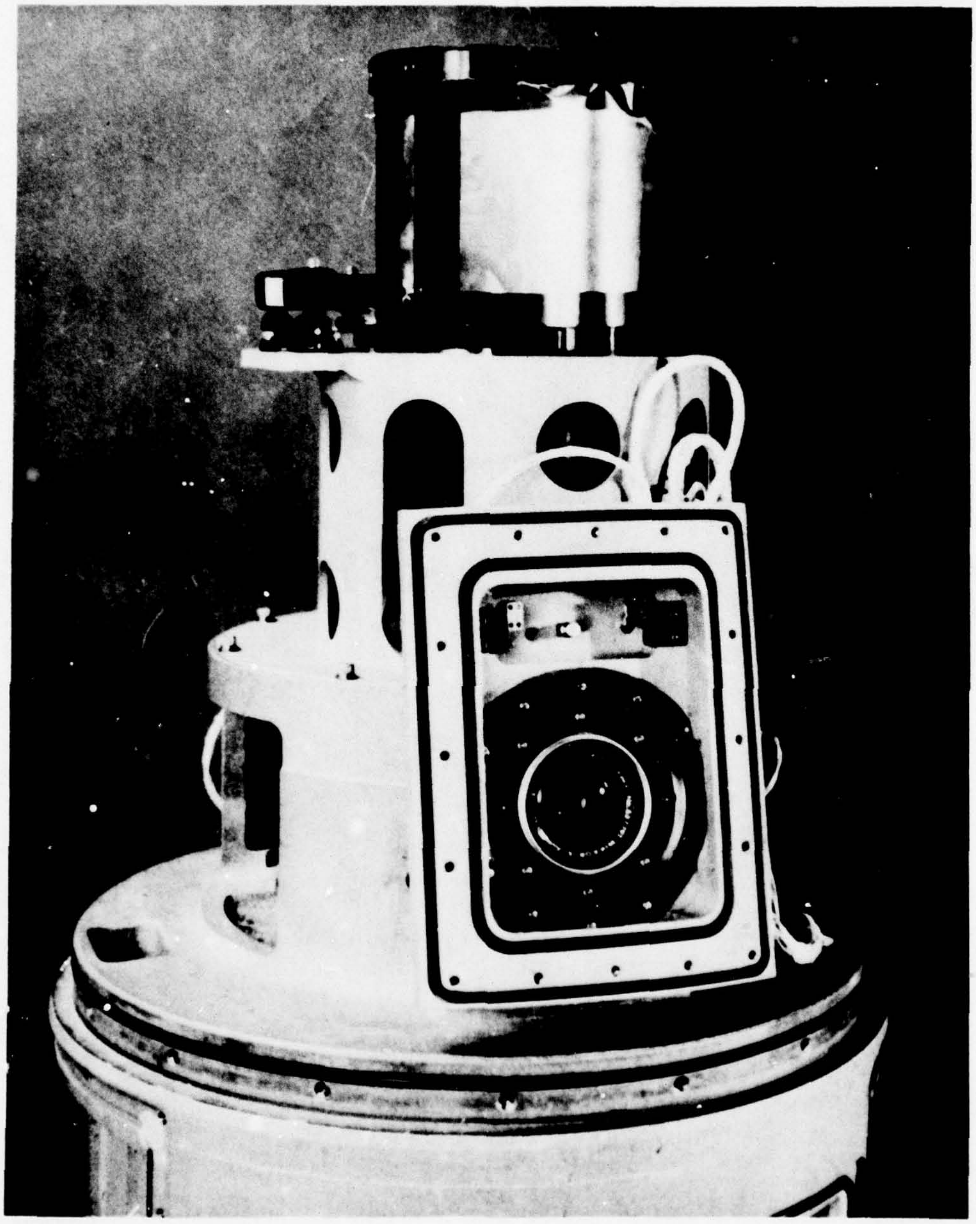

FIGURE 5 - STELLAR ASPECT SYSTEM PORT

stowed position. The surface of this cavity is treated with a hard glossy epoxy paint that allows a cling free, easily cleaned area. The cavity is separated from the stellar aspect sensor and stellar tracker section by a solid bulkhead and from the support section immediately below by a rubber gasket attached to the sensor cap. Servicing the infrared radiometer in the tower prior to launch is performed through an access door observed at the rear of the cavity and directly above the radiometer.

Purging of atmospheric pressure during rocket ascent is accomplished by two methods. First, the clean air in the sensor chamber is vented through one way 1.0 psi check valves mounted on the skin. Second, the contaminated air in the support section and tracker-aspect sensor section is vented to the side panel section, Figure 6, through clearances in the casting, and then out the side panels, Figure 7, through Millipore filters, effectively containing contamination inside a "dirty" area.

4.0 CLEANING

4.1 Clean Bench and Clean Room

Both the clean work station, used for the assembly and disassembly of the infrared radiometer, and the clean room provide a laminar flow of 100 feet per minute of filtered air. Prefiltering achieves 60% efficiency and final filters of the absolute type increases effectiveness to 99.97 percent on particles exceeding 0.3 microns diameter.

Preparation of the clean room requires complete vacuuming, soap and water scrubbing, rinsing, and a two day purge. Clean room efficiency is continuously monitored by instrumentation designed to detect particles greater than 0.5 micron diameter. A visual display counter gives digital particle counts and an audio alarm alerts the user to an unexpected violation of cleanliness standards. All work in the clean room ceases and remedial action initiated if a breakdown in standards occur. Normal operation is resumed when corrections have been completed and the required

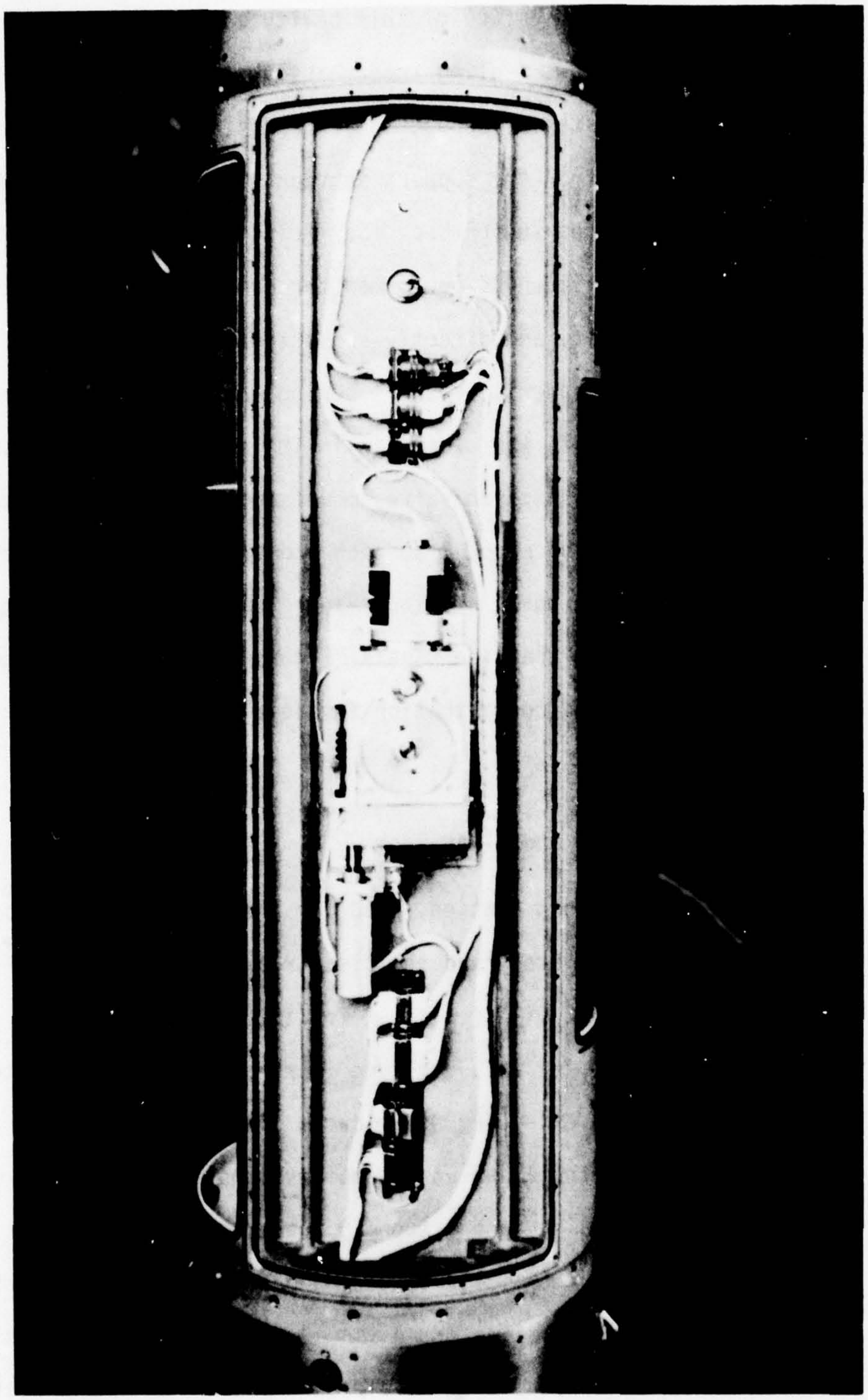

FIGURE 6 - SIDE PANEL SECTION SHOWING COMBINATION VENT AND CABLE HOLES AT THE TOP AND BOTTOM OF THE SECTION

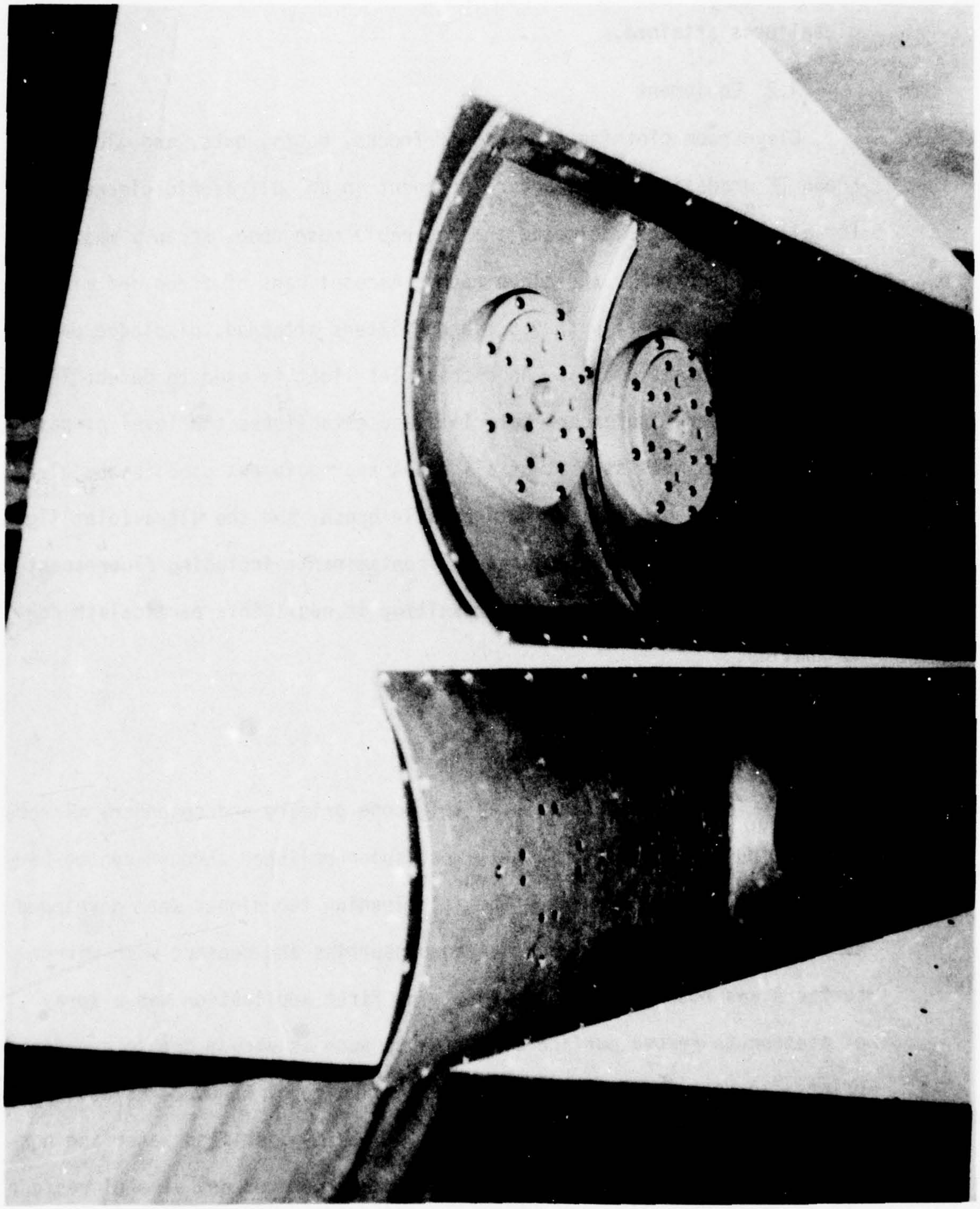

FIGURE 7 - SIDE PANELS WITH MILLIPORE FILTER HOLDERS ON THE INSIDE AND VENT HOLES ON THE OUTSIDE

cleanliness attained.

4.2 Equipment

Clean room clothing consists of frocks, boots, hats, and gloves. Freon TF grade is used as a purging agent in an ultrasonic cleaner for all small parts including the separable nose cone, screws, washers, and all tools used in the clean room. Aerosol cans of freon and microscopically clean air, with 0.5 micron filters attached, disolodge particles in inaccessable area. An ultraviolet light is used to detect lint, dust, and other fluorescent materials and establishes the level of payload cleanliness as well as that of all tools and equipment used in the clean room. A vacuum cleaner, a stiff bristle brush, and the ultraviolet light is used to examine and eliminate all contaminants including fluorescent materials from exposed surfaces resulting in negligible particalate contamination.

4.3 Procedures

4.3.1 Mirror Cleaning

The infrared radiometer telescope primary and secondary mirrors used during HI STAR SOUTH flights were super-polished canogen-coated-beryllium first surface mirrors. Special cleaning techniques were developed to prevent degradation of scattering properties and contact with mirror surfaces was restricted to liquids. The first application was a spray of acetone to remove surface contaminants such as vacuum grease and finger prints. A spray of 99.9 percent pure ethyl alcohol removed residual acetone and dissolved any grease or oil. A bath of distilled water and nonionic soap or very mild dishwashing detergent removed any alcohol residue. Finally, flooding the mirror with distilled water removed any residual soap solution. This process is repeated until visual inspection indicates all deposition is removed. If repeated applications of the above procedure fail to remove contamination, strips of Kay Dry tissues thoroughly saturated with each of the liquids are drawn, without surface pressure, across the mirrors. This technique has effectively removed contamination in all operations.

4.3.2 Payload Cleaning

Areas requiring absolute cleanliness include the nose cone, stellar tracker and stellar aspect system detents, radiometer section, and the entire outer skin of the payload. The payload, Figure 1, is positioned horizontally on a cradle designed with rollers to permit effortless rotation and maximum access to all sections to be cleaned. The nose cone end of the payload is canted slightly and positioned close to the clean room filter bank placing cleaned areas and those being cleaned between the filter bank and personnel during cleaning functions.

Nylon lint-free cloths are used to apply liberal quantitites of clean freon over the skin of the payload around the stellar tracker mounting area. This detent is then vacuumed and checked with the aid of an ultra violet light. The exposed tracker lens is cleaned with standard lens paper and Kodak lens cleaner. At this point the pre-cleaned separable nose cone is assembled and secured to the payload. Again the skin is flushed to below the stellar aspect system detent and vacuumed. The aspect system door, purged in the ultrasonic cleaner, is then secured to the payload and an ultraclean polyethylene antistatic bag cut to the full length of the payload is pulled over the nose and down along the payload to a point just below the aspect system door thereby isolating the upper cleaned portion from contamination.

The most intricate and complicated portion to undergo cleaning is the infrared radiometer sensor and cavity area. Once again the payload exterior from below the bagged area to below the cavity is washed with liberal amounts of freon and vacuumed. The radiometer exterior, casting cavity, cables, and connectors are cleaned in preparation for the opening of the infrared radiometer. The radiometer cap is then lowered, the sensor deployed some 90 degrees, and the interior vacuumed. The infrared radiometers are assembled on a clean bench and contaminants are rarely found inside at this time. On completion of the cleaning, the radiometer is stowed and the cap raised in place. Equipment used to service the radiometer in the launch tower consists of a helium fill line, a vacuum pump port, and a vent heater cable, all thoroughly cleaned and attached through a split access door. The sensor cavity is re-inspected for contaminants, cleaned if required, and isolated with the attachments of the pre-cleaned ejectable doors. The exposed outer payload skin is purged, re-cleaned, and the polyethylene bag moved along to cover the payload to below the sensor door. The remainder of the payload from a point below the radiometer section to the bottom of the payload separation joint is systematically cleaned with freon and vacuumed, isolating each section after cleaning by moving the clean bag along the skin.

To gain access for servicing of parts of the payload encased in the clean bag, polyethylene sleeves are fabricated and attached to the bag at strategic locations. One such place is at the temporary service door for the radiometer. In addition to the vacuum pump and liquid helium lines in this area, a small clean bag containing the pre-cleaned permanent door and other equipment used in preparation for final "buttoning up" is inserted in the sleeve. Other sleeves are fabricated to provide access to the payload timers, flight battery doors, umbilical connector section, and attitude control system battery door. A second clean bag is subsequently stretched over the entire payload to protect the package during transportation, mating with the rocket sustainer, and emplacement in the launch tower. Connector ends of all umbilical cables are cleaned with freon, ultraviolet light tested, vacuumed, and then doubly bagged to prevent contamination during mating with the payload on the launch tower.

All bagging material, Figure 9, remained on the payload until seventy five minutes before launch at which time it was washed down, slit, and peeled off.

5.0 RESULTS

Seven rockets have been successfully launched, Figure 10, at White Sands Missile Range, and three at Woomera, Australia. The ten launches of the HI STAR and HI STAR SOUTH program surveyed ninty percent of the sky at 11 and 20 microns locating and identifying some 3200 celestial objects, Figure 11.

6.0 ACKNOWLEDGEMENTS

The payload was designed by Paul Hartnett and Edwin LeBlanc of Wentworth Institute and C. Neil Stark of the Geophysics Laboratory. The attitude control system and recovery package were provided by Aerojet Liquid Rocket Co. Cleaning was done by David Akerstrom, Michael Mitchell, Dr. Thomas Murdock and Anthony Romanelli of AFGL with the assistance of Wentworth Institute personnel. The experiments described were conducted under the supervision of Dr. Russell G. Walker, Chief project scientist at AFGL.

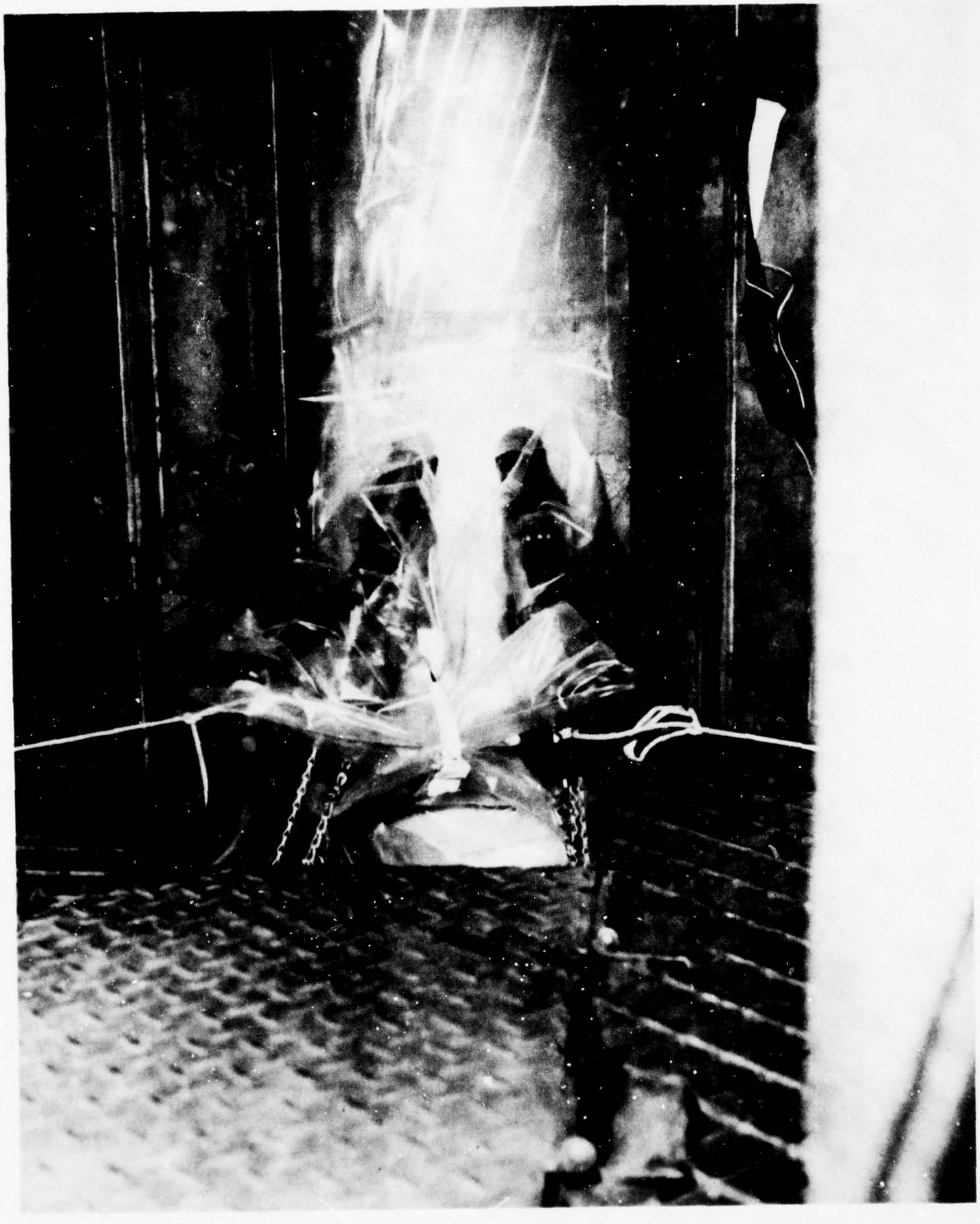

FIGURE 8 - PORTION OF BAGGED PAYLOAD AND UMBILICAL CABLE CONNECTIONS IN THE LAUNCH TOWER

FIGURE 9 - NOSE TIP OF PAYLOAD ENSHROUDED IN POLYETHYLENE BAGGING MATERIAL ON THE LAUNCH TOWER

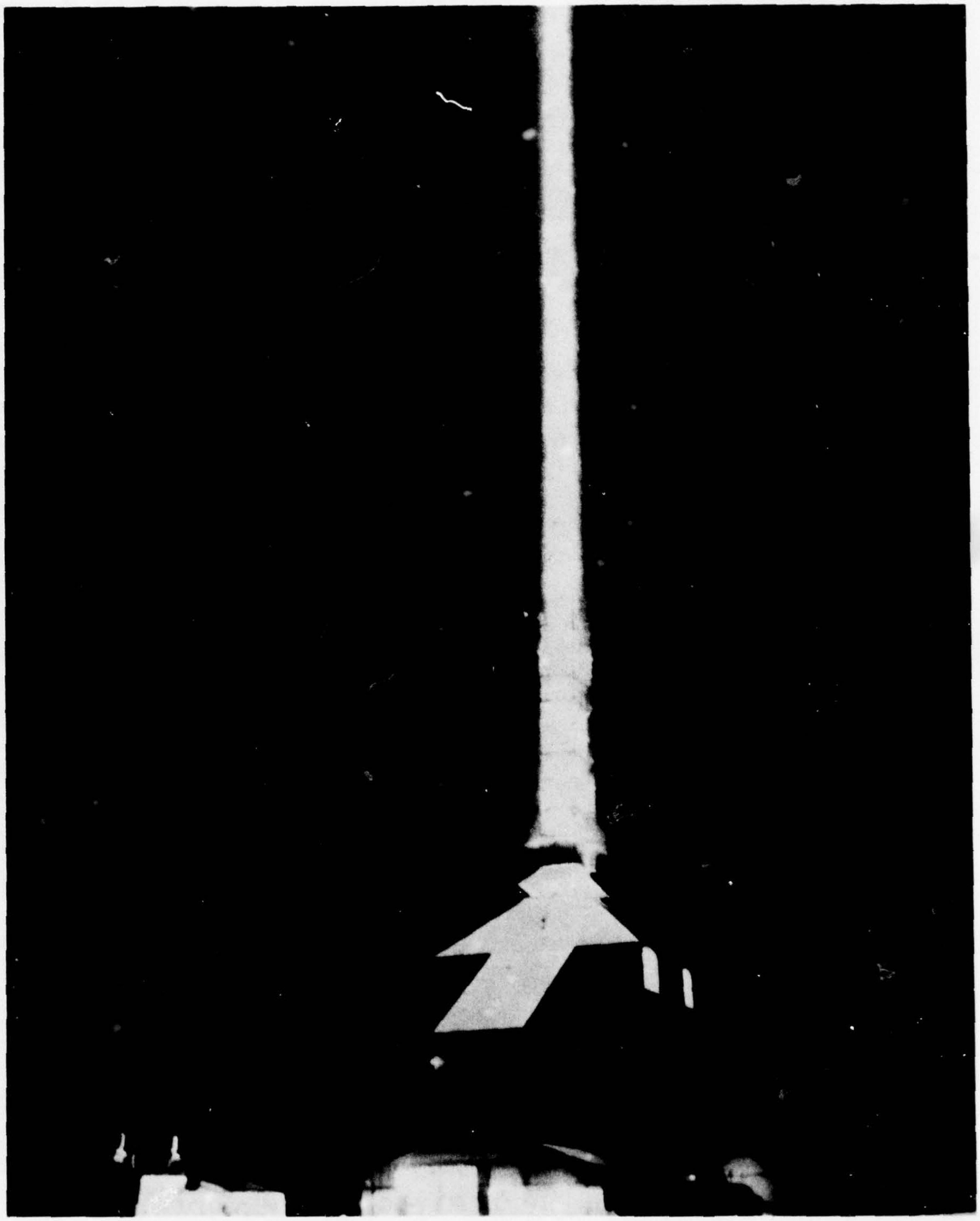

FIGURE 10 - TYPICAL HI STAR AEROBEE LAUNCH

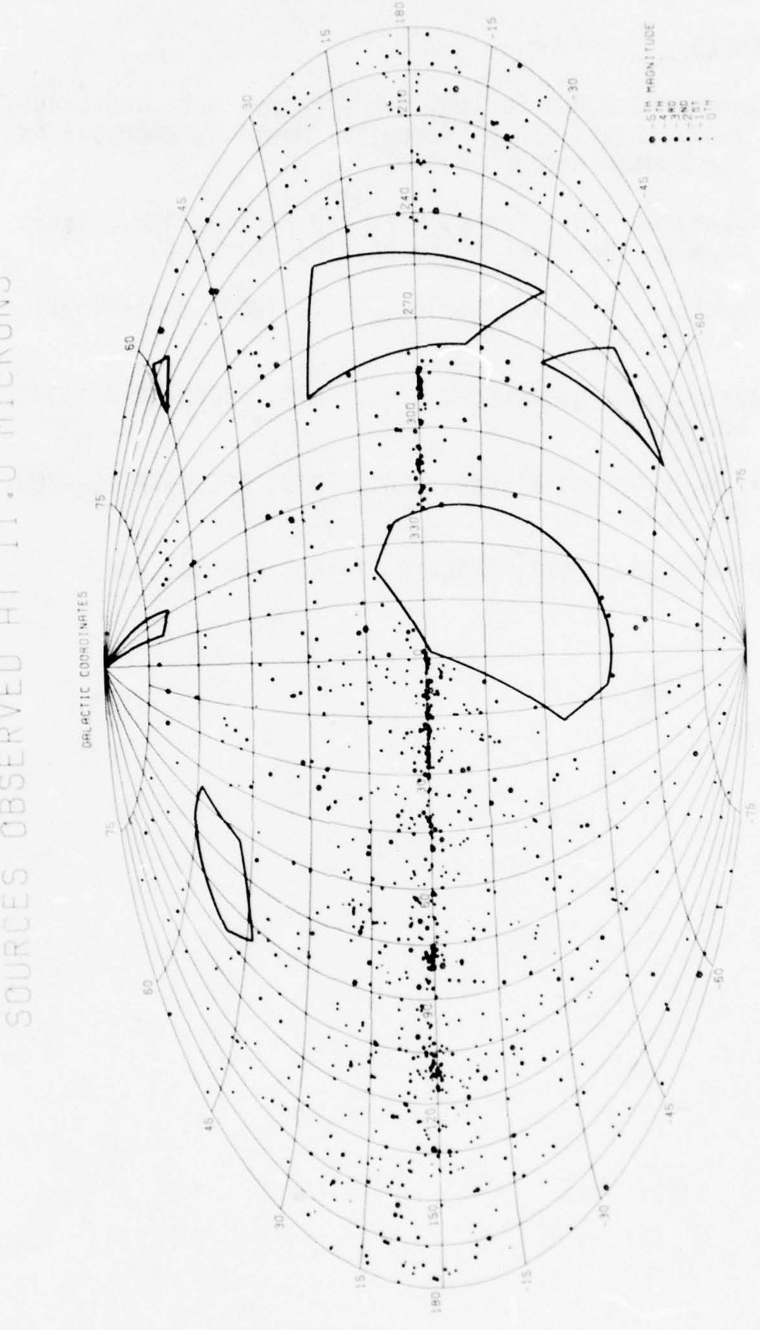

FIGURE 11 - INFRARED SOURCES AT 11 MICRONS AS OBSERVED DURING HI STAR FLIGHTS

7.0 REFERENCES

1. Blanchard, M.B., Farlow, N.H., Ferry, G.V. and Shade, H.D., 1967. Sixth Annual Technical Meeting, American Association for Contamination Control.

2. Blanchard, M.B., Ferry, G.V. and Farlow, N.H., 1968. J. Geophys. Research Space Physics, 73, 6343.

3. Blanchard, M.B. and Farlow, N.H., 1966, Contamination Control Vol. 5, 22.

4. Walker, R.G. and Price, S.D., 1975, AFCRL-TR-75-0373, ERP No. 522.

5. Price, S.D. and Walker, R.G., 1976, AFCRL-TR-76-0208, ERP No. 576.

6. Price, S.D., 1977, AFGL-TR-77-160, ERP No. 606.

PARTICULATE CONTAMINATION CONTROL FOR THE VIKING AND VOYAGER UNMANNED PLANETARY SPACECRAFT

by Alan R. Hoffman and Robert C. Koukol

Paper presented at the International Spacecraft Contamination Conference, 7-9 March 1978, Colorado Springs, Colorado.

ABSTRACT

Particles released during the flight of planetary spacecraft can result in either unacceptable performance of science instruments or in mission operations problems caused by particles interfering with the celestial sensors. Because of planetary protection requirements for spacecraft flying to planets of biological interest, a high degree of exterior particulate cleanliness is also desirable to reduce the likelihood of the accumulation of microbial burden on spacecraft surfaces. To minimize the accumulation of particulate matter on the spacecraft exterior surfaces, the Viking and Voyager projects contamination control programs consisted of establishing cleanliness requirements for facilities, equipment, and personnel. This paper discusses the effectiveness of these programs during the prelaunch operations at Cape Canaveral.

The final assembly and checkout of the Viking and Voyager unmanned planetary spacecraft occurred in Class 100,000 (or better) cleanrooms. Following spacecraft encapsulation, the payload was continuously subjected to Class 100 air during transport, hoist, and on-pad operations. Several different particulate determination approaches were used to verify not only spacecraft surface cleanliness but also air cleanliness. These included visual inspection of surfaces with and without magnifying aids, collection of visible surface particles for chemical analysis, light scattering particle measuring devices, and specially developed samples for monitoring exhaust air.

Visual inspections of spacecraft surfaces occurred periodically during the prelaunch operations. The contamination control inspection team would either certify cleanliness of the spacecraft or require additional cleaning. When it was necessary to identify the types of particles noted, particles were subject to chemical or spectral analyses.

Volumetric measurements of the air cleanliness of the cleanrooms and the encapsulated payload air conditioning systems were made using light scattering instruments. The data shows that the air cleanliness requirements for the cleanrooms and the air conditioning systems were satisfied. To obtain reliable measurements at high air velocities, as in the air conditioning ducts, specially designed isokinetic probes were used.

To evaluate air cleanliness during the transport and hoist operations of the encapsulated spacecraft, a pair of specially designed 45 mm disc samples were placed in the exhaust area of the payload. This technique proved acceptable for obtaining qualitative type of measurements during the five air conditioning changes during these operations as well as during on-pad operations if inlet air cleanliness became marginal.

Finally, in-flight bright particle occurrences as detected by the star trackers are used as an indirect indication of surface cleanliness. Based on comparisons with previous Mariner spacecraft, the Viking and Voyager spacecraft have had fewer bright particle occurrences.

This paper presents the results of one phase of research carried out by the Jet Propulsion Laboratory, California Institute of Technology, under Contract No. NAS 7-100, sponsored by the National Aeronautics and Space Administration.

1.0 INTRODUCTION

Two Viking and two Voyager unmanned planetary spacecraft were successfully launched from Cape Canaveral in 1975 and 1977, respectively. All of these spacecraft were prepared for launch in compliance with particulate contamination control programs that had evolved primarily from earlier unmanned projects (reference 1). However, there were significant differences for the Viking and Voyager programs. These included new facilities, different planetary protection constraints, and new on-pad particulate monitoring approaches. This paper discusses the Viking and Voyager particulate contamination control programs at Cape Canaveral including the hardware flow through the various facilities, the monitoring methods employed, the results obtained, and the in-flight experience.

For the Viking and Voyager spacecraft there were three reasons for implementing a particulate contamination control program; 1) minimize the likelihood of encountering particles in the field of view of optical guidance equipment, i.e., celestial sensors, 2) minimize particle liklihood in or on optics of scientific experiments, 3) enhance the chances of satisfying the spacecraft planetary protection constraints for the launch preparation activities.

There was a difference between the two programs in the importance of these reasons. For Viking, planetary protection was the dominant reason. For Voyager, optical guidance equipment and science instruments were dominant.

Three methods were used for controlling particulate contamination during spacecraft prelaunch preparation: facilities, personnel constraints, and special hardware protective measures such as dry nitrogen purging or equipment dust covers.

2.0 FACILITY AND PERSONNEL REQUIREMENTS

The facilities used for Viking and Voyager prelaunch preparation were similar, although there were modifications and changes to the payload transporter, and on-pad air conditioning system between the two programs. Table 1 summarizes the facility capabilities; and indicates their specific utilization during the Viking and Voyager programs for major payload items. Several points regarding these facilities should be emphasized. The air cleanliness level was a class 100,000 or better.* After payload encapsulation, the air cleanliness was class 100 or better to the time of launch. The encapsulated payload experienced five air conditioning changes from the time of encapsulation in the assembly facility to the time of installation on top of the launch vehicle at Launch Complex 41.

Personnel constraints imposed on the spacecraft test team included garment requirements and limited access to the facilities. The garment requirements are summarized in Table 2 and shown in Figure 1. Significant complaints noted by the team regarding the garments were 1) hoods restricted peripheral vision and 2) bunny suits and hoods caused discomfort, i.e., too warm, if worn continuously for long periods of time.

---

* Per Federal Standard 209b, Federal Standard Cleanroom and Work Station Requirements Controlled Environments, 1972

	Facility					
Payload Item	Hangar AE	Hangar AO	ESA 60A	SAEF 1 & 2	Transporter	Launch Complex 41
Facility Environments	Class 300,000 Air ~21°C ~45%	Class 10,000 Air 21^{+3}_{-0} °C 45 ±5%	Class 100,000 Air 21^{+3}_{-0} °C 45 ±5%	Class 100,000 Air 21^{+3}_{-0} °C 45 ±5%	Class 100 Air	Class 100 Air
VIKING						
Orbiter		X	X	X		
Lander				X		
Shroud	X			X		
Encap. Payload (a)				X	X	X
VOYAGER (b)						
Mission Module		X		X		
Propulsion Module			X	X		
Shroud	X					
Encap. Payload				X	X	X

a) Includes orbiter, lander and shroud in encapsulated configuration.

b) Includes mission module, propulsion module, shroud in encapsulated configuration.

Table 1 - Cape Canaveral Facilities Utilized by Viking and Voyager Payload Items

TABLE 2 - CLEANROOM GARMENT REQUIREMENTS FOR VIKING AND VOYAGER CAPE CANAVERAL OPERATIONS

	SAEF 1&2	ESA 60	HANGAR AO
HEAD	Fullhood, Tyvek Disposable (Moustache Covers)*	Fullhood, Tyvek Disposable (Moustache Covers)*	Fullhood, Tyvek Disposable (Moustache Covers)*
BODY	Bunny Suits, Nomex for all S/C and S/C/ transporter operations in designated area Bunny Suits, Dacron elsewhere in high bay	Bunny Suits, Nomex or if Nomex unavailable, Smock and Pants, Nomex	Bunny Suits, Tyvek Disposable
HANDS**	Gloves, ** --Nylon	Gloves, ** Nylon	Gloves, ** Nylon
FEET	Approved Cleanroom Shoes or Booties, Tyvek Disposable	Approved Cleanroom Shoes or Booties, Tyvek Disposable	Approved Cleanroom Shoes or Booties, Tyvek Disposable

*Required for personnel with moustaches.

**Gloves are required whenever flight equipment is handled except when an operation is so delicate that gloves impede the operation.

Figure 1 Example of Personnel Clothing Requirements

3.0 MONITORING METHODS

Several qualitative and quantitative particulate monitoring methods were applied during the Viking and Voyager programs. The qualitative methods included visual inspections of spacecraft surfaces with and without magnifying aids and collection of particles for chemical or physical analysis. The quantitative methods were based on the utilization of light scattering monitors for enumerating the number of dust particles in a given volume of air.

3.1 Visual Inspection

The spacecraft prelaunch visual inspections were performed by an inspection team consisting of quality assurance and contamination control personnel while work platforms were in positions favorable for viewing spacecraft surfaces. The inspection team would walk slowly around the spacecraft at each level looking for dirt particles. Magnifying aids (10X magnifying glasses) were occassionally used. Special attention was paid to cracks and crevices where dust particles could have been overlooked during earlier cleaning operations. The team would either certify cleanliness of the spacecraft or require additional cleaning. The principal visual inspection occurred just before the spacecraft was encapsulated in the protective shroud. The basic requirement that had to be satisifed was that the spacecraft surfaces had to be visually clean. When it was necessary to identify the types of particles visually observed on the surfaces, particles were removed by "picking them" with a lint free cloth, adhesive tape, or a cotton swab and placing the particle in a suitable container such as a clean petri dish. The particles were then taken to the chemical and spectral facility for analysis.

3.2 Facility Monitoring

To assure that the specified requirement "visually clean" was satisfied and that the spacecraft were not subsequently subjected to dirty air, a facility monitoring program was implemented. This program consisted of performing periodic measurements in the high bay areas of the clean room immediately before and during spacecraft operations using light scattering monitors, verifying air cleanliness of inlet air for the encapsulated payload using light scattering monitors with isokinetic probes, and monitoring the payload exhaust air using light scattering monitors and "disc" samples. A description of each of these methods is given in the following. Their utilization is summarized in Table 3.

3.2.1 Volumetric Light Scattering Monitor

The volumetric light scattering monitor pulls air into the instrument where a bright beam of light is projected through the airstream and detects the presence of particles by sensing the light scattered by the particles. Each particle passing through the viewing field generates a light pulse which is detected by a photomultiplier tube. Since the amount of light reaching the photomultiplier tube varies with the size of the particles, the output pulses from the tube can be used to count particles and to classify them according to size. The normally used size ranges, $\leq 0.5\mu$ and $\geq 5.0\mu$, were applied for the Viking and Voyager particle monitoring efforts and measurements were reported as the number of particles per cubic foot of sampled air.

In the high bay areas with daily activity, such as the SAEF's and Hanger AO, continuous measurements were taken using automatic light scattering monitors. The resulting strip charts were read by facility personnel to verify compliance of the clean room with air cleanliness requirements.

TABLE 3 - PARTICULATE MEASUREMENT REQUIREMENTS FOR VIKING AND VOYAGER CAPE CANAVERAL OPERATIONS.

Monitoring Method	Pre Encapsulation					Post Encap.		Transport				Launch Complex 41			
	Hanger AO	ESA 60(c)	SAEF 1 or 2	SAEF Payload Air		SAEF Payload Air		SAEF Airlock Air		Transporter Air		Hoist Air		Payload Air	
				Inlet	Nozzle Outlet	Inl	Exh	Inl	Exh	Inl	Exh	Inl	Exh	Inh	Exh
Particle Counter															
Std. particle counter aperature (high bay areas)															
•Continuous	X	X	X												
•Periodic (a)	X	X	X												
Isokinetic probe(s)															
(Ducted air to payload)															
•CSS airborne ducting cleanliness verification				X(f)	X(g)										
•Premate Survey(d)						X		X		X		X		X	
•Continuous														X	
•Periodic							X		X						X(e)
Disc Samples							X(b)		X		X		X		X(b)

(a) In close proximity to spacecraft.

(b) As required, see acceptance criteria.

(c) Requirements if ESA60 used for Ops.

(d) Premate survey of air conditioning system prior to connecting air to encapsulated payload.

(e) Once every 12 hrs. for a minimum of 30 minutes.

(f) Premate survey.

(g) After several hours of blowdown.

Light scattering monitors were used to periodically measure the number of particles in the air near the spacecraft during assembly and test operations. This data was also used to verify compliance of the clean room with air cleanliness requirements.

In conjunction with the isokinetic probes the light scattering monitors were used for premate surveys to verify air quality of air conditioning systems prior to connecting air to shroud or encapsulated payload and for periodic sampling of the inlet and exhaust air on the launch pad.

3.2.2 Isokinetic Probes

Because of the possibility of obtaining erroneous readings from the light scattering monitors while sampling air in an air conditioning duct (or exhaust port) moving at high flow velocities, specially designed isokinetic probes were required on the end of the inlet tube to the instrument. Figure 2 was used to select the proper probe inlet size. The methodology consisted of the following steps. First to measure the flow velocity at the location to be sampled using a manometer or a hot wire anemometer, and second to enter Figure 2 and select the probe nearest to the measured velocity always using the largest probe inlet size closest to the measured velocity. If velocities exceeded 20m/s, the higher (1m/s) sampling flow rate was used.

3.2.3 Disc Samples

For several post encapsulation operations, such as transport and hoist, particle measurements using light scattering monitors were impractical. To provide particles for performing qualitative assessments, special devices, called disc samples, were designed. The purpose of the samples was to provide a mechanism for trapping particles entrained in the payload exhaust air.

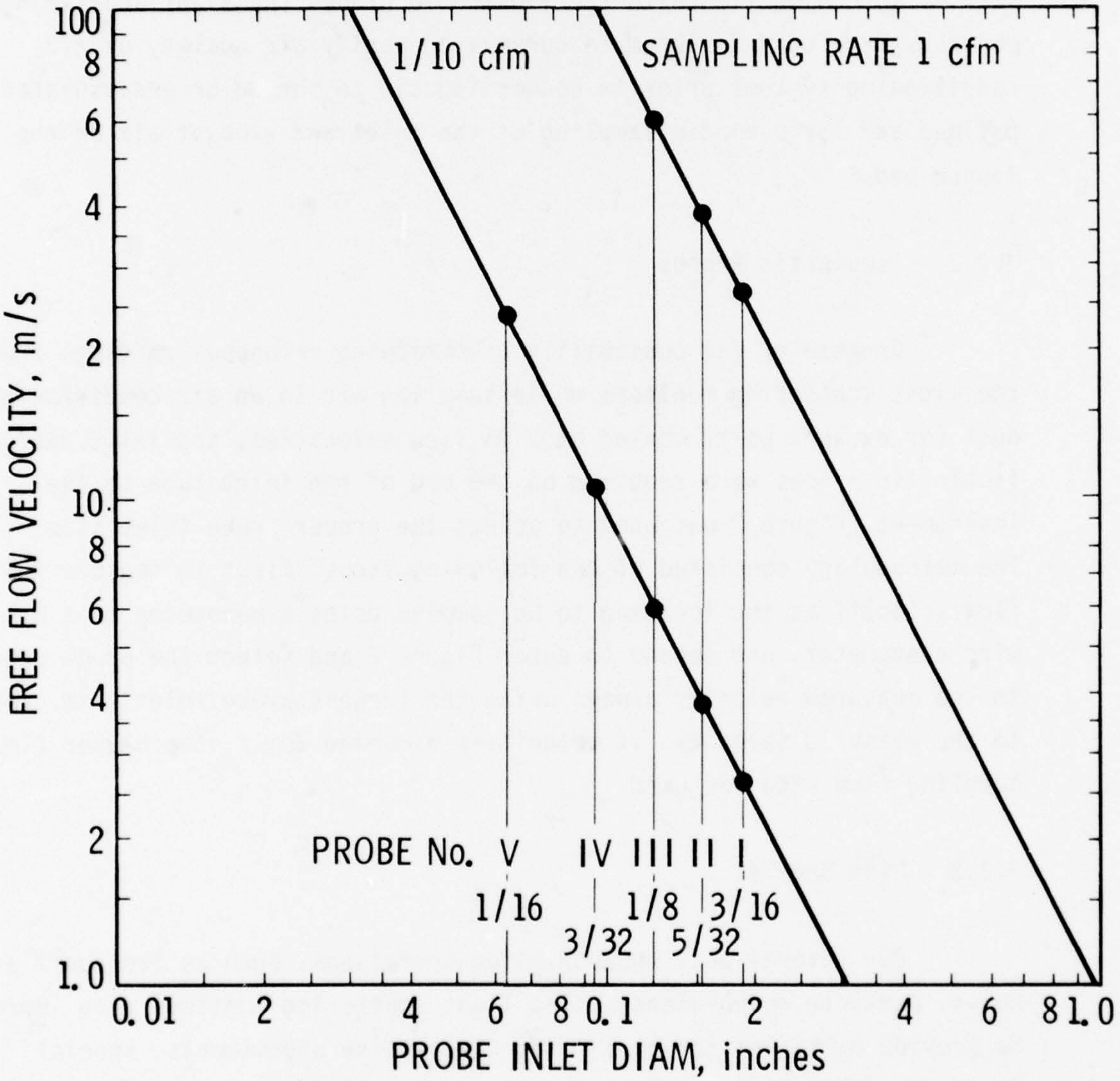

Figure 2. Isokinetic Probe Selection Chart

For Viking the discs were placed on the flapper valves of the payload diaphragm for transport, hoist, and as required on pad. For Voyager, the discs were placed on the flapper valves of the aft protective cover during transport and at the splitlines of the Voyager payload diaphragm during transport, hoist, and as required on pad. The discs were attached at the sampling location by using double-back tape.

After retrieval from the spacecraft, the discs were examined under a microscope and comparisons made against the previously determined background count. If appropriate, discs were sent to the chemical analysis lab for particle identification. This information was used to determine the particle source and to pinpoint possible contaminating mechanisms.

4.0 RESULTS

4.1 Visual Inspection Results

The encapsulation visual inspection for each Viking and Voyager spacecraft generally found no visible particles on the spacecraft surfaces. On Viking, one lander bioshield cap had a few black particles on it. On Voyager 1, the antenna and plume shields were dirty. In both instances, the hardware was cleaned and the subsequent visual inspection revealed that the spacecraft surfaces were acceptable.

For both Viking and Voyager, on-pad spacecraft problems required decapsulation of flight spacecraft. This provided opportunities to determine whether the indirect measurement methods, e.g., particle counters and disc samples, were providing a reasonable indication of what was occurring underneath the protective shroud. The indirect methods did provide early indications of problems for Viking which were confirmed by post decapsulation inspection. This will be discussed in more detail in the Launch Complex 41 air quality results. The decapsulation inspection of Voyager 1 showed that the spacecraft was visually clean. This result was consistent with the favorable results from the indirect measurements at the launch pad.

4.2 Clean Room Data

As noted in Table 1 Viking and Voyager hardware passed through several different clean rooms during the course of the Cape Canaveral operations. The principal clean rooms were in Hanger AO, ESA 60A, and SAEF's 1 and 2. These clean rooms were certified to meet Class 100,000 air cleanliness requirements prior to the arrival of flight hardware. Since these clean rooms were subjected to an extensive facility cleaning program preceding the certification, there was no difficulty in satisfying the requirements. Typical results from two of the clean rooms are shown in Table 4. This data was obtained by using light scattering particle counters.

TABLE 4 - CERTIFICATION DATA FROM SPACECRAFT ASSEMBLY AND ENCAPSULATION FACILITY CLEANROOMS

	No. Of Particles > 0.5 μ
Spacecraft Assembly and Encapsulation Facility #1	8 to 148
Spacecraft Assembly and Encapsulation Facility #2	1 to 75

4.3 Support and Launch Complex 41 Air Conditioning Systems Data

The air conditioning systems were environmentally certified by using a light scattering particle counter a few days prior to use, retested the day before use and again verified just prior to integration with flight hardware. The payload support air conditioning units which provided air to the encapsulated spacecraft in the Spacecraft Assembly and Encapsulation Facilities, in the airlock, and during transportation as well as the Launch Complex 41 systems consisting of the hoisting air conditioning (5th level), payload air conditioning (12th level) and Centaur Electronics Module air conditioning (11th level) were certified to meet or exceed the Federal Standard 209b for providing Class 100 air delivery. An example of this data is shown in Table 5.

At Launch Complex 41, the air quality of the inlet air for the payload was periodically monitored for Viking and continuously monitored for Voyager. Particle counts from the inlet air are shown in Table 6. This data was obtained using light scattering particle counters with isokinetic probes. The air cleanliness requirement for Class 100 air was satisfied at all times except when a High Efficiency Particulate Airfilter (HEPA) failed on Viking.

The exhaust air exiting from the bottom of the payload was qualitatively measured by disc samples during transport and hoist, and, if needed, at the top of the launch vehicle. The results from this data are given in Table 7. For Voyager 1, the microscopic examination of the pair of disc samples installed for the rollout, erection, and mating of the encapsulated payload to the launch vehicle showed particle counts significantly higher than the background count. Representative particles were subjected to a microchemical analysis. The results of this analysis are shown in Table 8. Subsequent sets of discs showed no indication of continued particulate shedding within the encapsulated payload.

TABLE 5 - PREMATE SURVEY DATA FOR ENCAPSULATED PAYLOAD AIR CONDITIONING SYSTEMS

	0.5μ	5.0μ
Payload Environmental Support Trailer	0-67	0
Launch Complex 41 Level 5	5-40	0
Level 11	0-2	0

TABLE 6 - ON-PAD PARTICLE MONITORING RESULTS TO PAYLOAD SHROUD

Range of Number of Particles Greater Than or Equal To
0.5 or 5μ Size Particle Diameter

	Particle Diameter	Requirement	Viking	Voyager
Inlet Air	0.5μ	≤100	5 to 50*	5 to 15
	5.0μ	0	0*	0
Exhaust Air	0.5μ	≤1000	5 to 230	20 to 180
	5.0μ	7	0 to 3	0 to 3**

* Except when HEPA filter failed.

** One reading, one day of 8.

TABLE 7 - SUMMARY OF VIKING AND VOYAGER DISC SAMPLING RESULTS

Number of Occurrences of Excessive Contamination

	Viking	Voyager
Post Encapsulation In Assembly Facility	0	0
Transport and Hoist	0	0
On-Pad	0	1

TABLE 8 - ANALYSIS RESULTS OF PARTICLES OBTAINED FROM VOYAGER DISC SAMPLES

Particle No.	Analysis Identification	Probable Source
1	Iron oxide, a steel corrosion product.	Common contaminants from facilities found in soils and atmosphere at Cape Canaveral.
2	A Latex paint particle.	
3	A zinc rich paint particle.	
4 and 5	Aggregates of aluminum corrosion products, coquira and sand.	Common contaminants from soil and atmosphere.
6	Coquina (Limestone)	Soil and atmosphere.
7	Aluminum alloy.	Disc sample.

Quantitative samples of the exhaust air were obtained periodically after installation of the payload on the launch vehicle. The Viking data is given in Figure 3, The following discussion provides two examples of how this type of data can be used to obtain an early indication of a problem in the air conditioning system or in the payload cavity. As the data shown in Figure 3 was being obtained during the Viking Program, the upward increase in particle contamination exhausting from the payload shroud was noted. Subsequent trouble shooting pinpointed the problem as a HEPA filter failure. The filter was taken "off-line". Because of an unrelated spacecraft problem the payload was decapsulated. Visible contaminants, most likely from the filter, were found on the spacecraft. Subsequent to the temporary repairs made to the air conditioning system, but prior to the decapsulation, another increase in exhaust air contamination was observed. Concerns were expressed as to the origin of the contamination, and it was speculated that something on the spacecraft or shroud had ruptured. Inspection of the internal structure of the shroud after decapsulation showed that the insulation matting was torn in several places. Speculated cause of the problem was the GN_2 purge (5#/minute) which entered the shroud impinging on the insulation matting at sonic speed for approximately 102 hours. The exhaust data in both of these instances proved to be useful to the launch team. During subsequent operations for both Viking and Voyager there were no recurrences of exhaust air quality exceeding the acceptance criteria.

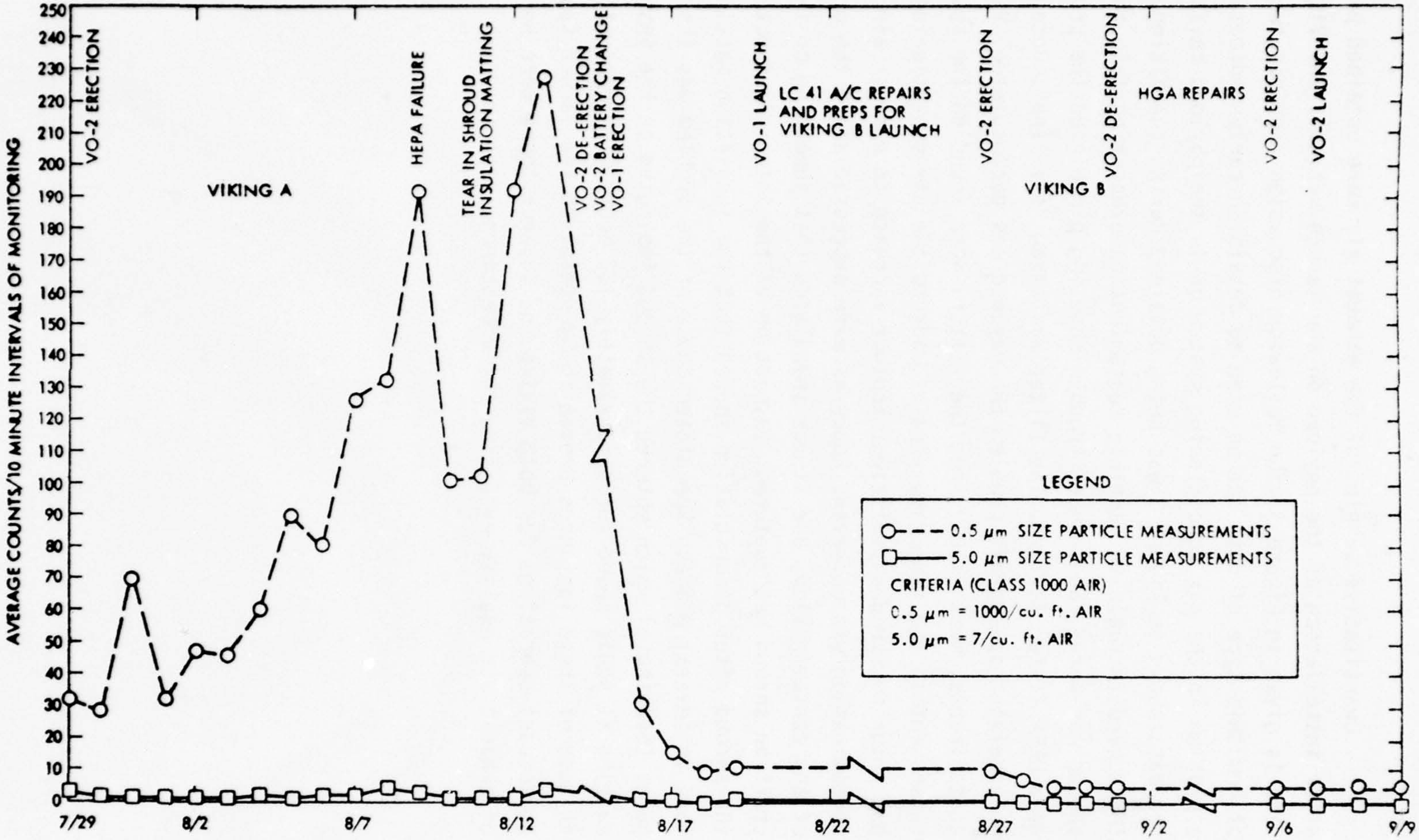

Figure 3. Particle Measurements of Viking Payload Exhaust Air at Launch Complex 41

5.0 IN-FLIGHT EXPERIENCE

Since the Viking and Voyager spacecraft were three axis stabilized, celestial sensors are used for guidance (Figures 4 and 5). If a particle comes into the star tracker's field of view, the intensity measurements increase. By determining the number of times "blips" occur, a relative measure of the number of particles passing through the field of view can be determined. Such a relative measure serves as a "report card" of the success of the particulate contamination control program. The bright particle occurrences for Viking and Voyager are shown in Figures 6, 7, 8. Release of particles were generally related to dynamic events on board the spacecraft such as the firing of pyrotechnic devices and the slewing of the science platform. Also, it should be noted that bright particle occurrences decrease as a function of time. This results from three factors: 1) particles released once generally do not re-attach and re-release, 2) the size of sensible particles increases as the spacecraft travels away from the sun, (e.g., 8μ diameter particle required near Earth, 15μ diameter near Mars, 3) no spacecraft material degradation generating particles is occurring. The conclusion to be drawn from these results is that there were relatively few bright particle occurrences and that the contamination control program for Viking and Voyager was very good. No science instrument has attributed any degradation in performance to particulate contamination. This again attests to the adequacy of the Viking and Voyager contamination control programs.

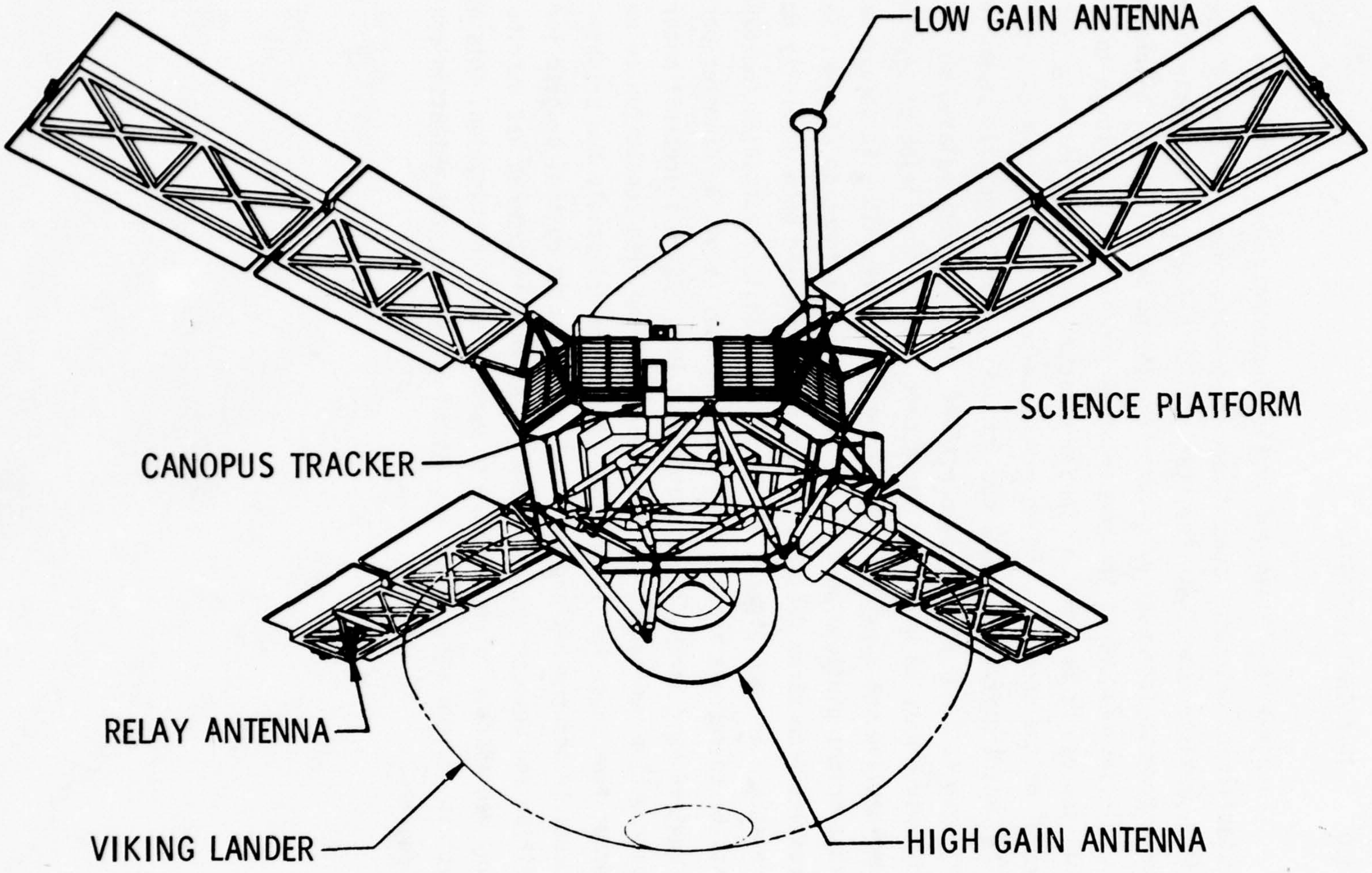

Figure 4. Viking Spacecraft

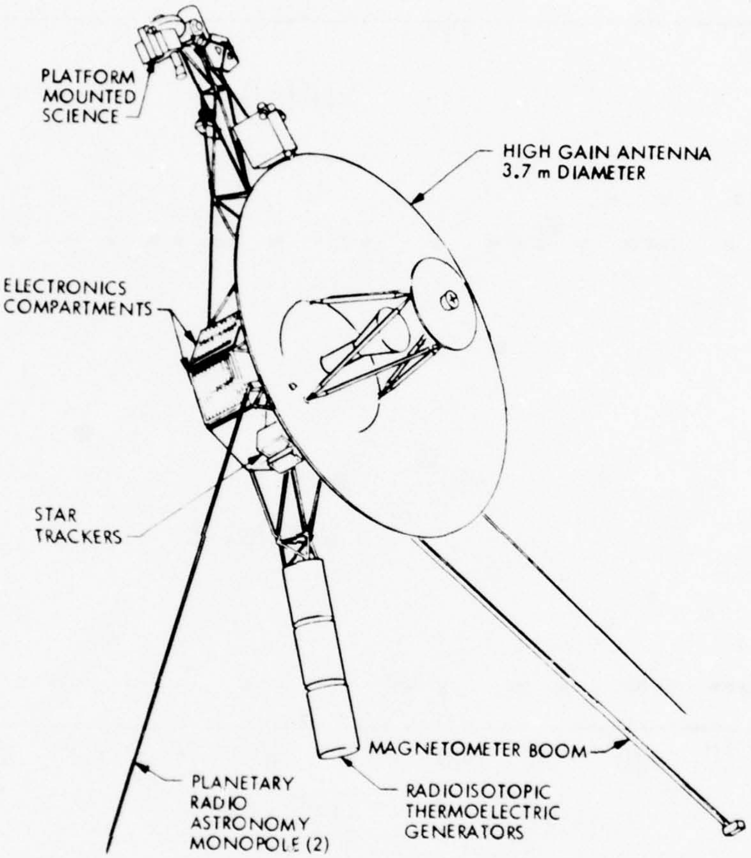

Figure 5. Voyager Spacecraft

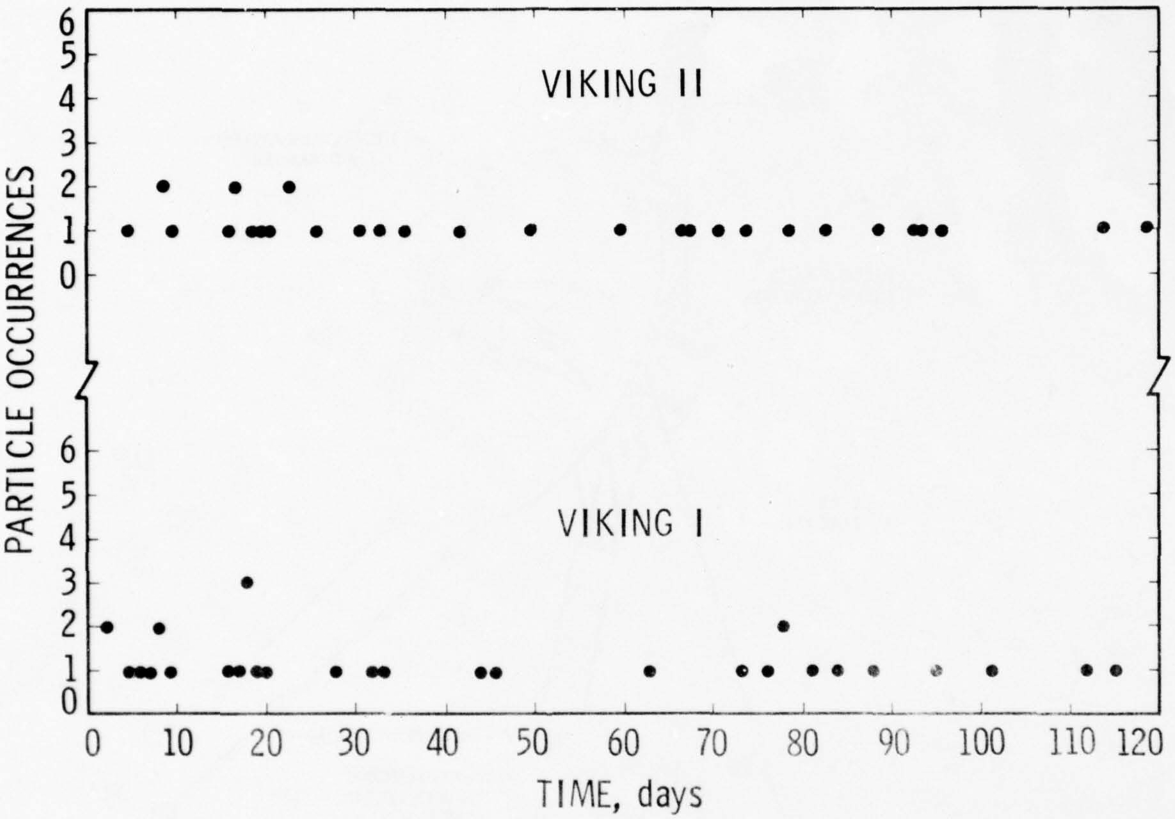

Figure 6. Viking In-Flight Particle Occurrences, Launch Through Four Months

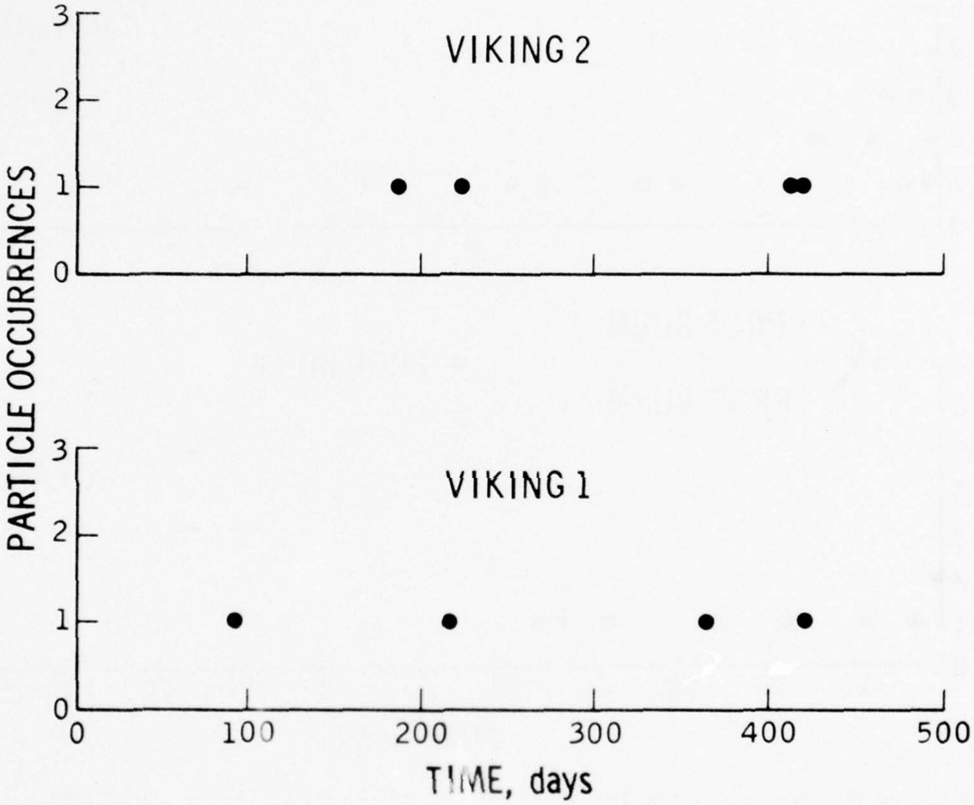

Figure 7. Viking Extended Mission In-Flight Particle Occurrences

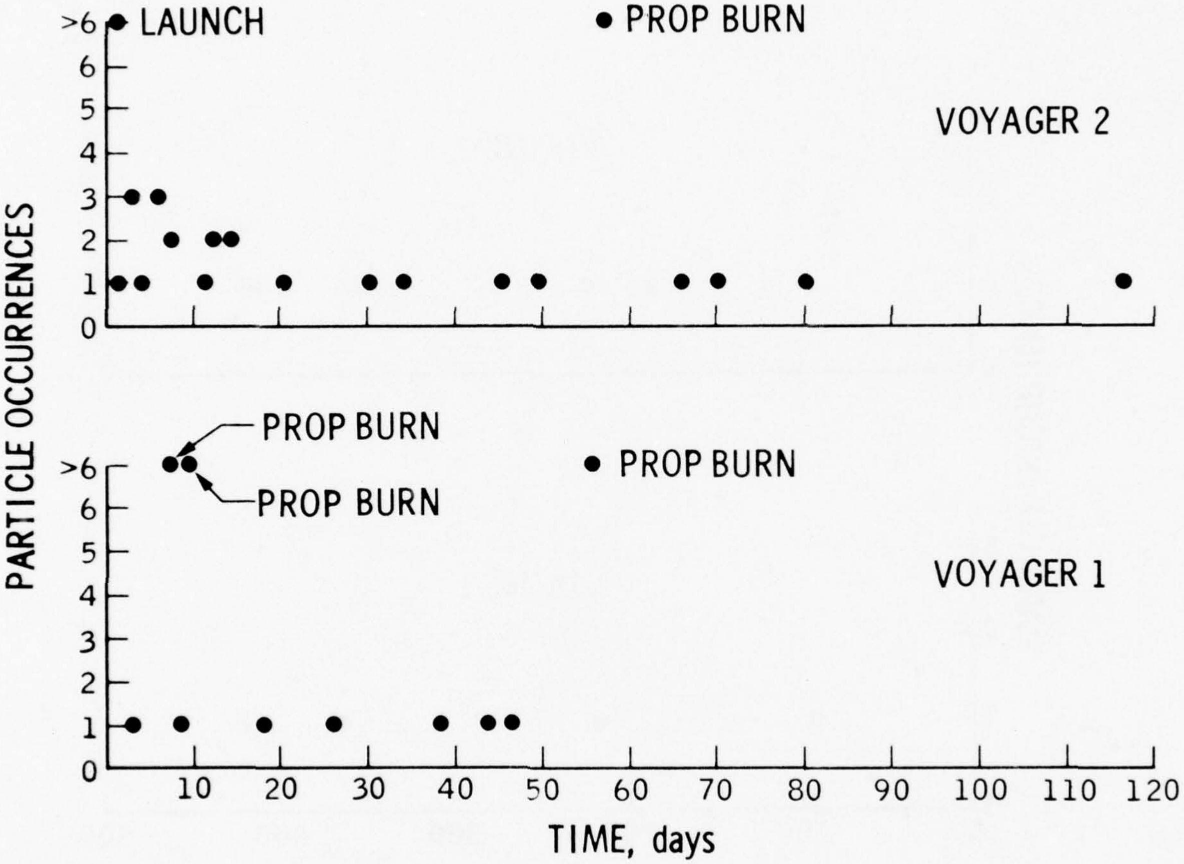

Figure 8. Voyager In-Flight Particle Occurrences, Launch Through Four Months

6.0 CONCLUSIONS

The particulate contamination control program implemented on the Viking and Voyager spacecraft resulted in visually clean spacecraft at encapsulation/launch and no in-flight anomalies attributable to particles

The particulate monitoring methods utilized provided useful quantitative and qualitative data for assessing the adequacy of the air delivered to the spacecraft. Monitoring both the inlet and exhaust air after encapsulation provides enhanced assurance that the spacecraft remains in a clean condition during transport and on-pad operations. Disc samples are a useful tool for collecting particulates for qualitative evaluation when it is appropriate to identify the source of the particles.

Acknowledgements

The contamination control programs for Viking and Voyager required cooperation of many people and several organizations all of whom made significant contributions to these efforts. F. Currington, Kennedy Space Center provided us with data and timely support during both programs. L. Daspit, Langley Research Center, Dr. J. Stern, Bionetics Co., and L. P. LaLime, formerly of Bionetics, provided untiring efforts and encouragement during the Viking Program. Appreciation to H. Schneider for his initial design concepts for the disc samples and isokinetic probes, as well as his advice throughout the programs is gratefully acknowledged.

References

1. Schneider, H. "Evaluation of Particulate Contamination for Unmanned Spacecraft Prelaunch Operations", the Journal of Environmental Sciences, January/February 1975

2nd Surface Mirror Cleaning and Verification

By

Dr. M. K. Barsh

Aerojet ElectroSystems Company
Azusa, California

The requirement that an advanced space satellite be free of contamination upon orbit insertion resulted in more stringent efforts to ensure maximum cleanliness at launch. Special techniques were developed to clean 2nd surface mirror thermal control radiator surfaces and ancillary procedures were invoked to verify their cleanliness level at launch.

Panels utilizing as many as 10,000 separate mirrors are used to achieve thermal control of the satellite system. Since the mirror panels can be exposed to a variety of potential contaminating environments during the satellite history of fabrication, assembly, ambient/vacuum testing, storage, shipment, and launch readiness, methods were studied to determine how best to clean and subsequently verify mirror cleanliness before launch. Whereas simple wiping of the surfaces with fabrics and appropriate solvents to achieve "visual clarity" may leave residues of as much as 1000 Å of surface contaminant, it was not evident how much improvement could be achieved by additional cleaning.

An effective cleaning procedure was established for 2nd surface-thermal-control mirrors using Auger Electron Spectroscopy to measure the contaminant residues on variously cleaned mirror panels. It was subsequently found that two sequential cleaning operations performed on individual mirror elements after the "visual clarity" condition had been obtained would achieve a minimal contamination level of less than 20 Å on the mirrors. In addition, a post-cleaning wipe-and-extraction procedure provided a means of verifying the level of cleanliness achieved. These techniques, currently employed to provide maximum 2nd surface-mirror cleanliness at launch of Aerojet space systems, will be described.

SURFACE CLEANLINESS

1.0 INTRODUCTION AND SUMMARY

The requirement that many of the newer more sophisticated satellite systems be relatively free of contamination for effective orbital performance demands that the cleanliness at launch be maximized. The thermal control surfaces of these satellite systems such as second surface mirrors are most critical with respect to the contamination levels. In order to effect initially "clean" critical surfaces, it was first necessary to evaluate the contamination levels of these surfaces, then to establish what levels of cleanliness could be achieved, and finally develop a practical procedure for obtaining and verifying the desired cleanliness level. Auger electron spectroscopy was utilized to determine the contamination levels on typical second surface mirror specimens and a cleaning and in-field verification procedure was developed which insured that the initial contamination levels on the mirrors would not be greater than approximately 20Å. The details are described below.

2.0 BACKGROUND

Satellite systems which require maintenance of low temperatures to insure optimum performance of critical subsystems often use passive radiators constituted of second surface mirrors whose ratio of absorptance to emissivity, α/ϵ is favorable for rejecting the maximum radiative energy while concomitantly absorbing the minimum. The presence of accumulated contamination on these mirrors increases their α and consequently degrades their thermal control characteristics. While it is evident that some contamination will collect on the systems during ascent and during orbital flight with time, it is obvious that the lower the initial level of contamination at launch, the longer the system will be able to perform efficiently. The identification that accumulated contamination could be responsible for a degradation in system performance with time, led to one phase of a dedicated contamination program effort to insure that a minimum of contaminants initially resided on the mirrors at launch.

Initial activities consisted of cleaning to visual clarity, but it was recognized that this might leave as much as 1000 Å on the surfaces. When preliminary studies with the Fullam Laboratories Corp.[1] indicated that moisture condensation on solid mirror surfaces would occur preferentially where surface contamination was significant, a cleaning study was instituted to explore what cleaning procedure would be required to guarantee minimum contamination. The initial cleaning study by Fullam involved an initial scrubbing with "Milk of Magnesia," followed by water rinses and with final detergent solution scrubbing and final water rinses. The last step constituted a final wipe with Freon 113 and drying in a clean environment. Unfortunately, interpretation of the results was muddied because it was found that the condensation patterns were strongly influenced by the thermal conductance related to the mode of attachment of the mirrors to their supportive substrate. Although the study did demonstrate that multiple

---

[1] Fullam, E.F. (Inc.), "The Attachment, Cleaning and Preservation of a Highly Reflective Surface," Report No. 1486 for Aerojet ElectroSystems Company, 9 Mar 1972.

cleanings, beyond visual clarity, could significantly improve the cleanliness level of the mirror surfaces, it was not evident how many recleanings were provident.

An alternate possibility of in-orbit cleaning by electrical discharge plasma was briefly investigated.[2] This required a bombardment of the mirror surfaces with energetic ions such as are found in an oxygen plasma. Whereas the laboratory results showed small but significant improvement by this technique, this approach was not pursued further because of the obvious difficulties in producing and maintaining a plasma over a large surface while in space.

Another approach to cleaning was considered. This consisted of applying collodion to the mirror surfaces, allowing the material to dry and then peeling the collodion away.[3] The procedure applied one or more times which requires a pure cellulose nitrate solution in ether-methanol mixture and a cheesecloth reinforcement, is purported to provide a very clean surface. Unfortunately attempts to apply this approach would wreak serious damage to the multimirror panels since the fluid collodion would migrate into the gap between the mirrors. Then, as the solidified collodion was peeled off to remove the contaminants, some of the individual mirrors might also be lifted off or damaged. Whereas the remaining mirrors might be reasonably clean, this would be offset by the extent of damage resulting from the peeling action. Consequently this approach was not pursued further.

---

2. Cruz, G.A. and Gillette, R.B., Active Cleaning Technique for Removing Contamination from Optical Surfaces in Space, The Boeing Co. Quarterly Progress Report No. 4 for GMSFC, Huntsville, Alabama, April 1, 1972 to June 1, 1972.

3. Tyndall, John B, Collodion Technique of Mirror Cleaning, NASA TECH BRIEF 70-10463, August 1970.

The primary problem in establishing the prerequisite cleaning procedure became one of determining quantitatively the resident contamination. A series of exploratory experiments with ellipsometry proved disappointing as it became evident that likely contaminants, such as silicone resin or adhesive could not be resolved effectively from the fused silica substrate because of the similarities in the indices of refraction. Ordinary optical techniques were rejected since the anticipated small thicknesses of contaminant (10-500 Å) precluded most of the techniques available.

A brief consideration of the constitution of probable contaminants revealed that the element carbon, in a wide variety of organic materials, would be a logical tracer of the presence of contaminants. Since the Auger Electron Spectroscopy technique provided a means of tracking elementary species down to very low levels, it was explored in depth. This technique, in conjunction with argon ion sputtering subsequently enabled quantitative estimation of residual contamination and permitted the establishment of a viable cleaning and verification technique. The details are discussed below.

2.1 Auger Electron Spectroscopy Studies

Preliminary studies were undertaken at Physical Electronics Inc. (PEI)[4] to evaluate the feasibility of quantitatively establishing the contamination thicknesses residing on cleaned second surface mirrors. Carbon, oxygen and silicon spectra were explored (Figure 1) and the peak-to-peak distances from the curve traces were used as a measure of the quantity of contaminant present when the contaminant levels were in the range of 50 Å. Further it was subsequently suggested by Dr. Palmberg (of PEI) that the C to Si peak-to-peak ratios would

---

4. Palmberg, H., Private Communication, Physical Electronics Industries, Inc., Edina, Minnesota, December 1972.

378-1173

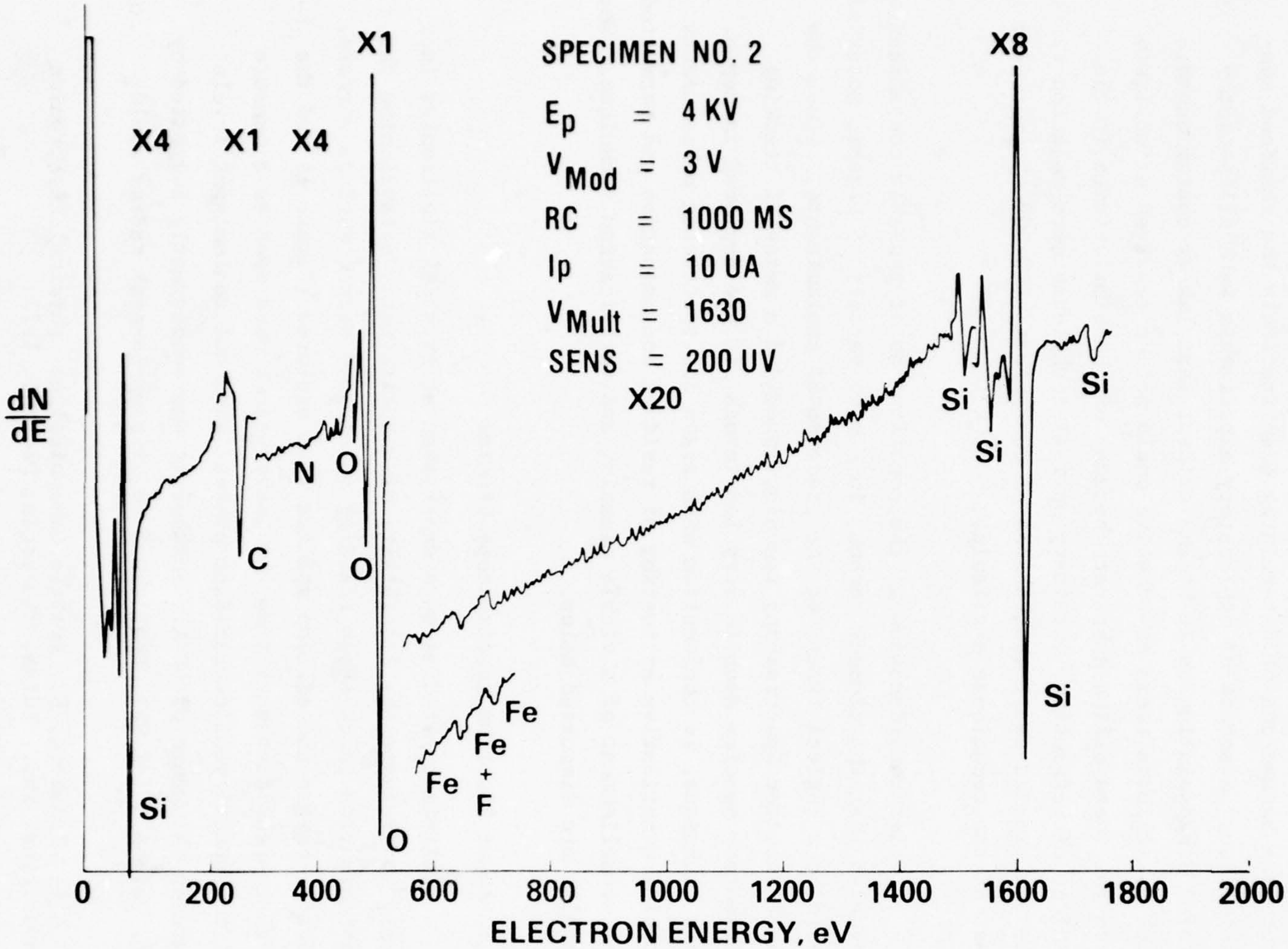

FIGURE 1 CONTAMINATION SPECTRA

provide a more accurate evaluation of the quantities of contaminant since the spectra of both would be evident during analysis. Further it was noted that the use of an argon ion sputtering beam could be used to etch away the contaminant while the Auger analysis was occurring so that a continuous record could be had of the contaminant removal with time. Using the etching technique it was relatively simple to establish when all of the contaminant was removed since the carbon peaks characteristic of the contaminants would disappear. Although silicon and oxygen peaks would vary somewhat during the sputtering, it was nevertheless not difficult to distinguish between the contaminant and substrate peaks.

A variant of the Argon sputtering and simultaneous Auger analysis was subsequently invoked which provided a relatively direct thickness calibration of the carbon-to-silicon peak ratios. Extensive exploration of a wide variety of organic materials had revealed that a sputtering beam of a given energy would etch away the organic material at a known fixed rate. The equipment was then programed to repetitively scan over a very narrow band in a sawtooth mode corresponding to the carbon peak. With the recording graph paper driven at constant speed, and the AES activated, the sputtering beam was turned on and maintained until the carbon peak-to-peak values had dwindled to zero (Figure 2). It was then a simple matter to estimate the initial thickness of contaminant and to correlate it with the C to Si ratios.

2.2 Cleaning Studies

The use of the thickness measuring tool described above enabled a cleaning evaluation study to be undertaken. This consisted of evaluating several cleaning materials and techniques. In order to fully appreciate the problem it is enlightening to consider the way in which the second-surface-mirror temperature control (TC) surfaces were constituted. The TC panels consisted of

378-1164

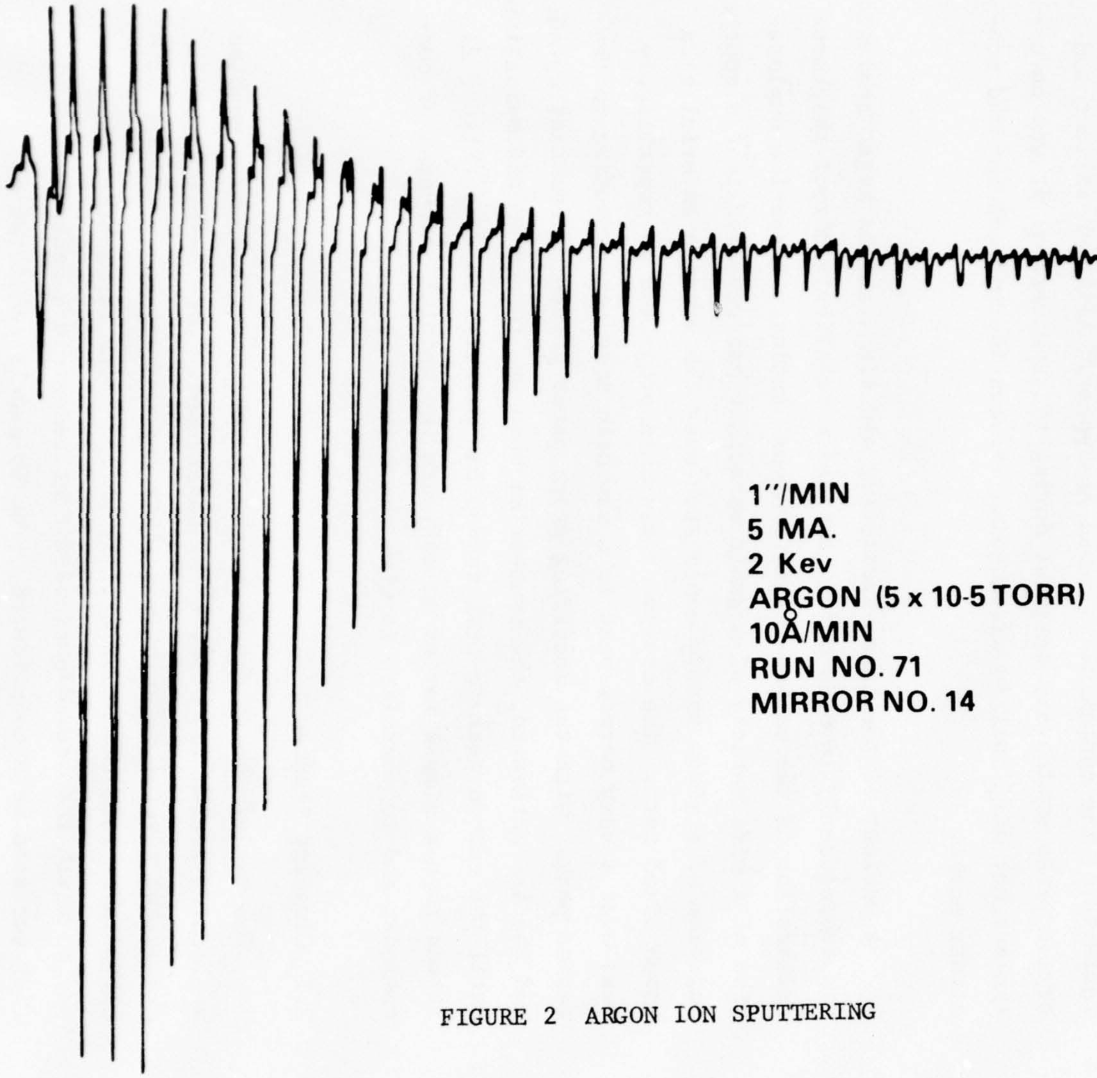

FIGURE 2 ARGON ION SPUTTERING

one inch square second-surface fused silica mirrors bonded to a magnesium substrate. However, in order to accommodate thermal excursions and accompanying expansion and contraction forces, the mirror panels, as fabricated, were separated by a gap of 0.006 inches. In order to clean these panels, account had to be taken of the problem of "wiping" contaminants into the gaps and subsequently extracting the contaminant out to spread over the mirror surfaces. Conceptually, the cleaning procedure was divided into two phases: (a) general overall wiping with appropriate cloths and solvent and (b) specific individual mirror cleanings to circumvent the gap problem. The questions which required resolution were: (1) how much initial/general wiping should be done and to what criteria; (2) what type of wiping material; (3) what solvents; (4) how should the individual mirrors be cleaned; (5) what type of cleaning materials; (6) what solvents; (7) how many repetitive cleanings are necessary to achieve minimum cleanliness; and (8) how could this level of cleanliness be verified both at the factory and at the launch site.

The first problem that was approached was to select a method and the materials for the cleaning. Since, at the inception of this effort, no major modification of the space system was considered acceptable, it was necessary to choose a technique that would be practical for both the factory and launch sites. The method selected was that implied above; namely, that an initial overall wiping to visual clarity would be followed by repetitive individual mirror recleaning wipings. Several materials and solvents were considered and were tried on individual mirrors of the mirror panels which had been artificially dirted with RTV566, a typical tenacious contaminant candidate. The mirrors were subsequently analyzed by the Auger technique and the results are shown in Figure 3. It may be seen that the smallest

SOLVENT SYSTEM	DEPOSITS REMAINING
Detergent*	> 50 Å
Detergent/Perchloroethane*	> 8 Å
Ethanol/90-10, 1,1,1 Trichloroethane, Ethanol**	6.5 Å

*Process studied by Aerospace Corporation

**Solvent mixture contains less than 1 ppm of non-volatile residue.

FIGURE 3 EFFECTS OF SOLVENT ON CLEANING EFFECTIVENESS deposit was obtained using the 1,1,1 trichlorethane/ethanol solvent mixture. The cloths selected for the wipings, optic cotton cloth, were those which would not degrade with 150 cycle Sohxlet extractions with methanol (found to be most effective) and would be reasonably wetted by the selected solvents.

The next problem approached was the maximum practical level of cleanliness that could be achieved assuming the use of a general precleaning followed by repetitive individual mirror cleanings. Clearly an infinite number of repetitive cleanings appear superficially to be ideal but it was anticipated that something less than this would prove to be adequate. The approach taken was to fabricate a series of 2 by 2 mirror panels (4 mirrors total) incorporating the expansion gaps described above (see Figure 4). These panels were limited to this size to accommodate their introduction into the Auger equipment. The panels were then variously "dirtied." Some were handled with incipient contamination whereas others were carefully and "excessively" precleaned and subsequently "redirtied" with RTV566 adhesive. The mirror panels were treated in various ways prior to insertion into the Auger system. They were all initially subjected to a general overall wipe-cleaning to visual clarity; i.e., no evidence of any contamination could be seen with the naked eye when illuminated by the use of a narrow collimated light beam. Then individual mirrors were carefully cleaned, some once, others twice, and more. Auger measurements were subsequently made on the panels and the results are summarized in Figure 5. It can be seen that no significant improvement is to be expected if the individual mirrors are cleaned more than 2 times each, after visual clarity had been achieved and that the minimum contaminant thickness would be about 8-10 Å.

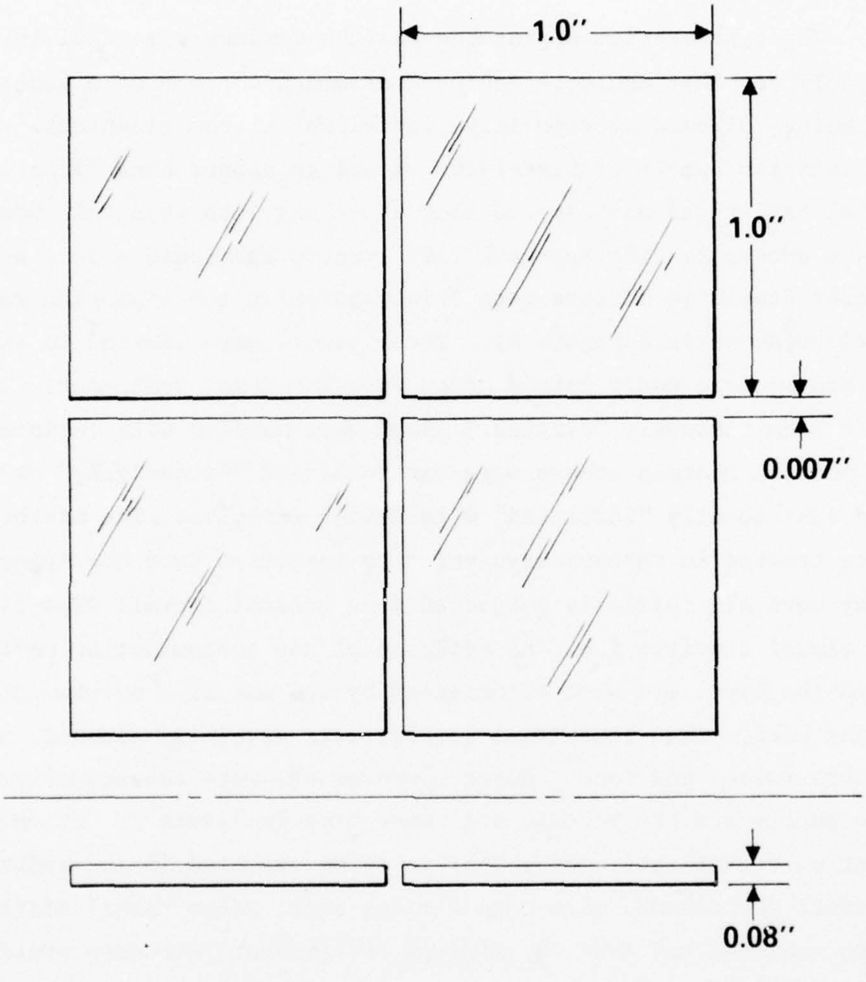

FIGURE 4 MIRROR TEST PANEL

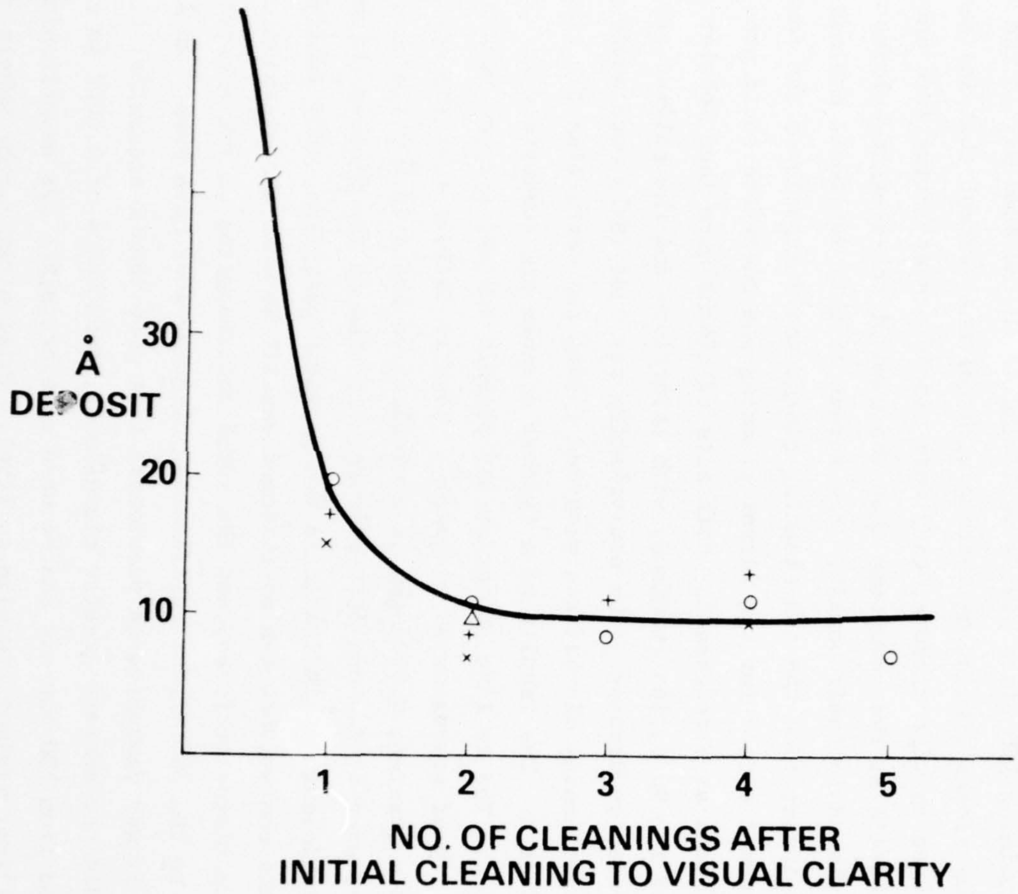

FIGURE 5 EFFECTS OF MULTIPLE CLEANINGS

The remaining problem, the development of a practical cleanliness verification technique, was solved using a variation of the cleaning procedures described above. A set of approximately 300 mirrors in a typically assembled panel were individually cleaned using one small piece of cloth for two mirrors after first having been cleaned overall to visual clarity. Another 300 pieces of extracted cloth were set aside for the second individual mirror cleaning. 150 pieces were used for cleaning the 300 mirrors and were subsequently stored in a clean bottle. The remaining 150 cloth pieces were handled in the same way as the cleaning cloths (including wetting with solvent) except that instead of being used to wipe mirrors, they were placed one-at-a-time into another clean bottle at the same time that the used mirror-cleaning-cloths were being placed in their bottle. The intent of this duplicate procedure was to insure that the non-cleaning cloths would experience the same environment except for the mirror cleaning and therefore could provide a valid blank as a reference. Both sets of cloths were then Sohxlet extracted for 90 cycles (minimum) with chloroform and the solvent carefully evaporated to dryness. The non-volatile residues (NVR) were weighed and the non-cleaning cloths data provided a tare for correcting the cleaning cloths data. The results of a typical example are summarized in Figure 6. The residue are primarily organic and are assumed to have a density of approximately 1 gm/cm^3. Thus it follows that the net amount extracted, 0.0002 gm, is equivalent to about 10 Å depth covering the area of 300 one inch mirrors. In view of the minimum thickness achievable as indicated in the previous paragraph, this implies that the contaminant was partitioned equally between the cleaning cloths and the mirror surfaces, and the total contamination on the mirrors, prior to the 300 mirror verification cleaning must have been ~ 20 Å. Since it was demonstrated previously that more than 2 sequential cleanings did not achieve greater cleanliness, this value of 0.0002 gm extracted from 300 mirrors can be used as a criterion for establishing a practical maximum cleanliness level. This, after mirror panels were

Sample	NVR Wt. (mg.)
• 150 cloths from cleaning 300 1-in. mirrors	0.57
• Tare from 150 cloths	0.37
• Net contaminant	0.20 mg.

FIGURE 6 VERIFICATION DATA

believed to have been adequately cleaned to visual clarity, a sample consisting of a 300 mirror panel was recleaned, one mirror at a time, with 150 pieces pre-extracted cloth and pure solvent mixture. The requirement was subsequently stipulated that the net extract from the cloths used for the 300 mirror cleaning shall be equal or less than 0.0002 gm to insure that the contamination on the mirror panels would be equal or less than 20 Å.

3.0 CONCLUSIONS AND RECOMMENDATIONS

The validity of the extractive approach is predicated on the assumption that all contaminants would be partitioned between the mirror surfaces and the cloths in the same manner as it was in the test procedure. For ordinary contaminants derived from handling or even from the possible deposition or surface migration of tenacious materials, such as the silicones, this is probably true. However, it is obvious that a fully cured epoxy resin on the mirror surface might not provide valid data in the cleaning-extraction process. Perhaps the crux of the matter lies in the fact that the first step in the cleaning procedure requires "visual" clarity; a condition which could hardly be obtained with a fully cured epoxy. Further, additional tests using mirrors predirtied with various silicone adhesives and oils, epoxy, acrylic and polyurethane adhesives gave essentially the same results once the condition was met that the initial visual clarity cleaning was achieved.

One of the concerns with the one-at-a-time mirror cleaning technique was the possibility that with the cleaning of large numbers of mirrors using extreme care to avoid crossing over the gaps between the mirrors, some of the mirrors might not be cleaned to their extremities as a result of fatigue, unintentional carelessness, etc. The resultant effects might not be picked up by the verification technique since it was basically the same as the cleaning technique.

Subsequent experiments with multiple overall wipes with larger pieces of cloth suggest that a 10-fold repetitive procedure might accomplish the same as one overall wipe to visual clarity followed by 2 sequential individual mirror cleanings. The 10-fold procedure appears more attractive than the separate mirror especially where 10,000 or more separate mirrors are involved. This alternate procedure is still under investigation as it has not yet been demonstrated that it might not wipe the surface contaminants into the gaps. Subsequently the contaminants might migrate out onto the mirror surfaces to defeat the intention.

With reference to verification techniques, the state-of-the-art of the configuration of spacecraft has developed recently to such an extent that it now appears attractive and feasible to incorporate small witness plates of 4 individual mirrors each into the second surface mirror thermal control surfaces. These witness plates could subsequently be removed to an Auger Spectrometer and their surfaces directly analyzed for contamination. This would circumvent the obvious shortcomings of the extractive verification procedure. This alternate approach appears most attractive and is currently under consideration for use with some of the space systems fabricated by Aerojet.

4.0 REFERENCES

1. Fullam,E.F. (Inc.), "The Attachment, Cleaning and Preservation of a Highly Reflective Surface," Report No. 1486 for Aerojet ElectroSystems Company, 9 Mar. 1972.
2. Cruz, G.A. and Gillette, R.B., Active Cleaning Technique for Removing Contamination from Optical Surfaces in Space, The Boeing Co. Quarterly Progress Report No. 4 for GMSFC, Huntsville, Alabama, April 1, 1972 to June 1, 1972.
3. Tyndall, John B, Collodion Technique of Mirror Cleaning, NASA TECH BRIEF 70-10463, August 1970.

4. Palmberg, H., Private Communication, Physical Electronics Industries, Inc., Edina, Minnesota, December 1972.

PUNCTURE DISCHARGES IN SURFACE DIELECTRICS AS CONTAMINANT SOURCES IN SPACECRAFT ENVIRONMENTS[+]

E. J. Yadlowsky, R. C. Hazelton, and R. J. Churchill
Colorado State University
Fort Collins, CO 80523

ABSTRACT

Spacecraft in geosynchronous orbits are known to become charged to large negative potentials during the local midnight region of the satellite orbit. This surface charging results in electrical discharges which can cause electrical interference with on-board electronic systems. The discharges also constitute a source of contamination for spacecraft sensors and thermal control surfaces because of the transport of charged and uncharged discharge products from the site of the electrical discharge. Such discharges have been studied in the present work by the electron beam irradiation of dielectric samples in a vacuum environment. In addition to static measurements and photographic examination of the puncture discharges in the Teflon samples, the transient characteristics of the electrical discharges are determined from oscillographs of voltage and current and by charged particle measurements employing a biased Faraday cup and a retarding potential analyzer. Using these latter techniques, studies of angular and energy distributions of charged particles have indicated an initial burst of high energy electrons (5 x 10^{13} per discharge at energies greater than

[+] Sponsored by NASA Grant No. NSG-3145.

3000 eV) followed by a less intense burst of lower energy negative particles. Positive ions are emitted from the discharge site in an initial high velocity burst followed by a lower velocity burst tentatively identified as carbon. The fact that these particles are measured some 15 cm from the discharge site dramatically indicates the extent to which the discharge constituents may contaminate the satellite environment with particulate deposition and radio frequency noise signals.

1.0 INTRODUCTION

The occurrence of electrical discharges on the surfaces of satellites which penetrate the magnetospheric plasmas is now recognized by spacecraft designers as a technological problem of not insignificant difficulty. For example, the ATS-5 and ATS-6 satellite data revealed the existence of particle fluxes which cause negative surface potentials as high as 20 kV. The spacecraft charging phenomena and the resultant deleterious effects are described in a number of publications and reports.[1-3]

Under a research grant from NASA (NSG-3145) Colorado State University has undertaken a program wherein the spacecraft charging phenomenon is simulated in a laboratory vacuum chamber by irradiating suitable dielectric targets with an electron beam operating at accelerating potentials from 0-34 kV. A circular Teflon sample is mounted on an annular ring and is enclosed by a grounded aluminum box whose entrance aperture assures that the edges of the Teflon sample are not directly irradiated by the electron beam. This arrangement facilitates the study of particle emission and material damage on both the front and

1. Spacecraft Charging by Magnetospheric Plasmas, (Progress in Astronautics and Aeronautics, Vol. 47) A. Rosen, ed., Cambridge, Mass., MIT Press (1976).
2. Proceedings of the Spacecraft Charging Technology Conference, eds. C. P. Pike and R. R. Lovell, Air Force Geophysics Laboratory (1977).
3. "Space Radiation Effects (Session D of the Annual Conference on Nuclear and Space Radiation Effects," IEEE Transactions on Nuclear Science, NS-24 (No. 6):2244-2304 (1977).

back surfaces of the Teflon sample. Measurements are made of electron beam charging current, charging time, and surface voltage under static conditions while oscillographs in conjunction with transient current probes, fast response potential dividers, loop antennas, photomultipliers and charged particle detectors record the transient nature of the electrical discharges. The physical appearance of the self-luminous electrical discharges is recorded with time-integrated photography, and the resultant damage to the dielectric surface as well as the sites of discharge punctures through the dielectric layer are examined by means of scanning electron beam micrographs. The charged particles emanating from the site of the puncture-type discharges have been measured with biased Faraday cups and retarding potential analyzers.

The most prominent damage feature revealed by the photographs is the existence of crater-like punctures, some 0.06 mm in diameter, through the Teflon layer from the front surface to the silver layer which coats the back surface of the sample. Puncture-type breakdowns occur in one mil Teflon samples at an electron beam voltage of 10 kV, whereas 3 mil Teflon samples break down at a 24 kV electron beam voltage. These values are to be compared with the 10-20 kV negative potentials to which spacecraft surfaces become charged.

Preliminary results indicate that both electrons and positive ions are emitted from the electrical discharge and that significant quantities of heated Teflon are transported from the discharge site to the nearby dielectric surfaces. Angular and energy distributions of charged particles have indicated an initial burst of high energy electrons with energies in excess of 3000 eV and ∿ 5 x 10^{13} electrons emitted per electrical discharge. This is followed some 5 μsec later by a less intense burst of lower energy (< 85 eV) negative particles. Positive ions are also emitted from the discharge site in an initial high velocity burst followed by a lower velocity burst of ions tentatively identified as carbon.

In the remainder of this paper the experimental system is discussed briefly. This is followed by a description of the experimental techniques and conditions of particular interest in the area of spacecraft contamination. Results are given for puncture discharges and a wide range of charged particle emissions. Tentative identification of several potential spacecraft contaminants is made.

2.0 EXPERIMENTAL SYSTEM

The spacecraft charging phenomenon is simulated in a vacuum chamber by irradiating a dielectric target with a high-energy electron beam. It is convenient to discuss the total system relative to the schematic diagram shown in Fig. 1.

The simulation chamber consists of a 30 cm diameter cylindical glass tube about 1 meter in length. Four cylindrical ports 15 cm in diameter located at the central section of the tube provide outlets for vacuum ports, introduction of electrical and photographic measurement systems and the installation of target assemblies. The electron beam

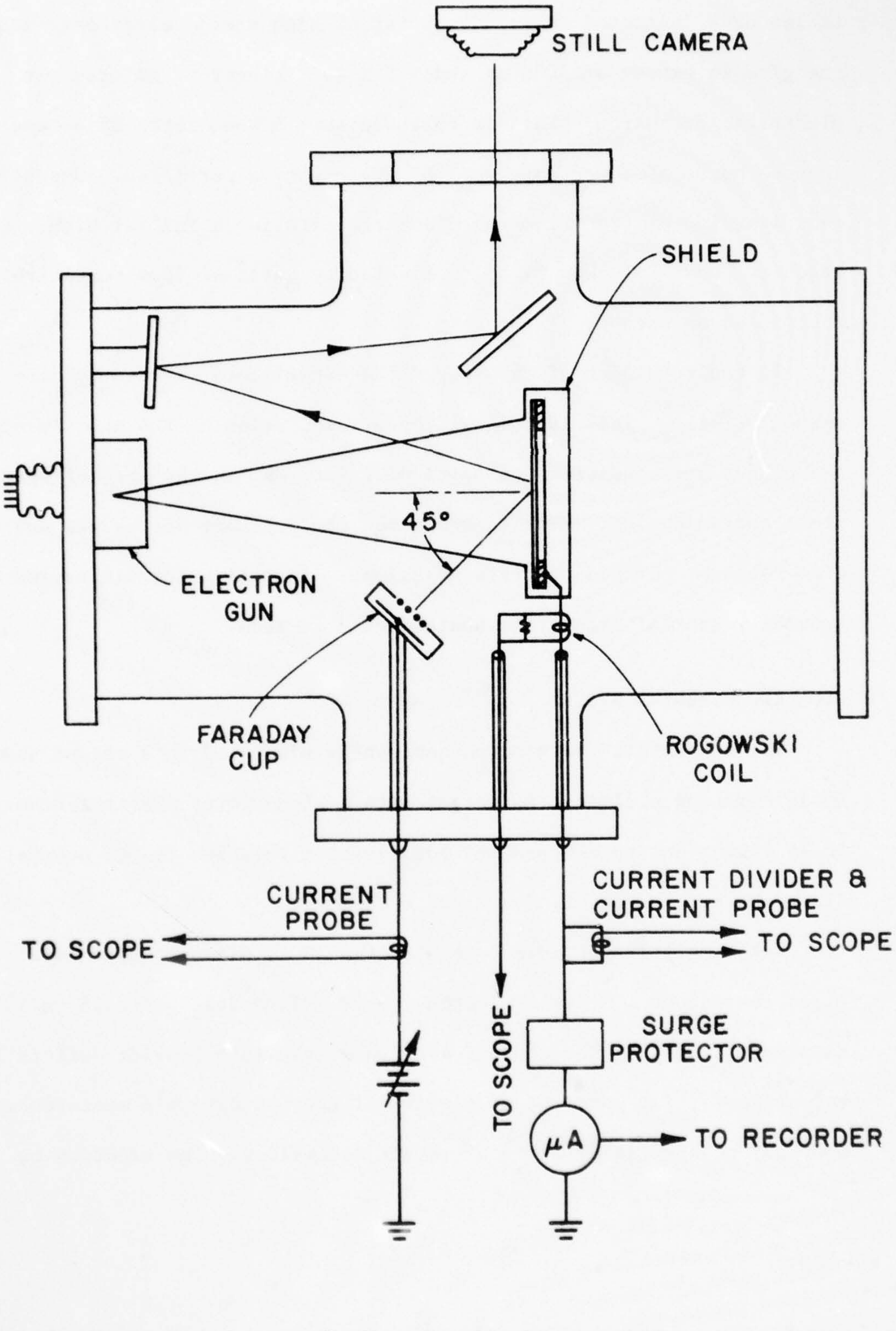

Figure 1. Spacecraft Charging Simulator and Measurement System.

AD-A070 386 AIR FORCE MATERIALS LAB WRIGHT-PATTERSON AFB OH F/G 22/2
PROCEEDINGS OF THE USAF/NASA INTERNATIONAL SPACECRAFT CONTAMINA--ETC(U)
1978 J M JEMIOLA
UNCLASSIFIED AFML-TR-78-190 NL

11 OF 13
AD
A070386

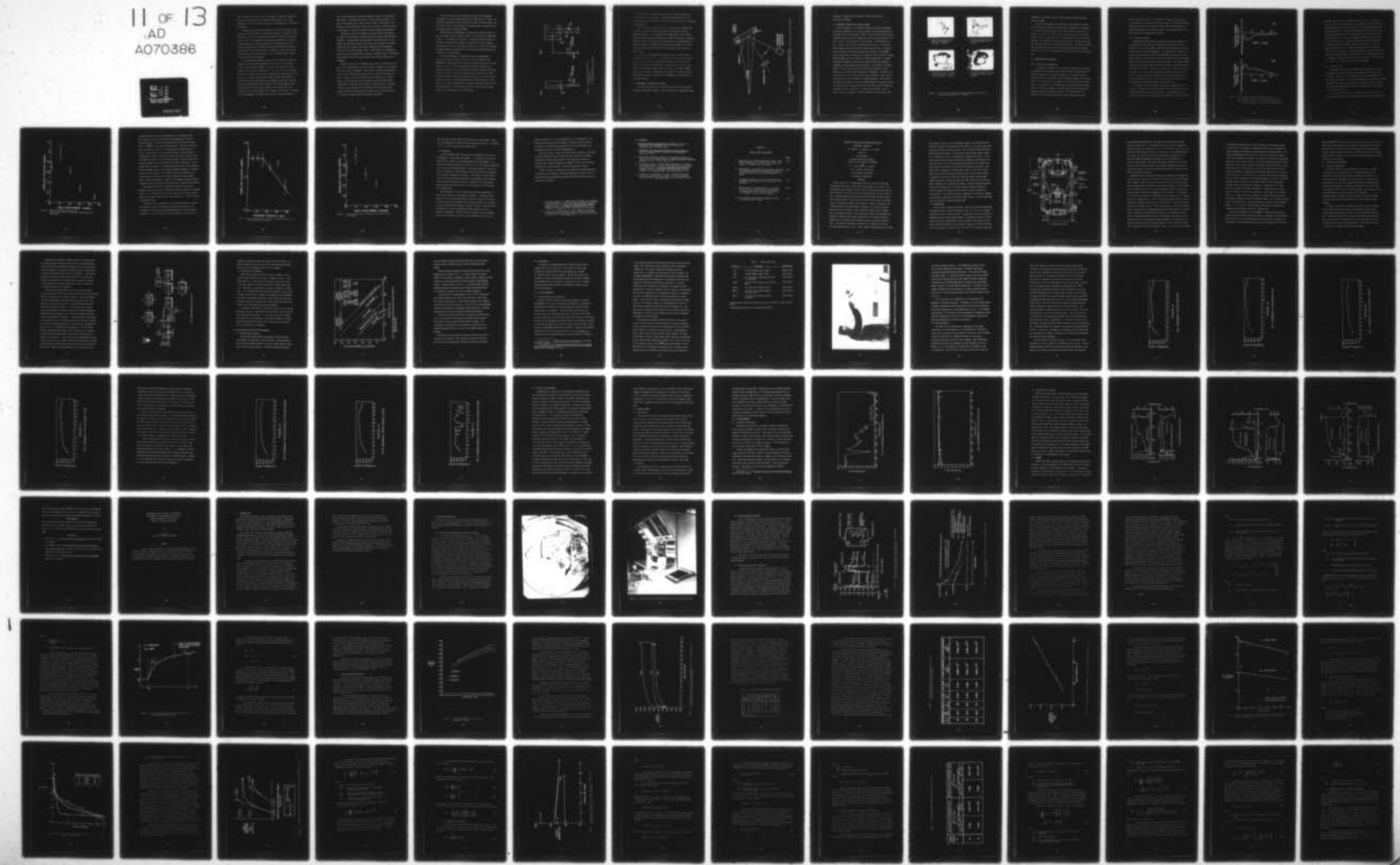

gun is located at one end of the 30 cm diameter cylinder and generates an axial electron beam to the centrally-located target area. Base pressures of 10^{-7} Torr are possible using a 10 cm diameter oil diffusion pump system.

To simulate the spacecraft charging the dielectric targets are bombarded with a mono-energetic electron beam having an acceleration potential from 0 to 34 kV and a beam current density at the target location of 0-5 nA/cm^2. The divergent electron beam is generated by a directly-heated filament and a grounded, spherical accelerating grid. Beam forming electrodes and the cathode are negatively biased with respect to the grounded accelerating electrode. Uniformity of the electron beam over the target area is about 25% for a 10 cm diameter target located 50 cm from the electron beam gun.

The silver-backed dielectrics used in the irradiation process are mounted on various target assemblies at the center of the four-port region of the simulation chamber so as to have the dielectric front surface of the target at right angles to the axis of the electron beam. The sample is supported by an annular aluminum ring providing electrical contact to the silver-backed Teflon sample through conducting paint. Some 10 cm of the target diameter are unobstructed from front and back so that observations may be readily made. The entire sample holder is placed within but electrically insulated from a grounded enclosure containing an aperture through which the sample is irradiated. By means of this arrangement, the sample edges are not irradiated directly by the electron beam thus facilitating breakdown studies not dominated by edge effects. Provisions are made to attach potential dividers to the back of the sample, and to insert current probes, electrometers, and Rogowski coils in the sample current paths to ground. The front surface of the sample is visible for inspection and photographic measurements.

During the process of charging the target surfaces, measurements are made of electron beam accelerating potential using a high impedance voltmeter, electron beam current magnitude and distribution over the target area utilizing a rake of five plane current probes with electrometers and chart recorder, and sample charging current employing an electrometer and chart recorder system. Time duration of charging and time to electrical breakdown are recorded to provide a means of estimating the potential to which the target surface has become charged prior to breakdown.

During the electrical discharges which occur at the dielectric targets, short time-duration voltage and current transients are associated with the electrical breakdown. The transient voltages associated with the electrical discharge are measured with a capacitive potential divider. Current transients are measured by a Tektronix CT-1 current probe. Both voltage and current transients are fed through coaxial vacuum-sealed connectors and recorded on a Tektronix 556 oscilloscope. A series of loop antennas 3 cm in diameter and an electronic event counter are used to record electrical signals at various points near the dielectric target during the discharge occurrence.

A system of mirrors and viewing ports permits time-integrated photographs of the self-luminous electrical discharges to be taken. The resultant photographs of the discharge path along the sample surface and the central site of the discharge are correlated with scanning electron microscope studies of material damage.

Charged particle measurements are made using a biased Faraday cup and a retarding potential analyzer (RPA), both of which are illustrated in Fig. 2. The Faraday cup consists of a shielded collector which can be biased to collect either positive or negative particles through a grid aperture of 2.5 cm. The output current of the collector is shunted to ground through a 50 ohm load and the resulting voltage measured with a Tektronix 556 oscilloscope.

The retarding potential analyzer used for the measurement of emitted particles, consists of a particle collector plate and two independently biasable grids enclosed in a grounded shield with an input aperture of 1.2 cm. For the measurement of positive particles the collector is biased at -9 V to capture the positive particles which pass through the grids. Grid G2, the suppressor grid, is biased at -800 V to prevent secondary electron emission from the collector surface which would give rise to erroneous measurements of positive particles. The first grid is then biased positively defining a threshold energy for the incoming particles. By varying the bias on the first grid the energy spectrum of the incoming ions can be measured.

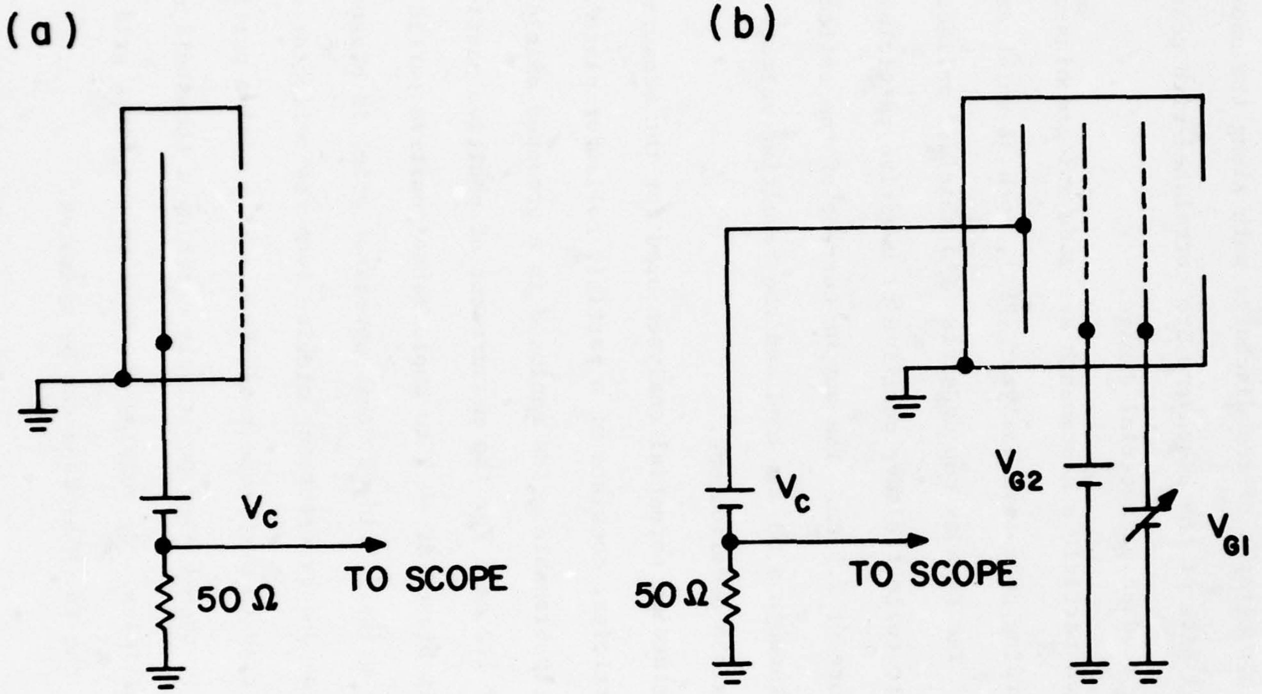

Figure 2. Charged Particle Detectors:

a) Faraday cup.

b) Retarding Potential Analyzer.

The output of the collector is measured in a manner identical to that used with the Faraday cup. A temporally-resolved particle flux is thereby derived and particle transit times and total particle emissions are determined.

With the collector biased to + 9 V, the second grid grounded, and the first grid biased negatively, similar measurements are made for negative particles. In all cases the true amplitudes of the incident particles are derived by multiplying the measured signal by the weighting factor of 1.8 which accounts for grid attenuation. The distribution of particle energies is obtained from the measured dependence of collector current on retarding grid voltage by differentiation with respect to grid voltage.

For the angular measurements presented herein, the probes were configured as shown in Fig. 3. The sample is set at ∿ 40° to the beam axis to allow observation of normally emitted particles without the detector interfering with the beam. The Faraday cup is set at a fixed angle of 40° below the sample center line and 9.5 cm from the sample surface while the RPA can pivot about the sample 15 cm from the center. The RPA has an angular resolution of 3° assuming a point discharge at the target surface.

3.0 MEASUREMENT TECHNIQUES AND RESULTS

In this section results are first given for the area of Puncture Discharges and Material Damage. This is followed by a somewhat detailed

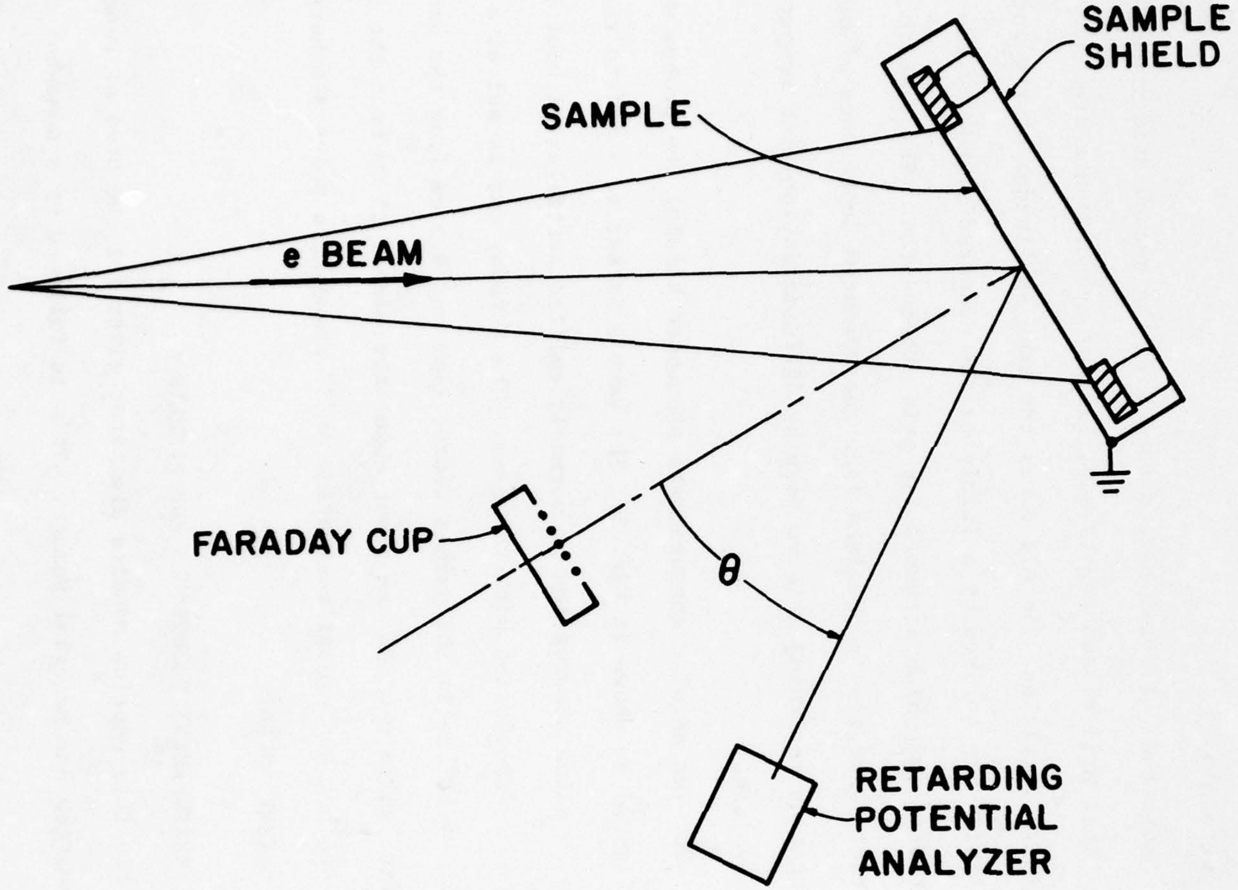

Figure 3. Angular Distribution Measurement System
(Relative orientation of dielectric sample, electron beam and charged particle detectors).

treatment of Charge Particle Emission from the sites of the electrical discharges.

3.1 PUNCTURE DISCHARGES AND MATERIAL DAMAGE

Material damage on the irradiated dielectric surface following an electrical discharge has been studied using an optical microscope and a scanning electron beam microscope (SEM). The optical microscope reveals information about sub-surface damage as well as surface damage while the SEM is used for high resolution surface studies. The photographs in Fig. 4 reveal a hole through the dielectric material to the grounded silver backing resulting from the discharge current flow. In addition, this microscopic investigation reveals the existence of filamentary surface tracks which terminate at the holes as in Fig. 4a and 4b. These material damage tracks are similar in form and appearance to luminous Lichtenberg streamers observed on the surface during the discharge although no direct comparison has been made. The tracks in the Teflon appear to be the results of currents which flow through the Teflon parallel to the surface when the sample is discharged. Ionization and recombination in the current channels are accompanied by light emission which gives rise to the luminous Lichtenberg patterns. The process of discharging the sample by currents flowing underneath the sample surface is consistent with puncture sites where filamentary material damage has occurred as in Fig. 4a and 4b. At other sites as shown in Fig. 4c, where there is no evidence of current channels near the puncture site,

a. Optical micrograph showing subsurface filamentary structure. (100 X)

b. Scanning electron micrograph of breakdown shown in 4a. (250 X)

c. Scanning electron micrograph of non-filamentary breakdown from Teflon side (300 X)

d. Scanning electron micrograph of damage to silver side. (300 X)

Figure 4. 3 mil silver-backed Teflon sample irradiated at 26 kV with a beam current density of ∿ 1 nA/cm^2.

discharge of the sample occurs by other processes having different electrical paths.

The micro photographs of the discharge sites dramatically demonstrate the material damage resulting from the discharges on the sample. It is evident that the energy in the current channel is sufficient to rupture the channel as in Fig. 4b and to eject molten Teflon from the puncture site. In addition, there is appreciable silver loss from the grounded silver backing as seen in Fig. 4d as well as extensive melting and ejection of material from the discharge sites. The material ejected from the discharge sites in the form of molten material and charged particles is a source of contamination of the spacecraft and its environment.

3.2 CHARGED PARTICLE EMISSION

3.2.1 Measurement Normalization

A correlation technique has been used to compensate for variations in discharge characteristics when measuring either the distribution of particle energies or the angular distribution of emitted particles because the entire distribution cannot be measured during one discharge event. In this approach, the Faraday cup with fixed bias and location serves as a monitor used to normalize the retarding potential analyzer signal. This allows changes in the RPA signal levels associated with changes in angle or energy distribution to be distinguished from variations in discharge characteristic. This procedure allows the results of certain events to be discarded if a significant departure of the signature on the monitor detector is noted. Since the normalized procedure does not remove variation between different measurements for fixed RPA parameters, an average of three or more normalized events is used to improve the measurement statistics.

3.2.2 Negative Particles

Using the particle detection techniques previously outlined, the time histories of the positive and negative emitted particles were recorded. Traces of the negative particles and positive particles are shown in Fig. 5a and 5b, respectively. The negative trace consists of an early spike followed by a much lower amplitude broader pulse. The early pulse of fast electrons is consistently present for each discharge while the later pulse is present only occasionally. The origin of these signals can be directly ascribed to the collection of particles because the signals are absent if the detector is rotated to a position behind the sample. Also, the signal attributed to positive particles on the RPA can be made to vanish by applying sufficiently positive biases to the retarding energy grid G1 in Fig. 2 while positive particles are still detected on the appropriately biased Faraday cup.

The energy of the early pulse of electrons is measured to be in excess of 3 KeV since a retarding potential of this value did not significantly attenuate the collector current. A determination of the electron energies was not possible since breakdowns in the RPA circuitry

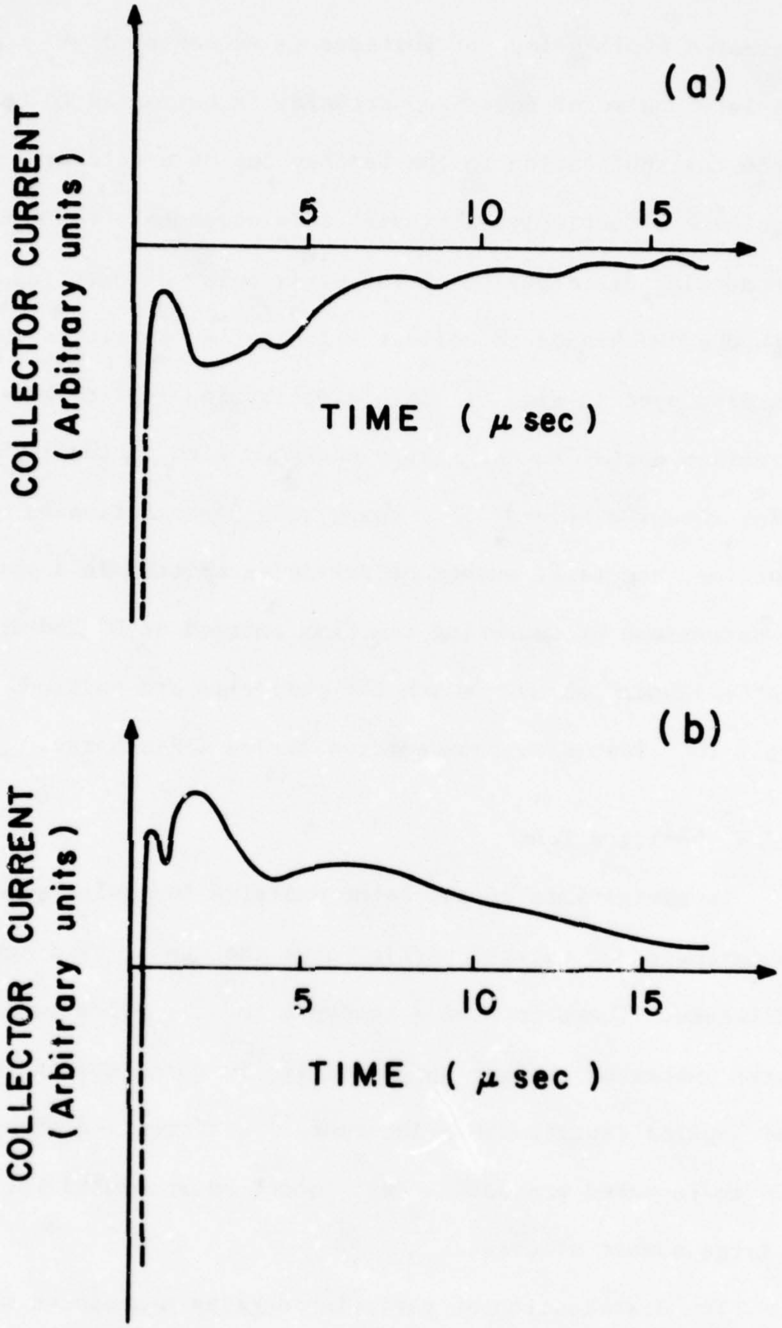

Figure 5. Oscilloscope Traces of Faraday Cup Current:

a) Faraday cup biased to collect negative particles

b) Faraday cup biased to collect positive particles.

prevented applications of voltages in excess of 3 kV. The energy of the later pulse of negative particles is estimated to be less than 85 eV since the application to the Faraday cup of a retarding voltage of this magnitude effectively eliminates this component from the particle flux. The angular distribution of the early pulse of electrons was measured with the RPA biased to collect all negative particles and the results are displayed in Fig. 6. This distribution is strongly peaked in the direction normal to the sample surface, with virtually no particles being observed beyond 45°. Using this distribution as a weighting function, the total number of particles emitted in a given discharge can be determined by measuring the flux emitted at 0° and integrating over the hemisphere through which the particles are emitted. Doing so gives 1-5 x 10^{13} fast electrons emitted during a discharge.

3.2.3 Positive Ions

Investigations of the later positive ion pulse reveal a decrease in intensity of emitted particles as the number of discharge events increases. There is also a tendency for the pulse to disappear after a large number of events. As a result, measurements of the particle energy and angular distributions incorporate a systematic change in character due to repeated breakdowns that cannot be accounted for by averaging a large number of events.

The distribution of particle energies associated with the later positive pulse has been studied immediately after a new sample has been

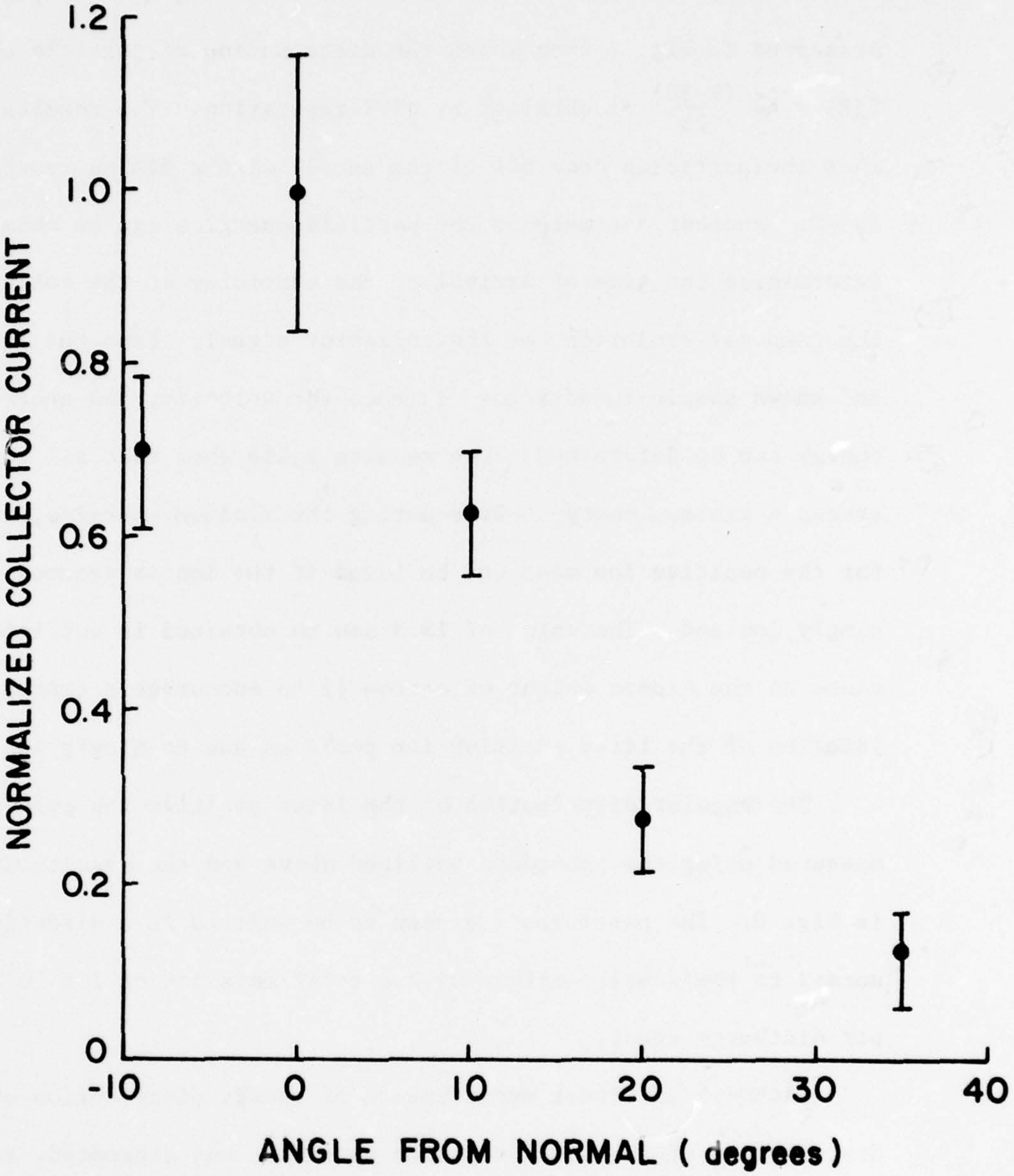

Figure 6. Angular Distribution of Electrons
(For the early burst of electrons emitted during the discharge).

installed for RPA orientation perpendicular to the sample surface. The variation in collector current with retarding grid voltage is presented in Fig. 7 from which the distribution of particle energies $f(E) = Ae^{-\frac{(E-30)}{23}}$ is obtained by differentiation. The results indicate that the particles come off of the sample with a minimum energy of 30 eV. Another estimate of the particle energies can be obtained by determining the time of arrival of the particles at the collector from the temporal evolution of the collector signal. From the transit time and known sample-to-detector distance the velocity, and hence, kinetic energy can be determined. The results again show that all the particles exceed a minimum energy. By equating the minimum energies, an estimate for the positive ion mass can be found if the ion is assumed to be singly ionized. The value of 13.3 amu so obtained is sufficiently close to the atomic weight of carbon 12 to encourage a tentative identification of the later positive ion peaks as due to singly ionized carbon.

The angular distribution of the later positive ion pulse was measured using the procedure outlined above and the results are presented in Fig. 8. The particles are seen to be emitted in a direction nearly normal to the sample surface with a total emission of 7×10^{12} particles per discharge event.

Although no direct measurements of energy distribution or angular distribution of the later negative particles was attempted, it is reasonable to assume that the angular distribution of these particles is similar to the later positive ion distribution in view of the fact

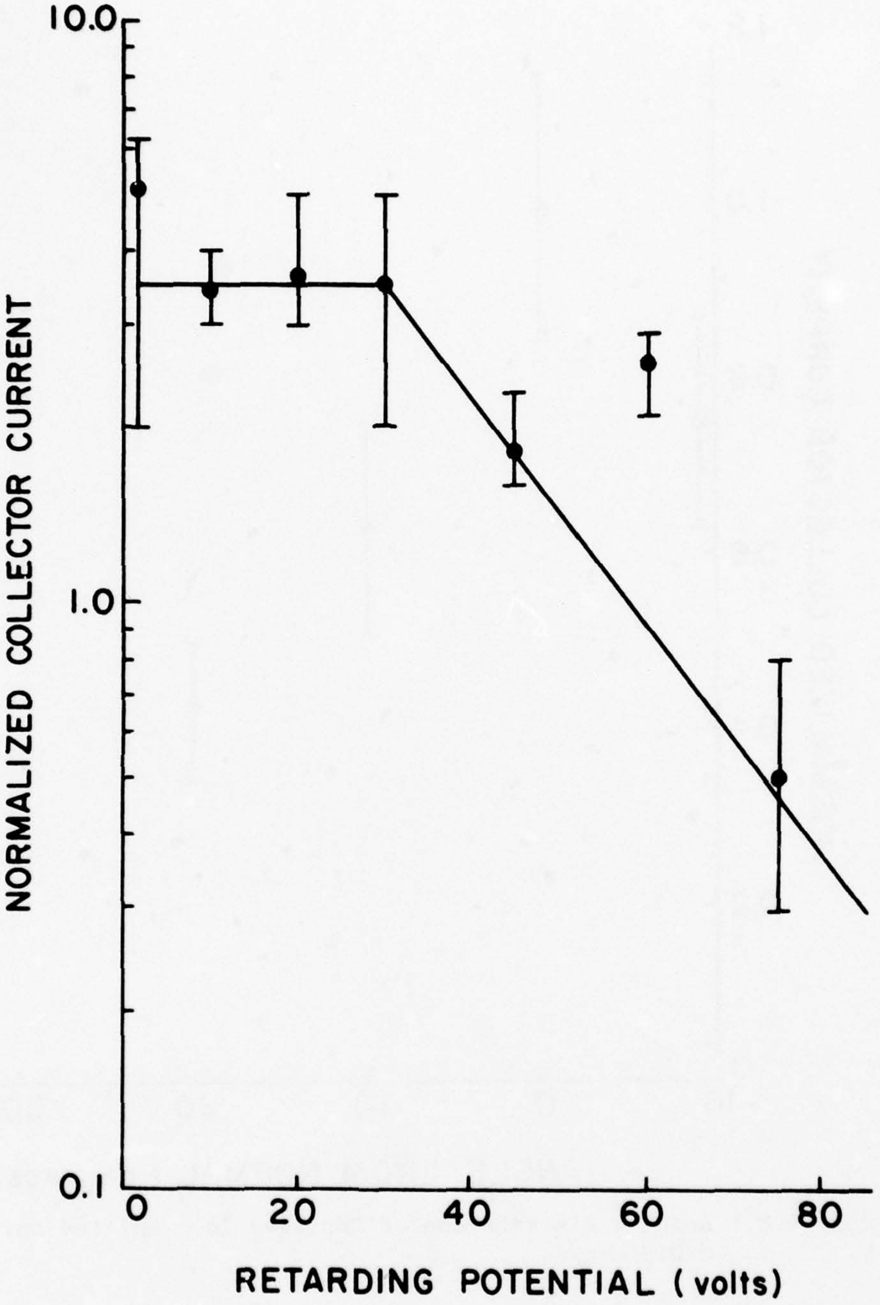

Figure 7. Energy Distribution of Positive Ions Measured with the Retarding Potential Analyzer.

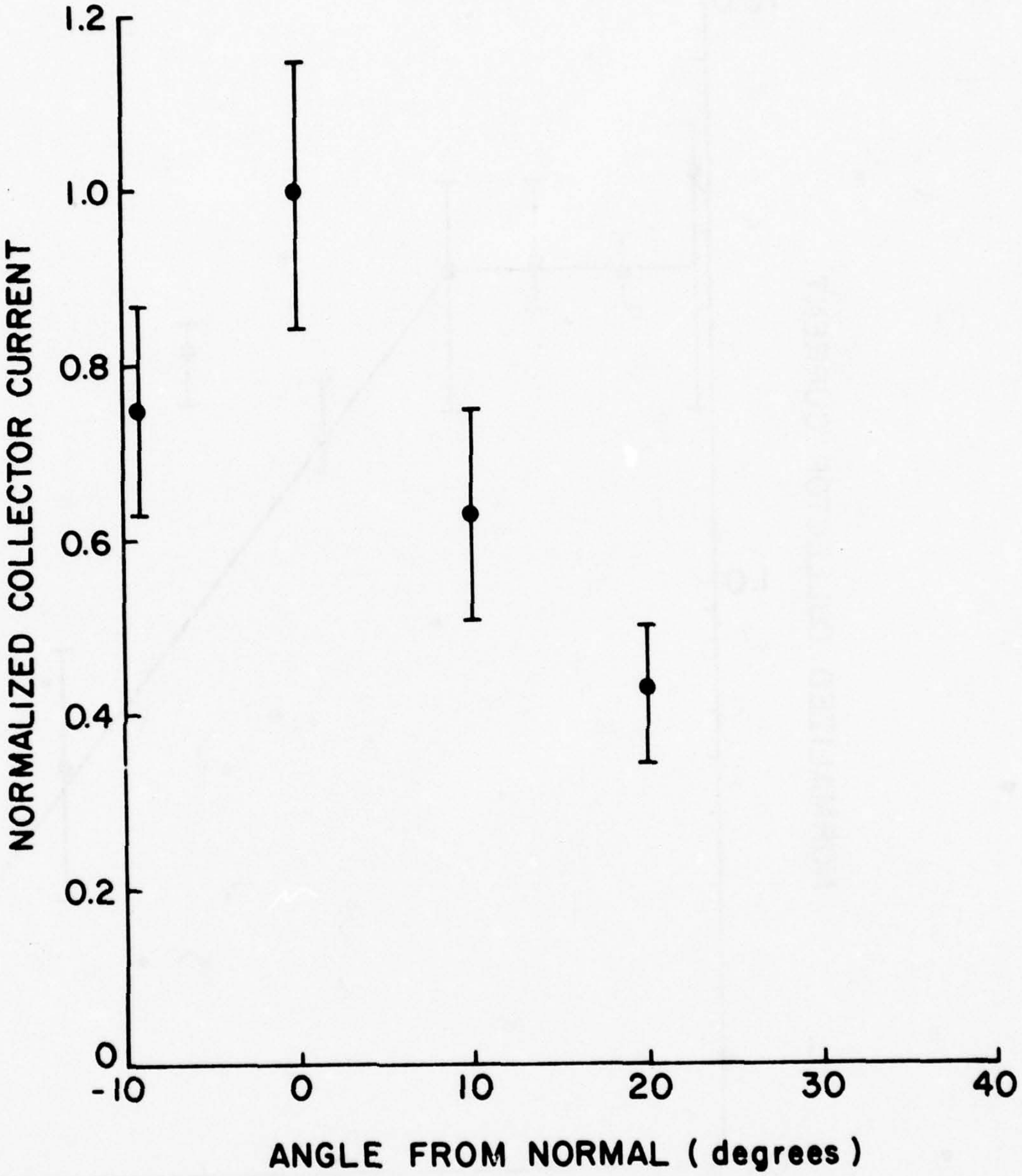

Figure 8. Angular Distribution of Positive Ions Emitted During a Discharge.

that the amplitude and width of these pulses are quite similar. Based on this assumption, the emission of later negative particles is estimated to be ∿ 6 x 10^{13} particles per discharge event.

4.0 DISCUSSION

Material damage resulting from puncture discharges is a source of contamination in spacecraft environments. In addition to expulsion of molten Teflon, emission of charged particles has been observed. The high energy electrons constitute a net loss of 5 x 10^{13} negative particles from the target per discharge event. The large energies of these particles (in excess of 3 KeV) indicate that the particles are accelerated by the negative voltage of the surface. The presence of later pulses of both positive and negative particles in approximately equal numbers indicates that the particles leave as a plasma with the ions having energies between 30 and 80 eV with a total emission of 10^{13} particles per discharge event.

The redeposition of the molten Teflon can affect performance of nearby solar panels and other sensitive surfaces. Although no direct emission of silver has been detected to date, the loss of silver from the back surface of the thermal control surfaces indicates the presence of silver redeposition on adjacent surfaces. The high energy electrons are expected to leave the negatively charged spacecraft and its immediate environment. The later pulses of positive ions and negative particles are expected to move in the electromagnetic fields of the spacecraft possibly as a neutral plasma and can be redeposited on adjacent surfaces and affect the response of sensors on the spacecraft. In addition, the emitted particles give rise to electromagnetic disturbances which affect on-board instrumentation.

The results tend to support the observations of Nanevicz and Adamo[4] and Sessler and West[5] that electrons are emitted during a discharge. Although the present results indicate a much narrower angular distribution than reported by Nanevicz and Adamo,[4] this is not surprising in view of the large difference in electron potentials involved.

Further work will be conducted on the emission of charged particles from electrical discharges on simulated spacecraft surfaces in order to identify deposited contaminants and some consideration will be given to alleviation techniques.

4. N. E. Nanevicz and R. C. Adamo, "Malter Discharges as a Possible Mechanism Responsible for Noise Pulses Observed on Synchronous-Orbit Satellites," in Spacecraft Charging by Magnetospheric Plasmas (Progress in Astronautics and Aeronautics, Vol. 47) A. Rosen, ed., Cambridge, Mass., MIT Press: 247-261 (1976).
5. B. Gross, G. M. Sessler and J. E. West, "Radiation Hardening and Pressure-Actuated Charge Release of Electron-Irradiated Teflon Electrets," Appl. Phys. Lett. 24 (No. 8):351-353 (1974).

5.0 REFERENCES

1. Spacecraft Charging by Magnetospheric Plasmas, (Progress in Astronautics and Aeronautics, Vol. 47) A. Rosen, ed., Cambridge, Mass., MIT Press (1976).

2. Proceedings of the Spacecraft Charging Technology Conference, eds. C. P. Pike and R. R. Lovell, Air Force Geophysics Laboratory (1977).

3. "Space Radiation Effects (Session D of the Annual Conference on Nuclear and Space Radiation Effects," IEEE Transactions on Nuclear Science, NS-24 (No. 6):2244-2304 (1977).

4. N. E. Nanevicz and R. C. Adamo, "Malter Discharges as a Possible Mechanism Responsible for Noise Pulses Observed on Synchronous-Orbit Satellites," in Spacecraft Charging by Magnetospheric Plasmas (Progress in Astronautics and Aeronautics, Vol. 47) A. Rosen, ed., Cambridge, Mass., MIT Press: 247-261 (1976).

5. B. Gross, G. M. Sessler and J. E. West, "Radiation Hardening and Pressure-Actuated Charge Release of Electron-Irradiated Teflon Electrets," Appl. Phys. Lett. 24 (No. 8):351-353 (1974).

SESSION VI

SPECIAL TOPICS AND EFFECTS

SPACECRAFT TEST CHAMBER CONTAMINATION STUDY

AEDC MARK I FACILITY

J. G. Pipes, D. F. Frazine, R. P. Young
ARO, Inc.
AEDC Division
A Sverdrup Corporation Company
Arnold Air Force Station, Tennessee
and
E. N. Borson and L. H. Rachal
Ivan A. Getting Laboratories
The Aerospace Corporation
El Segundo, California

ABSTRACT

Recent results of a contamination study in the Arnold Engineering Development Center Mark I space simulation chamber are presented. The measurements were associated with the Global Positioning System satellite test conducted in the Mark I facility between April 6, 1977, and July 24, 1977. Multiple internal reflection spectroscopy (MIRS) internal reflection elements (IRE's), thermal control surface witness plates, and quartz crystal microbalances (QCM's) were employed to measure contaminants condensible during an extended chamber evacuation. An automatic particle counter was used to measure airborne particle density when the chamber was at atmospheric pressure. The nonvolatile residue wipe technique was employed to determine the general cleanliness of the chamber hardware. Temperature of the IRE's during chamber operation, was between 150 and 200 K. One QCM was temperature controlled to a temperature of 238 K; the other QCM operated at 135 K. After chamber repressurization, the IRE's

were scanned in the 2 to 15 μm wavelength region. Resulting spectra indicated a coating of diffusion pump fluid (DC704) at a concentration level just above the limit of detectability. The cold QCM recorded deposition during chamber evacuation. This deposit sublimed during chamber warmup at a temperature of 170 K, the sublimation temperature of water. Since neither QCM indicated a mass addition after chamber repressurization, we have used the 1.7×10^{-8} g/cm^2 minimum detectable mass of the QCM as an upper limit for the mass of slicone fluid collected on the IRE's. This upper limit corresponds to two molecular layers of fluid for a twenty-nine-day evacuation period. The thermal control surface samples showed no change in IR spectral reflectance during the same twenty-nine-day chamber evacuation. Particle counts were taken during periods when the Mark I chamber was at atmospheric pressure. Particle densities measured for particles larger than 0.5 μm were nominally 6000 particles/ft^3. Particle density for particles larger than 5.0 μm were nominally 15 particles/ft^3. The airborne particle contamination in the Mark I chamber (at atmospheric pressure) was therefore below that of a class 10,000 clean room, as specified by Federal Standard 209.

1.0 INTRODUCTION

The Mark I space simulation chamber, located at the Arnold Engineering Development Center, Tullahoma, Tennessee, Fig. 1, is one of the largest facilities of its kind in the world. It measures 42 feet (12.8 meters) in diameter by 82 feet (25.6 meters) high, is constructed entirely of stainless steel and is equipped with a liquid nitrogen cooled liner over the floor, walls and portions of the ceiling to simulate the thermal environment of outer space. Eleven 32-inch (.81 meter) oil diffusion pumps form

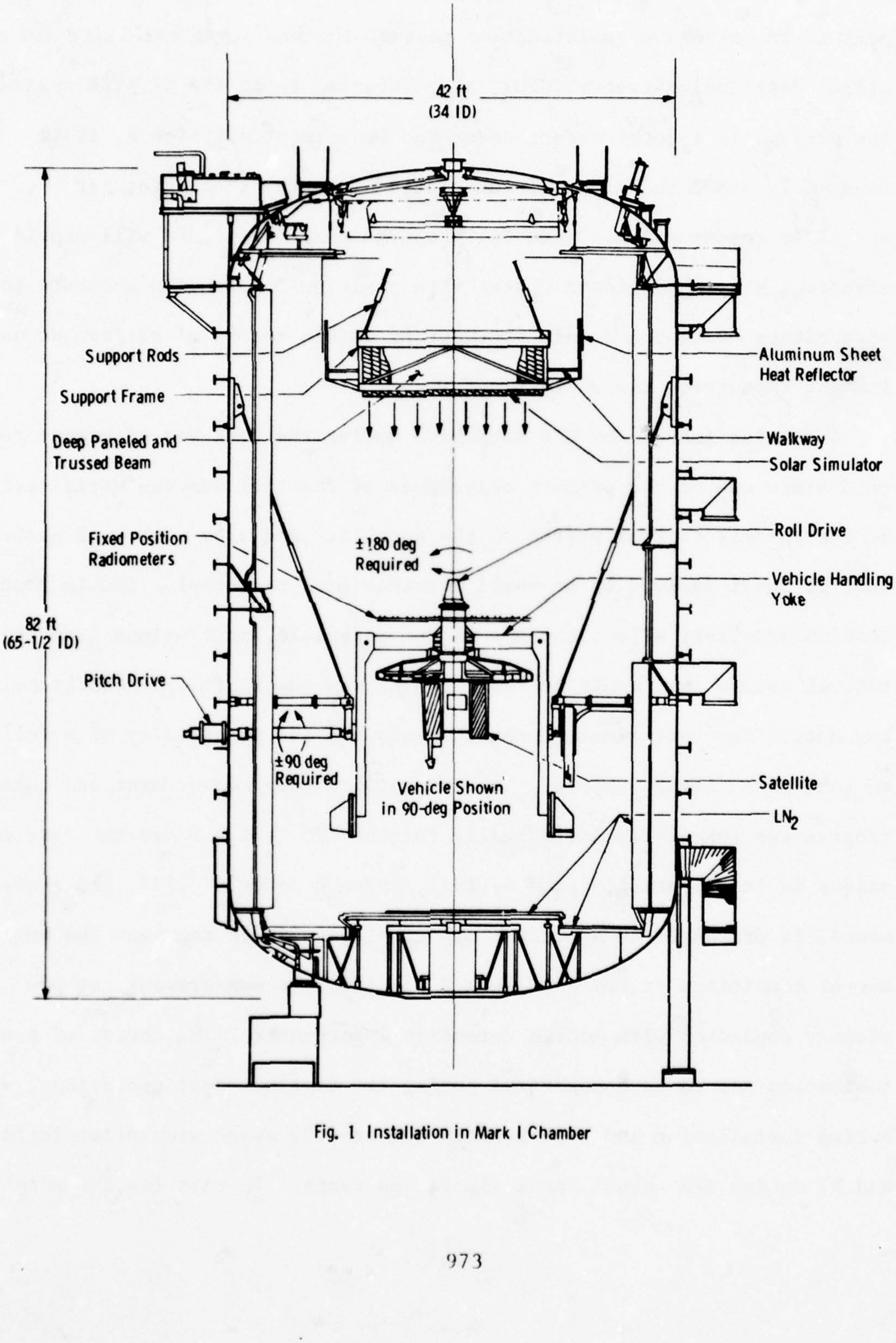

Fig. 1 Installation in Mark I Chamber

the primary pumping system and each pump has its own liquid nitrogen baffle and angle valve. This unique facility was recently employed to perform an extensive qualification test of the prototype satellite for the Global Positioning System (GPS), also referred to as the NAVSTAR system. The project is a joint effort under the Department of Defense, it is managed by SAMSO and Rockwell International is the contractor for satellite construction. When fully operational (1984) GPS will provide airborne, ship, and ground system with position information accurate to within tens of feet and velocity vectors within tenths of a ft/sec at any instant throughout the world.

Contamination of the GPS satellite during the test was of utmost concern since one of the primary objectives of the test was the verification of the thermal control system on the satellite and also a thermal mathematical model derived by Rockwell International personnel. Should contamination adversely affect the α/ϵ of the materials, conclusions from the thermal vacuum test would be ambiguous to say the least. An additional key motive for contamination measurements was the possibility of a follow-on test of a flight vehicle. Thus a contamination measurement and control program was formulated specifically for the GPS test. Since the test was unique in its duration, April 6, 1977, through July 24, 1977, and requirements, it presented an excellent opportunity to fully document the environmental conditions of the AEDC Mark I facility, a measurement not previously conducted with modern detection instruments. The threat of contamination was to be encountered during two distinct test operations, a) during installation and work periods between the space simulation tests, and b) during the actual space simulation tests. In case (a) the satellite is subjected to pariticulate fallout and personnel contamination while in case (b) it is subjected to vacuum pump fluid vapors and condensible vapors outgassed from umbilical wiring and general chamber hardware. The following instruments were selected on a basis of sensitivity, applicability and availability to measure the degree of contamination originating from each of the possible sources: a particle sensing instrument, Coulter Model 550, to monitor particulate contamination levels below 10^5 per cubic foot of air (R. P. Young, ARO, Inc., was the contact engineer for particulate measurement); a nonvolatile residue (NVR) wipe test to measure surface cleanliness (E. N. Borson and L. H. Rachal, The Aerospace Corporation, were the contact engineers for the NVR measruements); a series of infrared multiple internal reflection spectroscopy (MIRS) internal reflection elements (IRE) for qualitative assessment of condensbles (J. G. Pipes was contact engineer for MIRS measurement); a series of witness plates (wafers identical in form to the satellite's outer skin) for α/ε measurements (J. G. Pipes was contact engineer for witness plate measurements); and finally two quartz crystal microbalances (QCM) for quantitative measurement of condensibles (D. F. Frazine was contact engineer for QCM measurements). Dr. H. E. Scott, DOTR, AEDC AF, directed and coordinated the contamination measurement program for the Air Force.

Each of the instruments is individually described below along with typical data and conclusive results, however, in general it was determined that the Mark I as a space simulation facility performed well above all expectations. The particle density for particles larger than 0.5 μm was nominally 6000/ft^3 and 15/ft^3 for particles larger than 5.0 μm. This is below class 10,000 as specified by Federal Standard 209; the NVR wipes showed a moderate level of surface contamination on chamberhardware; the IRE's detected only trace amounts of vacuum pump fluid; the witness samples showed no change in α/ε; and the cooled QCM showed only a slight collection of water vapor.

2.0 PARTICULATE MEASUREMENTS

2.1 Instrument Description

The Mark I chamber is not equipped as a clean room. The GPS requirements of Class 340,000 are not stringent, however, and a series of particle count measurements were made near the start of test preparation to determine existing conditions. It showed that the chamber is close to the required Class 340,000 cleanliness level without special measures. Of particular importance is the fact that the chamber lid was off prior to the measurement. The addition of two room dehumidifiers, provided by Rockwell for humidity control, brought the chamber conditions within the required 340,000 class with 50% relative humidity for most of the ambient pressure periods.

In order to ensure that conditions were met around the vehicle at all times, a protective frame and surrounding cover was built for use when the vehicle was at the 0° position (antennas pointing up). The frame was attached to the vehicle lifting lug attachments. The cover was made of polyethylene with nylon mesh embedded to provide protection in event of falling objects. The vehicle was thus enclosed in an isolated volume inside the chamber.

Humidity and temperature control within the enclosed volume was maintained by a trailer mounted 15-ton air conditioning unit with attached filter furnished by Rockwell as part of the ground support equipment. This unit was located beneath the chamber and the output was ducted to the protective enclosure. A distribution manifold at the vehicle directed the output over the batteries, thermal control louvers, and SADAP drives as required. Because of the distribution manifold, these units could be cooled with or without the protective enclosure.

Particle count measurements were monitored during ambient pressure operation using a Coulter Model 550 counter; manufactured by Coulter Electronics, Inc., Hialeah, Florida. The counter employs the near-forward light scattering technique and can detect particles of size greater than .5μm. A simplified block diagram of the counter is given in Figure 2. Particles are detected and sized by collecting an air sample through a positive displacement flow system and passing the particle laden air between the light source and photoelectric detector. A resulting pulse, proportional to the particle size, is amplified and sorted by size in an amplifier card, then subsequently fed to a logic card for conversion to digital code. The digital code is displayed on the front panel and also accessible from a data card. Calibration of the counter is performed by the manufacturer using monosized particles in a range of .5μm to 20.0μm. An accurate absolute calibration accuracy for the instrument is not known. During the installation of the GPS and between-test operations the particle counter was located on the floor of the chamber since measurements under the satellite tent

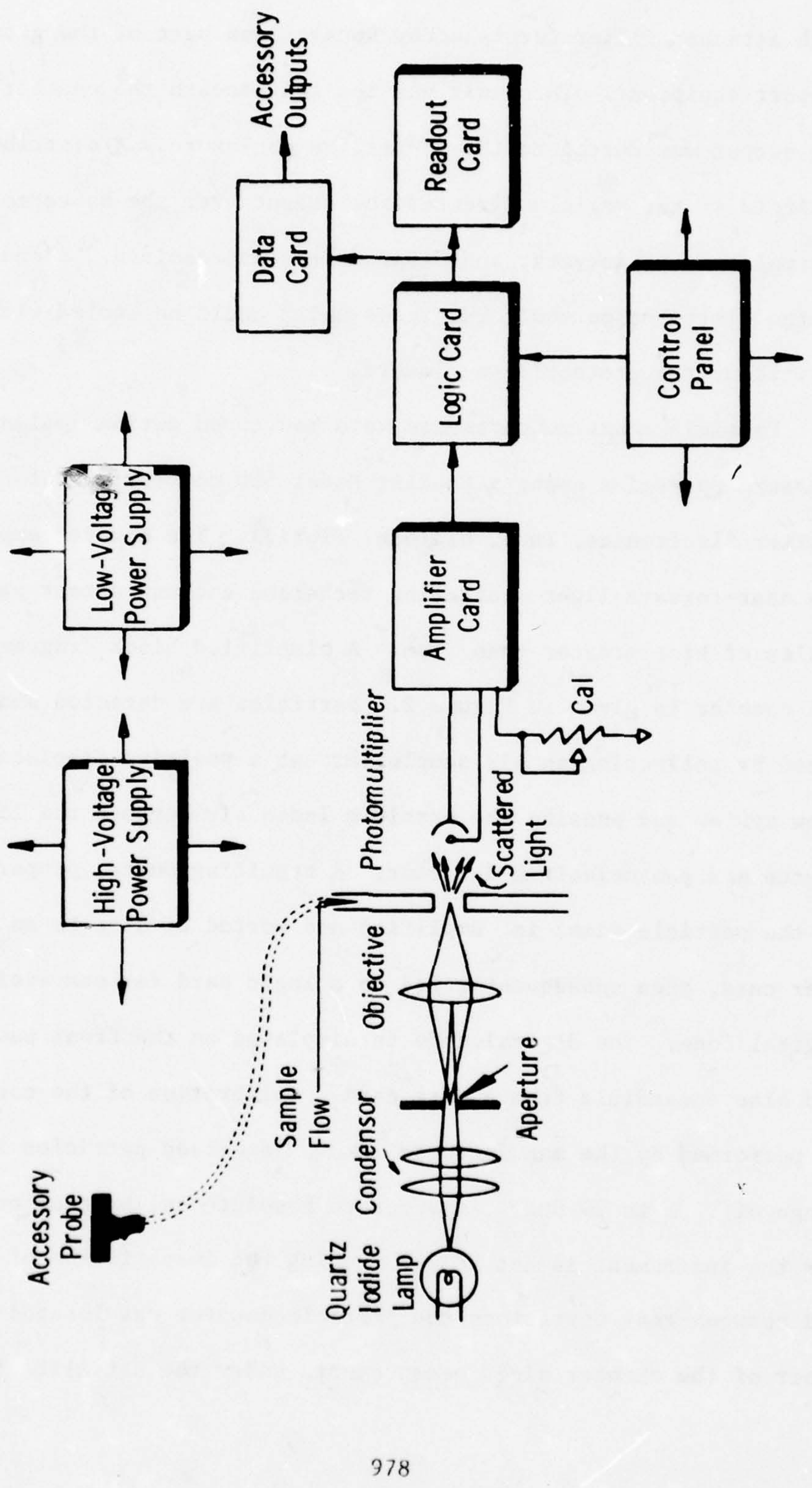

Fig. 2 Block Diagram of Particle Counter

showed no significant difference between the two locations. As would be expected the count level varied considerably depending upon the level of personnel activity in the chamber.

2.2 Typical Data and Results

Particle count data was hand recorded; see Figure 3 for a typical result during a work period of moderate activity. As is clear from Fig. 3, the particle density for sizes greater than 0.5 μm were nominally $6000/ft^3$ and $15/ft^3$ for sizes greater than 5 μm. The Mark I can therefore be classed as 10,000 for the GPS test. It is believed that this more than adequate low count level was due to the pre-test cleaning of the chamber and test hardware, the clean room personnel procedures during installation and modification periods (all personnel wore caps, gloves, smocks and shoe covers), and the operating procedures in general.

It should be noted that a correction to the particle count was made after the test. Originally class 100,000 was reported, based on a Royce Model 245 counter. It was later found that the Royce was severely out of calibration. Following calibration the Royce agreed closely with the Coulter, thus the Coulter data reported herein is believed to be accurate.

3. NVR (Non-Volatile Residue) Measurements

3.1 Solvents and Procedures

Non-volatile residue (NVR) was measured on both the Mark I test chamber and dummy space vehicle surfaces. NVR measurements were initially performed prior to and after chamber pumpdown tests with a simulated space vehicle. No additional NVR measurements

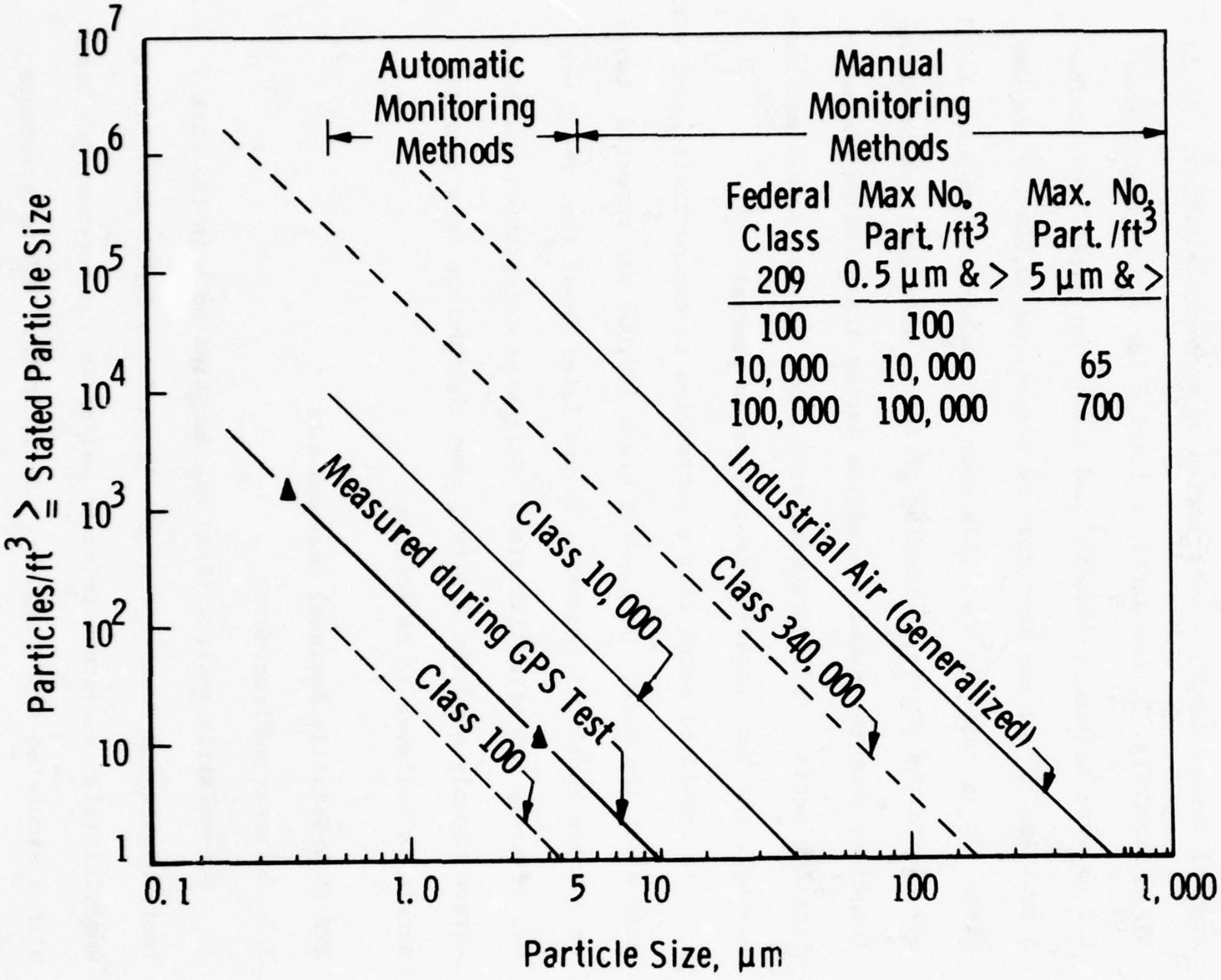

Federal Class 209	Max No. Part./ft^3 0.5 µm & >	Max. No. Part./ft^3 5 µm & >
100	100	
10,000	10,000	65
100,000	100,000	700

Fig. 3 Particle Size Measurement during a Work Period of Moderate Activity

were performed following the qualification test on the GPS space vehicle because the QCM's and IRE's indicated negligible NVR levels.

The NVR procedure consists of wiping the surface with a cloth dampened with a mixture of 1, 1, 1 trichloroethane and ethanol. Soxhlet of the cloths is employed to remove soluble residues, and the solvents are triple distilled to reduce the NVR to approximately 1 ppm. A solvent mixture of 75% 1, 1, 1 trichloroethane and 25% ethanol by volume is azeotropic (has a single boiling point) and is, therefore, convenient for use in Soxhlet extraction.

A surface area of approximately 0.1 m^2 (1 ft^2) is wiped with the solvent dampened cloth twice, each time with a fresh cloth. The cloths are retained in a clean sealed container until removed for the solvent extraction process. For this test, the used wiping cloths were returned to the Aerospace Corporation Ivan A. Getting Laboratories for solvent extraction and NVR determination.

The extraction process consists of removing the NVR from the cloth in an ultrasonic bath using the 75%/25% solvent mixture. The solvent is then evaporated and the NVR is weighed. The evaporation is performed at room temperature rather than at an elevated temperature such as is used in the ASTM standard test methods.

The NVR is usually retained for further analysis should such information be required. Infrared MIRS is frequently used because of the small quantities of NVR that usually are available.

3.2 NVR Results

The results of NVR measurements performed during the Mark I chamber tests are as follows for a wipe taken on a cable tray: 33 mg/m^2 (3.1 mg/ft^2) before the warm pumpdown and 15 mg/m^2 (1.4 mg/ft^2) after the cold pumpdown. The NVR levels were considered to be high, and additional cleaning of the Mark I chamber was performed prior to starting the qualification test. Infrared spectroscopy had shown the NVR to be primarily a lubricant used on the test fixture.

4.0 MIRS MEASUREMENTS

4.1 IRE Description and IR Spectrum

Multiple internal reflection spectroscopy (MIRS) at infrared wavelengths is one of the more sensitive techniques for qualitative identification of infrared active compounds where very low level concentrations are available. The principles of MIRS (also commonly referred to as ATR (attenuated total reflection), TIR (total internal reflection), and FTIR (frustrated total internal reflection)), as well as the instruments and applications of the technique are given by Harrick[1] in a fine test on internal reflection spectroscopy. There is also an ANSI/ASTM Standard on the subject.[2] Basically polychromatic radiation, in most cases infrared of the 2-25 μm wavelengths, is directed into a prism shaped crystal so that the angle of incidence

---

[1] Harrick, N. J., Internal Reflection Spectroscopy, John Wiley & Sons, Inc., (1967).

[2] ANSI/ASTM E573-76, Standard Recommended Practices for Internal Reflection Spectroscopy, American Society for Testing and Materials, Annual Book of Standards, Part 42.

at the points of internal reflection are greater than the critical angle. The radiation is totally reflected at the crystal-air interface but the electric field does penetrate the rarer medium (air), a distance not greater than a few wavelengths, and is damped exponentially. The waves that attempt to penetrate the rare medium are termed "evanescent" or "frustrated" and lead to the concept of frustrated total internal reflection. If the air (a dielectric) is replaced by a conductor, for example the condensation of a volatile contaminant onto the crystal, the evanescent waves will be attenuated, for wavelengths at which the contaminant is active, allowing absorption infrared spectroscopy to be performed. This condition leads to attenuated total reflection (ATR) which is the technique employed for contamination detection and identification during the GPS Mark I space simulation test. One other optical measurement was conducted, an IR specular reflection measurement of thermal control witness plates, which is described following the MIRS discussion.

The preceding paragraph described ATR using a prism shaped crystal, but in reality a trapezoidal-shaped crystal is employed so that multiple reflections occur, amplifying the detection sensitivity similar to a multipass transmission cell. Many geometric styles of IRE crystals have been fabricated[1], however, the trapezoidal shape is the most common commercially available configuration. For the GPS test KRS-5 single pass crystals (52.5 x 20 x 2 mm, with 45° face angles) mounted in Delrin® holders were employed. Three AEDC plates and four Aerospace Corporation (Mr. E. Borson was the primary contact for Aerospace Corporation) plates were mounted at

Table 1 IRE's on GPS Test

IRE I.D.	Location	Temperature*
IR-6	On GPS looking along -Y axis	Same as GPS
IR-8	On GPS looking along +Y axis	Same as GPS
IR-2	On radar tower looking down and out at cryopanels	150-to-200 K
IR-10	On radar tower looking up and out at GPS	150-to-200 K
AEDC #1	On pitch yoke looking at GPS	150-to-200 K
AEDC #2	On pitch yoke looking opposite direction as #1	150-to-200 K
AEDC #3	On pitch yoke looking at radar structure	150-to-200 K

*Thermocouples placed in reference ovens and referenced to other reference ovens.

**Thermocouples shorted at data system path panel.

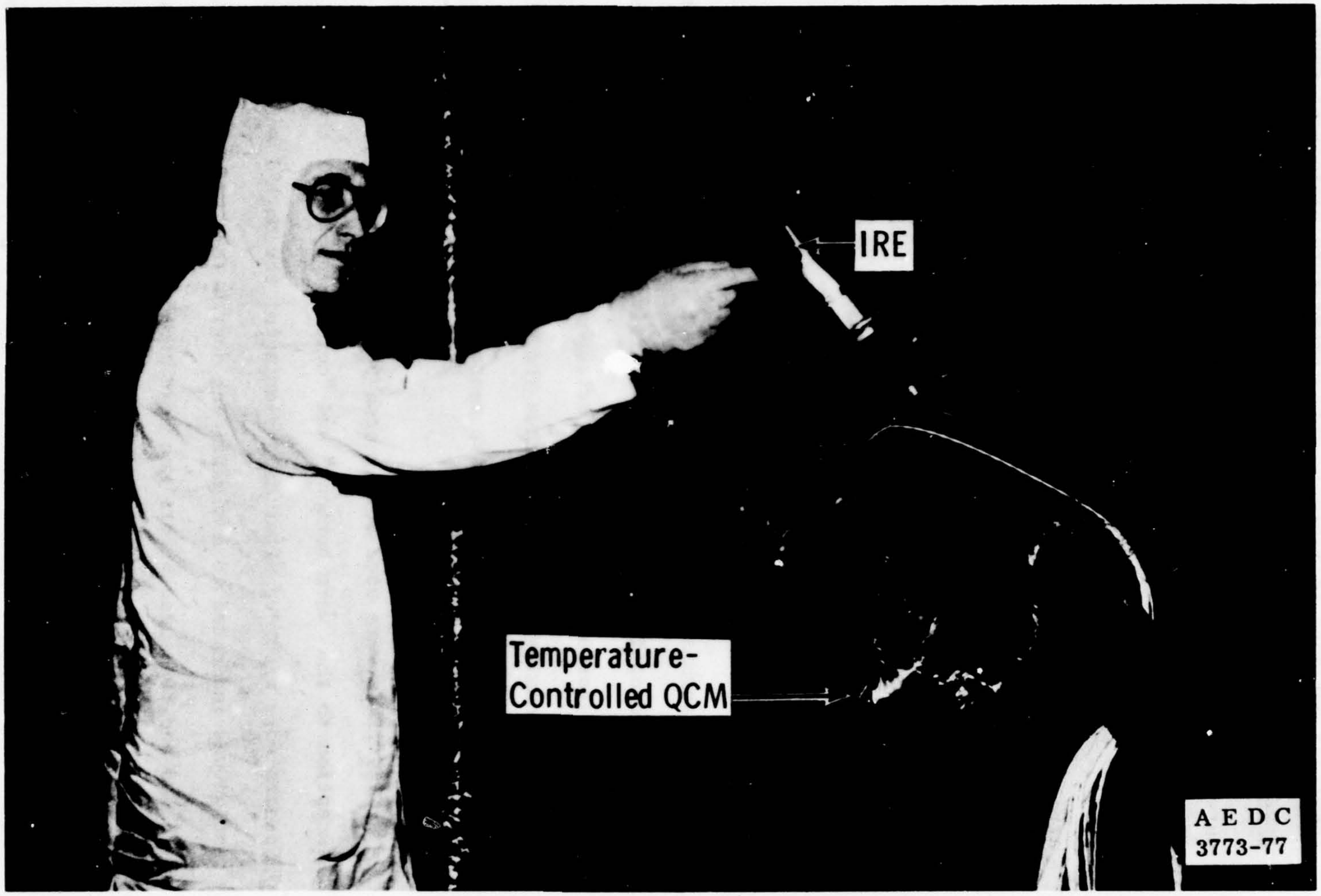

Fig. 4 Photograph of IRE and Temperature-Controlled QCM

locations outlined in Table 1. The temperature history of each plate is also indicated in this table. The KRS-5 IRE's were purchased from Wilks, Norwalk, Connecticut. One IRE and the QCM's are shown in Fig. 4. During the entire course of the test all MIRS spectra were obtained using the Wilks Model 9 internal reflection attachment and the Perkin-Elmer Model 21 doublé beam spectrophotometer, located at the AEDC Chemistry Laboratory. The Model 21 has a sodium chloride prism which resulted in a nominal spectral resolution of 1% for the slit program used for wavelengths between 2.0 and 15.0 μ m.

All of the IRE's were scanned prior to installation for a baseline or background spectrum. In general, all of the plates showed a smooth transmission spectrum rising from 40% at 2.0 μm to 90% near 10 μm then dropping off to 70% transmission at 15 μm. The reference beam attenuator on the Model 21 spectrophotometer was adjusted to give the 90% transmission at 10 μm, thus the transmission values for all MIRS data presented is a relative measurement.

4.2 Typical Results

The IRE's were used during each pumpdown-vent cycle with exception to the "warm bakeout" and "cold pumpdown" of the Mark I. Spectra were recorded after each venting of the Mark I and if contamination was indicated to a significant degree the IRE's were cleaned and rescanned before the next pumpdown. After the GPS was installed there were four pumpdowns and vents during the test sequence, i.e., 1) spin drift, 2) on-orbit #1, 3) on-orbit #2, and 4) on-orbit #3. The spin-drift test took five days after which the

IRE's were scanned for the first time after being under vacuum. A number of weak features were observed in all of the plates spectra which was not recognized as significant until after the on-orbit #1 MIRS measurements. The spectral features for IR-6 and IR-8 were interpreted as baseline fluctuations and the bands of all other plates (e.g., IR-2) were unexplained at the time (see Figs. 5 and 6). It was concluded that no contaminant was detected on the IRE's and they were reinstalled for the on-orbit #1 sequence. After the on-orbit #1 MIRS spectra were obtained (the on-orbit lasted 15 days) it became clear that the spectral features were real and a search for a matching spectrum (from the data by F. C. Gross, NASA Goddard Space Flight Center, "Infrared Characterized Spacecraft Contaminants and Related Compounds") revealed that DC-704 was identifiable. The broad weak band in the MIRS spectra at 9.4 μm is, no doubt, the 9.4 μm strong band in the DC-704 reference spectrum. The 3.5 μm, 12.5 μm, 13.75 μm and 14.4 μm absorption bands were also just identifiable in the MIRS spectra, see for example Fig. 7. IR-6 and -8 located on the GPS showed a slightly different spectrum with the 9.45 μm feature being more triangular shaped, as compared to the square 9.40 μm band shape in Fig. 7, see Fig. 8. Although it is recognized that this band could be an indication of another contaminant, it is felt that DC-704 fluid is the most probable candidate.

For the on-orbit #2 sequence the IRE's were not cleaned before installation so that a check for accumulation could be made. It was in question whether the DC-704 was deposited during the pumpdown or vent sequence or a gradual accumulation during the entire test sequence.

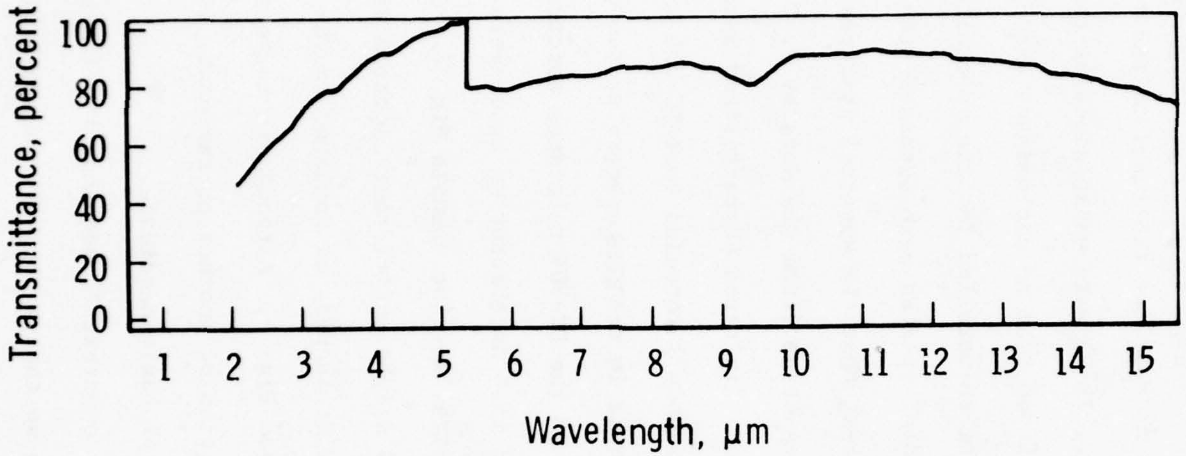

Fig. 5 IRE Spectrum--Post Spin-Drift (IR-8)

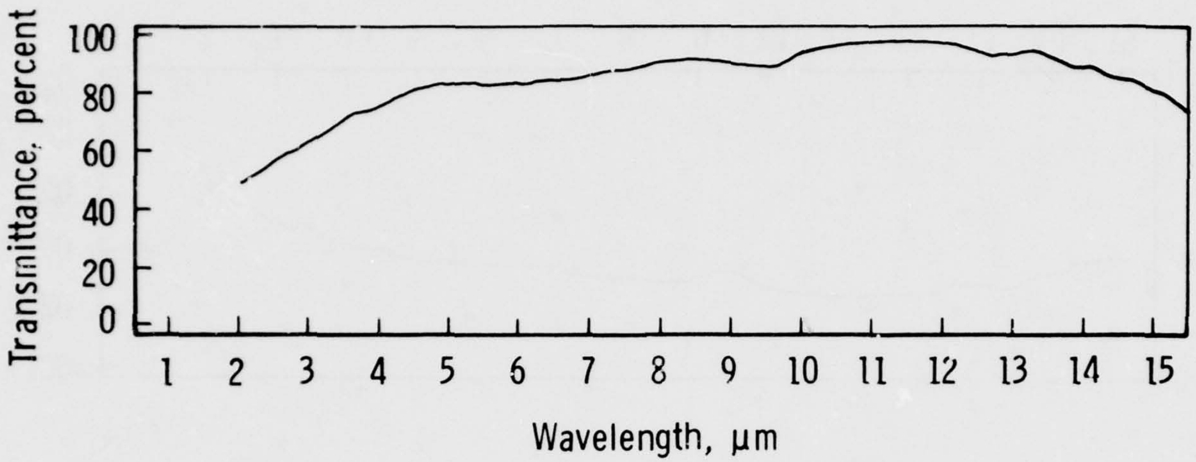

Fig. 6 IRE Spectrum--Post Spin-Drift (IR-2)

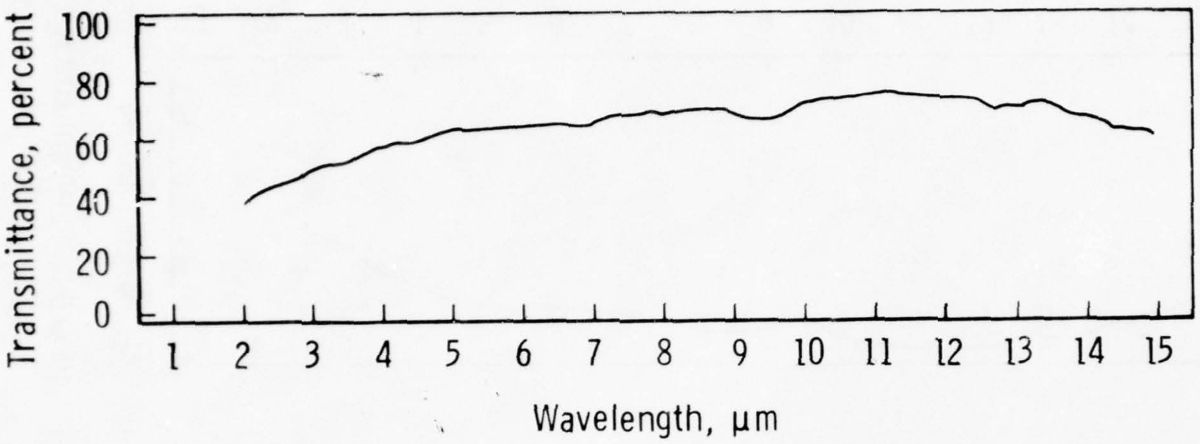

Fig. 7 IRE Spectrum--Post On-Orbit No. 1 (AEDC-1)

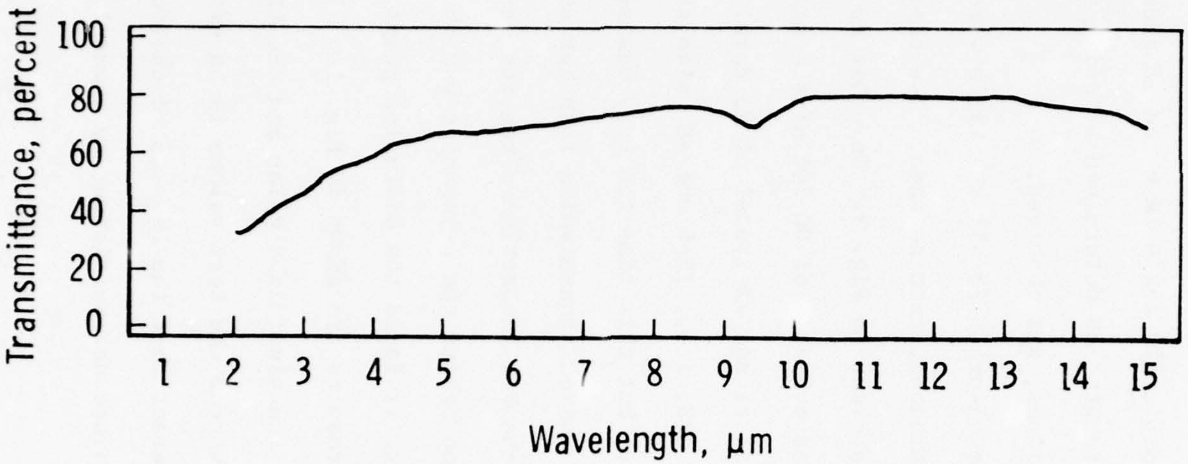

Fig. 8 IRE Spectrum--Post On-Orbit No. 1 (IR-8)

After the on-orbit #2 the MIRS spectra did not show a significant (doubling) increase in the DC-704 absorption bands thus it was concluded that the DC-704 deposition is a gradual continuous accumulation and not primarily occurring during the pumpdown or vent cycle. Also, during the on-orbit #2, IRE's IR-6 and -8 showed no increase in the 9.4 μm line strength, as determined by using neighboring transmission values as baselines, was observed.

Before the on-orbit #3 all the IRE's were cleaned with acetone and rinsed in ethanol, then scanned. The cleaning removed all evidence of DC-704 as is clear in Fig. 9. On-orbit #3 lasted 30 days and again the IRE's showed evidence of DC-704 of the same concentration as the scan of on-orbit #1 and #2 (total of 25 days), see Fig. 10. The plates located on the GPS, i.e., IR-6 and -8, also showed a slight transmission loss near 9.4 μm but this time the band was more indicative of DC-704, i.e., a square shaped transmission loss between 9 and 10 μm.

During a chamber inspection after the on-orbit #1 test, the mylar super-insulation behind the cryopanels was observed to have a haze, especially where it faced the diffusion pumps. A wipe sample was taken and the results are shown in Fig. 11. It is apparent that the combination of the aluminized mylar and the LN_2 wall separating the diffusion pumps from the test volume is an effective baffle. However, it is also apparent that the LN_2 cooled chevron baffles immediately above the pumps are not sufficient by themselves.

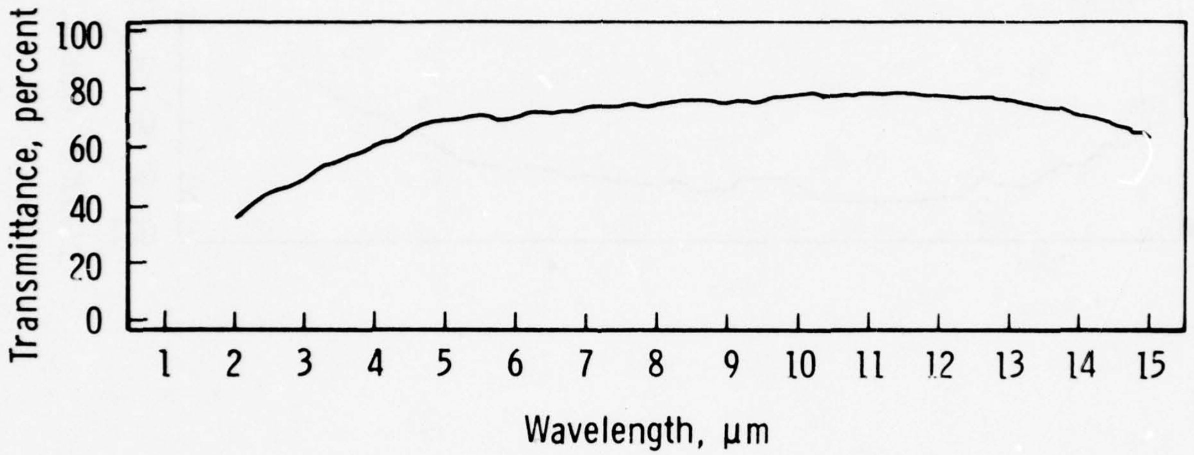

Fig. 9 IRE Spectrum--Prior to On-Orbit No. 3 (IR-8) after Cleaning

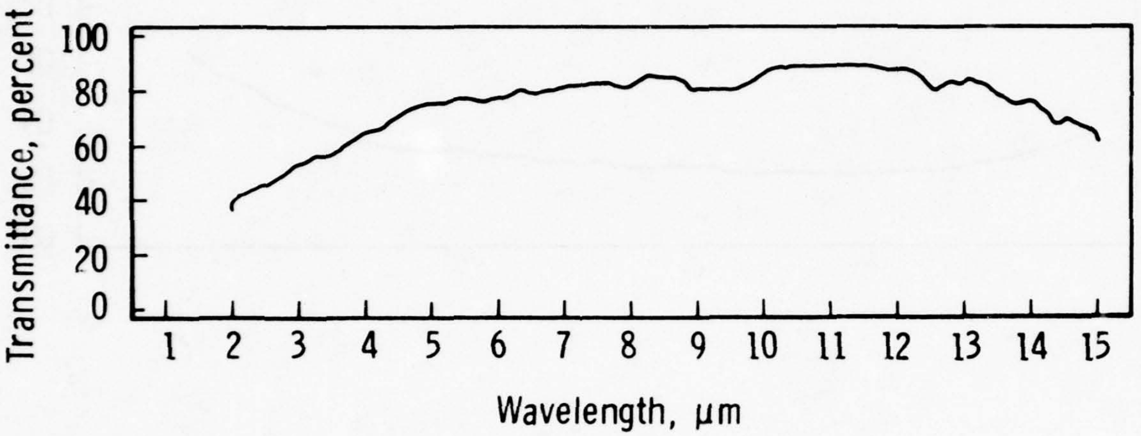

Fig. 10 IRE Spectrum--Post On-Orbit No. 3 (IR-10)

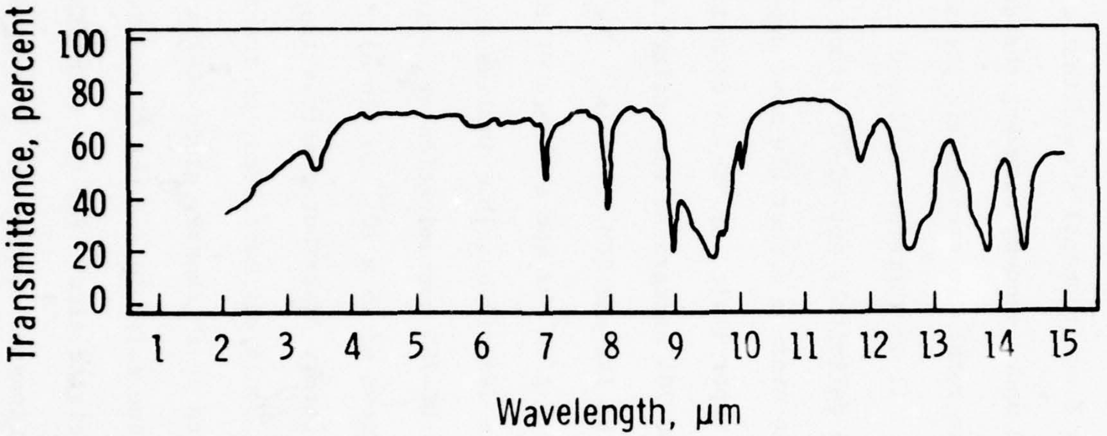

Fig. 11 Reference Spectrum--DC 704 Fluid from Al-Mylar Insulation

4.3 Quantitative Assessment

A quantitative assessment of DC-704 deposition required to produce the observed spectrum can be achieved with the aid of the quartz crystal microbalances (QCM's) results. The QCM's, temperature controlled to 290 ±10 K and one uncontrolled (T = 116 K after equilibration with the Mark I environment) showed that a deposition took place during each period under vacuum; however, the deposits sublimed immediately following the return to atmospheric pressure and temperature (see Section 6.2). It is therefore believed the deposit was probably water and definitely not DC-704 since it would not have sublimed. Thus the minimum detectable mass deposition of the QCM may be used as an upper limit for DC-704 deposition, which, of course, assumes that the DC-704 background was uniform throughout the chamber, equally exposing the IRE and QCM crystals. The QCM's have a sensitivity of 1.7×10^{-8} g/cm^2-Hz and a change of 10 Hz is needed to positively indicate deposition. This implies an upper limit of 17×10^{-8} g/cm^2 of DC-704 contamination or dividing by a density of 1.04 g/cm^3 a thickness of 16×10^{-8} cm (16 Å). If it is assumed that the DC-704 was uniformly distributed across the plate, then the DC-704 layer on the IRE's could not have been, on the average, more than two molecular layers in thickness, since DC-704 is a phentaphenyl-trimethyl-trisiloxane molecule and the CH and SiO groups are the order of 3 Å in characteristic size. For the size IRE's employed, the number of multiple reflections is 25 thus the loss of energy per reflection needed to yield a final loss of 5% is 0.25%. It must be left to the discretion of the thermal control engineer to determine if such a small loss (0.0025) in reflectance at 9.4 μm (reflectance loss at other wavelengths is negligible) is detrimental to a thermal control surface. If it is, then the two molecular layers of DC-704 must be considered a contaminant, if it isn't, then the GPS (or any other hardware placed in the Mark I chamber) was completely free of contamination during the test.

5.0 WITNESS PLATES

5.1 Description

The witness plates were one-inch-diameter laminated wafers identical in form to the outer thermal control skin of the satellite. Two styles were employed, an aluminum plus 0.001 inch of Kapton over-coated with aluminum and a gold coated inconel over-coated with FEP Teflon. Seven witness plates were mounted on the satellite with double back tape (3M Y966) at strategic locations. The α/ε ratio of the plate was determined by measuring the reflectance at visible and near IR wavelength. A Rockwell specification of 0.002 for the Ag-FEP Teflon plates and 0.004 for the Al-Kapton plates was set as an acceptable upper limit for change in reflectance, for all wavelengths. This criterion is below the absolute accuracy limit on the Cary 90 and the Beckman DK-2A reflectometers employed to measure the reflectance, they are more near 0.01 to 0.02 accurate in reflectance measurement capability. Nevertheless the samples were scanned after the first test period.

5.2 Results

The reflectance of all the witness plates was found to be consistently within the measurement accuracy of the reflectometers. Thus it was concluded that the reflectance had not changed more than one percent during a test period. Furthermore, after reviewing the MIRS results it was concluded that the reflectance measurements were unnecessary, since the IRE's which are twenty-five times more sensitive showed a very small level of contamination. The witness plates were still included on each test sequence but later stored for future reference in the event some concern arose regarding the thermal balance testing of the satellite. A typical infrared reflectance scan of an Al-Kapton and Ag-Teflon witness sample is shown in Figures 12 and 13, respectively, for illustration purposes.

6.0 QCM MEASUREMENTS

6.1 Instrument Description

During the entire GPS test, the Mark I chamber contained two quartz crystal microbalances which viewed the central volume of the chamber containing the satellite. These QCM's were of Jet Propulsion Laboratory origin, incorporating a 5 MHz crystal doublet (measuring and reference oscillators on the same 3/4 x 1-1/2-inch crystal) with both crystals cut at $40^{\circ}8'$ for cryogenic operation. See Chirivella[3] for a more complete description of the JPL QCM's.

QCM #1 was strapped to the LN_2-cooled frame of the fixed earth support tower and eventually reached a minimum temperature of 116 K; temperature variations were caused by changing solar simulator irradiance. QCM #2 was similarly mounted, but was wrapped with aluminized mylar and included a heater which maintained a crystal temperature of 284 K. (See Figure 4 four mounting arrangement of QCM's.)

---

[3] Chirivella, J. E., Hydrazine Engine Plume Contamination Mapping, AFRPL TR-75-16 (1975).

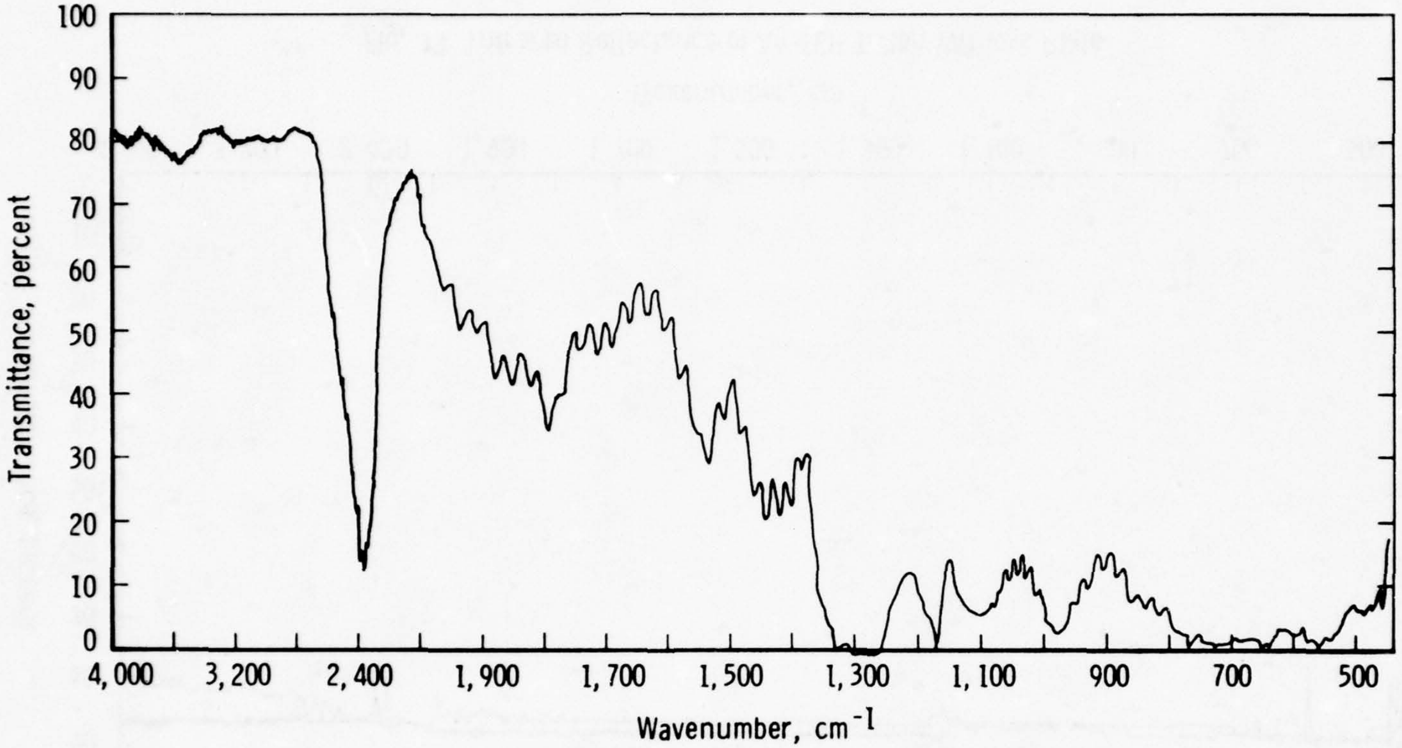

Fig. 12 Infrared Reflectance of Al-Kapton Witness Plate

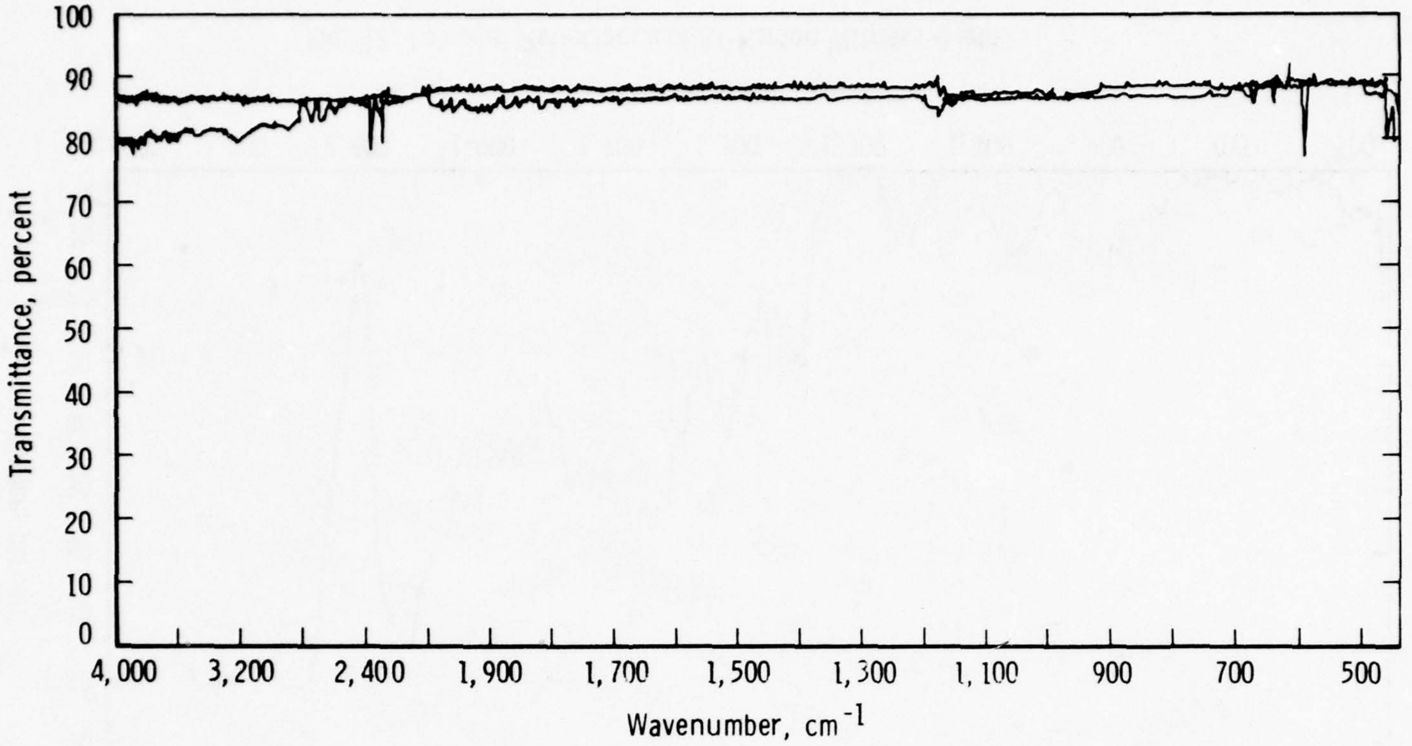

Fig. 13 Infrared Reflectance of Ag-FEP Teflon Witness Plate

6.2 Typical Data of Results

QCM output signals were recorded continuously via frequency-to-voltage converters and a dual pen strip chart, and hourly readings of a frequency counter were noted on the chart. Frequencies taken from the chart and counter are plotted along with crystal temperature in Figures 14 through 16. The actual frequency shown in the figures is a difference frequency between the measuring and reference oscillators on each QCM. As is clear in the figures the temperature controlled QCM (#2) showed a small change in difference frequency, the order of 70 Hz or a deposition of 1.2 μg in comparison to the cooled QCM (#1) which indicated a 4000 Hz maximum frequency change, or a deposition of 70 μg. The maximum deposition occurred during warmup of the chamber and is caused by a release of water vapor from portions of the chamber which warm at a higher rate than the QCM. The fact that the final frequencies after return to ambient conditions was within 10 Hz of the original frequencies and the QCM's indicated rapid loss of mass near 175 K (H_2O has a 10^{-5} torr vapor pressure at this temperature) it seems quite conclusive that the mass deposited on the QCM #1 was water vapor. Since the satellite is maintained at 300 K it was not subjected to contamination by water vapor.

7.0 SUMMARY

Through the usage of modern sensitive contamination measuring instruments a complete assessment of the contamination levels and types has been conducted for the AEDC Mark I space chamber. The general consensus is that the Mark I facility has a very low background contamination level (double layer level) of diffusion pump fluid. It must be

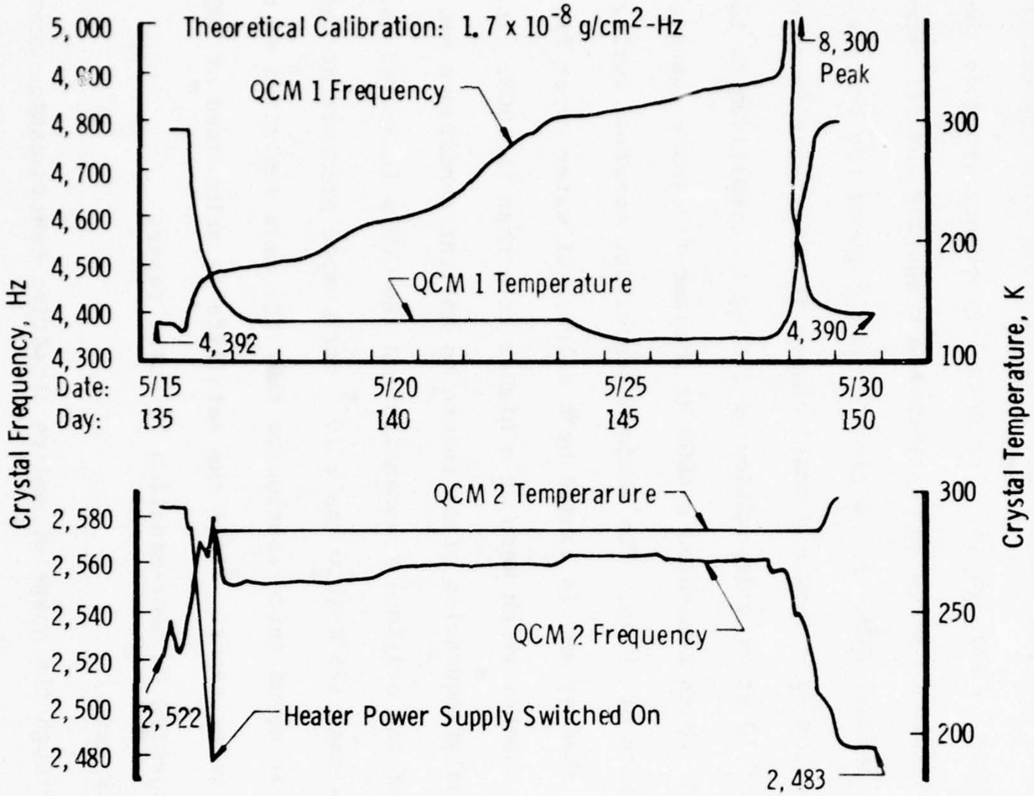

Fig. 14 QCM Measurements (On-Orbit No. 1)

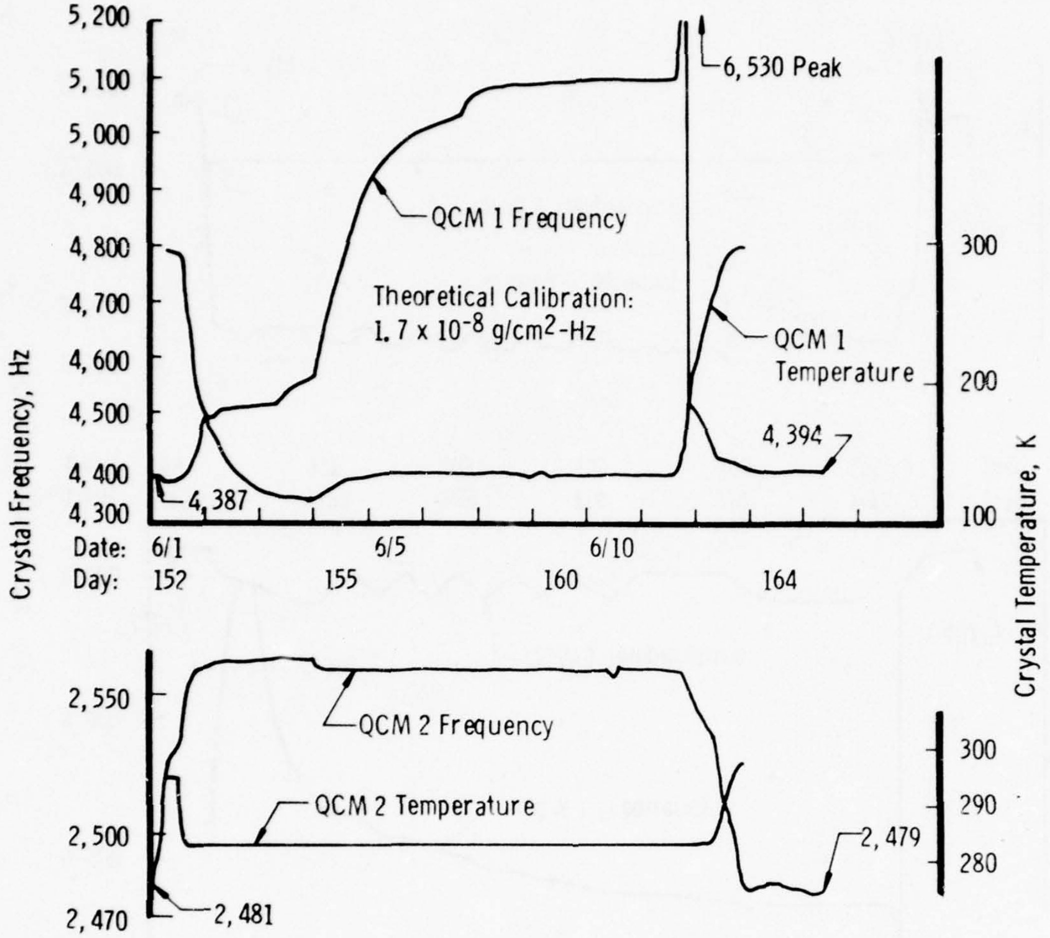

Fig. 15 QCM Measurements (On-Orbit No. 2)

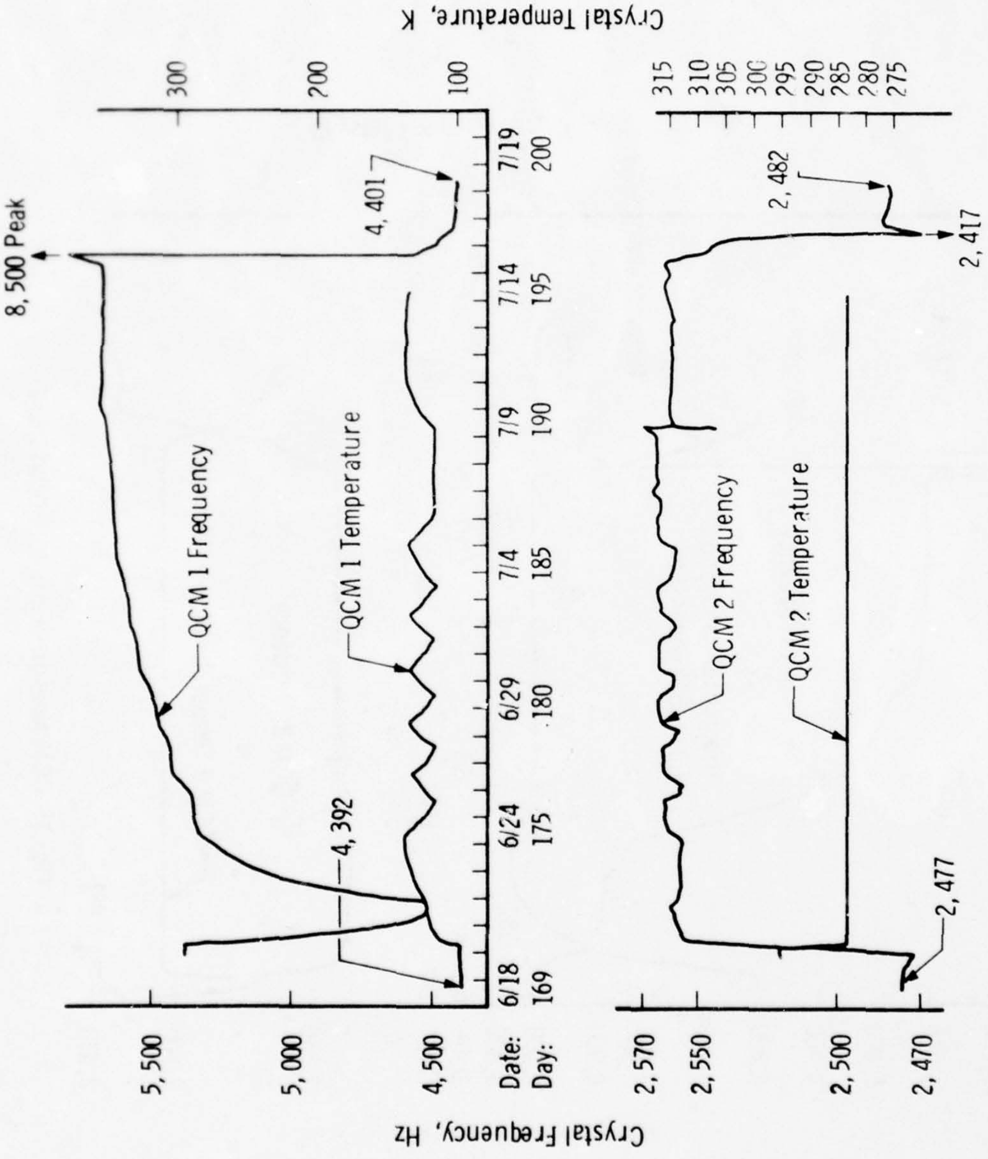

Fig. 16 QCM Measurements (On-Orbit No. 3)

decided by an expert thermal engineer if the level detected during the GPS test is detrimental or not. We feel, in general, that the background is acceptable in most cases and somewhat improvable if need be.

ACKNOWLEDGMENT

The work reported herein was conducted for the Arnold Engineering Development Center (AEDC), Air Force Systems Command (AFSC), by ARO, Inc., a Sverdrup Corporation Company, operating contractor for the AEDC.

REFERENCES

1. Harrick, N. J., Internal Reflection Spectroscopy, John Wiley & Sons, Inc. (1967).
2. ANSI/ASTM E573-76, Standard Recommended Practices for Internal Reflection Spectroscopy, American Society for Testing and Materials, Annual Book of Standards, Part 42.
3. Chirivella, J. E., Hydrazine Engine Plume Contamination Mapping, AFRPL TR-75-16 (1975).

Measurements of the Kinetics and Transport Properties of Contaminants Released from Polymeric Sources in Space and the Effects on Collecting Surfaces

by

E. A. Zeiner
Aerojet ElectroSystems Company

Abstract

Under a recent USAF contract, AESC performed measurements on the emission kinetics, reemission kinetics, and surface transport properties of the contaminants (CVCM) which are released by polymeric sources in space. In addition to these mass transfer properties, measurements were made on the optical effects these contaminants had on receptors upon which they deposit.

1. INTRODUCTION

The testing work done at AESC in support of the USAF Satellite Contamination Program covered five basic testing areas. These tasks were: 1) source emission kinetics, 2) receptor reemission kinetics, 3) surface transport properties, 4) laser induced kinetics, and 5) contaminated receptor optical effects. The laser kinetics work is not covered in this report due to classification.

Two primary test facilities were employed in which to make the necessary measurements. For the mass transfer measurements covering the first three of the above tests, the AESC Molecular Kinetics Test Facility (Molekit) was used. Its primary instrument consists of an array of four quartz crystal microbalances (QCMs) positioned directly in front of the source. The contamination effects measurements were made in the AESC Surface Materials Effects Facility (SMEF). For this effort, the SMEF used an integrating sphere to measure changes in the spectral reflectance and transmittance on five typical receptors which were contaminated by the source materials and then irradiated with ultraviolet light.

In addition to obtaining the source material properties themselves, a substantial amount of the work was directed at developing the test techniques to facilitate both the precision and the speed of the measurements. This is particularly true for the mass transfer tests in the Molekit. While the necessity of applying QCMs to evaluate reemission kinetics from contaminated surfaces is clear, it is not so clear that these same instruments can be used to evaluate source emission kinetics. This indirect technique, identified as cryogenic QCM thermogravimetric analysis (CQ/TGA) requires considerable knowledge of the test configuration and rigorous temperature control of all components of the facility. Since free molecule flow conditions are maintained, the only transport property evaluated is the surface capture coefficient.

This is primarily the probability that an incident molecule will become thermally accommodated upon collision with the surface of the receptor. Two typical source materials were studied; one, RTV-566 (0.2% catalyst), was studied fairly completely.

In the SMEF, reflectance measurements were made with about 1000 Å of volatile condensible materials (VCMs) from RTV-566 adhesive and after thirty-six hours of irradiation with thirty equivalent ultraviolet suns (30 EUVs) of light at 1236 Å. However, the data reduction was not completed in time to include the results in this report.

Significant characteristics of the Molekit and the SMEF are that their internal configurations and procedures were developed by direct application of the system contamination equations. This insures that the flux coupling geometry of the chamber components can be rigorously accounted for in evaluating material properties.

2. VCM MASS TRANSFER TESTS

This section covers a brief description of the Molekit and the three areas of testing performed in it. Included is an outline of the QCM calibration techniques necessary for CQ/TGA of source materials kinetics.

2.1 AESC Molecular Kinetics Test Facility (Molekit)

This facility is displayed in Figure 1. It is a vertical cylinder 2-1/2 feet high and 2-1/2 feet in diameter. The outer shell contains a complete cryogenic shroud which is maintained at LN_2 temperatures in all tests. The basic instrumentation consists of a coplanar array of four QCMs which can be positioned from about 1/2 inch to 6 inches in front of the source holder. This array can be held at any temperature from -170°C to 150°C with better than ±1/2°C accuracy. The source holder supports a 1-inch-diameter source specimen and it can be maintained from -170°C to about 140°C with the present temperature controllers. All internal cryogenic and LN_2 lines are covered with foil to minimize radiation coupling. The entire Molekit (without sources) can be baked out in vacuum at up to 150°C. The Molekit is fore pumped with 4 sorption pumps and will maintain near 10^{-8} torr with a 500 liter/sec ion pump; thus no pumps using hydraulic lubrication or diffusion oil are used which minimizes spurious gas loads. Temperatures are monitored throughout the Molekit at 15 locations.

All data is automatically acquired once the test starts using the HP-3050A automatic data acquisition system depicted on the control panel in Figure 2. Data is sampled at precisely programmed intervals, stored on magnetic tape, printed out, and plotted for real time "quick-look" analysis and system diagnosis. This is also true of the SMEF.

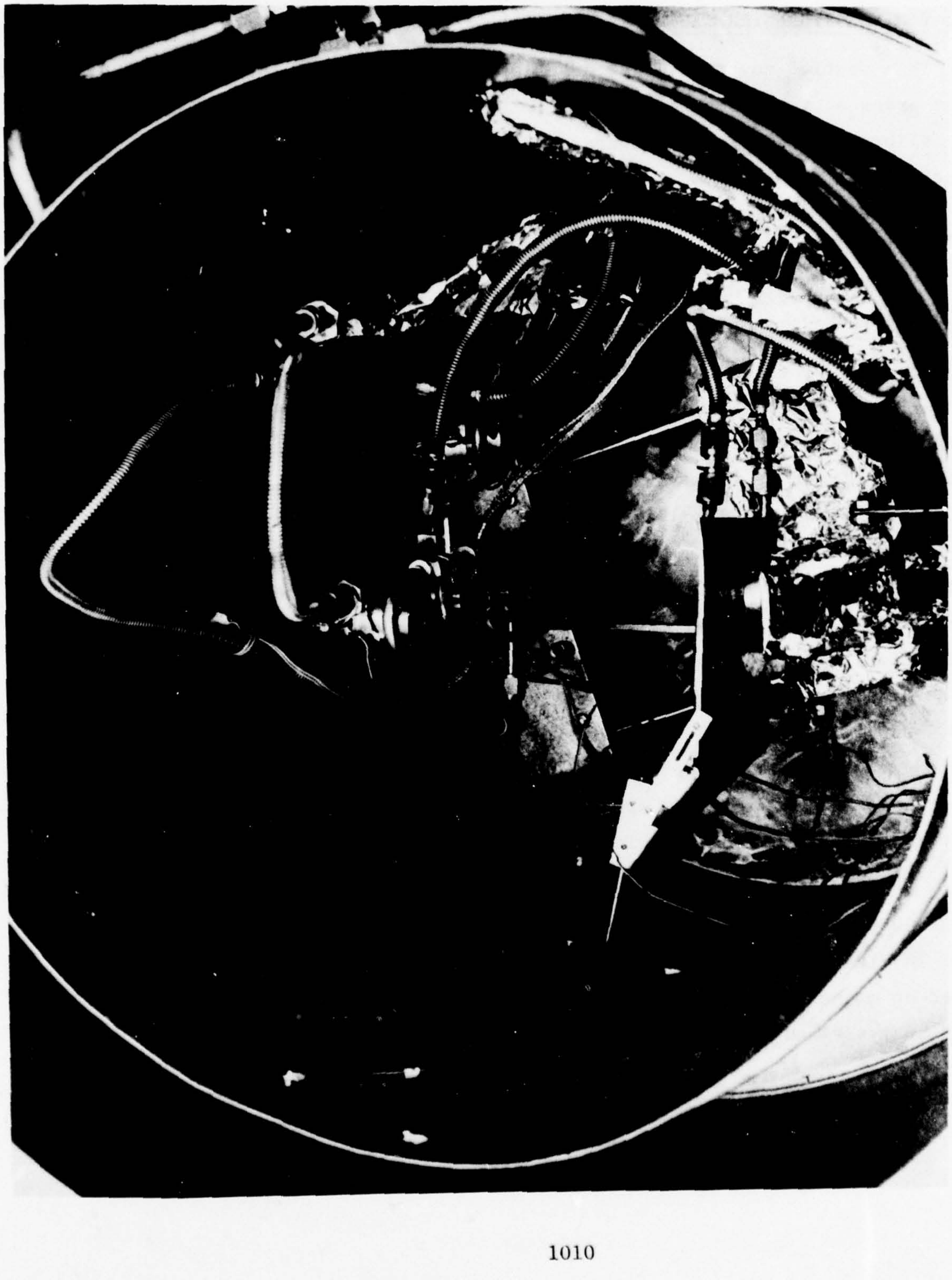

Figure 1. The Molecular Kinetics Test Facility

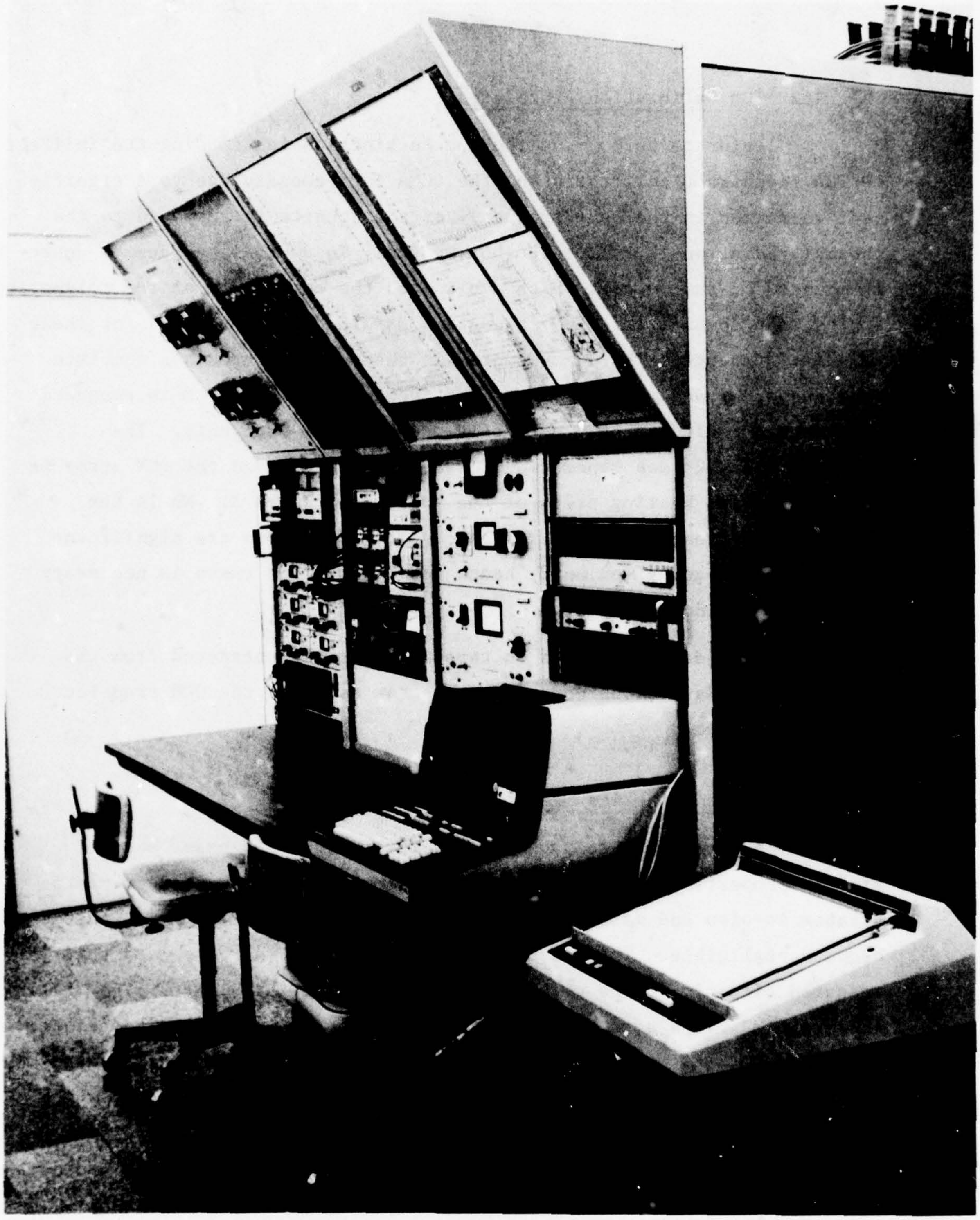

Figure 2. Control Console with HP-3050A Automatic Data Acquisition System

2.2 QCM Calibration Procedures

Prior to performing the source kinetics tests using the indirect CQ/TGA technique, calibration of the QCMs is necessary due to a significant variation in the beat frequency of these units in response to the thermal radiation flux from the hot source. To do this, a "dummy" source is mounted on the support which duplicates the emissivity of the polymeric source, but doesn't emit VCM. Baked-out marble discs were used for these calibration tests. The dummy source is then cycled through a complete test sequence, and the transient beat frequency of each QCM is recorded long enough until a steady output is obtained for each unit. The response for a 2-inch separation between the source and the QCM array is plotted for two heating steps of the source in Figure 3. While the basic mode of response is the same for each QCM, there are significant variations for any given unit, hence the calibration curve is necessary for each individual QCM unit.

This data is stored on tape and is then subtracted from the contamination data, thus correcting the raw data for the QCM transient thermal response.

2.3 Source Kinetics Tests Procedures

A direct and reliable method for determining exact source kinetic properties is to suspend the source specimen on a vacuum microbalance in-situ and maintain a constant temperature until the outgassing becomes negligible. This is classical isothermal TGA. The data that is measured directly is the weight remaining, M_s, in the source. The mass loss rate $\dot{M}_s$, is a second variable which can be obtained from the slope of the M_s versus time profile. For an isothermal first-order rate process, Figure 4 represents a typical M_s time profile for a source, which contains 2 active components. One important characteristic implicit on Figure 4 is that the activity or volatility of the two active components is sufficiently different so that by the time the high volatile

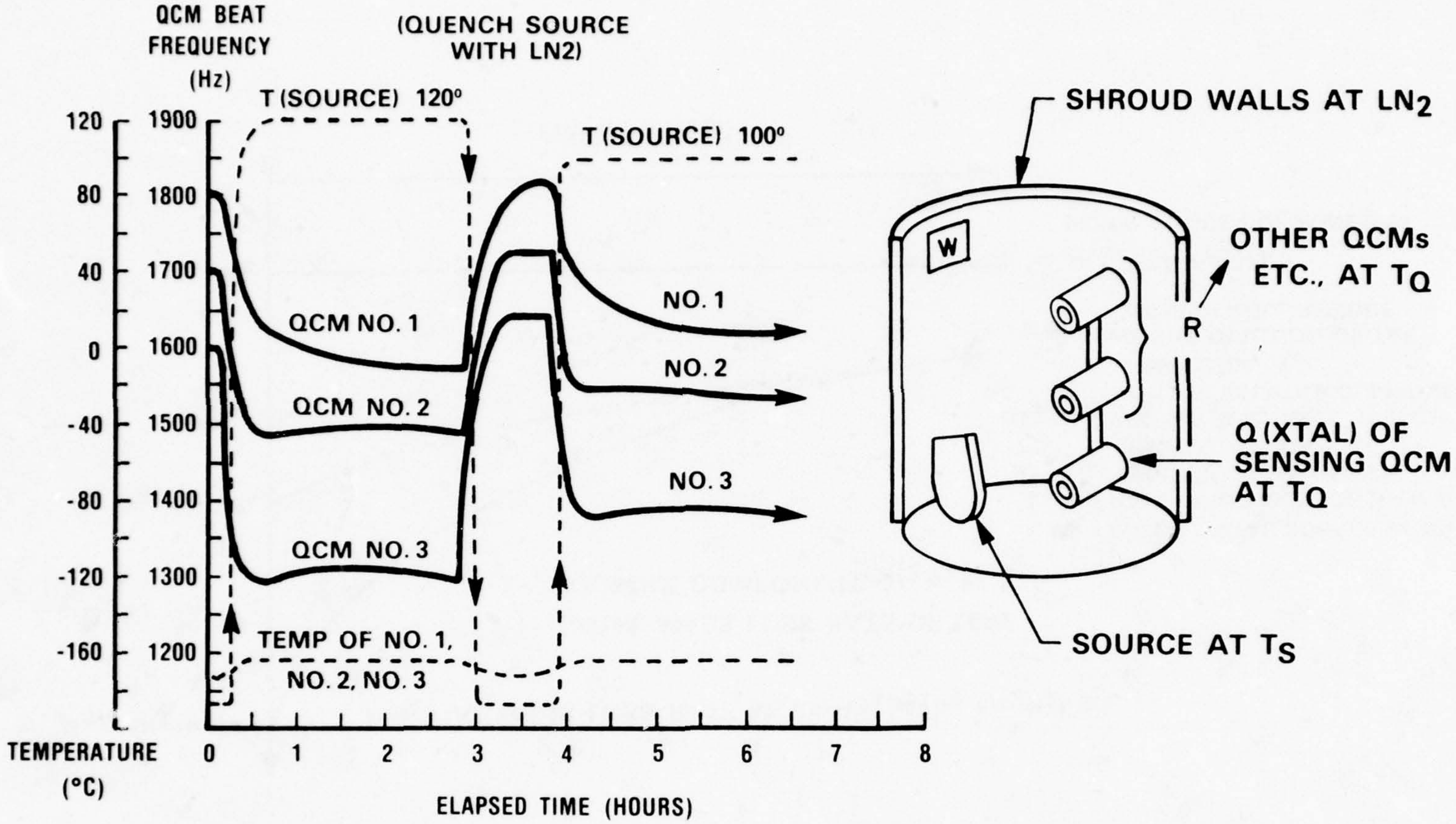

AEROJET AESC ELECTROSYSTEMS COMPANY

Figure 3. Transient Frequency Response of a QCM Held at -170°C to Step Heating by a Source Between -180°C and 120°C

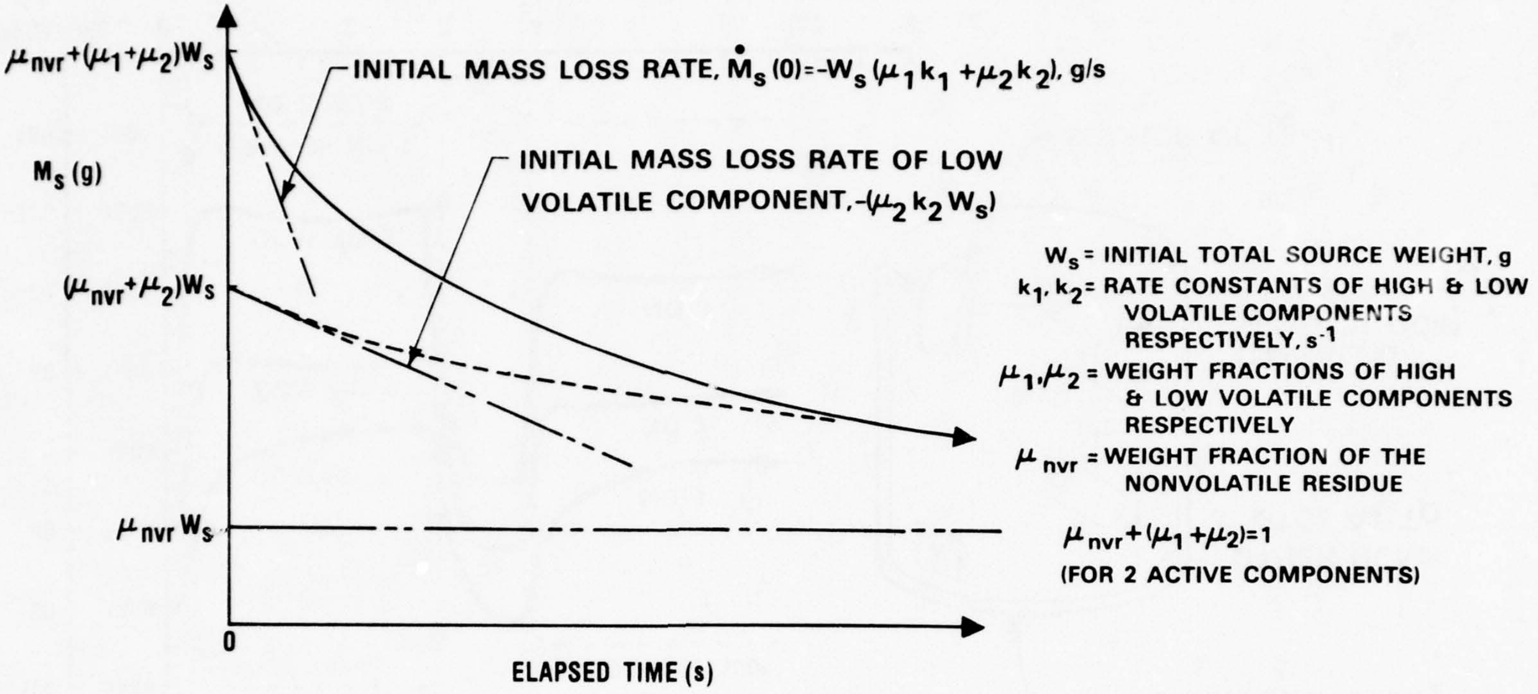

Figure 4. Source Kinetics Parameters Applied to a Typical 2 Component Polymer During Isothermal TGA

component (HVC, #1) is depleted, the low volatile component (LVC #2) is still active enough to exhibit measurable changes to the deposition rate. When this is true, then the data is "tail-of-the-test" data, where changes are due to the LVC only. Thus, the value of the rate constant of the LVC can be determined from the slope and weight fraction by extrapolating to the origin. The weight fraction of the non-volatile residue (μ_{nvr}) must also be known. The initial total mass loss rate together with any other point where both components are active, will give the weight fraction and the rate constant of the HVC. Independent measurements of the total initial source weight and the non-volatile residue mass fraction are required. More than two components can be evaluated with this general procedure provided the activity of the components is widely separated.

For source kinetic processes which are rate processes greater than first order processes, a completely analogous procedure applies. When more general kinetics such as surface-mediated diffusion is present, a somewhat similar procedure is used, but the process requires fitting the entire mass remaining profile to obtain the diffusion parameters. In general, this requires a polynomial regression analysis on a computer instead of the simple graphical procedures permissible in the case of first order kinetics.

For most real space qualified materials, the volatility of the active VCM components is quite low by design, hence a very long test time is required to perform the isothermal TGA using vacuum weighing systems with methods just described. This problem is further complicated by the mass sensitivity limitations of an in situ vacuum microbalance system if it is used. Measurements of this kind to obtain source kinetics were studied but were not performed.

Another method is available for measuring source kinetics. This technique uses QCMs which are maintained at LN_2 temperatures so that the VCM remission is negligible. The source temperature is maintained at a constant value so that this method is designated isothermal cryogenic QCM TGA (CQ/TGA). Its principle shortcoming is that the source directional mass loss distribution must be known. This distribution can be measured by an array of QCMs such as is employed in the Molekit. Its main advantages over the isothermal TGA are that the QCMs are extremely sensitive being able to detect nanograms of mass loss from the source, and that it can be applied to the most general complex source configurations used on typical satellite systems. CQ/TGA, being at the present a state-of-the-art isothermal procedure, requires about 48 hours including set-up time to evaluate a typical low volatile space qualified source. By virtue of CQ/TGA high sensitivity, it requires considerably less time than conventional isothermal TGA with vacuum balances. While dynamic TGA is the most rapid of all testing procedures, it is limited to the source configurations it can handle and at present it can only characterize sources in terms of rate ordered processes at relatively high temperatures. This is probably valid at temperatures in excess of 200°C for most source materials which are applied as relatively thin coatings. However, at near ambient source temperatures, even with thin coatings, much of the mass loss kinetics is probably diffusion limited, and isothermal methods are again necessary.

To reliably obtain the kinetic parameters of the source materials, it is necessary to accurately model the AESC Molekit configuration and then adjust the geometry of the internal components to establish the optimum configuration for testing. The Molekit can be modeled as a four-node system. These nodes are the crystal of the sensing QCM (Q), the cases of all four QCMs and their support structure (R), the source and its holder (S), and the Molekit shroud walls (W).

The basic equation for CQ/TGA to evaluate source kinetics is, assuming the source to emit diffusely (cosine distribution),

$$\dot{M}_Q = -F_{SQ}\dot{M}_S \tag{1}$$

where

$\dot{M}_Q$ = total mass deposition rate on the QCM, g/s

$\dot{M}_s$ = total mass loss rate from the source (a negative value), g/s

F_{SQ} = diffuse geometric view factor from the source to the QCM crystal

If an explicit functional form of $\dot{M}_s$ is known, which is integrable, equation (1) can be integrated to give the CQ/TGA equation for source kinetic testing. If it is assumed that the most likely source process is the exponential first order process, then two independent equations(M_Q and $\dot{M}_Q$) will characterize the CQ/TGA procedures allowing the simultaneous evaluation of 2 independent material properties. Thus a two component source is indicated which exhibits first order source emission. The QCM deposition expression assuming an initially clean QCM and a diffuse source, becomes

$$\left.\begin{aligned} M_Q &= F_{SQ}\, W_S \left[(\mu_1 + \mu_2) - \left(\mu_1\, e^{-k_1 t} \right) - \left(\mu_2 e^{-k_2 t} \right) \right] \\ \dot{M}_Q &= F_{SQ}\, W_S \left(\mu_1 k_1\, e^{-k_1 t} + \mu_2 k_2\, e^{-k_2 t} \right) \end{aligned}\right\} \qquad (2)$$

where

M_Q = mass on the QCM, g

W_S = total weight of source material before testing, g

μ_1, μ_2 = weight fractions in the source of the two source components

k_1, k_2 = rate constants at T_s, for the two source components, s^{-1}

The QCM is a "beat" frequency which is directly proportioned to the deposited mass. Analytically, this is expressed as

$$\left.\begin{aligned} M_Q &= A_Q C_Q (f - f_o) \quad , \quad g \\ \dot{M}_Q &= Q_Q C_Q \dot{f} \quad , \quad g/s \end{aligned}\right\} \qquad (3)$$

where

A_Q = 0.316 cm^2, the active area of the QCM crystal

C_Q = $4.43 \text{ x } 10^{-9}$ *g-cm*$^{-2}$ *- Hz; the mass sensitivity constant* for these QCMs

f = instantaneous beat frequency of the QCM, Hz and

f_o = initial baseline (clean) beat frequency of the QCM, Hz.

Combining equations (2) and (3) expresses the four source kinetic properties (μ_1, μ_2, k_1, k_2) in terms of two isothermal observables, $(f, \dot{f})$.

$$(\mu_1 + \mu_2) - \left(\mu_1 e^{-k_1 t} + \mu_2 e^{-k_2 t}\right) = C(f - f_o)$$

$$\left(\mu_1 k_1 e^{-k_1 t} + \mu_2 k_2 e^{-k_2 t}\right) = C\dot{f}$$

where

$$C = \left(\frac{A_Q C_Q}{F_{sq} M_{so}}\right) \text{ Hz}^{-1} \text{ and}$$

$$\dot{f} = \text{instantaneous rate of change in beat frequency, Hz}\cdot\text{s}^{-1}.$$

A basic requirement to use this method (and any other multi-component technique such as dynamic TGA) is that the two active components are sufficiently different in their kinetic activity that the high volatile component (HVC or μ_1) is completely depleted from the source while the lower volatile component (MVC, or μ_2) is still being released in significant amounts. The basic procedure allows the tests to run long enough for the high volatile component to be completely depleted so that the "tail" of the test can be analyzed when only the lower volatile material is still outgassing. Once the two properties of the low volatile have been determined, earlier data where both species are active can be used to compute the values of μ_1 and k_1. This "Tail of the Test" procedure can be used to analyze sources with more than two components provided that the rate constants of the components are significantly different. The method simply starts at the end of the test and works backwards to the beginning solving for the components of each successive active component.

It has been shown (Dow Corning, Ball Brothers, etc.[2]) that many organic polymers of the type currently being used in satellite applications do indeed exhibit a highly volatile component which offgasses relatively rapidly (about 10 to 15 hours for $T_s \approx 125°C$) followed by a very slowly emitting component which exhibits a nearly constant deposition rate when the high volatile component has been depleted. Figure 5 presents a representative example of such a typical two component polymer, and identifies the significant observables during a cryogenic QCM thermogravimetry test.

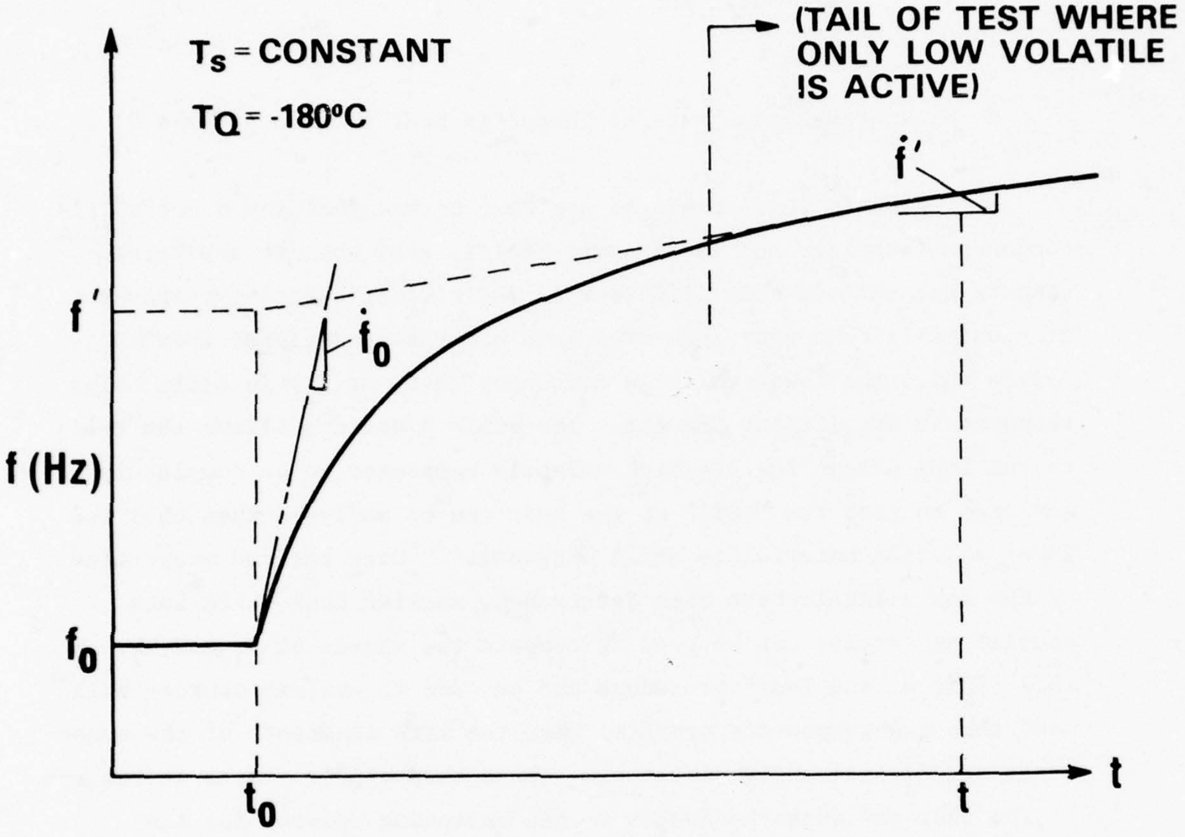

Figure 5. Typical Isothermal QCM Thermogravimetric Data for a Two Component Polymeric Source

If sufficient test time is allowed, the high volatile component is depleted and, assuming a constant outgassing rate for the low volatile component simplified graphical relationships develop as follows

$$\begin{aligned} \mu_2 k_2 &= C\dot{f}' \\ \acute{\mu}_1 k_1 &= C(\dot{f}_o - \dot{f}') \\ \mu_1 &= C(f' - f_o). \end{aligned} \tag{4}$$

If the constant slope, $\dot{f}'$, is projected to the starting time of the test, then the $(f' - f_o)$ measures the mass of the high volatile component which is present in the source sample during the test. This will always be slightly less than the actual mass fraction due to undetected losses which occur during the pumpdown and initial test procedures in vacuum prior to the start of deposition. The rate constant for the high volatile component is simply

$$k_1 = \left(\frac{\dot{f}_o - \dot{f}'}{f' - f_o} \right). \tag{5}$$

Of course the QCM calibration data must be applied to the raw test data to obtain the curve shown in Figure 5.

One limitation in these types of tests is that the source outgassing component which is the most volatile begins leaving the source as soon as the chamber is pumped. Thus, it is clear, that the source should be quenched with LN_2 as soon as possible after starting the pumpdown to preserve as much of these high volatiles as possible. There are two constraints to this procedure. The first is that if the source is chilled too fast, water vapor can condense on the cold sources, which can significantly change the initial mass loss characteristics. Secondly, if the chamber walls are not kept continually colder than the source, any condensibles on the walls (from previous tests, etc.) can be readily transferred to the source. Thus, the overall constraint is how fast the entire Molekit system can be brought to cryogenic temperatures.

The Molekit at present accomplishes this in about ten minutes using a sequence of aspirators and sorption pumps for the rough pumping. The optimum pressures at which the cryogen is admitted into each subsystem of the facility has been experimentally optimized so that it is estimated only about 5% of the high volatile is lost.

2.4 Source Kinetics Test Results

During the source kinetics testing phase of the program, two source materials were evaluated. A single source kinetics test was run on DC 92-007 at 100°C and three tests were run on RTV-566 at 40°C, 70°C and 120°C. The raw data is presented as it was obtained on the data acquisition plotter during the tests. The QCM calibration has not been applied to this raw data. The QCM array during the DC 92-007 test is 15.24 cm from the source.

The outgassing characteristics of DC 92-007 at 100°C are presented in Figure 6. The accumulation on 3 QCMs is shown. The first QCM is concentric with the source while the other two are coplanar with the on-axis QCM and make angles of about 26° and 53° with that axis. The ratio of the deposition on the first two QCMs clearly indicates Lambertian (diffuse) emission from the source. The outermost QCM gives values about 50% greater than diffuse, but subsequent tests have shown this QCM to be faulty. It has since been removed from the Molekit. Diffuse

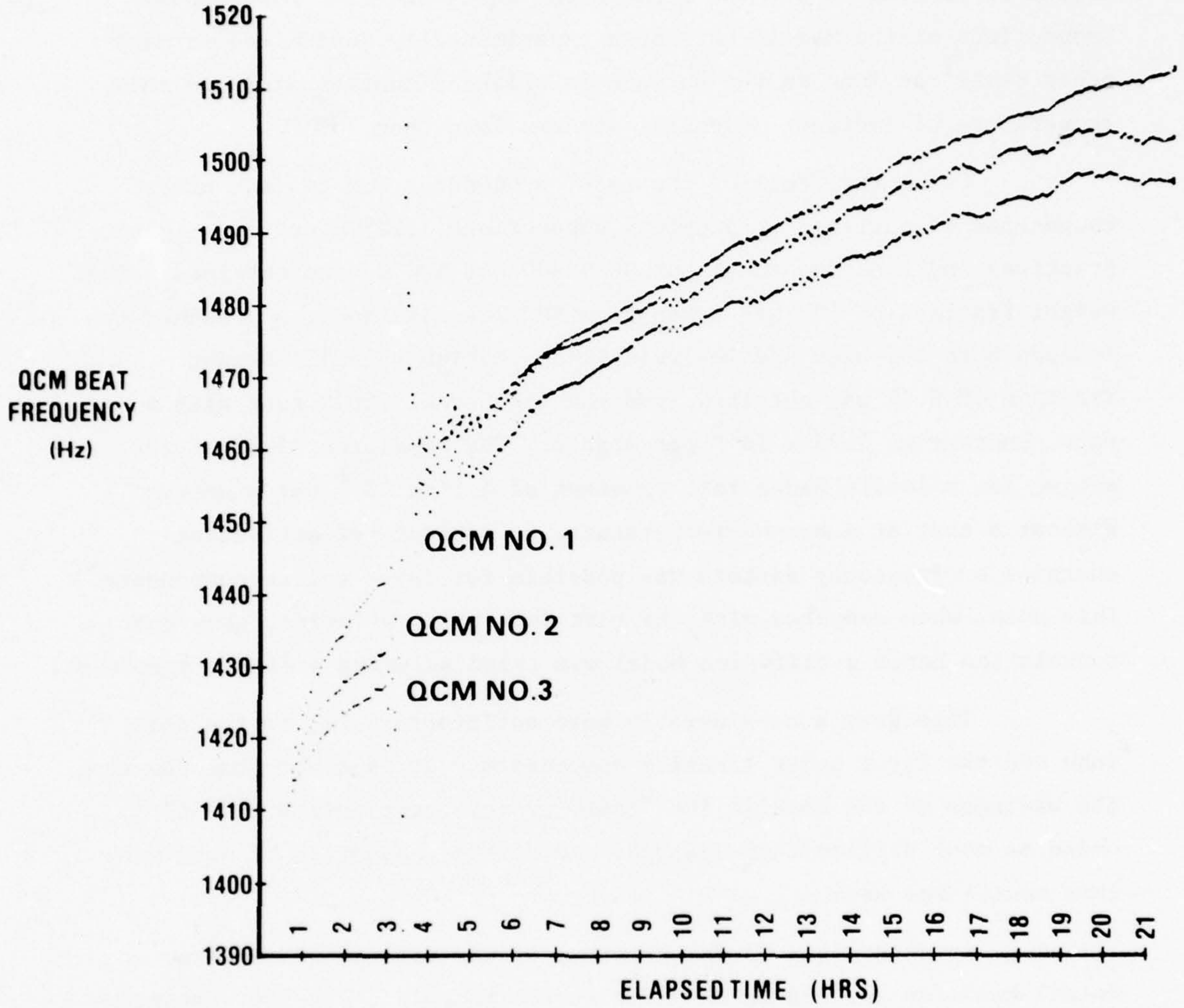

Figure 6. Isothermal QCM/TGA for DC 92-007 at a Temperature of 100°C

source emission is thus tentatively experimentally verified. Diffuse molecular reflection and VCM reemission, which are also fundamental assumptions of the model, have been experimentally determined in many other tests[1] so long as the surface is slightly contaminated and the temperature of incident molecular streams less than 700°C.

Using the "tail of the test" procedures for two 1st order components as outlined in previous subsections, the values of weight fractions and rate constants for DC 92-007 at 100°C were obtained. The weight fraction of 53% was taken from MMC TGA data and was presumed to include both the high and low volatiles. A high volatile weight fraction of 0.7% was obtained from the isothermal 100°C test with a rate constant of 1.75×10^{-3} per minute. The remaining 52.3% of the active low volatile had a rate constant of 4.24×10^{-6} per minute. Without a test at a second temperature, no estimate of activation energies or frequency factors was possible for these source components. This data, when compared with the test data point by point, gave poor correlation hence a diffusion model was tried assuming a single component.

This gave a considerably more satisfactory fit to the data than did the first order kinetics components. It is clear that due to the waviness of the data in the "tail" of this test unit DC 92-007 would be most difficult to analyze. No further reduction of data with this source was made.

At this point in the program, it was decided to continue detail kinetics testing on only one source material, RTV-566. Measurements of the isothermal outgassing kinetics for a 2.54 cm (1.0 inch) diameter coating of RTV-566 at four temperatures were made during this period. The temperatures were 40°C, 70°C, 100°C and 120°C. Data are presented in Figure 7 for these temperatures except for the 100°C run. A heater failure occurred during this test.

Additional information required are the physical dimensions of the sample coating itself. The procedures used are to peel the RTV

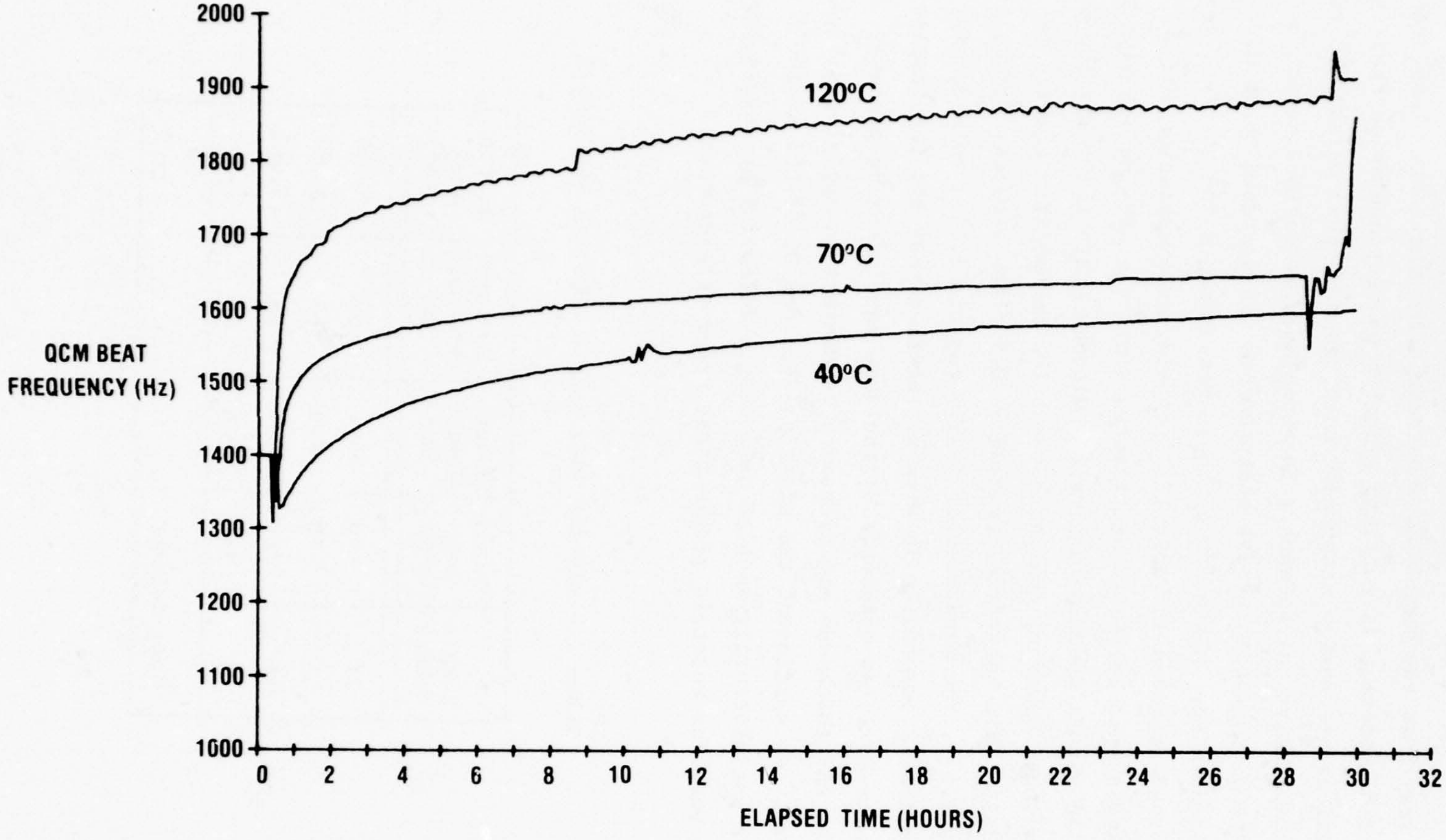

Figure 7. Isothermal QCM/TG Data for Three RTV-566 Coatings at 40, 70, and 120°C for Approximately 30 Hours Without UV Radiation

film away from the magnesium substrate after the test. Then, the resulting specimen is cut into a number of rectangular patches whose dimensions are easily measured. Each patch is then weighed to ±100 μg using an analytical balance. The thickness at various locations is measured, and the thickness measurements are averaged to obtain the reported value. A summary of these measurements for the four tests performed is given in Table I. A considerable variation in the thickness (±12 μm) is to be expected since the RTV-566 adhesive is applied with a spatula in a fairly viscous state following the vacuum degassing. However, the large variation in specific gravity is unusual. This has varied from about 0.90 (the samples readily float) up to 1.47. The manufacturer (G.E.) reports 1.51. This density variation is surprising in view of the fact that all the samples are from the same raw compounds of the same manufacturing process. The weight and thickness are necessary parameters in applying diffusion theory. As mentioned, the kinetics data for DC 92-007 at 100°C was quite satisfactorily modeled as a single diffusing process superimposed on a very low volatile single first order rate process.

TABLE I - RTV-566 TEST SAMPLE PHYSICAL PROPERTIES

Sample Number	Source Temp (°C)	Source Weight (mg)	Average Thickness (μm)	Source Area (cm^2)
27	40	45.1	69	5.067
28	70	47.9	109	5.067
*26	100	43.6	76	5.067
21	120	46.6	64	5.067

*Test deleted.

The basic nature of the RTV-566 and the measurement precision of the Molekit system necessitated the development of a relatively sophisticated data analysis algorithm to adequately reduce the QCM test data to obtain the desired source kinetic parameters.

A standard software package of polynomial regression and function analyzer routines was purchased from Hewlett Packard and these were linked together with the AESC plotter programs to be compatible with the data storage tapes. This system of programs, designated "POLYPLOT" (1) inputs the test data tapes and the QCM transient calibration, (2) fits a sequence of 9th order polynomials to the compensated QCM beat frequency data, (3) computes the derivatives of this function and (4) compares the regression analysis against the test data by plotting regression functions over the test data. The test data is therefore divided into a sequence of regression polynomials until the correlation coefficient is greater than 0.995. Then reliable slope and intercept determination from a log-linear plot of frequency rate versus time can be obtained. From these measurements, the kinetic parameters of the less volatile second component can be estimated, and subsequently the parameters for the first component evaluated by subtracting the effects of the second component from the test data at the start of the test when both components are active. With the assumption of first order kinetic processes for both components, the results of the data reduction are the percent by weight (weight fraction μ) of each component and the first order specific rate constant for each component (K). Table II presents this data at the three test source temperatures $40^\circ C$, $70^\circ C$ and $120^\circ C$. Figure 8 shows the nearly linear dependency of the weight fraction of the high volatile component (μ_1) with source temperature. This could indicate an adsorbed material where the quantity that the surface will hold is inversely proportional to its temperature. The weight fraction of the second component can be averaged to give a value of about 0.21 ± 0.07. While the uncertainty is rather large, the average fraction

TABLE II. 1st ORDER SOURCE KINETICS DATA FOR TWO HIGH VOLATILE COMPONENTS OF RTV-566 (0.2% CATALYST)

TEMP T (°C)	WEIGHT W_S (mg)	DEPTH h (μm)	1st FRAC. μ_1 (%)	2nd FRAC. μ_2 (%)	1st RATE CONSTANT k_1 (MIN^{-1})	2nd RATE CONSTANT k_2 (MIN^{-1})
40	45.1	69	0.153	0.131	8.668×10^{-3}	9.330×10^{-4}
70	47.9	109	0.251	0.282	2.959×10^{-2}	9.493×10^{-5}
120	46.6	64	0.348	0.229	4.656×10^{-2}	2.007×10^{-3}

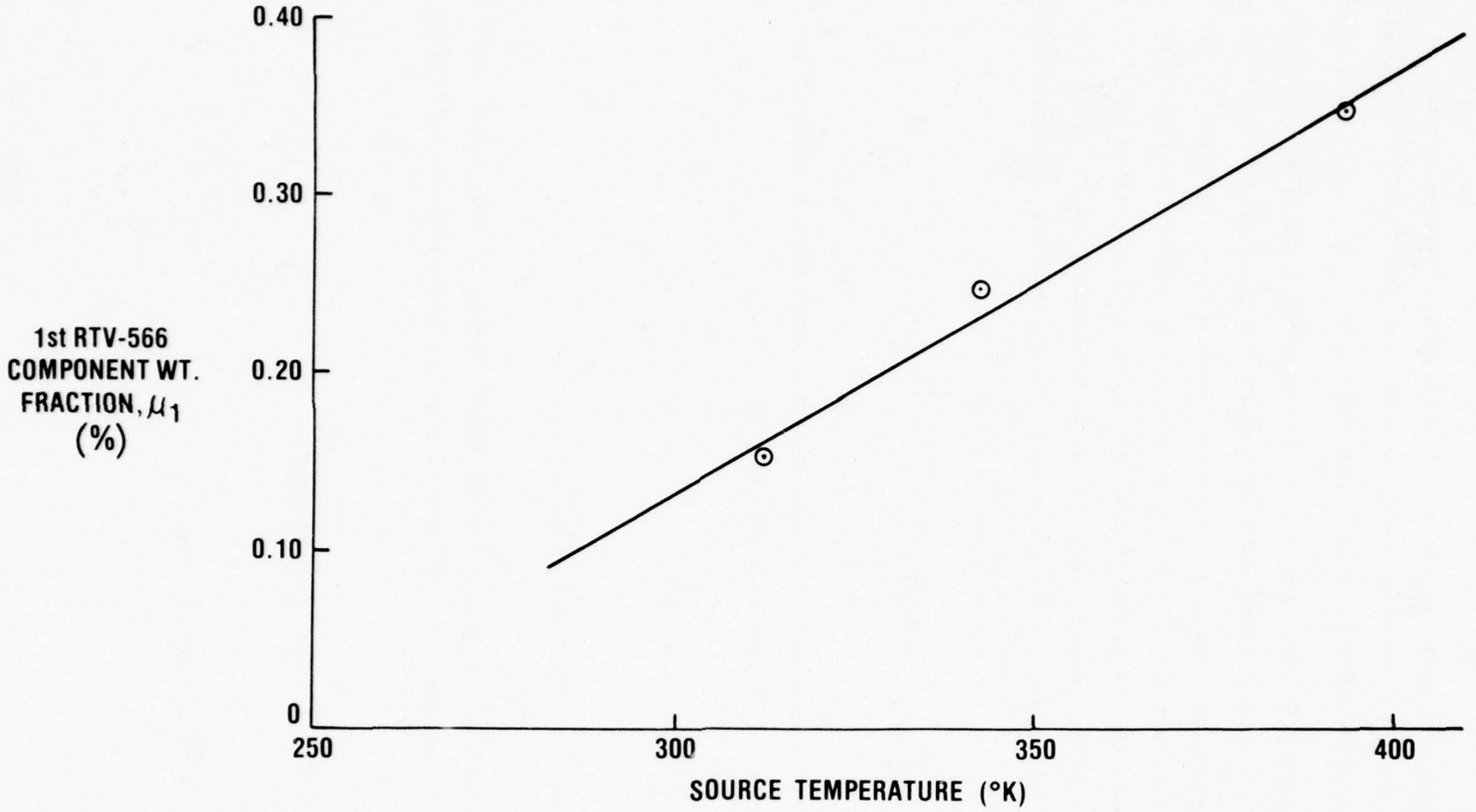

Figure 8. Variation of RTV-566 1st Component Wt. Fraction (%) with Source Temperature

of the second component which is released after twenty-four hours with the source at 120°C compares very closely with the NASA TND-8008 %TML of 0.23% for RTV-566 with 0.2% catalyst.

Figure 9 presents plot of the natural logarithm of the rate constants versus the reciprocal of the source temperature for both active components. The slope of such curves gives the value of the heat of activation for the process in question while the intercept at 1/T = 0 gives the so-called "frequency factor." The value of the rate constant at other temperatures can then be determined by using the Arrhenius relationship over the temperature range for which the slope is constant,

$$K(T) = A_o \, e^{-\Delta E/RT} \tag{6}$$

For the first component, a linear approximation with a correlation coefficient of 0.89 can be made showing

$$A_o^{(1)} = 32.15 \text{ min}^{-1}$$

$$\Delta E^{(1)} = 4990 \text{ cal mole}^{-1}.$$

For the second component, a linear relationship is not really indicated, but if it is assumed in spite of a very low correlation coefficient, then

$$A_o^{(2)} = 4.953 \times 10^{-1} \text{ min}^{-1}$$

$$\Delta E^{(2)} = 3083 \text{ cal mole}^{-1}.$$

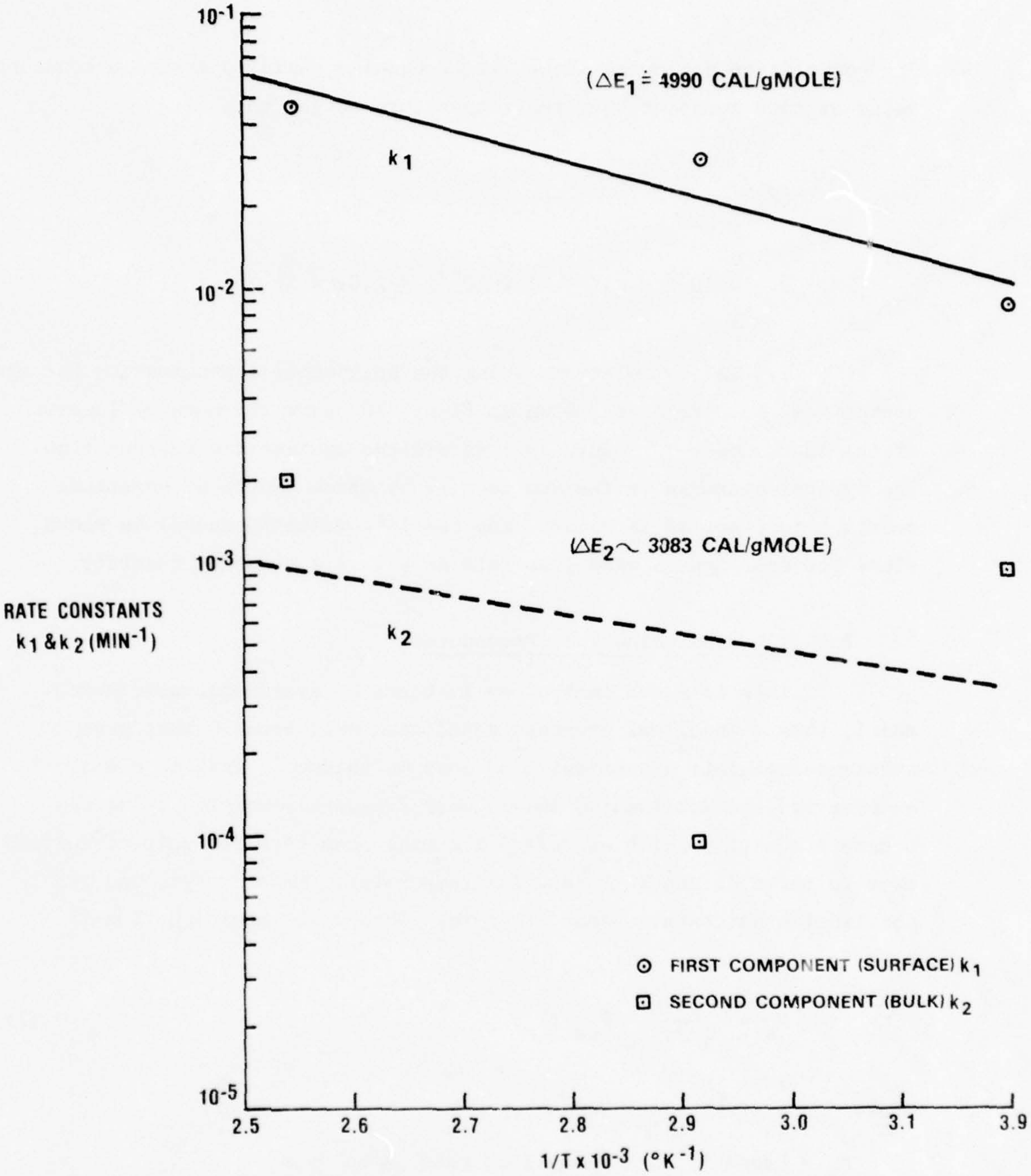

Figure 9. Rate Order Constants (Assuming First Order) of RTV-566 Versus Reciprocal Temperature for the Two High Volatile Components

For correlation as low as shown, it is equally valid to assume a constant value of rate constant over the temperature range; then

$$\Delta E^{(2)} = 0$$

$$9.5 \times 10^{-5} < \bar{K}_2(-1.01 \times 10^{-3}) < 2.01 \times 10^{-3} .$$

Typical calculations using the polynomial approximation for the source mass loss rate are shown in Figure 10 where the natural logarithm of the source mass loss rate $|\dot{M}_s|$ is plotted against the testing time. The typical decrease in the source rate by three orders of magnitude over the test period is clear. The absolute value (modulus) is shown since the real source mass loss rate is always a negative quantity.

2.5 VCM Reemission Test Procedures

This is a new technology in terms of systematic predictive model, thus a model was proposed based upon experience. Most pure substances exhibit a constant mass loss in vacuum.[3] This is classical evaporation and sublimation and is most frequently modeled using the Langmuir equation which expresses the mass loss rate per unit of surface area in terms of the bulk material temperature, mass number, and its equilibrium saturation vapor pressure. This well-known equation is

$$\dot{M}_s = \sqrt{\frac{M}{2\pi R T_s}}\, P_{sat}(T_s) \qquad (7)$$

where

$\dot{M}_s$ = Langmuir bulk reemission rate, g/cm^2 - s
M_s = VCM (a pure substance) atomic weight, AMU
R = universal gas constant, 1.986 cal/mole/^{0}K
T_s = bulk source temperature, ^{0}K

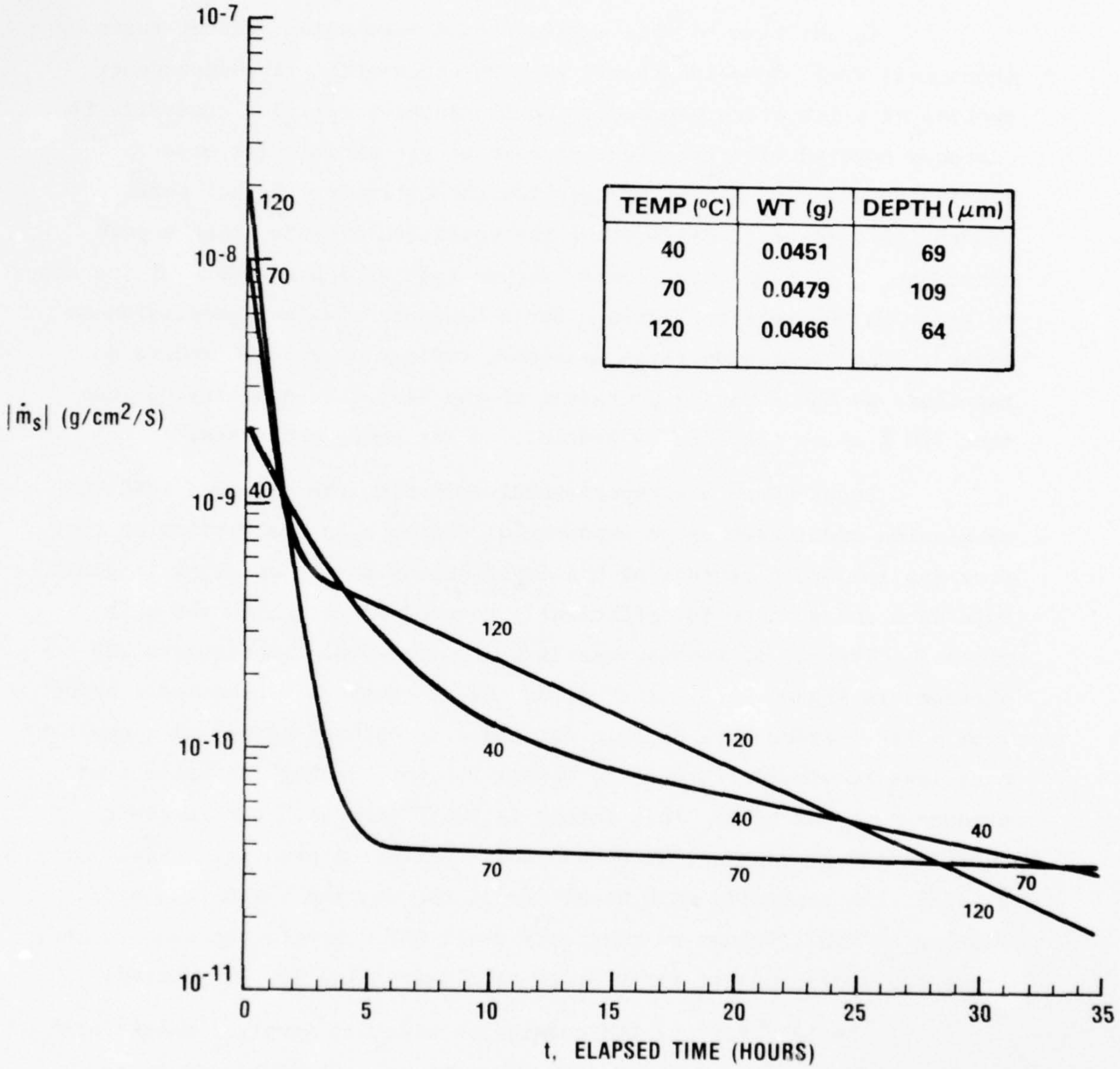

TEMP (°C)	WT (g)	DEPTH (μm)
40	0.0451	69
70	0.0479	109
120	0.0466	64

Figure 10. Mass Loss Rate for RTV-566 at 40, 70 and 120°C (0.2% Catalyst)

$P_{sat}(T_s)$ = equilibrium saturation vapor pressure at T_s, mm Hg(torr) .

In addition to this constant bulk reemission, recent tests have shown that small deposits reemit with an exponential time-dependency typical of a 1st order process[4], and it has been verified generally that surfaces covered with fractions of a monolayer exhibit 1st order reemission exactly[5] as for example the BET-Langmuir model of surface adsorption. In tests calibrating the precision of QCMs using a pure substance, ice, test data clearly showed that at least 1500 Å of ice had to exist on the receptor surface for a Langmuir constant reemission to occur[6]. The reemission rates decreased rapidly by several orders of magnitude as the coverage decreased to the very thin deposits of less than 500 Å which can then be modeled as 1st order processes.

Based upon this experimental evidence, the proposed AESC VCM reemission model assumes an exponential decrease in the reemission rate from the 1st order process at monolayer depths to the constant Langmuir rate when the surface is sufficiently covered to establish the bulk process. Typical of such processes at two receptor temperatures are sketched in Figure 11. The equation covers reemission kinetics ranging from a first order rate process for small receptor deposits to a constant mass loss reemission rate (zero order) for thick enough deposits that produce pure VCM bulk. This latter is identified with the Langmuir equation and is thus called a "Langmuir reemission process." With RTV-566, the basically high stability of the coating limits the outgassing to small values so that only small QCM deposits can be obtained, hence the small deposit first-order reemission kinetics is assured.

The test for the VCM reemission kinetics involves maintaining a clean QCM receptor at the temperature that the kinetics are to be evaluated. Then, the source is raised to a high temperature ($\approx 125^{\circ}C$), and the VCM allowed to deposit until a peak is reached, at which time the source is quenched with LN_2.

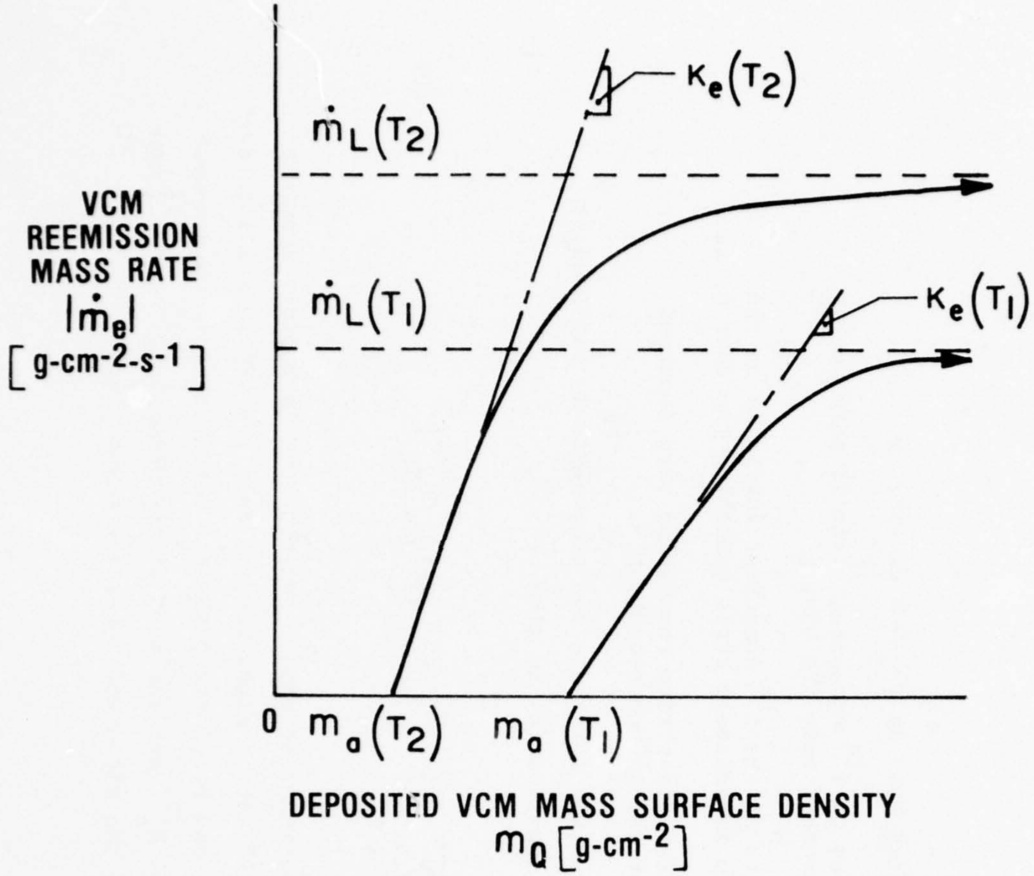

$$\boxed{\dot{m}_e \doteq \dot{m}_L \left[1 - e^{\frac{K_e}{\dot{m}_L}(m_a - m_Q)} \right]}$$

Figure 11. Schematic Diagram of VCM Reemission Mass Rate vs Deposited VCM Mass ($T_2 > T_1$)

The procedures for obtaining the VCM reemission rates constants for the two components can then be developed from the equation in Figure 11 for the QCM mass and mass rate equations assuming first order VCM reemission kinetics. The mass equation is

$$M_Q(t) = \sum_{i=1,2} \left[M_a^{(i)} \quad M_{QO}^{(i)} - M_a^{(i)} \quad e^{-K_e^{(i)} t} \right] \tag{8}$$

where

$M_Q(t)$ = total mass on the QCM at time, g

$M_a^{(i)}$ = mass of i^{th} component which is permanently adsorbed onto the QCM, g

$M_{QO}^{(i)}$ = mass of the i^{th} component initially on the QCM immediately after quenching the source, g

$k_e^{(i)}$ = first order rate reemission rate constant for the i^{th} component, s^{-1}.

The mass rate equation for these two components is obtained by differentiating equation (8) to give

$$\dot{M}_Q = -\sum_{i=1,2} k_e^{(i)} \left[M_{QO}^{(i)} - M_a^{(i)} \right] e^{-K_e^{(i)} t} \tag{9}$$

As typical deposition test data shows, the HVC is rapidly reemitted so that in the "tail" (after eight hours), only the LVC is still actively being reemitted, and by plotting LN $|\dot{M}_Q|$ versus time in this domain, the rate constant $K_e^{(2)}$ and the mass differential $\left[M_{QO}^{(2)} - M_a^{(2)} \right]$ can be obtained from the slope and intercept respectively.

At the beginning of the reemission test, the QCM mass loss rate is given by

$$\dot{M}_Q(0) = -\sum_{i-1,2} k_e^{(i)}\left[M_{Q0}^{(i)} - M_a^{(i)}\right] \tag{10}$$

Further, the total deposit on the QCM at the start and finish of the reemission test are respectively

$$\left.\begin{array}{ll} M_Q(0) = \sum\limits_i M_{Q0}^{(i)} & \quad (11a) \\ \\ M_Q(\infty) = \sum\limits_i M_a^{(i)} & \quad (11b) \end{array}\right\} \quad i = 1,2$$

By combining the data from the log-linear plot of $\dot{M}_Q$ versus t with equations (10) and (11), it is possible to evaluate the HVC rate constant

$$k_e^{(1)} = \frac{\left[M_Q(0)\right] - k_e^{(2)}\left[M_{Q0}^{(2)} - M_a^{(2)}\right]}{\left[M_Q(0) - M_Q(\infty)\right] - \left[M_{Q0}^{(2)} - M_a^{(2)}\right]} \tag{12}$$

2.6 VCM Reemission Test Results

Figure 12 shows a constant QCM mass loss rate at -20°C. It is a reasonable assumption that only the LVC is actively being reemitted and that its reemission rate constant is so small that a linear loss rate appears.

$$\dot{M}_Q = -k_e^{(2)}\left[M_{Q0}^{(2)} - M_a^{(2)}\right] \tag{13}$$

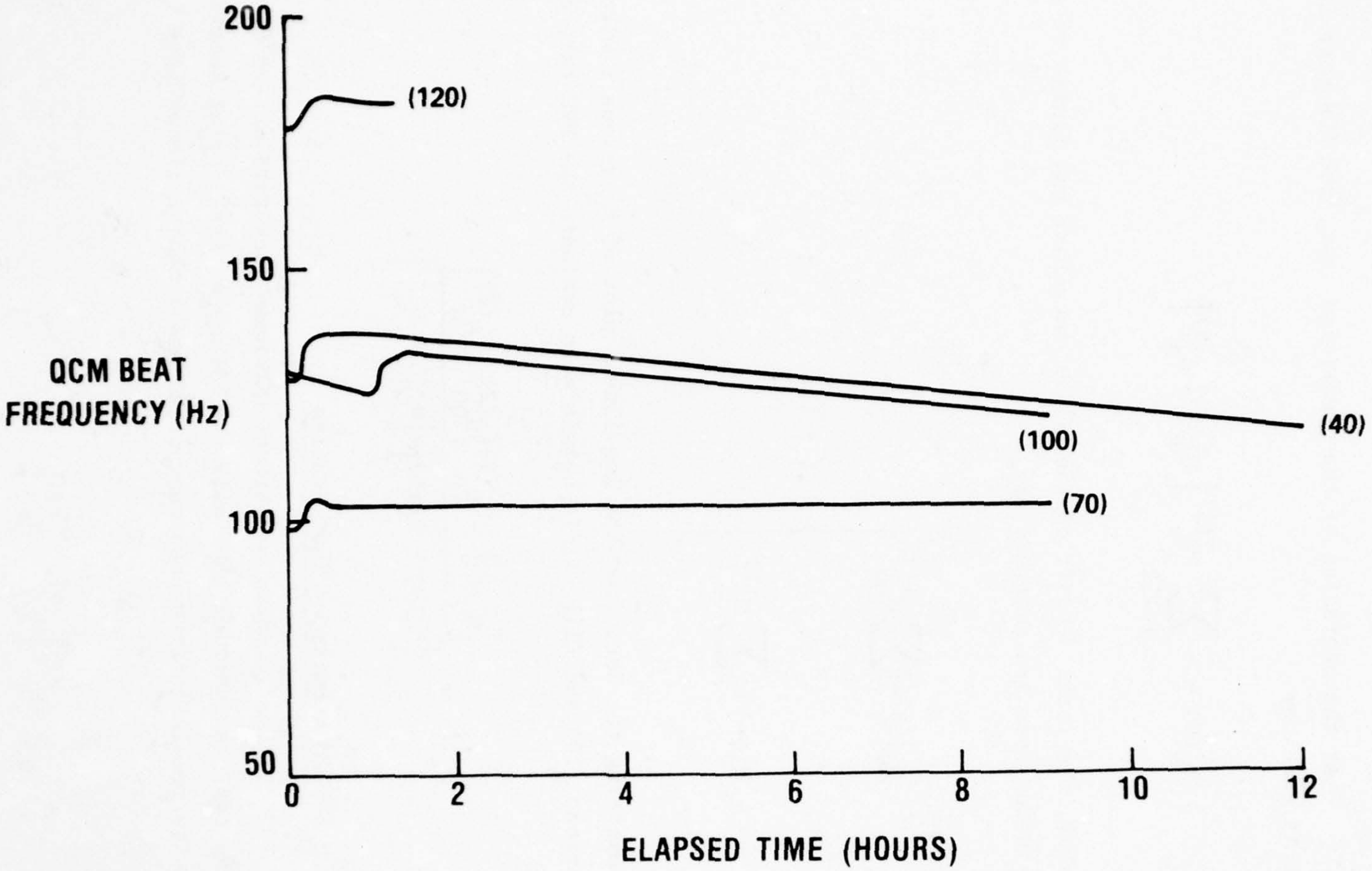

Figure 12. Reemission of Deposits from a QCM at -20°C After Termination of Deposition from RTV-566 at 40°, 70°, and 100°C

where

$$\dot{M}_Q = -2.115 \times 10^{12} \text{ g-s}^{-1}.$$

The initial quantity of LVC on the QCM, $M_{Q0}^{(2)}$, is obtained by extrapolating the constant reemission rate to the start of the test. The adsorbed quantity of the LVC, $M_a^{(2)}$, is assumed to be one-half of that shown in Figure 11.

For the QCM active crystal area of 0.316 cm^2, the mass surface density (MSD) becomes

$$m_a^{(2)}(-20^\circ\text{C}) = 1.82 \times 10^{-7} \text{ g-cm}^{-2}.$$

Assuming a VCM specific gravity of about 1.3, this gives deposit of LVC "thickness" of about 14 Å. The rate constant calculated for the LVC at -20°C is then

$$K_e^{(2)}(-20^\circ\text{C}) = 3.842 \times 10^{-4} \text{ min}^{-1} .$$

The reemission test for the source at 120°C and the QCM at 10°C showed an almost identical constant reemission about one hour after the HVC was emitted and by applying the same criteria as with the last case, the MSD

$$m_a^{(2)}(10^\circ\text{C}) = 1.557 \times 10^{-7} \text{ g-cm}^{-2}$$

which corresponds to a thickness of about 12 Å. The rate constant is

$$K_e^{(2)}(10^\circ\text{C}) = 9.311 \times 10^{4} \text{ min}^{-1} .$$

If classical ordered rate theory is assumed, then the LVC reemission rates will follow the Arrhenius relationship for temperature dependency. For the LVC data at -20°C and 10°C, these results are

$$K_e^{(2)} = A_o^{(2)} e^{\Delta Q^{(2)}/RT} \tag{14}$$

where

$A_o^{(2)} = 1.64 \text{ min}^{-1}$, the frequency factor for MVC reemission

$\Delta_Q^{(2)} = 4200 \text{ cal-g}^{-1} \text{ mole}^{-1}$, the heat of activation for MVC reemission.

The data for the reemission test at 10°C had sufficient VCM at the start of the tests to permit the use of equations (11) and (12) to compute the rate constant of the HVC at 10°C.

$$K_e^{(1)}(10^\circ\text{C}) = 6.12 \times 10^{-2} \text{ min}^{-1} .$$

All of the source and reemission processes of the two higher volatile components of RTV-566 studied with the isothermal QCM/TGA technique have exhibited low heats of activation characteristic of non-activated (physical) processes. In fact, they are all between 3000 and 5000 cal/g mole/°K. It is probably safe to assume that the HVC reemission would show a similar heat of activation of about 4000 cal-g^{-1} mole^{-1}. Then, the Arrhenius relation for the HVC becomes

$$K_e^{(1)} = A_o^{(1)} e^{\Delta Q^{(1)}/RT} \tag{15}$$

where

$A_o^{(1)} = 75.44\ \text{min}^{-1}$

$\Delta Q^{(1)} = 4000\ \text{cal-g}^{-1}\text{-mole}^{-1}$ (assumed).

Using this relationship, the HVC rate constant at $(-20^\circ C)$ becomes

$$k_e^{(1)}(-20^\circ C) = 2.63 \times 10^{-2}\ \text{min}^{-1}.$$

The VCM reemission kinetics results are summarized in Table III. The first order kinetic model for VCM reemission is probably only valid for a limited thickness (about 150 Å was deposited in these tests). The reemission rate increases with the net deposited mass up to a maximum rate which is identified with the Knudsen-Langmuir loss rate $(\dot{m}_L)$ classically related to the saturation vapor pressure. There is not enough VCM in the coated samples used in these tests to evaluate the Langmuir process.

2.7 Surface Transport Properties Test Procedures

This testing phase is primarily aimed at measuring the capture coefficients for VCM molecules emitting from the source at the source temperature, T_s, and impinging on the QCM receptor at T_Q. A temperature matrix of temperature combinations must be measured to account for the temperature range expected. The receptor temperatures were set at $-20^\circ C$, $+10^\circ C$ and $+25^\circ C$. Actually, above the $+10^\circ C$, almost no measurable deposit occurs. The source temperatures were the same as those used during the source kinetics testing.

The test procedures for these tests are obtained by integrating the QCM deposition differential equation which applies in the Molekit

TABLE III. REEMISSION KINETIC PROPERTIES FOR RTV-566 (0.2% CAT.)

QCM TEMP. °C	HIGH VOLATILE COMPONENT (HVC)		MEDIUM VOLATILE COMPONENT (MVC)	
	$A_0^{(1)} = 75.44\ \mathrm{MIN}^{-1}$ $\Delta Q^{(1)} \cong 4.0$ KCAL/gMOLE		$A_0^{(2)} = 1.64\ \mathrm{MIN}^{-1}$ $\Delta Q^{(2)} = 4.2$ KCAL/gMOLE	
	$m_a^{(1)}$, μg-cm^{-2}	$K_e^{(1)}$, MIN^{-1}	$m_a^{(2)}$, μg cm^{-2}	$K_e^{(2)}$, MIN^{-1}
-20	0.182	2.63×10^{-2}	0.182	3.84×10^{-4}
10	0.156	6.12×10^{-2}	0.156	9.31×10^{-4}

where the QCMs are at temperatures above LN_2. This expression is an extension of equation (1);

$$\dot{M}_Q + k_Q M_Q = -F_{SQ}\sigma_{SQ}\dot{M}_s \text{ g/s} \qquad (16)$$

where

k_Q = VCM reemission rate constant from the QCM, s^{-1}

σ_{SQ} = capture coefficient for VCM molecules leaving the source at T_s and impinging on the QCM surface at T_Q.

Since first order kinetics has been applied to the two components of RTV-566 source, equation (16) can be integrated to give the desired Q/TGA equations. Then, to compute the two corresponding capture coefficients, it is necessary to examine the QCM mass and mass rate equations for the deposition transport tests. For the condition of a small deposit, 1st order source and VCM kinetics is assumed.

The QCM mass deposition equation for the two components is

$$M_Q = \sum_{i=1,2} M_a^{(i)} + F_{SQ}W_S\left[\frac{\sigma_{SQ}^{(i)}\mu^{(i)}k_s^{(i)}}{k_e^{(i)} - k_s^{(i)}}\right] x\text{---}$$

$$\text{---}x\left(e^{-k_s^{(i)}t} - e^{-k_e^{(i)}t}\right) \qquad (17)$$

where

F_{SQ} = diffuse angle factor from the source to the QCM crystals

W_S = total source weight, g

$\sigma_{SQ}^{(i)}$ = capture coefficient of the i^{th} component arriving at the QCM from the source

$k_S^{(i)}$ = first order source rate constant for the i^{th} component, min^{-1} and

μ = weight factor of the i^{th} component in the source.

The QCM mass rate equation is obtained by differentiating equation (17) to give

$$\dot{M}_Q = \sum_{i=1,2} F_{SQ} W_S \left[\frac{\sigma_{SQ}^{(i)} \mu^{(i)} k_s^{(i)}}{k_e^{(i)} - k_s^{(i)}}\right] x---$$

$$---x \left(k_e^{(i)} e^{-k_e^{(i)} t} - k_s^{(i)} e^{-k_s^{(i)} t}\right) \qquad (18)$$

Allowing sufficient time (≈ eight hours) to deplete the source of the high volatile component (HVC), equation (18), which is now an expression involving only the low volatile component (LVC), can be rearranged to determine the corresponding capture coefficient as follows:

$$\sigma_{SQ}^{(2)} = \frac{\left[k_e^{(2)} - k_S^{(2)} \dot{M}_Q(t)\right]}{\left(F_{SQ}\, \mu^{(2)} W_S k_S^{(2)}\right)\left(k_e^{(2)} e^{-k_e^{(2)} t} - k_S^{(2)} e^{-k_S^{(2)} t}\right)} \qquad (19)$$

at any value of t ≥ eight hours.

All the parameters on the right hand side of equation (19) are known from the source kinetics test and the reemission test. For good results, considering the typical difficulties with data reduction in analyzing "tail" data, several values of $\sigma_{SQ}^{(2)}$ at different times in the "tail" domain are calculated and the results averaged. Finally, the capture coefficient for the HVC can now be calculated using equation (18) at any time during the initial hours of the transport test. The simplest result is the initial deposition, $\dot{M}_Q(0)$, rate which gives the following expression for the desired coefficient

$$\sigma_{SQ}^{(1)} = \frac{\dot{M}_Q(0) - F_{SQ}W_S\left[\sigma_{SQ}^{(2)}\ \mu^{(2)}\ K_S^{(2)}\right]}{F_{SQ}W_S\ \mu^{(1)}\ K_S^{(1)}} \tag{20}$$

Another convenient time at which to evaluate this coefficient is at the peak mass deposition when the mass rate vanishes. For many of the transport test conditions, this equilibrium point where the deposition rate vanishes is clearly evident and the elapsed time, t*, at which it occurs is easy to determine. When this occurs a particularly simple arrangement of the mass rate expressions allows simultaneous computation of both LVC and MVC capture coefficients knowing the initial QCM mass rate, $\dot{M}_Q(0)$, and the elapsed time at the peak deposition. Equations (18) and (20) can be combined into a matrix format as follows:

$$A_{ij}\ \sigma_{SQj} = B_i (i,j = 1,2) \tag{21}$$

where

σ_{SQj} = capture coefficient for i^{th} component of source onto the QCM

The elements of the coefficient matrix are given as follows:

$$A_{1,i} = \mu^{(i)}\ k_S^{(i)}\ (i = 1,2) \tag{22}$$

$$A_{2,i} = A_{1,i}\left\{\frac{k_e^{(i)}\ e^{-k_e^{(i)}t^*} - k_S^{(i)}\ e^{-k_S^{(i)}t^*}}{k_e^{(i)} - k_S^{(i)}}\right\} \tag{23}$$

$$B_1 = \left(\frac{\dot{M}_Q(0)}{F_{SQ} W_S} \right) \tag{24}$$

$$B_2 = 0 \; . \tag{25}$$

where

t^* = elapsed time at peak deposit, min and

$\dot{M}(0)$ = initial QCM mass accumulation, rate, g-min^{-1}

2.8 Surface Transport Properties Test Results

Transport deposit tests were made at QCM receptor temperatures of -20° and 10°C and at source temperatures of -40°C, 70°C, 100°C and 120°C. In addition, a single test was run with the source at 125°C and the QCM receptor at 25°C to compare Q/TGA testing results with those of the SRI-JPL TML/CVCM tests that are currently used to screen spacecraft materials.

The raw uncorrected QCM beat frequency data for the QCM at -20°C is presented in Figure 13. At the end of each deposition test, the source is quenched with LN_2. The QCM is maintained at -20°C and any subsequent VCM reemission measured. If there is still sufficient VCM in the QCM to make definitive reemission kinetics measurements, then this can be done. The data on VCM reemission kinetics of Figure 13 was taken after these transport deposition curves were made. At the QCM temperatures, no reemission was detected and separate reemission tests had to be performed.

Two general observations can be made based on the raw data. The first is that reemission rates exceed the incident flux rates, as is shown by the deposition peaks with the source at 70°C and 100°C. It also is true of the 120°C deposition curve, although it is not readily

AD-A070 386   AIR FORCE MATERIALS LAB WRIGHT-PATTERSON AFB OH   F/G 22/2
PROCEEDINGS OF THE USAF/NASA INTERNATIONAL SPACECRAFT CONTAMINA--ETC(U)
1978   J M JEMIOLA
UNCLASSIFIED   AFML-TR-78-190   NL

12 OF 13
AD
A070386

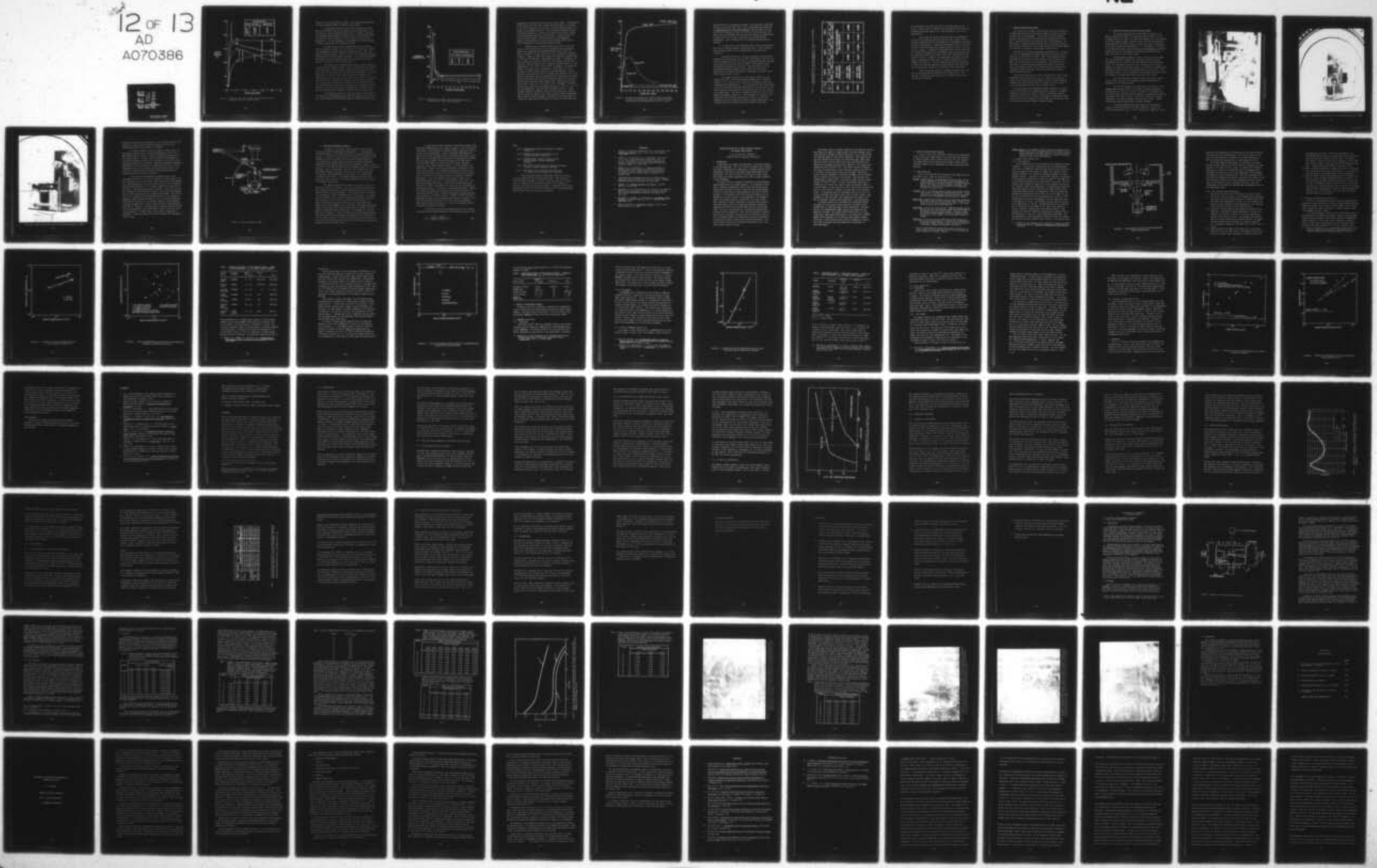

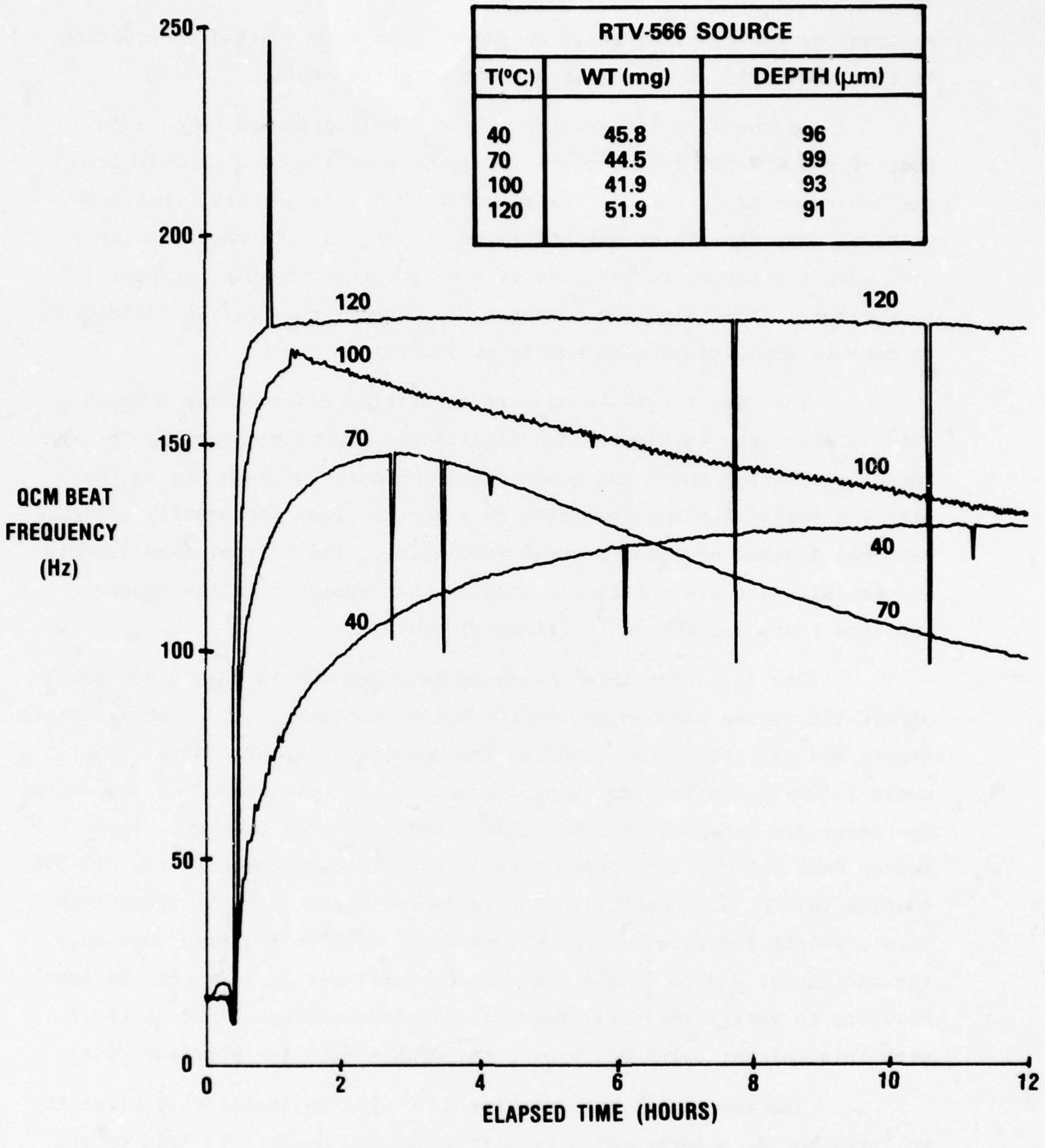

RTV-566 SOURCE		
T(°C)	WT (mg)	DEPTH (μm)
40	45.8	96
70	44.5	99
100	41.9	93
120	51.9	91

Figure 13. Deposition on a QCM at -20°C from RTV-566 (0.2% Cat.) Sources at 40°, 70°, 100° and 120°C

apparent on the plotting scale as shown. The second broad observation is that the residual amount of deposit is quite small.

If the specific gravity of the VCM is presumed to be about that of the RTV-566 resin or the catalyst, then the peak deposit from the source at 120°C corresponds to about 50 Å. It appears, therefore, that residual deposition may be limited to several adsorbed monolayers even when the source temperature is much greater than the receptor temperature. This also demonstrates the capability of Q/TGA techniques to measure depositions with monolayer precision.

The data for the transport deposition tests on the QCMs at +10° is presented in Figure 14. As with the -20°C test data, a "quick-look" examination shows two qualitative characteristics. One is the high VCM volatility and the other is a more or less permanently adsorbed residual deposit of about several monolayers. The initial mass deposit and deposit rate are noticeably greater than appeared in the source kinetics tests and the -20°C transport tests.

One cause for this increased mass release is that a new batch of RTV-566 source samples was made. While the identically same materials (resin and catalyst) were used and the manufacturing procedures rigorously followed, it is clear that the weight and thicknesses of the source specimens are from 50% to 150% greater than previous samples. The source data for the 10°C tests clearly shows the increase in the RTV-566 coating thickness. Hopefully, the intensive source kinetic properties (i.e., weight fractions and rate constants) will be invariant and only the additional source weight need be accounted for in reducing the data. However, to verify this will require additional source kinetics tests with this thicker batch of samples to compare with the previous data.

The transport test data for 10°C also indicates that after two to three hours, a permanently held residual VCM deposit is held on the QCM. This residual VCM (physisorbed) appears to depend upon the source

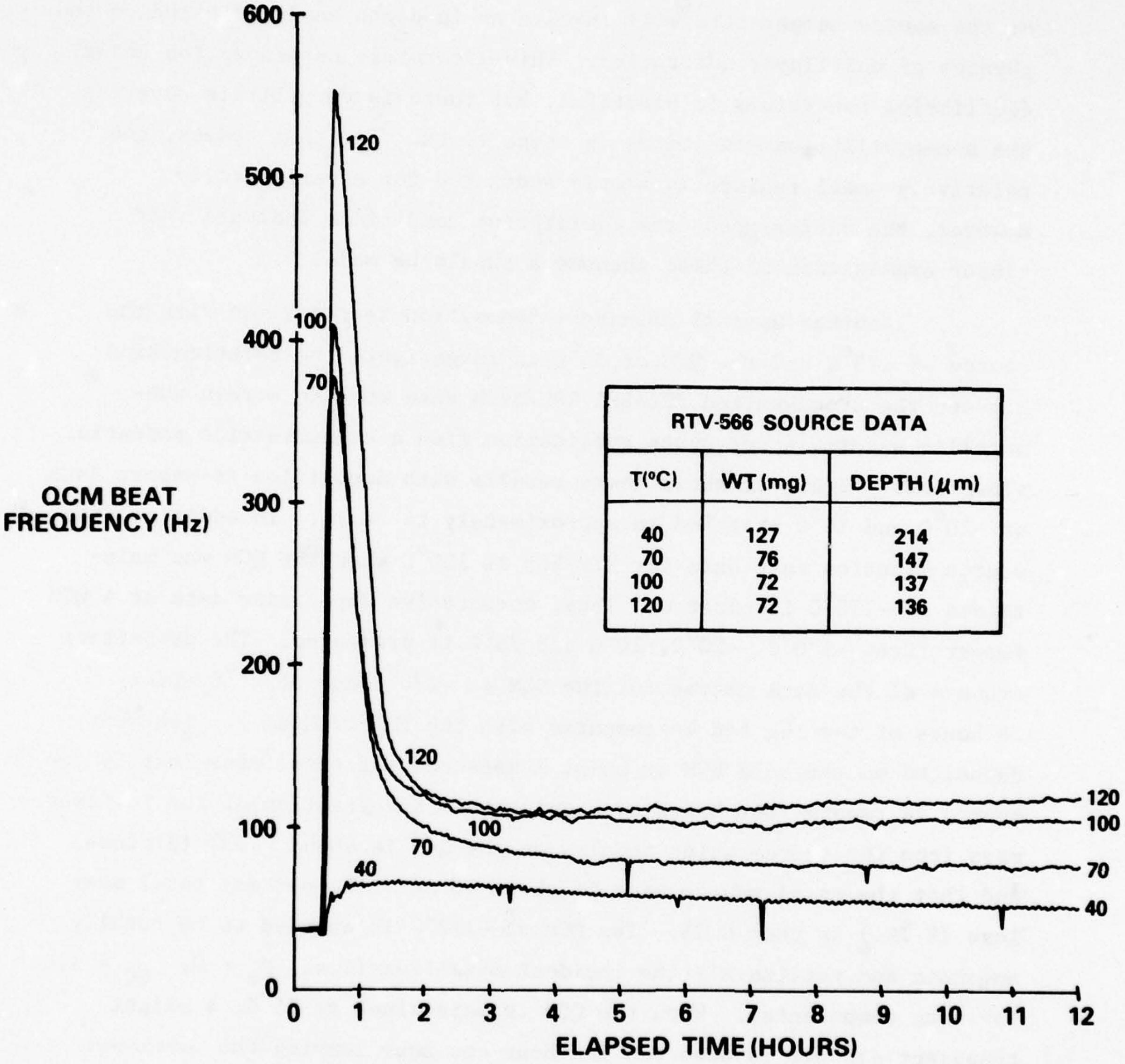

RTV-566 SOURCE DATA

T(°C)	WT (mg)	DEPTH (μm)
40	127	214
70	76	147
100	72	137
120	72	136

Figure 14. Deposition on a QCM at 10°C from RTV-566 (0.2% Cat.) Sources at 40°C, 70°C, 100°C and 120°C

temperature as the test data at the end of the test shows. An explanation of the variation of this final residual adsorbed deposit as a function of the source temperature will involve an in-depth analysis based on the physics of multilayer adsorption. This literature on adsorption under equilibrium conditions is plentiful, but there is very little covering the non-equilibrium conditions in these tests. For this reason, the relatively small residue is simply accounted for experimentally. However, the differences from equilibrium conditions indicate that a closer examination of these phenomena should be made.

Another special transport deposition test was run with the source at 125°C and the QCM at 25°C to investigate the relationships between the standardized JPL-SRI RML/CVCM data used to screen non-metallic materials for space application from a contamination potential viewpoint. Figure 15 shows these results with deposition transport data at -20°C and 10°C sketched in approximately to scale. In addition, the source kinetics test data for RTV-566 at 120°C when the QCM was maintained at -170°C is plotted. Thus, comparative deposition data at 4 QCM temperatures -170°C, -20°C, 10°C and 25°C is presented. The deposition amounts of the data curves for the QCM at -170°C and at 25°C after 24 hours of testing can be compared with the TML/CVCM data. The mass deposited on the cold QCM at point A measures the total mass lost by the source in twenty-four hours by knowing that the fraction of the released mass from the source which remains on the QCM is about 0.35% (diffuse) and that the total source mass is about 70 mg. The percent total mass loss (% TML) is then 0.3%. The QCM at -170°C is assumed to be totally anechoic and retains all the incident mass flux (i.e., $\dot{M}_e = 0$, $\sigma_{SQ} = 1.0$ for both components). When the QCM is maintained at 25°C, a slight transient deposit is desorbed in about one hour leaving the adsorbed deposit at point B, which is the percent collected volatile condensible mass (% CVCM) for both components. The ratio of the mass deposit at B to that at A shows that for the QCM at 25°C about 5% of that which hits

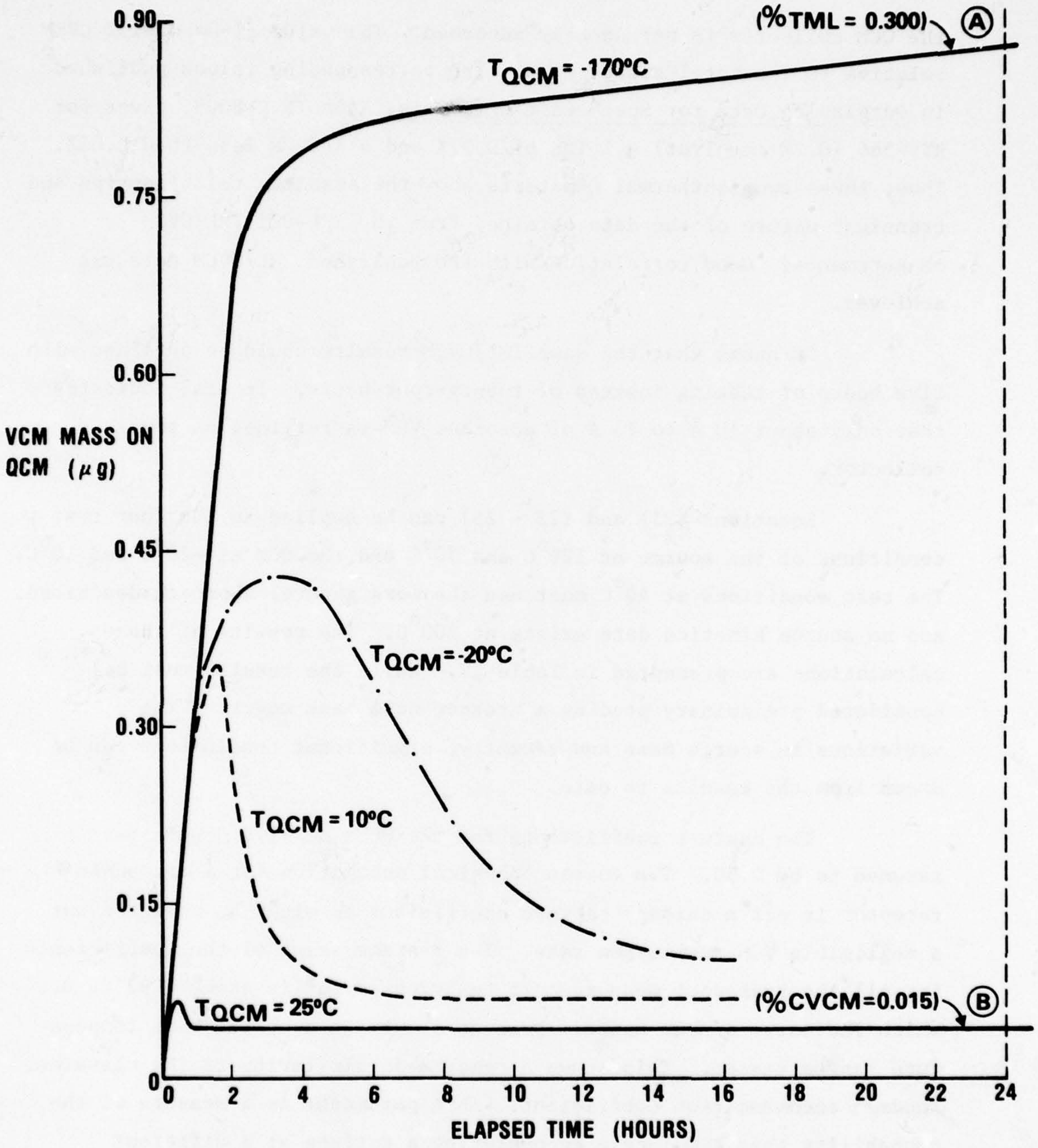

Figure 15. VCM Mass (μg) Deposited on a QCM Area 0.301 cm^2 Located 5.0 cm From a 2.54 cm. Dia. Source of RTV-566 (0.2% Cat.) Coated with 70 Mg and Maintained at 125°C for 24 Hrs.

the QCM collector is permanently adsorbed. The value gives 0.015% CVCM relative to the total source mass. The corresponding values published in Outgassing Data for Spacecraft Materials, NASA TN D-8008, gives for RTV-566 (0.2% catalyst) a % TML of 0.27% and a % CVCM less than 0.03%. Thus, these two isothermal QCM tests show the absolute relationships and transient nature of the data obtained from the JPL-SRI TML/CVCM measurements. Good correlation with the published TML/CVCM data was achieved.

It seems that the same TML/CVCM results could be obtained with five hours of testing instead of twenty-four hours. It also indicates that only about 10 Å to 15 Å of adsorbed VCM is retained on the collector.

Equations (21) and (22 - 25) can be applied to the four test conditions of the source at 120°C and 70°C and the QCM at -20°C and 10°C. The test conditions at 40°C must use the more general approach described, and no source kinetics data exists at 100°C. The results of these calculations are presented in Table IV. While the results must be considered preliminary pending a broader data base covering the variations in source mass and geometry, significant conclusions can be drawn from the results to date.

The capture coefficients for the QCMs at -170°C have been assumed to be 0.90. The correct physical assumption for a cryogenic receptor is not a unitary capture coefficient as might be expected but a negligible VCM reemission rate. The average value of the coefficients for all the transport measurements analyzed so far is about 0.92 to 0.04 which indicates a near uniform process occurring over the test temperature ranges tested. This shows a remarkable similarity to the classical Knudsen accommodation coefficient. This parameter is a measure of the probability that a molecule encountering a surface at a different temperature from the surface will attain the surface temperature. The incident molecule thus loses its previous identity, and becomes

TABLE IV. CAPTURE COEFFICIENTS FOR TWO COMPONENTS OF RTV-566 (0.2% CATALYST) FROM SOURCES AT (T_S) ONTO QCM RECEPTORS AT (T_Q)

T_Q / T_S	-170°C		-20°C		10°C	
	$\sigma_{SQ}^{(1)}$	$\sigma_{SQ}^{(2)}$	$\sigma_{SQ}^{(1)}$	$\sigma_{SQ}^{(2)}$	$\sigma_{SQ}^{(1)}$	$\sigma_{SQ}^{(2)}$
40°C	(0.9) (ASSUMED)	(0.9)	DATA PROCESSING INCOMPLETE			
70°C	(0.9) (ASSUMED)	(0.9)	0.883	0.923	0.955	0.885
120°C	(0.9) (ASSUMED)	(0.9)	0.927	0.938	0.924	0.891

indistinguishable from other molecules of the same species on the surface. Recent studies in surface physical chemistry[5] show that this accommodation process requires but a few picoseconds in the case of physisorption.

Identifying the capture coefficient with the accommodation coefficient is completely consistent with the mass transport model as presently formulated when the VCM reemission is independently determined. The broad significance of a temperature-independent capture coefficient is that it is valid whether the incident molecules are hotter or colder than the receptor. A gravimetric measurement with a source colder than the receptor would probably be indeterminant since the reemission rates are signficantly higher than incident rates (viz, the deposition data greater than 10°C). Hopefully, for engineering applications with the ranges of temperatures under study, all capture coefficients can be assumed to be about 0.9. The only materials testing then required is to obtain the Arrhenius temperature relationships for the source VCM and its reemission; no matrix of coefficients need be determined.

These conclusions should be considered tentative until more data on other materials and conditions are obtained, but it does indicate a significant simplification in the analysis and testing of VCM transport properties.

3. RECEPTOR SURFACE EFFECTS TESTS

This section of the report covers the tests that were performed in the SMEF where the spectral reflectance change on 5 typical satellite receptor surfaces was measured. The classical Fresnel reflection equations for specular spectral reflection and transmission[8] require that a uniform thickness of film deposit exist on the substrate. To insure this, the mass transfer equations used in the previous section were employed to design the source holder and the carousel which supports the receptors to establish a uniform deposit within ±0.2%.

The spectral reflectance measurements were made on all 5 receptors in a Carey 14 monochromator in ambient laboratory conditions prior to placing these receptors in the SMEF. Then a similar ambient spectral measurement of reflectance was made using the optical system on the SMEF. By rationing these sets of measurements, the SMEF optics is calibrated at all wavelength measurements for absolute reflectance. Then, only changes in these values following the LN_2 quenching, the contamination deposition event, and the UV radiation are needed to obtain the desired effects.

The original test plan was to use a PbS detector at $-80^{\circ}C$ to make measurements from about 0.75 μm to 2.5 μm. However, this detector failed, and the spectral data was taken from 0.25 μm using a tungsten filament lamp. An S20 PMT was used as the detector with both lamps to cover the wavelength band from 0.25 μm to about 0.90 μm.

The measurements were completed following a deposition of 1000 Å from an RTV-566 source and a subsequent 36 hour exposure to 30 EUVS of ultraviolet irradiation at 1236 Å. However, considerable computer processing of the data is required to determine if a measurable change occurred since such a change will be very slight and "quick-look" study of the data isn't precise enough to indicate change.

3.1 AESC Surface Materials Effect Facility (SMEF)

The general specifications for the SMEF are similar to the Molekit except that the SMEF is a horizontal cylinder which is 1.22 m in diameter and 2.44 m long. The larger size permits the in-situ assembly of the more complex hardware required to make the effects measurements. The photograph of the SMEF in Figure 16 shows the overall configuration to be used to perform the hemispherical $\rho - \tau$ measurements. It consists of an integrating sphere system which includes a monochromator positioned outside and on top of the chamber with aspherical transfer optics to direct the light into the in-situ sphere.

The photograph in Figure 17 shows a closer view of the SMEF (with the loading door removed) with the receptor carousel rotated horizontally into the position where the deposition and UV irradiation occur. The 5 mounting locations for the 5 receptors on the carousel pinwheel are shown as well as the position of a QCM which is symmetrically positioned to have the same contamination depth as the receptors. Then the entire carousel, with the exception of the stepper motor which rotates the pinwheel, is cryogenically cooled and held at about -160°C.

The final photograph in Figure 18 shows the carousel rotated into position in front of the integrating sphere following either a deposition or a UV radiation event.

The receptor pinwheel on the front end of the carousel can be indexed about the center line of the carousel through 360 degrees to position all the receptors in front of the sphere. The temperature of the source holder (not shown) and the carousel is maintained by precision controllers from -160°C to 130°C. The shroud is always at cryogenic temperature. The sphere components are typically at -80°C. Fifteen thermocouples monitor temperatures throughout the SMEF.

The Hewlett-Packard 3050A data acquisition system which is coupled to both the Molekit and the SMEF automatically samples and records the photometric data. It has a capability to sample up to sixty

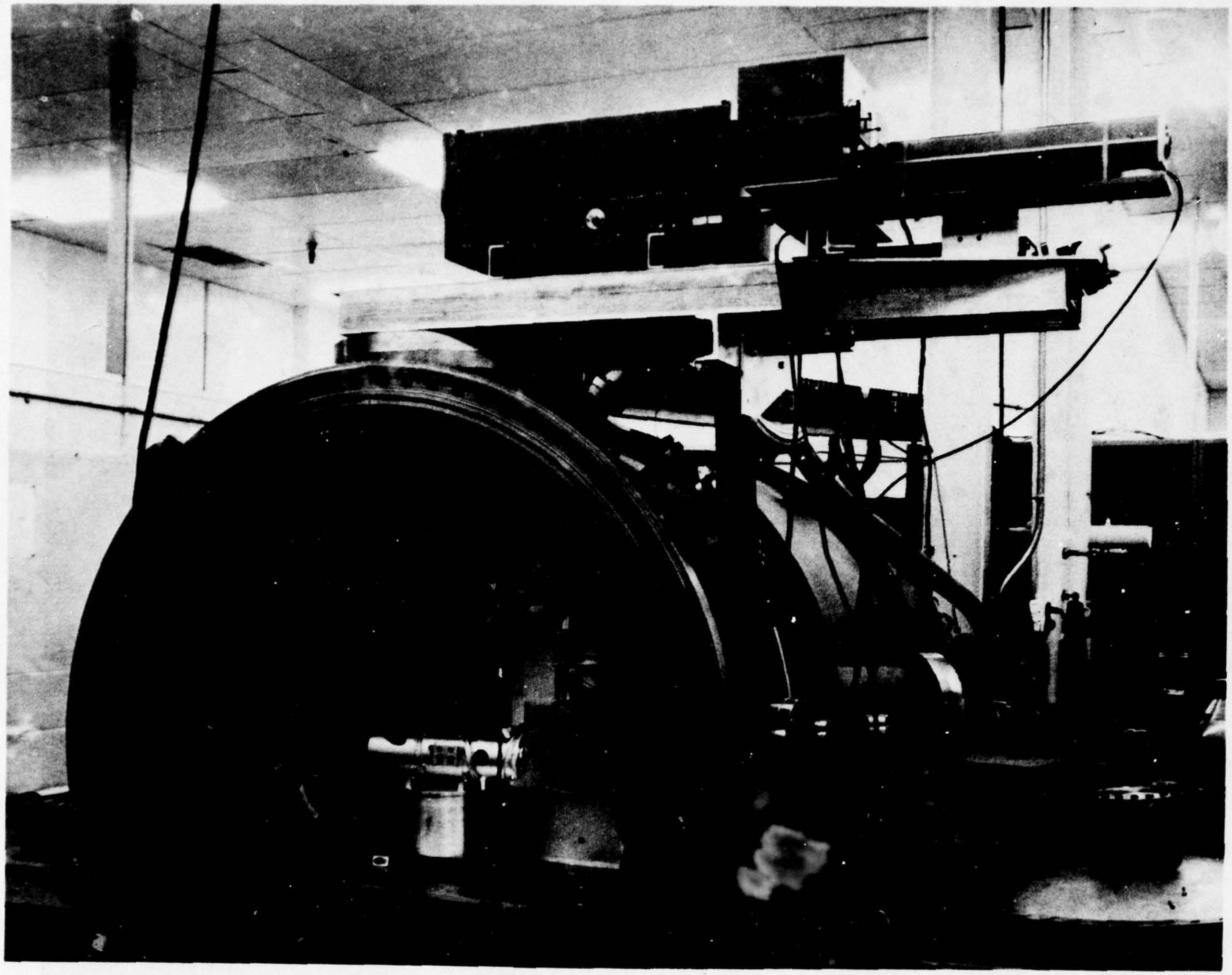

Figure 16. Surface Materials Effects Facility (SMEF) Configured for Spectral Reflectance/Transmittance Measurements

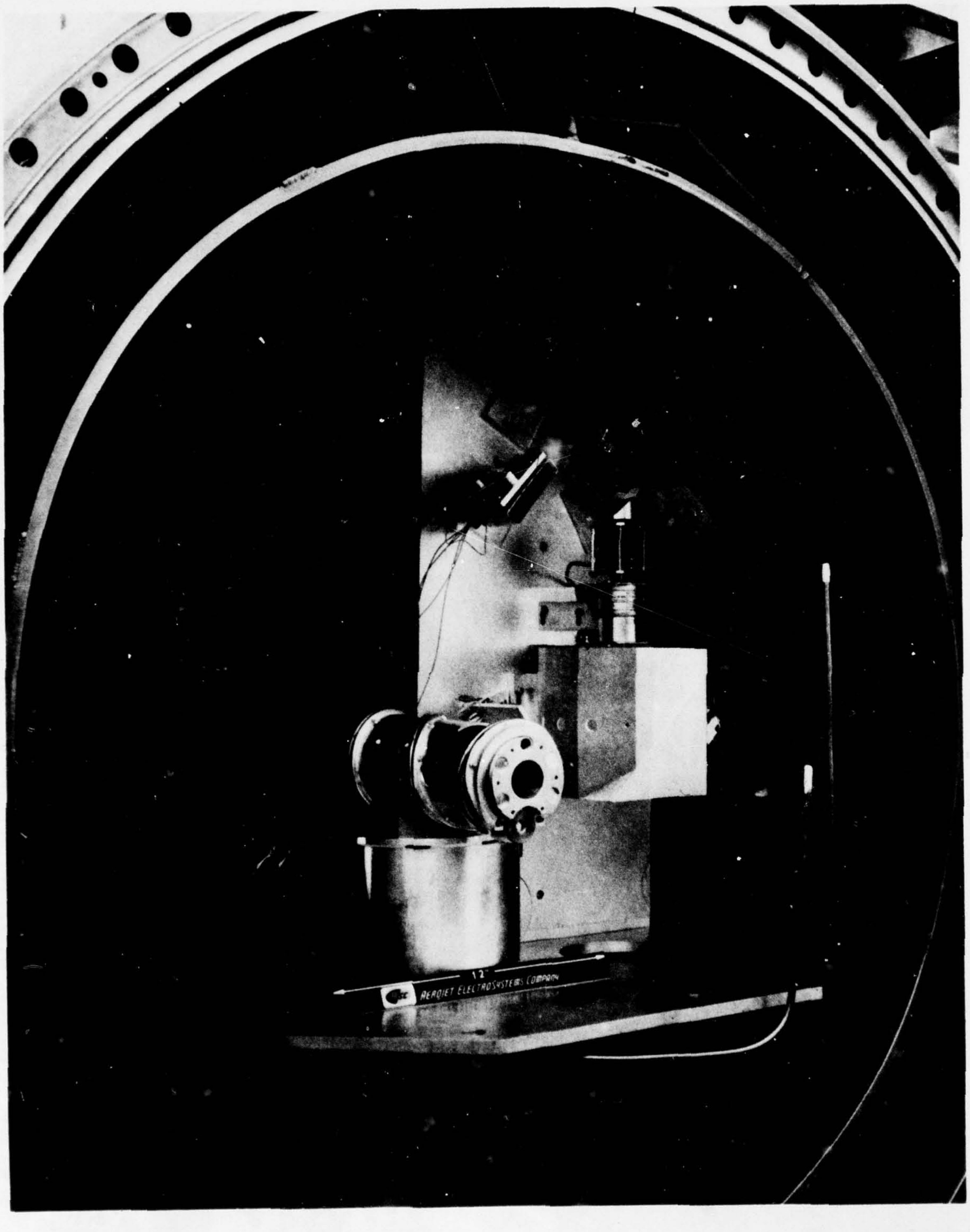

Figure 17. Sample Carousel Positioned for Deposition/Irradiation in SMEF

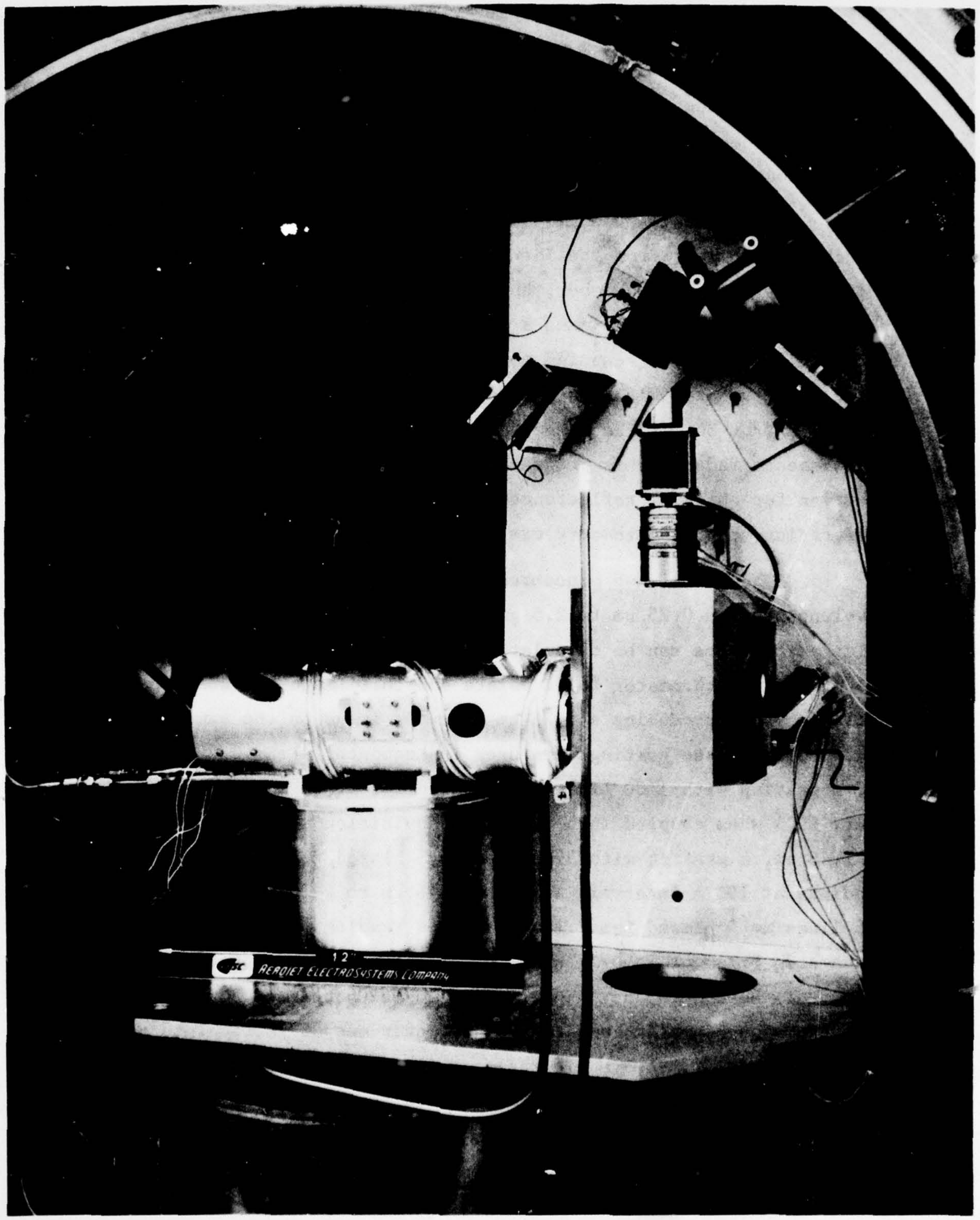

Figure 18. Sample Carousel Positioned for Effects Measurements in SMEF

channels of analog data with precision to 1 μV at a speed of about four channels per second. Data is stored on magnetic tape and can be simultaneously plotted and printed out as needed.

An optical schematic is shown in Figure 19 which traces the monochromatic light from the Jarral-Ash monochromator on top of the SMEF chamber into the chamber, through the integrating sphere and onto the desired receptor. To make a typical reflectance measurement, an oscillating rotatable scanning mirror is mounted in-situ on top of the integrating sphere which can provide a dual beam comparative photometric measurement of both reflectance and transmittance if desired. For the measurements made on this program, this mirror remained fixed in the position for spectral reflectance and the substitutional method of integrating sphere photometry was employed.

The Jarral-Ash monochromator can automatically scan the wavelengths from 0.25 μm to 2.5 μm at 500 Å min^{-1} so that values of the solar adsorptance can be calculated. Fixed circular slits 6 mm diameter are at the monochromator focal points and this image is put through the optical system producing a 1.25 cm diameter image on the sample part of the sphere. Three gratings are used in sequence. From 0.25 μm to 0.83 μm, a grating with 1180 $\text{lines}\cdot\text{mm}^{-1}$ blazed for 0.40 μm produces readings every 50 Å when coupled into the data acquisition system. From 0.83 μm to 1.46 μm, a grating with 590 $\text{lines}\cdot\text{mm}^{-1}$ blazed for 1.0 μm produces readings at 100 Å intervals and from 1.46 μm to 2.50 μm a grating with 295 $\text{lines}\cdot\text{mm}^{-1}$ blazed for 2.1 μm produces readings at 200 Å intervals. A tungsten filament lamp is used in conjunction with a photomultiplier tube (PMT) as a detector. The light beam is chopped at 200 Hz upon exit from the monochromator, and the PMT detector output is fed into a PAR lock-in amplifier. A dynamic range of five orders of magnitude is detectable. As with the Molekit, all data is automatically sampled and stored on tape.

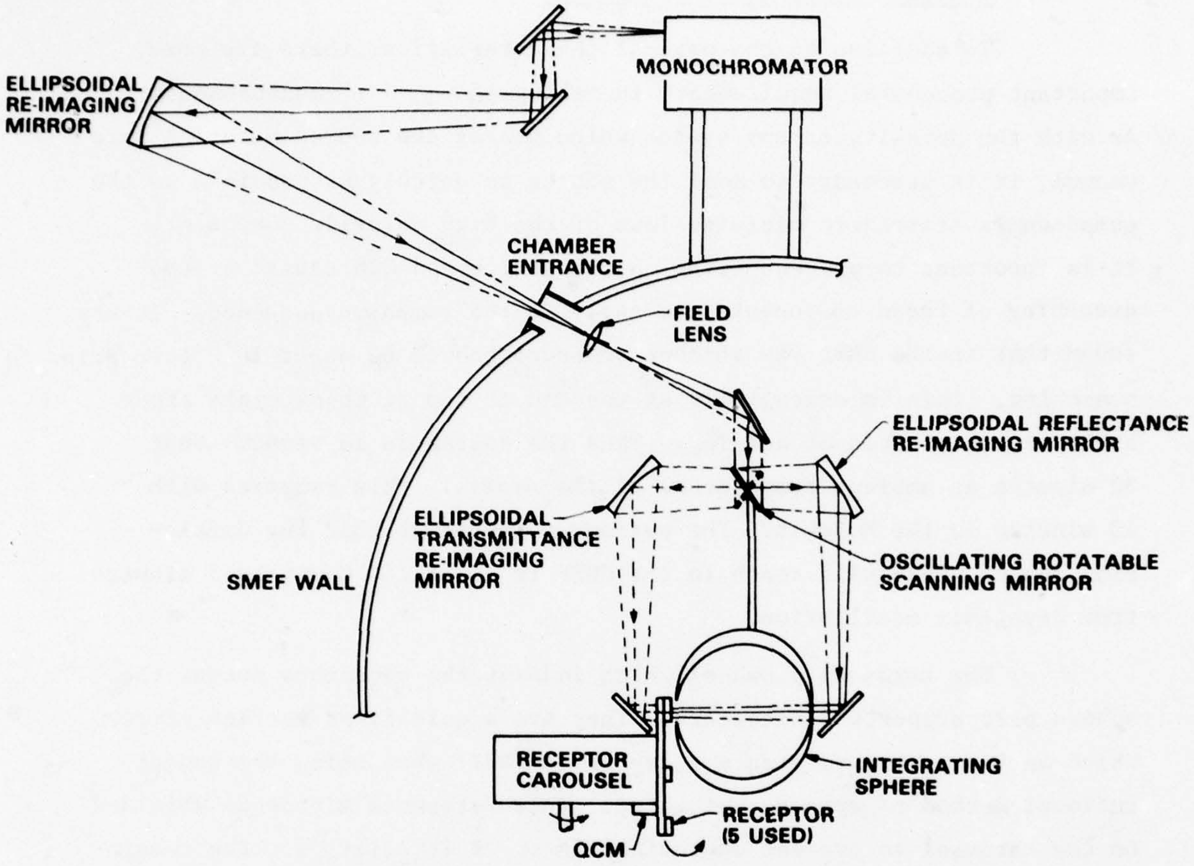

Figure 19. Optical Schematic of SMEF

3.2 Effects Measurements Procedures

In addition to the optical characteristics, there are some important procedural requirements in making the $\rho_\lambda - \tau_\lambda$ measurements. As with the Molekit, or any system which places the source material into vacuum, it is necessary to cool the source as quickly as possible as the pumpdown is started to minimize loss of the high volatile component. It is important to prevent icing on the source and QCM caused by LN_2 quenching of these components too early in the pumpdown sequence. It was found that in the SMEF the chamber pressure should be about 10^{-3} torr prior to quenching. This is essentially at the end of the roughing cycle after about thirty minutes of pumping. Thus the source is in vacuum about 30 minutes at ambient temperature at the start. This compares with 10 minutes in the Molekit. The maximum temperature that the double-ring source plate will reach in the SMEF is about 140°C within 5 minutes from cryogenic equilibrium.

The carousel pinwheel which indexes the receptors across the sphere part supports 5 receptors. They are a gold first surface mirror which serves as the reference receptor (Au/REF) when using the substitutional method of sphere photometry. This reference mirror is shielded on the carousel to prevent contamination or UV irradiation. The remaining four receptors receive the full contamination-irradiation procedure. These receptors are (1) a gold first surface mirror (Au/FSM), (2) a sample of aluminized Teflon with 0.002 inches of Teflon mounted as a second surface mirror (AgFEP), (3) a 0.010 fused silica wafer coated with 1000 Å of silver mounted as a second surface mirror (Ag/SSM), and (4) a sample of S13GLO white paint 0.003" thick. All receptors are circular discs 1/2" in diameter. A QCM is positioned in the 6th pinwheel position (but doesn't index) and thus measures the VCM mass that is deposited on the four sample receptors. During the test period of about one week, the entire carousel is cryogenically cooled with LN_2 and thus all the attached components are held at about -170°C.

An eight step procedure was used to evaluate the effects of UV irradiated contamination on the 4 sample receptors. First, the spectral reflectances of the Au/REF and the sample receptors were made ex-situ in a Carey 14 spectrophotometer. Second, reflectance measurements were made on each of the 5 receptors and of the baseline (no receptor at the sphere part) in the SMEF sphere system prior to evacuation and cooldown. This basically validates the basic performance of the SMEF sphere. Third, the SMEF chamber is evacuated and all internal components (carousel, source, shroud, sphere, optics, etc.) are quenched to LN_2 temperatures. Fourth, a reflectance measurement is again made on the clean, cool receptors. This measurement determines the optical path alignment distortion when the optical train is chilled to LN_2 temperatures. The optics are realigned as much as is possible for optimum measurements. Fifth, the carousel is positioned in front of the double-ring source, the source is quickly heated to about 135°C, and a deposition sequence takes place. About 1200 Å was deposited during these tests. Sixth, a measurement is then made of the contaminated but unirradiated receptors. The source is then quenched with LN_2. Seventh, the contaminated receptors are exposed to about 30 equivalent ultraviolet suns (30 EUVS) from a resonance electrodeless krypton lamp which emits radiation at 1236 Å for 36 hours. Eighth, a final reflectance measurement is made on the contaminated and irradiated receptors. This eight step procedure requires about one week with each measurement phase requiring about one working day. Most of the deposition and UV irradiation is performed overnight.

To calculate the spectral reflectance profile for a receptor using substitutional sphere photometry, the following equation is used

$$\rho_S(\lambda) = \left[\frac{I_S(\lambda) - I_B(\lambda)}{I_R(\lambda) - I_B(\lambda)}\right] \rho_R(\lambda) \qquad (26)$$

where

$\rho_S(\lambda)$ = hemispherical spectral reflectance of a sample receptor at λ

$\rho_R(\lambda)$ = hemispherical spectral reflectance of the reference receptor (Au/REF) at λ

$I_S(\lambda)$ = photomultiplier current of sphere detector when the sample is being illuminated, milliamps

$I_R(\lambda)$ = PMT current of sphere detector when the reflectance receptor is being illuminated, milliamps

$I_B(\lambda)$ = PMT current for the baseline measurement where no receptor covers the sphere port, milliamps

Thus, six scans through the wavelength range from 0.25 μm to 2.5 μm is required during each measurement phase. Each receptor is sampled at 250 wavelengths. A total of 1500 data points are stored on tape. To compute the profiles using equation (26), a computer is required. At present the software programs to completely perform these calculations and plot the reflectance profiles have just been completed and only "spot" checks of the data are available.

References

1. Nocilla, S. "The Surface Reemission Law in Free Molecule Flow" Rarefied Gas Dynamics, Supp. 2, Vol. 1, p. 327, Academic Press, 1963

2. Whipple, C. L. and Thorne, J. A. "Silicones in Outer Space" The Effects of Space Environment on Materials, Vol. II, p. 243, Proceedings of the 11th National Symposium and Exhibit of the Society of Aerospace Materials and Process Engineers (SAMPE), St. Louis, 1967

3. Buckley, P. H. and Johnson, R. L. "Evaporation Rates for Various Organic Liquid and Solid Lubricants in Vacuum to 10^{-8} mm Hg at 55°F to 1100°F", NASA TN D-2081, National Aeronautics and Space Administration, Washington, D.C., December 1963

4. "Investigation of Contamination Effects on Thermal Control Materials", AFML-TR-74-218, Final Technical Report, AFML/MBE, Wright-Patterson Air Force Base, Ohio, June 1974

5. Adamson, A. W. Physical Chemistry of Surfaces, Jim Wiley and Sons, 3rd Ed. 1976

6. Glassford, A. P. M. "An Analysis of the Accuracy of a Commercial Quartz Crystal Microbalance", Paper No. 76-438 presented at the 11th AIAA Thermophysics Conference, San Diego, Cal., July, 1976

7. Glasstone, S., Laidlor, K., and Eyring, H., The Theory of Rate Processes, McGraw-Hill Book Co., Inc., 1st Edition, 4th Impression, 1941

8. Born, M. and Wolf, E., Principles of Optics, 3rd Ed. (Rev.) Pereamon Press, N.Y., 1965

CONTAMINATION EFFECTS OF SOME SPACECRAFT MATERIALS AND ROCKET PLUME PRODUCTS

C. K. Liu and A.P.M. Glassford
Lockheed Palo Alto Research Laboratories

1. INTRODUCTION

Contamination can degrade the performance of spacecraft systems by two main mechanisms. One is the effect on thermal control surfaces and optical components due to deposition of condensed and particulate contaminants. The other is the signal scattering/attenuation and stray-light in the optical field of view caused by a debris cloud. Both effects are further compounded by the effect of space radiation on the contaminant.

Two major sources of spacecraft contamination are the material outgas products and rocket plume products. It is important to minimize or eliminate contamination effects from these sources at the design stage by careful selection of materials and system geometry. In order to perform such a design analysis in the case of critical surfaces, it is necessary to have data relating the amount of contaminant on a critical surface, to the magnitude of the change produced in the surface property. Generation of this type of data under completely realistic temperature, vacuum and space radiation conditions requires the use of complex and expensive simulation apparatus with relatively high associated costs and time per data point. The cost of solving specific contamination-related design problems could be minimized if a less costly experimental technique were used for preliminary screening tests. The results can then be used to determine whether the contamination problem was negligible, or significant enough to require more detailed measurements. This paper describes such low cost techniques and presents some of the data already obtained with them.

The primary concern of present study was to determine the relationship between the amount of outgas products from some candidate spacecraft materials condensed on typical spacecraft critical surfaces and the resulting change in their optical properties. The outgas sources used were RTV-560 silicon rubber, S-13 GLO white paint; Kapton tape, FEP Teflon-silver second surface mirror tape with SR-585 and P-223 adhesives and graphite-reinforced epoxy composite. The outgas source temperatures were 125°C and 177°C. The surface properties measured were the solar absorptance of aluminized quartz optical solar reflector (Al/OSR), flexible optical solar reflector made of FEP Teflon either silverized (Ag/FOSR) or aluminized (Al/FOSR), and the transmittance of fused silica solar cell cover glass. These surfaces were contaminated in vacuum at 25°C. The deposit surface densities ranged between 10^{-6} and 10^{-4} g/cm^2. The basic experimental method was to arrange the test surface and a quartz crystal microbalance (QCM) in a vacuum chamber, so that both were at 25°C, and both had the same view factor to the orifice of a Knudsen cell-type outgas source material holder. It was assumed that the contaminant mass per unit area collected on the QCM is the same as that on the collector surface. Measurements of solar absorptance and transmittance were made at 25°C and one atmosphere pressure using a Cary Model 14 spectrophotometer.

A secondary concern was to determine the relationship between the amount of rocket plume products deposited on thermal control surfaces and the resulting change in solar absorptance. The plume product of a methylhydrazine (MMH) thruster was synthesized and deposited on Al/OSR. The carbon particles which exist in a solid rocket motor (SRM) plume-induced deposit, were deposited on Al/FOSR, ALCLAD 7075-T6 Aluminum and S-13 GLO white paint sample surfaces. The amount of carbon deposited were found by weighing on a balance, while solar absorptance was again measured by a Cary Model 14 spectrophotometer.

2. EFFECT OF OUTGAS PRODUCTS DEPOSIT

A series of tests were conducted to determine the contamination threat posed by the outgas products of various spacecraft materials on selected thermal control surfaces and solar cell cover glasses. The outgas products were condensed on the sample surfaces and the resultant changes in solar absorptance and solar transmittance were measured.

2.1 Sample Materials

A total of six materials were selected as the outgas source for the present study. These are described below:

RTV-560 A methyl-phenyl room temperature vulcanizing (RTV) silicon rubber, manufactured by the General Electric Company, and used extensively in the Shuttle Orbiter's Thermal Protection System. The sample tested was prepared according to the manufacturer's instructions. Details of the preparation procedure are given in Ref. 1.

S-13 GLO This is a low-outgassing zinc oxide-silicate white thermal control paint for spacecraft hardware applications. It was supplied by the IIT Research Institute and mixed in accordance with the IITRI/NASA/MSFC specification No. 10M0183.

Kapton Tape Katpon/silicon adhesive tape, one inch wide, manufactured by TFE Industries, Warwick, Rhode Island. Kapton is the trade name of a Du Pont polyimide film Type H. The outgas source is mainly the silicone adhesive.

SR-585 Tape A 5-mil, one inch wide tape of FEP-Teflon/silver/Inconel flexible optical solar reflector (FOSR) with SR-585 adhesive for bonding to the spacecraft surface. The tape is manufactured by Sheldahl Company, Northfield, Minnesota, while the SR-585 silicone adhesive is from the General Electric Company.

P-223 Tape A 5 mil,four inch wide FOSR tape of FEP-Teflon/silver/Inconel with P-223 adhesive. The FOSR tape is manufactured by Sheldahl Company, Minnesota, while the P-223 adhesive is from Permacel Company, New Brunswick, New Jersey.

---

1. Liu, C. K. and Glassford, A.P.M.,Kinetics Data for Diffusion of Outgas Species from RTV 560, NASA CP-2007, Ninth Conference on Space Simulation, Los Angeles (1977).

Graphite Epoxy A fiber composite used as spacecraft structural material with the epoxy resin manufactured by the Fiberite Corp. of Winona, Minnesota. The sample material for current tests was supplied in the form of 0.059-inch thick laminate and 0.038-inch thick disks of 0.5-inch diameter.

2.2 Outgas Product Deposit Test

2.2.1 Test Apparatus

The contamination tests were conducted in the apparatus as shown in Figure 1. The principal components are the test surface holder (collector); the QCM that records the mass deposition rate during the test; the sample pot that houses the outgas source material; and a system of shrouds. All of these are thermally grounded to a liquid nitrogen reservoir. The QCM is a Celesco Model 700 unit, the accuracy of which has been established in a previous study.(2) The sample pot is a cylindrical container with a small orifice on the top. The test surface holder, QCM and the sample pot are all equipped with electrical resistance heater and thermocouples. By balancing the respective heat inputs against the heat leaks along the support struts to the cooled shielding structure, the temperature of the test surface and the QCM can be maintained at 25°C, while that of the sample pot can also be controlled at the prescribed temperatures of 125°C or 177°C. The QCM and the collector are arranged to have the same view factor of the sample pot orifice. The distance from the sample pot orifice to the QCM surface is 7.68 cms. The QCM and Collector are displaced 16° on either side of the normal line of sight of the sample pot orifice, viewing it through a hole with movable shutters. These shutters are controlled separately, permitting the impinging flux to the QCM and the collector to be interrupted when appropriate. The basic assumption in this experimental technique is that the contaminant mass per unit area condensed on the collector is the same as that

2. Glassford, A.P.M., Analysis of the Accuracy of a Commercial Quartz Crystal Microbalance, Progress in Astronautics and Aeronautics, 56 (1977).

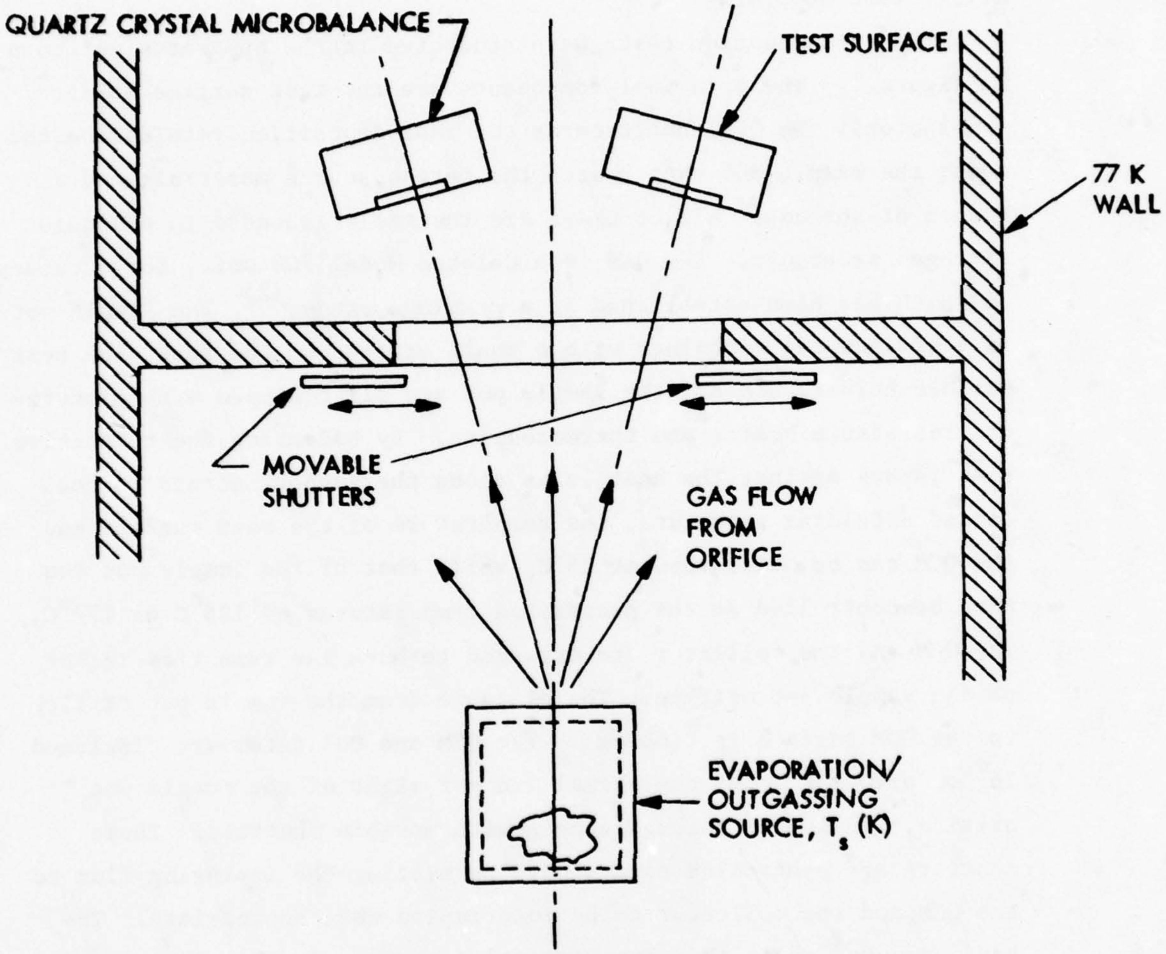

FIGURE 1 - SCHEMATIC OF OUTGAS CONTAMINATION STUDY APPARATUS

measured by the QCM when both are maintained at 25°C and the shutters are opened and closed simultaneously. The collector, QCM, and the sample pot are completely surrounded by the cooled shrouding to reduce the background outgassing rate to undetectably low levels.

The surface property was measured in a Cary Model 14 spectrophotometer, which measures the diffuse spectral reflectance and transmittance in the range of 0.27 to 1.8μm. It contains an integrating sphere and a recorder for providing the data in a permanent trace. The samples are measured in air at room temperature, with a maximum uncertainty of ± 0.02 reflectance unit. The solar reflectance can be calculated by integrating the spectral reflectance with respect to the solar spectral irradiance. The solar absorptance can then be calculated by subtracting the solar reflectance from unity. The solar transmittance is calculated the same way when the apparatus is run in the transmittance mode.

2.2.2 Test Procedure and Data Reduction

The general procedure used in the deposit test was as follows:

(1) Before each test, the surface to be contaminated was cleaned and its surface property (solar absorptance for thermal control surfaces and solar transmittance for solar cell cover glasses) was measured by the Cary Model 14 spectrophotometer. The clean test surface was then installed in the collector holder.

(2) A quantity of sample material was weighed and installed in the sample pot. The amount of sample used was not a critical test parameter, but had to be sufficient to provide a measurable deposit on the QCM and collector. The apparatus was assembled, the bell jar was replaced and the system evacuated. The liquid nitrogen container was filled when the pressure reached 10^{-4} torr, lowering the pressure to the final value of 2×10^{-7} torr or lower.

(3) During evacuation the sample pot was heated to its prescribed temperature, while the heat inputs to the QCM and collector were adjusted to maintain their temperatures at 25°C as the rest of

the apparatus cooled down. Steady state measurements with equilibrated QCM, collector, pot sample could be obtained within about one hour after evacuation of the system. The shutters were opened to allow the outgas flux to impinge on the 25°C QCM and collector surfaces. The deposition rate was measured by the QCM reading, which was recorded as a function of time.

(4) When the QCM had accumulated a substantial deposit, the shutters were closed and all heat inputs were removed. Inert gas was led into the system to bring the pressure up to one atmosphere.

(5) When the system reached thermal equilibrium with laboratory air, the test surface with the contaminant deposit was removed. Its surface property was measured again and compared to that before the test. The amount of deposit was given from the deposit mass per unit area on the QCM crystal. This is equal to the frequency shift from the clean condition multiplied by the QCM sensitivity constant, 4.43×10^{-9} g/cm^2/Hz. The source sample and holder were also removed and reweighted.

2.3 Results of Outgas Product Deposit Test

The effect of outgas products deposit from five spacecraft materials on the solar absorptance of optical solar reflectors (OSR) and FEP-Teflon flexible optical solar reflectors (FOSR), either aluminized or silverized on the back surface, is shown in Figures 2 and 3. A test summary is given in Table 1.

It is seen from Figure 2 that the effect of RTV-560 products is more pronounced on Al/OSR than on Ag/FOSR. However, the percentage change in solar absorptance, which is more useful to contamination control engineers, is of the same order of magnitude as shown in Figure 3. This seems to agree with the trend of reported flight data from Skylab D024 experiment.(3) One set of thermal control

3. Lehn, W. L. and Hurley, C. J., Skylab D024 Thermal Control Coatings and Polymeric Films Experiment, AIAA/AGU Conference on Scientific Experiments of Skylab, Huntsville, Ala (1974).

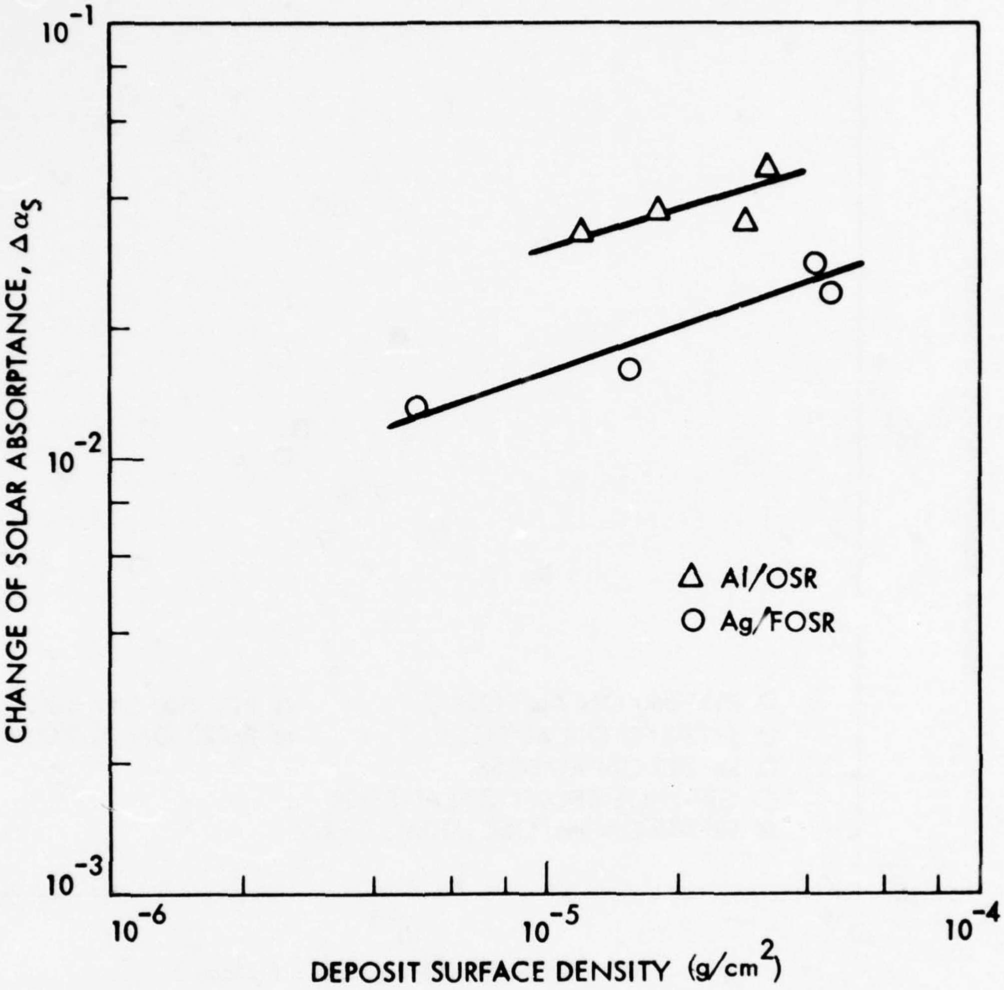

FIGURE 2 - CHANGE OF SOLAR ABSORPTANCE BY RTV-560 OUTGAS PRODUCTS

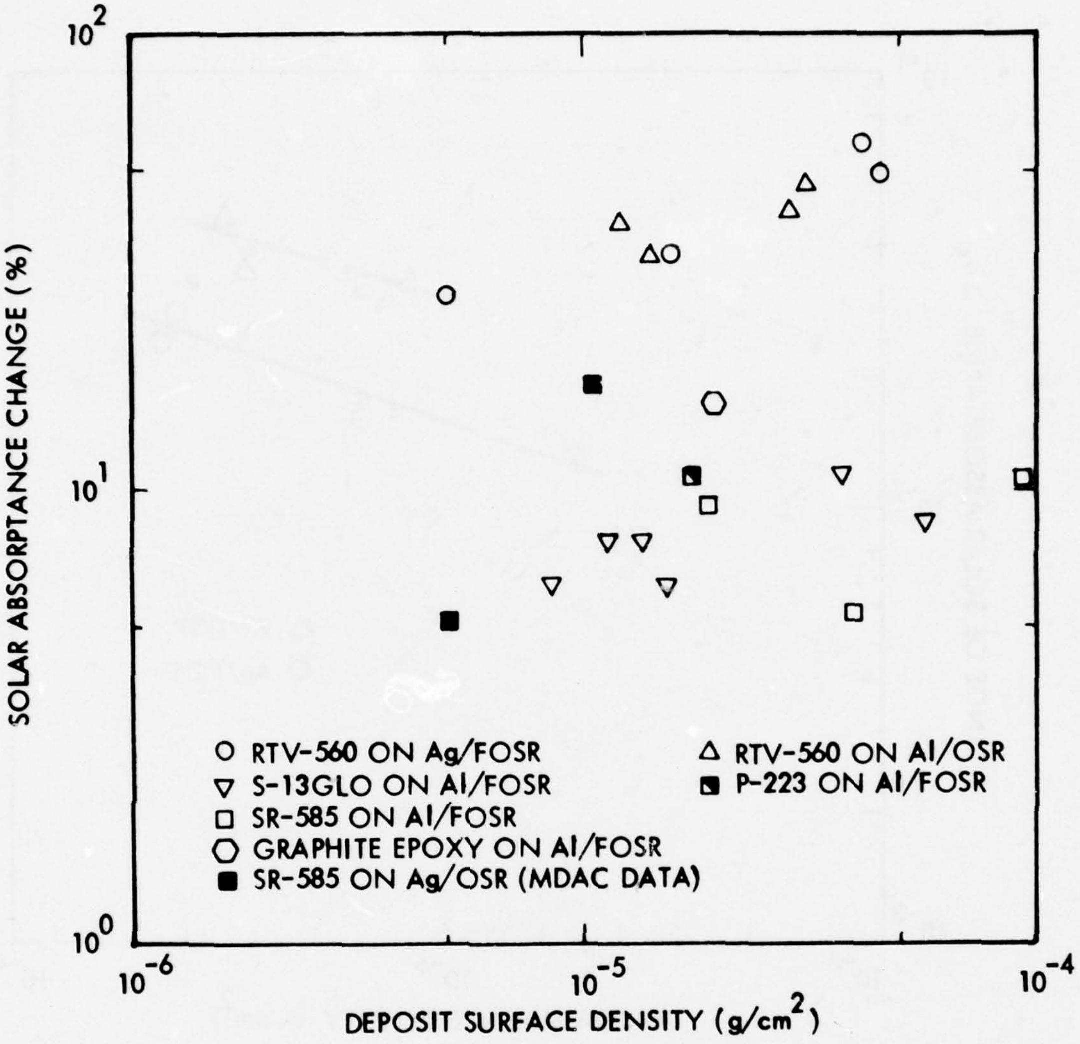

FIGURE 3 - SOLAR ABSORPTANCE CHANGE OF CONTAMINATED THERMAL CONTROL SURFACES

TABLE 1. CONTAMINATION EFFECT OF OUTGAS PRODUCTS DEPOSIT - CHANGE OF SOLAR ABSORPTANCE, $\Delta\alpha_s$, OF THERMAL CONTROL SURFACES

Source (T_s,C)	Collector (25^oC)	Deposit 10^{-5} g/cm^2	Initial α_s	$\Delta\alpha_s$
RTV-560 (125)	Ag/FOSR	.5 - 4.6	.061-.076	.013-.028
RTV-560 (125)	Al/OSR	1.2 - 3.2	.085-.113	.033-.046
S-13 GLO (177,125)	Al/FOSR	.53 - 7.8	.13	0 - .014
SR-585 (177,125)	Al/FOSR	1.9 - 9.4	.129	.007-.014
P-223 (177,125)	Al/FOSR	1.73-8.5	.129	.003-.014
Graphite Epoxy (177,125)	Al/FOSR	.06 - 2.0	.129	.009-.021
SR-585[(4)] (140)	Ag/OSR (-100^oC)	.51 - 1.0	.058	.003-.01

coating specimens, SL-4, experienced no exposure to Service Module Reaction Control System (SMRCS) Plume Products and exhibited twice as much change of solar absorptance in Al/FOSR as in Al/OSR. However, the percentage change in solar absorptance is identical (+8.23%) in both specimens. It should be noted that the degradation of the SL-4 specimens in Ref. 3 is due to a combination of outgas product deposit plus solar irradiation. No ultraviolet radiation was used in

4. Hughes, T.A., Bonham, T.E. and Allen, T.H., Investigation of Contamination Effects on Thermal Control Materials. AFML-TR-76-5 (1976).

current test.

The percentage change in solar absorptance in Al/FOSR due to the four other spacecraft materials is much lower with the exception of Graphite Epoxy. In this last case the outgas product deposit from the 125°C onto the 25°C collector was insignificant. The equivalent thickness of the deposit (based on an assumed effective density of 1.1 g/cm^3) was only 55 Å after a three-hour period. The larger value of degradation came from the source sample maintained at 177°C. This is to be expected since the outgas rate should increase significantly as the source sample temperature increases from 125°C to 177°C, resulting in a corresponding increase in the amount of deposit on the 25°C QCM.

Also included in Table 2 and Figure 3 are the measured solar absorptance data of Ag/OSR due to outgas products deposit of SR-585 from Reference 4. In this work, the results of Test Runs 1, 2 and 3 showed increase, decrease and no change of solar absorptance, respectively, for equal amount of the same contaminant on the same kind of substrate. Only the data from Run 1 are included here for comparison purpose. Although the collector temperature was much lower, the percentage changes of solar absorptance agree with the general trend of data from current tests.

The effect of outgas products deposits from five spacecraft materials on the solar transmittance of solar cell cover glass is shown in Figure 4. A test summary is given in Table 2. With the exception of graphite epoxy, the changes are insignificant for amounts of deposit up to 1.36×10^{-4} g/cm^2 (equivalent thickness of 1.3μm based on density of 1.1). In the case of graphite epoxy, the solar transmittance of the solar cell cover glass decreased from 0.93

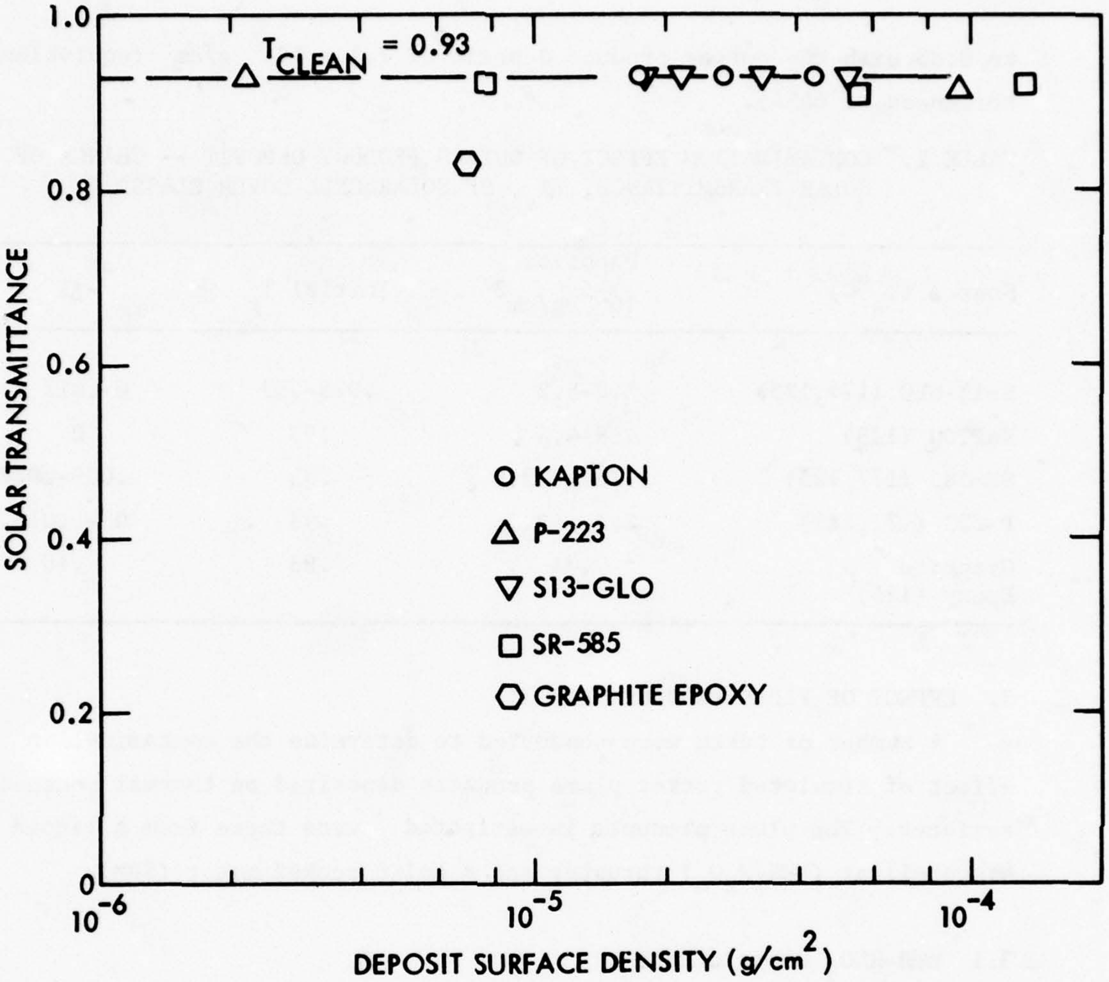

FIGURE 4 - SOLAR TRANSMITTANCE CHANGE OF CONTAMINATED SOLAR CELL COVER GLASS

to 0.83 with the outgas product deposit of 7.1 x 10^{-6} g/cm^2 (equivalent thickness of 645Å).

TABLE 2. CONTAMINATION EFFECT OF OUTGAS PRODUCT DEPOSIT -- CHANGE OF SOLAR TRANSMITTANCE, ΔT_s, OF SOLAR CELL COVER GLASS

Source (T_s °C)	Deposit, 10^{-5} g/cm^2	Initial T_s	$-\Delta T_s$
S-13-GLO (177,125)	1.8-5.2	.928-.93	0-.012
KAPTON (125)	1.8-4.4	.93	0
SR-585 (177,125)	.78 - 13.6	.93	.009-.022
P-223 (177,125)	2.2 - 9.5	.93	0 - .015
Graphite Epoxy (125)	.71	.93	.10

3. EFFECT OF PLUME PRODUCT DEPOSIT

A number of tests were conducted to determine the contamination effect of simulated rocket plume products deposited on thermal control surfaces. The plume products investigated were those from a liquid bipropellant (MMH/N_2O_4) thruster and a solid rocket motor (SRM).

3.1 MMH-HNO_3 Deposit Test

3.1.1 Background

It has been found$^{(5)}$ that the predominant species in the residue resulting from the combustion of MMH and N_2O_4 is monomethylhydrazine nitrate (MMH-HNO_3). At orbital altitude, it is also the most detrimental condensible as other species in the plume product or unburned

---

5. Etheridge, F. G. and Boudreaux, R. A., Attitude-Control Rocket Exhaust Plume Effect on Spacecraft Functional Surfaces, J. Spacecraft, 7 (No. 1): 44-48 (1970).

propellant droplets have vapor pressures too high to be of concern except in the near-plume field.(6) Previous investigations conducted at NASA/Lewis Research Center did not give the amount of MMH-HNO$_3$ on test samples. Hence, a series of tests were carried out to deposit MMH-HNO$_3$ to thermal control sample surfaces. The surface property was measured before and after the test with various amounts of MMH-HNO$_3$ deposit. The results can be used to update the plume contamination analysis in the prediction of critical stand-off distances.

3.1.2 Test Summary

The MMH-HNO$_3$ can be synthesized by the treatment of MMH with equimolar solution of dilute nitric acid and the removal of water under reduced pressure.(7) Due to the hypergolic nature of MMH, the mixing of MMH and HNO$_3$ was done at low temperatures (below 12°C). By use of a micro-pipette, the neutral solution was deposited with various calibrated amounts onto Al/OSR; front surface Aluminum and S-13G white paint sample surfaces. These surfaces were then placed in a vacuum dessicator as the MMH-HNO$_3$ salt is extremely hygroscopic. The removal of water under reduced pressure was not wholly successful and the deposits remained in liquid droplets form on the Al and S-13G surfaces. However, white crystal salt was observed on the Al/OSR surfaces and the change in solar absorptance was measured by a Cary Model 14 spectrophotometer in an inert gas environment.

3.1.3 Results of MMH-HNO$_3$ Deposit Test

The changes in solar absorptance due to MMH-HNO$_3$ deposit on the Al/OSR are given in Figure 5 and a test summary is given in Table 3.

---

6. Fong, M.C. and Liu, C.K., Contamination Control of Long Life Shuttle Payloads, Lockheed 1976 Independent Development Program Summary Report, LMSC-D569577 (1976).
7. Takimoto, H. H. and Denault, G. C., Rocket Plume (N$_2$O$_4$/MMH) Impingement on Alumin Surface, J. Spacecraft, 7 No.11):1372-1374 (1970)

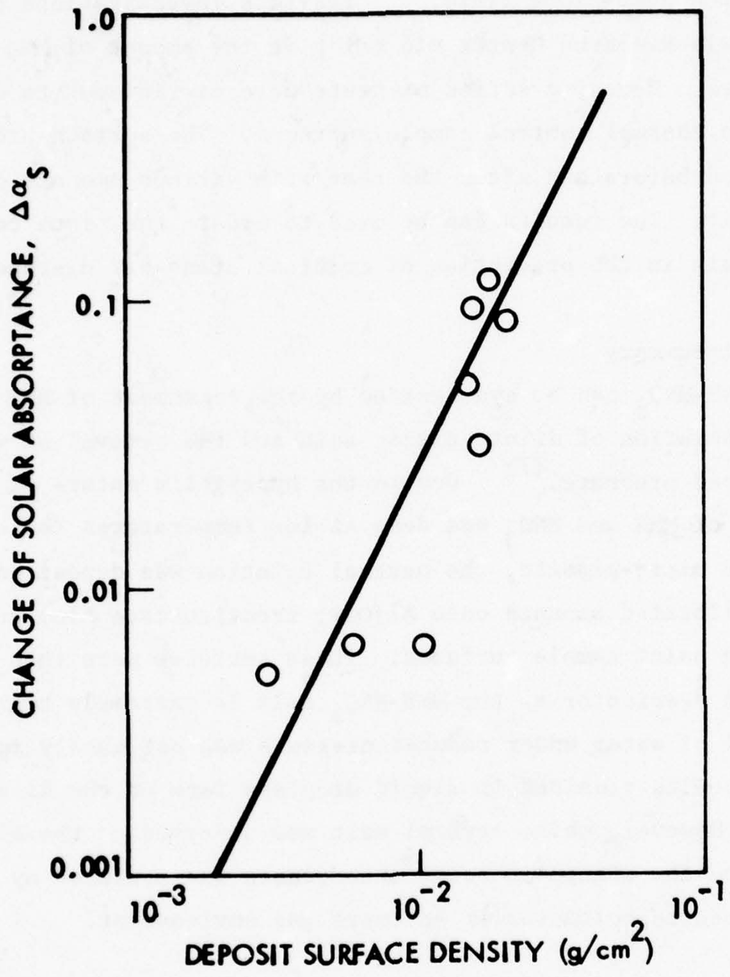

FIGURE 5 - CHANGE OF SOLAR ABSORPTANCE OF Al/OSR SURFACE DUE TO MMH-HNO_3 DEPOSIT

TABLE 3. CONTAMINATION EFFECT OF PLUME PRODUCT DEPOSIT - CHANGE OF SOLAR ABSORPTANCE, $\Delta\alpha_s$, OF THERMAL CONTROL SURFACES

SOURCE	COLLECTOR	DEPOSIT g/cm^2	INITIAL α_s	$\Delta \alpha_s$
MMH-HNO$_3$	Al/OSR	3×10^{-3} to 2.03×10^{-2}	.098-.11	.005-.117
CARBON PARTICLES (SIZE A)	Al/FOSR	6.7×10^{-6} to 1.26×10^{-4}	0.137	.421-.813
CARBON PARTICLES (SIZE A)	ALCLAD 7075-T6 Aluminum	2.4×10^{-6} to 2.9×10^{-5}	0.191	.212-.666
CARBON PARTICLES (SIZE A)	S-13 GLO	5×10^{-6} to 3.8×10^{-5}	0.24	.252-.654
CARBON PARTICLES (SIZE B)	S-13 GLO	1×10^{-5} 1.1×10^{-4}	0.249	.346-.648

Size A = 0.16 - 0.08μm

Size B = .012μm average

It is seen that for a deposit surface density of 3 to 20 mg/cm^2, the change of solar absorptance ranges from .005 to .117, equivalent to increases of 4.8 to 116 percent. This covers a larger range of plume deposit degradation than the reported increase in solar absorptance of S-13G due to various pulse duration and duration of a MMH/N_2O_4 thruster.(8) The results can be used to construct curves showing critical separation distance versus exposure time in terms of

---

8. Sommers, R.D. and Racquet, C.A., Effect of Thruster Pulse Length on Thruster-Exhaust Damage of S13G White Thermal Control Coatings, NASA-TMX-68213, 7th JANNAF Plume Technology Conference, Redstone Arsenal, Ala (1973).

representative values of $\Delta\alpha_s$ values.(6) These curves represent contamination constraints. When used in conjunction with the other applicable dynamic constraints, a separation distance envelop can be established for the design purpose.

3.2 Carbon Deposit Test

3.2.1 Background

During several ascent events, the SRM boosters, staging rockets and retro rockets create a plume-induced gaseous and particulate environment. The resulting contaminant deposit may cause degradation of thermal control surfaces. Recent review of limited flight data(9) revealed that the plume-induced deposit was of sub-micron size carbon-type substance rather than Al_2O_3, the major species in aluminized propellant plume. Hence, a test program was initiated to obtain solar absorptance change data as a function of carbon deposit for some candidate thermal control sample surfaces.

3.2.2 Test Summary

The sample surfaces to be contaminated were Al/FOSR, ALCLAD 7075-T6 Aluminum sheet and S-13 GLO white paint. The carbon particle sizes used were in the range of 0.08 to 0.16 microns, which is in the range to be expected from the SRM exhaust plumes. In addition, in order to assess the size effect, carbon particles with average size of 0.012 microns were deposited on a number of S-13 GLO white paint sample surfaces. The amount of deposit was determined by weighing the test sample before and after the contamination test. The change of solar absorptance was determined by comparing the solar absorptance of the contaminated surfaces to that of the clean test surface.

Carbon particles in the range of 0.08 to 0.16 microns were ob-

9. Hetrick, M. A. and Romine, G. L., Payload Contamination Environment for TILLC Launch Vehicles Using Launch Complex 40, Martin-Marietta Corp. Report MCR-75-118 (1975).

tained from the combustion products of diallylphthalate electrical insulation material. To verify that these products were indeed submicron carbon particles with negligible amounts of other materials, several analyses were made. No organic matter was found from the deposit in an IR absorption test. Other than carbon, only traces of potassium, chlorine, calcium and vanadium (less than 1% combined) were found by use of an electron microprobe. The sizes of the carbon particles in the deposit were determined from Scanning Electron Microscope pictures. The source of fine size carbon particles was the Carbon Black Carboloc 2 SRS-511 manufactured by Cabot. The average size of the particles is given as 12 millimicrons by the manufacturer.

For deposition of carbon particles with sizes of .08-.16 microns, the diallylphthalate material was placed on a wire screen supported in air and was ignited to produce a heavy smoke. A length of metal tube was then placed on the screen to generate a uniform plume. The test sample placed in a holder was then placed over the smoke with the test surface facing directly over the plume. The samples were held over the plume for various lengths of time to obtain a range of deposits. For deposit of fine carbon particles, the Carbon Black was dissolved in methyl alcohol and deposited on the test samples by use of a spray gun for various lengths of time. The test samples with the carbon deposit were then placed in the oven where the methyl alcohol was evaporated in a very short period of time, leaving a uniformly distributed carbon deposit on the test sample surfaces.

The test surfaces used in the carbon deposit test are: (a) Al/FOSR adhesively bonded onto metal circular discs of 1-in. diameter; (b) ALCLAD 7075-T6 Aluminum sheet of .032-in. diameter; and (c) S-13 GLO white paint mixed in accordance with the IITRI/NASA/MSFC specification No. 10M0183, poured and cured at room temperature on 7075-T6 Aluminum sheets of 0.063-in thickness. For the contamination test, the samples were cut into rectangular pieces of 1.1 by 1.3 in.

Before and after each contamination test the weight and solar absorptance of each sample were measured. Samples were weighed with an Ainsworth Type FHM Balance with sensitivity of one microgram (10^{-6} g). The uncertainty in the set of mass standards used for the current test is in the range of $\pm 4\text{x}10^{-6}$ g. The uncertainty during repeated weighing of a given sample was found to be less than $6\text{x}10^{-6}$ g. Solar absorptance was measured with the Cary 14 spectrophotometer as described in Section 2.2.1.

3.2.3 Results of Carbon Deposit Test

After weighing again by use of the Ainsworth Balance, the solar absorptance of the test surfaces with the carbon deposit, along with a clean test surface were measured by a Cary Model 14 spectrophotometer. The results are given in Table 3 and Figures 6 and 7. The carbon deposition was relatively high ($2.4\text{x}10^{-6}$ to $1.25\text{x}10^{-4}$ g/cm^2) and the change in solar absorptance was significant. In Figure 6, the increase in solar absorptance is seen to increase uniformly with the carbon deposit and is independent of the substrate. In Figure 7, as the carbon particles deposit increases, the increase in solar absorptance seems to be lower where the deposit particle size is much smaller. However, S-13 GLO is a highly diffuse surface, and the effect will be more meaningful if a specular surface, like ALCLAD Aluminum can be used in any future tests to determine the effect of contaminant particle size.

4. CONCLUSION

By use of relatively simple and inexpensive test equipment and instrumentation, a series of tests have been conducted and the contamination effect of some spacecraft materials and rocket plume products on selected thermal control surfaces and solar cell cover glasses have been determined. Although the apparatus and experiment-

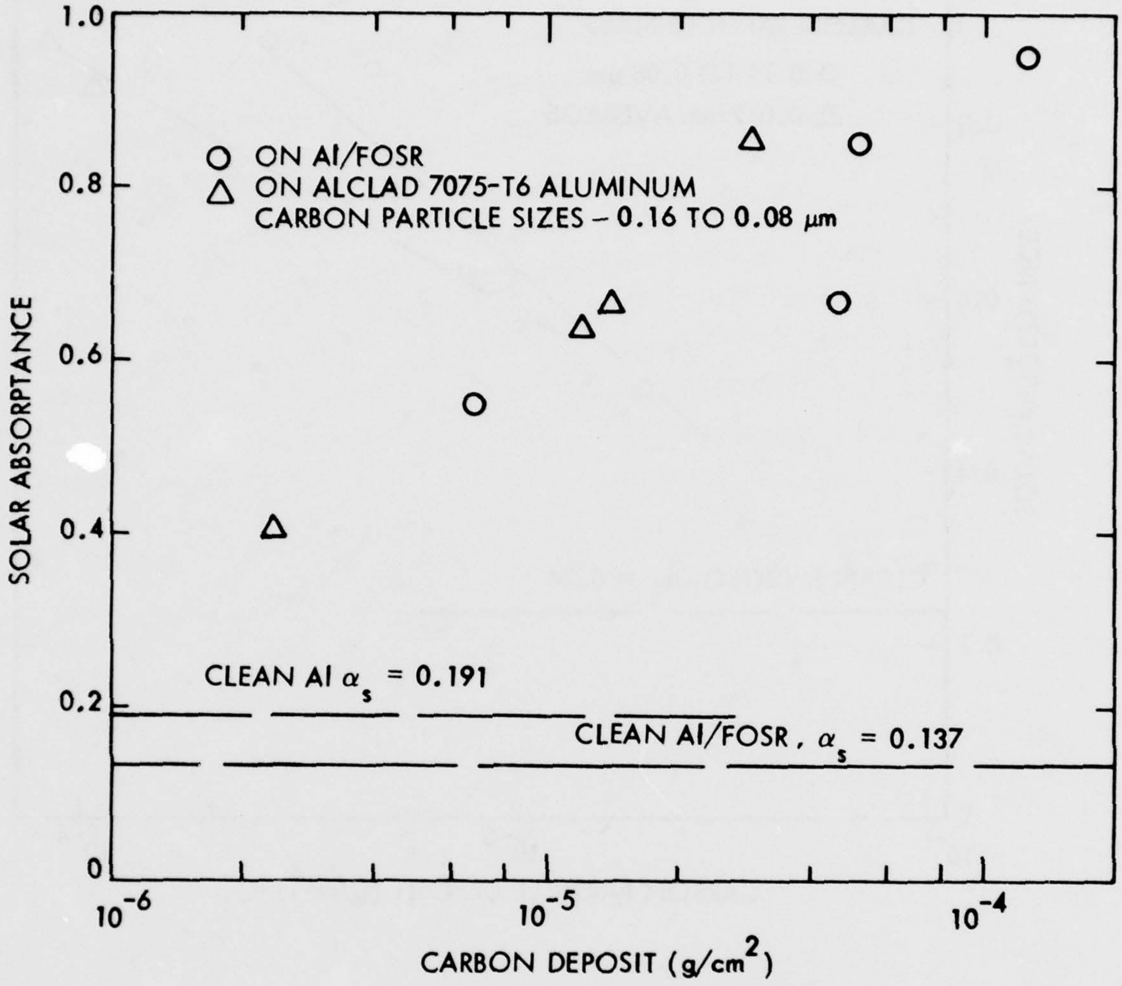

FIGURE 6 - CHANGE OF SOLAR ABSORPTANCE BY CARBON PARTICLE DEPOSIT

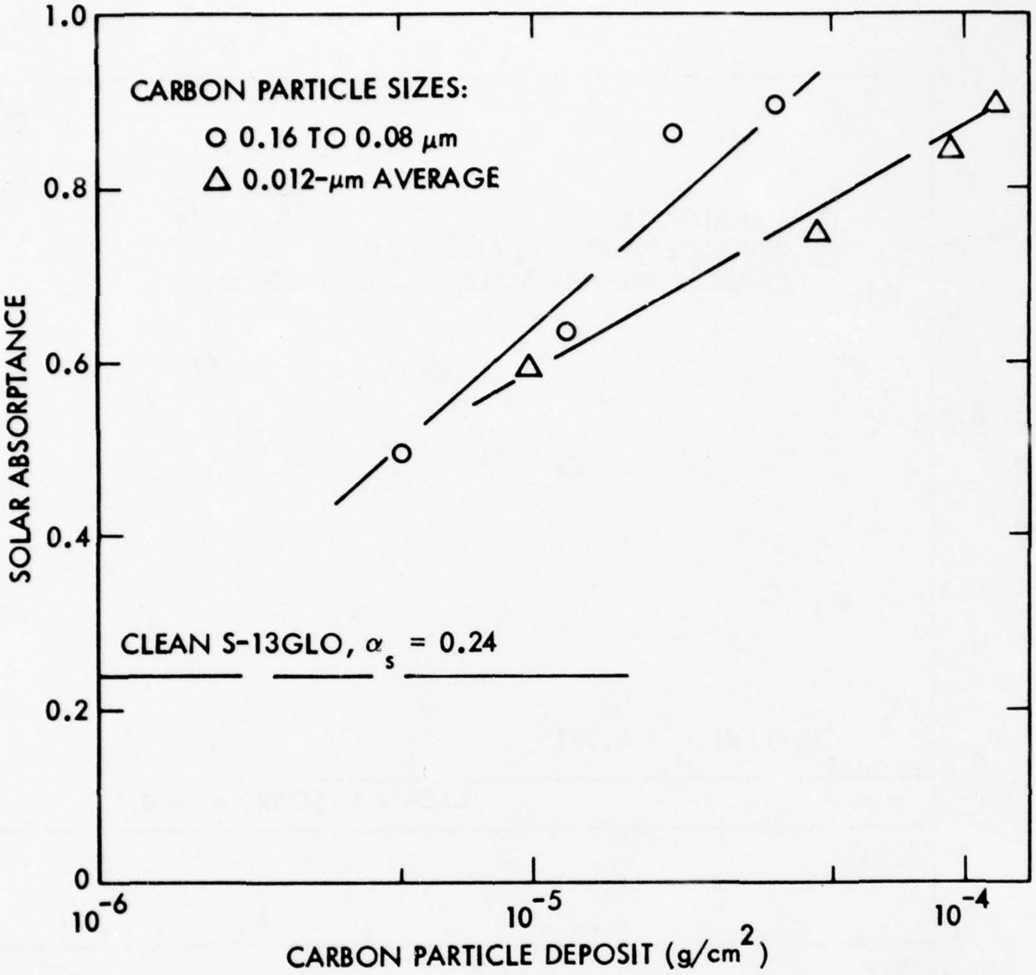

FIGURE 7 - EFFECT OF PARTICLE SIZES ON CHANGE OF SOLAR ABSORPTANCE

al techniques used were very simple and the degree of simulation less than perfect, the data obtained show trends and characteristics clearly enough to permit significant practical conclusions to be drawn and decisions made. In particular, the data clearly show that the contamination degradation due to RTV-560 outgas products to be higher than from all other contaminants. This type of low cost data have been used on several Lockheed programs as a basis for screening and for making preliminary design decisions. The simplified techniques described are thus expected to provide a useful complement to comprehensive in-situ environmental exposure and contamination effects measurement facilities.

Acknowledgement

This work was performed by Lockheed Palo Alto Research Laboratory in support of LMSC Space System Division, U. S. Air Force and NASA Program Offices, and as part of a Lockheed Independent Reseach Program.

REFERENCES

1. Liu, C.K. and Glassford, A.P.M., Kinetics Data for Diffusion of Outgas Species from RTV 560, NASA CP-2007, Ninth Conference on Space Simulation, Los Angeles (1977).
2. Glassford, A.P.M., Analysis of the Accuracy of a Commercial Quartz Crystal Microbalance, Progress in Astronautics and Aeronautics, 56 (1977).
3. Lehn, W. L. and Hurley, C. J., Skylab D024 Thermal Control Coatings and Polymeric Films Experiment, AIAA/AGU Conference on Scientific Experiments of Skylab, Huntsville, Ala (1974).
4. Hughes, T. A., Bonham, T.E. and Allen, T.H., Investigation of Contamination Effects on Thermal Control Materials. AFML-TR-76-5 (1976).
5. Etheridge, F. G. and Boudreaux, R. A., Attitude-Control Rocket Exhaust Plume Effect on Spacecraft Functional Surfaces, J. Spacecraft, 7 (No. 1): 44-48 (1970).
6. Fong, M. C. and Liu, C. K., Contamination Control of Long Life Shuttle Payloads, Lockheed 1976 Independent Development Program Summary Report, LMSC-D569577 (1976).
7. Takimoto, H. H. and Denault, G.C., Rocket Plume (N_2O_4/MMH) Impingement on Aluminum Surface, J. Spacecraft, 7 (No. 11): 1372-1374 (1970).
8. Sommers, R.D. and Racquet, C.A. Effect of Thruster Pulse Length on Thruster-Exhaust Damage of S13G White Thermal Control Coatings, NASA-TMX-68213, 7th JANNAF Plume Technology Conference, Redstone Arsenal, Ala (1973).
9. Hetrick, M. A. and Romine, G. L., Payload Contamination Environment for TIIIC Launch Vehicles Using Launch Complex 40, Martin-Marietta Corp. Report MCR-75-118 (1975).

The Influence of the UV-Intensity on I. F.-Filter Protected Second Surface Mirror α_s Stabilities, Including Surfaces with Conductive Top Layers.

Otto K. Husmann, Messerschmitt-Bölkow-Blohm GmbH,
Space Division Ottobrunn

K. Kerner, Robert Bosch GmbH, Stuttgart and

J. Naegele, Deutsche Balzers GmbH, Geisenheim, West Germany

ABSTRACT

The current MBB experimental research program for satellite thermal household control is directed toward improvement of the satellite thermal life time of passively controlled satellites. To retard the commonly experienced degradation of the solar absorption coefficient of SSM and OSR, several protective thin film coatings have been applied to Teflon FEP SSM and Suprasil glass OSR. Both substrate materials were chosen because of their superior stability under solar radiation exposure, compared to other plastics and glasses. The performance of these protected substrates was evaluated in terms of their α_s changes under accelerated solar radiation test conditions, with 7,5 solar constants (SK), 3,5 SK, and 2 SK. Several sets of samples were exposed to UV radiation only, and to UV and proton radiation simultaneously. A few samples were coated with a thin layer of In_2O_3 to study their surface resistance during the course of simulated solar radiation exposure.

This research program is sponsored by the DFVLR of West Germany.

Paper presented at the USAF/NASA International Spacecraft Contamination Conference, March 7 to 9, 1978, Colorado Springs, Colorado, U.S.A.

1.0 INTRODUCTION

Experimental studies point toward the short wave length UV radiation as the cause of SSM and OSR α_s degradation, besides particle radiation.[1,2,3] To protect the SSM and OSR against the influence of the short wave length solar UV radiation, without adding weight, interference filter may be deposited on such surfaces, which either reflect or absorb the detremental part of the UV spectrum of the sun.

Among the materials with sufficiently high stability under solar radiation exposure are ZnS with a high index of refraction, and ThF_4 as well as Al_2O_3, both with a low index of refraction. ZnS alone may be interesting as protective shield, because it strongly absorbs below 3500 Å even as a $\lambda/4$ layer. - Interference filter, fabricated from successive $\lambda/4$ layers of ZnS and ThF_4 or ZnS and Al_2O_3, have shown high stability under simulated solar radiation. Therefore they are candidate materials for IF filter fabrication on SSM and OSR. - In conjunction with static spacecraft surface charging in geostationary orbits, thin conductive In_2O_3 + 10% SnO_2 coats as top layers are of particular importance for undisturbed satellite communications. The conductivity of such films atop of the interference filters also has been tested under simulated solar radiation conditions.

The α_s stability of surface layers may depend on the intensity of the simulated solar radiation. Impressive results, obtained under highly accelerated test conditions may not necessarily repeat under exposure with less intense UV radiation.

To save time, selected samples first were exposed to 7,5 solar constants UV radiation over 3000 ESH and subsequently to 7,5 SK UV and proton radiation, with a total of 10^{16} protons/cm^2, at 10 KeVolt proton energy, again over 3000 ESH.

To study the dependence of α_s changes on the radiation intensities, above tests were repeated under similar conditions, first with 3,5 SK UV exposure, and 30 KeV proton energy, and subsequently with 2 SK and 20 KeVolt proton energy. Each time one set of samples was irradiated with UV alone, and thereafter a second set of identical samples was exposed to UV and protons simultaneously. All tests were extended over 3000 ESH.

It was not possible, to generate proton intensities below $10^{10}/cm^2$ sec. For this reason proton irradiation proceeded in intervals during the UV exposure, till 10^{16} protons/cm^2 were brought onto the samples. During proton irradiation the proton beam was not neutralized.

2.0 THE MBB SOLAR RADIATION SIMULATION TEST FACILITY

2.1 The Combined Effects Chamber

The MBB solar radiation simulation test facility consists of five main building blocks, the vacuum chamber with ion pump, the spectrophotometer with digital data reduction equipment for in situ on line α_s determination, the UV source, the proton generator and the electron gun. The UV intensities are adjustable between 7,5 solar constants and 2 solar constants, employing OSRAM XBO 900 W/4 and XBO

450 W/4 Xenon high pressure lamps with Suprasil bulbs. The proton intensities are adjustable between 10^{10} and 10^{11} protons/cm^2 sec; the electron intensities may be selected between 10^{10} and 10^{12} /cm^2 sec. Proton and electron energies range between 5 KeV and 50 KeV.

Both, the proton source and the electron gun were layed out to insure uniform intensity distribution accross the target area, independent of the acceleration potential. Both currents follow the $U^{3/2}$ law. The electron current density can be adjusted through its heater power input. Electron emitter is a L-cathode, which repeatedly may be exposed to air after formation.

The protons are extracted through a 0.6 mm diameter capillary, which takes care of the pressure difference between the RF ion source and the vacuum system. The hydrogen pressure within the RF ion source is around 50 microns. A unipotential lens beneath the capillary insures equal proton current density distribution, independent of the acceleration potential.

Three Faraday cups can be moved across the sample area, close to the samples, to scan electron and proton current densities. The current density distribution over the samples is affected by the build up of retarding potentials on nonconductive sample surfaces.

During the application of acceleration potentials exceeding 20 KVolt, occasionally discharges around and also through the 5 mil thick samples were observed. Such discharges can damage the plastic foil. In some cases, also the reflector was damaged by discharges, because here the reflector is isolated against ground through a thin layer of glue.

2.2 UV-Calibration of a OSRAM XBO 900 W/4 Light Source

Earlier studies pointed toward the short wave length UV radiation as the major cause of α_s deterioration under solar radiation.[1,2,3] For a better assessment of the UV inflicted damages to the SSM and OSR, efforts therefore were expended for calibration of the UV source, a Xenon high pressure lamp with Suprasil bulb, including all elements within the light beam.

For light projection onto the samples a parabolic mirror was employed. Through a sapphire window the light beam enters the vacuum chamber. Air and water vapor strongly absorb below 1860 Å. For this reason the light source is operated within a heat exchanger, which is filled with spectrally clean nitrogen. Suprasil absorbs between 1700 Å and 1600 Å. Beyond 1600 Å the UV intensities are practically zero.

A new XBO 900 W/4 was calibrated in the spectral range from 1600 Å to 3000 Å with a JOBIN-YVON H - 20 monochromator. Through application of three filters of known transmittance it was possible to eliminate stray radiation in particular below 2500 Å. As secondary standard served a D - 15 Deuterium lamp, which was calibrated at the DESY facility at Hamburg, West Germany. Since absolute calibration at an electron synchrotron is not a simple straight forward task, the calibration curve was fixed to the radiation intensity of a well known tungsten band lamp at 2800 Å. This calibration was accomplished with an integrating sphere, which was installed between light source and monochromator. Because of the short wave length UV under consideration the inside of this integrating sphere was aluminum coated after sandblasting the day before the calibration. All components but the heat exchanger were under vacuum. During the calibration the heat exchanger continously was rinsed with spectrally clean nitrogen.

In Fig. 1 the integrated irradiance from 1600 Å to λ is plotted. For comparison the integrated solar irradiance according to ASTM E 490 is added[4]. The steep increase of the UV intensity between 1600 Å and 1700 Å can be attributed to the transmittance of the Suprasil enveloppe within this wavelength range. In the short wave length range the UV output of the lamp by far exceeds that of the sun. However, with increasing wave length both curves come closer together. At 3000 Å the integral intensity amounts to about 13 solar constants and decreases further to 7,5 solar constants at 4000 Å, in good agreement with radiometer measurements.[5]

In conclusion it should be mentioned, that the UV intensities in the short wave length range exceed those of the sun. The integral intensity of a new XBO 900 W/4, operated at nominal current in this geometry, corresponds to 7,5 solar constants at the samples. With a XBO 450 W/4 intensities between 3,5 SK and 2 SK can be maintained.

2.3 In Situ α_s Evaluation

The sample holder accepts a total of fourty samples. Eight samples may be exposed simultaneously. The sample temperatures can be adjusted between -100° C and +100° C. Within

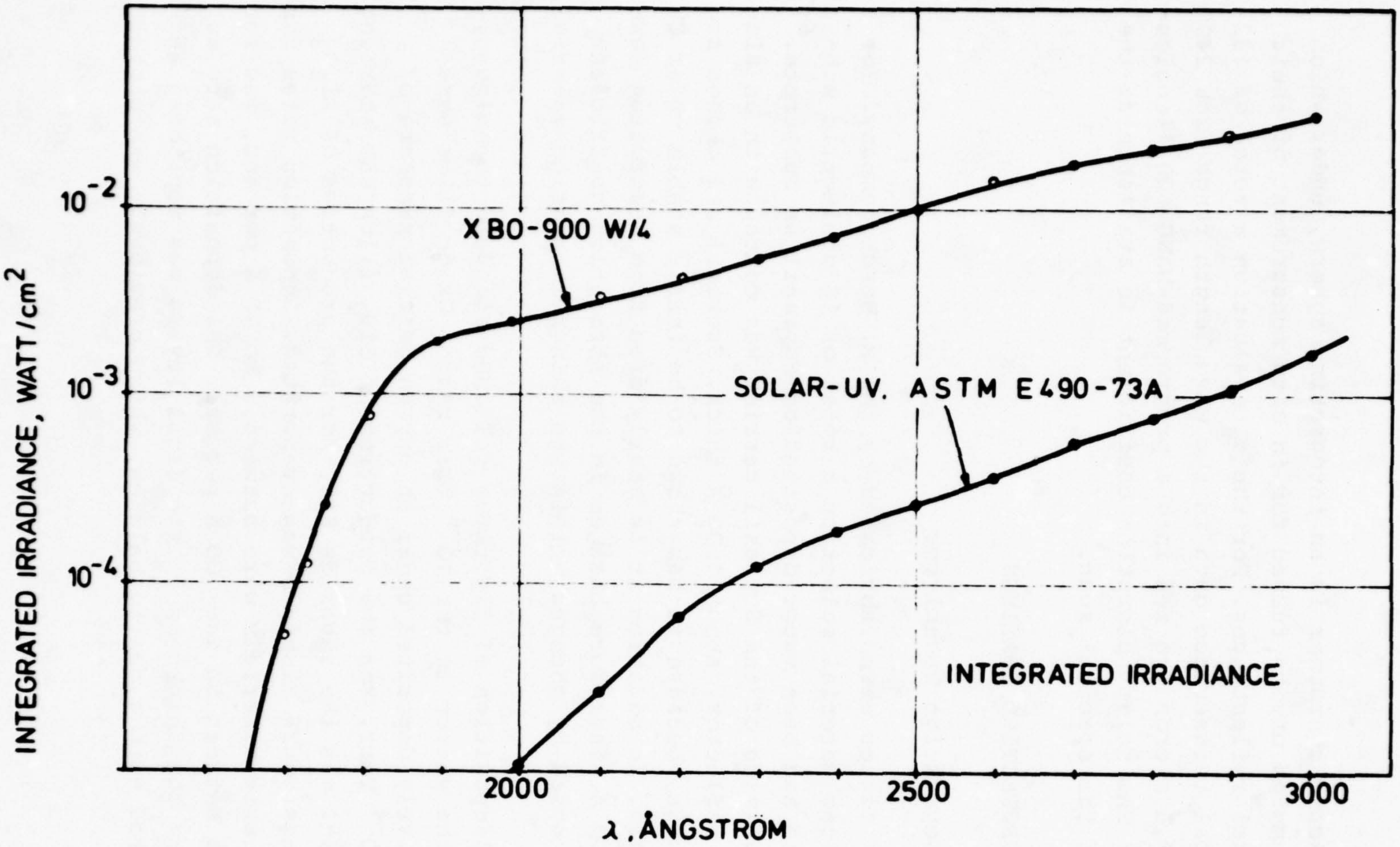

FIGURE 1 INTEGRATED IRRADIANCE FROM 1600 Å to λ, IN WATT/cm^2, OF A NEW XBO 900 W/4. FOR COMPARISON THE INTEGRATED SOLAR UV IRRADIANCE HAS BEEN ADDED.

the vacuum container is an integrating sphere, under which the samples may be turned for in situ measurement of their spectral reflectances. For the α_s evaluation a total of 132 spectral reflectance data in the wave length range from 2400 Å to 2,5 micron are fed into a programmed WANG 600/14 calculator. The solar absorption coefficient is available at the end of the spectral scan.

3.0 PROTECTIVE COATINGS

3.1 Deposition Techniques

The IF filter were fabricated by the R. Bosch company. For IF filter material selection a total of 13 dielectric substances had been vapor deposited on Suprasil as substrate.[6,7] The backside of the Suprasil carrier was coated with an aluminum reflector, about 1500 Å thick. Suprasil was chosen as substrate, because it has shown to be fairly stable under UV exposure. In addition it is nearly free from absorption down to 1700 Å. Therefore changes in the absorption coefficient were caused by changes within the thin film coating material.

Vapor deposition of fluorides followed standard techniques, with the vacuum in the 10^{-6} Torr range. Oxide films were reactively deposited under an oxygen partial pressure of 2×10^{-4} Torr. For the production of SiO_2 films the starting material was the suboxide SiO, for the production of Al_2O_3 coatings, pure aluminum was evaporated. Deposition rates for dielectric materials were between 5 to 10 Å per sec, and for metals between 50 and 100 Å per sec. The deposition rate as well as the thickness of the final layers was monitored and adjusted with a quartz balance, which previously was photometer calibrated with $\lambda/4$ layers.

To insure sufficient adherence of the IF filter to Teflon FEP, at first a thin aluminum layer, about 20 Å thick, is deposited on Teflon. Subsequently, the other compounds, always starting with ZnS, were vapor deposited. The 20 Å thick aluminum layer partly reacts with the fluor of the substrate, partly it reacts with oxygen from the residual gas atmosphere and forms a completely transparent layer, which improves the adherence of the IF filter to the substrate.

The Interference filter are composed of seven alternating layers, each $\lambda/4$ thick, starting with ZnS. ZnS has a high index of refraction. In addition, it efficiently absorbs the UV radiation below 3500 Å, and as top layer eliminates UV exposure below 3500 Å for the subsequent layers, including the Teflon FEP substrate.

The second layer was fabricated either from ThF_4 or AL_2O_3. In conjunction with its radioactivity, ThF_4 was considered less desirable, and more emphasis was placed on the development of highly transparent stoichiometric Al_2O_3 coats. Stoichiometric deposition of Al_2O_3 and SiO_2 layers is difficult. For Al_2O_3 deposition electron beam and reaction deposition techniques were compared, with and without annealing. Finally reaction deposition was selected after several tests, concerning the α_s stability of these coatings.

In conjunction with the strong UV absorption of ZnS below 3500 Å it is of no advantage to place the IF filter reflectance maximum into this region. Either reflection or absorption protect the underlying materials against the UV radiation. If radiation damage is inflicted to transparent materials, such damage may appear as increased absorption in any part or parts of the spectrum, depending on the material. To reduce or to eliminate the consequences of such damage (α_s-increase), e.g. yellow coloration of Teflon FEP, it is of advantage to place the reflection maximum of the IF filter over the spectral range of increased absorption. By application of this technique the light is reflected instead of being absorbed. Therefore the solar absorption coefficient shows less increase, compared to other placings of the IF filter reflection maximum.

3.2 SSM and OSR Transmission

Also the reflector of the SSM can excert some influence on the satellite thermal life time, if the short wave length UV is not absorbed by e. g. a ZnS layer.

Under such condition a silver reflector absorbs below about 3000 Å, in contrast to the high reflectance of aluminum reflectors in this wave length range. With Al-reflectors the UV passes twice through the transparent foil, with the Ag reflector only once.

During the exposure with 3,5 solar constants, a few samples without reflector were incorporated into the test array. These ZnS/Al_2O_3 IF filter on Suprasil were exposed to 3000 ESH UV and also to the same amount of UV simultaneously with protons of 30 KeVolt, to a total of 10^{16} protons/cm^2. One set of these samples consisted of eight layers, starting with Al_2O_3. The second set of samples with seven layers had ZnS on top.

After exposure to simulated solar radiation these samples again were checked for their spectral transmittance in air. Neither the depth nor the wave length of the transmission minimum had changed after exposure. The small differences measured can be attributed to the IF filter fabrication. The good agreement of the transmission curves, measured before and after solar radiation exposure, leads to the conclusion, that the ZnS/Al_2O_3 IF filter now remain unaffected, independent of the top layer material. (Fig. 2) Because of this favorable result, in subsequent tests at two solar constants, a few ZnS/ThF_4 samples were exchanged for ZnS/Al_2O_3 samples.

3.3 Conductive Coatings

The interference filter materials are insulators. Under UV and particle radiation they charge up. If high potentials develop, arc discharges between the satellite structure and these charged surfaces may cause interference with the satellite communications system. An efficient approach to eliminate such charges is the overcoating of thermal surfaces with a thin layer of transparent conductive material, such as In_2O_3.[8,9] This conductive layer must be connected to the satellite structure. The resistance of the conductive coating may be high, because of the low density charged particle streams in outer space, e. g., in a geosynchronous orbit.

For the two solar constant tests reported here, two Teflon FEP samples with ZnS/Al_2O_3 IF filter, conductive coating and Ag reflector were incorporated for exposure to UV + protons, protons, and electrons. Those samples, which were exposed to UV only, instead included two ZnS/ThF_4 IF filter protected

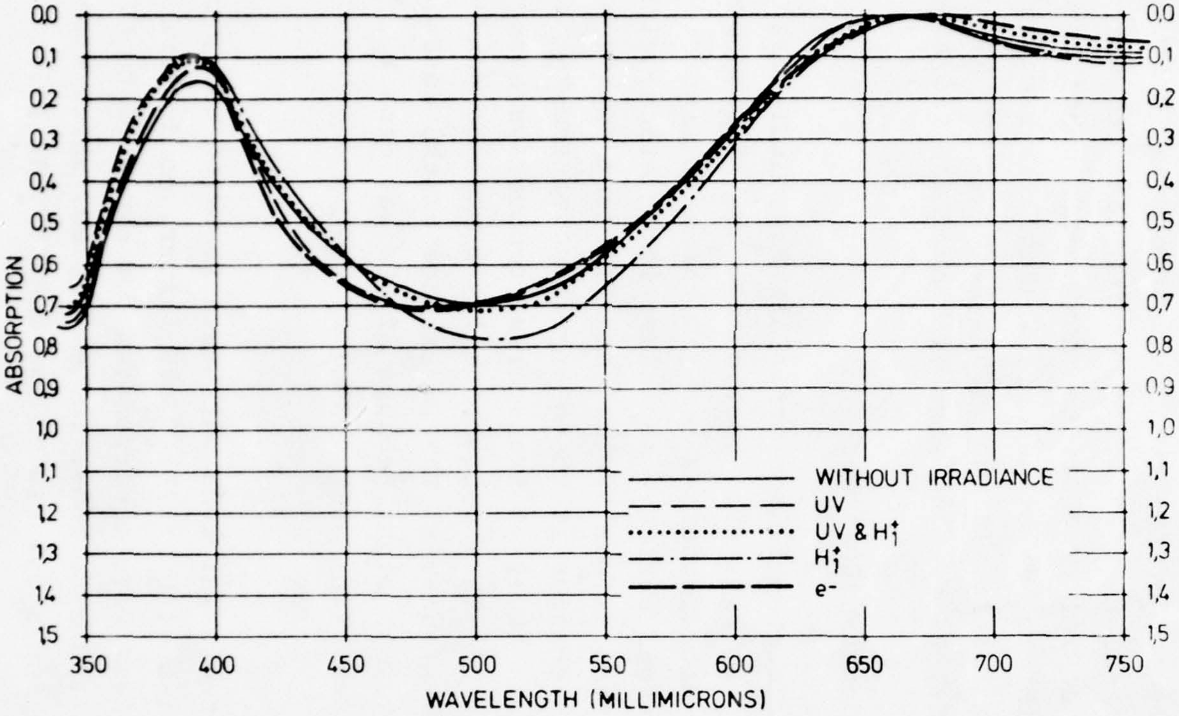

FIGURE 2 ABSORPTION OF A ZnS/Al_2O_3 INTERFERENCE FILTER BEFORE AND AFTER EXPOSURE TO UV, PROTONS, AND ELECTRONS. THIS IF-FILTER HAS NO REFLECTOR.

Teflon FEP SSM with In_2O_3 top layer and Ag reflector.

The CC was deposited on top of the IF filter by indium evaporation under about 10^{-4} Torr oxygen partial pressure. To improve its mechanical stability, 10 % SnO_2 simultaneously with the In_2O_3 was brought onto the sample.

For measurement of their square resistance, electric leads were glued with ECOBOND 57 C to the gold-electrodes, about 10 mm long, in 10 mm distance. For comparison, a total of four Suprasil samples with CC were added. On Teflon FEP the thickness of the CC was in the 100 Å range, on Suprasil it was about 700 Å thick.[11]

4.0 TEST RESULTS

4.1 α_s Performance of Protected SSM and OSR

Of all the IF filter materials investigated, ZnS, ThF_4, and Al_2O_3 showed considerable stability under simulated solar radiation. Seven layer IF filters, fabricated from these materials, performed well under prolonged exposure to UV, protons and electrons.[10] These IF filter efficiently protect the underlaying substrates against α_s increases within the stated times of test.

To ascertain, that these test results, gained under accelerated test conditions with 7,5 solar constants are true at lower radiation levels, the tests were repeated with 3,5 solar constants, and finally with 2 solar constants. The UV exposure always amounted to 3000 ESH (equivalent sun hours). The proton doses somewhat exceeded $10^{16}/cm^2$.

Proton energies ranged from 10 KeVolt to 30 KeVolt, with 10 KVolt application during the 7,5 solar constant exposure, and 30 KVolt in conjunction with 3,5 solar constant UV irradiation. To avoid discharge damages to Teflon FEP and to the reflector, during the final combined exposure the proton acceleration potential was maintained at 20 KVolt.

The proton radiation intensities were too high for continuous proton exposure. Therefore the protons were applied in intervals during the UV irradiation, until $10^{16}/cm^2$ were brought onto the samples. In Table I the α_s data of the investigated candidate IF-filter on Suprasil and on Teflon FEP are compiled. Samples with In_2O_3 top layer are not included in this comparison. However, they perform as well as the samples without conductive layer. -

Table I
Solar Absorption Coefficients of IF Filter Protected SSM and OSR Before and After Exposure to 3000 ESH UV and Protons. The underlined data were measured with Suprasil as substrate. For the other samples, the IF filter were deposited on 5 mil thick Teflon FEP. All samples had aluminum reflectors, 1500 Å thick.

The samples exposed to UV are identical to those exposed to UV + protons, provided they have been tested under the same solar radiation intensity.

Differences among the samples are the result of fabrication techniques, and the location of the IF filter reflection maximum, which was varied within the spectral range from 4600 Å to 5250 Å. During the course of this study these

RADIATION DOSES	IF-FILTER MATERIALS	ALPHA - S								
		2.0 SK			3.5 SK			7.5 SK		
		BEFORE	AFTER	$\Delta\alpha_s$ %	BEFORE	AFTER	$\Delta\alpha_s$ %	BEFORE	AFTER	$\Delta\alpha_s$ %
UV	ZnS / ThF_4	0.160	0.163	2	0.150	0.165	10	0.138	0.142	3
3000 ESH	ZnS / ThF_4	0.160	0.169	6	0.180	0.210	17	0.166	0.168	1
	ZnS / Al_2O_3	0.160	0.160	0	0.192	0.205	7	0.178	0.182	2
	ZnS / Al_2O_3	0.160	0.160	0	0.175	0.1	10	0.197	0.198	1
UV & PROTONS	ZnS / ThF_4	0.185	0.194	5	0.165	0.193	17	0.138	0.146	6
3000 ESH	ZnS / ThF_4	0.171	0.181	6	0.167	0.184	10	0.166	0.173	4
AND	ZnS / Al_2O_3	0.162	0.164	1	0.185	0.203	10	0.186	0.210*	13
10^{16} H_1^+/cm^2	ZnS / Al_2O_3	0.160	0.160	0	0.173	0.178	3	0.212	0.219	3

TABLE I SOLAR ABSORPTION COEFFICIENTS OF IF-FILTER PROTECTED SSM AND OSR BEFORE AND AFTER EXPOSURE TO 3000 ESH UV AND PROTONS ($10^{16}/cm^2$).

*REFLECTANCE DETERIORATION HERE IS THE MAIN CAUSE OF $\Delta\alpha s$.

fabrication techniques were improved. The IF filter tested during the two solar constant exposure represent the final design.

Samples that suffered discharge damages were omitted from further evaluation. In general, such samples showed steep increases of their α_s after such damage occurred. Damages were visually recognizable through light yellow coloration of Teflon FEP or as a fine discharge pattern in the Al-reflector (Lichtenberg figures).

The error of the α_s data reported here is within ± 3 %, due to instrumental limitations, and also in dependence of the DK-2A calibration.

The measured data, Table I, indicate, that α_s increases after completion of the exposure to 3000 ESH UV as well as to 3000 ESV UV + 10^{16} protons/cm^2 are small. Only three times the α_s exceeds 10 %. The 13 % increase after combined UV and proton exposure at 7,5 SK partially can be attributed to slight damage of its Al-reflector.

In particular, there is no α_s increase due to decreasing UV intensity. Therefore, from these accelerated test data the α_s performance of Teflon FEP SSM and Suprasil OSR with IF filter protection may be extrapolated to one solar constant exposure without underestimation of the consequences for satellite thermal household control.

4.2 Conductive Coating Resistance Performance

The resistances of the samples with conductive coating were repeatedly measured prior to and after evacuation of the test chamber. These measurements were continued during sample exposure to simulated solar radiation and encompassed all samples with conductive coatings within the vacuum chamber, also those, which were not yet irradiated.

Under vacuum the square resistance of the In_2O_3 layers soon increased. At the beginning these resistances were in the 3 K ohm range. Only the resistance of the In_2O_3 coats on Suprasil remained around 250 to 300 ohms.

After a few days under vacuum, without any radiation exposure, drastic increases of the resistance on all samples with Teflon FEP substrate were measured. The resistance varied between the samples from $10^8\ \Omega$ up to $10^{11}\ \Omega$, and remained within this range, with variations in the course of time under vacuum. After exposure to air, these resistances remained within above range. Only the conductive coatings on Suprasil maintained constant resistances.

Microscopic inspection of the top layers on all Teflon FEP samples revealed many fine cracks accross the sample surfaces. Such cracks frequently had parallel orientation, but often little isolated islands were found atop the substrate.

These fine cracks dont hurt the IF filter performance. Therefore they dont affect the SSM solar absorption coefficient. However, concerning the surface conductivity, these fine interruptions of the conductive path can lead to resistance increases of several orders of magnitude. Fortunately, charged particle currents even in a geosynchroneous orbit are low. For this reason surface resistances in the 10^8 ohm cm range are regarded to be tolerable.

For an efficient elimination of charges from thermal control surfaces it seems to be mandatory to ground connect conductive top layers all around to the satellite structure.

5.0 CONCLUSIONS

The results of this research program indicate, that it is possible to maintain within the error limits a constant solar absorption coefficient of IF filter protected SSM and OSR over an exposure time of 3000 ESH. Substrates were Teflon FEP and Suprasil. Extrapolation of these favorable results to other substrates may not be possible.

In conjunction with the thermal lay out of satellites, in general small increases of the thermal control surface solar absorption coefficient are tolerable. Therefore exposure times exceeding 3000 ESH are feasable.

Because of its radioactivity, ThF_4 was omitted from further consideration for fabrication of IF filter. Consequently, IF filter fabricated from alternating layers of ZnS and Al_2O_3 are the candidate design.

The IF filter under study are composed of seven layers. Five or three layer filter were not tested. - For improved IF filter stability a ZnS layer was placed on the outside, - because of its strong UV absorption below 3500 Å. Also, such eight layer IF filter with an Al_2O_3 $\lambda/4$ film a top showed no degradation of its spectral transmission after exposure to UV, UV+protons, protons, and electrons (UV at 3,5 SK) after 3000 ESH. ZnS alone may be sufficient as protective shield.[10]

The SSM and OSR α_s studies with exposures to three different UV radiation intensities lead to the conclusion, that for the IF filter tested solar radiation exposures up to 7,5 SK yield for constant ESH identical test results within the error limits, independent of the UV radiation intensity. Therefore, up to 7,5 SK α_s changes here are proportional to the number of ESH only.

All investigations were performed with samples 11 x 11 mm. Presently studies are under way to increase the sample size to dimensions interesting for the fabrication of satellite thermal control surfaces.

ACKNOWLEDGMENT

The authors wish to express their gratitude to Mrs. Mutschler of the Robert Bosch GmbH for deposition of the IF filter and to Mr. Ch. Bock of the Messerschmitt-Bölkow-Blohm Company for alpha-S measurements.

References

1 Aversen, J.C., Spectral Dependence of Ultraviolet-Induced Degradation of Coatings for Space Craft Thermal Control, in Progress in Astronautics and Aeronautics, vol. 20, G.B. Heller, edt., Thermophysics of Space Craft and Planetary Bodies, Academic Press Inc., New York, p.265-280 (1967)

2 Swofford, D.D., Mangold, V.L., and Johnson, St. W., Effects of Extreme Ultraviolet on the Optical Properties of Thermal Control Coatings, vol. 21, J.T.Bevans, edt., Thermal Design Principles of Space Craft and Entry Bodies, Academic Press Inc., p. 667-695, New York, (1969)

3 Paillous, A., and Buisson, J.P., Irradiations Ultraviolettes Monochromatiques ou Polychromatiques de Divers Materiaux. International Conference, Evaluation of Space Environment on Materials, Toulouse, June 17-21, p.467-487, (1974).

4 Solar Constant and Air Mass Zero Solar Spectral Irradiance, Standard Specification. - American Society for Testing and Materials, 1916 Race Street, 19103 Philadelphia/Pa., ASTM E 490 (1973).

5 Husmann, Otto K., Absolute Calibration of a XBO 900 W/4 Xenon Lamp with Suprasil Bulb in the Short Wave Lenght UV, and the Layout of the UV Light Source. - Materials Work Shop,

Toulouse, France, July 1977; published by the European Space Agency, ESTEC, Noordwijk, Netherlands, (1977)

6 Husmann, Otto K., The MBB Space Radiation Simulation Test Facility : Performance Data and In Situ Evaluation of the Optical Degradation of SSM under Ultraviolet and Proton Irradiation, International Conference, Evaluation of Space Environment on Materials, Toulouse, France, July 1974, published by CNES, Toulouse, p. 135-151, 1975

7 Husmann, Otto K., and Kerner, K., The Alpha-S Stability of Teflon FEP SSM Protected by Vapor Deposited Interference Filters under Accelerated Solar Radiation Test Conditions. Materials Work Shop, Toulouse, France, July 1977; published by the European Space Agency, ESTEC, Noordwijk, Netherlands, (1977).

8 E. Ritter, Transparent Conductive Coatings, in Progress in Electro - Optics, edt. by E. Camatini, Plenum-Publishing Corp., 227 West 17 th Street, 10011 New York, N.Y., p. 181-199, (1976)

9 Husmann, Otto K., Electrically Conducting Thermal Control Surface Study, MBB Report No. UR-204-1973, (1973).

10 Husmann, Otto K., and Kerner, K., Solar Radiation Resistance Improvement of Second Surface Mirrors and Optical Solar Reflectors by Deposition of Interference Filters,, J. Vac. Sci. Technol., vol. 14., No. 1, Jan/Feb., (1977), p. 200-204.

11 Fabricated at the Deutsche BALZERS GmbH, Geisenheim, West Germany.

SILVER-TEFLON CONTAMINATION UV RADIATION STUDY[+]

J. A. MUSCARI, MARTIN MARIETTA AEROSPACE
S. JACOBS, NASA/JOHNSON SPACE CENTER

1.0 INTRODUCTION

Silver-Teflon is currently being planned to be used as the thermal control material covering the radiator surfaces on the Shuttle Orbiter payload bay doors. These radiators require the use of materials that have a very low solar absorptance (α_s) and a high emittance for heat rejection. However, operationally, materials used on these critical radiator surfaces, such as silver-Teflon, will be exposed to a variety of conditions which include both the natural as well as the induced environments. It is very important to understand the influences of these environments upon these materials because of their impact upon on-orbit operational activities as well as ground operations such as refurbishment.

Although radiator surfaces are selected to be stable when exposed to the natural solar ultraviolet and particulate environment, the deposition of contaminants and the interaction of the contaminants with solar exposure can significantly degrade the performance of such an operational surface. Laboratory test programs and spacecraft experiments have shown that certain contaminants darken significantly when exposed to solar ultraviolet, resulting in an increased α_s.

With the present requirement to maintain changes in reflectance on Orbiter radiator surfaces to less than 1%, it becomes very important to understand the nature of spacecraft contaminants when exposed to a solar environment and their effect upon silver-Teflon. The purpose of this study is to determine the effects of radiation upon silver-Teflon surfaces after contamination by the CVCM (collected volatile condensible mass) from RTV-560 and MIL-H-83282 hydraulic fluid. The test procedure was depositing, irradiating, and measuring solar absorptance changes (via reflectance measurements) in-situ. Additionally, cleaning procedures will be developed for surfaces that experience a change in solar absorptance (α_s) greater than 0.03 so that the absorptance can be recovered to near 0.08. This program is still in progress and this paper presents the current results with RTV-560.

2.0 EQUIPMENT

Figure 1 presents a schematic of the test setup and facility. The equipment consists of an ultrahigh vacuum chamber with feedthroughs, manipulators, and LN_2 shroud; contaminant source holder heated by filament lamps; a receptor holder to position nine silver-Teflon (Ag/FEP) samples, a control Ag/FEP sample, and the barium sulfate calibration

---

[+] This work was supported by National Aeronautics and Space Administration Johnson Space Center, Houston, Texas, under contract NAS9-15436.

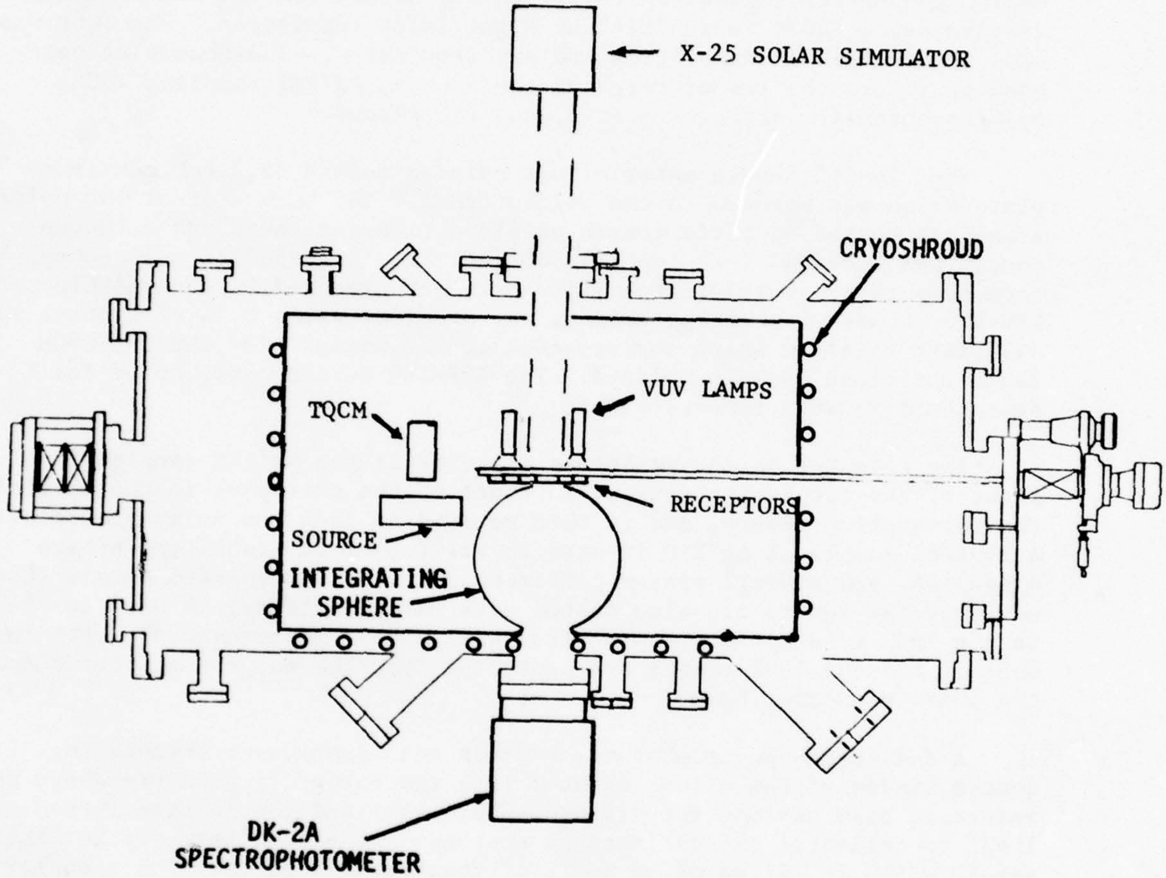

Figure 1 Schematic of the Test Setup and Facility

sample for deposition, irradiation, and measurement; a spectrophotometer with an integrating sphere mounted in the chamber; a solar simulator; two vacuum ultraviolet lamps; and a temperature controlled quartz crystal microbalance (TQCM).

The vacuum chamber normally operated in the low 10^{-6} Torr range. The LN_2 shroud prevented migration of any contaminants to the Ag/FEP except through direct line-of-sight from the test source. The shroud also cooled the Ag/FEP samples by radiation and maintained the contaminated samples below -40°C to inhibit any significant reemission. The TQCM was used to monitor the deposition and any reemission. Thermocouples were used to record the temperatures of the source, Ag/FEP samples, TQCM, spectrophotometer detector system, and the shroud.

The RTV-560 source material was painted onto a 32.3 cm^2 aluminum plate which was mounted to the holder frame. The back side of the holder frame was heated by three quartz envelope filament lamps and a thermocouple was embedded into the RTV-560 material. RTV-560 is a two-component room temperature vulcanizing silicone rubber produced by General Electric. RTV-560, a methyl-phenyl compound, was prepared using 0.5% of dibutyl tin dilaurate catalyst which corresponded to the mixture for the TML/CVCM tests performed by NASA Goddard. The RTV-560 samples were cured for seven days at room temperature.

The receptor holder positions all nine of the Ag/FEP samples in front of the outgassing source, in front of the exit port in the wall of the integrating sphere, and is then rotated to face the solar simulators. A control sample of Ag/FEP is used to verify sample stability, sphere alignment, and overall system performance. A barium sulfate sample (the walls of the sphere are also coated with barium sulfate) is used to obtain a 100% reading before and after each set of measurements. Both the control and the 100% sample are protected from the outgassing source and the solar simulator beams.

A dual beam spectrophotometer sends two light beams through the quartz window of the vacuum chamber into the integrating sphere where the reference beam strikes the diffuse sphere wall and the multireflected light is collected by the detector system. The second beam strikes the sample which is tilted at an angle of four degrees so that the specular scattered light does not exit through the entrance port and is scattered throughout the sphere. The sample and the reference signals are electronically ratioed, displayed on a chart recorder, and converted to digital data for storage on punch cards. The digital data is processed by the use of computer programs. A blocking screen covered with barium sulfate prevents the specular Ag/FEP samples from direct line-of-sight to the detectors which would give incorrect signals.

An external X-25 solar simulator provides solar intensities up to 2.5 equivalent suns (ES) at target samples 2A, 2B, and 2C after passing through a quartz vacuum chamber window. However, these standard high-pressure xenon lamps are depleted in the short wavelengths radiation (less than 230 nm) which have been shown to be necessary for changes in certain films.[1] Thus, two in-situ vacuum ultraviolet sources were included to irradiate three samples each. The xenon lamp has 90% of its total radiation (0.621 mW) in the wavelength band of 145 nm to 160 nm. This lamp provides 0.359 mW·cm^{-2} at one Ag/FEP sample and 0.0081 mW·cm^{-2} at two other samples. If it is assumed that one equivalent ultraviolet sun (EUVS) is the integrated standard solar zero air mass intensity for all wavelengths shorter than 230 nm (0.131 mW·cm^{-2}),[2] then the xenon lamp irradiates sample 1B with 2.74 EUVS and samples 1A and 1C with 0.062 EUVS. An in-situ hydrogen lamp failed during the testing and was replaced by a krypton resonance line lamp (124 nm; 0.166 mW·cm^{-2}) which produces about 1.3 EUVS on samples 3A, 3B, and 3C.

The TQCM, with a mass sensitivity of 3.5x10^{-9} g·cm^{-2}·Hz^{-1}, was kept at the same temperature as the Ag/FEP samples. The characteristics of the matched set of 10 MHz quartz crystals have been tested previously and are known to be relatively insensitive to temperature changes (+1.5 Hz·°C^{-1}) and have a low response to thermal radiation from heated sources (-7 Hz for a 125°C source). If it is assumed that the CVCM is a uniform film and its density is 1.2 g·cm^{-3}, then a change of 340 Hz is equivalent to a film of 10 nm.

3.0 TEST PROCEDURES

The stability of Ag/FEP to a vacuum environment and solar radiation, especially vacuum ultraviolet wavelengths, was first verified. Then the effect of the CVCM from RTV-560 and hydraulic fluid for five different CVCM thicknesses will be measured. The reflectance measurements are repeated after irradiating with solar radiation for periods of at least 48 hours up to 300 ESH. The 48 hour baseline correlates to near 48 orbits on the average, or a three day exposure for normal incidence during sunlight periods of the orbit. For surfaces not normal to the solar flux, the time to accumulate 48 hours of sunlight is increased by dividing by cos θ where θ is the angle with respect to the surface normal and the incident flux direction. For example, for a surface at 60 degrees, 48 ESH equates to 6 days on orbit and for 45 degrees it is 4.2 days. A current estimate of the expected initial deposition rate on the Ag/FEP surfaces of the Shuttle Orbiter (fixed attitude, flying nose first belly up in a fixed ZLV mode, zero degree beta angle, and at 296 km) is in the range 1.7x10^{-6} g·cm^{-2}·day^{-1}; assuming a CVCM density of 1.2 g·cm^{-3} gives a film thickness of 14 nm·day^{-1}.[3] Our planned range of CVCM deposition levels will be equivalent to a thickness from 10 nm to 400 nm and thus cover mission durations up to 30 days.

General cleaning techniques using solvents will be used to study the restoration of degraded Ag/FEP samples. Successful techniques will be reviewed for application to very large surfaces. The reflectance will be

---

[1] P. D. Fleischauer and L. Tolentino, 7th Conf. Space Simulation, NASA SP-336, 645 (1973).

[2] M. P. Thekaekara, Optical Spectra, 32 (March, 1972).

[3] R. O. Rantanen and D. A. Strange, Shuttle Orbiter-IUS/DSP Satellite Interface Contamination Study Final Report, MCR-78-512 (January, 1978).

remeasured to verify the original absorptance value or determine the ineffectiveness of the solvent.

4.0 RESULTS

After performing the initial tests, it became quite apparent that standard spectrophotometer techniques would not provide the resolution and repeatability necessary for the low solar absorptance of the Ag/FEP samples. With the typical solar absorptance for Ag/FEP of 0.08 and our computed solar intensity of 1310 $W \cdot m^{-2}$ (wavelength region from 0.25 μm to 2.5 μm), then a deviation of only 2% in the reflectance produces a change of 25% in α_S. Table 1 presents the solar absorptance values for the clean Ag/FEP samples verifying the stability of the surfaces to solar radiation.

Table 1 Solar Absorptance of Ag/FEP Samples When Exposed To A Solar Simulator (2.32 ES, Samples 2A,2B,2C), Xenon Lamp (0.062 EUVS, Samples 1A,1C; 2.74 EUVS, Sample 1B), and No Radiation (Control, 3A,3B,3C).

SAMPLE	SOLAR ABSORPTANCE					
	HOURS OF EXPOSURE				AVERAGE	STANDARD DEVIATION
	0	25.83	44.58	66.58		
CONTROL	0.076	0.054	0.069	0.060	0.065	±0.0097
3A	0.073	0.057	0.070	0.056	0.064	±0.0088
3B	0.071	0.054	0.065	0.052	0.061	±0.0090
3C	0.064	0.053	0.064	0.054	0.059	±0.0061
2A	0.065	0.055	0.064	0.055	0.060	±0.0055
2B	0.068	0.063	0.074	0.057	0.066	±0.0072
2C	0.076	0.075	0.080	0.070	0.075	±0.0041
1A	0.091	0.084	0.096	0.087	0.089	±0.0052
1B	0.100	0.093	0.103	0.095	0.098	±0.0046
1C	0.114	0.110	0.116	0.110	0.112	±0.0030

The values of solar absorptance are only relative due to an as yet undetermined geometrical factor. The average standard deviation for all ten runs is ±0.0063.

Eight repeated runs were performed on the control sample, moving and rotating the rod between measurements. The standard deviation for all eight runs was 0.0043 showing the repeatability of the measuring system.

Table 2 presents the data for the change in α_S for the Ag/FEP samples after they were contaminated by the CVCM from RTV-560 with an initial deposit of 2.54×10^{-5} $g \cdot cm^{-2}$ and allowed to reemit until 3.32×10^{-6}

$g \cdot cm^{-2}$ (equivalent to about 28 nm) remained. The samples were then irradiated up to 49 hours. During this period the TQCM slowly lost mass reaching 2.54×10^{-6} $g \cdot cm^{-2}$ after 49 hours. The temperatures of the TQCM and the samples were usually in the -80°C range with short excursions to -10°C. Thus, the data in Table 2 is complicated by the fact that any increases in α_s due to ultraviolet radiation may be masked by the decrease in contaminant thickness. The data up to the first 27.25 hrs of exposure shows no significant change in α_s except for samples 2A, 2B, and 2C. These samples show a decrease in α_s, probably due to the decreasing contaminant thickness. Solar radiation does not appear to affect the CVCM. After 27.25 hours of exposure, the data is inconclusive and is being studied further. The data at 49 hours is shown for completeness, but should not be taken as indicating a trend. The radiation was continued out to 147 hours, however, the TQCM frequency dropped to about 50 Hz when the temperature of the samples accidently reached 0°C. The solar absorptance of the samples returned essentially to the clean values. No discoloration or any other physical defects were observed on the samples after removing them from the vacuum chamber.

Table 2 Change in Solar Absorptance of Silver-Teflon Samples Contaminated by the CVCM of RTV-560 and Exposed to a Solar Simulator (2.32 ES, Samples 2A,2B,2C), Xenon Lamp Radiation 147 nm (0.062 EUVS, Samples 1A,1C; 2.74 EUVS, Sample 1B), and no Radiation (Control,3A,3B,3C). The Initial Deposition on the TQCM was 2.54×10^{-5} $g \cdot cm^{-2}$ and was Allowed to Reemit Until 3.32×10^{-6} $g \cdot cm^{-2}$ (Equivalent to 28 nm) Remained.

SAMPLE	CLEAN α_s	CHANGE IN SOLAR ABSORPTANCE			
		HOURS OF EXPOSURE			
		0.0	21.0	27.25	49.0
3A	0.056	0.002	0.006	-0.001	0.012
3B	0.052	0.003	0.008	-0.002	0.022
3C	0.054	0.001	0.008	-0.003	0.026
2A	0.055	0.011	0.015	0.010	0.034
2B	0.057	0.025	0.017	0.012	0.038
2C	0.070	0.024	0.013	0.015	0.034
1A	0.087	0.007	0.008	0.008	0.031
1B	0.095	0.016	0.006	0.009	0.027
1C	0.110	0.017	0.004	-0.006	0.029

The TRASYS computer program was used to calculate the ratio of each sample/source view factor to the TQCM/source view factor to verify the uniformity of contaminant deposition. Table 3 shows this view factor ratio.

Table 3 Ratio of Sample/Source View Factor to the TQCM/Source View Factor

SAMPLE	$(VF_S)/(VF_{TQCM})$
3A	0.94
3B	0.97
3C	0.99
2A	1.00
2B	1.00
2C	1.00
1A	0.99
1B	0.97
1C	0.94

Table 4 shows the data for the change in α_s for the samples contaminated with an initial deposit of 4.06×10^{-5} g·cm^{-2} (equivalent to 340 nm), decreasing to 3.45×10^{-5} g·cm^{-2} and remaining relatively constant throughout the 134.98 hour test period ending at 3.12×10^{-5} g·cm^{-2}. The number in parenthesis below each exposure time is the frequency of the TQCM above its initial clean value. The temperature control of the LN$_2$ shroud was improved, resulting in the samples and the TQCM staying at about $-46^{\circ}C \pm 5^{\circ}C$. The temperature of samples 2A, 2B, and 2C was continuously monitored during the entire test period. The data in Table 4 indicates that both the solar beam and the vacuum ultraviolet radiation had little effect on the CVCM/FEP/Ag surface and the initial change in α_s decreased as the thickness of the CVCM decreased. Samples 3A, 3B, and 3C which were not exposed to any radiation show the same decrease in α_s as the exposed samples. Also, samples 1A and 1C which were exposed to 8.37 EUVSH show the same change in α_s as 1B which was exposed to 370 EUVSH. Figure 2 presents the change in α_s as a function of time, illustrating the similar decrease in α_s for these example samples. Once again, when the TQCM was brought up to room temperature only a very small residual CVCM remained. The samples were also visibly the same as their initial condition.

Table 5 presents the change in α_s when contaminated by the CVCM deposited sequentially in five steps to a total of 4.46×10^{-5} g·cm^{-2}. The data shows an unexpected decrease in α_s from the clean condition. The maximum temperature of the RTV-560 source, T_s, started at 33°C for the first layer and reached 65°C for the last step. The maximum temperature of the silver-Teflon samples during deposition was -10°C, nominal temperature was -51°C.

The samples used in the above test (4.46×10^{-5} g·cm^{-2}) were then irradiated up to 85.41 hours and the data is shown in Table 6. Once again, even for this heavier coating of CVCM, radiation exposure does not significantly affect the contaminated surface α_s. Figure 3 shows a photograph (22x magnification) of the contaminated area (atmospheric pressure, 25°C) for samples 1A, 1B, and 1C; 1C is the area to the left of center,

Table 4 Change in Solar Absorptance of Silver-Teflon Samples Contaminated by the CVCM of RTV-560 and Exposed to a Solar Simulator and Xenon Lamp. The Initial Deposition on the TQCM was $4.06\text{x}10^{-5}$ $\text{g}\cdot\text{cm}^{-2}$ and After 134.98 Hours $3.12\text{x}10^{-5}$ $\text{g}\cdot\text{cm}^{-2}$ Remained. The Number in Parenthesis Below the Hours of Exposure is the Frequency of the TQCM above the Initial Clean Condition

SAMPLE	CHANGE IN SOLAR ABSORPTANCE							
	HOURS OF EXPOSURE							
	0.0 (11602)	17.23 (9855)	22.23 (9507)	38.37 (9427)	60.48 (9288)	65.98 (9265)	84.73 (8943)	134.98 (8926)
3A	0.024	0.011	0.010	0.015	0.017	0.010	0.016	-0.001
3B	0.013	0.018	0.020	0.019	0.045	0.022	0.026	0.020
3C	0.001	0.005	0.008	0.008	0.025	0.010	0.014	0.005
2A	0.011	0.006	0.011	0.011	0.023	0.009	0.010	-0.003
2B	0.025	0.013	0.017	0.018	0.033	0.014	0.018	0.001
2C	0.021	0.012	0.016	0.014	0.033	0.014	0.012	-0.001
1A	0.028	0.030	0.023	0.026	0.045	0.026	0.015	0.011
1B	0.042	0.034	0.022	0.028	0.052	0.030	0.016	0.019
1C	0.046	0.044	0.030	0.022	0.053	0.032	0.026	0.023

Table 5 Change in Solar Absorptance of Silver-Teflon Samples Contaminated by the CVCM of RTV-560 Sequentially in Five Steps to a Total of $4.46\text{x}10^{-5}$ $\text{g}\cdot\text{cm}^{-2}$. The Change in Solar Absorptance is From the Initial Clean Value. The Sensitivity of the TQCM is $3.5\text{x}10^{-9}$ $\text{g}\cdot\text{cm}^{-2}\cdot\text{Hz}^{-1}$.

SAMPLE	CHANGE IN SOLAR ABSORPTANCE				
	(TQCM FREQUENCY IN Hz)				
	(1088)	(2558)	(3873)	(8176)	(12742)
3A	-0.014	0.000	-0.004	-0.013	-0.019
3B	-0.009	-0.003	-0.011	-0.029	-0.027
3C	-0.011	-0.006	-0.020	-0.037	-0.036
2A	-0.011	-0.010	-0.021	-0.040	-0.040
2B	-0.006	-0.006	-0.019	-0.039	-0.037
2C	-0.007	-0.007	-0.024	-0.033	-0.033
1A	-0.014	-0.003	-0.020	-0.041	-0.043
1B	-0.031	-0.027	-0.028	-0.049	-0.051
1C	-0.046	-0.036	-0.038	-0.060	-0.070
T_s	33°C	37°C	40°C	57°C	65°C

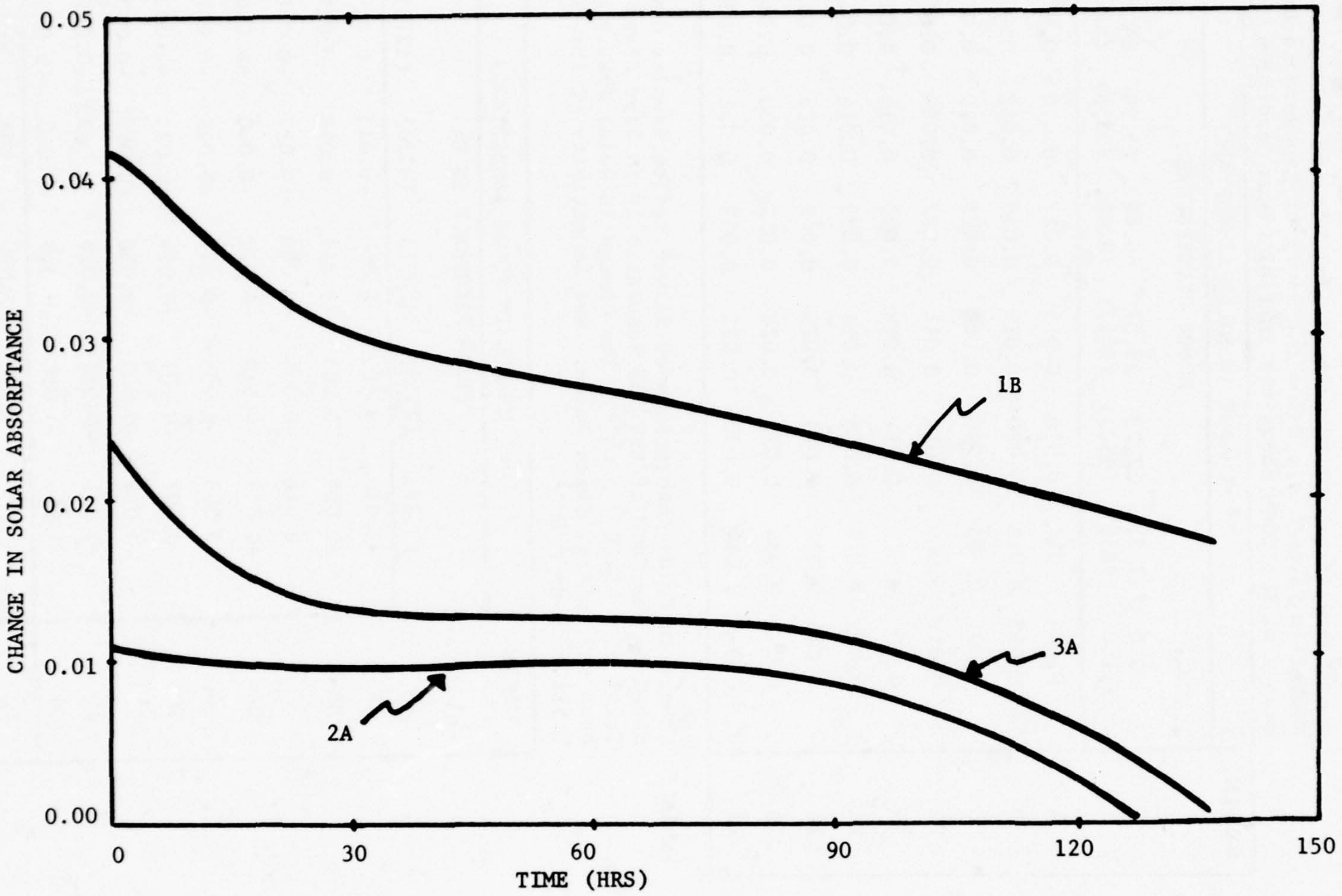

Figure 2 Change In Solar Absorptance Of Contaminated (CVCM From RTV-560) Silver-Teflon When Exposed To No Radiation (3A), X-25 Solar Simulator (2A, 2.32 ES), And Vacuum Ultraviolet Radiation (1B, 2.74 EUVS, 147 nm).

Table 6 Change in Solar Absorptance of Silver-Teflon Samples Contaminated by the CVCM of RTV-560 and Exposed to no Radiation (3A,3B,3C), Solar Radiation (2A,2B,2C 2.32 ES), and to a Xenon Lamp 147 nm (1B 2.74 EUVS; 1A,1C 0.062 EUVS). The Initial Deposition on the TQCM was 4.46×10^{-5} g·cm^{-2} and After 85.41 Hours 4.44×10^{-5} g·cm^{-2} Remained. The Change in Solar Absorptance is From the Contaminated Condition Zero Hours Radiation.

SAMPLE	CHANGE IN SOLAR ABSORPTANCE		
	HOURS OF EXPOSURE		
	15.0	65.83	85.41
3A	0.008	0.005	0.015
3B	0.006	0.005	0.009
3C	0.002	0.010	0.020
2A	-0.009	-0.007	-0.006
2B	-0.005	-0.005	-0.008
2C	-0.007	-0.004	-0.009
1A	0.003	-0.005	0.004
1B	-0.001	-0.002	0.001
1C	0.007	0.011	0.009

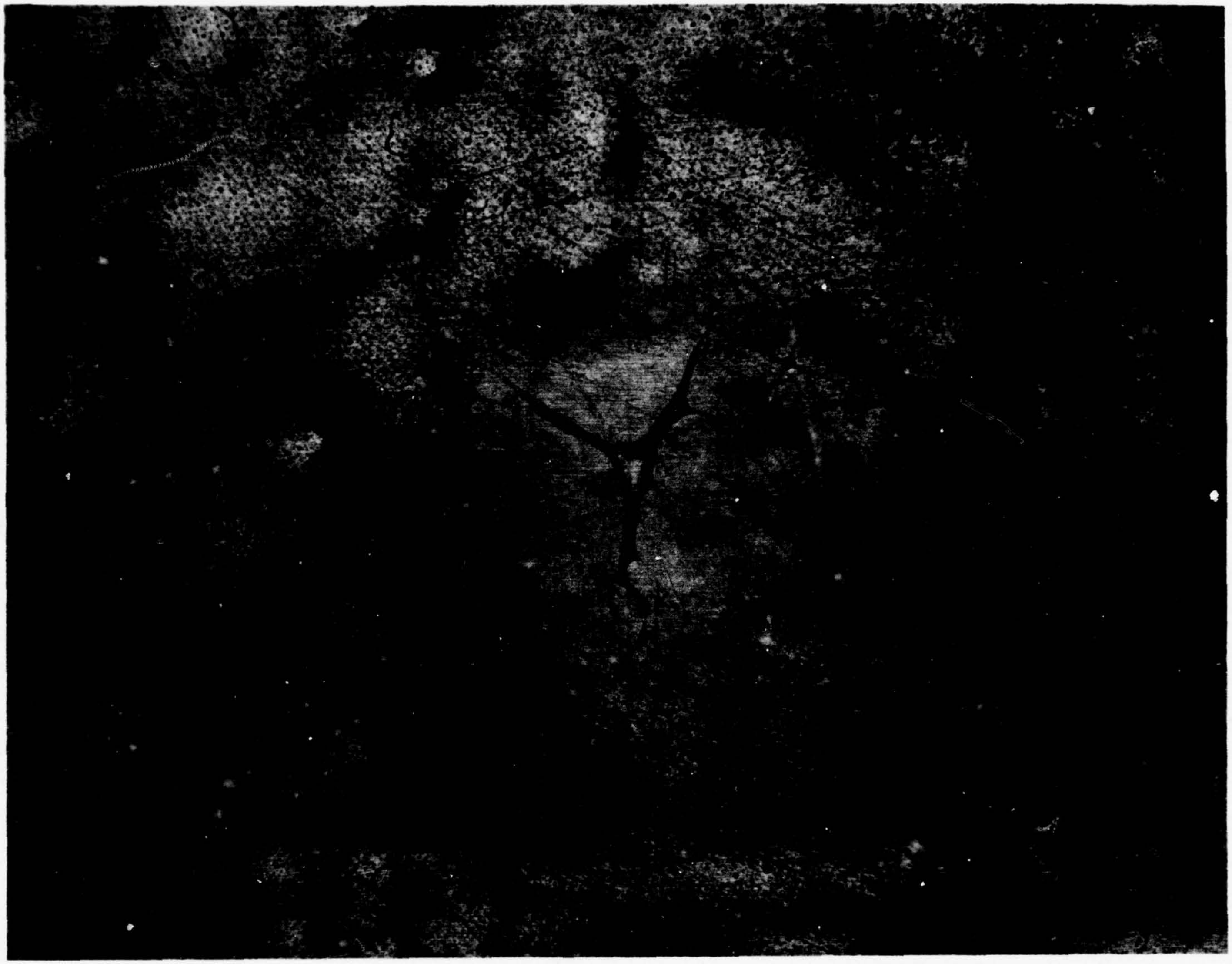

Figure 3 Photograph of the silver-Teflon sample 1C (area to the left of center), 1B (center area), 1A (area to the right of center) contaminated by the CVCM from RTV-560. Sample 1B was exposed to xenon vacuum ultraviolet radiation, 2.74 EUVS (147 nm); 1A and 1C were exposed to 0.062 EUVS.

1B is the area in the center, and 1A is the area to the right of center. It appears that the intense vacuum ultraviolet causes the CVCM to collect in large droplets, effectively clearing the surface around it. The CVCM that remains after removing the samples from the vacuum chamber was not a uniform film but consists of various size droplets. Figure 4 shows a photograph (22x magnification) of sample 2C (area to the left of center), 2B (center area), and 2A (area to the right of center). These samples were all exposed to the X-25 solar simulator (2.32 ES). The clear area to the extreme right was that part of the sample which was under 3C. The vertical streaks were from an accidental brush by a gloved hand. Notice that the cross hatched area just to the right of center is similar to that found on sample 3A. Figure 5 shows a photograph (22x magnification) of sample 3C (area to the left of center), 3B (center area), and 3A (area to the right of center). No radiation was applied directly to this sample however some of the X-25 light can just strike the extreme left side of sample 3C. The spider web character of the CVCM on these samples differs from the droplets found on the samples irradiated with vacuum ultraviolet. Figure 6 shows a photograph of the control sample.

Table 7 presents the data for the change in α_s for a deposition level of $9.67\mathrm{x}10^{-6}$ g$\cdot$cm^{-2}, the RTV-560 reached a maximum temperature of 48°C. No reemission of the CVCM was measured and the silver-Teflon samples did not reach a temperature above -40°C for the entire test. Once again, the data does not show any strong trends. The irradiated samples, including 3A, 3B, and 3C which were exposed to the krypton lamp, did not show any different changes in α_s than the samples 2A, 2B, and 2C which were not exposed to any radiation. When the samples were brought back to room temperature, 58% of the CVCM had been reemitted. Visual inspection of the samples did not show any significant characteristic.

Table 7 Change in Solar Absorptance of Silver-Teflon Samples Contaminated by the CVCM of RTV-560 and Exposed to a Krypton Vacuum Ultraviolet Lamp 124 nm (3A,3B,3C), no Radiation (2A,2B,2C), and a Xenon Vacuum Ultraviolet Lamp 147 nm (1B, 2.74 EUVS; 1A,1C 0.062 EUVS). The Initial Deposition on the TQCM was $9.67\mathrm{x}10^{-6}$ g$\cdot$cm^{-2} and no Reemission was Measured. All the Columns Show The Change in Solar Absorptance From the Initial Clean Value.

SAMPLE	CHANGE IN SOLAR ABSORPTANCE			
	HOURS OF EXPOSURE			
	0.00	3.67	21.17	64.76
3A	0.005	-0.001	-0.001	-0.003
3B	0.010	0.004	0.005	0.004
3B	0.013	-0.001	-0.002	-0.001
2A	-0.001	-0.010	-0.017	0.002
2B	0.008	-0.007	-0.012	0.003
2C	0.007	-0.015	-0.011	-0.005
1A	0.007	-0.012	-0.015	-0.015
1B	0.011	0.002	-0.012	-0.009
1C	0.003	0.004	-0.007	-0.010

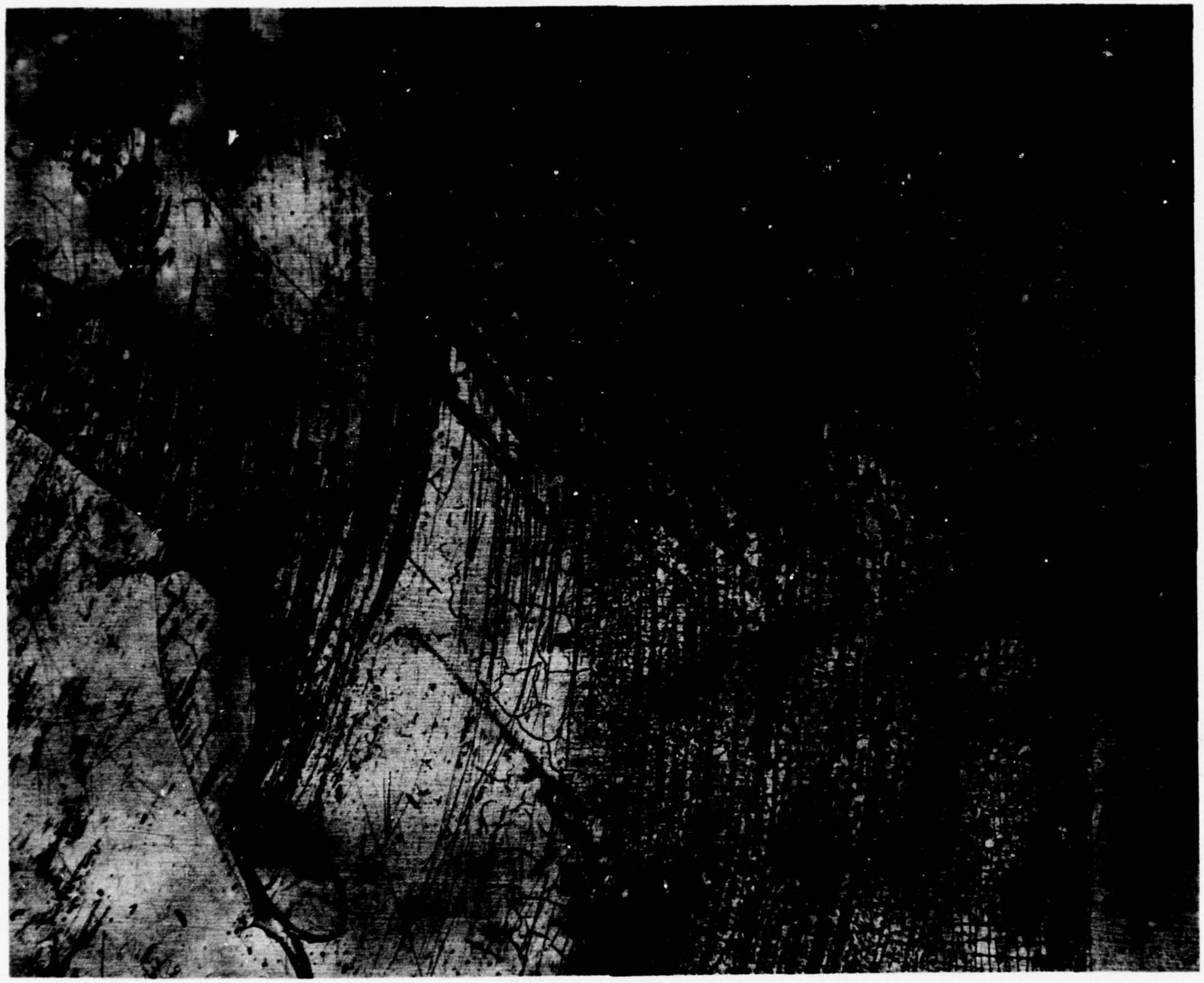

Figure 4 Photograph of the silver-Teflon sample 2C (area to the left of center), 2B (center area), 2A (area to the right of center) contaminated by the CVCM from RTV-560 and exposed to 2.32 ES. Vertical streaks are from an accidental brush by a glove. The clear area to the extreme right was that part of the sample covered up by sample 3C.

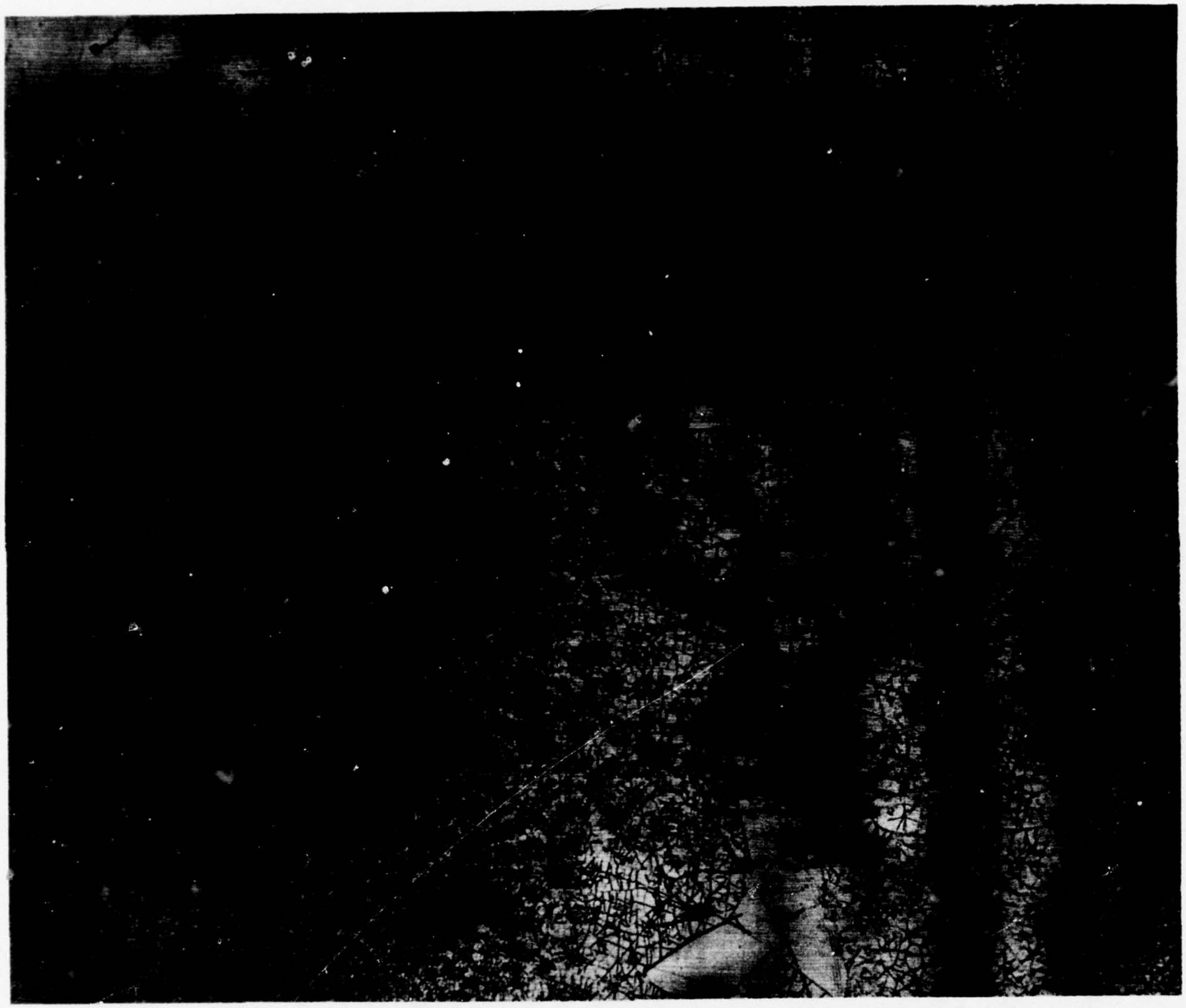

Figure 5 Photograph of the silver-Teflon sample 3C (area to the left of center), 3B (center area), 3A (area to the right of center) contaminated by the CVCM from RTV-560. No radiation was applied directly to this sample, however some of the solar (2.32 ES) can just irradiate the extreme left side of sample 3C.

Figure 6 Photograph of the silver-Teflon control sample.

5.0 CONCLUSIONS

The stability of Ag/FEP to a vacuum environment and solar radiation, especially vacuum ultraviolet wavelengths, up to 370 EUVSH was verified. Although an undetermined geometrical factor produced solar absorptance values differing from the nominal 0.08, the sensitivity and repeatability of the instrumentation and analysis techniques were sufficient to determine a change of α_s by 0.01.

Temperatures below -40°C were necessary to inhibit significant reemission of the CVCM from RTV-560. The CVCM from a fresh RTV-560 source almost entirely reemits when the contaminated Ag/FEP reaches room temperature. RTV-560 sources that are used repeatedly produce a CVCM that will remain on the surface at room temperature, for one case 42% of the CVCM remained. The CVCM from RTV-560 is colorless and does not darken when exposed to solar radiation up to 2.74 EUVS for 370 EUVSH.

The change in α_s is not a linear function of the amount of CVCM. The major increase in α_s occurs for CVCM at least as small as a 28 nm equivalent film. Increasing the surface density of CVCM by a factor of 13 only increases the change in α_s by a factor of 2. An equivalent film of 370 nm only increases α_s by about 0.04. The solar absorptance of the contaminated Ag/FEP is not affected by solar radiation (wavelengths greater than 250 nm, 313 ESH) nor vacuum ultraviolet line emission (147 nm, 370 EUVSH; 124 nm, 82 EUVSH).

The CVCM from RTV-560 that remains on the Ag/FEP surface at room temperature is deposited uniformly in small droplets. The droplets can combine occupying a smaller surface area then the sum of the individual droplets. Intense vacuum ultraviolet enhances the formation of very large droplets. Thus, an initial increase in α_s can be decreased by both reemission of the CVCM and by large droplet formation reducing the effective contaminated surface area.

SESSION VII

PANEL DISCUSSION

THE CONTROL OF SPACECRAFT CONTAMINATION -- WHERE ARE WE GOING?

E. N. BORSON

MATERIALS SCIENCES LABORATORY

IVAN A. GETTING LABORATORIES

THE AEROSPACE CORPORATION

The last conference exclusively on the subject of spacecraft contamination that I attended was held in 1969 as Aspen, Colorado. A review of the program from that conference shows that most of the topics discussed then were also discussed here in Colorado Springs, nearly nine years later. Therefore, it seems appropriate to spend some time reviewing where we are and discussing where we are going with respect to spacecraft contamination control.

The NASA Contamination Control Handbook(1) defines "contaminant" as "any material, substance, or energy which is unwanted or adversely affects the contaminee."

Because this definition can include a wide range of contaminants, it would be worthwhile to eliminate some types of control activities that are already adequately covered by other groups. For example, radio frequency interference could fall within the above definition of a contaminant, but it is typically considered as a separate technical specialty.

Background radiation of other types is of importance to the accomplishment of space missions. For example, the use of magnesium alloys containing thorium 232 may result in unacceptably high levels of background gamma radiation for some scientific experiments. Other potential gamma sources include potassium 40 in potassium silicate paints and uranium 238 found in some glasses. This can affect the selection of materials for use with some experiments.

Spacecraft contamination control was derived from the technologies developed for aircraft and missile systems. Fluid systems had to be free from particulates that could damage components; liquid and gaseous oxygen systems had to be free of materials that could react with the fluid; and a "visually clean" environment was maintained for good housekeeping. Procedures and equipment were developed to control the particulate environment, and instruments became available to monitor the environment. It would appear that the control of particulate and organic contaminants in fluid systems are, for the most part, adequate to meet the needs of spacecraft systems.

More stringent cleanliness requirements resulted from the needs of components using high speed bearings and the manufacture of miniature electronics components. The technology for these areas of contamination control appear to be satisfactory to meet the needs of spacecraft systems, although all the problems have not been solved.

During orbital operations, it soon became apparent that there were additional types of contamination problems. Spacecraft windows have become clouded; thermal control surfaces have degraded at higher than anticipated rates; and, particulates around spacecraft have appeared as false targets for star sensors.

Thermal-vacuum tests on spacecraft and components revealed large quantities of outgassing materials that condensed on cooler surfaces. Vacuum bakeout of components was initiated to reduce the condensable products, but this was not always satisfactory. Screening tests were initiated to help select materials for minimum outgassing, and some new materials were formulated using specially processed, low-outgassing constituents. We now have an ASTM standard screening test for materials(2), and most spacecraft programs exercise controls on the use of materials. The move towards the use of the Space Shuttle System is resulting in more programs now employing the same criterion as is used in the NASA Space Shuttle specification for vacuum stability of polymeric materials.(3)

The typical screening test criterion is less than 1% of TML (total mass loss) and less than 0.1% CVCM (collected volatile condensable material). This provides the type of quantitative requirement that is needed for inclusion in contract work statements and for the initial selection of potentially satisfactory materials. I emphasize "initial selection" and "potentially satisfactory" because this is just the first step in the selection of materials. The functional performance of materials, including contamination, often requires additional tests on materials and components. These additional tests are used to provide information on the performance of materials for specific applications. These functional tests may be tailored to the use in one system or may be more general in nature. Final proof of satisfactory material selection and processing usually occurs during ground thermal-vacuum tests, or, unfortunately, sometimes not until in orbit.

Waiting until a system is in orbit to have some confidence in the performance is not the ideal approach. Designers and systems engineers want to know the effect of using specific quantities of known materials under the predicted temperature environments.

The large number of papers on modeling presented at this conference is evidence of the importance of providing engineers with quantitative predictions of the contamination on spacecraft systems.

I have formulated a list of topics and added some comments that I hope will serve as a basis for discussions during this morning's session.

1. Standards and Requirements
2. Cleaning
3. Ground Operations
4. Contamination Monitoring on the Ground and In-Flight
5. Rocket Motor Plumes
6. Modeling
7. Systems Engineering

Standards and requirements are closely related subjects. It is necessary to define the required cleanliness and to have suitable techniques to verify that the requirements have been achieved. Some requirements state that the components shall be clean but do not define "clean." "Visibly clean" is being specified, but this requires well defined procedures. Other requirements have merely specified "Class 100,000" or "Class 10,000" environment per FED-STD-209.(4) It is important to distinguish between the "Class of a clean room" and the "Class of the environment." FED-STD-209(4) defines the general requirements for a clean room, and additional requirements are defined in references 5 and 6. A clean room class is based on the design, construction, and operating procedures. In addition, the actual cleanliness can vary over a wide range depending upon the number of people in the room and the types of operations being performed. For example, a Class 10,000 room can provide a Class 5,000, or even a Class 100 environment, when appropriate procedures are used.

The significance of the above is that it may be necessary to specify the required environment in addition to the class of clean room. For example, a system that has been operating in a Class 100,000 clean room may be exposed to no greater than a Class 10,000 or 5,000 environment for most of the time. If a Class 100,000 environment is specified and maintained, the system may not achieve the required cleanliness levels. It should be noted that standard HEPA (high efficiency particulate air) filter(7) provides Class 100 or cleaner air.

Although it is necessary to specify the work environment, the primary goal is the maintenance of a clean spacecraft rather than a "clean room."

The procedures being used in a clean area can be much more important than the design of the room.

One area of extreme concern for many space system applications is that clean room standards do not consider molecular contaminants that may deposit onto exposed surfaces.(4,5,6) A review of additional references on contamination control specifications and standards(8,9) also do not appear to include molecular contaminants.

This includes outgassing from materials and dioctylphthalate (DOP) used to test clean rooms and HEPA filters. Liquid DOP is atomized to form aerosol droplets of approximately 0.3 μm in diameter. Holes in the filter and leaks in the system can then be detected using a standard particle counter. Unfortunately, DOP can be a contaminant, especially for optical surfaces.

Clean room and filter standards, such as references 4 through 7, should be revised to incorporate controls on molecular contaminants because many applications of clean facilities do not require controls on molecular contaminants; therefore, the standards should contain the necessary options for alternate verification techniques. For example, the NASA Johnson Space Center allows the use of a probe and particle counter to scan filters for defects.(10)

There is a definite need for quantitative descriptions of surface cleanliness. The current approach is to use MIL-STD-1246A(11) or NASA SN-C-0005(12) to describe particulates and NVR (non-volatile residue) on surfaces. These standards define the numbers of particulates per unit surface area as a function of size. One drawback to requiring a specific cleanliness level per MIL-STD-1246A or SN-C-0005 is that it becomes necessary to measure both the numbers and sizes of particulates to satisfy the letter of the requirement. This is difficult because a spacecraft usually cannot be cleaned and verified by the standard procedures used for small components. For components, a typical procedure is to flush them with solvent, collect and filter the solvent, and then count and size the particles that have been removed. The solvent flushing technique is not practical for the total spacecraft, and it only measures what has been removed from the surface, not what remains on the surface.

Photographic techniques have been used for non-contact or limited contact with a surface.(13) In addition, techniques such as vacuuming surfaces and the use of pressure sensitive adhesive tapes to remove particulates have been used. Each of these techniques has limitations.

Witness surfaces that are kept with the spacecraft and are removed for measurement on a scheduled basis provide an additional approach to monitoring cleanliness without having to contact sensitive areas. This requires that the witness surfaces be exposed to exactly the same environment as the spacecraft. The human element enters into the measurement because it may not be possible to verify that the witness surfaces are not given special treatment during the various spacecraft operations. Workers may treat the witness surfaces very carefully while leaving fingerprints on the spacecraft surfaces.

For many components, the cleanliness can be evaluated by measuring a quantity related to the function of a component. For example, the cleanliness of optical and thermal control surfaces can be evaluated by measuring their performance. Because it may not be convenient to measure the surfaces directly, optical techniques can be used in conjunction with witness plates.

Particulates or non-uniform molecular deposits on surfaces can be detected by measuring the increase in scattered light from highly specular witness plates (such as mirrors). Deposited molecular contaminants can be detected by the increase in infrared light absorption on plates used for multiple internal reflectance spectroscopy.(14,15)

Contaminants from rocket motors are still a matter of concern as they were in 1969. Since that time, considerable analytical and experimental work has been performed on bipropellant and monopropellant thrusters, resulting in the development of the CONTAM model.(16) There is a current effort being sponsored by the Air Force Rocket Propulsion Laboratory to revise the model. The Shuttle Orbiter RCS and VCS thrusters were designed to minimize the production of contaminants.

Unfortunately, solid propellant thrusters have not been adequately studied. Several areas need to be studied with analytical and experimental programs. These include the composition of contaminants in the exhaust plume (molecular and particulate) and the motion of small particles in the gas plume.

Another aspect of modeling includes the total spacecraft system in flight. Design studies have been performed in support of the Space Shuttle Orbiter system, and studies on fundamental mechanisms of contaminant sources and transport are in progress. The prediction of the effects of contaminants is still difficult; however, in spite of the shortcomings of modeling and prediction, the technique is proving to be extremely useful. This is especially true in the identification of potential problems. The accuracies of the techniques are still uncertain, but, I believe that contamination analyses will become as important and standard in the near future as thermal analyses are now.

The systems engineering and management aspects of contamination control are as important as the technical aspects. It may be technically possible to achieve a particular objective, but it is necessary to consider cost. This gets back to defining requirements. A cleanliness requirement that is more stringent than necessary for mission performance can result in higher program costs. Requirements that are deficient can result in premature failure and performance degradation that can also increase costs. The cost aspect may become more important in the Space Shuttle era when anything that affects ground turn around times will also affect costs.

Because contamination control involves many different technologies and affects systems from design through flight operations, management at the Project Office level becomes more important.

In closing, although the titles of the presentations and the subject matter of today's conference appear similar to those of nine years ago, there have been significant accomplishments and contributions to spacecraft performance.

REFERENCES

1. Sandia Laboratories, Contamination Control Handbook, NASA CR-61264, 1969 (NASA Marshall Space Flight Center)
2. ASTM E595-77, Standard Test Method for Total Mass Loss and Collected Volatile Condensable Materials from Outgassing in a Vacuum Environment, American Society for Testing and Materials, Annual Standards, Part 41
3. SP-R-0022A, General Specification, Vacuum Stability Requirements of Polymeric Material for Spacecraft Application, NASA Johnson Space Center, 9 September 1974
4. FED Std. No. 209B, Clean Room and Work Station Requirements, Controlled Environment, April 24, 1973
5. T.O. 00-25-203, Technical Order, Contamination Control of Aerospace Facilities, U.S. Air Force, 1 December 1972; Change 1, 1 October 197
6. Air Force Manual 88-4, Chapter 5, Criteria for Air Force Clean Facility Design and Construction, 13 November 1964
7. MIL-F-51068C, Military Specification, Filter, Particulate, High-Efficiency, Fire Resistant, 8 June 1970
8. Jan Gustavsson, Survey of International Standards in the Field of Contamination Control, Proceedings, 3rd International Symposium on Contamination Control, Copenhagen, 1976
9. Susuke Mikami, Systemization of Specifications and Standards on Contamination Control, Survey Report, Proceedings, 3rd International Symposium on Contamination Control, Copenhagen, 1976
10. JSCM 5322, Rev. A, Contamination Control Requirements Manual, NASA Johnson Space Center, December 1974
11. MIL-STD-1246A, Product Cleanliness Levels and Contamination Control Program, 18 August 1967
12. SN-C-0005, Specification, Contamination Control Requirements for the Space Shuttle Program, NASA Johnson Space Center, March 1974

REFERENCES (Continued)

13. O. Hamberg, Photographic Measurement of Particulate Surface Contamination, Space Simulation, Proceedings of the 7th Space Simulation Conference, NASA SP-336, U.S. Government Printing Office, 1973

14. J. G. Pipes, et al, Spacecraft Test Chamber Contamination Study, USAF/NASA International Spacecraft Contamination Conference

15. ANSI/ASTM E573-76, Standard Recommended Practices for Internal Reflection Spectroscopy, American Society for Testing and Materials, Annual Standards, Part 42

16. R. J. Hoffman, et al, Plume Contamination Effects Prediction, the CONTAM Computer Program, Version II, AFRPL-TR-73-46, August 1973

J. DAUPHIN (ESTEC, Netherlands) - European Contamination Concerns

First, I would like to thank the management of this symposium for giving me this occasion to explain what we are doing in Europe on the problem of contamination. This presentation has been called the European Contamination Program. I don't like this title. I don't know what it means exactly. Is Europe contaminated or is the United States contaminated? I don't know. Anyway, in order to understand the future you have to know what happened in the past. What I'm going to show you is what we have done and how we have been brought to study this problem of contamination. In fact, in the beginning our organization was devoted only to scientific satellites. We had our first contact with contamination in the case of the TD satellite, which was a UV astronomical satellite.

On this occasion we had our first contact with Goddard Space Flight Center, JPL, etc., because prior to this time we were sure our satellites were totally immaculate and now we had to learn something; so we learned from them. This brought us to the use of the micro VCM system. We installed this system and we took precautions from the beginning to be compatible as possible with the American test method. As you can see (Figure 1) we published the first issue of our specification on the micro VCM method on September 1971. This method remains in use since that period. It has been used in the material selection process on scientific satellites. I can site ESRO IV as a satellite in which this process was used (ESRO IV was a satellite used for astronomy at this time but with a mass spectrometer for measuring density and composition of the atmosphere). After that, we have used this system (VCM) constantly. We also began some cleanliness activities on the ground because careful selection of materials alone is not sufficient to insure spacecraft cleanliness. We had to look also at the ground operations. We have utilized mainly infrared techniques first with crystals which would be exposed at the same time as the spacecraft during operation and test, and after that with wipes and with witness plates, where we can concentrate the deposit which is a bit more efficient.

Now you have to understand that Europe is not like the United States--a country, so in place of the two labels you have for national organizations and industry, we have three. We have an international organization, ESA, and we have a national organization in at least the main countries: France, Germany, and Italy. We have to treat many problems through these organizations so we have three levels of organizations. Industry was also concerned at the time by the contamination problem and you see here (Figure 1) a list of companies who did something on contamination during this period. Particularly to be sited is the work of MBB who was the prime contractor of ESRO IV at the time. They were the first ones in Europe to make a model of the gas cloud around the spacecraft and they did so with a reasonable amount of success. Also, the work of DFVLR on the satellite HELIOS, which was in fact not a real satellite but a sort of probe and was very near the sun, raised some interesting problems on cleanliness at high temperatures. So this is the follow-up on the history we have had to coordinate and we have a greater need in fact in Europe to coordinate because we are many countries.

We had our first coordination with the United States when we led some round-robin tests on the VCM system, the results of which have been published by John Park of Goddard Spaceflight Center. After that we conducted some coordination experiments in the space materials activity in Europe. We have organized a system of data exchange for micro VCM results. We have also had a round-robin which was devoted not only to the VCM technique, but also compared the micro-VCM technique to the balance methods. These results were published at the Nineth Space Simulation

Conference. So finally we arrive at what is a bit more recent (See Figure 2).

Now we have on practically all our scientific or application satellites (because in the meantime our organization has switched also to application satellites) special cleanliness measures. We also now have special cleanliness problems. GEOS, for example, was the first satellite to have a full cleanliness program because this satellite was devoted to an extremely accurate class of measurements and had to be just so. Now it's on orbit and it's working. RBB, a joint program with NASA, has followed the same policy. METEOSAT. I will comment later on it; I've devoted one full slide to that one. On OTS, a communication satellite, the problem of contamination is limited normally to the radiators of the traveling wave tubes (TWT). We have also tried to develop a European specification system to formalize the cleanliness policy.

We published specification QRM-02T, which was rewritten at the time of the issue of the ASTM #595-77 in order to make all of the nomenclature parallel and compatible. Specification QRM-05 represents our specification of cleanliness of the ground operation by taking wipes and so on, so this was also formalized. We have specifications which are devoted to material selection before a project comes. We have also a specification devoted to the operation of the clean rooms and to cleanliness control in general. This is in particular specification QRA-23 which in principle covers all the aspects of contamination from the beginning of satellite construction through launch. We have also looked at the question of particulate fallout. As Gene Borson was saying, we are not very happy with the Federal Standard 209B because it seems to be used mainly as a blessing for some project manager who says everything is alright and working and nothing can happen. That's not really true. So we are looking at the particle fallout measurements mainly by a method of light diffusion. On this we are helped mainly by the Scandenavian Air Systems Company as they are also working this matter. We have now recorded a number of contamination cases either during tests or in space. This has been extremely useful because it's the only way that you can convince a project manager that a contamination problem exists. And in fact, we have had some visible contamination during the GEOS qualification model which has helped in finding a solution later. Also a note here on METEOSAT. You will see later that on METEOSAT we have an example of contamination in space which has been corrected. We have recent information about a French experiment on the Russian satellite, CYGNE 3. The experiment is a UV spectrometer which was sent into space and has stopped operation because it was fully contaminated. We think that the main cause of contamination is the lack of feeling by people not directly engaged in this type of work so they just don't care. They just don't take the necessary precautions.

These are our current projects (Figure 3). Most of these projects are following policies which have been established previously for similar satellites. The French satellite, SPOT, which is a satellite for earth observation will probably follow all procedures set up for METEOSAT. On the space telescope we again have a joint project with NASA. This program will be run stricter than GEOS policy because there are some cryogenic optics and the problem is a little more difficult. OUT of ECLIPTIC is also a joint program and is following the ISEE-B policy. We have also some new requirements. For example, in the case of EXOSAT, which is a x-ray astronomy satellite. It has an x-ray reflecting surface which is probably extremely sensitive to contamination. But we do not know a lot about contamination on x-ray telescopes for the moment. In the case of Spacelab we are engaged again in a joint program and here we are following Shuttle policies. We have been faced with the new problem of reuseability and contamination on the ground, etc. EOCS is a satellite full of sensitive optics and spectrometers to look at the radiation coming up from the earth. Surface cleanliness control and checking continues. It is now a common practice in our house and in most of our contractors for all thermal vacuum tests to achieve a cleanliness level of 2 x 10^{-7} grams per square centimeter at the end of a blank test.

Now a development of the test methods we use (Figure 4). Micro VCM. I think no more development is necessary. This method is adopted and an ASTM standard is published. We have had some special requirements for some spacecraft. For example, we have used double pass VCM to look at the effect of vacuum bake on materials in a standard way. We have also had a request from the space telescope that the VCM be run with a -20°C condensation plate in place of +25°C. This is always possible. The balance methods are growing and will certainly grow more and more because the demand of the computer programs. This is the only type of input data that you can reasonably put into a computer program. And in fact we have two systems which are now working or nearly working in effect. Germany as you see (Figure 4) still has a very active laboratory at MBB but DFVLR at the Braunschweig laboratory, which is a national German organization, has stopped activity in this area. Another crucial activity in our sense is the effect of irradiation on the contaminant, but unfortunately, we cannot put a lot of effort on this because these tests are expensive. We have a lack of funding rather than a lack of will in this area. There was an apparatus working at DFVLR in Braunschweig but this has been dismantled.

More development is needed now in the dust fallout area and we are following up on that also. We are trying to prepare a specification but to work with a specification people must understand exactly what a cleanliness level means. So what we

AD-A070 386 AIR FORCE MATERIALS LAB WRIGHT-PATTERSON AFB OH F/G 22/2
PROCEEDINGS OF THE USAF/NASA INTERNATIONAL SPACECRAFT CONTAMINA--ETC(U)
1978 J M JEMIOLA
UNCLASSIFIED AFML-TR-78-190 NL

13 OF 13
AD
A070386

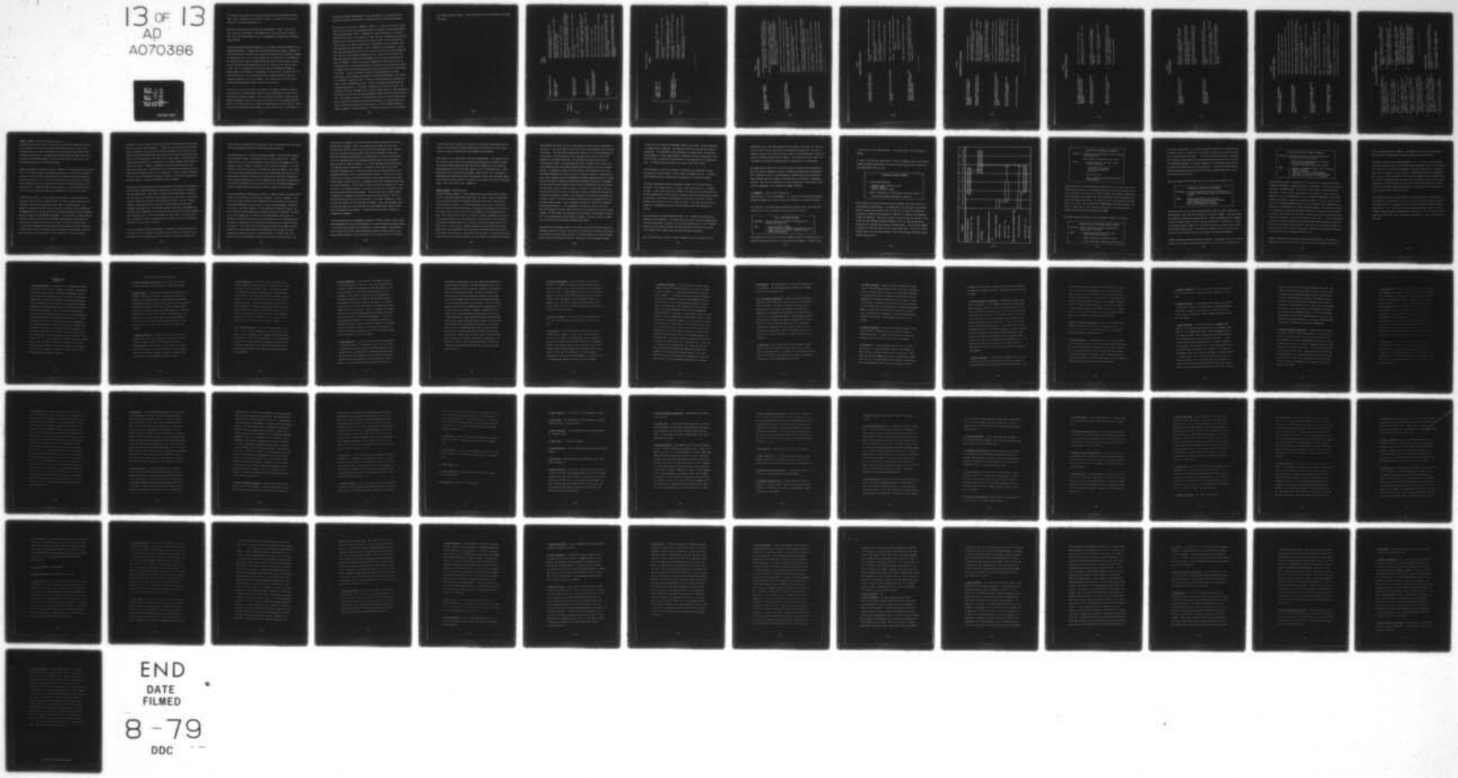

END
DATE
FILMED
8-79
DDC

are trying for the moment is to correlate dust fall values with Federal Standard 209B. This correlation is not valid in all cases. It requires that you fix the condition of air flow, turbulance, etc.

There will be also some tests which will be performed in flight. The only one that I know of, at the moment, on contamination is a test which will be flown on one of the first HELIOS flights to see if contamination is coming from the shroud during liftoff.

We have also developed some new materials but our general policy is normally to use commercial materials. I suppose you are faced with the same problem. Whatever we do in space we don't represent such a market that producers are interested in making new materials for us. We try to get the best out of what exists on the market and for that we use all types of cleaning methods for materials like baking in vacuum. We still develop some new materials, but very few. There are two cases of which I know. One is a competitor for RTV 566 and which is developed in Germany by Wacker-Chemie (D) and there is a development of a white paint, a competitor for our friend S13G-LO that we get either directly from the United States or from the European subsidiaries of these companies. But I think there will not be a very large material development program in Europe in the future.

Now what can I see for the future? We (ESA) will certainly continue our present policy and act as a documentation center for all our contractors and also for the contractors of national programs. We try to provide all projects a clear and well defined cleanliness policy at the start with the use of all our published specifications. But also we will try to tailor the requirements to the end purpose. There is no need for excessive specifications, it is too costly and so we look mainly to tailoring our specifications exactly to our requirements. On the national side there will certainly be some effort in Germany mainly for the Spacelab program.

Now let me pass to the case of METEOSAT (Figure 7), a satellite which had a cleanliness policy from the start aimed specifically at keeping a space facing radiator clean and cooled down to 85°K. Contamination has been considered as a critical problem from the start of this project so there have been cleanliness specifications imposed on the prime and the subcontractor from the start There has been some study contracts with DFVLR for modeling and experimental study on internal radiometer contamination and the effect of this contamination on performance. Here I have given some evaluation of the costs. You see that these costs are expressed in KAU. The AU is the European accounting unit and I think it is now worth $1.20. There has been strict material and contamination control during integration and tests of METEOSAT. We have also required engineering change notices on all the cleanliness aspects covering manufacturing, integration, tests and storage activity. All design tests and the orbital operation have been influenced by the cleanliness requirements. We have had heaters installed for decontamination in space, jettisonable covers, hermetic pyrotechnics and hermeting mechanisms. All of them to be verified by ground testing. A special ejection sequence was instituted in order to avoid contamination on orbit. Special containers were used during the transportation and so on. But still, contamination was observed in space. We launched on the 22nd of November 1977 and after eight weeks the cooler temperature had increased to 91°K and two infrared channels showed a rather big signal degradation. The probable cause was ice contamination on the cool optics of the cooler. This was cured by the heater which had been installed, by a warmup period of 48 hours to 40°C which has been entirely successful. The IR channels returned to normal operation. And this (Figure 8) to close up is just a list of the publication through official channels. These publications are also referenced in the NASA STAR system.

FIGURE 1

HISTORY

AT ESRO (LATER ESA)	- TRIGGERING OF ACTIVITIES	- TD Astronomical satellite (UV astronomy) Contacts with NASA-GSFC and JPL.
	- MATERIALS SELECTION STARTS IN 1968	- Contract with INTA (Spain) to make a micro-VCM system following U.S. drawings. Equipment ready: end of 1969. - First issue of spec QRM-02T: 10-9-1971. - The method is used to select materials for TD and ESRO IV (the latter has a requirement for cleanliness due to a mass spectrometry experiment) and on later spacecraft.
	- CLEANLINESS ACTIVITIES STARTS ALSO IN 1968	- Check in vacuum chambers by IR discs, later by metal foils and wipes. - First issue QRM-05T: September 1972. - Method used on TD, ESRO IV, COS B, ANS (Dutch), SIRIO (Italian) . . . at ESTEC, CNES (F) and IABG (D).
	- A SECOND VCM SYSTEM STARTS IN 1974	- This is the system installed at ESTEC. Design of JPL modified but local geometry maintained.
ELSEWHERE IN EUROPE	- EUROPEAN INDUSTRY AND NATIONAL SPACE ORGANIZATIONS FOLLOW	- INTA (SP) as a contractor to ESTEC. - MBB (D) builds a balance under vacuum. - CNES (F) starts a modified VCM system (not standard). - DFVLR (D) builds many balance systems.
	- THE INVESTIGATION AREA EXPANDS	- MBB (D) as prime contractor of ESRO IV makes a first trial of modelization of the gas cloud around the spacecraft. (1970) - DFVLR (D) works on problems raised by HELIOS: High temperature, cleanliness requirements, conductivity requirements.

FIGURE 1 (Continued)

HISTORY

COORDINATION	- A FIRST ROUND-ROBIN EUROPE - USA TAKES PLACE IN 1971	- Participants are GSFC, JPL, ESTEC (INTA) - only Micro-VCM systems. - A second round-robin is run on to clarify some discrepancies. - Results of both are published by J. J. Park & all at the 7th Space Simulation Conference 1973.
	- EUROPEAN COORDINATION OF SPACE MATERIALS ACTIVITIES STARTS IN JANUARY 1974	- A data exchange system on Micro-VCM (and other data) is established. - A European round-robin is run on Micro-VCM and balance systems. - Results are published by A. Zwaal at the 9th Space Simulation Conference 1976.

FIGURE 2

RECENT ACCOMPLISHMENTS

- **MOST OF THE SATELLITE PROGRAMS REQUIRE NOW SPECIAL CLEANLINESS MEASURES**	- GEOS: High accuracy plasma measurements, conductive surfaces. First satellite to have a comprehensive cleanliness policy in Europe. Launched in 1977. ISEE-B follows the same policy.
	- METEOSAT: Critical surfaces in the radiometer and passive cooler. Specification: less than 10^{-7} g/cm^2 of contaminant. Triggered a study by DFVLR on modelization of condensation and on effects of irradiation on contaminants. First to be equipped of heaters for decontamination (used in orbit January 1978).
	- OTS/MAROTS: Critical surfaces in the radiators (facing solar panels).
- **THE ESA SPECIFICATIONS SYSTEM IS DEVELOPED IN ORDER TO FORMALIZE CLEANLINESS POLICY**	- QRM-02T is revised to make it compatible with ASTM nomenclature.
	- Large experience is gained by the use of QRM-05T in many projects and many simulation chambers: ESTEC, CNES (F), IABG (D).
	- QRM-01 and QRM-16 which cover selection and qualification of materials are now implemented on all projects.
	- QRA-18 (on clean rooms) and QRA-23 (on cleanliness control) are published.
	- Studies have started to cover the "particle fall-out" and correlate it with Fed. Std. 209B which is considered insufficient. ESTEC, ESTL (UK), and SAS (Scandinavia) are working on this.
- **SEVERAL CONTAMINATION CASES ARE RECORDED AND EVENTUALLY CORRECTED**	- During tests on GEOS Qual. Model, on OTS Qual. Model.
	- In Orbit on Meteosat. Corrected by warming up the cooler and cold optics (48 h/40°C).
	- In French experiment on Russian satellite Cygne 3 (UV optics).
	- Cause is mainly the "lack of feeling" for this type of problem by project people and/or contractors.

FIGURE 3

CURRENT SPACECRAFT PROJECTS

- MOST PRESENT PROJECTS FOLLOW-UP CLEANLINESS WISE SOME PAST ONES	- ECS/H.SAT/MARECS are using the experience gained on OTS.
	- SPOT (a French programme by CNES) will utilize METEOSAT experience.
	- SPACE TELESCOPE (European part) is following a stricter GEOS policy.
	- OUT of ECLIPTIC is following ISEE-B policy.
- SOME PROJECTS BRING NEW REQUIREMENTS IN LIGHT	- EXOSAT. Problem of x-ray reflecting surfaces.
	- SPACELAB. - Use of full modeling (Martin Marietta program) - Re-usability and associated ground operations.
	- SEOCS. Satellite full of sensitive optics.
- SURFACE CLEANLINESS CONTROL & CHECK IS NOW A COMMON PRACTICE DURING INTEGRATION AND TEST	- All projects are using QRM-05T particularly during T.V. tests. A requirement is set at 2.10^{-7} $g.cm^{-2}$ during blank test.

FIGURE 4

DEVELOPMENTS OF TEST METHODS

- THE MICRO-VCM HAS REACHED WIDE ACCEPTANCE; FEW DEVELOPMENTS FORESEEN	- Publication of ASTM E 595-77. - Specification QRM-31T which is a "double-VCM" to assess cleanability by vacuum bake.
- BALANCE METHODS ARE GROWING DUE TO THE DEMAND OF COMPUTER MODELIZATION	- VBQC I system in operation at ESTEC. System has provided data for Spacelab pallet. VBQC II including UV irradiation of the sample in development phase at ESTEC. - In Germany MBB balance system still operational but DFVLR stopped all effort in Braunschweig Laboratory. - Little effort in the modelization area (CNES).
- EFFECTS OF IRRADIATION ON CONTAMINANTS IS INVESTIGATED BUT WITH LITTLE EFFORT	- DFVLR Braunschweig also dropped that activity. - DERTS (Toulouse) is working on the subject but not with in-situ contamination. Drawings for a complete equipment exist but funding is lacking.
- MORE DEVELOPMENT IS NEEDED ON THE DUST FALL OUT MEASUREMENTS	- ESTEC intends to prepare an ESA specification to cover this method. - The SAAB(S) equipment is already used at IAL (B), ESTL (UK), and ESTEC.
- TESTS IN FLIGHT WILL BE PERFORMED	- CNES will embark a quartz balance experiment on an Ariane test flight.

FIGURE 5

DEVELOPMENT OF NEW MATERIALS

- THE GENERAL POLICY IN EUROPE IS TO USE COMMERCIAL MATERIALS WITH SOMETIMES A SPECIAL CLEANING TREATMENT	- Selection is made by Micro-VCM tests. - Cleaning methods are frequently bake, vacuum bake, solvent extraction....
- SOME NEW MATERIALS ARE DEVELOPED FOR CRITICAL APPLICATIONS	- Development of a clean silicone adhesive to replace RTV 566 by DFVLR/AEG (D)/WACKER-CHEMIE (D). - Development of a clean silicone white paint by CNES/ASTRAL (F) to replace S13 GLO.
- MANY PROBLEMS ARE STILL SOLVED BY THE USE OF U.S. MATERIALS	- Dow Corning "Controlled Volatility" Silicones (incidentally the removal of DC 6-1102 from the market creates a problem). - General Electric RTV 566/567.

FIGURE 6

FUTURE PROSPECTS

- AT ESA THE PRESENT POLICY WILL CONTINUE TO BE APPLIED AND PERFECTED
    - ESTEC acts as a documentation center, as a consultant to industry on ESA or national projects, as a test house.
    - All ESA projects will have now a clear, well-defined cleanliness policy and will use the relevant ESA specifications.
    - The level of cleanliness will continue to be "modulated" depending on the mission requirements.
- A LIMITED EFFORT WILL STILL BE AVAILABLE FROM THE NATIONAL SPACE CENTERS
    - Germany may increase its effort if first Spacelab/Shuttle flight tests show a contamination problem.
    - France is starting the SPOT program. Cleanliness will be at premium in this application.
    - Other countries have relied and will probably continue to rely on ESTEC for their support in that area.

FIGURE 7

A CASE HISTORY: METEOSAT

- METEOSAT IS THE FIRST EUROPEAN METEOROLOGICAL SATELLITE	- Geostationary orbit with Europe/Africa coverage. - Apogee boost motor jettisoned before operation. - Scanning radiometer working in the visible and infrared. - Infrared detector passively cooled by a radiative cooler (85°K).
- CONTAMINATION HAS BEEN CONSIDERED AS A CRITICAL PROBLEM FROM THE START	- Cleanliness specification imposed on prime and other contractors. - Study contract passed to DFVLR for modeling and experimental study of the radiometer contamination and effects. Cost ∿100 KAU. - Strict materials control and contamination control during integration and tests. Cost ∿100 KAU. - Cleanliness E.C.P. covering manufacture, integration, tests, storage, etc.... Cost ∿500 KAU.
- DESIGN, TESTS, AND ORBITAL OPERATION WERE INFLUENCED BY CLEANLINESS REQUIREMENT	- Heaters foreseen for decontamination in space. - Jettisonable covers, hermetic pyrotechnics, hermetic mechanisms. All of them to be verified by suitable ground tests. - Special ejection sequence when in orbit to avoid contamination risks. - Purge of containers during ground transportation.
- CONTAMINATION HAS BEEN EFFECTIVELY OBSERVED - AND REMOVED - IN SPACE	- Launch took place on 22nd November 1977. After 6 weeks operation, cooler temperature had raised to 91°K - 2 IR channels showed signs of degradation. - Probable cause: Ice contamination of cooled optics and cooler. - Recovery by warming up 48 hours at 40°C entirely successful.

FIGURE 8

LIST OF ESA PUBLICATIONS ON CONTAMINATION

1) ESRO TN 110 - February 1971. A. ZWAAL and J. DAUPHIN, "Screening of Space Materials with the Micro VCM Weight Loss Test."
Presented at 3rd Intern. Conf. of Space Technology - Rome, 1971.

2) ESRO TN 86 - January 1973. J. DAUPHIN, G. SCHAMLE, A. ZWAAL, "Some Contamination Problems in the Astronomical Satellite TD-1A."
Also NASA SP 298 - 1972 - Paper No. 53

3) CNES Simulation Symposium - Toulouse - 1973. J. DAUPHIN, A. ZWAAL, "Le dégazage des Matériaux Spatiaux et sa mesure."
English version - ESRO TN 124 - February 1975.

4) ESRO TM 147 - September 1973. J. DAUPHIN and G. PREMAT, "Contamination risks raised by apogee motors after burn-out."

5) ESRO TM 157 - April 1974. B.D. DUNN and J.A. STEINZ, "Contamination and Heating Effects of a Hydrazine Thruster Intended for Use on Board of the Scientific Geostationary Satellite."

6) International Conference - "Evaluation de l'Action de l'Environnement Spatial sur les Matériaux" - Toulouse - 1974, G. PREMAT, B.D. DUNN, A. ZWAAL, "Risques de contamination provoqués par les moteurs embarqués sur satellites."

7) ESA TN 128 - September 1976, J. DAUPHIN, "Testing Materials for Space Application."

8) ESA TM 158 - February 1977. G. PREMAT, "Etude du dégazage de manchons soudables fabriqués par Raychem."

9) NASA CP 2007 - 1977 - Paper No. 26 - A. ZWAAL, "European tests on Materials Outgassing."
Published also in ESA Scient. & Techn. review (1976) 2 287

10) Materials Workshop - Toulouse - 1977. DERTS/ESA. G. PREMAT, "Mesure continue du dégazage des Matériaux dans le vide."
R. W. DAVIS, "The variation of standard test parameters in the micro VCM test method and the effects on the outgassing of materials."

11) International Spacecraft Contamination Conference - Colorado Springs, 1978, A. ZWAAL, "Outgassing Measurements on Materials in a Vacuum using a Vacuum Balance and Quartz Crystal Balances."

Contractor Report

"Configuration Study of the Meteosat Radiometer and Cooler with respect to the Contamination of Sensitive Surfaces."

ESA Contract Nb 1930/73/CG - September 1973 by W. GANZ, H. SWOBODA, and W. WILKENS - DFVLR.

LUBERT J. LEGER - Gaseous Contamination Concerns

Reiterating what Jacques said, I've enjoyed the conference tremendously and there are two people, in particular, who have worked extremely hard to bring us all together and discuss these common problems and I think that we should give them recognition at this time. Jim Jemiola and Ed Miller have both worked very hard in putting this conference toegether. Let's give them a hand. Thank you Jim - Ed. We certainly appreciate the Academy facilities.

Gaseous contamination concerns is my topic. Whatever I say will naturally be tainted with a lot of Shuttle aspects and hopefully when we get to the question and answer session, you will be able to ask questions about the basic approach and design we have taken on Shuttle. It is only by good constructive criticism that we develop better programs and we are certainly anxious to have an effective dialog in that particular area. In terms of gas transport; however, or gas contamination concerns, I'll just try to quickly make some brief comments about, first of all, theory.

I think from the basics, if we're concerned with viscous or free molecular flow mechanisms, they're fairly straight forward. We're able to handle them until the point where the molecule interacts with the surface or another molecule. For example, in the Shuttle we have return flux which constitutes a fairly significant contamination load for certain types of very sensitive payloads and these outgassing molecules interact with the ambient environment. Cross sections for those reactions are sorely needed so that we can better model these particular interactions and therefore get a better handle on the return flux. No data is available there. I think the basic modeling techniques that have been developed should be usable but we still have a lot of data lacking. Once the molecule hits the surface the whole question comes up of how long does it stick, how does it come off and we get quickly into the area where we need to use quartz crystal microbalances and we get data that we don't really understand. I think this is one area which will become much more important as we get into the Shuttle era because if you really look at Shuttle, a unique difference between the present launch vehicles and Shuttle is the contact of the payload with itself and the bay is much longer in Shuttle than for present day launch vehicles. The payload is in a vacuum chamber (Shuttle Bay) for a period of an hour. Chances for transport via multiple collisions exist and therefore we need to get a good handle on the interaction of the molecule with the surface and the resultant effects on its transport. In terms of source emissions, we've had a lot of discussions yesterday, especially in the areas of outgassing. The basic physics, I think can be separated into two regimes.

One, basically dealing with physical processes which are controlled by diffusion and surface effects primarily dealing or associated with the problems of outgassing under low temperatures. The results of the other area which people are getting into and that's laser radiation where temperatures are high enough to cause actual chemical decomposition and their chemical bonds are broken. This is a totally different regime and may be the reason why we keep talking about TGA versus isothermal vacuum mass loss. TGA has been typically applied to high temperature reactions where decomposition occurs and where you can get some activation energies and frequencies factors that are appropriate for that rnage. If you go down to the low temperature region, isothermal mass loss seems to be the more appropriate technique to use, at least in my mind.

As far as taking the theory and applying it to modeling I think again there has been quite a bit of discussion in the model area but really if you look at both the models, it's my opinion that they both revert to basically the same basis.

Each model has a description of the geometry, a set of viewfactors and then a great deal of assumptions about what the emission characteristics are.

In plume measurements, I think we've made some headway. We've made some measurement of the water plume. The RCS plume area is a more difficult one. I think there has been a lot of data presented at this conference that suggests that the question, as far as Shuttle is concerned, is the 25 and 875 pounders. It is very difficult to get good test data on the ground for those two engines. But I think that basically the modeling activity that we've gone through over the last two to three years has been very effective in pointing out at least order of magnitude type problems and enabling us to better understand the operational characteristics of vehicles and therefore be able to make a better case to program management in terms of changes needed on the vehicle as well as support in certain areas.

As far as measurement techniques are concerned, I think we should just keep clearly in mind that the VCM is a screening type technique. It is not a panacea. It is just a first level evaluation and I think when you start looking at Shuttle with its closed payload bay, the first level cut is just not good enough, especially if you have a very large surface or a very large mass of material involved. We have to get some rather unique data, basically rate data as a function of probably two or three temperatures, as a function of vacuum exposure time and just as importantly we need to know what are the characteristics of the outgassed species in terms of interacting with those sensitive surfaces which are always the point in question. I don't know if we are developing a second level standard test but I know that the last eight months in our particular area the data we've been generating is going back to the old outgassing rates. It doesn't seem to be appropriate to me to standardize right now but we may do so in the future. The question asked is why can't you use previously generated outgassing data that was obtained many years ago. Well, if you understand how complex all these real materials that you have to deal with are, you worry considerably about variations that have occurred in the last several years in the development of materials. Usually the materials have differed, the conditions that the rates were obtained at are not representative of the conditions existing today, and the quantative rates are just not readily available. So it looks like some detailed evaluations of outgassing rates are appropriate. In contrast to what Jacques said in the materials development area, I think he's pointed out one area that seems to be an immediate problem and that's a good white paint is needed. S13G-LO is one option in that area, but again if you start looking at large surface areas in the closed vacuum chamber of the Shuttle bay, low outgassing rates and considerably lower than 0.1% VCM are necessary. They're hard to come by and they're expensive but I think there will be a continuing need for such paints as we get into the Shuttle era and sensitive payloads become more prevalent. There are some other problems equally as important, for example, electrical tie wraps for the payload bay. We use 30 pounds of electrical tie wrap in the bay and it's just about impossible to find a tie wrap that passes the 0.1 percent VCM requirement. People are beginning to see the need for items such as this and there are some organizations which are interested in developing such products. I think they will do so as the interest in contamination increases.

In this particular area of outgassing for Shuttle I'd like to point out that acceptable outgassing rates for the entire payload is a unique consideration again because of the close contact between the payload and its support package. Many payloads have not had to worry about cross contamination between the support part of the payload and the sensors. You now have to do so if you are going to fly in Shuttle.

I think an easy way to negate this problem is by carefully incorporating into the thermal vacuum acceptance program considerations for sufficient time and vacuum exposure to reduce the outgassing rates and make them acceptable.

There remain a lot of areas where we need some measurements. For example, in the RCS areas we are not able to get good ground measurements and through the flight of the Induced Environmental Contamination Monitor (IECM) we will be hopefully getting some data that will shed some light in a lot of different areas. We will be getting a lot of data from that program. There will be a lot of problems in interpreting the IECM data, I'm sure, but hopefully the data will shed some light on these problems and help redirect our efforts in all aspects even down to the theory level. That's all I have to say. Thank you.

RUSSELL RHOADES - Ground Operations

My name is Russell Rhoades. I'm from Kennedy Space Center and I plan to talk to you for a few minutes about ground operations. The topic I plan to discuss with you is primarily the main line Shuttle flow because this area is the one that involves the new facilities. For those facilities that we plan to use for off line work they are pretty much existing. The existing facilities, for you who are not aware of what we have at KSC, are well documented in two documents that we have. One is KSM-14 and the other is a TR-1351. Shuttle contamination control is also well documented in that each element has a control plan by which we control contamination through manufacturing, acceptance tests and through delivery to the launch site. At KSC we have a Shuttle Integration and Turn Around Control Plan. This control plan is KSTSM-09.7 and for any of you that would get with me after this session I would be glad to see that we send you copies. It specifies the type of control that we plan for the Shuttle, for the Oribiter Processing Facility (OPF), which handles the Orbiter in a turn around mode, and in checkout and refurbishment. Of course, at this point (OPF) we will also unload and load payloads that are loaded horizontally. The only payload identified at present to be loaded horizontally is the Spacelab. The contamination control technique that we use is that the OPF highbays are controlled work areas. Now you might ask, "What do you mean by controlled work areas?" The controlled work area is primarily that we purge the entire high bay with a gas system of mainly 100,000 class air at four air changes per hour. In addition to that, we control access to and operations in the area. We schedule operations such that if you are installing a payload or removing a payload, other operations that are contamination producing operations would be stopped, and the area would be monitored with portable contamination monitors to determine that the area has become quiessant and it should be acceptable to open the payload bay and either install or remove a payload. One area in the OPF that's still an open issue area is the need for an enclosure in which to perform this operation of removing and installing a payload. The technique that's presently being looked at is either a gas air curtain, essentially the process that is presently used or an enclosure would be added to that. Presently the plan is to identify the approach before Spacelab Mission 1. The technique we are using for that is to use the Shuttle contamination monitor (IECM) that flies in the payload for the first several flights. To gather data in the payload area we also plan to take samples to determine if the contamination control system is adequate. The next area that I would like to discuss is the pad Payload Changeout Room (PCR).

There has been considerable interest in the PCR in that it's the primary means for installing payloads at the pad. Of course, in the PCR they're installed vertically. The technique of control there, again it's a controlled work area, it has the same controls that we would plan for the OPF. One aspect of this technique, however, is that we do not verify the cleanliness level of area itself. We are controlling it primarily with a purge gas. You might ask, "Well how do we know that area is acceptable?" The technique is that we maintain it visually clean. We use either vacuum systems or a white light approach to maintain its visual cleanliness. The PCR at the pad is purged with 5,000 class air. The change rate is 15 changes per hour. It's HEPA filtered and also we use carbon in the filter system.

The crew module at the pad for access to the Orbiter crew compartment is again controlled in a similar manner. The air supply is 100,000 class air. It again is HEPA filtered and the air change rate is maintained at 23 pounds per minute.

The Orbiter payload bay itself is continually purged in all of these various locations. The technique there is to purge it with 5,000 class air. It's HEPA filtered. It has carbon filters also except at the pad we do not carbon filter it. The only period that we do not maintain a purge on the Orbiter payload bay is during the erection of the Orbiter and integration to the rest of the stack. We have estimated that period will be up to about 12 hours. So an area to look at in the future as a contamination concern is when the Shuttle goes from horizontal to vertical.

Those areas that do contain contamination that are visible would probably get replaced in the payload bay. For what I see in the future as to these capabilities versus the discussions I've heard, I don't see any problem areas. As Mr. Hoffmann pointed out in his paper for those that were fortunate to hear him this morning for the Viking, this technique was used there and used successfully.

One of the areas that is going to require considerable effort is going to be the manifesting of all these multi-payloads and the reason I bring that up is the fact that the concern for the electrostatic contamination possibilities. The need to maintain a moisture level which has been expressed by some organizations versus the concern of moisture contamination of others. So we are going to have to pay a lot of attention to placing the payloads that are compatible in the same mission.

One comment that I would like to make in terms of the paper sessions this week is that I've heard no comments in regard to avoidance techniques other than shields and I would like to hear a little discussion, possibly during the question and answer session about why we haven't considered the use of getters or cryosorbers for that. They are used effectively in vacuum technology so I would like to offer that as a suggestion. That completes my message, thank you.

LT ZLOTKOWSKI - Rocket Plumes Contamination

Good afternoon. I'm Lt Joe Zlotkowski. I'm from the Air Force Rocket Propulsion Laboratory (AFRPL) and I'm here in place of Dan Stewart, who sends his regrets.

The objective of the rocket plume contamination program at RPL is to develop the capability to detect contamination from various space thrusters.

AFRPL CONTAMINATION PROGRAM

OBJECTIVE: Develop capability to predict contamination from various space thrusters.

USES:
- Assess potential problems
- Design thrusters to minimize contamination sources
- Design spacecraft systems to minimize effects
- Solve system problems

This capability will allow us to assess potential problems, to design thrusters to minimize contamination sources, to design spacecraft systems, to minimize these effects, and to solve system problems. The emphasis here is on the system in general.

I'd like to lead off with some history. This is a summary of some of the contamination programs we have done in the past and as you can see they are mostly in the liquid engine data base area.

CONTAMINATION PROGRAM SUMMARY

- o Liquid Engine Data base
  - Monoprop contam production, (JPL)
  - Consett, (AEDC)
  - Biprop contam meas, (AEDC)
- o Model verification for liquids/assess solids and electric
  - Contam analysis/model improvement, (contract)

They include the mono-prop contam production program at JPL, which fired a 0.1 pound Hamilton Standard Engine. The condensation conset program, which had two phases, includes a gas mixture as well as the same 0.1 pound force engine and the bi-prop contamination measurements at AEDC that Dr. Hermann Scott discussed during this symposium. This data is going to be used as part of the model verification for the contaminationcomputer program. This is a road map showing how everything fits together (see roadmap on following page). As you can see CONTAM is going to be the final version of our liquid engine work. I'd like to discuss briefly some of the particular programs. First, the mono-prop propellant contamination program at JPL.

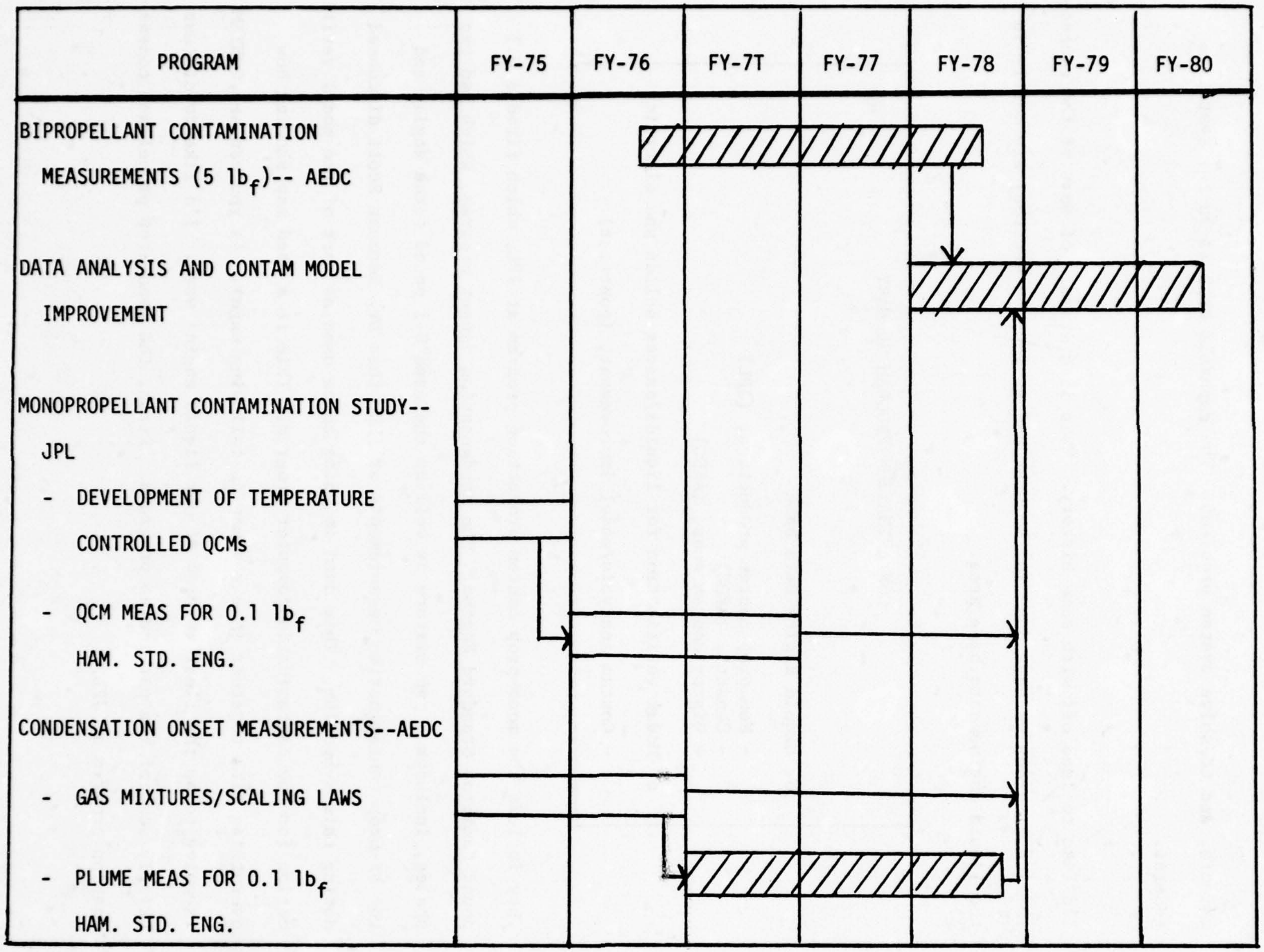
PROGRAM
FY-75
FY-76
FY-7T
FY-77
FY-78
FY-79
FY-80
BIPROPELLANT CONTAMINATION MEASUREMENTS (5 lb_f)-- AEDC
DATA ANALYSIS AND CONTAM MODEL IMPROVEMENT
MONOPROPELLANT CONTAMINATION STUDY-- JPL
- DEVELOPMENT OF TEMPERATURE CONTROLLED QCMs
- QCM MEAS FOR 0.1 lb_f HAM. STD. ENG.
CONDENSATION ONSET MEASUREMENTS--AEDC
- GAS MIXTURES/SCALING LAWS
- PLUME MEAS FOR 0.1 lb_f HAM. STD. ENG.

MONOPROPELLANT CONTAMINATION PRODUCTION

OBJECTIVE: Provide monoprop contamination data for CONTAM verification (JPL)

Verify CONTAM code against JPL data (I/H)

SCOPE:
1. Measure deposition rates over varying thruster conditions
   - propellant water content
   - catalyst bed temperature
   - duty cycle
2. Analyze test data
3. Compare CONTAM model prediction with data (I/H Wax/Davis)

The objective here is to provide mono-prop propellant data for verification of the CONTAM code and as part of this program we did exercise the code using that data as an in-house effort. The scope of the effort included a measurement of deposition rates using QCMs in the JPL Mole Sink. We used different types of propellant varying the propellant water content. We varied the catalyst bed temperature and duty cycle of the engine. And we compared the CONTAM model predictions with data. The results of this study are in the Wax-Davis report which I think most people are familiar with especially those familiar with CONTAM.

The CONSET program (condensation onset measurement) consisted of two parts,

CONDENSATION ONSET MEASUREMENTS PROGRAM (CONSET)

OBJECTIVE: Develop capability to predict condensation of rocket exhaust plume gases

SCOPE:
1. Measure condensation properties of gas mixtures/develop scaling laws
2. Measure condensation in mono-prop plume
3. Verify laws against simulated mono-prop plume

the gas flow region where we are trying to measure the outset of condensation with a simulated nozzle. The objective is to develop a capability to predict condensation of rocket exhaust plume gases. The effort included measurement of condensation properties of gas mixtures and developing scaling laws which will be used in the CONTAM model program, to measure condensation in a mono-prop plume which was 0.1 pound force engine used in the JPL experiment. To verify these laws against a simulated mono-prop plume they went back and used a simulated gas flow to see if our scaling laws were correct.

The bi-prop program which Hermann Scott gave you most of the details on-----

BIPROPELLANT CONTAMINATION MEASUREMENTS

OBJECTIVE:	To provide experimental data for verification of the biprop CONTAM computer model for plume contamination.
SCOPE:	Chamber design/modification/checkout Instrumentation design/acquisition/checkout Engine firings/plume measurements Data reduction/analysis & reporting

The objective here is to provide experimental data again for verification of the CONTAM program. The scope of the effort was to design a chamber. The penze chamber was modified to improve the pumping capacity. Special instrumentation was designed. During the engine firings, the exit ratio was varied 50 to 1 and 100 to 1. We had two different types of injectors, 0° and 45° flush plate. We varied the O/F ratios and we varied the duty cycle. The product was complete analysis of the 5 pound bi-prop, one of the best efforts to date dealing with plume contamination.

Finally CONTAM data analysis and model improvement. I'm going to have to be a little careful here as this is a RFP that has gone out so I can't get too specific about

CONTAM DATA ANALYSIS AND MODEL IMPROVEMENT

OBJECTIVE: Determine the effect of plume contamination on spacecraft mission effectiveness

- Define facility/instrumentation limitations
- Upgrade/verify CONTAM model
- Demonstrate importance for specific systems

SCOPE:

1. Review and assessment (liquid, solid, electric)
2. CONTAM II upgrade
3. Verification against mono/bi-prop data
4. Assessment of system-related CONTAM problems
5. Spacecraft sensitivities to contamination

this particular program. The objective of this effort is to determine the effect of plume contamination of spacecraft mission effectiveness. It's more than just an updating of the CONTAM model. The idea is to find facility and instrumentation limitations. Then to go back and determine to what extent the data is valid, to upgrade or verify the CONTAM model (as you all know the CONTAM model has not been completely verified), to improve its useability, make it easier so that you won't have to be a plume contamination expert to use the program, and to demonstrate the importance of contamination on specific spacecraft systems. The scope of the effort is to review data (flight data and chamber data) and to assess this data in terms of liquid, solid, and electric thrusters. The initial work done by Aerojet Electro-Systems is a beginning. They have done some very basic work. It kind of embarrasses me because the Rocket Propulsion Lab should have done that work about two years ago. That type of work should have been done a long time ago. The electric thruster is a new area that we are starting to enter into. Some work has been done in the past at Fairchild and some is ongoing right now at JPL.

CONTAM II upgraded and verification and increased reuseability of the program----- Nothing more needs to be said about that except that certain models we know are no longer accurate and must be upgraded. The mono-prop and the bi-prop programs are about the best information you are going to get on plume contamination.

Assessment of system related CONTAM problems------- We want to look at specific space systems running through the computer program, assess the impact plume contamination has had on that system and determine spacecraft sensitivities to contamination. This is something we have a void on. CONTAM and rocket plume contamination work goes up to the point where we tell you what is coming out of the rocket engine. Air Force Materials Laboratory knows what their materials are going to do as far as outgassing. But nobody really tells you what's going to happen when the contaminants from your rocket plume deposit them on your particular system components and this is something that we need to look at.

When Gene Borson asked me to participate in this panel he said to say something controversial. An observation. As far as the JPL Propulsion Contamination Experiment Module (PCEM), it's a good idea and I think we possibly may end up having to go into space. But I think there is some preliminary work that needs to be done. Primarily through CONTAM, the assessment of ground data. We may not have to go into space to do this type of work. Then again you may have to. That's undefined at this time.

MARCH 09, 1978
SESSION VII

E. Miller (NASA/MSFC) - The approach for a contamination control on Shuttle is not to impose stringent cross-border requirements, which would be very costly, but to impose requirements that we know from these past experiences that we need and to measure and verify where we have met the contamination control requirements. These measurements will be furnished by the Induced Environment Contamination Monitor during all phases of the Shuttle operation. If we do have problems, we hope to pinpoint the contamination sources during these different phases. And, also to provide data for updating and hopefully improving modeling efforts. We also recognize that we have a further responsibility to disseminate the contamination data to as widely distribution as possible and as quickly as possible. Plan to publish quick-look reports on the order of weeks after each flight and I am not going to make any promises about the further analysis reports that will be coming out later on. I will make mine very brief since we are running late on time. One thing I did want to announce; we have guest sample positions available on the passive sample array for those of you that are interested. Contact me or Roger Linton at the Marshall Space Flight Center. Thank you.

GENERAL QUESTION AND ANSWER SESSION

G. Borson (Aerospace Corporation) - Now would be a good time for some questions, comments, whatever. Why don't we begin.

M. Barsch (AESC) - I had a specific question related that I will address to the group as a whole. It has to do with this dissemination of information which I think everybody acknowledges as being most important and also this problem of having the quick-look information which I think all of us agree would be great, except for one thing--I would like to hear comments. It has been my experience, at least at our company in relationship to other companies, that any time you release a quick-look program it gets cast into concrete and you are held up to hang at a later time because it's in print. Now, how do we get around that problem?

J. Dauphin (ESA/ESTEC) - At least in ESTEC we haven't found a solution for that. We don't publish our data, but we have installed a computer system. All our contractors who want information cannot access directly to the computer, but they have to pass through the material specialist so they give them their problem and get an answer as quickly as possible, which takes a matter of hours normally, but it's filtrated.

L. Leger (NASA/JSC) - I don't know Max, but in terms of the Shuttle Program I think what we see is the release that Ed kind of referred to as a quick-look report. We utilize that means of communicating to the Apollo program and I think everybody took the data in the right light; it was early data, it was preliminary, but it was out and it was to be able to be used by everyone involved. I think we will probably be able to take the same approach in terms of releasing quick-look reports like that and hopefully being able to give presentations to people that are concerned about it and to discuss the data because I think, again to repeat, there will be a lot of data, a lot of complex data that will need a lot of time to unravel.

R. Moss (Ford/Aerospace) - I have a couple questions for Russ first. Who is acting as load master on the Shuttle and assign space to various experiments to be launched, decide which ones are compatible? That's the first question. The second question is; when you have the inevitable contamination experience, who is going to establish who is at fault and who is going to pay for cleaning up everybody elses spacecraft once that fault has been established?

R. Rhodes (NASA/KSC) - I don't know if I can answer either one of those questions, but I will try. The first question was who is going to establish the manifesting, and quite frankly I can't tell you right now, I think that is being worked, but to my knowledge I don't believe it has been firmly established yet. The question about who is at fault if you find that you get a contamination problem, that's part of the reason. As a matter of fact, that is the reason for flying the contamination monitor system that Ed told you about. To try to determine if our operations are effective ground operations and the flight operations as far as that goes in controlling contamination. Now, as far operation, when we get out to the 20th flight, you have an experiment that fails, I guess if you didn't measure the contamination for yourselves, should we try to find out what caused it with the information available, and as far as establishing fault, I don't think that is really a problem.

L. Leger (NASA/JSC) - I think that as far as payload integration is concerned right now, at least before we get out the SPIDPO, at Johnson Space Center the Shuttle Payload Development and Integration Office is taking care of integrating payloads within the Shuttle bay and it appears that the responsibility for compatibility with wing payloads is also beginning to fall upon them. If it does, then we will get involved in terms of a contamination assessment, if you will, from cross-contamination from one payload to another. We talked long about, well, the cross-contamination from one payload to another is the responsibility of the integrating center. So far, the payload we've talked about, at least from a general standpoint, there seems to be a mission where there is not just one integrating center for all the payloads that go on the mission. So, for all those cases it has fallen back on SPIDPO and we are beginning to look at those particular problems. Yesterday, I mentioned that in terms of cross-contamination and responsibility for the cross-contamination there is again SPIDPO asking questions like--okay there is some contract satellites that we want to fly, but their fee is based on their performance and they want to be insured that if there is contamination that occurs on that satellite that they can at least identify where it came from so the fee can be fairly assessed, and I see that there is a need for that, there is going to be a smaller complement of instruments to the IECM and, I think, as far as placing the blame. It's more an assessable fee than placing the blame that I think we will be better off with.

R. Kruger (NASA/Goddard) - If I can go back to the earlier question for a moment. In regard to data, Ed mentioned that he would try to get the data out to the users as soon as possible after the flight. I might suggest that if he could it would be helpful to the users to get data before the flight on the performance of the instruments if you are running things like chamber tests. The users, I think, would get a big leg up if they could get some feel for how the instruments perform before they actually get flight data.

E. Miller (NASA/MSFC) - I don't know if we can promise that or not, Ray. That's an awfully busy period for us, but we will try.

C. Maag (AESC) - I have three specific questions; one to each individual panel member. The first one; I guess to Dauphin. You have a very impressive contamination control program in Europe and Arie Zwaal, and his paper showed that the Chemglaze material (The Chenglaze white), that was going to be used as a primary thermal coating, appeared to be extremely high in outgassing. Other data has shown that it is also extremely susceptible to ultraviolet radiation damage. Is there any plan for changing that coating, or would you care to comment?

J. Dauphin (ESA/ESTEC) - We are putting the situation of the support laboratory versus the project group, and it is always a tricky situation. In fact, the project group has the last word, normally. I could say that when this specific paint was chosen in the laboratory, we were not in agreement with that for two reasons: One is the outgassing you have seen in the curve; the second one is the UV stability which is not very good. Now on the outgassing side, most of the outgassing occurred within the first day. We can say that the day is still already a lot for a mission that is seven days, and our role has been to say to the project manager, this is your risk, you would have one day where your operation will be purging, but it's his job to accept that amount. Second, about the UV, we have run a comprehensive test on this paint to show what was exactly the degradation versus specification, which has been given by the Spacelab people, and we told them this time where you would have to repaint your pallet and he told us we accept it. So, for us, it is difficult to go further away and I agree since you know these people are mainly mechanical engineers; they have the tendency to look more at the practical aspect of this thing. They want to climb on this paint to fit things on it, and I am more inclined to put the mechanical properties at a preminum.

C. Maag (AESC) - The second question I would like to address to Lt. Zlotkowski. Are there any plans for using the 10V chamber at AEDC for a solid motor test?

Lt. J. Zlotkowski (AFRPL/PACP) - There are no plans presently. There were plans in the past, but due to certain constraints we don't have plans in the future. But what the rocket lab is waiting to do at this stage, two things we are waiting for, CONTAM and the assessment of solid rocket motor contamination to see if it is a significant impact to space systems and in the short term we are looking for support from SAMSO SPO's, in particular, to come out and say that they do have a potential contamination problem and that they want to look at a solid rocket motor contamination. That is my position right now--I can't--there are no active plans for a solid rocket motor contamination.

C. Maag (AESC) - Our third question will be addressed to Russ Rhodes. You stated that PCR will have what you call visibly clean contamination checks. We heard a lot in different sessions about the use of ATR. Has there been any thought to using IRS techniques to look at contamination in the PCR?

R. Rhodes (NASA/KSC) - I guess in order to answer that I would say no. And the reason being that first of all its our position to do the minimal effort to reduce cost, as possible, and until you establish that there is a problem in that we don't plan to implement any different technique to try to do better. Now one of the reasons I say that is that the PCR is not really opened to the payload itself, the payload comes in in the canister which again is purged and is removed from the canister in the PCR once you establish the environment in the PCR and open the payload bay to the Orbiter. So we really don't see this as a problem.

J. Dauphin (ESA/ESTEC) - I would like to make a comment on that, since nobody ever commanded this type of panel, to make an offensive statement. I would like the word visibly clean and reasonably clean be crossed out of the space vocabulary.

C. Maag (AESC) - I have one comment for Russ and I will drop that subject. You had a question, I guess of the audience, of people looking at methods of say getters or cryosorbs. I know that there has been suggestions to NASA, not for specific spacecraft, but for a long-term space station program, to be looking at utilizing getters to say collect waste dumps, to look at ionizing the waste dumps to eliminate that type of contamination from getting to primary radiators. Some people have been looking at them.

E. Borson (Aerospace Corporation) - I would like to make a comment, also to Russ. I see a number of payload type requirements that are going to come forth that will ask what is the cleanliness in the PCR before we go into it, and I think this will have to be monitored, checked out in some sort of way as a facility checkout and then I also see monitoring being performed during the payload operations within the PCR. Now that part of it may very well be payload peculiar, but I do see that there will be different operations for different payloads, so I don't visualize the PCR or the Shuttle operations as being the same on every launch. There may be a standard way of doing things and hopefully we will have an idea of how clean the standard way is. But payloads that will come in and ask for something special, I think these will have to be worked on a program by program basis. Any comments?

R. Rhodes (NASA/JSC) - I would like to comment on the fact that I guess we can't see any reason why we should do something in the PCR we are not doing in the payload bay of the Orbiter. Our turnaround plans for the payload bay of the Orbiter is to maintain it visibly clean even though you don't like those words. Now there again, if we find evidence of contamination in there, through visual techniques, we would attempt to clean that either by wipe or vacuum cleaning. These are the techniques we used on Apollo. We haven't heard anything, to date, that says that we should do better than that. For instance, if you have a break in one of those hydraulic lines, and you get hydraulic fluid in there, we are going to clean it up the best we can.

E. Borson (Aerospace Corporation) - Yeah, I'm not talking about accidents necessarily, that will be a problem to assess. If there is an accident, what effect has that had on the payload? I am thinking about standard operations.

R. Rhodes (NASA/JSC) - I understand that if you had an accident you are going to have to go to more extensive cleaning techniques to remove that contaminant, but we don't see why that concentration on the PCR primrarily any more so than any other element of the Shuttle Transportation System. I don't think it's the concentration on the PCR, I think the PCR is just one of the aspects; I think all apsects will be looked at like this one.

J. Dauphin (ESA/ESTEC) - What I criticize in "visibly clean level" is not the level itself because I don't know what it is. Just that.

R. Rhodes (NASA/KSC) - I understand, and my answer to that really is that we don't intend to take any special monitoring equipment, that's what I mean by visibly clean. If you don't see it, we are not going to worry about it until someone establishes that's not good enough.

L. Leger (NASA/JSC) - I think you have got to remember that right at this point in time we've got a set of requirements that Russ and I are implementing at KSC. Those requirements based on a Shuttle Program. Many, many missions, and what drives KSC, is the frequency in use of a particular requirement. I think they have been doing an amicable effort in trying to implement the requirements we have given them. The IRS requirements that Carl talked about I think falls in a category of a specialized requirement rather than a general requirement. Obviously, you're not going to have a KRS crystal riding through the ground turnaround operations if its not needed, and if you talk about a general requirement, Russ and them would be doing that. Hopefully, special requirements, the KRS crystal, the special witness plates, or the special particle measurement, will be able to be worked out with KSC for that specific mission. They are ready to work with each individual payload on that particular basis. But what drives the general facilities is the general requirement and what drives the specific implementation of those requirements is the frequency of need. That is why you guys, payload people in particular, have to start talking to KSC about your needs in the contamination area, not just the mechanical requirements, your electrical requirements, but also your contamination requirements because it is that upon which KSC bases its approach in implementing the various requirements.

E. Borson (Aerospace Corporation) - I might add that to that in that when I looked at these things, whether it be the Orbiter or the PCR or other facilities, I've looked at the point of view that regardless of what the requirements are, will it do the job we want it to do, even if we have to implement some special additional type of controls. And so far, I think for the most part it looks like it can be done. There are certain areas that need to be looked into, but I think that people should be aware that there will be some variation from payload to payload and hopefully that standard requirement will be adequate for the great majority of payloads.

L. Leger (NASA/JSC) - One more comment, Gene, in terms of somebody suggesting shrouding as a protective means for contamination. It's a very expensive approach, especially if you are talking about a large program like IUS, for example, or the specific satellites that fly IUS. It is a very expensive flight hardware development program. I think it behooves us to look in a great amount of detail using whatever analysis tools we've got and whatever data or test data that we have in assessing the contamination problem insuring that we do need shrouds when you're flying in Shuttle before going out and developing them. It's a difficult problem to address because of the shroud; it's going to have to be developed now, and hopefully, in the near future with some of the base studies that are being done now, that we can better define when and when you don't need a shroud.

A. Hoffman (JPL) - I guess I'd like to address this to Russ. Would you comment a little bit on what the plans are--cleanliness plans--as they currently exist in between the various flights of the Shuttle and, in particular, the cleaning of the payload liner and will one previous flight contamination problem that we see in one flight would we have to worry about that on the subsequent one?

R. Rhodes (NASA/KSC) - That's a good question, and I guess I tried to answer that before, but apparently not adequately. In turnaround activity we plan to go in and inspect the payload bay after we remove the payload. Now I guess we wouldn't take any special pains about cleaning up the payload bay unless we had evidence that the prior mission in fact did contaminate it. Now, if we know that there is contamination from that payload, then we would do what is necessary as would be pointed out from that payload. There again, that substantiates the requirement for being able to identify the possible contaminant sources from the payload. I would like to point out one other thing about the PCR in the fact that there was a very strong emphasis on putting capability in the PCR to do checkout and servicing. We resisted that heavily in that it complicates the operation of PCR. It takes a long timeline, it adds to the contamination problem, as you well know, and we do have limited capability to do just that in the PCR. Now one of the things we implemented in that exercise was to add a spigot that will allow us to have a purge capability inside the PCR that would - you would have the capability of purging the enclosure within that, if that be necessary. So that it is added precaution that the facility capabilities built in.

D. Smith (HAC) - I am now thoroughly confused about the cleanliness requirements for Shuttle. We have talked about visibly clean and whatever that means; some of the specs say visibly clean or they will call out level 300 per MIL-Standard 1246 or 0005. I don't want to get into a discussion as to whether you can equate those two requirements. One is obviously a very simple inspection procedure in order to quantitize the contamination to prove that you had level 300. Then you obviously have to get in there and take a tremendous number of samples in order to have any statistically valid average. And I am just wondering now what are the real requirements going to be? I have documents that call out level 300. Now if you are going to quantitize it in that way, then you have got to do something to prove it. Also, when we talk about a level A, with respect to NVR, my eyeballs certainly aren't calibrated to see that kind of a level.

L. Leger (NASA/JSC) - I want to apologize for the confusion. First of all, the contamination requirements ought to be reemphasized are basically providing a capability at KSC--okay? If you don't request or indicate to KSC that your payload is contamination sensitive, there may be nothing special done for your payload. That's the first thing that you need to be, is establish a requirement with KSC, say this is a contamination system mission, I need the full requirements for developing the Shuttle system requirements documentation. That documentation does call out once the enclosure in the bay, if I can drop quite a few steps here, is established in a visibly clean level within the bay. The visibly clean level is referenced to us the spec SMC-0005. Gene, you might help me with this. I think it is a visual inspection with the unaided eye with appropriate lighting conditions. That is the consistent level or the level of contamination control that is consistent with a quick turnaround If you need something more quantitative than that, if you need a level 300 again, that's a special requirement. Go to KSC and say I need level 300 requirements on this particular mission and they'll be glad to help you implement that. But not all payloads, in fact, very small portion of our total traffic model, requires a level 300 cleanliness requirements in the bay and if on that basis it is senseless, implement an expensive time consuming procedure for something that is not required by the payload. You've got to remember that this program is flexible. Try to utilize the flexibility.

E. Borson (Aerospace Corporation) - I would like to make a comment on some of that confusion. Confusion stems from the various documents that have been written. The basic Shuttle specs are visibly clean. If you look at the NASA payload contamination requirements and definition group document that they put out, which has not been accepted as a system requirement, that calls out something like the 300A. If you look at some of the DOD documents, they'll call out 300A, but these are not imposed upon all the Shuttle systems so as I commented before in my looking at these things I've looked at it at a point of view, can we achieve this or is there a reasonable chance of achieving these more stringent requirements with the current design and I say right now it looks like it's certainly feasible if you are willing to put the extra effort into it.

D. Smith (HAC) - I am concerned about the contamination going the other way. I am making Shuttle compatibility studies on spacecraft that have already been designed and, in some cases, may be even partially built. Now they do not meet the requirements of SP-R-0022 for outgassing, they will not meet level 300 and they will not meet level A for NVR. Now where are we? Can I put my spacecraft into your Shuttle?

L. Leger (NASA/JSC) - First of all, there is only one illustrated requirement basically imposed upon payloads; it's not a rigorous imposition, it's the VCM requirement, and again, as I mentioned in my little brief discussion here, try to incorporate that into your thermal vacuum acceptance program for those spacecraft. I think it is very simple to sit down and say okay. I've exposed my spacecraft to a seven-day thermal vacuum exposure and be able to show that you're way below the VCM requirements and indeed probably eliminate your . . . . . .

D. Smith (HAC) - No way. There are many components on the spacecraft that couldn't possibly expose to that kind of a bakeout cycle.

L. Leger (NASA/JSC) - Well, in your thermal vacuum acceptance for the satellite, do you do thermal vacuum acceptance to the satellite?

D. Smith (HAC) - Yes.

L. Leger (NASA/JSC) - Then in what particular step--you expose it to vacuum--right?

D. Smith (HAC) - We expose it to hard vacuum.

L. Leger (NASA/JSC) - You expose it to sun temperature--right?

D. Smith (HAC) - The temperatures are very benign, most surfaces probably wouldn't go above ambient.

L. Leger (NASA/JSC) - What temperature does your system operate at - ambient--right?

D. Smith (HAC) - It operates at ambient.

L. Leger (NASA/JSC) - Well, then good--you have done a good vacuum bakeout.

D. Smith (HAC) - The requirements for outgassing are at a much higher temperature.

L. Leger (NASA/JSC) - Like I say, I think you can easily develop --there is a first screening requirement in that it's a standard procedure, but logic still prevails. You can still go one step beyond that and say; look, I do a thermal vacuum acceptance at 25°C in hard vacuum, my spacecraft does not see any more than that during Shuttle launch, my spacecraft is acceptable and there won't be any problem--right?

G. Borson (Aerospace Corporation) - Other people may not want to fly with you.

A. McClure (BAC) - For the IUS in the Orbiter bay it is still a valid requirement and that would assume that most of the spacecraft flying with the IUS would also have to meet that same level. Are you going to be able to maintain that level--300 in the Orbiter bay, Russ?

R. Rhodes (NASA/KSC) - The simplest way to answer that question is yes. If that is necessary, the answer is yes. I guess, if I wasn't aware that it is in fact documented, we have to meet level 300A for all missions that fly with IUS. If that is the case, we will look at what that would mean to us based on the mission models we know today. If that did not turn out to be a tremendous cost we will probably get back and talk to people about it. Is that really required? Because, let's face it, this program is a cost effective approach to working in space. That's number one priority. And if in fact we can meet the 300A without any big imposition, maybe it's a little more time consuming, but on the front end of the program when we are flying the IUS, that may not be a big problem to us. So the answer is yes - maybe.

G. Borson (Aerospace Corporation) - I would like to comment on that. I may be sticking my neck out but I suspect that the IUS as a general purpose vehicle will meet the requirements that will be generated by the specific payload and what it means in the current spec that they're asking for the capability of meeting that type of cleanliness. And it may be that all payloads are not going to ask for that, and it would not be cost effective to have to go through stringent cleaning for every mission whether they want it or not.

A. McClure (BAC) - I would like to see those modifications.

L. Leger (NASA/JSC) - It is interesting; they ask what actual design change does that require when imposed on the vehicle. Probably doesn't mean one iota as far as what the hardware does.

E. Borson (Aerospace Corporation) - I think you are right. The cost really comes in during the ground operations.

H. Peohlmann (Ball Brothers) - I guess Lubert has brought up a question in my mind in answer to Don's question about meeting SP-R-0022. I think what you said is the requirement currently on payload--is that right?

L. Leger (NASA/JSC) - With tongue in cheek, I think that is correct.

H. Poehlmann (Ball Brothers) - And then you implied, I thought, that as long as he wasn't going to operate at a temperature above ambient and obviously could therefore meet the tenth of a percent VCM, he would be safe which then seems to throw out the whole idea of testing at 125 for all of the materials that we have been doing for all this time. Obviously, a great many of the materials that we are using are only used at ambient temperature. The reason that we tested at 125 is to accelerate the outgassing, etc., and to get the VCM in a short period of time. If you are now saying that as long as we don't operate above 25C, we are home free if the materials don't produce a VCM greater than a tenth of a percent that seems to fly in the face of past testing and also in the face of what I would have assumed is the philosophy behind SP-R-0022.

L. Leger (NASA/JSC) - Certainly I did not mean that we can draw back to 25°C on the standard evaluation. The SP-R-0022, the micro VCM, whatever you want to refer to, is a good standard screening technique. But it does not take into account previous vacuum exposure of the material. That is what I was pointing out, that previous vacuum exposure during thermal vacuum acceptance testing for hardware that goes through that is a very effective way of reducing the VCM, also from an economical standpoint, as well as a . . . . .

J. Dauphin (ESA/ESTEC) - I don't agree with that statement. I don't agree with that statement. It's just admitting the spreading of the VCM all over the spacecraft.

H. Poehlmann (Ball Brothers) - I don't think that at least from our experience you went through a hard vacuum at essentially ambient temperature that you would in any way get your VCM down to meet that tenth of a percent requirement if you ran the test subsequent to that. If you ran the test at 125.

L. Leger (NASA/JSC) - You've got to take one additional thing into account and that's the operational temperature. And SP-R-0022A has a qualification that if you cannot meet the VCM requirement and you can show that your used temperature is considerably lower than 125°C. Develop a special test and come up with a rationale.

H. Poehlmann (Ball Brothers) - You are going to real temperature, but then I have to go to real time for testing.

L. Leger (NASA/JSC) - Oh yes, most definitely. You have passed the screening step and you are now into the detail evaluation step.

H. Poehlmann (Ball Brothers) - If I can then run my spacecraft or my payload at its maximum temperature, whatever that may be for a real time--a period of time equal to what is going to see in space--and I don't unnecessarily crud things up, I can meet the requirement. Okay, I'll buy that.

E. Borson (Aerospace Corporation) - As Lubert says, that is a screening test and I think that various analytical techniques and measurements can be used to justify a particular system that may have some portion of the materials in it that do not meet the requirements.

L. Leger (NASA/JSC) - The requirements is not to meet the VCM, it's to have a successful spacecraft. So that is what I am saying; use all the data and vacuum exposure you have at hand and granted, for some spacecraft where you are conductance limited or for some reason of peculiar configuration, you just have to sweat it out.

J. Dauphin (ESA/ESTEC) - The advantage of the VCM test is not this one in fact. What you are saying is in fact what we are doing also for a lot a different spacecraft. We cannot claim that there are spacecraft that have flown only with material which pass the VCM test. It's not true. The problem is that we apply it exactly as submitted when the material, as such, does not pass a VCM test. We consider it as a waiver case. So you have to go deeper in the matter and normally it is more costly. So you cannot apply that without the material so the most cost effective approach is as much as possible pass the VCM for most of the material, and leave only those cases that you cannot solve, say for a technical reason, to be looked at deeper because it will cost money.

R. Flaaton (HAC) - The qualification test for the materials were designed for one thing and that was to screen them. It is not necessarily the case that because something meets the specification that you can use it in all applications. If you have something that is very sensitive to the outgassing product and you put it right by the source of the contaminant, you can wipe it out even though it can meet it with those specs.

J. Dauphin (ESA/ESTEC) - Yes, that is entirely true.

R. Flaaten (HAC) - It is just a screening thing and you got to still look at it and say how is it going to affect the payload. And, in fact, there are other data that should be available like; is that contaminant going to affect certain things like optics, mirrors, radiators, etc. It might be such that what the outgassing product, even though it's a condensable, might not hurt a lot of things, but there are other ones where it cannot tolerate it. Another comment I don't understand; if you are going to apply the same kind of nonvolatile residue to a whole spacecraft. Are you going to weigh the spacecraft and say I can't have any more than .01% of the total weight of the spacecraft--as a contaminant?

J. Dauphin (ESA/ESTEC) - No, but our approach on that is very simple. It's again the question of cost you know. It's evident that on some application you need a more complicated balance wave operation task, eventually spectrometer test of the contaminant--the way it absorbs. Eventually, irradiation of the contaminant, and so on. But these being extremely costly experiments, you can run them only for the material which are placed at very critical positions and on a few of them, by the way. So it is exactly that the VCM does not insure you that you will get good results. You have to pass this test first as a screening for general application in close to an optic or something like that you have necessary need to go to a modernization in some other kind of method. But say, to fix difference, we evaluate that the VCM test on the material could cost 200 accounting units when balance test cost 3000.

L. Leger (NASA/JSC) - You have to answer that question. Is .01 the weight of the spacecraft or the weight of the outgassing material acceptable for the spacecraft? That is precisely the question you have to answer for that specific mission. It involves looking at all the detail material, their outgassing characteristics, computing the load, transport mechanisms, and determining how much you are going to get to that sensor.

R. Flaaten (HAC) - Somebody made a statement, that the materials were not processed if they were qualified. In 8008, Mr. Parks and company, they have put down what the processing was to qualify it and, therefore, if you are going to use the material you have to at least go through the processing they have used or you should go through the processing they have used to establish those numbers. In other words, if Parks ran a test and he baked it for 96 hours at 250°F prior to running the test and the material qualified, that's the same way you have to use it in your application. If you are going to say I use a--and that's the same way with the silicone 560. It has to be baked to meet those qualifications and it just happens to be that the testing of the space simulation chamber might help it a little bit, but not necessarily with the environments we have, really to be that process. It has to be processed separately from the space simulation test.

L. Leger (NASA/JSC) - Not necessarily.

J. Dauphin (ESA/ESTEC) - My answer is yes on that.

L. Leger (NASA/JSC) - What we are faced with is a bunch of spacecraft that are built just like we pointed out earlier that have components on them that we can't change. You can't go back and say I am going to change that material and make it acceptable. What are you faced with? You have a spacecraft that you have to fly. It does not pass the one-tenth of a percent VCM, you have to fall back and say okay, what has that material seen. You have to compare the vacuum chamber exposure, pressure and temperature, the vacuum mass loss data at the same temperature and pressure, and on that base, make a logical decision as to whether it has seen a significant amount of vacuum degassing.

R. Kruger (NASA/GSFC) - I like Lubert's suggestion that if you put the thing through a vacuum test you have already done yourself a lot of good as far as that and you can easily see it when you run a spacecraft full all up spacecraft in the chamber and you pull it out for something or other and two weeks later you put it back in and the chamber takes about half the time to pump down. To borrow something Russ Crutcher mentioned, the cost effectiveness is starting to rear its head again and we are getting the cheapy payloads where the requirement is no testing and I'm a little afraid of that. And there is a large segment of the test population which says thermal vacuum testing is expensive, which is true, and don't do it unless you have an absolute need to do it. Now we may be talking about big spacecraft with no thermal vacuum testing going into the Shuttle. I guess I am just throwing that out as a caveat.

R. Scott (AESC) - I would like to make a comment about modeling. The last comment you made was that it's really upon the payload people to determine if their system is adequate, is going to fly and be free of contaminants. And that involves quite a number of things heard talked about here. Ground concerns, launch, Shuttle bay, IUS, FEX, if you are on that vehicle, and on-orbit concerns out of yourself, contamination, if you will.

I think the importance in accurate modeling is a key to this whole thing. That if we can really identify what the processes are, and how they apply to all these processes by good modeling, then we've got a leg up and we begin to stand where we are. And it's really a systems problem, you know, it's not a taking of individual materials and doing a viewfactor calculation and that saying so much goes to here. It's really doing a multiple reflection of that material to all the surfaces in the system from all of the emitters. Receivers can become emitters after they absorb contaminants from other pieces, and so the modeling must address the system. Now, one of the things that was presented here and I think was a fundamental breakthrough. Gene Zeiner gave a couple of papers on what we believe to be some very carefully done tests which indicates that there is a factor variously called sticking coefficient, condensation coefficient, or whatever, and Gene has found from his testing that the amount of material that comes in that's stuck, is a constant regardless of what it is. That's based on a very simple approach and it's based upon a limited number of tests. But that's a significant finding. And that sez, at least to the point, that what we see when we test materials is the difference between that constant sticking and the reemission that comes off. Reemission is a function of temperature so as you take the samples to a low temperature, you stop emitting. That's been coined to be--it has 100% sticking coefficient. If the sticking coefficient is really .9, then you really have an outgassing material that can condense--10% that are still floating around the system and being reflected around the system and can get to other surfaces. And I think we fool ourselves sometimes with the bulk approach and the bulk modeling technique where we don't separate the two processes of what's absorbed and what's reemitted, and I think that is something. I hope everyone here really looks at Gene's paper to agree or disagree that we really ought to look at that issue because that would imply even very cold payloads that the contaminants are still moving around and are not stuck and that has some big implications, I think.

J. Dauphin (ESA/ESTEC) - I think I would agree entirely with your approach. If you know, say the outgassing property, the transport property, and so on, and you have a good model, you can calculate everything, but that would cost. The cost of modeling, the cost of getting all the materials property, because this is lacking for the moment, and this is extremely expensive and a lot of spacecraft cannot afford that.

L. Leger (NASA/JSC) - Let me disagree a little bit. From the Shuttle standpoint, we have been doing a detailed analysis for an IUS and payload associated mission. And that is precisely what you get into. You have material coming out of the surface and is being transported to some other area by a multiple reflection. It bounces off the payload liner, in this case a teflon surface, but there is, how much sticks and how much is reemitted as a function of time. It really has to be looked at. If we do an equilibrium calculation because the bay's at high pressure and really doesn't come into play at this particular analysis, but in some it will. That where the QCM is a good representation of that side surface for those contaminants hit and will be reemitted and you have to look I think at this point, the QCM data and determine what your reemission characteristic is from your second map.

R. Scott (AESC) - These characteristics are the same as the other characteristics of the spacecraft or what you are looking at. In other words, the QCM has to have the same sort of absorption characteristics that the sensitive . . . . . .

L. Leger (NASA/JSC) - There is always some limitations. Of course, one thing you can do is coat the QCM with teflon--make your measurement.

J. Dauphin (ESA/ESTEC) - After the deposition of the first layer the materials deposit on itself.

E. Miller (NASA/JSC) - I would like to make a comment here in my simple way of looking at this. It appears we tend to oversimplify the problem of interrelationship of different--whereever you have confined payloads. Each payload user evaluates his payload, but when you bring the payloads together in a common bay, will it in fact produce the same results, or will you get some chemical interreaction. And change some of those factors that you now are using in your model.

L. Leger (NASA/JSC) - Well, you have to use the configurations for that particular mission. You have to look at it on a mission to mission basis--that's the only way. And I think that at this point in time it's not just the payload problem hopefully at least I would like to think that we are working at least this IUS particular payload to try to define the level of the contamination and from that level determine whether or not protective shrouds are needed. I think we will be in that mode for sometime and to the Shuttle operational era until we begin to understand well the characteristics of the----I think we will be able to generate a standard set of rules of some kind into the Shuttle operation.

W. Moss (TRW) - I would like to get back to particulate matter for just a second and toss out an idea here which I think has probably occurred to lots of people here. I have come to feel that these lines in 1246 level 300, level 500, have very little meaning. I know Gene and I have had a lot of experience on P74 and we know that real contamination lines do not follow these lines. It always drops off into smaller particles and we both know that if you accept percent obscuration, the equivalent percent obscuration to level 300 for instance, it's easy to achieve that on a spacecraft. But actual level 300 cannot be achieved because I don't care how well you achieve--clean something--you are always going to have particle or two in every square foot that 500 microns, 750 microns--something like that--and 1246 implies the size of the largest particle. And in mecahnical systems perhaps, whether there is interference, or something like that, perhaps it is important, but in the case of spacecraft, obscuration most of the time is the important thing so I would like to suggest that we start thinking in terms of specifying particulate contamination levels on the basis of percent obscuration and I would just like to toss that out for people to consider.

<u>H. Scott (AEDC/DOTR)</u> - At the risk of being in the minority, let me remind everyone that at the joint Air Force/NASA conference I would like to turn the attention a little bit back to some of the plume questions. Let me respond to Carl Maag's question earlier about the possibility of solid rocket motor contamination measurements. As you know, I think everyone agrees that a dedicated solid rocket motor measurement contamination study is needed very badly. And it has been considered, but the comment that I would like to make is simply that if and when it does come we are going to have to be sure to allow some time for developing decent two-face flow diagnostics. We have the particles and the gasses both to consider and the properties are very difficult to separate when one is making insitu measures on them. Secondly, I would like to comment on something Lubert said--this is only a comment--that it was very difficult to test something like the 25-lb and 900-lb bi-prop motors in ground facilities. Having anticipated some of these things, we have considered the feasibility of a large bi-prop motor being fired in the Mark 1 chamber at AEDC and it looks quite reasonable to say that we can fire--we can make a contamination measurement in the back flow region nothing like we have done on the 5-lb motor in the case of a motor of about 100-lb thrust. Certainly, the 25-lb, maybe 200- or 300-lb by adding some cryo pumps to pump

hydrogen and the cost would be in the neighborhood of $300,000 to $400,000, not 4 million dollars, which I have heard for PCEM system. And, finally, then I would like to reiterate something that I mentioned earlier yesterday because I don't feel like I got a satisfactory response at the time. Sort of let me give you what I consider to be a logical sequence and somebody tell me where the flaw is in my logic. Everyone knows that DOD is principally interested in the STS system (Space Transportation System) for putting various sensor systems into orbit. Many of these we know will be cryogenically cooled to very low temperatures; many of you are aware of what the temperatures are. If I remember correctly, there is something like 32- to 25-lb bi-prop motors on the Shuttle. Is that right? How Many?

L. Leger (NASA/JSC) - 38.

H. Scott (AEDC/DOIR) - We heard yesterday that mean free path would be longer than the Shuttle itself, it was described rather graphically as a cloud around the Shuttle, possibly in terms of exhaust products. We know that major bi-propellant exhaust products, and I am not just talking about minor constituants now, I'm talking about the major products like water vapor, CO_2, nitrogen, and hydrogen. Let me eliminate hydrogen since it is not going to be a problem. That these condense at temperatures like in the case of water vapor 160^oK, CO_2 at about 85^oK, and nitrogen about 28, and we have shown in the case of the small rocket motor that these get into the backflow region of the motor. So there are certainly going to be problems in my view of these major exhaust products from the bi-prop motors on the Shuttle contaminating low temperature sensor systems that I am sure DOD is going to be very concerned about. So, I have not been involved in interface meetings between NASA, and primarily SAMSO in this sort of question, but has anything been resolved--is there some flaw in my logic?

L. Leger (NASA/JSC) - No, there is no flaw to your logic. Those are major sources on-board the vehicle. I guess there are two things that might be worth considering. Shuttle is a large vehicle and the engines are located, generally speaking, at one end and the other so that there are fairly far distances away from surfaces in general for the direct flow standpoint. In almost all cases, they are shadowed completely from direct line-of-sight to the payload so the back field flow is transport from the engine to the spacecraft center--I think it's going to be one that will be a minimal problem. From the standpoint of recondensation, however, while the telescope is operating at cool temperature, it's a real problem. As far as measurements are concerned, we can operate the Orbiter in certain attitude modes where firings can be minimized considerably. For example, there have been some studies that show you can fly for as much as an hour--hour and a half with deviations, say from a nose down to a tail down attitude of 10^{o} along say all the major axes. If you have an attitude pointing system for spacecraft that may be acceptable and you may be able to indeed fly a long period of time making measurements without requiring an engine. If you don't indeed have a good attitude pointing system, then you are faced with every hour and a half of having to reorient the vehicle and indeed having a real potential for depositing the engine effluents onto the surfaces. For those particular cases you have to be concerned first thing about the attitude of the vehicle if the sensor is flying in the wake of the Orbiter, for example, then scattering of the plume back into the sensor is minimized and might indeed be acceptable for a reasonable wide payload as long as you are not trying to operate it for a very long period of time. So attitude is the first thing you have to consider. If you indeed do not have a trade or--you can't exercise if you will that flexibility, then you have to consider items such as closing the telescope for a period of time at your blind end. So there is a whole series of steps that you have to go through to make sure that you have exercised all your options before you go to the closing of the telescope during firing of the engines. In addition, most cryo telescopes are considering purging the helium through the tube and, therefore, preventing a lot of intrusion of the water vaporing inside the telescope itself. And I think some of the people from Martin, and certainly people from Ames, have been considering utilizing that protective means for the telescopes.

E. Borson (Aerospace Corporation) - Also, I guess, keep in mind most free fliers or payloads that are deployed from the Shuttle have cool system--will probably either have a cover to protect that system or may not be cooled down until after deployment. You have to look at the mode of operation.

R. Hoffman (SAI) - A couple of comments about the potential differences between solid rocket motors and liquid rocket motors I think that's been very briefly discussed here and, while there are some differences, there are also many similarities and I personally do not see a great deal of difference in many of the modeling mechanisms between liquid rocket motor contamination and solid rocket motor contamination. I will give you some examples. The present version of CONTAM, which was developed for liquid rocket motors, has an abrasion subroutine as part of the surface effect mechanisms and that was put in for unburnt fuel and oxidizing droplets. Now I'll not say that the wear rate equations that go along with that will hold exactly for aluminum particles, but some upgrade of that may well be appropriate. The two-phase flow program within content, which is the subroutine called MULTRAN, actually stemmed from a solid motor transport program and modifications had to be made to that to make it into a liquid rocket mechanism. With regard to backflow with liquid rocket motors, which we have done a little more accurately than is presently in CONTAM. You can get expansion close to 150 to 160°, at least, and then taking into account what might go beyond that boundary I think you can account for it that way. And I think the same mechanisms, therefore, hold for solid rocket motors. I can summarize it by saying it's not clear that we need to go into very exotic mechanisms for backflow of solid rocket motors any more so than we have before with liquid motors.

E. Borson (Aerospace Corporation) - I will just make one comment on that. We know less about what is coming out of a solid motor than what we do about what is coming out of a liquid motor. I think that's a big difference--it's hard to model something that you don't know what it is.

C. Maag (AESC) - One quicky, directed to Ron. How do you get dribble out of solid rocket motor?

J. Youngblood (NASA/LRC) - As a result of the recent demise of the Soviet satellite in the wilds of Canada, the Skylab spacecraft is very much in the news and my information is that there will most likely be a rendezvous, perhaps as early as 1979, with that spacecraft and the decision will have to be made whether or not to deboost; that is, cause the spacecraft to entry in a control way, or else to reboost it, kick it in a higher orbit so that we can save if for awhile. My observation is that this piece of hardware may be a national treasure in terms of hardware that has been exposed in space for a long period of time, and if it is indeed worth something to look at that material, I would ask the panel, and even members of the audience, if this rendezvous takes place what kind of monitoring should be done during that rendezvous, what kind of measurement should me made and to go one step further, what kinds of samples should be brought back to earth for analysis. It is a big question, but I think it is an idea that ought to be considered.

E. Borson (Aerospace corporation) - Unfortunately, we don't have time to talk about it right now. I guess Jim Jemiola would like to make a few remarks.

J. Jemiola (AFML/MBE) - I guess being conference co-chairman always means being able to have the last word. I would like to make a couple of announcements. First of all, I have not received a couple of copies of a number of papers; one was Session 1, Paper 4, Applications of TGA; one was Section 5, Paper 2, Ron Dawbarn's paper. I understand why he couldn't have them, but I would like to get them as soon as possible. Session 7, Paper 1, Gene Borson's paper (G. Borson/Aerospace Corporation)--did you get a copy? I would like to ask any of the panel members if they have a hard copy of their paper would they try to pass it to Lubert Leger since he is going to try to have these tapes transcribed, and I am sure that it would help him. I want to thank you all for attending this conference and I want to say that your attendance--I really mean this--helped make this a success and I want to thank you all for coming and I hope you all have a good trip home and like I have said a number of times before the-buses are waiting down stairs.

☆U.S.Government Printing Office: 1979 — 657-002/598